CONTROL OF POWER ELECTRONIC CONVERTERS AND SYSTEMS

VOLUME 3

EDITED BY
FREDE BLAABJERG

Control of Power Electronic Converters and Systems

Volume 3

This page intentionally left blank

This book belongs to Kitab Liaison (ocd1996@gmail.com)

Copyright Elsevier 2023

Control of Power Electronic Converters and Systems

Volume 3

Edited by

Frede Blaabjerg

ELSEVIER

ACADEMIC PRESS

An imprint of Elsevier

This book belongs to Kitab Liaison (ocd1996@gmail.com)

Copyright Elsevier 2023

Academic Press is an imprint of Elsevier
125 London Wall, London EC2Y 5AS, United Kingdom
525 B Street, Suite 1650, San Diego, CA 92101, United States
50 Hampshire Street, 5th Floor, Cambridge, MA 02139, United States
The Boulevard, Langford Lane, Kidlington, Oxford OX5 1GB, United Kingdom

Copyright © 2021 Elsevier Ltd. All rights reserved

No part of this publication may be reproduced or transmitted in any form or by any means, electronic or mechanical, including photocopying, recording, or any information storage and retrieval system, without permission in writing from the publisher. Details on how to seek permission, further information about the Publisher's permissions policies and our arrangements with organizations such as the Copyright Clearance Center and the Copyright Licensing Agency, can be found at our website: www.elsevier.com/permissions.

This book and the individual contributions contained in it are protected under copyright by the Publisher (other than as may be noted herein).

Notices

Knowledge and best practice in this field are constantly changing. As new research and experience broaden our understanding, changes in research methods, professional practices, or medical treatment may become necessary.

Practitioners and researchers must always rely on their own experience and knowledge in evaluating and using any information, methods, compounds, or experiments described herein. In using such information or methods they should be mindful of their own safety and the safety of others, including parties for whom they have a professional responsibility.

To the fullest extent of the law, neither the Publisher nor the authors, contributors, or editors, assume any liability for any injury and/or damage to persons or property as a matter of products liability, negligence or otherwise, or from any use or operation of any methods, products, instructions, or ideas contained in the material herein.

Library of Congress Cataloging-in-Publication Data
A catalog record for this book is available from the Library of Congress

British Library Cataloguing-in-Publication Data
A catalogue record for this book is available from the British Library

ISBN: 978-0-12-819432-4

For information on all Academic Press publications visit our website at https://www.elsevier.com/books-and-journals

Publisher: Brian Romer
Acquisitions Editor: Lisa Reading
Editorial Project Manager: Joshua Mearns
Production Project Manager: Sojan P. Pazhayattil
Cover Designer: Greg Harris

Typeset by TNQ Technologies

ELSEVIER Book Aid International Working together to grow libraries in developing countries
www.elsevier.com • www.bookaid.org

This book belongs to Kitab Liaison (ocd1996@gmail.com) Copyright Elsevier 2023

Contents

Contributors xv
Preface xvii

1. **Advanced control of power electronic systems—an overview of methods**
Chao Wu and Frede Blaabjerg

1.1 Introduction 1
1.2 Linear controller implementation and analysis 5
1.2.1 Implement PI controller 5
1.2.2 Implement PR controller 6
1.2.3 Implement repetitive controller 7
1.2.4 Pole placement control 9
1.2.5 Linear quadratic regulator 9
1.3 Nonlinear controller implementation and analysis 10
1.3.1 Hysteresis control 11
1.3.2 Lookup table—based direct power control 11
1.3.3 Model predictive control 14
1.3.4 Backstepping control 15
1.3.5 Sliding mode control 19
1.3.6 Feedback linearization 23
1.3.7 Passivity control 23
1.3.8 Adaptive control 24
1.3.9 H_∞ control 25
1.3.10 Artificial intelligence 26
1.4 Summary 28
References 28

2. **Robust design and passivity control methods**
Yonghao Gui, Jianzhe Liu, Jan Dimon Bendtsen and Jakob Stoustrup

2.1 Introduction 35
2.2 State space model of power electronic systems 36
2.2.1 Introduction 37
2.2.2 Grid-connected voltage source inverter 38
2.2.3 An example of a VSC (STATCOM) 40

This book belongs to Kitab Liaison (ocd1996@gmail.com) Copyright Elsevier 2023

2.3 Robust controller design 42
2.3.1 Voltage-modulated direct power control 43
2.3.2 Tracking controller 44
2.3.3 Robust control design 46
2.3.4 Simulation results 47
2.4 Robust small-signal stabilization control design 49
2.4.1 Introduction 49
2.4.2 Lur'e type model 51
2.4.3 Robust small-signal stability analysis problem 57
2.4.4 Robust stability analysis method 58
2.4.5 Robust stabilization control design 58
2.5 Passivity-based control design 61
2.5.1 Introduction 62
2.5.2 Port-controlled Hamiltonian system 62
2.5.3 Passivity-based control design in a microgrid 63
2.5.4 Passivity control design in STATCOM 67
2.6 Conclusions and future prospective 71
Acknowledgment 73
References 73

3. Sliding mode controllers in power electronic systems

Hosein Gholami-Khesht, Pooya Davari and Frede Blaabjerg

3.1 Introduction 77
3.2 System dynamics of a voltage source inverter 78
3.3 Introduction to sliding mode control 79
3.3.1 Reachability condition in the sliding mode control 81
3.3.2 Control input calculation 82
3.4 Classical sliding mode control 82
3.5 Boundary-layer sliding mode control 85
3.5.1 Adaptive boundary-layer sliding mode control 85
3.6 Adaptive sliding mode control 85
3.7 Integral sliding mode control 87
3.8 Terminal sliding mode control 87
3.9 Second-order sliding mode control 89
3.9.1 Twisting SMC 89
3.9.2 Super-twisting 90
3.9.3 Adaptive super-twisting 91
3.10 Comparison of different SMCs 91
3.11 Experimental results 93
3.11.1 Steady-state performance 94
3.11.2 Dynamic performance 96
3.12 Conclusions 96
References 98

This book belongs to Kitab Liaison (ocd1996@gmail.com) Copyright Elsevier 2023

4. Model predictive control of power converters, motor drives, and microgrids

Zhenbin Zhang, Tomislav Dragicevic, Yu Li, Yongdu Wang, Changming Zheng, Minrui Leng and Jose Rodriguez

4.1 Introduction on MPC 101
4.2 MPC for permanent-magnet synchronous motor drives 102
4.2.1 Model of PMSM 106
4.2.2 FCS-MPC for PMSM drives 108
4.2.3 Performance evaluations of MPC with simulations 109
4.2.4 Summary 109
4.3 MPC for microgrids 110
4.3.1 Dynamics and predictive model of VSC-based MG 111
4.3.2 MPC for robust and fast operation of an islanded AC MG 112
4.3.3 Dynamic stabilization of a DC MG using MPC 113
4.3.4 Performance evaluation with experimental results 113
4.3.5 Summary 115
4.4 MPC for renewable energy applications (PMSG wind turbine) 115
4.4.1 Modeling of PMSG wind turbine system with back-to-back power converter 116
4.4.2 Direct model predictive current control 118
4.4.3 FCS-MPC for three-level PMSG systems 119
4.5 Conclusions and future trends 121
References 122

5. Adaptive control in power electronic systems

Hosein Gholami-Khesht, Pooya Davari and Frede Blaabjerg

5.1 Introduction 125
5.2 System dynamics on a UPS system 127
5.3 System identification 128
5.3.1 Parameters identification 129
5.3.2 State identification 130
5.4 Indirect adaptive predictive control 135
5.4.1 Experimental results 136
5.5 Model reference direct adaptive control of UPS 136
5.5.1 The outer voltage control loop 137
5.5.2 The inner current control loop 142
5.5.3 Experimental results 142
5.6 Conclusion 145
References 145

6. Machine learning technique for low-frequency modulation techniques in power converters

Amirhossein Moeini, Morteza Dabbaghjamanesh, Tomislav Dragičević, Jonathan W. Kimball and Jie Zhang

This book belongs to Kitab Liaison (ocd1996@gmail.com) Copyright Elsevier 2023

6.1 Introduction 149
6.2 Cascaded H-bridge active power filter configuration 151
6.3 ANN for the asymmetric selective harmonic current mitigation-PWM 152
6.4 The proposed technique simulation and experimental results 157
6.4.1 Simulation results 157
6.4.2 Experimental results 162
6.5 Conclusion 164
References 165

7. Overview of stability analysis methods in power electronics

Qianwen Xu

7.1 Introduction 169
7.2 Small-signal stability analysis methods 171
7.2.1 Modeling of power converter 172
7.2.2 Eigenvalue method 174
7.2.3 Impedance-based method 177
7.2.4 Comparison of methods 179
7.3 Large-signal stability analysis methods 180
7.3.1 Time-domain simulations 180
7.3.2 Lyapunov-based analytical methods 180
7.4 Case studies with practical examples 183
7.4.1 Small-signal stability analysis 183
7.4.2 Large-signal stability analysis on a power electronic system 192
7.5 Summary 195
References 195

8. Cyber security in power electronic systems

Subham Sahoo

8.1 Introduction 199
8.2 Cyber physical architecture of power electronic converters 200
8.2.1 Physical stage 201
8.2.2 Cyber stage 202
8.3 Vulnerability analysis of cyber attacks on control of VSCs 203
8.3.1 Cyber security 203
8.3.2 Vulnerability assessment 204
8.4 Cyber attack detection and mitigation mechanisms in power electronic systems 205
8.4.1 Detection 205
8.4.2 Mitigation 210
8.5 Test cases 212
8.5.1 Test case I 212
8.5.2 Test case II 213

This book belongs to Kitab Liaison (ocd1996@gmail.com) Copyright Elsevier 2023

8.6 Conclusions and future challenges 217
References 217

9. Advanced modeling and control of voltage source converters with LCL filters

Bochen Liu, Dao Zhou and Frede Blaabjerg

9.1 Introduction 221
9.2 Modeling of the VSCs with *LCL* filters 222
9.2.1 Modeling methods in balanced three-phase systems 222
9.2.2 Modeling methods in unbalanced three-phase systems 226
9.2.3 Simulation examples 236
9.3 Alternative current control of the VSCs with LCL filters 238
9.3.1 Control in synchronous reference (*dq*) frame 239
9.3.2 Resonance damping technique 242
9.3.3 Control under unbalanced grid voltages 251
9.4 Impedance-based stability analysis under weak grid conditions 256
9.4.1 System control of the *LCL*-filtered VSCs in $\alpha\beta$ frame and *dq* frame 258
9.4.2 Impedance-based stability analysis 262
References 266

10. Phase-locked loops and their design

Wenzhao Liu and Frede Blaabjerg

10.1 Introduction 269
10.2 PLL's control and design 270
10.3 Three-phase PLLs 271
10.3.1 Conventional synchronous reference frame PLL 271
10.3.2 Moving average filter—based PLLs 277
10.3.3 Notch filter—based PLLs 278
10.3.4 Sinusoidal signal integrator—based PLLs 278
10.3.5 Second-order generalized integrator—based PLLs 279
10.3.6 Complex coefficient filter—based PLLs 280
10.3.7 Delayed signal cancellation—based PLLs 282
10.3.8 Multiple SRF filter—based PLLs 283
10.3.9 Other three-phase PLLs 284
10.3.10 Performance comparison and recommendation 285
10.4 Single-phase PLLs 287
10.4.1 Standard P-PLLs 287
10.4.2 Low pass filter—based P-PLLs 288
10.4.3 Moving average filter—based P-PLLs 288
10.4.4 Notch filter—based P-PLLs 289
10.4.5 Double-frequency and amplitude compensation—based P-PLLs 290
10.4.6 Modified mixer PD-Based P-PLLs 291
10.4.7 Transfer delayed—based PLLs 291

This book belongs to Kitab Liaison (ocd1996@gmail.com) Copyright Elsevier 2023

10.4.8 Inverse park transformation—based PLLs 292
10.4.9 Generalized integrator—based PLLs 293
10.4.10 Synthesis circuit PLLs 295
10.4.11 Performance comparison and recommendation 296
10.5 Summary 298
References 298

11. Stability and robustness improvement of power converters

Xiongfei Wang, Yicheng Liao and Zichao Zhou

11.1 Introduction 303
11.2 Stability and robustness improvement of current control 304
11.2.1 Small-signal modeling 305
11.2.2 Passivity-based stability analysis 309
11.2.3 Robustness enhancement 313
11.3 Stability and robustness improvement of outer-loop control 319
11.3.1 Small-signal modeling 319
11.3.2 MIMO-based stability analysis 326
11.3.3 Robustness enhancement 332
References 336

12. High switching frequency three-phase current-source converters and their control

Dapeng Lu and Frede Blaabjerg

12.1 Challenges of high switching frequency CSCs control 339
12.1.1 Multiple timescale dynamics of high switching frequency CSCs 339
12.1.2 Control methods of high switching frequency CSCs 340
12.2 Stability analysis of the single-loop DC-link current control 342
12.2.1 Small-signal modeling 342
12.2.2 Stable region of single-loop DC-link current control 343
12.2.3 Experimental validation 346
12.3 Active damping methods for high switching frequency CSCs 348
12.3.1 Virtual impedance analysis 350
12.3.2 Experimental validation of active damping 357
12.4 Summary 364
References 365

13. High-power current source converters

Li Ding and Yunwei Li

13.1 Introduction 367
13.2 Current source converters and applications 368

This book belongs to Kitab Liaison (ocd1996@gmail.com) Copyright Elsevier 2023

13.2.1 Thyristor-based technology 368
13.2.2 PWM CSC-based medium-voltage drives 370
13.2.3 More potential application 371
13.3 Parallel CSC system and modulation strategies 373
13.3.1 Parallel CSC topology 374
13.3.2 CSC modulation strategies 375
13.4 Parallel CSC and circuit analysis 381
13.4.1 CM loop circuit of parallel CSC 381
13.4.2 DC-link circuit of parallel CSC 385
13.5 DC current balance and CMV reduction methods 387
13.5.1 SVM-based methods 387
13.5.2 Carrier-shifted SPWM-based methods 394
13.5.3 Case study results 397
13.6 Conclusions 400
References 401

14. Parallel operation of power converters and their filters

Ghanshyamsinh Gohil

14.1 Introduction 403
14.2 Circulating current modeling 405
14.2.1 Parallel converters with a common DC bus 405
14.2.2 Parallel converters with separate DC bus 409
14.3 Circulating current control 410
14.3.1 Current sharing schemes 411
14.3.2 Droop control scheme 412
14.3.3 Zero vector dwell time control 415
14.4 Harmonic performance improvement through interleaved operation 419
14.4.1 Modulation of parallel interleaved converters 419
14.4.2 Symmetrically interleaved converters 419
14.4.3 Harmonic performance evaluation 425
14.4.4 Nearest three vector modulation 428
14.5 Circulating current suppression in parallel interleaved converters 430
14.5.1 Galvanic isolation 432
14.5.2 Coupled inductor 433
14.5.3 Common-mode inductor 437
14.5.4 Integrated inductor 440
14.6 Summary 442
References 444

15. Advanced power control of photovoltaic systems

Ariya Sangwongwanich, Jinkui He and Yiwei Pan

15.1 Introduction 447
15.2 Overview of PV inverter control 448

This book belongs to Kitab Liaison (ocd1996@gmail.com) Copyright Elsevier 2023

15.2.1 Control structure 448
15.2.2 MPPT algorithm 450
15.3 Requirement of advanced control functionality 453
15.3.1 Grid code 453
15.3.2 Active power control requirement 454
15.4 Constant power generation control strategy 455
15.4.1 Direct power control (P-CPG) 457
15.4.2 Current-limiting control (I-CPG) 458
15.4.3 Perturb and observe—based control (P&O-CPG) 460
15.5 Benchmarking of constant power generation control strategy 463
15.5.1 Dynamic responses 463
15.5.2 Steady-state responses 466
15.5.3 Tracking error 466
15.5.4 Stability 467
15.5.5 Complexity 467
15.6 Summary 468
References 468

16. Low voltage ride-through operation of single-phase PV systems

Zhongting Tang and Yongheng Yang

16.1 Introduction 471
16.2 Low voltage ride-through operations 475
16.2.1 LVRT control using the single-phase PQ theory 477
16.2.2 LVRT control based on the power-voltage curve 482
16.3 Reactive power injection strategies under LVRT 488
16.3.1 Constant average active power control strategy (*Const.-P*) 491
16.3.2 Constant active current control strategy (*Const.-*I_d) 492
16.3.3 Constant peak current control (*Const.-*I_{gmax}) 494
16.4 Summary 495
References 496

17. Grid-following and grid-forming PV and wind turbines

P. Rodriguez and N.B. Lai

17.1 Introduction 499
17.2 PV and wind turbine systems 500
17.2.1 PV structures 500
17.2.2 Grid converter for wind turbine systems 501
17.3 Grid-following power converters 502
17.3.1 Definition 502
17.3.2 Synchronization strategies 503
17.3.3 Current controllers 506

This book belongs to Kitab Liaison (ocd1996@gmail.com) Copyright Elsevier 2023

17.4 Grid-forming power converters 508
17.4.1 Definition 508
17.4.2 Control schemes for grid-forming power converter 509
17.4.3 Droop control in grid-forming power converters 510
17.4.4 The synchronous power controller 516
17.5 Conclusions 519
References 519

18. Virtual inertia operation of renewables
Rasool Heydari, Mehdi Savaghebi and Frede Blaabjerg

18.1 Introduction 523
18.2 Evolution of green energy transition 525
18.2.1 Low-inertia grid challenges 525
18.2.2 Control of power converter—interfaced renewables 527
18.3 Virtual inertia-based control 529
18.3.1 Virtual synchronous machine 530
18.3.2 Concepts and fundamentals 531
18.4 VSM implementation 532
18.4.1 NSG penetration level 533
18.4.2 VSM performance 534
18.4.3 Fault right through capability 534
18.5 Summary and future trend 536
References 538

19. Virtual inertia emulating in power electronic—based power systems
Yousef Khayat, Mobin Naderi, Hassan Bevrani and Frede Blaabjerg

19.1 Introduction 541
19.2 Inertia concept 542
19.3 Inertia challenges of power electronic—based power systems 547
19.4 Adaptive inertia for grid-connected VSGs 549
19.4.1 VSG principle 550
19.4.2 Adaptive inertia 551
19.5 Simulation and experimental results 553
19.5.1 Simulation results 553
19.5.2 Experimental results 555
19.6 Summary 557
References 558
Further reading 560

20. Abnormal operation of wind turbine systems
Dao Zhou and Mads Graungaard Taul

20.1 Introduction 561
20.1.1 Classification of grid faults 561

This book belongs to Kitab Liaison (ocd1996@gmail.com) Copyright Elsevier 2023

20.1.2 Grid code requirements on low-voltage ride-through 562
20.1.3 Fundamental wind turbine configurations 566
20.2 Control of type III wind turbine during grid faults 568
20.2.1 Existing challenges during grid faults 568
20.2.2 Control strategies during symmetrical grid faults 573
20.2.3 Control strategies during asymmetrical grid faults 578
20.3 Control of type IV wind turbine during grid faults 582
20.3.1 Modeling and control of grid-side converter 583
20.3.2 Symmetrical grid fault control 587
20.3.3 Asymmetrical grid fault control 593
20.4 Summary 604
References 604

21. Wind farm control and optimization

Weihao Hu, Qi Huang, Xiawei Wu, Jian Li and Zhenyuan Zhang

21.1 Introduction 609
21.2 Wind farm active dispatch 611
21.2.1 Wake effect 611
21.2.2 Single MPPT and global MPPT 612
21.2.3 Noise impact reduction 614
21.3 Wind farm reactive dispatch 618
21.3.1 Regular method 618
21.3.2 Loss minimization 622
21.3.3 Levelized production cost minimization 625
21.4 Wind farm layout optimization 636
21.4.1 Topography and wind direction impact for layout 636
21.4.2 Layout optimization for minimum levelized production cost 641
21.5 Conclusion 643
References 643

22. Power converters and control of LEDs

Xiaohui Qu and Huai Wang

22.1 Introduction 645
22.2 Characteristics of LEDs and drivers 650
22.2.1 Physical principle of LEDs 650
22.2.2 Optoelectrical properties of LEDs 651
22.2.3 Characteristics of drivers for LEDs 653
22.3 Color control with a power converter 654
22.4 Efficiency and lifetime improvement 658
22.5 Current sharing schemes 669
22.5.1 Passive current sharing schemes 669
22.5.2 Active current sharing schemes 673
22.6 Reliability assessment 678
References 685

Index 689

This book belongs to Kitab Liaison (ocd1996@gmail.com) Copyright Elsevier 2023

Contributors

Jan Dimon Bendtsen, Aalborg University, Aalborg, Denmark

Hassan Bevrani, University of Kurdistan, Sanandaj, Kurdistan, Iran

Frede Blaabjerg, Department of Energy Technology, Aalborg University, Aalborg, Denmark

Morteza Dabbaghjamanesh, Department of Mechanical Engineering, The University of Texas at Dallas, Richardson, TX, United States

Pooya Davari, Aalborg University, Aalborg, Denmark

Li Ding, Department of Electrical and Computer Engineering, University of Alberta, Edmonton, AB, Canada

Tomislav Dragičević, Department of Electrical Engineering, Technical University of Denmark, Lyngby, Denmark

Hosein Gholami-Khesht, Aalborg University, Aalborg, Denmark

Ghanshyamsinh Gohil, University of Texas at Dallas, Richardson, TX, United States

Yonghao Gui, Aalborg University, Aalborg, Denmark

Jinkui He, Aalborg University, Aalborg, Denmark

Rasool Heydari, University of Southern Denmark, Odense, Denmark

Weihao Hu, University of Electronic Science and Technology of China, Chengdu, Sichuan, China

Qi Huang, University of Electronic Science and Technology of China, Chengdu, Sichuan, China

Yousef Khayat, University of Kurdistan, Sanandaj, Kurdistan, Iran

Jonathan W. Kimball, Electrical and Computer Engineering Department, Missouri University of Science and Technology, Rolla, MO, United States

N.B. Lai, Luxembourg Institute of Science & Technology, Esch-Sur-Alzette, Luxembourg

Minrui Leng, School of Electrical Engineering, Southwest Jiaotong University, Chengdu, China

Yunwei Li, Department of Electrical and Computer Engineering, University of Alberta, Edmonton, AB, Canada

Yu Li, School of Electrical Engineering, Shandong University, Jinan, China

Jian Li, University of Electronic Science and Technology of China, Chengdu, Sichuan, China

This book belongs to Kitab Liaison (ocd1996@gmail.com)

Copyright Elsevier 2023

Yicheng Liao, Aalborg University, Aalborg, Denmark

Bochen Liu, Department of Energy Technology, Aalborg University, Aalborg, Denmark

Wenzhao Liu, Aalborg University, Aalborg, Denmark

Jianzhe Liu, Argonne National Laboratory, Lemont, IL, United States

Dapeng Lu, Aalborg University, Aalborg, Denmark

Amirhossein Moeini, Electrical and Computer Engineering Department, Missouri University of Science and Technology, Rolla, MO, United States

Mobin Naderi, University of Kurdistan, Sanandaj, Kurdistan, Iran

Yiwei Pan, Aalborg University, Aalborg, Denmark

Xiaohui Qu, Southeast University, Nanjing, Jiangsu, China

P. Rodriguez, Luxembourg Institute of Science & Technology, Esch-Sur-Alzette, Luxembourg

Jose Rodriguez, Faculty of Engineering, Universidad Andres Bello, Santiago, Chile

Subham Sahoo, Department of Energy Technology, Aalborg University, Aalborg East, Nordjylland, Denmark

Ariya Sangwongwanich, Aalborg University, Aalborg, Denmark

Mehdi Savaghebi, University of Southern Denmark, Odense, Denmark

Jakob Stoustrup, Aalborg University, Aalborg, Denmark

Zhongting Tang, Central South University, Changsha, China

Mads Graungaard Taul, Department of Energy Technology, Aalborg University, Aalborg, Denmark

Xiongfei Wang, Aalborg University, Aalborg, Denmark

Huai Wang, Aalborg University, Aalborg, North Jutland, Denmark

Yongdu Wang, School of Electrical Engineering, Shandong University, Jinan, China

Chao Wu, Department of Energy Technology, Aalborg University, Aalborg, Denmark

Xiawei Wu, University of Electronic Science and Technology of China, Chengdu, Sichuan, China

Qianwen Xu, Electric Power and Energy Systems Division, KTH Royal Institute of Technology, Stockholm, Sweden

Yongheng Yang, Aalborg University, Aalborg, Denmark

Zhenbin Zhang, School of Electrical Engineering, Shandong University, Jinan, China

Jie Zhang, Department of Mechanical Engineering, The University of Texas at Dallas, Richardson, TX, United States

Zhenyuan Zhang, University of Electronic Science and Technology of China, Chengdu, Sichuan, China

Changming Zheng, School of Electrical and Power Engineering, China University of Mining and Technology, Xuzhou, Jiangsu, China

Dao Zhou, Department of Energy Technology, Aalborg University, Aalborg, Denmark

Zichao Zhou, Aalborg University, Aalborg, Denmark

This book belongs to Kitab Liaison (ocd1996@gmail.com) Copyright Elsevier 2023

Preface

In 2018 I published two volumes in my edited book series *Control of Power Electronic Converters and Systems,* which have been very well received by society. Now, 3 years later, it is very clear that such a broad topic has become more and more important as the world has acknowledged the fact that carbon emission from energy consumption is a major contribution to global warming. Countries all over the world have already specified dedicated goals of 2030 and 2050 for carbon emission reduction. One of the important technologies is renewable generation because this technology leaves only the slightest of carbon footprints when electrical power is generated. Further concerns are that more electricity is needed to "fuel" the heavy transportation sector, to make the energy chain more efficient, and to deal with more seasonal-based power generation. These include different levels and sizes of storage as well as performing energy vector coupling to make modern society operate with a safe energy supply. The outcome of all this is that power electronics technology will be increasingly needed to control energy/power throughout the energy chain and different kinds of control are unavoidable.

In general, my preference for control technology is to keep it as simple as possible to solve a necessary problem. However, we are now seeing more advanced control methodologies coming into play in industrial applications, which offer a lot of added value. As a consequence, I decided to edit a Volume 3 in the series *Control of Power Electronic Converters and Systems,* which explores emerging topics in the control of power electronics and converters in different applications, which are all important in the energy transition we are now facing. The book covers the theory behind control, but also practical implementation and operation, which are always important. What is also evident is that in the power grid, controller interactions exist due to increasing renewable energy penetration in the power system and challenges with stability and power quality are beginning to appear. So, in this book, with contributions from all over the world, the focus is on small scale to large scale renewable generation. Also under scrutiny are terminal behavior at the connection to the grid and how to ensure better performance. I have also decided to cover a few important applications seen from a load perspective, which can also be used to control the grid.

I will like to thank all my colleagues who worked with me on this book, as well as the contributions from outside Aalborg University. I would also like

This book belongs to Kitab Liaison (ocd1996@gmail.com)

Copyright Elsevier 2023

thank the Villum Fonden for supporting my research as a Villum investigator through the project Reliable Power Electronic-based Power System. Such support is important to be able to realize a book like this.

Frede Blaabjerg
Aalborg University
March 2021

This book belongs to Kitab Liaison (ocd1996@gmail.com) Copyright Elsevier 2023

Chapter 1

Advanced control of power electronic systems—an overview of methods

Chao Wu[1], **Frede Blaabjerg**[1]
[1]*Department of Energy Technology, Aalborg University, Aalborg, Denmark*

1.1 Introduction

With the rapid development of semiconductor devices, power electronic technology has also been expanding rapidly and widely used in modern power system. Therefore, the power system is gradually changing toward a power electronic–based power system, which can be seen from these three aspects: power generation, power transmission and distribution grid, and electrical load.

For the power generation, environmental and energy crisis call for the extensive application of renewable energy like wind power and photovoltaics. These power generations are highly dependent on power electronic converters to transform the generated electricity to grid [1,2]. For the power transmission and distribution grid, flexible AC transmission systems and static synchronous compensator are needed to improve grid voltage quality, which are also mostly based on power electronic devices [3–5]. On the electrical load side, the wide application of variable frequency drive further increases the proportion of versatile inverters as well as many others like computer centers, lighting, and so on [6,7].

In summary, the modern power system will be with particularly high penetration rate of power electronic devices, so it is of great importance to study how to efficiently and stably control these power electronic equipment.

According to different applications, it may have different control objectives such as position control and speed control of electric motor, active and reactive power control of renewable energies, and voltage and current control of diverse power converters. In order to realize these different control objectives, different and reliable control strategies need to be adopted. This chapter will

Control of Power Electronic Converters and Systems. https://doi.org/10.1016/B978-0-12-819432-4.00020-2
Copyright © 2021 Elsevier Ltd. All rights reserved.

This book belongs to Kitab Liaison (ocd1996@gmail.com)
Copyright Elsevier 2023

summarize the advanced control technologies in modern power electronic systems. Based on the characteristics of controllers, it can generally be divided into linear controller and nonlinear controller.

When it comes to linear controllers, it means that the structure of the controller is linear and the controller design is based on a linear model of the controlled plant. The most commonly used linear controller is proportional and integral (PI) controller, which can track a DC reference without steady-state error [8–11]. The structure is simple and easy to be applied. However, only the DC reference signal can be controlled through a PI controller. Other kinds of reference signals like the sinusoidal reference cannot be tracked without errors. Hence, the proportional and resonant (PR) controller is proposed to track the sinusoidal reference [12–15]. In essence, the resonant controller is an extension of integral control in the frequency domain, which is not just aimed at the zero frequency but can be used at any desired frequency. Through the PR controller, the sinusoidal current or voltage can be controlled in the stationary frame without complex coordinate transformation. However, when the frequency is various, an adaptive resonant controller should be designed, otherwise the control accuracy cannot be guaranteed [16,17]. When the grid voltage is distorted with multifrequency harmonics, a series of resonant controllers should be employed in the control structure which will make the controller design complex and cumbersome to do the discretization in digital controller [18]. In this context, repetitive controller (RC) is a good choice for controlling multifrequency component simultaneously, since the RC is equivalent to a series of resonant controllers in parallel [19–21]. Nevertheless, the delay time in the RC structure may deteriorate the dynamic performance if the basic fundamental frequency is low. Furthermore, the bandwidth and stability of RC should be paid serious attention to when applying it to the digital controller. When it comes to the dynamic performance design process, the pole placement control is an effective method to set all desired poles of system according to the state space equation [22–26]. Sometimes there are special requirements of the control performance, and the linear quadratic regulator (LQR) is an effective method to achieve an optimized control like finite time to the steady point or least energy consumed during dynamic process [27–30]. The LQR is also based on the linear state space equation of the system, and the key point is to find the weighting matrix of state and input, and then calculate the feedback gain matrix. This procedure is dependent on the system parameters, which will jeopardize the system performance with parameter deviations.

It should be noted that the application and design of these linear controllers are dependent on the linear model of the controlled plant. The PI controller, resonant controller, and RC are all based on the linear transfer function, and the pole placement control and the LQR are both based on the linear state space equation. Nevertheless, most of the power electronic–based system are nonlinear when considering the power control, synchronization block, switching process, and so on. In order to achieve an accurate and robust

This book belongs to Kitab Liaison (ocd1996@gmail.com) Copyright Elsevier 2023

control during the whole operation range, many nonlinear and advanced control methods are taken into consideration in the power electronic systems.

Hysteresis control is a simple nonlinear control method with the advantages of easy implementation, strong robustness, and low parameter dependence [31–38]. However, the switching frequency of the hysteresis control is uncertain, so that the theoretical frequency band of the output current can be as high as twice the operating frequency of its hysteresis comparator, which causes unnecessary difficulties in the design of the output filter.

Model predictive control (MPC) is an optimization control method which is not limited to the linear system but dependent on how to choose the cost function. Based on the cost function and the system model, the MPC method can directly get the PWM signals without any synchronization block. However, the switching frequency of the basic MPC method is variable which may make the filter design difficult [39–47].

Backstepping (BS) control technique has received much attention due to its merits of systematic and recursive design methodology [48–55]. The idea of BS control strategy is to select the proper Lyapunov function according to control targets on different design stages and form a final Lyapunov function by summing up the previous ones on every stage. The characteristics of the Lyapunov function can guarantee the stability of the control systems. The parameters needed to be tuned are less than PI controller; however, the control performance might have steady-state error when the system parameter changes.

In order to enhance the robustness of the BS control, sliding mode control (SMC) is widely used in power electronic systems because of the immunity to system parameters variation [56–61]. The sliding mode variable structure control strategy can change its own control structure in real time according to the change of the operating state of the system, and finally make the state variables of the system enter the predesigned sliding mode surface. However, due to the discontinuous control input for varying, the structure will lead to chatter problem.

In order to deal with the nonlinear block in power electronic systems, feedback linearization (FBL) is a good choice to change the nonlinear to linear system by constructing new intermediate variables. The FBL is particularly useful in power electronics to tackle the nonlinear problem. The technique is widely used while developing the control for electric machines, such as the DC machine, induction machine, switched reluctance machine, and permanent-magnet synchronous machine using power electronic converters, where a nonlinear process is transformed into a linear one by forcing the output to follow the input in a closed-loop fashion [62–66]. However, FBL control cannot tackle with parameter variations and disturbance uncertainty.

In order to enhance the robustness of the control system, the robust control can also be applied to tackle with the uncertain disturbance. The aforementioned controllers are mainly focusing the self-performance of converters

This book belongs to Kitab Liaison (ocd1996@gmail.com) Copyright Elsevier 2023

without considering the interaction with the grid. The impedance characteristic of converters with different control strategies changes dramatically in a wide frequency range. When it is connected to weak grid, resonance or unstable divergence is frequently occurred due to the impedance interaction. Thus, the passivity control is proposed for regulating the phase of converter impedance between −90 and 90 degrees, which can avoid the instability caused by the impedance interaction [67−73].

When considering the parameter variations during working period and reducing the negative effect caused by parameter changes, adaptive control is an effective way to estimate the state and change the control parameter real time according to the current working status [74−77].

To deal with this stability problem, an H_∞ controller with explicit robustness in terms of grid impedance variations is proposed to incorporate the desired tracking performance and the stability margin [73,79−83]. By properly selecting the weighting functions, the synthesized H_∞ controller exhibits high gains at the vicinity of the line frequency, similar to the traditional PR controller; meanwhile, it has enough high-frequency attenuation to keep the control loop stable.

Furthermore, artificial intelligence (AI) is developing rapidly and is one of the most salient research areas during the last several decades [83,84]. The aim of AI is to facilitate systems with intelligence that is capable of human-like learning and reasoning. There are various applications, including design optimization of power module heatsink [85], intelligent controller for multi-color light-emitting diode [86], maximum power point tracking control for wind energy conversion systems [87,88], anomaly detection for inverter [89], remaining useful life prediction for supercapacitors [90], etc. By implementing AI, power electronic systems are embedded with capabilities of self-learning and self-adaptation, and therefore the system autonomy can be improved.

In conclusion, many advanced control methods can be applied in power electronic systems with different objectives, which can be generally divided into two categories: linear controller and nonlinear controller. The overview of these advanced control methods can be seen in Fig. 1.1. This chapter tries to give a comprehensive and systematic review of these advanced control methods, which will start with the linear controller in the first section. Then, various nonlinear controllers are introduced in the next section. In order to give an intuitive interpretation of different control methods, the simple three-phase voltage source converter (VSC) is utilized as the controlled plant. In the last section, the comparison of different advanced control methods is compared through different aspects, such as the tracking performance, disturbance rejection ability and complexity of control algorithm, and so on. According to different performance requirements, different advanced control methods should be chosen. Along with the quick development of digital controller and signal processing ability, the advanced nonlinear control method will be a trend for improving the performance of power electronic systems.

This book belongs to Kitab Liaison (ocd1996@gmail.com) Copyright Elsevier 2023

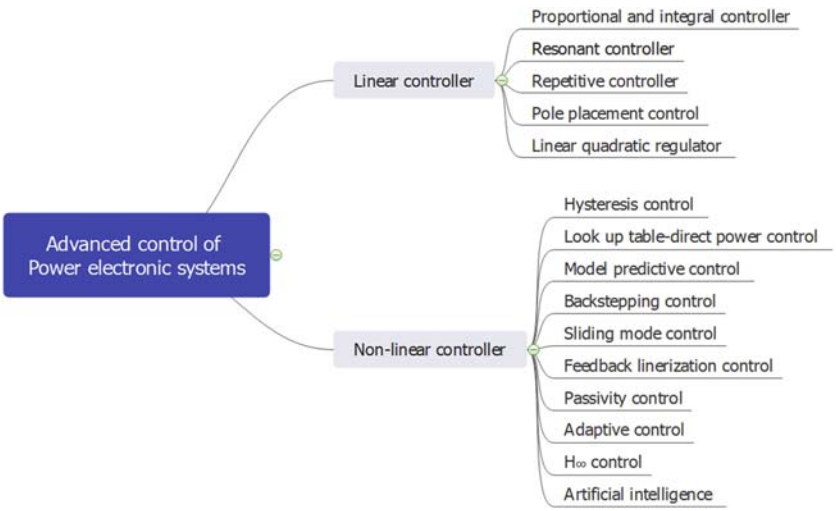

FIGURE 1.1 Overview of advanced control methods in power electronic systems.

1.2 Linear controller implementation and analysis

Due to the simple structure and easy to be implemented, linear controllers such as PI controller, resonant controller, and RC are widely used in the power electronic systems. It should be noted that an important characteristic of linear controller is that the application and design of linear controller are all based on a linear system. In this section, all the linear controllers are elaborated in details to better understand the advantages and disadvantages of different methods.

1.2.1 Implement PI controller

The PI regulator is a linear controller. The input of PI controller is the deviation of a given reference value and a feedback value. The output is a linear combination of the PI of the deviation. The PI controller is the most widely and extensively used controller in the power electronics, since it is simple and stable. The transfer function of conventional PI controller in the continuous domain can be expressed as

$$G_{pi}(s) = k_p + \frac{k_i}{s}. \tag{1.1}$$

where k_p and k_i are the proportional and integral gains, respectively.

A three-phase two-level VSC is very often used in the power electronic system and it is taken as the controlled plant. The control diagram of PI controller applied for the current control in VSC is shown in Fig. 1.2, where

This book belongs to Kitab Liaison (ocd1996@gmail.com) Copyright Elsevier 2023

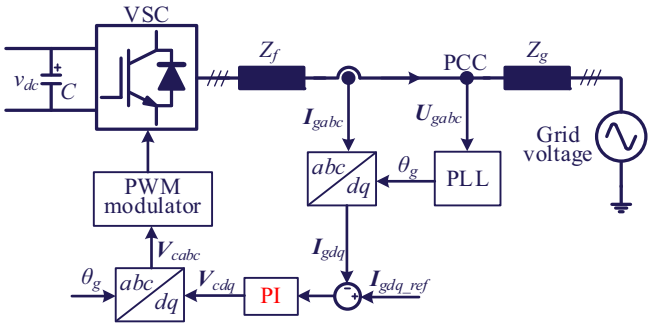

FIGURE 1.2 Control diagram of proportional and integral controller applied in a three-phase voltage source converter to control the current.

$\boldsymbol{U}_{gabc}$ is the grid voltage of point of common coupling, $\boldsymbol{I}_{gabc}$ is the grid current, Z_f is the impedance of filter which can be a simple L filter or LCL filter, Z_g represents the impedance of weak grid, $\boldsymbol{V}_{cabc}$ is the converter voltage, v_{dc} is the DC voltage, and C is the DC capacitance.

As can be seen from Fig. 1.2, the three-phase alternative currents in stationary frame need to be changed to DC signals in the synchronous frame, since the PI controller can only achieve a zero steady-state control of DC signal. Thus, the phase-locked loop and coordinate transformation are necessary in this control structure.

1.2.2 Implement PR controller

The transfer function of PR controller can be obtained by shifting the integrator part of the conventional PI controller to both positive and negative fundamental frequency:

$$G_{PR_ideal}(s) = k_p + \frac{k_i}{s - j\omega} + \frac{k_i}{s + j\omega} = k_p + \frac{2k_i s}{s^2 + \omega^2}. \tag{1.2}$$

where k_p, k_i are the proportional and integral parameters of the PI part, ω is the tuned resonant frequency.

However, it should be pointed out that the PR controller expression in Eq. (1.2) is an ideal one, which is quite sensitive to the grid frequency variation. Thus, the practical PR controller is adopted by the following equation:

$$G_{PR}(s) = k_p + \frac{k_r \omega_c s}{s^2 + \omega_c s + \omega_0^2}. \tag{1.3}$$

where k_r is the resonant gain, ω_c is the resonant bandwidth introduced to increase the control bandwidth and improve the robustness against the grid frequency variation, ω_0 is the resonant frequency of 50 Hz.

This book belongs to Kitab Liaison (ocd1996@gmail.com) Copyright Elsevier 2023

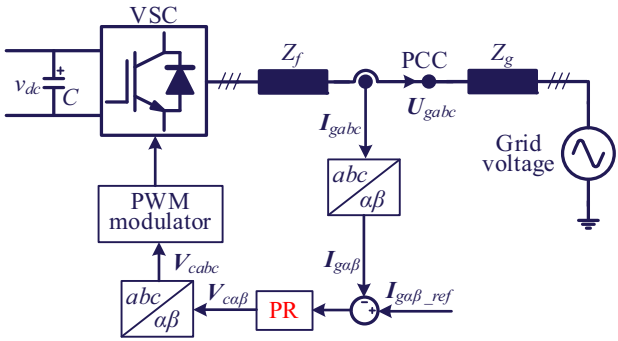

FIGURE 1.3 Control diagram of proportional and resonant controller applied in a three-phase voltage source converter to control the current.

The PR controller can be applied for the current control in VSC as illustrated in Fig. 1.3. Since the resonant controller is capable of regulating the alternating signal, the Park transformation can be avoided and the control structure is implemented in the stationary frame.

1.2.3 Implement repetitive controller

In some cases, the grid might be distorted by the nonlinear load like a diode bridge. Hence, the distorted harmonic voltage will cause multifrequency harmonic currents. In such case, a single PI controller or PR controller is not enough for dealing with all the harmonics with different frequencies. Under this situation, it is necessary to apply some controllers which are able to deal with multiple frequencies simultaneously.

The conventional repetitive controller (CRC) in the continuous domain can be expressed as follows:

$$G_{\mathrm{CRC}}(s) = k_{\mathrm{RC}} \frac{e^{-sT_0}}{1 - e^{-sT_0}}. \tag{1.4}$$

where k_{RC} is the gain parameter of CRC regulator, T_0 is the period of the fundamental control frequency, and $T_0 = 1/300$ s if considering the harmonics caused by diode bridge [21].

Moreover, based on the nature of exponential function, the conventional RC given in Eq. (1.4) can also be written as

$$G_{\mathrm{CRC}}(s) = -\frac{k_{\mathrm{RC}}}{2} + \frac{k_{\mathrm{RC}}}{T_0 s} + \frac{2k_{\mathrm{RC}}}{T_0} \sum_{n=1}^{\infty} \frac{s}{s^2 + (n\omega_0)^2}. \tag{1.5}$$

From the above expression, it can be concluded that an RC is equivalent to a parallel combination of a negative proportional term, an integral element,

This book belongs to Kitab Liaison (ocd1996@gmail.com) Copyright Elsevier 2023

and an infinite number of resonant controllers connected in parallel at specific harmonic frequencies. This implies that an RC contains lots of resonant frequencies, while a PR controller contains only one.

An ideal RC has an infinite open-loop gain at the resonant frequencies and can make the control system to track the reference signals without steady-state error. However, it also results in poor stability inevitably and has poor robustness against the deviation of resonant frequencies. To improve the stability and robustness, a low-pass filter $Q(s)$ or a constant Q less than 1 is added to the internal model. When Q is a constant less than 1, the expression of the RC with a certain bandwidth becomes

$$G_{\mathrm{BRC}}(s) = \frac{k_{\mathrm{RC}} Q e^{-T_0 s}}{1 - Q e^{-T_0 s}}. \tag{1.6}$$

Based on the nature of exponential function, Eq. (1.6) can be rewritten as follows:

$$G_{\mathrm{BRC}}(s) = \frac{k_{\mathrm{RC}} Q e^{-T_0 s}}{1 - Q e^{-T_0 s}} = -\frac{k_{\mathrm{RC}}}{2} + \frac{k_{\mathrm{RC}}}{T_0 s + T_0 \omega_c} + \frac{2k_{\mathrm{RC}}}{T_0} \sum_{n=1}^{\infty} \frac{s + \omega_c}{s^2 + 2\omega_c s + \omega_c^2 + (n\omega_0)^2}$$

$$\approx -\frac{k_{\mathrm{RC}}}{2} + \frac{k_{\mathrm{RC}}}{T_0 s + T_0 \omega_c} + \frac{2k_{\mathrm{RC}}}{T_0} \sum_{n=1}^{\infty} \frac{s + \omega_c}{s^2 + 2\omega_c s + (n\omega_0)^2}. \tag{1.7}$$

When ω_c is far smaller than ω_0, the symbol of approximate equal holds. ω_c is the resonant bandwidth and $\omega_c = -\ln Q/T_0$. From Eq. (1.7), it can be seen that the integral element in Eq. (1.5) becomes an inertial element, and the resonant controllers become quasiresonant controllers. Therefore, it can be concluded that the modified RC with Q corresponds to a parallel combination of a negative proportional term, an inertial element, and a series of quasiresonant controllers connected in parallel at harmonic frequencies, which can tackle with multifrequency component simultaneously. The control diagram of RC applied for a three-phase VSC is shown in Fig. 1.4, which is aimed to

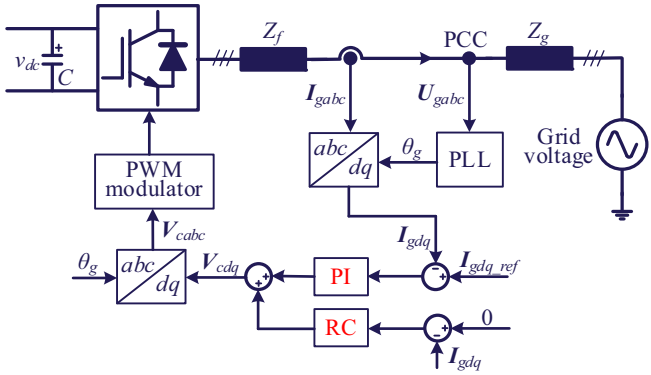

FIGURE 1.4 Control diagram of repetitive controller applied in a three-phase voltage source converter to suppress harmonic currents.

This book belongs to Kitab Liaison (ocd1996@gmail.com) Copyright Elsevier 2023

suppress the harmonics in grid current. It should be noted that the input of RC is not only limited to the current error but it can also be chosen as power error when the control objective is to suppress power ripple under distorted grid voltages.

1.2.4 Pole placement control

Pole placement is a method used in feedback control system theory which allows all the dominant closed-loop poles of a plant to be placed in a desired location in the s-plane. If all the system state variables are considered to be measurable and controllable, then poles of the closed-loop system may be placed at any desired location by means of state feedback through an appropriate state feedback gain matrix [22]. The location of the poles directly corresponds to the roots of the system characteristic equation, which controls the characteristics of the response of the system [23]. In this way, the dynamic and steady-state performance can be designed flexibly by regulating the dominant closed-loop poles to have a desired damping ratio and an undamped natural frequency [24].

Based on the system data considered and the operating condition, the state equation of the system under study is given by $\dot{X} = AX + BU$, where the state feedback control is used, $U = -KX$. The use of state feedback control modifies the system state equation to $\dot{X} = (A - BK)X$ which is the state variable presentation of the compensated system. The characteristic equation of the compensated system is $|sI - A + BK| = 0$. Here, the state feedback gain matrix K can be determined using the Ackermann's formula [25], which is

$$K = \begin{bmatrix} 0 & 0 & \cdots & 1 \end{bmatrix} \begin{bmatrix} B & AB & \cdots & A^{n-1}B \end{bmatrix}^{-1} \phi(A). \tag{1.8}$$

where $\phi(A) = A^n + \alpha_1 A^{n-1} + \ldots + \alpha_{n-1}A + \alpha_n I$, α_i are the coefficients of the desired characteristic polynomial [26].

However, the pole placement control is based on an accurate model of the system. The control performance will be deteriorated if the system parameters are deviated. Furthermore, the pole placement control is only applicable for a linear plant, which might be a limitation for this method, since most power electronic plants are nonlinear.

1.2.5 Linear quadratic regulator

LQR is a linear optimal control scheme based on a state space equation. By establishing a linear model and introducing a quadratic integral function of the control objective as an evaluation function, the feedback matrix is acquired based on solving the minimum value of the quadratic integral function. Compared with the proportional integral PI regulator, the control objectives of LQR are more flexible. At present, this LQR method has been initially used in active power filters, wind turbine pitch control, motor speed control, and other control systems [27–30].

This book belongs to Kitab Liaison (ocd1996@gmail.com) Copyright Elsevier 2023

The control object of LQR is a linear system given in the form of state space in modern control theory, and the objective function is a quadratic function of the object state and control input. The optimal design of LQR refers to the state feedback controller K designed to minimize the quadratic objective function J, and K is uniquely determined by the weight matrices Q and R, so the selection of Q and R is particularly important. The LQR theory is the earliest and the most mature state space design method in modern control theory. Especially valuable is that LQR can obtain the optimal control law of state linear feedback, which is easy to form a closed-loop optimal control. Moreover, the application of Matlab provides conditions for theoretical LQR simulations, and it also provides convenience for us to achieve stable, accurate, and fast control goals.

The LQR method is based on the state space equation, and the linear state space equation of the three-phase VSC can be expressed as

$$\dot{X} = AX + BU. \tag{1.9}$$

where X is the state vector, U is the input vector which normally contains the grid voltage and converter voltage.

In the LQR method, the optimal state feedback control law is derived as

$$u = -K(X^* - X). \tag{1.10}$$

where X^* is the desired state vector, X is the actual state vector, and K is the feedback gain matrix. The value of K is obtained by solving the Algebraic Riccati equation

$$A^T P + PA + Q - PBR^{-1}B^T P = 0. \tag{1.11}$$

where Q is a symmetrical positive semidefinite diagonal matrix, which is the weighing matrix of X. R is a symmetrical positive definite diagonal matrix, which is the weighing matrix of control action U. The weights are selected according to the task to be done in this control method. In this way, the control objectives can be set flexibly in LQR method.

1.3 Nonlinear controller implementation and analysis

As commonly known, all the power electronic converters are made up of switching components, which are nonlinear blocks, and the controlled plant belongs to a nonlinear system. Thus, it is often not applicable to achieve the performance by simply using a linear control method when encountering some hostile environment such as unbalanced or distorted grid voltage. Furthermore, when considering the system parameter variation and disturbance uncertainty, a nonlinear controller is more suitable for enhancing the robustness and being adaptive to different occasions. In this context, some advanced nonlinear control methods may be necessary in order to improve the performance of power electronic systems. In recent years, the FBL method, BS method, SMC,

This book belongs to Kitab Liaison (ocd1996@gmail.com) Copyright Elsevier 2023

adaptive control, and MPC are all applied in the power electronic system to better satisfy the control requirements of the power electronic system in versatile applications.

1.3.1 Hysteresis control

The hysteresis current controller is simple to implement and independent of load parameters. But the switching frequency changes according to the load which leads to high switching losses and resonance problems. This limits the usage of hysteresis controllers to low power levels. The control logic for the hysteresis controller per phase is shown in Fig. 1.5.

The reference inverter current and the actual inverter current $\boldsymbol{I}_{gabc}$ are compared and the pulses are generated according to the error. The switching logic is expressed as

$$S_{abc} = \begin{cases} -1, \boldsymbol{I}_{gabc} \geq \boldsymbol{I}_{abc_ref} + h \\ 1, \boldsymbol{I}_{gabc} \leq \boldsymbol{I}_{abc_ref} - h \end{cases}. \tag{1.12}$$

where S_{abc} is the switching signal, 1 means upper switch is on, -1 means lower switch is on, and h is the hysteresis band. The actual current is made to follow the reference current by forcing the actual current to stay within the hysteresis band.

1.3.2 Lookup table−based direct power control

Direct power control (DPC) is another kind of high-performance control strategy for PWM rectifier based on instantaneous power theory, which was first proposed in Ref. [33] and more clearly presented in Ref. [34]. The basic principle of DPC is similar to direct torque control in motor drives [35]. It directly selects the desired voltage vector from a predefined switching table, according to the grid voltage position (or virtual flux position) and the errors between the reference active/reactive power and feedback value. The internal current loop existing in voltage-oriented control is eliminated in DPC. As a result, DPC features very quick dynamic response with simple structure.

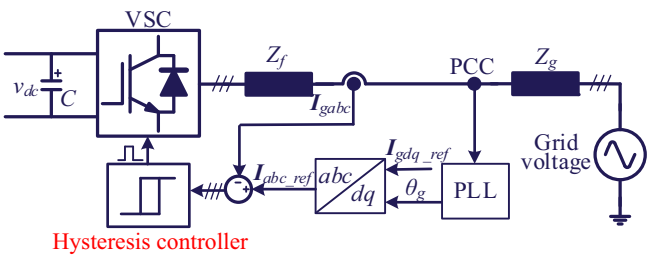

FIGURE 1.5 Hysteresis control scheme applied in a three-phase voltage source converter.

This book belongs to Kitab Liaison (ocd1996@gmail.com) Copyright Elsevier 2023

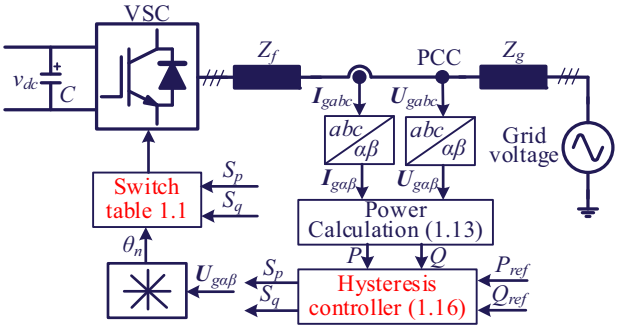

FIGURE 1.6 Control diagram of lookup table—based direct power control applied in a three-phase voltage source converter [34].

The control structure of a typical LUT-DPC is shown in Fig. 1.6, where the switch table is shown in Table 1.1. The power calculation block can be expressed as

$$\begin{cases} P = \dfrac{3}{2}(\boldsymbol{U}_{g\alpha\beta} \cdot \boldsymbol{I}_{g\alpha\beta}) = \dfrac{3}{2}(u_{g\alpha} i_{g\alpha} + u_{g\beta} i_{g\beta}) \\ Q = \dfrac{3}{2}(\boldsymbol{U}_{g\alpha\beta} \times \boldsymbol{I}_{g\alpha\beta}) = \dfrac{3}{2}(u_{g\beta} i_{g\alpha} - u_{g\alpha} i_{g\beta}) \end{cases}. \tag{1.13}$$

where $\boldsymbol{U}_{g\alpha\beta} = u_{g\alpha} + ju_{g\beta}$ and $\boldsymbol{I}_{g\alpha\beta} = i_{g\alpha} + ji_{g\beta}$.

In order to obtain the position of grid voltage vector, the angle of grid voltage can be calculated based on $u_{g\alpha}$ and $u_{g\beta}$ as

$$\theta = \arctan(u_{g\beta} / u_{g\alpha}). \tag{1.14}$$

The switch table is based on the position of grid voltage vector. In order to optimize the performance of converter, the grid voltage can be divided into 12 sectors. The angle of 12 sectors can be expressed as

$$(n-2)\frac{\pi}{6} \le \theta_n \le (n-1)\frac{\pi}{6},\ n = 1, 2, \cdots, 12. \tag{1.15}$$

The power hysteresis controller consists of active power and reactive power hysteresis controller. The inputs are the power error between the power reference and the real power. The output reflects the status of power deviation, which can be expressed as S_p and S_q. S_p and S_q only have two status, which can be expressed as

$$S_p = \begin{cases} 0 & P < P_{\text{ref}} - H_p \\ 1 & P > P_{\text{ref}} + H_p \end{cases},\ S_q = \begin{cases} 0 & Q < Q_{\text{ref}} - H_q \\ 1 & Q > Q_{\text{ref}} + H_q \end{cases}. \tag{1.16}$$

where H_p and H_q are the hysteresis band.

Although LUT-DPC has been considered as a powerful and robust control scheme for PWM rectifier, high-power ripples and variable switching

This book belongs to Kitab Liaison (ocd1996@gmail.com) Copyright Elsevier 2023

TABLE 1.1 Switch table applied in lookup table–based direct power control.

S_p	S_q	θ_1	θ_2	θ_3	θ_4	θ_5	θ_6	θ_7	θ_8	θ_9	θ_{10}	θ_{11}	θ_{12}
1	0	101	111	100	000	110	111	010	000	011	111	001	000
1	1	111	111	000	000	111	111	000	000	111	111	000	000
0	0	101	100	100	110	110	010	010	011	011	001	001	101
0	1	100	110	110	010	010	011	011	001	001	101	101	100

This book belongs to Kitab Liaison (ocd1996@gmail.com)

Copyright Elsevier 2023

frequency are two of the most notable drawbacks of conventional LUT-DPC. Furthermore, the required sampling frequency is usually very high in order to achieve relative satisfactory performance, which increases the hardware burden and might limit the application of this method.

1.3.3 Model predictive control

As a more advanced control theory, MPC has received extensive attention in the field of power electronic systems in recent years. In MPC, a cost function should first be defined according to an expected control target, and then calculate and compare the cost function when different voltage vectors are applied in each control cycle. Then, the optimal voltage vector is selected for the system control in a specific sample period.

Compared with the traditional lookup table method, this vector selection method based on the cost function is more accurate in selecting the voltage vector due to the great flexibility in the selection of the cost function. The objectives that can be achieved by this control strategy are very diverse not only to achieve conventional power or current control but it can also optimize other performances such as reducing switching loss, mitigating power/torque ripple, etc.

In addition, by adjusting the weighting factors of different variables in the cost function, different control performances can also be achieved. In Ref. [39], the author designed a control algorithm for the active and reactive power error in the cost function. The weighting factors are adjusted in real time, optimizing the dynamic performance of the entire system. Some studies aimed at the effect of system delay in the control process on the control accuracy of the MPC strategy and proposed a two-step prediction method to compensate for the delay error and thereby effectively reduce the current harmonics and power ripple [40–43]. Other studies have proposed a method to optimize the control accuracy of the MPC strategy by adding a duty cycle modulation. This control strategy adds zero vectors to modulate on the basis of the optimal effective vector selected in each control cycle. The execution time of the effective vector and the zero vector is calculated through the deadbeat principle, so that the control error at the end of each control cycle is effectively suppressed, and the overall control performance of the control system is optimized [44–48]. However, the MPC strategy based on the finite set needs to calculate and compare the objective functions of all voltage vectors in each control cycle, which demands a large amount of calculation and requires high performance of the processor when the sampling frequency is high and also to achieve a high bandwidth.

In summary, some open questions for the MPC can be concluded as follows: 1. When the cost function is a combination of multitarget optimization, how to choose the weighting factor? 2. How to ensure the switching frequency is constant of MPC? 3. How to reduce the effect of parameter deviation on the

This book belongs to Kitab Liaison (ocd1996@gmail.com) Copyright Elsevier 2023

control accuracy of MPC? Such detailed discussions about MPC methods will be addressed in Chapter 4 of this book.

1.3.4 Backstepping control

The BS control technique has received much attention due to its merits of systematic and recursive design methodology. The idea of BS control strategy is to select a proper Lyapunov function according to the control targets in different design stages and form a final Lyapunov function by summing up the previous ones in every stage. The characteristics of the Lyapunov function can guarantee stability of the control systems. The BS control strategy has been widely used in aeronautical and astronautical systems [49–51], and satisfied control performance is achieved. In addition, the BS control technique can also be applied to power electronic system [52–55].

In order to take an intuitive example of BS applied in power electronic system, a BS-DPC strategy is designed for the grid-connected AC/DC converter. The main objective for the BS-DPC strategy is to maintain the DC-bus voltage of the AC/DC converter to be a given value by regulating the active power. The other two objectives are the control of active and reactive powers to the given reference. Since the three-phase VSC is working as a rectifier in this case, the reference direction of the grid current is shown in Fig. 1.7. For simplification, the inductance filter is applied. L_f is the inductance of filter and R_f is the resistance of filter.

According to Fig. 1.7, the relationship between the grid voltages, converter voltages, and the grid currents in the stationary $\alpha\beta$ frame can be expressed as

$$\boldsymbol{U}_{g\alpha\beta} = \boldsymbol{I}_{g\alpha\beta}R_f + L_f\frac{d\boldsymbol{I}_{g\alpha\beta}}{dt} + \boldsymbol{V}_{c\alpha\beta}. \tag{1.17}$$

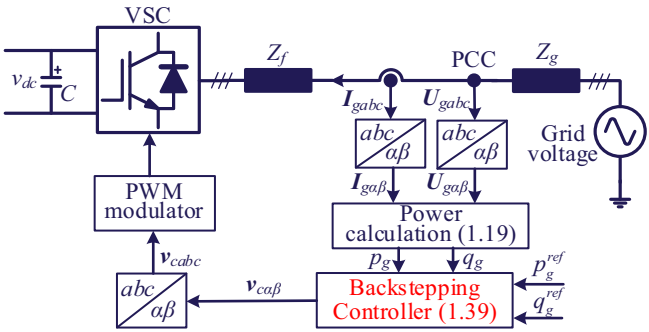

FIGURE 1.7 Control scheme of backstepping control applied in a three-phase voltage source converter [55].

This book belongs to Kitab Liaison (ocd1996@gmail.com)
Copyright Elsevier 2023

In the stationary $\alpha\beta$ frame and for a balanced three-phase system, the instantaneous active and reactive power outputs, seen from the grid side, can be defined as

$$p_g + jq_g = \frac{3}{2}\left(\boldsymbol{U}_{g\alpha\beta}\widehat{\boldsymbol{I}}_{g\alpha\beta}\right). \tag{1.18}$$

where ˆ denotes the conjugate of the complex vector. In such case, p_g and q_g can be deduced as

$$\begin{aligned} p_g &= \frac{3}{2}\left(u_{g\alpha}i_{g\alpha} + u_{g\beta}i_{g\beta}\right) \\ q_g &= \frac{3}{2}\left(u_{g\beta}i_{g\alpha} - u_{g\alpha}i_{g\beta}\right). \end{aligned} \tag{1.19}$$

Differentiating Eq. (1.19) results in the instantaneous active and reactive power variations as

$$\begin{aligned} \frac{dp_g}{dt} &= \frac{3}{2}\left(u_{g\alpha}\frac{di_{g\alpha}}{dt} + i_{g\alpha}\frac{du_{g\alpha}}{dt} + u_{g\beta}\frac{di_{g\beta}}{dt} + i_{g\beta}\frac{du_{g\beta}}{dt}\right) \\ \frac{dq_g}{dt} &= \frac{3}{2}\left(u_{g\beta}\frac{di_{g\alpha}}{dt} + i_{g\alpha}\frac{du_{g\beta}}{dt} - u_{g\alpha}\frac{di_{g\beta}}{dt} - i_{g\beta}\frac{du_{g\alpha}}{dt}\right). \end{aligned} \tag{1.20}$$

Assuming the grid voltage is an ideal sinusoidal wave form, namely,

$$\begin{aligned} u_{g\alpha} &= U_g \sin(\omega_1 t) \\ u_{g\beta} &= -U_g \cos(\omega_1 t). \end{aligned} \tag{1.21}$$

The instantaneous grid voltage variation can be obtained as

$$\begin{aligned} \frac{du_{g\alpha}}{dt} &= \omega_1 U_g \cos(\omega_1 t) = -\omega_1 u_{g\beta} \\ \frac{du_{g\beta}}{dt} &= \omega_1 U_g \sin(\omega_1 t) = \omega_1 u_{g\alpha}. \end{aligned} \tag{1.22}$$

Based on Eq. (1.17), the instantaneous grid current variations can be expressed as

$$\begin{aligned} \frac{di_{g\alpha}}{dt} &= \frac{1}{L_f}\left(u_{g\alpha} - i_{g\alpha}R_f - v_{c\alpha}\right) \\ \frac{di_{g\beta}}{dt} &= \frac{1}{L_f}\left(u_{g\beta} - i_{g\beta}R_f - v_{c\beta}\right). \end{aligned} \tag{1.23}$$

Substituting Eqs. (1.22) and (1.23) into Eq. (1.20) yields

$$\begin{aligned} \frac{dp_g}{dt} &= \frac{3}{2L_f}\left[\left(u_{g\alpha}^2 + u_{g\beta}^2\right) - \left(u_{g\alpha}v_{c\alpha} + u_{g\beta}v_{c\beta}\right)\right] - \omega_1 q_g - \frac{R_f}{L_f}p_g \\ \frac{dq_g}{dt} &= \frac{3}{2L_f}\left(u_{g\alpha}v_{c\beta} - u_{g\beta}v_{c\alpha}\right) + \omega_1 p_g - \frac{R_f}{L_f}q_g. \end{aligned} \tag{1.24}$$

This book belongs to Kitab Liaison (ocd1996@gmail.com)
Copyright Elsevier 2023

The relationship between DC-bus voltage and active power can be written as

$$C\frac{dv_{\mathrm{dc}}}{dt}=\frac{p_g}{v_{\mathrm{dc}}}-i_{\mathrm{load}}. \tag{1.25}$$

where i_{load} is the load current and C is the value of capacitor.

For the whole design procedures of the nonlinear BS controller, there are two steps in order to force the system states to track the desired reference commands. The first step is to design the DC-bus voltage BS controller to control the v_{dc}, and the output is regarded as the reference value of active power p_g^{ref}. The second step is to design the power BS controller to control the active and reactive powers according to p_g^{ref} and q_g^{ref} (which is always set to zero for unity power factor control). The BS-DPC design procedures are described as follows:

The tracking error of DC-bus voltage e_v is defined as

$$e_v=v_{\mathrm{dc}}^{\mathrm{ref}}-v_{\mathrm{dc}}. \tag{1.26}$$

where $v_{\mathrm{dc}}^{\mathrm{ref}}$ is the reference value of DC-bus voltage.

$$\frac{de_v}{dt}=-\frac{dv_{\mathrm{dc}}}{dt}=\frac{1}{C}\left(\frac{p_g}{v_{\mathrm{dc}}}-i_{\mathrm{load}}\right). \tag{1.27}$$

Then, a Lyapunov function V_1 is defined as

$$V_1=\frac{1}{2}e_v^2. \tag{1.28}$$

The differentiation of V_1 can be calculated as

$$\frac{dV_1}{dt}=e_v\frac{de_v}{dt}=-\frac{e_v}{C}\left(\frac{p_g}{v_{\mathrm{dc}}}-i_{\mathrm{load}}\right). \tag{1.29}$$

The active power tracking error e_p is introduced as

$$e_p=p_g^{\mathrm{ref}}-p_g. \tag{1.30}$$

The active power reference can be designed as

$$p_g^{\mathrm{ref}}=(k_vCe_v+i_{\mathrm{load}})v_{\mathrm{dc}}. \tag{1.31}$$

where k_v is the BS parameter for the DC-bus voltage control loop.

Substituting Eq. (1.31) into Eq. (1.29), the differentiation of V_1 can be rewritten as

$$\frac{dV_1}{dt}=-k_ve_v^2+\frac{e_ve_p}{Cv_{\mathrm{dc}}}. \tag{1.32}$$

This book belongs to Kitab Liaison (ocd1996@gmail.com) Copyright Elsevier 2023

As the tracking error e_p tends to be zero for an appropriate control, it is obvious that the differentiation of V_1 will be negative; thus, the tracking error e_v will tend to be zero according to the Lyapunov stability analysis.

The tracking error of reactive power is defined as

$$e_q = q_g^{\text{ref}} - q_g. \tag{1.33}$$

According to Eq. (1.24), the differentiation of the power tracking errors (e_p and e_q) can be represented by

$$\begin{cases} \dfrac{de_p}{dt} = \dfrac{dp_g^{\text{ref}}}{dt} - \dfrac{dp_g}{dt} = \dfrac{dp_g^{\text{ref}}}{dt} - \dfrac{3}{2L_g}\left(U_g^2 - (u_{g\alpha}v_{c\alpha} + u_{g\beta}v_{c\beta})\right) + \omega_1 q_g \\ \dfrac{de_q}{dt} = -\dfrac{dq_g}{dt} = \dfrac{3}{2L_g}(u_{g\alpha}v_{c\beta} - u_{g\beta}v_{c\alpha}) - \omega_1 p_g \end{cases}. \tag{1.34}$$

where $U_g^2 = u_{g\alpha}^2 + u_{g\beta}^2$ is used for simplicity.

Define a Lyapunov function V_2 to realize the global tracking control of DC-bus voltage and power as

$$V_2 = V_1 + \frac{1}{2}\left(e_p^2 + e_q^2\right). \tag{1.35}$$

The differentiation of V_2 can be deduced as

$$\frac{dV_2}{dt} = \frac{dV_1}{dt} + e_p\frac{de_p}{dt} + e_q\frac{de_q}{dt} = -k_v e_v^2 + e_p\left(\frac{e_v}{Cv_{\text{dc}}} + \frac{de_p}{dt}\right) + e_q\frac{de_q}{dt}. \tag{1.36}$$

For the purpose of $(dV_2/dt) < 0$, it can be designed as follows

$$\begin{cases} \dfrac{e_v}{Cv_{\text{dc}}} + \dfrac{de_p}{dt} = -k_p e_p \\ \dfrac{de_q}{dt} = -k_q e_p \end{cases}. \tag{1.37}$$

where k_p and k_q are the BS parameters of the active power control loop and the reactive power control loop.

Since the differentiation of V_2 is a negative definite function, it implies that e_v, e_p, and e_q go to zero asymptotically. According to the Lyapunov stability theorem, the stability of the proposed BS-DPC strategy can be guaranteed.

Substituting Eq. (1.37) into Eq. (1.34), we can obtain

$$\begin{cases} \dfrac{dp_g^{\text{ref}}}{dt} - \left\{\dfrac{3}{2L_g}\left[U_g^2 - (u_{g\alpha}v_{c\alpha} + u_{g\beta}v_{c\beta})\right] - \omega_1 q_g\right\} = -k_p e_p - \dfrac{e_v}{Cv_{\text{dc}}} \\ \dfrac{3}{2L_g}(u_{g\alpha}v_{c\beta} - u_{g\beta}v_{c\alpha}) + \omega_1 p_g = k_q e_q \end{cases}. \tag{1.38}$$

This book belongs to Kitab Liaison (ocd1996@gmail.com)
Copyright Elsevier 2023

It can be concluded from Eq. (1.38) that the BS-DPC law for the AC/DC converter can be designed as

$$\begin{cases} v_{c\alpha} = \dfrac{2L_f}{3U_g^2}\left[-u_{g\alpha}\left(k_p\left(p_g^{\text{ref}} - p_g\right) + \dfrac{e_v}{Cv_{\text{dc}}} + \dfrac{dp_g^{\text{ref}}}{dt}\right) - u_{g\beta}k_q\left(q_g^{\text{ref}} - q_g\right)\right. \\ \qquad\qquad \left. -\omega_1 u_{g\alpha}q_g + \omega_1 u_{g\beta}p_g\right] + u_{g\alpha} \\ v_{c\beta} = \dfrac{2L_f}{3U_g^2}\left[-u_{g\beta}\left(k_p\left(p_g^{\text{ref}} - p_g\right) + \dfrac{e_v}{Cv_{\text{dc}}} + \dfrac{dp_g^{\text{ref}}}{dt}\right) + u_{g\alpha}k_q\left(q_g^{\text{ref}} - q_g\right)\right. \\ \qquad\qquad \left. -\omega_1 u_{g\beta}q_g - \omega_1 u_{g\alpha}p_g\right] + u_{g\beta} \end{cases} \tag{1.39}$$

As can be seen from Fig. 1.7, the advantages of BS method are that the control structure is pretty simple and having good steady-state and dynamic performance. Compared with the conventional PI controller, only one parameter needs to be tuned which can simplify the parameter design process. However, the BS control method is highly dependent on the system parameters, which will cause steady-state error if the parameter deviation is large.

1.3.5 Sliding mode control

As a nonlinear control strategy, the SMC strategy has excellent dynamic performance and good parameter robustness and has been widely studied in the field of power electronic systems.

The main idea of the sliding mode variable structure control strategy is to design the sliding mode surface and the approaching law according to the desired dynamic characteristics of the system, so that the system state moves from outside the sliding mode surface to the sliding mode surface, which is achieved by discontinuous control. Once the system reaches the sliding mode surface, it is not affected by the system parameters and external disturbances and moves along the sliding mode surface, effectively solving the problem of poor robustness of the BS control strategy. But the sliding mode variable structure control strategy might produce chattering problems because of the introduction of the switching function in discontinuous control, which will affect the control accuracy of the system. In Ref. [57], a sliding mode variable structure DPC strategy is applied to a three-phase DC/AC converter. The design of the sliding mode surface selects the form of PI of power error. The SMC strategy with a variable control structure is based on the design of discontinuous control signal that drives the system operation states toward

This book belongs to Kitab Liaison (ocd1996@gmail.com) Copyright Elsevier 2023

special manifolds in the state space. These manifolds are chosen in such a way that the control system will have the desired behavior as the states converge to them. In order to understand the SMC principle well, an SMC scheme for regulating the instantaneous active and reactive powers of grid-connected three-phase DC/AC converter is elaborated as an example.

The first step is to design the sliding surface. The DC voltage of the three-phase PWM converters is assumed constant, and the control objectives are to track the predefined active power and reactive power accurately and quickly. Thus, the sliding surface is based on the power error. In order to maintain the enhanced transient response and minimize the steady-state error, the switching surfaces can be in the integral forms as

$$S = [S_P \quad S_Q]^T. \tag{1.40}$$

$$\begin{cases} S_P = e_p + K_p \int_0^t e_p(\tau)d\tau \\ S_Q = e_q + K_q \int_0^t e_q(\tau)d\tau \end{cases}. \tag{1.41}$$

where $e_p = p_g^{\text{ref}} - p_g$ and $e_q = q_g^{\text{ref}} - q_g$ are the respective errors between the references and the actual active and reactive powers. K_p and K_q are the positive control gains. The manifolds $S_P = 0$ and $S_Q = 0$ represent the precise tracking of converter's active and reactive powers.

The second step is to design the approaching law of SMC, namely, how to ensure the states can come to the sliding with arbitrary initial states. The task is to force the system state trajectory to the interaction of the switching surfaces as aforementioned. In this example, an SMC scheme is suggested to generate the converter output voltage reference as the input to SVM module.

Based on Eq. (1.41), the differential of the sliding surface can be expressed as

$$\begin{aligned} \frac{dS_P}{dt} &= \frac{de_p}{dt} + K_p e_p = -\frac{d}{dt}p_g + K_p\left(p_g^{\text{ref}} - p_g\right) \\ \frac{dS_Q}{dt} &= \frac{de_q}{dt} + K_q e_q = -\frac{d}{dt}q_g + K_q\left(q_g^{\text{ref}} - q_g\right). \end{aligned} \tag{1.42}$$

Substituting Eq. (1.24) into Eq. (1.42) leads to

$$\frac{d\boldsymbol{S}}{dt} = \boldsymbol{F} + \boldsymbol{D}\boldsymbol{V}_g. \tag{1.43}$$

where $\boldsymbol{F} = [F_P \quad F_Q]^T$, $\boldsymbol{V}_g = [v_{g\alpha} \quad v_{g\beta}]^T$

This book belongs to Kitab Liaison (ocd1996@gmail.com) Copyright Elsevier 2023

$$D = -\frac{3}{2L_f}\begin{bmatrix} u_{g\alpha} & u_{g\beta} \\ u_{g\beta} & -u_{g\alpha} \end{bmatrix}$$

$$F_P = \frac{3}{2L_f}\left(u_{g\alpha}^2 + u_{g\beta}^2\right) + \frac{R_f}{L_f}p_g + \omega_1 q_g + K_P\left(p_g^{\text{ref}} - p_g\right) \tag{1.44}$$

$$F_Q = \frac{R_f}{L_f}q_g - \omega_1 p_g + K_q\left(q_g^{\text{ref}} - q_g\right).$$

In the SMC, a Lyapunov approach is usually used for deriving conditions on the control law that will drive the state orbit to the equilibrium manifold. The quadratic Lyapunov function is selected as

$$W = 0.5\boldsymbol{S}^T\boldsymbol{S} \geq 0. \tag{1.45}$$

The time derivative of W on the state trajectories of Eq. (1.43) is then given by

$$\frac{dW}{dt} = \frac{1}{2}\left(\boldsymbol{S}^T\frac{d\boldsymbol{S}}{dt} + \boldsymbol{S}\frac{d\boldsymbol{S}^T}{dt}\right) = \boldsymbol{S}^T(\boldsymbol{F} + \boldsymbol{D}\boldsymbol{V}_g). \tag{1.46}$$

The approaching law must be properly chosen so that the time derivative of W is definitely negative with $S \neq 0$. Therefore, the following control law is selected as

$$\boldsymbol{V}_{c\alpha\beta} = -\boldsymbol{D}^{-1}\left\{\begin{bmatrix} F_P \\ F_Q \end{bmatrix} + \begin{bmatrix} K_{P1} & 0 \\ 0 & K_{Q1} \end{bmatrix}\begin{bmatrix} \text{sgn}(S_P) \\ \text{sgn}(S_Q) \end{bmatrix}\right\}. \tag{1.47}$$

where K_{P1} and K_{Q1} are the positive control gains, sgn(S_P) and sgn(S_Q) are the respective switch functions for active and reactive powers.

The robustness analysis, in practical operation, the sliding surface S will be affected by the parameter variations, AD sample errors and measurement noise, etc. Thus, Eq. (1.43) should be rearranged as

$$\frac{d\boldsymbol{S}}{dt} = \boldsymbol{S} + \boldsymbol{D}\boldsymbol{V}_g + \boldsymbol{H}. \tag{1.48}$$

where $H = [H_P \quad H_Q]^T$ represents the system disturbances.

In this way, Eq. (1.46) can be rewritten as

$$\frac{dW}{dt} = \boldsymbol{S}^T\frac{d\boldsymbol{S}}{dt} = \boldsymbol{S}^T\left\{\begin{bmatrix} H_P \\ H_Q \end{bmatrix} - \begin{bmatrix} K_{P1} & 0 \\ 0 & K_{Q1} \end{bmatrix}\begin{bmatrix} \text{sgn}(S_P) \\ \text{sgn}(S_Q) \end{bmatrix}\right\}. \tag{1.49}$$

It is worth noting that if the positive control gains fulfill the following condition, $K_{P1} > |HP|$ and $K_{Q1} > |HQ|$, the time derivative of Lyapunov function dW/dt is still definitely negative. Therefore, the SMC obviously features strong robustness.

This book belongs to Kitab Liaison (ocd1996@gmail.com) Copyright Elsevier 2023

Remedy of the Power Chattering Problem: The SMC scheme developed earlier guarantees a fast tracking of instantaneous active and reactive powers of grid-connected DC/AC converters. However, fast switching may generate unexpected chattering, which may excite unmodeled high-frequency system transients and even result in unforeseen instability. To eliminate this problem, the discontinuous part of the controller is smoothed out by introducing a boundary layer around the sliding surface. As a result, a continuous function around the sliding surface neighborhood is obtained as

$$\mathrm{sgn}(S_j) = \begin{cases} 1, \ if S_j > \lambda_j \\ \dfrac{S_j}{\lambda_j}, \ if |S_j| \le \lambda_j \\ -1, \ if S_j < -\lambda_j \end{cases} . \tag{1.50}$$

where $\lambda_j > 0$ is the width of the boundary layer and j represents p_g and q_g, respectively.

According to Eq. (1.47), the converter output voltage reference is obtained in the stationary reference frame and can be directly transferred to the SVM module for generating the required switching voltage vectors and their respective duration times. The control diagram of SMC applied in VSC can be shown in Fig. 1.8.

The improved sign function is designed for approaching law, which effectively reduces the chattering problem of the system. This sliding mode variable structure DPC strategy can be realized in a static coordinate system, which has good steady-state and dynamic performance and has strong

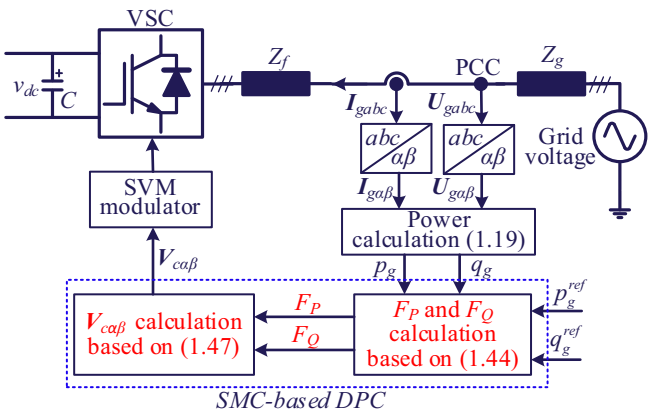

FIGURE 1.8 Control diagram of sliding mode control applied for power control in a three-phase voltage source converter [57].

This book belongs to Kitab Liaison (ocd1996@gmail.com)
Copyright Elsevier 2023

parameter robustness. However, how to choose the appropriate sliding mode surface and how to design the approaching law are various, which will be thoroughly discussed in Chapter 3 for different applications.

1.3.6 Feedback linearization

FBL is a common nonlinear control approach, whose main idea is to transform a nonlinear system into a fully or partially decoupled linear one by means of state feedback and nonlinear transformation, so that linear control strategies can be used. The basic theory of the FBL of nonlinear system is to linearize the nonlinear system in a wide range by choosing a proper nonlinear transformation $z = T(x)$ and a nonlinear state feedback variable $v = \alpha(x)+\beta(x)u$. At the same time, for a multivariable nonlinear system, decoupled control can also be realized [62]. Such linearization has higher accuracy, since the linear approximation is not employed, which means that no higher order nonlinear terms are ignored.

Recently, the FBL method has been widely used in power electronics, motor control, distributed generation, and other fields [63–66]. In Ref. [63], an adaptive input–output FBL-based torque control of synchronous reluctance motor is proposed without any mechanical sensor. In Ref. [66], the dynamic performance of the system is improved by configuring zeros and poles of the feedback-linearized system. Although the FBL method can transform the nonlinear system to a linear system and using the linear control method, it is based on the accurate system model without considering the parameter deviations or disturbance uncertainty.

1.3.7 Passivity control

The passivity-based control of VSCs recently emerges as a promising way to tackle the instability challenge and achieve robustness. The concept of passivity in the frequency domain implies that the real part of the output impedance/admittance of VSC is nonnegative.

To keep the real part of the VSC output admittance always larger than zero, which can maintain the phase of output admittance belong to -90 from 90 degrees. Since the grid impedance is always passive, the interaction between the VSC and the grid would always be stable if the output admittance of VSC is controlled to be passivity.

The first step of passivity control is to get the impedance/admittance model of the VSC, then trying to control the real part of the impedance/admittance to be larger than zero, which can be expressed as

$$\mathrm{Re}(G_{\mathrm{VSC}}(j\omega)) > 0. \tag{1.51}$$

where $G_{\mathrm{VSC}}(j\omega)$ represents the frequency characteristic of VSC impedance/admittance, which is a complex variable and the real part denotes

This book belongs to Kitab Liaison (ocd1996@gmail.com) Copyright Elsevier 2023

resistance/conductance. If the real part is above zero, which means the VSC is passive and will be stable even under weak grid conditions.

It should be noted that the passivity control of VSC is a sufficient condition but not a necessary condition for the stable operation under weak grid. The detailed discussions of the passivity control can be seen in Chapter 2 of this book.

1.3.8 Adaptive control

Most of the aforementioned control methods are based on the model parameters without considering the parameters uncertainty and deviation due to different operation points. Large parameter deviations can be detrimental for the system performance like steady-state error or oscillating dynamic process. In this context, adaptive control methods have attracted much attention, since it is robust to parameter variations or other uncertainties. Adaptive control is a control algorithm with adjustable control gains that are adaptive to variable or initially uncertain parameters of a controlled system [74–76]. Hence, this control method can keep the system performance and stability at the desired or optimum level under different conditions.

The model reference adaptive system (MRAS) is the mostly commonly applied control structure which is used for acquiring the rotor speed or position in motor drive field. The classical rotor flux MRAS speed observer is shown in Fig. 1.9, where u_s and is represent the stator voltage and stator current vector, $\boldsymbol{\phi}_r$ is the actual rotor flux acquired from the reference model, $\hat{\boldsymbol{\phi}}_r$ is the estimated rotor flux vector obtained from the adaptive model, and $\widehat{\omega}_r$ is the estimated rotor speed. The steps of MRAS control can be elaborated as follows: a reference model and an adaptive model are firstly constructed, then the error between these two models is calculated, and an appropriate controller is lastly designed to regulate the error to be zero. There are also other types of adaptive control structures, which can be seen from Chapter 5 in this book.

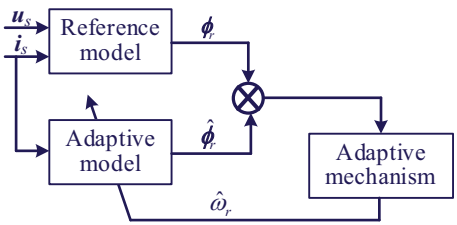

FIGURE 1.9 Classical rotor flux model reference adaptive system speed observer for an induction motor [77].

This book belongs to Kitab Liaison (ocd1996@gmail.com) Copyright Elsevier 2023

1.3.9 H_∞ control

The H_∞ control has been introduced in the early 1980s and opened a new direction in robust control design. Recently, this approach has been applied to the control of active power filters [73,78]. The feature is that the quantitative measure (H_∞-norm) of robustness may be explicitly included in the design goal. But its application to practical design problems was not so popular as the conventional control methods such as PI and pole assignment because the degree of the resulting controller is usually too high to be implemented by analog circuits. Moreover, the synthesis of the optimal controller involves complex manipulation on the system transfer functions, and a general and reliable numerical algorithm was not available. Although the state space solution approach [79] provides an attractive way to synthesize the controller by solving two Riccati equations, it is restricted to the so-called regular case where transfer function of the plant suffers from some inherent limitations. Recently, Gahinet and Apkarian [80] proposed the LMI approach which relaxes the above restrictions and provides a more general and numerically sound way to synthesize the controller.

The design of loop-shaping controller based on H_∞ control method is displayed in Fig. 1.10, in which $P(s)$ is the augmented plant obtained by appending the weighting function to the output of the transfer function of the desired loop shapes, w is in the original input, u is the additional input to enhance the system performance, v is the output, H(s) is the plant, $\Delta(s)$ represents the system uncertainty, and $W(s)$ is the system weighting function. The design goal is to synthesize the stabilizing controller $K(s)$ so that the H_∞ gain from w to z is less than 1 [82].

The H_∞ method is a robust control method; however, the derived controller and weighting function always are high orders which will increase the computation burden of the digital controllers.

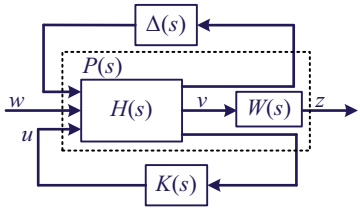

FIGURE 1.10 Control configuration for generalized H_∞ control [82].

This book belongs to Kitab Liaison (ocd1996@gmail.com)
Copyright Elsevier 2023

1.3.10 Artificial intelligence

The AI contains many smart algorithms, one of them mostly used is the neural network (NN). The main advantages of NN are parallel processing, learning ability, robustness, and generalization. They can be not only effectively used for current controller but also for other functions in a controller structure. NN-based controller can be named as a black-box technique, and it can approximate a wide range of nonlinear functions to arbitrary accuracy. An exemplary application of NN-based current vector control for a three-phase voltage converter is shown in Fig. 1.11 [91]. The NN is applied for generating the converter voltage reference. The inputs of the NN are the grid current, the error of grid current, and the integration of error. The action network in Ref. [91] had two hidden layers of six nodes each and 2 output nodes, and short-cut connections between all pairs of layers, with hyperbolic tangent functions at all nodes.

Even though the NN-based controller possesses several advantages such as robustness, being model free, also adaptive, universal approximation, etc., however, it needs massive training data in order to obtain accurate results. There are also other intelligent control methods, like fuzzy control, reinforcement control [92–95], which are elaborated in detail in more details in Chapter 6 of this book.

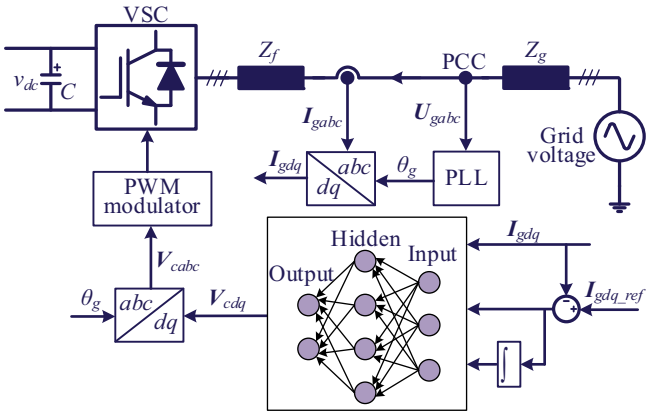

FIGURE 1.11 Control diagram of neural network applied in a three-phase voltage source converter for current control [91].

This book belongs to Kitab Liaison (ocd1996@gmail.com)
Copyright Elsevier 2023

TABLE 1.2 The comparison between different advanced control methods applied in power electronic systems.

Control methods		Reference signal	Control flexibility	Algorithm complexity	Parameter dependency	Robustness to disturbance	Easy to design
Linear controller	PI	DC	Low	Low	High	Poor	Easy
	Resonant controller	AC	Low	Low	High	Poor	Easy
	RC	AC	Low	Medium	High	Poor	Easy
	PPC	DC	Medium	Medium	High	Poor	Medium
	LQR	DC	High	High	High	Poor	Medium
Nonlinear controller	Hysteresis control	AC and DC	High	Low	Low	Medium	Easy
	LUT-DPC	AC and DC	Low	Low	Medium	Medium	Easy
	MPC	AC and DC	High	Medium	Medium	Medium	Medium
	BS	AC and DC	High	High	High	Poor	Medium
	SMC	AC and DC	High	Medium	Low	Good	Medium
	FBL	AC and DC	High	Medium	Medium	Medium	Medium
	Passivity control	AC and DC	Medium	Medium	Medium	Good	Medium
	Adaptive control	AC and DC	High	High	Low	Good	Complex
	H_∞ control	AC and DC	High	High	Low	Good	Complex
	AI	AC and DC	High	High	Low	Good	Complex

This book belongs to Kitab Liaison (ocd1996@gmail.com)

Copyright Elsevier 2023

1.4 Summary

In conclusion, there are many different advanced control methods applied in power electronic systems. Different control performances can be achieved through different methods under diverse application. In order to make a systematic and comprehensive comparison of these advanced control methods, Table 1.2 compares the performance of each control method from five aspects: reference signal, control flexibility, algorithm complexity, parameter dependency, and robustness to disturbance. There is no universal principle or criterion for choosing each control method. How to choose control methods should be analyzed according to the specific applications. For example, when a VSC is working in grid connection, the conventional linear controller is capable enough for tracking the reference, like the PI controller or PR controller. Nevertheless, for the stand-alone application like the uninterruptible power supply system, the load is unknown which can change in a wide range and in such situation, the advanced robust control like H_∞ controller is more suitable for operating well under wide range disturbances and uncertainties.

References

[1] F. Blaabjerg, Y. Yang, D. Yang, X. Wang, Distributed power-generation systems and protection, Proc. IEEE 105 (7) (July 2017) 1311–1331.

[2] F. Blaabjerg, K. Ma, Future on power electronics for wind turbine systems, IEEE J. Emerg. & Sel. Top. Power Electron. 1 (3) (September 2013) 139–152.

[3] F.B. Alhasawi, J.V. Milanovic, Techno-economic contribution of FACTS devices to the operation of power systems with high level of wind power integration, IEEE Trans. Power Syst. 27 (3) (August 2012) 1414–1421.

[4] M. Nagpal, C. Henville, Impact of power-electronic sources on transmission line ground fault protection, IEEE Trans. Power Deliv. 33 (1) (February 2018) 62–70.

[5] L.K. Haw, M.S.A. Dahidah, H.A.F. Almurib, A new reactive current reference algorithm for the STATCOM system based on cascaded multilevel inverters, IEEE Trans. Power Electron. 30 (7) (July 2015) 3577–3588.

[6] E.B. Agamloh, Power and efficiency measurement of motor-variable-frequency drive systems, IEEE Trans. Ind. Appl. 53 (1) (January-February 2017) 766–773.

[7] M. Malekpour, R. Azizipanah-Abarghooee, F. Teng, G. Strbac, V. Terzija, Fast frequency response from smart induction motor variable speed drives, IEEE Trans. Power Syst. 35 (2) (March 2020) 997–1008.

[8] J. Dannehl, F.W. Fuchs, P.B. Thogersen, PI state space current control of grid-connected PWM converters with LCL filters, IEEE Trans. Power Electron. 25 (9) (September 2010) 2320–2330.

[9] J. Selvaraj, N.A. Rahim, Multilevel inverter for grid-connected PV system employing digital PI controller, IEEE Trans. Ind. Electron. 56 (1) (January 2009) 149–158.

[10] F.D. Freijedo, A. Vidal, A.G. Yepes, J.M. Guerrero, O. Lopez, J. Malvar, J. Doval-Gandoy, Tuning of synchronous-frame PI current controllers in grid-connected converters operating at a low sampling rate by MIMO root locus, IEEE Trans. Ind. Electron. 62 (8) (August 2015) 5006–5017.

This book belongs to Kitab Liaison (ocd1996@gmail.com) Copyright Elsevier 2023

[11] M.P. Kazmierkowski, L. Malesani, Current control technique for three-phase voltage-source PWM converters: a survey, IEEE Trans. Ind. Electron. 45 (5) (October 1998) 691−703.

[12] D.N. Zmood, D.G. Holmes, Stationary frame current regulation of PWM inverters with zero steady-state error, IEEE Trans. Power Electron. 18 (3) (May 2003) 814−822.

[13] M. Castilla, J. Miret, J. Matas, L.G. Vicuña, J.M. Guerrero, Control design guidelines for single-phase grid-connected photovoltaic inverters with damped resonant harmonic compensators, IEEE Trans. Ind. Electron. 56 (11) (November 2009) 4492−4501.

[14] F. Wang, M.C. Benhabib, J.L. Duarte, M.A.M. Hendrix, Sequence decoupled resonant controller for three-phase grid-connected inverters, in: In Proc. IEEE APEC, Washington, DC, February 2009, pp. 121−127.

[15] D.G. Holmes, T.A. Lipo, B.P. McGrath, W.Y. Kong, Optimized design of stationary frame three phase AC current regulators, IEEE Trans. Power Electron. 24 (11) (November 2009) 2417−2426.

[16] S. Gómez Jorge, C.A. Busada, J.A. Solsona, Frequency-adaptive current controller for three-phase grid-connected converters, IEEE Trans. Ind. Electron. 60 (10) (October 2013) 4169−4177.

[17] S. Golestan, E. Ebrahimzadeh, J.M. Guerrero, J.C. Vasquez, An adaptive resonant regulator for single-phase grid-tied VSCs, IEEE Trans. Power Electron. 33 (3) (March 2018) 1867−1873.

[18] J.B. Hu, Y.K. He, Multi-frequency proportional-resonant (MFPR) current controller for PWM VSC under unbalanced supply conditions, J. Zhejiang Univ. - Sci. 8 (10) (2007) 1527−1531.

[19] D. Chen, J. Zhang, Z. Qian, Research on fast transient and 6n $\pm$ 1 harmonics suppressing repetitive control scheme for three-phase grid-connected inverters, IET Power Electron. 6 (3) (March 2013) 601−610.

[20] M. Abusara, S. Sharkh, P. Zanchetta, Adaptive repetitive control with feedforward scheme for grid-connected inverters, IET Power Electron. 8 (8) (August 2015) 1403−1410.

[21] Y. Song, H. Nian, Sinusoidal output current implementation of DFIG using repetitive control under a generalized harmonic power grid with frequency deviation, IEEE Trans. Power Electron. 30 (12) (December 2015) 6751−6762.

[22] S. Gubbala, M.R.P. Reddy, Improvement of dynamic stability using conventional, fuzzy controlled and PSO power system stabilizer, Int. J. Ind. Electron. & Electr. Eng. (IJIEEE) 2 (1) (2014) 6−13.

[23] P.P. Kumar, M.R. Babu, Saraswathi, Dynamic analysis of single machine infinite bus system using single input and dual input PSS, Int. Electr. Eng. J. (IEEJ) 3 (2) (2012) 632−641.

[24] F.M. Serra, A. Doria-Cerezo, C.H. De Angelo, L.L. Martín Fernández, M. Bodson, Complex pole placement control for a three-phase voltage source converter, in: 2020 IEEE International Conference on Industrial Technology (ICIT), Buenos Aires, Argentina, 2020, pp. 901−906.

[25] H. Saadat, Power System Analysis, WCB/McGraw-Hill, 1999.

[26] C.A.B. Karim, M.A. Zamee, Design and analysis of pole-placement controller for dynamic stability improvement of VSC-HVDC based power system, in: 2014 9th International Forum on Strategic Technology (IFOST), Cox's Bazar, 2014, pp. 272−275.

[27] C. Olalla, R. Leyva, A. El Aroudi, I. Queinnec, Robust LQR control for PWM converters: an LMI approach, IEEE Trans. Ind. Electron. 56 (7) (July 2009) 2548−2558.

[28] B. Kedjar, K. Al-Haddad, DSP-based implementation of an LQR with integral action for a three-phase three-wire shunt active power filter, IEEE Trans. Ind. Electron. 56 (8) (August 2009) 2821−2828.

This book belongs to Kitab Liaison (ocd1996@gmail.com) Copyright Elsevier 2023

[29] T. Qoria, et al., Tuning of AC voltage-controlled VSC based linear quadratic regulation, in: 2019 IEEE Milan PowerTech, Milan, Italy, 2019, pp. 1−6.

[30] U. Markovic, Z. Chu, P. Aristidou, G. Hug, LQR-based adaptive virtual synchronous machine for power systems with high inverter penetration, IEEE Trans. Sustain. Energy 10 (3) (July 2019) 1501−1512.

[31] M. Mohseni, S.M. Islam, A new vector-based hysteresis current control scheme for three-phase PWM voltage-source inverters, IEEE Trans. Power Electron. 25 (9) (September 2010) 2299−2309.

[32] M. Mohseni, S.M. Islam, M.A.S. Masoum, Enhanced hysteresis-based current regulators in vector control of DFIG wind turbines, IEEE Trans. Power Electron. 26 (1) (January 2011) 223−234.

[33] T. Ohnishi, Three phase PWM converter/inverter by means of instantaneous active and reactive power control, in: In Proceedings IECON '91: 1991 International Conference on Industrial Electronics, Control and Instrumentation, 1991, pp. 819−824.

[34] T. Noguchi, H. Tomiki, S. Kondo, I. Takahashi, Direct power control of PWM converter without power-source voltage sensors, IEEE Trans. Ind. Appl. 34 (3) (May-June 1998) 473−479.

[35] R. Datta, V.T. Ranganathan, Direct power control of grid-connected wound rotor induction machine without rotor position sensors, IEEE Trans. Power Electron. 16 (3) (May 2001) 390−399.

[36] Y. Zhang, Z. Li, Y. Zhang, W. Xie, Z. Piao, C. Hu, Performance improvement of direct power control of PWM rectifier with simple calculation, IEEE Trans. Power Electron. 28 (7) (July 2013) 3428−3437.

[37] D. Zhi, L. Xu, B.W. Williams, Improved direct power control of grid-connected DC/AC converters, IEEE Trans. Power Electron. 24 (5) (May 2009) 1280−1292.

[38] M. Malinowski, M.P. Kazmierkowski, S. Hansen, F. Blaabjerg, G.D. Marques, Virtual-flux-based direct power control of three-phase PWM rectifiers, IEEE Trans. Ind. Appl. 37 (4) (July-August 2001) 1019−1027.

[39] D. Choi, K. Lee, Dynamic performance improvement of AC/DC converter using model predictive direct power control with finite control set, IEEE Trans. Ind. Electron. 62 (2) (February 2015) 757−767.

[40] P. CortÉs, J. RodrÍguez, P. Antoniewicz, M. Kazmierkowski, Direct power control of an AFE using predictive control, IEEE Trans. Power Electron. 23 (5) (September 2008) 2516−2523.

[41] R. Vargas, U. Ammann, J. RodrÍguez, Predictive approach to increase efficiency and reduce switching losses on matrix converters, IEEE Trans. Power Electron. 24 (4) (April 2009) 894−902.

[42] W. Xie, X.C. Wang, F.X. Wang, et al., Finite-control-set model predictive torque control with a deadbeat solution for PMSM drives, IEEE Trans. Ind. Electron. 62 (9) (September 2015) 5402−5410.

[43] R. Vargas, P. Cortes, U. Ammann, J. Rodriguez, J. Pontt, Predictive control of a three-phase neutral-point-clamped inverter, IEEE Trans. Ind. Electron. 54 (5) (October 2007) 2697−2705.

[44] Y. Zhang, W. Xie, Z. Li, Y. Zhang, Model predictive direct power control of a PWM rectifier with duty cycle optimization, IEEE Trans. Power Electron. 28 (11) (November 2013) 5343−5351.

This book belongs to Kitab Liaison (ocd1996@gmail.com) Copyright Elsevier 2023

[45] Y. Zhang, W. Xie, Z. Li, Y. Zhang, Low-complexity model predictive power control: double-vector-based approach, IEEE Trans. Ind. Electron. 61 (11) (November 2014) 5871−5880.

[46] H. Fang, Z. Zhang, X. Feng, R. Kennel, Ripple-reduced model predictive direct power control for active front-end power converters with extended switching vectors and time-optimised control, IET Power Electron. 9 (9) (September 2016) 1914−1923.

[47] Y. Zhang, Y. Peng, H. Yang, Performance improvement of two-vectors-based model predictive control of PWM rectifier, IEEE Trans. Power Electron. 31 (8) (August 2016) 6016−6030.

[48] F. Lin, L. Teng, P. Shieh, Intelligent adaptive backstepping control system for magnetic levitation apparatus, IEEE Trans. Magn. 43 (5) (May 2007) 2009−2018.

[49] B. Xian, J. Guo, Y. Zhang, Adaptive backstepping tracking control of a 6-DOF unmanned helicopter, IEEE/CAA J. Autom. Sinica 2 (1) (January 2015) 19−24.

[50] C. Peng, Y. Bai, X. Gong, Q. Gao, C. Zhao, Y. Tian, Modeling and robust backstepping sliding mode control with adaptive RBFNN for a novel coaxial eight-rotor UAV, IEEE/CAA J. Autom. Sinica 2 (1) (January 2015) 56−64.

[51] K. Kim, Y. Kim, Robust backstepping control for slew maneuver using nonlinear tracking function, IEEE Trans. Contr. Syst. Technol. 11 (6) (2003) 822−829.

[52] S.M.J. Rastegar Fatemi, N.R. Abjadi, J. Soltani, S. Abazari, Speed sensorless control of a six-phase induction motor drive using backstepping control, IET Power Electron. 7 (1) (January 2014) 114−123.

[53] M. Salimi, J. Soltani, G.A. Markadeh, N.R. Abjadi, Indirect output voltage regulation of DC-DC buck/boost converter operating in continuous and discontinuous conduction modes using adaptive backstepping approach, IET Power Electron. 6 (4) (April 2013) 732−741.

[54] G. Wang, R. Wai, Y. Liao, Design of backstepping power control for grid-side converter of voltage source converter-based high-voltage dc wind power generation system, IET Renew. Power Gener. 7 (2) (March 2013) 118−133.

[55] D. Sun, X. Wang, Y. Fang, Backstepping direct power control without phase-locked loop of AC/DC converter under both balanced and unbalanced grid conditions, IET Power Electron. 9 (8) (2016) 1614−1624.

[56] V.I. Utkin, Sliding mode control design principles and applications to electric drives, IEEE Trans. Ind. Electron. 40 (1) (February 1993) 23−36.

[57] J. Hu, L. Shang, Y. He, Z.Q. Zhu, Direct active and reactive power regulation of grid-connected DC/AC converters using sliding mode control approach, IEEE Trans. Power Electron. 26 (1) (January 2011) 210−222.

[58] A. Hemdani, M. Dagbagi, W.M. Naouar, L. Idkhajine, I. Slama Belkhodja, E. Monmasson, Indirect sliding mode power control for three phase grid connected power converter, IET Power Electron. 8 (6) (2015) 977−985, 6.

[59] J. Hu, H. Nian, B. Hu, Y. He, Z.Q. Zhu, Direct active and reactive power regulation of DFIG using sliding-mode control approach, IEEE Trans. Energy Convers. 25 (4) (December 2010) 1028−1039.

[60] R.P. Burgos, E.P. Wiechmann, J. Holtz, Complex state-space modeling and nonlinear control of active front-end converters, IEEE Trans. Ind. Electron. 52 (2) (April 2005) 363−377.

[61] K.H. Kim, M.J. Youn, A nonlinear speed control for a PM synchronous motor using a simple disturbance estimation technique, IEEE Trans. Ind. Electron. 49 (3) (June 2002) 524−535.

This book belongs to Kitab Liaison (ocd1996@gmail.com) Copyright Elsevier 2023

[62] H. Chen, Z. Xu, F. Zhang, Nonlinear control for VSC based HVDC system, in: 2006 IEEE Power Engineering Society General Meeting, Montreal, Que., 2006, pp. 1−5, p. 5.

[63] H. Abootorabi Zarchi, J. Soltani, G. Arab Markadeh, Adaptive input-output feedback-linearization-based torque control of synchronous reluctance motor without mechanical sensor, IEEE Trans. Ind. Electron. 57 (1) (January 2010) 375−384.

[64] J. Matas, M. Castilla, J.M. Guerrero, L. Garcia de Vicuna, J. Miret, Feedback linearization of direct-drive synchronous wind-turbines via a sliding mode approach, IEEE Trans. Power Electron. 23 (3) (May 2008) 1093−1103.

[65] L. Yacoubi, K. Al-Haddad, F. Fnaiech, L.-A. Dessaint, A DSP-based implementation of a new nonlinear control for a three-phase neutral point clamped boost rectifier prototype, IEEE Trans. Ind. Electron. 52 (1) (February 2005) 197−205.

[66] D.E. Kim, D.C. Lee, Feedback linearization control of three-phase UPS inverter systems, IEEE Trans. Ind. Electron. 57 (3) (March 2010) 963−968.

[67] W. Gil-González, O.D. Montoya, A. Garces, Direct power control for VSC-HVDC systems: an application of the global tracking passivity-based PI approach, Int. J. Electr. Power Energy Syst. 110 (2019) 588−597.

[68] L. Harnefors, L. Zhang, M. Bongiorno, Frequency-domain passivity based current controller design, IET Power Electron. 1 (4) (December 2008) 455−465.

[69] Y. Gui, Y.O. Lee, Y. Han, C.C. Chung, Novel passivity-based controller design for back-to-back STATCOM with asymmetrically structured converters, in: In IEEE Power and Energy Society General Meeting, 2012.

[70] Y. Gui, B. Wei, M. Li, J.M. Guerrero, J.C. Vasquez, Passivity-based coordinated control for islanded AC microgrid, Appl. Energy 229 (2018) 551−561.

[71] L. Harnefors, A. Yepes, A. Vidal, J. Doval-Gandoy, Passivity-based controller design of grid-connected VSCs for prevention of electrical resonance instability, IEEE Trans. Ind. Electron. 62 (2) (2014) 702−710.

[72] Y. Gui, W. Kim, C.C. Chung, Passivity-based control with nonlinear damping for type 2 STATCOM systems, IEEE Trans. Power Syst. 31 (4) (2016) 2824−2833.

[73] Z. Yao, S. Lahaie, V. Rajagopalan, Robust compensator of harmonics and reactive power, In Proc. IEEE PESC (1995) 215−220.

[74] A. Vidal, et al., A method for identification of the equivalent inductance and resistance in the plant model of current-controlled grid-tied converters, IEEE Trans. Power Electron. 30 (12) (December 2015) 7245−7261.

[75] A. Vidal, A.G. Yepes, F.D. Freijedo, J. Malvar, Ó. López, J. Doval-Gandoy, A technique to estimate the equivalent loss resistance of grid-tied converters for current control analysis and design, IEEE Trans. Power Electron. 30 (3) (March 2015) 1747−1761.

[76] T.D. Do, V.Q. Leu, Y. Choi, H.H. Choi, J. Jung, An adaptive voltage control strategy of three-phase inverter for stand-alone distributed generation systems, IEEE Trans. Ind. Electron. 60 (12) (December 2013) 5660−5672.

[77] I. Benlaloui, S. Drid, L. Chrifi-Alaoui, M. Ouriagli, Implementation of a new MRAS speed sensorless vector control of induction machine, IEEE Trans. Energy Convers. 30 (2) (June 2015) 588−595.

[78] P. Chevrel, F. Auger, M. Machmoum, "H_∞-control for a single phase active power filter: a systematic approach, In Proc. IEEE PESC (1996) 1112−1118.

[79] J. Doyle, K. Glover, P.P. Khargonekar, B.A. Francis, "State space solution to standard H_2 and H_∞ control problem, IEEE Trans. Autom. Control 34 (August 1989) 831−847.

[80] P. Gahinet, P. Apkarian, "Linear matrix inequality approach to H_∞ control, Int. J. Robust Nonlinear Control 4 (1994) 421−448.

This book belongs to Kitab Liaison (ocd1996@gmail.com) Copyright Elsevier 2023

[81] D. McFarlane, K. Glover, "A loop shaping desing procedure using H_∞ synthesis, IEEE Trans. Automat. Contr. 37 (June 1992) 759−769.

[82] T.S. Lee, S.J. Chiang, J.M. Chang, $H\infty$ loop-shaping controller designs for the single-phase UPS inverters, IEEE Trans. Power Electron. 16 (4) (July 2001) 473−481.

[83] C.M. Bishop, Pattern Recognition and Machine Learning, Springer, 2006.

[84] I. Goodfellow, Y. Bengio, A. Courville, Deep Learning, MIT press, 2016.

[85] T. Wu, Z. Wang, B. Ozpineci, M. Chinthavali, S. Campbell, Automated heatsink optimization for air-cooled power semiconductor modules, IEEE Trans. Power Electron. 34 (6) (June 2019) 5027−5031.

[86] X. Zhan, W. Wang, H. Chung, A neural-network-based color control method for multi-color LED systems, IEEE Trans. Power Electron. 34 (8) (August 2019) 7900−7913.

[87] C. Wei, Z. Zhang, W. Qiao, L. Qu, Reinforcement-learning-based intelligent maximum power point tracking control for wind energy conversion systems, IEEE Trans. Ind. Electron. 62 (10) (October 2015) 6360−6370.

[88] C. Wei, Z. Zhang, W. Qiao, L.Y. Qu, An adaptive network based reinforcement learning method for MPPT control of PMSG wind energy conversion systems, IEEE Trans. Power Electron. 31 (11) (November 2016) 7837−7848.

[89] I. Bandyopadhyay, P. Purkait, C. Koley, Performance of a classifier based on time-domain features for incipient fault detection in inverter drives, IEEE Trans. Ind. Inf. 15 (1) (January 2019) 3−14.

[90] A.E. Mejdoubi, H. Chaoui, J. Sabor, H. Gualous, Remaining useful life prognosis of supercapacitors under temperature and voltage aging conditions, IEEE Trans. Ind. Electron. 65 (5) (May 2018) 4357−4367.

[91] S. Li, M. Fairbank, C. Johnson, D.C. Wunsch, E. Alonso, J.L. Proao, Artificial neural networks for control of a grid-connected rectifier/inverter under disturbance, dynamic and power converter switching conditions, IEEE Trans. Neural Netw. & Learn. Syst. 25 (4) (April 2014) 738−750.

[92] M.A. Dzieniakowski, M.P. Kazmierkowski, Self-tuned fuzzy PI current controller for PWM-VSI, in: In Proc. EPE Conf., Seville, Spain, 1995, pp. 1.308−1.313.

[93] M.G. Simoes, B.K. Bose, R.J. Spiegel, Design and performance evaluation of a fuzzy-logic-based variable-speed wind generation system, IEEE Trans. Ind. Appl. 33 (4) (July-August 1997) 956−965.

[94] M. Glavic, R. Fonteneau, D. Ernst, Reinforcement learning for electric power system decision and control: past considerations and perspectives, IFAC Papersonline 50 (1) (July 2017) 6918−6927.

[95] P. Kofinas, S. Doltsinis, A.I. Dounis, G.A. Vouros, A reinforcement learning approach for MPPT control method of photovoltaic sources, Renew. Energy 108 (August 2017) 461−473.

This book belongs to Kitab Liaison (ocd1996@gmail.com) Copyright Elsevier 2023

This page intentionally left blank

This book belongs to Kitab Liaison (ocd1996@gmail.com)

Copyright Elsevier 2023

Chapter 2

Robust design and passivity control methods

Yonghao Gui[1], Jianzhe Liu[2], Jan Dimon Bendtsen[1], Jakob Stoustrup[1]
[1]*Department of Energy Technology, Aalborg University, Aalborg, Denmark;* [2]*Argonne National Laboratory, Lemont, IL, United States*

2.1 Introduction

Power electronic systems are used in the wide range of applications like flexible AC transmission systems, renewable energy sources (RESs) (e.g., solar and wind), and smart grids [1–4]. Numerous control strategies have been researched for those power electronic systems to improve their stability, performance, robustness, etc.

Linear control methods (e.g., proportional and integral (PI), linear quadratic regulator (LQR), linear quadratic Gaussian (LQG), etc.) have been designed to control power electronic systems. Normally, for three-phase voltage source converters, a PI control with a decoupling feedforward term is designed separately for controlling d–q axes currents in a synchronously rotating reference frame [5]. Though it is easy to do stability analysis when using the PI methods, there are some disadvantages, e.g., the performance will be highly sensitive to the accuracy of controller gains and parameters, the completeness of the current decoupling, the grid voltage conditions, etc. Linear optimal controller based on LQR/LQG control, with better robustness properties than a PI controller, has also been designed for inverters [6,7], and wind turbine (WT) systems [8]. However, due to the fact that these control strategies are designed via a model linearized around the nominal operating point, and inherently nonlinear property of power electronic systems, it is difficult to guarantee a uniform performance in the range of the whole operating points by using the aforementioned techniques.

To handle these problems, various nonlinear control strategies have been designed in the literature. One of the efficient control strategies for nonlinear systems to handle trajectory tracking problems is input–output feedback linearization method, since a linearized closed-loop system is obtained [9]. The input–output linearization (IOL) method has been applied to rectifiers [10,11], WT systems [12,13], STATCOMs [14,15], modular multilevel

Control of Power Electronic Converters and Systems. https://doi.org/10.1016/B978-0-12-819432-4.00010-X
Copyright © 2021 Elsevier Ltd. All rights reserved.

This book belongs to Kitab Liaison (ocd1996@gmail.com) Copyright Elsevier 2023

converters [16], etc. With the input−output feedback linearization method, it is easy to obtain a satisfactory tracking performance of the output and to guarantee the stability of the output. However, the performance and stability of the internal dynamics are not easy to be guaranteed. In addition, the input−output feedback linearization method is sensitive to the model mismatches, parameter uncertainties, disturbances, etc.

To improve the robustness properties, sliding mode control was introduced in Ref. [17]. The sliding mode control method guarantees the trajectory converges to a specified manifold in finite time, and once it reaches the target manifold, it then remains on it even in the presence of parametric uncertainties. Due to such advantages, the sliding mode control method has been applied to various applications such as rectifiers [18−20], WT systems [21,22], STATCOM [23,24], modular multilevel converter [25,26], etc. The sliding mode control method has advantages that it obtains a fast-transient response and has robustness property against parameter uncertainties. However, one disadvantage of the method is the issue of *chattering* due to the requirement of variable switching frequency.

The aforementioned control methods are designed without the consideration of the system's physical structure such as its passivity feature, which describes energy conservation, acting a central role in control techniques [27]. Employing passivity-based control (PBC), it is able to improve the robustness and simplify the implementation compared with the aforementioned control methods because it prevents the system canceling the nonlinearities that are helpful for its stability [28]. Due to these advantages, PBC is employed into WT system [29], STATCOM [30], modular multilevel converter [31], etc.

In this chapter, we introduce how to design robust controllers as well as PBC methods for power electronic systems. At first, a state space model of the power electronic systems, e.g., grid-connected voltage source inverter and STATCOM, is given in Section 2.2. Then, a robust controller is designed for a grid-connected voltage source inverter in Section 2.3. In Section 2.4, a robust small-signal stabilization control design for DC microgrids is introduced. In Section 2.5, a PBC design for an islanded microgrid and multipulse STATCOM is shown. Finally, the conclusions and future perspectives are summarized in Section 2.6.

2.2 State space model of power electronic systems

In this section, a state space model of grid-connected voltage source inverter is described in order to use modern control theory rather than traditional control theory such as a transfer function. Moreover, an active and reactive power−based model is introduced where direct power control (DPC) method is applied.

This book belongs to Kitab Liaison (ocd1996@gmail.com) Copyright Elsevier 2023

2.2.1 Introduction

The calculations of a three-phase AC power system are substantially simplified by introducing "Phasor" concept, which is an arrow in the complex plane that has a one-to-one relation with a sinusoidal signal as shown in Fig. 2.1. For example, the voltage has the angular frequency, ω, then a radius with a length $\sqrt{2}$ times the length of the phasor rotates counterclockwise in the complex plane with the same frequency [32]. The phasor of a signal represents a sinusoidal signal as follows: the length of the voltage phasor equals the effective or the RMS value of the signal. Moreover, the angle of the signal equals to the phase shift of the signal with respect to a voltage reference.

For the sake of the simplicity of the analysis for three-phase circuits, the Clark transformation is introduced, which transforms a three-phase model to one in the stationary reference frame ($\alpha-\beta$ frame), as shown in Fig. 2.2. The Clark transformation is given as follows:

$$T_{abc2\alpha\beta} = \frac{2}{3}\begin{bmatrix} 1 & -\frac{1}{2} & -\frac{1}{2} \\ 0 & -\frac{\sqrt{3}}{2} & -\frac{\sqrt{3}}{2} \end{bmatrix}. \tag{2.1}$$

Then, in order to obtain a model in the synchronously rotating reference frame, Park transformation is given as follows:

$$T_{\alpha\beta 2dq} = \begin{bmatrix} \cos(\theta) & \sin(\theta) \\ -\sin(\theta) & \cos(\theta) \end{bmatrix} \tag{2.2}$$

where θ is a phase angle of the grid voltage, which is obtained via a phase-locked loop (PLL) system in a grid-connected power converter. It should be noted that, the d-axis is always coincident with the instantaneous voltage, whereas the q-axis is in quadrature with it, i.e., $v_{gd} = V_g$ and $v_{gq} = 0$, as it is shown in Fig. 2.3.

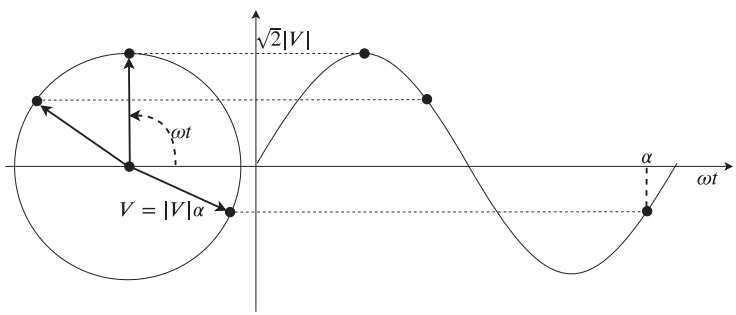

FIGURE 2.1 Relationship between a phasor and a sinusoidal of signal.

This book belongs to Kitab Liaison (ocd1996@gmail.com) Copyright Elsevier 2023

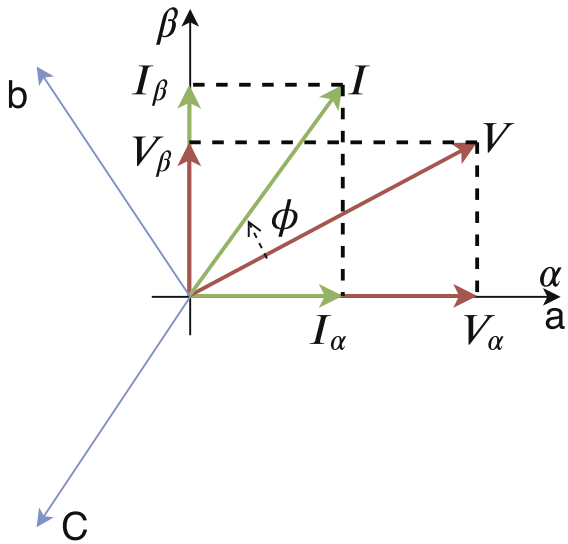

FIGURE 2.2 Transformation from *abc* frame to $\alpha-\beta$ frame.

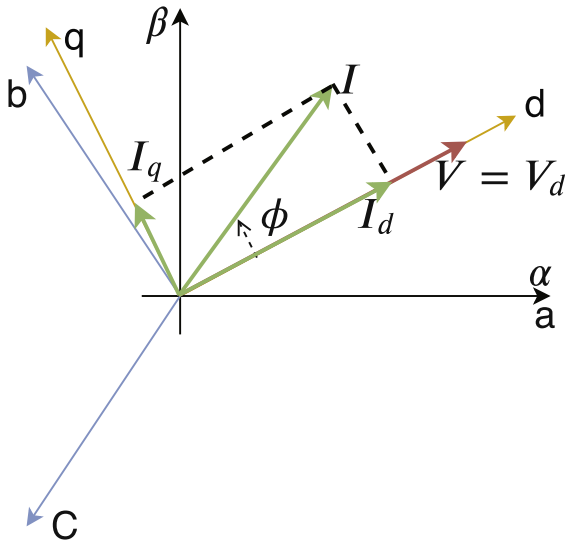

FIGURE 2.3 Transformation from $\alpha-\beta$ frame to $d-q$ frame.

2.2.2 Grid-connected voltage source inverter

A DPC model of voltage source inverter is briefly introduced where the active and reactive powers are directly controlled without inner-loop current controller.

This book belongs to Kitab Liaison (ocd1996@gmail.com) Copyright Elsevier 2023

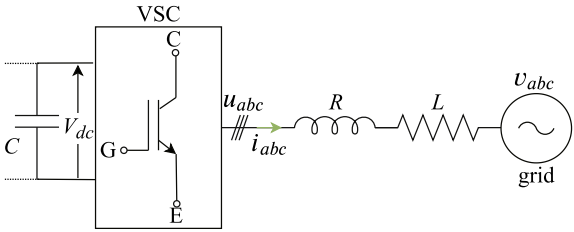

FIGURE 2.4 Grid-connected voltage source inverter.

Fig. 2.4 shows a two-level grid-connected voltage source inverter, which uses an L-filter to filter out the high frequency of harmonics from the switching operation. At the DC side, RESs (e.g., wind and PV) or energy storage systems (ESSs) can be connected through a capacitor C. For the AC side, the dynamics regarding the grid voltages, the output voltages, and the output currents is able to be formulated as follows:

$$\begin{aligned} u_a &= Ri_a + L\frac{di_a}{dt} + v_{ga}, \\ u_b &= Ri_b + L\frac{di_b}{dt} + v_{gb}, \\ u_c &= Ri_c + L\frac{di_c}{dt} + v_{gc}, \end{aligned} \tag{2.3}$$

where $v_{ga,b,c}$, $i_{a,b,c}$, and $u_{a,b,c}$ indicate the three phases of grid voltages, the output currents, and the output voltages at the inverter, respectively. R and L indicate the filter resistance and inductance, respectively. It should be noted that we assume that $R_a = R_b = R_c = R$ and $L_a = L_b = L_c = L$. In this study, a balanced grid voltage condition will be considered. Consequently, the dynamics in Eq. (2.3) is transformed in the stationary reference frame through the Clark transformation introduced in Eq. (2.1) such as

$$\begin{aligned} u_\alpha &= Ri_\alpha + L\frac{di_\alpha}{dt} + v_{g\alpha}, \\ u_\beta &= Ri_\beta + L\frac{di_\beta}{dt} + v_{g\beta}, \end{aligned} \tag{2.4}$$

where u_α and u_β are the inverter output voltages, i_α and i_β are the output currents, and $v_{g\alpha}$ and $v_{g\beta}$ are the grid voltages in the $\alpha-\beta$ frame, respectively.

The instantaneous active and reactive powers of the inverter in the $\alpha-\beta$ frame is given as

This book belongs to Kitab Liaison (ocd1996@gmail.com) Copyright Elsevier 2023

$$P = \frac{3}{2(v_{g\alpha} i_\alpha + v_{g\beta} i_\beta)},$$
$$Q = \frac{3}{2(v_{g\beta} i_\alpha - v_{g\alpha} i_\beta)}, \tag{2.5}$$

where P and Q indicate the instantaneous active and reactive powers of the inverter, respectively. Variations in P and Q are able to be expressed via the grid voltages and output currents variations by differentiating Eq. (2.5) as follows:

$$\frac{dP}{dt} = \frac{3}{2}\left(i_\alpha \frac{dv_{g\alpha}}{dt} + v_{g\alpha}\frac{di_\alpha}{dt} + i_\beta \frac{dv_{g\beta}}{dt} + v_{g\beta}\frac{di_\beta}{dt}\right),$$
$$\frac{dQ}{dt} = \frac{3}{2}\left(i_\alpha \frac{dv_{g\beta}}{dt} + v_{g\beta}\frac{di_\alpha}{dt} - i_\beta \frac{dv_{g\alpha}}{dt} - v_{g\alpha}\frac{di_\beta}{dt}\right). \tag{2.6}$$

Since only a balanced nondistorted grid voltage is considered, the following relationship can be formulated:

$$v_{g\alpha} = V_g \cos(\omega t),$$
$$v_{g\beta} = V_g \sin(\omega t), \tag{2.7}$$

where V_g indicates the amplitude of the grid voltage. Furthermore, the grid voltage variations can be formulated by differentiating Eq. (2.7).

$$\frac{dv_{g\alpha}}{dt} = -\omega V_g \sin(\omega t) = -\omega v_{g\beta},$$
$$\frac{dv_{g\beta}}{dt} = \omega V_g \cos(\omega t) = \omega v_{g\alpha}. \tag{2.8}$$

Substituting Eqs. (2.4) and (2.8) into Eq. (2.6), a state space model of P and Q can be expressed such as

$$\frac{dP}{dt} = -\frac{R}{L}P - \omega Q + \frac{3}{2L\left(v_{g\alpha}u_\alpha + v_{g\beta}u_\beta - V_g^2\right)},$$
$$\frac{dQ}{dt} = \omega P - \frac{R}{L}Q + \frac{3}{2L(v_{g\beta}u_\alpha - v_{g\alpha}u_\beta)}. \tag{2.9}$$

Notice that the dynamics in Eq. (2.9) is a nonlinear multi-input-multi-output (MIMO) system. Notice also that $V_g = \sqrt{v_{\alpha,g}^2 + v_{\beta,g}^2}$.

2.2.3 An example of a VSC (STATCOM)

In Fig. 2.5, a STATCOM system injects/absorbs the reactive power to the grid to enhance voltage stability and power quality in the transmission line. The inductance, L, denotes the leakage of the power transformer. The resistance, R_s,denotes the converter and transformer conduction losses, whereas the

This book belongs to Kitab Liaison (ocd1996@gmail.com) Copyright Elsevier 2023

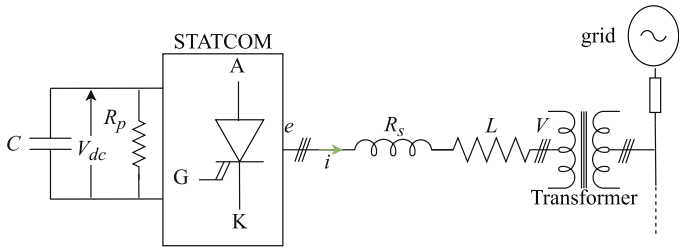

FIGURE 2.5 Equivalent circuit of an STATCOM.

resistance, R_p, at the DC link denotes the switching losses of the STATCOM where a capacitor, C, connects in parallel. $V_{(a,b,c)}$ denote the phase-to-neutral bus voltages. $e_{(a,b,c)}$ denote the voltage of the STATCOM at the AC side [33]. The STATCOM dynamics is formulated as

$$\begin{bmatrix} \frac{dI'_a}{dt} \\ \frac{dI'_b}{dt} \\ \frac{dI'_c}{dt} \end{bmatrix} = \begin{bmatrix} -\frac{R'_s\omega_b}{L'} & 0 & 0 \\ 0 & -\frac{R'_s\omega_b}{L'} & 0 \\ 0 & 0 & -\frac{R'_s\omega_b}{L'} \end{bmatrix} \begin{bmatrix} I'_a \\ I'_b \\ I'_c \end{bmatrix} + \begin{bmatrix} e'_a - V'_a \\ e'_b - V'_b \\ e'_c - V'_c \end{bmatrix} \tag{2.10}$$

where $I_{(a,b,c)}$ represent three-phase currents. ω_b is the angular speed at the nominal frequency of the grid. The state variables and parameters with the apostrophe represent the values in per-unit based on the following definitions:

$$z_{base} = \frac{V_{base}}{I_{base}}.\ I'_{(a,b,c)} = \frac{i_{(a,b,c)}}{I_{base}},\ V'_{(a,b,c)} = \frac{V_{(a,b,c)}}{V_{base}},\ e'_{(a,b,c)} = \frac{e_{(a,b,c)}}{V_{base}},$$

$$L' = \frac{\omega_b L}{z_{base}},\ C' = \frac{1}{\omega_b C z_{base}},\ R'_s = \frac{R_s}{z_{base}},\ R'_p = \frac{R_p}{z_{base}}$$

By applying the transformation Eqs. (2.1) and (2.2) into Eq. (2.10), a model of STATCOM can be formulated on the $d-q$ frame as

$$\begin{bmatrix} \dot{I'_d} \\ \dot{I'_q} \\ \dot{V'_{dc}} \end{bmatrix} = \begin{bmatrix} -\frac{R'_s\omega_b}{L'}I'_d + \omega I'_q + \frac{k\omega_b}{L'}V'_{dc}cos\alpha - \frac{\omega_b}{L'}|V'| \\ -\omega I'_d - \frac{R'_s\omega_b}{L'}I'_q + \frac{k\omega_b}{L'}V'_{dc}sin\alpha \\ -\frac{3}{2}kC'\omega_b I'_d cos\alpha - \frac{3}{2}kC'\omega_b I'_q sin\alpha - \frac{\omega_b C'}{R'_p}V'_{dc} \end{bmatrix}, \tag{2.11}$$

where I'_d, I'_q, and V'_{dc} indicate the active current, reactive current, and DC-link voltage, respectively. Since the synchronously rotating reference frame is

This book belongs to Kitab Liaison (ocd1996@gmail.com) Copyright Elsevier 2023

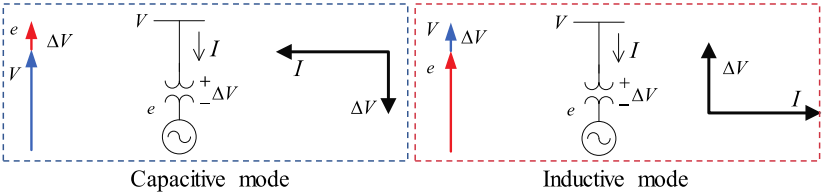

FIGURE 2.6 Operation modes of STATCOM.

oriented along the grid voltage, V_q' is zero. ω is the angular velocity of the fundamental frequency of the grid voltage. α is the phase-shift angle by which the converter voltage vectors $e_{a,b,c}$ lead the line voltage vectors $V_{a,b,c}$. It should be noted that α is only one control input. k is a constant factor relating the DC-link voltage to the maximum amplitude of the voltage at the STATCOM AC side. In this study, when the STATCOM voltage is larger than the grid voltage, the STATCOM works in the capacitive mode, i.e., I_q' is negative and the STATCOM generates the reactive power to the grid as shown in Fig. 2.6A. When the STATCOM voltage is smaller than the grid voltage, the STATCOM operates in the inductive mode, i.e., I_q' is positive and it absorbs the reactive power from the grid as shown in Fig. 2.6B.

2.3 Robust controller design

In this section, robust but simple control law, called a voltage-modulated direct power control (VM-DPC) with additional damping scheme is introduced for grid-connected inverter, as shown in Fig. 2.7. The main objective of the VM-DPC method is to obtain not only a fast-transient response but also a good steady-state performance, where the power ripples as well as total harmonics distortion (THD) of the output currents are decreased. The VM-DPC with additional damping method has four components. The first one is a nonlinear controller, which defines the VM inputs that transform the inverter system into a linear time-invariant (LTI) one. Then, a feedback controller is designed to control active and reactive powers independently. The VM-DPC obtains two separate second-order error dynamics of active and reactive powers, which guarantee the exponentially stable of the closed-loop system in the whole operating range. The third one is the additional damping term, which is designed to enhance the robustness properties against uncertainties in terms of the model and parameter as well as guarantee the exponential stability. Finally, the last one is the inverse of VM, which generates the original control input of the inverter.

This book belongs to Kitab Liaison (ocd1996@gmail.com) Copyright Elsevier 2023

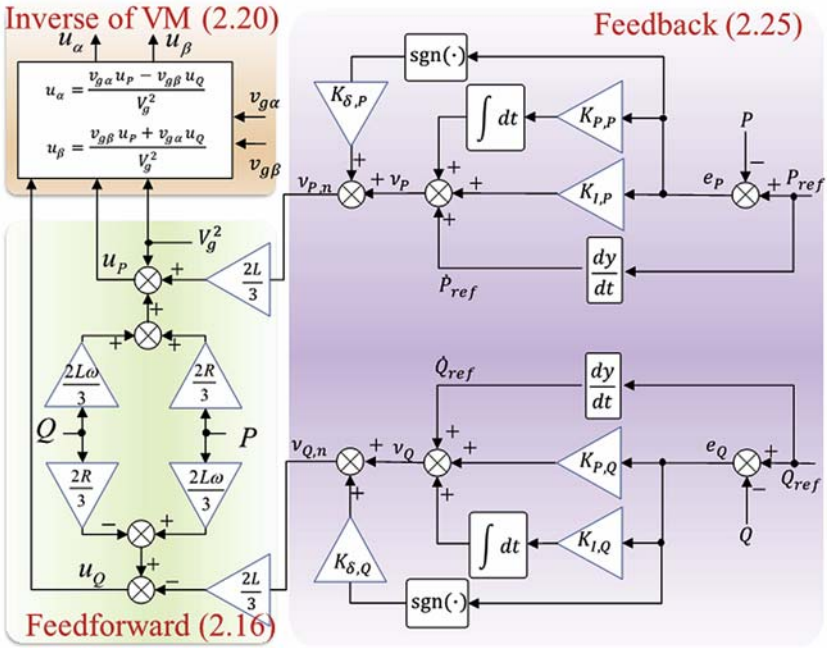

FIGURE 2.7 Control block diagram of the voltage-modulated (VM) direct power control with addition damping.

2.3.1 Voltage-modulated direct power control

It should be noted that the dynamics Eq. (2.9) is a time-varying MIMO system. In addition, the control inputs are coupled with the states P and Q. Let us define the VM inputs as [34].

$$\begin{aligned} u_P &:= v_{g\alpha}u_\alpha + v_{g\beta}u_\beta, \\ u_Q &:= -v_{g\beta}u_\alpha + v_{g\alpha}u_\beta. \end{aligned} \tag{2.12}$$

Through the relationship of the grid voltage in Eq. (2.7), the new VM inputs are the new control inputs expressed in the $d-q$ frame such as

$$\begin{bmatrix} u_P \\ u_Q \end{bmatrix} = V_g \begin{bmatrix} \cos(\omega t) & \sin(\omega t) \\ -\sin(\omega t) & \cos(\omega t) \end{bmatrix} \begin{bmatrix} u_\alpha \\ u_\beta \end{bmatrix} = V_g \begin{bmatrix} u_d \\ u_q \end{bmatrix}, \tag{2.13}$$

where u_d and u_q are the inverter voltages on the $d-q$ frame. V_g is the magnitude of the grid voltage. From Eq. (2.13), it can be seen that the VM inputs are the inputs in the $d-q$ frame. The system in Eq. (2.9) can be rewritten as

This book belongs to Kitab Liaison (ocd1996@gmail.com)
Copyright Elsevier 2023

$$\begin{aligned} \frac{dP}{dt} &= -\frac{R}{L}P - \omega Q + \frac{3}{2L\left(u_P - V_g^2\right)}, \\ \frac{dQ}{dt} &= \omega P - \frac{R}{L}Q - \frac{3}{2L}u_Q, \end{aligned} \tag{2.14}$$

where ω is angular frequency of the grid voltage. Notice that the system in Eq. (2.14) has been converted into a simple linear MIMO system.

2.3.2 Tracking controller

This subsection introduces a traditional tracking control strategy, which is designed to make P and Q to track their references exponentially. At first, let us define the following errors of P and Q:

$$\begin{aligned} e_P &:= P_{ref} - P, \\ e_Q &:= Q_{ref} - Q, \end{aligned} \tag{2.15}$$

where P_{ref} and Q_{ref} indicate the reference of P and Q, respectively. For the system in Eq. (2.9), we design a tracking control law consisting of a feedforward and feedback such as

$$u_P = \underbrace{V_g^2 + \frac{2R}{3}P + \frac{2L\omega}{3}Q}_{\text{feedforward}} + \underbrace{\frac{2L}{3}\nu_P}_{\text{feedback}}, u_Q = \underbrace{\frac{2L\omega}{3}P - \frac{2R}{3}Q}_{\text{feedforward}} - \underbrace{\frac{2L}{3}\nu_Q}_{\text{feedback}}, \tag{2.16}$$

where ν_P and ν_Q are the new feedback controller that can be designed as follows:

$$\begin{aligned} \nu_P &= \dot{P}_{ref} + K_{P,P}e_P + K_{I,P}\int_0^t e_P(\tau)d\tau, \\ \nu_Q &= \dot{Q}_{ref} + K_{P,Q}e_Q + K_{I,Q}\int_0^t e_Q(\tau)d\tau, \end{aligned} \tag{2.17}$$

where $K_{P,P}$, $K_{I,P}$, $K_{P,Q}$, and $K_{I,Q}$ are the controller gains. Substituting Eqs. (2.16) and (2.17) into Eq. (2.14), the following error dynamics can be obtained:

$$\begin{aligned} \dot{P}_{ref} - \dot{P} &= \dot{e}_P = -K_{P,P}e_P - K_{I,P}\int_0^t e_P(\tau)d\tau, \\ \dot{Q}_{ref} - \dot{Q} &= \dot{e}_Q = -K_{P,Q}e_Q - K_{I,Q}\int_0^t e_Q(\tau)d\tau. \end{aligned} \tag{2.18}$$

This book belongs to Kitab Liaison (ocd1996@gmail.com) Copyright Elsevier 2023

If we define $\dot{\psi}_P = e_P$ and $\dot{\psi}_Q = e_Q$, the error dynamics Eq. (2.18) are transformed into the following form:

$$\underbrace{\begin{bmatrix} \dot{e}_P \\ \dot{\psi}_P \\ \dot{e}_Q \\ \dot{\psi}_Q \end{bmatrix}}_{\dot{x}} = \underbrace{\begin{bmatrix} -K_{P,\mathrm{P}} & -K_{I,\mathrm{P}} & 0 & 0 \\ 1 & 0 & 0 & 0 \\ 0 & 0 & -K_{P,\mathrm{Q}} & -K_{I,\mathrm{Q}} \\ 0 & 0 & 1 & 0 \end{bmatrix}}_{A} \underbrace{\begin{bmatrix} e_P \\ \psi_P \\ e_Q \\ \psi_Q \end{bmatrix}}_{x} \tag{2.19}$$

From Eq. (2.19), it can be found that if $K_{P,P}$, $K_{I,P}$, $K_{P,Q}$, and $K_{I,Q}$ are larger than zero, then A is Hurwitz matrix, i.e., it has all negative eigenvalues, which guarantee the exponential stability. It should be noted that it is possible to design $K_{P,p}$, $K_{P,i}$, $K_{Q,p}$, and $K_{Q,i}$ with the consideration of the damping ratio and settling time of the closed-loop system [11]. Consequently, the original control inputs can be calculated through inverse of Eq. (2.12), which is formulated as follows:

$$u_\alpha = \frac{v_{g\alpha} u_P - v_{g\beta} u_Q}{V_g^2}, \; u_\beta = \frac{v_{g\beta} u_P + v_{g\alpha} u_Q}{V_g^2} \tag{2.20}$$

By using the VM-DPC method, the system in Eq. (2.9) is converted into an LTI MIMO system. Fig. 2.8 shows a comparison between the inputs of the conventional DPC and the VM-DPC when $P = 1$ kW and $Q = 1$ kVAr. It can be seen that the VM-DPC control inputs, u_P and u_Q, are constant, i.e., the VM-DPC has the same construction to the conventional vector current control designed on the $d-q$ frame, which has been proven in Ref. [3]. That means various linear control methods can be designed by using the VM-DPC concept to overcome the corresponding issues [35–40].

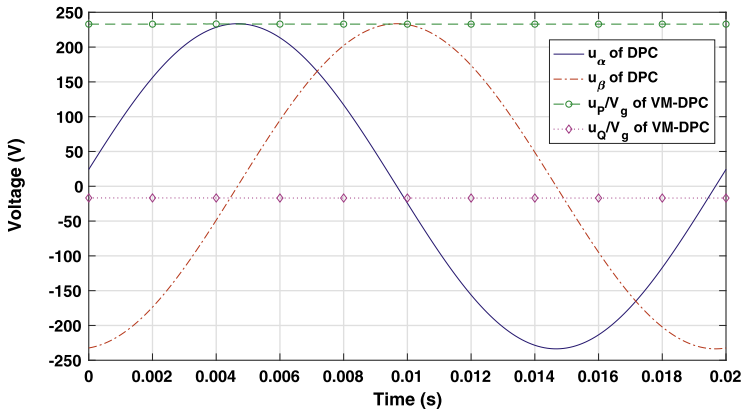

FIGURE 2.8 Conventional direct power control (DPC) and voltage-modulated direct power control (VM-DPC) of inputs.

This book belongs to Kitab Liaison (ocd1996@gmail.com)
Copyright Elsevier 2023

2.3.3 Robust control design

In a practical system, the stability obtained by Eq. (2.19) will be affected by uncertainties including measurement noises, parameter uncertainties, discretization errors, etc. Consequently, it is assumed that there exist some uncertainties as δ_P, δ_Q, and Δ in the LTI MIMO system Eq. (2.14), which are formulated as follows:

$$\begin{aligned} \dot{x} &= f_a(x, u_P.u_Q, \delta_P, \delta_Q) \\ &= \begin{bmatrix} -\dfrac{R}{L}x_1 - \omega x_2 + \dfrac{3}{2L\left(u_P - V_g^2\right)} + \delta_P \\ \\ \omega x_1 - \dfrac{R}{L}x_2 + \dfrac{3}{2L}u_Q + \delta_Q \end{bmatrix}, \end{aligned} \tag{2.21}$$

It should be noted that the uncertainties, δ_P and δ_Q, are bounded such as

$$0 \le |\delta_P| \le \Delta,\ 0 \le |\delta_Q| \le \Delta. \tag{2.22}$$

In the grid-connected voltage source inverter, the parameter uncertainties can, e.g., be the frequency, grid voltage, the inductance of filter, or change of gains in measurement. For a practical system with limited operating range, it should estimate an upper bound of uncertainties, Δ. From Eq. (2.19), it is always guaranteed the exponential stability of the nominal plant with the control law Eq. (2.16) in the operating range. The integral action in Eq. (2.17) is designed to compensate for any DC offset due to model or parameter uncertainties. Moreover, a small perturbation from the operation point is ultimately bounded through the exponential stability property [41]. Consequently, assumptions Eqs. (2.21) and (2.22) are reasonable without loss of generality.

When $\delta_P = 0$ and $\delta_Q = 0$, it has been proved that the closed loop is exponentially stable. When $\delta_P \neq 0$ or $\delta_Q \neq 0$, only δ_P and δ_Q terms are considered for the sake of simplicity. Let us define a Lyapunov function candidate as

$$V = \frac{1}{2}e_P^2 + \frac{1}{2}e_Q^2. \tag{2.23}$$

Then, the derivative of the Lyapunov function candidate Eq. (2.23) in terms of time is calculated such as

$$\dot{V} = e_P\dot{e}_P + e_Q\dot{e}_Q = e_P\left(\delta_P - K_{\delta,P}\mathrm{sgn}(e_P)\right) + e_Q\left(\delta_Q - K_{\delta,Q}\mathrm{sgn}(e_Q)\right). \tag{2.24}$$

This book belongs to Kitab Liaison (ocd1996@gmail.com) Copyright Elsevier 2023

If the new feedback controllers are taken as

$$\begin{aligned} \nu_{P,n} &= \dot{P}_{ref} + K_{P,P}e_P + K_{I,P}\int_0^t e_P(\tau)d\tau + K_{\delta,P}\mathrm{sgn}(e_P), \\ \nu_{Q,n} &= \dot{Q}_{ref} + K_{P,Q}e_Q + K_{I,Q}\int_0^t e_Q(\tau)d\tau + K_{\delta,Q}\mathrm{sgn}(e_Q), \end{aligned} \tag{2.25}$$

where $K_{\delta,P}$ and $K_{\delta,Q}$ are the new controller gains, then the derivative of the Lyapunov function candidate in terms of time is changed into the following one:

$$\dot{V} = e_P\big(\delta_P - K_{\delta,P}\mathrm{sgn}(e_P)\big) + e_Q\big(\delta_Q - K_{\delta,Q}\mathrm{sgn}(e_Q)\big). \tag{2.26}$$

If $K_{\delta,P} > \Delta$ and $K_{\delta,Q} > \Delta$ are taken, then

$$\dot{V} \le -K_{\Delta P}|e_P| - K_{\Delta Q}|e_Q|, \tag{2.27}$$

where $K_{\Delta P} = K_{\delta,P} - \Delta$ and $K_{\Delta Q} = K_{\delta,Q} - \Delta$.

Notice that the VM-DPC with additional damping term scheme presents the dynamics of the inverter on the $d-q$ frame without a PLL [3].

2.3.4 Simulation results

MATLAB/Simulink and PLECS are used to validate the control method introduced in this study. The grid-connected voltage source inverter is built in the PLECS, and the control strategy is built in MATLAB/Simulink. The performance of the VM-DPC is compared with the PBC-DPC proposed in Ref. [42], which obtains a better performance compared to the SMC-DPC designed in Ref. [43]. The parameters of the system are listed in Table 2.1.

Figs. 2.9 and Fig. 2.10 show the performance of the VM-DPC and PBC-DPC, respectively, when P changes from 0 W to 1 kW at 0.03 s and is back

TABLE 2.1 Parameters of system in simulation.

DC-link voltage	250 V	AC frequency	50 Hz
Line-to-line voltage (RMS)	133 V	Switching frequency	10 kHz
$R_{a,b,c}$	0.16 Ω	Sampling frequency	10 kHz
$L_{a,b,c}$	4 mH	Power rate	2 kVA
$K_{P,P}\&K_{P,Q}$	200	$K_{I,P}\&K_{I,Q}$	2000
$K_{\delta,'p}\&K_{\delta,Q}$	10		

This book belongs to Kitab Liaison (ocd1996@gmail.com) Copyright Elsevier 2023

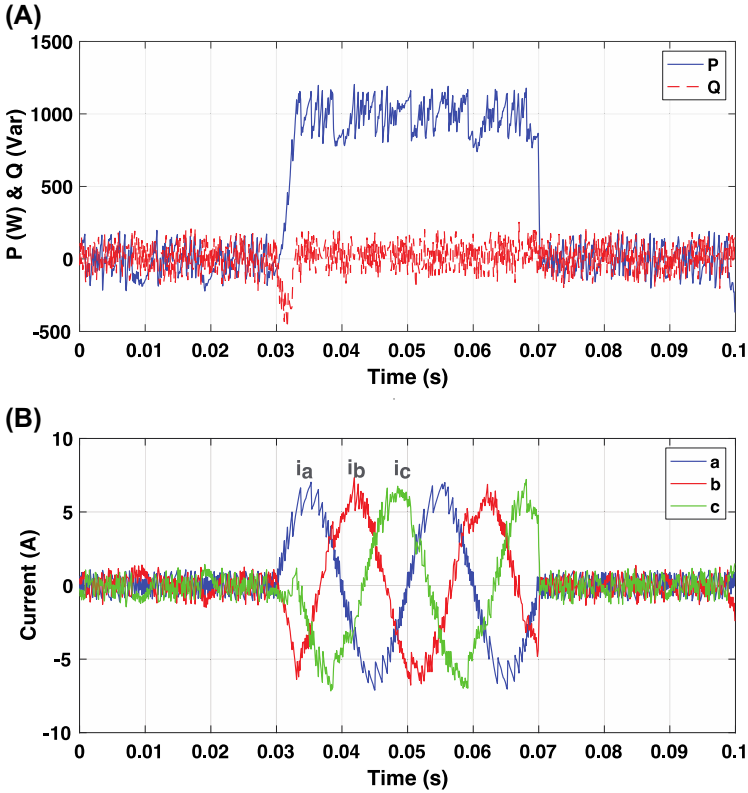

FIGURE 2.9 Simulation results of the PBC-DPC when Q is 0 VAr and P changes from 0 W to 1 kW. (A) P and Q, (B) output currents. *DPC*, direct power control; *PBC*, passivity-based control.

to 0 W at 0.07 s. Among this period, Q is regulated to 0 VAr. Comparing to P tracking performance of the PBC-DPC, the VM-DPC significantly reduces ripples both in P and Q as well as in the output current. The VM-DPC has no need to consider the switching delay as well as harmonics. Furthermore, the VM-DPC obtains two independent decoupled error dynamics of P and Q that guarantee the exponential stability in the operating range. Those features are similar with the vector current controller designed in the $d-q$ frame. Figs. 2.11 and Fig. 2.12 show the case when Q changes from 0 VAr to 1 kVAr at 0.03 s and then returns to 0 VAr at 0.07 s. P is regulated to 0 W. As it is similar with the case obtained from P tracking performance, the VM-DPC has smaller ripples both in P and Q as well as in output current compared to the PBC-DPC.

The steady-state performance (i.e., power ripples) is the main disadvantage of DPC methods compared with the vector current controller designed on the $d-q$ frame. However, the VM-DPC method overcomes the steady-state performance problem since two decoupled LTI error dynamics are obtained and

This book belongs to Kitab Liaison (ocd1996@gmail.com) Copyright Elsevier 2023

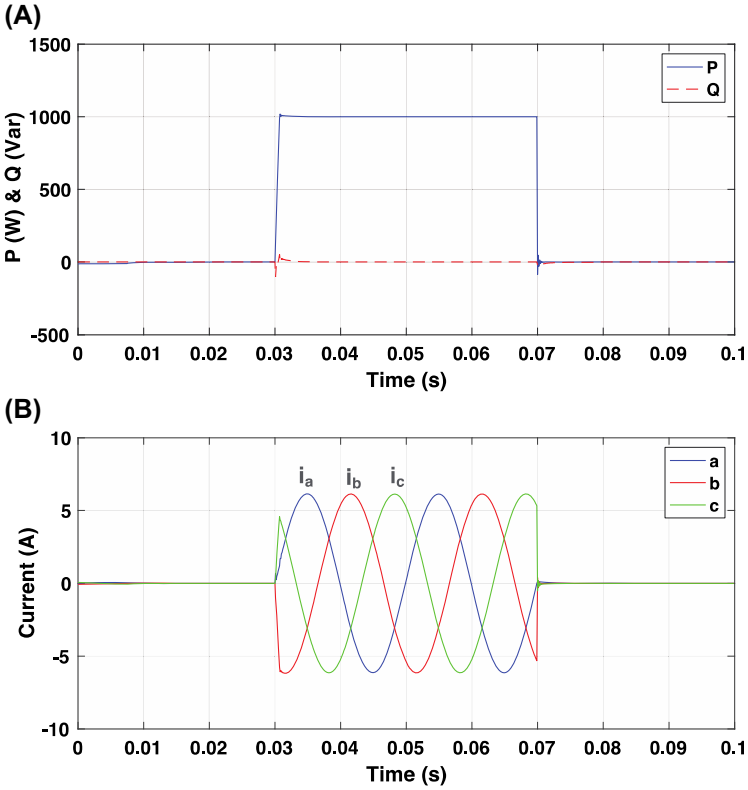

FIGURE 2.10 Simulation results of the voltage-modulated direct power control when Q is 0 VAr and P changes from 0 W to 1 kW. (A) P and Q, (B) output currents.

they are guaranteed to be globally exponentially stable by Eqs. (2.19) and (2.27). To compare the steady-state performance of the two methods, the case is tested where $P = 1$kW and $Q = 1$ kVAr, as shown in Figs. 2.13 and Fig. 2.14. Fig. 2.15 shows the harmonic spectra of the output currents from 3rd up to 25th harmonics. The VM-DPC obtains a THD of the output current as 1.4%, which is lower than 5% required for grid connection. However, the PBC-DPC obtains THD = 5.6%. Therefore, it can be concluded that the VM-DPC decreases the THD of the output current but maintains the same transient performance as the PBC-DPC.

2.4 Robust small-signal stabilization control design

2.4.1 Introduction

From the previous discussions, the linearized system model is dependent on the desired states. Variations in the desired states cause entries of the linearized

This book belongs to Kitab Liaison (ocd1996@gmail.com) Copyright Elsevier 2023

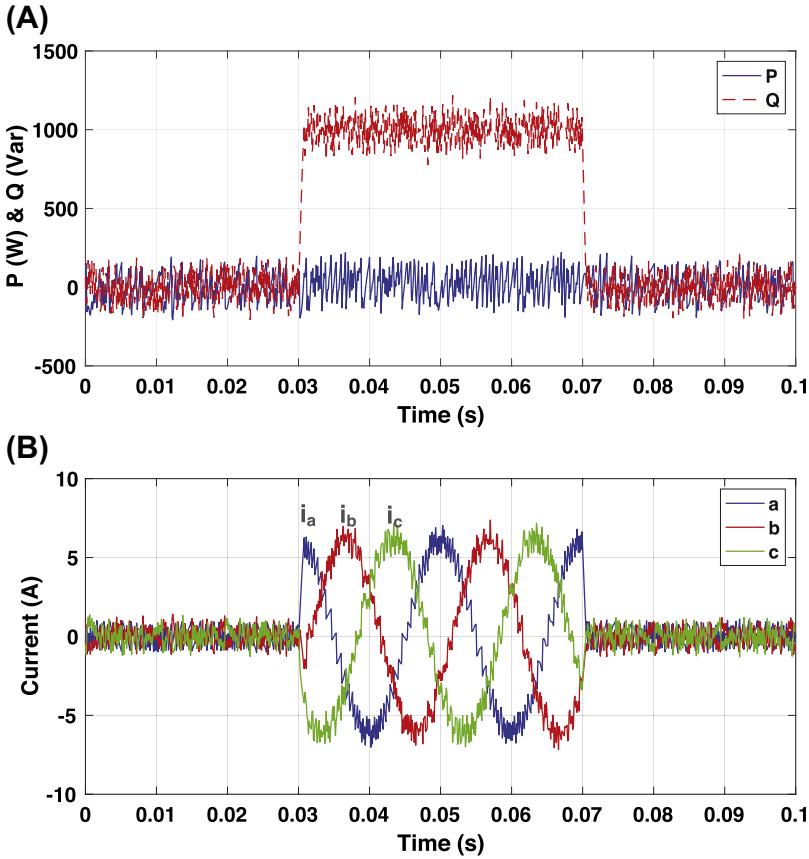

FIGURE 2.11 Simulation results of the PBC-DPC when P is 0 W and Q changes from 0 VAr to 1 kVAr. (A) P and Q, (B) output currents. *DPC*, direct power control; *PBC*, passivity-based control.

system matrix to change. Such changes can drive the eigenvalues away from the designated positions, which can lead to instability in certain circumstances.

Stability analysis of a linearized system requires small-signal stability analysis methods. However, the conventional small-signal stability methods could be hard to apply to study a system with strong uncertainty, since the variations in the equilibria are usually hard to precisely characterize for such systems, whereas most existing small-signal stability analysis results require exact knowledge about the equilibria [44].

To tackle this difficulty, a computationally efficient method is shown in this section to design a robust small-signal stabilization control. The method does not require knowing the exact system equilibria for a power electronic device

This book belongs to Kitab Liaison (ocd1996@gmail.com) Copyright Elsevier 2023

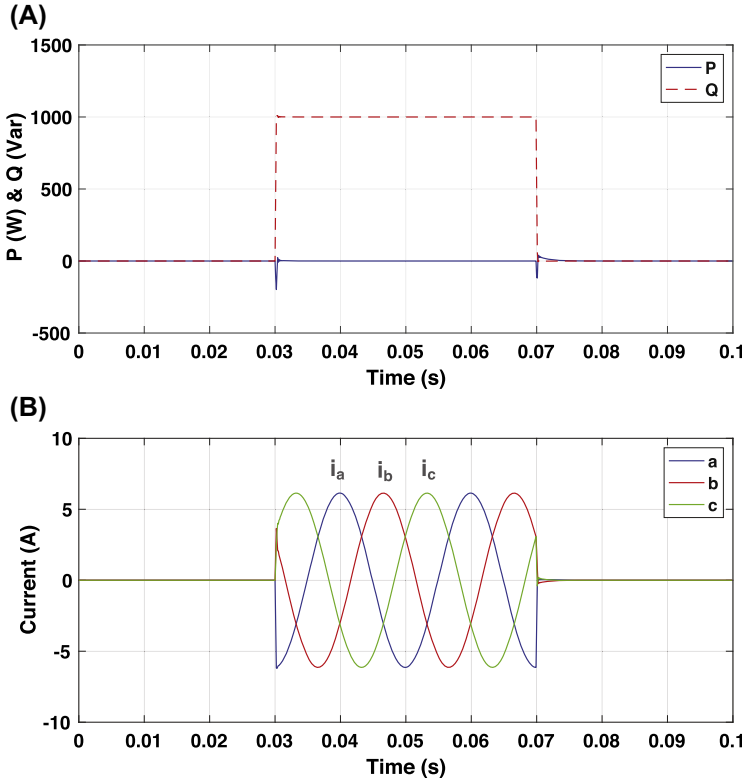

FIGURE 2.12 Simulation results of the voltage-modulated direct power control when P is 0 W and Q changes from 0 VAr to 1 kVAr. (A) P and Q, (B) output currents.

or a power electronic interfaced system. The equilibria are assumed to be an arbitrary point lying in a polytopic set that represents the operational constraints, such as voltage and current bounds. A stability condition is shown that certifies whether all elements lying in the set are stable. Then, a stabilization control is designed to make sure the condition is always satisfied.

The theoretical results are first shown using a general model derived from Lur'e type system. Several examples concerning DC/DC converters and DC microgrids are shown to illustrate the usefulness of the method.

2.4.2 Lur'e type model

The technical results are based on a general model. Many power engineering control systems have separate linear and nonlinear parts added together in the system dynamics, thus can be categorized into Lur'e type systems [45].

This book belongs to Kitab Liaison (ocd1996@gmail.com) Copyright Elsevier 2023

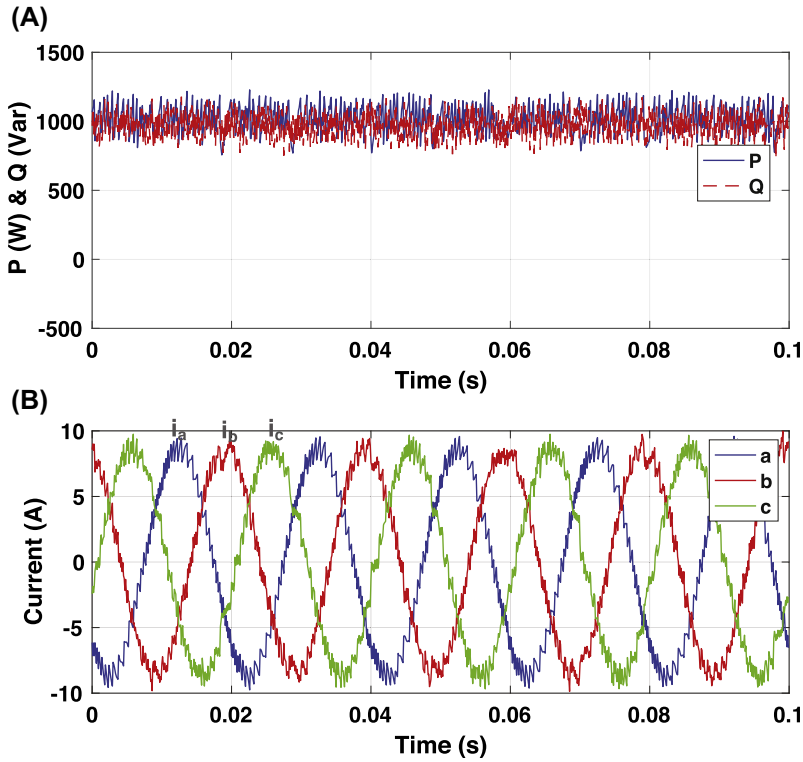

FIGURE 2.13 Simulation results of the PBC-DPC when P is 1 kW and Q is 1 kVAr. (A) *P* and *Q*, (B) output currents. *DPC*, direct power control; *PBC*, passivity-based control.

As shown in Fig. 2.16, a Lur'e type system is described by the following model:

$$\begin{cases} \dot{x} = Ax + B_1 p + B_2 u, \\ y = Cx + D_1 p + D_2 u \end{cases} \tag{2.28}$$

where p is an additive nonlinear input given by $p = \phi(x, u, w)$, and w is an unknown variable that represents disturbance or modeling errors, x, u, and y are the system state, input, and output variables. Inserting $p = \phi(x, u, w)$ into Eq. (2.28) yields the classic Lur'e type system model for the state dynamics:

$$\dot{x} = \underbrace{Ax + B_2 u}_{\text{linear part}} + \underbrace{B_1 \phi(x, u, w)}_{\text{nonlinear part}} . \tag{2.29}$$

It can be seen that the Lur'e type system has two additive parts: the linear part resembles a common LTI system, and the nonlinear part is in a general function form. Throughout the following content in this section, it is assumed

This book belongs to Kitab Liaison (ocd1996@gmail.com) Copyright Elsevier 2023

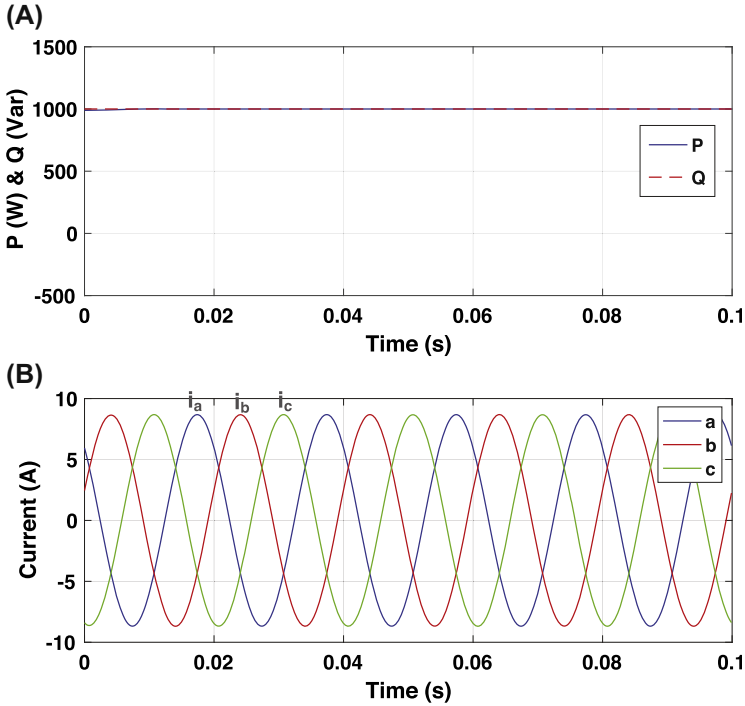

FIGURE 2.14 Simulation results of the voltage-modulated direct power control when P is 1 kW and Q is 1 kVAr. (A) P and Q, (B) output currents.

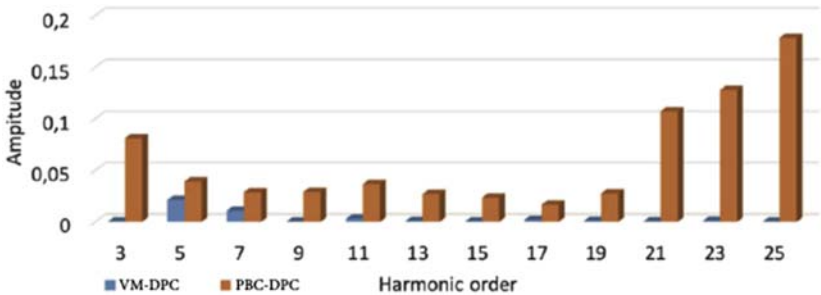

FIGURE 2.15 Current harmonic spectra of Figs. 2.13 and Fig. 2.14, where total harmonics distortion of the voltage-modulated direct power control (VM-DPC) is 1.4% and PBC-DPC is 5.6%. *DPC*, direct power control; *PBC*, passivity-based control.

that ϕ is a rational function where both the nominator and denominator are polynomials. It can be seen that AC inverter model Eq. (2.9) follows from this general form.

Two examples involving DC/DC converter model and DC microgrid demonstrate the wide applicability of the model.

This book belongs to Kitab Liaison (ocd1996@gmail.com) Copyright Elsevier 2023

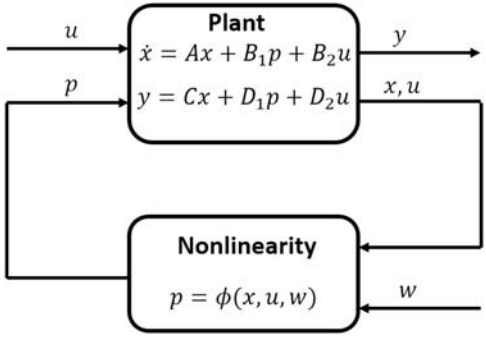

FIGURE 2.16 Control diagram for Lur'e type system.

2.4.2.1 Example 1: DC/DC buck converter model

A buck converter is widely used in DC-bus voltage regulation. Consider a buck converter interfaced voltage source supplying a constant power load P. Let the voltage source be V_i; it is the input of the buck converter. The dynamics of the output voltage V_o and the current I are given as follows:

$$\begin{cases} L\dfrac{dI}{dt} = V_iD - V_o \\ C\dfrac{dV_o}{dt} = I - \dfrac{P}{V_o} \end{cases} \tag{2.30}$$

where D is the duty ratio of the DC/DC buck converter, L and C are the inductance and capacitance of the converter. Notice that the duty ratio can be determined through controllers like a primary droop controller. It can be clearly seen from the model that there is a nonlinear input P/V_o where the constant power P is often unknown and the reciprocal form makes the term nonlinear in the system state.

Since source voltage V_i is usually a constant, the term V_iD can be considered as a control input to the system. Let $x = [I, V_o]^\top$. The model can be written in a more compact form as follows:

$$\dot{x} = \underbrace{\begin{bmatrix} & -1 \\ 1 & \end{bmatrix} x}_{Ax} + \underbrace{\begin{bmatrix} 1 \\ 0 \end{bmatrix} V_iD}_{B_2u} + \underbrace{\begin{bmatrix} 0 \\ -1 \end{bmatrix} P/V_o}_{B_1\phi(x,p)}, \tag{2.31}$$

It can be seen clearly that the model follows the general Lur'e type model.

2.4.2.2 Example 2: DC microgrid model

In addition, many power electronic interfaced systems can be modeled as Lur'e type system as well. DC microgrid can be used as an example to

This book belongs to Kitab Liaison (ocd1996@gmail.com) Copyright Elsevier 2023

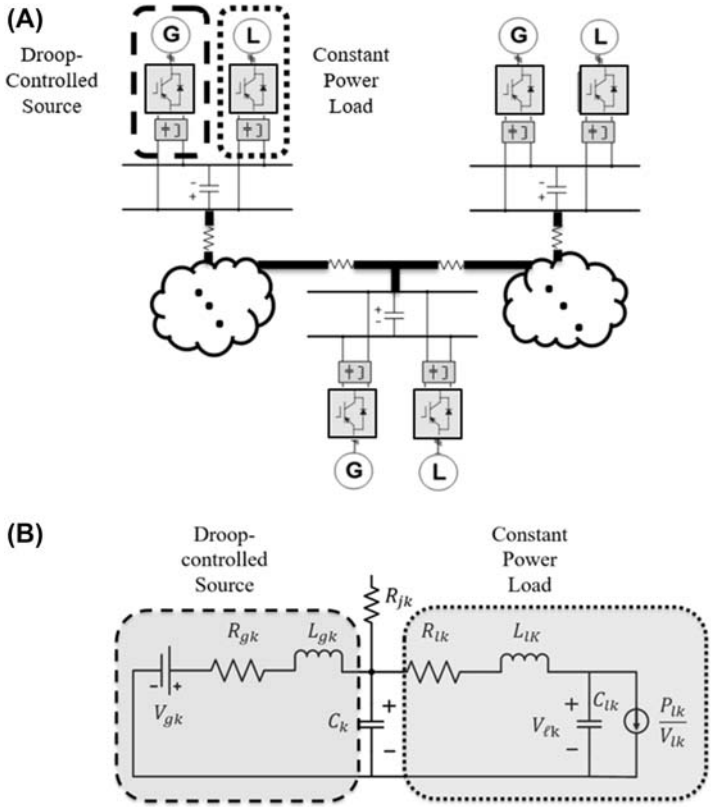

FIGURE 2.17 Example of a (A) DC microgrid topology and (B) power electronic circuit.

illustrate this. An example DC microgrid is shown in Fig. 2.17. The DC microgrid is composed of multiple DC buses. Each DC bus can be connected to several DC/DC converter interfaced loads and sources. For simplicity, we use one composite source and load to integrate all the sources and loads on each bus.

It is well known that many DC sources are controlled under primary droop control. The duty ratio is updated in order to control the terminal voltage following the droop control. For the k-bus, the output voltage of the source is given as follows:

$$V_{gk} = V_{gk}^{*} - I_{gk} d_k, \tag{2.32}$$

where d_k is a droop gain, V_{gk} is the output voltage of the source, I_{gk} is the output current, and V_{gk}^{*} is a droop reference. From Eq. (2.32), the desired terminal output voltage is an affine function in the output current.

This book belongs to Kitab Liaison (ocd1996@gmail.com) Copyright Elsevier 2023

The time scale for finding the desired duty ratio is often negligible when comparing to that of the primary droop control, hence it is often assumed that the instantaneous terminal voltage output of a source is determined by Eq. (2.32).

In addition, the constant power loads are still a nonlinear function in the terminal voltage, and it is assumed that the instantaneous power is always the desired power demand.

Bearing this in mind, the circuit model of a DC bus is given as follows:

$$\begin{cases} L_{gk}\dfrac{dI_{gk}}{dt} = V_{gk} - I_{gk}R_{gk} - V_{bk} \\ C_k\dfrac{dV_{bk}}{dt} = I_{gk} - I_{lk} - I_{kj} \\ L_{lk}\dfrac{dI_{lk}}{dt} = V_{bk} - I_{lk}R_{lk} - V_{lk} \\ C_{lk}\dfrac{dV_{lk}}{dt} = I_{lk} - \dfrac{P_{lk}}{V_{lk}} \\ V_{gk} = V_{gk}^{*} - I_{gk}d_k \end{cases} \tag{2.33}$$

where I_{gk} and I_{lk} are the source and load currents, I_{jk} is the transiting current between bus j and k, V_{bk} is the DC-bus voltage, V_{lk} is the voltage across the load capacitor, L_{gk} and L_{lk} are the source and load inductance, R_{gk} and R_{lk} are the source and load resistance, C_k is the DC-bus capacitance, and C_{lk} is the load capacitance, at last, R_{jk} is the line resistance between bus j and k.

It can be seen that the model has linear part with respect to the source current, DC-bus voltage, and load current; meanwhile, it has also a nonlinear part concerning the constant power load. It thus resembles the single DC/DC converter model and further resembles a Lur'e type system. Extending this model to the entire system, one can see that Lur'e type system can be used to describe a DC microgrid system.

A salient feature of a Lur'e type system is that the system equilibria depend on the control input, uncertain disturbances, as well as the nonlinear function $\phi(x, u, w)$. This can be seen from the derivation below. Suppose the equilibrium is x^d, so it must satisfy the following steady-state equation:

$$0 = Ax^d + B_1\phi\left(x^d, u, w\right) + B_2u, \tag{2.34}$$

which is the steady-state equation, and it verifies that x^d is determined by both the linear and the nonlinear parts.

This book belongs to Kitab Liaison (ocd1996@gmail.com) Copyright Elsevier 2023

If the nonlinear function is not concerned with the system state, i.e., when it is given by $\phi(u, w)$, and the system matrix is nonsingular, the equilibrium is given as follows:

$$x^d = -A^{-1}(B_1\phi(u, w) + B_2u), \tag{2.35}$$

it can be seen that the system equilibrium is dependent on the uncertainty and the control.

Nevertheless, when the nonlinear part involves the state variables, it is often difficult to find an analytical expression of the system equilibria. For example, in the DC microgrid system with the reciprocal nonlinear function owing to the constant power loads, the system steady-state equations are multidimensional quadratic equations that are in lack of analytical solutions.

2.4.3 Robust small-signal stability analysis problem

Classic small-signal stability analysis results cannot be applied when the system equilibria are not known. In the following, it is shown that when x^d lies in a known constraint set, robust stability analysis results can be applied to ascertain the small-signal stability.

To simplify the discussion, suppose the system control follows a linear state feedback control as follows:

$$u = Kx, \tag{2.36}$$

hence, the closed-loop system is now given by $\dot{x} = (A + B_2K)x + B_1\phi(x, w)$ where the dependence of the equilibria on the control variable is removed. This control gain matrix K can be obtained through classic power electronic control design methods and are considered known for now.

Let the uncertainty be subject to box constraint arising from capacity limits (physical disturbances are generally bounded) as follows: $w \in \mathscr{W}$, where $\mathscr{W} = \{w : w \in [w^-, w^+]\}$. Furthermore, let $x^d \in \mathscr{X}^d$ with $\mathscr{X}^d = \{x^d : x^d \in [x^{d-}, x^{d+}]\}$ being box constraint sets for the system equilibria. Notice that x^{d-} and x^{d+} are the elementwise lower and upper bounds. This constraint set can represent the operational constraints for a power electronic device or system. For example, it can represent a constraint set for the terminal voltage of an inverter.

Any desired system equilibria must lie in the operational constraint set $\mathscr{X}^d$. If $x^d \in \mathscr{X}^d$ is known, a conventional linearization method can be applied to study the eigenvalues of the system Jacobian matrix. Now that x^d could be an arbitrary point in $\mathscr{X}^d$, the Jacobian matrix is unknown, and we cannot directly study its eigenvalues. Fortunately, with x^d and w lying in a constraint set the Jacobian matrix is bounded as well.

Definition 2.1. *The system is* ***robustly small-signal stable*** *when any equilibrium lying in $\mathscr{X}^d$ is small-signal stable for any $w \in \mathscr{W}$.*

This book belongs to Kitab Liaison (ocd1996@gmail.com) Copyright Elsevier 2023

Let the linearized nonlinear function with respect to arbitrary $x^d \in \mathscr{X}^d$ and $w \in \mathscr{W}$ be $\widetilde{\phi}(x^d, w)$ and the linearized Jacobian matrix is $J = A + B_2K + B_1\widetilde{\phi}(x^d, w)$.

It is well known that as long as ϕ is a rational function (i.e., the nominator and denominator are polynomials in x^d and w), and $x^d \in [x^{d-}, x^{d+}]$, $w \in [w^-.w^+]$, a box constraint can always be found for the linearized function $\widetilde{\phi} \in \left[\widetilde{\phi}^-, \widetilde{\phi}^+\right]$. Both the lower and upper bounds are dependent on x^{d-}, x^{d+}, w^- and w^+, thus are known.

As a result, the Jacobian now lies in a known interval matrix constraint, $J \in [J^-, J^+]$. So long as any J in this set is small-signal stable, the system is **robustly small-signal stable.**

Now the robust stability analysis problem is transformed into determining the stability of a matrix lying in an interval. Several methods exist to solve this problem [44]. A method based on linear matrix inequality testing is shown in the following.

2.4.4 Robust stability analysis method

Knowing that $\widetilde{\phi} \in \left[\widetilde{\phi}^-, \widetilde{\phi}^+\right]$, each element of this vector lies in a box constraint. Let the i-th element lie in the following constraint set, $\widetilde{\phi}_i \in \left[\widetilde{\phi}_i^-, \widetilde{\phi}_i^+\right]$, and define $\widetilde{\Phi} = \left\{\widetilde{\phi} : \widetilde{\phi}_i \in \left[\widetilde{\phi}_i^-, \widetilde{\phi}_i^+\right], \forall i\right\}$.

Equivalently, the problem is to determine the stability of $J$with $\widetilde{\phi} \in \widetilde{\Phi}$. Although there are infinitely many elements in $\widetilde{\Phi}$, there are finitely many vertices for this set. Let the number of vertices be m. (If $\widetilde{\phi}$ is a n-dimensional vector, there are $m = 2^n$ vertices). With regard to the k-th vertex of Φ, let it be $\widetilde{\phi}^k$, and let the Jacobian matrix be $J^k = A + B_2K + B_1\widetilde{\phi}^k$.

Theorem 2.1. *The system is robustly small-signal stable if there exists a positive semidefinite matrix P that satisfies the following linear matrix inequality constraint:*

$$P \succ 0, P\left(J^k\right)^\top + J^kP \prec 0, k = 1, \cdots, m \tag{2.37}$$

Notice that the condition derived in Eq. (2.37) is a semidefinite programming problem, that can be solved through off-the-shelf algorithms like interior point algorithm [46].

2.4.5 Robust stabilization control design

In the robust stability analysis, it is shown how to determine whether the system equilibrium is always small-signal stable with a given control law $u = Kx$ where the control gain matrix K is known.

This book belongs to Kitab Liaison (ocd1996@gmail.com) Copyright Elsevier 2023

If an initial design K cannot ensure the robust small-signal stability, it can be redesigned using the method below.

The following **robust small-signal stabilization problem** is considered: a control gain matrix K is to be designed such that the system Jacobian $J = A + B_2K + B_1\widetilde{\phi}(x^d, w)$ is **robustly small-signal stable** with $x^d \in \mathscr{X}^d$ and $w \in \mathscr{W}$.

The design problem is formulated as follows:

$$\min_{K,P,\alpha} -\alpha$$
$$P\left(A + B_2K + B_1\widetilde{\phi}^k\right)^\top + \left(A + B_2K + B_1\widetilde{\phi}^k\right)P \prec -\alpha I,$$
$$k = 1, \cdots, m$$
$$\alpha > 0, \qquad P \succ 0. \tag{2.38}$$

If problem Eq. (2.38) is feasible, then any solution K ensures that the system is **robustly small-signal stable.**

As there is no extra constraint on K, an interpolation method can be applied to efficiently solve the problem. Let $Y = PK^\top$ and substituting it into Eq. (2.38) yields

$$\min_{P,\alpha,Y} -\alpha$$
$$P\left(A + B_1\widetilde{\phi}^k\right)^\top + \left(A + B_1\widetilde{\phi}^k\right)P + YB_2^\top + B_2Y^\top \prec -\alpha I,$$
$$k = 1, \cdots, m \qquad \alpha > 0, \quad P \succ 0. \tag{2.39}$$

Problem Eq. (2.39) is again a linear matrix inequality problem.

Often there are constraints on K, for example, with decentralized or distributed control design, there is always structural constraint on K as much system information is not available to the controller. The interpolation method cannot be used in this case. Fortunately, problem Eq. (2.38) is a bilinear matrix inequality constraint problem, and there exist effective methods to solve such a problem as well [47].

2.4.5.1 Example 3: robust small-signal stability of a DC microgrid

Example is based on a nine-bus DC microgrid system as shown in Fig. 2.18. Each source uses the V−I droop control and is considered as a DC voltage source [48]. The power electronic circuit of the k-th bus is shown in Fig. 2.17. The parameters of the k-th bus can be found in Table 2.2.

From Eq. (2.33), the nonlinear part is the constant power load $-P_{lk}/V_{lk}$, and its linearized form is P_{lk}/V_{lk}^2. Suppose that each load power is uncertain and may take values in the range [0, 20 kW] and let the load voltage be in the range [360 V, 440 V]. Hence, the linearized term P_{lk}/V_{lk}^2 is in the range [0, 0.193].

From the results about robust small-signal stabilization, problem Eq. (2.37) is infeasible when the droop gains are 0.06. This infeasibility indicates that with this design the system is not robustly small-signal stable as shown in Fig. 2.19. For the simulation we let each load to gradually increase from 5 to 20 kW. During the increase of load, the system becomes unstable.

This book belongs to Kitab Liaison (ocd1996@gmail.com) Copyright Elsevier 2023

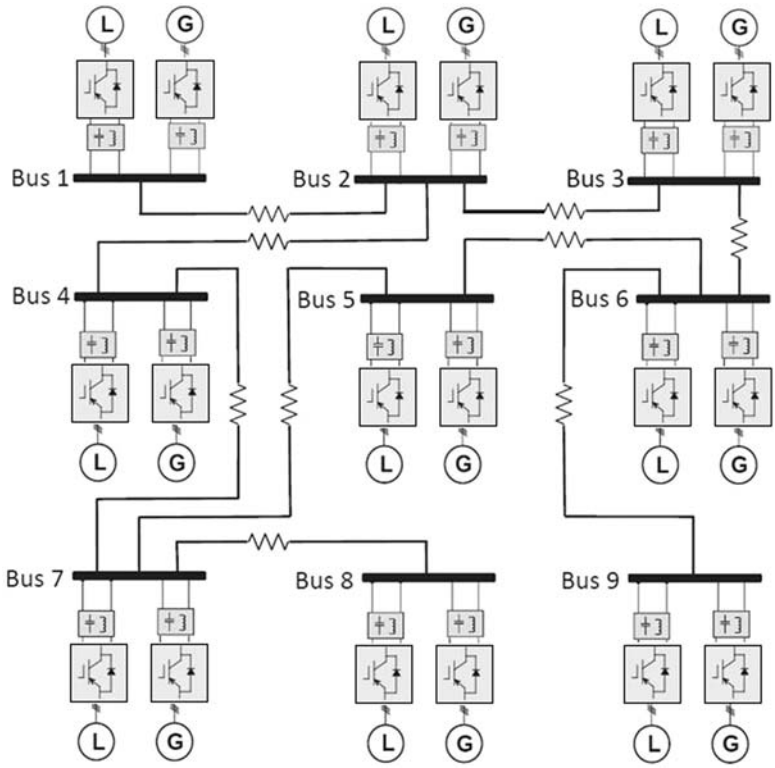

FIGURE 2.18 DC microgrid with nine buses for robust small-signal stability analysis.

TABLE 2.2 Parameters of nine-bus DC microgrid.

R_{gk}	0.05 Ω	R_{lk}	0.05 Ω	L_{gk}	0.9 mH
L_{lk}	0.9 mH	C_k	0.75 mF	C_{lk}	0.75 mF
$[P_{lk-}, P_{lk+}]$	[0.20 kW]	R_{jk}	1 Ω	P_k^n	15 kW
$[V_{lk-}, V_{lk+}]$	[360 V,440 V]	V_{gk}^*	400 V	d_k	0.06

Let p_{lk}^n be the nominal power, and it is set as 15 kW.

The droop gain is redesigned according to Problem Eq. (2.38) and it shows that when the droop gains are set to 0.2, system will be robustly stable. This is verified by Fig. 2.20 as when each load again increases to 20 kW the system remains stable.

This book belongs to Kitab Liaison (ocd1996@gmail.com) Copyright Elsevier 2023

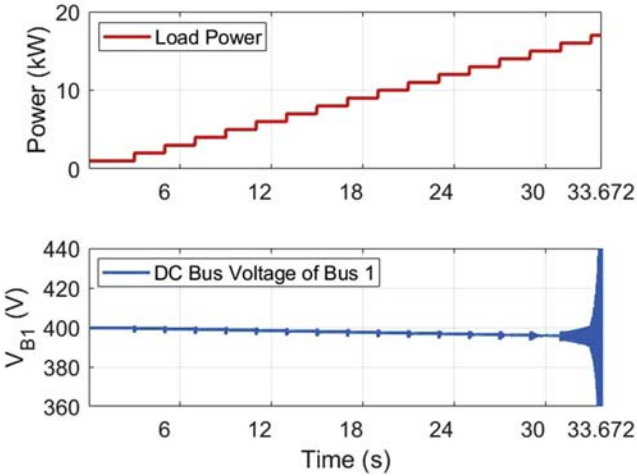

FIGURE 2.19 Instability with inappropriate control design.

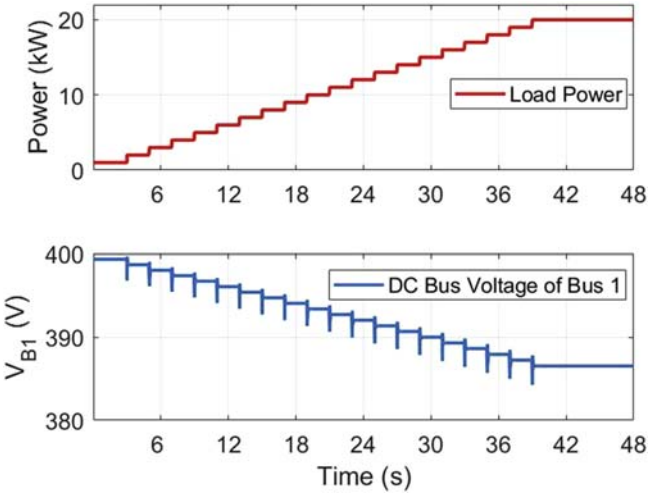

FIGURE 2.20 System is robustly small-signal stable.

2.5 Passivity-based control design

The port-controlled Hamiltonian (PCH) system is introduced in this section in order to get the passivity properties, which has the advantage that if a group of passive subsystems are in the parallel or feedback connection, the whole system is also stable and passive [49]. This property can be applied to heterogenous RESs in, e.g., a microgrid in order to guarantee the stability of the microgrid, and an STATCOM system in order to guarantee the exponential stability in the whole operating range.

This book belongs to Kitab Liaison (ocd1996@gmail.com) Copyright Elsevier 2023

2.5.1 Introduction

Generally, PCH systems can formulate a classification of the variables and the equations into a special model where the interconnection structure related with the exchanges of energy is defined [50]. It is easy to modify the energy function and add dissipation into the system, which are the basic steps of PBC. Moreover, the geometric structure of the state space of PCH systems can profitably be used for PBC. The PCH system has received an increasing amount of interest from the field of control engineering [51,52]. It has been proven effective for a wide range of applications [50]. Many power electronic applications can be modeled as PCH systems where multiple simpler components are interconnected to form a more complicated and complete system.

2.5.2 Port-controlled Hamiltonian system

In this study, at first, a general state and input sets are introduced. Let $x \in \mathbb{R}^n$ and $u \in \mathbb{R}^m$ indicate the state and input vector, respectively. A system is formulated in the following form:

$$\dot{x} = f(x, u), \tag{2.40}$$

where $x \in X \subset \mathbb{R}^n$ and $u \in U \subset \mathbb{R}^m$ are the state and the input vector, respectively. $f(\cdot, \cdot)$ is sufficiently smooth in the open connected sets X [53].

Definition 2.2. [54] *If a system in Eq. (2.40) satisfies the following form Eq. (2.41), it can be called as a PCH system.*

$$\dot{x} = (\mathfrak{J} - \mathfrak{R})\frac{\partial H(x)}{\partial x} + G(u), \tag{2.41}$$

where H represents *the Hamiltonian function, which is given as*

$$\begin{aligned} H(x) &= \frac{1}{2}x^T S x,\ S = S^T \succ 0, \\ \mathfrak{J}^T &= -\mathfrak{J},\ \mathfrak{R} = \mathfrak{R}^T \succ 0. \end{aligned} \tag{2.42}$$

In Definition 2.2, $\succ$ represents positive definite, $\mathfrak{R}$ represents the dissipative forces, $\mathfrak{J}$ represents the conservative forces, and $G(u)$ represents the energy acquisition term in the system [55]. It should be noted that S and $\mathfrak{R}$ are $n \times n$ matrices.

Assumption 2.1. *Suppose that there exist state and input $x^d(t)$ and $u^d(t)$, which satisfy the PCH form in Eq. (2.41),*

$$\dot{x}^d = (\mathfrak{J} - \mathfrak{R})\frac{\partial H(x^d)}{\partial x^d} + G(u^d). \tag{2.43}$$

This book belongs to Kitab Liaison (ocd1996@gmail.com) Copyright Elsevier 2023

It should be noted that the system dynamics considered in this study are sufficiently smooth in the open connected set X, hence, Assumption 2.1 is reasonable.

Theorem 2.2. [54] *Suppose one system satisfies the PCH form* Eq. (2.41). *Given a reference trajectory, $x^d(t)$, which satisfies* Eq. (2.43), *if a control input is taken as $u = u^d$, then the tracking error exponentially converges to be zero, i.e., $lim_{t\to\infty} x(t) = x^d(t)$.*

Proof: We suppose that $x(t) \in X \subset \mathbb{R}^n$ to be the trajectory of the system Eq. (2.41) corresponding to the input, $u = u^d \in U \subset \mathbb{R}$,

$$\dot{x} = \left(\mathfrak{J}\left(u^d\right) - \Re\right)\frac{\partial H(x)}{\partial x} + G\left(u^d\right). \tag{2.44}$$

Since $x^d(t)$ and $x(t)$ have different initial conditions, they are not the same signals, but satisfy the same dynamic equations. Let us define an error, $e := x^d - x$. As a consequence, the error dynamics can be expressed as

$$\dot{e} = \dot{x}^d - \dot{x} = \left(\mathfrak{J}\left(u^d\right) - \Re\right)\frac{\partial H(e)}{\partial e}. \tag{2.45}$$

Let $H(e)$ in Eq. (2.42) be a Lyapunov function candidate. Then, the time derivative of $H(e)$ is formulated as

$$\begin{aligned}\dot{H}(e) &= \frac{1}{2}\left(\dot{e}^T\left(\frac{\partial H(e)}{\partial e}\right) + \left(\frac{\partial H(e)}{\partial e}\right)^T\dot{e}\right)\\ &= -e^T S^T \Re S e.\end{aligned} \tag{2.46}$$

Since S and $\Re$ are positive definite, e exponentially converges to zero. Consequently, $\lim_{t\to\infty}\left\| x^d(t) - x(t)\right\| = 0$.

Notice that although x and x^d have the same dynamics, their initial conditions are different. u^d can easily be calculated if the flatness property is used [54].

2.5.3 Passivity-based control design in a microgrid

It should be noted that the dynamics of the grid-connected voltage source inverter in Eq. (2.14) also satisfies the form in Eq. (2.41). For the dynamics in Eq. (2.14), if a Hamiltonian function is taken as

$$H(x) = \frac{1}{2}x^T S x \tag{2.47}$$

where $x = [x_1, x_2]^T = [P, Q]^T$, and $S = I_2$. Thus, the inverter system Eq. (2.14) is transformed into the PCH form in Eq. (2.41) such as

$$\dot{x} = (\mathfrak{J} - \Re)\frac{\partial H(x)}{\partial x} + G(u), \tag{2.48}$$

This book belongs to Kitab Liaison (ocd1996@gmail.com) Copyright Elsevier 2023

where

$$\Im = \begin{bmatrix} 0 & \omega \\ -\omega & 0 \end{bmatrix}, \Re = \begin{bmatrix} \frac{R}{L} & 0 \\ 0 & \frac{R}{L} \end{bmatrix}, G(u) = \begin{bmatrix} \frac{3}{2L(u_P - V_g^2)} \\ \frac{3}{2L} u_Q \end{bmatrix}. \tag{2.49}$$

Assumption 2.2. *It is supposed that the control input generated by the VM-DPC in Eq. (2.16) is u^*, and the inverter system trajectory using u^*, x converges to x^*, which has the following relationship with x^d of Eq. (2.45) such as*

$$x^d - x^* = \begin{bmatrix} exp^{-\lambda_1 t}\left(x_1^d - x_1\right) \\ exp^{-\lambda_2 t}\left(x_2^d - x_2\right) \end{bmatrix}. \tag{2.50}$$

where $\lambda_{1,2}$ are the decay ratios of $x_{1,2}$.

Assumption 2.2 is reasonable in this study, because from Eq. (2.19) in Subsection 2.3.3, the VM-DPC guarantees the exponential stability of the closed-loop system. Based on Assumption 2.1 and Assumption 2.2, the following relationship between the desired control value in Eq. (2.43), u^d, and the VM-DPC in Eq. (2.16), u^*, can be obtained.

$$\begin{aligned} \delta u_1 = u_1^d - u_1^* &= \frac{3exp^{-\lambda_1 t}}{2L}\left(-\lambda_1 \dot{e}_1 + \frac{R}{L} e_1 + \omega e_2\right), \\ \delta u_2 = u_2^d - u_2^* &= \frac{3exp^{-\lambda_2 t}}{2L}\left(\lambda_2 \dot{e}_2 - \frac{R}{L} e_2 + \omega e_1\right), \end{aligned} \tag{2.51}$$

where λ_1 and λ_2 are the decay ratio of $e_1$and e_2, respectively [53].

Assumption 2.3. *In addition, we also suppose that $\forall x \in X_o$, where X_o is operating points set for the grid-connected voltage source inverter, there exist Δ_1 and Δ_2 that satisfy the following relationship:*

$$\sup_{\forall x \in X_o} \dot{e}_1 = \Delta_1, \quad \sup_{\forall x \in X_o} \dot{e}_2 = \Delta_2. \tag{2.52}$$

Since the capacities of grid-connected voltage source inverters and RESs are always limited, the generated powers of RESs are also limited. In addition, the system is stabilized and regulated in the whole operating range by using the VM-DPC. As a consequence, $\dot{e}$ and e are also bounded in regard to the given references [53]. Hence, Assumption 2.3 is reasonable as well.

Theorem 2.3. [53] *For a given dynamic system of VSC in Eq. (2.14), suppose that from Assumption 2.1 to Assumption 2.3 are all held. If a control law*

This book belongs to Kitab Liaison (ocd1996@gmail.com) Copyright Elsevier 2023

consisting of the VM-DPC Eq. (2.16) is taken and a new feedback is introduced as follows:

$$\widehat{u}_{vm} = u^* + u_{fb}, \tag{2.53}$$

where $u_{fb} = [-\kappa_1|e_1|, \kappa_2|e_2|]^T$ *with* $\kappa_1 \geq \lambda_1\Delta_1$ *and* $\kappa_2 \geq \lambda_2\Delta_2$*, then the tracking error converges to zero exponentially.*

A detailed proof of Theorem 2.3 is omitted, which can be found in Ref. [53]. It should be noted that additional damping term is added by the feedback term in Eq. (2.53). Fig. 2.22 shows the control block diagram of the method designed by using Theorem 2.3. In normal operation, RES generates as much as possible active power. Consequently, it is assumed that RESs are operated at their own maximum power point. By using Theorem 2.3, all new integrated RES guarantees the passivity property, and the ESS guarantees the passivity property through a proportional resonant controller with active damping method designed in Ref. [56]. Consequently, it is guaranteed that the microgrid is stable based on the passivity principle [49], i.e., the entire microgrid including the RESs and ESS is asymptotically stable.

In order to validate the PBC method of RESs in the microgrid, the test system is implemented in MATLAB/Simulink, Simscape Power Systems. The case study is studied in a microgrid including a PV, WT, ESS, and two loads, as shown in Fig. 2.21. The detailed parameters are listed in Table 2.3.

In the microgrid, the ESS regulates its bus voltage (230 V) and frequency (50 Hz). At first, the load 1 is connected and consumes the active power (5 kW), which leads to decrease in the frequency in the microgrid. At this time, the ESS injects more active power into the microgrid in order to keep the balance between the generation and consumption with its own controller, as shown in Fig. 2.23A. At 0.51 s, the WT is connected into the microgrid and generates 10 kW shown in Fig. 2.23C, which leads to an increase in the frequency of the microgrid. The ESS starts to charge surplus active power to keep the balance in the microgrid. When the PV is connected and generates its maximum power 5 kW at 0.72 s, as it is shown in Fig. 2.23D, the ESS charge more active power to keep the balance in the microgrid. At 1 s, the total load in the microgrid increases to 10 kW, as it is shown in Fig. 2.23B, the ESS starts to decrease its power in order to keep the balance in the microgrid since the WT and PV have generated their maximum power. Notice that there is no synchronization process in the PBC method, which is the benefit from the VM-DPC. Moreover, the WT decreases its power to 6 kW at 1.25 s. The red (gray in printed version) dashed line indicates the performance of the conventional method (vector current control). From the results, it can be seen that the conventional method has a larger overshoot when the WT and PV are connected into the microgrid, because the PLL has slow dynamics of the phase angle estimation. When the PLL supports the correct phase angle for the conventional method, both methods get the similar results. As a consequence, it can be concluded that the PBC for the microgrid has a good effect on the stable operation and the RESs could easily plug into the microgrid.

This book belongs to Kitab Liaison (ocd1996@gmail.com) Copyright Elsevier 2023

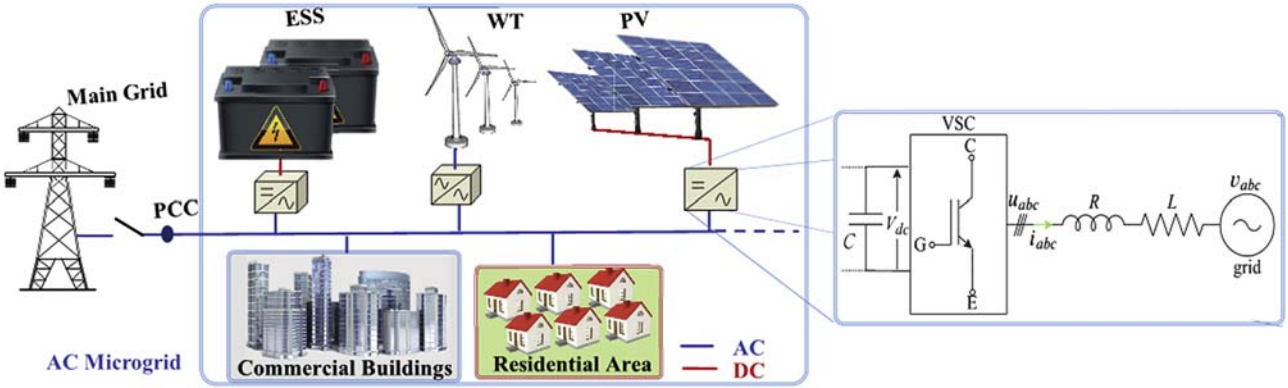

FIGURE 2.21 Islanded microgrid including renewable energy sources, energy storage system (ESS), and loads.

This book belongs to Kitab Liaison (ocd1996@gmail.com)

Copyright Elsevier 2023

TABLE 2.3 Microgrid system parameters in simulation.

V^*_{rms}	230 V	f^*	50 Hz	$L_{in,ess}$	1.8 mH
C	27 μF	$L_{o,ess}$	1.8 mH	L_{pv}&L_{wt}	3.6 mH
PV	5 kW	WT	6.5 kW	Load 1 and 2	5 kW

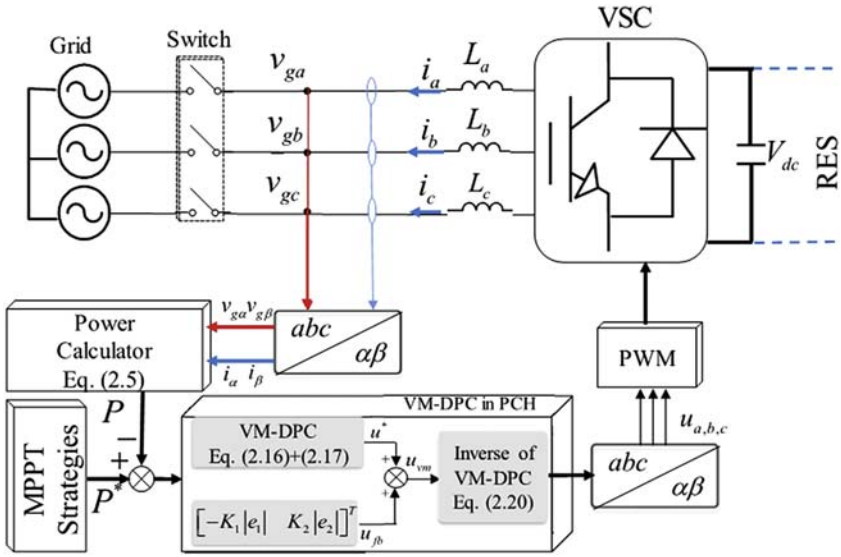

FIGURE 2.22 Control block diagram of the method design in port-controlled Hamiltonian for renewable energy sources (RESs) applied in a microgrid.

2.5.4 Passivity control design in STATCOM

The methodology is also illustrated in a STATCOM system. In order to design a PBC strategy with a nonapproximation model, the STATCOM system is to be rewritten in the PCH form in Eq. (2.41). Unfortunately, the STATCOM system does not satisfy the flatness property [30], which can generate the desired control input from the desired output. As a consequence, a dynamic extension algorithm is use to obtain an input-affine system for the STATCOM, in which the tracking control law is generated based on the IOL framework. It is guaranteed that the error dynamics of the system is exponentially stable over the entire operating range via the passivity property. In addition, there is a uniform damping over the whole operating range. This means that the convergence of the dynamics is not affected by the operating point, which is a main difference from the other methods.

This book belongs to Kitab Liaison (ocd1996@gmail.com) Copyright Elsevier 2023

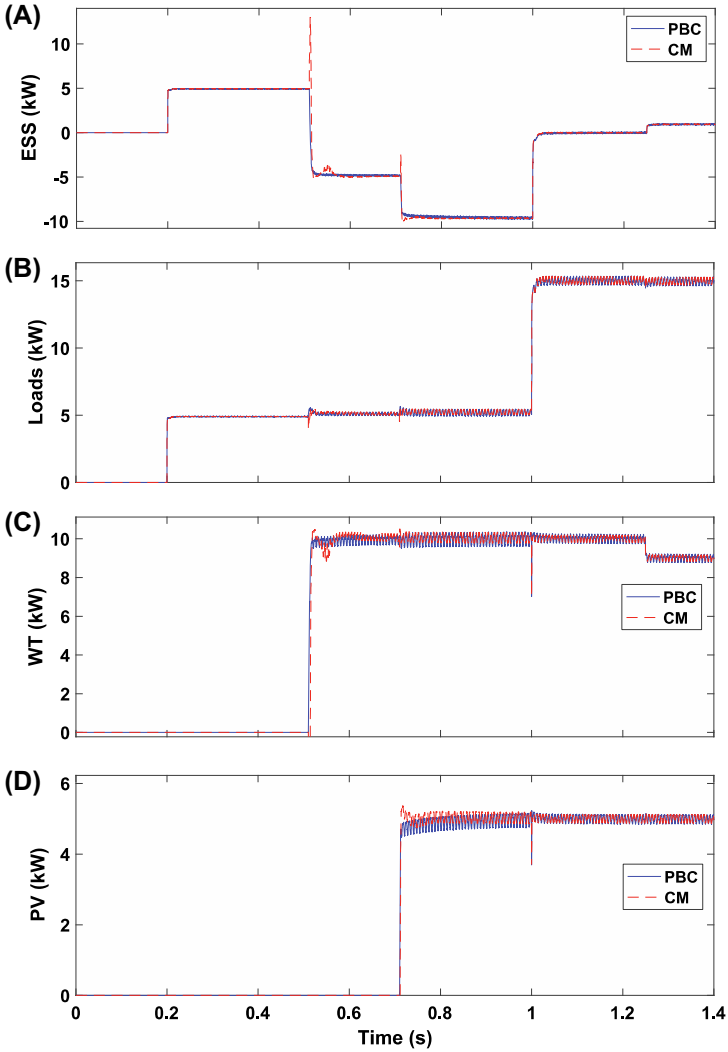

FIGURE 2.23 Simulation results of active power of the passivity-based control for the microgrid shown in Fig. 2.21: (A) energy storage system, (B) load, (C) wind turbine, (D) PV. *CM*, conventional method; *PBC*, passivity-based control.

At first, the dynamic extension of the STATCOM is introduced. Let $u_a = \dot{\alpha} \in U_a \subset \mathbb{R}$ be a new control input, and $x_4 = \sin\alpha$ be a new state. Thus, the new state vector, $x_a = [x_1, x_2, x_3, x_4]^T \in D_a \subset \mathbb{R}^4$, is redefined [24]. Consequently, the original STATCOM system (2.11) is transformed into an input affine one given as

This book belongs to Kitab Liaison (ocd1996@gmail.com)
Copyright Elsevier 2023

$$\begin{aligned} \dot{x}_a &= f_a(x_a) + g_a(x_a)u_a \\ y &= h_a(x_a), \end{aligned} \tag{2.54}$$

where

$$f_a(x_a) = \begin{pmatrix} -\frac{R'_s\omega_b}{L'}x_1 + \omega x_2 + \frac{k\omega_b}{L'}x_3\sqrt{1-x_4^2} - \frac{\omega_b}{L'}|V'| \\ -\omega x_1 - \frac{R'_s\omega_b}{L'}x_2 + \frac{k\omega_b}{L'}x_3x_4 \\ -\frac{3}{2}kC'\omega_b x_1\sqrt{1-x_4^2} - \frac{3}{2}kC'\omega_b x_2x_4 - \frac{\omega_b C'}{R'_p}x_3 \\ 0 \end{pmatrix},$$

$$g_a(x_a) = \begin{pmatrix} 0 \\ 0 \\ 0 \\ \sqrt{1-x_4^2} \end{pmatrix},$$

$$h_a(x_a) = x_2,$$

where $f_a(x_a)$, $g_a(x_a)$, and $h_a(x_a)$ are sufficiently smooth functions in the compact set $D_a \in \mathbb{R}^4$ [24]. Since $-22.1^\circ \leq \alpha \leq 22.1^\circ$ is the operating range of the STATCOM [15], $\cos(\alpha) = \sqrt{1-x_4^2}$.

Notice that the dynamic extended STATCOM system Eq. (2.54) is used to obtain the desired control input (u^d) from the desired output (y^d). However, in this study, we omitted the process of u^d generation, which is calculated by using an IOL method. The detailed design process can be found in Ref. [57].

For the original STATCOM system Eq. (2.11), if a Hamiltonian function is taken as

$$H(x) = \frac{1}{2}x^T Sx, \tag{2.55}$$

where $S = \begin{bmatrix} 1 & 0 & 0 \\ 0 & 1 & 0 \\ 0 & 0 & \frac{2}{3L'C'} \end{bmatrix}$, then the STATCOM system Eq. (2.11) is converted into the PCH form Eq. (2.41) as

This book belongs to Kitab Liaison (ocd1996@gmail.com) Copyright Elsevier 2023

$$\dot{x} = (\Im(\alpha) - \Re)\frac{\partial H(x)}{\partial x} + G, \tag{2.56}$$

where

$$\Im(\alpha) = \begin{bmatrix} 0 & \omega & \frac{3}{2}kC'\omega_b \cos\alpha \\ -\omega & 0 & \frac{3}{2}kC'\omega_b \sin\alpha \\ -\frac{3}{2}kC'\omega_b \cos\alpha & -\frac{3}{2}kC'\omega_b \sin\alpha & 0 \end{bmatrix},$$

$$\Re = \begin{bmatrix} \frac{R'_s\omega_b}{L'} & 0 & 0 \\ 0 & \frac{R'_s\omega_b}{L'} & 0 \\ 0 & 0 & \frac{3\omega'_b C'}{2R'_p} \end{bmatrix}, \; G = \begin{bmatrix} -\frac{\omega_b}{L'}|V'| \\ 0 \\ 0 \end{bmatrix}.$$

If the original control input for the STATCOM Eq. (2.11) is taken and the following is valid:

$$\alpha^d = \int_0^t u^d(\tau)d\tau, \tag{2.57}$$

then the errors of the STATCOM system Eq. (2.11) converge to zero exponentially based on Theorem 2.2. The control block diagram of the PCH method of the STATCOM system is shown in Fig. 2.24.

The simulations are done to validate the effectiveness of the PBC (PCH) method in MATLAB/Simulink, Simscape Power Systems. The parameters tested in this simulation are listed in Table 2.4.

Fig. 2.25 shows the time response of the STATCOM when $I_q^{'d}$ changes from −0.8 pu to 0.8 pu, which is a lightly damped operating point [15]. As shown in Fig. 2.25A, the performance of I'_q using the PBC method is slightly improved as compared with the IOL with a nonlinear damping (IOLMD) method designed in Ref. [15]. However, the PBC has a smaller overshoot and a faster convergence time in I'_d and V'_{dc} compared with the IOLMD, as shown in Fig. 2.25B and C, because the PBC considers the passivity property of the STATCOM.

This book belongs to Kitab Liaison (ocd1996@gmail.com) Copyright Elsevier 2023

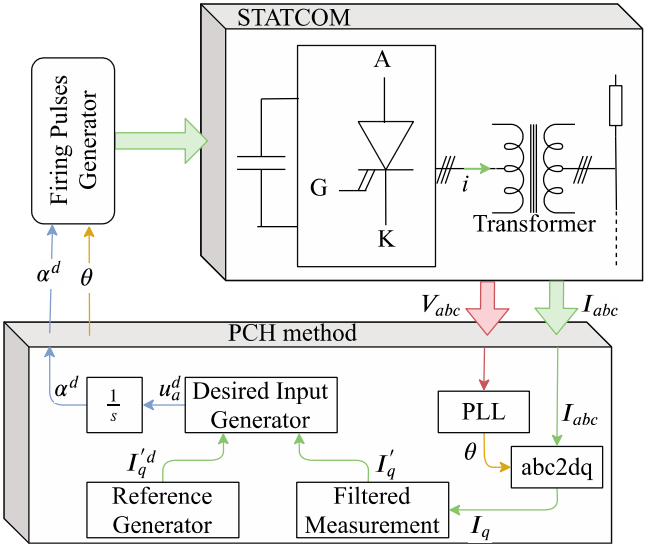

FIGURE 2.24 Controller block diagram of the port-controlled Hamiltonian (PCH) method for STATCOM system.

TABLE 2.4 STATCOM system parameters in simulation.

Power rate	100 MVA	Gird voltage	345 kV
R_s'	0.00071 pu	R_p'	727.5846 pu
L'	0.15 pu	k	0.6312
C'	2.78 pu	f	60 Hz

2.6 Conclusions and future prospective

This chapter has introduced how to design and analyze the robust control law for power electronic systems. At first, a grid-connected inverter is introduced in order to design a robust controller. It is shown that the VM-DPC is robust to the grid variations and line filter parameter variations. Moreover, the exponential stability of the closed-loop system is guaranteed in the whole operating range. Then, a computationally efficient method is introduced to design a robust small-signal stabilization control without knowing the exact system equilibria for a DC/DC converter and DC microgrid. It is easy to analyze the stability of the system even if there exists strong uncertainties. Finally, the PBC shows that it is easy to modify the energy function and add dissipation

This book belongs to Kitab Liaison (ocd1996@gmail.com) Copyright Elsevier 2023

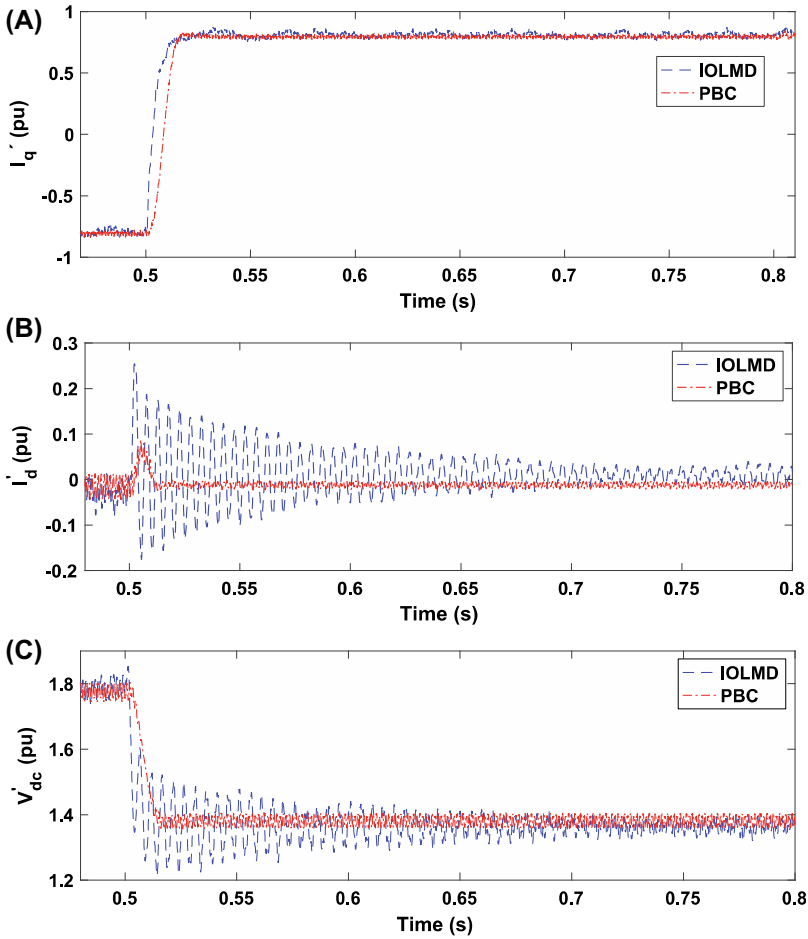

FIGURE 2.25 Simulation result of the STATCOM when $I_q^{'d}$ changes from -0.8 pu to 0.8 pu. (A) I'_q, (B) I'_d, (C) V'_{dc}.

into the system. The PBC is applied to STATCOM and microgrid applications, where it is proven that the PBC is an effective method to obtain robust properties.

In the future work, parallel converters control with the above methods should be studied, e.g., also by considering communication. Due to the increase of the power electronic penetration in the power system, an optimum management strategy of power electronic systems is needed to obtain efficient and economic performance. The stability can be guaranteed easily with the aforementioned methods, and the references of each power electronic system are calculated based on the system characteristics to improve the reliability and efficiency of the overall system.

This book belongs to Kitab Liaison (ocd1996@gmail.com) Copyright Elsevier 2023

Another potential research direction is to study the impact of cyber-attacks on system stability and control performance. Controllers designed in this section generally require measurements taken from the system like state feedback. These measurements, when sent through communication networks such as a wireless network, can be vulnerable to cyber-attacks. A cyber-attack can jeopardize the integrity and availability of the transmitted data. Maliciously modified or incomplete data convey false system information, and may mislead controllers to make incorrect decisions. Most control design only considers the system performance in the normal operation case. While working under cyber-attack threats, incorrect actions taken by a controller may not accomplish the control objective and in some cases may even cause instability. The controllers designed in this section have certain robustness against uncertainties, but their performance against attacks is still an open question.

Acknowledgment

Argonne National Laboratory's work is based upon work supported by the US Department of Energy's Office of Energy Efficiency and Renewable Energy under the Solar Energy Technologies Office Award Number 34230.

References

[1] F. Blaabjerg, R. Teodorescu, M. Liserre, A.V. Timbus, Overview of control and grid synchronization for distributed power generation systems, IEEE Trans. Ind. Electron. 53 (5) (2006) 1398−1409.

[2] J. Stoustrup, A. Annaswamy, A. Chakrabortty, Z. Qu, Smart Grid Control, Springer, 2019, ISBN 978-3-319-98309-7.

[3] Y. Gui, X. Wang, F. Blaabjerg, D. Pan, Control of grid-connected voltage-source converters: the relationship between direct-power control and vector-current control, IEEE Ind. Electron. Mag. 13 (2) (2019) 31−40.

[4] R. Wang, Q. Sun, P. Zhang, Y. Gui, D. Qin, P. Wang, Reduced-Order Transfer Function Model of the Droop-Controlled Inverter via Jordan Continued-Fraction Expansion, IEEE Trans. Energy Convers. 35 (3) (2020) 1585−1595.

[5] M.P. Kazmierkowski, L. Malesani, Current control techniques for three-phase voltage-source PWM converters: a survey, IEEE Trans. Ind. Electron. 45 (5) (1998) 691−703.

[6] F. Huerta, J. Pérez, S. Cóbreces, M. Rizo, Frequency-adaptive multiresonant LQG state-feedback current controller forLCL-filtered VSCs under distorted grid voltages, IEEE Trans. Ind. Electron. 65 (11) (2018) 8433−8444.

[7] N. Arab, H. Vahedi, K. Al-Haddad, LQR control of single-phase grid-tied PUC5 inverter with LCL filter, IEEE Trans. Ind. Electron. 67 (1) (2020) 297−307.

[8] M. Ghafouri, U. Karaagac, H. Karimi, S. Jensen, J. Mahseredjian, S. Faried, An LQR controller for damping of subsynchronous interaction in DFIG-based wind farms, IEEE Trans. Power Syst. 32 (6) (2017) 4934−4942.

[9] A. Isidori, Nonlinear Control Systems, Springer Science & Business Media., 1995, ISBN 978-1-4471-3909-6.

This book belongs to Kitab Liaison (ocd1996@gmail.com) Copyright Elsevier 2023

[10] T.S. Lee, Input-output linearization and zero-dynamics control of three-phase AC/DC voltage-source converters, IEEE Trans. Power Electron. 18 (1) (2003) 11−22.

[11] Y. Gui, M. Li, J. Lu, S. Golestan, J.M. Guerrero, J.C. Vasquez, A voltage modulated DPC approach for three-phase PWM rectifier, EEE Trans. Ind. Electron. 65 (10) (2018) 7612−7619.

[12] A. Mullane, G. Lightbody, R. Yacamini, Wind-turbine fault ride-through enhancement, IEEE Trans. Power Syst. 20 (4) (2005) 1929−1937.

[13] K.H. Kim, Y.C. Jeung, D.C. Lee, H. Kim, LVRT scheme of PMSG wind power systems based on feedback linearization, IEEE Trans. Power Electron. 27 (5) (2012) 2376−2384.

[14] N.C. Sahoo, B.K. Panigrahi, P.K. Dash, G. Panda, Application of a multivariable feedback linearization scheme for STATCOM control, Elec. Power Syst. Res. 62 (2) (2002) 81−91.

[15] Y. Han, Y.O. Lee, C.C. Chung, Modified non-linear damping of internal dynamics via feedback linearisation for static synchronous compensator, IET Gener., Transm. Distrib. 5 (9) (2011) 930−940.

[16] S. Yang, P. Wang, Y. Tang, Feedback linearization-based current control strategy for modular multilevel converters, IEEE Trans. Power Electron. 33 (1) (2018) 161−174.

[17] V. Utkin, J. Guldner, J. Shi, Sliding Mode Control in Electro-Mechanical Systems, CRC press, 2009. ISBN: 9781420065602 - CAT# 65602.

[18] M. Zhang, Y. Li, F. Liu, L. Luo, Y. Cao, M. Shahidehpour, Voltage stability analysis and sliding-mode control method for rectifier in DC systems with constant power loads, IEEE J. Emerg. Select. Top. Power Electron. 5 (4) (2017) 1621−1630.

[19] Y. Gui, J.D. Bendtsen, J. Stoustrup, Sliding mode control with grid voltage modulated direct power control for three-phase AC-DC converter, in: 38th Chinese Control Conference (CCC), 2019, pp. 7436−7441.

[20] Y. Gui, F. Blaabjerg, X. Wang, J.D. Bendtsen, D. Yang, J. Stoustrup, Improved DC-link voltage regulation strategy for grid-connected converters, IEEE Trans. Ind. Electron. (2020) 1−11 (in press).

[21] X. Zheng, Y. Feng, F. Han, X. Yu, Integral-type terminal sliding-mode control for grid-side converter in wind energy conversion systems, IEEE Trans. Ind. Electron. 66 (5) (2019) 3702−3711.

[22] D. Jeong, C. Kim, Y. Gui, C.C. Chung, Sliding mode control for LVRT of a PMSG wind turbine using stored energy in rotor inertia, in: IEEE Power and Energy Society General Meeting (PESGM), 2016, pp. 1−5.

[23] J. Wu, Q. Chen, M. Du, S. Yu, Sliding-mode variable structure controller for cascade STATic var COMpensator, IET Power Electron. 6 (2) (2013) 343−352.

[24] Y. Gui, C.C. Chung, Integral sliding mode control for type 2 STATCOM systems via input-output linearization with dynamic extension, in: 54th IEEE Conference on Decision and Control (CDC), 2013, pp. 1991−1996.

[25] Q. Yang, M. Saeedifard, M. Perez, Sliding mode control of the modular multilevel converter, IEEE Trans. Ind. Electron. 66 (2) (2019) 887−897.

[26] X. Yang, Z. Li, T.Q. Zheng, X. You, P. Kobrle, Virtual impedance sliding mode control-based MMC circulating current suppressing strategy, IEEE Access 7 (2019) 26229−26240.

[27] R. Ortega, J.A.L. Perez, P.J. Nicklasson, H.J. Sira-Ramirez, Passivity-based Control of Euler-Lagrange Systems: Mechanical, Electrical and Electromechanical Applications, Springer Science & Business Media, 2013, ISBN 978-1-84996-852-2.

[28] T.S. Lee, Lagrangian modeling and passivity-based control of three-phase AC/DC voltage-source converters, IEEE Trans. Ind. Electron. 51 (4) (2004) 892−902.

This book belongs to Kitab Liaison (ocd1996@gmail.com) Copyright Elsevier 2023

[29] Y. Gui, C. Kim, C.C. Chung, Improved low-voltage ride through capability for PMSG wind turbine based on port-controlled Hamiltonian system, Int. J. Contr. Autom. Syst. 14 (5) (2016) 1195−1204.

[30] Y. Gui, Y.O. Lee, Y. Han, W. Kim, C.C. Chung, Passivity-based control with nonlinear damping for STATCOM system, in: 51st IEEE Conference on Decision and Control (CDC), 2012, pp. 1715−1720.

[31] G.Z.D. Bergna-Diaz, S. Sanchez, R. Ortega, E. Tedeschi, PI passivity-based control and performance analysis of MMC multi-terminal HVDC systems, IEEE J. Emerg. Select. Top. Power Electron. 7 (4) (2019) 2453−2466.

[32] P. Schavemaker, L. Van Der Sluis, Electrical Power System Essentials, John Wiley & Sons, 2008, ISBN 978-0-470-98768-1.

[33] Y. Gui, W. Kim, C.C. Chung, Passivity-based control with nonlinear damping for type 2 STATCOM systems, IEEE Trans. Power Syst. 31 (4) (2016) 2824−2833.

[34] Y. Gui, C. Kim, C.C. Chung, Grid voltage modulated direct power control for grid connected voltage source inverters, in: 2017 American Control Conference (ACC), 2017, pp. 2078−2084.

[35] Y. Gui, X. Wang, H. Wu, F. Blaabjerg, Voltage modulated direct power control for a weak grid-connected voltage source inverters, IEEE Trans. Power Electron. 34 (11) (2019) 11383−11395.

[36] Y. Gui, Q. Xu, F. Blaabjerg, H. Gong, Sliding mode control with grid voltage modulated DPC for voltage source inverters under distorted grid voltage, CPSS Trans. Power Electron. Appl. 4 (3) (2019) 244−254.

[37] Y. Gui, X. Wang, F. Blaabjerg, Vector current control derived from direct power control for grid-connected inverters, IEEE Trans. Power Electron. 34 (9) (2019) 9224−9235.

[38] W. Gil-González, O.D. Montoya, A. Garces, Direct power control for VSC-HVDC systems: an application of the global tracking passivity-based PI approach, Int. J. Electr. Power Energy Syst. 110 (2019) 588−597.

[39] R.J. Wai, Y. Yang, Design of backstepping direct power control for three-phase PWM rectifier, IEEE Trans. Ind. Appl. 55 (3) (2019) 3160−3173.

[40] S. Gao, H. Zhao, Y. Gui, D. Zhou, F. Blaabjerg, An Improved Direct Power Control for Doubly Fed Induction Generator, IEEE Trans. Power Electron. 36 (4) (2021) 4672−4685.

[41] Y. Gui, C. Kim, C.C. Chung, J.M. Guerrero, Y. Guan, J.C. Vasquez, Improved direct power control for grid-connected voltage source converters, IEEE Trans. Ind. Electron. 65 (10) (2018) 8041−8051.

[42] Y. Gui, G.H. Lee, C. Kim, C.C. Chung, Direct power control of grid connected voltage source inverters using port-controlled Hamiltonian system, Int. J. Contr. Autom. Syst. 15 (5) (2017) 2053−2062.

[43] J. Hu, L. Shang, Y. He, Z. Zhu, Direct active and reactive power regulation of grid-connected DC/AC converters using sliding mode control approach, IEEE Trans. Power Electron. 26 (1) (2011) 210−222.

[44] J. Liu, W. Zhang, G. Rizzoni, Robust stability analysis of DC microgrids with constant power loads, IEEE Trans. Power Syst. 33 (1) (2018) 851−860.

[45] C. Li, L. Chen, K. Aihara, Stability of Genetic Networks With SUM Regulatory Logic: Lur'e System and LMI Approach, IEEE Trans. Circuit. Syst. I: Regular Paper. 53 (11) (2006) 2451−2458.

[46] S. Boyd, L. Vandenberghe, Convex Optimization, Cambridge University Press, 2004, ISBN 9780511804441.

This book belongs to Kitab Liaison (ocd1996@gmail.com) Copyright Elsevier 2023

[47] J.G. VanAntwerp, R.D. Braatz, A tutorial on linear and bilinear matrix inequalities, J. Process Contr. 10 (4) (2000) 363−385.

[48] P.C. Loh, D. Li, Y.K. Chai, F. Blaabjerg, Autonomous operation of hybrid microgrid with AC and DC subgrids, IEEE Trans. Power Electron. 28 (5) (2013) 2214−2223.

[49] H.K. Khalil, Nonlinear Systems, 2002, ISBN 0-13-067530-X. Upper Saddle River.

[50] R. Ortega, A. Van Der Schaft, B. Maschke, G. Escobar, Interconnection and damping assignment passivity-based control of port-controlled Hamiltonian systems, Automatica 38 (4) (2002) 585−596.

[51] S. Gugercin, R. Polyuga, C. Beattie, A. Van Der Schaft, Structure-preserving tangential interpolation for model reduction of port-Hamiltonian systems, Automatica 48 (9) (2012) 1963−1974.

[52] Y. Gui, Y.O. Lee, Y. Han, C.C. Chung, Novel passivity-based controller design for back-to-back STATCOM with asymmetrically structured converters, in: IEEE Power and Energy Society General Meeting, 2012, pp. 1−6.

[53] Y. Gui, B. Wei, M. Li, J.M. Guerrero, J.C. Vasquez, Passivity-based coordinated control for islanded AC microgrid, Appl. Energy 229 (2018) 551−561.

[54] Y. Gui, D.E. Chang, C.C. Chung, Tracking controller design methodology for passive port-controlled Hamiltonians with application to type-2 STATCOM systems, in: 52nd IEEE Conference on Decision and Control, 2013, pp. 1653−1658.

[55] H.J. Sira-Ramirez, R. Silva-Ortigoza, Control Design Techniques in Power Electronics Devices, Springer Science & Business Media, 2006, ISBN 978-1-84996-605-4.

[56] L. Harnefors, A. Yepes, A. Vidal, J. Doval-Gandoy, Passivity-based controller design of grid-connected VSCs for prevention of electrical resonance instability, IEEE Trans. Ind. Electron. 62 (2) (2014) 702−710.

[57] Y. Gui, C.C. Chung, F. Blaabjerg, M.G. Taul, Dynamic extension algorithm based tracking control of STATCOM via port-controlled Hamiltonian system, IEEE Trans. Ind. Inform. 16 (8) (2020) 5076−5087 (in press).

This book belongs to Kitab Liaison (ocd1996@gmail.com) Copyright Elsevier 2023

Chapter 3

Sliding mode controllers in power electronic systems

Hosein Gholami-Khesht, Pooya Davari, Frede Blaabjerg
Aalborg University, Aalborg, Denmark

3.1 Introduction

Nowadays, power electronic converters have become one of the critical components in the energy sectors, and they are widely used in the generation, transmission, and consumption parts in this sector due to their various advantages that they offer. The most important benefits are full controllability, flexibility, high control performance, and high efficiency in their power conversion. However, power electronic converters are prone to instability, since they are subject to various nonlinearities, uncertainties, unmolded dynamics, and disturbances. Consequently, developing a control strategy with a strong robustness feature, which is the heart of the whole power converter system, is highly desired.

Sliding mode control (SMC) or variable structure control (VSC) is known as a good control solution to comply with these issues that offers important benefits such as high robustness against system uncertainties, unknown disturbances, fast dynamic response, and simple structure and the concept. Due to these advantages, SMC is implemented in the power electronic applications such as photovoltaic power system [1–3], wind turbine systems [4–6], high-performance control of AC drives [7,8], microgrids [9,10], grid-connected voltage source inverters (VSIs) [11–16], active front end rectifiers [17–19], uninterruptible power supplies (UPSs) [20], and active power filters [21,22], and more applications are seen day by day.

In this respect, the first aim of this chapter is thus to describe and investigate this powerful control method and its new advances. The classic or traditional SMC is very robust and simple and also independent of system uncertainties and disturbances. However, it suffers from two main shortcomings, as it has high chattering in the control input [1,5,10,22] as well as asymptotically and infinite time convergence of tracking variables to the desired values. To reduce chattering in the control action, boundary-layer SMC and adaptive boundary-layer SMC have been presented. Moreover, in order to provide finite-time

Control of Power Electronic Converters and Systems. https://doi.org/10.1016/B978-0-12-819432-4.00005-6
Copyright © 2021 Elsevier Ltd. All rights reserved.

This book belongs to Kitab Liaison (ocd1996@gmail.com)
Copyright Elsevier 2023

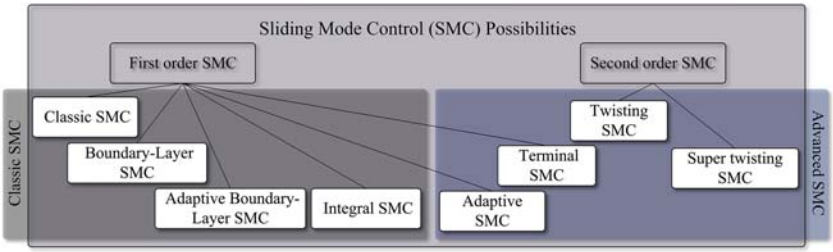

FIGURE 3.1 Classification of different sliding mode controls (SMCs).

convergence of tracking variables, the terminal SMC (TSMC) concept has been introduced [23,24]. Recently due to the existence of powerful digital processors, second-order SMC (SOSMC) have been attracted considerable attention from researchers because these methods can preserve the advantages of the classic SMC, while compensating its shortcomings such as high chattering and infinite time convergence [6,7,17,18]. So far, different algorithms for SOSMC have been proposed. The most practical control methods are twisting controller and its modified versions super-twisting controller, which will be discussed in this chapter in more details. To give an overview of the methods, a classification of different SMCs is shown in Fig. 3.1. In the following sections, the basic concept of SMC and its new advances will be presented, and it will be applied on a three-phase VSI in an UPS application.

3.2 System dynamics of a voltage source inverter

The first step before implementing the SMC control law is to find the dynamic model of the system under consideration. A schematic diagram of the investigated three-phase UPS is shown in Fig. 3.2, which consists of a three-phase VSI connected to loads through an LC filter. Based on Fig. 3.2 and Kirchhoff's Laws, the system equation can be readily written as

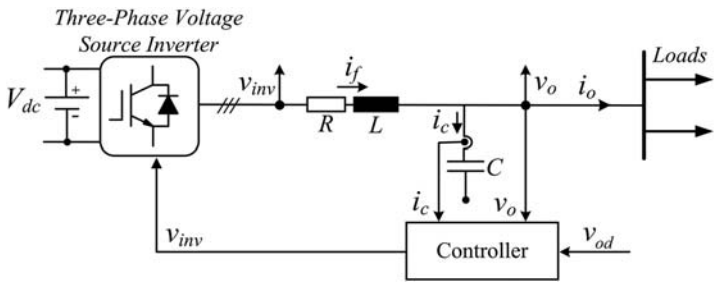

FIGURE 3.2 Single-phase diagram of three-phase voltage source inverter (VSI) in an uninterruptible power supply (UPS) application.

This book belongs to Kitab Liaison (ocd1996@gmail.com) Copyright Elsevier 2023

$$\begin{cases} L\dfrac{di_f}{dt} = v_{inv} - v_o - Ri_f \\ C\dfrac{dv_o}{dt} = i_f - i_o \\ i_f = i_c + i_o \end{cases} \tag{3.1}$$

where v_{inv}, v_o, are output voltage of the inverter and capacitor voltage or voltage at the point of common coupling (PCC), i_f, i_o, and i_c are the inverter or inductor current, capacitor current, and load current. Besides, L and R are filter inductance, and its equivalent resistance and C is the filter capacitance. In practice, the value of parameters L, R, and C is not exactly known, and they could vary from the nominal values. Therefore, the impact of parameter variations must be investigated on the control system performance. By considering v_o and i_c as system states and i_o as input disturbance, Eq. (3.1) can be rewritten in standard state space form:

$$\frac{dx}{dt} = Ax + Bu + d$$

$$x = \begin{bmatrix} x_1 \\ x_2 \end{bmatrix} = \begin{bmatrix} i_c \\ v_o \end{bmatrix}, d = \begin{bmatrix} d_1 \\ d_2 \end{bmatrix}, u = v_{inv}, A = \begin{bmatrix} -\dfrac{R_n}{L_n} & -\dfrac{1}{L_n} \\ \dfrac{1}{C_n} & 0 \end{bmatrix}, B = \begin{bmatrix} \dfrac{1}{L_n} \\ 0 \end{bmatrix} \tag{3.2}$$

where x and u are system states and control input, d is disturbance inputs, which include all system uncertainties and disturbances, A and B are the state and input matrixes, and parameters with subscript n show the nominal values of the system parameters.

3.3 Introduction to sliding mode control

The classic SMC has been applied in power electronic and electric drive applications in Refs. [25–27] for the first time. After that, it has been quickly extended to various implementations of these systems as discussed in the introduction. The primary aim of this section is to review the basic idea of classic SMC and the reachability conditions. After that, the structure of control input in SMC is introduced and calculated. Interested readers can refer to some primary and basic works in this topic for more details in Ref. [25–30]. It is worth to note that the application of classic SMC to three-phase UPS will be presented in the next section.

This book belongs to Kitab Liaison (ocd1996@gmail.com) Copyright Elsevier 2023

The dynamic equation of a nonlinear single-input system can be represented as

$$\mathbf{x}^n = f(\mathbf{x}) + b(\mathbf{x})u \tag{3.3}$$

where scalar variables x and u are system output and control input. Therefore, the state vector would be

$$\mathbf{x} = \begin{bmatrix} x & \dot{x} & \dots & x^{(n-1)} \end{bmatrix}^T \tag{3.4}$$

In Eq. (3.3), $f(x)$ and $b(x)$ are uncertain nonlinear functions, but upper bounded by known, continuous function of x (i.e., $|f(\mathbf{x})| < F_1(\mathbf{x}), |b(\mathbf{x})| < B_1(\mathbf{x})$, where F_1 and B_1 are known continuous functions). The sign of $b(x)$ is also known. It is worth to note that Eq. (3.3) is a general form that also includes the studied linear system in Eq. (3.2) by simply assuming $f(\mathbf{x}) = Ax$ and $b(\mathbf{x}) = B$.

The control objective is the convergence of the state vector to the desired or reference state vector in the presence of the system uncertainties and disturbances.

Therefore, the tracking error can be defined as

$$\mathbf{e_x} = \mathbf{x} - \mathbf{x_d} = \begin{bmatrix} \mathbf{e_x} & \dot{\mathbf{e}}_\mathbf{x} & \dots & \mathbf{e}_\mathbf{x}^{(n-1)} \end{bmatrix}^T \tag{3.5}$$

where $\mathbf{x_d} = \begin{bmatrix} x_d & \dot{x}_d & \dots & x_d^{(n-1)} \end{bmatrix}^T$ is the reference state vector.

Now, let us define the time-variant surface $s(t)$ with the scalar equation $s(\mathbf{e_x}, t) = 0$ as [30]

$$s(\mathbf{e_x}, t) = \left(\frac{d}{dt} + \lambda\right)^{n-1} \mathbf{e_x} \tag{3.6}$$

here λ is a positive constant that determines the convergence rate of the dynamic error to zero. And $s(\mathbf{e_x}, t) = 0$ shows a differential equation, which has only one solution $\mathbf{e_x} \equiv 0$.

Therefore, if we can bring and remain the system states on the sliding surface $(s(\mathbf{e_x}, t) = 0)$, the dynamic error Eq. (3.5) converges to zero by the specified dynamics in Eq. (3.6), which is independent of either the plant parameters or the external disturbances. This so-called "invariance" feature looks interesting for designing a controller for the dynamic system operating under plant uncertainties. Another exciting feature is changing the reference-tracking problem Eq. (3.5) by keeping the scalar s to zero for all $t > 0$. In other words, the tracking problem of n dimension vector ($\mathbf{x_d}$) is reduced to the stabilizing problem of one scalar variable (s).

The sliding surface is attractive,[1] and system states move and remain on this surface $(s(\mathbf{e_x}, t) = 0)$, if the control input fulfills the reachability condition. So, our goals would be

1. Attractive sliding surface means that trajectories outside the surface converge to it.

This book belongs to Kitab Liaison (ocd1996@gmail.com)
Copyright Elsevier 2023

1. Defining the reachability condition, which guarantees the moving of the system states to the sliding surface, anywhere in the state plane and under all system uncertainties and disturbances.
2. Calculating the control input to fulfill the reachability condition and maintaining the system state on the sliding surface for all further times.

3.3.1 Reachability condition in the sliding mode control

The system state goes and remains on the sliding surface ($s(t)$) from anywhere in the state plane when the reaching condition is fulfilled. There are different forms of reaching conditions, and generally, they can be classified into three categories of switching functions, Lyapunov function, and dynamic method.

The earliest and oldest reaching condition is

$$s\dot{s} < 0 \tag{3.7}$$

It is worth noting that s can be selected simply as Eq. (3.6) or any desirable differentiable linear or nonlinear dynamic error. The condition in Eq. (3.7) is universal. However, it does not guarantee a finite and limited reaching time. Another choice that belongs to this category is

$$\frac{1}{2}\frac{d}{dt}s^2 \leq -\eta|s| \tag{3.8}$$

In this condition, η is a positive constant value. If the mentioned condition is fulfilled, the reaching time (t_r) would be less than $t_r < \frac{|s(t=0)|}{\eta}$ [30].

In the second method, a positive definite Lyapunov function V is considered as follows:

$$V(x,t) = \frac{1}{2}s^2 \tag{3.9}$$

To ensure the system stability, the time derivative of V must be negative definite:

$$\dot{V}(x,t) = s\dot{s} < 0, \quad s \neq 0 \tag{3.10}$$

To guarantee the finite reaching time, Eq. (3.10) can be modified to

$$\dot{V}(x,t) = s\dot{s} < -\eta|s|, \quad s \neq 0, \ \eta > 0 \tag{3.11}$$

In the last method, the dynamics of the switching surface are directly defined by the following differential equation:

$$\dot{s} = -Q\mathrm{sgn}(s) - k \times f(s) \tag{3.12}$$

The above equation is also called the reaching law. Here, Q and k are definite positive gains, and sgn(s) indicates the sign function, which is

This book belongs to Kitab Liaison (ocd1996@gmail.com) Copyright Elsevier 2023

$$\mathrm{sgn}(s) = \begin{cases} +1 & , s > 0 \\ -1 & , s < 0 \end{cases} \tag{3.13}$$

Different choices for k and Q result in different state trajectories to the sliding plane. Besides, it provides implementing different structures for the reaching law.

3.3.2 Control input calculation

The control law in sliding mode usually consists of the following terms:

$$u = u_{eq} + u_{un} = u_{eq} - k \times \mathrm{sgn}(s) \tag{3.14}$$

where u_{eq} is a linear and continuous part, which is called equivalent control. It is only effective when the system state is in the sliding mode and maintains the system on the sliding surface. It is calculated from

$$\dot{s} = 0 \rightarrow u_{eq} \tag{3.15}$$

For calculating u_{eq} it is assumed that uncertainties and disturbances are zeros. These uncertainties and disturbances would be compensated by the second nonlinear and discontinuous part of the control input. u_{un} brings the system state, everywhere on the state plane, to the sliding surface and keeps them on the surface under all bounded disturbances. This term is calculated to accomplish the reachability conditions, which is defined in Section 3.1.

3.4 Classical sliding mode control

The control objective in a UPS system is to track the desired or reference output voltage (v_{od}) under different system uncertainties and disturbances. Therefore, using Eq. (3.2) and doing some manipulations, the tracking error and second-order derivative of it can be calculated as

$$e_{v_o} = v_o - v_{od} \tag{3.16}$$

$$\begin{cases} \ddot{e}_{vo} = \ddot{v}_o - \ddot{v}_{od} = \dfrac{1}{C_n L_n}(v_{inv} - v_o - R_n i_c) - \ddot{v}_{od} + \dfrac{d_1}{C_n} + \dot{d}_2 \\ \ddot{e}_{vo} = \ddot{v}_o - \ddot{v}_{od} = \varphi + \gamma v_{inv} + h(t) \end{cases} \tag{3.17}$$

where φ and γ are functions based on the system nominal parameters and measured states, and all system uncertainties and unmeasured disturbances are lumped into $h(t)$ as being represented:

This book belongs to Kitab Liaison (ocd1996@gmail.com) Copyright Elsevier 2023

$$\begin{cases} \gamma = \dfrac{1}{C_n L_n} \\ \varphi = \dfrac{1}{C_n L_n}(-v_o - R_n i_c) - \ddot{v}_{od} \\ h(t) = \dfrac{d_1}{C_n} + \dot{d}_2 \end{cases} \tag{3.18}$$

The system under study is of order 2. Thus, the sliding surface Eq. (3.6) can be defined as

$$s(e_{vo}, t) = \dot{e}_{vo} + \lambda e_{vo} \tag{3.19}$$

To have a stable system and an attractive sliding surface (s), the control input must fulfill the following condition based on the Lyapunov stability theorem in Eq. (3.11):

$$s\dot{s} < -\eta|s|, \quad s \neq 0, \ \eta > 0 \tag{3.20}$$

By the time derivative of s, one has

$$\begin{cases} \dot{s}(e_{vo}, t) = \ddot{e}_{vo} + \lambda \dot{e}_{vo} = \varphi_1 + \gamma v_{inv} + h(t) \\ \varphi_1 = \varphi + \lambda \dot{e}_{vo} \end{cases} \tag{3.21}$$

Based on Eqs. (3.15) and (3.21), the equivalent control law is calculated as

$$\dot{s}(e_{vo}, t) = h(t) = 0 \rightarrow \varphi_1 + \gamma v_{eq} = 0 \rightarrow v_{eq} = \frac{-\varphi_1}{\gamma} \tag{3.22}$$

By considering the nonlinear part of the control law in Eq. (3.14) to guarantee attractivity of s and to compensate for system uncertainties, the final control law can be written

$$v_{inv} = v_{eq} + v_{un} = \frac{-\varphi_1}{\gamma} - \frac{k}{\gamma} \times \mathrm{sgn}(s) \tag{3.23}$$

The implementation of the obtained control law in the classic SMC is shown in Fig. 3.3.

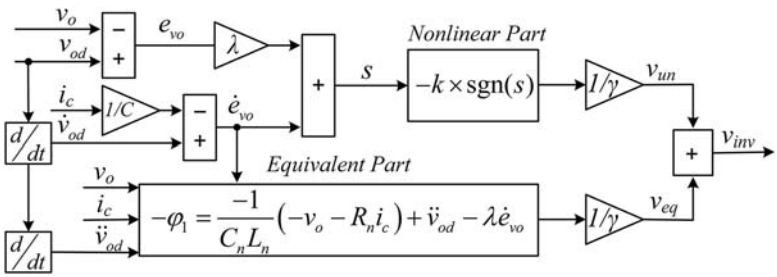

FIGURE 3.3 Structure diagram of the classic sliding mode control Eq. (3.23) to control an uninterruptible power supply system.

This book belongs to Kitab Liaison (ocd1996@gmail.com) Copyright Elsevier 2023

By replacing Eqs. (3.21) and (3.23) into Eq. (3.20) and doing some simplifications, one can have

$$s\dot{s} = s(\varphi_1 + \gamma v_{inv} + h(t)) = s(-k \times \mathrm{sgn}(s) + h(t)) \leq s(-k \times \mathrm{sgn}(s) + H) \tag{3.24}$$

where h(t) is bounded and $|h(t)| < H$. Choosing $k > H + \eta$:

$$s\dot{s} < -\eta|s| \tag{3.25}$$

which completely fulfills Eq. (3.20), and therefore v_{inv} is a stabilizing controller, and s is an attractive surface without any concern about the initial state of system and uncertainties.

After that the system reaches to the sliding surface, the error dynamics will be

$$s(e_{vo}, t) = \dot{e}_{vo} + \lambda e_{vo} = 0 \tag{3.26}$$

Its solution is

$$e_{vo}(t) = e_{vo}(0)e^{(-\lambda t)} \tag{3.27}$$

which is independent of system uncertainties and system disturbances. However, as it can be seen, the error dynamics on the sliding surface goes exponentially to zero at infinite time, i.e., $e_{vo}(t) \rightarrow 0$ when $t \rightarrow \infty$. It is one major drawback of the classic SMC.

It is worth to remark that a sliding mode controller has the two following dynamics, as it is shown in the phase portrait in Fig. 3.4:

(1) **A reaching phase** with limited time $((t_r < \eta^{-1}|s(t = 0)|))$, in which the system states reach the sliding surface in the presence of system uncertainties and disturbances with the help of control input, that is obtained by the reachability condition.

(2) **A sliding phase** with infinite time $(t_s = \infty)$, in which states remain on the sliding surface for all further times and thus converges to the desired state according to the specified dynamic by the sliding surface Eq. (3.26).

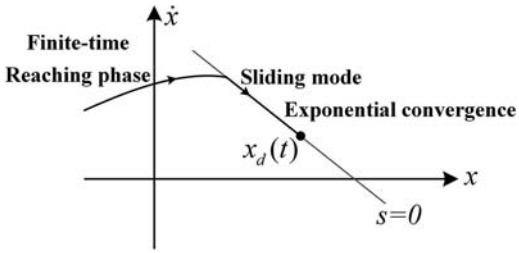

FIGURE 3.4 Main phases in sliding mode control of a second-order system [30].

This book belongs to Kitab Liaison (ocd1996@gmail.com) Copyright Elsevier 2023

3.5 Boundary-layer sliding mode control

Although classic SMC is a robust and straightforward control method, however, it suffers from a "chattering" phenomenon due to the unavoidable unmodelled dynamics of the plant and discontinuous sign function in the control law. In many practical applications, chattering makes it impossible to implement the classic SMC. A simple solution to have a continuous/smooth control input is approximating the discontinuous function sgn(s) by some continuous/smooth function like sigmoid function, saturation function, hyperbolic tangent, etc. A good approximation can be achieved by using the saturation function [1]:

$$sat\left(\frac{s}{\varepsilon}\right) = \begin{cases} \frac{s}{\varepsilon}, & |s(e_{vo}, t)| < \varepsilon \\ \mathrm{sgn}(s), & |s(e_{vo}, t)| > \varepsilon \end{cases} \tag{3.28}$$

where ε is a small positive constant. Selecting ε is a compromise between ideal performance and robustness of the ideal SMC and smooth/continuous control action. It is worth to note that under nonideal SMC, the sliding and state variables do not converge to zero at all. However, they go close to the origin ($|e_{v_o}(t = \infty)| < \varepsilon/\lambda$), which provides an acceptable performance and accuracy in most applications [30].

3.5.1 Adaptive boundary-layer sliding mode control

As discussed in Section 3.5, selection of ε is a trade-off between maintaining an ideal performance and ensuring a smooth control action. However, tuning of this parameter may be a difficult task in many applications. In Ref. [30], a useful and straightforward adaption law to update this parameter is presented, which ensures a good compromise. The proposed adaption law is

$$\dot{\varepsilon} + \lambda\varepsilon = k(x_d) \tag{3.29}$$

It is worth to remark that to stabilize system, the control gain must fulfill $k > H + \eta$ in Eq. (3.24). Here, H is a bounded, known continuous function of x. To implement the adaption law Eq. (3.29), x in H is replaced by the desired values (x_d) [30].

3.6 Adaptive sliding mode control

As discussed in Section 3.4, in order to have a stable closed-loop system, the control gain k must be greater than the upper bound of the system uncertainties and disturbances, i.e., $k > H + \eta$. If an accurate value of the upper band is not available, the control gain k must be overestimated to have a stable system and an attractive s. However, a high control gain k can lead to too large amplitude and high chattering in the control action, which is not desirable at all. Therefore, an adaption method seems to be necessary to find a proper value of

This book belongs to Kitab Liaison (ocd1996@gmail.com) Copyright Elsevier 2023

control gain that minimizes discontinuity of the control law and consequently reducing the chattering effect. To accomplish this, the Lyapunov function in Eq. (3.9) is modified to include the unknown control gain as [31]

$$V(x,t)=\frac{1}{2}s^2+\frac{1}{2\rho}\widetilde{k}^2,\quad \widetilde{k}=k-\widehat{k},\ \rho>0 \tag{3.30}$$

where k and $\widehat{k}$ are the accurate and estimated value of the control gain. To ensure the system stability and attractivity of s, the time derivative of V must be negative definite:

$$\dot{V}(x,t)=s\dot{s}+\rho^{-1}\widetilde{k}\dot{\widetilde{k}} \tag{3.31}$$

By assuming that $\begin{cases}\dot{k}=0\\ \dot{s}=m(t)-\widehat{k}\mathrm{sgn}(s)\\ |m(t)|\leq M\end{cases}$, and replacing them in Eq. (3.31), one has

$$\dot{V}(x,t)=s\times\left(m(t)-\widehat{k}\mathrm{sgn}(s)\right)+\rho^{-1}\widetilde{k}\dot{\widehat{k}}=s\times m(t)-\widehat{k}|s|-\rho^{-1}\dot{\widehat{k}}\left(k-\widehat{k}\right) \tag{3.32}$$

Considering the following adaption law for the control gain:

$$\dot{\widehat{k}}=\rho|s| \tag{3.33}$$

Eq. (3.32) can be simplified to

$$\dot{V}(x,t)\leq M|s|-\rho^{-1}\dot{\widehat{k}}\,k=M|s|-\rho^{-1}\rho|s|k=M|s|-k|s|=(M-k)|s|=-\eta|s| \tag{3.34}$$

where $M-k=-\eta,\ \eta>0$. Therefore $\dot{V}(x,t)$ is a definite negative for all $s\neq 0$, Eq. (3.30) is a Lyapunov function, and the closed loop is stable, s is attractive, and all signals are bounded under adaption law Eq. (3.33). The implementation of adaptive SMC is shown in Fig. 3.5.

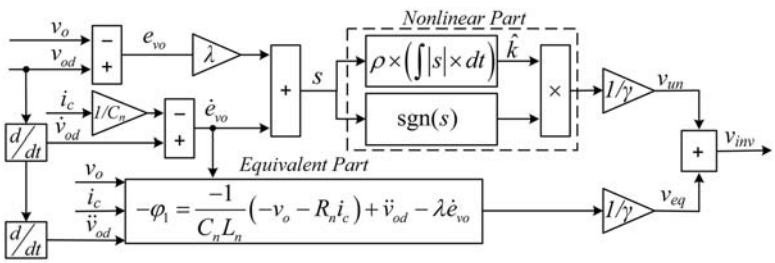

FIGURE 3.5 Structure diagram of the adaptive SMC to control an UPS system.

This book belongs to Kitab Liaison (ocd1996@gmail.com) Copyright Elsevier 2023

3.7 Integral sliding mode control

To have better disturbance rejection and zero steady-state error for DC signals, the sliding surface by the integration of an integrator can be modified as

$$s(e_{vo},t) = \dot{e}_{vo} + \lambda e_{vo} + \frac{\lambda^2}{4}\int e_{vo}dt \tag{3.35}$$

Thus, the time derivative of the sliding variable results in

$$\dot{s}(e_{vo},t) = \ddot{e}_{vo} + \lambda \dot{e}_{vo} + \frac{\lambda^2}{4}e_{vo} = \varphi_2 + \gamma v_{inv} + h(t) \tag{3.36}$$

where $\varphi_2 = \varphi_1 + \frac{\lambda^2}{4}e_{vo}$.

Based on Eq. (3.36), the equivalent control law is

$$\dot{s}(e_{vo},t) = h(t) = 0 \rightarrow \varphi_2 + \gamma v_{eq} = 0 \rightarrow v_{eq} = \frac{-\varphi_2}{\gamma} \tag{3.37}$$

Again the final control law that must fulfill the attractivity of s $(s\dot{s} < -\eta|s|, \quad s \neq 0, \ \eta > 0)$ in the presence of uncertainties and disturbances which can be calculated as

$$v_{inv} = v_{eq} + v_{un} = \frac{-\varphi_2}{\gamma} - \frac{k}{\gamma} \times \mathrm{sgn}(s), \quad k > H + \eta \tag{3.38}$$

3.8 Terminal sliding mode control

The idea of TSMC was proposed to solve the infinite time convergence of the state variables (e_{vo}) when the error dynamics reach and remain on the sliding surface [23,24]. To overcome this issue, the terminal sliding surface is proposed to be

$$s(e_{vo},t) = \dot{e}_{vo}^{\frac{p}{q}} + \lambda e_{vo} \tag{3.39}$$

where p and q must be chosen as two positive odd integers that satisfy the following conditions:

$$\begin{cases} p > q > 0 \\ 1 < \dfrac{p}{q} < 2 \end{cases} \tag{3.40}$$

when the states reach on the sliding surface and they follow the specified dynamics by

$$s(e_{vo},t) = \dot{e}_{vo}^{\frac{p}{q}} + \lambda e_{vo} = 0 \rightarrow \dot{e}_{vo}^{\frac{p}{q}} = -\lambda e_{vo} \tag{3.41}$$

This book belongs to Kitab Liaison (ocd1996@gmail.com) Copyright Elsevier 2023

By integrating both sides of Eq. (3.41) in period ($t_s = t_f - t_r$), and doing some manipulations, one has

$$\begin{aligned}
&\int_{t_r}^{t_f} \dot{e}_{vo}{}^{\frac{p}{q}} = -\lambda \int_{t_r}^{t_f} e_{vo}{}^{\frac{q}{p}} \rightarrow \\
&\int_{t_r}^{t_f} e_{vo}{}^{\frac{-q}{p}} \times de_{vo} = -\lambda \int_{t_r}^{t_f} dt \rightarrow \\
&\frac{1}{1-\frac{q}{p}}\left(e_{vo}(t_f)^{-\frac{q}{p}} - e_{vo}(t_r)^{-\frac{q}{p}}\right) = -\lambda(t_f - t_r) \rightarrow \\
&t_s = t_f - t_r = \frac{e_{vo}(t_r)^{-\frac{q}{p}}}{\lambda\left(1-\frac{q}{p}\right)} < \infty
\end{aligned} \tag{3.42}$$

It is worth to remark that t_r is the time that state variables (s) reach from initial location at the plane to the sliding surface ($s(e_{vo}, t) = 0$), and t_s is the time that the state variables (e_{vo}) converge to zero or desired values on the sliding surface, and t_f is the sum of these two periods.

It is evident from Eq. (3.42) that t_s is a finite time in TSMC, unlike the classical SMC.

The control input can be calculated as shown below. By time derivating of the sliding variable in Eq. (3.41), one has

$$\dot{s}(e_{vo}, t) = \frac{p}{q}\ddot{e}_{vo}\dot{e}_{vo}{}^{\frac{p}{q}-1} + \lambda\dot{e}_{vo} \tag{3.43}$$

By replacing Eqs. (3.16) and (3.17) into Eq. (3.43) and make it equal to zero:

$$\dot{s}(e_{vo}, t) = \varphi + \gamma v_{inv} + \frac{q}{p}\lambda\dot{e}_{vo}{}^{2-\frac{p}{q}} + h(t) = 0 \tag{3.44}$$

The above equation can be summarized as

$$\dot{s}(e_{vo}, t) = \varphi_3 + \gamma v_{inv} + h(t) = 0 \tag{3.45}$$

where $\varphi_3 = \varphi + \frac{q}{p}\lambda\dot{e}_{vo}{}^{2-\frac{p}{q}}$. Based on Eqs. (3.15) and (3.45), the equivalent control law is

$$\dot{s}(e_{vo}, t) = h(t) = 0 \rightarrow \varphi_3 + \gamma v_{eq} = 0 \rightarrow v_{eq} = \frac{-\varphi_3}{\gamma} \tag{3.46}$$

This book belongs to Kitab Liaison (ocd1996@gmail.com)
Copyright Elsevier 2023

The final control law to accomplish the attractivity condition of s can be calculated as

$$v_{inv} = v_{eq} + v_{un} = \frac{-\varphi_3}{\gamma} - \frac{k}{\gamma} \times \mathrm{sgn}(s), \quad k > H + \eta \tag{3.47}$$

3.9 Second-order sliding mode control

The primary motivation for the development of SOSMC was to eliminate the chattering. However, it is verified that they cannot provide chattering-free control action. Although they are able to reduce and adjust chattering effectively [32], it is worth to note that chattering is also reducible in the first-order SMC (like boundary-layer SMC), however, at the cost of accepting some steady-state output errors. Whereas in SOSMC, the chattering is adjustable, and zero steady-state error is also kept. Another advantage of SOSMC in contrast to the first-order ones is both sliding (s) and state (e_{vo}) variables converge to zero in a finite time, whereas in the first-order SMC (except TSMC) only the sliding variables converge to zero in a limited time and not the state variables.

Before continuing this section, it is appropriate to define the second-order or higher-order algorithms. In simple words, the SMC algorithm is of degree n, if the control input appears in the nth derivative of s, i.e.,

$$\begin{cases} \dot{s}(e_{vo}, v_{inv}, t) = \varphi(t) + \gamma(t)v_{inv} + h(t) \rightarrow \text{First} - \text{order SMC} \\ \ddot{s}(e_{vo}, v_{inv}, t) = \varphi(t) + \gamma(t)v_{inv} + h(t) \rightarrow \text{Second} - \text{order SMC} \\ \dddot{s}(e_{vo}, v_{inv}, t) = \varphi(t) + \gamma(t)v_{inv} + h(t) \rightarrow \text{Third} - \text{order SMC} \\ \dfrac{d^n(s(e_{vo}, v_{inv}, t))}{dt^n} = \varphi(t) + \gamma(t)v_{inv} + h(t) \rightarrow \text{n} - \text{order SMC} \end{cases} \tag{3.48}$$

where φ, γ, and h can be linear or nonlinear functions of the system state or disturbances, etc. So far, different algorithms for SOSMC have been proposed as twisting controller, suboptimal algorithm, control algorithm with prescribed convergence law, and quasi-continuous control algorithm [32]. In the following, the twisting controller and its modified versions (super-twisting and adaptive super-twisting controllers) are introduced as the most commonly used SOSMC.

3.9.1 Twisting SMC

The twisting algorithm is the first presented SOSMC, which is defined by the following controller equation [32]:

$$v_{inv} = v_{eq} + v_{un} = v_{eq} - \left(r_1' \mathrm{sgn}(s) + r_2' \mathrm{sgn}(\dot{s})\right), \quad r_1' > r_2' > 0 \tag{3.49}$$

This book belongs to Kitab Liaison (ocd1996@gmail.com) Copyright Elsevier 2023

For this algorithm, the sliding variable can be defined as

$$\begin{cases} s(e_{vo},t) = e_{vo} \\ \ddot{s}(e_{vo},t) = \ddot{e}_{vo} = \varphi + \gamma v_{inv} + h(t), \end{cases} \tag{3.50}$$

It can be proved that the twisting controller provides $s\dot{s} < 0$ and the convergence of s and $\dot{s}$ to zero in a finite time [32]. Since s is equal to e_{vo} in Eq. (3.50), therefore, the state variable also converges to zero in a finite time as well. In this algorithm, v_{eq} is calculated to guarantee $\ddot{s}(e_{vo},t) = 0$, i.e.,

$$\ddot{s}(e_{vo},t) = \ddot{e}_{vo} = h(t) = 0 \rightarrow \varphi + \gamma v_{inv} = 0 \rightarrow v_{eq} = \frac{-\varphi}{\gamma} \tag{3.51}$$

And thus the final control law to guarantee a reachability condition can be rewritten as

$$v_{inv} = v_{eq} + v_{un} = -\gamma^{-1}\left(\varphi + r_1 \mathrm{sgn}(s) + r_2 \mathrm{sgn}(\dot{s})\right), \quad r_1 > r_2 > 0 \tag{3.52}$$

3.9.2 Super-twisting

The super-twisting algorithm is not precisely an SOSMC; however, it produces a continuous control action and preserves the accuracy and robustness features of a SOSMC and a classic SMC, respectively. Moreover, unlike the twisting algorithm Eq. (3.49), this method does not require a time derivative of the sliding surface function ($\dot{s}$), which is another important feature of this method. The proposed control law for a super-twisting controller is [6,7,32]

$$v_{inv} = v_{eq} + v_{un} = v_{eq} - \left(\alpha'\sqrt{S}\,\mathrm{sgn}(s) + \beta'\int \mathrm{sgn}(s)\right), \quad \alpha' > \beta' > 0 \tag{3.53}$$

From Eq. (3.53), it is obvious that both terms of the control input are continuous, and the chattering is attenuated. Considering the following sliding surface of degree one:

$$\begin{cases} s(e_{vo},t) = \dot{e}_{vo} + \lambda e_{vo} \\ \dot{s}(e_{vo},t) = \varphi_1 + \gamma v_{inv} + h(t) \end{cases} \tag{3.54}$$

The equivalent control law can be calculated as

$$\dot{s}(e_{vo},t) = h(t) = \varphi_1 + \gamma v_{eq} \rightarrow v_{eq} = \frac{-\varphi_1}{\gamma} \tag{3.55}$$

And thus the final control law can be rewritten as

$$\begin{cases} v_{inv} = v_{eq} + v_{un} = -\gamma^{-1}\left(\varphi_1 + \alpha\sqrt{s}\,\mathrm{sgn}(s) + \beta\int \mathrm{sgn}(s)\right) \\ \alpha > \beta > 0, \end{cases} \tag{3.56}$$

In [7,32], some guidelines to tune the control gains (α, β) of Eq. (3.56) and stability analysis of the super-twisting controller are investigated. In summary,

This book belongs to Kitab Liaison (ocd1996@gmail.com) Copyright Elsevier 2023

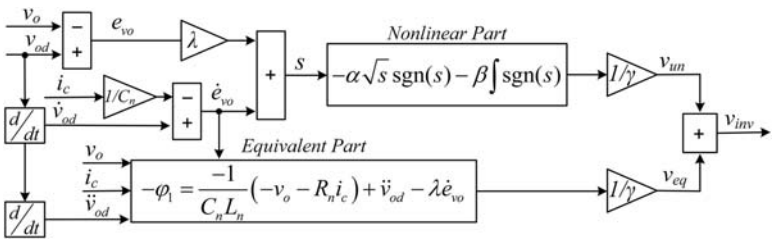

FIGURE 3.6 Structure diagram of the super-twisting algorithm Eq. (3.56) to control an uninterruptible power supply system.

if the upper bound of disturbance is known Eq. (3.24), a good start to choose and tune the control gains would be

$$\begin{cases} \alpha = 1.5\sqrt{H} \\ \beta = 1.1H \end{cases} \tag{3.57}$$

where H is upper bound of the system disturbance h(t), and is already defined in Eqs. (3.18) and (3.24). The implementation of the obtained control law in the super-twisting controller is shown in Fig. 3.6.

3.9.3 Adaptive super-twisting

To avoid trial and error to find proper values of control gains (α, β) which have an essential effect on the performance of the super-twisting algorithm, they can be calculated based on the following adaption laws [33]:

$$\begin{cases} \dot{\widehat{\alpha}} = \begin{cases} C_1 > 0, & s \neq 0 \\ 0, & s = 0 \end{cases} \\ \widehat{\beta} = C_2\widehat{\alpha} + C_3, \quad C_2 \& C_3 > 0 \end{cases} \tag{3.58}$$

Consequently, based on estimated control gains, the control input can be updated as

$$v_{inv} = -\gamma^{-1}\left(\varphi_1 + \widehat{\alpha}\sqrt{s}\,\mathrm{sgn}(S) + \widehat{\alpha}\int \mathrm{sgn}(s)\right) \tag{3.59}$$

3.10 Comparison of different SMCs

The different discussed SMCs are summarized in Table 3.1. The controllers are calculated for the studied UPS system. However, these equations are applicable to any second-order systems, which have the following form:

$$\ddot{e} = \varphi + \gamma v_{inv} + h \tag{3.60}$$

This book belongs to Kitab Liaison (ocd1996@gmail.com) Copyright Elsevier 2023

TABLE 3.1 Comparison of different sliding mode control (SMCs) used for a second-order system.

Controller	Sliding variables	Control input	Chattering	Stability	
				Sliding variables	State variables
Classic SMC	$\begin{cases} s = \dot{e} + \lambda e \\ \dot{s} = v + h \end{cases}$	$v = -k\text{sign}(s)$	High	Finite time	Asymptotically
Boundary-layer SMC	$\begin{cases} s = \dot{e} + \lambda e \\ \dot{s} = v + h \end{cases}$	$v = -k \times sat\left(\frac{s}{\varepsilon}\right),\ \varepsilon = \text{constant}$	Low	Lyapunov stable	Bounded
Adaptive boundary-layer SMC	$\begin{cases} s = \dot{e} + \lambda e \\ \dot{s} = v + h \end{cases}$	$\begin{cases} v = -k \times sat\left(\frac{s}{\varepsilon}\right), \\ \dot{e} + \lambda\varepsilon = k(x_d) \end{cases}$	Low	Lyapunov stable	Bounded
Adaptive SMC	$\begin{cases} s = \dot{e} + \lambda e \\ \dot{s} = v + h \end{cases}$	$\begin{cases} v = -k \times sat\left(\frac{s}{\varepsilon}\right), \\ \dot{k} = \rho\lvert s\rvert \end{cases}$	Low	Lyapunov stable	Bounded
PI SMC	$\begin{cases} s = \dot{e} + \lambda e + \frac{\lambda^2}{4}\int edt \\ \dot{s} = v + h \end{cases}$	$v = -k\text{sign}(s)$	High	Finite time	Asymptotically
Terminal SMC	$\begin{cases} s = \dot{e}^{\frac{p}{q}} + \lambda e \\ \dot{s} = v + h \end{cases}$	$v = -k\text{sign}(s)$	High	Finite time	Finite time
Twisting SMC	$\begin{cases} s = e \\ \ddot{s} = \ddot{e} = v + h \end{cases}$	$v = -\alpha\text{sign}(s) - \beta\text{sign}(\dot{s})$	Low	Finite time	Finite time
Super-twisting SMC	$\begin{cases} s = \dot{e} + \lambda e \\ \dot{s} = v + h \end{cases}$	$v = -\alpha\sqrt{\lvert s\rvert}\text{sign}(s) - \beta\int \text{sign}(s)$	Low	Finite time	Asymptotically

This book belongs to Kitab Liaison (ocd1996@gmail.com)

Copyright Elsevier 2023

3.11 Experimental results

In order to evaluate the performance of SMCs in practical situations, a laboratory prototype has been built, which includes a three-phase 5 kW PWM-VSC, which is supplied from a constant DC voltage, three-phase resistive load, and LC-type output filter (Fig. 3.7). Moreover, the control methods are realized on a DS1007 dSPACE system. To measure capacitor currents and voltages, the DS2004 high-speed A/D board, and to apply generated switching pulses, the DS5101 digital waveform output board are employed. The system and control parameters of three-phase UPS are given in Table 3.2. To evaluate and compare the SMCs features, the most conventional SMC method, i.e., classical SMC with the boundary-layer, and one advanced control method, i.e., super-twisting controller, are chosen and implemented in the following subsection. It is worth to remark that the control gains of both control methods are

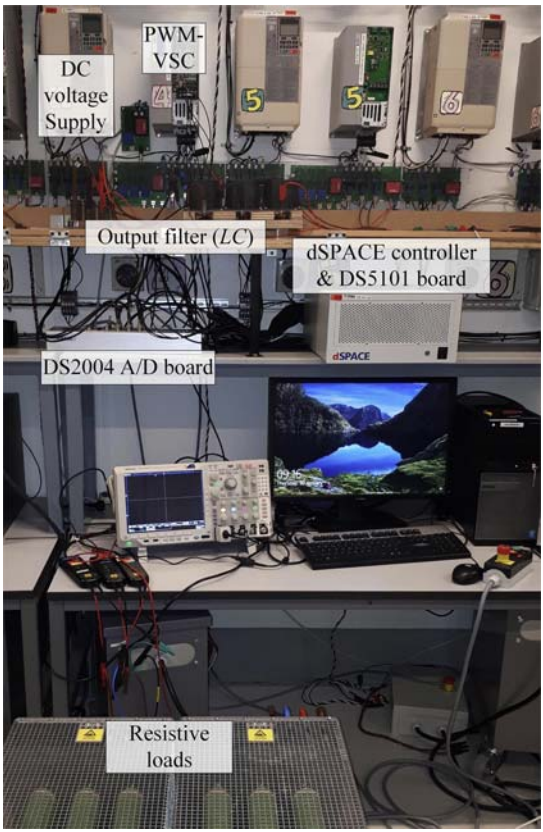

FIGURE 3.7 Experimental setup to implement sliding mode controls on a three-phase voltage source inverter in uninterruptible power supply application.

This book belongs to Kitab Liaison (ocd1996@gmail.com) Copyright Elsevier 2023

TABLE 3.2 System and control parameters for three-phase UPS system.

System parameters	
Nominal power	5 [kW]
Line voltage (rms)	380 [V]
Output frequency (f)	50 [hz]
Inductor and the series resistance (L_n, R_n)	3 [mH], 0.3 [Ω]
Capacitor (C_n)	15 [μF]
DC-link voltage (V_{dc})	720 [V]
Sampling frequency	20 [kHz]
Switching frequency	10 [kHz]
Control parameters	
Classical sliding mode control	
k	8.6e9
λ	1e4
ε	1.2e6
Super-twisting controller	
α	7e5
β	7e11

calculated based on the guidelines in Sections 3.4 And 3.5 and Section 3.9.2 and then doing some trials and errors, to finally tune the system.

3.11.1 Steady-state performance

Steady-state performance of classical SMC and super-twisting controller under nominal load is shown in Fig. 3.8. Both methods have excellent steady-state performance. It is worth to note that, the steady-state error of the super-twisting controller ($e_{vo} = 2.8$ V) is improved to half of the classic SMC ($e_{vo} = 5.3$V), whereas both control methods have approximately the same chattering in the control inputs. As discussed in Section 3.5, the steady-state tracking error of classic SMC can be reduced by reducing the boundary layer. However, it increases the control input chattering and also vulnerability against noise. The effect of the boundary-layer thickness on the steady-state error and also control input chattering is investigated in Fig. 3.9, which confirms the discussion in Section 3.5.

This book belongs to Kitab Liaison (ocd1996@gmail.com) Copyright Elsevier 2023

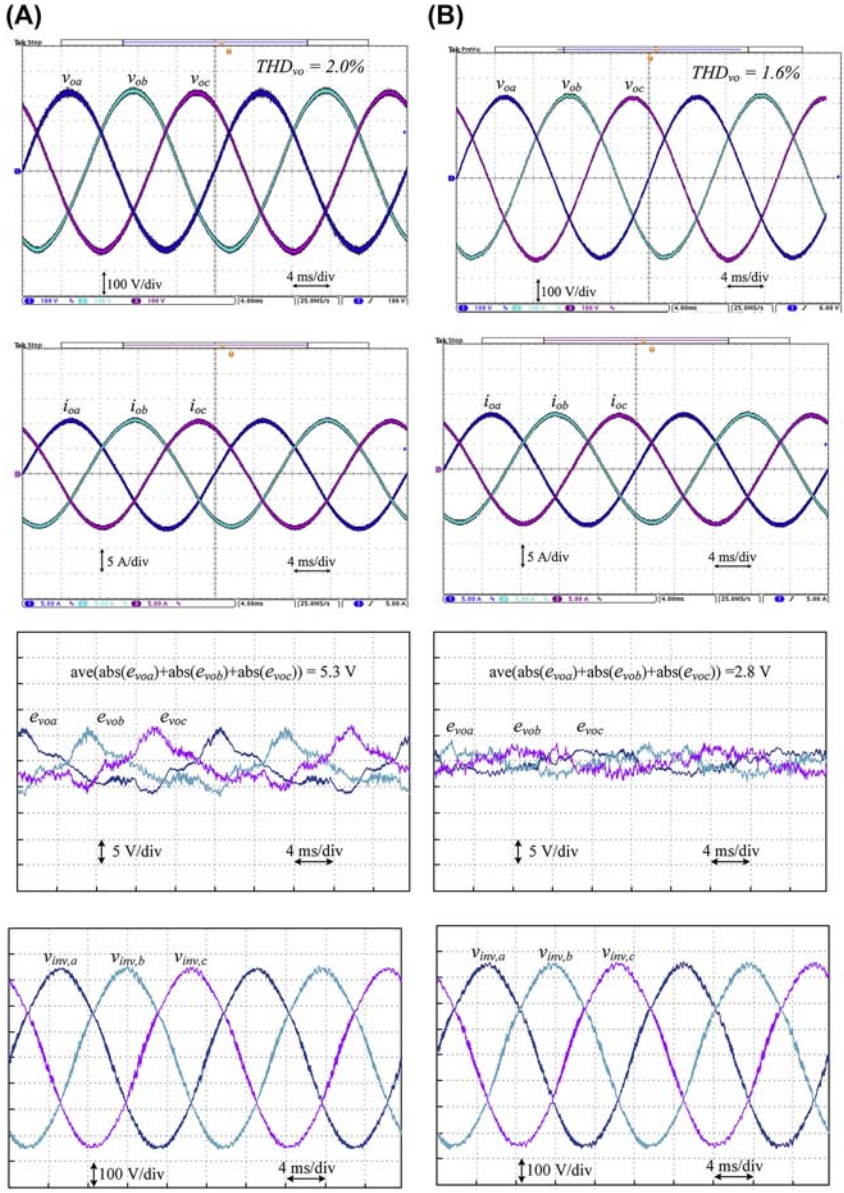

FIGURE 3.8 Obtained experimental results showing steady-state performance of two control methods under nominal load (5 kW) for uninterruptible power supply system, (A) classical sliding mode control, (B) super-twisting controller.

This book belongs to Kitab Liaison (ocd1996@gmail.com) Copyright Elsevier 2023

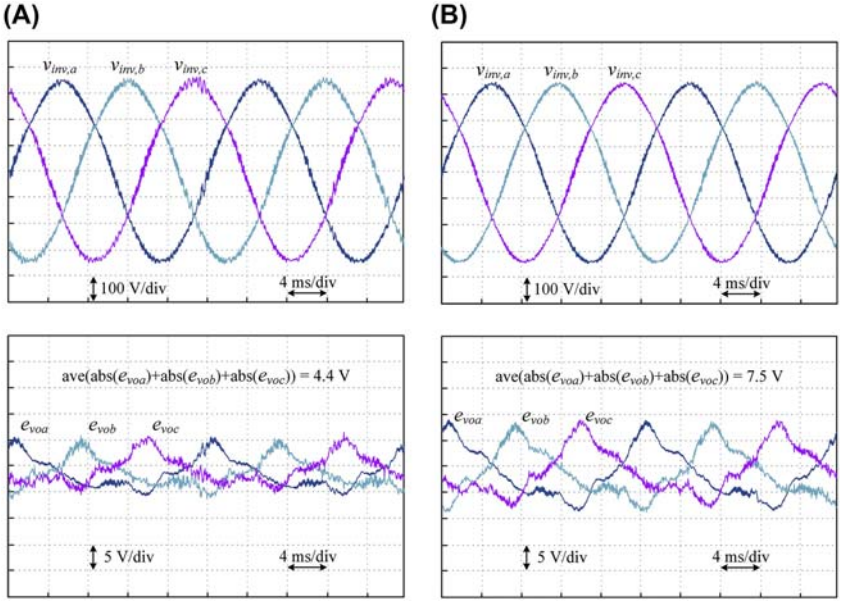

FIGURE 3.9 Obtained experimental results showing steady-state performance of classic sliding mode control under two different boundary-layer selection (A) $\varepsilon = 1e^6$, (B) $\varepsilon = 1.7e^6$.

3.11.2 Dynamic performance

The dynamic performance of two control methods under a step change in the resistive load is shown in Fig. 3.10. In this figure, the load power has been suddenly changed from zero to the nominal value. It shows good transient response and disturbance rejection of both control methods.

From this figure, it can be seen that the classic SMC has a little better transient performance than the super-twisting controller, due to larger gain in the nonlinear part of the control input. However, it is achieved on the cost of more control input chattering and steady-state errors, as discussed in the previous sections.

3.12 Conclusions

Thanks to the simple structure and concept, fast dynamic response, and good robustness and disturbance rejection, SMC has attracted considerable attention from power electronic researchers in recent years. In this chapter, the basic concept of different types of SMCs is investigated. The two most important SMCs, i.e., classic and super-twisting, have been implemented to make voltage control of a UPS. Experimental results confirm their excellent performance in both steady-state and transient operation as well as good load current disturbance rejection.

This book belongs to Kitab Liaison (ocd1996@gmail.com) Copyright Elsevier 2023

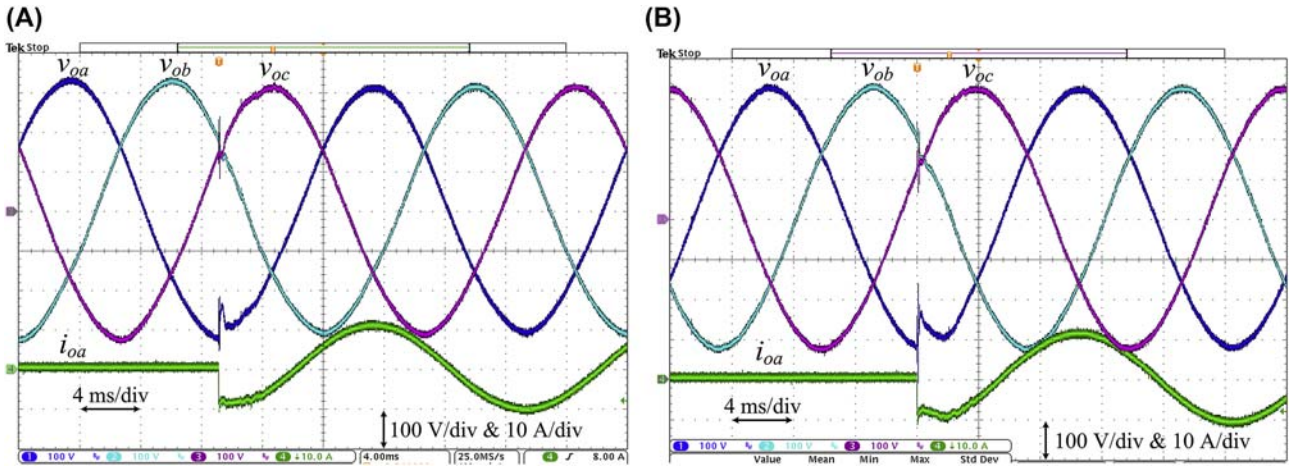

FIGURE 3.10 Obtained experimental results showing transient performance of two control methods under step change of load from zero to 5 kW, (A) classic sliding mode control, (B) super-twisting controller.

This book belongs to Kitab Liaison (ocd1996@gmail.com)

Copyright Elsevier 2023

References

[1] M. Rezkallah, S.K. Sharma, A. Chandra, B. Singh, D.R. Rousse, Lyapunov function and sliding mode control approach for the solar-PV grid interface system, IEEE Trans. Ind. Electron. 64 (1) (January, 2017) 785−795.

[2] A. Merabet, L. Labib, A.M.Y.M. Ghias, C. Ghenai, T. Salameh, Robust feedback linearizing control with sliding mode compensation for a grid-connected photovoltaic inverter system under unbalanced grid voltages, IEEE J. Photovoltaics 7 (3) (2017) 828−838.

[3] N. Kumar, T.K. Saha, J. Dey, Sliding-mode control of PWM dual inverter-based grid-connected PV system: modeling and performance analysis, IEEE J. Emerg. Sel. Top. Power Electron. 4 (2) (June, 2016) 435−444.

[4] D. Sun, X. Wang, H. Nian, Z.Q. Zhu, A sliding-mode direct power control strategy for DFIG under both balanced and unbalanced grid conditions using extended active power, IEEE Trans. Power Electron. 33 (2) (2018) 1313−1322.

[5] L. Xiong, J. Wang, X. Mi, M.W. Khan, Fractional order sliding mode based direct power control of grid-connected DFIG, IEEE Trans. Power Syst. 33 (3) (May, 2018) 3087−3096.

[6] R. Sadeghi, S.M. Madani, M. Ataei, M.R. Agha Kashkooli, S. Ademi, Super-twisting sliding mode direct power control of a brushless doubly fed induction generator, IEEE Trans. Ind. Electron. 65 (11) (2018) 9147−9156.

[7] C. Lascu, A. Argeseanu, F. Blaabjerg, Supertwisting sliding-mode direct torque and flux control of induction machine drives, IEEE Trans. Power Electron. 35 (5) (May, 2020) 5057−5065.

[8] G. Sun, Discrete-time fractional order terminal sliding mode tracking control for linear motor, IEEE Trans. Ind. Electron. 65 (4) (2018) 3386−3394.

[9] A. Pilloni, A. Pisano, E. Usai, Robust finite-time frequency and voltage restoration of inverter-based microgrids via sliding-mode cooperative control, IEEE Trans. Ind. Electron. 65 (1) (2018) 907−917.

[10] H. R. Baghaee, M. Mirsalim, G. B. Gharehpetian, and H. A. Talebi, "A decentralized power management and sliding mode control strategy for hybrid AC/DC microgrids including renewable energy resources," IEEE Trans. Ind. Informatics, https://doi.org/10.1109/TII.2017.2677943.

[11] R.P. Vieira, L.T. Martins, J.R. Massing, M. Stefanello, Sliding mode controller in a multiloop framework for a grid-connected VSI with LCL filter, IEEE Trans. Ind. Electron. 65 (6) (June, 2018) 4714−4723.

[12] R. Guzman, L.G. De Vicuña, M. Castilla, J. Miret, J. De La Hoz, Variable structure control for three-phase LCL-filtered inverters using a reduced converter model, IEEE Trans. Ind. Electron. 65 (1) (2018) 5−15.

[13] M. Huang, Q. Tan, H. Li, W. Wu, Improved sliding mode control method of single-phase LCL filtered VSI, in: 2018 9th IEEE Int. Symp. Power Electron. Distrib. Gener. Syst. PEDG vol. 2018, 2018, pp. 1−5, 2.

[14] T.G. Converters, I.M. Hassine, M.W. Naouar, N. Mrabet-bellaaj, Model predictive-sliding mode control for, IEEE Trans. Ind. Electron. 64 (2) (2017) 1341−1349.

[15] N.M. Dehkordi, N. Sadati, M. Hamzeh, A robust backstepping high-order sliding mode control strategy for grid-connected DG units with harmonic/interharmonic current compensation capability, IEEE Trans. Sustain. Energy 8 (2) (2017) 561−572.

[16] H. Komurcugil, S. Ozdemir, I. Sefa, N. Altin, O. Kukrer, Sliding-mode control for single-phase grid-connected LCL filtered VSI with double-band hysteresis scheme, IEEE Trans. Ind. Electron. 63 (2) (February, 2016) 864−873.

This book belongs to Kitab Liaison (ocd1996@gmail.com) Copyright Elsevier 2023

[17] J. Saeed, J.P. Mishra, L. Wang, X. Yu, A second-order sliding mode voltage oriented control of three-phase Active front end rectifier, in: 2018 IEEE 27th International Symposium on Industrial Electronics (ISIE) vol. 2018, June, 2018, pp. 175−180.

[18] J. Liu, S. Vazquez, S. Member, L. Wu, S. Member, Extended state observer-based sliding-mode control for three-phase power converters, IEEE Trans. Ind. Electron. 64 (1) (2017) 22−31.

[19] R. Guzman, L.G. de Vicuna, J. Morales, M. Castilla, J. Matas, Sliding-mode control for a three-phase unity power factor rectifier operating at fixed switching frequency, IEEE Trans. Power Electron. 31 (1) (January, 2016) 758−769.

[20] Z. Li, C. Zang, P. Zeng, H. Yu, S. Li, J. Bian, Control of a grid-forming inverter based on sliding-mode and mixed H2\Hinf control, IEEE Trans. Ind. Electron. 64 (5) (May, 2017) 3862−3872.

[21] J. Morales, L.G. De Vicuna, R. Guzman, M. Castilla, J. Miret, Modeling and sliding mode control for three-phase Active power filters using the vector operation technique, IEEE Trans. Ind. Electron. 65 (9) (2018) 6828−6838.

[22] Y. Chen, J. Fei, Dynamic sliding mode control of active power filter with integral switching gain, IEEE Access vol. 7 (c) (2019) 21635−21644.

[23] W. Le Zhu, X. Yang, F. Duan, Z. Zhu, B.F. Ju, Design and adaptive terminal sliding mode control of a fast tool servo system for diamond machining of freeform surfaces, IEEE Trans. Ind. Electron. 66 (6) (2019) 4912−4922.

[24] C. Mu, H. He, Dynamic behavior of terminal sliding mode control, IEEE Trans. Ind. Electron. 65 (4) (2018) 3480−3490.

[25] S.-L. Jung, Y.-Y. Tzou, Discrete sliding-mode control of a PWM inverter for sinusoidal output waveform synthesis with optimal sliding curve, IEEE Trans. Power Electron. 11 (4) (July, 1996) 567−577.

[26] J.F. Silva, Sliding-mode control of boost-type unity-power-factor PWM rectifiers, IEEE Trans. Ind. Electron. 46 (3) (June, 1999) 594−603.

[27] V.I. Utkin, Sliding mode control design principles and applications to electric drives, IEEE Trans. Ind. Electron. 40 (1) (1993) 23−36.

[28] J.Y.J.C. Hung, W. Gao, J.Y.J.C. Hung, Variable structure control: a survey, IEEE Trans. Ind. Electron. 40 (1) (1993) 2−22.

[29] K.D. Young, V.I. Utkin, Ü. Özgüner, "A control engineer's guide to sliding mode control, IEEE Trans. Contr. Syst. Technol. 7 (3) (1999) 328−342.

[30] J. Slotine, W. Li, Applied Nonlinear Control, Pearson, 1990.

[31] Y.J. Huang, T.C. Kuo, S.H. Chang, Adaptive sliding-mode control for nonlinear systems with uncertain parameters, IEEE Trans. Syst. Man Cybern. B Cybern. 38 (2) (2008) 534−539.

[32] Y. Shtessel, C. Edwards, L. Fridman, A. Levant, Sliding Mode Control and Observation, Birkhäuser, 2014.

[33] Y.B. Shtessel, J.A. Moreno, F. Plestan, L.M. Fridman, A.S. Poznyak, Super-twisting adaptive sliding mode control: a Lyapunov design, in: 49th IEEE Conference on Decision and Control (CDC), 2010, pp. 5109−5113.

This book belongs to Kitab Liaison (ocd1996@gmail.com) Copyright Elsevier 2023

This page intentionally left blank

This book belongs to Kitab Liaison (ocd1996@gmail.com)

Copyright Elsevier 2023

Chapter 4

Model predictive control of power converters, motor drives, and microgrids

Zhenbin Zhang[1], Tomislav Dragičević[2], Yu Li[1], Yongdu Wang[1], Changming Zheng[4], Minrui Leng[5], Jose Rodriguez[3]

[1]*School of Electrical Engineering, Shandong University, Jinan, China;* [2]*Department of Electrical Engineering, Technical University of Denmark, Lyngby, Denmark;* [3]*Faculty of Engineering, Universidad Andres Bello, Santiago, Chile;* [4]*School of Electrical and Power Engineering, China University of Mining and Technology, Xuzhou, Jiangsu, China;* [5]*School of Electrical Engineering, Southwest Jiaotong University, Chengdu, China*

4.1 Introduction on MPC

In this chapter, the basic concept and classification of model predictive control (MPC) will be introduced first. Afterward, typical applications of MPC in electrical drives, microgrids (MGs), and wind generation will be presented in detail. Finally, conclusions and future trends in power electronic systems are discussed.

MPC, also referred to as receding horizon control, was introduced to petrochemical industrial processes in the early 1970s [1,2]. MPC takes the entire system model into consideration and can penalize the (multiple) system control targets with a flexible cost function. The optimum values of the actuating variables are not computed based on the "post-error" between the reference and the feedback signals. Instead, this is done through minimizing a flexibly-designed cost function (a.k.a. objective function) with penalized "predicted behaviors" of the system, fully using the system model and the past control actions over a receding prediction horizon [2–4]. MPC has more freedom to further improve the system control performance, since the "predicted behaviors" of the system are utilized within the control/decision process. Additionally, using a cost function to define the control targets makes it more straightforward (at least from a concept perspective) for more complicated systems with multiple control targets.

The objective of MPC is to ensure that the output tracks the reference with minimal error, given only information about the system model and the state of

Control of Power Electronic Converters and Systems. https://doi.org/10.1016/B978-0-12-819432-4.00017-2
Copyright © 2021 Elsevier Ltd. All rights reserved.

This book belongs to Kitab Liaison (ocd1996@gmail.com) Copyright Elsevier 2023

the controlled output [5]. As illustrated in Fig. 4.1, the measured variable $\vec{x}_{[k]}$ and predictive model are used to predict the output $\vec{y}_{[k]}$. This predicted output is taken through an optimization algorithm to generate the input switching signal, $\vec{u}_{[k]}$, that will minimize the cost function of the control objectives. The reference output is $\vec{y}^{*}_{[k]}$. The measured variable $\vec{x}_{[k]}$ could be current, voltage, or frequency.

Table 4.1 shows the categories of MPC techniques. These strategies are broadly grouped as finite control set MPC (FCS-MPC) and continuous control set MPC (CCS-MPC), as shown in Fig. 4.2.

Generally, FCS-MPC does not require a modulator, while CCS-MPC utilizes a modulator for its operation. Thus, there is an inherent advantage of CCS-MPC, which is the fact that it has constant switching frequency, while FCS-MPC has variable and dynamic switching frequency. This latter quality creates some undesirable harmonics in the output signal. As illustrated in Table 4.1, FCS-MPC comprises optimal switching vector MPC (OSV-MPC) and optimal switching sequence MPC (OSS-MPC). CCS-MPC includes generalized predictive control (GPC) and explicit model predictive control (EMPC).

The MPC concept for controlling power electronics and electrical drives is applied in a variety of ways. As previously mentioned, CCS-MPC requires an extra modulator to generate the switching sequences based on the controller outputs, and these are usually continuous values of duty cycles or reference voltages (see Fig. 4.1). In contrast, FCS-MPC combines both the cost optimization and modulation into one single process and directly gives the output switching sequence. No extra modulation scheme is required (see Fig. 4.3).

FCS-MPC classes of MPC are useful to solving both linear and nonlinear problems with multiple constraints and control objectives. EMPC can also be applied to nonlinear and constrained systems. On the other hand, GPC is only useful for linear unconstrained systems. FCS-MPC is relatively easier than CCS-MPC because it is more intuitive and does not lead to any complex algorithms. The computational cost of EMPC is the lowest of the four categories because there is no need for online optimization at each sampling time. FCS-MPC has a shortcoming with its prediction horizon which is relatively short because longer horizon would increase the computational burden excessively.

4.2 MPC for permanent-magnet synchronous motor drives

In this section, the model of permanent-magnet synchronous motor (PMSM) is firstly described in Section 4.2.1, and the direct model predictive current control schemes with prediction horizon-one for two-level (2L) power converter of PMSM is discussed in Section 4.2.2. Its performances are evaluated with simulation results in Section 4.2.3. Summary is given in Section 4.2.4.

This book belongs to Kitab Liaison (ocd1996@gmail.com) Copyright Elsevier 2023

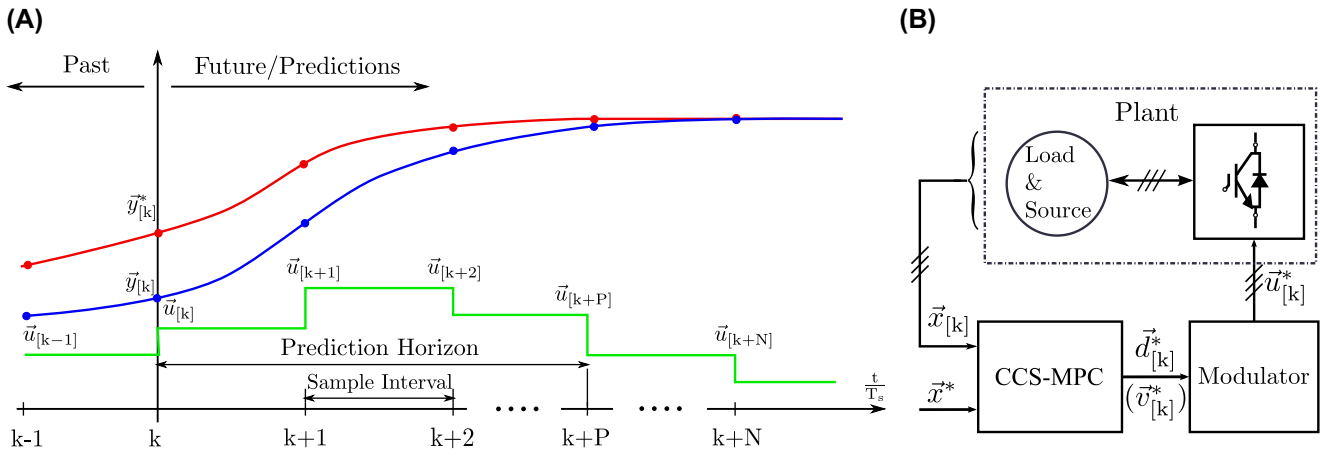

FIGURE 4.1 Continuous control set MPC concept (R. Kennel et al., 1983). (A) The reference trajectory $\vec{y}^*_{[k]}$ and predicted trajectory $\vec{y}_{[k]}$ with continuous control set MPC. (B) The block diagram of continuous control set MPC for power electronics and electrical drives.

This book belongs to Kitab Liaison (ocd1996@gmail.com)

Copyright Elsevier 2023

TABLE 4.1 Classification of model predictive control [5].

Description	Finite control set MPC (FCS-MPC)		Continuous control set MPC (CCS-MPC)	
	Optimal switching vector MPC (OSV-MPC) [6–9]	**Optimal switching sequence MPC (OSS-MPC) [10–12]**	**Generalized predictive control (GPC) [13,14]**	**Explicit MPC (EMPC) [15–17]**
Problem type	Linear and nonlinear	Linear and nonlinear	Linear unconstrained	Nonlinear constrained
Computational cost	High	Highest	Lowest	Low
Modulator	Not required	Not required	SVM and PWM	SVM and PWM
Switching frequency	Variable	Fixed	Fixed	Fixed
Cost function minimization	Online	Online	Online	Offline
Constraints	Allowed	Allowed	Allowed (with higher computational burden)	Allowed
Prediction horizon	Mostly short	Mostly short	Long	Long
Algorithm complexity	Intuitive	Intuitive	High	High

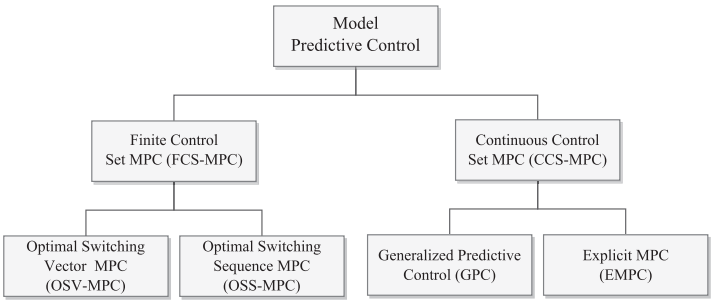

FIGURE 4.2 Categories of MPC schemes.

This book belongs to Kitab Liaison (ocd1996@gmail.com)
Copyright Elsevier 2023

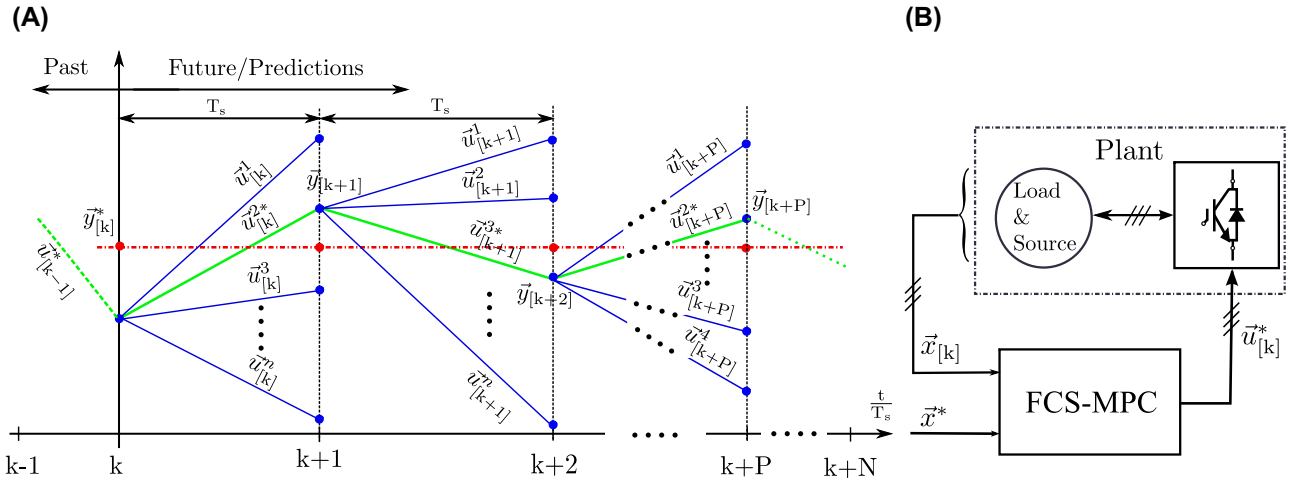

FIGURE 4.3 Finite control set MPC concept (J. Rodriguez et al., 2004). (A) The reference trajectory $\vec{y}^*_{[k]}$ and predicted trajectory $\vec{y}_{[k]}$ with finite control set MPC. (B) The block diagram of finite control set MPC for power electronics and electrical drives.

This book belongs to Kitab Liaison (ocd1996@gmail.com)

Copyright Elsevier 2023

4.2.1 Model of PMSM

In many industrial cases, for an electric-drive system, a smooth surface multipole (pole pair defined as N_p) PMSM is used [18]. Both the physical (structural) and saturation salience are, in practice, quite small and can be neglected, i.e., $L_s^d = L_s^q, \frac{\partial L_s}{\partial \theta_e} = 0$.[1] Moreover, the armature reaction affect is assumed to be negligible.

- PMSM in $\alpha\beta$ frame

A smooth surface multipole PMSM can be modeled in $\alpha\beta$-reference frame. The dynamics in the current can be described with the following nonlinear model

$$\frac{d\,\vec{i}_m^{\alpha\beta}(t)}{dt} = \frac{-R_s}{L_s}\vec{i}_m^{\alpha\beta}(t) + \frac{1}{L_s}\left(\vec{v}_m^{\alpha\beta}(t) - \underbrace{\begin{pmatrix} -\psi_{pm}\omega_e(t)\sin(\theta_e(t)) \\ -\psi_{pm}\omega_e(t)\cos(\theta_e(t)) \end{pmatrix}}_{=:\,\vec{e}_m^{\alpha\beta}(t)}\right),$$

$$\vec{i}_m^{\alpha\beta}(0) = \vec{i}_m^{0} \in \mathscr{R}^2, \tag{4.1}$$

where R_s [Ω] is the stator resistance, $\vec{e}_m^{\alpha\beta} = \left(e_m^\alpha, e_m^\beta\right)^T[\mathrm{V}]^2$ is the back-EMF vector, $\vec{v}_m^{\alpha\beta} = \left(v_m^\alpha, v_m^\beta\right)^T[\mathrm{V}]^2$ is the output voltage vector of the converter, $\vec{i}_m^{\alpha\beta} = \left(i_m^\alpha, i_m^\beta\right)^T[\mathrm{V}]^2$ is the stator current vector: all in $\alpha\beta$ frame. $\omega_e(t) = N_p\omega_m(t)[\mathrm{rad/s}]$ is the electrical angular velocity of the rotor (rotating with ω_m), N_p [1] is the pole pair number, ψ_{pm} [Wb] is the permanent-magnet flux linkage, θ_e [rad] is the electrical position of the rotor flux.

The stator flux and electromagnetic torque in the $\alpha\beta$ frame can be modeled as

$$\vec{\psi}_s^{\alpha\beta}(t) = \int\left(\vec{v}_m^{\alpha\beta}(t) - R_s\vec{i}_m^{\alpha\beta}(t)\right)dt,\ \vec{\psi}_s^{\alpha\beta}(0) = \vec{\psi}_s^{0} \in \mathbb{R}^2; \tag{4.2}$$

$$T_e(t)N_p\left(\psi_s^\alpha i_m^\beta - \psi_s^\beta i_m^\alpha\right) \tag{4.3}$$

The dynamics of the mechanical system are given by

$$\Theta_m\frac{d\omega_m(t)}{dt} = T_e(t) - T_l(t) = \mathscr{F}(\omega_m)(t), \omega_m(0) = \omega_m^0 \in \mathbb{R}; \tag{4.4}$$

where Θ_m [kgm^2] is the overall inertia (of the whole motor), T_e [Nm] is the electromagnetic torque, T_l [Nm] is the torque from the load, and $\mathscr{F}(\omega_m)$

1. For salience based encoderless control, the true property of $\frac{\partial L_s}{\partial \theta_e} \neq 0$ is utilized.

This book belongs to Kitab Liaison (ocd1996@gmail.com) Copyright Elsevier 2023

models nonlinear, dynamic friction effects; in this work, a constant coefficient B is used to model the friction effects.

Applying the Euler-forward method, the following discrete format of the motor in $\alpha\beta$ frame can be obtained:

$$\left.\begin{aligned}
\vec{i}^{\,\alpha\beta}_{\mathrm{m[k+1]}} &= \left(1-\frac{T_{\mathrm{s}}R_{\mathrm{s}}}{L_{\mathrm{s}}}\right)\vec{i}^{\,\alpha\beta}_{\mathrm{m[k]}} + \frac{T_{\mathrm{s}}}{L_{\mathrm{s}}}\left(\vec{v}^{\,\alpha\beta}_{\mathrm{m[k]}} - \underbrace{\begin{pmatrix} -\psi_{\mathrm{pm}}\omega_{\mathrm{e[k]}}\sin(\theta_{\mathrm{e[k]}}) \\ -\psi_{\mathrm{pm}}\omega_{\mathrm{e[k]}}\cos(\theta_{\mathrm{e[k]}}) \end{pmatrix}}_{=:\vec{e}^{\,\alpha\beta}_{\mathrm{e[k]}}}\right), \\
\vec{\psi}^{\,\alpha\beta}_{\mathrm{s[k+1]}} &= \vec{\psi}^{\,\alpha\beta}_{\mathrm{s[k]}} + \left(\vec{v}^{\,\alpha\beta}_{\mathrm{m[k]}} - R_{\mathrm{s}}\vec{i}^{\,\alpha\beta}_{\mathrm{m[k]}}\right)T_{\mathrm{s}}, \\
\omega_{\mathrm{e[k+1]}} &= \omega_{\mathrm{e[k]}} + \frac{T_{\mathrm{s}}N_{\mathrm{p}}}{\Theta_{\mathrm{m}}}\left(\underbrace{N_{\mathrm{p}}\left(\psi^{\alpha}_{\mathrm{s[k]}}i^{\beta}_{\mathrm{m[k]}} - \psi^{\beta}_{\mathrm{s[k]}}i^{\alpha}_{\mathrm{m[k]}}\right)}_{=:T_{\mathrm{e[k]}}} - T_{\mathrm{l[k]}} - B\bullet\omega_{\mathrm{m[k]}}\right).
\end{aligned}\right\} \tag{4.5}$$

- PMSM in dq frame

The mathematical model of a PMSM in direct-quadrature (dq) reference frame (indicated by superscript ^{dq}) is given by

$$\vec{v}^{\,\mathrm{dq}}_{\mathrm{m}}(t) = R_{\mathrm{s}}\vec{i}^{\,\mathrm{dq}}_{\mathrm{s}}(t) + \frac{\mathrm{d}\vec{\psi}^{\,\mathrm{dq}}_{\mathrm{s}}(t)}{\mathrm{d}t} + \omega_{\mathrm{e}}(t)\underbrace{\begin{bmatrix} 0 & -1 \\ 1 & 0 \end{bmatrix}}_{:=\mathrm{J}}\vec{\psi}^{\,\mathrm{dq}}_{\mathrm{s}},\ \vec{\psi}^{\,\mathrm{dq}}_{\mathrm{s}}(0) = \vec{\psi}^{\,0}_{\mathrm{s}} \in \mathbb{R}^2 \tag{4.6}$$

where $\vec{v}^{\,\mathrm{dq}}_{\mathrm{m}}(t) = \left(v^{\mathrm{d}}_{\mathrm{m}}(t), v^{q}_{\mathrm{m}}(t)\right)^T[\mathrm{V}]^2$ is the converter output voltage vector (to be specified later), R^{s} is the stator resistance, $\vec{i}^{\,\mathrm{dq}}_{\mathrm{m}}(t) = \left(i^{\mathrm{d}}_{\mathrm{m}}(t), i^{\mathrm{q}}_{\mathrm{m}}(t)\right)^T[\mathrm{A}]^2$ is the stator current vector, $\vec{\psi}^{\,\mathrm{dq}}_{\mathrm{s}}(t) = \left(\psi^{\mathrm{d}}_{\mathrm{s}}(t), \psi^{\mathrm{q}}_{\mathrm{s}}(t)\right)^T[\mathrm{Wb}]^2$ is the flux linkage (in the stator of the motor). The flux linkage is assumed linearly related to the current $\vec{i}^{\,\mathrm{dq}}_{\mathrm{m}}(t)$, stator inductance L_{s} [$\mathrm{V_s/A}$] and (constant) permanent-magnet flux linkage ψ_{pm} as follows:

$$\vec{\psi}^{\,\mathrm{dq}}_{\mathrm{s}}(t) = L_s\vec{i}^{\,\mathrm{dq}}_{\mathrm{m}}(t) + \left(\psi_{\mathrm{pm}}, 0\right)^T \tag{4.7}$$

$$T_{\mathrm{e}}(t) = N_{\mathrm{p}}\psi_{\mathrm{pm}}i^{\mathrm{q}}_{\mathrm{m}}. \tag{4.8}$$

This book belongs to Kitab Liaison (ocd1996@gmail.com) Copyright Elsevier 2023

Taking equations (4.4), (4.6)–(4.8) into consideration, and applying the Euler-forward method, yields the discrete format of the generator as

$$\left.\begin{aligned}
\vec{i}^{\,\mathrm{dq}}_{\mathrm{m[k+1]}} &= \begin{pmatrix} 1-\dfrac{T_\mathrm{s}R_\mathrm{s}}{L_\mathrm{s}} & T_\mathrm{s}\omega_{\mathrm{e[k]}} \\ -T_\mathrm{s}\omega_{\mathrm{e[k]}} & 1-\dfrac{T_\mathrm{s}R_\mathrm{s}}{L_\mathrm{s}} \end{pmatrix} \vec{i}^{\,\mathrm{dq}}_{\mathrm{m[k]}} + \begin{bmatrix} \dfrac{T_\mathrm{s}}{L_\mathrm{s}} & 0 \\ 0 & \dfrac{T_\mathrm{s}}{L_\mathrm{s}} \end{bmatrix} \vec{v}^{\,\mathrm{dq}}_{\mathrm{m[k]}} + \underbrace{\begin{pmatrix} 0 \\ -\dfrac{T\psi_\mathrm{pm}}{L_\mathrm{s}}\omega_{\mathrm{e[k]}} \end{pmatrix}}_{=:H_{\mathrm{m[k]}}} \\
\vec{\psi}^{\,\mathrm{dq}}_{\mathrm{s[k+1]}} &= L_s\,\vec{i}^{\,\mathrm{dq}}_{\mathrm{m[k+1]}} + \left(\psi_\mathrm{pm}, 0\right)^T, \\
\omega_{\mathrm{e[k+1]}} &= \omega_{\mathrm{e[k]}} + \frac{T_\mathrm{s}N_\mathrm{p}}{\Theta_\mathrm{m}} \underbrace{\left(N_\mathrm{p}\psi_\mathrm{pm} i^\mathrm{q}_{\mathrm{m[k]}} - T_{\mathrm{l[k]}} - B\cdot\omega_{\mathrm{m[k]}}\right)}_{=:T_{\mathrm{e[k]}}}
\end{aligned}\right\} \tag{4.9}$$

4.2.2 FCS-MPC for PMSM drives

For a two-level power converter driving PMSM system depicted in Fig. 4.4A, the torque tracking subject to a so-called "maximum torque per Ampere" (MTPA) law (i.e.$i^{\mathrm{d}*}_\mathrm{m} + \frac{L^\mathrm{d}_\mathrm{s}-L^\mathrm{q}_\mathrm{s}}{\psi_\mathrm{pm}}\left(\left(i^\mathrm{d}_\mathrm{m}\right)^2 - \left(i^\mathrm{q}_\mathrm{m}\right)^2 = 0\right)$) is desired. In the setup, $L^\mathrm{d}_\mathrm{s} \approx L^\mathrm{q}_\mathrm{s} = L_\mathrm{s}$. Therefore, $i^{\mathrm{d}*}_\mathrm{m} := 0$ can be set in the controller. The current reference is generated by a proper outer control loop (here a PI controller regulating the speed control is used for generating the q-axis current and the d-axis current reference is set to be zero for an MTPA control. These references are then transferred into $\alpha\beta$ frame to assign to the inner predictive

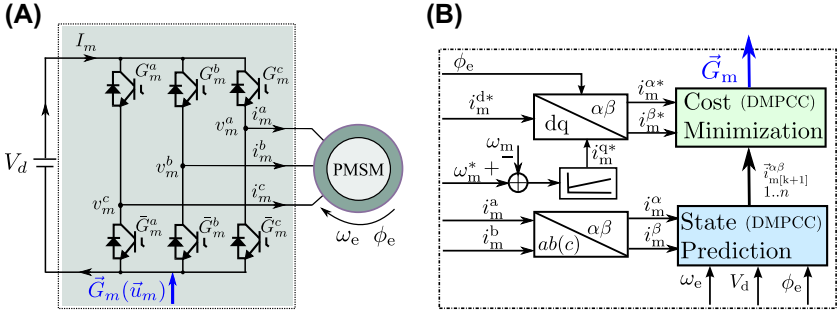

FIGURE 4.4 FCS-MPC scheme for the two-level power converter–fed PMSM system. (A) PMSM drive system under control with two-level converter. (B) Control diagram of direct model predictive control.

This book belongs to Kitab Liaison (ocd1996@gmail.com) Copyright Elsevier 2023

current control loop). The inner loop itself can be designed in the $\alpha\beta$ frame to eliminate the otherwise required synchronous frame transformations. This method is also named direct model predictive current control (DMPCC) because the main objective here is the current of the motor. Therefore, the cost function $J^{\mathrm{m}}_{\mathrm{DMPCC}}$ for predictive current control is defined as

$$J^{\mathrm{m}}_{\mathrm{DMPCC}}\left(\overrightarrow{u}_{\mathrm{m}}\right) = \left(i^{\alpha *}_{\mathrm{m}} - i^{\alpha}_{\mathrm{m[k+1]}}\left(\overrightarrow{u}_{\mathrm{m}}\right)\right)^2 + \left(i^{\beta *}_{\mathrm{m}} - i^{\beta}_{\mathrm{m[k+1]}}\left(\overrightarrow{u}_{\mathrm{m}}\right)\right)^2. \quad (4.10)$$

The predicted current vector of $i^{\alpha\beta}_{\mathrm{m[k+1]}}$ is calculated by Eq. (4.5), with $\overrightarrow{u}_{\mathrm{m}} \in \mathscr{U}_8$. Note that because the currents in both α- and β-axis are equally important to the system, no extra weightings are required for these targets. After evaluating and minimizing the costs obtained from Eq. (4.10) for $\sim\overrightarrow{u}_{\mathrm{m}} \in \mathscr{U}_8$ for the two-level converter, an optimal gate vector of $\overrightarrow{G}^{*}_{\mathrm{m}} = \mathscr{G}^{-1}\left(\overrightarrow{u}^{*}_{\mathrm{m}}\right)$ will be obtained and assigned to the motor drive converter. The overall control diagram of DMPCC is given in Fig. 4.4B.

4.2.3 Performance evaluations of MPC with simulations

In this section, the control performances of the aforementioned direct model predictive current control with simulation results are presented.

In the following, the overall testing scenarios are as follows: It is assumed that the optimal speed reference ω^{*}_{m} is already known. A rated torque is mounted under such (fast) speed changing rate to test the harshest operational situations. The control interval is set to be 50[μs], and no compensation is inserted into the predictions. The overall control performances are shown in Fig. 4.5A. The zoomed-in steady-state control performances of the motor currents are illustrated in Fig. 4.5B. As it can be seen, besides its good control dynamics, a big change of the switching frequency is seen. The current tracking performances are also quite good.

4.2.4 Summary

In this section, the direct model predictive current control and its application guidelines have been summarized. Based on this, its application has been demonstrated on a two-level power converter driving PMSM system taking "currents" as the targeting set.[2] In comparison with switching table−based direct torque and power control methods, the direct MPC methods, by using the cost function−based solution, make both the controller design and tuning process much more straightforward. In particular when the frequency regulation and DC-link capacitor voltage balancing control are considered with

2. This concept can also be applied to deal with "flux" and "voltage" control.

This book belongs to Kitab Liaison (ocd1996@gmail.com) Copyright Elsevier 2023

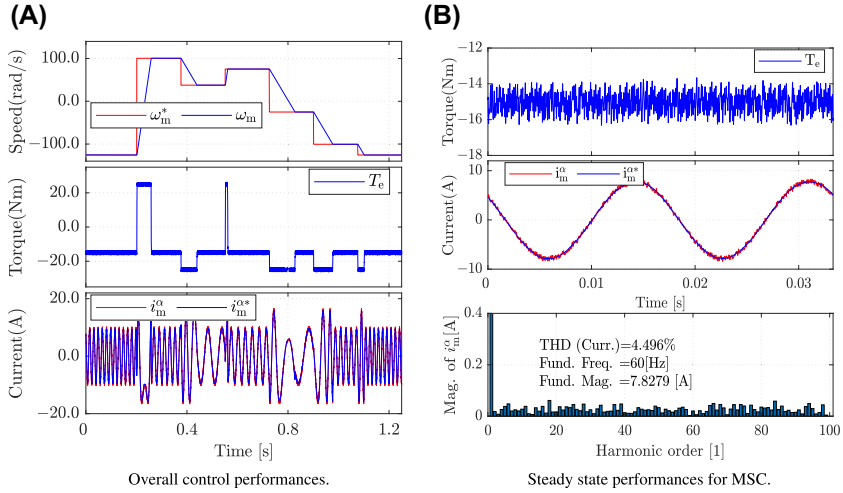

FIGURE 4.5 Simulation of **FCS-MPC** for the **two-level power converter−fed PMSM system**. From top to bottom for subfigure (A) are motor speed, motor torque, and motor stator current in α phase, respectively. Subfigure (B) illustration of the zoomed performance of the electromagnetic torque, machine phase currents, and corresponding Fourier analysis, respectively.

more level converters. The shown simulation results using PLECS software validates that FCS-MPC is a promising solution for motor drive system.

4.3 MPC for microgrids

Voltage source converters (VSCs) act as interfaces between the distributed energy resources and the MG [19]. Reliable control of VSCs is a critical function to achieve a high penetration of renewable energy on such systems. Generally, MG can be configured as AC or DC architecture, which can either work in stand-alone or in grid-connected mode, as it is shown in Fig. 4.6

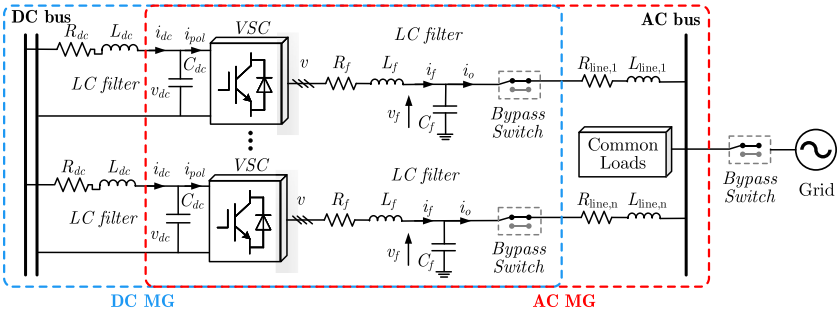

FIGURE 4.6 Basic structure of an MG which can be either AC or DC configured.

This book belongs to Kitab Liaison (ocd1996@gmail.com)
Copyright Elsevier 2023

[20–22]. In this chapter, both the applications of MPC in AC and DC MGs are discussed.

4.3.1 Dynamics and predictive model of VSC-based MG

In this section, the dynamics of AC and DC MG are modeled. Typically, an MG consists of multiple VSCs using *LC* filters in the AC and/or DC side (see Fig. 4.6).

- Load-filter side dynamics: *LC* filter

A two-level three-phase VSC with an output *LC* filter connected to a balanced load is described in stationary $\alpha\beta$ frame as [23]

$$\underbrace{\frac{\mathrm{d}}{\mathrm{d}t}\begin{bmatrix}\mathbf{i}_f\\ \mathbf{v}_f\end{bmatrix}}_{\dot{\mathbf{x}}(t)} = \underbrace{\begin{bmatrix}-\dfrac{R_f}{L_f} & -\dfrac{1}{L_f}\\ \dfrac{1}{C_f} & 0\end{bmatrix}}_{\mathbf{A}}\underbrace{\begin{bmatrix}\mathbf{i}_f\\ \mathbf{v}_f\end{bmatrix}}_{\mathbf{x}(t)} + \underbrace{\begin{bmatrix}\dfrac{1}{L_f} & 0\\ 0 & -\dfrac{1}{C_f}\end{bmatrix}}_{\mathbf{B}}\underbrace{\begin{bmatrix}\mathbf{u}\\ \mathbf{i}_o\end{bmatrix}}_{\mathbf{u}(t)} \tag{4.11}$$

where L_f and C_f are filter inductance and capacitance. The filter-capacitor voltage $\boldsymbol{v}_f = v_{f\alpha} + jv_{f\beta}$, inductor current $\mathbf{i}_f = i_{f\alpha} + ji_{f\beta}$, converter voltage vector $\mathbf{u} = u_\alpha + ju_\beta$, and load current $\mathbf{i}_\mathrm{o} = i_{o\alpha} + ji_{o\beta}$.

Correspondingly, the ZOH discretization–based predictive model is constructed using Eq. (4.11) as [24]

$$\begin{bmatrix}\mathbf{i}_{f[k+1]}\\ \mathbf{v}_{f[k+1]}\end{bmatrix} = \mathbf{A}_d\begin{bmatrix}\mathbf{i}_{f[k]}\\ \mathbf{v}_{f[k]}\end{bmatrix} + \mathbf{B}_d\begin{bmatrix}\mathbf{u}_{[k]}\\ \mathbf{i}_{o[k]}\end{bmatrix} \tag{4.12}$$

where $\mathbf{A}_d = e^{\mathbf{A}T_s}, \mathbf{B}_d = \int_0^{T_s} e^{\mathbf{A}\tau}\mathbf{B}d\tau$, a and T_s is the sampling time.

- DC-link dynamics

Apart from the dynamics of the AC side, dynamics are also derived for the DC link. Here, only a differential equation describing v_{dc} is used for modeling the DC link dynamics, where the current i_{dc}, which flows through the inductor, is treated as an external disturbance

$$C_{dc}\frac{dv_{dc}}{dt} = i_{dc} - i_{pol} \tag{4.13}$$

where i_{pol} is the current flowing into the inverter, which can be synthesized from the filter current and the gating signals. For the DC-link dynamics, the following approximation is used on the DC side to estimate how much the DC-link capacitor is charged/discharged during each sample period, i.e., using predictive DC-bus voltage model

This book belongs to Kitab Liaison (ocd1996@gmail.com) Copyright Elsevier 2023

$$v_{dc[k+1]} = v_{dc[k]} + \frac{1}{C_{dc}}\left(i_{dc} - \frac{i_{pol,i} + i_{pol,p}}{2}\right)T_s \tag{4.14}$$

$i_{pol,i}$ and $i_{pol,p}$ are the initial and final current flowing into the inverter during the following time step, respectively. The above discrete models on the AC side and DC side are used to predict $\boldsymbol{i}_f$, $\boldsymbol{v}_f$, and $\boldsymbol{v}_{dc}$ at the end of the next sampling instant in order to control the MG systems.

4.3.2 MPC for robust and fast operation of an islanded AC MG

An islanded AC MG usually consists of multiple parallel VSCs, which are connected to a common AC bus (see Fig. 4.6). The typical primary control contains normally of two control loops. Outer-loop control (e.g., droop control) aims to share the load power, while the inner-loop control (e.g., cascaded linear control) is responsible for voltage and frequency regulation. Generally, MPC is applied in the inner control loop to enhance the reference voltage tracking and system dynamic performance, and the cost function is defined as [25]

$$g_{ac} = \left(v^*_{f\alpha} - v_{f\alpha[k+1]}\right)^2 + \left(v^*_{f\beta} - v_{f\beta[k+1]}\right)^2 + \lambda_d g_{der} \tag{4.15}$$

with a voltage reference derivative tracking term as

$$g_{der} = \left(C_f \boldsymbol{\omega}^* v^*_{f\beta} - i_{f\alpha[k+1]} + i_{o\alpha[k]}\right)^2 + \left(C_f \boldsymbol{\omega}^* v^*_{f\alpha} + i_{f\beta[k+1]} - i_{o\beta[k]}\right)^2 \tag{4.16}$$

where $\boldsymbol{\omega}^*$ and v^*_f are the voltage and frequency reference generated by the outer droop control loop. λ_d is a weighting factor [26]. The predicted $\mathbf{v}_{f[k+1]}$ and $\mathbf{i}_{f[k+1]}$ are obtained by Eq. (4.12).

Note that Eq. (4.15) simultaneously tracks both voltage reference and its derivative, which can achieve an improved static performance compared to the conventional MPC with only voltage reference tracking [25]. After evaluating

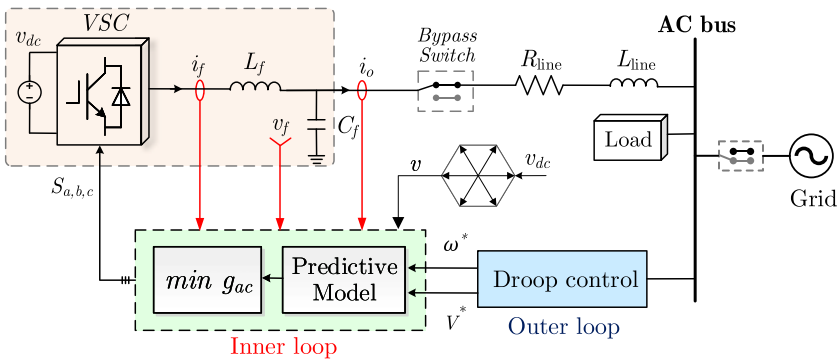

FIGURE 4.7 Block diagram of MPC for an islanded AC MG and a droop control for the outer loop.

This book belongs to Kitab Liaison (ocd1996@gmail.com)
Copyright Elsevier 2023

and minimizing the costs obtained from Eq. (4.15) for each converter voltage vector u, an optimal voltage vector will be achieved and applied to the VSC. The block diagram of the MPC for an islanded AC MG is shown in Fig. 4.7.

4.3.3 Dynamic stabilization of a DC MG using MPC

As shown in Fig. 4.6, the control objective is to achieve an excellent voltage regulation performance on the AC side as well as a stable voltage on the DC side. The cost function used for AC-side tracking is shown in Eq. (4.15). For the DC side, a simple solution to the instability problem is to introduce a stabilization term $g_{dc} = \left(v_{dc}^{*} - v_{dc}\right)$. As a result, the complete cost function for a DC MG is formed as [27]

$$g_p = g_{ac} + \lambda_{dc} g_{dc} \tag{4.17}$$

where g_{ac} is given in Eq. (4.15), and λ_{dc} is the weighting factor, which balances the performance between AC and DC side. A good load performance is achieved with a low setting of λ_{dc}, while a higher λ_{dc} ensures better DC-link dynamic response. Hence, an adaptive selection of λ_{dc} can be employed as

$$\lambda_{dc} = 0.1 \cdot \exp\left(\left|v_{dc}^{*} - v_{dc}\right| \cdot \frac{\ln(10)}{5}\right) \tag{4.18}$$

Similarly, by evaluating the cost function g_p, the optimal actuation can be determined.

4.3.4 Performance evaluation with experimental results

In this section, the experimental results for validating the MPC schemes for stabilization of AC and DC MGs are evaluated in Figs. 4.8 and 4.9 with the overall experimental parameters as listed in Table 4.2.

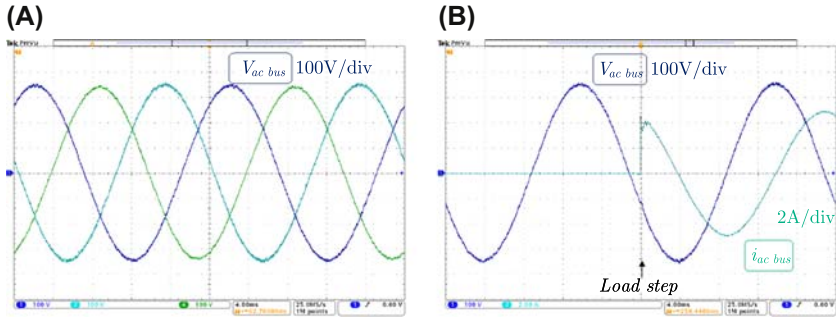

FIGURE 4.8 [Measured:] Overall control performance with inner-loop MPC (Eq. 4.15) for an islanded AC MG. (A) Steady-state load-side voltage (Voltage THD: 1.10%). (B) Dynamic response of load-side voltage under a load step change from open circuit to $R_l = 33\ \Omega$.

This book belongs to Kitab Liaison (ocd1996@gmail.com) Copyright Elsevier 2023

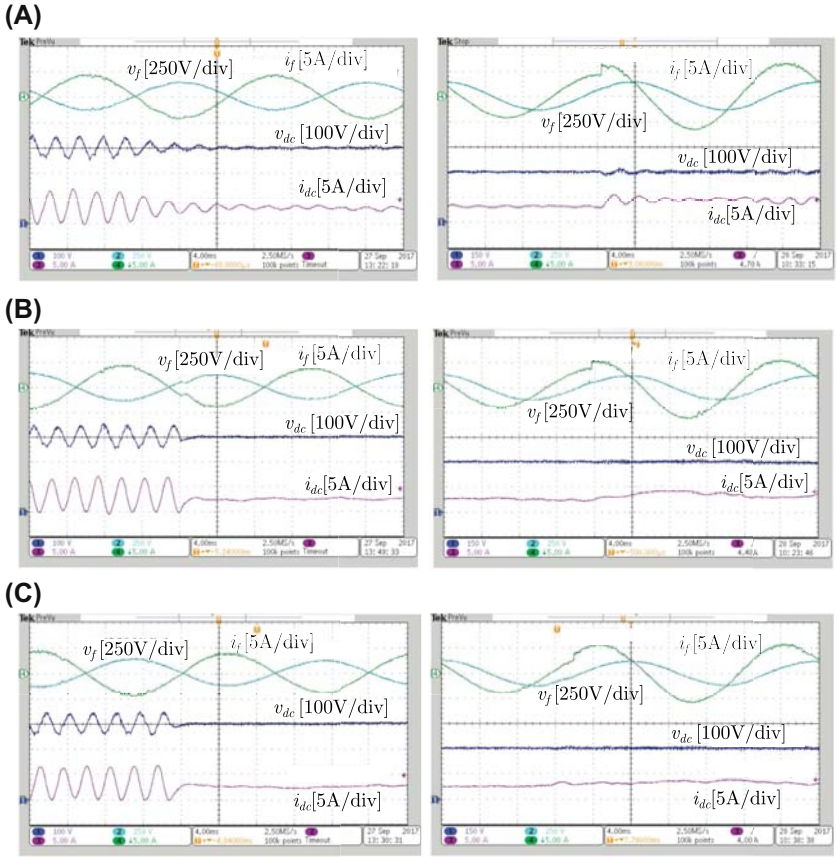

FIGURE 4.9 [Measured:] Overall control performance of stabilization for DC link and step load change for a DC MG using MPC in Eq. (4.17). (A) $\lambda_{dc} = 0.1$. (B) $\lambda_{dc} = 1$. (C) Adaptive λ_{dc} using Eq. (4.18).

TABLE 4.2 Experimental Parameters of an MG as shown in Fig. 4.6.

Parameter description	Symbols and values
DC-bus voltage	$V_{dc} = 700$ V
Load reference voltage for AC MG	$V_{ref} = 347$ V, $f_{ref} = 50$ Hz
Load reference voltage for DC MG	$V_{ref} = 208$ V, $f_{ref} = 50$ Hz
VSC dead time	$T_d = 4$ μs
Sampling time T_s	$T_s = 25$ μs
AC-side LC filter	$L_f = 2.4$ mH, $C_f = 25$ μF
DC-side LC filter	$L_{dc} = 5$ mH, $C_{dc} = 30$ μF
Linear resistive load	$R_l = 33\ \Omega$

This book belongs to Kitab Liaison (ocd1996@gmail.com) Copyright Elsevier 2023

As it can be seen in Fig. 4.8, for the AC side, a very fast dynamic response of the voltage under a load step change can be achieved. Meanwhile, the steady-state performance is also quite good with a low THD. As is shown in Fig. 4.9, for the DC side, with $\lambda_{dc} = 0.1$, a significant ringing can be seen on the DC side. On the other hand, for $\lambda_{dc} = 1$, very good dynamic performance on the DC link can be observed, but there is a drop in the steady-state voltage drop on the AC side. Finally, with the employed adaptive λ_{dc} in Eq. (4.18), the DC link is very fast stabilized after a step change in the load, while the load-side voltage has excellent dynamic response and negligible steady-state tracking error.

4.3.5 Summary

It can be seen that the MPC-based stabilization method, on the one hand, stabilizes an MG without implementing any additional active or passive components, thus providing higher energy efficiency and better cost-effectiveness than methods that rely on such components. On the other hand, this method has a significantly lower influence on AC-side voltage regulation performance.

4.4 MPC for renewable energy applications (PMSG wind turbine)

Wind energy, in particular high power wind energy installation, has steadily increased over the last decade. Currently, 12 MW systems are available in the market and numerous research activities aim at 10−14 MW level for offshore applications. For such demands, wind turbine systems (WTSs) using full power scale back-to-back power converter and permanent-magnet synchronous generator (PMSG) with direct drive structure (without mechanical gear) have attracted much interest over the last decade.

Compared with double-fed induction generator (DFIG)-based WTSs, which are equipped with partial power rating power converters, PMSG wind turbine configuration shows many advantages [28], such as wider wind speed operating range, higher power energy density and efficiency, better grid-side

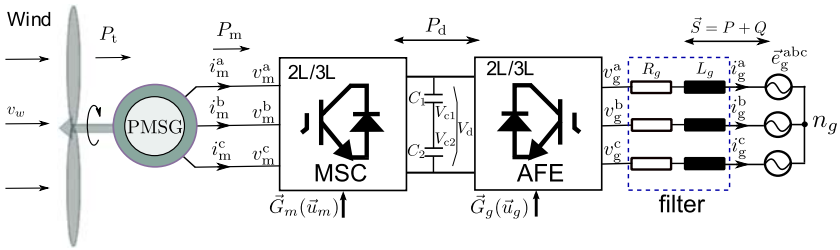

FIGURE 4.10 Simplified structure of a voltage source back-to-back power converter PMSG wind turbine system with active front-end (*AFE*); *MSC*, machine-side converter; 2*L*/3*L*, two-level/three level.

This book belongs to Kitab Liaison (ocd1996@gmail.com)
Copyright Elsevier 2023

support and fault ride-through capabilities, and, more importantly, reduced maintenance requirements. These properties make the PMSG WTSs with back-to-back power converter and direct-drive configuration a more attractive solution in particular for offshore wind energy systems. Fig. 4.10 shows a simplified structure of such a system.

4.4.1 Modeling of PMSG wind turbine system with back-to-back power converter

In this section, the PMSG WTS is modeled. In Fig. 4.10, the back-to-back power converter and PMSG have already been described in Section 4.2, so only the dynamics of the grid-side needs to be modeled here.

- Grid-side dynamics: grid and filter

Typically, for MW level WTS, an LCL or LC filter is usually used to connect and interface the power converter to the grid. A proper design of an LCL[3] or LC filter results in much smaller inductance values to achieve comparable filtering performances as L filter (see Refs. [29,30] and the references therein). However, given a properly designed hardware system, both the LC and LCL filter can be simplified as the same type of an L filter in the fundamental frequency domain for the controller design process. Therefore, in this work, only an (R) L filter is considered and constructed in the laboratory due to its simplicity.

The (controllable) grid-side power converter (GSC) is also named an active front end (AFE) power converter or (boost) PWM rectifier in many publications in this chapter, it is named as GSC or AFE for consistency. A typical three-level AFE with RL filter can be described in $\alpha\beta$ frame.

- AFE with RL filter modeling in $\alpha\beta$ frame

An AFE with RL filter connected to an ideal (balanced) grid in $\alpha\beta$ frame is given by (see, e.g. Refs. [31,32])

$$\vec{v}_{\mathrm{g}}^{\alpha\beta}(t) = \vec{e}_{\mathrm{g}}^{\alpha\beta}(t) + R_{\mathrm{g}} \cdot \vec{i}_{\mathrm{g}}^{\alpha\beta}(t) + L_{\mathrm{g}} \cdot \frac{d\,\vec{i}_{\mathrm{g}}^{\alpha\beta}}{\mathrm{d}t}, \quad \vec{i}_{\mathrm{g}}^{\alpha\beta}(0) = \vec{i}_{\mathrm{g}}^{0} \in \mathbb{R}^2. \tag{4.19}$$

Transferring into the discrete format, one obtains

$$\vec{i}_{\mathrm{g[k+1]}}^{\alpha\beta} = \underbrace{\left(1 - \frac{T_{\mathrm{s}} R_{\mathrm{g}}}{L_{\mathrm{g}}}\right)}_{:=\widehat{\mathrm{A}}_{\mathrm{g}}} \vec{i}_{\mathrm{g[k]}}^{\alpha\beta} + \underbrace{\frac{T_{\mathrm{S}}}{L_{\mathrm{g}}}}_{:=\widehat{\mathrm{B}}_{\mathrm{g}}} \left(\vec{v}_{\mathrm{g[k]}}^{\alpha\beta} - \vec{e}_{\mathrm{g[k]}}^{\alpha\beta}\right), \tag{4.20}$$

3. For which a damping of the resonant frequency is very important.

This book belongs to Kitab Liaison (ocd1996@gmail.com) Copyright Elsevier 2023

where R_g [Ω] and L_g [V_s/A] are the filter resistance and inductance, respectively, $\overrightarrow{i}_g^{\alpha\beta} = \left(i_g^{\alpha}, i_g^{\beta}\right)^T [A]^2$ is the current vector to the grid, $\overrightarrow{v}_g^{\alpha\beta} = \left(v_g^{\alpha}, v_g^{\beta}\right)^T [V]^2$ is the output voltage vector of the GSC, and $\overrightarrow{e}_g^{\alpha\beta} = \left(e_g^{\alpha}, e_g^{\beta}\right)^T [V]^2$ is the grid voltage: all are represented in the $\alpha\beta$ frame.

- Grid-side power dynamics

In the following, the power dynamics are used to model the system. Therefore, the relevant equations of the grid-side power dynamics are given. Invoking the instantaneous power theory [33,34], the grid-side power can be calculated as

$$\begin{aligned}\overrightarrow{S} = (P, Q)^T &= \left(\left(\overrightarrow{e}_g^{\alpha\beta}\right)^T \overrightarrow{i}_g^{\alpha\beta}, \left(\overrightarrow{e}_g^{\alpha\beta}\right)^T \mathrm{J}\, \overrightarrow{i}_g^{\alpha\beta}\right)^T \\ &= \left(\left(\overrightarrow{e}_g^{dq}\right)^T \overrightarrow{i}_g^{dq}, \left(\overrightarrow{e}_g^{dg}\right)^T \mathrm{J}\, \overrightarrow{i}_g^{dq}\right)^T,\end{aligned} \tag{4.21}$$

where P and Q are active and reactive power at the point of common coupling, respectively. For $\frac{d}{dt}P = \left(\overrightarrow{e}_g^{dg}\right)^T \frac{d}{dt}\overrightarrow{i}_g^{dq}$ and $\frac{d}{dt}Q = \left(\overrightarrow{e}_g^{dq}\right)^T \mathrm{J}\frac{d}{dt}\overrightarrow{i}_g^{dq}$ (assuming $\overrightarrow{e}_g^{dq} = \left(\widehat{e}_g, 0\right) = \left(\widehat{e}_g^{d}, 0\right)^T$ is constant, i.e., $e_g^{dg} = \widehat{e}_g > 0$), the dynamics of active and reactive power in the dq-reference frame can be computed as

$$\left.\begin{aligned}\frac{d}{dt}P &= \frac{1}{L_g}\left(-R_g P + v_g^{d}\widehat{e}_g + \omega_g L_g Q - \widehat{e}_2^{g}\right) \\ \frac{d}{dt}Q &= \frac{1}{L_g}\left(-R_g Q + v_g^{q}\widehat{e}_g + \omega_g L_g P\right).\end{aligned}\right\} \tag{4.22}$$

For a balanced grid, the grid-side source voltage is in the format of $\overrightarrow{e}_g^{\alpha\beta} = Ae^{j\omega_g t}$, where A and ω_g are the magnitude and frequency, respectively. Therefore, $\frac{d\overrightarrow{e}_g^{\alpha\beta}}{dt} = j\omega_g \overrightarrow{e}_g^{\alpha\beta}$. So the dynamics of the grid-side power can be

This book belongs to Kitab Liaison (ocd1996@gmail.com) Copyright Elsevier 2023

obtained in the αβ frame in the discrete format invoking Euler-forward method, given as[4]

$$\overrightarrow{G}_{\mathrm{S[k]}} = \frac{\mathrm{d}\overrightarrow{S}}{\mathrm{d}t} = \left[g_{\mathrm{P[k]}}, g_{\mathrm{Q[k]}}\right]^{\mathrm{T}}$$

$$= \frac{1}{L_{\mathrm{g}}}\begin{bmatrix} e^{\alpha}_{\mathrm{g[k]}} & e^{\beta}_{\mathrm{g[k]}} \\ e^{\beta}_{\mathrm{g[k]}} & -e^{\alpha}_{\mathrm{g[k]}} \end{bmatrix}\begin{pmatrix} e^{\alpha}_{\mathrm{g[k]}} & -v^{\alpha}_{\mathrm{g[k]}} \\ e^{\beta}_{\mathrm{g[k]}} & -v^{\beta}_{\mathrm{g[k]}} \end{pmatrix} - \begin{pmatrix} \frac{R_{\mathrm{g}}}{L_{\mathrm{g}}}P_{\mathrm{[k]}} + \omega_{\mathrm{g}}Q_{\mathrm{[k]}} \\ \frac{R_{\mathrm{g}}}{L_{\mathrm{g}}}Q_{\mathrm{[k]}} - \omega_{\mathrm{g}}P_{\mathrm{[k]}} \end{pmatrix}. \tag{4.23}$$

Therefore, the grid-side power at k + 1 can be predicted as

$$\overrightarrow{S}_{\mathrm{[k+1]}} = \left(P_{\mathrm{[k+1]}}, Q_{\mathrm{[k+1]}}\right)^{\mathrm{T}} = \left(P_{\mathrm{[k]}}, Q_{\mathrm{[k]}}\right)^{\mathrm{T}} + T_{\mathrm{s}} \cdot \overrightarrow{G}_{\mathrm{S[k]}} \tag{4.24}$$

4.4.2 Direct model predictive current control

For PMSG WTSs, DMPCC is applied for GSC and MSC. The DMPCC is illustrated in Section 4.2; only DMPCC for GSC is presented in this section. In the analogy to DMPCC for MSC, instead of using the grid-side instantaneous power as tracking targets, the grid-side current performances are of higher level priority for direct model predictive current control. The inner loop itself can be designed in the αβ frame, and the grid-side cost function is defined as

$$J^{\mathrm{g}}_{\mathrm{DMPC}}\left(\overrightarrow{u}_{\mathrm{g}}\right) = \left(i^{\alpha *}_{\mathrm{g}} - i^{\alpha}_{\mathrm{g[k+1]}}\left(\overrightarrow{u}_{\mathrm{g}}\right)\right)^{2} + \left(i^{\beta *}_{\mathrm{g}} - i^{\beta}_{\mathrm{g[k+1]}}\left(\overrightarrow{u}_{\mathrm{g}}\right)\right)^{2}. \tag{4.25}$$

The predicted current vector $i^{\alpha\beta}_{\mathrm{g[k+1]}}\left(\overrightarrow{u}_{\mathrm{g}}\right)\left(\overrightarrow{u}_{\mathrm{m}} \in \mathscr{U}_{8}\right)$ can be obtained by Eq. (4.20). The current references are generated/set by a proper outer control loop (here a PI controller for the DC-link control is used to generate the d-axis current reference and the q-axis current is set to be zero for unity power factor control. These two references are then transferred into $\alpha\beta$ frame). In the analogy, due to the currents both in α- and β-axis are equally important to the system, again no extra weightings are required for these targets.

After evaluating and minimizing the costs obtained from (4.25) for $\overrightarrow{u}_{\mathrm{m}} \in \mathscr{U}_{8}$ for the two-level MSC, an optimal voltage vector of $\overrightarrow{G}_{\mathrm{g}}$ will be obtained

4. $\overrightarrow{G}_{\mathrm{s}}(t)$ can be regarded as a slope/gradient of the power, with the same definition, which can also be applied in the dq, frame, as $\overrightarrow{G}_{\mathrm{s}}(t) := \frac{d\overrightarrow{S}_{(t)}}{\mathrm{d}t} = \hat{e}^{\mathrm{d}}_{\mathrm{g}}\left(\frac{di^{\mathrm{d}}_{\mathrm{g}}}{\mathrm{d}t}, \frac{di^{\mathrm{q}}_{\mathrm{g}}}{\mathrm{d}t}\right)^{\mathrm{T}}$.

This book belongs to Kitab Liaison (ocd1996@gmail.com) Copyright Elsevier 2023

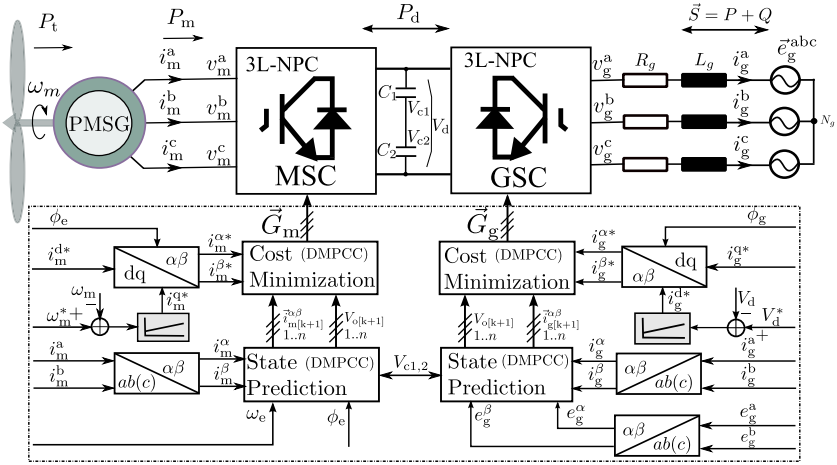

FIGURE 4.11 Control structure of direct model predictive current control for three-level NPC back-to-back power converter PMSG wind turbine system.

and assigned to the machine-side converter. An overview of the predictive current control method for both the grid- and machine-side control is shown in Fig. 4.11.

4.4.3 FCS-MPC for three-level PMSG systems

In this section, the direct FCS-MPC control method for **3L back-to-back power converter PMSG WTS** is evaluated. Both the overall control performances and the steady state of the machine- and grid-side control performances are given.

The simulation data of direct model predictive current control method (for both MSC and GSC) of the 3L back-to-back power converter PMSG WTS are depicted in Table 4.3. The simulations of this chapter are based on a per-unit model. The control interval is set to be 20 [μs], without compensation applied to the predictions. The DC-link voltage reference is set at 5200 [V], while the reactive power reference is set to be 0 [Var]. The overall control performances are shown in Fig. 4.12A. The steady-state control performances of both the generator and grid-side currents are illustrated in Fig. 4.12B. As it can be seen, besides its good control dynamics, a big change of the switching frequency is seen. The current tracking performances are also (quite) good. Besides, it is a non-fixed switching frequency control strategy. At the sampling frequency of 50 kHz, its real switching frequency is about 10 kHz. By adding penalty terms

This book belongs to Kitab Liaison (ocd1996@gmail.com) Copyright Elsevier 2023

TABLE 4.3 Parameters of the PMSG system in Fig. 4.11.

Parameter	Symbol	Value
Generator stator resistance	R_s	0.05362 [Ω]
Generator stator inductance	L_s	17.4 [mH]
Permanent-magnet flux linkage	ψ_{pm}	42 [Wb]
Generator rotor inertia	Θ_m	40,000 [kg/m^2]
Number of pairs	N_p	40 [1]
Grid (phase) voltage	e_g	1905 [V]
Grid frequency	ω_g	100π [rad/s]
Grid-side resistance	R_g	0 [Ω]
Grid-side inductance	L_g	1 [mH]
DC-link capacitance	$C_1(C_2)$	8.4 [mF]
DC-link voltage	V_{dc}	5200 [V]
Sampling time	T_s	20 [μs]
Power level	P	5 [MW]

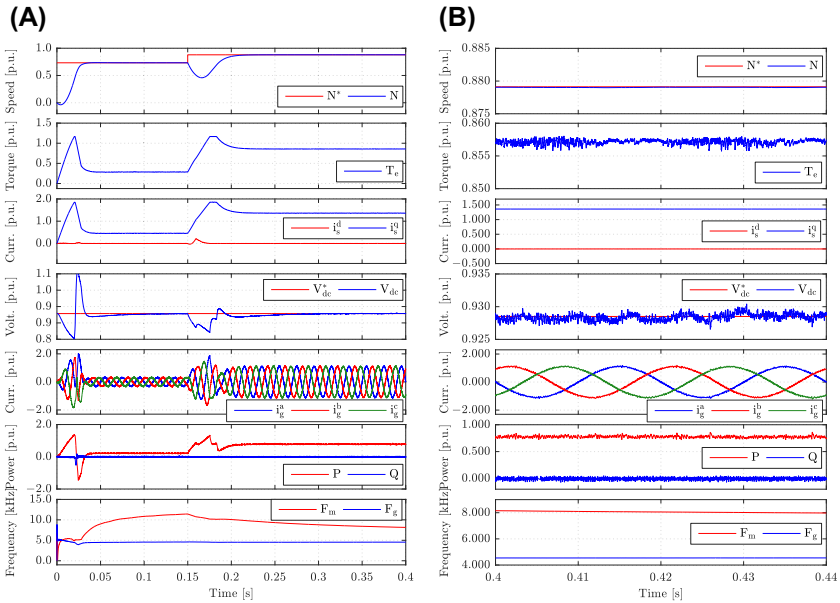

Overall control performances. Steady state control performances.

FIGURE 4.12 Simulated Control performance of **FCS-MPC** for the **three-level back-to-back power converter PMSG wind turbine system** shown in Fig. 4.11. From top to bottom are generator speed, torque, generator stator current in dq frame, DC-link voltage, grid-side current, active and reactive power, and grid- and machine-side switching frequency, respectively.

This book belongs to Kitab Liaison (ocd1996@gmail.com) Copyright Elsevier 2023

to the cost function, the switching frequency can be further reduced at the expense of current control performance.

This section has elaborated and verified the application of MPC in wind power generation system. According to the analysis using simulations, it can be seen that MPC has excellent transient and steady-state performance on such systems, and the algorithm is straightforward and easy to implement. It is foreseeable that MPC will be more widely used in wind power generation systems and other renewable systems.

4.5 Conclusions and future trends

This chapter has overviewed the application of MPC methods in power electronic systems. This chapter was started with introduction of the basic definitions of the MPC as a control methodology and then with categorization of various methods belonging to the broad family of MPC, which have been applied in the general power electronic area.

Afterward, important practical application details have been presented for several selected MPC applications, i.e., in electrical drives, MGs, and wind generation systems. Each of these applications has been discussed in a dedicated section. From the presented results, it can be concluded that MPC offers competitive performance advantages over conventional cascaded linear control strategies that are commonly used for controlling power electronic converters in these applications. In particular, it has been discussed that these advantages arise either from the avoidance of the use of modulator stage or from avoidance of the cascaded structure. While such measures enable better dynamic performance, as well as handling large disturbances and nonlinearities, they also introduce some application-dependent disadvantages. The most prominent disadvantages are increased computational burden, variable switching frequency (in case of non-modulated MPC such as FCS-MPC), and increased sensitivity to parameter variations due to reliance of the control strategy on the model of the plant. However, recent results have shown that some MPC strategies are very robust to parameter variations despite that fact they rely on the model of the plant.

A clear future trend for the MPC in power electronic systems is the development of new MPC methods that operate with constant switching frequencies using a modulator. The target is then to maximize the dynamic performance of power converters, while having the predictable switching pattern at the same time. This facilitates the output filter design and provides low levels of EMI and acoustic noise. Another prominent research area is development of MPC methods that provide state-of-the-art performance but reduce the number of sensors. Low number of sensors reduces the cost of power electronic systems and increases their reliability at the same time (i.e., by reducing the number of failure modes). Hence, this area of research is very important from an industrial standpoint. Finally, another very promising future

This book belongs to Kitab Liaison (ocd1996@gmail.com) Copyright Elsevier 2023

research approach is the combination of MPC with data-based methods where advantages of both can be combined. There are numerous implementation possibilities in this area, from using data-based methods as surrogate models of the parts of the plant that are difficult to model to training the overall data-based controller using the data generated by the MPC.

References

[1] S. Kouro, M.A. Perez, J. Rodriguez, A.M. Llor, H.A. Young, Model predictive control: Mpc's role in the evolution of power electronics, IEEE Trans. Ind. Electron. 9 (4) (Dec. 2015) 8−21.

[2] R. Kennel, a. Linder, Predictive control of inverter supplied electrical drives, in: 2000 IEEE 31st Annual Power Electron. Specialists Conference. Conference Proceedings (Cat. No.00CH37018), vol. 2, 2000, pp. 761−766.

[3] P. Cortes, M. Kazmierkowski, R. Kennel, D. Quevedo, J. Rodriguez, Predictive control in power electronics and drives, IEEE Trans. Ind. Electron. 55 (12) (2008) 4312−4324.

[4] R. Kennel, A. Linder, M. Linke, Generalized predictive control (GPC)-ready for use in drive applications?, in: Power Electron. Spec. Conf. 2001. PESC. 2001 IEEE 32nd Annu., 4, 2001, pp. 1839−1844, vol. 4.

[5] S. Vazquez, J. Rodriguez, M. Rivera, L.G. Franquelo, M. Norambuena, Model predictive control for power converters and drives: advances and trends, IEEE Trans. Ind. Electron. 64 (2) (Feb. 2017) 935−947.

[6] T. Geyer, N. Oikonomou, F.D. Kieferndorf, Direct model predictive control: a review of strategies that achieve long prediction intervals for power electronics, IEEE Trans. Ind. Electron. 8 (2014) 32−43.

[7] L.M. Caseiro, A.M. Mendes, S.M. Cruz, Dynamically weighted optimal switching vector model predictive control of power converters, IEEE Trans. Ind. Electron. 66 (2) (Feb. 2019) 1235−1245.

[8] Z. Zhang, Z. Li, M.P. Kazmierkowski, J. Rodriguez, R. Kennel, Robust predictive control of three-level NPC back-to-back power converter PMSG wind turbine systems with revised predictions, IEEE Trans. Power Electron. 33 (11) (Nov. 2018) 9588−9598.

[9] Y. Li, F. Grimm, Z. Zhang, Model predictive control for three-phase four-wire voltage source converters in standalone mode, in: 2019 21st European Conference on Power Electronics and Applications, EPE 2019 ECCE Europe, IEEE, Sept. 2019.

[10] S. Vazquez, A. Marquez, R. Aguilera, D. Quevedo, J.I. Leon, L.G. Franquelo, Predictive optimal switching sequence direct power control for grid-connected power converters, IEEE Trans. Ind. Electron. 62 (4) (2015) 2010−2020.

[11] S. Vazquez, R.P. Aguilera, P. Acuna, J. Pou, J.I. Leon, L.G. Franquelo, V.G. Agelidis, Model predictive control for single-phase NPC converters based on optimal switching sequences, IEEE Trans. Ind. Electron. 63 (12) (Dec. 2016) 7533−7541.

[12] A. Mora, R. Cárdenas-Dobson, R.P. Aguilera, A. Angulo, F. Donoso, J. Rodriguez, Computationally efficient cascaded optimal switching sequence MPC for grid-connected three-level NPC converters, IEEE Trans. Power Electron. 34 (12) (Dec. 2019) 12464−12475.

[13] M.G. Judewicz, S.A. Gonzalez, N.I. Echeverria, J.R. Fischer, D.O. Carrica, Generalized predictive current control (GPCC) for grid-tie three-phase inverters, IEEE Trans. Ind. Electron. 63 (7) (Jul. 2016) 4475−4484.

This book belongs to Kitab Liaison (ocd1996@gmail.com) Copyright Elsevier 2023

[14] S. Vazquez, C. Montero, C. Bordons, L.G. Franquelo, Design and experimental validation of a Model Predictive Control strategy for a VSI with long prediction horizon, in: IECON Proceedings (Industrial Electronics Conference), 2013, pp. 5788−5793.

[15] S. Mariethoz, M. Morari, Explicit model-predictive control of a PWM inverter with an LCL filter, IEEE Trans. Ind. Electron. 56 (2) (2009) 389−399.

[16] S. Almér, S. Mariéthoz, M. Morari, Sampled data model predictive control of a voltage source inverter for reduced harmonic distortion, IEEE Trans. Control Syst. Technol. 21 (5) (Sept. 2013) 1907−1915.

[17] A. Mora, M. Urrutia, R. Cardenas, A. Angulo, M. Espinoza, M. Diaz, P. Lezana, Modelpredictive- control-based capacitor voltage balancing strategies for modular multi-level converters, IEEE Trans. Ind. Electron. 66 (3) (Mar. 2019) 2432−2443.

[18] Y. Zhang, W. Xie, Z. Li, Y. Zhang, Model predictive direct power control of a PWM rectifier with duty cycle optimization, IEEE Trans. Power Electron. 28 (11) (2013) 5343−5351.

[19] J. Rocabert, A. Luna, F. Blaabjerg, P. Rodríguez, Control of power converters in ac microgrids, IEEE Trans. Power Electron. 27 (11) (Nov. 2012) 4734−4749.

[20] F. Blaabjerg, R. Teodorescu, M. Liserre, A. Timbus, Overview of control and grid synchronization for distributed power generation systems, IEEE Trans. Ind. Electron. 53 (5) (Oct. 2006) 1398−1409.

[21] T. Dragicevic, X. Lu, J.C. Vasquez, J.M. Guerrero, DC microgrids-part I: a review of control strategies and stabilization techniques, IEEE Trans. Power Electron. 31 (7) (Jul. 2016) 4876−4891.

[22] T. Dragicevic, X. Lu, J.C. Vasquez, J.M. Guerrero, DC microgrids - part II: a review of power architectures, applications, and standardization issues, IEEE Trans. Power Electron. 31 (5) (May 2016) 3528−3549.

[23] P. Cortés, G. Ortiz, J.I. Yuz, J. Rodríguez, S. Vazquez, L.G. Franquelo, Model predictive control of an inverter with output LC filter for UPS applications, IEEE Trans. Ind. Electron. 56 (6) (Jun. 2009) 1875−1883.

[24] C. Zheng, T. Dragicevic, F. Blaabjerg, Current-sensorless finite-set model predictive control for LC-filtered voltage source inverters, IEEE Trans. Power Electron. 35 (1) (Jan. 2020) 1086−1095.

[25] T. Dragicevic, Model predictive control of power converters for robust and fast operation of ac microgrids, IEEE Trans. Power Electron. 33 (7) (Jul. 2018) 6304−6317.

[26] T. Dragicevic, M. Novak, Weighting factor design in model predictive control of power electronic converters: an artificial neural network approach, IEEE Trans. Ind. Electron. 66 (11) (Nov. 2019) 8870−8880.

[27] T. Dragicevic, Dynamic stabilization of DC microgrids with predictive control of point-of-load converters, IEEE Trans. Power Electron. 33 (12) (Dec. 2018) 10872−10884.

[28] J.L. Li, S.J. Hu, M. Li, Y. Zhu, D.G. Kong, H.H. Xu, Research on the application of parallel back-to-back PWM converter on direct-drive wind power system, in: 3rd International Conference on Deregulation and Restructuring and Power Technologies, DRPT 2008, 2008, pp. 2504−2508.

[29] Z. Zhang, R. Kennel, Novel ripple reduced direct model predictive control of three level NPC active front end with reduced computational effort, in: Predictive Control of Electrical Drives and Power Electronics (PRECEDE 2015), Valparaiso, Chile, 2015.

This book belongs to Kitab Liaison (ocd1996@gmail.com) Copyright Elsevier 2023

[30] Z. Zhang, F. Wang, M. Acikgoz, X. Cai, R. Kennel, FGPA HiL simulation of back-to-back converter PMSG wind turbine systems, in: Power Electronics and ECCE Asia (ICPE-ECCE Asia), 2015 9th International Conference on, Jun. 2015, pp. 99−106.

[31] Z. Zhang, F. Wang, T. Sun, J. Rodriguez, R. Kennel, FPGA based experimental investigation of a quasi-centralized model predictive control for back-to-back converters, IEEE Trans. Power Electron. 31 (1) (2016) 662−672.

[32] Z. Zhang, R. Kennel, Direct model predictive control of three-level NPC back-to-back power converter PMSG wind turbine systems under unbalanced grid. Predictive Control of Electrical Drives and Power Electronics (PRECEDE 2015), Valparaiso, Chile, 2015, pp. 97−102.

[33] H. Akagi, Y. Kanazawa, A. Nabae, Instantaneous reactive power compensators comprising switching devices without energy storage components, IEEE Trans. Ind. Appl. IA-20 (3) (1984) 625−630.

[34] X. Dai, G. Liu, R. Gretsch, Generalized theory of instantaneous reactive quantity for multiphase power system, IEEE Trans. Power Deliv. 19 (3) (2004) 965−972.

This book belongs to Kitab Liaison (ocd1996@gmail.com) Copyright Elsevier 2023

Chapter 5

Adaptive control in power electronic systems

Hosein Gholami-Khesht, Pooya Davari, Frede Blaabjerg
Department of Energy Technology, Aalborg University, Aalborg, Denmark

5.1 Introduction

Nowadays, the control systems are known as the main intelligence of the power converter systems, and their major roles are to keep the stability and high performance of the power electronic system. Therefore, so far, many control strategies have been examined and applied in power electronic applications such as using linear control methods (proportional integral), robust control methods (μ analysis), nonlinear control methods (sliding mode control), adaptive control methods, fuzzy control methods, digital and predictive control methods, and also identification techniques can be applied in any control in order online to improve the control.

Among them, adaptive control methods have attracted much attention for decades. Adaptive control is a control method with adjustable control gains that are changeable due to variable or initially uncertain parameters in the controlled system. Therefore, this control method keeps the system performance and stability at the desired or optimum level under different conditions.

In addition to the ability to consider time-variant parameters and the presence of learning parts like nonlinear and smart control methods, another advantage of the adaptive control methods is the existence of powerful mathematical stability and convergence proofs like in classic and linear control methods. Consequently, the adaptive control method is a bridge between the classic and the more intelligent directions of control engineering and includes all advantages of both areas.

In this respect, the first aim of this chapter is to describe and investigate the concept, advantages and disadvantages, and new advances in adaptive control methods and also their application in the power electronic systems are discussed. Generally, adaptive control methods can be classified into two categories [1]: indirect adaptive control (IAC) and direct adaptive control (DAC). In IAC methods, firstly, an appropriate online identification is used for system

Control of Power Electronic Converters and Systems. https://doi.org/10.1016/B978-0-12-819432-4.00008-1
Copyright © 2021 Elsevier Ltd. All rights reserved.

This book belongs to Kitab Liaison (ocd1996@gmail.com)
Copyright Elsevier 2023

parameters' estimation; afterward, control gains are updated based on the estimated values [2–18]. So far, many different IAC methods are based on various online identification techniques, where the most important are the Luenberger observer [2–6], the sliding mode observer [7], the Kalman filter [8], the neural network [9], the steepest descent [10], recursive least-square (RLS) estimator [11], estimator based on Immersion and Invariance (I&I) theory [12], and the Lyapunov stability theory [13]. Although these identification parts make the control system immune against the system parameter variations and uncertainties, it will increase the computational burden in the control system. In contrary to the IAC, the DAC directly updates the controller gains based on a proper adaption mechanism, which brings simplicity and reduces the computational demand [19–26]. Besides, mathematical stability analysis is more straightforward and simple in DAC compared to IAC. One of the most practical and accessible DAC is known as model reference adaptive control (MRAC) [20,21,24–26]. In this control method, the desired characteristics of the closed-loop system are expressed in a reference model. There, the reference model generates the desired closed-loop response for the controller, and the controller takes the proper action concerning error between real and reference outputs. It is the main difference between MRAC and other control methods when the controller follows the reference output instead of the reference input.

To better clarify, the general structure of DAC and IAC methods is shown in Fig. 5.1. Moreover, the block diagram of the MRAC, which is known as one of the essential adaptive control methods, is shown in Fig. 5.2.

In the following sections, firstly, the dynamics of an uninterruptible power supply (UPS) system are described in Section 5.2. Section 5.3 presents system identification techniques, which includes both parameter and state estimation methods. The IAC based on the combination of model predictive control (MPC) and an adaptive observer, is presented in Section 5.4. In this structure,

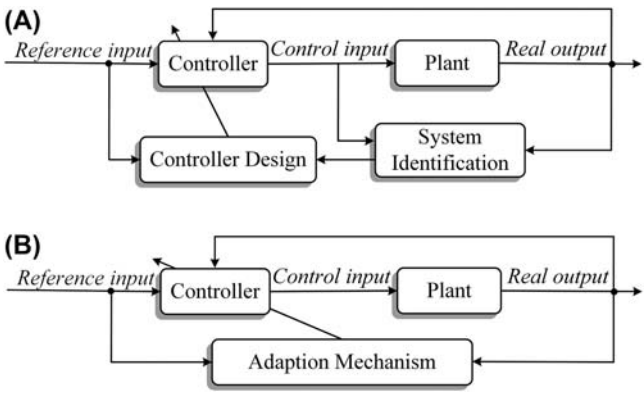

FIGURE 5.1 Block diagram of (A) indirect adaptive control and (B) direct adaptive control to be applied in power electronic system.

This book belongs to Kitab Liaison (ocd1996@gmail.com) Copyright Elsevier 2023

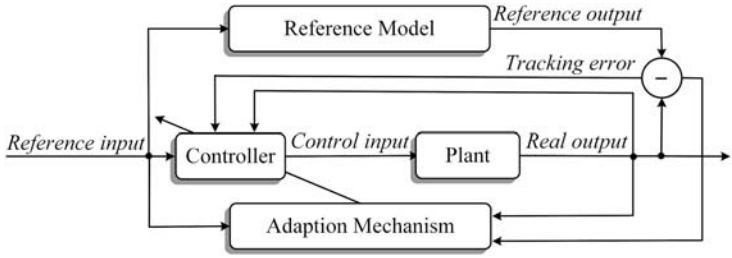

FIGURE 5.2 Block diagram of direct adaptive control based on the model reference adaptive concept.

the adaptive observer improves performance of the conventional MPC by estimating system uncertainties and load current disturbances. In Section 5.5, DAC based on the MRAC techniques is discussed. Both presented IAC and DAC methods in Sections 5.4 and 5.5 are demonstrated on a three-phase voltage source inverter (VSI) in UPS applications experimentally. Finally, conclusions are drawn in Section 5.6.

5.2 System dynamics on a UPS system

Single-line diagram of the studied three-phase UPS is shown in Fig. 5.3, which consists of a three-phase VSI connected to loads through an LC filter. Based on Fig. 5.3 and Kirchhoff's Laws, the system equation can be written as follows:

$$\begin{cases} L\dfrac{di_f}{dt} = v_{inv} - v_o \\ C\dfrac{dv_o}{dt} = i_f - i_o \end{cases} \tag{5.1}$$

where v_{inv}, v_o, are output voltage of the inverter and capacitor voltage/voltage at the point of common coupling (PCC), i_f and i_o are the inverter/inductor

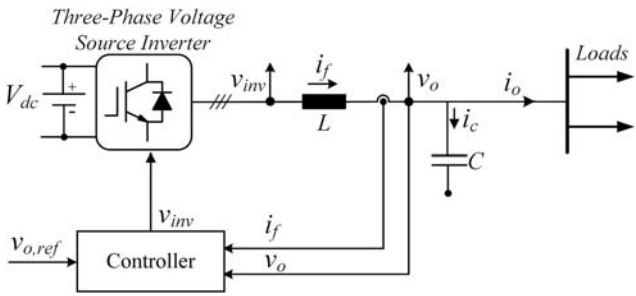

FIGURE 5.3 Single-phase diagram of three-phase voltage source inverter in uninterruptible power supply application.

This book belongs to Kitab Liaison (ocd1996@gmail.com) Copyright Elsevier 2023

current and load current. L and C are the filter inductance and capacitance to filter the PWM (pulse-width modulation) harmonics. It is worth to note that the value of parameters L and C are not precisely known, and they could vary from the nominal amounts in practice. Eq. (5.1) can be converted into standard state space form like the following:

$$\frac{dx}{dt} = Ax + Bv_{inv} + Di_o,$$
$$x = \begin{bmatrix} i_f \\ v_o \end{bmatrix}, A = \begin{bmatrix} 0 & -\frac{1}{L} \\ \frac{1}{C} & 0 \end{bmatrix}, B = \begin{bmatrix} \frac{1}{L} \\ 0 \end{bmatrix}, D = \begin{bmatrix} 0 \\ \frac{-1}{C} \end{bmatrix} \tag{5.2}$$

where x, v_{inv}, and i_o are system states, control, and disturbance inputs, and A, B, and D are the state and input matrixes.

The digital implementation of the control algorithm can be based on the discrete state space model of the plant dynamics. Discretizing (5.2) with sampling period of T_S yields the following discrete state space equations:

$$\begin{cases} x(k+1) = A_d x(k) + B_d v_{inv}(k) + D_d i_o(k) \\ y(k) = C_d x(k),\ C_d = \begin{bmatrix} 1 & 0 \\ 0 & 1 \end{bmatrix} \\ A_d = e^{AT_S} = L^{-1}\left\{(sI - A)^{-1}\right\}_{t=T_S} \\ B_d = \int_0^{T_S} e^{A_d(T_S-\tau)} B d\tau \\ D_d = \int_0^{T_S} e^{A_d(T_S-\tau)} D d\tau \end{cases} \tag{5.3}$$

5.3 System identification

The identification part is an essential part of any adaptive control methods (i.e., IAC and DAC), as discussed in the introduction and shown in Fig. 5.1. When this part is appropriately added to any control methods, in order to compensate for uncertain and variable parameters and disturbances inputs, then a strong adaptive control method can be obtained. Due to the importance of the identification part, the most practical identification methods include both parameter estimators and state observers, which are discussed in this section.

This book belongs to Kitab Liaison (ocd1996@gmail.com) Copyright Elsevier 2023

5.3.1 Parameters identification

5.3.1.1 Recursive least-square estimation

The performance of many control methods depends on the accuracy of the system parameters. Consequently, uncertainty in these parameters causes large output ripples as well as nonzero tracking errors and even system instability. As yet, various identification methods have been proposed for system parameter estimation. Among them, the RLS estimator is known as the best linear unbiased estimator and it is commonly used in adaptive control systems [1]. The general algorithm to implement RLS is given by the following equations:

$$\begin{aligned} \theta_{est}(k) &= \theta_{est}(k-1) + K(k)(y(k) - \Phi^T(k)\theta_{est}(k-1)) \\ K(k) &= P(k-1)\Phi(k)(\lambda I + \Phi^T(k)P(k-1)\Phi(k))^{-1} \\ P(k) &= (I - K(k)\Phi^T(k))P(k-1)/\lambda \end{aligned} \tag{5.4}$$

where θ_{est}, Φ^T, and $P(k)$ are the estimated parameter vector, the regressor vector, and the covariance matrix, respectively. Also, λ is the forgetting factor and is selected in the range [0−1], small values of λ ensure fast convergence with the cost of larger oscillations in the estimated parameters and vice versa. Moreover, once the system parameters approach the real values, $P(k)$ approaches zero, and the RLS does not work correctly and eventually cannot track the upcoming parameter variations. So, periodic resetting of $P(k)$ to αI (where α is a large constant value) would be the right solution and it is well discussed in the adaptive and identification books.

To use RLS algorithm and estimate filter inductance and capacitance of the studied UPS system, the system equation can be written as follows:

$$y(k) = \Phi^T(k)\theta$$
$$\begin{cases} y(k) = [\,(i_f(k) - i_f(k-1)) \quad (v_o(k) - v_o(k-1))\,]^T \\ \Phi^T(k) = \begin{bmatrix} v_{inv}(k-1) - v_o(k-1) & 0 \\ 0 & i_f(k-1) - i_o(k-1) \end{bmatrix} \\ \theta = [\,a \quad b\,]^T \end{cases} \tag{5.5}$$

This Eq. (5.5) is achieved by discretizing (5.2) with the first-order Euler method and considering the system parameters as being $a = \frac{T_S}{L}$ and $b = \frac{T_S}{C}$. Consequently, using the system model (5.5) and the RLS algorithm (5.4), the system parameters can be estimated as $\theta_{est} = [a_{est} \cdot b_{est}]^{\mathrm{T}}$. In our system, since the filter parameters change slowly with time, it is desirable to select the value of λ very close to one like 0.999. With this choice, a smooth estimation of the parameters is realized.

This book belongs to Kitab Liaison (ocd1996@gmail.com) Copyright Elsevier 2023

5.3.2 State identification

In many power electronic applications, it is necessary to measure all system states to shape the closed-loop transfer function, minimize the steady-state errors, and to do better disturbance rejection. However, measuring all signals with related sensors increases system cost, volume, and weight. Besides, physical sensors and related communication lines may worsen the system reliability due to additional physical components, which might be subject to damages and thereby failures.

A great solution to maintain the system performance and simultaneously to reduce the number of sensors is to employ an observer. In simple words, an observer is a closed-loop estimator that uses the state space model of the system to predict the states of the system from the measured inputs and outputs based on the minimization of the difference between the measured and the estimated outputs. High accuracy and reliability, cost and size reduction, and noise immunity are important advantages of determining signals by the observer. Moreover, an observer allows us to predict the desired quantities one sample ahead and therefore helps the control system to compensate for delays introduced by the digital implementation of power converters.

There are different types of observers. The most commonly used is a Luenberger observer, which is normally used for deterministic systems, while Kalman filter is developed for stochastic and noisy systems, and finally adaptive observers for robust estimation of system states under strong uncertainties.

5.3.2.1 Observability condition

Before implementing any observers, the observability condition of the system must be investigated. The whole system state will be estimated, if and only if the observability matrix of the system (5.6) has a full column rank.

$$\begin{bmatrix} C_d & C_dA_d & \dots & C_dA_d^{n-1} \end{bmatrix}^T \tag{5.6}$$

For the used system in this chapter, two different cases exist:

1. i_f and i_o are measured signals and v_o is nonmeasured variable, which can be estimated by the observer

   In such case the observability matrix can be constructed as follows:

$$C_d = \begin{bmatrix} 1 & 0 \end{bmatrix} \rightarrow obv = \begin{bmatrix} C_d & C_dA_d \end{bmatrix}^T = \begin{bmatrix} 1 & 0 \\ A_d(1,1) & A_d(1,2) \end{bmatrix} \tag{5.7}$$

2. v_o and i_o are measured signals and i_f is the nonmeasured variable, which can be estimated by the observer

   Therefore, in the second case, the observability matrix is

$$C_d = \begin{bmatrix} 0 & 1 \end{bmatrix} \rightarrow obv = \begin{bmatrix} C_d & C_dA_d \end{bmatrix}^T = \begin{bmatrix} 0 & 1 \\ A_d(2,1) & A_d(2,2) \end{bmatrix} \tag{5.8}$$

This book belongs to Kitab Liaison (ocd1996@gmail.com) Copyright Elsevier 2023

It is evident from the observability matrixes (5.7) and (5.8) that two systems are observable, and employing an observer is possible.

It is worth to note that there is also third case when v_o and i_f are measured signals, and it is preferable to eliminate the sensors for the disturbance input (i_o), which will also be investigated in this section as a disturbance estimator.

5.3.2.2 Luenberger observer

A full-order Luenberger observer can be constructed as follows:

$$\widehat{x}(k+1) = A_d\widehat{x}(k) + B_d v_{inv}(t) + D_d i_o(k) + GC_d\Big(x(k) - \widehat{x}(k)\Big) \tag{5.9}$$

where symbol "^" denotes the estimated values, and G is the observer gain. The estimation error ($e(k)$) dynamics using (5.3) and (5.9) is

$$\begin{cases} e(k+1) = (A_d - GC_d)e(k) \\ e(k) = x(k) - \widehat{x}(k) \end{cases} \tag{5.10}$$

The observer gain is chosen such that the estimation error dynamics of (5.10) is asymptotically stable and the eigenvalues of the observer are placed in desired locations, which is also discussed in Refs. [27–31]. To make the observer dynamically faster than the system, observable poles must be chosen proportional to the system poles (the proportionality constant is k and $k < 1$). However, a very small proportionality constant causes more sensitivity to the noise. Therefore, selecting the proportionality constant is a trade-off between the observer dynamics and the noise immunity.

5.3.2.3 Kalman filter

Kalman filter, also known as linear quadratic estimation technique, is an optimal recursive estimator, which can estimate system states in the presence of the measurement noises and model uncertainties [8,32–34]. The implementation of the Kalman filter includes two main steps:

1. Prediction step (or time update equations)

   In this step, based on the dynamic model (physical model) and estimated states $\big(\widehat{x}(k)\big)$ in the previous sample, an initial estimation of the system states is produced.

$$\begin{cases} \widehat{x}(k+1|k) = A_d\widehat{x}(k) + B_d u(k) + D_d i_o(k) \\ P(k+1|k) = A_d P(k|k) A_d^{\mathrm{T}} + Q \end{cases} \tag{5.11}$$

   where $\widehat{x}(k+1|k)$ and $P(k+1|k)$ are predicted states and error covariance, respectively.

This book belongs to Kitab Liaison (ocd1996@gmail.com) Copyright Elsevier 2023

2. Update step (update equations based on measurements)

Once the outcome of the next measurement is achieved, these estimated variables are updated using a weighted estimation error between the measured and estimated signals given as

$$\begin{cases} K(k+1) = P(k+1|k)C^T(CP(k+1|k)C^T + R)^{-1} \\ x(k+1|k+1) = x(k+1|k) + K(k+1)(y - Cx(k+1|k)) \\ P(k+1|k+1) = (I - K(k+1)C)P(k+1|k) \end{cases} \tag{5.12}$$

where $K(k+1)$ is the filter gain, $x(k+1|k+1)$ and $P(k+1|k+1)$ are updated and filtered state and error covariance, based on the last measured data. Moreover, Q and R are the covariance of the process noise (model uncertainties) and the measurement noise. Proper estimations of Q and R have a significant impact on the performance of the Kalman filter. However, there is no straightforward algorithm to find appropriate values of them, and they are usually tuned by trial and error using simulations and experiments.

5.3.2.4 Disturbance estimation based on an adaptive observer

In practice, the certainty of the system model is subjected to unmodeled dynamics, parameter uncertainties, and external disturbances. In this subsection, to cope with the problem, an augmented discrete state space model is presented, which includes all system parameters uncertainties and unmodeled dynamics [6,7,35]. To do so, by using the nominal system parameters (A_n, B_n, D_n) and considering the load current as a dynamic disturbance, the system dynamics (5.3) can be rewritten as

$$\begin{aligned} x(k+1) &= (A_n + \Delta A)x(k) + (B_n + \Delta B)v_{inv}(k) + D_d i_o(k) \\ x(k+1) &= A_n x(k) + B_n v_{inv}(k) + Mw(k) \\ w(k) &= \left(M^{-1}D_d\right)i_o(k) + \left(M^{-1}\Delta A\right)x(k) + \left(M^{-1}\Delta B\right)v_{inv}(k) \end{aligned} \tag{5.13}$$

where $(\Delta A, \Delta B, \Delta D)$ are the differences between the real and the nominal system matrixes, and $w(k)$ shows new disturbance input, which represents lumped uncertainties and disturbances. Moreover, M is defined as

$$M = \begin{bmatrix} \dfrac{-T_S}{L_n} & 0 \\ 0 & \dfrac{-T_S}{C_n} \end{bmatrix} \tag{5.14}$$

Here the parameters with subscript n (L_n, C_n) show the nominal values of system parameters (L, C). The augmented state space model can be obtained if the disturbance input $w(k)$ is known. This subsection presents a simple with low computational burden technique to online estimate the disturbance input

This book belongs to Kitab Liaison (ocd1996@gmail.com) Copyright Elsevier 2023

by using an adaptive observer. Based on the augmented model, a simple adaptive observer can be realized as follows:

$$\widehat{x}(k+1) = A_n x(k) + B_n v_{inv}(k) + M\widehat{w}(k) \tag{5.15}$$

where $\widehat{x}(k+1)$ is the output of the adaptive observer, and $\widehat{w}(k)$ is the estimated disturbance input. By comparing (5.15) with (5.13), it can be perceived when the estimation error $e(k) = x(k) - \widehat{x}(k)$ converges to zero, the estimated disturbance input approaches the actual disturbance input vector. Therefore, a steepest descent method is included in the observer system to estimate the disturbance input. This method searches for the minimum of a cost function of many variables. An appropriate cost function to formulate the steepest descent algorithm mathematically is the quadratic error function, which is described as follows:

$$E(k) = 0.5e(k)^T e(k) \tag{5.16}$$

The steepest descent adaptation law can be expressed as

$$\begin{cases} \widehat{w}(k+1) = \widehat{w}(k) + \Delta\widehat{w}(k) \\ \Delta\widehat{w}(k) = -\lambda\left(\dfrac{\partial E}{\partial \widehat{w}}\right) \end{cases} \tag{5.17}$$

Here, $\left(\frac{\partial E}{\partial \widehat{w}}\right)$ is the gradient of the cost function to the disturbance input, and λ is a positive adaptation gain, which controls the rate of convergence and system stability.

$$\begin{cases} \dfrac{\partial E}{\partial \widehat{w}} = \dfrac{\partial E}{\partial e}\dfrac{\partial e}{\partial \widehat{x}}\dfrac{\partial \widehat{x}}{\partial \widehat{w}} = -Me \\ \lambda = \begin{bmatrix} \lambda_1 & 0 \\ 0 & \lambda_2 \end{bmatrix} \end{cases} \tag{5.18}$$

Too large value for λ causes an overshoot or in the worst case instability and also too small value gives a low convergence rate and higher computational burden. Therefore, an adaptive gain selection has an essential impact on the adaptive observer stability and efficiency.

Therefore, the presented adaptive disturbance observer can be summarized as

$$\begin{cases} \widehat{x}(k+1) = A_n x(k) + B_n v_{inv}(k) + M\widehat{w}(k) \\ \widehat{w}(k+1) = \widehat{w}(k) + \lambda M\left(x(k) - \widehat{x}(k)\right) \end{cases} \tag{5.19}$$

This book belongs to Kitab Liaison (ocd1996@gmail.com) Copyright Elsevier 2023

In the following, the stability analysis of the adaptive observer in the sense of the Lyapunov functions is presented. The Lyapunov function is selected as

$$V_T(e(k),k) = 0.5e(k)^T e(k) \tag{5.20}$$

The closed-loop stability of the observer is obtained if the following requirements are satisfied:

$$\begin{cases} (1): V_T(k) > 0 \\ (2): \Delta V_T(k) < 0 \end{cases} \tag{5.21}$$

where $\Delta V_T\ (k)$ is the change in the Lyapunov function. The first stability condition in (5.21) is satisfied, because the Lyapunov function in (5.20) is a squaring function. Therefore, Lyapunov's convergence criterion is completely fulfilled if the negative change in the Lyapunov function is to be verified. The difference in the Lyapunov function is defined as

$$\Delta V_T(k) = V_T(e(k+1)) - V_T(e(k)) < 0 \tag{5.22}$$

Eq. (5.22) can be rewritten as

$$\Delta V_T(k) = e(k)^T \Delta e(k) + 0.5\Delta e(k)^T \Delta e(k) \tag{5.23}$$

where $\Delta e(k)$ is the change in the estimation error due to adaption law and disturbance input can be given by

$$\Delta e(k) = e(k+1) - e(k) = \frac{\partial e(k)}{\partial \widehat{w}(k)}\Delta \widehat{w}(k) = \frac{\partial e(k)}{\partial \widehat{x}(k)}\frac{\partial \widehat{x}(k)}{\partial \widehat{w}(k)}\Delta \widehat{w}(k) = -M\lambda M e(k) \tag{5.24}$$

Consequently, $\Delta V_T\ (k)$ by substituting (5.24) in (5.23) can be represented as

$$\Delta V_T(k) = -e(k)^T [M\lambda M(I_{2*2} - 0.5M\lambda M)]e(k) \tag{5.25}$$

To satisfy the second stability condition in (5.21), the adaptation gains are chosen as

$$\begin{cases} 0 < \lambda_1 < \dfrac{2{L_n}^2}{{T_{samp}}^2} \\ 0 < \lambda_2 < \dfrac{2{C_n}^2}{{T_{samp}}^2} \end{cases} \tag{5.26}$$

This book belongs to Kitab Liaison (ocd1996@gmail.com) Copyright Elsevier 2023

5.4 Indirect adaptive predictive control

The performance of many control methods, such as deadbeat and predictive control methods and also classical linear controllers of UPS, depends on the accuracy of the system parameters. Consequently, uncertainty in these parameters may give large output disturbances as well as nonzero tracking errors and even system instability. In this section, for real-time estimation of system uncertainties and disturbances, an identification part is added to the MPC method. So, a combination of the MPC and an identification part realizes an indirect adaptive predictive voltage control, as shown in Fig. 5.4 [6,28].

The proposed control strategy is based on two-step MPC. In this method, in each sampling period and based on the predicted converter quantities and augmented model, optimal converter voltage that minimizes a cost function is selected. The cost function usually consists of the voltage tracking errors (5.27), but others could be included too. Then the optimal voltage vector is saved and applied at the beginning of the next sampling period. So in the two-step MPC, a whole sampling period is available for computations, and consequently, delays due to calculations and digital implementation can be eliminated Fig. 5.4.

A conventional choice for cost function of the MPC is:

$$g = \left(v_o(k+2) - v_{o,ref}(k+1)\right)^2 \tag{5.27}$$

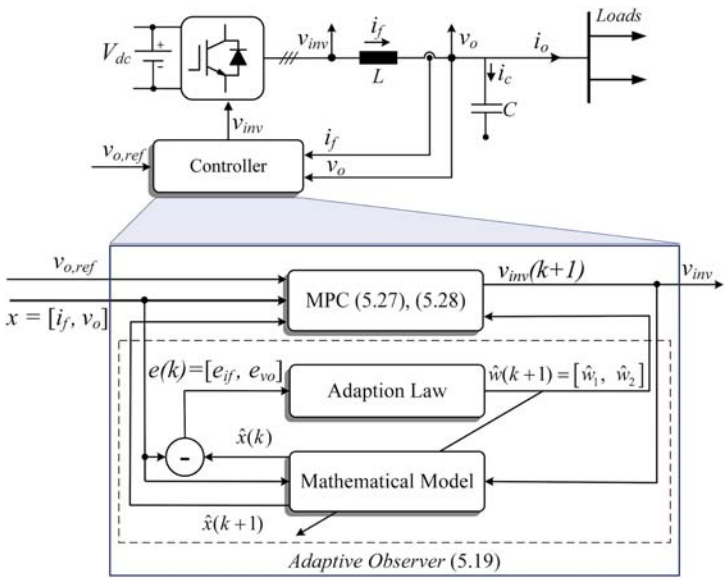

FIGURE 5.4 Block diagram of indirect adaptive control method based on predictive controller and adaptive observer.

This book belongs to Kitab Liaison (ocd1996@gmail.com) Copyright Elsevier 2023

where $v_o(k+2)$ is the output voltage at the beginning of the $(k+2)$th period, which is calculated based on the augmented model (5.13) for different available converter output voltage vectors given as

$$v_o(k+2) = A_n(2,1)i_f(k) + A_n(2,2)v_o(k+1) + B_n(2,1)v_{inv}(k+1) + M(2,2)w_2(k+1) \tag{5.28}$$

In the above equation, the system states at sample $(k+1)$ and disturbance dynamic w are estimated via the proposed adaptive observer in (5.19).

5.4.1 Experimental results

To evaluate the performance of adaptive MPC, an experimental setup has been prepared, which is shown in Fig. 5.5. The laboratory setup includes three-phase 5 kW PWM-VSC, which is supplied from a constant DC voltage, three-phase resistive load, and LC-type output filter. Moreover, the control method is realized on a DS1007 dSPACE system platform. Finally, for current and voltage measurements and switching pulses generation, the DS2004 high-speed A/D board and the DS5101 digital waveform output board are employed, respectively. The parameters of three-phase UPS are given in Table 5.1.

The steady-state performance of indirect adaptive MPC is shown in Fig. 5.6, which includes output voltage, output voltage tracking error, output current, and outputs of adaptive disturbance observer. Results show excellent steady-state performance of control method under unmeasured load currents and disturbances, unlike in the conventional MPC, which needs the load currents measurements. Moreover, the transient performance of adaptive MPC under a step change of resistive load is shown in Fig. 5.7. In this figure, the load power has been suddenly changed from zero to nominal ones. This figure shows very good transient response and also disturbance rejection using the indirect adaptive MPC control method.

5.5 Model reference direct adaptive control of UPS

In this section, a two-loop adaptive control of UPS is proposed. Both the outer capacitor voltage control and the inner inductor current control loops are based on the MRAC theorem. The block diagram of the proposed MRAC scheme is shown in Fig. 5.8, which includes a reference model that defines the desired closed-loop response for both the inner and outer control loops. Moreover, an adaption mechanism to force the system outputs to track the reference outputs and update the control gains in the presence of parameter uncertainties is designed based on the Lyapunov stability theorem. In the following, more details of the proposed control method are discussed.

This book belongs to Kitab Liaison (ocd1996@gmail.com) Copyright Elsevier 2023

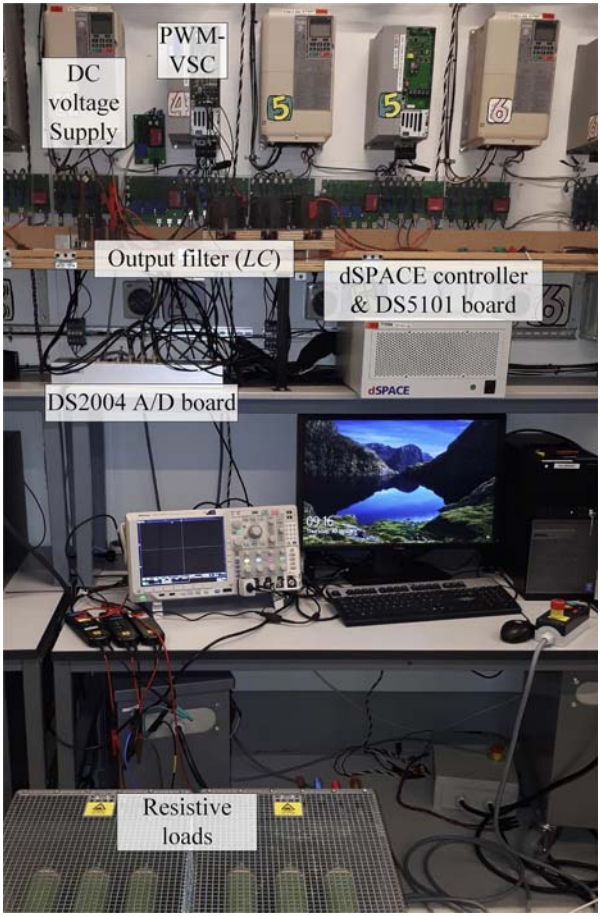

FIGURE 5.5 Experimental setup to implement adaptive model predictive control on a three-phase voltage source inverter in uninterruptible power supply application.

5.5.1 The outer voltage control loop

The capacitor voltage dynamics are given as

$$\dot{v}_o = a_2(i_f - i_o), a_2 = \frac{1}{C} \tag{5.29}$$

For this equation and the outer control loop, the inductor current is control input and can be defined as

$$i_f(t) = -k_1 v_o(t) + k_2 v_{o,ref}(t) + i_o \tag{5.30}$$

k_1 and k_2 are feedback control gains.

This book belongs to Kitab Liaison (ocd1996@gmail.com) Copyright Elsevier 2023

TABLE 5.1 System parameters for uninterruptible power supply system under the adaptive MPC.

Nominal power	5 [kW]
Line voltage (rms)	380 [V]
Output frequency (f)	50 [Hz]
Inductor (L)	4.5 [mH]
Capacitor (C)	15 [μF]
DC-link voltage (V_{dc})	720 [V]
Sampling time	22 [μs]

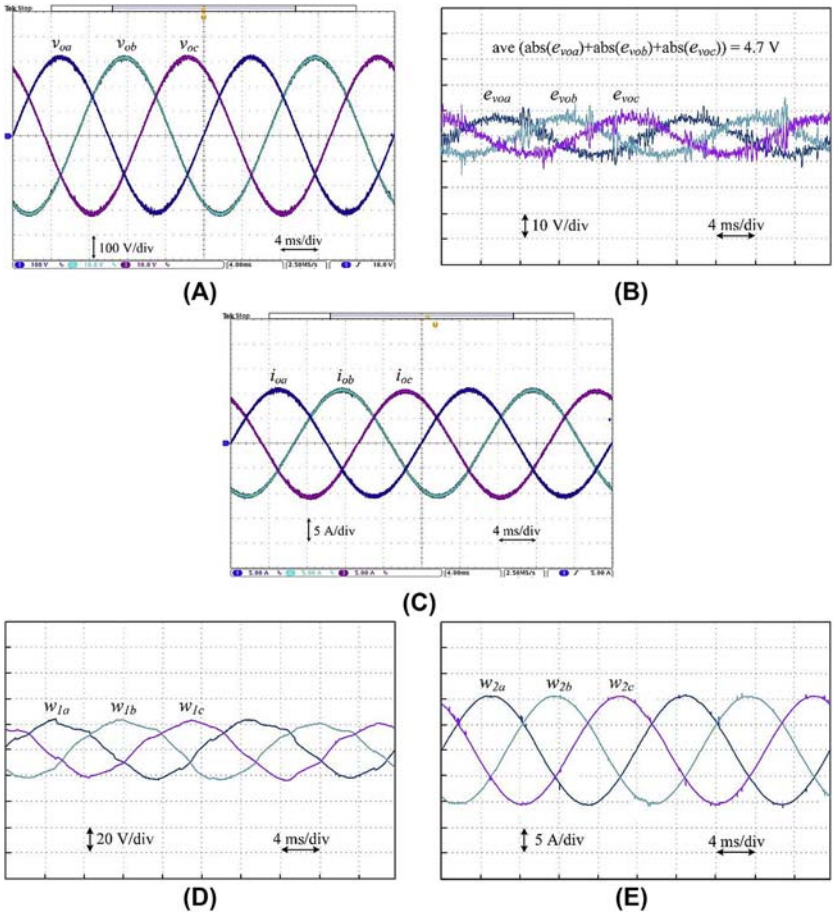

FIGURE 5.6 Obtained experimental results showing steady-state performance of the adaptive model predictive control under nominal load (5 kW). (A) Output voltage, (B) steady-state error, (C) output current, (D) and (E) adaptive observer outputs.

This book belongs to Kitab Liaison (ocd1996@gmail.com) Copyright Elsevier 2023

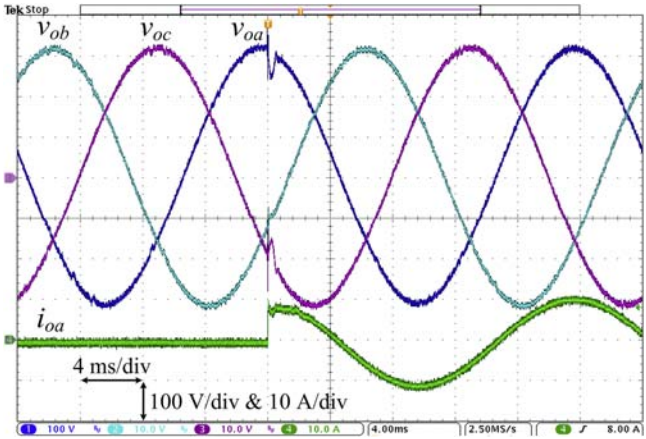

FIGURE 5.7 Obtained experimental results showing transient performance of the adaptive model predictive control under step change of the load from zero to 5 kW of the uninterruptible power supply.

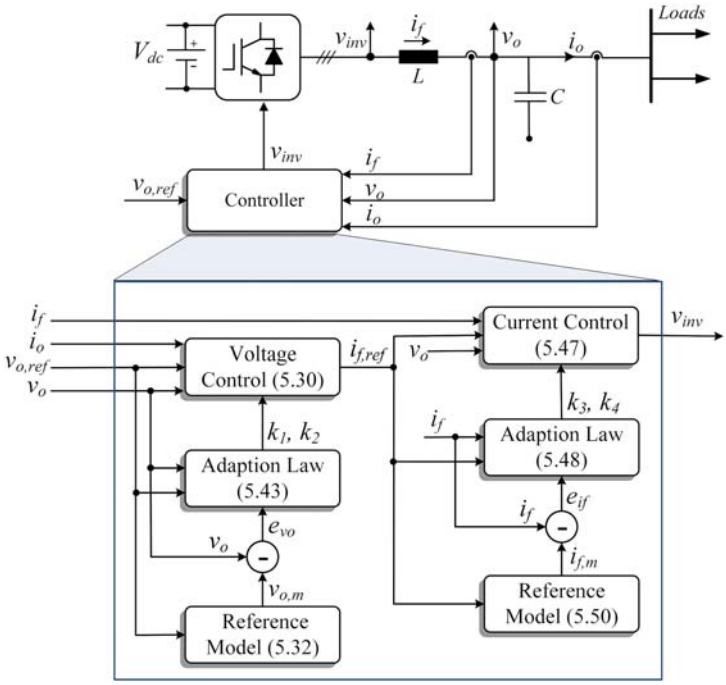

FIGURE 5.8 Block diagram of model reference adaptive control of uninterruptible power supply.

This book belongs to Kitab Liaison (ocd1996@gmail.com) Copyright Elsevier 2023

It is worth to note that (5.30) generates the inductor reference current for the inner loop as well as $\left(i_{f,ref}(t) \simeq i_f(t)\right)$. The closed-loop system under the proposed control law (5.30) is

$$\dot{v}_o = a_2\left(-k_1 v_o(t) + k_2 v_{o,ref}(t)\right) \tag{5.31}$$

Based on the system state space model of (5.31), the following reference model is proposed:

$$\dot{v}_{o,m}(t) = -a_{2m} v_{o,m}(t) + b_{2m} v_{o,ref}(t) \tag{5.32}$$

where $v_{o,m}$ and $v_{o,ref}$ are the output of the reference system and the reference input, and a_m is positive constant, which assigns the desired closed-loop pole in the reference model.

The voltage tracking error is

$$e_{v_o}(t) = v_o(t) - v_{o,m}(t) \tag{5.33}$$

Therefore, the tracking error dynamics can be calculated as

$$e_{v_o}(t) = -a_{2m} e_{v_o} - (a_2 k_1 - a_{2m}) v_o + (-a_2 k_2 + b_{2m}) v_{o,ref} \tag{5.34}$$

The above can be rewritten as

$$e_{v_o}(t) = -a_{2m} e_{v_o} - a_2\left(k_1 - k_1^*\right) v_o + a_2\left(k_2 - k_2^*\right) v_{o,ref} \tag{5.35}$$

where k_1^*, k_2^* are the nominal values of the control parameters.

$$\begin{cases} k_1^* = a_2^{-1} a_{2m} \\ k_2^* = a_2^{-1} b_{2m} \end{cases} \tag{5.36}$$

If the controller parameters are selected from (5.36), then the input–output relation of the real system and the reference model is identical, which is called a perfect-matching of the reference model (5.32) and the closed-loop system (5.31).

Due to nonlinearities and uncertainties of the plant parameters, (5.36) cannot be directly used for the calculation of the controller parameters. Thus, to fine-tune the control gains, a proper adaption law must be employed. In the following, a parameter updating law to tune the control gains based on the Lyapunov stability theory is proposed.

The voltage tracking error by defining the control parameters errors is recalculated again as

$$\begin{cases} \dot{e}_{v_o}(t) = -a_{2m} e_{v_o} + a_2 v_o \Delta k_1 - a_2 v_{o,ref} \Delta k_2 \\ e_{k1} = k_1 - k_1^*, e_{k2} = k_2 - k_2^* \end{cases} \tag{5.37}$$

The differential equation (5.37) contains adjustable parameters, k_1 and k_2. So, the main goal is to select a proper Lyapunov function and afterward determine an adjustment mechanism, such that the voltage tracking error,

This book belongs to Kitab Liaison (ocd1996@gmail.com) Copyright Elsevier 2023

defined by (5.37), converges to zero. One solution for the positive-definite radially unbounded normal and conventional Lyapunov function is

$$V(e_{v_o},k)=\frac{1}{2}e_{v_o}^2+\frac{\gamma_2^{-1}}{2}\left(e_{k1}^2+e_{k2}^2\right) \tag{5.38}$$

For the Lyapunov function to ensure asymptotic stability, the time derivative of (5.38), defined in (5.39), must be negative-definite.

$$\dot{V}(e_{v_o},k)=\dot{e}_{v_o}e_{v_o}+\gamma_2^{-1}(\dot{e}_{k1}e_{k1}+\dot{e}_{k2}e_{k2}) \tag{5.39}$$

Considering the following relationship:

$$\dot{e}_{K1}=\dot{k}_1,\ \dot{e}_{K2}=\dot{k}_2 \tag{5.40}$$

(5.39) is simplified as

$$\begin{aligned}\dot{V}(e_{v_o},k)&=-a_{2m}e_{v_o}^2+e_{v_o}a_2\left(v_{o,ref}e_{k2}-v_oe_{k1}\right)+\gamma_2^{-1}(\dot{k}_1e_{k1}+\dot{k}_2e_{k2})\\ \dot{V}(e_{v_o},k)&=-a_{2m}e_{v_o}^2+\left(\gamma_2^{-1}\dot{k}_1-a_2e_{v_o}v_o\right)e_{k1}+\left(\gamma_2^{-1}\dot{k}_2+a_2e_{v_o}v_{o,ref}\right)e_{k2}\end{aligned} \tag{5.41}$$

So the first term of (5.41) is negative-definite if the second and third term at the right-hand side equals to zero, i.e.,

$$-a_2e_{v_o}v_o+\gamma_2^{-1}\dot{k}_1=0a_2e_{v_o}v_{o,ref}+\gamma_2^{-1}\dot{k}_2=0\}\Rightarrow\dot{V}(e_{v_o},k)=-a_{2m}e_{v_o}^2 \tag{5.42}$$

Therefore, the proposed adaption laws are given as

$$\begin{cases}\dot{k}_1=\gamma_2a_2e_{v_o}v_o\\ \dot{k}_2=-\gamma_2a_2e_{v_o}v_{o,ref}\end{cases} \tag{5.43}$$

Hence, with e_{v_o} being nonzero, the time derivative of the Lyapunov function is negative-definite, which translates to $V(t)\le V(0)$ for $t>0$; therefore, e_{v_o}, and k in (5.38) are bounded. To ensure global exponential stability, the vector T is described as

$$T=\left[e_{v_o}\quad e_{k1}\quad e_{k2}\right] \tag{5.44}$$

with respect to (5.38)

$$\lim_{T\to\infty}V(T)=\infty \tag{5.45}$$

Consequently, the closed-loop system is globally exponentially stable, and the only equilibrium point of the system has occurred at $T=0$. Therefore, (5.38) is a Lyapunov function, and the overall control system under the adaption law of (5.43) is globally exponentially stable. Also, $e_{v_o}(t)\to 0$ and all signals are bounded.

This book belongs to Kitab Liaison (ocd1996@gmail.com) Copyright Elsevier 2023

5.5.2 The inner current control loop

The same procedure as done for the outer voltage control loop design can be employed to design the model reference current control. The inductor current dynamics is given as

$$\dot{i}_f = a_1(v_{inv} - v_o),\ a_1 = \frac{1}{L} \tag{5.46}$$

The converter reference voltage (control input) can be selected as

$$v_{inv}(t) = -k_3 i_f + k_4 i_{fref}(t) + v_o(t) \tag{5.47}$$

k_3 and k_4 are adaption parameters, which can be updated as

$$\begin{cases} \dot{k}_3 = \gamma_1 a_1 e_{i_f} i_f \\ \dot{k}_4 = -\gamma_1 a_1 e_{i_f} i_{f,ref} \end{cases} \tag{5.48}$$

where γ_1 is a positive adaption gain, $i_{f,ref}$ is the reference input, and e_{if} is the current tracking error that is defined as

$$e_{i_f}(t) = i_f(t) - i_{f,m}(t) \tag{5.49}$$

here $i_{f,m}$ is the output of the following reference system:

$$\dot{i}_{f,m}(t) = -a_{1m} i_{f,m}(t) + b_{1m} i_{f,ref}(t) \tag{5.50}$$

a_{1m} and b_{1m} are positive constants, and a_{1m} defines the desired closed-loop pole.

5.5.3 Experimental results

To evaluate the performance of direct MRAC, several experimental tests have been done on the three-phase 5 kW UPS. The system parameters are the same as Section 5.4.1 and Table 5.1 and given in Table 5.2. The only difference is

TABLE 5.2 System parameters for uninterruptible power supply system under the MRAC.

Nominal power	5 [kW]
Line voltage (rms)	380 [V]
Output frequency (f)	50 [Hz]
Inductor (L)	3 [mH]
Capacitor (C)	15 [μF]
DC-link voltage (V_{dc})	720 [V]
Sampling and switching frequencies	100 [μs]

This book belongs to Kitab Liaison (ocd1996@gmail.com) Copyright Elsevier 2023

the value of the inductor filter. MRAC, unlike MPC, uses a modulator and fixed switching frequency at 10 kHz in this case, and therefore it is possible to implement this control method with a lower inductor filter. Thus, the inductor filter is chosen $L = 3$ mH.

The steady-state performance of MRAC is shown in Fig. 5.9, which includes output voltage, output voltage tracking error, output current, and adaptive control gains. As it can be seen in Fig. 5.9, the control gains converge to desired and constant values in the steady state. The output of the real plant follows the desired output of the reference plant very well. Results confirm

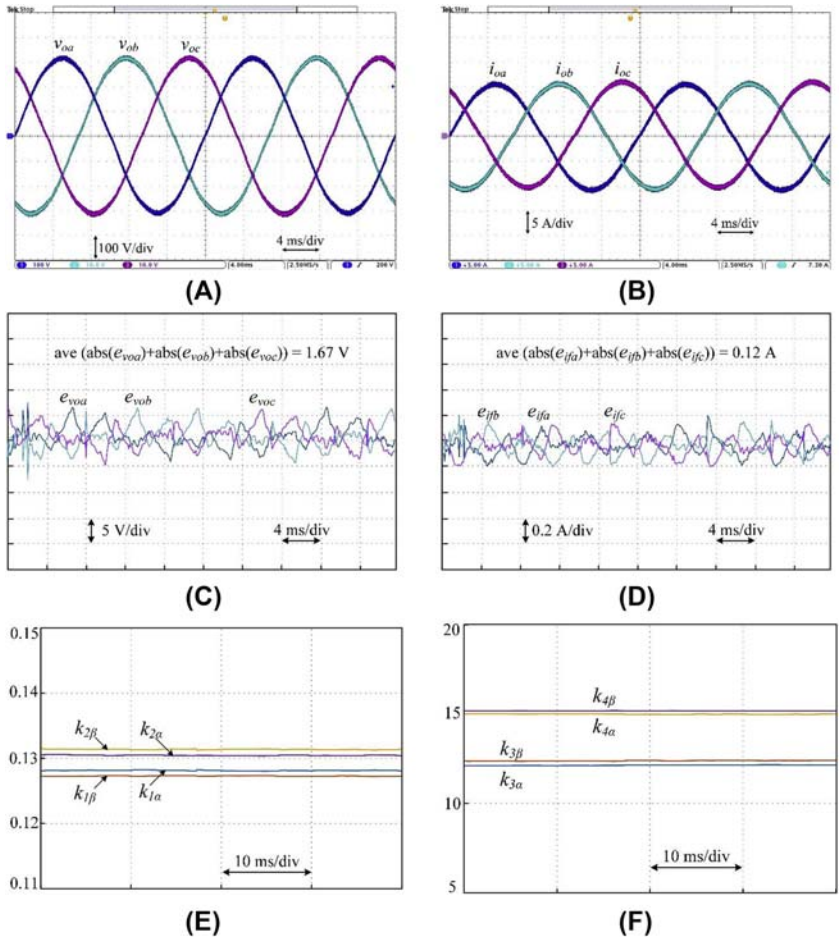

FIGURE 5.9 Obtained experimental results showing steady-state performance of model reference adaptive control under nominal load (5 kW). (A) Output voltage, (B) output current, (C) steady-state error of output voltage, (D) steady-state error of inductor current, (E) control gains (voltage outer loop), and (F) control gains (current inner loop).

This book belongs to Kitab Liaison (ocd1996@gmail.com) Copyright Elsevier 2023

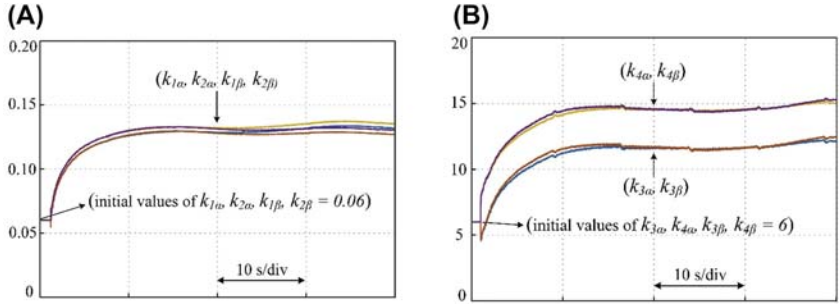

FIGURE 5.10 Obtained experimental results showing the start-up performance of model reference adaptive control. (A) Control gains convergence of voltage outer loop and (B) control gains convergence of current inner loop.

good steady-state performance of the control method under unknown system parameters. It is worth to note that these results have been obtained by considering more than 50% error of initial values of the controller gains, which is shown in Fig. 5.10. It shows a smooth and fast convergence of the control gains in the start-up process. Moreover, the transient performance of the adaptive MPC under a step change of resistive load (from zero power to nominal ones) is shown in Fig. 5.11, and it demonstrates a good transient response and disturbance rejection when using the MRAC.

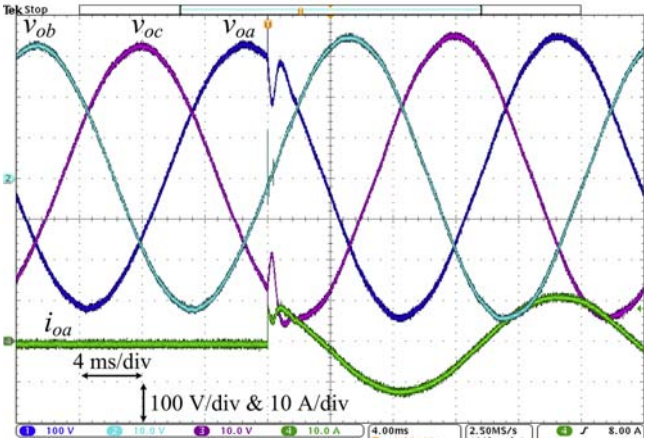

FIGURE 5.11 Obtained experimental results showing transient performance of model reference adaptive control under step change of load from zero to 5 kW.

This book belongs to Kitab Liaison (ocd1996@gmail.com) Copyright Elsevier 2023

5.6 Conclusion

Power electronic systems are subject to uncertain and time-variant parameters and also disturbances, e.g., due to aging, thermal effects, load changes, etc. Therefore, a fixed and linear control structure may not be able to present and give the desired performance under all conditions. Adaptive control methods have been proposed by power electronic researchers to overcome these issues. These control methods have the capability to work with unknown and uncertain parameters based on a rich mathematical background and using stability analysis. Thus, in this chapter, different types of adaptive control methods, including direct and IAC methods and also identification techniques (which is the essential part of adaptive control system), are presented. Moreover, their application on a three-phase UPS system is examined.

References

[1] K.J. Astrom, B. Wittenmark, Adaptive Control, second ed., Prentice-Hall, 1994.

[2] J.M. Espi, J. Castello, R. Garcia-Gil, G. Garcera, E. Figueres, An adaptive robust predictive current control for three-phase grid-connected inverters, IEEE Trans. Ind. Electron. 58 (8) (August 2011) 3537−3546.

[3] C. Xia, M. Wang, Z. Song, T. Liu, Robust model predictive current control of three-phase voltage source PWM rectifier with online disturbance observation, IEEE Trans. Ind. Inf. 8 (3) (August 2012) 459−471.

[4] K.J. Lee, B.G. Park, R.Y. Kim, D.S. Hyun, Robust predictive current controller based on a disturbance estimator in a three-phase grid-connected inverter, IEEE Trans. Power Electron. 27 (1) (2012) 276−283.

[5] Y.A.-R.I.A.I. Mohamed, M. A-Rahman, R. Seethapathy, Robust line-voltage sensorless control and synchronization of LCL -filtered distributed generation inverters for high power quality grid connection, IEEE Trans. Power Electron. 27 (1) (January 2012) 87−98.

[6] H. Gholami-Khesht, M. Monfared, Adaptive predictive voltage control of three-phase PWM-VSCs in UPS applications, in: 2016 International Siberian Conference on Control and Communications (SIBCON), 2016, pp. 1−6.

[7] Y.A.R.I. Mohamed, E.F. El-Saadany, Robust high bandwidth discrete-time predictive current control with predictive internal model - a unified approach for voltage-source PWM converters, IEEE Trans. Power Electron. 23 (1) (January 2008) 126−136.

[8] N. Hoffmann, F.W. Fuchs, Minimal invasive equivalent grid impedance estimation in inductive−resistive power networks using extended kalman filter, IEEE Trans. Power Electron. 29 (2) (Febuary 2014) 631−641.

[9] Y.A.-R.I.R.I. Mohamed, E.F. El-Saadany, Adaptive discrete-time grid-voltage sensorless interfacing scheme for grid-connected DG-inverters based on neural-network identification and deadbeat current regulation, IEEE Trans. Power Electron. 23 (1) (January 2008) 308−321.

[10] Y.A.R. Ibrahim Mohamed, et al., An improved deadbeat current control scheme with a novel adaptive self-tuning load model for a three-phase PWM voltage-source inverter, IEEE Trans. Ind. Electron. 54 (2) (April 2007) 747−759.

[11] Q. Liu, K. Hameyer, High-performance adaptive torque control for an IPMSM with real-time MTPA operation, IEEE Trans. Energy Convers. 32 (2) (June 2017) 571−581.

This book belongs to Kitab Liaison (ocd1996@gmail.com) Copyright Elsevier 2023

[12] Y.A. Zuniga-Ventura, D. Langarica-Cordoba, J. Leyva-Ramos, L.H. Diaz-Saldierna, V.M. Ramirez-Rivera, Adaptive backstepping control for a fuel cell/boost converter system, IEEE J. Emerging Sel. Top. Power Electron. 6 (2) (June 2018) 686−695.

[13] R.M. Milasi, A.F. Lynch, Y.W. Li, Adaptive vector control for voltage source converters, IET Control Theory Appl. 7 (8) (May 2013) 1110−1119.

[14] Z. Chen, J. Qiu, M. Jin, Adaptive finite-control-set model predictive current control for IPMSM drives with inductance variation, IET Electr. Power Appl. 11 (5) (May 2017) 874−884.

[15] J. Liu, W. Wu, H.S.-H. Chung, F. Blaabjerg, Disturbance observer-based adaptive current control with self-learning ability to improve the grid-injected current for LCL-filtered grid-connected inverter, IEEE Access 7 (July 2019) 105376−105390.

[16] A. Vidal, et al., A method for identification of the equivalent inductance and resistance in the plant model of current-controlled grid-tied converters, IEEE Trans. Power Electron. 30 (12) (December 2015) 7245−7261.

[17] A. Vidal, A.G. Yepes, F.D. Freijedo, J. Malvar, Ó López, J. Doval-Gandoy, A technique to estimate the equivalent loss resistance of grid-tied converters for current control analysis and design, IEEE Trans. Power Electron. 30 (3) (2015) 1747−1761.

[18] C. Zheng, T. Dragicevic, F. Blaabjerg, Current-sensorless finite-set model predictive control for LC-filtered voltage source inverters, IEEE Trans. Power Electron. 35 (1) (2019), 1−1.

[19] R.M. Milasi, A.F. Lynch, Y.W. Li, Adaptive control of a voltage source converter for power factor correction, IEEE Trans. Power Electron. 28 (10) (2013) 4767−4779.

[20] J.R. Massing, M. Stefanello, H.A. Grundling, H. Pinheiro, Adaptive current control for grid-connected converters with LCL-filter, in: 2009 35th Annual Conference of IEEE Industrial Electronics, vol. 59, 2009, pp. 166−172, no. 12.

[21] J.R. Massing, et al., Adaptive current control for grid-connected converters with LCL filter, IEEE Trans. Ind. Electron. 59 (12) (2012) 4681−4693.

[22] D. Xuan Ba, H. Yeom, J. Kim, J. Bae, Gain-adaptive robust backstepping position control of a BLDC motor system, IEEE/ASME Trans. Mechatron. 23 (5) (October 2018) 2470−2481.

[23] X. Fu, S. Li, Control of single-phase grid-connected converters with LCL filters using recurrent neural network and conventional control methods, IEEE Trans. Power Electron. 31 (7) (July 2016) 5354−5364.

[24] J. Kim, H. ho Choi, J.-W. Jung, MRAC-based voltage controller for three-phase CVCF inverters to attenuate parameter uncertainties under critical load conditions, IEEE Trans. Power Electron. 35 (1) (2019), 1−1.

[25] K. Shyu, M. Yang, Y. Chen, Y. Lin, Model reference adaptive control design for a shunt active-power-filter system, IEEE Trans. Ind. Electron. 55 (1) (January 2008) 97−106.

[26] T.D. Do, V.Q. Leu, Y.S. Choi, H.H. Choi, J.W. Jung, An adaptive voltage control strategy of three-phase inverter for stand-alone distributed generation systems, IEEE Trans. Ind. Electron. 60 (12) (2013) 5660−5672.

[27] T.S. Kwon, M.H. Shin, D.S. Hyun, Speed sensorless stator flux-oriented control of induction motor in the field weakening region using Luenberger observer, IEEE Trans. Power Electron. 20 (4) (July 2005) 864−869.

[28] P. Cortés, et al., Model predictive control of an inverter with output LC filter for UPS applications, IEEE Trans. Ind. Electron. 56 (6) (June 2009) 1875−1883.

[29] J.M. Espi Huerta, J. Castello-Moreno, J.R. Fischer, R. Garcia-Gil, A synchronous reference frame robust predictive current control for three-phase grid-connected inverters, IEEE Trans. Ind. Electron. 57 (3) (March 2010) 954−962.

This book belongs to Kitab Liaison (ocd1996@gmail.com) Copyright Elsevier 2023

[30] V. Miskovic, V. Blasko, T.M. Jahns, A.H.C.C. Smith, C. Romenesko, Observer-based active damping of LCL resonance in grid-connected voltage source converters, IEEE Trans. Ind. Appl. 50 (6) (November 2014) 3977−3985.

[31] H. Gholami-Khesht, M. Monfared, Deadbeat direct power control for grid connected inverters using a full-order observer, in: 2015 4th International Conference on Electric Power and Energy Conversion Systems, EPECS 2015, 2015, pp. 0−4.

[32] F. Auger, M. Hilairet, J.M. Guerrero, E. Monmasson, T. Orlowska-Kowalska, S. Katsura, Industrial applications of the kalman filter: a review, IEEE Trans. Ind. Electron. 60 (12) (2013) 5458−5471.

[33] R. Guzman, et al., Model based control for a three-phase shunt active power filter, IEEE Trans. Ind. Electron. 63 (7) (July 2016) 3998−4007.

[34] R. Guzman, L.G. De Vicuna, A. Camacho, J. Miret, J.M. Rey, Receding-horizon model-predictive control for a three-phase VSI with an LCL filter, IEEE Trans. Ind. Electron. 66 (9) (September 2019) 6671−6680.

[35] A.T. Nguyen, M.S. Rafaq, H.H. Choi, J.W. Jung, A model reference adaptive control based speed controller for a surface-mounted permanent magnet synchronous motor drive, IEEE Trans. Ind. Electron. 65 (12) (December 2018) 9399−9409.

This book belongs to Kitab Liaison (ocd1996@gmail.com) Copyright Elsevier 2023

This page intentionally left blank

This book belongs to Kitab Liaison (ocd1996@gmail.com)

Copyright Elsevier 2023

Chapter 6

Machine learning technique for low-frequency modulation techniques in power converters

Amirhossein Moeini[1], Morteza Dabbaghjamanesh[2], Tomislav Dragičević[3], Jonathan W. Kimball[1], Jie Zhang[2]

[1]*Electrical and Computer Engineering Department, Missouri University of Science and Technology, Rolla, MO, United States;* [2]*Department of Mechanical Engineering, The University of Texas at Dallas, Richardson, TX, United States;* [3]*Department of Electrical Engineering, Technical University of Denmark, Lyngby, Denmark*

6.1 Introduction

Nowadays power systems have many new challenges due to the fast growth of electric vehicle charging stations, renewable energy sources, smart grid technologies, and other power electronic−based loads [1−8]. Active power filters (APFs) have been used more and more for compensating the harmonics of nonlinear loads in power systems at the point of common coupling (PCC) [9]. Moreover, both reactive and active power of the power grid at the PCC can be managed by using an APF [9]. Different AC−DC converters have been proposed in the literature for APF applications. Between all available topology, for high-power applications, multilevel converters are growing in popularity due to their low stress on the semiconductor switches, low total harmonic distortion, and modular structure [10,11].

Based on the switching frequency of the converter, the modulation techniques of multilevel converters can be categorized. High-switching frequency modulation techniques such as space vector modulation (SVM) and phase shift−pulse width modulation (PS-PWM) are commonly used due to real-time control on the fundamental and harmonics of the converter and their simple implementation [12]. However, the switching losses of the high-switching frequency modulation techniques are high and undesirable. Moreover, the base-band and side-band harmonics of high-switching frequency modulation techniques are uncontrollable, which are undesirable for the power quality

Control of Power Electronic Converters and Systems. https://doi.org/10.1016/B978-0-12-819432-4.00009-3
Copyright © 2021 Elsevier Ltd. All rights reserved.

This book belongs to Kitab Liaison (ocd1996@gmail.com)
Copyright Elsevier 2023

requirements of grid-tied converters. On the other hand, low-frequency modulation techniques, e.g., selective harmonic elimination-PWM (SHE-PWM) [13,14], selective harmonic mitigation-PWM (SHM-PWM) [15,16], and selective harmonic current mitigation-PWM (SHCM-PWM) [9,10,17–19], have low switching losses. Contrarily, implementation of these techniques requires huge memory storage to save all possible solutions. By solving transcendental (trigonometric) Fourier series equations, these offline solutions are often obtained.

Different techniques (such as mathematical approaches and linearization techniques) have been proposed in the literature to implement the low-frequency modulation techniques in real time [20]. Contrarily, they are difficult to be implemented for a high-switching frequency. For example, in Ref. [20], an approach was proposed to linearize the trigonometric equations of a low-frequency modulation technique to control harmonic phases and magnitudes of a cascaded H-bridge (CHB) converter. However, the number of harmonics that can be controlled by using [20] is limited.

Artificial intelligence, especially machine learning, has become popular in different applications such as health science, meteorology, military, and education [21]. Machine learning can be used for regression or classification by using different training techniques [21]. One of the most commonly used machine learning techniques is artificial neural network (ANN) [22–30]. In ANN, the learning behavior of the human brain is modeled by using mathematical equations. The ANN has also been used for the grid-tied converter low-frequency modulation technique in Refs. [22,31], to utilize the DC-link voltages of the grid-tied converter for controlling the switching angles of the SHE-PWM. Contrarily, existing work in the literature have not extensively investigated how to apply ANN for a real-time implementation of the low-frequency modulation technique with a high number of switching transitions, how to generate training dataset, or how to control both magnitudes and phases of the voltage harmonics of grid-tied converters for the APF application.

As discussed in Ref. [9], the quarter-wave symmetric modulation techniques such as SHE-PWM, SHCM-PWM, and SHM-PWM cannot control both magnitude and phase of the voltage harmonic of the grid-tied converters. To solve this issue, when the low-frequency modulation technique is applied for the grid-tied converter, a half-wave symmetric modulation technique, e.g., asymmetric selective harmonic current mitigation-PWM (ASHCM-PWM) [18] can be used as discussed in Ref. [9]. As a result, when the low-frequency modulation technique is applied for the grid-tied converter, the ASHCM-PWM is the only option for controlling the APF current harmonics. The proposed technique has not been investigated so far by using ASHCM-PWM technique for the grid-tied converter. In this chapter, an asymmetric selective harmonic current mitigation-PWM (ASHCM-PWM) real-time implementation is investigated by using the ANN technique. As it will be shown in this chapter, the conventional lookup tables can be replaced by a trained ANN for controlling harmonics and the fundamental of the APF. Furthermore, when

This book belongs to Kitab Liaison (ocd1996@gmail.com) Copyright Elsevier 2023

nonlinear loads are connected at the PCC, the current harmonic requirements of the IEEE Std. 519 [32] can be met by using the proposed technique at the PCC. To reach this goal, a 3-cell 7-level CHB grid-tied converter is employed in both simulations and experiments of this chapter.

The remaining of this chapter is organized as follows. Section 6.2 briefly discusses the APFs fundamental principles. Section 6.3 explains the proposed ANN technique for the low-frequency modulation technique. The proposed ANN technique simulation and experimental results are shown and discussed in Section 6.4. Finally, Section 6.5 concludes the work.

6.2 Cascaded H-bridge active power filter configuration

Fig. 6.1 shows a CHB converter configuration for the APF application. As shown in Fig. 6.1, the CHB converter N cells are connected to the grid by using the coupling inductance (L_F). The nonlinear loads are also connected to the PCC and inject the nonlinear load current ($i(_{NLL})$). The converter generates the current ($i(_{ac-CHB})$) as shown in Fig. 6.1 to compensate for the nonlinear load current. By applying KCL,

$$i_{in}(t) = i_{(ac-CHB)}(t) + i_{(NLL)}(t). \tag{6.1}$$

where i_{in} is the injected current to the power grid. R_{grid} and L_{grid} are the resistance and inductance of the power grid, respectively. In this chapter, the power grid parameters are ignored. $v(_{ac-Grid})(t)$, $v(_{ac-CHB})(t)$, and $v(_{pcc})(t)$ are the AC voltages of the grid, CHB, and PCC in Fig. 6.1, respectively.

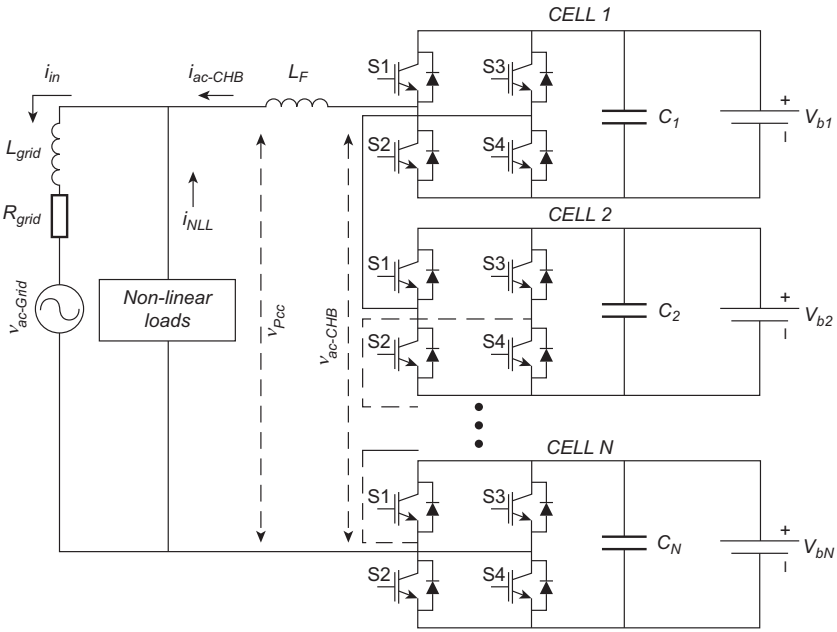

FIGURE 6.1 Configuration of the CHB for APF application.

This book belongs to Kitab Liaison (ocd1996@gmail.com) Copyright Elsevier 2023

6.3 ANN for the asymmetric selective harmonic current mitigation-PWM

One of the key challenges in low-frequency modulation techniques is to find real-time solutions of the Fourier equations for different phases and magnitudes of fundamental and harmonics. The proposed ANN-based technique can be used to reach this goal. The CHB voltage Fourier series equations in Fig. 6.2, with half-wave symmetry for the CHB voltage, is

$$\begin{cases} v_{(ac-CHB)}(t) = \sum_{h=1}^{\infty}(a_h \cos(h\omega t) + b_h \sin(h\omega t)) \\ a_h = \dfrac{2V_{dc}}{h\pi}\begin{pmatrix} -\sin(h\theta_{11}) + \sin(h\theta_{12}) - \cdots - \sin(h\theta_{in1}) \\ +\sin(h\theta_{i(n_i+1)}) - \cdots + \sin(h\theta_{1(2n1)}) \end{pmatrix} \\ b_h = \dfrac{2V_{dc}}{h\pi}\begin{pmatrix} \cos(h\theta_{11}) - \cos(h\theta_{12}) + \cdots + \cos(h\theta_{ini}) \\ -\cos(h\theta_{i(n_i+1)}) + \cdots - \cos(h\theta_{1(2n1)}) \end{pmatrix} \\ 0 \le \theta_{11} \le \theta_{12} \le \cdots \\ \ldots \le \theta_{in_i} \le \theta_{i(n_i+1)} \le \ldots \theta_{1(2n_1)} \le \pi \end{cases} \tag{6.2}$$

where b_h and a_h are the h_{th} order sine and cosine components of the CHB voltage, respectively; V_{dc} is the DC-link voltage of the converter ($V_{dc} = V_{b1} = V_{b2} = \ldots = V_{bN}$); θ_{jk} is the jth cell kth switching transition of the converter. The KVL equation of Fig. 6.1, when the effects of the impedance of the grid and the resistance of L_F are ignored, is written as

$$v_{(ac-CHB)}(t) = v_{(pcc)}(t) + L_F \frac{di_{(ac-CHB)}}{dt}. \tag{6.3}$$

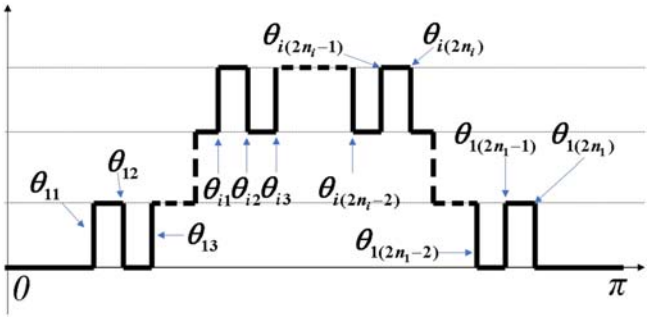

FIGURE 6.2 The time-domain waveform of the active power filter generating the voltage $v_{(ac-CHB)}(t)$.

This book belongs to Kitab Liaison (ocd1996@gmail.com) Copyright Elsevier 2023

TABLE 6.1 Odd order current harmonic requirements of the IEEE Std. 519 [32].

Harmonic order	Current limit (%)
$1 < h < 11$	4
$11 < h < 17$	2
$17 \leq h < 23$	1.5
$23 \leq h < 35$	0.6
$35 \leq h < 50$	0.3
TDD	5

The IEEE Std. 519 [32] requirements are then used to impose restrictions on the frequency-domain components of I_{in}. In ASHCM-PWM, where C_h is the hth order current harmonic requirement of IEEE Std. 519 [32] as shown in Table 6.1, the hard equalities of SHE-PWM are replaced by inequalities given in (6.4), when $\frac{I_L}{I_{sc}} \leq 20$. I_L is the maximum demand load at the PCC. I_{sc} is the converter short circuit current at the PCC. K is the switching transitions total number of the ASHCM-PWM.

In order to meet the current harmonic requirements, the ASHCM-PWM technique must generate the CHB voltage. In conventional approaches, off-line solutions of (6.4) are obtained for a wide range of phases and magnitudes for the harmonics and fundamental, which requires an impractically large memory for embedded implementation. In the present work, an ANN structure is used instead. In order to meet the current harmonic requirements listed in Table 6.1, the injected current harmonic $I_{ac-CHB-h}$ should have equal magnitude as, and 180 degrees phase shift from, I_{NLL-h}. When the magnitude is changed from 0 to $|I_{NLL-h}|$ and the phase is changed from 0 to 360 degrees, a low number of switching angles in the ASHCM-PWM technique cannot mitigate the h_{th} nonlinear load current harmonic. Therefore, the maximum circle whole range of nonlinear load current harmonics can be divided into several sections (24 sections in Fig. 6.3). This helps to have all solutions that are close to each other in a same section of Fig. 6.3. This helps the proposed learning-based technique to better divide all solutions (training data) based on the section into which each order of harmonics is placed.

This book belongs to Kitab Liaison (ocd1996@gmail.com) Copyright Elsevier 2023

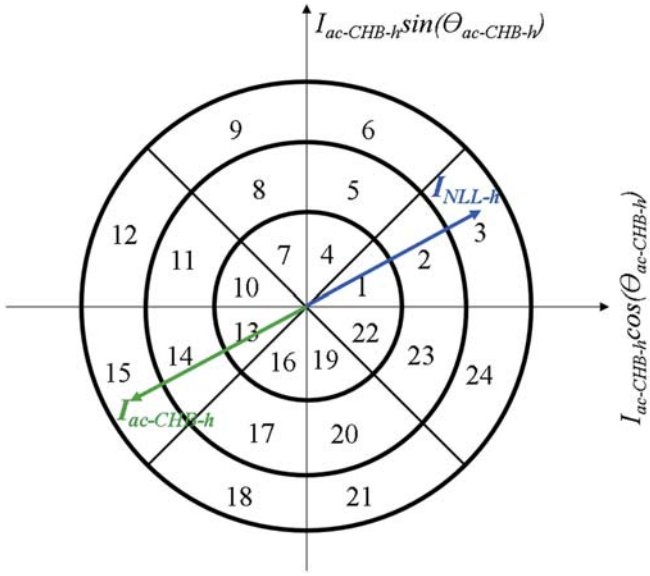

FIGURE 6.3 The proposed ANN technique for controlling current harmonics of APF.

$$
\begin{cases}
a_1 = \dfrac{2V_{dc}}{\pi}\left(-\sin(\theta_{11}) + \sin(\theta_{12}) - \ldots + \sin(\theta_K)\right), \\
b_1 = \dfrac{2V_{dc}}{\pi}\left(\cos(\theta_{11}) - \cos(\theta_{12}) + \ldots - \cos(\theta_K)\right), \\
\left|\dfrac{b_1 + ja_1 - V_{(pcc-1)}\left(\cos\left(\angle V_{(pcc-1)}\right) + j\sin\left(\angle V_{(pcc-1)}\right)\right)}{j\omega L_F} \ldots + I_{(NLL-1)}\left(\cos\left(\angle I_{(NLL-1)}\right) + j\sin\left(\angle I_{(NLL-1)}\right)\right) \ldots - I_{(in-1)}\left(\cos\left(\angle I_{(in-1)}\right) + j\sin\left(\angle I_{(in-1)}\right)\right)\right| \le \varepsilon_1, \\
\left|\dfrac{I_{(in-3)}}{I_L}\right| = \left|\dfrac{b_3 + ja_3 - V_{(pcc-3)}\left(\cos\left(\angle V_{(pcc-3)}\right) + j\sin\left(\angle V_{(pcc-3)}\right)\right)}{(j3\omega L_F I_L)} \ldots + I_{NLL-3}\left(\cos\theta_{NLL-3} + j\sin\theta_{NLL-3}\right)\right| \le C_3, \\
\left|\dfrac{I_{(in-5)}}{I_L}\right| = \left|\dfrac{b_5 + ja_5 - V_{(pcc-5)}\left(\cos\left(\angle V_{(pcc-5)}\right) + j\sin\left(\angle V_{(pcc-5)}\right)\right)}{(j5\omega L_F I_L)} \ldots + I_{NLL-5}\left(\cos\theta_{NLL-5} + j\sin\theta_{NLL-5}\right)\right| \le C_5, \\
\left|\dfrac{I_{(in-h)}}{I_L}\right| = \left|\dfrac{b_h + ja_h - V_{(pcc-h)}\left(\cos\left(\angle V_{(pcc-h)}\right) + j\sin\left(\angle V_{(pcc-h)}\right)\right)}{(jh\omega L_F I_L)} \ldots + I_{NLL-h}\left(\cos\theta_{NLL-h} + j\sin\theta_{NLL-h}\right)\right| \le C_h,
\end{cases}
\tag{6.4}
$$

This book belongs to Kitab Liaison (ocd1996@gmail.com)
Copyright Elsevier 2023

In Fig. 6.3, there are 24 sections for different magnitudes and phases of I_{NLL-h}. Using a high number of sections can improve the ANN performance to meet the power quality standards in the ASHCM-PWM technique. Contrarily, this can also significantly increase the size of the dataset. Thus, the proposed technique computational burden is significantly increased. In this technique, the total demand distortion (TDD) is not controlled and just the current harmonics are controlled, given by

$$\mathrm{TDD} = \sqrt{\left(\frac{I_{in-3}}{I_L}\right)^2 + \left(\frac{I_{in-5}}{I_L}\right)^2 + \cdots + \left(\frac{I_{in-h}}{I_L}\right)^2} \tag{6.5}$$

However, controlling the individual harmonics will generally achieve the desired TDD as well.

In Fig. 6.3, the $I_{ac-CHB-h}$ can be determined as

$$\begin{cases} I_{(ac-CHB-1)} = \dfrac{b_1 + ja_1 - V_{(pcc-1)}\left(\cos\left(\angle V_{(pcc-1)}\right) + j\sin\left(\angle V_{(pcc-1)}\right)\right)}{(j\omega L_F)}, \\ I_{(ac-CHB-3)} = \dfrac{b_3 + ja_3 - V_{(pcc-3)}\left(\cos\left(\angle V_{(pcc-3)}\right) + j\sin\left(\angle V_{(pcc-3)}\right)\right)}{(j3\omega L_F)}, \\ I_{(ac-CHB-5)} = \dfrac{b_5 + ja_5 - V_{(pcc-5)}\left(\cos\left(\angle V_{(pcc-5)}\right) + j\sin\left(\angle V_{(pcc-5)}\right)\right)}{(j5\omega L_F)} \\ \cdots \\ I_{(ac-CHB-h)} = \dfrac{b_h + ja_h - V_{(pcc-h)}\left(\cos\left(\angle V_{(pcc-h)}\right) + j\sin\left(\angle V_{(pcc-h)}\right)\right)}{(jh\omega L_F)} \end{cases} \tag{6.6}$$

The solutions of (6.6) are solved for various phases and magnitudes of V_{PCC-h}. By checking the phase and magnitude of (6.6), one of the sectors in Fig. 6.3 is selected. In this paper, it is assumed that the PCC voltage harmonic magnitudes are close to zero. Contrarily, the PCC voltage harmonics can be obtained from

$$\begin{aligned} & sL_F V_{(ac-Grid)}(s) \\ & V_{(PCC)}(s) = \frac{+Z_{Grid}(s)\left(V_{(ac-CHB)}(s) + sL_F I_{NLL}(s)\right)}{(sL_F + Z_{Grid}(s))}, \end{aligned} \tag{6.7}$$

where $Z_{Grid}(s)$ is the grid impedance. From (6.7), a high value of $Z_{Grid}(s)$ increases the $V(_{ac-CHB})$ effect on the V_{PCC}. However, a low value of $Z_{Grid}(s)$ increases the effect of $V(_{ac-Grid})(s)$ on the $V_{PCC}(s)$. From (6.6) and (6.7), $I(_{ac-CHB})$ is a function of $V(_{ac-CHB})$ and V_{PCC}. Furthermore, V_{PCC} is also function of $V(_{ac-CHB})$. Thus, changing the $V(_{ac-CHB})$ affects both V_{PCC}

This book belongs to Kitab Liaison (ocd1996@gmail.com)
Copyright Elsevier 2023

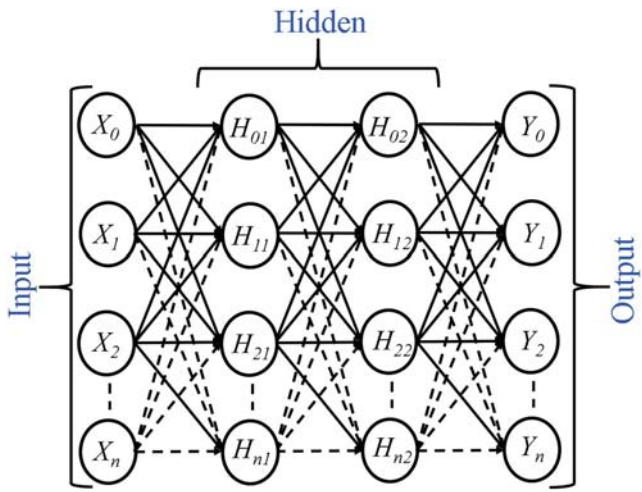

FIGURE 6.4 The ANN block diagram to be applied in the active power filter.

and $I(_{ac-CHB})$. This can complicate the controller design when the grid has an impedance, and is beyond the scope of the present work. Eq. (6.6) data for various switching angles of the CHB converter are obtained.

A general block diagram of the ANN [21] is shown in Fig. 6.4. As it can be seen, three main layers are used for the ANN technique: an input layer (X), an output layer (Y), and two hidden layers (H). Several nodes are used as shown in Fig. 6.4. Among consecutive layers (i (previous layer) and j (current layer)), a line which has a weight (ω_{ij}) is used. Each node output can be calculated using

$$O_j^l = \sigma_j^l\left(\sum_{i=0}^{n_{l-1}}\left(O_i^{l-1}\omega_{ij}\right) + b_j^l\right) \tag{6.8}$$

where O_j^l is the output of the lth layer jth node, O_j^{l-1} is the output of the $(l-1)$th layer jth node, O_j^l is the jth node activation function in the lth layer, b_j^l is the bias of the jth node in the lth layer of the ANN, and n_{l-1} is the number of nodes in the $(l-1)$th layer.

In the proposed method, values of θ_{11}, θ_{12}, …, and θ_K that satisfy (6.4) are determined for a PCC voltage harmonic magnitudes and phases range. Given the large number of variables and the range of inputs, the search space is very large. Thus, the technique given in Algorithm 6.1 is used to randomly sample the search space.

This book belongs to Kitab Liaison (ocd1996@gmail.com) Copyright Elsevier 2023

Algorithm 6.1 is used to generate random training data. First, based on the accuracy that is required for the harmonics and the available computational power, a time step is chosen. Switching angles that cover the whole range of search space are produced using random numbers. For the present work, the time step is set to 8 degrees; a smaller time step corresponds to an increase in the dataset size, an increase in the time required for training, and an increase in accuracy. The proposed algorithm first sorts the angles produced. Next, the angles are checked to all lie within the range of [0 degree; 180 degrees] to enforce half-wave symmetry. By using (6.4) and the obtained switching angles, current harmonics are checked to determine whether they meet the IEEE Std. 519 limits [32]. Variables O_3, O_5, …, O_h, O_{TDD} are logical indicators of whether the results satisfy the given limits; additional constraints can be included for other power quality standards. Finally, O_1 assigns the fundamental voltage (b_1).

6.4 The proposed technique simulation and experimental results

To validate the advantages and effectiveness of the proposed ASHCM-PWM with the ANN technique, simulation and experimental results are obtained for a 3-cell 7-level CHB converter. The parameters (i.e., the circuit parameters and the number of hidden layers of the ANN) of the grid-tied converter during the simulations and experiments are shown in Tables 6.2 and 6.3. The open-source KERAS [33] software is used to train the ANN, which is written in Python. The main objective in both simulations and experiments is to prove that the ANN technique can control harmonic phases and magnitudes by using the ASHCM-PWM technique.

6.4.1 Simulation results

In addition to the parameters that are mentioned in Table 6.2, a diode bridge connected to a parallel combination of a 20 resistor and a 50 μF capacitor is

TABLE 6.2 The number of nodes in ANN hidden layers.

Technique	1st hid.	2nd hid.	3rd hid.	4th hid.
ANN	50	50	50	50

This book belongs to Kitab Liaison (ocd1996@gmail.com) Copyright Elsevier 2023

TABLE 6.3 Multilevel converter parameters in simulations and experiments.

Parameter	Symbol	Value
AC grid voltage	$V_{ac-Grid-1}$	110 V
Fundamental frequency	F	60 Hz
Coupling inductance	L_F	0.49 pu
DC-link voltage	V_{dc}	65 V
Maximum output demand current	I_L	20 A
Number of cells in CHB	i	3
Number of switching transitions in each cell	n	1
Number of switching transitions	K	3
Number of mitigated harmonics	h	49
Decoupling DC capacitance	C	600 μF

used as a nonlinear load in the first simulation. Grid impedance is neglected here so the rectifier does not affect the PCC voltage. MATLAB/Simulink[1] is used to simulate the nonlinear load combination and the CHB grid-tied converter. Fig. 6.5A illustrates the time-domain waveforms of $i_{in}(t)$, $v_{(ac-CHB)}(t)$, $v_{(ac-Grid)}(t)$, and $i_{NLL}(t)$. The ANN technique increases the $i_{in}(t)$ fundamental current from 7:77 to 19:2 A at the PCC. Fig. 6.5B shows the current harmonic spectra of the nonlinear load ($i_{NLL}(t)$), which cannot meet the current harmonic requirements (the red (gray in print version) line in Fig. 6.5B) of the IEEE Std. 519 [32] for the third and fifth harmonics. Moreover, the nonlinear load current TDD cannot meet the 5% limit of the IEEE Std. 519. Fig. 6.5C shows the current harmonic spectra of $i_{in}(t)$ at the PCC, when the nonlinear load ($i_{NLL}(t)$) is injected to the grid. Now, the harmonics do meet the requirements due to the compensation provided by the CHB. The ANN achieves harmonic control with only six switching transitions per half-period.

1. MATLAB and Simulink are registered trademarks of The MathWorks, Inc.

This book belongs to Kitab Liaison (ocd1996@gmail.com) Copyright Elsevier 2023

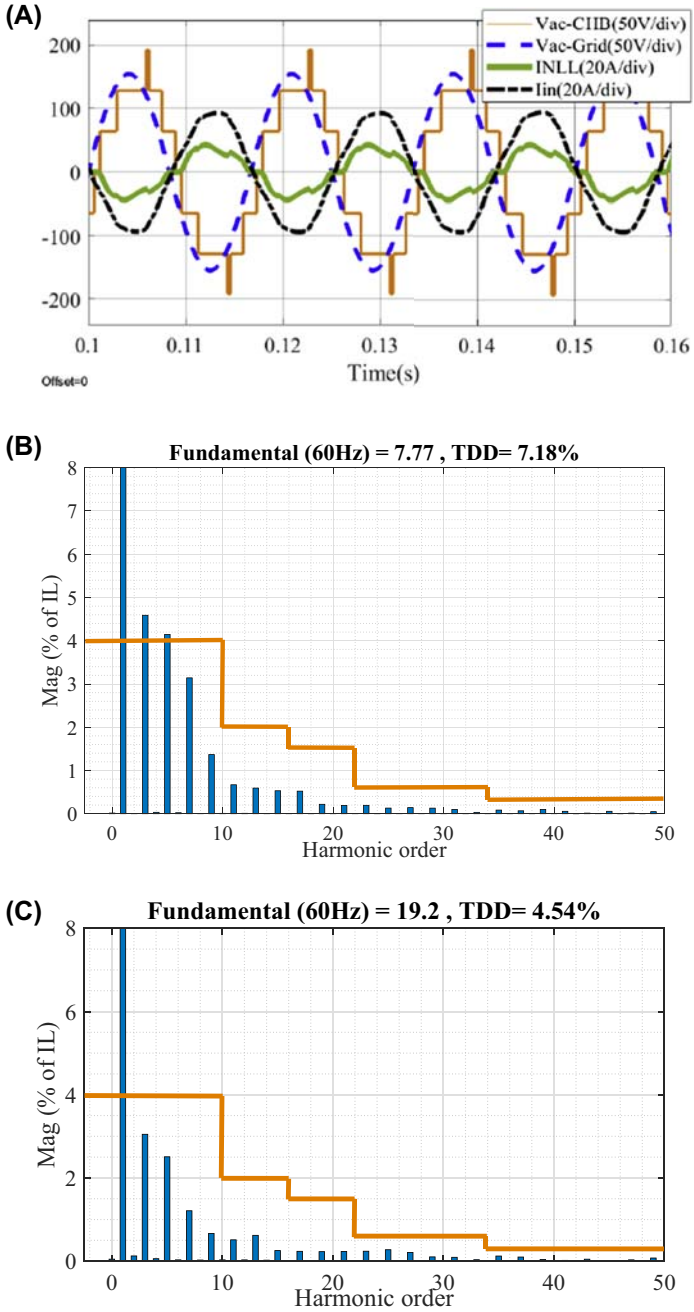

FIGURE 6.5 Simulation results using ASHCM-PWM technique for the grid-tied CHB converter with a nonlinear load, (A) time-domain waveforms of the $v(_{ac-CHB})(t)$, $v(_{ac-Grid})(t)$, $i_{in}(t)$, and $i(_{NLL})(t)$; (B) current harmonic spectra of $i(_{NLL})(t)$; (C) current harmonic spectra of $i_{in}(t)$.

This book belongs to Kitab Liaison (ocd1996@gmail.com)
Copyright Elsevier 2023

Algorithm 6.1. (*The proposed ASHCM-PWM algorithm with ANN.*)

Algorithm 1 The proposed ASHCM-PWM algorithm with ANN

```
for sw_11 = 1, 8, 16, ..., 180 − 8k do
    for sw_12 = sw_11, sw_11 + 8, sw_11 + 16, ..., 172 − 8k do
        ...
        for sw_in_i = sw_in_(i−1), sw_in_i = sw_in_(i−1) + 8, sw_in_i = sw_in_(i−1) + 16, ..., sw_in_i = 180 do
            θ_11 = 8 * random number + sw_11
            ...
            θ_in_i = 8 * random number + sw_in_i
            sort(θ_11, θ_12, ..., θ_in_i)
            for j=1:number of cells of converter do
                for p=1:number of switching in jth cell do
                    if θ_jp ≤ 180^o then
                        θ_jp = 180^o
                    end
                end
            end
            if (|I_in−3 / I_L| ≤ C_3) then
                O_3=1
            else
                O_3=0
            end
            ...
            if (|I_in−h / I_L| ≤ C_h) then
                O_h=1
            else
                O_h=0
            end
            if (|TDD| > 5%) then
                O_TDD=0
            else
                O_TDD=1
            end
            O_1 = b_1
        end
    end
end
```

This book belongs to Kitab Liaison (ocd1996@gmail.com)

Copyright Elsevier 2023

Fig. 6.6 shows the ANN technique second simulation result when the modulation index of the converter with the ASHCM-PWM is 2.45. The second simulation result objective is to prove that the ANN can control the current harmonic for the ASHCM-PWM without injecting the nonlinear load to the grid. After training the ANN technique, the proposed technique switching angles are 3, 26, 48, 121, 147, and 165 degrees. The grid-tied converter current magnitude is 12:9 A with a phase of 104 degrees. Thus, the proposed technique can be applied to the grid-tied converter for any reactive and active power. Fig. 6.6A shows the time-domain waveforms of $i_{in}(t)$, $v_{ac-CHB}(t)$, and

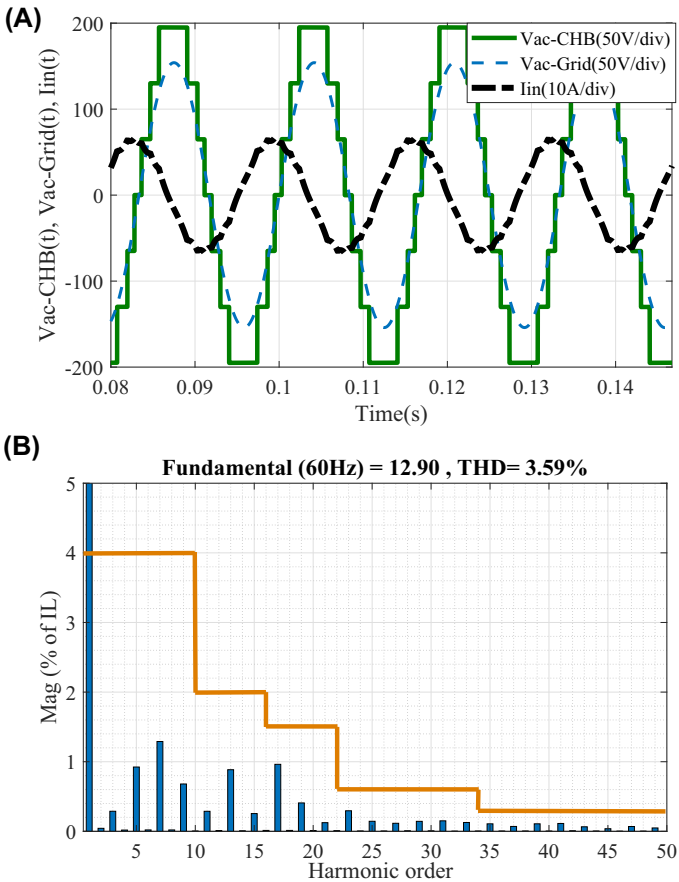

FIGURE 6.6 ASHCM-PWM technique simulation results for the grid-tied CHB converter without the nonlinear load, (A) time-domain waveforms of $v(_{ac-CHB})(t)$, $v(_{ac-Grid})(t)$, and $i_{in}(t)$, (B) current harmonic spectra of $i(_{in})(t)$.

This book belongs to Kitab Liaison (ocd1996@gmail.com)
Copyright Elsevier 2023

$v_{ac-Grid}(t)$. In this figure, a sinusoidal waveform is generated for the AC current ($i_{in}(t)$) by using the low-frequency modulation technique. Moreover, there is no variation in $v_{ac-CHB}(t)$ time-domain waveform due to neglecting the parasitic resistance at the DC link. On the contrary, the proposed technique can meet the power quality standard, when there is a parasitic resistance at the DC link of the CHB converter (internal resistance of the battery) as proven in Ref. [34]. The AC current time-domain waveform (($i_{in}(t)$)) is shown in Fig. 6.6B with the requirements of the IEEE Std. 519 indicated. From this figure, the proposed ANN can control all 25 odd low-order current harmonics. Also, as shown in Fig. 6.6B, the TDD 5% limit in IEEE Std. 519 can be met by using the ANN.

6.4.2 Experimental results

An ANN technique is further validated with experimental results using the same parameters, a 3-cell 7-level CHB converter. The second simulation in Fig. 6.6 is experimentally repeated using the same parameters. The grid-tied CHB converter hardware prototype that is used in experiments is shown in Fig. 6.7. Texas Instruments TMS320F28335 is used for applying the switching angles to the CHB converter. In each H-bridge of the CHB converter, an intelligent power module (IPM) (rated 30 A and 600 V) that uses a 3-leg IGBT is used as shown in Fig. 6.7. The block diagram in Fig. 6.8 illustrates the proposed technique implementation during the experiments, which is an open-loop control that applies the ASHCM-PWM switching angles technique with the ANN. The grid impedance is small and may be ignored as shown in Fig. 6.8. A phase-locked loop is used in this figure to detect the phase and frequency of the grid voltage. Moreover, θ_{CHB} is the CHB converter initial phase. In both simulation and experimental results,

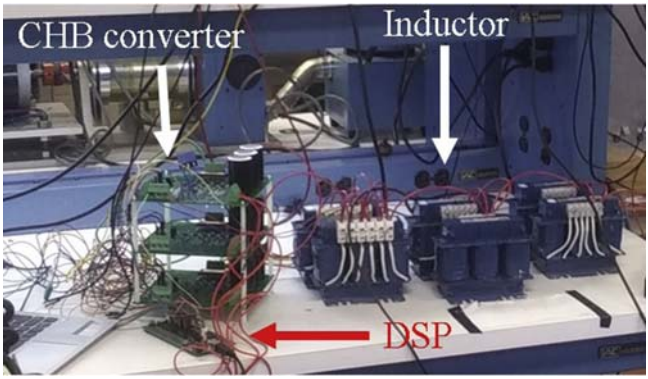

FIGURE 6.7 3-cell grid-tied CHB converter hardware prototype.

This book belongs to Kitab Liaison (ocd1996@gmail.com) Copyright Elsevier 2023

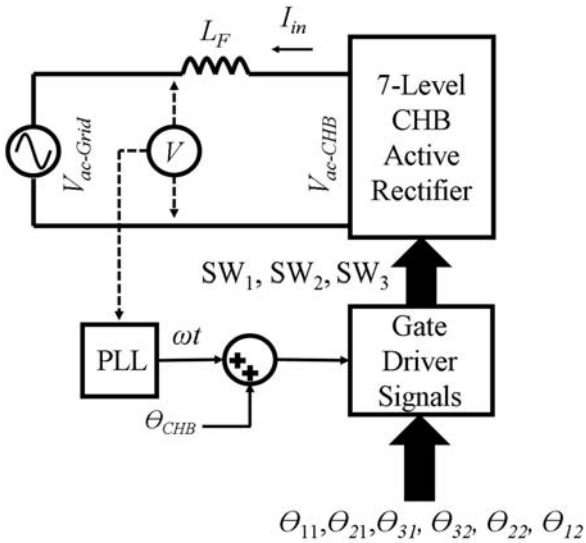

FIGURE 6.8 Grid-tied converter block diagram during the experiments and simulations.

the θ_{CHB} is assumed to be 0 degree. The optimal solutions (switching angles) (θ_{11}, θ_{21}, θ_{31}, θ_{32}, θ_{22}, θ_{12}) in Fig. 6.8 from the ANN are used in the grid-tied CHB converter. The switching transition values that are employed in the experiment are the same as in the second simulation result shown in Fig. 6.6. SW_1; SW_2; and; SW_3 are the converter switchings for the first, second, and third H-bridge cells, respectively. The converter has the lowest possible switching frequency, equal to the line frequency, 60 Hz. As a result, the proposed technique has the lowest possible switching losses for hard switching AC−DC converters.

The experimental results of the proposed ANN technique for ASHCM-PWM are shown in Fig. 6.9, when the CHB converter modulation index is 2.45, the same as the simulation result in Fig. 6.6. The grid-tied converter AC current is 13:4 A with a phase of 102. The $v_{ac-CHB}(t)$, $v_{ac-Grid}(t)$, and $i_{in}(t)$ time-domain waveforms are shown in Fig. 6.9A. The AC input current ($i_{in}(t)$) has a pure sinusoidal current waveform similar to the simulation result. The experimental current harmonic spectrum is shown in Fig. 6.9B. The IEEE Std. 519 [32] current requirements are shown by the red (gray in print version) line in Fig. 6.9B. As illustrated in the experimental results, all low-order current harmonics meet the IEEE Std. 519 requirements at the PCC. Moreover, using the proposed ANN technique for the ASHCM-PWM in the experiment in Fig. 6.9B, the 5% limit specified in the IEEE Std. 519 for the TDD is met.

This book belongs to Kitab Liaison (ocd1996@gmail.com) Copyright Elsevier 2023

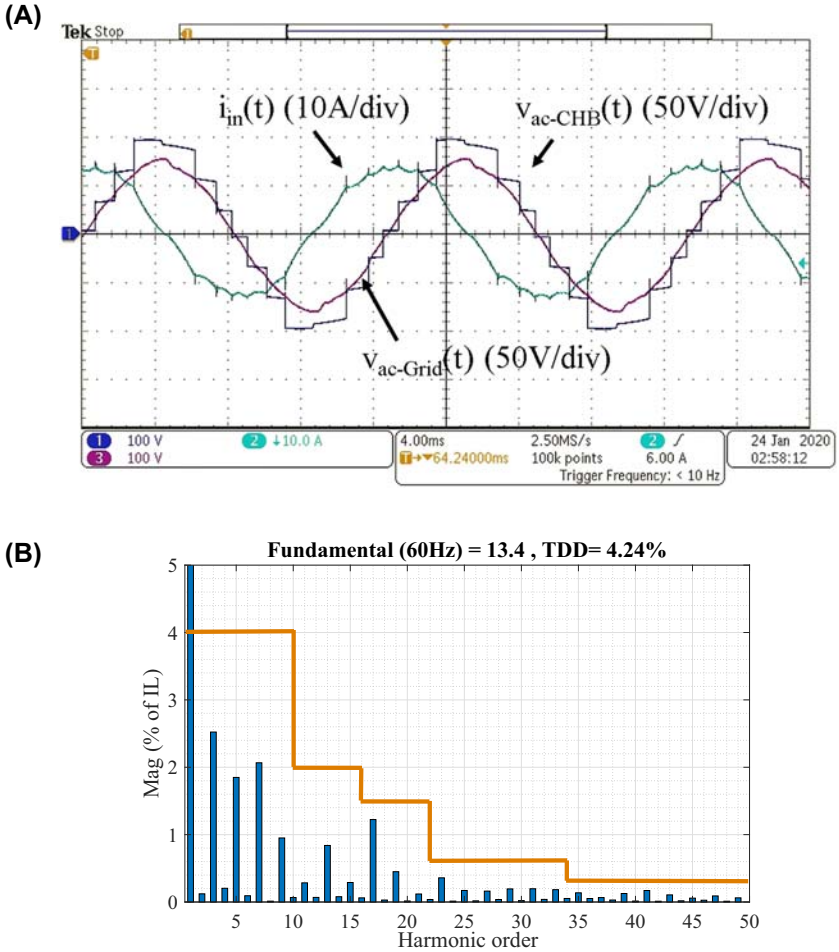

FIGURE 6.9 ASHCM-PWM technique experimental results for the grid-tied CHB converter, (A) time-domain waveforms of $v(_{ac-CHB})(t)$, $v(_{ac-Grid})(t)$, and $i_{in}(t)$, (B) current harmonic spectra of $i(_{in})(t)$.

6.5 Conclusion

In this chapter, an ANN technique to implement asymmetric selective harmonic current mitigation-PWM was proposed to control the current harmonics at the PCC in order to meet the power quality standards. The proposed technique does not need to save all phases and magnitudes of the fundamental and harmonics of the APF application AC current. The low-frequency ASHCM-PWM technique was implemented in both simulations and experiments to prove the advantages of the proposed technique for controlling the APF

This book belongs to Kitab Liaison (ocd1996@gmail.com) Copyright Elsevier 2023

current harmonic. To reach this goal, a technique was proposed to categorize the voltage harmonic vectors of the grid-tied converter. As demonstrated in the simulation and experimental results, the proposed technique that uses an ANN could meet the power quality standard low-order current harmonics such as the IEEE Std. 519. Furthermore, in this chapter, a guideline for generating the ANN technique training data was proposed. Using the guidelines in this chapter, the ANN could completely search the solutions whole search space of the low-frequency modulation techniques.

References

[1] M. Dabbaghjamanesh, A. Kavousi-Fard, Z. Dong, A novel distributed cloud-fog based framework for energy management of networked microgrids, IEEE Trans. Power Syst. 35 (4) (2020) 2847−2862.

[2] M. Dabbaghjamanesh, A. Kavousi-Fard, S. Mehraeen, J. Zhang, Z.Y. Dong, Sensitivity analysis of renewable energy integration on stochastic energy management of automated reconfigurable hybrid ac−dc microgrid considering DLR security constraint, IEEE Trans. Industr. Inform. 16 (1) (January 2020) 120−131.

[3] M. Dabbaghjamanesh, B. Wang, A. Kavousi-Fard, S. Mehraeen, N.D. Hatziargyriou, D. Trakas, F. Ferdowsi, A novel two-stage multi-layer constrained spectral clustering strategy for intentional islanding of power grids, IEEE Trans. Power Deliv. 35 (2) (2019) 560−570.

[4] M. Dabbaghjamanesh, A. Kavousi-Fard, S. Mehraeen, Effective scheduling of reconfigurable microgrids with dynamic thermal line rating, IEEE Trans. Ind. Electron. 66 (2) (February 2019) 1552−1564.

[5] E. Taherzadeh, M. Dabbaghjamanesh, M. Gitizadeh, A. Rahideh, A new efficient fuel optimization in blended charge depletion/charge sustenance control strategy for plug-in hybrid electric vehicles, IEEE Trans. Intell. Veh. 3 (3) (September 2018) 374−383.

[6] M. Dabbaghjamanesh, B. Wang, S. Mehraeen, J. Zhang, A. Kavousi-Fard, Networked microgrid security and privacy enhancement by the blockchain-enabled internet of things approach, in: 2019 IEEE Green Technologies Conference (GreenTech), April 2019, pp. 1−5.

[7] A. Kavousi Fard, B. Wang, O. Avatefipour, M. Dabbaghjamanesh, R. Sahba, A. Sahba, Superconducting fault current limiter allocation in reconfigurable smart grids, in: 2019 3rd International Conference on Smart Grid and Smart Cities (ICSGSC), June 2019, pp. 76−80.

[8] M. Dabbaghjamanesh, S. Mehraeen, A. Kavousi-Fard, F. Ferdowsi, A new efficient stochastic energy management technique for interconnected ac microgrids, in: 2018 IEEE Power Energy Society General Meeting (PESGM), August 2018, pp. 1−5.

[9] A. Moeini, S. Wang, An asymmetric selective harmonic current and voltage modulation-PWM technique for electric vehicle charging stations with cascaded h-bridge converters to meet power quality standards, in: 2019 IEEE Energy Conversion Congress and Exposition (ECCE), September 2019, pp. 4395−4402.

[10] A. Moeini, H. Zhao, S. Wang, A current-reference-based selective harmonic current mitigation PWM technique to improve the performance of cascaded h-bridge multilevel active rectifiers, IEEE Trans. Ind. Electron. 65 (1) (2016) 727−737.

This book belongs to Kitab Liaison (ocd1996@gmail.com) Copyright Elsevier 2023

[11] A. Moeini, H. Iman-Eini, M. Bakhshizadeh, Selective harmonic mitigation-pulse-width modulation technique with variable dc-link voltages in single and three-phase cascaded h-bridge inverters, IET Power Electron. 7 (4) (2013) 924−932.

[12] M.S.A. Dahidah, G. Konstantinou, V.G. Agelidis, A review of multilevel selective harmonic elimination PWM: formulations, solving algorithms, implementation and applications, IEEE Trans. Power Electron. 30 (8) (August 2015) 4091−4106.

[13] S.R. Pulikanti, V.G. Agelidis, Hybrid flying-capacitor-based active-neutral-point-clamped five-level converter operated with she-PWM, IEEE Trans. Ind. Electron. 58 (10) (October 2011) 4643−4653.

[14] H. Zhao, S. Wang, A. Moeini, Critical parameter design for a cascaded h-bridge with selective harmonic elimination/compensation based on harmonic envelope analysis for single-phase systems, IEEE Trans. Ind. Electron. 66 (4) (April 2019) 2914−2925.

[15] L.G. Franquelo, J. Napoles, R.C.P. Guisado, J.I. Leon, M.A. Aguirre, A flexible selective harmonic mitigation technique to meet grid codes in three-level PWM converters, IEEE Trans. Ind. Electron. 54 (6) (December 2007) 3022−3029.

[16] M. Najjar, A. Moeini, M.K. Bakhshizadeh, F. Blaabjerg, S. Farhangi, Optimal selective harmonic mitigation technique on variable dc link cascaded h-bridge converter to meet power quality standards, IEEE J. Emerging Sel. Top. Power Electron. 4 (3) (September 2016) 1107−1116.

[17] A. Moeini, H. Zhao, S. Wang, Improve control to output dynamic response and extend modulation index range with hybrid selective harmonic current mitigation-PWM and phase-shift PWM for four-quadrant cascaded h-bridge converters, IEEE Trans. Ind. Electron. 64 (9) (2017) 6854−6863.

[18] A. Moeini, S. Wang, B. Zhang, L. Yang, A hybrid phase shift-PWM and asymmetric selective harmonic current mitigation-PWM modulation technique to reduce harmonics and inductance of single-phase grid-tied cascaded multilevel converters, IEEE Trans. Ind. Electron. (2019), 1−1.

[19] A. Moeini, S. Wang, Analyzing and reducing current harmonics of ac and dc sides of cascaded h-bridge converters for electric vehicle charging stations, in: 2019 IEEE Energy Conversion Congress and Exposition (ECCE), September 2019, pp. 193−200.

[20] H. Zhao, T. Jin, S. Wang, L. Sun, A real-time selective harmonic elimination based on a transient-free inner closedloop control for cascaded multilevel inverters, IEEE Trans. Power Electron. 31 (2) (February 2016) 1000−1014.

[21] J.M. Zurada, Introduction to Artificial Neural Systems, vol. 8, West Publishing Company St. Paul, 1992.

[22] F. Filho, L.M. Tolbert, Y. Cao, B. Ozpineci, Real-time selective harmonic minimization for multilevel inverters connected to solar panels using artificial neural network angle generation, IEEE Trans. Ind. Appl. 47 (5) (September 2011) 2117−2124.

[23] M. Balasubramonian, V. Rajamani, Design and real-time implementation of shepwm in single-phase inverter using generalized hopfield neural network, IEEE Trans. Ind. Electron. 61 (11) (November 2014) 6327−6336.

[24] K. Yang, J. Hao, Y. Wang, Switching angles generation for selective harmonic elimination by using artificial neural networks and quasi-newton algorithm, in: 2016 IEEE Energy Conversion Congress and Exposition (ECCE), September 2016, pp. 1−5.

This book belongs to Kitab Liaison (ocd1996@gmail.com) Copyright Elsevier 2023

[25] P. Farhadi, M. Navidi, M. Gheydi, M. Pazhoohesh, H. Bevrani, Online selective harmonic minimization for cascaded half-bridge multilevel inverter using artificial neural network, in: 2015 Intl Aegean Conference on Electrical Machines Power Electronics (ACEMP), 2015 Intl Conference on Optimization of Electrical Electronic Equipment (OPTIM) 2015 Intl Symposium on Advanced Electromechanical Motion Systems (ELECTROMOTION), September 2015, pp. 331−335.

[26] P. Shanmuga Aravind, S. Albert Alexander, Harmonic minimization of a solar fed cascaded H bridge inverter using artificial neural network, in: 2013 International Conference on Energy Efficient Technologies for Sustainability, April 2013, pp. 163−167.

[27] I. Khoukha, C. Hachemi, B. El Madjid, Ann control of nine level NPC voltage inverter based on selective harmonics elimination, in: 2007 International Aegean Conference on Electrical Machines and Power Electronics, September 2007, pp. 587−591.

[28] M.G. Fakhry, A. Massoud, S. Ahmed, Quasi seven-level operation of multilevel converters with selective harmonic elimination, in: 2014 26th International Conference on Microelectronics (ICM), December 2014, pp. 216−219.

[29] J. Hao, G. Zhang, Y. Zheng, W. Hu, K. Yang, Solution for selective harmonic elimination in asymmetric multilevel inverter based on stochastic configuration network and levenberg-marquardt algorithm, in: 2019 IEEE Applied Power Electronics Conference and Exposition (APEC), March 2019, pp. 2855−2858.

[30] M. Mohaddes, A.M. Gole, P.G. McLaren, Application of an artificial neural network to harmonic reduction in PWM ac-dc converter, in: IEEE WESCANEX 95. Communications, Power, and Computing. Conference Proceedings, vol. 1, May 1995, pp. 123−128.

[31] F. Filho, H.Z. Maia, T.H.A. Mateus, B. Ozpineci, L.M. Tolbert, J.O.P. Pinto, Adaptive selective harmonic minimization based on ANNs for cascade multilevel inverters with varying dc sources, IEEE Trans. Ind. Electron. 60 (5) (May 2013) 1955−1962.

[32] Ieee Recommended Practice and Requirements for Harmonic Control in Electric Power Systems, IEEE Std 519-2014, June 2014, pp. 1−29 (Revision of IEEE Std 519-1992).

[33] F. Chollet, et al., Keras, 2015. https://keras.io.

[34] A. Moeini, S. Wang, A dc link sensor-less voltage balancing technique for cascaded h-bridge multilevel converters with asymmetric selective harmonic current mitigation-PWM, IEEE Trans. Power Electron. 33 (9) (2017) 7571−7581.

This book belongs to Kitab Liaison (ocd1996@gmail.com) Copyright Elsevier 2023

This page intentionally left blank

This book belongs to Kitab Liaison (ocd1996@gmail.com)

Copyright Elsevier 2023

Chapter 7

Overview of stability analysis methods in power electronics

Qianwen Xu
Electric Power and Energy Systems Division, KTH Royal Institute of Technology, Stockholm, Sweden

7.1 Introduction

Power electronic converters are widely adopted as the interface for the integration of various distributed generation systems (e.g., fuel cell, photovoltaic (PV), wind turbine, and energy storage) into the power grid [1], resulting in the emergence of power electronic−based power systems, like PV power plants [2], wind power plants [3], microgrids [4], electric railway systems [5], high-voltage DC transmission (HVDC), flexible AC transmission [6], etc. These interface converters enable full controllability, sustainability, and improved efficiency of the systems [7]. However, due to their negligible physical inertia, they also make the system susceptible to oscillations resulting from the network disturbances and the interactions with the systems [8,9].

Power system stability has been a significant issue since the 19th century. In conventional power system, stability analysis is well established: there are standard models of synchronous machines, governors, and excitation systems of varying orders to capture the important modes for particular problems; the electromechanical stability of synchronous generators, which is normally caused by slow control and dynamics that below the fundamental frequency, is the major concern [10]. However, in the modern power electronic−based power systems, the wide timescale control dynamics of power converters can cause interactions with both electromechanical dynamics in electrical machines and electromagnetic transients in power networks, resulting in wide timescale stability issues, e.g., low-frequency oscillations associated with the outer power control and grid synchronization loops, and high-frequency oscillations (typically from hundreds of hertz to several kilohertz) driven by mutual interactions between the fast inner control loops of the grid-connected converters [9]. Another significant concern is the high complexity of the power electronic−based power system caused by the large number of power

Control of Power Electronic Converters and Systems. https://doi.org/10.1016/B978-0-12-819432-4.00018-4
Copyright © 2021 Elsevier Ltd. All rights reserved.

This book belongs to Kitab Liaison (ocd1996@gmail.com)
Copyright Elsevier 2023

electronic converters with dedicated control loops, which complicates the system level modeling and analysis, and also increases difficulties in locating the instabilities present in power electronic—based power system [11,12]. Therefore, it is of significant importance to perform accurate stability analysis for design and operation of power electronic—based power systems.

Many research works have been conducted for power system small-signal stability analysis, either using eigenvalue method or impedance-based method. In eigenvalue method, a system state space model is derived and linearized at the operating point, then system stability is assessed by examining eigenvalues of the system state space matrix. The advantages of the eigenvalue method are the identification of oscillation modes and instability roots. The eigenvalue method has been widely applied for stability analysis of wind farms [3], inverter-based microgrid [4], grid-connected PV systems [13], HVDC system [6], etc. For a large-scale power system with high penetration of power electronic converters, there would be a lot of state variables from the detailed models of power converter dynamics, sources, lads, cables, etc. To make the eigenvalue method with modularity and scalability, some integration techniques like component connection method (CCM) or module-based approach are adopted for the system level integration [14,15]. The drawback of the eigenvalue approach is that it needs to know the full system information which may be kept privacy by different vendors of components to the power system [8]. In impedance-based approach, a system is divided as a source equivalent and a load equivalent, and system stability can be determined by the impedance ratio of the load and source using Nyquist criterion [8,16]. The advantages of impedance-based method are its modularity and its black box feature, where detailed knowledge of the parameters and properties of the system is not required as long as measurements can be obtained. The impedance can be extracted based on the measured signals with frequency scanning [17]. This also provides a promising technique for the online stability assessment. The impedance-based method is widely used in cascaded converter systems and grid-connected converter systems [18], grid-connected converter systems [19], and wind power systems [20]. The drawbacks of the impedance-based method include the conservative results and difficulty in identifying the oscillation modes and instability roots.

Small-signal stability can only ensure system stability at small disturbance. Due to the nonlinearity and complexity of the power electronic—based power system, it is significant to use large-signal analysis methods to ensure system stability at large disturbances, which may be caused by faults, protection, sudden load connections or disconnections, etc [21,22]. The stability behavior under such conditions differs from the small-signal case. Large-signal analysis provides characterization of stability boundary and transient behavior of system following a large disturbance. The objective is to estimate the domain of attraction of the system operation point, i.e., how large deviations from the operating point can be tolerated by the system. Currently, there are two kinds

This book belongs to Kitab Liaison (ocd1996@gmail.com) Copyright Elsevier 2023

of large-signal analysis methods, one is time-domain—based simulation method and the other is Lyapunov-based analytical methods. Time-domain simulations can provide high accuracy and validity but numerous simulations should be conducted over a wide operating point under various conditions [23]. There are several Lyapunov-based analytical methods, including Takagi—Sugeno (TS) multimodeling approach [24], Brayton—Moser's Mixed Potential method [25], and genetic algorithm—based Lyapunov function searching method [26]. Lyapunov-based analytical methods can provide the estimation of domain of attractions for stability, but it is a significant challenge to find a proper Lyapunov function.

In this chapter, the stability analysis methods for power electronic—based power systems are introduced, which is summarized in Fig. 7.1. Then Section 7.2 presents small-signal stability analysis methods and Section 7.3 presents large-signal stability analysis tools. Then two case studies are presented in Section 7.4 with small-signal stability analysis and large-signal stability analysis. Finally, conclusion is drawn.

7.2 Small-signal stability analysis methods

Small-signal stability is the system stability when subject to small-signal disturbances. The wide timescale oscillation issues caused by the interactions of power electronic converters with each other and with the grid are small-signal stability issues [10]. In this section, the modeling approaches of power converters are introduced. Then two widely used small-signal analysis methods, i.e., the eigenvalue method and impedance-based method, are introduced to perform small-signal stability analysis.

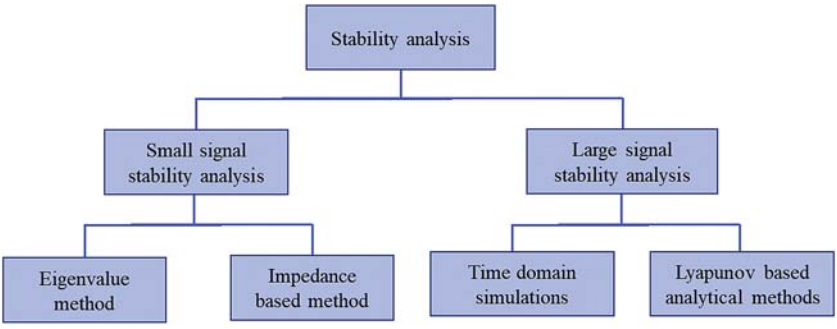

FIGURE 7.1 Stability analysis for power electronic—based power systems.

This book belongs to Kitab Liaison (ocd1996@gmail.com) Copyright Elsevier 2023

7.2.1 Modeling of power converter

Before stability analysis, it is necessary to build linearized models of power electronic converters due to their switching dynamics and nonlinearities. Several approaches can be adopted considering different level of accuracy requirement and the available information, i.e., state space averaging (SSA) approach, generalized SSA model method, harmonic state space (HSS) modeling method, and black box method. The first three methods require detailed system information and the black box method is based on measured data.

7.2.1.1 State space averaging method

The SSA method is a classical method for modeling power converters [27]. The instantaneous value of a state variable can be approximately represented by its one cycle average, expressed as

$$\langle x \rangle_0(t) = \frac{1}{T} \int_{t-T}^{t} x(\tau) d\tau \tag{7.1}$$

where $T = 2\pi/\omega_s$, ω_s is the switching frequency of the converter.

The SSA method can be directly applied to get linearized models of DC/DC converters as the obtained models are time invariant with steady-state operating points. But for AC/DC or AC/DC converters, the linearized models cannot be directly obtained due to time-varying variables of three-phase system with no steady-state operating points. To get linearized models of AC systems, dq transformation method [14] or harmonic linearization method [8] is applied with the SSA method. Dq transformation method is to do Park transformation for the three-phase variables, then the linearized model can be obtained in dq domain with steady-state operating points [14]. Harmonic linearization method is to superimpose the system with two sinusoidal perturbations, one in positive sequence and the other in negative sequence [8]. Then the linearized model can be obtained in sequence domain with steady-state operating points.

The SSA method is widely adopted. But it only considers fundamental frequency, when frequency coupling dynamics have large effects, the following two methods will be adopted, which provide more detailed models.

7.2.1.2 Generalized state space averaging method

The generalized state space averaging (GSSA) method [28] is based on Fourier transform of nonperiodic signals. A signal $x(t)$ can be approximated with arbitrary precision in the interval $\tau \in (t-T, t]$ by a Fourier series:

$$x(t) = \sum_{k=-\infty}^{\infty} X_k(t) e^{jk\omega_s \tau} \tag{7.2}$$

where Fourier coefficients $X_k(t)$ are given by

This book belongs to Kitab Liaison (ocd1996@gmail.com) Copyright Elsevier 2023

$$X_k(t) = \frac{1}{T}\int_{t-T}^{t} x(\tau)e^{jk\omega_s\tau}d\tau \tag{7.3}$$

It should be noted that SSA model is a special case for the GSSA model where $k = 0$.

7.2.1.3 Harmonic state space method

HSS model is a powerful technique to analyze linear time periodic systems [10]. It establishes an analogy to the state space model by introducing an exponentially modulated periodic signal, expressed as

$$x(t) = \sum_{k=-\infty}^{\infty} X_k(t)e^{st}e^{jk\omega_s t} \tag{7.4}$$

$$\dot{x}(t) = \sum_{k=-\infty}^{\infty} (s + jk\omega_s)X_k(t)e^{(s+jk\omega_s)t} \tag{7.5}$$

Both GSSA and HSS methods can capture the frequency coupling of power converters. However, they lead to higher order with complicated expressions.

7.2.1.4 Black box method

The previous three modeling methods require detailed information of models. However, in many situations, detailed information of components may be kept confidential by different vendors of components. Then data-based black box method provides a good solution for this case, where models can be built based on measured output dynamics of components. The impedance measurement approach is a widely used black box modeling method for power electronic systems and is briefly introduced here [8,16,18].

The main concept of impedance measurement method is to inject small disturbance signals (voltages or currents) at various frequencies in the operating system and then appropriate currents and voltages can be extracted to obtain the desired impedance or admittance [8,16]. This method can be directly applied to extract impedance of DC/DC converters or single-phase systems. For AC/DC and DC/AC converters, measurement of impedances in dq frame can be obtained by the two-step injection procedure: the first injection is on the d-axis while keeping q-axis perturbation null and then converted into abc frame to inject into the system; the corresponding voltage and current responses will be measured and converted back to dq frame; then the second injection is implemented q-axis with d-axis being zero to get the system responses. Then impedances in dq frame can be calculated [18].

The impedance measurement techniques make it possible to monitor the operational region of the system and assessing the system stability during

This book belongs to Kitab Liaison (ocd1996@gmail.com) Copyright Elsevier 2023

operation. For online applications, the ideal impedance measurement technique should complete the measurement in a short time, in order not to disturb normal operation for too long time, allowing a fast response to system variations. Wideband identification methods are proposed which inject a high-frequency content signal to excite all frequencies of interest simultaneously [19].

As a summary of the modeling methods, the first three modeling methods, i.e., SSA, GSSA, and HSS, are analytical solutions based on detailed information of models, and the black box method provides a powerful solution when detailed information is not available. Among the three analytical methods, the SSA method is the most commonly used approach, which approximates the instantaneous value of a state variable by its one cycle average. But it can only predict the dynamics below half the switching frequency. To further capture the frequency coupling dynamics caused by power electronic converters and provide more accurate assessment, the HSS method and GSSA method can be selected, which are based on Fourier transform of nonperiodic signals. But they also lead to higher orders with complicated expressions, resulting in increased computational burden and are difficult to use in very complex systems. When the information of models is not available, we will use black box method (e.g., impedance measurement approach) to build power converter models for systematic assessment; but the drawback is that the mechanisms inside models cannot be analyzed. These modeling methods can be selected for modeling power converters considering the available information and different levels of accuracy requirements and model complexity.

7.2.2 Eigenvalue method

Eigenvalue method is widely adopted for power system stability analysis. The detailed procedure of the small-signal stability analysis using eigenvalue method is presented in this part, including modeling and integration, stability analysis and verification, which is also illustrated in Fig. 7.2.

7.2.2.1 Component modeling and system integration

First, components are modeled in the state space form using an analytical modeling method presented in 7.2.1. Normally, SSA method is adopted to build state space models of components and then a system model is integrated for eigenvalue analysis.

For a large-scale power system with a high penetration of power electronic converters, there would be a lot of state variables from the detailed models of components. To address the high computation burden and complexity for

This book belongs to Kitab Liaison (ocd1996@gmail.com) Copyright Elsevier 2023

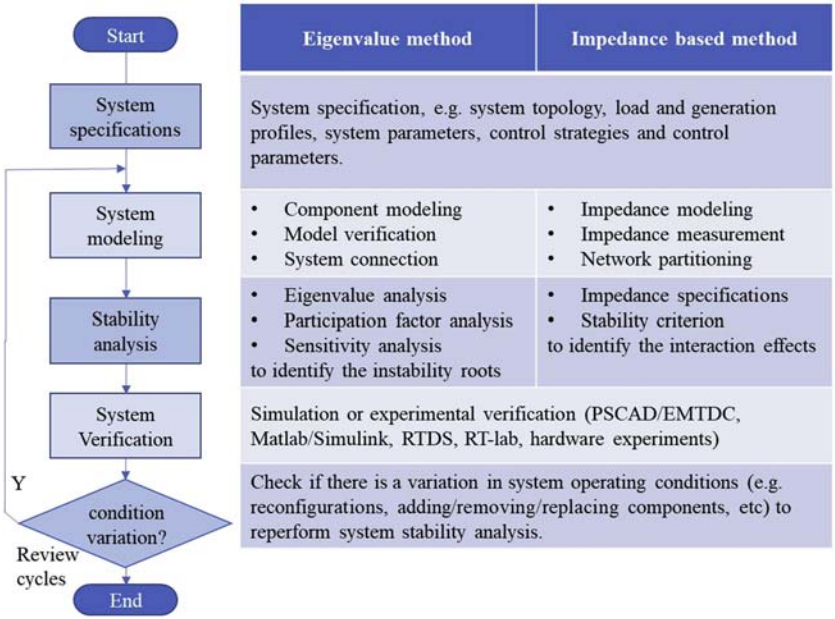

FIGURE 7.2 Procedures of small-signal analysis with the eigenvalue method and impedance-based method.

deriving the overall system state space model, the CCM or a module-based approach can be employed for system integration [14,15]. In the CCM, the power system is divided into multiple components with the interconnected relationship. The state space models of components are obtained and linearized as

$$\begin{aligned} \Delta\dot{x} &= A_i\Delta x + B_i\Delta u \\ \Delta y_i &= C_i\Delta x + D_i\Delta u \end{aligned} \tag{7.6}$$

where A_i, B_i, C_i, and D_i are state matrices for the i_{th} subsystem.

The interconnection relationship is extracted from the network architecture, given by

$$\begin{aligned} u &= L_1 y + L_2 a \\ b &= L_3 y + L_4 a \end{aligned} \tag{7.7}$$

where L_1, L_2, L_3, and L_4 are component interconnection matrices.

Then the small-signal model of the whole system is integrated as

$$\begin{aligned} \Delta\dot{x} &= F\Delta x + G\Delta a \\ \Delta b &= H\Delta x + J\Delta a \end{aligned} \tag{7.8}$$

where $F = A + BL_1(I - DL_1)^{-1}C, G = BL_1(I - DL_1)^{-1}DL_2 + BL_2,$

This book belongs to Kitab Liaison (ocd1996@gmail.com) Copyright Elsevier 2023

$$H = L_3(I - DL_1)^{-1}C, J = L_3(I - DL_1)^{-1}DL_2 + L_4.$$

The CCM and modular approach provide a modular and scalable solution for the large-scale power electronic—based power system integration.

7.2.2.2 Eigenvalue stability analysis

7.2.2.2.1 Eigenvalue analysis

The linearized state space model in (7.8) is analyzed by examining the eigenvalue of the system matrix F. The eigenvalue analysis shows different oscillation modes and damping characteristics. For a complex eigenvalue λ_i that corresponds to an oscillatory mode of the system in (7.9), the frequency f_{osci} and damping ratio ζ_i of the oscillation are expressed as (7.10) and (7.11).

$$\lambda_i = \sigma_i \pm j\omega_i \tag{7.9}$$

$$f_{osci} = \frac{\omega_i}{2\pi} \tag{7.10}$$

$$\zeta_i = -\frac{\sigma_i}{\sqrt{\sigma_i^2 + \omega_i^2}} \tag{7.11}$$

The damping ratio determines the rate at which the amplitude of the oscillations decreases. The dominant eigenvalues at different oscillation frequency ranges can be identified by eigenvalue analysis.

7.2.2.2.2 Participation factor analysis

Then participation factor analysis is performed [14,15,29], which calculates the contribution of each state to a certain mode, given by

$$p_{ki} = \frac{|w_{ki}||v_{ik}|}{\sum |w_{ki}||v_{ik}|} \tag{7.12}$$

where p_{ki} is the participation of kth state to ith mode; w_{ki} and v_{ik} are kth elements in the ith left eigenvector and right eigenvector, respectively.

The participation factor matrix can identify the states that have dominant effects on the dominant eigenvalues.

7.2.2.2.3 Sensitivity analysis

System stability can be predicted by calculating eigenvalue loci under different operating conditions [14,15,29]. The system becomes unstable if positive eigenvalues appear.

Parameters associated with the dominant states will be investigated through sensitivity analysis. The effect of these parameters (e.g., line impedance, filters, controller gain, delay time, PLL bandwidth, etc.) on system stability can be assessed by calculating the eigenvalue loci with the variation of these parameters. Then the ranges of the parameters for system stable operation of

This book belongs to Kitab Liaison (ocd1996@gmail.com) Copyright Elsevier 2023

the system can be obtained. This also provides a guideline to improve the system damping by tuning control parameters.

7.2.2.3 Verification

Time-domain simulations and experiments are typically performed to study stable and unstable conditions to verify the analysis and results.

7.2.3 Impedance-based method

Impedance-based methods are widely used to analyze power electronic—based systems. The detailed procedure of the small-signal stability analysis using an impedance—based approach is presented, including impedance modeling/measurement, stability analysis and verification, which is also illustrated in Fig. 7.2.

7.2.3.1 Impedance modeling

7.2.3.1.1 Impedance modeling

In impedance-based method, a system can be divided into a source subsystem and a load subsystem, as shown in Fig. 7.3 [8]. Z_{out_S} and Z_{in_L} are the output impedance of source and input impedance of load in the source—load interface, respectively. The total input to output transfer function is obtained as

$$G_{SL} = \frac{V_{out_L}}{V_{in_S}} = G_S\, G_L \frac{Z_{in_L}}{Z_{in_L} + Z_{out_S}} = G_S\, G_L \frac{1}{1 + T_{MLG}} \tag{7.13}$$

where the minor loop gain T_{MLG} is expressed as

$$T_{MLG} = \frac{Z_{out_S}}{Z_{in_L}} \tag{7.14}$$

For DC systems, impedance models are derived based on single-input and single-output transfer functions from current to voltage in a small-signal sense.

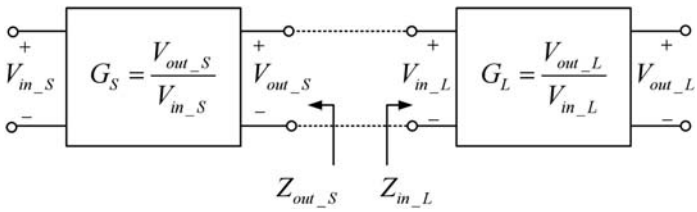

FIGURE 7.3 Impedance representation of an interconnected source—load system.

This book belongs to Kitab Liaison (ocd1996@gmail.com) Copyright Elsevier 2023

For AC systems, impedance models are built as multiple-input and multiple-output transfer functions either in dq domain or sequence domain [17]. For example, by applying a dq-reference frame transformation to the variables in abc domain, the AC system becomes a DC system in dq domain with the source and load impedances expressed as

$$Z_{S_dq} = \begin{bmatrix} Z_{S_dd}(s) & Z_{s_dq}(s) \\ Z_{s_qd}(s) & Z_{s_qq}(s) \end{bmatrix}, Z_{L_dq} = \begin{bmatrix} Z_{L_dd}(s) & Z_{L_dq}(s) \\ Z_{L_qd}(s) & Z_{L_qq}(s) \end{bmatrix} \tag{7.15}$$

If the detailed model information is not available, the impedance models can be obtained from experiments or simulations using impedance measurement technique discussed in 7.2.1.4.

7.2.3.1.2 Network partitioning

The impedance-based method is actually a local method. The impacts of some components may be neglected due to the lumping effect. Thus, the selection of network partitioning points to divide the system into source and load subsystems may lead to different system stability analysis results. It is also necessary to investigate the stability at different interfacing points.

7.2.3.2 Stability analysis

Based on (7.13), as G_s and G_L are stable transfer functions, system stability is determined by T_{MLG}. According to Nyquist criterion, the system is stable if and only if the Nyquist contour of T_{MLG} does not encircle $(-1, 0)$ point [16]. Many stability criteria are further developed based on this concept [16], such as Middlebrook criterion, Gain Margin and Phase Margin criterion, Opposing

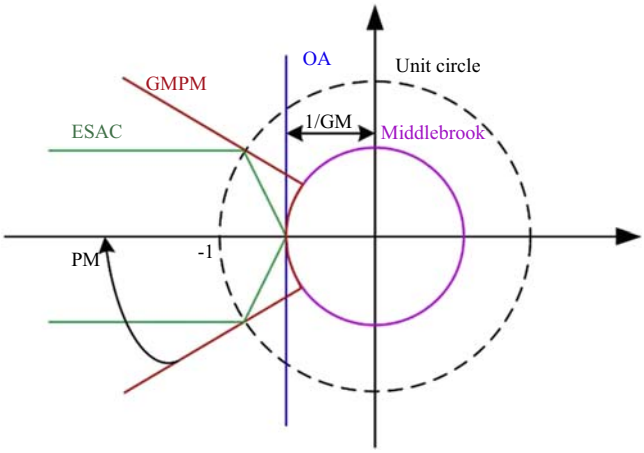

FIGURE 7.4 Stability boundaries based on different stability criteria.

This book belongs to Kitab Liaison (ocd1996@gmail.com) Copyright Elsevier 2023

Component criterion, Root Exponential Stability Criterion, etc. Fig. 7.4 depicts the stability boundaries based on different stability criteria.

For DC system, system stability can be evaluated directly in this way. For three-phase AC system, impedances of AC systems can be represented in dq domain or sequence domain. Then system stability can be evaluated and predicted by using the generalized Nyquist stability criterion to the impedance ratio [17].

To study the interaction between a converter system and the grid, a specific interfacing point needs to be selected with the converter as the load and the rest of the system as the source. Then the interaction dynamics can be analyzed in detail. The stability region can be predicted by investigating the impedance ratio with the stability criterion by varying operating profiles and different parameters to be studied.

This method also provides a design-oriented analysis. If a new converter system is to be integrated into the grid, given the interface and the grid impedance, the converter should be designed to ensure its impedance compatibility to the grid impedance with the stability criterion for stable operation. Moreover, with the plotted impedance characteristics, the interaction effects at different frequency ranges can be identified.

7.2.3.3 Verification of analysis

The stability analysis results should be verified by simulation or experimental results, otherwise, the impedance models should be reexamined in frequency domain.

7.2.4 Comparison of methods

The eigenvalue method has advantages in identifying oscillation modes and instability roots of system variables and it is preferred for comprehensive systematic analysis. However, it requires to know the full system information to perform stability analysis, which may be kept confidential by different vendors.

The impedance-based method analyses the whole system based on the I/O character (impedance) of each subsystem, once the impedance of each subsystem is obtained, system stability can easily be assessed; adding or removing or modifying a subsystem will not affect other subsystems and the new system can easily be reformulated. Thus, it is suitable for analyzing interactions of subsystems and the design of converters. Moreover, the impedance-based method has black box feature, which makes it a powerful technique when the system details are unavailable or for online stability assessment. However, the conservativeness of some impedance stability criteria may lead to

This book belongs to Kitab Liaison (ocd1996@gmail.com) Copyright Elsevier 2023

TABLE 7.1 Comparison of eigenvalue method and impedance-based method.

Stability analysis requirements	Eigenvalue method	Impedance method
Identification of oscillation modes	√	–
Participation factor of state variables	√	–
Black box (privacy)	–	√
Converter design–oriented analysis	–	√
Interaction effects of two subsystems	–	√

conservative design and it is unable to identify the oscillation modes and participation factors.

A comparison is made as a criterion for selecting the small-signal stability analysis method based on different requirements, which is shown in Table 7.1.

7.3 Large-signal stability analysis methods

Large-signal stability (i.e., transient stability) is the stability subject to large-signal disturbances caused by faults, protection, sudden load connections or disconnections, etc [21,22]. Two kinds of approaches are used to conduct large-signal stability analysis, one is using time-domain simulations with switched models [23], and the other is to use Lyapunov-based analytical methods [21]. In this section, time-domain simulation method is briefly introduced, and three Lyapunov-based analytical methods are illustrated to estimate domain of attraction that can ensure system stability under large-signal disturbances.

7.3.1 Time-domain simulations

Time-domain simulation approach is a common way to investigate system large-signal stability and electromechanical transient simulation tools have been developed for analyzing system behavior under different large-signal disturbances. It provides high accuracy and validity. But the problem is the extremely high computation burden as numerous simulations should be conducted to ensure system stability over a wide operating range under various disturbances [22].

7.3.2 Lyapunov-based analytical methods

Lyapunov-based analytical methods can estimate the domain of attraction, within which the system is stable under large-signal disturbances. Then

This book belongs to Kitab Liaison (ocd1996@gmail.com) Copyright Elsevier 2023

numerous time-domain simulations are not needed. Three analytical tools for large-signal stability analysis are introduced here.

7.3.2.1 Takagi–Sugeno multimodel method

TS multimodeling method can model nonlinear systems with multiplication, division, exponential, or square root nonlinearities. In this method, a nonlinear system is represented by a set of linear models based on a set of "if-then" fuzzy rules. At each rule, local behavior of the nonlinear model will be represented by a local linear model. The TS models are equivalent to the nonlinear model with sufficient number of fuzzy rules [24]. For the ith rule of total r rules, the relevant local model is expressed as

$$\begin{cases} \dot{x}(t) = A_i x(t) + B_i u(t) \\ y(t) = C_i x(t) \end{cases} \tag{7.16}$$

where A_i, B_i, and C_i are constant matrices.

Then the nonlinear model can be expressed as

$$\begin{cases} \dot{x}(t) = \sum_{i=1}^{r} h_i (A_i x(t) + B_i u(t)) \\ y(t) = \sum_{i=1}^{r} h_i C_i x(t) \end{cases} \tag{7.17}$$

where h_i is the respective weight of the ith rule that $\sum_{i=1}^{r} h_i = 1, h_i \geq 0$.

The nonlinear system is asymptotically stable if the linear matrix inequality (LMI) condition in (7.18) is satisfied.

$$\begin{cases} M = M^T > 0 \\ A_i^T M + M A_i < 0, \forall i \in \{1, 2, \ldots, r\} \end{cases} \tag{7.18}$$

where is M is a matrix and its existence indicates the stability of the system.

Once the matrix of LMI problem is known, the Lyapunov function is selected as

$$V(x) = x^T M x \tag{7.19}$$

The following algorithm is utilized to estimate the domain of attraction:

Algorithm 7.1.

1. - Set all nonlinearities to the operating point values $f_{j\min} = f_{j\max} = f_j(0)$, $j = 1,2,\ldots q$ ($x_{j\min} = x_{j\max} = 0$), q is the number of nonlinearities of the function f.
2. - Check LMI problem in (7.19), if it is feasible, go to Step 3, else go to Step 4.

This book belongs to Kitab Liaison (ocd1996@gmail.com) Copyright Elsevier 2023

3. - Decrease $f_{j\min}$ and increase $f_{j\max}$ by modifying $x_{j\min}$ and $x_{j\max}$, $j = 1,2,\ldots, q$. Then go to Step 2.
4. - The estimated domain of attraction can be calculated by $x_{j\min}$ and $x_{j\max}$, $j = 1,2,\ldots, q$.

This method can estimate domain of attraction with an obtained Lyapunov function. However, if the number of nonlinearities increases, the order of matrix will grow rapidly and the problem will be very complicated to solve.

7.3.2.2 Brayton–Moser's mixed potential

This method is based on Lyapunov-type mixed potential function using the elements and circuits of the studied system [25]. Based on circuit topology and Kirchhoff's laws, the dynamics of a nonlinear circuit can be expressed by a set of inductor currents i and capacitor voltages v. Then the mixed potential is developed as

$$P(v,i) = A(i) - B(v) + \langle i, \gamma \cdot v \rangle \tag{7.20}$$

where γ is a constant matrix determined by circuit topology; current potential $A(i)$ and voltage potential $B(v)$ are the sum of integration of current set and voltage set, respectively, given by

$$A(i) = \sum_{\rho \in N_i} \int_{\Gamma} v_\rho di \tag{7.21}$$

$$B(i) = \sum_{\rho \in N_v} \int_{\Gamma} i_\rho dv \tag{7.22}$$

A candidate Lyapunov function is selected as

$$P^*(v,i) = \lambda \cdot P(v,i) + \frac{1}{2}\left\langle \frac{\partial P(v,i)}{\partial v}, \frac{1}{C} \cdot \frac{\partial P(v,i)}{\partial v} \right\rangle + \frac{1}{2}\left\langle \frac{\partial P(v,i)}{\partial i}, \frac{1}{L} \cdot \frac{\partial P(v,i)}{\partial i} \right\rangle \tag{7.23}$$

According to Lyapunov theorem and LaSalle invariance principle [25], an estimated domain of attraction can be obtained as large-signal stability boundary of the system. However, this method is mainly for nonlinear LC circuits, other nonlinear systems such as motor drive system, it is often difficult to find a Lyapunov function.

This book belongs to Kitab Liaison (ocd1996@gmail.com) Copyright Elsevier 2023

7.3.2.3 Optimal Lyapunov function generation

The problem of finding the large-signal stability boundary can be formulated as an optimization problem which is to find the maximum domain of attraction for a proper Lyapunov function $V(x)$ [26].

The optimization problem is formulated as (7.24) and a genetic algorithm is applied to solve it.

$$\begin{array}{ll} \min & V(x) \\ \text{Subject to} & \dot{V}(x) \geq 0 \end{array} \tag{7.24}$$

Several candidate Lyapunov functions are presented in Ref. [30].

To solve the optimization problem, it is better to have more variables to ensure enough degrees of freedom. Therefore, this method is more helpful to solve complex systems.

As can be observed from the above methods, large-signal stability analysis is much more complicated than small-signal stability analysis. The major challenge for Lyapunov-based analytical method is to find a proper Lyapunov function for a high-order power electronic−based power system.

7.4 Case studies with practical examples

7.4.1 Small-signal stability analysis

To illustrate the small-signal analysis method of power electronic−based power system using the eigenvalue method and impedance-based method in Section 7.2, a grid-connected three-inverter system in Fig. 7.5 is studied by using eigenvalue method and impedance-based method as a demonstration. The inverters are in current-controlled mode with PR controllers in the stationary frame (only current loop is considered) [9], as shown in Fig. 7.6. System parameters and control parameters are given in Table 7.2.

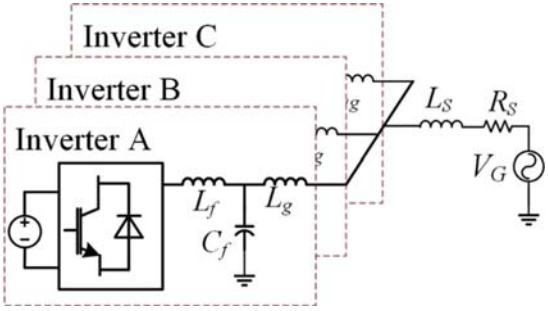

FIGURE 7.5 A grid-connected three-inverter system for case study.

This book belongs to Kitab Liaison (ocd1996@gmail.com) Copyright Elsevier 2023

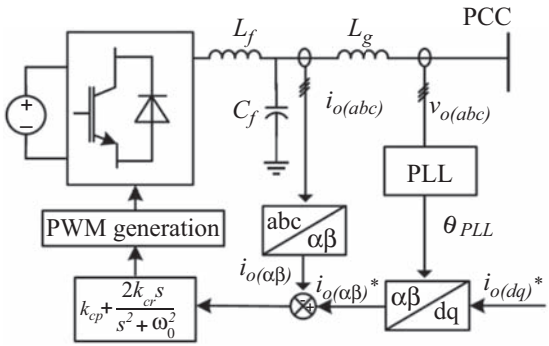

FIGURE 7.6 Control implementation of the grid-connected inverter using PR controllers.

TABLE 7.2 System parameters for system in Fig. 7.3.

		Inverters		
		Inv. A	Inv. B	Inv. C
Switching frequency [kHz]		10		
Filter values	L_f[mH] C_f[uF] L_g[mH]	3 3 3	2 5 2	1.5 5 1.5
Parasitic values	r_{Lf}[mΩ] r_{Cf}[mΩ] r_{Lg}[mΩ]	0.0628 0.1061 0.0942	0.0471 0.0637 0.0628	0.0471 0.0637 0.0471
Control gain	K_p k_R	20 600	12 600	12 600
Grid impedance	L_S[mH] Rs [Ω]	2e−3 0.4e−3		

7.4.1.1 Eigenvalue method

By following the procedure in Section 7.2.2, the eigenvalue method is applied for stability analysis of the system in Fig. 7.5.

7.4.1.1.1 System modeling

The most widely used SSA method is applied. According to the system topology in Fig. 7.5 and control structure in Fig. 7.6, state space model of Inverter i ($i = A$, B, and C) and grid can be derived as

This book belongs to Kitab Liaison (ocd1996@gmail.com) Copyright Elsevier 2023

$$\begin{cases} \dfrac{di_{Lfd,i}}{dt} = -\dfrac{r_{Lf,i}}{L_{f,i}} i_{Lfd,i} + \omega i_{Lfq,i} + \dfrac{1}{L_{f,i}} v_{ind,i} - \dfrac{1}{L_{f,i}} v_{Cfd,i} \\ \dfrac{di_{Lfq,i}}{dt} = -\dfrac{r_{Lf,i}}{L_{f,i}} i_{Lfq,i} + \omega i_{Lfd,i} + \dfrac{1}{L_{f,i}} v_{inq,i} - \dfrac{1}{L_{f,i}} v_{Cfq,i} \\ \dfrac{dv_{Cfd,i}}{dt} = \dfrac{1}{C_{f,i}} i_{Lfd,i} + \omega v_{Cfq,i} - \dfrac{1}{C_{f,i}} i_{Lgd,i} \\ \dfrac{dv_{Cfq,i}}{dt} = \dfrac{1}{C_{f,i}} i_{Lfq,i} + \omega v_{Cfd,i} + \dfrac{1}{C_{f,i}} i_{Lgq,i} \\ \dfrac{di_{Lgd,i}}{dt} = -\dfrac{r_{Lg,i}}{L_{g,i}} i_{Lgd,i} + \omega i_{Lgq,i} + \dfrac{1}{L_{g,i}} v_{Cfd,i} - \dfrac{1}{L_{g,i}} v_{pccd,i} \\ \dfrac{di_{Lgq,i}}{dt} = -\dfrac{r_{Lg,i}}{L_{g,i}} i_{Lgq,i} + \omega i_{Lgd,i} + \dfrac{1}{L_{g,i}} v_{Cfq,i} - \dfrac{1}{L_{g,i}} v_{pccq,i} \\ \dfrac{dx_{1d,i}}{dt} = i^*_{Lgd,i} - i_{Lgd,i} \\ \dfrac{dx_{1q,i}}{dt} = i^*_{Lgq,i} - i_{Lgq,i} \\ v_{ind,i} = k_{cp,i}\left(i^*_{Lgd,i} - i_{Lgd,i}\right) + k_{cr,i} X_{1d,i} \\ v_{inq,i} = k_{cp,i}\left(i^*_{Lgq,i} - i_{Lgq,i}\right) + k_{cr,i} X_{1q,i} \end{cases} \tag{7.25}$$

$$\begin{cases} \dfrac{di_{Gd}}{dt} = -\dfrac{r_S}{L_S} i_{Gd} + \omega i_{Gq} + \dfrac{1}{L_S} v_{Gd} - \dfrac{1}{L_S} v_{pccd} \\ \dfrac{di_{Gq}}{dt} = -\dfrac{r_S}{L_S} i_{Gq} + \omega i_{Gd} + \dfrac{1}{L_S} v_{Gq} - \dfrac{1}{L_S} v_{pccq} \\ \dfrac{dv_{pccd}}{dt} = -\dfrac{1}{C_{pcc}} i_{gd} + \omega v_{pccq} + \dfrac{1}{C_{pcc}} i_{Gd} \\ \dfrac{dv_{pccq}}{dt} = -\dfrac{1}{C_{pcc}} i_{gq} - \omega v_{pccd} + \dfrac{1}{C_{pcc}} i_{Gq} \end{cases} \tag{7.26}$$

The small-signal models of Inverter i ($i = A$, B, and C) and grid can be obtained by linearizing (7.25) and (7.26) at the operating point as

$$\Delta \dot{x}_{inv,i} = A_{inv,i} \Delta x_{inv,i} + B_{inv,i} C_G \Delta x_G \tag{7.27}$$

This book belongs to Kitab Liaison (ocd1996@gmail.com)
Copyright Elsevier 2023

$$\Delta\dot{x}_G = A_G \Delta x_G + \sum_{i=11-n} B_G C_{inv,i} \Delta x_{inv,i} \tag{7.28}$$

where $\Delta x_{inv,i} = \left[\Delta i_{Lfd,i}\ \Delta i_{Lfq,i}\ \Delta v_{cfd,i}\ \Delta v_{cfq,i}\ \Delta i_{Lgd,i}\ \Delta i_{Lgq,i}\ \Delta X_{1d,i}\ \Delta i_{1q,i}\right]^T$

$$\Delta x_G = \left[\Delta v_{pccd} \quad \Delta v_{pccq} \quad \Delta i_{gd} \quad \Delta i_{gq}\right]^T$$

By using component connection approach or module-based approach, the overall small-signal model of the system is expressed as

$$A_s = \begin{bmatrix} A_{inv,A} & 0 & 0 & B_{inv,A}C_G \\ 0 & A_{inv,B} & 0 & B_{inv,B}C_G \\ 0 & 0 & A_{inv,C} & B_{inv,C}C_G \\ B_G C_{inv,A} & B_G C_{inv,B} & B_G C_{inv,C} & A_G \end{bmatrix} \tag{7.29}$$

Then system stability can be evaluated by examining eigenvalues of the system matrix As. Fig. 7.7 shows the corresponding eigenvalue loci. As can be observed, the modes λ11-14 are in the right half plane and the system will be unstable.

Then the participation factor analysis is conducted to localize the instability roots. Following (7.12), the participation factors for the system are calculated and depicted in Fig. 7.8. The dominant states to the unstable modes λ11-14 are $i_{Lfd,C}$, $i_{Lfq,C}$, $v_{Cfd,C}$, $v_{Cfq,C}$, $i_{Lgd,C}$, $i_{Lgq,C}$ with the participation factors 0.124, 0.124, 0.249, 0.249, 0.125, and 0.125, respectively. Therefore, Inverter C has a dominant impact on the unstable result.

Fig. 7.9 shows the eigenvalue loci with the variation of the current control gain from 9 to 14. As can be observed, when the current control gain is larger than 11, some eigenvalues move to the right half plane. Therefore, to ensure system stability, controller gain should be selected as 10 or smaller.

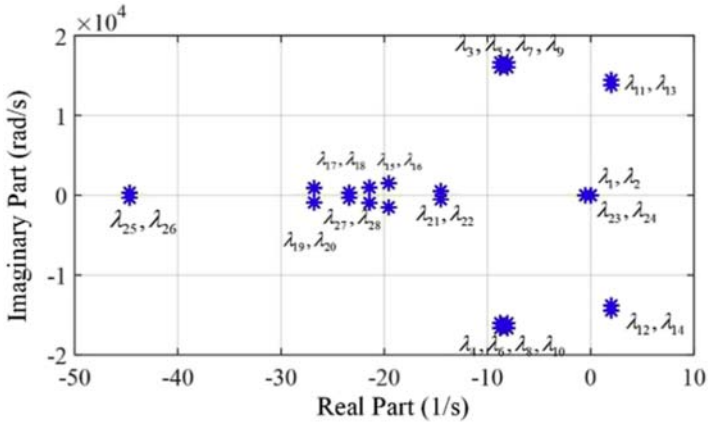

FIGURE 7.7 Eigenvalue loci of the system under study in Fig. 7.3.

This book belongs to Kitab Liaison (ocd1996@gmail.com)
Copyright Elsevier 2023

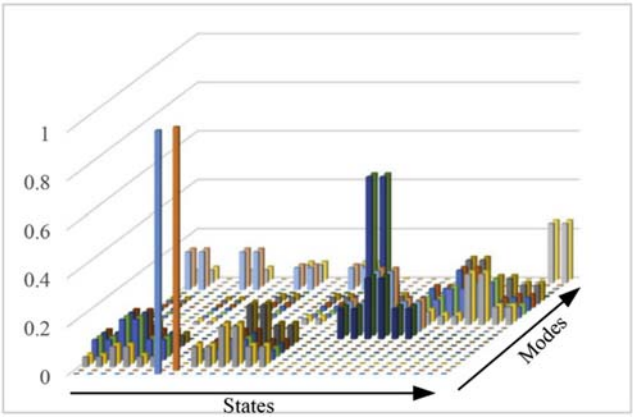

FIGURE 7.8 Participation factors for the system under study in Fig. 7.3.

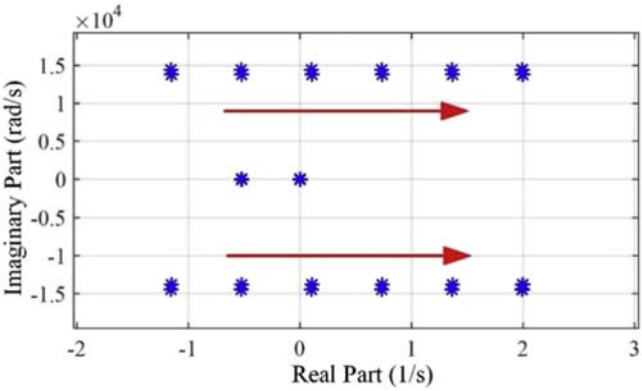

FIGURE 7.9 Eigenvalue loci with the variation of the current control gain *kcp,C* in Inverter C from 9 to 14.

7.4.1.2 Impedance-based method

7.4.1.2.1 Impedance modeling

Based on [9], the output admittance of Inverter i with an LCL filter $Y_{oi}(i = A, B, C)$ can be derived as

$$Y_{oi,i} = \frac{Y_{o,i}(s)}{1 + G_{cgi}(s)G_{PWM}(s)Y_{gi,i}(s)} \tag{7.30}$$

$$\text{with } Y_{gi,i}(s) = \frac{Z_{Cf,i}}{Z_{Cf,i}Z_{Lf,i} + Z_{Lg,i}Z_{Lf,i} + Z_{Cf,i}Z_{Lg,i}}$$

This book belongs to Kitab Liaison (ocd1996@gmail.com) Copyright Elsevier 2023

$$Y_{o,i}(s) = \frac{Z_{Cf,i} + Z_{Lf,i}}{Z_{Cf,i}Z_{Lf,i} + Z_{Lg,i}Z_{Lf,i} + Z_{Cf,i}Z_{Lg,i}}$$

$$G_{cgi}(s) = k_{cp,i}\frac{k_{cr,i}s}{s^2 + \omega_1^2}$$

$$G_{PWM}(s) = e^{-1.5T_s s}$$

The grid admittance Y_g is derived as

$$Y_g = \frac{1}{R_S + sL_S} \tag{7.31}$$

Here the integration of Inverter C to the grid-connected inverter system is studied with Inverters $A + B$ as an example. Then partitioning point can be selected where the Inverter C is seen as the load side and the rest of the system is the source side, with the minor loop gain calculated as

$$T_{MLG} = \frac{Y_{oC}}{Y_g + Y_{oA} + Y_{oB}} \tag{7.32}$$

Fig. 7.10depicts the Nyquist plot for the system with original parameters in red (dark gray in print version) color. It can be observed that Nyquist plot encircles $(-1, 0j)$ point and thus, the system is unstable with the integration of Inverter C.

The parameter is redesigned to stabilize system, i.e., to make Nyquist plot encircle $(-1, 0j)$ point. The system is stable with proportional gain redesigned as 10, as it is shown in Fig. 7.10 with blue (dark gray in printed version) color line.

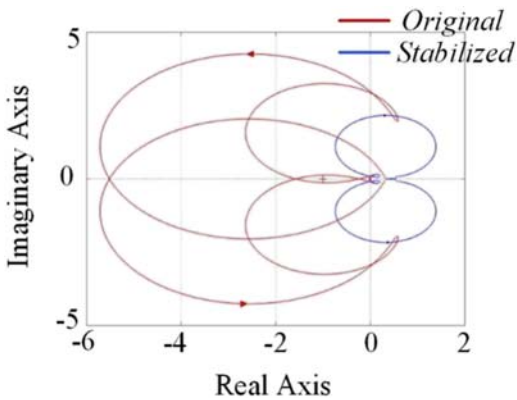

FIGURE 7.10 Nyquist plot for the system with original control parameter (unstable) and redesigned control parameter (stable).

This book belongs to Kitab Liaison (ocd1996@gmail.com) Copyright Elsevier 2023

7.4.1.3 Verification

Simulations are done in Matlab/Simulink based on Figs. 7.5 and 7.6 for the verification of the results of the above two methods.

Fig. 7.11 demonstrates the simulation results of output currents of three inverters and the grid voltage with the original parameters in Table 7.2. The results indicate that the system is unstable, which verifies the analytical results of eigenvalue method in Section 7.4.1.1 and impedance-based method in Section 7.4.1.2.

Fig. 7.12 presents the simulation results with the redesigned proportional gain in Inverter C, as suggested by the eigenvalue method and impedance-based method in Section 7.4.1. The results of the current dynamics and voltage dynamics show that the system is stable, which validates the analytical results.

A laboratory platform of the grid-connected multiinverter system is established for further verification of the results, as shown in Fig. 7.13. Three inverters are integrated into the grid simulator though LCL filters and grid line inductor. The parameters are the same as that for simulations. The control algorithm is implemented in dSPACE 1007 to generate PWM signals for the inverters.

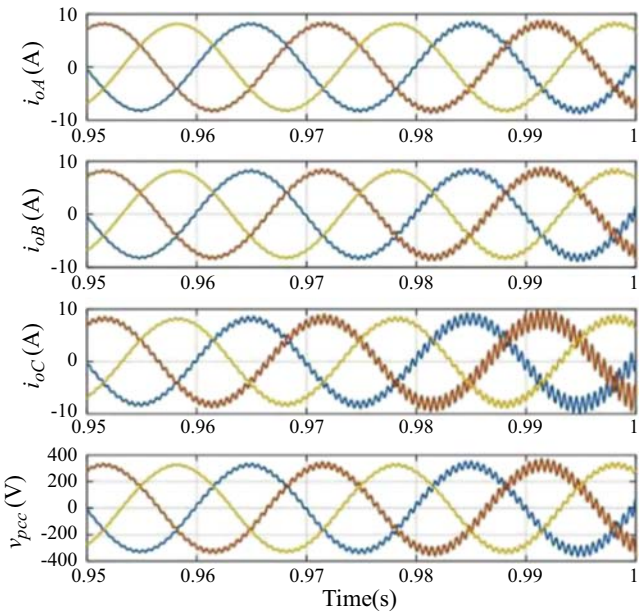

FIGURE 7.11 Simulation results with the original control parameter ($kcp,C = 12$) for the system under study.

This book belongs to Kitab Liaison (ocd1996@gmail.com) Copyright Elsevier 2023

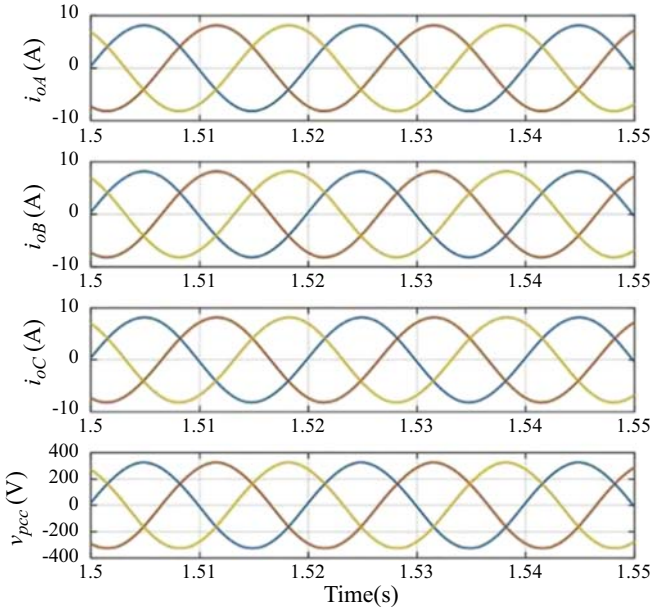

FIGURE 7.12 Simulation results with the redesigned control parameter ($kcp,C = 10$) for the system under study.

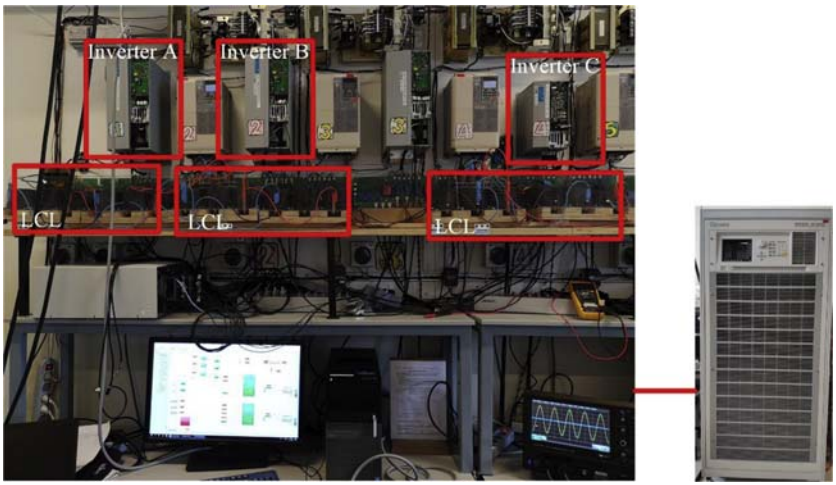

FIGURE 7.13 Experimental platform using three-inverter systems connected to a grid.

The experimental results of the system with original parameters listed in Table 7.2 are shown in Fig. 7.14. The current response of three inverters and the voltage response at PCC show that the system is unstable, which verifies the analytical and simulation results.

This book belongs to Kitab Liaison (ocd1996@gmail.com) Copyright Elsevier 2023

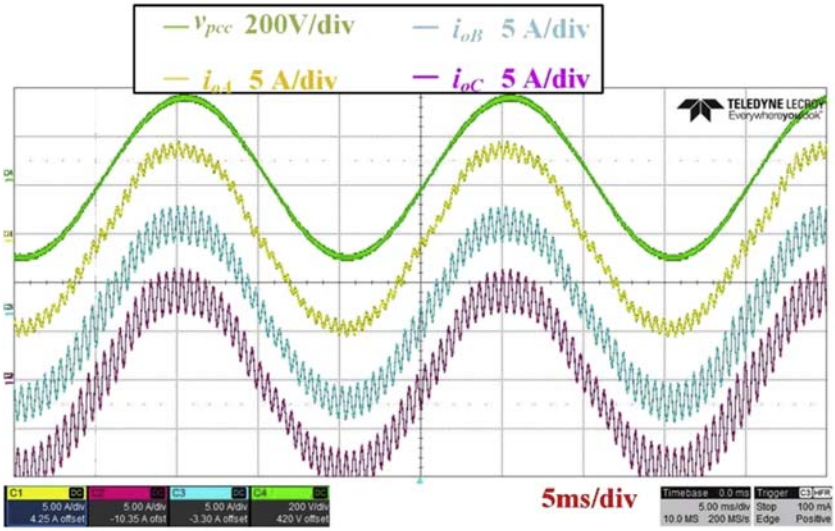

FIGURE 7.14 Experimental results with the original control parameter ($kcp,C = 12$) for the system under study.

Fig. 7.15 shows the experimental results with the redesigned current loop proportional gain of Inverter C to be 10. The system is stable, which validates the analytical and simulation results are feasible to be used.

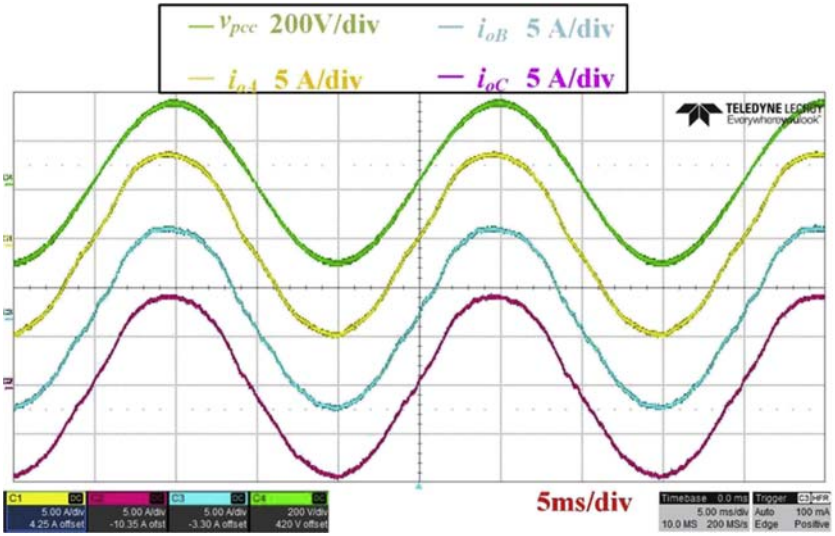

FIGURE 7.15 Experimental results with the redesigned control parameter ($kcp,C = 10$) for the system under study.

This book belongs to Kitab Liaison (ocd1996@gmail.com) Copyright Elsevier 2023

7.4.2 Large-signal stability analysis on a power electronic system

Here an example of a large signal stability analysis is shown for a simple DC system with constant power load (CPL) by using TS multimodeling approach [20,24] illustrated in Section 7.3.2.1.

Stability issues caused by a high penetration of power electronic converters in DC microgrid attract much attention in recent years. Tightly controlled power electronic converters behave as CPLs with destabilizing effects. The interaction of CPLs with an LC filter is studied in a simple DC distribution system, as shown in Fig. 7.16. The parameters for the system under study are given in Table 7.3.

The model of the system is expressed as

$$\dot{x} = \begin{bmatrix} \dot{x}_1 \\ \dot{x}_2 \end{bmatrix} = \begin{bmatrix} -\dfrac{r_f}{L_f} & -\dfrac{1}{L_f} \\ \dfrac{1}{C} & \dfrac{p_{s0}}{CV_{s0}} f_1(x_2) \end{bmatrix} \begin{bmatrix} x_1 \\ x_2 \end{bmatrix} = A_1(x_2)x \tag{7.33}$$

$$\text{with } f_1(x_2) = \frac{1}{x_2 + V_{s0}}.$$

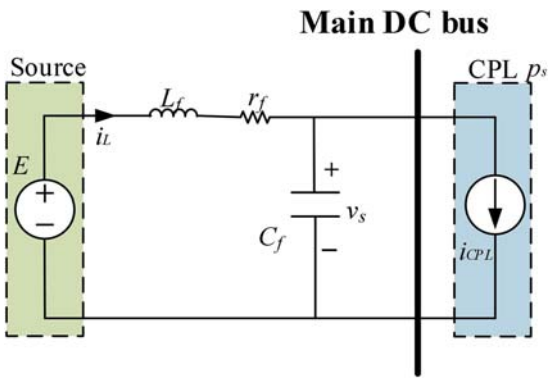

FIGURE 7.16 A simplified DC distribution system.

TABLE 7.3 Parameters for the DC distribution system.

DC-link voltage (E)	200 V
DC-link filter (L_f, r_f, C_f)	39.5 mH, 1.1 Ω, 0.501 mF
Constant power load P_s	300 W

This book belongs to Kitab Liaison (ocd1996@gmail.com)
Copyright Elsevier 2023

As can be observed from (7.33), there is only one nonlinearity. Following the TS modeling method in 7.3.1, suppose x_2 belongs to the interval $[x_{2\min}, x_{2\max}]$, which is to be determined by Algorithm 7.1. Let

$$\begin{cases} f_{1\min} = \dfrac{1}{x_{2\max} + V_{s0}} \\ f_{1\max} = \dfrac{1}{x_{2\min} + V_{s0}} \end{cases} \tag{7.34}$$

Here two local models using two fuzzy rules can be applied:

Rule 1: if x_2 is $x_{2\min}$, the model is obtained as

$$\dot{x} = \begin{bmatrix} -\dfrac{r_f}{L_f} & -\dfrac{1}{L_f} \\ \dfrac{1}{C} & \dfrac{p_{s0}}{CV_{s0}} f_{1\min} \end{bmatrix} x = A_1 x \tag{7.35}$$

Rule 2: if x_2 is $x_{2\max}$, the model is obtained as

$$\dot{x} = \begin{bmatrix} -\dfrac{r_f}{L_f} & -\dfrac{1}{L_f} \\ \dfrac{1}{C} & \dfrac{p_{s0}}{CV_{s0}} f_{1\max} \end{bmatrix} x = A_2 x \tag{7.36}$$

Then the border of the domain can be calculated considering the LMI condition in (7.37) and the algorithm in Section 7.3.1.

$$\begin{cases} M = M^T > 0 \\ A_1^T M + M A_1 < 0 \\ A_2^T M + M A_2 < 0 \end{cases} \tag{7.37}$$

Then the domain of attraction is calculated as

$$103.1x_1^2 + 2.86x_1x_2 + 1.31x_2^2 = 10292 \tag{7.38}$$

with M obtained as $M = \begin{bmatrix} 103.1 & 1.43 \\ 1.43 & 1.31 \end{bmatrix}$ at $x_{2\min} = -89.4$.

The domain of attraction using TS multimodeling method is plotted in Fig. 7.17.

The effect of the load power on the domain of attraction can be explored and it is shown that the maximum load of the system is 500 W beyond which the domain of attraction vanishes. Fig. 7.18 shows the time-domain simulation result when load power increases from 200 to 400 to 600 W. It shows that system becomes unstable when load increases from 400 to 600 W, which is coherent with the stability region of the analytical method.

This book belongs to Kitab Liaison (ocd1996@gmail.com) Copyright Elsevier 2023

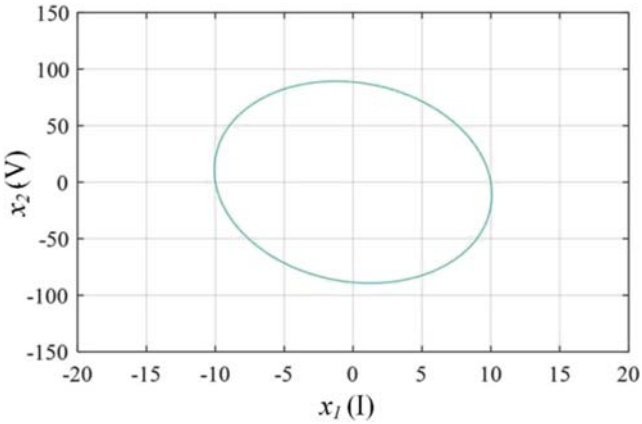

FIGURE 7.17 Estimated domain of attraction using TS multimodeling method for large-signal stability analysis.

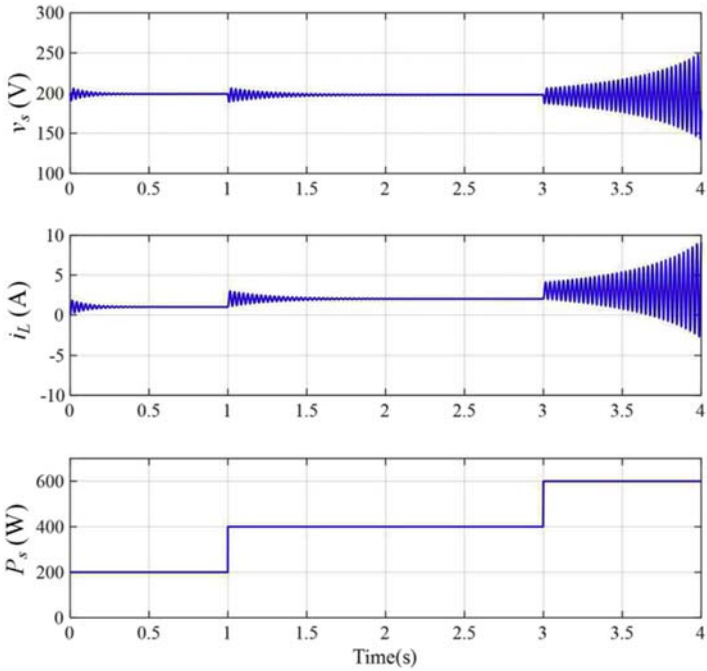

FIGURE 7.18 Time-domain simulation of the DC system with load power variation.

This book belongs to Kitab Liaison (ocd1996@gmail.com) Copyright Elsevier 2023

7.5 Summary

In this chapter, we introduce small-signal stability analysis and large-signal stability methods. First, modeling methods are introduced, and a proper modeling method can be selected based on information availability and accuracy requirement. Then the commonly used small-signal stability analysis tools, i.e., eigenvalue method and impedance-based method, are demonstrated in details, with case studies and simulation/experimental verifications. It shows that the eigenvalue method is a good solution to find the unstable root of the overall system and design the stable parameters; while impedance method is suitable to investigate the interactions of two subsystems or when the information of subsystems is not available. The large-signal stability analysis tools are introduced which include time-domain simulation method and Lyapunov-based analytical methods with a small case study of a DC system for demonstration. For small-signal stability analysis, it is necessary to develop a technique that is able to identify the unstable root and does not require detailed model information, i.e., have both advantages of the eigenvalue method and impedance-based method. For large-signal stability analysis, it is challenging to find a proper Lyapunov function for large power electronic−based power systems to estimate domain of attraction, which should be explored in the future.

References

[1] F. Blaabjerg, Z. Chen, S.B. Kjaer, Power electronics as efficient interface in dispersed power generation systems, IEEE Trans. Power Electron. 19 (5) (2004) 1184−1194.

[2] M. El-Shimy, A. Sharaf, H. Khairy, G. Hashem, Reduced-order modelling of solar-PV generators for small-signal stability assessment of power systems and estimation of maximum penetration levels, IET Gener. Transm. Distrib. 12 (8) (2018) 1838−1847.

[3] Y. Mishra, S. Mishra, F. Li, Z.Y. Dong, R.C. Bansal, Small-signal stability analysis of a DFIG based wind power system under different modes of operation, IEEE Trans. Energy Convers. 24 (4) (2009) 972−982.

[4] N. Pogaku, M. Prodanovic, T.C. Green, Modeling, analysis and testing of autonomous operation of an inverter-based microgrid, IEEE Trans. Power Electron. 22 (2) (2007) 613−625.

[5] E. Mollerstedt, B. Bernhardsson, Out of control because of harmonics-an analysis of the harmonic response of an inverter locomotive, IEEE Control Syst. Mag. 20 (4) (2000) 70−81.

[6] M. Amin, M. Molinas, Understanding the origin of oscillatory phenomena observed between wind farms and HVdc systems, IEEE J. Emerging Sel. Top. Power Electron. 5 (1) (2017) 378−392.

[7] F. Blaabjerg, R. Teodorescu, M. Liserre, A. V Timbus, Overview of control and grid synchronization for distributed power generation systems, IEEE Trans. Ind. Electron. 53 (5) (2006) 1398−1409.

[8] J. Sun, Small-signal methods for AC distributed power systems–a review, IEEE Trans. Power Electron. 24 (11) (2009) 2545−2554.

This book belongs to Kitab Liaison (ocd1996@gmail.com) Copyright Elsevier 2023

[9] X. Wang, F. Blaabjerg, W. Wu, Modeling and analysis of harmonic stability in an AC powerelectronics- based power system, IEEE Trans. Power Electron. 29 (12) (2014) 6421−6432.

[10] X. Wang, F. Blaabjerg, Harmonic stability in power electronic-based power systems: concept, modeling, and analysis, IEEE Trans. Smart Grid 10 (3) (May 2019) 2858−2870.

[11] Y. Wang, X. Wang, F. Blaabjerg, Z. Chen, Harmonic instability assessment using state-space modeling and participation analysis in inverter-fed power systems, IEEE Trans. Ind. Electron. 64 (1) (2017) 806−816.

[12] E. Ebrahimzadeh, F. Blaabjerg, X. Wang, C.L. Bak, Harmonic stability and resonance analysis in large PMSG-based wind power plants, IEEE Trans. Sustain. Energy 9 (1) (2018) 12−23.

[13] S. Eftekharnejad, V. Vittal, G.T. Heydt, B. Keel, J. Loehr, Small signal stability assessment of power systems with increased penetration of photovoltaic generation: a case study, IEEE Trans. Sustain. Energy 4 (4) (2013) 960−967.

[14] Q. Xu, P. Wang, J. Chen, C. Wen, M.Y. Lee, A module-based approach for stability analysis of complex more-electric aircraft power system, IEEE Trans. Transp. Electrif. 3 (4) (2017) 901−919.

[15] Y. Wang, X. Wang, Z. Chen, F. Blaabjerg, Small-signal stability analysis of inverter-fed power systems using component connection method, IEEE Trans. Smart Grid 9 (5) (2018) 5301−5310.

[16] S.D. Sudhoff, S.F. Glover, Admittance space stability analysis of power electronic systems, IEEE Trans. Aerosp. Electron. Syst. 36 (3 PART 1) (2000) 965−973.

[17] B. Wen, R. Burgos, D. Boroyevich, P. Mattavelli, Z. Shen, AC stability analysis and dq frame impedance specifications in power-electronics-based distributed power systems, IEEE J. Emerging Sel. Top. Power Electron. 5 (4) (2017) 1455−1465.

[18] B. Wen, D. Boroyevich, R. Burgos, P. Mattavelli, Z. Shen, Small-signal stability analysis of three-phase AC systems in the presence of constant power loads based on measured d-q frame impedances, IEEE Trans. Power Electron. 30 (10) (2015).

[19] A. Riccobono, M. Mirz, A. Monti, Noninvasive online parametric identification of three-phase AC power impedances to assess the stability of grid-tied power electronic inverters in LV networks, IEEE J. Emerging Sel. Top. Power Electron. 6 (2) (2017) 629−647.

[20] M. Amin, M. Molinas, Understanding the origin of oscillatory phenomena observed between wind farms and HVDC systems, IEEE J. Emerging Sel. Top. Power Electron. 5 (1) (2016) 378−392.

[21] D. Marx, P. Magne, B. Nahid-Mobarakeh, S. Pierfederici, B. Davat, Large signal stability analysis tools in DC power systems with constant power loads and variable power loads-A review, IEEE Trans. Power Electron. 27 (4) (2012) 1773−1787.

[22] M. Kabalan, P. Singh, D. Niebur, Large signal Lyapunov-based stability studies in microgrids: a review, IEEE Trans. Smart Grid 8 (5) (Sepember 2017) 2287−2295.

[23] E. Nasr-azadani, et al., Stability analysis of unbalanced distribution systems with synchronous machine and DFIG based distributed generators, IEEE Trans. Smart Grid 5 (5) (2014) 2326−2338.

[24] P. Magne, B. Nahid-Mobarakeh, S. Pierfederici, General active global stabilization of multiloads DC-power networks, IEEE Trans. Power Electron. 27 (4) (April 2012) 1788−1798.

[25] A. Griffo, J. Wang, Large signal stability analysis of 'more electric' aircraft power systems with constant power loads, IEEE Trans. Aerosp. Electron. Syst. 48 (1) (January 2012) 477−489.

This book belongs to Kitab Liaison (ocd1996@gmail.com) Copyright Elsevier 2023

[26] B.P. Loop, S.D. Sudhoff, S.H. Zak, E.L. Zivi, Estimating regions of asymptotic stability of power, IEEE Trans. Control Syst. Tech. 18 (5) (2010) 1011−1022.

[27] S.R. Sanders, G.C. Verghese, Synthesis of averaged circuit models for switched power converters, IEEE Trans. Circuits Syst. 38 (8) (1991) 905−915.

[28] H. Ebrahimi, H. El-kishky, A novel generalized state-space averaging (GSSA) model for advanced aircraft electric power systems, Energy Convers. Manag. 89 (January 2015) 507−524.

[29] G.O. Kalcon, G.P. Adam, O. Anaya-Lara, S. Lo, K. Uhlen, Small-signal stability analysis of multi-terminal VSC-based DC transmission systems, IEEE Trans. Power Syst. 27 (4) (2012) 1818−1830.

[30] C.J. Sullivan, S.D. Sudhoff, E.L. Zivi, H.Ż. Stanislaw, Methods of Optimal Lyapunov Function Generation with Application to Power Electronic Converters and Systems, 2007, pp. 267−274.

This book belongs to Kitab Liaison (ocd1996@gmail.com) Copyright Elsevier 2023

This page intentionally left blank

This book belongs to Kitab Liaison (ocd1996@gmail.com)

Copyright Elsevier 2023

Chapter 8

Cyber security in power electronic systems

Subham Sahoo
Department of Energy Technology, Aalborg University, Aalborg East, Nordjylland, Denmark

8.1 Introduction

The development of carbon-neutral electrical power systems is one of the most important global technical targets and a challenge at the same time in this century. It will not only minimize emissions and the impact of global warming but will also reduce the overall public reliance on unreliable fossil fuel supplies. Wide-scale deployment of renewable energy sources (RES) such as wind and photovoltaic (PV) transmission systems, energy storage systems (ESSs), electric vehicles (EVs), and high-voltage DC (HVDC) transmission systems is seen as critical initiatives for achieving this objective [1].

Under these circumstances, grid-tied voltage source converters (VSCs) play a key role as they act as the most common energy conversion interfaces between these technologies and the electrical grid [2]. It should also be noted that VSCs allow the creation of intelligent microgrids (MGs), which are seen as intermediate aggregation entities that can either function in stand-alone mode or facilitate the integration of distributed energy resources in grid-tied mode on a large scale [3,4]. As the number of VSCs in the power grid increases, their impact on these grids is also becoming more pronounced. With the grid modernization being carried out swiftly, several VSCs are integrated into the existing distribution network to provide grid-supportive services.

In reality, the assimilation of these facilities has led to a plight, creating a direct tradeoff between reliability and security for larger interconnected VSC network. In fact, such large-scale monitoring using supervisory control and data acquisition (SCADA) makes it highly susceptible to malicious intrusions. In addition, the reliability aspect involved in deep integration of communication layers in order to achieve synchronization often leads to new safety issues. These threats range from theft to cyber attack, which may eventually lead to system collapse, cascaded failure, damage to consumer loads, endangered activities in the energy market, etc [5]. Many cyber power outage

Control of Power Electronic Converters and Systems. https://doi.org/10.1016/B978-0-12-819432-4.00007-X
Copyright © 2021 Elsevier Ltd. All rights reserved.

This book belongs to Kitab Liaison (ocd1996@gmail.com)
Copyright Elsevier 2023

incidents in Brazil have been published [6], including the SQL Slammer worm attack, the Stuxnet attack, and numerous industrial calamities. In addition, the McAfee Study [7] reported that 80% of the utility companies encountered at least one denial of service (DoS) attack in their communication network, with 85% of unit data penetrated by an adversary. Since the most popular mode of communication in smart grids is wireless, IT security customers control different data protection policies to tackle data transmission device unreliability. However, smartly designed cyber attacks with abundant system information create disparity in securing the electrical grid, as they easily bypass the model verification tests [8]. It emanates additional vulnerabilities from the perspective of control systems in the smart grid, since the newly established methods of verification are mostly based on information technologies.

Intelligent attacks often seek to monitor the integrity of the system as a concealed disorder. This mandates the detection of cyber attacks in a timely manner in order to avoid unnecessary system casualties, taking into account a considerable timescale separation of the control phases of the VSC with a value of no more than 0.1 s. Apart from the said liabilities, it also violates confidentiality and the optimal functioning of the system almost immediately on one hand. On the other hand, the attacker can initiate the attack in slightly alarming circumstances to arrange drastic system shutdowns, since the penetration of intelligent attacks continues stealthily without being detected by control-theoretical solutions. Such situations would be considered as alternatives to planning and power backup. Therefore, the emphasis on resolving these critical safety issues needs to be the suitable design for VSC for secure, robust, and intelligent control methodologies.

For the purpose of better understanding of security problems in the control of cyber physical power electronic systems, this chapter will discuss the following points:

1. Control and operational challenges faced by the VSCs used in different applications due to cyber attacks.
2. A brief overview of the vulnerabilities in the control and cyber layer of VSCs (in grid-connected and stand-alone mode) is provided. Further, more aspects on how it disorients their operation from the state of normalcy is detailed.
3. Directions and viewpoints, especially in the design of resilient control formulation for VSCs.

8.2 Cyber physical architecture of power electronic converters

A typical architecture of the network of VSCs connected to the AC grid is shown in Fig. 8.1. There are several phases in the total power conversion chain, such as input, input-side power transformer, DC voltage phase, VSC

This book belongs to Kitab Liaison (ocd1996@gmail.com) Copyright Elsevier 2023

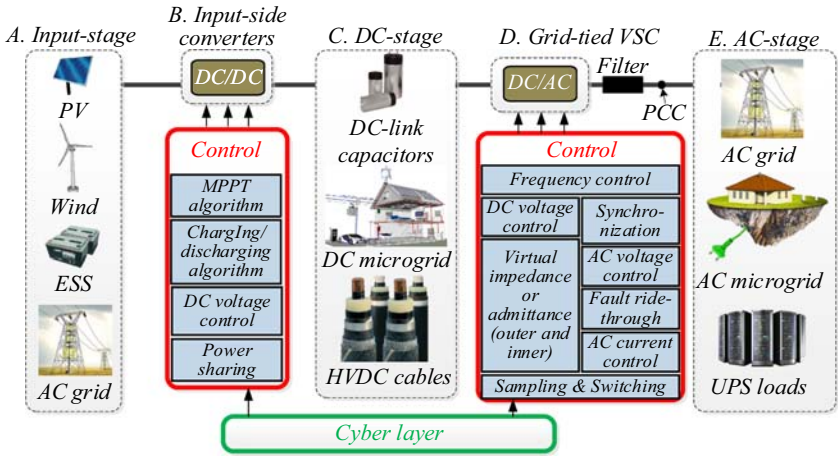

FIGURE 8.1 Control and physical stages in an individual grid-tied voltage source converter system connected in different configurations.

network stage, AC grid stage, and cyber stage, as shown in Fig. 8.1. This kind of power architecture is used most commonly for RES interfaces such as wind and PV [9], ESS [10], and the electric grids EV charging network [11]. In order to improve the strength and reliability of smart grids, it is anticipated that individual VSC systems will be interconnected through a unique all-inclusive cyber physical smart grid through communication links in the near future. The control stages which are referred to the above segments are listed in the sections below.

8.2.1 Physical stage

The exemplary input power sources/sinks are located on the far left side of Fig. 8.1. Some units in the input stage such as grid or ESS can either inject or absorb the electric power.

Input-side converters may also be programmed to automatically shift the operating modes online. These mode shifts are implemented in systems that have multiple units connected to the common DC bus and their purpose is to maintain the power balance in the common DC bus under all operating conditions. For instance, RES may change the operation from MPPT mode to voltage control mode and vice-versa. Similarly, ESSs may move from charging mode to DC voltage control mode and back. These mode shifts can be done either through a centralized supervisory control system enabled by communication technologies [12], or in a decentralized way [13,14]. The output of AC grid−tied VSC is connected through the interface filter either to an AC electrical power grid, AC MG, or to stand-alone AC loads, as shown in Fig. 8.1. The most common filter structures are *L*, *LC*, and *LCL*.

This book belongs to Kitab Liaison (ocd1996@gmail.com) Copyright Elsevier 2023

The connection point is commonly referred to as the point of common coupling (PCC). Depending on the type of connection, different standards are applicable. For instance, in the case of grid connection, voltage at the PCC is defined by the legacy AC grid so primary concern of VSC is to regulate the grid current with high quality in steady state and with predefined behavior during transients (e.g., voltage sags, swells, and unbalances) [15]. Recently, an increasing number of grid-ancillary services related to grid voltage and frequency support are also required [15]. Based on its interconnection with different AC stages, various standards are applicable. For electric grid, the primary concern lies with the regulation of grid current with high power qualitative signatures during transients (voltage sags, swells, and unbalances) [15]. In recent years, increased numbers of grid-ancillary services are also required in terms of grid stress reduction and frequency support [15]. On the other hand, its output in an inertia-free autonomous system, such as MG systems, is effectively regulated with the ability to share active and reactive control. Such objectives are accomplished by primary control of the quantities described above, which will be discussed later in this chapter.

8.2.2 Cyber stage

As smart grid comprising of numerous VSCs, together with conventional synchronous generators, jointly regulate the grid, each of these units is termed as an agent for an exemplary portion of a smart grid with interconnected VSCs.

The sensors and controllers that operate jointly in the smart grid are linked by a communication network. Each agent can interact in two different ways: (a) to a central controller and (b) among each other in a distributed manner. A pictorial description of both the cyber structures is provided in Fig. 8.2, where the dotted lines represent the flow of information. Since the control objectives is highly vulnerable to single point-of-failure in a centralized network, the distributed control theory in Fig. 8.2B is used prominently to improve the reliability and scalability in power electronic—based cyber physical systems.

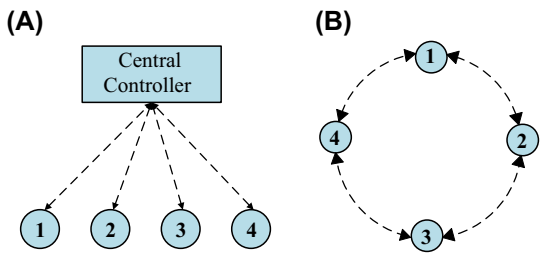

FIGURE 8.2 Communication topologies with four units: (A) Centralized control, (B) Distributed control.

This book belongs to Kitab Liaison (ocd1996@gmail.com) Copyright Elsevier 2023

Each agent has a distributed controller that uses data from local and neighboring agents. These data are typically obtained via phasor measurement units (PMUs), consisting of dynamic voltage phasors. Communication between the PMUs and local controllers can be carried out centrally, where measurements are obtained from all the agents for analysis and decision making. The SCADA framework is typically used to alleviate surveillance in smart grid networks [16]. This strategy not only requires substantial means of communication but is also vulnerable to possible cyber attacks, if the number of agents is high. Another method, commonly known as decentralized control, involves a scheme that uses only local steps. Although the communication network here is totally avoided, the capability to monitor is restricted. As already explained above, a distributed control paradigm introduces flexibility since the computational resources are uniformly dispersed across the system to achieve coordination. Hence, low bandwidth communication channels can be employed to achieve the same function. Although it offers an obvious evaluation criterion for intrusion attempts, resistance to cyber attacks cannot automatically be assured for coordinated attacks [17–20]. This can be explained owing to the inadequate information in each node for cyber attack detection.

A brief description of the control functions of AC grid–tied VSCs according to their timescales is provided in Fig. 8.3. Each control loop (as highlighted in Fig. 8.3) is shown next to each other, indicating that they are concurrently controlled (e.g., active damping and AC current control [21], DC-link voltage control and synchronization [22], or fault ride and virtual impedance/admittance control [23]). The VSC's roles in renewable-based power systems and MGs can be divided into two main categories, i.e., grid-following, and grid-forming [24].

On the other hand, the internal control loops, as shown in Fig. 8.3, are resilient to cyber attacks, because they operate for each state with a tracking objective. It is worth noting that the internal control loop only becomes vulnerable to cyber attacks when the outer control loop is unattacked. Since the secondary control layer exploits communication to alter the outer control loop references, any bad-data injection into the upper control layer (highlighted in Fig. 8.3) disorients stability or causes system shutdown. The shutdown is usually caused by the involuntary activation of overvoltage and overcurrent layers of protection. More discussion on VSC's vulnerable control layers will be conducted in the next section after a brief theory about cyber security is provided.

8.3 Vulnerability analysis of cyber attacks on control of VSCs

8.3.1 Cyber security

Cyber threats are becoming a reality with the emergence of networking technologies. These disruptions can dramatically affect the efficiency of smart

This book belongs to Kitab Liaison (ocd1996@gmail.com) Copyright Elsevier 2023

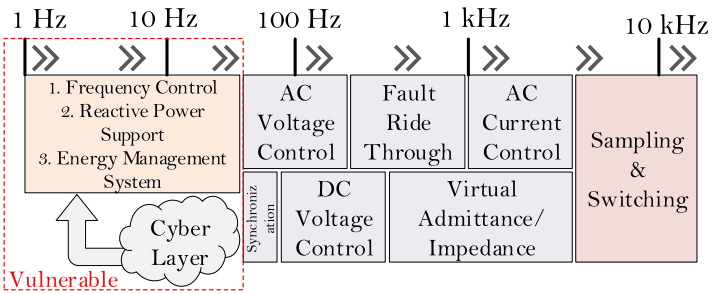

FIGURE 8.3 Conventional control structure for two-level VSC—Vulnerable control layer against cyber attacks.

grids, as it is evident from multiple real-world examples. Rapidly growing penetration of VSC technologies and their impact on the system is approaching a point, where it is difficult to disregard the risk of cyber attacks. In particular, researchers are focusing more on developing secure control methodologies rather than improving the conventional encryption-based techniques. Spoofing attacks can usually be triggered on sensors and communication links, where the signals are disrupted, quantized, or coerced. To name a few, false data injection attacks (FDIAs) are triggered by injecting auxiliary signals or altering the output of the sensor measurements [25]. It is generally referred to as the man-in-the-middle (MITM) attack when a similar activity is detected in the communication channels [26]. In addition, signal jamming can also be triggered to disrupt signal transmission, which is generally known as service denial (DoS) attack [27]. These are some of the prominent cyber attacks that have precipitated in real time [28].

8.3.2 Vulnerability assessment

A conventional single-line representation for the grid-forming VSCs is shown in Fig. 8.4. Grid-forming VSCs control local voltage and frequency. The general principle is to coordinate primary droop control locally using the available measures to synchronize with other AC sources. This decentralized system is considerably secure from a cyber space perspective, as it is difficult for the attackers to penetrate the physical layer. Additionally, effective physical layer protection alternatives such as beamforming are widely used these days [29]. However, the philosophies of decentralized management suffer from an organizational point of view when it comes to conforming to commercial regulatory requirements. Normally secondary controller conceived this drawback using the details from other VSCs. Referring to the cyber framework in Fig. 8.2, distributed or centralized secondary control systems may be placed on the primary control legislation to account for the offsets. However, this leaves the attackers a large vulnerable space to locate the

This book belongs to Kitab Liaison (ocd1996@gmail.com) Copyright Elsevier 2023

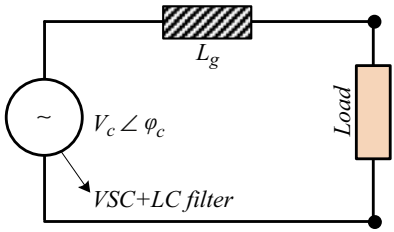

FIGURE 8.4 Simplified representation of grid-forming VSC.

attacked data in the sensors, communication links, or the controller. Below are some of the common methods of intrusion approaches to manipulate each component:

- **Sensors:** Data from the sensors are normally manipulated within the control platform by penetration of the adversary. *Trojan Horse* [30] can easily achieve this penetration by using remote systems as host. The sensor output from the acquisition panel is usually within signed 15 V. Acquisition gains using a linear plotting method are used to calibrate it against the actual measurement. The attacker usually attempts to change the acquisition gains which creates a bias in the reported measurements.
- **Communication Links:** The communicated data can be manipulated either inside the controller or in a router/encoder/decoder communication point. There are several ways in which the transmitted data can be manipulated, such as infringement of authorization, interruption of signal transmission, illegal opening of information logs, replay of the transmitted information from the past, etc.
- **Controller:** As already mentioned, the controller can be illegitimately accessed using *Trojan Horse* to modify the reference input(s) used for control of VSCs either in the outer control loop or in the secondary controller.

All the vulnerable points for grid-forming VSCs have been detailed in Table 8.1. A detailed vulnerability assessment of grid-following and grid-supporting VSCs including applications such as DFIG, HVDC, etc., follows the same hypothesis with maximum threat from the controller [31].

8.4 Cyber attack detection and mitigation mechanisms in power electronic systems

8.4.1 Detection

When the control layers of a VSC are implemented in real-time processors, intrusion into the control layer only allows access to the reference setpoints (DC-link voltage, frequency) during run-time instead of the internal control layers.

This book belongs to Kitab Liaison (ocd1996@gmail.com) Copyright Elsevier 2023

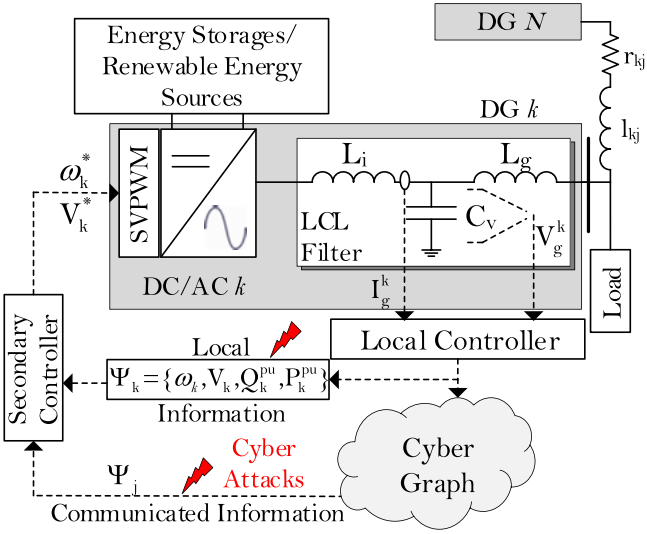

FIGURE 8.5 Basic $V-f$ control of grid-forming VSCs: Attack elements injected into sensors/communication link.

TABLE 8.1 Vulnerable points in control of grid-forming VSCs in Fig. 8.5.

Control layer	Vulnerable?
Current control	–
Voltage control	FDIA on ω^*, V^*(only without secondary controller)
Secondary control	DoS[a]/MITM[b] attack on V_j, ω_j [c] FDIA[d] on V_k, ω_k

[a]*Denial of Service.*
[b]*Man-in-the-middle.*
[c]*Communicated.*
[d]*False data injection attack.*

Since the internal loops are compiled into the processor's read-only memory portion, the device operation cannot be dissembled by intrusion into the sensor values. However, when the references are modified to cause instability or activation of the protection layer, the device dynamics can vary. Mathematically, this can be explained using the state space representation of ith VSC for a system with N VSCs using

$$\begin{aligned} \dot{x}_i(t) &= Ax_i(t) + Bu_i(t) \\ y_i(t) &= Cx_i(t) + Du_i(t) \end{aligned} \tag{8.1}$$

This book belongs to Kitab Liaison (ocd1996@gmail.com) Copyright Elsevier 2023

$\forall\ i \in N$, where $x_i = [v_g\ i_g\ P\ Q\ v_{dc}]^T$ and $u = [\omega^*\ v_{dcref}\ P^*\ Q^*\ V^*]^T$ with the state parameters x_i denoted by grid voltage, grid current, active power, reactive power, DC voltage, respectively; and the input consisting of the reference parameters of frequency, DC voltage, active power, reactive power, and inverter voltage for i^{th} VSC, respectively. Further, $x \in \mathbb{R}^N$, $u \in \mathbb{R}^M$, $y \in \mathbb{R}^S$, $A \in \mathbb{R}^{N\times N}$, $B \in \mathbb{R}^{N\times M}$, $C \in \mathbb{R}^{P\times N}$, and $D \in \mathbb{R}^{P\times M}$. Without loss of generality, it can be assumed that each state and output variable can be independently compromised by an attacker. An attack signal $\xi_i(t) \in \mathbb{R}^{P+N}$ depends specifically upon the attack strategy. If $\Sigma = \{\xi_1, \xi_2, \ldots, \xi_{N+P}\}$ is a null vector, then the system response is unbiased. To detect the presence of cyber attack elements, a residual signal r: $\mathbb{R}_{\geq 0} \rightarrow \mathbb{R}^P$ test can be followed. It is worth notifying that ξ_i is not a design parameter; as it completely depends on the intent of the attacker.

To detect attacks using a centralized attack detection filter based on a modified Luenberger observer, the estimated dynamics of ith VSC with known initial states $x(0)$ can be given by

$$\begin{aligned} \dot{\widehat{x}}_i(t) &= (A + GC)\widehat{x}_i(t) - Gy_i(t) \\ r_i(t) &= C\widehat{x}_i(t) - y_i(t) \end{aligned} \tag{8.2}$$

where $\widehat{x}_i(t)$ denote the estimated states. Further, $\widehat{x}_i(0) = x_i(0)$ and the output injection matrix $G \in \mathbb{R}^{N\times P}$ is such that $(A + GC)$ is Hurwitz. Hence, $r_i(t) \leq \overline{r}$ if and only if $\xi_i(t) = 0$ for $t \in \mathbb{R}_{\geq 0}$, where $\overline{r}$ is an infinitesimal value. It is intuitive from Fig. 8.6 that the normal residual test is passed for the violet (light gray in print version) trajectory since the residual value remains within the threshold $\overline{r}$.

Otherwise, it could be inferred that the ith VSC contains an attack element. As these attacks cause system response alteration due to modified model, the residual item overshoots out of the shaded circle in Fig. 8.6. Hence, any

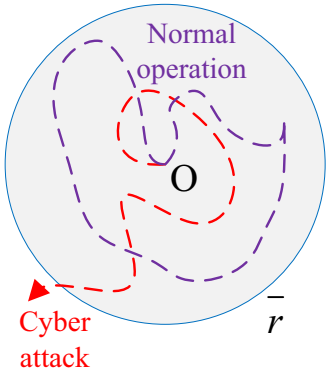

FIGURE 8.6 Attack detection filter law—Trajectories outside $\overline{r}$ denote the presence of cyber attack.

This book belongs to Kitab Liaison (ocd1996@gmail.com) Copyright Elsevier 2023

physical disturbances such as load change, faults, and line breakdown will always satisfy the abovementioned detection criteria as the dynamics of the model will always be unchanged using the unbiased measurements during these disturbances.

Based on the attacked point(s) in cyber physical power electronic systems, the designed anomaly detection model in (8.2) can be used to detect compromised controllers, sensors, and cyber links. Various cyber attack detection techniques in Table 8.2 have been designed from a control theory perspective to disregard the false data injected by the attacker. To eliminate false data in the control inputs, the vulnerable states are often adjoined using an alias relationship, also termed as the watermarking strategy [32], which theoretically is unknown to the attacker. Further to detect the presence of bad data in incoming/outgoing cyber links via an MITM attack, an improved version of the bad-data detector in (8.2) is designed only using local measurements, such that the localization principle can be leveraged [33]. Apart from maligning the communicated signal, they can also be interrupted leading to loss of information, commonly referred as DoS attacks. These attacks can be modeled as a fuzzy disturbance to the plant, leaving behind insufficient information of the attacked agent. To solve this issue, a signal temporal logic—based controller is designed in Ref. [34] to assimilate the

TABLE 8.2 Detectability of different cyber attacks in electrical networks.

Vulnerable points					
Controller	Sensors	Cyber link	Detection techniques	Attack	Remarks
✓	–	–	Watermarking [32]	Hijacking	False control inputs
✓	✓	–	Bad-data detectors [35]	FDIA	False sensing
–	–	✓	Localization [33]	MITM	Observable attacks
–	–	✓	Signal temporal logic [34]	DoS	Observable attacks
–	✓	✓	Hyperproperties [36] PI-based consensus [17–20]	Generalized FDIA	Difficult to detect
✓	✓	✓	–	Generalized FDIA	Undetectable

This book belongs to Kitab Liaison (ocd1996@gmail.com)
Copyright Elsevier 2023

time-stamped behavior of the missing communicated signal. Additionally using an artificial intelligence perspective, data-driven techniques such as artificial neural network−based controllers can also be designed to predict the missing information by studying the input−output behavior of the system.

Extending this theory for interconnected VSCs, the artificial dynamics created by the attack element can be nullified in (1), only when

$$\sum_{i=1}^{N} \xi_i = 0 \tag{8.3}$$

holds true. Further, these attacks in the attack set Σ can be categorized as *undetectable* from the monitors, if and only if $x \in \mathbb{R}^N$ such that $||sI - A||_0 + ||Cx||_0 = \phi$, where $|\Sigma| = \phi$. Such attacks are commonly termed as *coordinated* attacks, since they easily bypass the attack filters in (8.2). These attacks have also been tabulated in Table 8.2, where generalized FDIAs are detected using a systematic and sophisticated model identification tool by extracting the hyperproperties [36] or analyzing the system outputs using PI-based extended consensus algorithms [17−20], only when the sensors and cyber links are attacked concurrently. On the other hand, if all of the cyber physical entities such as controller, sensors, and cyber links are compromised, it is impossible to detect the attack element using any security conventions since the attack element has completely encapsulated the property of the system and its response to physical disturbances.

Using (8.3), it can be concluded that an external entity can manipulate the control inputs either in the controller or on the communication link(s). A brief overview of the attack detection techniques subjected to various vulnerabilities in the control layer has been schematically demonstrated in Fig. 8.7. As the cyber and control layer are closely linked, the vulnerability to cyber attacks worsens for an interconnected VSC network. As attack-vulnerable points

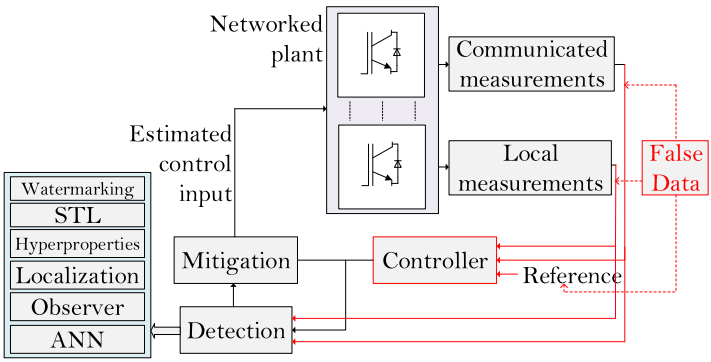

FIGURE 8.7 A schematic of detection techniques and vulnerabilities in the control layer for cyber secure measures on control of networked power electronic system.

This book belongs to Kitab Liaison (ocd1996@gmail.com)
Copyright Elsevier 2023

increase, the ancillary support provided by interconnected VSCs can be easily misled, resulting in system collapse. These effects inevitably trigger technoeconomic catastrophes by inserting false data attack vectors into the cyber physical layer to malign the electric network.

8.4.2 Mitigation

To remove the aforementioned cyber attacks in power electronic systems, the mitigating action needs to be fast, otherwise the network can become unstable or even lead to shutdown. Most cyber security papers in power electronic systems are limited to detection without providing any comprehensive steps of countermeasures for normal system operation to remove the attack element(s). Some papers also tend to remove the compromised information received from the attacked unit(s) is as an elementary approach to prevent the propagation of attack into the system [37]. As a result, the network connectivity is affected degrading the control performance. In Ref. [34], O. Beg et al. have proposed an attack impact quantification technique and suppressed the impact of attack element using a deterministic number in the low-pass filter. However, the scalability of the mitigation approach is not largely discussed. Another well-defined mitigation approach is to employ an observer for each unit to operate with the estimated states using the preattack points upon detection of attack [38]. Even though these approaches are quite efficient, they have model-intensive requirements, where their performance is highly prone to model uncertainties. Moreover, the design of observer can be complex, while its real-time execution may require heavy computational resources. Additionally, an upper bound−based mitigation condition is also proposed in Ref. [39], where the mitigation strategy is selectively determined based on the total number of compromised units, termed as F-total, or the local compromised agents in the neighborhood of each unit, termed as F-local. Although it counteracts against attacks on sensors, actuators, and communication links, it might affect the cyber graph connectivity by unnecessarily abandoning neighbor€s information during a load change even when there is no attack. As a result, its operation becomes a point of serious concern for stealth attacks, which entails zero dynamics in distributed networks. Since the abovementioned approaches are based on restrictive assumption on the information exchange in the cyber network, a self-healing mitigation strategy needs to be developed, which provides maximum resilience for the system to recover without losing the cyber network connectivity.

To address these issues, a signal reconstruction−based strategy is devised in Ref. [40], where the presence of a cyber attack in a given agent is classified as an *event*. As compared to event-triggered schemes [41], the attack detection criteria can be used as an event-triggering mechanism for the said countermeasure to operate immediately. As soon as the authentication is checked for the monitor signals, the signal reconstruction process is activated as shown in Fig. 8.8. This mandates the requirement of at least one *trustworthy* converter,

This book belongs to Kitab Liaison (ocd1996@gmail.com) Copyright Elsevier 2023

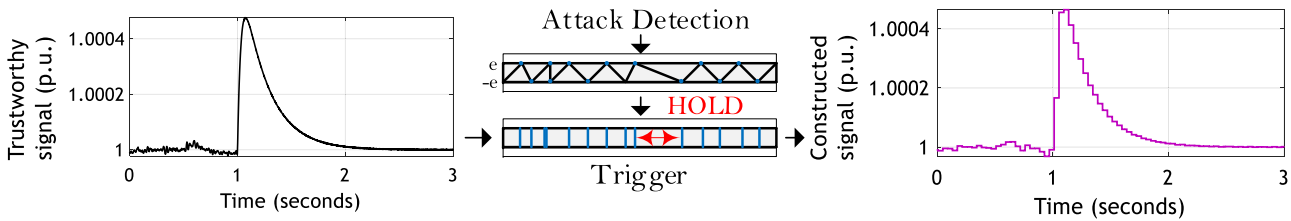

FIGURE 8.8 Signal reconstruction–based mitigation strategy against cyber attacks in power electronic systems.

This book belongs to Kitab Liaison (ocd1996@gmail.com)

Copyright Elsevier 2023

which is used as a reference to reconstruct the digital signal to be used in the compromised agent. This requirement is coordinated based on the control objectives and define an error surface to limit the difference between the trustworthy and constructed signal within $||e||$. This leads to triggering instants, wherein the intertriggering space is held to the last triggered value. In this way, the new constructed signal is generated as shown in Fig. 8.8. The resolution of the constructed signal will improve as e is kept smaller. As described in Ref. [20], the value of e can be as small as possible yet it should be sufficiently higher than the measurement noise to avoid unnecessary triggering.

Finally using the above-mentioned strategies, the most prominent cyber attacks can be removed from the conventional controllers defined for power electronic systems. Although they provide resiliency against false intrusion attempts, there could be many other shortcomings such as stability issues, determination of critical detection, and mitigation time period, which needs further investigation.

8.5 Test cases

8.5.1 Test case I

In this scenario, a ramp-based cyber attack on frequency reference is conducted on a single grid-forming VSC ($N = 1$) (as shown in Fig. 8.5) operating at a global voltage and frequency reference of 311 V and 50 Hz, respectively. More details on the system and control parameters can be referred here [42]. At t = 0.2 s, a ramp signal ω_a is injected into the frequency reference for control of grid-forming VSC in Fig. 8.9 using

$$\omega_a^* = \omega^* + \underbrace{2\pi 1000t}_{\omega_a} \tag{8.4}$$

As soon as the attack is conducted in Fig. 8.9, the frequency at which the voltage is formulated ramps up leading to issues such as heating in the LC filter and operability issues of critical loads. As this attack acts like an exogeneous disturbance to the state space equations defined for grid-forming VSC in (8.1), a

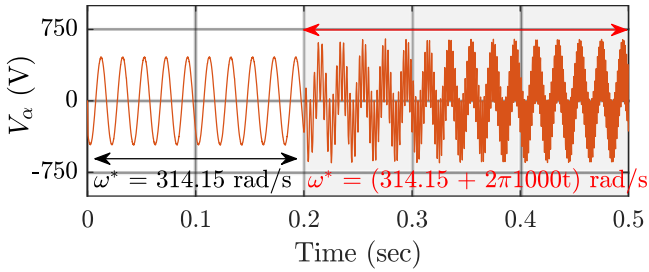

FIGURE 8.9 A ramp-based attack element is injected into the frequency reference of single VSC at t = 0.2 s—Frequency increases leading to heating and operability issues of critical loads.

This book belongs to Kitab Liaison (ocd1996@gmail.com)
Copyright Elsevier 2023

residue can be dynamically calculated using the Luenberger observer. However, such attacks conducted in multiple grid-forming VSCs at the same time can bypass the detection norms easily. This has been studied in the next case study, which mandates a robust detection scheme for *coordinated* attacks.

8.5.2 Test case II

In this scenario, a coordinated attack on frequency is carried out in a distributed AC MG (as shown in Fig. 8.5) operating at a global voltage and frequency reference of 311 V and 50 Hz, respectively, with $N = 4$ grid-forming VSCs. Since each VSC is of equal capacity of 10 kVA, the active power droop coefficients m_k are equal and, hence, active power will be shared equally. More details on the system and control parameters and control structure can be referred here [43].

As shown in Fig. 8.5, the kth distributed generators consist of a DC source (e.g., renewable energy or ESSs), VSC, LCL filter, and a controller using local measurements. In the system shown in Fig. 8.5 comprising of N agents, each communication digraph is represented via edges to constitute an adjacency matrix $\mathbf{A} = [a_{kj}] \in R^{N \times N}$, where the communication weights are given by $a_{kj} > 0$, if $(\psi_k, \psi_j) \in \mathbf{E}$, where $\mathbf{E}$ is an edge connecting two nodes, with ψ_k and ψ_j being the local and neighboring node, respectively. Otherwise, $a_{kj} = 0$. $N_k = \{j | (\psi_k, \psi_j) \in \mathbf{E}\}$ denotes the set of all neighbors of kth agent. Further, the in-degree matrix $\mathbf{Z}_{in} = \text{diag}\{z_{in}\}$ is a diagonal matrix with its elements given by $z_{in} = \sum_{j \in N_k} a_{kj}$. Further, the Laplacian matrix $\mathbf{L}$ is defined as $\mathbf{L} = \mathbf{Z}_{in} - \mathbf{A}$.

To improve their performance, neighboring VSCs' measurements, which are transmitted to the local VSC and vice-versa, are used in a cooperative secondary controller to regulate their respective bus' average voltage $\overline{V}_g^k$ and frequency ω_k. The control objectives of the cooperative controller can be mathematically represented as

$$\lim_{t \to \infty} \omega_k(t) = \omega^*, \lim_{t \to \infty} \overline{V}_g^k(t) = V^* \forall\ k \in N \tag{8.5}$$

where ω^* and V^* denote the global reference for frequency and voltage, respectively. Detailed control equations of cooperative secondary controller in AC MG can be referred from Refs. [44]. To achieve proportionate active power sharing alongwith frequency restoration, the primary layer droop control is modified into

$$\omega_k(t) = \omega^* - m_k\left(P_k(t) - P_k^{ref}(t)\right) \tag{8.6}$$

where m_p, P_k, and P_k^{ref} denote the active power droop coefficient, measured active power, and secondary control active power reference in k^{th} agent.

This book belongs to Kitab Liaison (ocd1996@gmail.com) Copyright Elsevier 2023

Basically, P_k^{ref} compensates for the error introduced by the droop coefficient in (8.6). This is done using

$$\dot{P}_k^{ref}(t) = k_1(\omega^* - \omega_k(t)) + k_2 \sum_{j \in N_k} a_{kj}(x_j(t) - x_k(t)) \tag{8.7}$$

with k_1 and k_2 being positive variables and $x = mP$. Further, N_k denotes the set of neighbors of kth agent. Substituting (8.7) in (8.6), we obtain $\mathbf{L}\boldsymbol{\omega}(t) = 0$.

However, the objectives in (8.5) can be misconstrued in the presence of cyber attacks on the frequency signal in k^{th} agent using

$$\omega_k^f(t) = \omega_k(t) + \kappa\omega_k^a \tag{8.8}$$

where $\kappa = 1$ denotes the presence of an attack element ω_k^a in k^{th} agent, or 0 otherwise. Further, these attacks can be conducted in a *coordinated* manner to deceive the system operator using

$$\dot{\boldsymbol{\omega}}(t) = -(\mathbf{L}\boldsymbol{\omega}(t) + \boldsymbol{\omega}^a) \tag{8.9}$$

where $\boldsymbol{\omega}$ and $\boldsymbol{\omega}^a$ denote column matrices of the measured frequency and attack signal for N VSCs, respectively.

Considering the attack model in (8.9), the attack can be termed as

1. **coordinated** attack, if $\dot{\boldsymbol{\omega}}(t) = 0$. Such attacks always lead to a stable and feasible solution, thereby satisfying the objectives in (8.5).
2. **noncoordinated** attack, if $\dot{\boldsymbol{\omega}}(t) \neq 0$. They disregard the objectives in (8.5).

Based on the definition of *coordinated* attacks, it can be concluded that $\sum_{k=1}^{N} \omega^a = 0$ for cooperative synchronization holds true. Conversely, $\sum_{k=1}^{N} \omega^a \neq 0$ for *noncoordinated* attacks.

In Fig. 8.10, when an attack of $\boldsymbol{\omega}^a = 2\pi\{0.1, 0, -0.1, 0\}$ rad/s is introduced at $t = 0.5$ s, frequency and active power converge back to the corresponding references, as defined in the control objectives. As defined above, all the necessary conditions are met, which certifies it as a *coordinated* attack. However, at $t = 1.5$ s, the attacker maintains this discretion and increases one attack element in $\boldsymbol{\omega}^a = 2\pi\{10, 0, -0.1, 0\}$ rad/s. As a result, it can be seen that ω_1 immediately goes outside the boundary of operation [49.5, 50.5] Hz (as highlighted in Fig. 8.10) defined for the MG. As the frequencies reach close to the aforementioned threshold, it could unnecessarily lead to the activation of protective relays, which could cause shutdown of the whole MG.

Finally, the resilience capability of the signal reconstruction strategy in Fig. 8.8 is studied for test case II using only one trustworthy frequency input. In Fig. 8.11, it can be seen that the detection mechanism for the attack model in (8.9) activates the proposed signal reconstruction strategy at $t = 0.5$ s, which immediately brings the system to follow the control objectives despite the presence of attacks. Following the *coordinated* attack, it also bypasses the

This book belongs to Kitab Liaison (ocd1996@gmail.com) Copyright Elsevier 2023

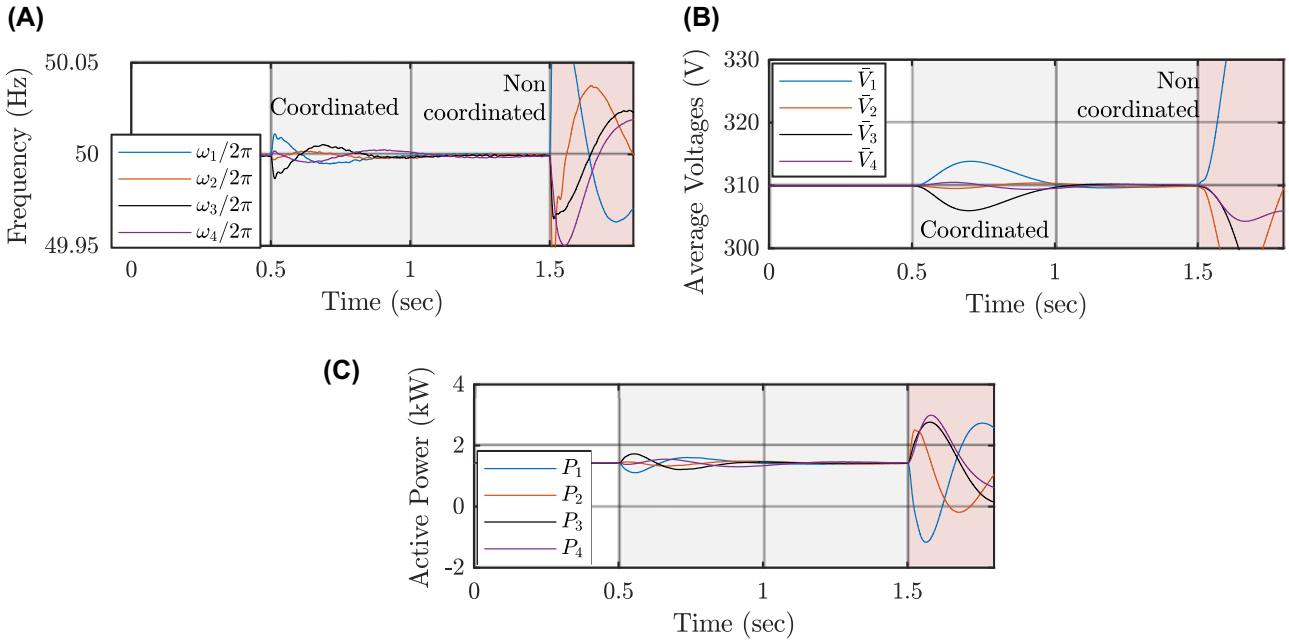

FIGURE 8.10 Case study for $N = 4$ grid-forming VSCs in Fig. 8.5—(a) Frequency, (b) Average Voltages and (c) Active Power. Attacker conducts a *coordinated* attack first to deceive the system operator and then conducts a *non-coordinated* attack resulting in operation outside the allowable range.

This book belongs to Kitab Liaison (ocd1996@gmail.com)

Copyright Elsevier 2023

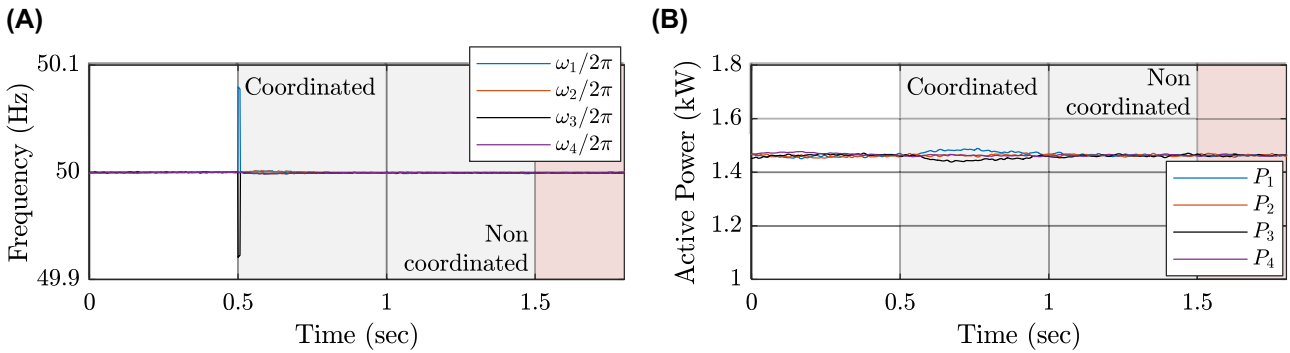

FIGURE 8.11 Case study for $N = 4$ grid-forming VSCs in Fig. 8. 5—(a) Frequency, (b) Active Power. The event-driven resilient controller mitigates the *coordinated* attack immediately based on the detection philosophy proposed in Ref. [40].

This book belongs to Kitab Liaison (ocd1996@gmail.com)

Copyright Elsevier 2023

impact of *noncoordinated* attack at $t = 1.5$ s. Hence, this strategy can be effectively used to mitigate cyber attacks to maximum degree of resiliency.

As it is evident from the impact and behavior of the system, it is important to establish a generic strategy for detection and mitigation of attacks to provide a resilient networked control norm. In addition, network observability needs to be accommodated to develop a robust control mechanism for cyber attacks to improve security in the modern electric grid.

8.6 Conclusions and future challenges

In this chapter, from power electronic system point of view, the challenges and vulnerabilities associated with controlling modern grid-tied power converters due to cyber attacks were analyzed. Initially, the basic concepts of local control used by VSCs in different fields and applications were updated. Then, we provided an overview of possible attacks and their effect on interconnected converters. A comprehensive tutorial is given about the vulnerable points in the control and communication layer used for controlling grid-forming converters. Two test cases considering grid-forming VSCs are conducted using these attack models as proof of concept to illustrate the implications of cyber attacks. Cyber attacks with limited complexity have been shown to result in system failure, cause disruption, and potentially harm to consumer appliances. To resolve these issues, resilient control systems need to be established as a potential scope of work to reduce the effect of cyber attacks on the electrical grid. The design of resilient strategies includes a clear understanding of the layer of control and security. Ideally, eliminating the communication channel to promote localized control strategies will enable the protection of the electronic power converters. However, from an efficiency viewpoint, this notion elevates up as an overstatement. Therefore, it is important to restrict the cyber physical interactions to a minimum synergy by targeting a manageable system output tradeoff. Accommodating these perspectives, designing resilient technology and planning a line of defense against cyber attacks is a new objective to improve the security and efficiency of the power electronic converters in the electric grid.

References

[1] B.V. Mathiesen, H. Lund, K. Karlsson, 100% renewable energy systems, climate mitigation and economic growth, Appl. Energy 88 (2) (2011) 488–501.

[2] F. Blaabjerg, R. Teodorescu, M. Liserre, A.V. Timbus, Overview of control and grid synchronization for distributed power generation systems, IEEE Trans. Ind. Electron. 53 (5) (October 2006) 1398–1409.

[3] J. Rocabert, A. Luna, F. Blaabjerg, P. Rodriguez, Control of power converters in AC microgrids, IEEE Trans. Power Electron. 27 (11) (November 2012) 4734–4749.

This book belongs to Kitab Liaison (ocd1996@gmail.com) Copyright Elsevier 2023

[4] T. Dragicevic, X. Lu, J.C. Vasquez, J.M. Guerrero, DC microgrids-Part II: a review of power architectures, applications, and standardization issues, IEEE Trans. Power Electron. 31 (5) (May 2016) 3528−3549.

[5] Y. Mo, T.H.-J. Kim, K. Brancik, D. Dickinson, H. Lee, A. Perrig, B. Sinopoli, "Cyber−physical security of a smart grid infrastructure, Proc. IEEE 100 (1) (2011) 195−209.

[6] F. Pasqualetti, F. Dorfler, F. Bullo, Control-theoretic methods for cyberphysical security: geometric principles for optimal cross-layer resilient control systems, IEEE Contr. Sys. Mag. 35 (1) (2015) 110−127.

[7] S.A. Baker, N. Filipiak, K. Timlin, In the Dark: Crucial Industries Confront Cyber Attacks, McAfee, 2011. Incorporated.

[8] F. Pasqualetti, F. Dörfler, F. Bullo, Attack detection and identification in cyber-physical systems, IEEE Trans. Automat. Contr. 58 (11) (2013) 2715−2729.

[9] J.M. Carrasco, L.G. Franquelo, J.T. Bialasiewicz, E. Galvan, R.C. PortilloGuisado, M.A.M. Prats, J.I. Leon, N. Moreno-Alfonso, Power-electronic systems for the grid integration of renewable energy sources: a survey, IEEE Trans. Ind. Electron. 53 (4) (June 2006) 1002−1016.

[10] C.A. Hill, M.C. Such, D. Chen, J. Gonzalez, W.M. Grady, Battery energy storage for enabling integration of distributed solar power generation, IEEE Trans. Smart Grid 3 (2) (June 2012) 850−857.

[11] M. Yilmaz, P.T. Krein, Review of battery charger topologies, charging power levels, and infrastructure for plug-in electric and hybrid vehicles, IEEE Trans. Power Electron. 28 (5) (May 2013) 2151−2169.

[12] T. Dragicevic, J. Guerrero, J. Vasquez, D. Skrlec, Supervisory control of an adaptive-droop regulated dc microgrid with battery management capability, IEEE Trans. Power Electron 29 (2) (2014) 695−706.

[13] J. Schonberger, R. Duke, S. Round, DC-Bus signaling: a distributed control strategy for a hybrid renewable nanogrid, IEEE Trans. Ind. Electron. 53 (5) (Oct. 2006) 1453−1460.

[14] D. Boroyevich, I. Cvetkovic, D. Dong, R. Burgos, F. Wang, F. Lee, Future electronic power distribution systems a contemplative view, in: 2010 12th International Conference on Optimization of Electrical and Electronic Equipment, IEEE, May 2010, pp. 1369−1380.

[15] "Ieee Standard for Interconnection and Interoperability of Distributed Energy Resources with Associated Electric Power Systems Interfaces," *IEEE Std 1547-2018* (Revision of IEEE Std 1547-2003), April 2018, pp. 1−138.

[16] S.A. Boyer, SCADA: Supervisory Control and Data Acquisition, International Society of Automation, 2009.

[17] S. Sahoo, S. Mishra, J.C. Peng, T. Dragicevic, A stealth cyber attack detection strategy for dc microgrids, IEEE Trans. Power Electron. 34 (8) (2019) 8162−8174, https://doi.org/10.1109/TPEL.2018.2879886.

[18] S. Sahoo, J.C. Peng, A. Devakumar, S. Mishra, T. Dragičević, "On detection of false data in cooperative dc microgrids€"a discordant element approach, IEEE Trans. Ind. Electron. 67 (8) (2020) 6562−6571.

[19] S. Sahoo, J.C. Peng, S. Mishra, T. Dragičević, Distributed screening of hijacking attacks in dc microgrids, IEEE Trans. Power Electron. 35 (7) (2020) 7574−7582.

[20] S. Sahoo, T. Dragicevic, F. Blaabjerg, Resilient operation of heterogeneous sources in cooperative dc microgrids, IEEE Trans. Power Electron. 35 (12) (2020) 12601−12605, https://doi.org/10.1109/TPEL.2020.2991055.

This book belongs to Kitab Liaison (ocd1996@gmail.com) Copyright Elsevier 2023

[21] W. Wu, Y. Liu, Y. He, H.S.H. Chung, M. Liserre, F. Blaabjerg, Damping methods for resonances caused by lcl-filter-based current-controlled grid-tied power inverters: an overview, IEEE Trans. Ind. Electron. 64 (9) (Sept 2017) 7402−7413.

[22] L. Harnefors, X. Wang, A.G. Yepes, F. Blaabjerg, Passivity-based stability assessment of grid-connected vscs: an overview, IEEE J. Em. Sel. Topics Power Electron. 4 (1) (March 2016) 116−125.

[23] D.M. Vilathgamuwa, P.C. Loh, Y. Li, Protection of microgrids during utility voltage sags, IEEE Trans. Ind. Electron. 53 (5) (Oct 2006) 1427−1436.

[24] K.D. Brabandere, B. Bolsens, J.V. den Keybus, A. Woyte, J. Driesen, R. Belmans, A voltage and frequency droop control method for parallel inverters, IEEE Trans. Power Electron. 22 (4) (July 2007) 1107−1115.

[25] Y. Liu, P. Ning, M.K. Reiter, False data injection attacks against state estimation in electric power grids, ACM Trans. Inf. Syst. Secur. 14 (1) (2011) 13.

[26] F. Callegati, W. Cerroni, M. Ramilli, Man-in-the-middle attack to the https protocol, IEEE Security and Privacy 7 (1) (2009) 78−81.

[27] A.D. Wood, J.A. Stankovic, Denial of service in sensor networks, Computer 35 (10) (2002) 54−62.

[28] G. Liang, J. Zhao, F. Luo, S.R. Weller, Z.Y. Dong, A review of false data injection attacks against modern power systems, IEEE Trans. Smart Grid 8 (4) (2016) 1630−1638.

[29] Y.-S. Shiu, S.Y. Chang, H.-C. Wu, S.C.-H. Huang, H.-H. Chen, Physical layer security in wireless networks: a tutorial, IEEE Wireless Comm. 18 (2) (2011) 66−74.

[30] A. Stefanov, C.-C. Liu, Cyber-power system security in a smart grid environment, in: 2012 IEEE PES Innovative Smart Grid Technologies (ISGT), IEEE, 2012, pp. 1−3.

[31] S. Sahoo, T. Dragičević, F. Blaabjerg, "Cyber security in control of grid-tied power electronic converters€"challenges and vulnerabilities, IEEE J. Emerg. Select. Topics Power Electron. (2019), pp. 1−1.

[32] B. Satchidanandan, P.R. Kumar, "Dynamic watermarking: active defense of networked cyber€"physical systems, Proc. IEEE 105 (2) (2017) 219−240.

[33] K. Pan, A. Teixeira, M. Cvetkovic, P. Palensky, Cyber risk analysis of combined data attacks against power system state estimation, IEEE Trans. Smart Grid 10 (3) (2018) 3044−3056.

[34] O.A. Beg, L.V. Nguyen, T.T. Johnson, A. Davoudi, Signal temporal logic-based attack detection in dc microgrids, IEEE Trans. Smart Grid 10 (4) (2018) 3585−3595.

[35] E. Handschin, F.C. Schweppe, J. Kohlas, A. Fiechter, Bad data analysis for power system state estimation, IEEE Trans. Power Apparatus Syst. 94 (2) (1975) 329−337.

[36] O.A. Beg, T.T. Johnson, A. Davoudi, Detection of false-data injection attacks in cyber-physical dc microgrids, IEEE Trans. Ind. Informat. 13 (5) (2017) 2693−2703.

[37] S. Sundaram, C.N. Hadjicostis, Distributed function calculation via linear iterative strategies in the presence of malicious agents, IEEE Trans. Automat. Contr. 56 (7) (2010) 1495−1508.

[38] K. Manandhar, X. Cao, F. Hu, Y. Liu, Detection of faults and attacks including false data injection attack in smart grid using kalman filter, IEEE Trans. Control Network Syst. 1 (4) (2014) 370−379.

[39] S. Sundaram, B. Gharesifard, Consensus-based distributed optimization with malicious nodes, in: 2015 53rd Annual Allerton Conference on Communication, Control, and Computing (Allerton), IEEE, 2015, pp. 244−249.

This book belongs to Kitab Liaison (ocd1996@gmail.com) Copyright Elsevier 2023

[40] S. Sahoo, Y. Yang, F. Blaabjerg, Resilient synchronization strategy for ac microgrids during cyber attacks, IEEE Trans. Power Electron. 36 (1) (2021) 73−77, https://doi.org/10.1109/TPEL.2020.3005208.

[41] S. Sahoo, S. Mishra, An adaptive event-triggered communication-based distributed secondary control for dc microgrids, IEEE Trans. Power Electron. 9 (6) (2017) 6674−6683.

[42] T. Dragičević, Model predictive control of power converters for robust and fast operation of ac microgrids, IEEE Trans. Power Electron. 33 (7) (2018) 6304−6317.

[43] Q. Shafiee, J.M. Guerrero, J.C. Vasquez, "Distributed secondary control for islanded microgrids−a novel approach, IEEE Trans. Power Electron. 29 (2) (2013) 1018−1031.

[44] R. Rana, S. Sahoo, S. Mishra, J.C. Peng, Performance validation of cooperative controllers in autonomous ac microgrids under communication delay, in: 2019 IEEE Power Energy Society General Meeting (PESGM), 2019, pp. 1−5.

This book belongs to Kitab Liaison (ocd1996@gmail.com) Copyright Elsevier 2023

Chapter 9

Advanced modeling and control of voltage source converters with LCL filters

Bochen Liu[1], Dao Zhou[1], Frede Blaabjerg[1]
[1]*Department of Energy Technology, Aalborg University, Aalborg, Denmark*

9.1 Introduction

In this chapter, various switched models of the *LCL*-filtered voltage source converters (VSCs) in *abc*-, $\alpha\beta$-, and *dq*-reference frames are firstly introduced in Section 9.2. Especially, the original sinusoidal AC voltage and currents are transformed to the constant DC components in *dq* frame, together with the rotating grid phasor. This can facilitate the simplification of the steady-state grid current control and help to build the continuous time-independent averaged model in *dq* frame. However, this model can only predict the converter open-loop behavior with a given switching function, and it cannot model the cross-coupling of different harmonic components. By addressing this harmonic coupling issue and considering unbalanced grid situations, the dynamic phasor model is introduced, where the averaged values of different harmonic components are included and thus is also called generalized averaged model (GAM). Next, in order to further describe the transient response of each harmonic component in the VSC, which can be regarded as a linear time-periodic (LTP) system, the harmonic state space (HSS) model can be used. Besides, this model is developed by imitating the linear time-invariant (LTI) system and therefore the already developed control and analysis methods for LTI systems can also be applied.

Afterward, in terms of the converter control, a fundamental *dq*-frame–based DC-link voltage and alternating current control are firstly introduced in Section 9.3. Therein, each variable is expressed by the complex form and is ready to further analyze the system performance (e.g., stability and harmonic effect) using the tools of complex space factors and complex transfer function. In order to tackle the resonance phenomenon caused by *LCL* filter, different damping methods including passive damping (PD) and active damping (AD)

Control of Power Electronic Converters and Systems. https://doi.org/10.1016/B978-0-12-819432-4.00015-9
Copyright © 2021 Elsevier Ltd. All rights reserved.

This book belongs to Kitab Liaison (ocd1996@gmail.com)
Copyright Elsevier 2023

are introduced to suppress the peak resonance. Moreover, an alternating current control procedure is presented for unbalanced grid situations, where the grid-phase extraction and positive/negative-sequence decoupling submodules are explained in detail.

Besides, considering the widely varying grid impedance in increasing distribution generation systems, the converter stability analysis in weak grids is conducted in Section 9.4. By integrating the capacitor current feedback into the system control so as to damp the *LCL* filter resonance, the system control procedure is firstly illustrated in $\alpha\beta$ and dq frame. On this basis, the equivalent VSC output impedance can be derived and the converter stability analysis can be implemented. Simulation results are presented to validate the analysis.

9.2 Modeling of the VSCs with *LCL* filters

Firstly, which is developed in DC−DC power converters, the state space averaging approach [1] is often used to filter out the switching ripples and thus an averaged nonlinear but time-invariant model can be obtained. However, this approach cannot directly be applied to VSCs due to the time-periodic operating trajectory of the AC system [2]. Hence, a reference frame transformation technique (i.e., Clarke transformation and Park transformation) is introduced to transfer the static three-phase system to a rotating two-phase system, where the AC operating trajectory is transformed as the DC operating point. On the other hand, in an unbalanced power grid, more frequency terms need to be considered due to the positive-sequence and negative-sequence components of the AC system. By addressing this, a generalized averaging model (GAM [3,4], also known as the dynamic phasor model [5−7]) and the HSS model [8−10] can be developed to transform the discrete switching events into a continuous model, which is much more easier to analyze. Due to the page limitation, only the large signal model using these three modeling methods is illustrated. But the similar modeling procedure can be applied to derive the small-signal model for linearizing at an equilibrium operating point.

9.2.1 Modeling methods in balanced three-phase systems

A typical VSC with LCL filter is shown in Fig. 9.1 and the three-phase system equations can be obtained from the circuit

$$\begin{cases} L_f \dfrac{d\mathbf{i_f}}{dt} + R_f \mathbf{i_f} = \dfrac{u_{dc}}{2}\mathbf{S} - \mathbf{u_{cf}} - u_n \mathbf{I} \\ C_f \dfrac{d\mathbf{u_{cf}}}{dt} = \mathbf{i_f} - \mathbf{i_g} \\ L_g \dfrac{d\mathbf{i_g}}{dt} + R_g \mathbf{i_g} = \mathbf{u_{cf}} - \mathbf{u_g} + \left(u_n - u_n'\right)\mathbf{I} \\ C \dfrac{du_{dc}}{dt} = i_{dc} - \mathrm{S}^{\mathrm{T}} \mathbf{i_f} \end{cases} \tag{9.1}$$

This book belongs to Kitab Liaison (ocd1996@gmail.com) Copyright Elsevier 2023

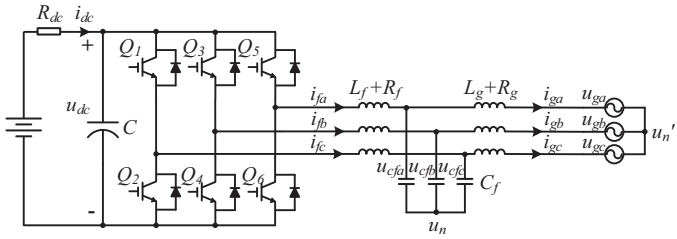

FIGURE 9.1 Typical structure of three-phase grid-tied voltage source converter with LCL filter.

where $\mathbf{i_g} = [i_{ga}\ i_{gb}\ i_{gc}]^{\mathrm{T}}$ is the grid-side current vector, $\mathbf{i_f} = [i_{fa}\ i_{fb}\ i_{fc}]^{\mathrm{T}}$ the inverter-side current vector, $\mathbf{i_{cf}} = [i_{cfa}\ i_{cfb}\ i_{cfc}]^{\mathrm{T}}$ the filtering capacitor current vector, $\mathbf{u_{cf}} = [u_{cfa}\ u_{cfb}\ u_{cfc}]^{\mathrm{T}}$ the capacitor voltage vector, $\mathbf{u_g} = [u_{ga}\ u_{gb}\ u_{gc}]^{\mathrm{T}}$ the grid voltage vector, $\mathbf{S} = [S_a\ S_b\ S_c]^{\mathrm{T}}$ the control signal vector ($S_a\ S_b\ S_c = 1,\ -1$), u_n and u_n' are the voltages at neutral points, and $\mathbf{I}$ is a unit column vector defined as $[1\ 1\ 1]^{\mathrm{T}}$.

Due to the Kirchhoff's laws, there are

$$\begin{cases} i_{ga} + i_{gb} + i_{gc} = 0 \\ i_{cfa} + i_{cfb} + i_{cfc} = 0 \\ i_{fa} + i_{fb} + i_{fc} = 0 \end{cases} \tag{9.2}$$

Combining Eqs. (9.1) and (9.2), the neutral point voltages u_n and u_n' can be derived as

$$\begin{cases} u_n = \dfrac{u_{dc}}{6}(S_a + S_b + S_c) - \dfrac{1}{3}(u_{cfa} + u_{cfb} + u_{cfc}) \\ u_n' = \dfrac{u_{dc}}{6}(S_a + S_b + S_c) - \dfrac{1}{3}(u_{ga} + u_{gb} + u_{gc}) \end{cases} \tag{9.3}$$

In balanced three-phase power grids, $u_{ga} + u_{gb} + u_{gc} = 0$ and $u_{ca} + u_{cb} + u_{cc} = 0$, and thus Eq. (9.3) is simplified to be

$$u_n = u_n' = \frac{u_{dc}}{6}(S_a + S_b + S_c) \tag{9.4}$$

According to Eq. (9.4), the new expressions for balanced three-phase systems can be written as

$$\begin{cases} L_f \dfrac{d\mathbf{i_f}}{dt} + R_f \mathbf{i_f} = \dfrac{u_{dc}}{2}\mathbf{S} - \mathbf{u_{cf}} - u_n \mathbf{I} \\ C_f \dfrac{d\mathbf{u_{cf}}}{dt} = \mathbf{i_f} - \mathbf{i_g} \\ L_g \dfrac{d\mathbf{i_g}}{dt} + R_g \mathbf{i_g} = \mathbf{u_{cf}} - \mathbf{u_g} \\ C \dfrac{du_{dc}}{dt} = i_{dc} - \mathbf{S}^{\mathrm{T}} \mathbf{i_f} \end{cases} \tag{9.5}$$

This book belongs to Kitab Liaison (ocd1996@gmail.com)
Copyright Elsevier 2023

Eq. (9.5) is the switched model of the VSC with LCL filters in balanced three-phase power systems. Without loss of generality, applying a moving average technique to an n-length signal vector $\mathbf{x} = [x_1, x_2, x_3 \ldots x_n]$, the result is

$$\langle \mathbf{x} \rangle_{avg} = \frac{1}{T_{sw}} \left[\int_{t-T_{sw}}^{t} x_1(\tau)d\tau, \int_{t-T_{sw}}^{t} x_2(\tau)d\tau, \int_{t-T_{sw}}^{t} x_3(\tau)d\tau \ldots \int_{t-T_{sw}}^{t} x_n(\tau)d\tau \right] \tag{9.6}$$

Therein, T_{sw} is the width of the averaged time window, and it is usually equal to one switching period in power electronic converters. Applying moving average technique to the switched model in Eq. (9.5), the averaged model of the VSC with *LCL* filter can be derived as

$$\begin{cases} L_f \dfrac{d\langle \mathbf{i_f} \rangle_{avg}}{dt} + R_f \langle \mathbf{i_f} \rangle_{avg} = \dfrac{\langle u_{dc} \rangle_{avg}}{2} \langle \mathbf{S} \rangle_{avg} - \langle \mathbf{u_{cf}} \rangle_{avg} - \langle u_n \rangle_{avg} \mathbf{I} \\ C_f \dfrac{d\langle \mathbf{u_{cf}} \rangle_{avg}}{dt} = \langle \mathbf{i_f} \rangle_{avg} - \langle \mathbf{i_g} \rangle_{avg} \\ L_g \dfrac{d\langle \mathbf{i_g} \rangle_{avg}}{dt} + R_g \langle \mathbf{i_g} \rangle_{avg} = \langle \mathbf{u_{cf}} \rangle_{avg} - \langle \mathbf{u_g} \rangle_{avg} \\ C \dfrac{d\langle u_{dc} \rangle_{avg}}{dt} = \langle i_{dc} \rangle_{avg} - \langle \mathbf{S^T} \rangle_{avg} \langle \mathbf{i_f} \rangle_{avg} \end{cases} \tag{9.7}$$

It should be noted that by assuming that the DC output voltage u_{dc} and the converter-side current $\mathbf{i_f}$ hardly change in one switching period, the items $\langle u_{dc}\mathbf{S} \rangle_{avg}$ and $\langle \mathbf{S^T i_f} \rangle_{avg}$ in Eq. (9.5) are approximately equal to $\langle u_{dc} \rangle_{avg} \langle \mathbf{S} \rangle_{avg}$ and $\langle \mathbf{S^T} \rangle_{avg} \langle \mathbf{i_f} \rangle_{avg}$ in Eq. (9.7), respectively.

In this way, the variables in Eq. (9.5) are transformed to be continuous, and thus Eq. (9.7) is named as continuous-time averaged model of VSC converter. However, the model in Eq. (9.7) is still nonlinear and time varying due to the AC currents (i.e., $\mathbf{i_f}$, $\mathbf{i_g}$) and AC voltages (i.e., $\mathbf{u_{cf}}$, $\mathbf{u_g}$). In order to linearize the averaged model in Eq. (9.7), a coordinate transformation technique is usually adopted. In balanced power systems, the AC voltages or currents contain no zero-sequence components. Hence, by using Clarke transformation, the three-phase *abc* frame can be converted into the two-phase static $\alpha\beta$-reference frame, i.e.,

$$\begin{bmatrix} x_\alpha \\ x_\beta \end{bmatrix} = \underbrace{\frac{2}{3} \begin{bmatrix} 1 & -\frac{1}{2} & -\frac{1}{2} \\ 0 & \frac{\sqrt{3}}{2} & -\frac{\sqrt{3}}{2} \end{bmatrix}}_{T_{\alpha\beta}} \begin{bmatrix} x_a \\ x_b \\ x_c \end{bmatrix} \tag{9.8}$$

where x_a, x_b, x_c represent the three-phase voltages or currents and x_α, x_β are the converted variables in $\alpha\beta$-reference frame. The constant coefficient 2/3 is used

This book belongs to Kitab Liaison (ocd1996@gmail.com) Copyright Elsevier 2023

to keep the same peak value in both coordinate frames ($\sqrt{2}/3$ or $\sqrt{2/3}$ for root-mean-square and power-invariant scaling, respectively). Although the three-phase quantities are transformed into two-phase quantities, x_α and x_β are still time-dependent variables. Thus, a Park transformation is needed to further transform the static two-phase $\alpha\beta$ frame to the synchronous rotating dq frame, which is

$$\begin{bmatrix} x_d \\ x_q \end{bmatrix} = \underbrace{\begin{bmatrix} \cos\omega t & \sin\omega t \\ -sin\ \omega t & \cos\omega t \end{bmatrix}}_{T_{dq}} \begin{bmatrix} x_\alpha \\ x_\beta \end{bmatrix} \tag{9.9}$$

Therein, x_d, x_q are the transformed components in dq-reference frame, and ω is the angular speed of the rotating frame, which can be obtained by grid synchronization technique. Taking the voltage vector $\mathbf{u_g}$ in Eq. (9.1) as an example, if V_g is defined as the peak value of the grid phase voltage, the three-phase voltages are

$$\mathbf{u_g} = [u_{ga}\ u_{gb}\ u_{gc}]^T = V_g[\cos(\omega t)\ \cos(\omega t - 2\pi/3)\ \cos(\omega t + 2\pi/3)]^T \tag{9.10}$$

Then the dq transformation can be conducted as

$$\mathbf{u_{g,dq}} = [u_{gd}\ u_{gq}]^T = T_{dq} \cdot T_{\alpha\beta} \cdot \mathbf{u_g} = [V_g\ 0]^T \tag{9.11}$$

Consequently, the three static variables in abc-reference frame can be represented by two DC variables in the dq-reference frame. By applying the Clarke transformation in Eq. (9.8) to the three-phase static switched model Eq. (9.5), the expressions of the VSC with LCL filter in $\alpha\beta$ coordinate can be achieved as

$$\begin{cases} L_f \dfrac{d\mathbf{i_{f,\alpha\beta}}}{dt} + R_f \mathbf{i_{f,\alpha\beta}} = \dfrac{u_{dc}}{2}\mathbf{S_{\alpha\beta}} - \mathbf{u_{cf,\alpha\beta}} \\ C_f \dfrac{d\mathbf{u_{cf,\alpha\beta}}}{dt} = \mathbf{i_{f,\alpha\beta}} - \mathbf{i_{g,\alpha\beta}} \\ L_g \dfrac{d\mathbf{i_{g,\alpha\beta}}}{dt} + R_g \mathbf{i_{g,\alpha\beta}} = \mathbf{u_{cf,\alpha\beta}} - \mathbf{u_{g,\alpha\beta}} \\ C \dfrac{du_{dc}}{dt} = i_{dc} - \dfrac{3}{2}\mathbf{S^T_{\alpha\beta}}\mathbf{i_{f,\alpha\beta}} \end{cases} \tag{9.12}$$

where $\mathbf{i_{f,\alpha\beta}} = [i_{f\alpha}\ i_{f\beta}]^{\mathrm{T}}$, $\mathbf{i_{g,\alpha\beta}} = [i_{g\alpha}\ i_{g\beta}]^{\mathrm{T}}$, $\mathbf{u_{cf,\alpha\beta}} = [u_{cf\alpha}\ u_{cf\beta}]^{\mathrm{T}}$, $\mathbf{u_{g,\alpha\beta}} = [u_{g\alpha}\ u_{g\beta}]^{\mathrm{T}}$ and $\mathbf{S_{\alpha\beta}} = [S_\alpha\ S_\beta]^{\mathrm{T}}$, all of which are converted into two-phase static $\alpha\beta$ components. As the control signals are symmetrical in a balanced power system, the term $u_n\mathbf{I}$ in Eq. (9.5) is omitted by $\alpha\beta$ transformation.

Similarly, based on Eq. (9.12) and the Park transformation Eq. (9.9), the expressions in the rotating dq-reference frame can be derived as

This book belongs to Kitab Liaison (ocd1996@gmail.com) Copyright Elsevier 2023

$$\begin{cases} L_f \dfrac{d\mathbf{i}_{\mathrm{f,dq}}}{dt} + R_f \mathbf{i}_{\mathrm{f,dq}} = -\omega L_f \mathbf{J}\mathbf{i}_{\mathrm{f,dq}} + \dfrac{u_{dc}}{2}\mathbf{S}_{\mathrm{dq}} - \mathbf{u}_{\mathrm{cf,dq}} \\ C_f \dfrac{d\mathbf{u}_{\mathrm{cf,dq}}}{dt} = -\omega C_f \mathbf{J}\mathbf{u}_{\mathrm{cf,dq}} + \mathbf{i}_{\mathrm{f,dq}} - \mathbf{i}_{\mathrm{g,dq}} \\ L_g \dfrac{d\mathbf{i}_{\mathrm{g,dq}}}{dt} + R_g \mathbf{i}_{\mathrm{g,dq}} = -\omega L_g \mathbf{J}\mathbf{i}_{\mathrm{g,dq}} + \mathbf{u}_{\mathrm{cf,dq}} - \mathbf{u}_{\mathrm{g,dq}} \\ C \dfrac{du_{dc}}{dt} = i_{dc} - \dfrac{3}{2}\mathbf{S}_{\mathrm{dq}}^{\mathrm{T}} \mathbf{i}_{\mathrm{f,dq}} \end{cases} \tag{9.13}$$

where $\mathbf{i_{f,dq}} = [i_{fd}\ i_{fq}]^{\mathrm{T}}$, $\mathbf{i_{g,dq}} = [i_{gd}\ i_{gq}]^{\mathrm{T}}$, $\mathbf{u_{cf,dq}} = [u_{cfd}\ u_{cfq}]^{\mathrm{T}}$, $\mathbf{u_{g,dq}} = [u_{gd}\ v_{gq}]^{\mathrm{T}}$ and $\mathbf{S_{dq}} = [S_d\ S_q]^{\mathrm{T}}$, all of which are converted into two-phase synchronous dq components. $\mathbf{J}$ is an assistant matrix equaling to

$$\mathbf{J} = \begin{bmatrix} 0 & -1 \\ 1 & 0 \end{bmatrix} \tag{9.14}$$

Applying the moving average technique to Eq. (9.13), the averaged dq-frame model of the VSC for a balanced three-phase system can thus be obtained, which is

$$\begin{cases} L_f \dfrac{d\langle \mathbf{i_{f,dq}} \rangle_{avg}}{dt} + R_f \langle \mathbf{i_{f,dq}} \rangle_{avg} = -\omega L_f \mathbf{J} \langle \mathbf{i_{f,dq}} \rangle_{avg} + \dfrac{\langle u_{dc} \rangle_{avg}}{2} \langle \mathbf{S_{dq}} \rangle_{avg} - \langle \mathbf{u_{cf,dq}} \rangle_{avg} \\ C_f \dfrac{d\langle \mathbf{u_{cf,dq}} \rangle_{avg}}{dt} = -\omega C_f \mathbf{J} \langle \mathbf{u_{cf,dq}} \rangle_{avg} + \langle \mathbf{i_{f,dq}} \rangle_{avg} - \langle \mathbf{i_{g,dq}} \rangle_{avg} \\ L_g \dfrac{d\langle \mathbf{i_{g,dq}} \rangle_{avg}}{dt} + R_g \langle \mathbf{i_{g,dq}} \rangle_{avg} = -\omega L_g \mathbf{J} \langle \mathbf{i_{g,dq}} \rangle_{avg} + \langle \mathbf{u_{cf,dq}} \rangle_{avg} - \langle \mathbf{u_{g,dq}} \rangle_{avg} \\ C \dfrac{d\langle u_{dc} \rangle_{avg}}{dt} = \langle i_{dc} \rangle_{avg} - \dfrac{3}{2} \langle \mathbf{S_{dq}^{T}} \rangle_{avg} \langle \mathbf{i_f} \rangle_{avg} \end{cases} \tag{9.15}$$

Eq. (9.15) is the averaged model of the VSC with LCL filter in dq-reference frame. Compared to the original averaged time-variant model Eq. (9.7) in abc-reference frame, the AC variables (e.g., $\mathbf{i_f}$, $\mathbf{i_g}$) are transferred into DC operating variables (e.g., $\mathbf{i_{f,dq}}$, $\mathbf{i_{g,dq}}$), and thus the dq-frame model becomes nonlinear and time invariant. It should be noted that the cross-coupling between the d-axis and q-axis components also appears (i.e. $\omega L_f \mathbf{J}\mathbf{i_{f,dq}}$, $\omega L_g \mathbf{J}\mathbf{i_{g,dq}}$) due to the Park transformation.

9.2.2 Modeling methods in unbalanced three-phase systems

As discussed above, the balanced three-phase power system can be modeled by averaging the variables within one switching period. However, in unbalanced three-phase system, more frequency coupling terms need to be

This book belongs to Kitab Liaison (ocd1996@gmail.com) Copyright Elsevier 2023

considered. Besides, the state averaged model can only predict the converter dynamics below half the switching frequency, and the model is restricted to the assumption of small switching ripples. In order to extend these limitations, a multifrequency model is introduced to represent the behavior of converters containing AC stages, especially to handle the high-order harmonics. Two modeling methods of the VSC with *LCL* filters will be introduced for unbalanced three-phase systems, i.e., GAM (also called dynamic phasor model) and HSS model.

9.2.2.1 Generalized averaged model

The GAM was firstly proposed to capture the switching-frequency component of DC−DC converters. The GAM is based on the fact that a periodic waveform $x(t)$ can be represented by infinite complex Fourier series, which is

$$x(t) = \sum_{k=-\infty}^{+\infty} \langle x \rangle_k(t) \cdot e^{jk\omega t} \tag{9.16}$$

The coefficient of the kth harmonic is defined by

$$\langle x \rangle_k(t) = \frac{1}{T} \int_{t-T}^{T} x(\tau) \cdot e^{-jk\omega\tau} d\tau \tag{9.17}$$

where $T = 2\pi/\omega$ and ω is the constant fundamental frequency pulsation. It can be found that $k = 0$ in Eq. (9.17) corresponds to the moving average operator in Eq. (9.6) with T equaling the switching period T_{sw}. There are two fundamental properties in GAM, as can be expressed by

$$\frac{d}{dt}\langle x \rangle_k(t) = \langle \frac{d}{dt} x \rangle_k(t) - jk\omega \langle x \rangle_k(t) \tag{9.18}$$

$$\langle x \cdot y \rangle_k(t) = \sum_i \langle x \rangle_{k-i}(t) \cdot \langle y \rangle_i(t) \tag{9.19}$$

Eqs. (9.18) and (9.19) describe the properties of the derivative of the moving average and the variables coupling in GAM, respectively. For the convenience of analysis, the Fourier coefficients are simplified by

$$\langle x \rangle_k(t) \rightarrow \langle x \rangle_k, \quad \langle x \cdot y \rangle_k(t) \rightarrow \langle x \cdot y \rangle_k \tag{9.20}$$

Furthermore, the following relationships between the real (denoted by "*R*") and imaginary (denoted by "*I*") parts of the *k*th coefficient and the $(-k)^{th}$ coefficient can be readily obtained and they are satisfied for arbitrary harmonic component

$$\begin{cases} \langle x \rangle_{kR} = \dfrac{1}{T} \displaystyle\int_{t-T}^{t} x(\tau)\cos(k\omega\tau) d\tau = \langle x \rangle_{-kR} \\ \langle x \rangle_{kI} = \dfrac{1}{T} \displaystyle\int_{t-T}^{t} x(\tau)\sin(k\omega\tau) d\tau = -\langle x \rangle_{-kI} \end{cases} \tag{9.21}$$

This book belongs to Kitab Liaison (ocd1996@gmail.com) Copyright Elsevier 2023

Therefore, if only first-order harmonic (i.e., fundamental component) is studied, the actual signal can be modeled as

$$x(t) \approx \langle x\rangle_1 e^{j\omega t} + \langle x\rangle_{-1} e^{-j\omega t} = 2[\langle x\rangle_{1R}\cos(\omega t) - \langle x\rangle_{1I}\sin(\omega t)] \tag{9.22}$$

On the basis of Eqs. (9.17)–(9.21) and combining with the original switched model (cf. Eq. 9.1) of VSC with *LCL* filter, the *k*th-order harmonic component contained in the AC currents/voltages can be obtained with

$$\begin{cases} L_f\dfrac{d\langle \mathbf{i_f}\rangle_k}{dt} + R_f\langle \mathbf{i_f}\rangle_k = -jk\omega L_f\langle \mathbf{i_f}\rangle_k + \dfrac{1}{2}\langle u_{dc}\mathbf{S}\rangle_k - \langle \mathbf{u_{cf}}\rangle_k - \langle u_n\mathbf{I}\rangle_k \\ C_f\dfrac{d\langle \mathbf{u_{cf}}\rangle_k}{dt} = -jk\omega C_f\langle \mathbf{u_{cf}}\rangle_k + \langle \mathbf{i_f}\rangle_k - \langle \mathbf{i_g}\rangle_k \\ L_g\dfrac{d\langle \mathbf{i_g}\rangle_k}{dt} + R_g\langle \mathbf{i_g}\rangle_k = -jk\omega L_g\langle \mathbf{i_g}\rangle_k + \langle \mathbf{u_{cf}}\rangle_k - \langle \mathbf{u_g}\rangle_k + \langle (u_n - u_n')\mathbf{I}\rangle_k \\ C\dfrac{d\langle u_{dc}\rangle_k}{dt} = \langle i_{dc}\rangle_k - \langle \mathbf{S^T i_f}\rangle_k \end{cases} \tag{9.23}$$

where the symbol meanings are the same as Eq. (9.1). Next, by setting k to different values (e.g., 1, 5, 7, 11, 13 … for AC variables and 0, 2, 6, 12 … for DC variables), the corresponding *k*th-order harmonic can be solved using Eq. (9.23), and then the GAM of the VSC with *LCL* filter can be achieved by adding up these harmonic components. As a result, if up to *h*th-order harmonics are considered, the final results are

$$\begin{cases} L_f\dfrac{d\sum_{k=1}^{h}\langle \mathbf{i_f}\rangle_k}{dt} + R_f\sum_{k=1}^{h}\langle \mathbf{i_f}\rangle_k = \sum_{k=1}^{h}(-jk\omega L_f\langle \mathbf{i_f}\rangle_k) + \dfrac{1}{2}\sum_{k=1}^{h}\langle u_{dc}\mathbf{S}\rangle_k - \sum_{k=1}^{h}\langle \mathbf{u_{cf}}\rangle_k - \sum_{k=1}^{h}\langle u_n\mathbf{I}\rangle_k \\ C_f\dfrac{d\sum_{k=1}^{h}\langle \mathbf{u_{cf}}\rangle_k}{dt} = \sum_{k=1}^{h}(-jk\omega C_f\langle \mathbf{u_{cf}}\rangle_k) + \sum_{k=1}^{h}\langle \mathbf{i_f}\rangle_k - \sum_{k=1}^{h}\langle \mathbf{i_g}\rangle_k \\ L_g\dfrac{d\sum_{k=1}^{h}\langle \mathbf{i_g}\rangle_k}{dt} + R_g\sum_{k=1}^{h}\langle \mathbf{i_g}\rangle_k = \sum_{k=1}^{h}\left(-jk\omega L_g\langle \mathbf{i_g}\rangle_k\right) + \sum_{k=1}^{h}\langle \mathbf{u_{cf}}\rangle_k - \sum_{k=1}^{h}\langle \mathbf{u_g}\rangle_k + \sum_{k=1}^{h}\langle (u_n - u_n')\mathbf{I}\rangle_k \\ C\dfrac{d\sum_{k=0}^{h}\langle u_{dc}\rangle_k}{dt} = \sum_{k=0}^{h}\langle i_{dc}\rangle_k - \sum_{k=0}^{h}\langle \mathbf{S^T i_f}\rangle_k \end{cases} \tag{9.24}$$

Clearly, if more harmonics are taken into account, the GAM will be more accurate, but in the meantime, the model will become more complex. In sight of this, a balance between the modeling accuracy and complexity needs to be

This book belongs to Kitab Liaison (ocd1996@gmail.com) Copyright Elsevier 2023

considered in practical applications, which usually depends on the harmonic components of interest.

If the first-order harmonic components (i.e., fundamental components) of the AC variables (e.g., $\mathbf{i_g}, \mathbf{i_f}$) and the zeroth-order components (i.e., average values) of the DC variables (e.g., $u_{dc},\ i_{load}$) are considered in Eq. (9.24), the modeling procedure of GAM is explained as the following. Firstly, substituting $h = 1$ and $h = 0$ into the first three expressions and the last expression in Eq. (9.24), respectively, the result is

$$\begin{cases} L_f \dfrac{d\langle \mathbf{i_f}\rangle_1}{dt} + R_f\langle \mathbf{i_f}\rangle_1 = -j\omega L_f\langle \mathbf{i_f}\rangle_1 + \dfrac{1}{2}\langle u_{dc}\mathbf{S}\rangle_1 - \langle \mathbf{u_{cf}}\rangle_1 - \langle u_n\mathbf{I}\rangle_1 \\ C_f \dfrac{d\langle \mathbf{u_{cf}}\rangle_1}{dt} = -j\omega C_f\langle \mathbf{u_{cf}}\rangle_1 + \langle \mathbf{i_f}\rangle_1 - \langle \mathbf{i_g}\rangle_1 \\ L_g \dfrac{d\langle \mathbf{i_g}\rangle_1}{dt} + R_g\langle \mathbf{i_g}\rangle_1 = -j\omega L_g\langle \mathbf{i_g}\rangle_1 + \langle \mathbf{u_{cf}}\rangle_1 - \langle \mathbf{u_g}\rangle_1 + \langle (u_n - u_n')\mathbf{I}\rangle_1 \\ C \dfrac{d\langle u_{dc}\rangle_0}{dt} = \langle i_{dc}\rangle_0 - \langle \mathbf{S^T i_f}\rangle_0 \end{cases} \tag{9.25}$$

with $\langle \mathbf{i_f}\rangle_1 = [\langle i_{fa}\rangle_1, \langle i_{fb}\rangle_1, \langle i_{fc}\rangle_1]^T$, $\langle \mathbf{i_g}\rangle_1 = [\langle i_{ga}\rangle_1, \langle i_{gb}\rangle_1, \langle i_{gc}\rangle_1]^T$, $\langle \mathbf{u_{cf}}\rangle_1 = [\langle u_{cfa}\rangle_1, \langle u_{cfb}\rangle_1, \langle u_{cfc}\rangle_1]^T$.

Based on [11], the Fourier coefficients of the switching functions $\mathbf{S} = [S_a\ S_b\ S_c]^{\mathrm{T}}$ can be obtained with

$$\langle \mathbf{S}\rangle_0 = \begin{bmatrix} \langle S_a\rangle_0 \\ \langle S_b\rangle_0 \\ \langle S_c\rangle_0 \end{bmatrix} = \begin{bmatrix} 0 \\ 0 \\ 0 \end{bmatrix} \quad \langle \mathbf{S}\rangle_1 = \begin{bmatrix} \langle S_a\rangle_1 \\ \langle S_b\rangle_1 \\ \langle S_c\rangle_1 \end{bmatrix} = \begin{bmatrix} j\left(-\dfrac{m}{2}\right) \\ j\left(-\dfrac{m}{2}\right)e^{-j\frac{2\pi}{3}} \\ j\left(-\dfrac{m}{2}\right)e^{-j\frac{4\pi}{3}} \end{bmatrix} \tag{9.26}$$

where m is the modulation index. On this basis, the term $\langle u_{dc}\mathbf{S}\rangle_1$ can be expressed by

$$\langle u_{dc}\mathbf{S}\rangle_1 = \begin{bmatrix} \langle u_{dc}S_a\rangle_1 \\ \langle u_{dc}S_b\rangle_1 \\ \langle u_{dc}S_c\rangle_1 \end{bmatrix} = \begin{bmatrix} \langle u_{dc}\rangle_0\langle S_a\rangle_1 \\ \langle u_{dc}\rangle_0\langle S_b\rangle_1 \\ \langle u_{dc}\rangle_0\langle S_c\rangle_1 \end{bmatrix} \tag{9.27}$$

and the term $\langle S_a i_{fa}\rangle_0$ in $\langle \mathbf{S^T i_f}\rangle_0 = \langle S_a i_{fa}\rangle_0 + \langle S_b i_{fb}\rangle_0 + \langle S_c i_{fc}\rangle_0$ can be derived as

$$\langle S_a i_{fa}\rangle_0 = \langle S_a\rangle_1\langle i_{fa}\rangle_{-1} + \langle S_a\rangle_{-1}\langle i_{fa}\rangle_1 = 2(\langle S_a\rangle_{1R}\langle i_{fa}\rangle_{1R} + \langle S_a\rangle_{1I}\langle i_{fa}\rangle_{1I}) \tag{9.28}$$

and similar results can be obtained for $\langle S_b i_{fb}\rangle_0$ and $\langle S_c i_{fc}\rangle_0$. Combining with Eqs. (9.21)−(9.28) and separating the real part and imaginary part for each expression, the final form of Eq. (9.25) can be derived as

This book belongs to Kitab Liaison (ocd1996@gmail.com) Copyright Elsevier 2023

$$\begin{cases} L_f \dfrac{d\langle \mathbf{i_f}\rangle_{1R}}{dt} + R_f\langle \mathbf{i_f}\rangle_{1R} = \omega L_f\langle \mathbf{i_f}\rangle_{1I} + \dfrac{1}{2}\langle u_{dc}\rangle_0\langle \mathbf{S}\rangle_{1R} - \langle \mathbf{u_{cf}}\rangle_{1R} + \dfrac{1}{3}\sum\limits_{i=a,b,c}\langle u_{cfi}\rangle_{1R} \\ L_f \dfrac{d\langle \mathbf{i_f}\rangle_{1I}}{dt} + R_f\langle \mathbf{i_f}\rangle_{1I} = -\omega L_f\langle \mathbf{i_f}\rangle_{1R} + \dfrac{1}{2}\langle u_{dc}\rangle_0\langle \mathbf{S}\rangle_{1I} - \langle \mathbf{u_{cf}}\rangle_{1I} + \dfrac{1}{3}\sum\limits_{i=a,b,c}\langle u_{cfi}\rangle_{1I} \\ C_f \dfrac{d\langle \mathbf{u_{cf}}\rangle_{1R}}{dt} = \omega C_f\langle \mathbf{u_{cf}}\rangle_{1I} + \langle \mathbf{i_f}\rangle_{1R} - \langle \mathbf{i_g}\rangle_{1R} \\ C_f \dfrac{d\langle \mathbf{u_{cf}}\rangle_{1I}}{dt} = -\omega C_f\langle \mathbf{u_{cf}}\rangle_{1R} + \langle \mathbf{i_f}\rangle_{1I} - \langle \mathbf{i_g}\rangle_{1I} \\ L_g \dfrac{d\langle \mathbf{i_g}\rangle_{1R}}{dt} + R_g\langle \mathbf{i_g}\rangle_{1R} = \omega L_g\langle \mathbf{i_g}\rangle_{1I} + \langle \mathbf{u_{cf}}\rangle_{1R} - \langle \mathbf{u_g}\rangle_{1R} + \dfrac{1}{3}\sum\limits_{i=a,b,c}\langle u_{gi}\rangle_{1R} + \dfrac{1}{3}\sum\limits_{i=a,b,c}\langle u_{cfi}\rangle_{1R} \\ L_g \dfrac{d\langle \mathbf{i_g}\rangle_{1I}}{dt} + R_g\langle \mathbf{i_g}\rangle_{1I} = -\omega L_g\langle \mathbf{i_g}\rangle_{1R} + \langle \mathbf{u_{cf}}\rangle_{1I} - \langle \mathbf{u_g}\rangle_{1I} + \dfrac{1}{3}\sum\limits_{i=a,b,c}\langle u_{gi}\rangle_{1I} + \dfrac{1}{3}\sum\limits_{i=a,b,c}\langle u_{cfi}\rangle_{1I} \\ C\dfrac{d\langle u_{dc}\rangle_0}{dt} = \langle i_{dc}\rangle_0 - 2\sum\limits_{i=a,b,c}\left(\langle S_i\rangle_{1R}\langle i_{fi}\rangle_{1R} + \langle S_i\rangle_{1I}\langle i_{fi}\rangle_{1I}\right) \end{cases} \tag{9.29}$$

Then Eq. (9.29) can be directly used to model the VSC with an *LCL* filter.

Three-phase voltages can become unbalanced and distorted because of the effect of the nonlinear loads and transient grid faults. In such case, one general way is to rewrite the AC voltages as

$$\mathbf{v_{abc}} = [v_a \quad v_b \quad v_c]^T = \sum_{k=1}^{+\infty}\left(\mathbf{v}_{abc}^{+k} + \mathbf{v}_{abc}^{-k} + \mathbf{v}_{abc}^{0k}\right) = \sum_{k=1}^{+\infty}\left\{ V^{+k}\begin{bmatrix} \cos\left(k\omega t + \phi^{+k}\right) \\ \cos\left(k\omega t - \frac{2}{3}\pi + \phi^{+k}\right) \\ \cos\left(k\omega t - \frac{4}{3}\pi + \phi^{+k}\right) \end{bmatrix} + V^{-k}\begin{bmatrix} \cos\left(k\omega t + \phi^{-k}\right) \\ \cos\left(k\omega t - \frac{4}{3}\pi + \phi^{-k}\right) \\ \cos\left(k\omega t - \frac{2}{3}\pi + \phi^{-k}\right) \end{bmatrix} + V^{0k}\begin{bmatrix} \cos\left(k\omega t + \phi^{0k}\right) \\ \cos\left(k\omega t + \phi^{0k}\right) \\ \cos\left(k\omega t + \phi^{0k}\right) \end{bmatrix} \right\} \tag{9.30}$$

where superscripts $+k$, $-k$, and $0k$ represent, respectively, the positive-, negative-, and zero-sequence components of the kth-order harmonic of the

This book belongs to Kitab Liaison (ocd1996@gmail.com) Copyright Elsevier 2023

voltage vector $\mathbf{v_{abc}}$. Likewise, the unbalanced AC currents can be generally expressed as

$$\mathbf{i_{abc}} = [i_a \quad i_b \quad i_c]^T = \sum_{k=1}^{+\infty}\left(\mathbf{i}_{abc}^{+k} + \mathbf{i}_{abc}^{-k}\right)$$
$$= \sum_{k=1}^{+\infty}\left\{ I^{+k}\begin{bmatrix} \sin\left(k\omega t + \varphi^{+k}\right) \\ \sin\left(k\omega t - \frac{2}{3}\pi + \varphi^{+k}\right) \\ \sin\left(k\omega t - \frac{4}{3}\pi + \varphi^{+k}\right) \end{bmatrix} + I^{-k}\begin{bmatrix} \sin\left(k\omega t + \varphi^{-k}\right) \\ \sin\left(k\omega t - \frac{4}{3}\pi + \varphi^{-k}\right) \\ \sin\left(k\omega t - \frac{2}{3}\pi + \varphi^{-k}\right) \end{bmatrix} \right\} \tag{9.31}$$

Due to that the three-wire connection VSC injects no zero-sequence current into the grid, the zero-sequence component of the voltage vector $\mathbf{v_{abc}}$ can be ignored. The voltage vectors ($\mathbf{v}_{abc}^{+k}$, $\mathbf{v}_{abc}^{-k}$) in Eq. (9.30) and the current vector ($\mathbf{i}_{abc}^{+k}$, $\mathbf{i}_{abc}^{-k}$) in Eq. (9.31) can be used to describe the voltage and current vectors in Eq. (9.23), resulting in positive- and negative-sequence GAMs of the VSC converter for the *kth* harmonic components. In practical situations, the first-order harmonic (i.e., fundamental component) is usually focused on, and hence the instantaneous positive- and negative-sequence components of the unbalanced AC voltages can be obtained by

$$\begin{bmatrix} v_a^+ \\ v_b^+ \\ v_c^+ \end{bmatrix} = \frac{1}{3}\begin{bmatrix} 1 & a & a^2 \\ a^2 & 1 & a \\ a & a^2 & 1 \end{bmatrix}\begin{bmatrix} v_a \\ v_b \\ v_c \end{bmatrix} \qquad \begin{bmatrix} v_a^- \\ v_b^- \\ v_c^- \end{bmatrix} = \frac{1}{3}\begin{bmatrix} 1 & a^2 & a \\ a & 1 & a^2 \\ a^2 & a & 1 \end{bmatrix}\begin{bmatrix} v_a \\ v_b \\ v_c \end{bmatrix} \tag{9.32}$$

where v_a^+, v_b^+, v_c^+ and v_a^-, v_b^-, v_c^- are the positive- and negative-sequence components of the first-order harmonic voltage, and v_a, v_b, v_c are the measured unbalanced AC voltages. The symbol a denotes the operation $a = e^{j2\pi/3}$. The AC currents can also be expressed similar to Eq. (9.32). Consequently, the first-order GAM of the VSC with *LCL* filter can be achieved by substituting Eq. (9.32) into Eq. (9.23), which is

$$\begin{cases} L_f\dfrac{d\langle\mathbf{i_f^{\pm}}\rangle_1}{dt} + R_f\langle\mathbf{i_f^{\pm}}\rangle_1 = -j\omega L_f\langle\mathbf{i_f^{\pm}}\rangle_1 + \dfrac{V_{dc}}{2}\langle\mathbf{u}^{\pm}\rangle_1 - \langle\mathbf{u_c^{\pm}}\rangle_1 \\ C_f\dfrac{d\langle\mathbf{u_c^{\pm}}\rangle_1}{dt} = -j\omega C_f\langle\mathbf{u_c^{\pm}}\rangle_1 + \langle\mathbf{i_f^{\pm}}\rangle_1 - \langle\mathbf{i_g^{\pm}}\rangle_1 \\ L_g\dfrac{d\langle\mathbf{i_g^{\pm}}\rangle_1}{dt} + R_g\langle\mathbf{i_g^{\pm}}\rangle_1 = -j\omega L_g\langle\mathbf{i_g^{\pm}}\rangle_1 + \langle\mathbf{u_c^{\pm}}\rangle_1 - \langle\mathbf{u_g^{\pm}}\rangle_1 \end{cases} \tag{9.33}$$

Eq. (9.33) is the combination of the positive- and negative-sequence GAMs, denoted by the superscripts + and −, respectively.

This book belongs to Kitab Liaison (ocd1996@gmail.com) Copyright Elsevier 2023

9.2.2.2 Harmonic state space model

A typical LTP system can be defined by

$$\begin{cases} \dot{x}(t) = A(t)x(t) + B(t)u(t) \\ y(t) = C(t)x(t) + D(t)u(t) \end{cases} \tag{9.34}$$

where $x(t)$, $u(t)$, $y(t)$ are the, respectively, state, input, and output variables and $A(t)$, $B(t)$, $C(t)$, $D(t)$ are time-periodic matrices, i.e., $A(t) = A(t + \mathrm{T})$ and similarly for others. In order to apply the frequency separation property to LTP systems, instead of the expression Eq. (9.16) in GAM, another form of exponentially modulated periodic (EMP) signal expressed by the following is used:

$$x(t) = e^{st} \sum_{k=-\infty}^{+\infty} x_k e^{jk\omega t} \tag{9.35}$$

where s is a complex number in order to represent the transient evolution of the harmonic components.

Then, by posing the variables $x(t)$, $u(t)$, $y(t)$ in Eq. (9.34) as EMP signals and the time-periodic matrices $A(t)$, $B(t)$, $C(t)$, $D(t)$ in Eq. (9.34) as complex Fourier series, i.e.,

$$\begin{cases} x(t) = e^{st} \sum_{k=-\infty}^{+\infty} x_k e^{jk\omega t}, \quad y(t) = e^{st} \sum_{k=-\infty}^{+\infty} Y_k e^{jk\omega t}, \quad u(t) = e^{st} \sum_{k=-\infty}^{+\infty} U_k e^{jk\omega t}, \\ A(t) = \sum_{k=-\infty}^{+\infty} A_k e^{jk\omega t}, B(t) = \sum_{k=-\infty}^{+\infty} B_k e^{jk\omega t} C(t) = \sum_{k=-\infty}^{+\infty} C_k e^{jk\omega t}, \ D(t) = \sum_{k=-\infty}^{+\infty} D_k e^{jk\omega t} \end{cases} \tag{9.36}$$

the LTP system description can be transferred to

$$\begin{cases} \sum_{k=-\infty}^{+\infty} (jk\omega + s) X_k e^{(jk\omega+s)t} = \sum_{k,m=-\infty}^{+\infty} A_{k-m} X_m e^{(jk\omega+s)t} + \sum_{k,m=-\infty}^{+\infty} B_{k-m} U_m e^{(jk\omega+s)t} \\ \sum_{k=-\infty}^{+\infty} Y_k e^{(jk\omega+s)t} = \sum_{k,m=-\infty}^{+\infty} C_{k-m} X_m e^{(jk\omega+s)t} + \sum_{k,m=-\infty}^{+\infty} D_{k-m} U_m e^{(jk\omega+s)t} \end{cases} \tag{9.37}$$

The m in Eq. (9.37) indicates the frequency cross-coupling among difference harmonic components.

Considering the harmonic balance principle, which refers to the linear independency of every harmonic component, the summation symbol and the term $e^{(jk\omega+s)t}$ can be canceled on the both sides of the expressions in Eq. (9.37), leading to

This book belongs to Kitab Liaison (ocd1996@gmail.com) Copyright Elsevier 2023

$$\begin{cases} sX_k = \sum_{m=-\infty}^{+\infty} A_{k-m}X_m + \sum_{m=-\infty}^{+\infty} B_{k-m}X_m - jk\omega X_k \\ Y_k = \sum_{m=-\infty}^{+\infty} C_{k-m}X_m + \sum_{m=-\infty}^{+\infty} D_{k-m}U_m \end{cases} \tag{9.38}$$

Then, the HSS form can be obtained by including all harmonic component coefficients of Eq. (9.38) in a matrix, resulting in

$$\begin{cases} \mathbf{sX} = (\mathbf{A}\text{-}\mathbf{N})\mathbf{X} + \mathbf{BU} \\ \mathbf{Y} = \mathbf{CX} + \mathbf{DU} \end{cases} \tag{9.39}$$

Therein, **A**, **B**, **C**, and **D** are Toeplitz matrices constructed by respective Fourier coefficients of $A(t)$, $B(t)$, $C(t)$, and $D(t)$. For example, instead of the infinite Fourier series of Eq. (9.36), if up to hth-order components are considered in practice, **A** can be written as

$$A = \begin{bmatrix} A_0 & A_{-1} & \cdots & A_{-h} & \mathbf{0} & \mathbf{0} & \mathbf{0} \\ A_1 & \ddots & \ddots & \ddots & \ddots & \mathbf{0} & \mathbf{0} \\ \vdots & \ddots & A_0 & A_{-1} & \ddots & A_{-h} & \mathbf{0} \\ A_h & \ddots & A_1 & A_0 & A_{-1} & \ddots & A_{-h} \\ \mathbf{0} & A_h & \ddots & A_1 & A_0 & \ddots & \vdots \\ \mathbf{0} & \mathbf{0} & \ddots & \ddots & \ddots & \ddots & A_{-1} \\ \mathbf{0} & \mathbf{0} & \mathbf{0} & A_h & \cdots & A_1 & A_0 \end{bmatrix} \tag{9.40}$$

and similarly for **B**, **C**, and **D**. On the other hand, **X**, **U**, and **Y** in Eq. (4.39) denote respective Fourier coefficients of their complex Fourier series expansion, and **N** is the diagonal matrix of the sequence $\{jk\omega\}_{k=-h}^{+h}$, resulting in

$$\mathbf{X} = \begin{bmatrix} X_{-h} \\ \vdots \\ X_{-1} \\ X_0 \\ X_1 \\ \vdots \\ X_h \end{bmatrix} \mathbf{U} = \begin{bmatrix} U_{-h} \\ \vdots \\ U_{-1} \\ U_0 \\ U_1 \\ \vdots \\ U_h \end{bmatrix} \mathrm{Y} = \begin{bmatrix} Y_{-h} \\ \vdots \\ Y_{-1} \\ Y_0 \\ Y_1 \\ \vdots \\ Y_h \end{bmatrix} \mathbf{N} = \begin{bmatrix} -jh\omega & & & & & & \\ & \ddots & & & & & \\ & & -j\omega & & & & \\ & & & 0 & & & \\ & & & & j\omega & & \\ & & & & & \ddots & \\ & & & & & & jh\omega \end{bmatrix} \tag{9.41}$$

In order to obtain the HSS model of the VSC in Fig. 9.1, the original switched model Eq. (9.1) is firstly transferred to the LTP form

This book belongs to Kitab Liaison (ocd1996@gmail.com)
Copyright Elsevier 2023

$$\begin{cases} \dot{\mathbf{i_f}} = -\dfrac{R_f}{L_f}\mathbf{i_f} + \dfrac{u_{dc}}{2L_f}\mathbf{S} - \dfrac{1}{L_f}\mathbf{u_{cf}} - \dfrac{u_n}{L_f}\mathbf{I} \\ \dot{\mathbf{u_{cf}}} = \dfrac{1}{C_f}\mathbf{i_f} - \dfrac{1}{C_f}\mathbf{i_g} \\ \dot{\mathbf{i_g}} = -\dfrac{R_g}{L_g}\mathbf{i_g} + \dfrac{1}{L_g}\mathbf{u_{cf}} - \dfrac{1}{L_g}\mathbf{u_g} + \dfrac{1}{L_g}\left(u_n - u_n'\right)\mathbf{I} \\ \dot{u}_{dc} = \dfrac{1}{C}i_{dc} - \dfrac{1}{C}\mathbf{S^T i_f} \end{cases} \tag{9.42}$$

If the average and first-order harmonic components are considered for each state variable, the HSS model of Eq. (9.42) can be derived based on Eqs. (9.39)–(9.41). For example, the differential expression of a phase converter-side current is

$$\dot{i}_{fa} = -\frac{R_f}{L_f}\cdot i_{fa} + \begin{bmatrix} \dfrac{u_{dc}}{2L_f} & -\dfrac{1}{L_f} & -\dfrac{1}{L_f} \end{bmatrix} \cdot \begin{bmatrix} S_a \\ u_{cfa} \\ u_n \end{bmatrix} \tag{9.43}$$

and the HSS model of Eq. (9.43) can be derived as

$$\mathbf{sI_{fa}} = (\mathbf{A_{ifa}}\text{-}\mathbf{N_{ifa}})\mathbf{I_{fa}} + \mathbf{B_{ifa}}\mathbf{U_{ifa}} \tag{9.44}$$

Therein, the matrices $\mathbf{I_{fa}} = [\,I_{fa-1} \quad I_{fa0} \quad I_{fa1}\,]^T$, $\mathbf{U_{ifa}} = [\,S_{a-1} \quad S_{a0} \quad S_{a1} \quad U_{cfa-1} \quad U_{cfa0} \quad U_{cfa1} \quad U_{n-1} \quad U_{n0} \quad U_{n1}\,]^T$, $\mathbf{N_{ifa}} = diag[\,-j\omega_0 \quad 0 \quad j\omega_0\,]$, and $\mathbf{A_{ifa}}$, $\mathbf{B_{ifa}}$ are

$$\mathrm{A_{ifa}} = \begin{bmatrix} -\dfrac{R_f}{L_f} & 0 & 0 \\ 0 & -\dfrac{R_f}{L_f} & 0 \\ 0 & 0 & -\dfrac{R_f}{L_f} \end{bmatrix} \mathrm{B_{ifa}} = \begin{bmatrix} \dfrac{U_{dc0}}{2L_f} & \dfrac{U_{dc-1}}{2L_f} & 0 & -\dfrac{1}{L_f} & 0 & 0 & -\dfrac{1}{L_f} & 0 & 0 \\ \dfrac{U_{dc1}}{2L_f} & \dfrac{U_{dc0}}{2L_f} & \dfrac{U_{dc-1}}{2L_f} & 0 & -\dfrac{1}{L_f} & 0 & 0 & -\dfrac{1}{L_f} & 0 \\ 0 & \dfrac{U_{dc1}}{2L_f} & \dfrac{U_{dc0}}{2L_f} & 0 & 0 & -\dfrac{1}{L_f} & 0 & 0 & -\dfrac{1}{L_f} \end{bmatrix} \tag{9.45}$$

Similar to Eq. (9.44), the other expressions in Eq. (9.42) can also be transformed into HSS models. Firstly, Eq. (9.42) can be rewritten as the LTP state space form (similar to Eq. 9.34), which is

This book belongs to Kitab Liaison (ocd1996@gmail.com) Copyright Elsevier 2023

$$\begin{bmatrix} \dot{\mathbf{i}}_{\mathbf{f}} \\ \dot{\mathbf{u}}_{\mathbf{cf}} \\ \dot{\mathbf{i}}_{\mathbf{g}} \\ \dot{u}_{dc} \end{bmatrix} = \begin{bmatrix} -\frac{R_f}{L_f} & -\frac{1}{L_f} & 0 & \frac{1}{2L_f}\mathbf{S} \\ \frac{1}{C_f} & 0 & -\frac{1}{C_f} & 0 \\ 0 & \frac{1}{L_g} & -\frac{R_g}{L_g} & 0 \\ -\frac{1}{C}\mathbf{S}^{\mathbf{T}} & 0 & 0 & 0 \end{bmatrix} \begin{bmatrix} \mathbf{i}_{\mathbf{f}} \\ \mathbf{u}_{\mathbf{cf}} \\ \mathbf{i}_{\mathbf{g}} \\ u_{dc} \end{bmatrix} + \begin{bmatrix} -\frac{u_n}{L_f} & 0 & 0 \\ 0 & 0 & 0 \\ \frac{1}{L_g}\left(u_n - u_n'\right) & -\frac{1}{L_g} & 0 \\ 0 & 0 & \frac{1}{C} \end{bmatrix} \begin{bmatrix} \mathbf{I} \\ \mathbf{u}_{\mathbf{g}} \\ i_{dc} \end{bmatrix} \tag{9.46}$$

Then, the HSS model of Eq. (9.46) can be obtained by following Eqs. (9.39)−(9.41). For a clear view, the HSS model of each phase in Eq. (9.46) is shown separately. By setting $i = a, b, c$, there are

$$s\mathbf{u}_{\mathbf{cfi}} = -\mathbf{N}_{\mathbf{ucfi}}\mathbf{u}_{\mathbf{cfi}} + \mathbf{B}_{\mathbf{ucfi}}\mathbf{U}_{\mathbf{ucfi}}$$

$$\Downarrow$$

$$\mathbf{u}_{\mathbf{cfi}} = \begin{bmatrix} u_{cfi-1} \\ u_{cfi0} \\ u_{cfi1} \end{bmatrix} \mathbf{N}_{\mathbf{cfi}} = \begin{bmatrix} -j\omega_0 & & \\ & 0 & \\ & & j\omega_0 \end{bmatrix} \mathbf{U}_{\mathbf{ucfi}} = \begin{bmatrix} i_{fi-1} \\ i_{fi0} \\ i_{fi1} \\ i_{gi-1} \\ i_{gi0} \\ i_{gi1} \end{bmatrix} \mathbf{B}_{\mathbf{ucfi}} = \begin{bmatrix} \frac{1}{C_f} & & & -\frac{1}{C_f} & & \\ & \frac{1}{C_f} & & & -\frac{1}{C_f} & \\ & & \frac{1}{C_f} & & & -\frac{1}{C_f} \end{bmatrix} \tag{9.47}$$

$$s\mathbf{i}_{\mathbf{gi}} = (\mathbf{A}_{\mathbf{igi}} - \mathbf{N}_{\mathbf{igi}})\mathbf{i}_{\mathbf{gi}} + \mathbf{B}_{\mathbf{igi}}\mathbf{U}_{\mathbf{igi}}$$

$$\Downarrow$$

$$\mathbf{i}_{\mathbf{gi}} = \begin{bmatrix} i_{gi-1} \\ i_{gi0} \\ i_{gi1} \end{bmatrix} \mathbf{A}_{\mathbf{igi}} = \begin{bmatrix} -\frac{R_g}{L_g} & & \\ & -\frac{R_g}{L_g} & \\ & & -\frac{R_g}{L_g} \end{bmatrix} \mathbf{N}_{\mathbf{igi}} = \begin{bmatrix} -j\omega_0 & & \\ & 0 & \\ & & j\omega_0 \end{bmatrix} \tag{9.48}$$

$$\mathbf{B}_{\mathbf{igi}} = \begin{bmatrix} \frac{1}{L_g} & & & -\frac{1}{L_g} & & & \frac{1}{L_g} & \\ & \frac{1}{L_g} & & & -\frac{1}{L_g} & & & \frac{1}{L_g} \\ & & \frac{1}{L_g} & & & -\frac{1}{L_g} & & \frac{1}{L_g} \end{bmatrix}$$

$$\mathbf{U}_{\mathbf{igi}} = \begin{bmatrix} u_{cfi-1} & u_{cfi0} & u_{cfi1} & u_{gi-1} & u_{gi0} & u_{gi1} & u_{n-1} - u_{n-1}' & u_{n0} - u_{n0}' & u_{n1} - u_{n1}' \end{bmatrix}^T$$

This book belongs to Kitab Liaison (ocd1996@gmail.com)

Copyright Elsevier 2023

$$s\mathbf{u_{dc}} = -\mathbf{N_{udc}}\mathbf{u_{dc}} + \mathbf{B_{udc}}\mathbf{U_{udc}}$$

$$\Downarrow$$

$$\mathbf{u_{dc}} = \begin{bmatrix} u_{dc-1} \\ u_{dc0} \\ u_{dc1} \end{bmatrix} \mathbf{N_{udc}} = \begin{bmatrix} -j\omega_0 & & \\ & 0 & \\ & & j\omega_0 \end{bmatrix} \mathbf{U_{udc}} = [\, i_{dc-1} \quad i_{dc0} \quad i_{dc1} \quad i_{fa-1} \quad i_{fa0} \quad i_{fa1} \quad i_{fb-1} \quad i_{fb0} \quad i_{fb1} \quad i_{fc-1} \quad i_{fc0} \quad i_{fc1} \,]$$

$$\mathbf{B_{udc}} = \begin{bmatrix} \frac{1}{C} & & & -\frac{1}{C}S_{a0} & -\frac{1}{C}S_{a-1} & 0 & -\frac{1}{C}S_{b0} & -\frac{1}{C}S_{b-1} & 0 & -\frac{1}{C}S_{c0} & -\frac{1}{C}S_{c-1} & 0 \\ & \frac{1}{C} & & -\frac{1}{C}S_{a1} & -\frac{1}{C}S_{a0} & -\frac{1}{C}S_{a-1} & -\frac{1}{C}S_{b1} & -\frac{1}{C}S_{b0} & -\frac{1}{C}S_{b-1} & 0 & -\frac{1}{C}S_{c0} & -\frac{1}{C}S_{c-1} \\ & & \frac{1}{C} & 0 & -\frac{1}{C}S_{a1} & -\frac{1}{C}S_{a0} & 0 & -\frac{1}{C}S_{b1} & -\frac{1}{C}S_{b0} & 0 & -\frac{1}{C}S_{c1} & -\frac{1}{C}S_{c0} \end{bmatrix} \tag{9.49}$$

Similar procedure can be applied to derive the HSS model of the controller, which is not shown here due to page limitation.

9.2.3 Simulation examples

Taking the GAM as an example, a simulation model using PLECS is built to validate the effectiveness of the modeling method, and the system parameters are shown in the following Table 9.1. Applying the conventional *dq*-axis current control (converter current feedback), which will be introduced in the next section, the steady-state working waveforms including the grid voltages, the grid-side inductor current, and the converter-side current are shown in Fig. 9.2.

TABLE 9.1 Parameters of 15 kW grid-tied voltage source converters with LCL filter.

Operating power P_o (kW)	7.5
Grid peak phase voltage U_g (V)	311
DC-link voltage V_{dc} (V)	650
Converter-side inductor L_f (mH)	3
Capacitor branch C_f (uF)	25
Grid-side inductor L_g (mH)	1.8
Grid voltage frequency f_g (Hz)	50
Switching frequency f_{sw} (kHz)	4
Converter-side inductor equivalent resistance R_f (Ω)	0.15
Grid-side inductor equivalent resistance R_g (Ω)	0.15

This book belongs to Kitab Liaison (ocd1996@gmail.com)
Copyright Elsevier 2023

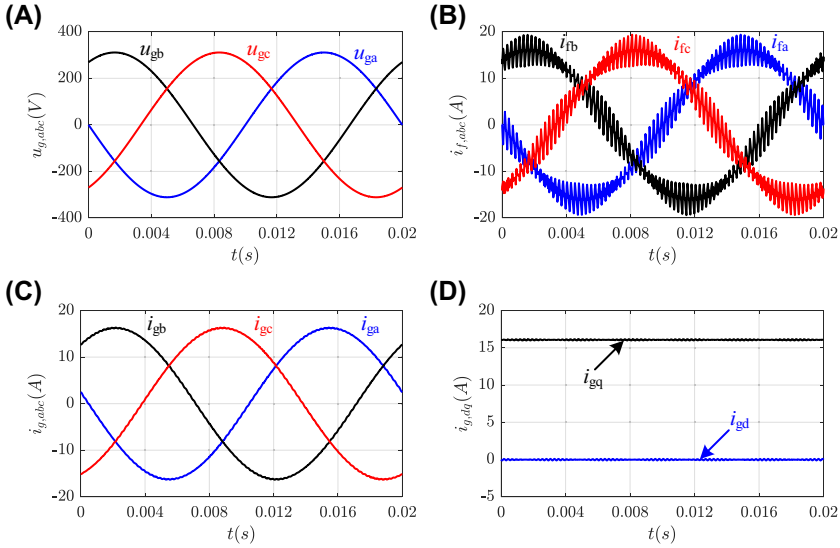

FIGURE 9.2 Steady-state working waveforms of the voltage source converter with *LCL* filter with $P_o = 7.5$ kW. (A) Grid voltages, (B) converter-side currents, (C) grid-side currents, and (D) grid-side *dq*-axis currents.

For the purpose of validating the GAM model, the simulated phase *a* current on the converter side and grid side is compared with the modeled *a* phase current from the first-order GAM of the VSC with *LCL* filter, as shown in Fig. 9.3A and B, respectively. In the modeling procedure, Eq. (9.22) is used to generate the actual AC current from the calculated real and imaginary parts of the first-order Fourier series coefficient in GAM. In the figure, $I_{ga1}(t)$, $I_{fa1}(t)$ are the modeled currents and i_{fa}, i_{ga} are the simulated currents. It can be seen that the first-order generalized average model can track the fundamental component of the converter current and grid current properly.

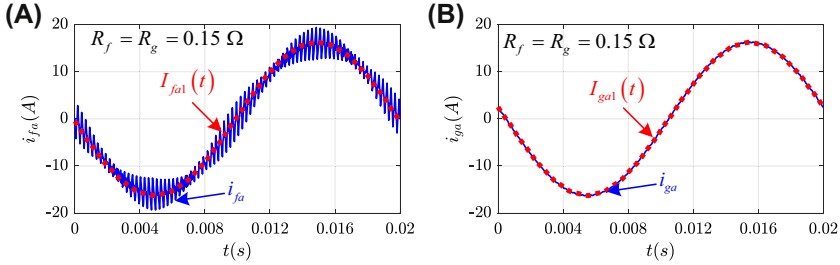

FIGURE 9.3 Comparison of the simulated *a* phase current and the modeling *a* phase current from first-order GAM under $R_f = R_g = 0.15\ \Omega$. (A) Converter-side current comparison, (B) grid-side current comparison.

This book belongs to Kitab Liaison (ocd1996@gmail.com) Copyright Elsevier 2023

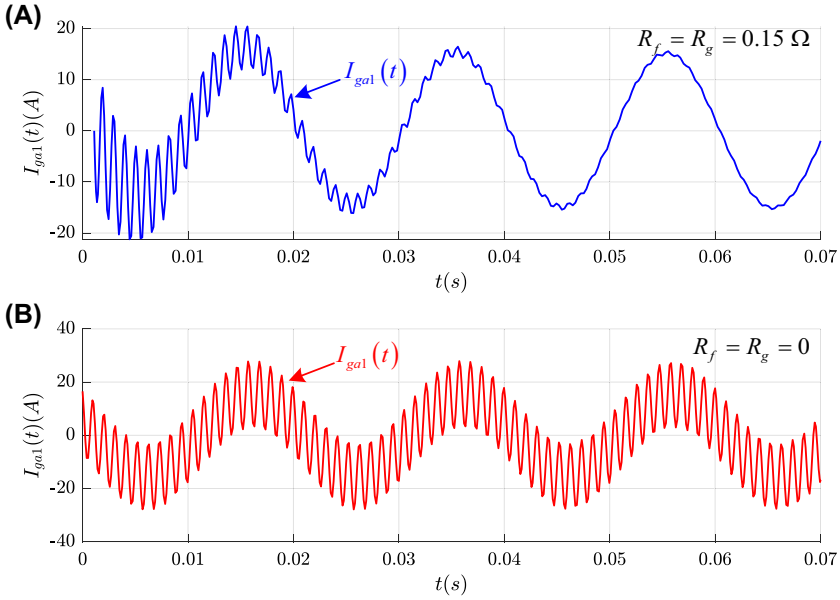

FIGURE 9.4 Modeling start-up waveforms of *a* phase current under (A) $R_f = R_g = 0.15\ \Omega$ and (B) $R_f = R_g = 0$ in the GAM of voltage source converter with *LCL* filter.

Besides, by setting the resistance parts in the converter inductor and grid inductor as zero, the start-up waveform of the modeled *a* phase current is shown in Fig. 9.4B. As comparison, the start-up waveform with nonzero resistance is shown in Fig. 9.4A. It can be seen that the resonance in the beginning is gradually debilitated in Fig. 9.4A due to the existence of the resistance. On the contrary, the resonance caused by *LCL* filter will retain in the current waveforms in Fig. 9.4B if the resistive parts are zero. From this point, the GAM can also be used to study the damping effect of different damping methods, which can be achieved by proper *LCL* filter design in hardware or AD control from software perspective.

9.3 Alternative current control of the VSCs with LCL filters

There are mainly two types of *L* and *LCL* filters for the grid connection of VSCs. In terms of *L*-type filter, one drawback is the need of higher value of inductance to decrease the harmonics of the line current, and another one is the necessity of higher switching frequency to achieve desired dynamic performance. If *LCL*-type filter is used, the size of passive elements and the switching frequency can be lower [12]. However, using *LCL* filter might cause instability problems at zero impedance occurred by its resonance frequency. In order to avoid this instability problem, the inherent, active, or PD methods can be employed [12–15].

This book belongs to Kitab Liaison (ocd1996@gmail.com) Copyright Elsevier 2023

9.3.1 Control in synchronous reference (*dq*) frame

The power circuit of VSCs with the *LCL* filter is as shown in Fig. 9.1. Due to the fact that the impedance of the capacitor branch in *LCL* filter is negligibly small at grid frequency, the *LCL* filter converges to *L* filter at low frequencies. The merit of *LCL* filter becomes evident at higher frequencies, because the impedance of the capacitor branch decreases considerably and the high-frequency ripple attenuation extent rises from 20 to 60 dB/dec. Thus, the *LC* part of the *LCL* filter is in charge of the attenuation of the high-frequency current ripple and current controllers do not have to deal with the high-frequency ripple conduction. Besides, proportional−integral (PI)-based current controllers have limited control bandwidth that primarily depends upon the sampling frequency of the system, and this does not enable the controllers to regulate the high-frequency oscillations. Therefore, PI-based current control can be done in accordance with the *L* filter approximation by neglecting the influence of the capacitor branch. On this basis, the system *dq*-frame control of VSC is shown in Fig. 9.5.

Consequently, the averaged *dq*-frame model in Eq. (9.13) can be simplified as

$$(L_f + L_g)\frac{d\vec{i}_{dq}}{dt} + (R_f + R_g)\vec{i}_{dq} = \frac{V_{dc}}{2}\vec{d}_{dq} - \vec{u}_{g,dq} - j\omega_g(L_f + L_g)\vec{i}_{dq} \tag{9.50}$$

Note that in Eq. (9.50), complex vectors are introduced for the convenience of the analysis, i.e., $\vec{i}_{dq} = i_d + ji_q$, $\vec{d}_{dq} = d_d + jd_q$, $\vec{u}_{g,dq} = u_{gd} + ju_{gq}$.

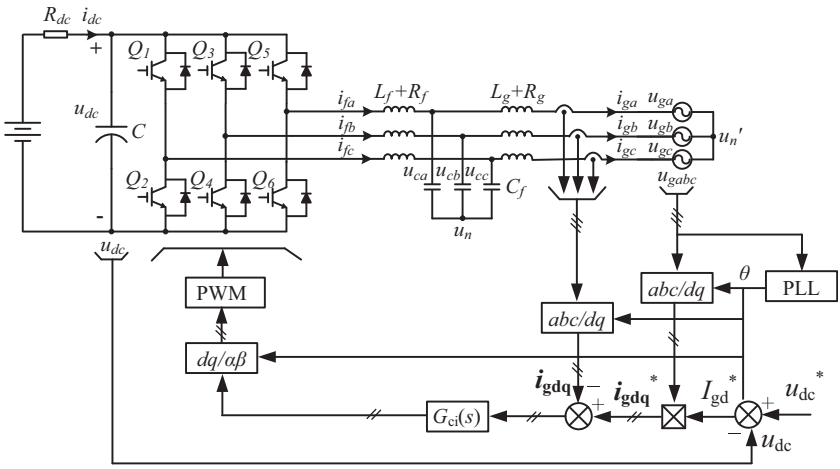

FIGURE 9.5 System *dq*-frame control of voltage source converter in stiff grid.

This book belongs to Kitab Liaison (ocd1996@gmail.com) Copyright Elsevier 2023

ω_g is the grid angular frequency and d_d, d_q are the dq-frame transmission of averaged switching functions.

In order to model a worst-case undamped scenario, the resistive part of the LCL filter components is often neglected in controller design phase, i.e., R_f and R_g in Eq. (9.50) equal zero, leading to

$$(L_f + L_g)\frac{d\vec{i}_{dq}}{dt} = \frac{V_{dc}}{2}\vec{d}_{dq} - \vec{u}_{g,dq} - j\omega_g(L_f + L_g)\vec{i}_{dq} \tag{9.51}$$

Then, the relationship of the s-domain currents $\vec{I}_{dq}(s) = I_d(s) + jI_q(s)$ and input variables $\vec{D}_{dq}(s) = D_d(s) + jD_q(s)$ can be deduced from (9.51), which are

$$P(s) = \frac{\vec{I}_{dq}(s)}{\vec{D}_{dq}(s)} = \frac{V_{dc}}{2(s + j\omega_g)(L_f + L_g)} \tag{9.52}$$

The model of Eq. (9.52) can be equivalently expressed in the transfer function matrix form as

$$\begin{bmatrix} I_d \\ I_q \end{bmatrix} = \mathbf{P}(s)\cdot\frac{V_{dc}}{2}\begin{bmatrix} D_d \\ D_q \end{bmatrix} = \begin{bmatrix} P_1(s) & -P_2(s) \\ P_2(s) & P_1(s) \end{bmatrix}\cdot\frac{V_{dc}}{2}\begin{bmatrix} D_d \\ D_q \end{bmatrix} \tag{9.53}$$

with

$$P_1(s) = \frac{s}{\left(s^2 + \omega_g^2\right)(L_f + L_g)} \qquad P_2(s) = \frac{-\omega_g}{\left(s^2 + \omega_g^2\right)(L_f + L_g)} \tag{9.54}$$

In Eq. (9.53), a nonzero $P_2(s)$ indicates that there exists axis cross-coupling in the converter plant, which means that the input variable D_d or D_q will not only control the corresponding current (I_d or I_q) but also disturb the other current (I_q or I_d). Thus, a decoupling control is needed.

Depending on the current sensor positions, there are two types of current controllers, i.e., converter current feedback (CCF) and grid current feedback (GCF). Accordingly, there are two types of decoupling schemes corresponding to $\vec{i}_{dq} = \vec{i}_{f,dq} = i_{fd} + ji_{fq}$ or $\vec{i}_{dq} = \vec{i}_{g,dq} = i_{gd} + ji_{gq}$ in Eq. (9.50). If the converter complex output voltages are introduced as

$$\vec{u}_o = u_{od} + ju_{oq} = \frac{V_{dc}}{2}(D_d + jD_q) \tag{9.55}$$

the controller block diagrams of these two decoupling methods are as shown in Fig. 9.6. The superscript notation * denotes the reference value. For the purpose of achieving zero displacement between the grid current and the grid voltage (i.e., unity power factor), the given q-axis current should be zero if GCF is used (cf. $i_{gq}^* = 0$ in Fig. 9.6B). Otherwise, if the CCF is employed, the influence of the capacitor branch should be taken into account since the grid

This book belongs to Kitab Liaison (ocd1996@gmail.com) Copyright Elsevier 2023

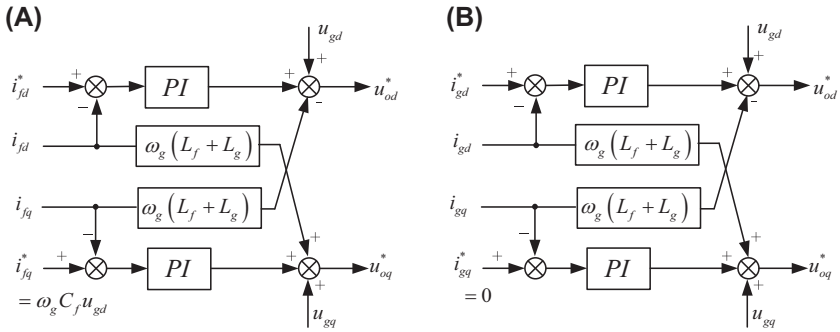

FIGURE 9.6 Decoupling block diagrams of d-axis and q-axis currents. (A) Converter-side current feedback, (B) grid-side current feedback.

current is not directly controlled, and hence a nonzero i^*_{fq} is required. According to the second expression in Eq. (9.13), the q-axis components can be expanded to be

$$C_f \frac{du_{cq}}{dt} = -\omega_g C_f u_{cd} + i_{fq} - i_{gq} \tag{9.56}$$

In steady state, it can be derived from Eq. (9.56) that

$$i^*_{fq} = \omega_g C_f u_{cd} = \omega_g C_f u_{gd} \tag{9.57}$$

which is as shown in Fig. 9.6A.

Then, the overall block diagram of the current loop control can be obtained, as shown in Fig. 9.7. The variables in the figure are expressed in the form of complex vectors. The current controller part in Fig. 9.7 is equivalent to the decoupling control as in Fig. 9.6A or Fig. 9.6B, depending on the current sensor positions. Therein, $G_{PI}(s)$ denotes the PI controller and can be expressed by

$$G_{PI}(s) = K_p + \frac{K_i}{s} \tag{9.58}$$

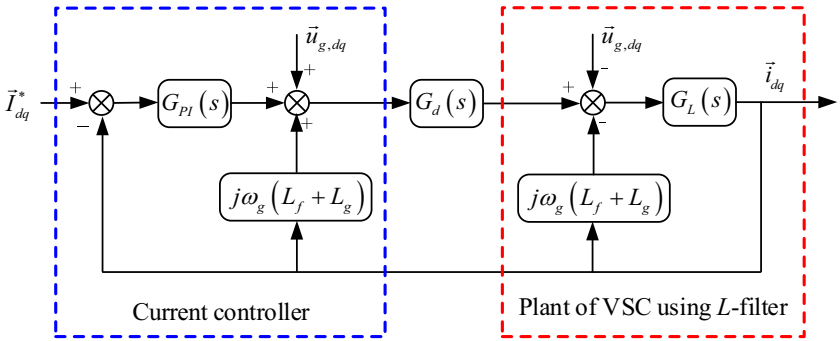

FIGURE 9.7 Overall block diagram of the current loop control.

This book belongs to Kitab Liaison (ocd1996@gmail.com) Copyright Elsevier 2023

Besides, $G_d(s)$ means the transfer function of the total time delay caused by sampling, computation, updating of the compare registers, and the zero-order-hold effect of pulse width modulation [16], which can be estimated as

$$G_d(s) = e^{-sT_d} \approx e^{-s \cdot 1.5T_{samp}} \tag{9.59}$$

with T_d as the time delay and T_{samp} as the sampling cycle of the controller. The last part in Fig. 9.7 is the simplified L-type filter plant (i.e., Eq. 9.51) where

$$G_L(s) = \frac{1}{s(L_f + L_g)} \tag{9.60}$$

9.3.2 Resonance damping technique

Despite that *LCL* filter has the advantages of smaller size and better harmonic attenuation performance over the *L* filter, the utilization of *LCL* filters makes the control design more complicated. One main drawback is the amplification of undesired harmonic components around the resonant frequency. Thus, the harmonics generated by VSC at this frequency are amplified through the *LCL* filter and injected into the grid, leading to the inevitable closed-loop control instability. In the literature, there are various methods to deal with this phenomenon, such as PD provided with resistors connected in several ways to the *LCL* filter [17], AD supplied with the modification of the current control structure using filter capacitor current [14,15], or capacitor voltage [18], inherent damping (ID) [14] achieved by only using the converter-side current feedback and sensorless AD-based estimation of the state variables by using complex state observers [19]. Some of these methods are selected and will be introduced in the following.

The resistive part of the *LCL* filter components is neglected to nullify all internal damping, and the grid voltages are assumed to contain only positive-sequence fundamental components. Thus, the simplified equivalent circuit per phase is shown as in Fig. 9.8, and the plant model transfer function $G_p(s)$ (which is also the *LCL* filter s-domain admittance) is

$$Y_{LCL}(s) = G_p(s) = \frac{I_g(s)}{U_o(s)} = \frac{1}{L_f C_f L_g s^3 + (L_f + L_g)s} \tag{9.61}$$

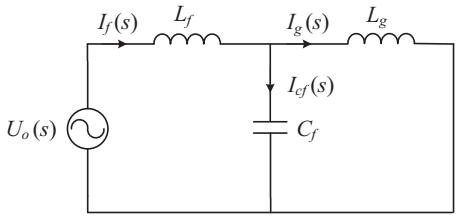

FIGURE 9.8 Simplified equivalent circuit per phase at nonfundamental frequencies of Fig. 9.5.

This book belongs to Kitab Liaison (ocd1996@gmail.com) Copyright Elsevier 2023

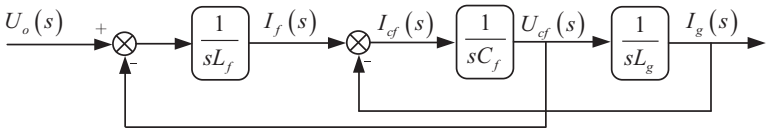

FIGURE 9.9 Block diagram of *LCL* network shown in Fig. 9.8.

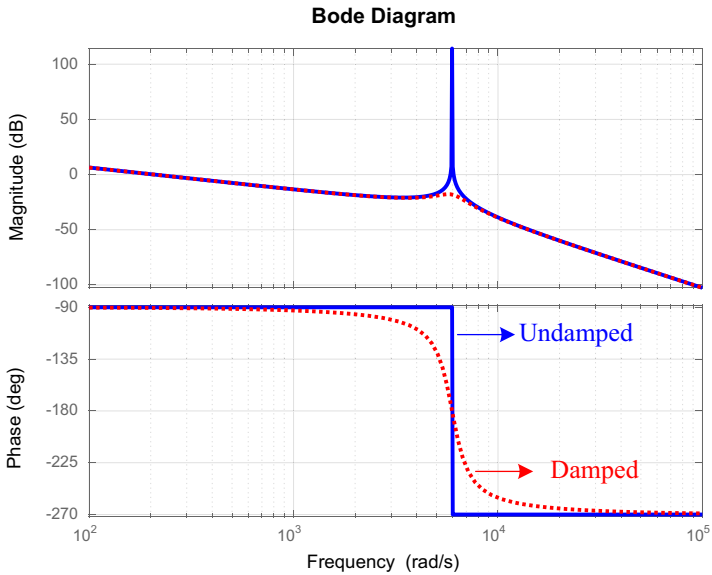

FIGURE 9.10 Bode plot of the open-loop voltage source converter with *LCL* filter under non-damped and damped conditions.

where the capitalized notations represent the variables in the s-domain and $U_o(s)$ is s-function of the converter output voltages. The expression of $G_p(s)$ can also be obtained using the block diagram of the *LCL* filter plant shown in Fig. 9.9. Based on Eq. (9.61), the magnitude and phase response of the undamped *LCL* filter is plotted in Fig. 9.10. An obvious resonance can be observed at the resonance frequency, which should be avoided since the rapid phase transition may cause instability issues. With the utilization of damping methods, the resonance can be suppressed as shown in Fig. 9.10 with the "damped" label, where the peaky magnitude response and the rapid phase transition are softened.

9.3.2.1 Passive damping technique

There are several ways to implement PD [12], among which the minimization of the damping power losses is the vital point to determine the most suitable PD configuration. In light of comprehensive analysis on distinct resistor

This book belongs to Kitab Liaison (ocd1996@gmail.com) Copyright Elsevier 2023

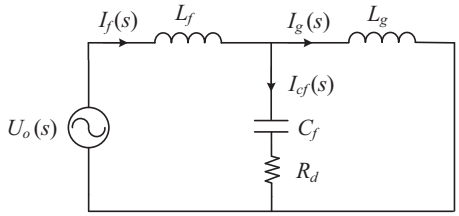

FIGURE 9.11 Equivalent per phase circuit of *LCL* filter with passive damping.

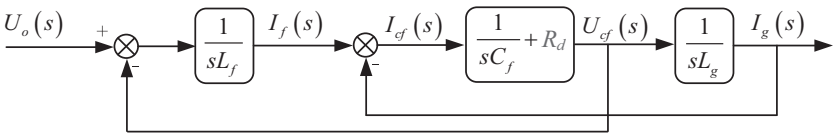

FIGURE 9.12 Block diagram of *LCL* network with passive damping.

configurations, inserting simple resistors into the capacitor branch in *LCL* filters is proved to deliver the least PD losses [20,21], the structure of which is as shown in Fig. 9.11. The equivalent block diagram of the *LCL* filter with PD is shown in Fig. 9.12, and the transfer function between the grid current and the converter output voltage can be derived as

$$G_{PD}(s)=\frac{I_g(s)}{U_o(s)}=\frac{R_dC_fs+1}{L_fC_fL_gs^3+C_fR_d(L_f+L_g)s^2+(L_f+L_g)s} \tag{9.62}$$

The magnitude and phase response are plotted in Fig. 9.13, where the peak resonance response is clearly suppressed. In the low-frequency range, the impact of PD is not considerable due to the much lower impedance of the damping resistor R_d than that of the filter capacitor C_f . In higher frequency range, the impedance of damping resistor is increased, and the high-frequency current components (especially the switching harmonics) begin to flow into the grid. Therefore, there is a tradeoff between the system stability and the low switching ripple injected to the grid.

9.3.2.2 Active damping technique using filter capacitor current feedback

Due to the fact that the resonance is caused by the filter capacitor, it is reasonable to process the current/voltage information of the capacitor part. The block diagram shown in Fig. 9.14 employs the capacitor current feedback to realize AD control. The AD block $K(s)$ can be modeled as a simple proportional controller with a constant gain K_d. Seen from Fig. 9.14, it is not convenient to analyze the resonance damping because the feedback current is tapped from the middle of the *LCL* plant. By moving the connection point backward to the grid current side, an equivalent block diagram can be obtained

This book belongs to Kitab Liaison (ocd1996@gmail.com) Copyright Elsevier 2023

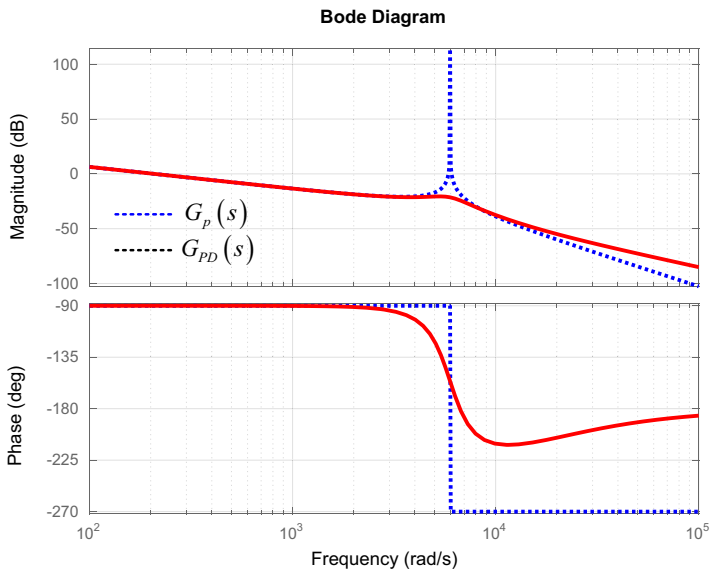

FIGURE 9.13 Comparison of the attenuation capability between undamped and passive-damped *LCL* filter.

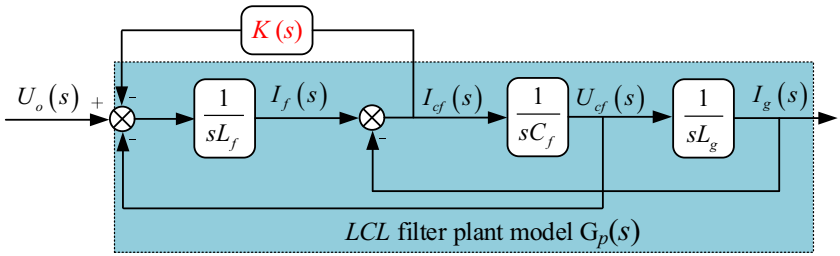

FIGURE 9.14 Block diagram of the *LCL* network with capacitor current feedback for active damping.

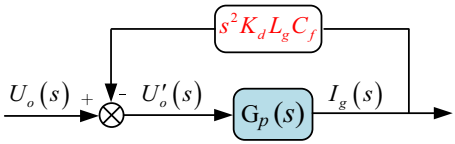

FIGURE 9.15 Equivalent block diagram of the *LCL* network using active damping.

as shown in Fig. 9.15. The *LCL* filter plant is denoted by $G_p(s)$ (cf. Eq. 9.61) in the figure. It can be found that the converter output voltage to the *LCL* plant is modified by the AD block, and the transfer function from the original $U_o(s)$ to the new $U_o'(s)$ is

This book belongs to Kitab Liaison (ocd1996@gmail.com) Copyright Elsevier 2023

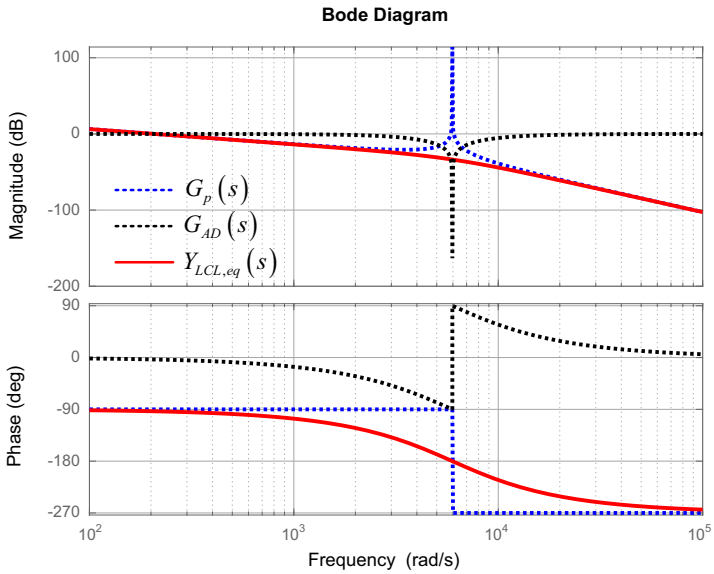

FIGURE 9.16 Impact of the capacitor current feedback on resonance damping.

$$G_{AD}(s) = \frac{U_o'(s)}{U_o(s)} = \frac{L_f C_f L_g s^3 + (L_f + L_g)s}{L_f C_f L_g s^3 + K_d C_f L_g s^2 + (L_f + L_g)s} \tag{9.63}$$

Then the equivalent admittance transfer function between the grid current and the converter output voltage can be derived as

$$Y_{LCL,eq}(s) = \frac{I_g(s)}{U_o(s)} = G_p(s) \cdot \frac{U_o'(s)}{U_o(s)} = \frac{1}{L_f C_f L_g s^3 + K_d C_f L_g s^2 + (L_f + L_g)s} \tag{9.64}$$

Comparing Eq. (9.64) and undamped Eq. (9.61), the s^2-term appears in the denominator resulting from the capacitor current feedback, which can effectively avoid a phase jump and the resonance peak. In order to verify this, the magnitude and phase responses of $G_p(s)$, $G_{AD}(s)$, and $Y_{LCL,eq}(s)$ are plotted in Fig. 9.16. It can be seen that the AD block transfer function $G_{AD}(s)$ behaves like a notch filter (NF), providing a negative peak response as opposed to the undamped *LCL* filter resonance. If a proper K_d value is selected, these two peaks might cancel out each other at the resonant frequency and an improved damped system can be obtained, as highlighted by the solid red (gray in print version) line in the figure.

9.3.2.3 Active damping technique under grid current feedback

The closed-loop system consisting of the *LCL* filter plant $G_p(s)$, the PI current controller $G_{PI}(s)$, and the grid-side current feedback i_g is as shown in Fig. 9.17.

This book belongs to Kitab Liaison (ocd1996@gmail.com) Copyright Elsevier 2023

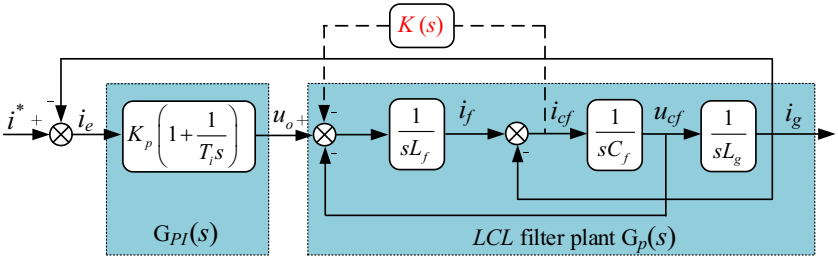

FIGURE 9.17 Block diagram of the grid-side current feedback control without/with active damping.

It should be noted that the time delay, as shown in the overall system control block diagram Fig. 9.7, is treated as pure amplifier gain here and thus is integrated into the front-end current controller [14]. Detailed information of the impact of time delay on the controller design and system stability can be found in Refs. [22–24], where the method of equivalent impedance model in discrete domain is often employed.

The open-loop transfer function without AD in Fig. 9.17 can be derived as

$$G_{PI}(s)G_p(s) = \frac{K_p(s + 1/T_i)}{L_f C_f L_g s^4 + (L_f + L_g)s^2} \tag{9.65}$$

from which the third-order term is absent, indicating the difficulty to reach stability for closed-loop control. In spite of the PD resulting from the resistive part of the *LCL* components, the damping extent is generally inadequate. Thus, the aforementioned AD block is added, as shown by the dashed feedback in Fig. 9.17. The open-loop function changes to

$$\frac{I_g(s)}{I_e(s)} = \frac{K_p(s + 1/T_i)}{L_f C_f L_g s^4 + K_d C_f L_g s^3 + (L_f + L_g)s^2} \tag{9.66}$$

The current controller parameters do not appear in the resulting s^3 term in Eq. (9.66), revealing that $G_{PI}(s)$ has no impact on the resonant damping under GCF. Besides, the damping extent can also be evaluated by the damping factor ζ, which can be regulated by

$$\frac{K_d}{L_f} = 2\zeta\omega_{res} = 2\zeta\sqrt{\frac{L_f + L_g}{L_f L_g C_f}} \tag{9.67}$$

In Eq. (9.67), the term K_d/L_f is the proportion of the constant coefficients of the second highest order variable (s^3 in Eq. 9.66) to the highest order variable (s^4 in Eq. 9.66) and ω_{res} is the resonant angular frequency. Generally, an optimum damping factor $\zeta = 0.707$ is recommended in literature [14,15].

In order to validate the effectiveness of the AD in GCF control, the simulated working waveforms of the converter-side current and the grid-side

This book belongs to Kitab Liaison (ocd1996@gmail.com) Copyright Elsevier 2023

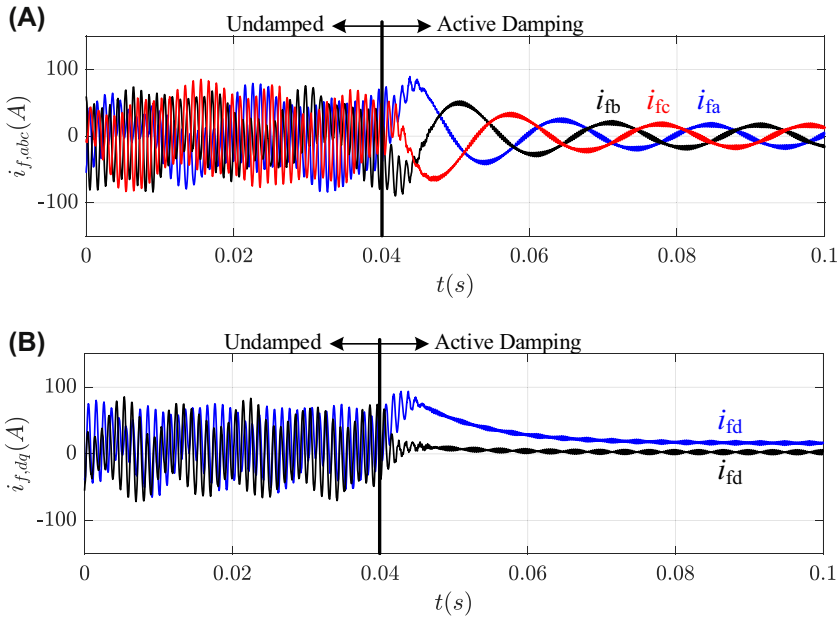

FIGURE 9.18 Simulated waveforms of the converter-side current under grid current feedback control with $P_o = 7.5$ kW. (A) Three-phase converter-side AC currents, (B) transformed dq frame converter-side currents.

current are shown in Figs. 9.18 and 9.19, respectively. The converter parameters are as listed in Table 9.1, except that the equivalent series resistance of the converter inductor and the grid inductor is set at zero in undamped case. In the following Figs. 9.18 and 9.19, the capacitor current feedback−based AD is activated at $t = 0.04$ s, and it can be seen that the resonant three-phase AC currents are immediately damped and reach steady state after one fundamental operating period.

9.3.2.4 Active damping technique under converter current feedback

A block diagram of the converter-side current feedback control is shown in Fig. 9.20, which can be equivalently modified to the control in Fig. 9.21. Compared to the GCF control in Fig. 9.17, an additional GCF appears in the loop, which can be seen as the ID characteristic of CCF. The open-loop transfer function can be derived as

$$\frac{I_g(s)}{I_e'(s)} = \frac{K_p(s + 1/T_i)}{L_f C_f L_g s^4 + K_p C_f L_g s^3 + (K_p C_f L_g/T_i + L_f + L_g)s^2} \tag{9.68}$$

This book belongs to Kitab Liaison (ocd1996@gmail.com)
Copyright Elsevier 2023

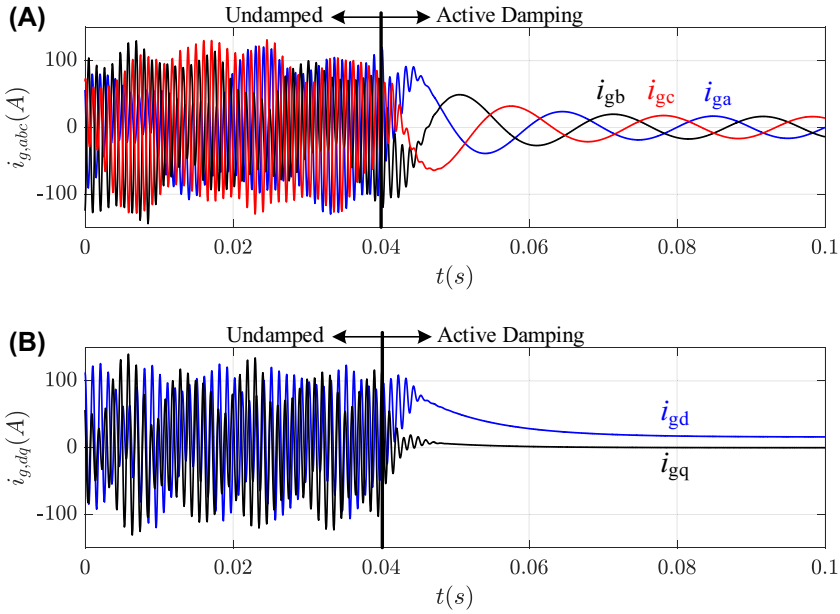

FIGURE 9.19 Simulated waveforms of the grid-side currents under grid current feedback control with $P_o = 7.5$ kW. (A) Three-phase grid-side AC currents, (B) transformed dq frame grid-side currents.

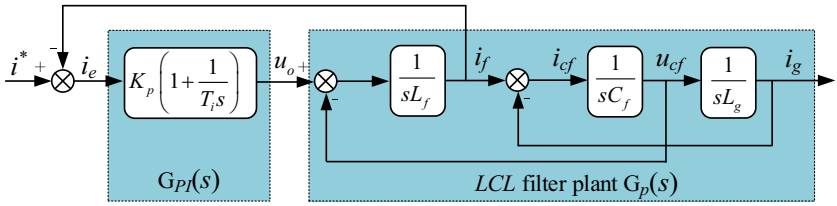

FIGURE 9.20 Block diagram of converter-side current feedback control.

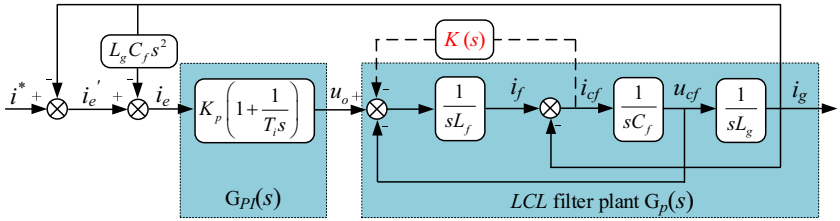

FIGURE 9.21 Equivalent block diagram of converter-side current feedback with active damping.

This book belongs to Kitab Liaison (ocd1996@gmail.com)
Copyright Elsevier 2023

Comparing Eq. (9.68) with Eq. (9.65), it can be found that due to the existence of the extra GCF in CCF, the s^3 term also appears in the denominator of the open-loop transfer function, indicating an intrinsic damping control of CCF. Similarly, the damping can be obtained with

$$\frac{K_p}{L_f} = 2\zeta\omega_{res} \tag{9.69}$$

where either K_p or L_f can be used to adjust the damping factor ζ. If the required damping factor cannot be achieved by only adjusting K_p or L_f, then additional damping terms $K(s)$ could be introduced into the loop. Consequently, the open-loop transfer function becomes

$$\frac{I_g(s)}{I_e'(s)} = \frac{K_p(s + 1/T_i)}{L_f C_f L_g s^4 + (K_p + K_d)C_f L_g s^3 + (K_p C_f L_g/T_i + L_f + L_g)s^2} \tag{9.70}$$

Likewise, the damping can be adjusted by

$$\frac{K_p + K_d}{L_f} = 2\zeta\omega_{res} \tag{9.71}$$

In order to compare the effectiveness of the damping method under GCF and CCF control, the closed-loop poles corresponding to Eqs. (9.65), (9.66), (9.68), and (9.70) are shown in Fig. 9.22. The original GCF (denoted by blue

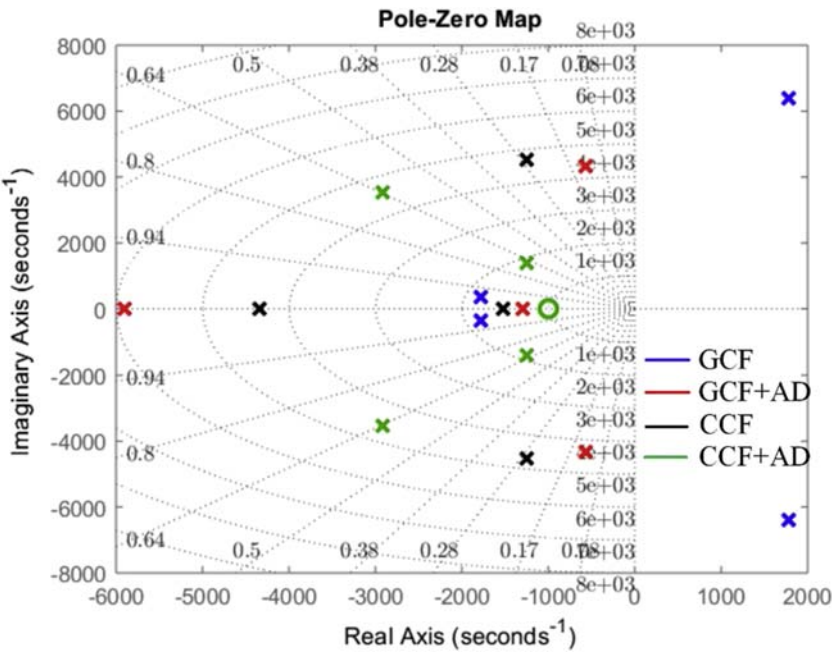

FIGURE 9.22 Pole locations under grid current feedback (GCF) control and converter current feedback (CCF) control using active damping.

This book belongs to Kitab Liaison (ocd1996@gmail.com) Copyright Elsevier 2023

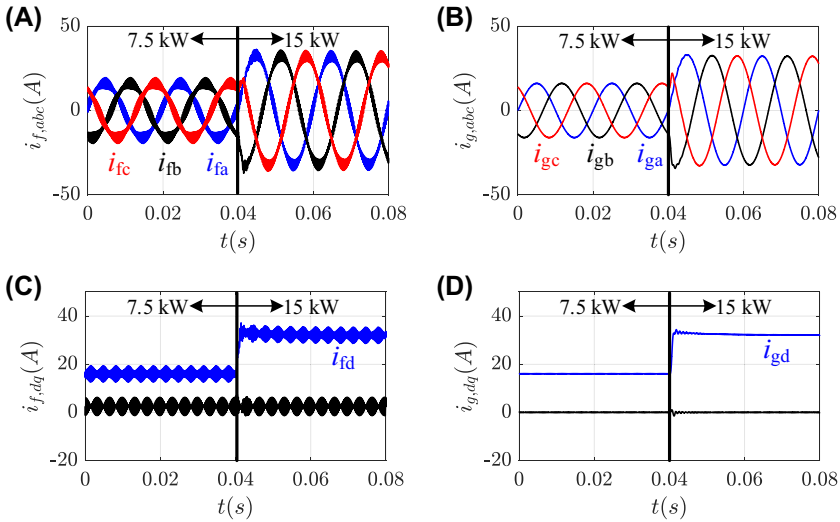

FIGURE 9.23 Simulated waveforms under converter current feedback with P_o changing from 7.5 to 15 kW at $t = 0.04$ s. (A) Three-phase converter-side AC currents, (B) three-phase grid-side AC currents, (C) dq frame converter-side currents, (D) dq frame grid-side currents.

(gray in print version) points) control is not stable since there are poles in the right s plane, while the other three cases can achieve stability if proper LCL filter components and controller/damping parameters are selected.

By operating the converter with CCF control method, the simulated waveforms including the converter-side current and the grid-side current are shown in Fig. 9.23. In order to keep the grid currents in phase with grid voltages (i.e., unity power factor), the q-axis reference current is given as $\omega_g C_f u_{gd}$, as shown in Fig. 9.6. The operating power is changed from 7.5 to 15 kW at $t = 0.04$ s in Fig. 9.23. It can be seen that there is no clear resonance in the converter current and the grid current due to the ID characterization in CCF control, which is in agreement with the discussions before.

9.3.3 Control under unbalanced grid voltages

As discussed previously, the AC voltages/currents can be divided into positive- and negative-sequence components when the grid voltages are unbalanced or distorted. Thus, a common way to control the grid current under unbalanced power system is to regulate the positive- and negative-sequence currents separately based on synchronous dq-reference frame [25]. Of course, grid currents can also be controlled in a stationary reference frame (e.g., $\alpha\beta$ frame) and resonant controllers (e.g., proportional resonant controller) instead of PI control are often utilized in this situation.

In order to control the grid currents under unbalanced grid voltages, the dq components of the positive- and negative-sequence voltages/currents should be

This book belongs to Kitab Liaison (ocd1996@gmail.com) Copyright Elsevier 2023

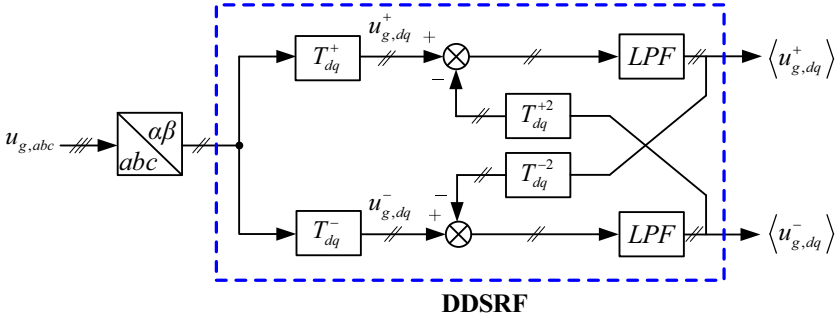

FIGURE 9.24 Block diagram of decoupled synchronous reference frame (DDSRF) to be applied in unbalanced grid.

extracted from the original signals at first. Focusing on the fundamental components (i.e., first-order harmonic) of the AC variables, if U_g^+ and U_g^- are supposed being as the amplitudes of the positive- and negative-sequence voltages, the respective dq components can be obtained through Park transformation (cf. Eq. 9.9) and the reverse Park transformation, i.e.,

$$\begin{bmatrix} U_{gd}^{+} \\ U_{gq}^{+} \end{bmatrix} = \underbrace{\begin{bmatrix} \cos\omega t & \sin\omega t \\ -sin\omega t & \cos\omega t \end{bmatrix}}_{T_{dq}^{+}} \begin{bmatrix} U_{g\alpha} \\ U_{g\beta} \end{bmatrix} = U_g^{+} \begin{bmatrix} 1 \\ 0 \end{bmatrix} + U_g^{-} \begin{bmatrix} \cos(-2\omega t) \\ \sin(-2\omega t) \end{bmatrix} \tag{9.72}$$

$$\begin{bmatrix} U_{gd}^{-} \\ U_{gq}^{-} \end{bmatrix} = \underbrace{\begin{bmatrix} \cos\omega t & -\sin\omega t \\ sin\omega t & \cos\omega t \end{bmatrix}}_{T_{dq}^{-}} \begin{bmatrix} U_{g\alpha} \\ U_{g\beta} \end{bmatrix} = U_g^{+} \begin{bmatrix} \cos(2\omega t) \\ \sin(2\omega t) \end{bmatrix} + U_g^{-} \begin{bmatrix} 1 \\ 0 \end{bmatrix} \tag{9.73}$$

It can be seen that the DC values of the transformed results are equal to the amplitudes of positive/negative-sequence voltages, and the twice angular frequency (i.e., 2ω) terms indicate the component coupling between d-axis and q-axis. From this perspective, a decoupling network [26] similar to Fig. 9.6 can be used to cancel out the effect of the 2ω oscillations, which is as shown in Fig. 9.24.

In Fig. 9.24, the transformation matrices T_{dq}^{+2} and T_{dq}^{-2} are

$$T_{dq}^{+2} = \left[T_{dq}^{-2}\right]^T = \begin{bmatrix} \cos(2\omega t) & \sin(2\omega t) \\ -sin(2\omega t) & \cos(2\omega t) \end{bmatrix} \tag{9.74}$$

The LPF block in Fig. 9.24 is a first-order low-pass filter, and the final outputs $\langle u_{g,dq}^{+} \rangle$ and $\langle u_{g,dq}^{-} \rangle$ are the average decoupled dq voltages of the positive- and negative-sequence components, respectively.

This book belongs to Kitab Liaison (ocd1996@gmail.com) Copyright Elsevier 2023

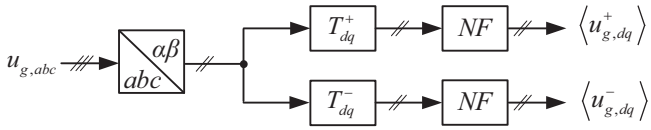

FIGURE 9.25 Block diagram of average dq-component calculation using notch filters to be applied in unbalanced grid.

On the other hand, from a filtering point of view, the positive/negative-sequence components can also be obtained by using a NF and the transfer function of which can be expressed by

$$G_{NF}(s) = \frac{s^2 + \omega_n^2}{s^2 + 2\omega_n s + \omega_n^2} \tag{9.75}$$

where ω_n is the notch frequency and it should be equal to the 2ω value in Eq. (9.74). The schematic block is shown in Fig. 9.25.

Other than the dq-component calculation as discussed above, the grid synchronization technique to extract the grid voltage–phase angle is another key part in the unbalanced current control. The commonly used dual second-order generalized integrator–phase-locked loop (DSOGI-PLL) is introduced into the control system [27], and the schematic diagram is shown in Fig. 9.26. Therein, the second-order generalized integrator (SOGI) submodule is the second-order generalized integrator, which is as shown in Fig. 9.27. The input

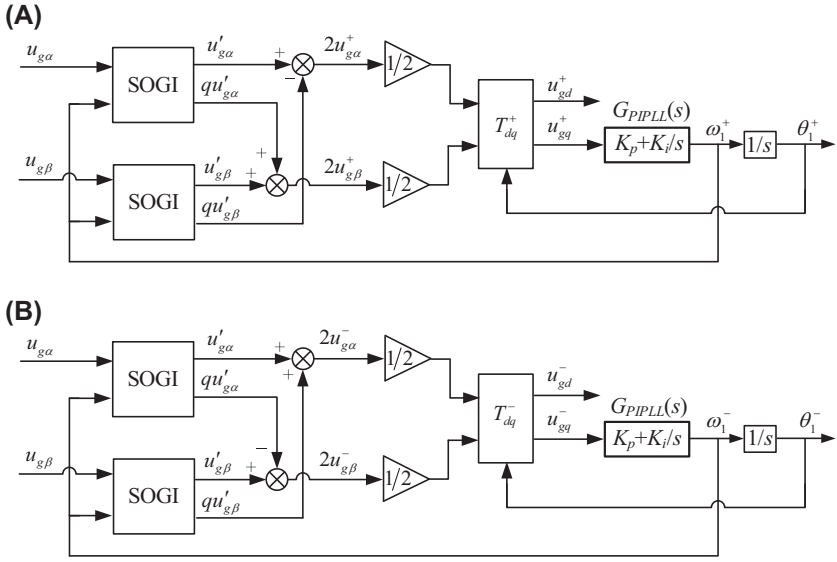

FIGURE 9.26 Schematic diagram of the DSOGI-PLL. (A) Positive-sequence grid voltage–phase angular extraction, (B) negative-sequence grid voltage–phase angular extraction.

This book belongs to Kitab Liaison (ocd1996@gmail.com) Copyright Elsevier 2023

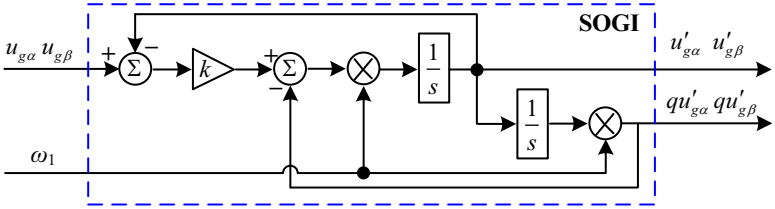

FIGURE 9.27 Schematic diagram of the second-order generalized integrator (SOGI) block in Fig. 9.26.

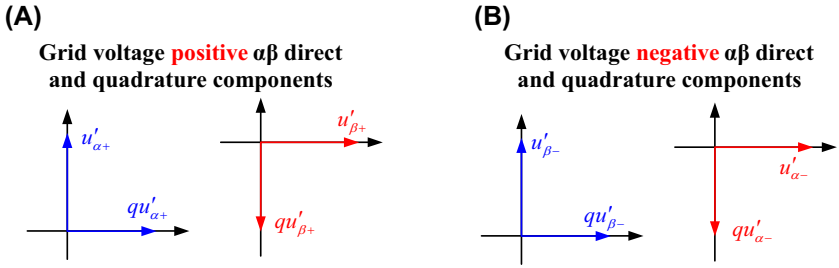

FIGURE 9.28 Phasor diagram of (A) grid voltage positive $\alpha\beta$ direct/quadrature components and (B) negative $\alpha\beta$ direct/quadrature components.

to SOGI can be either the α-axis or the β-axis component, and the outputs $qu'_{g\alpha}$ $qu'_{g\beta}$ denote the orthogonal signals of $u'_{g\alpha}$ and $u'_{g\beta}$ with a 90 degrees lag, respectively. The relationships among these output signals of SOGI are shown in Fig. 9.28. Therefore, the following equations can be derived for calculating the positive- and negative-sequence components in $\alpha\beta$-reference frame.

$$u'_{\alpha} - qu'_{\beta} = \left(u'_{\alpha+} + u'_{\alpha-}\right) - \left(qu'_{\beta+} + qu'_{\beta-}\right) = u'_{\alpha+} - qu'_{\beta+} = 2u'_{\alpha+} \tag{9.76}$$

$$qu'_{\alpha} + u'_{\beta} = \left(qu'_{\alpha+} + qu'_{\alpha-}\right) + \left(u'_{\beta+} + u'_{\beta-}\right) = qu'_{\alpha+} + u'_{\beta+} = 2u'_{\beta+} \tag{9.77}$$

$$u'_{\alpha} + qu'_{\beta} = \left(u'_{\alpha+} + u'_{\alpha-}\right) + \left(qu'_{\beta+} + qu'_{\beta-}\right) = u'_{\alpha-} + qu'_{\beta-} = 2u'_{\alpha-} \tag{9.78}$$

$$-qu'_{\alpha} + u'_{\beta} = -\left(qu'_{\alpha+} + qu'_{\alpha-}\right) + \left(u'_{\beta+} + u'_{\beta-}\right) = -qu'_{\alpha+} + u'_{\beta-} = 2u'_{\beta+} \tag{9.79}$$

On the basis of average dq-component extraction (cf. Fig. 9.24 or Fig. 9.25) and the grid synchronous method DSOGI-PLL (cf. Fig. 9.26), the overall current control procedure under unbalanced grid voltages can be achieved, as shown in Fig. 9.29. Therein, the decoupling positive- and negative-sequence current control blocks are shown in Fig. 9.30.

This book belongs to Kitab Liaison (ocd1996@gmail.com) Copyright Elsevier 2023

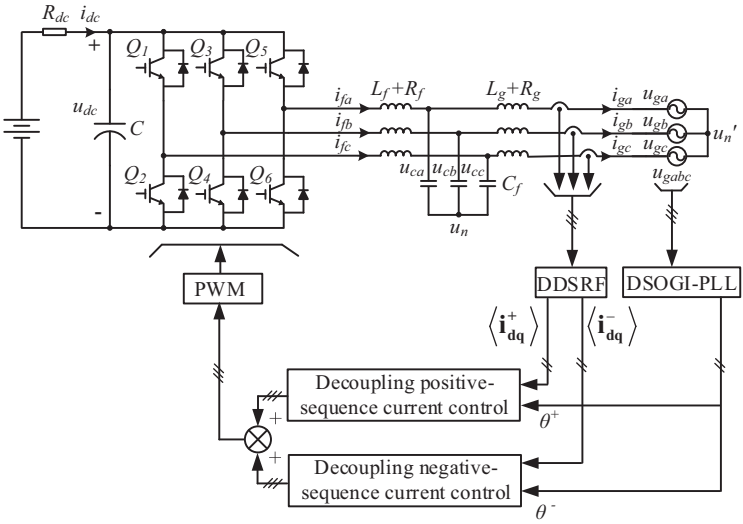

FIGURE 9.29 Block diagram of the overall current control under unbalanced grid voltages.

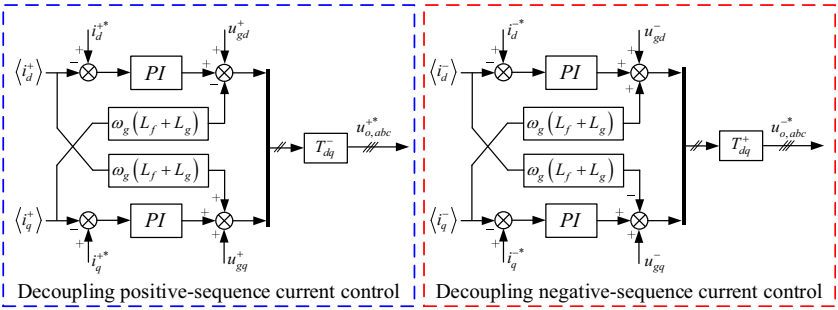

FIGURE 9.30 Block diagram of the decoupling positive- and negative-sequence current control.

In Fig. 9.30, the reference values of the positive/negative-sequence *dq*-axis currents are usually obtained from an outer power control loop in unbalanced grid. There are several power control methods in the literature [28], such as instantaneous active-reactive control, positive- and negative-sequence control, average active-reactive control, and balanced positive-sequence control (BPSC). In this chapter, the BPSC method is considered, and the goal is to inject a set of balanced sinusoidal current with only positive-sequence components into the grid.

In order to validate the current control under unbalanced grid voltages, a PLECS simulation model with the parameters shown in Table 9.2 is built. Considering the BPSC power control method, the reference negative-sequence *dq*-axis currents are zero. Besides, in order to avoid the current resonance in

This book belongs to Kitab Liaison (ocd1996@gmail.com) Copyright Elsevier 2023

TABLE 9.2 Parameters of 15 kW grid-tied voltage source converters with LCL Filter under unbalanced grid voltages.

Operating power P_o (kW)	7.5/15
Balanced grid peak phase voltage U_g (V)	311
DC-link voltage V_{dc} (V)	650
Converter-side inductor L_f (mH)	3
Capacitor branch C_f (uF)	25
Grid-side inductor L_g (mH)	1.8
Grid voltage frequency f_g (Hz)	50
Switching frequency f_{sw} (kHz)	4
The proportional gain in SOGI block k (Fig. 9.27)	10
The proportional gain in DSOGI-PLL block K_p (Fig. 9.25)	10
The integral coefficient in DSOGI-PLL block K_i (Fig. 9.25)	1000
Unbalanced a phase grid voltage u_{ga} (V)	311 $\cos(\omega_g t)$
Unbalanced b phase grid voltage u_{gb} (V)	280 $\cos(\omega_g t - 2\pi/3)$
Unbalanced c phase grid voltage u_{gc} (V)	342 $\cos(\omega_g t + 2\pi/3)$

GCF as discussed before, the CCF-based control is applied to the converter. Thus, the reference positive-sequence q-axis current is set as $\omega_g C_f u_{gd}^{+}$ to maintain unity power factor, where ω_g is the grid voltage frequency, C_f is the capacitor in LCL filter, and u_{gd}^{+} is the positive-sequence d-axis grid voltage. The simulated working waveforms of the converter-side currents and grid-side currents are shown in Figs. 9.31–9.33. During the simulation procedure, the reference positive d-axis converter-side current is changed from 16 to 32 A at time $t = 0.06$ s. In Fig. 9.31, the unbalanced three-phase AC grid voltages (u_{ga}, u_{gb}, u_{gc}) and the balanced grid-side currents (i_{ga}, i_{gb}, i_{gc}) are in phase with each other, indicating a unity power factor. By using the DDSRF technique, the positive- and negative-sequence dq-axis converter-side currents are extracted and shown in Fig. 9.32. Similarly, the transient response of the grid-side currents is shown in Fig. 9.33. The converter can effectively follow the reference value, which implies the feasibility of the decoupled double synchronous reference frame current control method.

9.4 Impedance-based stability analysis under weak grid conditions

In weak grid conditions, one big difference from the strong power system is that the grid-side impedance might vary widely, which is mainly dependent on

This book belongs to Kitab Liaison (ocd1996@gmail.com) Copyright Elsevier 2023

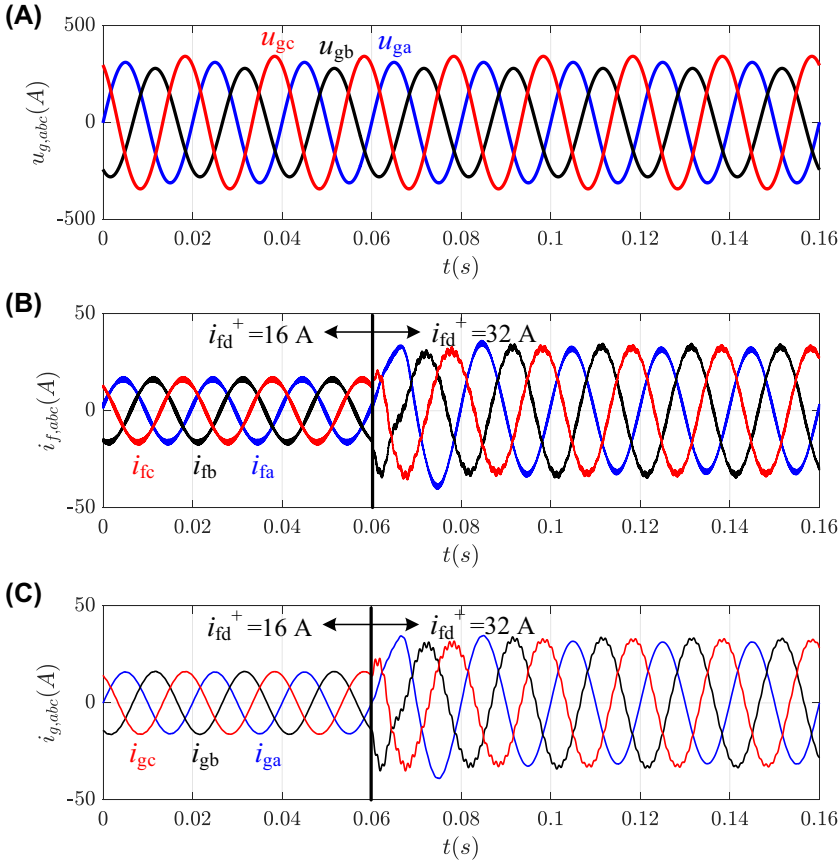

FIGURE 9.31 Simulated waveforms under unbalanced grid voltages with the given positive-sequence d-axis converter current changing from 16 to 32 A at $t = 0.06$ s. (A) Grid voltages, (B) converter-side currents, (C) grid-side currents.

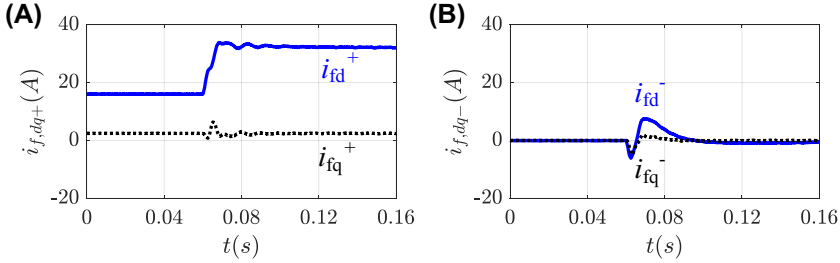

FIGURE 9.32 Simulated transient response of dq-axis converter-side currents with the given positive-sequence d-axis converter current changing from 16 to 32 A at $t = 0.06$ s. (A) Positive-sequence dq currents, (B) negative dq currents.

This book belongs to Kitab Liaison (ocd1996@gmail.com) Copyright Elsevier 2023

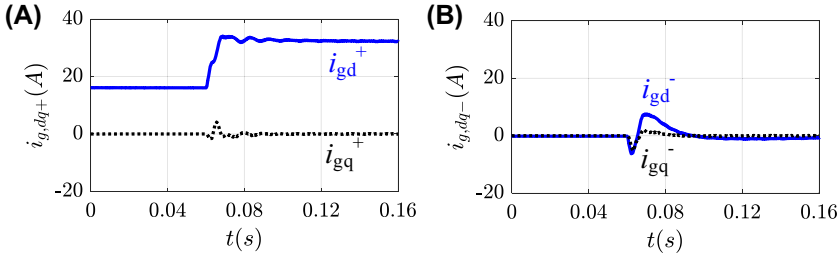

FIGURE 9.33 Simulated transient response of *dq*-axis grid-side currents with the given positive-sequence *d*-axis converter current changing from 16 to 32 A at $t = 0.06$ s. (A) Positive-sequence *dq* currents, (B) negative *dq* currents.

the linear transformers and distribution feeders. Consequently, the grid impedance is possibly close to or larger than the converter-side impedance, especially when multiple grid-connected converters are interconnected at the point of common coupling (PCC). In that case, the grid impedance cannot be neglected as in the strong power system. In order to reveal the effect of the grid impedance on the converter stability, the impedance-based analysis method is introduced in the following.

9.4.1 System control of the *LCL*-filtered VSCs in $\alpha\beta$ frame and *dq* frame

Based on the derived $\alpha\beta$-frame model (9.12), the system control scheme in $\alpha\beta$ frame is as shown in Fig. 9.34. As discussed previously, in order to damp the resonance caused by the *LCL* filter, the filter capacitor current−based AD method is applied. Compared to the strong-grid configuration, the grid impedance between the PCC and the grid voltage is considered and is denoted

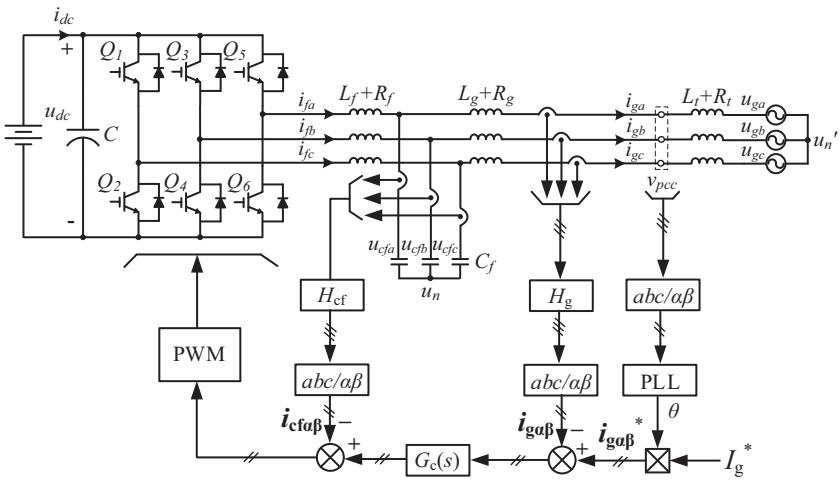

FIGURE 9.34 Block diagram of the system control in $\alpha\beta$-reference frame.

This book belongs to Kitab Liaison (ocd1996@gmail.com)
Copyright Elsevier 2023

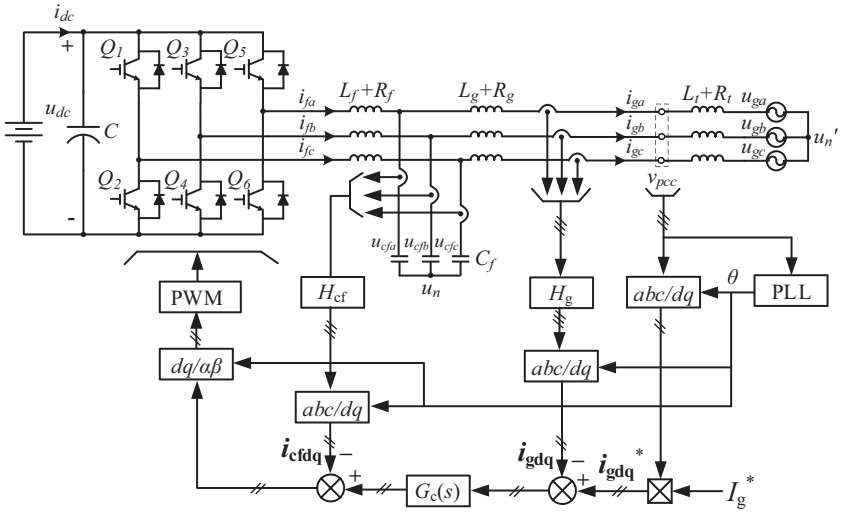

FIGURE 9.35 Block diagram of the system control in *dq*-reference frame.

by $L_t + R_t$ in Fig. 9.34. Therein, $\mathbf{i}^*_{\mathbf{g\alpha\beta}} = \left[i^*_{g\alpha} \quad i^*_{g\beta} \right]^T$ is the reference grid current, $\mathbf{i_{g\alpha\beta}} = \left[i_{g\alpha} \quad i_{g\beta} \right]^T$ is the actual grid current, and $\mathrm{i}_{cf\alpha\beta} = \left[i_{cf\alpha} \quad i_{cf\beta} \right]^T$ is the capacitor branch current in the *LCL* filter, all of which are represented by the $\alpha\beta$-frame form. H_{cf} and H_g are the sensor gains of the grid current i_{gabc} and the capacitor branch current i_{cfabc}, respectively. $G_c(s)$ is the current controller. Note that the DC-link voltage is assumed constant and the current control is the focus.

Besides, the grid voltage phase θ is detected using the sampled three-phase voltages at PCC. It can be easily found that there is a phase difference between the PCC voltages and the actual grid voltages, which will cause a small error between the detected θ and the actual θ. The impact of this error and the methods to omit it are described in detail in Refs. [29,30]. In terms of the reference current amplitude I_g^*, it is directly given in Fig. 9.34, instead of being generated by the outer voltage loop as in Fig. 9.5. Similarly, based on the *dq*-frame model (9.13), the grid current control diagram in *dq* frame is as shown in Fig. 9.35, where $\mathbf{i}^*_{\mathbf{gdq}} = \left[i^*_{gd} \quad i^*_{gq} \right]^T$ is the reference grid current, $\mathbf{i_{g\alpha\beta}} = \left[i_{gd} \quad i_{gq} \right]^T$ is the actual grid current, and $\mathbf{i_{cfdq}} = \left[i_{cfd} \quad i_{cfq} \right]^T$ is the capacitor branch current in the *LCL* filter, all of which are represented by the *dq*-frame form.

According to the control procedures in Figs. 9.34 and 9.35, the block diagrams of the grid current *s*-domain control in $\alpha\beta$ frame and *dq* frame are shown in Figs. 9.36 and 9.37, respectively. The VSC is represented by a proportional gain K_{PWM}, and considering the practical time delay in digital control, the delay block $G_d(s)$ is introduced and can be expressed by

$$G_d(s) = e^{-1.5sT_s} \tag{9.80}$$

This book belongs to Kitab Liaison (ocd1996@gmail.com) Copyright Elsevier 2023

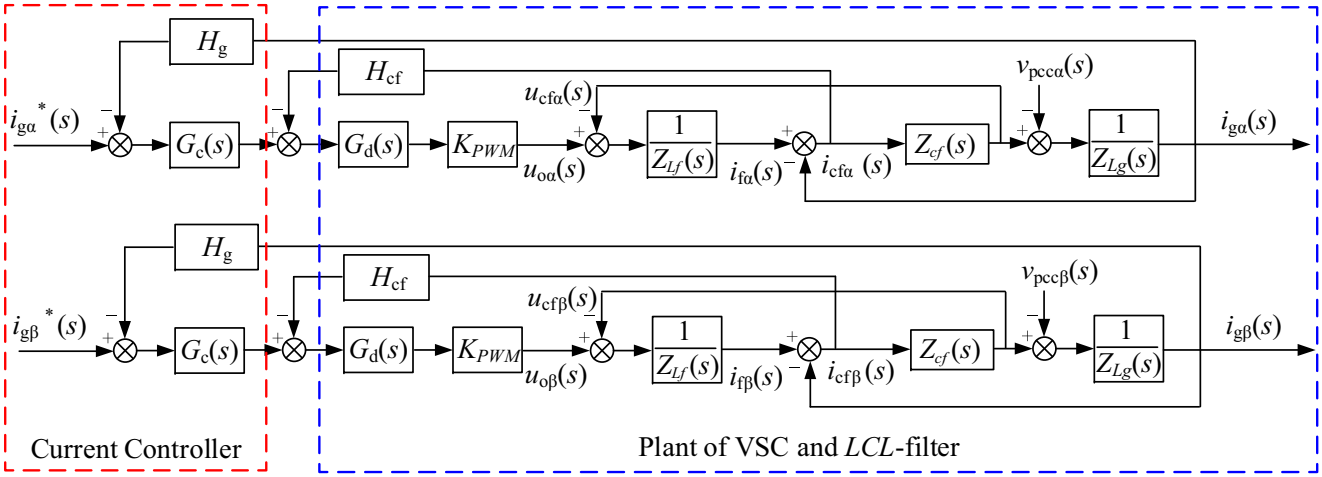

FIGURE 9.36 Block diagram of the s-domain current controller for the LCL-filtered voltage source converter (VSC) under stationary $\alpha\beta$ frame.

This book belongs to Kitab Liaison (ocd1996@gmail.com)

Copyright Elsevier 2023

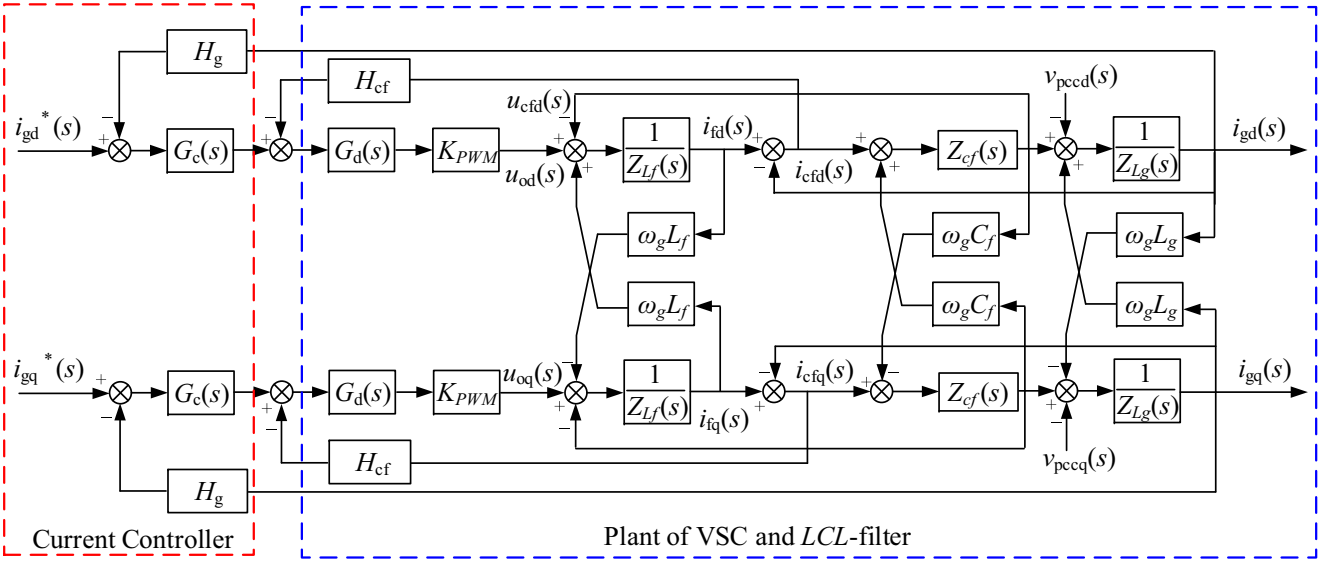

FIGURE 9.37 Block diagram of the s-domain current controller for the LCL-filtered voltage source converter (VSC) under rotating dq frame.

This book belongs to Kitab Liaison (ocd1996@gmail.com)

Copyright Elsevier 2023

where T_s is the sampling period. Alternatively, $G_d(s)$ can also be expressed by Pade approximation and the accuracy can be regulated by selecting different orders [31]. With respect to the current controller $G_c(s)$, it can be denoted by a quasiproportional-resonant (PR) controller in $\alpha\beta$ frame or a PI controller in dq frame, by considering the sinusoidal form and the constant value of the grid current in $\alpha\beta$ frame and dq frame, respectively. Thus, the $G_c(s)$ in Fig. 9.36 can be expressed by

$$G_c(s) = K_p + \frac{2K_r\omega_c s}{s^2 + 2\omega_c s + \omega_0^2} \tag{9.81}$$

where K_p and K_r are the proportional and resonance coefficients, respectively, and $\omega_c = 5$ rad/s (assuming grid fundamental frequency is within 50 Hz $\pm$ 0.8 Hz), ω_0 is the fundamental angular frequency.

9.4.2 Impedance-based stability analysis

Taking the $\alpha\beta$-frame control as an example, the grid-connected converter model in weak grids can be represented by a current source $\mathbf{i_{r\alpha\beta}} = [\, i_{r\alpha} \quad i_{r\beta} \,]^T$ in parallel with an output impedance $Z_o(s)$, as shown in Fig. 9.38. Therein, Z_t(s) denotes the grid impedance, $\mathbf{u_{g\alpha\beta}} = [\, u_{g\alpha} \quad u_{g\beta} \,]^T$ is the grid voltage, and $\mathbf{v_{pcc\alpha\beta}} = [\, v_{pcc\alpha} \quad v_{pcc\beta} \,]^T$ is the PCC voltage. Therefore, the grid current $\mathbf{i_{g\alpha\beta}} = [\, i_{g\alpha} \quad i_{g\beta} \,]^T$ can be calculated by

$$\begin{aligned} \mathbf{i_{g\alpha\beta}}(s) &= \frac{Z_o(s)}{Z_o(s) + Z_t(s)}\mathbf{i_{r\alpha\beta}}(s) - \frac{1}{Z_o(s) + Z_t(s)}\mathbf{u_{g\alpha\beta}}(s) \\ &= \frac{1}{1 + Z_t(s)/Z_o(s)}\left[\mathbf{i_{r\alpha\beta}}(s) - \frac{\mathbf{u_{g\alpha\beta}}(s)}{Z_o(s)}\right] \end{aligned} \tag{9.82}$$

On the other hand, the α-channel control block in Fig. 9.36 can be simplified, as shown in Fig. 9.39. Due to that the α-channel and β-channel control blocks are similar in Fig. 9.36, the α-channel is selected as an example here. The aggregated transfer functions $G_{a1}(s)$ and $G_{a2}(s)$ can be derived as

$$G_{a1}(s) = \frac{K_{PWM}G_c(s)G_d(s)Z_{cf}(s)}{Z_{Lf}(s) + Z_{cf}(s) + K_{PWM}H_{cf}G_d(s)} \tag{9.83}$$

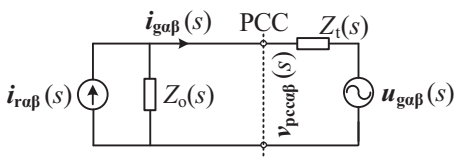

FIGURE 9.38 Equivalent circuit of grid-connected converter system.

This book belongs to Kitab Liaison (ocd1996@gmail.com)
Copyright Elsevier 2023

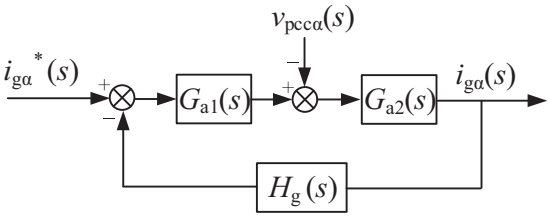

FIGURE 9.39 Equivalent transformation of the α-channel current control block in Fig. 9.36.

$$G_{a2}(s) = \frac{Z_{Lf}(s) + Z_{cf}(s) + K_{PWM}H_{cf}G_d(s)}{Z_{Lf}(s)Z_{Lg}(s) + [Z_{Lf}(s) + Z_{Lg}(s)]Z_{cf}(s) + K_{PWM}H_{cf}G_d(s)Z_{Lg}(s)} \tag{9.84}$$

Then the closed-loop control of the grid current $i_{g\alpha}$(s) in Fig. 9.39 can be obtained with

$$\begin{aligned} i_{g\alpha}(s) &= \frac{G_{a1}(s)G_{a2}(s)}{1 + H_gG_{a1}(s)G_{a2}(s)} i_{g\alpha}^{*}(s) - \frac{G_{a2}(s)}{1 + H_gG_{a1}(s)G_{a2}(s)} v_{pcc\alpha}(s) \\ &= G_{ig}(s)i_{g\alpha}^{*}(s) - \frac{1}{Z_o(s)} v_{pcc\alpha}(s) \end{aligned} \tag{9.85}$$

Comparing Eqs. (9.82) and (9.85), the current loop gain $G_{ig}(s)$ and the converter output capacitance $Z_o(s)$ can be expressed by

$$\begin{aligned} G_{ig}(s) &= \frac{G_{a1}(s)G_{a2}(s)}{1 + H_gG_{a1}(s)G_{a2}(s)} \\ &= \frac{K_{PWM}G_c(s)G_d(s)}{s^3L_fC_fL_g + s^2K_{PWM}L_gC_fH_{cf}G_d(s) + s(L_f + L_g) + K_{PWM}H_gG_c(s)G_d(s)} \end{aligned} \tag{9.86}$$

$$\begin{aligned} Z_o(s) &= \frac{1 + H_gG_{a1}(s)G_{a2}(s)}{G_{a2}(s)} \\ &= \frac{s^3L_fC_fL_g + s^2L_gC_fK_{PWM}H_{cf}G_d(s) + s(L_f + L_g) + K_{PWM}H_gG_c(s)G_d(s)}{s^2L_fC_f + sC_fK_{PWM}H_{cf}G_d(s) + 1} \end{aligned} \tag{9.87}$$

According to Eq. (9.82), if the converter is stable in strong grid (i.e., $Z_t(s) = 0$), the stability of the *LCL*-filtered VSC is determined by $Z_t(s)/Z_o(s)$. Using the parameters listed in Table 9.3, the Bode plots of $Z_t(s)$ and $Z_o(s)$ are shown in Fig. 9.40. It can be seen that phase difference at the crossing frequency of $Z_t(s)$ and $Z_o(s)$ is larger than 180 degrees, indicating an unstable grid current control according to the Nyquist stability criterion [32]. It should be

This book belongs to Kitab Liaison (ocd1996@gmail.com) Copyright Elsevier 2023

TABLE 9.3 Parameters of 15 kW grid-tied voltage source converter with LCL Filter under weak grids.

Operating power P_o (kW)	7.5
Balanced grid peak phase voltage U_g (V)	311
DC-link voltage V_{dc} (V)	650
Converter-side inductor L_f (mH)	3
Capacitor branch C_f (uF)	10
Grid-side inductor L_g (mH)	1.8
Grid voltage frequency f_g (Hz)	50
Switching frequency f_{sw} (kHz)	4
Switching frequency f_s (kHz)	8
Proportional gain of the quasiPR controller K_p	0.5
Integral coefficient of the quasiPR controller K_r	50
Sensor gain of the capacitor current H_{cf}	0.1
Sensor gain of the grid current H_g	0.1
Converter gain K_{PWM}	90
Grid impedance $Z_t(s)$	$0.5 + 0.002$ s

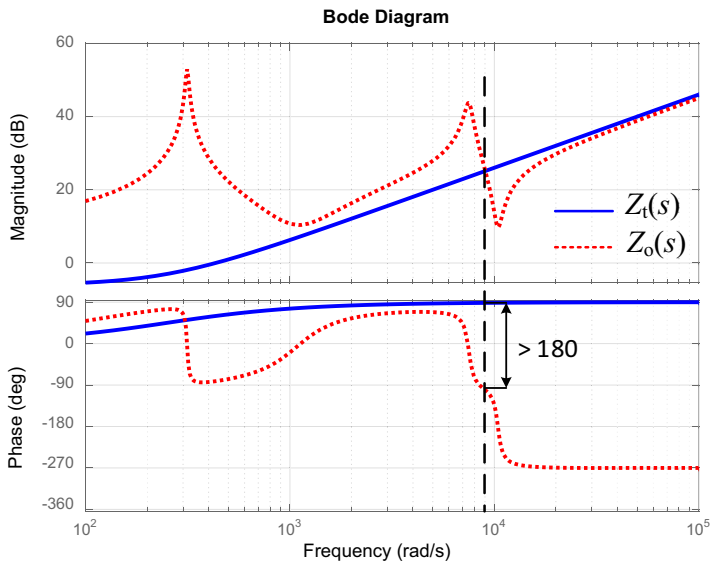

FIGURE 9.40 Bode plots of the converter output impedance $Z_o(s)$ and the grid impedance $Z_t(s)$.

This book belongs to Kitab Liaison (ocd1996@gmail.com)
Copyright Elsevier 2023

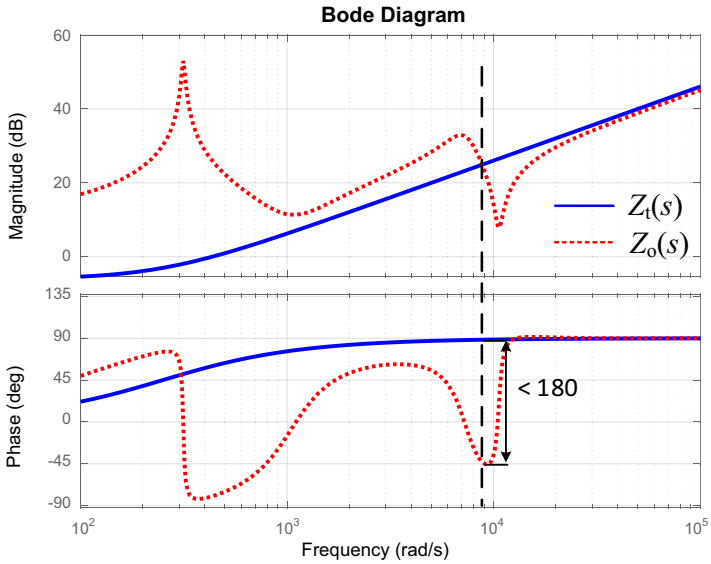

FIGURE 9.41 Bode plots of the converter output impedance $Z_o(s)$ and the grid impedance $Z_t(s)$ with reduced time delay.

noted that there are other factors that may lead to an unstable control. For example, the reference current I^* is directly given in Fig. 9.36. But in practical situation, this reference value is usually generated by the outer DC-link voltage control loop, and this will worsen the converter stability [33].

There are many ways to improve the system stability, such as reducing the time delay [34], proper design of the *LCL* filter (mainly the capacitor [35]), or AD control [36]. Taking the time-delay reduction as an example, if the time delay in $G_d(s)$ is reduced from $1.5T_s$ to T_s, the obtained Bode plot of $Z_o(s)$ is shown in Fig. 9.41. It can be seen that phase difference becomes lower than 180 degrees, indicating a stable grid current control.

In order to validate the stability analysis above, the same parameters in Table 9.3 are utilized to simulate the *LCL*-filtered VSC under the $\alpha\beta$-frame control in Fig. 9.35. The simulation results are shown in Fig. 9.42, including the three-phase voltages $v_{pcc,abc}$ at PCC as shown in Fig. 9.42A and the three-phase grid currents $i_{g,abc}$ in Fig. 9.42B. At $t = 0.05$ s, the VSC is connected to the PCC, and it can be seen that the PCC voltages and the grid-injected current are unstable with the time delay $t_d = 1.5T_s$. Then the time delay is reduced to $t_d = T_s$ at the time instant $t = 0.13$ s in Fig. 9.42. It can be seen the working waveforms become stable after a short transient period, which validates the effectiveness of the time-delay reduction for a stability improvement.

This book belongs to Kitab Liaison (ocd1996@gmail.com) Copyright Elsevier 2023

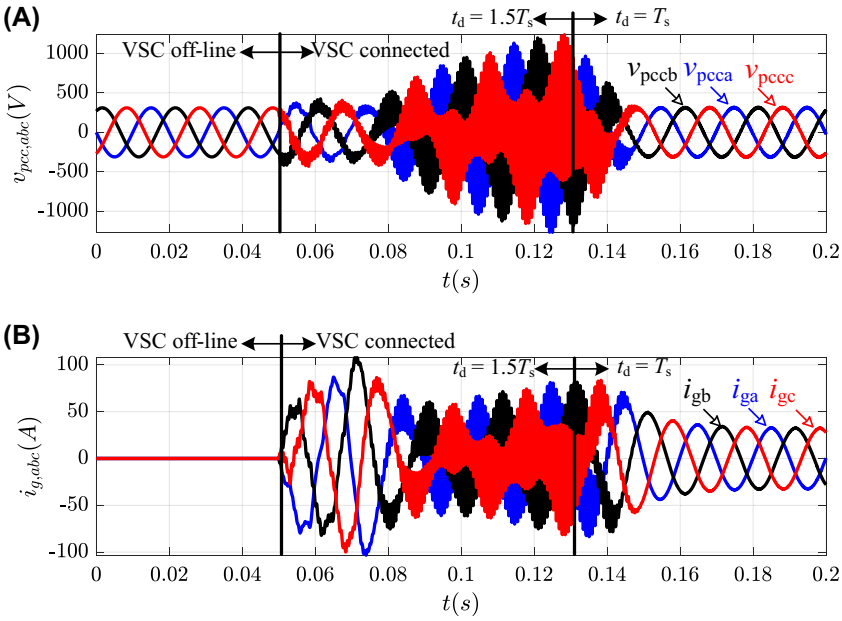

FIGURE 9.42 Simulation results of the (A) point of common coupling (PCC) voltage and (B) grid current when different time delays are applied to the *LCL*-filtered voltage source converter (VSC), using the $\alpha\beta$-frame control shown in Fig. 9.36.

References

[1] G.W. Wester, R.D. Middlebrook, Low-frequency characterization of switched DC-DC converters, in: Proc. IEEE Power Processing and Electronics Specialists Conf, 1972, pp. 9–20.

[2] A.R. Wood, D.J. Hume, C.M. Osauskas, Linear analysis of waveform distortion for HVDC and facts devices, in: Proc. (Cat. No.00EX441) Ninth Int Conf. Harmonics and Quality of Power, vol. 3, 2000, pp. 967–972.

[3] S.R. Sanders, J.M. Noworolski, X.Z. Liu, G.C. Verghese, Generalized averaging method for power conversion circuits, IEEE Trans. Power Electron. 6 (2) (April 1991) 251–259.

[4] V.A. Caliskan, G.C. Verghese, A.M. Stankovic, Multi-frequency averaging of DC/DC converters, in: Proc. 5th IEEE Workshop Computers in Power Electronics, 1996, pp. 113–119.

[5] A.M. Stankovic, S.R. Sanders, T. Aydin, Dynamic phasors in modeling and analysis of unbalanced polyphase AC machines, IEEE Trans. Energy Convers. 17 (1) (2002) 107–113.

[6] P.C. Stefanov, A.M. Stankovic, Modeling of UPFC operation under unbalanced conditions with dynamic phasors, IEEE Trans. Power Syst. 17 (2) (2002) 395–403.

[7] A.M. Stankovic, T. Aydin, Analysis of asymmetrical faults in power systems using dynamic phasors, IEEE Trans. Power Syst. 15 (3) (2000) 1062–1068.

[8] N.M. Wereley, Analysis and Control of Linear Periodically Time Varying Systems, Ph.D. thesis, Massachusetts Institute of Technology, 1990.

This book belongs to Kitab Liaison (ocd1996@gmail.com) Copyright Elsevier 2023

[9] J.R.C. Orillaza, A.R. Wood, Harmonic state-space model of a controlled TCR, IEEE Trans. Power Deliv. 28 (1) (2013) 197−205.
[10] J.J. Rico, M. Madrigal, E. Acha, Dynamic harmonic evolution using the extended harmonic domain, IEEE Trans. Power Deliv. 18 (2) (2003) 587−594.
[11] Y. Peng, Z. Shuai, Y. Li, J.M. Guerrero, Z.J. Shen, Dynamic-phasor modeling and transient analysis of inverter-based microgrid under unbalanced and harmonic condition, in: 2018 IEEE Energy Conversion Congress and Exposition (ECCE), IEEE, 2018, pp. 3760−3764.
[12] M. Liserre, F. Blaabjerg, S. Hansen, Design and control of an LCL-filter-based three-phase active rectifier, IEEE Trans. Ind. Appl. 41 (5) (2005) 1281−1291.
[13] J. Dannehl, F.W. Fuchs, S. Hansen, P.B. Thøgersen, Investigation of active damping approaches for pi-based current control of grid-connected pulse width modulation converters with LCL filters, IEEE Trans. Ind. Appl. 46 (4) (2010) 1509−1517.
[14] Y. Tang, P.C. Loh, P. Wang, F.H. Choo, F. Gao, Exploring inherent damping characteristic of LCL-filters for three-phase grid-connected voltage source inverters, IEEE Trans. Power Electron. 27 (3) (2011) 1433−1443.
[15] S.G. Parker, B.P. McGrath, D.G. Holmes, Regions of active damping control for LCL filters, IEEE Trans. Ind. Appl. 50 (1) (2013) 424−432.
[16] J. Wang, J.D. Yan, L. Jiang, J. Zou, Delay-dependent stability of single-loop controlled grid-connected inverters with LCL filters, IEEE Trans. Power Electron. 31 (1) (2015) 743−757.
[17] B.G. Cho, S.K. Sul, LCL filter design for grid-connected voltage-source converters in high power systems, in: 2012 IEEE Energy Conversion Congress and Exposition (ECCE), IEEE, 2012, pp. 1548−1555.
[18] J. Dannehl, C. Wessels, F.W. Fuchs, Limitations of voltage-oriented pi current control of grid-connected PWM rectifiers with LCL filters, IEEE Trans. Ind. Electron. 56 (2) (2008) 380−388.
[19] V. Blasko, V. Kaura, A novel control to actively damp resonance in input LC filter of a three-phase voltage source converter, IEEE Trans. Ind. Appl. 33 (2) (1997) 542−550.
[20] R. Pena-Alzola, M. Liserre, F. Blaabjerg, R. Sebastian, J. Dannehl, F.W. Fuchs, Analysis of the passive damping losses in LCL-filter-based grid converters, IEEE Trans. Power Electron. 28 (6) (2012) 2642−2646.
[21] M. Liserre, A. Dell'Aquila, F. Blaabjerg, Stability improvements of an LCL-filter based three-phase active rectifier, in: 2002 IEEE 33rd Annual IEEE Power Electronics Specialists Conference. Proceedings (Cat. No. 02CH37289), IEEE, vol. 3, 2002, pp. 1195−1201.
[22] J. Xu, S. Xie, T. Tang, Active damping-based control for grid-connected LCL-filtered inverter with injected grid current feedback only, IEEE Trans. Ind. Electron. 61 (9) (2013) 4746−4758.
[23] W. Xia, J. Kang, Stability of LCL-filtered grid-connected inverters with capacitor current feedback active damping considering controller time delays, J Mod. Power Syst. Clean Energy 5 (4) (2017) 584−598.
[24] X. Wang, F. Blaabjerg, P.C. Loh, Grid-current-feedback active damping for LCL resonance in grid-connected voltage-source converters, IEEE Trans. Power Electron. 31 (1) (2015) 213−223.
[25] A. Doria-Cerezo, M. Bodson, Design of controllers for electrical power systems using a complex root locus method, IEEE Trans. Ind. Electron. 63 (6) (2016) 3706−3716.
[26] P. Rodríguez, J. Pou, J. Bergas, J.I. Candela, R.P. Burgos, D. Boroyevich, Decoupled double synchronous reference frame PLL for power converters control, IEEE Trans. Power Electron. 22 (2) (2007) 584−592.

This book belongs to Kitab Liaison (ocd1996@gmail.com) Copyright Elsevier 2023

[27] Y. Yang, L. Hadjidemetriou, F. Blaabjerg, E. Kyriakides, Benchmarking of phase locked loop based synchronization techniques for grid-connected inverter systems, in: 2015 9th International Conference on Power Electronics and ECCE Asia (ICPE-ECCE Asia), IEEE, 2015, pp. 2167−2174.

[28] R. Teodorescu, M. Liserre, P. Rodriguez, Control of Grid Converters under Grid Faults, 2007.

[29] D. Yang, X. Wang, F. Liu, K. Xin, Y. Liu, F. Blaabjerg, Symmetrical PLL for SISO impedance modeling and enhanced stability in weak grids, IEEE Trans. Power Electron. 35 (2) (2019) 1473−1483.

[30] X. Wang, L. Harnefors, F. Blaabjerg, Unified impedance model of grid-connected voltage-source converters, IEEE Trans. Power Electron. 33 (2) (2017) 1775−1787.

[31] X. Wang, F. Blaabjerg, P.C. Loh, An impedance-based stability analysis method for paralleled voltage source converters, in: 2014 International Power Electronics Conference (IPEC-Hiroshima 2014-ECCE ASIA), IEEE, 2014, pp. 1529−1535.

[32] B. Wen, D. Boroyevich, R. Burgos, P. Mattavelli, Z. Shen, Inverse nyquist stability criterion for grid-tied inverters, IEEE Trans. Power Electron. 32 (2) (2016) 1548−1556.

[33] D. Lu, X. Wang, F. Blaabjerg, Impedance-based analysis of dc-link voltage dynamics in voltage-source converters, IEEE Trans. Power Electron. 34 (4) (2018) 3973−3985.

[34] D. Yang, X. Ruan, H. Wu, A real-time computation method with dual sampling mode to improve the current control performance of the *LCL*-type grid-connected inverter, IEEE Trans. Ind. Electron. 62 (7) (2014) 4563−4572.

[35] X. Wang, F. Blaabjerg, P.C. Loh, Passivity-based stability analysis and damping injection for multi-paralleled VSCS with LCL filters, IEEE Trans. Power Electron. 32 (11) (2017) 8922−8935.

[36] L. Harnefors, A.G. Yepes, A. Vidal, J. Doval-Gandoy, Passivity-based controller design of grid-connected VSCs for prevention of electrical resonance instability, IEEE Trans. Ind. Electron. 62 (2) (2014) 702−710.

This book belongs to Kitab Liaison (ocd1996@gmail.com) Copyright Elsevier 2023

Chapter 10

Phase-locked loops and their design

Wenzhao Liu, Frede Blaabjerg
Department of Energy Technology, Aalborg University, Aalborg, Denmark

10.1 Introduction

The development of the phase-locked loops (PLLs) dates back to 1930s when it was designed to the synchronous reception of radio signals [1]. After that, the PLL technologies have been widely developed in different industry areas such as communication systems, motor drive systems, contactless power supplies, and grid synchronization of the power electronic–based renewable energy systems, etc. Furthermore, the detailed applications can be divided into the estimation of fundamental parameters of electrical signals [2], electrical synchronization of power quality instruments [3], measurement of harmonics and interharmonics [4], control of AC and DC electrical machines [5], implementing adaptive filters and robust controllers, islanding detection of microgrids [6], grid faults and voltage sags detection [7,8], etc.

In recent years, the PLLs are probably the most widely used in grid-connected synchronization applications. For the renewable-based power generation systems, power converters playing as the interface devices are usually employed connecting to the main grid and local loads. Generally, the synchronization technology is defined as a procedure of coordinating power generation units and main AC grid so that they are able to effectively operate in parallel. This procedure may often require PLLs to extract the grid voltage information such as its amplitude, phase, and frequency and provide necessary reference signals to system controllers [9]. However, the main challenge of all synchronization techniques for power electronic–based electrical system is facing a number of disturbances (i.e., the presence of unbalances, harmonics, asymmetrical amplitude sags/swells and DC offset, etc.) in the grid voltage. These nonideal but widely existing disturbances are depending on many factors, which are mainly attributable to the high penetration of distributed

Control of Power Electronic Converters and Systems. https://doi.org/10.1016/B978-0-12-819432-4.00013-5
Copyright © 2021 Elsevier Ltd. All rights reserved.

This book belongs to Kitab Liaison (ocd1996@gmail.com)
Copyright Elsevier 2023

generation systems especially equipped with nonlinear power electronic loads or power electronic—based devices, which may affect the accuracy and/or response speed of synchronization technology.

However, it should be noted that a highly important unit in the control of the power converters is the synchronization part, which performs a series of action to ensure the power converter and the main grid to be able to work safely and effectively. The information provided by the synchronization unit may be used for different monitoring and further protection purposes. The synchronization techniques in power converters may be categorized to open-loop and closed-loop methods [10]. The implementations of closed-loop synchronization always require feeding back one or more signals, and there are two main categories (PLLs and frequency-locked loop (FLLs)) [11]. The open-loop synchronization is free of any feedback signals in their structures. This chapter focuses on the discussion of popular closed-loop PLL and their design in practiced application.

On the other hand, much research efforts focused on solving power quality issues have been proposed to improve the performance of PLLs under different working conditions [11—13]. However, these efforts often result in very complicated or highly nonlinear control structures. That lead to some shortcomings such as high computational burden, implementation complexity, difficult to model and do stability analysis for the system, and inefficient under large frequency drifts etc. Therefore, this chapter aims at presenting a comprehensive survey on various PLL synchronization techniques to facilitate quick and proper selection for further development and applications for researchers and engineers.

10.2 PLL's control and design

A grid-connected converter with a closed-loop PLL synchronization control to a time-varying grid voltage signal can be simplified as shown in Fig. 10.1. The mentioned PLL is usually devided into three parts: phase detection (PD), loop filter (LF), and voltage-controlled oscillator (VCO). And the difference between phase angle of the grid voltage input signal and that of the output signal is detected by PD and then sent to the LF. The LF output signal drives the VCO to generate the output signal, which could track the grid voltage phase information. More specifically, the PD is mainly responsible to generate a signal containing the phase error information, and the LF also known as the loop controller, which drives the phase error signal to be zero. Finally, the VCO produces a synchronized unit vector with a phase $\widehat{\theta}$ in its outputs.

Furthermore, more detailed PLLs can be classified into three-phase and single-phase applications. A good PLL usually requires lower computational burden, higher robust grid disturbances (i.e., voltage imbalance, harmonics,

This book belongs to Kitab Liaison (ocd1996@gmail.com) Copyright Elsevier 2023

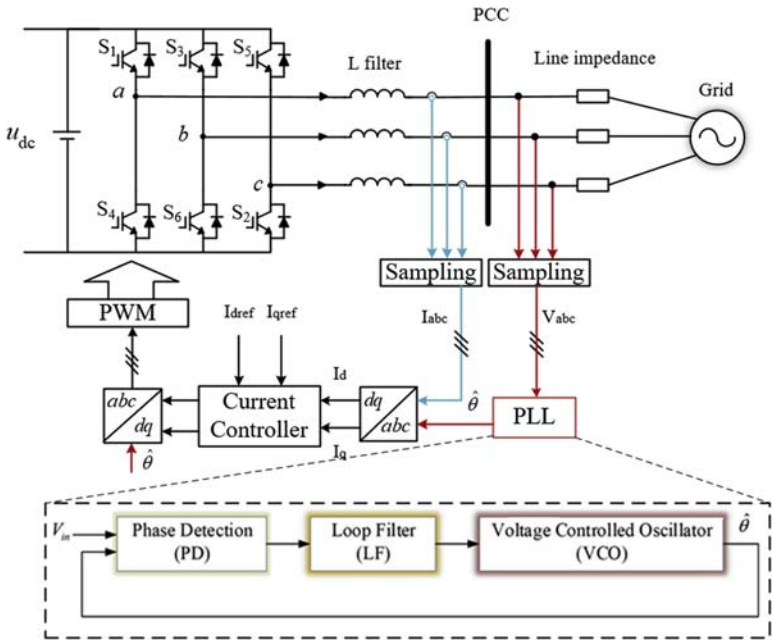

FIGURE 10.1 Classical phase-locked loop (PLL) control structure in three-phase grid-connected converter.

frequency variations), and fast dynamic response ability and enhanced stability. The following will present some advanced three-phase and single-phase PLLs and their design.

10.3 Three-phase PLLs

10.3.1 Conventional synchronous reference frame PLL

The synchronous reference frame PLL (SRF-PLL) may be the most famous PLL in three-phase grid-connected converter applications [2,9,14]. The typical SRF-PLL structure is shown in Fig. 10.2, where $\widehat{V}$, $\widehat{\omega}_g$, and $\widehat{\theta}$ are the estimated amplitude, frequency, and phase angle, respectively. The ω_n is the nominal frequency of the detected grid voltage signal.

The operation principle of the SRF-PLL can be summarized as follows: firstly, transform the three-phase grid voltage V_{abc} to the V_{dq} in the synchronous frame, then the PI controller is adopted to suppress the V_q to zero, and consequently align the grid voltage to d-axis. The output of the PI controller together with the integrator finally produces the grid voltage phase angle, which is also delivered back to the Park transformation applied in the mentioned power circuit in Fig. 10.1.

This book belongs to Kitab Liaison (ocd1996@gmail.com) Copyright Elsevier 2023

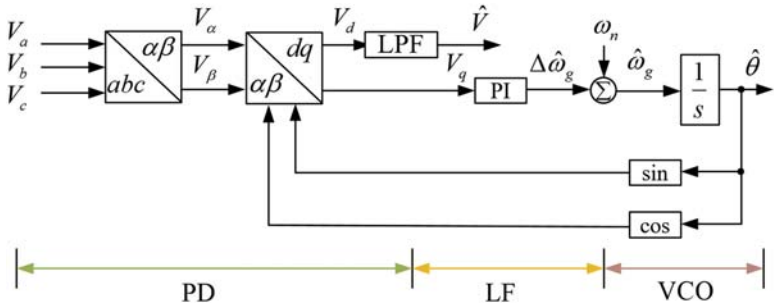

FIGURE 10.2 Schematic diagram of the conventional synchronous reference frame—based phase-locked loop.

In order to further understand the working principle the SRF-PLL, it is assumed that the three-phase grid voltage (input of the SRF-PLL) can be expressed as

$$\begin{bmatrix} V_a(t) \\ V_b(t) \\ V_c(t) \end{bmatrix} = \begin{bmatrix} V_1 \cos(\theta_1) + \sum_{-\infty, h \neq 1}^{+\infty} V_h \cos(\theta_h) \\ V_1 \cos\left(\theta_1 - \frac{2\pi}{3}\right) + \sum_{-\infty, h \neq 1}^{+\infty} V_h \cos\left(\theta_h - \frac{2\pi}{3}\right) \\ V_1 \cos\left(\theta_1 + \frac{2\pi}{3}\right) + \sum_{-\infty, h \neq 1}^{+\infty} V_h \cos\left(\theta_h + \frac{2\pi}{3}\right) \end{bmatrix} \tag{10.1}$$

where V_1 and θ_1 represent the fundamental frequency amplitude and phase angle of the three-phase signals, respectively. V_h and θ_h represent the h-order harmonic amplitude and phase angle of the three-phase signals, respectively.

$$T_{clark(abc \to \alpha\beta)} = \frac{2}{3} \begin{bmatrix} 1 & -\frac{1}{2} & -\frac{1}{2} \\ 0 & \frac{\sqrt{3}}{2} & -\frac{\sqrt{3}}{2} \end{bmatrix} \tag{10.2}$$

$$T_{park(\alpha\beta \to dq)} = \begin{bmatrix} \cos(\widehat{\theta}_1) & \sin(\widehat{\theta}_1) \\ -\sin(\widehat{\theta}_1) & \cos(\widehat{\theta}_1) \end{bmatrix} \tag{10.3}$$

This book belongs to Kitab Liaison (ocd1996@gmail.com)
Copyright Elsevier 2023

Applying the Clark and Park transformation, which is expressed as (10.2) and (10.3), into (10.1), the d-axis and q-axis component can be obtained as follows:

$$\begin{bmatrix} V_d(t) \\ V_q(t) \end{bmatrix} = \begin{bmatrix} V_1 \cos(\theta_1 - \widehat{\theta}_1) \\ V_1 \sin(\theta_1 - \widehat{\theta}_1) \end{bmatrix} + \begin{bmatrix} \sum_{-\infty, h \neq 1}^{+\infty} V_h \cos(\theta_h - \widehat{\theta}_h) \\ \sum_{-\infty, h \neq 1}^{+\infty} V_h \sin(\theta_h - \widehat{\theta}_h) \end{bmatrix} \tag{10.4}$$

$$\begin{bmatrix} \theta_h \\ \widehat{\theta}_h \end{bmatrix} = \begin{bmatrix} \int \omega_g dt = \int (\omega_n + \Delta\omega_g) dt = \overbrace{\int \omega_n dt}^{\theta_h} + \overbrace{\int \Delta\omega_g dt}^{\Delta\theta_h} \\ \int \widehat{\omega}_g dt = \int \left(\omega_n + \Delta\widehat{\omega}_g\right) dt = \overbrace{\int \omega_n dt}^{\theta_h} + \overbrace{\int \Delta\widehat{\omega}_g dt}^{\Delta\widehat{\theta}_h} \end{bmatrix} \tag{10.5}$$

Substitute (10.5) into (10.4), then the following equations can be obtained:

$$\begin{aligned} \begin{bmatrix} V_d(t) \\ V_q(t) \end{bmatrix} &= \begin{bmatrix} V_1 \cos(\theta_1 - \widehat{\theta}_1) \\ V_1 \sin(\theta_1 - \widehat{\theta}_1) \end{bmatrix} + \begin{bmatrix} \sum_{-\infty, h \neq 1}^{+\infty} V_h \cos(\theta_h - \widehat{\theta}_h) \\ \sum_{-\infty, h \neq 1}^{+\infty} V_h \sin(\theta_h - \widehat{\theta}_h) \end{bmatrix} \\ &\approx \begin{bmatrix} V_1 + D_d(t) \\ V_1(\theta_1 - \widehat{\theta}_1) + D_q(t) \end{bmatrix} \end{aligned} \tag{10.6}$$

As it can be observed in (10.6), the signal $V_d(t)$ is a measure of the amplitude of the three-phase signals, and $V_q(t)$ contains the phase error information. Based on these characteristics and the diagram in Fig. 10.2, the linearized models of the SRF-PLL can be derived as shown in Fig. 10.3.

According to this model, the open-loop and closed-loop transfer functions of the SRF-PLL can be determined as follows:^

$$\Delta\widehat{\theta}_1(s) = \frac{V(k_p s + k_i)}{s^2} \theta_e(s) \tag{10.7}$$

$$\Delta\dot{\hat{\theta}}_1(s) = \frac{V(k_p s + k_i)}{s^2 + Vk_p s + V_n k_i} \Delta\theta_1(s) + \frac{k_p s + k_i}{s^2 + Vk_p s + V_n k_i} D_q(s) \tag{10.8}$$

This book belongs to Kitab Liaison (ocd1996@gmail.com)
Copyright Elsevier 2023

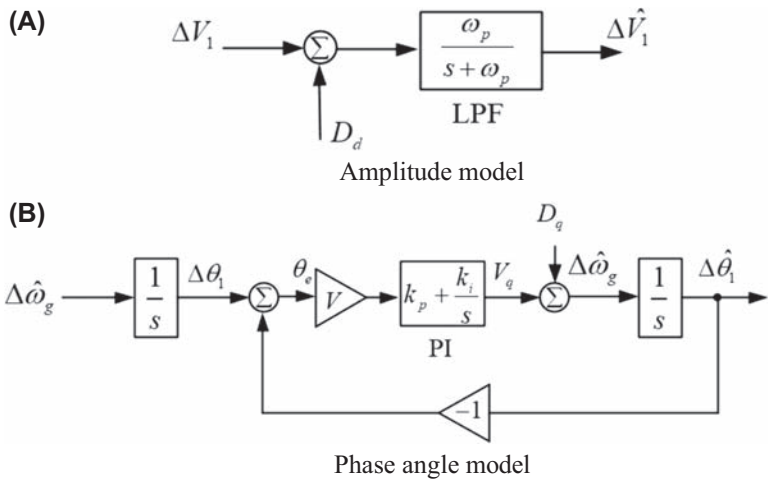

FIGURE 10.3 Linearized models of the typical synchronous reference frame−based phase-locked loop. (A) Amplitude model, (B) phase angle model.

$$\Delta\widehat{\omega}_g(s) = \frac{V(k_p s + k_i)}{s^2 + Vk_p s + V_n k_i}\Delta\omega_g(s) + \frac{s(k_p s + k_i)}{s^2 + Vk_p s + Vk_i}D_q(s) \tag{10.9}$$

$$\Delta\widehat{V}_1(s) = \frac{\omega_p}{s+\omega_p}\Delta V_1(s) + \frac{\omega_p}{s+\omega_p}D_d(s) \tag{10.10}$$

In fact, these models provide quite useful information for the better understanding of the characteristics of the SRF-PLL as follows:

- In Fig. 10.3, the amplitude V is a gain in the forward path of the SRF-PLL model, which means that the variations of the three-phase input amplitude may change the loop gain and affect the stability margin and dynamic performance. Consequently, the input amplitude variations will change the loop gain, dynamics, and stability.
- According to (10.7), where the impact of $D_q(s)$ has been neglected, it has two open-loop poles, so the SRF-PLL can be treated as a type-II control system. Therefore, the SRF-PLL can track phase angle jumps and frequency steps with zero steady-state phase error, but it is difficult to achieve frequency ramps, which may happen in the power system. Furthermore, the phase error during the frequency ramps can be reduced by increasing the PLL bandwidth but degrading the noise immunity of SRF-PLL.
- According to (10.8)−(10.10), the phase angle, frequency, and amplitude estimated by the SRF-PLL suffer from the disturbance of $D_d(s)$ and $D_q(s)$. If there is DC offset and unbalances in the input signal, there will be fundamental frequency and double-frequency components in $D_d(s)$ and

This book belongs to Kitab Liaison (ocd1996@gmail.com) Copyright Elsevier 2023

$D_q(s)$, and h-order harmonic will appear as $h - 1$ order harmonic, which will decrease the tracking accuracy of SRF-PLL.

More specifically, Figs. 10.4–10.6 show simulation results of SRF-PLL under different grid voltage cases. It can be included that the conventional SRF-PLL has a very limited capability to mitigate the grid voltage disturbances (i.e., grid voltage imbalance or harmonics), since the fundamental frequency and double-frequency disturbances will appear or more harmonics will be presented in the control loop of SRF-PLL. Nevertheless, narrowing the loop bandwidth of SRF-PLL will significantly degrade the dynamic performance and still cannot mitigate the above disturbances. These drawbacks of the SRF-PLL are the main motivation to design the PLLs to be more efficient.

On the other hand, with the increased penetration of renewable energy sources to the power grid and the proliferation of nonlinear loads have caused serious power quality issues and require better synchronization performance.

In order to deal with the above problems, many advanced PLLs are proposed and designed with enhanced disturbance rejection capabilities [9,14].

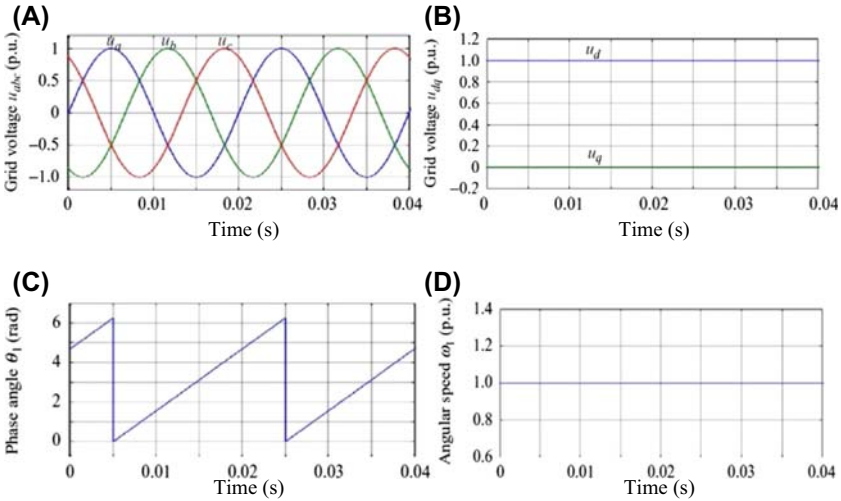

FIGURE 10.4 Simulation results of synchronous reference frame phase-locked loop in the three-phase normal grid voltage. (A) Three-phase grid voltage, (B) grid voltage components at dq frame, (C) estimated phase angle, (D) angular speed.

This book belongs to Kitab Liaison (ocd1996@gmail.com)
Copyright Elsevier 2023

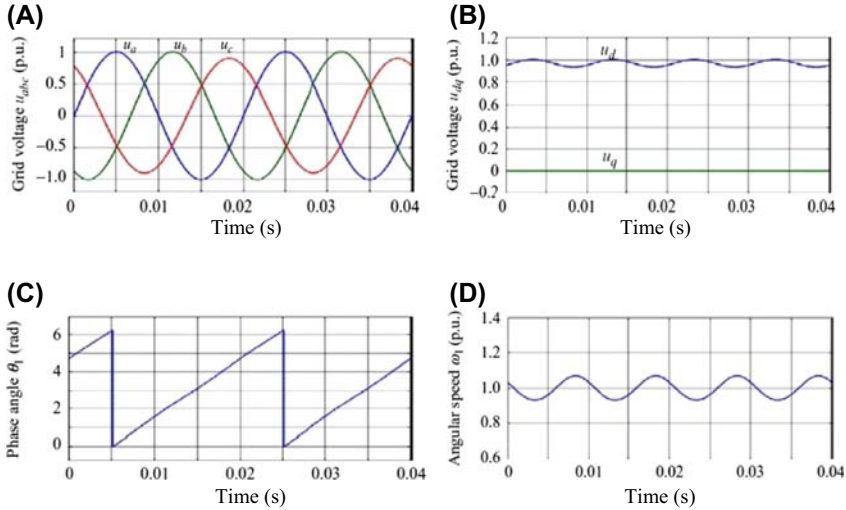

FIGURE 10.5 Simulation results of synchronous reference frame phase-locked loop in the three-phase unbalanced grid voltage. (A) Three-phase grid voltage (unbalance is 3.5%), (B) grid voltage components at *dq* frame, (C) estimated phase angle, (D) angular speed.

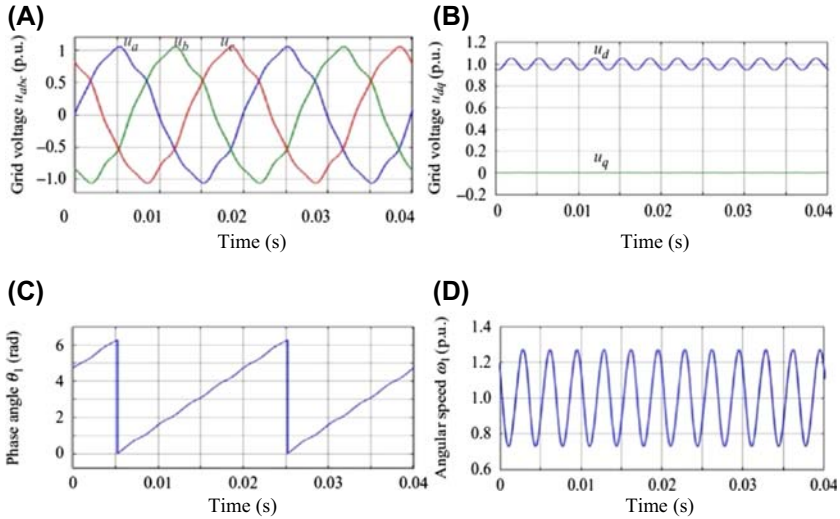

FIGURE 10.6 Simulation results of synchronous reference frame phase-locked loop in the three-phase grid voltage with harmonics. (A) Grid voltage (4% of fifth harmonics, 3% of seventh harmonic), (B) grid voltage components at *dq* frame, (C) estimated phase angle, (D) angular speed.

This book belongs to Kitab Liaison (ocd1996@gmail.com) Copyright Elsevier 2023

10.3.2 Moving average filter–based PLLs

Fig. 10.7 shows a conventional SRF-PLL with moving average filter (MAF), which is referred as MAF-PLL [15]. The MAF is a linear-phase filter which can be described as

$$G_{MAF}(s) = \frac{1 - e^{-T_{\omega s}}}{T_{\omega s}} \tag{10.11}$$

Notice that including the MAF inside the SRF-PLL control loop can significantly improve its filtering capability, but slow down its dynamic response considerably [15]. The reason is that the MAF in-loop will cause a phase delay. It is on the condition that the window length of MAF is equal to the nominal period of the input signals. The selection for the window length is recommended to be equal to the fundamental period of the grid voltage ($T_\omega = T$), when the grid harmonic is unclear and DC offset may be presented in the PLL input [15,16]. T_ω is the window length of MAF, more choices for the window length of the MAF such as $T_\omega = T/2$ and $T_\omega = T/6$ are suitable for applications when there are possible odd-order harmonics in the input of PLLs [17]. The MAF will pass the DC component and completely block frequency components of integer multiples of $1/T_\omega$.

Furthermore, in order to improve the dynamic of the MAF-PLL while maintaining better harmonics-filter performance, several methods are proposed in the literature. In Ref. [18], a proportional integral derivative (PID) controller is used instead of the conventional PI controller as the LF of the MAF-PLL, which can provide an additional degree of freedom. Therefore, it enables the designer to effectively compensate for the phase delay caused by the MAF by arranging a pole-zero cancellation in the design [9].

In addition, a special lead compensator is added before the PI controller in the MAF-PLL [19], where the transfer function of the compensator is inverse of the MAF's transfer function; therefore, it will be able to reduce the phase delay in the MAF-PLL control loop. It should be emphasized here that, the MAF-PLL with a window length equal to the input fundamental period can remove all of the harmonics up to the aliasing frequency in addition to the fundamental-frequency disturbance components.

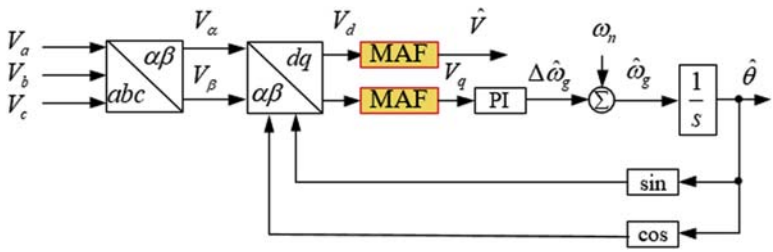

FIGURE 10.7 Schematic diagram of the moving average filter–based phase-locked loop.

This book belongs to Kitab Liaison (ocd1996@gmail.com) Copyright Elsevier 2023

10.3.3 Notch filter–based PLLs

A notch filter (NF) is a band-rejection filter that significantly attenuates specific frequency signals but passes all other frequency components with negligible attenuation. This feature makes the NF attractive in order to cancel the selected desired harmonic components presented in the input signal [9,14,20]. In fact, the NFs can be divided into adaptive or nonadaptive filters. The former one is very preferred by designers because it is easier to select a narrow bandwidth for NFs to minimize the phase delay in the control loop of the PLL. However, this advantage increases computational burden of the PLL. The structure of NF-PLL is similar to the standard MAF-PLL, except that the MAF is replaced with NFs as shown in Fig. 10.8.

In industry, more than one NF in the PLL control loop can be extended with cascaded topology [21] and parallel-connecting topology [22]. The main difference between these topologies is their frequency estimation method, the latter topology uses the same frequency estimator for all of the NFs. However, in the cascaded topology, every NF is equipped with its own frequency estimator and there is a tradeoff between the filtering capability and computational burden in both topologies. To achieve a satisfactory compromise, three NFs with notch frequencies at $2\omega_g$, $6\omega_g$, and $12\omega_g$ are usually suggested by designers to obtain a robust PLL [9].

10.3.4 Sinusoidal signal integrator–based PLLs

Fig. 10.9 shows the schematic diagram of sinusoidal signal integrator PLL (SSI-PLL) which tracks the grid voltage by extracting the fundamental positive-sequence component with the structure of SRF-PLL. Therefore, it can operate well under unbalanced and harmonic voltage conditions. The parameter K in Fig. 10.9 is designed to control the loop bandwidth and the response speed of the SSI-PLL.

In addition, a similar structure with single SSI can be found in Ref. [23], where the positive-sequence component is extracted by using a single SSI as a filter for the detected grid voltage, and calculated from grid voltage by

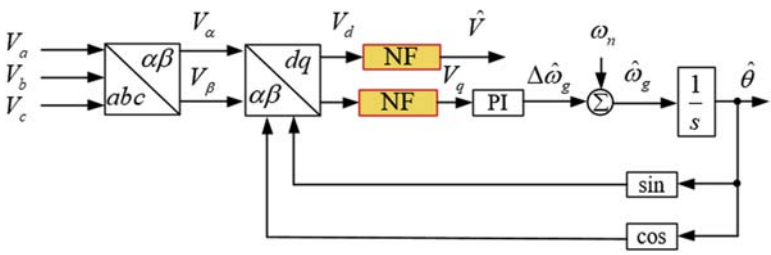

FIGURE 10.8 Schematic diagram of the notch filter–based phase-locked loop.

This book belongs to Kitab Liaison (ocd1996@gmail.com) Copyright Elsevier 2023

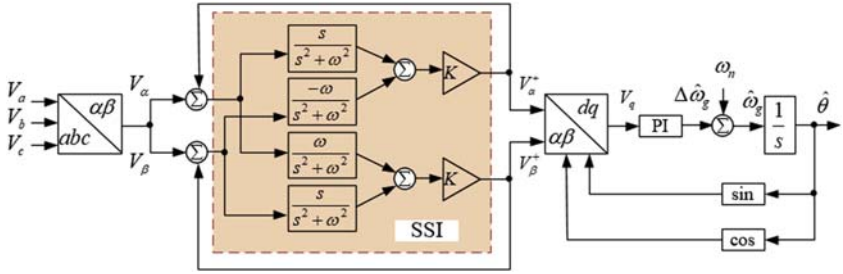

FIGURE 10.9 Schematic diagram of the sinusoidal signal integrator–based phase-locked loop.

delaying the signal with 90 degrees. The main advantages of SSI-PLL are immunity to the voltage distortion and being able to operate in unbalanced grid conditions. Moreover, it can be more simplified and applied to single-phase power system with a few modifications [24].

10.3.5 Second-order generalized integrator–based PLLs

The second-order generalized integrator–based PLL (SOGI-PLL) can be treated as SSI and acts as a quadrature signal generator and band-pass filter (BPF) by feeding back its output signal. The SOGI-PLL is a useful tool for the extraction and separation of the fundamental positive- and negative-sequence components of three-phase grid signals [9,24]. It implies that its structure is somehow mathematically equivalent to the DSRF-PLL [25], DCCF-PLL [26], and dual SOGI-based PLL (DSOGI-PLL) [11].

In Fig. 10.10, two SOGIs are applied to extract the filtered direct and quadrature components of V_α and V_β, and its components are calculated based on the instantaneous symmetrical component method. In addition, in order to improve the harmonic filtering capability of the DSOGI-PLL, some additional

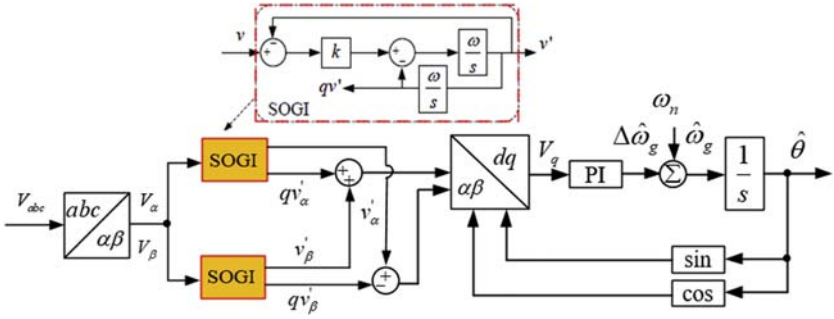

FIGURE 10.10 Schematic diagram of the dual second-order generalized integrator–based phase-locked loop.

This book belongs to Kitab Liaison (ocd1996@gmail.com) Copyright Elsevier 2023

SOGIs tuned at harmonic frequencies can be added to the standard structure [11,27]. Another interesting solution is to apply the third-order generalized integrator—based BPF and can be found in Ref. [27], which can further improve the dynamic response ability.

It is worth mentioning that an accurate fundamental positive- and negative-sequence component extraction in DSOGI-PLL requires 90 degree phase shift of the grid voltage. This method is not frequency-adaptive and will give rise to errors in the positive-sequence estimation. Therefore, a combination of a low pass filter (LPF) and a BPF is developed, where the BPF (Eq. 10.12) only provides harmonic filtering functions and the LPF (Eq. 10.13) offers both the harmonic filtering and 90 degree phase shift at the same time.

$$G_{BPF}(s) = \frac{v'}{v} = \frac{k\omega s}{s^2 + k\omega s + \omega^2} \tag{10.12}$$

$$G_{LPF}(s) = \frac{qv'}{v} = \frac{k\omega^2}{s^2 + k\omega s + \omega^2} \tag{10.13}$$

Besides, the parameters of the filter can be updated to achieve the frequency-adaptive purpose for the PLL. In addition, it could be applied to single-phase power system, i.e., SSI-PLL [28].

10.3.6 Complex coefficient filter—based PLLs

The complex coefficient filter—based PLLs (CCF-PLLs) can be characterized by introducing an asymmetrical frequency response around zero frequency, which implies the CCFs can make a distinction between the positive- and negative-sequence components at different frequencies [26]. Therefore, the CCF-PLLs are interesting for the selective extraction and/or cancellation of different harmonic components from the grid voltage.

Fig. 10.11 shows the schematic diagram of a decoupled CCF-PLL (DCCF-PLL), which uses two complex-coefficient BPFs as the SRF-PLL prefiltering

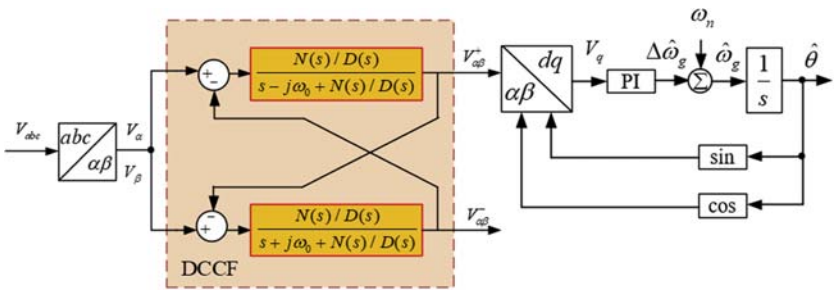

FIGURE 10.11 Schematic diagram of decoupled complex coefficient filter—based phase-locked loop.

This book belongs to Kitab Liaison (ocd1996@gmail.com) Copyright Elsevier 2023

stage [26]. The N(s)/D(s) can be extended to different transfer functions to affect the steady and dynamic performance of the CCF-PLLs. In addition, the CCFs in the input of the SRF-PLL are working in a collaborative way, each CCF is responsible for extracting a particular component of the input signal.

The fundamental frequency positive- and negative-sequence grid voltage components can be expressed as

$$V_{\alpha\beta}^{+}(s) = \frac{N(s)(s + j\omega_0)}{D(s)\left(s^2 + \omega_0^2\right) + 2N(s)s} V_{\alpha\beta}(s) \tag{10.14}$$

$$V_{\alpha\beta}^{-}(s) = \frac{N(s)(s - j\omega_0)}{D(s)\left(s^2 + \omega_0^2\right) + 2N(s)s} V_{\alpha\beta}(s) \tag{10.15}$$

when $N(s) = \omega_c$, $D(s) = 1$, the Bode diagram of DCCF-PLL can be illustrated as shown in Fig. 10.12. It can be seen that the positive-sequence curve has a magnitude of 1.0 p.u at 50 Hz and a magnitude of 0 at −50 Hz.

On the contrary, the amplitude of the negative-sequence curve is 0 at 50 Hz and 1.0 p.u at −50 Hz. Therefore, the DCCF can achieve accurate decoupling of positive- and negative-sequence components at the fundamental grid voltage frequency.

In addition, the DCCF equipped with LPFs can be used to reduce the potential DC offset components from three-phase grid voltage and the structure can be found in Fig. 10.13 [26], where ω_1 is the cut-off frequency of the LPF inside of the DCCF-PLL to extract the potential DC offset components in grid voltage. The ω_0 represents the detected grid voltage frequency and V^0 is the DC offset components measured from the grid voltage.

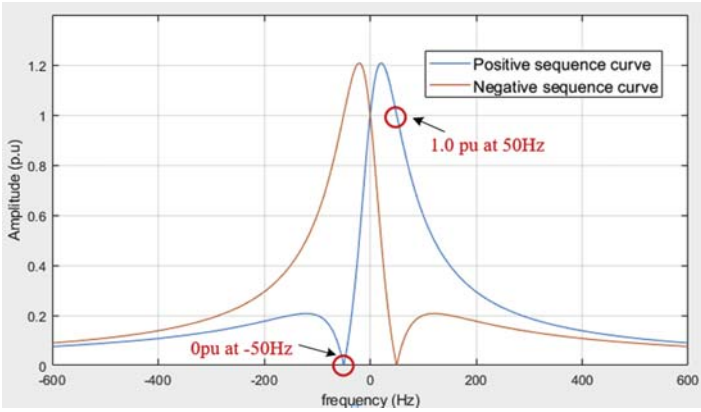

FIGURE 10.12 Bode diagram of the decoupled complex coefficient filter−based phase-locked loop.

This book belongs to Kitab Liaison (ocd1996@gmail.com)
Copyright Elsevier 2023

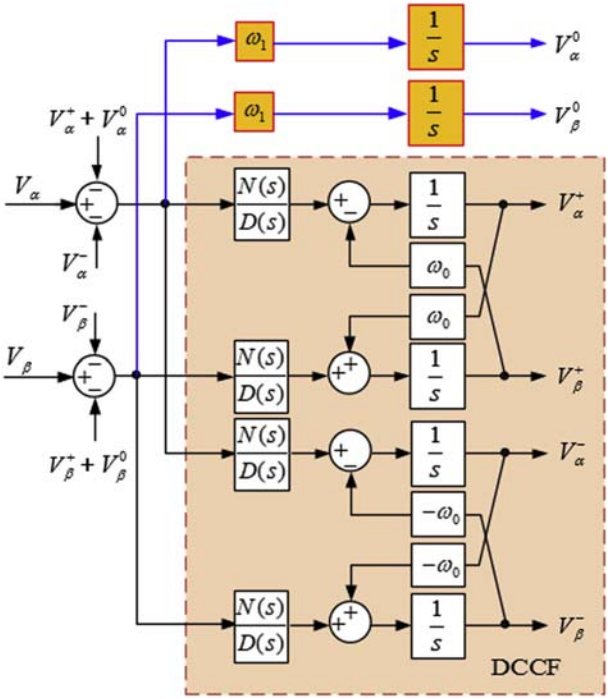

FIGURE 10.13 Physical implementation diagram of the decoupled complex coefficient filter–based phase-locked loop.

However, it should be noted that the LPFs inside of DCCM-PLL may lead to a slow dynamic response. As one possible solution, the dynamic response can be improved by using a PID controller as the LF of the SRF-PLL in order to provide a pole-zero cancellation. On the other hand, the CCF-PLLs can be extended to the dominant harmonic components by using extra complex BPFs centered at the desired harmonic frequencies. The CCF-PLLs are not limited to the study cases as described in Figs. 10.12 and 10.13. The topology of CCFs can be used as an in-loop filter of different PLLs, but the potential efforts and design optimization still need further research investigations under different case studies and tests.

10.3.7 Delayed signal cancellation–based PLLs

The delayed signal cancellation–based PLLs (DSC-PLLs) are generally designed to improve the filtering capacity of the conventional PLLs due to their easier tailored characteristic under different grid voltage cases [29]. It usually severs as an in-loop filter in the SRF-PLL or as a preprocessing filter before the SRF-PLL input. However, the DSC may increase the phase delay

This book belongs to Kitab Liaison (ocd1996@gmail.com) Copyright Elsevier 2023

and slow down the dynamic response, and even affect the stability of the PLLs. Therefore, the DSC operators in most cases are usually playing as a pre-processing filter tool to improve the filtering capability of the SRF-PLL [9], and the number of DSCs in the PLL control loop depends on the anticipated harmonic components from three-phase grid voltages.

On the other hand, the frequency estimated by the SRF-PLL is often fed back to adapt frequency variations in the system. More DSC operating in the control loop of SRF-PLLs will increase the implementation complexity and the computational burden. The frequency feedback loop makes the PLLs system highly nonlinear and hard to analyze in terms of stability. Some alternative approaches are introduced in Refs. [9,30], but still require more computational efforts. In addition, the method of correcting the phase and amplitude errors in PLLs is suggested to reduce computational burden, as the length of the delays of the DSC remains fixed, and the stability analysis can be carried out easily [31]. However, this method does not improve the disturbance rejection ability of the nonadaptive DSCs when the grid frequency deviates from its nominal value, so that there are some limitations for further application under large frequency drifts and severe also during asymmetrical grid voltage faults.

10.3.8 Multiple SRF filter–based PLLs

Multiple SRF filter–based PLLs (MSRF-PLLs) are another popular extended version of SRF-PLLs. As an example, in Fig. 10.14, the DSRF-PLL is equipped with two SRFs rotating at the same angular speed but with opposite directions, and a cross-feedback structure is applied to extract and separate the fundamental frequency positive/negative-sequence components of the grid voltage [25].

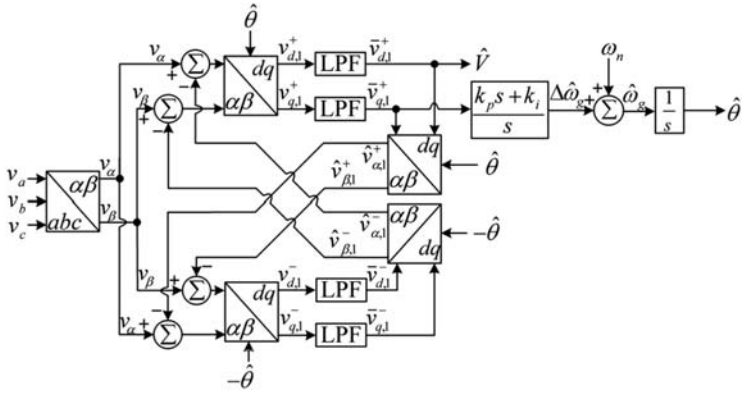

FIGURE 10.14 Schematic diagram of the dual synchronous reference frame–based phase-locked loop [25].

This book belongs to Kitab Liaison (ocd1996@gmail.com) Copyright Elsevier 2023

In addition, it should be noted that the grid voltage imbalance has no steady-state negative effect on the DSRF-PLL performance. However, the presence of grid voltage harmonics in the DSRF-PLL input may cause oscillatory errors in the estimated quantities. This problem can be solved by adding several SRFs rotating at the targeted harmonic frequencies to the standard structure [25,32]. Therefore, this kind of PLLs is usually called the MSRF-PLL.

However, more SRFs will cause a considerable increase in the PLL computational burden. A systematic approach for tuning the control parameters of the MSRF-PLL can be found in Ref. [33]. It is also worth mentioning that the DSRF-PLL is mathematically equivalent with the decoupled double SRF-PLL (DDSRF-PLL) if the input signal of the PI controller is adjusted to $V_{q,1}^{+}$.

10.3.9 Other three-phase PLLs

There are also some other interesting three-phase PLLs. The selective cancellation of harmonic components by using a repetitive regulator/controller inside the SRF-PLL control loop (RR-PLL) is suggested in Ref. [34]. The controller of RR-PLL is based on the discrete transformation, and its computational burden is independent of the number of grid voltage harmonics that are intended to be blocked, which means removing a single harmonic or more grid harmonics using this regulator requires the same computational efforts. This is one of the obvious advantages for RR-PLL. However, the regulator of RR-PLL highly depends on the sampling frequency, and increasing the sampling frequency drives up the potential computational cost. Therefore, the RR-PLL may not be suitable for applications where the sampling frequency is very high.

On the other hand, in order to remove the fundamental frequency negative-sequence component, reforming the imbalanced signals to the balanced ones, a zero-crossing detection-based PLL (ZCD-PLL) is proposed in Ref. [35]. The ZCD-PLL is simple to implement and can operate effectively even in the presence of multiple zero crossings in the PLL input. However, the ZCD-PLL only considers the amplitude imbalance in the grid voltages, but cannot remove the components of phase imbalance in the grid voltages. Furthermore, the harmonic filtering capability of ZCD-PLL is very limited.

In Ref. [36], the Space Vector Fourier Transforms (SVFT) are employed as the SRF-PLL prefiltering stage. The SVFT can effectively reject almost all of harmonic components with a very low computational effort. However, the recursive implementation of the SVFT-based filter may involve potential stability problems in the power system. This stability issues can be avoided by implementing the SVFT in the nonrecursive form, but at the expense of increasing computational cost.

This book belongs to Kitab Liaison (ocd1996@gmail.com) Copyright Elsevier 2023

In Ref. [37], a scheme of Second-Order Lead Compensators (SOLC) included into SRF-PLL is proposed. These compensators have pairs of purely imaginary zeros and poles, which means they can provide a selective harmonic cancellation like NFs without causing a big phase delay in the PLLs. Consequently, these compensators can improve the filtering capability but at the cost of a low noise immunity.

Furthermore, the three-phase PLLs should also have a DC offset rejection ability as required in Ref. [9]. Noted that the presence of the DC offset components may be caused by the incorrected installation of the electrical devices, half-wave rectification, geomagnetic phenomena, and the short-term grid faults. To deal with these problems, a simple and effective method by adding an integrator-based DC offset estimation loop to the standard PLL structure is proposed in Ref. [38]. In addition, a method by subtracting the αβ-axis voltage components from their delayed versions and with a frequency-adaptive correction unit improves the robustness perfomance of the PLL [9]. This technique ensures a complete and fast rejection of the DC offset in PLLs. A performance comparison of five DC offset rejection strategies for three-phase PLLs can be found in Ref. [39].

10.3.10 Performance comparison and recommendation

A summary of the typical three-phase PLLs can be found in Fig. 10.15 and their performance comparison between the mentioned PLLs is summarized in Table 10.1. Notice that the performance results reported in Table 10.1 are corresponding to the typical structure of each three-phase PLL.

In case of the ideal grid synchronization, the SRF-PLL is still the most common PLL due to its design simplicity and lower computational burden as well as fast dynamic response ability. However, the SRF-PLL is very sensitive to the grid voltage harmonics and imbalances. Therefore, several PLLs such as SSI-PLL, SOGI-PLL, and DCCF are recommended to enhance the robustness to the system disturbances and unbalanced grid voltage faults. On the other

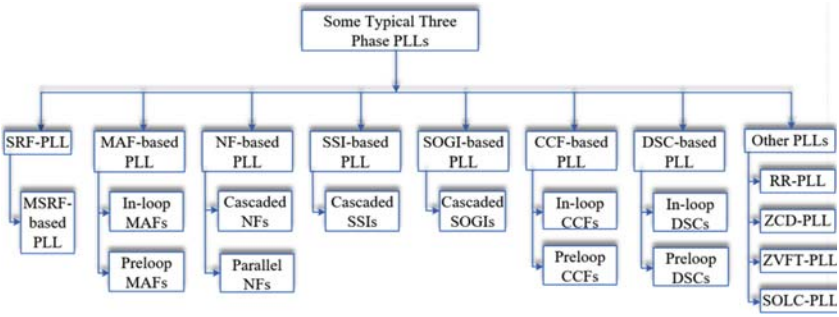

FIGURE 10.15 Summary of the typical three-phase phase-locked loops (PLLs).

This book belongs to Kitab Liaison (ocd1996@gmail.com) Copyright Elsevier 2023

TABLE 10.1 Performance comparison between three-phase phase-locked loops (PLLs) shown in Fig. 10.15.

PLLs type	Features					
	Design simplicity	Frequency adaptive	Harmonic robustness	Imbalance robustness	Computational burden	Dynamic response
SRF-PLL [9]	Good	Average	No	Poor	Average	Fast
MAF-PLL [15]	Average	Average	No	Poor	Low	Average
NF-PLL [20]	Good	Average	Yes	Average	High	Fast
SSI-PLL [23]	Average	Average	Yes	Good	High	Fast
SOGI-PLL [24]	Average	Average	Yes	Good	High	Fast
MSRF-PLL [25]	Average	Average	Yes	Poor	High	Fast
DCCF-PLL [26]	Average	Average	Yes	Good	High	Fast
DSC-PLL [29]	Average	Average	No	Good	Low	Average
RR-PLL [34]	High	Average	No	Average	High	Average
ZCD-PLL [35]	Good	Poor	No	Poor	Low	Fast
SVFT-PLL [36]	Average	Average	No	Average	High	Fast
SOLC-PLL [37]	Average	Average	No	Average	Average	Fast

This book belongs to Kitab Liaison (ocd1996@gmail.com)

Copyright Elsevier 2023

hand, the dynamic response and stability performance is the main concern of the PLLs. Almost all of the mentioned PLL in Table 10.1 has a good dynamic response performance, but the MAF-PLL, DSC-PLL, and ZCD-PLL usually need the PID-type prefilter or extra phase compensator to improve the dynamic performance, which may increase the computational burden. In addition, the ZCD-PLL is not suggested to be applied directly in the grid-connected power system, since it is frequency nonadaptive and its harmonic filtering capability is quite limited. It shows that almost all of the PLLs in Table 10.1 benefit from different disturbance rejection capacity and there will be a direct relation between the their filtering capability and computational burden, which means the harmonic filtering capability of PLLs can be improved by adding more extended modules but at the cost of a higher computational burden.

In a short conclusion, the operating principle of three-phase PLLs was explained and their advantages and disadvantages were briefly discussed in this section. The provided information can be very useful for researchers to select a proper synchronization technique for their particular application.

10.4 Single-phase PLLs

In recent years, single-phase PLLs have been widely applied for monitoring and diagnostic purposes in the power electric system and energy areas. With the development of a large number of single-phase PLLs with different topologies and properties, it is necessary to provide an insight into the characteristics of different single-phase PLLs. The details of each typical single-phase PLLs are described in the following section.

10.4.1 Standard P-PLLs

In fact, the single-phase PLLs are mainly categorized into the power-based PLLs (P-PLLs) and quadrature signal generation—based PLLs (QSG-PLLs) [28]. Fig. 10.16 shows the schematic diagram of a standard P-PLL, which is a very basic PLL in single-phase applications [28].

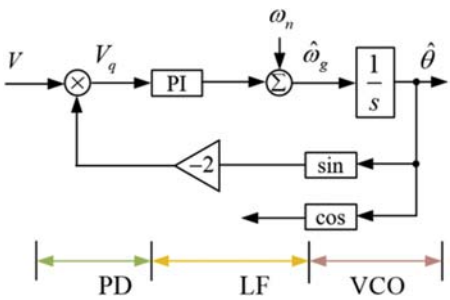

FIGURE 10.16 Schematic diagram of a single-phase standard power—based phase-locked loop.

This book belongs to Kitab Liaison (ocd1996@gmail.com) Copyright Elsevier 2023

In this standard P-PLL, V is the single-phase signal input, $\widehat{\omega}_g$ and $\widehat{\theta}$ are the estimated amplitude of frequency and phase, ω_n is the nominal value of the frequency, and the PI controller serves as the LF of PLLs. The P-PLL uses a mixer or product-type PD to generate the phase error information. Such PD has a double-frequency term, which may cause a double-frequency oscillatory error and DC offset error in the P-PLL. The shortcoming of a standard P-PLL is that it does not provide any information about the input voltage amplitude. It implies a decoupling between P-PLL dynamics and the input voltage amplitude variations.

10.4.2 Low pass filter–based P-PLLs

In order to mitigate the double-frequency disturbance terms in the standard P-PLL, a P-PLL equipped with a high-order infinite impulse response (IIR) or LPF is proposed in Ref. [40]. The schematic diagram of LPF-P-PLL is shown in Fig. 10.17. Notice that the LPF requires a low cut-off frequency to remove the double-frequency disturbance item, which results in a considerably high phase delay in the PLLs and causes a very slow dynamic performance. However, the LPF-P-PLL benefits from a high harmonic filtering capability and noise immunity. Tuning the parameters of the LPF-P-PLL is carried out by the trial-and-error procedure suggested in Ref. [40].

10.4.3 Moving average filter–based P-PLLs

In a similar way, Fig. 10.18 shows an alternative approach to eliminate the double-frequency disturbance term by using an in-loop MAF in the P-PLL [15,41]. The MAF is a linear phase–based LPF, which is also known as a rectangular window filter, which may cause a slow dynamic response.

To mitigate the effect of the dynamics of MAF-PLL, the PI controller could be instead a PID controller and arranging a pole-zero cancellation inside the control loop [15]. However, the pole-zero cancellation in MAF-PLL reduces the ability of rejecting the double-frequency grid disturbance. Therefore, the

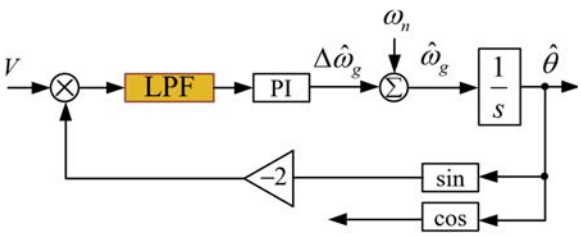

FIGURE 10.17 Schematic diagram of a low pass filter power–based phase-locked loop PLL.

This book belongs to Kitab Liaison (ocd1996@gmail.com) Copyright Elsevier 2023

frequency-adaptive—based MAF is suggested in Ref. [42], and the frequency adaptability of MAF-PLL is designed by using a variable sampling frequency and altering the MAF window length according to the frequency variations of the single-phase input signal.

In addition, the MAFs can be achieved with both recursive and non-recursive forms [28]. The recursive realization is usually preferred with lower computational burden, and the amplitude estimation function can be obtained by adding more MAFs into the selected PLLs.

10.4.4 Notch filter—based P-PLLs

A nonadaptive IIR-NF-P-PLL is proposed to cancel the double-frequency items in single-phase applications [43]. The structure is similar to the LPF-P-PLL except that the LPF is replaced by an IIR-NF. However, the notch bandwidth of the IIR-NF highly depends on the expected range of the grid frequency variations. Therefore, a wide bandwidth for the NF should be carefully designed under the condition of large frequency drifts. Furthermore, it should be noted that the selection effectively removes the double-frequency term at the expense of causing a large phase delay, and hence, slowing down the transient response of P-PLL.

On the other hand, the harmonic filtering capability of IIR-NF-PLLs can be enhanced by additional NFs in a serial manner or in a parallel configuration, and the tuning of the control parameters of IIR-NF-P-PLL can be obtained by using the symmetrical optimum methods [28].

Moreover, the finite impulse response notch filter—based PLL (FIR-NF-P-PLL) is proposed to reject the double-frequency term in Ref. [44]. The schematic diagram of FIR-NF-P-PLL can be seen in Fig. 10.19. The FIR-NF is implemented by using T/4 delay units (T is the grid fundamental period), rather effectively blocks the double-frequency term even the grid frequency variations are large. In addition, the FIR-NF-P-PLL rejects some specific

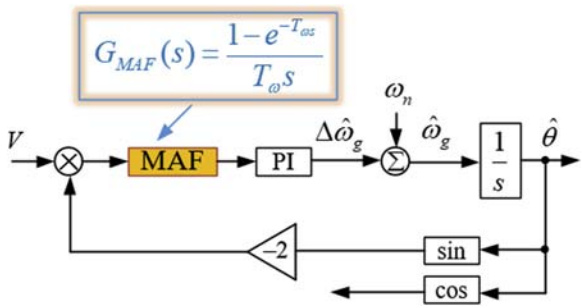

FIGURE 10.18 Schematic diagram of the moving average filter power—based phase-locked loop.

This book belongs to Kitab Liaison (ocd1996@gmail.com) Copyright Elsevier 2023

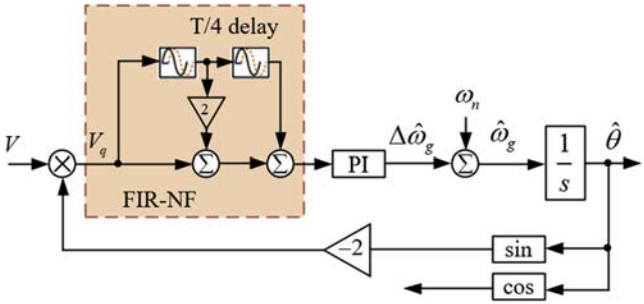

FIGURE 10.19 Schematic diagram of the finite impulse response notch filter—based phase-locked loop.

harmonic components inside the control loop. However, these advantages are at the expense of a slower transient response of the P-PLL due to large phase delay caused by FIR-NF unit.

10.4.5 Double-frequency and amplitude compensation—based P-PLLs

The schematic diagram of DFAC-P-PLL is shown in Fig. 10.20 [28,45], where an amplitude estimation loop is added to the standard P-PLL, and thereby the double-frequency terms are canceled by compensating the opposite double-frequency components. On contrary to other single-phase P-PLLs, the

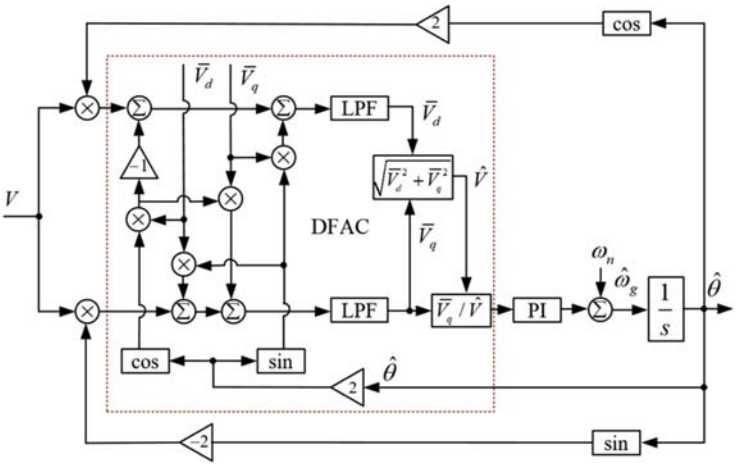

FIGURE 10.20 Schematic diagram of the double-frequency and amplitude compensation—based phase-locked loop [28,45].

This book belongs to Kitab Liaison (ocd1996@gmail.com) Copyright Elsevier 2023

dynamics of the DFAC-P-PLL is independent of the grid amplitude variations. And the first-order LPFs used in the DFAC structure contribute to higher harmonic filtering capabilities.

It is worth mentioning that the extended version of the DFAC-P-PLL with an excellent harmonic filtering capability is at the cost of slower dynamic response in practice.

10.4.6 Modified mixer PD-Based P-PLLs

A modified mixer PD-Based P-PLL (MMPD-P-PLL) to tackle the double-frequency problem is proposed in Ref. [46]. In this approach, the double-frequency item is canceled before the PI controller by adding an equal but opposite component, which is constructed by using the information of the estimated phase angle. This approach works effectively in the condition that the grid voltage is always assumed as 1.0 p.u. However, it is difficult to create this condition since an accurate amplitude estimation in real time is required.

10.4.7 Transfer delayed–based PLLs

Another important type of single-phase PLL is the QSG-PLLs. However, most of QSG-PLLs are the variants from the conventional SRF-PLL (see Fig. 10.3) with additional filter/circuit/algorithms to generate the required quadrature signals. In Fig. 10.21, the TD-PLLs based on the transfer delay create a quadrature signal as one typical approach. The quadrature signal is obtained by delaying the original single-phase signal by T/4, where T is the grid fundamental frequency period.

On the other hand, it should be noted that the delayed signal is not perfectly orthogonal to the original signal under grid frequency variations/drifts cases and it is easy to cause the double-frequency and offset errors in the estimated quantities by the standard structure of the TD-PLL. Therefore, some extended TD-PLLs have been developed such as NTD-PLL [47], ETD-PLL [48], ATD-PLL [49], VTD-PLL [50], etc.

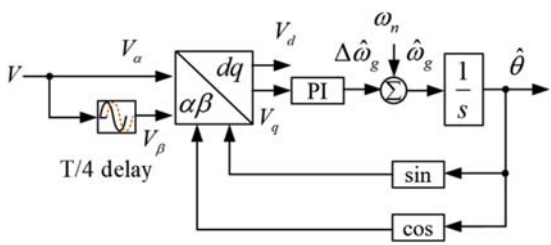

FIGURE 10.21 Schematic diagram of a standard transfer delayed–based phase-locked loop.

This book belongs to Kitab Liaison (ocd1996@gmail.com) Copyright Elsevier 2023

TABLE 10.2 Performance comparison between some single-phase PLLs in terms of calculation operation.

	Calculation operations		
	Storage samples	Trigonometric functions	Basic calculation (+−×÷)
NTD-PLL [47]	80	0	0
ETD-PLL [48]	140	0	22
ATD-PLL [49]	40	2	4
VTD-PLL [50]	80	0	124

As one of the most concerns, their computational burden should be carefully considered. Therefore, the number of operations required for the quadrature signal generation in different TD-PLLs is summarized in Table 10.2. Based on these results, it seems that the ATD-PLL and ETD-PLL are the best choices.

However, the VTD-PLL with a linear interpolation can be an interesting option when the sampling frequency is high, as it requires lower calculations in practice. The NTD-PLL and the VTD-PLL are not recommended, as the former suffers from double-frequency oscillations/ripples under frequency drifts and the latter requires a high computational effort. It should be noted that the ETD-PLL is the only available choice among TD-PLLs when a high harmonic filtering capability is required.

10.4.8 Inverse park transformation−based PLLs

The inverse park transformation−based PLL (IPT-PLL) is one of another popular single-phase PLLs and it is shown in Fig. 10.22. Its virtual orthogonal signal is generated by applying the IPT to the filtered dq-axis voltage components. Note that an in-loop phase delay may be caused by LPF inside the IPT-PLL, but the filtering capability and noise immunity are increased. More control design and detailed analysis of the IPT-PLL can be found in Refs. [28,40].

Furthermore, in addition to the fundamental component, extracting the DC offset and some harmonic components may be required for the faulty grid conditions, an extended IPT-PLL structure is shown in Fig. 10.23 [51]. However, selecting the number of filtering modules involves a tradeoff between the detection accuracy and computational burden, which should be carefully considered.

This book belongs to Kitab Liaison (ocd1996@gmail.com) Copyright Elsevier 2023

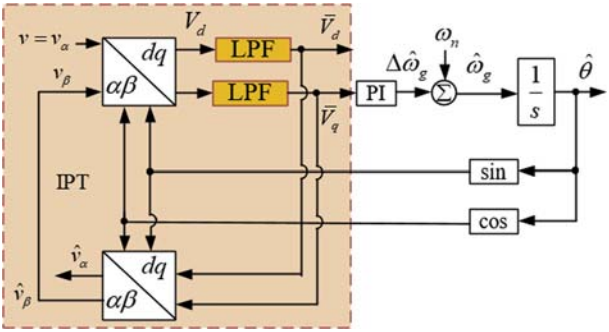

FIGURE 10.22 Schematic diagram of a standard inverse park transformation−based phase-locked loop.

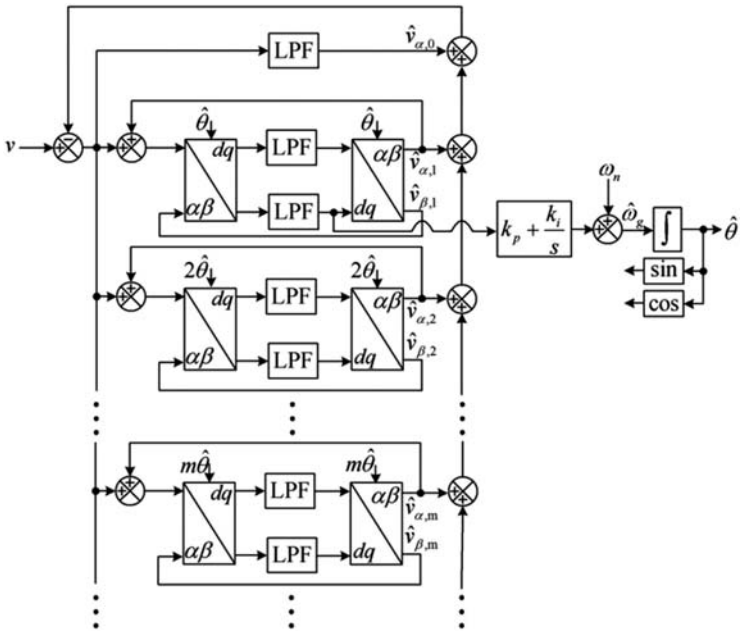

FIGURE 10.23 Extended structure of the inverse park transformation−based phase-locked loop [51].

10.4.9 Generalized integrator−based PLLs

Generalized integrator−based PLLs (GI-PLLs) are also very attractive since they can be effectively customized according to different grid scenarios. In Fig. 10.24, the single-phase SOGI-PLL can create a virtual quadrature signal and attenuate the harmonic components in the same structure. Notice that the

This book belongs to Kitab Liaison (ocd1996@gmail.com) Copyright Elsevier 2023

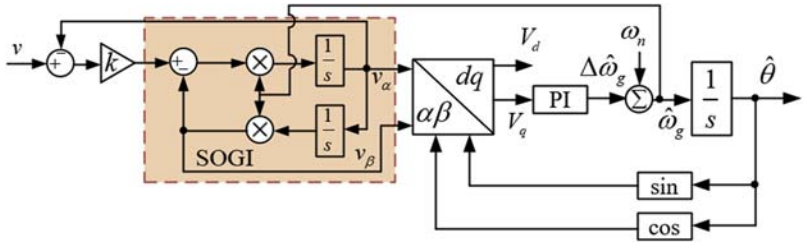

FIGURE 10.24 Structure of standard single-phase second-order generalized integrator—based phase-locked loop.

frequency estimated by the PLL is fed back to the SOGI for adapting it to the grid frequency variations. The small-signal modeling and control design of the single-phase SOGI-PLL can be found in Ref. [52].

In addition, some attempts for frequency-fixed SOGI-PLLs (FFSOGI-PLLs) have been proposed in recent years [53]. In these PLLs, the resonance frequency of SOGIs is fixed at the nominal grid frequency.

Fig. 10.25 shows the structure for implementing the FFSOGI-PLLs, the β-axis output of the nonadaptive SOGI is multiplied by $\hat{\omega}_g/\omega_n$ to create balanced two-phase signals for the PLL input. The α-axis component has a phase difference with the grid voltage caused by SOGI, which results in a phase error in the PLL output, which can be corrected by a phase error compensator.

Fig. 10.26 shows another approach for implementing the FFSOGI-PLLs [54], which has employed two nonadaptive SOGI-QSGs in the PLL. The first SOGI-QSG operates as a prefilter, which may cause phase and amplitude errors under grid frequency drifts. The second SOGI-QSG generates the same phase shift angle and amplitude to compensate the measured errors. More analysis and design of the FFSOGI-PLLs can be found in Ref. [54].

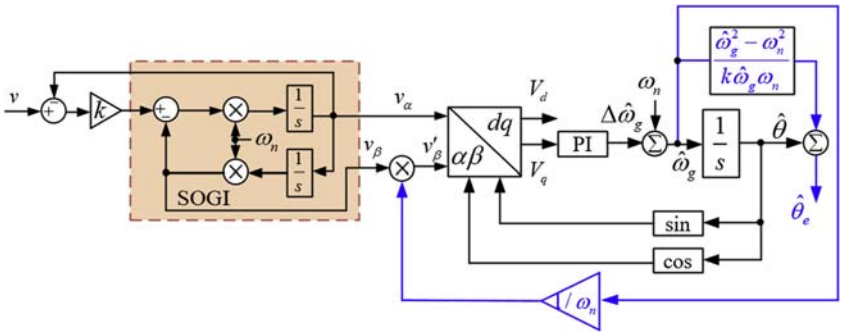

FIGURE 10.25 Structure of single-phase frequency-fixed second-order generalized integrator—based phase-locked loop.

This book belongs to Kitab Liaison (ocd1996@gmail.com) Copyright Elsevier 2023

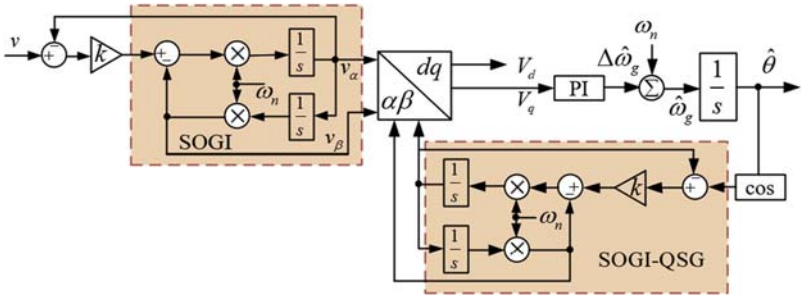

FIGURE 10.26 Extended structure of single-phase frequency-fixed second-order generalized integrator—based phase-locked loop.

10.4.10 Synthesis circuit PLLs

The SC-PLLs are the simplest extended single-phase SRF-PLL due to its easy implementation and characteristics [28]. The schematic diagram of standard SC-PLL is shown in Fig. 10.27.

In addition, when it is necessary to extract more information of grid voltage phase, amplitude, or more harmonic components, the structure of SC-PLL can be extended as shown in Fig. 10.28. However, the computations will increase, especially considering the grid voltage harmonic effects. It is worth mentioning that the SC-PLL demonstrates a very similar performance to the IPT-PLL.

One of the other attractive PLLs in single-phase applications is the E-PLL, which is mathematically equivalent to the standard SC-PLL [55]. However, the E-PLL has modified the integrator output signal as the estimated frequency, which make a higher filtering capability and a more damped dynamic response in the frequency estimation. Furthermore, the extended E-PLLs have been proposed in Refs. [38,56] to improve the ability of harmonic and DC offset components rejection. It should be mentioned that these strategies are also applicable to other single-phase and three-phase PLLs, which could be applied to modern distributed power systems [57,58].

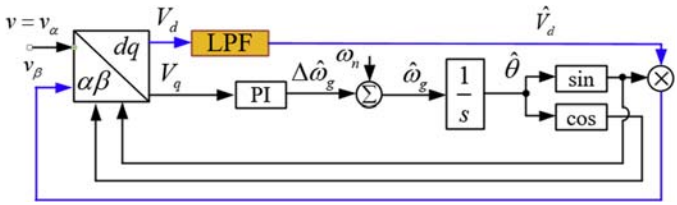

FIGURE 10.27 Schematic diagram of the standard synthesis circuit—based phase-locked loop.

This book belongs to Kitab Liaison (ocd1996@gmail.com) Copyright Elsevier 2023

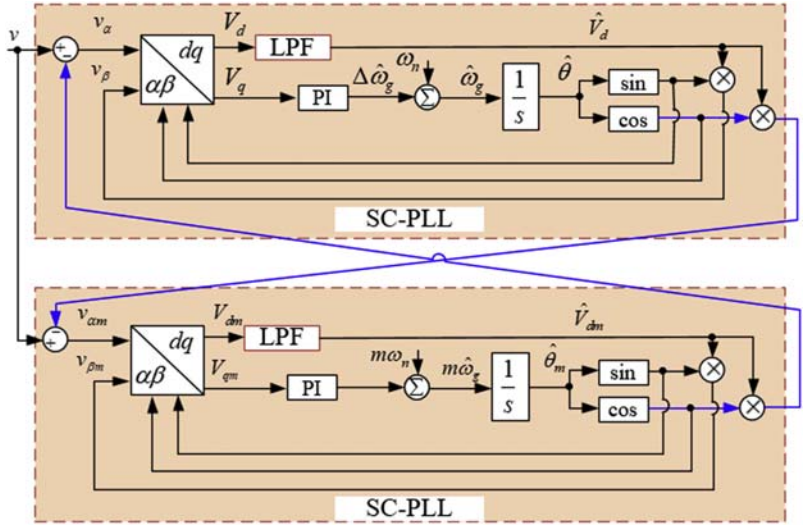

FIGURE 10.28 Extended schematic diagram of the synthesis circuit–based phase-locked loop.

10.4.11 Performance comparison and recommendation

A summary of the mentioned single-phase PLLs is presented in Fig. 10.29 and a performance comparison between these single-phase PLLs can be summarized in Table 10.3. The signal-phase PLL can be devided into two main categories.

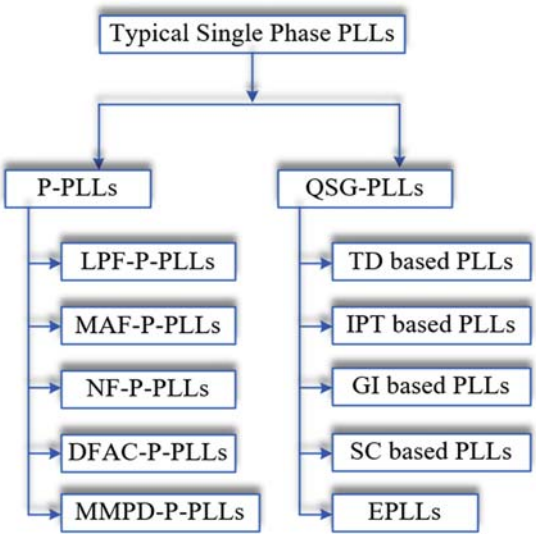

FIGURE 10.29 Two main categories of the typical single-phase phase-locked loops.

This book belongs to Kitab Liaison (ocd1996@gmail.com) Copyright Elsevier 2023

TABLE 10.3 Performance comparison between single-phase phase-locked loops mentioned in Fig. 10.29.

PLLs type	Features			
	Double-frequency robustness	Harmonic robustness	Computational burden	Dynamic response
LPF-P-PLL [40]	Good	Medium	Low	Slow
MAF-P-PLL [41]	Good	Medium	Low	Slow
NF-P-PLL [43]	Good	Medium	Low	Slow
DFAC-P-PLL [45]	Good	Good	Average	Average
MMPD-P-PLL [46]	Good	Good	Average	Average
TD-PLL [47]	Good	Medium	Low	Fast
IPT-PLL [40]	Good	Good	Average	Fast
GI-PLL [52–54]	Good	Good	Average	Fast
Standard E-PLL [55]	Good	Low	Low	Fast
SC-PLL [28,59]	Good	Low	Low	Fast

Based on the performance comparison, the LPF-P-PLL [40], MAF-P-PLL [41], and NF-P-PLL [43] are not suggested due to their slow dynamic performance and limited harmonic filtering capacities. The DFAC-P-PLL [45] and MMPD-P-PLL [46] provide some interesting and optimized features, but the overall design complexity and computational efforts of the PLLs are increased.

In addition, the TD-PLL and its extensions [47–50], SC-PLL [28,59], and standard E-PLL [55] are good options only when the grid voltage contains little harmonics since they have limited harmonic filtering capacity. In practice, the best possible choices are probably the IPT-PLL [40] and GI-PLLs [52–54] since they can provide a satisfactory compromise between the dynamic response, harmonic filtering capacity, and computational complexity, and they can be effectively customized for adverse grid conditions.

Compare with the three-phase PLLs, the single-phase PLL algorithm still presented the fast responses to frequency and phase disturbances, but they are more stiff to single-phase voltage sags and harmonics due to the low cut-off frequency of their designed filters. However, the three-phase PLL algorithm

This book belongs to Kitab Liaison (ocd1996@gmail.com) Copyright Elsevier 2023

is more efficient from the computational point of view, which is demanding about half the number of calculations on three-phase detector stage than the single-phase PLL algorithm. And the three-phase PLL may use three generated single-phase input signal to operate as normal working case.

10.5 Summary

This chapter provides a comprehensive overview of the recent attempts for designing advanced three-phase and single-phase PLLs to be applied in the power electronic area. The operating principle of both three-phase and single-phase PLLs is carefully explained. Furthermore, the different features and applications of the PLLs are discussed. The research considers the enhancement of the PLLs filtering capacities, different grid disturbance rejections, control structure simplification, dynamic response performance, and proper compromise selections under different grid conditions. Finally, the performance comparison guidance is provided and that could be a quick reference for proper selections of appropriate PLLs for researchers and engineers.

References

[1] H. de Bellescize, La Reception Synchrone, E. Chiron., June 1932.
[2] F. Blaabjerg, R. Teodorescu, M. Liserre, A.V. Timbus, Overview of control and grid synchronization for distributed power generation systems, IEEE Trans. Ind. Electron. 53 (5) (October 2006) 1398–1409.
[3] A. Cataliotti, V. Cosentino, S. Nuccio, A phase-locked loop for the synchronization of power quality instruments in the presence of stationary and transient disturbances, IEEE Trans. Instrum. Meas. 56 (6) (December 2007) 2232–2239.
[4] M. Karimi-Ghartemani, M. Iravani, Measurement of harmonics/inter-harmonics of time-varying frequencies, IEEE Trans. Power Deliv. 20 (1) (January 2005) 23–31.
[5] G. Zhang, et al., ADALINE network based PLL for position sensorless interior permanent magnet synchronous motor drives, IEEE Trans. Ind. Electron. 31 (2) (Febuary 2016) 1450–1460.
[6] T. Tran, T. Chun, H. Lee, et al., PLL based seamless transfer control between grid- connected and islanding modes in grid-connected inverters, IEEE Trans. Power Electron. 29 (10) (October 2014) 5218–5228.
[7] M. Ohrstrom, L. Soder, Fast protection of strong power systems with fault current limiters and PLL-aided fault detection, IEEE Trans. Power Deliv. 26 (3) (July 2011) 1538–1544.
[8] G. Chen, L. Zhang, R. Wang, et al., A novel SPLL and voltage sag detection based on LES filters and improved instantaneous symmetrical components method, IEEE Trans. Power Electron. 30 (3) (March 2015) 1177–1188.
[9] S. Golestan, et al., Three-phase PLLs: a review of recent advances, IEEE Trans. Power Electron. 32 (3) (March 2017) 1894–1907.

This book belongs to Kitab Liaison (ocd1996@gmail.com) Copyright Elsevier 2023

[10] M. Karimi-Ghartemani, M. Iravani, A method for synchronization of power electronic converters in polluted and variable-frequency environments, IEEE Trans. Power Syst. 19 (3) (August 2004) 1263−1270.

[11] P. Rodriguez, A. Luna, I. Candela, et al., Multiresonant frequency-locked loop for grid synchronization of power converters under distorted grid conditions, IEEE Trans. Ind. Electron. 58 (1) (January 2011) 127−138.

[12] Z. Xin, R. Zhao, F. Blaabjerg, et al., An improved flux observer for field-oriented control of induction motors based on dual second-order generalized integrator frequency-locked loop, IEEE J. Emerg. Sel. Top. Power Electron. 5 (1) (March 2017) 513−525.

[13] S. Golestan, J.M. Guerrero, J.C. Vasquez, DC-offset rejection in phase-locked loops: a novel approach, IEEE Trans. Ind. Electron. 63 (8) (August 2016) 4942−4946.

[14] M. Ciobotaru, V.G. Agelidis, R. Teodorescu, F. Blaabjerg, Accurate and less-disturbing active antiislanding method based on PLL for grid-connected converters, IEEE Trans. Power Electron. 25 (6) (June 2010) 1576−1584.

[15] S. Golestan, et al., Moving average filter based phase-locked loops: performance analysis and design guidelines, IEEE Trans. Power Electron. 29 (6) (June 2014) 2750−2763.

[16] E. Robles, S. Ceballos, J. Pou, et al., Variable-frequency grid-sequence detector based on a quasi-ideal lowpass filter stage and a phase-locked loop, IEEE Trans. Power Electron. 25 (10) (October 2010) 2552−2563.

[17] J.Y. Wang, J. Liang, F. Gao, et al., A method to improve the dynamic performance of moving average filter-based PLL, IEEE Trans. Power Electron. 30 (10) (October 2015) 5978−5990.

[18] I. Carugati, S. Maestri, P.G. Donato, et al., Variable sampling period filter PLL for distorted three-phase systems, IEEE Trans. Power Electron. 27 (1) (January 2012) 321−330.

[19] S. Golestan, et al., MAF-PLL with phase-lead compensator, IEEE Trans. Ind. Electron. 62 (6) (June 2015) 3691−3695.

[20] F.D. Freijedo, et al., An optimized implementation of phase locked loops for grid applications, IEEE Trans. Instrum. Meas. 60 (9) (September 2011) 3110−3119.

[21] F. Gonzalez-Espin, et al., An adaptive control system for three-phase photovoltaic inverters working in a polluted and variable frequency electric grid, IEEE Trans. Power Electron. 27 (10) (October 2012) 4248−4261.

[22] S. Eren, M. Karimi-Ghartemani, A. Bakhshai, Enhancing the threephase synchronous reference frame PLL to remove unbalance and harmonic errors, in: Proc. 35th Annu. Conf. IEEE Ind. Electron., November 2009, pp. 437−441.

[23] P. Rodriguez, R. Teodorescu, I. Candela, et al., New positivesequence voltage detector for grid synchronization of power converters under faulty grid conditions, in: IEEE Power Electronics Specialists Conference, 2006, pp. 1−7.

[24] M. Ciobotaru, R. Teodorescu, F. Blaabjerg, A new single phase PLL structure based on second order generalized integrator, in: IEEE Power Electronics Specialists Conference, 2006, pp. 1−6.

[25] P. Xiao, K.A. Corzine, G.K. Venayagamoorthy, Multiple reference frame-based control of three-phase PWM boost rectifiers under unbalanced and distorted input conditions, IEEE Trans. Power Electron. 23 (4) (July 2008) 2006−2017.

[26] X. Guo, W. Wu, Z. Chen, Multiple-complex coefficient-filter-based phase-locked loop and synchronization technique for three-phase grid interfaced converters in distributed utility networks, IEEE Trans. Ind. Electron. 58 (4) (April 2011) 1194−1204.

This book belongs to Kitab Liaison (ocd1996@gmail.com) Copyright Elsevier 2023

[27] W. Li, X. Ruan, C. Bao, et al., Grid synchronization systems of three-phase grid-connected power converters: a complex vector-filter perspective, IEEE Trans. Ind. Electron. 61 (4) (April 2014) 1855−1870.

[28] S. Golestan, J.M. Guerrero, J.C. Vasquez, Single-phase PLLs: a review of recent advances, IEEE Trans. Power Electron. 32 (12) (December 2017) 9013−9030.

[29] J. Svensson, M. Bongiorno, A. Sannino, Practical implementation of delayed signal cancellation method for phase-sequence separation, IEEE Trans. Power Deliv. 22 (1) (January 2007) 18−26.

[30] Y.N. Batista, H.E.P. de Souza, F.A.S. Neves, et al., Variable structure generalized delayed signal cancellation PLL (VS-GDSC-PLL) to improve convergence time, IEEE Trans. Ind. Electron. 62 (11) (November 2015) 7146−7150.

[31] W. Liu, F. Blaabjerg, D. Zhou, S.F. Chou, Modified instantaneous power control with phase compensation and current-limited function under unbalanced grid faults, IEEE J. Emerg. Sel. Top. Power Electron. (2020), https://doi.org/10.1109/JESTPE.2020.2984475.

[32] L. Hadjidemetriou, E. Kyriakides, F. Blaabjerg, A robust synchronization to enhance the power quality of renewable energy systems, IEEE Trans. Ind. Electron. 62 (8) (August 2015) 4858−4868.

[33] S. Golestan, M. Monfared, F.D. Freijedo, Design-oriented study of advanced synchronous reference frame phase-locked loops, IEEE Trans. Power Electron. 28 (2) (Febuary 2013) 765−778.

[34] A.V. Timbus, R. Teodorescu, F. Blaabjerg, et al., PLL algorithm for power generation systems robust to grid voltage faults, in: Proc. 37th IEEE Power Electron. Spec. Conf., June 2006, pp. 1−7.

[35] B. Liu, F. Zhou, Y. Zhu, et al., A three-phase PLL algorithm based on signal reforming under distorted grid conditions, IEEE Trans. Power Electron. 30 (9) (September 2015) 5272−5283.

[36] F.A.S. Neves, et al., A space-vector discrete Fourier transform for unbalanced and distorted three-phase signals, IEEE Trans. Ind. Electron. 57 (8) (August 2010) 2858−2867.

[37] F.D. Freijedo, A.G. Yepes, O. Lopez, et al., Three-phase PLLs with fast postfault retracking and steady-state rejection of voltage unbalance and harmonics by means of lead compensation, IEEE Trans. Power Electron. 26 (1) (January 2011) 85−97.

[38] M. Karimi-Ghartemani, S.A. Khajehoddin, P. Jain, et al., Addressing DC component in PLL and notch filter algorithms, IEEE Trans. Power Electron. 27 (1) (January 2012) 78−86.

[39] S. Golestan, J.M. Guerrero, G. Gharehpetian, Five approaches to deal with problem of DC offset in phase-locked loop algorithms: design considerations and performance evaluations, IEEE Trans. Power Electron. 31 (1) (January 2016) 648−660.

[40] R.M. Santos Filho, et al., Comparison of three single-phase PLL algorithms for UPS applications, IEEE Trans. Ind. Electron. 55 (8) (August 2008) 2923−2932.

[41] M.A. Perez, et al., A robust phase-locked loop algorithm to synchronize static-power converters with polluted AC systems, IEEE Trans. Ind. Electron. 55 (5) (May 2008) 2185−2192.

[42] I. Carugati, P. Donato, S. Maestri, et al., Frequency adaptive PLL for polluted single-phase grids, IEEE Trans. Power Electron. 27 (5) (May 2012) 2396−2404.

[43] F.D. Freijedo, J. Doval-Gandoy, O. Lopez, et al., Robust phase locked loops optimized for DSP implementation in power quality applications, in: Proc. IEEE 34th Annu. Conf. Ind. Electron. Soc., November 2008, pp. 2390−2395.

This book belongs to Kitab Liaison (ocd1996@gmail.com) Copyright Elsevier 2023

[44] A. Elrayyah, Y. Sozer, M. Elbuluk, Robust phase locked-loop algorithm for single-phase utility-interactive inverters, IET Power Electron. 7 (5) (May 2014) 1064−1072.

[45] S. Golestan, M. Monfared, F.D. Freijedo, et al., Design and tuning of a modified power-based PLL for single-phase grid-connected power conditioning systems, IEEE Trans. Power Electron. 27 (8) (August 2012) 3639−3650.

[46] T. Thacker, et al., Phase-locked loop noise reduction via phase detector implementation for single-phase systems, IEEE Trans. Ind. Electron. 58 (6) (June 2011) 2482−2490.

[47] S.B. Kjaer, Design and Control of an Inverter for Photovoltaic Applications, Ph.D. dissertation, Inst. Energy Technol., Aalborg Univ, Aalborg, Denmark, 2005.

[48] S. Golestan, et al., Small-signal modeling, stability analysis and design optimization of single-phase delay-based PLLs, IEEE Trans. Power Electron. 31 (5) (May 2016) 3517−3527.

[49] S. Golestan, et al., An adaptive quadrature signal generation based single phase phase-locked loop for grid-connected applications, IEEE Trans. Ind. Electron. 64 (4) (April 2017) 2848−2854.

[50] A. Ozdemir, I. Yazici, Fast and robust software-based digital phaselocked loop for power electronics applications, IET Gener. Transm. Distrib. 7 (12) (May 2013) 1435−1441.

[51] L. Hadjidemetriou, Y. Yang, E. Kyriakides, F. Blaabjerg, A synchronization scheme for single- phase grid-tied inverters under harmonic distortion and grid disturbances, IEEE Trans. Power Electron. 32 (4) (April 2017) 2784−2793.

[52] M. Ciobotaru, R. Teodorescu, F. Blaabjerg, A new single-phase PLL structure based on second order generalized integrator, in: Proc. 37th IEEE Power Electron. Spec. Conf., June 2006, pp. 1511−1516.

[53] F. Xiao, L. Dong, L. Li, X. Liao, A frequency-fixed SOGI based PLL for single-phase grid-connected converters, IEEE Trans. Power Electron. 32 (3) (March 2017) 1713−1719.

[54] Q. Guan, Y. Zhang, Y. Kang, et al., Single-phase phase-locked loop based on derivative elements, IEEE Trans. Power Electron. 32 (6) (June 2017) 4411−4420.

[55] M.K. Ghartemani, Enhanced Phase-Locked Loop Structures for Power and Energy Applications, Wiley-IEEE Press, New York, NY, USA, 2014.

[56] M.K. Ghartemani, S.A. Khajehoddin, P.K. Jain, et al., Problems of startup and phase jumps in PLL systems, IEEE Trans. Power Electron. 27 (4) (April 2012) 1830−1838.

[57] W. Liu, et al., An evaluation method for voltage dips in shipboard microgrid under quasi-balanced and unbalanced voltage conditions, IEEE Trans. Ind. Electron. 66 (10) (October 2019) 7683−7693.

[58] W. Liu, et al., Power quality assessment in shipboard microgrids under unbalance and harmonic ac bus voltage, IEEE Trans. Ind. Appl. 55 (1) (January 2019) 7683−7693.

[59] F. Xiong, et al., A novel frequency-adaptive PLL for single-phase grid- connected converters, in: Proc. of IEEE Energy Convers. Congr. Expo., September 2010, pp. 414−419.

This book belongs to Kitab Liaison (ocd1996@gmail.com) Copyright Elsevier 2023

This page intentionally left blank

This book belongs to Kitab Liaison (ocd1996@gmail.com)

Copyright Elsevier 2023

Chapter 11

Stability and robustness improvement of power converters

Xiongfei Wang, Yicheng Liao, Zichao Zhou
Aalborg University, Aalborg, Denmark

11.1 Introduction

There have been increasing deployments of converter-based power sources and loads in electric power systems. The stability and control of power converters tend to be more sensitive to the variabilities and uncertainties of the connected electrical systems. A number of power disruptions that are resulted from the instability of grid−converter interactions have been reported in recent years.

Voltage source converters (VSCs) are commonly used with converter-based power sources and loads. Differing from synchronous generators, VSCs enable full control of electric power, and thus the control dynamics of VSCs play a critical role in grid−converter interactions. There have been numerous control schemes developed for grid-connected VSCs. The vector current control, among others, is still the mostly used approach to regulating the power exchanged between VSCs and the grid. The dynamic analysis and controller design for current-controlled VSCs have been extensively studied over the years. The focus of research has also been shifted from the reference tracking of control loops under various disturbances, such as the voltage harmonics and unbalances, to the stability and robustness of VSCs with a wide range of grid impedances, e.g., a low short circuit ratio (SCR) grid, and series/parallel resonant impedance.

In this chapter, the stability and robustness improvements of current-controlled VSCs are addressed. The dynamic impacts of control loops, including the inner current loop, the phase-locked loop (PLL), and the outer DC-link voltage control (DVC) loop, on the stability robustness of VSCs are systematically discussed. In Section 11.2, the small-signal modeling of current control for a three-phase VSC with L or LCL filter, where both the

Control of Power Electronic Converters and Systems. https://doi.org/10.1016/B978-0-12-819432-4.00016-0
Copyright © 2021 Elsevier Ltd. All rights reserved.

This book belongs to Kitab Liaison (ocd1996@gmail.com)
Copyright Elsevier 2023

converter- and grid-side current control are considered. The theoretical basis and assumption for representing the inner current loop by single-input and single-output (SISO) transfer functions are elaborated. Then, the impedance modeling of the inner current control loop is discussed. Based on the impedance modeling of inner current loop, the frequency-domain passivity-based analysis is introduced to evaluate the stability robustness of current control, where the effect of time delay involved in the current control is illustrated. Then, three approaches for improving the passivity of inner current control are discussed, including the time delay reduction, the passivity-based design of passive filters, and the active damping control.

Following the SISO impedance modeling of inner current loop, the dynamic impacts of PLL and the outer DVC loop are discussed in Section 11.3. Unlike the inner current control loop, which is generally designed with symmetrical dynamics, the DVC loop and PLL lead to asymmetrical control dynamics on the *d*- and *q*-axes, which necessitate the use of multiple-input and multiple-output (MIMO) model to analyze their dynamic effect. Further, the PLL and DVC loop are nonlinear and time varying, whose small-signal dynamics are highly dependent on the operating (equilibrium) points of VSCs. The MIMO impedance modeling of VSCs, considering the inner current loop, the PLL, and the DVC loop, is illustrated step by step. It is shown that the DVC loop can destabilize the grid—converter interaction when VSCs operate in the rectifier mode, while the PLL can induce oscillations when VSCs operate in the inverter mode. Then, the generalized Nyquist stability criterion is applied to predict the stability of VSCs in weak grids. This is followed by the controller parameter tuning of the PLL and DVC for improving the stability robustness.

11.2 Stability and robustness improvement of current control

Fig. 11.1 shows a single-line representation of a three-phase VSC with L or LCL filter. The current control can be performed on either the converter side or

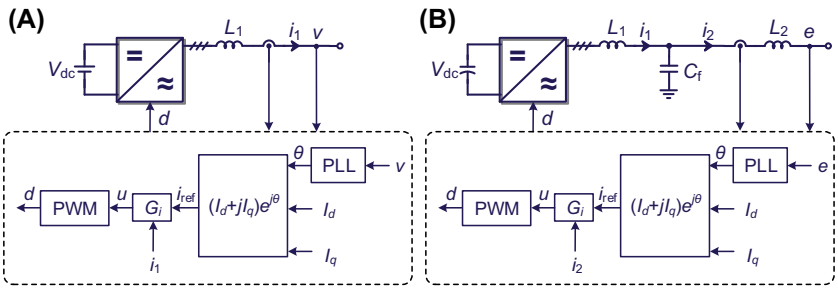

FIGURE 11.1 Single-line representation of a three-phase voltage source converter. (A) Converter-side current control; (B) Grid-side current control.

This book belongs to Kitab Liaison (ocd1996@gmail.com) Copyright Elsevier 2023

the grid side. The current control performance is usually determined by a PLL and an inner-loop current controller [1]. The PLL provides the phase reference of the voltage for the current control, which has slower dynamics than the inner-loop current control, thus it is usually neglected for analyzing the current control dynamics [2].

The current control has faster dynamics, whose control bandwidth (BW) can be high up to one-tenth of the converter switching frequency, yet still with enough stability margin [2]. Thus, the time delay introduced by converter digital control can have a significant impact on the current control dynamics, which also tends to result in harmonic instability issues in grid-connected applications [3]. This section derives the small-signal model of current control loop first, then performs the stability analysis and introduces different ways to robustness enhancement.

11.2.1 Small-signal modeling

The small-signal models of the VSC with the converter-side current control and the grid-side current control are derived, respectively, which are based on a linearization of the converter power stage.

11.2.1.1 Linearization of the converter power stage

Fig. 11.2 gives the circuit diagram of a VSC with switches. The switching signals for different phases are defined as s_a, s_b, and s_c, which can be either 1 or 0 to represent the on or off state of the upper switch or the lower switch during a normal operation. They are thus determined by the status of the switches, s_1–s_6, i.e.,

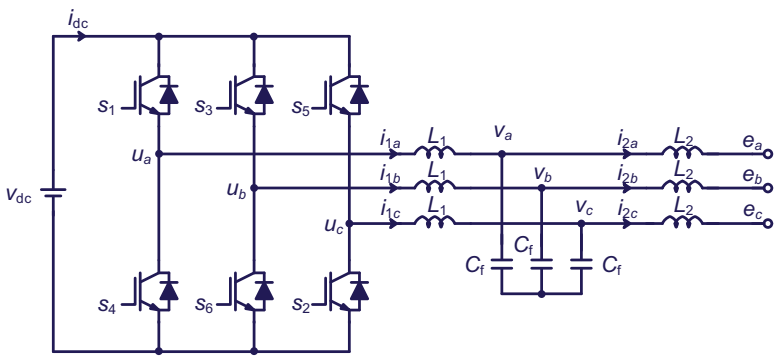

FIGURE 11.2 Switching model of the voltage source converter.

This book belongs to Kitab Liaison (ocd1996@gmail.com) Copyright Elsevier 2023

$$s_a = \begin{cases} 1, \ s_1 = \text{on} \cap s_4 = \text{off} \\ 0, \ s_1 = \text{off} \cap s_4 = \text{on} \end{cases}, \ s_b = \begin{cases} 1, \ s_3 = \text{on} \cap s_6 = \text{off} \\ 0, \ s_3 = \text{off} \cap s_6 = \text{on} \end{cases}, \\ s_c = \begin{cases} 1, \ s_5 = \text{on} \cap s_2 = \text{off} \\ 0, \ s_5 = \text{off} \cap s_2 = \text{on} \end{cases} \tag{11.1}$$

Then the AC-side voltage and DC-side current through the switching modulation can be represented as

$$\begin{bmatrix} u_a \\ u_b \\ u_c \end{bmatrix} = v_{\text{dc}} \begin{bmatrix} s_a \\ s_b \\ s_c \end{bmatrix}, \ i_{\text{dc}} = \begin{bmatrix} s_a & s_b & s_c \end{bmatrix} \begin{bmatrix} i_a \\ i_b \\ i_c \end{bmatrix}. \tag{11.2}$$

It can be seen from Eq. (11.2) that the converter system is a nonlinear and discontinuous system. By applying the averaging operator over the switching period [4], the switching ripples can be neglected. The duty cycles are defined as the averaged switching functions, i.e.,

$$d_{a/b/c} = \frac{1}{T_{\text{sw}}} \int_{t-T_{\text{sw}}}^{t} S_{a/b/c} d\tau. \tag{11.3}$$

Then a continuous dynamic model of the converter power stage is derived as

$$\begin{bmatrix} u_a \\ u_b \\ u_c \end{bmatrix} = v_{\text{dc}} \begin{bmatrix} d_a \\ d_b \\ d_c \end{bmatrix}, \ i_{\text{dc}} = \begin{bmatrix} d_a & d_b & d_c \end{bmatrix} \begin{bmatrix} i_a \\ i_b \\ i_c \end{bmatrix}. \tag{11.4}$$

It is noted that the averaging operator determines the validity of the model till half of the switching frequency [4]. By linearizing the converter model, the small-signal model for the AC-side equivalent circuit can be derived as shown in Fig. 11.3, where the DC-side dynamics can be neglected when V_{dc} is assumed as constant ($v_{\text{dc}} = 0$).

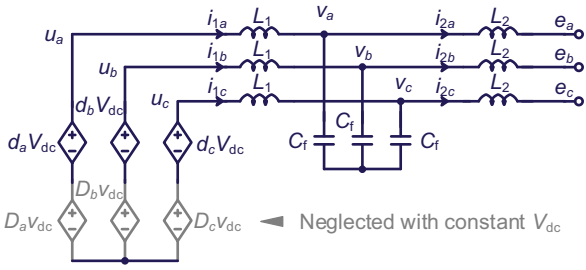

FIGURE 11.3 Linearized AC-side equivalent circuit of the voltage source converter.

This book belongs to Kitab Liaison (ocd1996@gmail.com)
Copyright Elsevier 2023

Under three-phase balanced conditions, the three-phase circuit in the *abc* frame can be transformed into a two-phase system in the $\alpha\beta$ frame. If the converter current control is assumed symmetrical in the *dq* frame [5] or identical in the $\alpha\beta$ frame, thus, the two-phase stationary-frame model can be further simplified as a single-phase system. Considering the converter control, the stationary-frame model can be represented by Fig. 11.4. The switching modulation with V_{dc} is canceled by the normalization with $1/V_{dc}$ in the converter control.

11.2.1.2 Small-signal model of VSC with converter-side current control

For the converter-side current control, the filters C_f and L_2 can be excluded for the converter modeling. Consequently, only an L-filter is considered and the capacitor voltage v is seen as the disturbance input. According to the circuit in Fig. 11.4, the plant model from the modulation voltage u to the converter output current i_1 and the converter open-loop output admittance can be derived, respectively, as

$$Y_{ui}(s) = \left.\frac{i_1}{u}\right|_{v=0} = \frac{1}{sL_1}, \tag{11.5}$$

$$Y_{ol}(s) = -\left.\frac{i_1}{v}\right|_{u=0} = \frac{1}{sL_1}. \tag{11.6}$$

The pulse width modulation (PWM) can be modeled by a zero-order hold block, which usually introduces a time delay of $0.5T_s$ [6], where T_s is the sampling rate. Then, considering a one-period calculation delay of digital controller, the total time delay is characterized as $1.5T_s$, which can be represented as a transfer function (G_d) in series with the current controller, i.e.,

$$G_d(s) = e^{-sT_d} = e^{-1.5sT_s}. \tag{11.7}$$

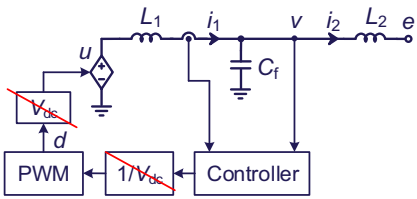

FIGURE 11.4 Stationary-frame model of the voltage source converter with converter-side current control.

This book belongs to Kitab Liaison (ocd1996@gmail.com)
Copyright Elsevier 2023

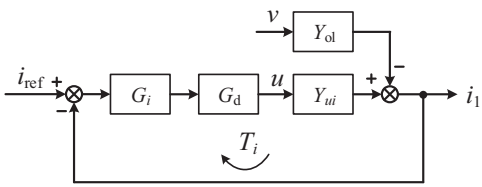

FIGURE 11.5 Closed-loop small-signal model of the voltage source converter with converter-side current control.

Then the closed-loop control diagram for the converter can be depicted in Fig. 11.5, where G_i represents the transfer function of the current controller, which utilizes a proportional + resonant (PR) controller in the $\alpha\beta$ frame, i.e.,

$$G_i(s) = K_{\text{pi}} + \frac{K_{\text{ri}} s}{s^2 + \omega_1^2} \overset{\text{high frequency}}{\approx} K_{\text{pi}}, \tag{11.8}$$

where ω_1 is the fundamental angular frequency. The resonant controller gain, K_{ri}, is merely designed for the steady-state tracking performance at ω_1, thus it has negligible effect on the frequency response at the higher crossover frequency [2].

Based on the control diagram in Fig. 11.5, the loop gain and the closed-loop output admittance of the current control can be derived, respectively, as

$$T_i(s) = G_i(s) G_d(s) Y_{\text{ui}}(s), \tag{11.9}$$

$$Y_o(s) = \frac{Y_{\text{ol}}(s)}{1 + G_i(s) G_d(s) Y_{\text{ui}}(s)}, \tag{11.10}$$

which can be utilized for controller design and stability analysis.

11.2.1.3 Small-signal model of VSC with grid-side current control

For the grid-side current control, the converter small-signal model can be derived in a similar way. The only difference lies in the transfer functions of the plant model Y_{ui} and the open-loop admittance model Y_{ol}. They are derived based on the LCL filter with the voltage e as the disturbance input, which are represented as

$$Y_{\text{ui}}(s) = \left.\frac{i_2}{u}\right|_{e=0} = \frac{Z_{\text{Cf}}}{Z_{\text{Cf}} Z_{L1} + Z_{\text{Cf}} Z_{L1} + Z_{L1} Z_{L2}}, \tag{11.11}$$

$$Y_{\text{ol}}(s) = -\left.\frac{i_2}{e}\right|_{u=0} = \frac{Z_{\text{Cf}} + Z_{L1}}{Z_{\text{Cf}} Z_{L1} + Z_{\text{Cf}} Z_{L1} + Z_{L1} Z_{L2}}, \tag{11.12}$$

where Z_{L1}, Z_{L2}, and Z_{Cf} are the impedances of L_1, L_2, and C_{f}, respectively. Then, the closed-loop small-signal model can be derived in the same way as shown in Fig. 11.5, with v replaced by e and i_1 replaced by i_2.

This book belongs to Kitab Liaison (ocd1996@gmail.com) Copyright Elsevier 2023

11.2.2 Passivity-based stability analysis

For a grid-connected VSC, its output admittance plays a significant role in the grid—converter interaction. The overall system stability is contributed by minor loop gain composed by the grid impedance and the converter output admittance at their point of connection [7]. However, the external grid impedance profile is usually unknown, which makes it difficult to predict the system stability based on a specific minor loop gain. Therefore, the passivity-based stability analysis can be utilized—the interconnected system is passive and stable if the converter output admittance and the grid impedance are both passive [8]. Such a method provides a sufficient condition for system stability. The grid impedance is composed of passive components, thus it is always passive. Then the stability performance can be simply analyzed by the converter output admittance.

The passivity condition implied that the converter output admittance dissipates energy, i.e., the real part of the admittance model is nonnegative at all frequencies. If the converter admittance has negative real part, it tends to result in negative damping to the stability of grid interaction. The passivity-based stability analysis for converter-side current control and grid-side current control is thus analyzed, respectively.

11.2.2.1 Passivity-based stability analysis for converter-side current control

To further investigate the passivity of the converter close-loop output admittance, Y_o can be further derived as two admittances in series [9], i.e.,

$$Y_o(s) = \frac{1}{\dfrac{1}{Y_{\mathrm{ol}}(s)} + \dfrac{1}{Y_{\mathrm{oa}}(s)}}, \tag{11.13}$$

where one admittance is the open-loop output admittance Y_{ol}, which is passive, and the other is an active admittance, which is defined as Y_{oa}.

For the converter-side current control, it is derived that Y_{oa} is merely determined by the current controller and the time delay, i.e.,

$$Y_{\mathrm{oa}}(s) = \frac{Y_{\mathrm{ol}}(s)}{G_i(s)G_d(s)Y_{\mathrm{ui}}(s)} = \frac{1}{G_i(s)G_d(s)}. \tag{11.14}$$

Neglecting the effect of the resonant current controller, the high-frequency response of Y_{oa} is derived as

$$Y_{\mathrm{oa}}(j\omega) \overset{\text{high frequency}}{\approx} \frac{1}{K_{\mathrm{pi}}} e^{j\omega T_d} = \frac{1}{K_{\mathrm{pi}}}[\cos(\omega T_d) + j\sin(\omega T_d)]. \tag{11.15}$$

This book belongs to Kitab Liaison (ocd1996@gmail.com) Copyright Elsevier 2023

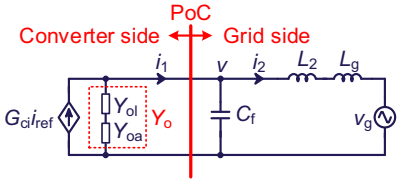

FIGURE 11.6 Equivalent circuit of the grid-connected converter with converter-side current control.

It is seen that $Y_{oa}(j\omega)$ is a function of time delay, whose real part is determined by the function of $\cos(\omega T_d)$. Consequently, the negative real part of Y_{oa} locates in the frequency range of $(1/(4T_d), 3/(4T_d))$, i.e., $(f_s/6, f_s/2)$ with $T_d = 1.5T_s$. Since Y_{ol} is passive, the nonpassive region of the total converter admittance Y_o should also locate in the nonpassive region of Y_{oa}.

Consequently, the equivalent circuit of a grid-connected converter can be represented by Fig. 11.6. It is noted that the converter admittance only considers the converter-side filter L_1; thus, the filters C_f and L_2 are included in the model of the grid admittance, which is given by

$$Y_g(s) = sC_f + \frac{1}{s(L_2 + L_g)}. \tag{11.16}$$

The converter-side current controller design and the passivity-based analysis are carried out based on the circuit and control parameters provided in Table 11.1. Fig. 11.7A plots the Bode diagram of the current loop gain, where the current control BW is designed as 1/10 of the switching frequency. Fig. 11.7B plots the Bode diagrams of the converter output admittance Y_o and the grid admittance Y_g.

It is seen that the negative real part of Y_o appears in the frequency range $(f_s/6, f_s/2)$, since its phase response has exceeded -90 degrees. This nonpassive behavior of Y_o makes the phase difference between the Y_o and Y_g exceed 180 degrees within the frequency range where $|Y_o|>|Y_g|$, thus the grid-connected converter system is unstable according to the Nyquist stability criterion [7].

A simulation verification is provided in Fig. 11.8 for this scenario. It is seen that high-frequency oscillations are observed in the converter output current waveforms. The oscillation frequency is estimated as 1.73 kHz, which agrees with the admittance magnitude crossover frequency shown in Fig. 11.7B.

This book belongs to Kitab Liaison (ocd1996@gmail.com) Copyright Elsevier 2023

TABLE 11.1 Circuit and control parameters of the grid-connected converter.

Parameter	Symbol	Value	Parameter	Symbol	Value
Grid voltage	V_g	380 V_{RMS}	Grid frequency	f_1	50 Hz
DC-link voltage	V_{dc}	650 V	Power rating	P_0	2 kW
Grid inductor (ESR)	L_g (R_g)	10 mH (0.1 Ω)	Converter-side inductor (ESR)	L_1 (R_{L1})	2.2 mH (0.1 Ω)
Filter capacitor	C_f	10 μF	Converter-side inductor (ESR)	L_2 (R_{L2})	1 mH (0.1 Ω)
Switching frequency	f_{sw}	10 kHz	Sampling frequency/ period	f_s/T_s	10 kHz/100 μs
P gain of converter-side current control	K_{pi}	13.8 Ω	R gain of converter-side current control	K_{pr}	8685 Ω/s
P gain of grid-side current control	K_{pi}	5.8 Ω	R gain of grid-side current control	K_{pr}	1094 Ω/s
P gain of grid-side current control with $C_f = 1$ μF	K_{pi}	18 Ω	R gain of grid-side current control with $C_f = 1$ μF	K_{pr}	1129 Ω/s

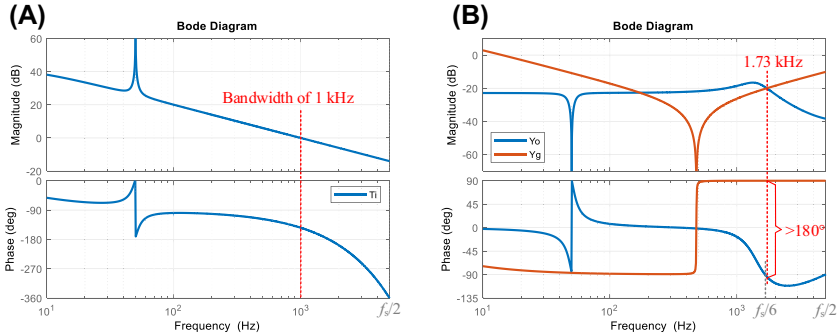

FIGURE 11.7 Converter-side current control design and admittance analysis for the grid-connected converter. (A) Current control loop gain; (B) Admittance-based passivity and stability analysis.

This book belongs to Kitab Liaison (ocd1996@gmail.com)
Copyright Elsevier 2023

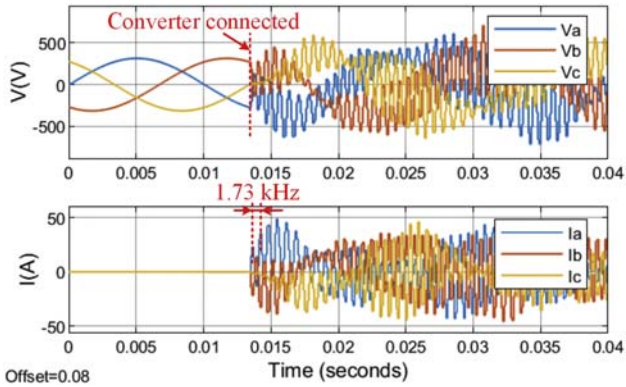

FIGURE 11.8 Simulation result of the grid-connected converter with converter-side current control.

11.2.2.2 Passivity-based stability analysis for converter-side current control

For the grid-side current control, the output admittance can also be seen as the open-loop admittance Y_{ol} in series with the active admittance Y_{oa}. The latter one is derived as

$$Y_{\mathrm{oa}}(s) = \frac{Y_{\mathrm{ol}}(s)}{G_i(s)G_d(s)Y_{\mathrm{ui}}(s)} = \frac{Z_{C\mathrm{f}} + Z_{L1}}{Z_{C\mathrm{f}}G_i(s)G_d(s)}, \tag{11.17}$$

whose high-frequency response can be approximated as

$$Y_{\mathrm{oa}}(j\omega) \overset{\text{high frequency}}{\approx} \frac{1 - L_1 C_{\mathrm{f}}\omega^2}{K_{\mathrm{pi}}} e^{sT_d} = \frac{1 - L_1 C_{\mathrm{f}}\omega^2}{K_{\mathrm{pi}}} [\cos(\omega T_d) + j\sin(\omega T_d)]. \tag{11.18}$$

It is found that the passivity of Y_{oa} is not only dependent on the time delay but also related to the resonant frequency of L_1 and C_{f}, i.e., f_{L1C}. It is thus further derived that the negative real part of Y_{oa} locates in the frequency range of (f_{L1C}, $1/(4T_d)$), i.e., (f_{L1C}, $f_s/6$) with $T_d = 1.5T_s$. It is noted that if f_{L1C} is larger than $1/(4T_d)$, the nonpassive region should be ($1/(4T_d)$, f_{L1C}).

The equivalent circuit for a grid-connected converter with the grid-side current control is shown in Fig. 11.9. Since the LCL filters are internal parameters of the converter, the external grid admittance is merely composed of L_g. Based on the same circuit parameters in Table 11.1, the current control loop gain is designed with control BW of 300 Hz, whose Bode diagram is shown in Fig. 11.10A. It is noted that the BW of the grid-side current control cannot be designed as too large, because of the impact of the LCL resonance in the high-frequency range. It is seen that the BW of 300 Hz results in a gain margin of 4.5 dB and a phase margin of 8.7 degrees. The admittance plots for

This book belongs to Kitab Liaison (ocd1996@gmail.com) Copyright Elsevier 2023

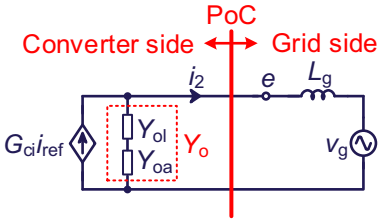

FIGURE 11.9 Equivalent circuit of the grid-connected converter with grid-side current control.

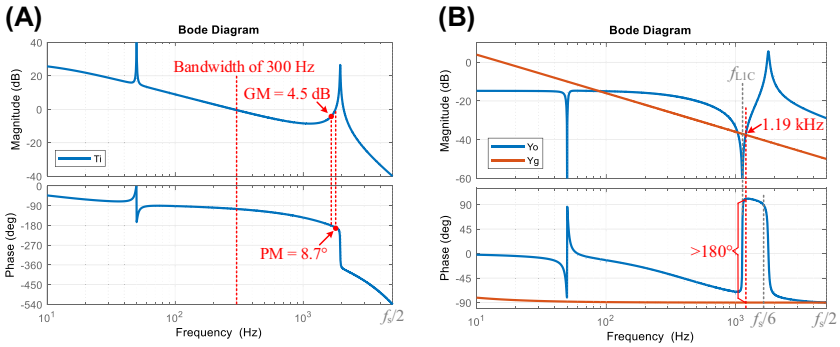

FIGURE 11.10 Grid-side current control design and admittance analysis for the grid-connected converter. (A) Current control loop gain; (B) Admittance-based passivity and stability analysis.

the converter and the grid are shown in Fig. 11.10B. It is seen that the converter admittance only has the negative real part within the frequency range of (f_{L1C}, $f_s/6$), whose phase response has exceeded +90 degrees. At the magnitude crossover frequency of 1.19 kHz, the phase difference between the converter admittance and the grid admittance has exceeded 180 degrees, which results in instability.

The simulation result for the grid-connected converter with the grid-side current control is provided in Fig. 11.11. When the converter is connected, an oscillation at the frequency of 1.18 kHz can be observed in the current waveform, which also agrees with the stability analysis provided in Fig. 11.10B.

11.2.3 Robustness enhancement

Based on the admittance passivity analysis, the stability of the grid-connected converter can be improved by reducing the nonpassive frequency range. There are several approaches to enhance the system robustness by improving the converter admittance passivity.

This book belongs to Kitab Liaison (ocd1996@gmail.com) Copyright Elsevier 2023

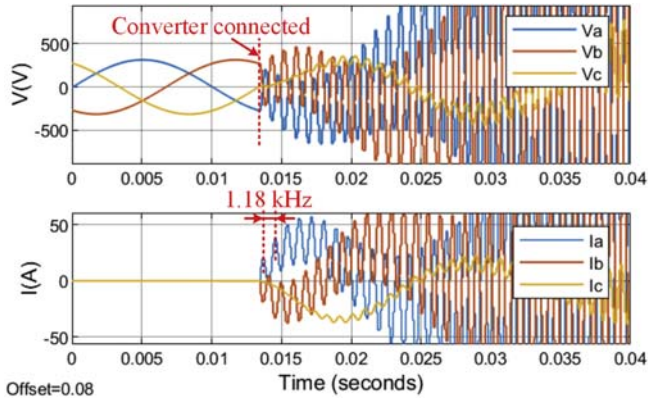

FIGURE 11.11 Simulation result of the grid-connected converter with grid-side current control.

11.2.3.1 Time delay reduction

For the converter-side current control, it has been found that the nonpassive region of the converter admittance locates within $(1/(4T_d), 3/(4T_d))$, which is merely dependent on the time delay. Therefore, an effective approach to improving the converter passivity is to reduce the time delay, which could push the nonpassive region to a higher frequency range, thus the admittance phase difference over 180 degrees can be prevented at the magnitude crossover frequency.

There are several ways to reduce the time delay:

(a) Increasing the sampling frequency to twice as the switching frequency and the double PWM update within a switching period, where $T_d = 1.5T_s$ still holds but the value of T_d is reduced [6].

(b) Shifting the sampling instant toward the PWM update instant, by which the calculation delay is reduced as $0.5T_s$, then the total time delay reduces to $T_d = T_s$ [10].

Considering the two ways, with a fixed switching frequency of 10 kHz, the output admittances of the converter compared against the grid admittance are plotted in Fig. 11.12. It can be seen that the passivity at the admittance magnitude crossover frequency has been improved by reducing the time delay, which makes the admittance phase difference less than 180 degrees and thus contributes to stability. Simulation results for the two cases are provided in Fig. 11.13, where the converter can be stabilized.

It is noted that the time delay reduction approach may not well apply to the grid-side current control, since the nonpassive region is $(f_{L1C}, 1/(4T_d))$. In such a case, a reduction of time delay can even widen the nonpassive region.

This book belongs to Kitab Liaison (ocd1996@gmail.com) Copyright Elsevier 2023

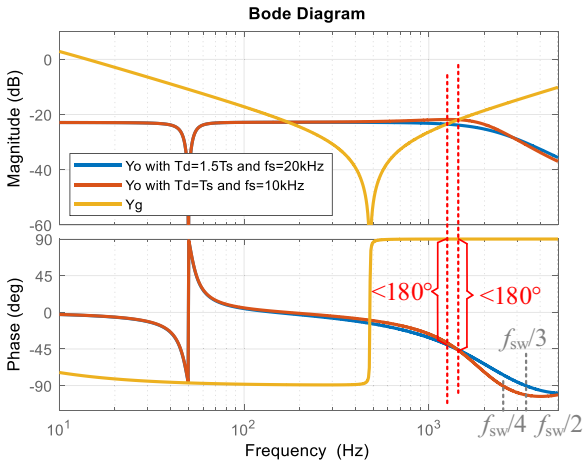

FIGURE 11.12 Equivalent circuit of the grid-connected converter with grid-side current control.

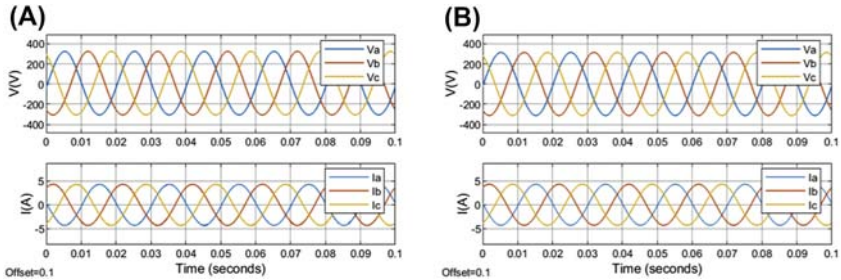

FIGURE 11.13 Stability enhancement by reducing time delay for the grid-connected converter with converter-side current control. (A) $T_d = 1.5T_s$ and $f_s = 20$ kHz; (B) $T_d = T_s$ and $f_s = 10$ kHz.

11.2.3.2 Design of passive filters

For the grid-side current control, it has been found that the nonpassive region of the converter admittance locates within (f_{L1C}, $1/(4T_d)$). Therefore, the nonpassive region of the converter can be eliminated by designing $f_{L1C} = 1/(4T_d)$ [9]. Based on the principle, the filter capacitance is redesigned as 1 μF and the filter inductance remains unchanged. With the new parameters of the LCL filter, the current control loop can be redesigned with much higher BW but still guarantee the loop gain stability. The Bode diagrams of redesigned current control loop gain and the converter output admittance are plotted in Fig. 11.14. It can be seen that with $f_{L1C} = 1/(4T_d)$, the passivity of the converter admittance can be guaranteed till half of the sampling frequency. Therefore, there is no instability issue in connection with the grid. The simulation result shown in Fig. 11.15 indicates that the stability of the grid-connected converter can be improved by designing $f_{L1C} = 1/(4T_d)$.

This book belongs to Kitab Liaison (ocd1996@gmail.com) Copyright Elsevier 2023

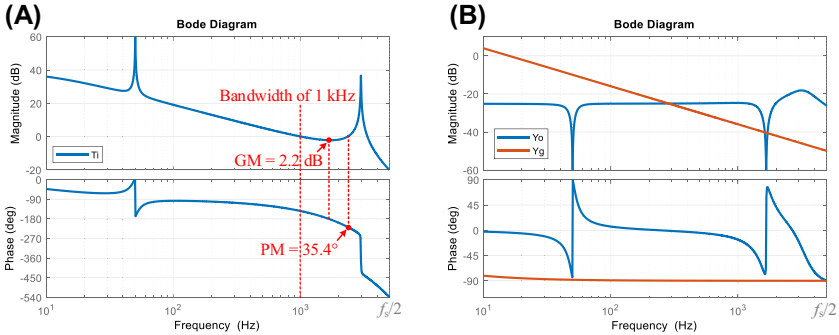

FIGURE 11.14 Grid-side current control design and admittance analysis for the grid-connected converter with $f_{L1C} = 1/(4T_d)$. (A) Current control loop gain; (B) Admittance-based passivity and stability analysis.

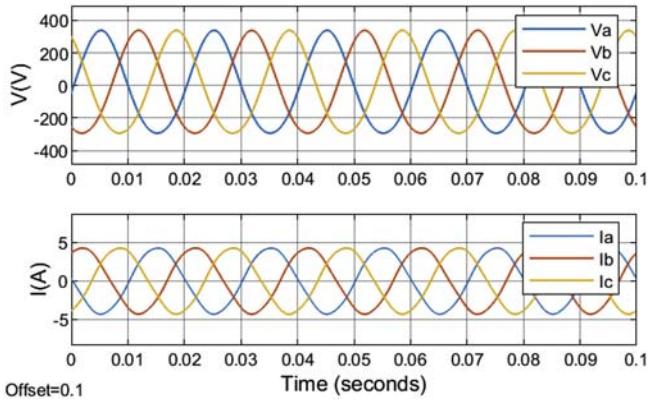

FIGURE 11.15 Stability enhancement of the grid-connected converter with grid-side current control and $f_{L1C} = 1/(4T_d)$.

11.2.3.3 Active damping

Another way to improve the converter passivity is the active damping method implemented in the current control. One simple way of active damping is to employ a differential voltage feedforward control with the converter-side current control [11]. The control diagram is provided in Fig. 11.16. Then, the output admittance can be derived as

$$Y_o(s) = \frac{Y_{\mathrm{ol}}(s)(1 - KsG_d(s))}{1 + G_i(s)G_d(s)Y_{\mathrm{ui}}(s)} = \frac{1 - sKe^{-sT_d}}{(s + \alpha_c e^{-sT_d})L_1}, \tag{11.19}$$

where α_c is defined as the current control BW (rad/s), i.e., $\alpha_c = K_{\mathrm{pi}}/L_1$. Through the frequency response analysis of Y_o, its real part can be derived as

This book belongs to Kitab Liaison (ocd1996@gmail.com) Copyright Elsevier 2023

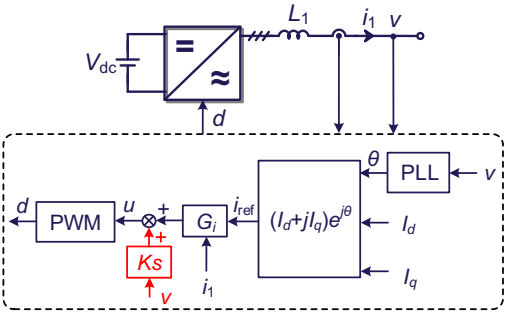

FIGURE 11.16 Control diagram of the grid-connected converter with the converter-side current control and the voltage feedforward control for active damping.

$$\mathrm{Re}\{Y_o(j\omega)\} = \frac{(\alpha_c - \omega^2 K)\cos\omega T_d}{\left(\alpha_c^2 + \omega^2 - 2\alpha_c\omega\sin\omega T_d\right)L_1}. \tag{11.20}$$

The denominator of Eq. (11.20) is always positive; thus, the sign of Re $\{Y_o(j\omega)\}$ is determined by the sign of $(\alpha_c - \omega^2 K)\cos\omega T_d$. It is known that $\cos\omega T_\mathrm{d}$ changes its sign from positive to negative at $\omega = \pi/(2T_d)$, and $\alpha_c - \omega^2 K$ changes its sign from positive to negative at $\omega = \sqrt{\alpha_c/K}$. Consequently, the passivity of Y_o can be achieved till half of the sampling frequency if and only if the two critical frequencies are the same, i.e.,

$$K = \frac{4\alpha_c T_d^2}{\pi^2}. \tag{11.21}$$

Fig. 11.17 gives the admittance plots of the converter and the grid by employing the differential voltage feedforward controller with Eq. (11.21). It is seen that such an active damping method guarantees the passivity till half of the sampling frequency. And at the critical frequency $\omega = \pi/(2T_d)$, i.e., $f = f_s/6$, the converter has the worst stability, where the admittance phase response gets closest to -90 degrees. Thus, the stability of the grid-connected converter can be improved.

It is noted that the performance of a differentiator could be affected by the digital implementation in the high-frequency range. Such a differential voltage feedforward control can be equivalently realized by employing a P controller with the gain of K/C_f on the capacitor current. Fig. 11.18 provides the simulation result with the P controller applied to the current difference of $(i_1 - i_2)$. It is seen that the stability is improved by the active damping method.

It should be noted that the differential voltage feedforward control may fail in impedance passivation when the time delay is longer than $1.5T_s$, since multiple nonpassive regions are present below $f_s/2$. A virtual-flux–based voltage feedforward control is thus proposed in Ref. [12], which adopts an integral controller in the voltage feedforward loop, which successfully

This book belongs to Kitab Liaison (ocd1996@gmail.com) Copyright Elsevier 2023

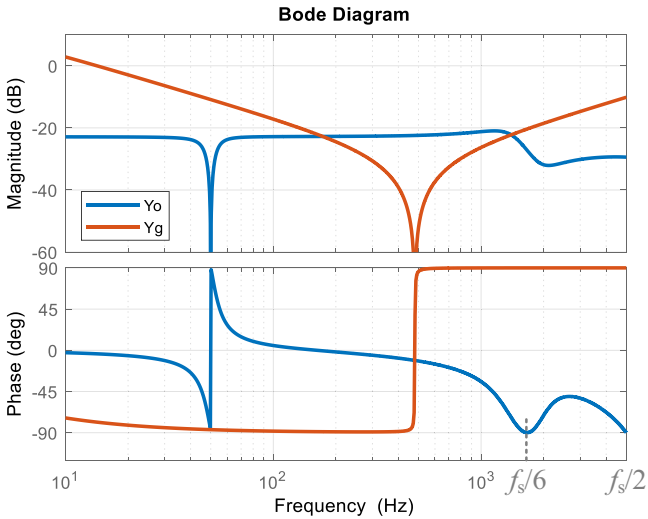

FIGURE 11.17 Control diagram of the grid-connected converter with the converter-side current control and the voltage feedforward control for active damping.

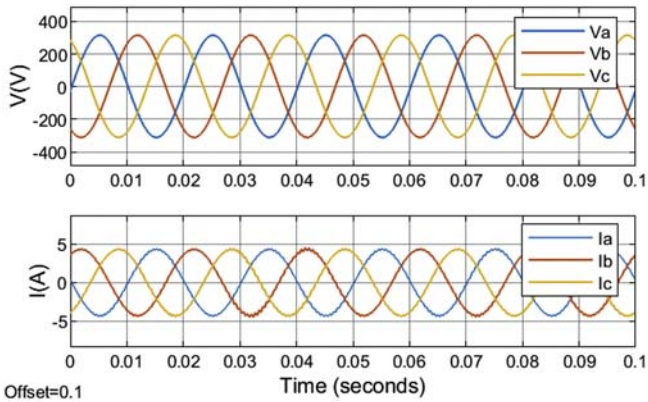

FIGURE 11.18 Stability enhancement of the grid-connected converter with active damping for the converter-side current control.

eliminates the multiple nonpassive regions. This virtual-flux—based active damping results in similar impedance passivation and stability improvement; thus, it is not further analyzed here. In addition to the voltage feedforward control, there are some other active damping methods for current-controlled VSCs, such as the damping injection method codesigned with the current controller proposed in Ref. [9]. This method relies on a discrete-domain modeling, thus is not further discussed in this chapter.

This book belongs to Kitab Liaison (ocd1996@gmail.com) Copyright Elsevier 2023

11.3 Stability and robustness improvement of outer-loop control

Fig. 11.19 shows the single-line representation of a three-phase grid-connected converter with converter-side current control and the outer-loop controls. The converter-side current loop control is the same as previous section, and the outer-loop controls include the PLL and the DVC. The BW of the outer-loop control is much slower than the inner-loop current control; thus, for the outer-loop control dynamic analysis, both the outer and inner loops should be modeled [3].

In the outer loop, the PLL controls the q-axis voltage for the phase detection, which can introduce negative damping in the q-axis dynamic for grid-connected converter operating as inverter [13]. The DVC loop generates the d-axis current reference, which can introduce a negative damping in d-axis dynamics when the grid-connected converter is operating as a rectifier [14]. This section derives the small-signal model of the PLL and the DVC loop first, then performs the stability analysis for these two loops. Finally, different ways to robustness enhancement are introduced.

11.3.1 Small-signal modeling

The small-signal models of the PLL and the DVC loops with the converter-side current control are derived, respectively, in this section.

Unlike the inner current control loop, both the PLL and DVC loops are asymmetrical in the dq frame, and hence the outer control loop cannot be simply modeled as an SISO system like the inner current control loop modeling. This asymmetrical system dynamic should be modeled as an MIMO model for stability analysis. The transfer function matrices and space vectors are utilized in this section, which are useful to represent the MIMO system dynamics [5].

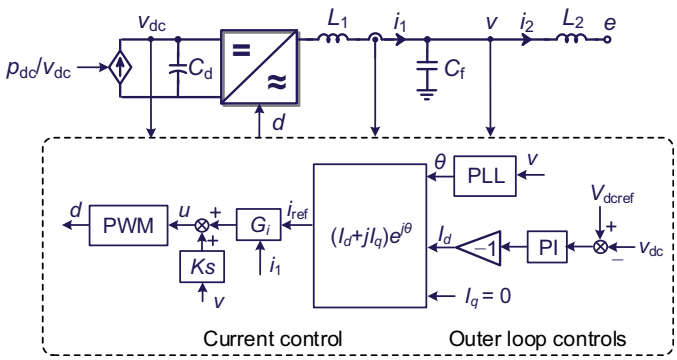

FIGURE 11.19 Single-line representation of a three-phase voltage source converter with converter-side current control and outer-loop controls.

This book belongs to Kitab Liaison (ocd1996@gmail.com)
Copyright Elsevier 2023

In this section, the italic letters are used to denote space vectors in the $\alpha\beta$ frame, e.g., $v = [v_\alpha, v_\beta]^T$ for the PoC voltage, and the corresponding complex space vectors are denoted by the bold letters. The transfer function matrices are denoted with an additional superscript "m." A subscript "dq" is added for space vectors and transfer functions in the dq frame. The small-signal variables are represented by the lowercases, and the uppercases denote the steady-state variables.

11.3.1.1 Linearization of the PLL

The synchronous reference frame PLL is shown in Fig. 11.20. The q-axis voltage is regulated by a PI controller $H_{\mathrm{PI}}(s)$ for the phase tracking [15].

The relationship between the $\alpha\beta$ frame and the dq frame PoC voltage is

$$(\boldsymbol{V} + \boldsymbol{v})e^{-j\omega_1 t} = \boldsymbol{V}_{dq} + \boldsymbol{v}_{dq}. \tag{11.22}$$

In steady state, the PoC voltage is aligned to the d-axis, so the steady-state dq frame voltage vector is $\boldsymbol{V}_{dq} = V_d + j0$.

According to Fig. 11.20, the voltage generated by the dq transformation in PLL is

$$\boldsymbol{V}_{PLLdq} + \boldsymbol{v}_{PLLdq} = (\boldsymbol{V} + \boldsymbol{v})e^{-j\theta} = (\boldsymbol{V}_{dq} + \boldsymbol{v}_{dq})e^{-j\Delta\theta} \approx (\boldsymbol{V}_{dq} + \boldsymbol{v}_{dq})(1 - j\Delta\theta). \tag{11.23}$$

From Eq. (11.23), it can be deduced that

$$V_{PLLq} = v_q - V_d\Delta\theta. \tag{11.24}$$

According to Fig. 11.20, the small signal of phase is given by

$$\Delta\theta = \frac{H_{PI}(s)}{s} V_{PLLq}. \tag{11.25}$$

Substituting Eq. (11.25) into Eq. (11.24), the small-signal transfer function from v_q to $\Delta\theta$ can be derived as

$$H_{PLL}(s) = \frac{H_{PI}(s)}{s + H_{PI}(s)V_d}. \tag{11.26}$$

The small-signal model of the PLL is thus shown in Fig. 11.21.

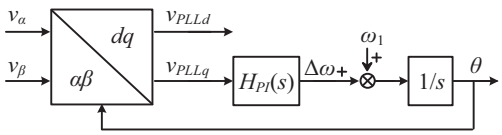

FIGURE 11.20 Block diagram of the synchronous reference frame phase-locked loop.

This book belongs to Kitab Liaison (ocd1996@gmail.com)
Copyright Elsevier 2023

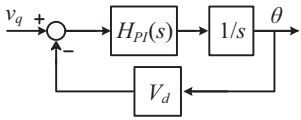

FIGURE 11.21 Block diagram of the small-signal model of the synchronous reference frame phase-locked loop.

11.3.1.2 Small-signal model of VSC with PLL

The control diagram of the grid-connected converter with current control loop and PLL is represented by Fig. 11.22 in the $\alpha\beta$ frame. The transfer functions in Fig. 11.5 should be represented by MIMO transfer function matrices, which are denoted with the additional superscript "m." The current reference in dq frame is transformed to the $\alpha\beta$ frame at the input of current control loop. With this dq transformation, the PLL effect will be introduced to the current reference signal.

According to Fig. 11.22, the current reference signal generated by the dq transformation is

$$\begin{aligned}\boldsymbol{I}_{\text{refcc}} + \boldsymbol{i}_{\text{refcc}} &= (\boldsymbol{I}_{\text{ref}dq} + \boldsymbol{i}_{\text{ref}dq})e^{j\theta} = (\boldsymbol{I}_{\text{ref}dq} + \boldsymbol{i}_{\text{ref}dq})e^{j(\omega_1 t + \Delta\theta)} \\ &\approx (\boldsymbol{I}_{\text{ref}dq} + \boldsymbol{i}_{\text{ref}dq})(1 + j\Delta\theta)e^{j\omega_1 t}.\end{aligned} \tag{11.27}$$

From Eq. (11.27), the current reference signal can be derived as

$$\boldsymbol{i}_{\text{refcc}dq} = \boldsymbol{i}_{\text{ref}dq} + j\Delta\theta \boldsymbol{I}_{\text{ref}dq}, \tag{11.28}$$

where $\boldsymbol{i}_{\text{refcc}dq}$ represents $\boldsymbol{i}_{\text{refcc}}$ in dq frame.

Substituting Eq. (11.27) into Eq. (11.28) leads to

$$\boldsymbol{i}_{\text{refcc}dq} = \boldsymbol{i}_{\text{ref}dq} + jH_{PLL}(s)\boldsymbol{I}_{\text{ref}dq}v_q. \tag{11.29}$$

From Eq. (11.29), it can be found that the q-axis small-signal voltage has influence on the d-axis and d-axis small-signal current reference, while the d-axis small-signal voltage makes no difference to the current reference.

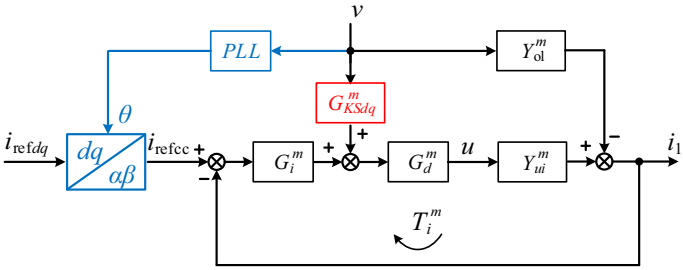

FIGURE 11.22 Block diagram of the voltage source inverter with current control and phase-locked loop (PLL).

This book belongs to Kitab Liaison (ocd1996@gmail.com) Copyright Elsevier 2023

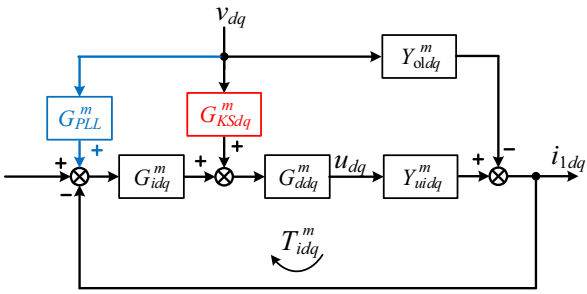

FIGURE 11.23 Small-signal model of current control with phase-locked loop effect.

This leads to an asymmetric transfer function matrix from the PoC voltage to the current reference in the dq frame as follows:

$$G^m_{PLL}(s) = \begin{bmatrix} 0 & -H_{PLL}(s)I_{\mathrm{ref}q} \\ 0 & H_{PLL}(s)I_{\mathrm{ref}d} \end{bmatrix}. \tag{11.30}$$

Fig. 11.23 illustrates the small-signal model of the current control with PLL effect in dq frame. The subscript "dq" means they are transformed to dq frame by the frequency translation $sI \rightarrow sI + J\omega_1$, where the I and J are the matrix forms of real unit 1 and imaginary unit j:

$$I = \begin{bmatrix} 1 & 0 \\ 0 & 1 \end{bmatrix}, \; J = \begin{bmatrix} 0 & -1 \\ 1 & 0 \end{bmatrix}. \tag{11.31}$$

For example, the PR controller elaborated in Eq. (11.8) can be represented by the dq frame transfer function matrix form as

$$G^m_{idq}(s) = K_{pi}I + \frac{K_{\mathrm{ri}}}{2s}I + \frac{K_{\mathrm{ri}}}{2}(sI + 2J\omega_1). \tag{11.32}$$

Combining the PLL with the current control, the equivalent closed-loop output admittance of the VSC, namely the closed-loop transfer function from v_{dq} to $-i_{1dq}$, can be derived as

$$Y^m_{PLL\&CC}(s) = Y^m_{PLL}(s) + Y^m_{odq}(s) = -G^m_{cldq}(s)G^m_{PLL}(s) + Y^m_{odq}(s), \tag{11.33}$$

where $Y^m_{odq}(s)$ is the matrix form of closed-loop output admittance of the current control, which is represented by Eq. (11.19), in dq frame, and $G^m_{cldq}(s)$ is the closed-loop transfer function matrix of the current control in dq frame.

11.3.1.3 Linearization of the DC-link voltage control

In Fig. 11.19, an active load or source p_{dc} (p_{dc} is positive if generating power in DC side, and is negative if consuming power) is applied to the DC side of the grid-connected converter. According to the power balance rule, the

This book belongs to Kitab Liaison (ocd1996@gmail.com) Copyright Elsevier 2023

instantaneous power output from the DC side should be equal to the power output from the AC side [8,16]. This power balance relationship can be expressed as

$$p_{\mathrm{dc}} - \frac{1}{2}C_d\frac{dv_{\mathrm{dc}}^2}{dt} = p = v_{dq}^T i_{1dq} + R_{L1}\left(i_{1d}^2 + i_{1q}^2\right) + \frac{1}{2}L_1\frac{d\left(i_{1d}^2 + i_{1q}^2\right)}{dt}, \quad (11.34)$$

where p is the instantaneous active power.

It is worth mentioning that although the filter inductor does not consume the active power, but the instantaneous active power will flow into or out from the filter inductor, which will influence the dynamic of the system. Thus, the power dynamic of the filter inductor should be included in p, which is represented by the third term of Eq. (11.34). The first and second terms of Eq. (11.34) represent the output power and the power dissipated in the equivalent series resistor (ESR) of the filter inductor. Since the ESR is usually very small, it can be neglected for system modeling.

Linearizing Eq. (11.34) yields

$$p_{\mathrm{dc}} - sC_dV_{\mathrm{dc}}v_{\mathrm{dc}} = V_{dq}^T i_{1dq} + I_{1dq}^T v_{dq} + \left(2R_{L1}I_{1dq}^T + sL_1I_{1dq}^T\right)i_{1dq}. \quad (11.35)$$

From the Eq. (11.34), the small-signal model of the DVC loop can be derived, as shown in Fig. 11.24.

In the small-signal model, the transfer functions of the DC-side plant and DC controller are

$$G_{\mathrm{dc}p}(s) = \frac{1}{sC_dV_{\mathrm{dc}}}, \quad (11.36)$$

$$G_{\mathrm{dc}c}^m(s) = \begin{bmatrix} G_{\mathrm{dc}cd}(s) \\ 0 \end{bmatrix} = \begin{bmatrix} K_{pv} + K_{iv}\dfrac{1}{s} \\ 0 \end{bmatrix}. \quad (11.37)$$

It is supposed that both the d-axis and q-axis current references are provided by the DC-link voltage controller $G_{\mathrm{dc}c}^m(s)$, but the q-axis channel of $G_{\mathrm{dc}c}^m(s)$ is set to zero, so the q-axis current reference is actually not under the control of DC-link voltage controller. This two-by-one matrix form of DC-link voltage

Controller can directly multiply by the inner current control close-loop gain, which is a two-by-two symmetrical transfer function matrix in dq frame.

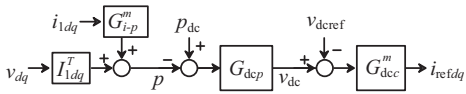

FIGURE 11.24 Block diagram of the small-signal model of the DC-link voltage control loop.

This book belongs to Kitab Liaison (ocd1996@gmail.com) Copyright Elsevier 2023

Then, according to Eq. (11.35), the transfer function from the output current to the AC-side power is

$$G_{i-p}^{m}(s) = V_{dq}^{T} + 2R_{L1}I_{1dq}^{T} + sL_1 I_{1dq}^{T}, \tag{11.38}$$

which is a one-by-two matrix.

Eq. (11.34) elaborate the power balance relationship between AC side and DC side with DC-side active power load or source. The similar methodology can be applied to other kinds of loads, such as passive load, constant current load, or source shown in Fig. 11.25. The change of DC-side plant will only change the expression of $G_{\mathrm{dc}p}(s)$. The AC-side linearization model will remain unchanged.

In the system with DC-side passive power load shown in Fig. 11.25A, the power balance relationship can be expressed as

$$-p_{Rd} - \frac{1}{2}C_d\frac{dv_{\mathrm{dc}}^2}{dt} = p, \tag{11.39}$$

$$p_{Rd} = \frac{v_{\mathrm{dc}}^2}{R_d}. \tag{11.40}$$

In the small-signal model, the transfer function of DC-side plant with the passive power load can be derived by linearizing Eqs. (11.39) and (11.40), which gives rise to

$$G_{\mathrm{dc}p}(s) = \frac{1}{(2R_d + sC_d)V_{\mathrm{dc}}}, \tag{11.41}$$

Similarly, the transfer function of DC-side plant with constant current source or load shown in Fig. 11.25B is

$$G_{\mathrm{dc}p}(s) = \frac{1}{(I_{\mathrm{dc}} + sC_d)V_{\mathrm{dc}}}, \tag{11.42}$$

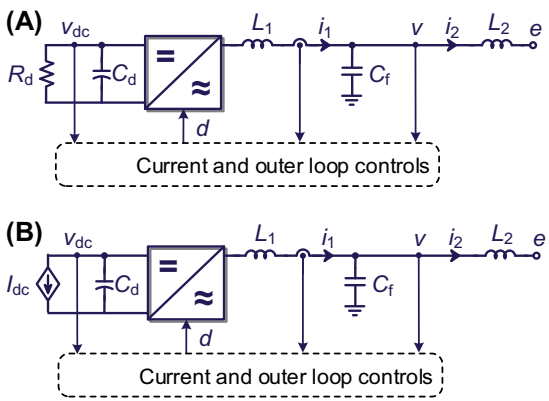

FIGURE 11.25 Single-line representation of a three-phase voltage source converter. (A) Passive load in DC side; (B) Constant current source or load in DC side.

This book belongs to Kitab Liaison (ocd1996@gmail.com) Copyright Elsevier 2023

11.3.1.4 Small-signal model of VSC with DC-link voltage control loop

The control diagram of VSC with current control loop, PLL, and the DVC loop is represented by Fig. 11.26. The equivalent output admittance impacted by the current control and PLL is illustrated as $Y^m_{odq}(s)$ and $Y^m_{\mathrm{PLL}}(s)$ in Fig. 11.26. Their expressions are derived by Eqs. (11.19) and (11.33).

From Fig. 11.26, it can be found that the equivalent output admittance introduced by the current control and PLL control is reshaped by the outer DVC loop. In addition, it can be seen that the DVC introduces a new equivalent output admittance through the steady-state output current I^T_{1dq}.

According Fig. 11.26, the open-loop gain of the DVC loop can be given by

$$T^m_{\mathrm{dc}}(s) = G^m_{cl}(s)G^m_{\mathrm{dc}c}(s)G_{\mathrm{dc}p}(s)G^m_{i-p}(s), \tag{11.43}$$

which is a two-by-two matrix.

The overall output admittance, namely the close-loop transfer function from v_{dq} to $-i_{1dq}$, can be derived as

$$Y^m_{\mathrm{dc\ \&\ PLL\&CC}}(s) = Y^m_{\mathrm{dc}}(s) + Y^m_{\mathrm{PLLdc}}(s) + Y^m_{o\mathrm{dc}}(s), \tag{11.44}$$

where

$$\begin{aligned} Y^m_{\mathrm{dc}}(s) &= \left[I + T^m_{\mathrm{dc}}(s)\right]^{-1} Y^m_{\mathrm{dc0}}(s) = \left[I + T^m_{\mathrm{dc}}(s)\right]^{-1} G^m_{cl}(s)G^m_{\mathrm{dc}c}(s)G_{\mathrm{dc}p}(s)I^T_{1dq} \\ Y^m_{\mathrm{PLLdc}}(s) &= \left[I + T^m_{\mathrm{dc}}(s)\right]^{-1} Y^m_{\mathrm{PLL}}(s) \\ Y^m_{o\mathrm{dc}}(s) &= \left[I + T^m_{\mathrm{dc}}(s)\right]^{-1} Y^m_{odq}(s). \end{aligned} \tag{11.45}$$

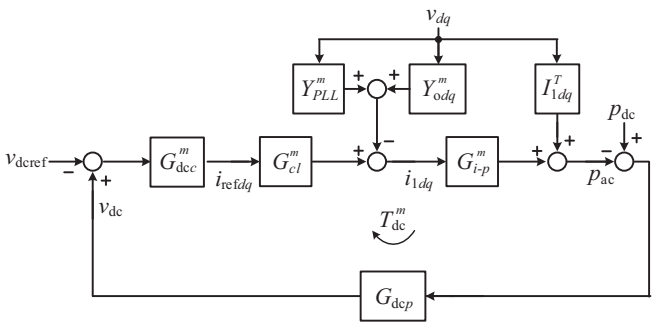

FIGURE 11.26 Block diagram of the voltage source inverter with current control, phase-locked loop control, and DC-link voltage control.

This book belongs to Kitab Liaison (ocd1996@gmail.com) Copyright Elsevier 2023

The $Y^m_{\mathrm{PLLdc}}(s)$ and $Y^m_{o\mathrm{dc}}(s)$ are the reshaped equivalent output admittances introduced by the PLL control loop and converter-side current control loop. $Y^m_{\mathrm{dc}}(s)$ is the new equivalent output admittance introduced by the outer DVC loop. They are all two-by-two matrices.

It is worth mentioning that the coupling between the v_{dc} and duty cycle d is not considered in this modeling method because the v_{dc} is assumed to be canceled by the normalization as shown in Fig. 11.4. However, the normalization variable is a constant in this case and cannot cancel the dynamic of v_{dc}, which will cause a complex coupling between the DVC loop and current control loop. The real-time DC-link voltage sampled for normalization will alleviate this coupling effect, but due to the control and sensor delay, the dynamic of v_{dc} cannot be fully eliminated in the real system. A more precise model based on switching function can be used to model the coupling effect [17].

11.3.2 MIMO-based stability analysis

For a VSC with PLL and DVC loop, the control is asymmetrical in the dq frame. In this situation, the impedance-based method can also be applied to analyze the stability. The VSC system can be represented by an equivalent output admittance matrix, and the MIMO-based dynamic analysis tool, such as generalized Nyquist stability criterion [18], can be applied to evaluate the system stability. Table 11.2 provides the VSC circuit and control system parameters that are used in the following analysis.

11.3.2.1 Dynamic impact of PLL

From the Eq. (11.33), it can be found that the equivalent closed-loop output admittance of the VSC with PLL and current control loop can be derived as two admittances in parallel, namely $Y^m_{\mathrm{PLL}}(s) + Y^m_{odq}(s)$. One admittance is the closed-loop output admittance of the current control, namely $Y^m_{odq}(s)$, which has been analyzed in the previous section. The other is the closed-loop output admittance caused by the PLL, which is defined as $Y^m_{\mathrm{PLL}}(s)$. The equivalent circuit of the grid-connected converter with converter-side current control and PLL control in dq frame is shown in Fig. 11.27.

Since the $d-d$ channel and $q-d$ channel in Eq. (11.30) are zero, the $d-d$ channel and $q-d$ channel of $Y_{\mathrm{PLL}}(s)$ will also be zero, which leads to

$$Y^m_{PLL}(s) = \begin{bmatrix} 0 & Y_{PLLdq}(s) \\ 0 & Y_{PLLqq}(s) \end{bmatrix}, \tag{11.46}$$

Fig. 11.28 illustrates the $d-q$ channel and $q-q$ channel plot of the $Y^m_{\mathrm{PLL}}(s)$ when the VSC works in the inverter mode. The BW of current control loop is set as 700 Hz. It can be seen that when the BW of PLL increases, the region with negative real part of $q-q$ channel will be expanded to the higher

This book belongs to Kitab Liaison (ocd1996@gmail.com) Copyright Elsevier 2023

TABLE 11.2 Circuit and control parameters of the grid-connected converter.

Parameter	Symbol	Value	Parameter	Symbol	Value
Grid voltage	V_g	380 V_{RMS}	Grid frequency	f_1	50 Hz
DC-link voltage	V_{dc}	650 V	Power rating in inverter mode/ rectifier mode	P_0	2 kW/−2 kW
Grid inductor (ESR)	L_g (R_g)	10 mH (0.1 Ω)	Converter-side inductor (ESR)	L_1 (R_{L1})	2.2 mH (0.1 Ω)
Filter capacitor	C_f	10 μF	Converter-side inductor (ESR)	L_2 (R_{L2})	1 mH (0.1 Ω)
Switching frequency	f_{sw}	10 kHz	Sampling frequency/ period	f_s/T_s	10 kHz/ 100 μs
P gain of converter-side current control	K_{pi}	9.7 Ω	R gain of converter-side current control	K_{pr}	4255 Ω/s
P gain of PLL controller with BW = 260 Hz	K_{pPLL}	3.2 rad/ (s·V)	I gain of PLL controller	K_{iPLL}	1973 rad/(s^2·V)
P gain of DC-link voltage controller with BW = 200 Hz	K_{pdc}	2.1/Ω	P gain of DC-link voltage controller	K_{idc}	540/(s·Ω)

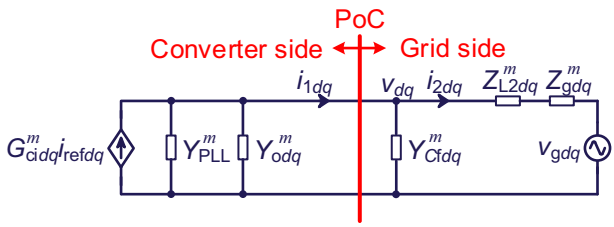

FIGURE 11.27 Equivalent circuit of the grid-connected converter with converter-side current control and phase-locked loop control in *dq* frame.

This book belongs to Kitab Liaison (ocd1996@gmail.com)
Copyright Elsevier 2023

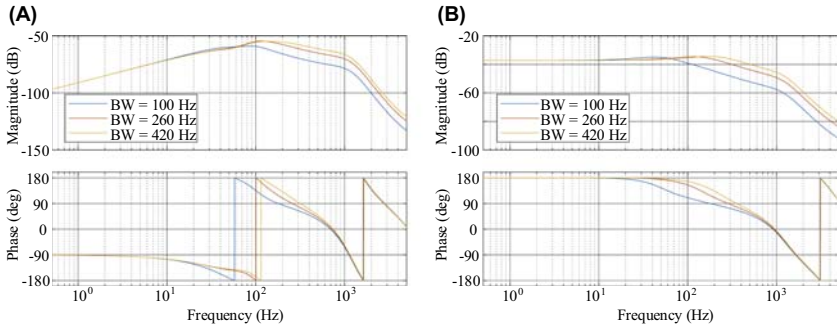

FIGURE 11.28 Equivalent output admittance of voltage source converter caused by the phase-locked loop effect. (A) $d-q$ channel plot; (B) $q-q$ channel plot.

frequency range, which may cause instability with the interaction with grid impedance and the equivalent output admittance of the current control loop.

The negative real part region in the $q-q$ channel admittance can be explained by Fig. 11.29. In the steady state, the PLL dq frame aligns with the constant speed dq frame. Suppose that the closed-loop gain of current control is 1 (current control loop has relative high BW), then the d-axis output current i_{1d} is overlapped with $i_{\mathrm{ref}d}$, as shown in Fig. 11.29A. If v_q increases, then according to Eq. (11.26), $\Delta\theta$ will also increase. This causes the PLL dq frame to lead the constant speed dq frame, and $i_{\mathrm{ref}d}$, which rotates with PLL dq frame, will introduce a projection i_{1q} in the q-axis of constant speed dq frame as shown in Fig. 11.29B. If the converter works on the inverter mode, $i_{\mathrm{ref}d}$ should be positive. And then, the output q-axis current i_{1q} is positive. Therefore, the converter behaves like a negative resistor in the $q-q$ channel.

Compared with the $q-q$ channel admittance, the $d-q$ channel admittance is relatively small in this case. The $d-q$ channel admittance is introduced by the interaction between the dynamic of PLL and current control loop. Both the $d-q$ and $q-q$ channel admittances should be taken into consideration for stability analysis in most of the cases.

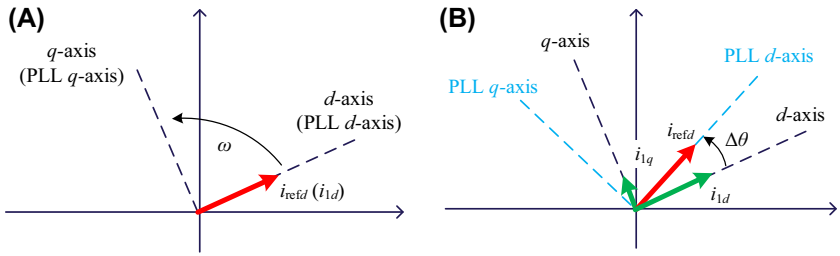

FIGURE 11.29 Vector diagram of output current. (A) Steady state; (B) v_q increase.

This book belongs to Kitab Liaison (ocd1996@gmail.com)
Copyright Elsevier 2023

The impedance-based method can be applied to study the stability of this MIMO system in the *dq* frame [19]. According to Fig. 11.24, the impedance ratio between the equivalent output admittance of the grid-connected converter and the grid impedance is expressed as

$$T^m_{PLL\&Grid}(s) = \left[Z^m_{L2dq}(s) + Z^m_{gdq}(s)\right]\left[Y^m_{PLL}(s) + Y^m_{odq}(s) + Y^m_{Cfdq}(s)\right]. \quad (11.47)$$

According to the generalized Nyquist criterion [18], the impedance ratio T^m can be used to predict the overall system stability. For this MIMO transfer function matrix, the frequency responses of the eigenvalues can be derived by

$$\det\left[\lambda I - T^m_{PLL\ \&\ Grid}\right] = 0. \quad (11.48)$$

Based on the same circuit parameters in Table 11.1, the PLL is designed with control BW of 100 Hz, 260, and 420 Hz to compare the influence of PLL BW. The Bode diagrams of the eigenvalues of the impedance ratio T^m are shown in Fig. 11.26. In Fig. 11.30A, when the magnitudes of the two eigenvalues are smaller than 0 dB at the phase crossing over frequency of −180 degrees, the system is stable. In Fig. 11.30B, when the phase crosses

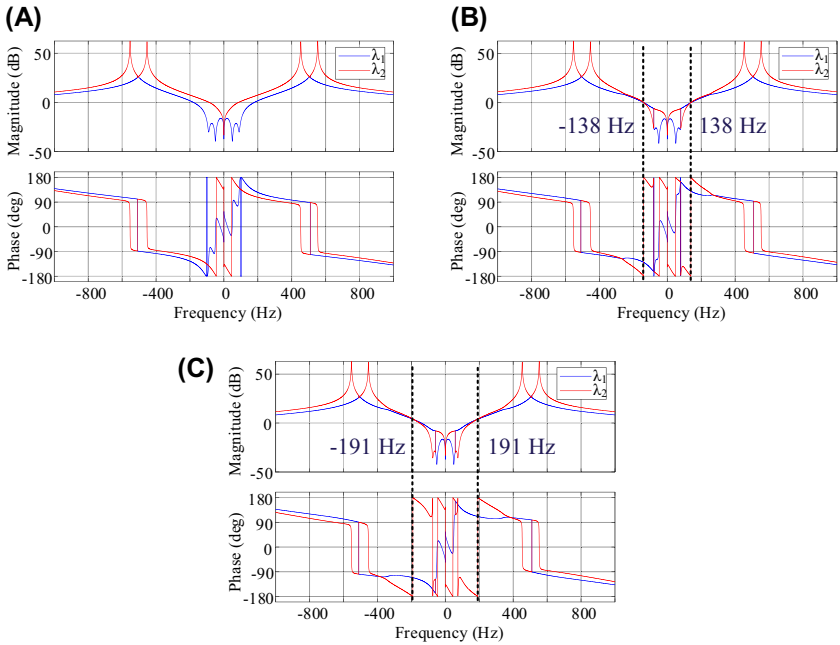

FIGURE 11.30 Frequency response of the eigenvalues in the inverter mode. (A) PLL BW = 100 Hz; (B) PLL BW = 260 Hz; (C) PLL BW = 420 Hz. *BW*, bandwidth; *PLL*, phase-locked loop.

This book belongs to Kitab Liaison (ocd1996@gmail.com)
Copyright Elsevier 2023

over −180 degrees, the magnitude is 0.12 dB, slightly larger than 0 dB. It means the system is critically unstable. In Fig. 11.30C, the magnitude is 4 dB at the frequency where the phase crosses over −180 degrees, which means the system is unstable.

The simulation result for the grid-connected converter with the converter-side current control and PLL is provided in Fig. 11.31. When the converter is connected, an oscillation at the frequency of 138 Hz can be observed in the *dq* frame PoC voltage waveform, which agrees with the stability analysis provided in Fig. 11.30B.

11.3.2.2 Dynamic impact of DVC

In Eq. (11.38), with unity power factor, the steady-state *q*-axis voltage and current are equal to zero, so the transfer function from the output current to AC-side power can be simplified to

$$G_{i-p}^{m}(s) = [\,G_{i-pd}(s) \quad 0\,] = [\,V_d + (2R_{L1} + sL_1)I_{1d} \quad 0\,]. \tag{11.49}$$

Substituting Eqs. (11.36), (11.37), and (11.49) into Eq. (11.43), the open-loop gain of the DVC loop can be derived as

$$T_{\mathrm{dc}}^{m}(s) = \begin{bmatrix} T_{\mathrm{dc}dd}(s) & 0 \\ T_{\mathrm{dc}qd}(s) & 0 \end{bmatrix} = \begin{bmatrix} G_{cldd}(s)G_{\mathrm{dc}cd}(s)G_{\mathrm{dc}p}(s)G_{i-pd}(s) & 0 \\ G_{clqd}(s)G_{\mathrm{dc}cd}(s)G_{\mathrm{dc}p}(s)G_{i-pd}(s) & 0 \end{bmatrix}, \tag{11.50}$$

where the $G_{cldd}(s)$ and $G_{clqd}(s)$ are the d−d channel and q−d channel of the current control closed-loop transfer function matrix $G_{cl}^{m}(s)$.

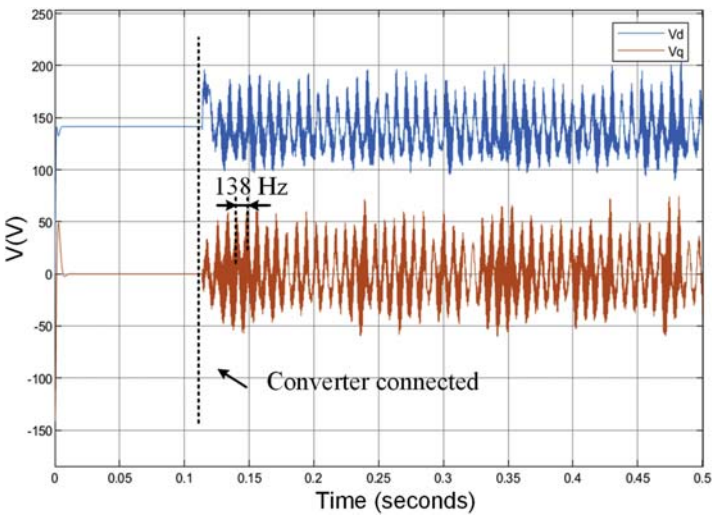

FIGURE 11.31 Simulation result of the grid-connected converter when PLL BW = 260 Hz. *BW*, bandwidth; *PLL*, phase-locked loop.

This book belongs to Kitab Liaison (ocd1996@gmail.com)
Copyright Elsevier 2023

From Eq. (11.50), it can be seen that although the DVC only generates the d-axis current reference for the inner current control loop, meanwhile, it will influence the q-axis current dynamic due to the nonzero $q-d$ channel of $G_{cl}^{m}(s)$. Similarly, the outer DVC loop will reshape all the channels of $Y_{\mathrm{PLL}}^{m}(s)$ and $Y_{odq}^{m}(s)$, but not only the $d-d$ channel.

In Eq. (11.44), the equivalent closed-loop output admittance of the grid-connected converter with converter-side current control, PLL control, and DVC can be derived as three admittances in parallel, namely $Y_{\mathrm{dc}}^{m}(s) + Y_{\mathrm{PLLdc}}^{m}(s) + Y_{o\mathrm{dc}}^{m}(s)$. The equivalent circuit is shown in Fig. 11.32.

Fig. 11.33 illustrates Bode plot of equivalent admittance when the VSC works in the rectifier mode. To minimize the influence of PLL, the BW of PLL is set to 5 Hz, which is much smaller that the DVC BW, and the current control loop BW is 700 Hz. It can be seen that the DVC loop has a great influence to the $d-d$ channel equivalent admittance with different BW.

The negative real part region in the $d-d$ channel is caused by the constant power load effect in the rectifier mode. When the converter consumes constant active power, an increase in d-axis PoC voltage will cause a decrease in input d-axis current and vice versa. Thus, the converter behaves like a negative resistor in $d-d$ channel and the phase of $d-d$ channel equivalent admittance is 180° at low frequency. Meanwhile, the other channels are also reshaped slightly by the DC-link loop.

According to Fig. 11.32, the impedance ratio between the equivalent output admittance of the grid-connected converter and the grid impedance is expressed as

$$T_{\mathrm{dc\ \&\ Grid}}^{m}(s) = \left[Z_{L2dq}^{m}(s) + Z_{gdq}^{m}(s)\right]\left[Y_{\mathrm{dc}}^{m}(s) + Y_{\mathrm{PLLdc}}^{m}(s) + Y_{o\mathrm{dc}}^{m}(s) + Y_{Cfdq}^{m}(s)\right], \tag{11.51}$$

Based on the same circuit parameters in Table 11.1, the DVC loop is designed with control BW of 100, 200, and 300 Hz to compare the influence of DVC loop BW.

The Bode diagrams of the eigenvalues of the impedance ratio T^{m} are shown in Fig. 11.34. In Fig. 11.34A, when the phase of the two eigenvalues crosses

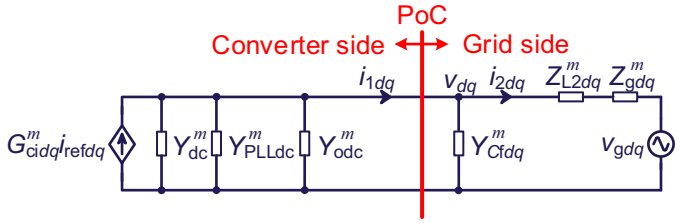

FIGURE 11.32 Equivalent circuit of the grid-connected converter with converter-side current control, phase-locked loop control, and DC-link voltage control in dq frame.

This book belongs to Kitab Liaison (ocd1996@gmail.com)
Copyright Elsevier 2023

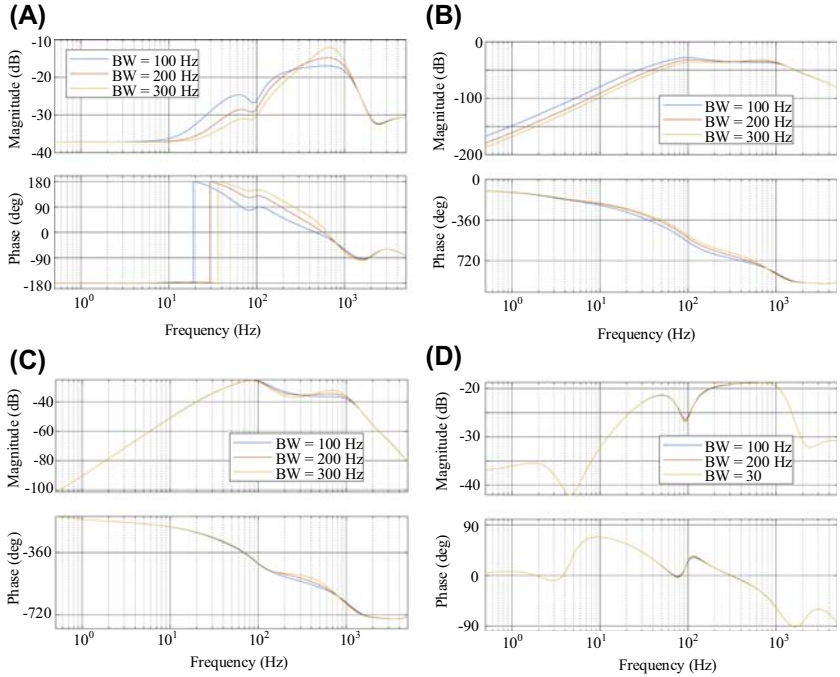

FIGURE 11.33 Equivalent output admittance of voltage source converter caused by the phase-locked loop effect and DC-link voltage loop. (A) $d-d$ channel plot; (B) $d-q$ channel plot; (C) $q-d$ channel plot; (D) $q-q$ channel plot.

over -180 degrees, the magnitude is smaller than 0 dB, which means the system is stable. In Fig. 11.34B, when the phase crosses over -180 degrees, the magnitude is 0.11 dB, slightly larger than 0 dB. It means the system is critically unstable. In Fig. 11.34C, the magnitude is 7 dB when the phase crosses over -180 degrees, which means the system is unstable.

The simulation result for the grid-connected converter with the converter-side current control, PLL control loop, and DVC loop is provided in Fig. 11.35. When the converter is connected, an oscillation at the frequency of 173 Hz can be observed in the d-axis current reference waveform, which closely agrees with the stability analysis provided in Fig. 11.34B.

11.3.3 Robustness enhancement

Based on the admittance analysis, the stability of PLL and DVC loop is mainly affected by their $q-q$ and $d-d$ channel profiles, respectively. The stability of the PLL and DVC loop can be improved by reducing the frequency range with negative real part in these channels.

This book belongs to Kitab Liaison (ocd1996@gmail.com) Copyright Elsevier 2023

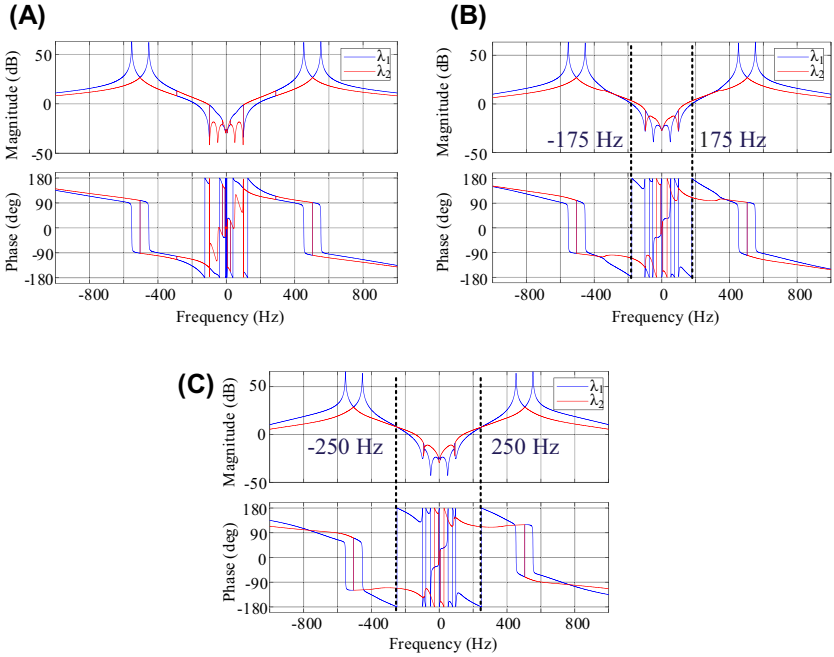

FIGURE 11.34 Frequency response of the eigenvalues in the rectifier mode. (A) DVC BW = 100 Hz; (B) DVC PLL BW = 200 Hz; (C) DVC BW = 300 Hz. *BW*, bandwidth; *DVC*, DC-link voltage control.

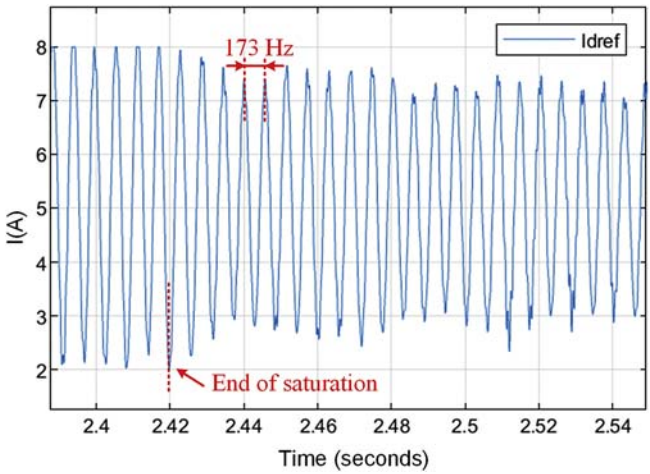

FIGURE 11.35 Simulation result of the grid-connected converter when DVC BW = 200 Hz. *BW*, bandwidth; *DVC*, DC-link voltage control.

This book belongs to Kitab Liaison (ocd1996@gmail.com)
Copyright Elsevier 2023

11.3.3.1 PLL design

For the PLL control, it has been found that the negative real part region of the $Y^m_{\mathrm{PLL}}(s)$ locates within the low frequency range of the $q-q$ channel admittance, which is mainly dependent on the BW of the PLL. To improve the converter stability, the most effective way is to reduce the BW of the PLL. With this method, the range with negative real part can be reduced.

Fig. 11.36 show the poles of the equivalent admittance seen from the grid, namely

$$Y^m_{\mathrm{eqg}} = \left(Y^m_{PLL} + Y^m_{odq} + Y^m_{\mathrm{C}fdq}\right)\left[I + T^m_{PLL\ \&\ Grid}(s)\right]^{-1}. \tag{11.52}$$

From Fig. 11.36, it can be seen that a pair of poles, which locates along the red (dark gray in printed version) arrow, will move to the right half plane when the BW of PLL increases and leads to the instability issue. In Fig. 11.37, it is shown that the same pair of poles will move to the right half plane with low SCR. The instability is more sensitive to the variation of SCR, which means that weak grid condition can significantly degrade the synchronization stability of PLL. To keep the system stable, this pair of poles should be set away from the imaginary axis in the left half plane. A low BW should be chosen for a grid-connected converter working in a low-SCR condition.

11.3.3.2 DVC design

For the DVC, it has been found that the negative real part region of the output admittance locates within the low frequency range of the $d-d$ channel plot in

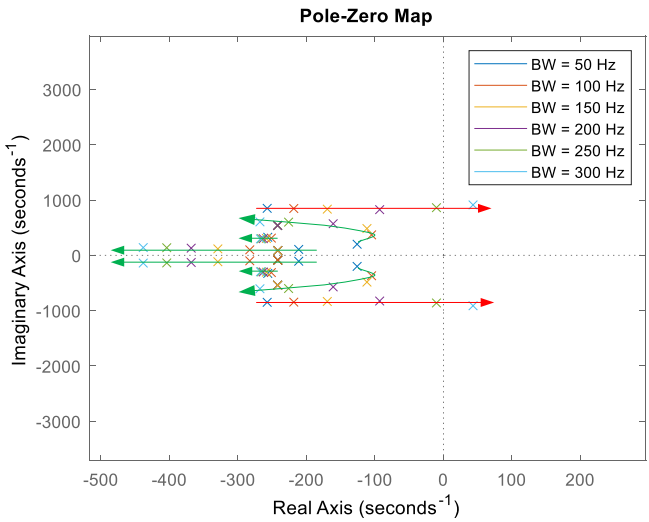

FIGURE 11.36 Poles of the Y^m_{eqg} with the change of phase-locked loop bandwidth (SCR = 9).

This book belongs to Kitab Liaison (ocd1996@gmail.com)
Copyright Elsevier 2023

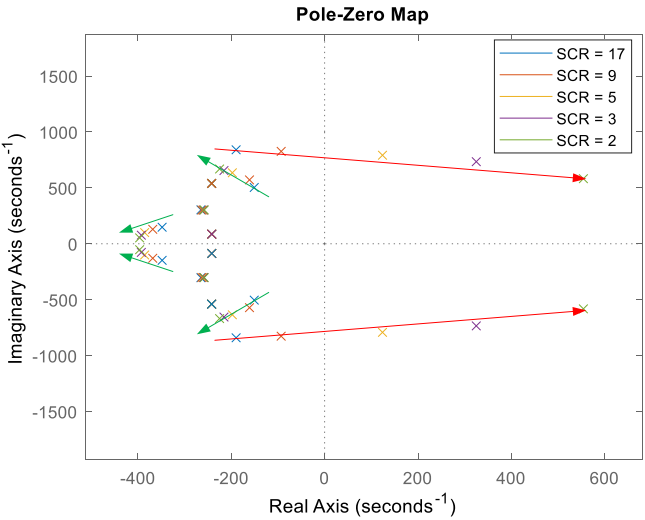

FIGURE 11.37 Poles of the Y_{eqg}^{m} with the change of short circuit ratio (phase-locked loop bandwidth = 200 Hz).

Fig. 11.33, when the converter is working in rectifier mode. Like the PLL control, the negative real part region in $d-d$ channel admittance is related to the BW of DVC. A lower BW will cause a smaller negative real part region, which can lead to a larger stability margin. Fig. 11.38 shows the poles of the

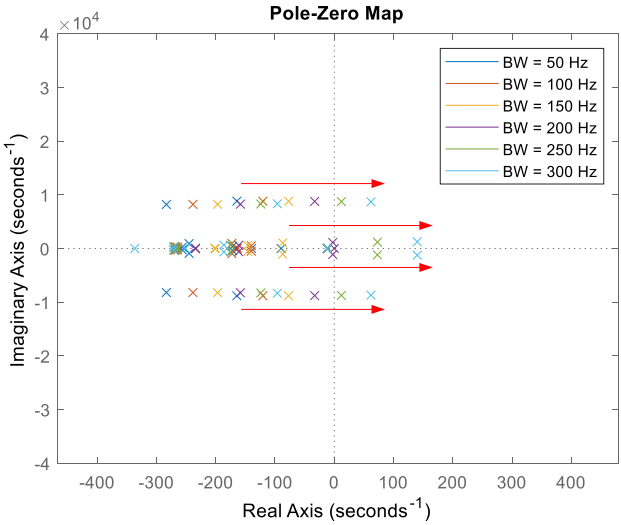

FIGURE 11.38 Poles of the Y_{eqg}^{m} with the change of DC-link voltage control bandwidth.

This book belongs to Kitab Liaison (ocd1996@gmail.com) Copyright Elsevier 2023

equivalent admittance seen from the grid in Eq. (11.52); it can be seen that all poles will move to the right half plane when the BW of DVC increases with values specified in Fig. 11.38.

References

[1] F. Blaabjerg, R. Teodorescu, M. Liserre, A.V. Timbus, Overview of control and grid synchronization for distributed power generation systems, IEEE Trans. Ind. Electron. 53 (5) (October 2006) 1398−1409.

[2] D.G. Holmes, T.A. Lipo, B.P. McGrath, W.Y. Kong, Optimized design of stationary frame three phase AC current regulators, IEEE Trans. Power Electron. 24 (11) (November 2009) 2417−2426.

[3] X. Wang, F. Blaabjerg, Harmonic stability in power electronic-based power systems: concept, modeling, and analysis, IEEE Trans. Smart Grid 10 (3) (May 2019) 2858−2870.

[4] S.R. Sanders, J.M. Noworolski, X.Z. Liu, G.C. Verghese, Generalized averaging method for power conversion circuits, IEEE Trans. Power Electron. 6 (2) (April 1991) 251−259.

[5] L. Harnefors, Modeling of three-phase dynamic systems using complex transfer functions and transfer matrices, IEEE Trans. Ind. Electron. 54 (4) (August 2007) 2239−2248.

[6] S. Buso, P. Mattavelli, Digital Control in Power Electronics, Morgan & Claypool, 2015.

[7] Y. Liao, X. Wang, Impedance-based stability analysis for interconnected converter systems with open-loop RHP poles, IEEE Trans. Power Electron. 35 (4) (April 2020) 4388−4397.

[8] L. Harnefors, X. Wang, A.G. Yepes, F. Blaabjerg, Passivity-based stability assessment of grid-connected VSCs—an overview, IEEE J. Emerg. & Sel. Top. Power Electron. 4 (1) (March 2016) 116−125.

[9] X. Wang, F. Blaabjerg, P.C. Loh, Passivity-based stability analysis and damping injection for multiparalleled VSCs with LCL filters, IEEE Trans. Power Electron. 32 (11) (November 2017) 8922−8935.

[10] D. Yang, X. Ruan, H. Wu, A real-time computation method with dual sampling mode to improve the current control performance of the LCL-type grid-connected inverter, IEEE Trans. Ind. Electron. 62 (7) (July 2015) 4563−4572.

[11] L. Harnefors, A.G. Yepes, A. Vidal, J. Doval-Gandoy, Passivity-based controller design of grid-connected VSCs for prevention of electrical resonance instability, IEEE Trans. Ind. Electron. 62 (2) (February 2015) 702−710.

[12] H. Wu, X. Wang, Virtual-flux-based passivation of current control for grid-connected VSCs, IEEE Trans. Power Electron. 35 (12) (May. 2020) 12673−12677, https://doi.org/10.1109/TPEL.2020.2997876.

[13] X. Wang, L. Harnefors, F. Blaabjerg, Unified impedance model of grid-connected voltage-source converters, IEEE Trans. Power Electron. 33 (2) (February 2018) 1775−1787.

[14] N. Bottrell, M. Prodanovic, T.C. Green, Dynamic stability of a microgrid with an active load, IEEE Trans. Power Electron. 28 (11) (November 2013) 5107−5119.

[15] S.-K. Chung, A phase tracking system for three phase utility interface inverters, IEEE Trans. Power Electron. 15 (3) (May 2000) 431−438.

[16] D. Lu, X. Wang, F. Blaabjerg, Impedance-based analysis of DC-link voltage dynamics in voltage-source converters, IEEE Trans. Power Electron. 34 (4) (April 2019) 3973−3985.

This book belongs to Kitab Liaison (ocd1996@gmail.com) Copyright Elsevier 2023

[17] Y. Liao, Z. Liu, H. Zhang, B. Wen, Low-frequency stability analysis of single-phase system with dq-frame impedance approach—part I: impedance modeling and verification, IEEE Trans. Ind. Appl. 54 (5) (September-October 2018) 4999–5011.

[18] A.G.J. MacFarlane, Return-difference and return-ratio matrices and their use in analysis and design of multivariable feedback control systems, in: Proceedings of the Institution of Electrical Engineers, vol. 117, October 1970, pp. 2037–2049, 10.

[19] B. Wen, D. Boroyevich, R. Burgos, P. Mattavelli, Z. Shen, Small-signal stability analysis of three-phase AC systems in the presence of constant power loads based on measured d-q frame impedances, IEEE Trans. Power Electron. 30 (10) (October 2015) 5952–5963.

This book belongs to Kitab Liaison (ocd1996@gmail.com) Copyright Elsevier 2023

This page intentionally left blank

This book belongs to Kitab Liaison (ocd1996@gmail.com)

Copyright Elsevier 2023

Chapter 12

High switching frequency three-phase current-source converters and their control

Dapeng Lu, Frede Blaabjerg
Department of Energy Technology, Aalborg University, Aalborg, Denmark

Current-source converters (CSCs) are widely used in the high-power AC motor drive systems as cost-effective solutions. Moreover, with recent advances in power semiconductor devices, high switching frequency CSCs are increasingly interesting for improving the power efficiency and power density in many new applications, including photovoltaic systems [1,2], wind power generation systems [3,4], data center power supplies [5,6], solid-state transformers [7,8], harmonics suppression [9,10], and on-board EV chargers [11]. Equipment of single-stage buck rectifiers and boost inverters, reduced electromagnetic interference, inherent short circuit protection, and high reliability contribute to the potential of using CSCs in these new applications. However, only a few works have been devoted to the stability analysis and control of the high switching frequency CSCs.

12.1 Challenges of high switching frequency CSCs control

To meet the requirements of low grid current harmonics and constant DC-link current, an *LC*-type filter is employed in the AC side and an inductor is used in the DC-link, which is the same with high-power CSCs. However, by increasing the switching frequency, the value of the passive filters can be significantly reduced, which leads to a different dynamic analysis and design of the control system.

12.1.1 Multiple timescale dynamics of high switching frequency CSCs

Generally, the control system consists of the DC-link current control for achieving constant DC-link, the grid synchronization control for obtaining the

Control of Power Electronic Converters and Systems. https://doi.org/10.1016/B978-0-12-819432-4.00014-7
Copyright © 2021 Elsevier Ltd. All rights reserved.

This book belongs to Kitab Liaison (ocd1996@gmail.com)
Copyright Elsevier 2023

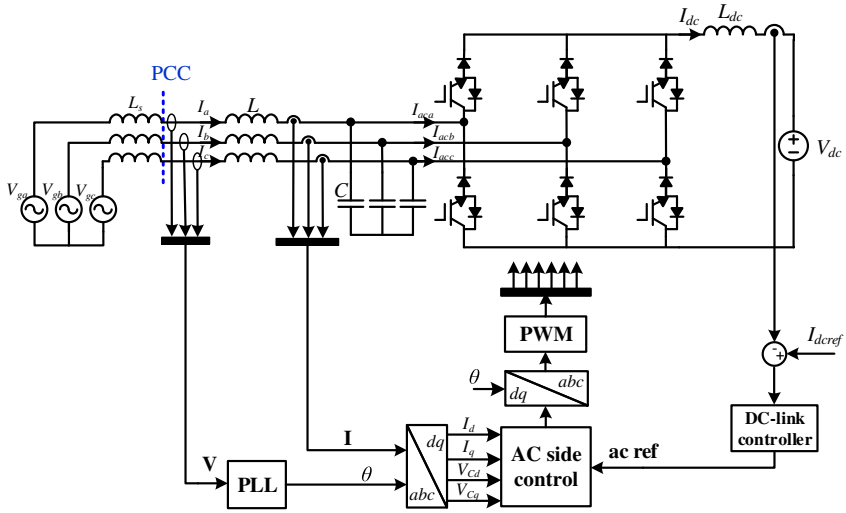

FIGURE 12.1 Control system implementation of the current source controller in the *dq* frame.

grid phase and frequency, and the inner loop aiming to obtain a low-distorted grid current with a fast-transient response, which are shown in Fig. 12.1. Furthermore, the three control loops have different timescale dynamics according to their bandwidths, e.g., 100 ms for DC-link control, 10 ms for the grid synchronization, and 1 ms for the inner loop in a 10 kHz switching frequency grid-connected converter. The dynamic impact of the grid synchronization can be neglected under a stiff grid condition [12]. In high-power CSCs, the dynamics of the AC side and the DC-link are considered independent, where the dynamic impact of DC-link is ignored by assuming a constant DC-link current due to a large DC-link inductor L_{dc}. However, as mentioned before, the DC-link inductor can be reduced significantly in high switching frequency CSCs, which may cause interactions between the AC-side control and DC-link current control. Consequently, modeling of the high switching frequency CSCs with involving both the AC side and the DC-link is a challenge.

12.1.2 Control methods of high switching frequency CSCs

By ignoring the dynamic interactions of the AC side and the DC-link, several control methods have been proposed for high switching frequency CSCs. Fig. 12.2 shows the control scheme of the DC-link current in the synchronous reference frame. Based on Fig. 12.1, according to the power balance, with a lossless converter and a fast AC current control loop, the active power P in the grid side and the power to the DC-link are equal, which is given as

This book belongs to Kitab Liaison (ocd1996@gmail.com) Copyright Elsevier 2023

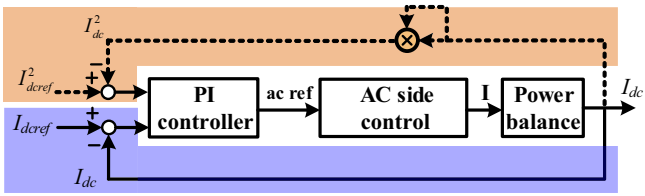

FIGURE 12.2 Block diagram of DC-link current control in current source controllers based on the active power balance.

$$P = \underbrace{V_d I_d + V_q I_q}_{\text{Active power in ac side}} = \underbrace{\frac{L_{dc} I_{dc}^2}{2} + P_L}_{\text{Active power to the dc-link}} \tag{12.1}$$

where V_d and V_q are the d- and q-axis voltage of the PCC voltage $\boldsymbol{V}$. I_d and I_q are the d- and q-axis current of the AC input current $\boldsymbol{I}$. $L_{dc} I_{dc}^2/2$is the energy stored in the DC-link inductor L_{dc} and P_L is the load power. Thus, the DC-link current dynamics is derived by linearizing Eq. (12.1) as

$$\widehat{P} = V_d \widehat{I}_d + V_q \widehat{I}_q = \frac{L_{dc}}{2} \frac{d\left(\widehat{I}_{dc}^2\right)}{dt} + V_{dc} \widehat{I}_{dc} \Rightarrow G_d = \frac{\widehat{I}_{dc}}{\widehat{I}_d} = \frac{V_d}{sL_{dc} I_{dc} + V_{dc}} \tag{12.2}$$

$$\widehat{P} = V_d \widehat{I}_d + V_q \widehat{I}_q = \frac{C_{dc}}{2} \frac{d\left(\widehat{V}_{dc}^2\right)}{dt} + \widehat{P}_L \Rightarrow G_d = \frac{\widehat{I}_{dc}^2}{\widehat{I}_d} = \frac{2V_d}{sL_{dc}} \tag{12.3}$$

where "$\widehat{\cdot}$" denotes the small-signal perturbation of a variable. G_d is the transfer function from d-axis AC current to the DC-link current. Thus, both $I_{dc}$and I_{dc}^2can be used as the feedback control variable for the DC-link current control. Since G_d is of first order, a PI controller can be employed.

In the AC side control, existing works focus on the suppression of the harmonics caused by the LC filter. Active damping methods are proposed to address this issue. It is found that the active damping in Ref. [13] can improve the transient dynamics of CSCs, where the CSC system is stable in steady state under DC-link current control. However, in Refs. [14–17], the active damping is an essential part to maintain the stability of CSCs. Moreover, a single-loop DC-link current control is documented in Ref. [18], which indicates that an open-loop control is also effective in the AC side. Therefore, the mechanism of the active damping in the dynamic analysis of high switching frequency CSCs is not clear.

Thus, by including the dynamic interactions between the AC side and DC-link, the design of the control system is also a challenge.

This book belongs to Kitab Liaison (ocd1996@gmail.com) Copyright Elsevier 2023

12.2 Stability analysis of the single-loop DC-link current control

12.2.1 Small-signal modeling

Building the small-signal model is a general method to analyze the dynamics of CSCs. The small-signal circuit including the linearization in the *dq* frame is shown in Fig. 12.3, where D_d and D_q are the *d*- and *q*-axis duty cycle in the *dq* frame. V_{cd} and V_{cq} are the *d*- and *q*-axis capacitor voltage. ω_1 is the grid frequency. Based on that, the control plant of the single-loop DC-link current control, i.e., the transfer function $G_{dc\text{-}d}$ from the *d*-axis duty cycle to the DC-link current, can be derived as

$$G_{dc-d} = \frac{1}{L_{dc}L^2C^2s}\frac{N_{dc}}{D} \tag{12.4}$$

$$\begin{aligned} N_{dc} &= L^2C^2V_{cd}s^4 - L^2CD_dI_{dc}s^3 + \left(\omega L^2CD_qI_{dc} + 2\omega^2L^2C^2V_{cd} + 2LCV_{cd}\right)s^2 \\ &+ \left(-\omega L^2CD_dI_{dc} - LD_dI_{dc}\right)s + \left(\omega_1^2LC - 1\right)\left(\omega_1^2LCV_{cd} + \omega_1LD_qI_{dc} - V_{cd}\right) \end{aligned} \tag{12.5}$$

$$\begin{aligned} D &= \left(s^2 + \omega_{c1}^2\right)\left(s^2 + \omega_{c2}^2\right) \\ \omega_{c1}^2 &= \frac{1}{LC} + \omega_1^2 + \frac{D_d^2 + D_q^2}{2L_{dc}C} - \sqrt{\left(\frac{D_d^2 + D_q^2}{2L_{dc}C}\right)^2 + \frac{4\omega_1^2}{LC}} \\ \omega_{c2}^2 &= \frac{1}{LC} + \omega_1^2 + \frac{D_d^2 + D_q^2}{2L_{dc}C} + \sqrt{\left(\frac{D_d^2 + D_q^2}{2L_{dc}C}\right)^2 + \frac{4\omega_1^2}{LC}} \end{aligned} \tag{12.6}$$

It is noted that the open-loop control is applied to the reactive power regulation, where the calculated reactive power compensation reference is

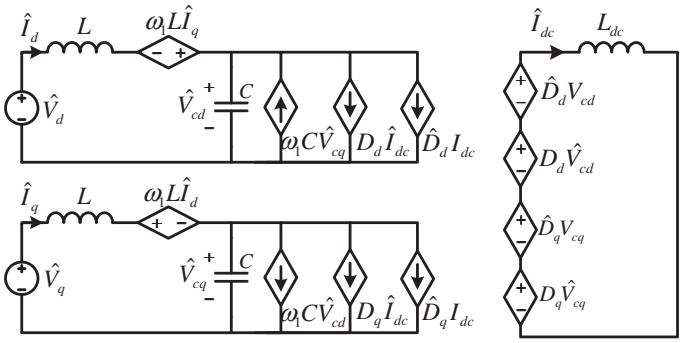

FIGURE 12.3 Small-signal circuit model of current source controllers (CSCs) (e.g., circuit shown in Fig. 12.1).

This book belongs to Kitab Liaison (ocd1996@gmail.com) Copyright Elsevier 2023

TABLE 12.1 Main circuit and control parameters in a three-phase current source converter.

Symbol	Parameter	Value
V_g	Grid voltage (line to line)	173 V, 50 Hz
I_{dc}	DC-link current	10 A
V_{dc}	DC-link voltage	−100/100 V
L	Inductance of the input *LC* filter	0.5/1/2 mH
C	Capacitance of the input *LC* filter	5/10 μF
L_{dc}	DC-link inductor	3 mH
f_s	Switching frequency	10 kHz
T_s	Sampling time	100 μs
k_{pdc}	Proportional gain of PI controller	0.01 S
k_{idc}	Integral gain of PI controller	0.5 rad/s

given to the q-axis duty cycle. Therefore, only $G_{dc\text{-}d}$ is considered in the single-loop DC-link current control.

To investigate the stability of the single-loop DC-link current control, parameters listed in Table 12.1 will be used as an example in the following.

12.2.2 Stable region of single-loop DC-link current control

According to the Nyquist stability criterion, a system can be stabilized by tuning the proportional gain under the condition, i.e., the magnitude is not above 0 dB at the frequency where the phase of the open-loop gain is $(-1-2k)\pi$ ($k = 0, 1, 2$.) [19]. Four sets of *LC*-filter parameter values from Table 12.1, as listed in Table 12.2, are thus used to investigate the stability of the single-loop

TABLE 12.2 Parameters of *LC* filter used in the stability analysis.

Case	*LC*-filter value
I	$L = 0.5$ mH $C = 5$ μF
II	$L = 1$ mH
	$C = 5$ μF
III	$L = 1$ mH
	$C = 10$ μF
IV	$L = 2$ mH
	$C = 10$ μF

This book belongs to Kitab Liaison (ocd1996@gmail.com) Copyright Elsevier 2023

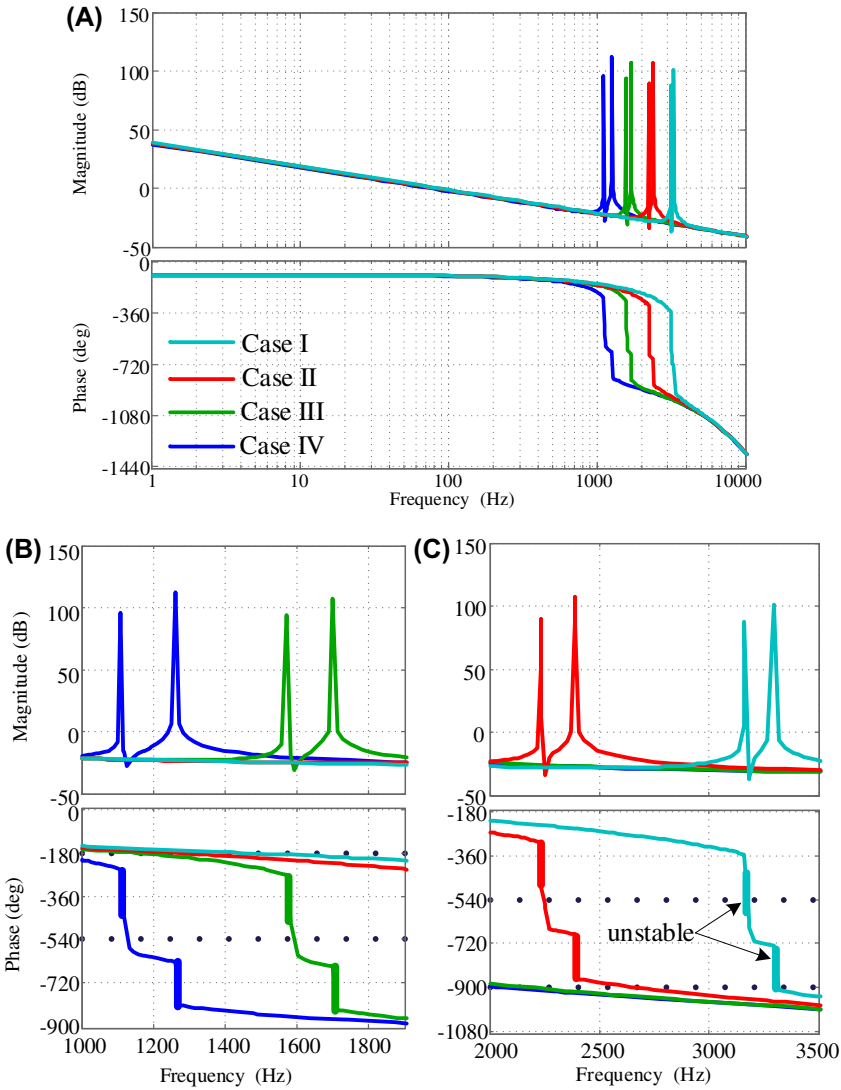

FIGURE 12.4 Bode plots of the open-loop gain G_o of the single-loop DC-link current control ($k_{pdc} = 0.01$) corresponding to Table II. (A) Overall view. (B) Zoom-in view, 1000−1900 Hz. (C) Zoom-in view, 2000−3500 Hz.

DC-link current control. Fig. 12.4 shows the Bode plots of the open-loop gain of the single-loop DC-link current control G_o, which can be expressed as

$$G_o = G_c G_{del} G_{dc-d} \tag{12.7}$$

where G_{del} is the time delay, i.e., $G_{del} = e^{-1.5T_s}$ and G_c is the DC-link current PI controller, i.e., $G_c = k_{pdc} + k_{idc}/s$. The proportional gain k_{pdc} of the PI

This book belongs to Kitab Liaison (ocd1996@gmail.com) Copyright Elsevier 2023

controller is set to 0.01 and the integrator is ignored since it will not affect the frequency responses around ω_{c1} and ω_{c2}. It can be seen that the CSC system is stable in Cases II, III, and IV. However, it turns out to be unstable in Case I, because the phase crosses -540 and -900 degrees at ω_{c1} and ω_{c2}, respectively.

To further verify the relationship between the *LC*-filter parameters and the stability, root loci in the *z*-domain with varying k_{pdc} under the four sets of the *LC*-filter parameters are shown in Fig. 12.5. It can be seen that the stable region of k_{pdc} becomes narrow from Case IV to Case II. When using the *LC*-filter parameters as Cases I, i.e., $L = 0.5$ mH and $C = 5$ μF, the root locus is always outside the unity circle, which indicates that the system is always unstable. Thus, the single-loop DC-link current control can be stabilized with low resonance frequency *LC* filter, while showing instability by using high resonance frequency *LC* filter. The in-depth reason is that the phase lag coming from the time delay effect becomes larger at the resonances from low frequencies to high frequencies, which affect the stability of the single-loop DC-link current control.

Thus, the single-loop DC-link current control can be stabilized with low resonance frequency *LC* filter, while showing instability by using high resonance frequency *LC* filter. The in-depth reason is that the phase lag coming from the time delay effect becomes larger at the resonances from low frequencies to high frequencies, which affects the stability of the single-loop DC-link current control.

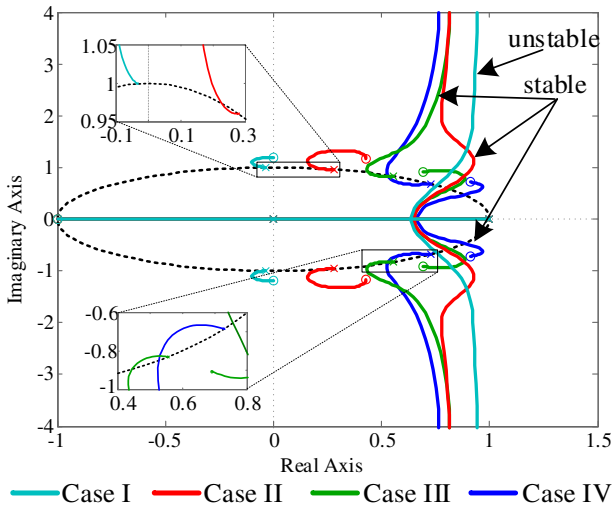

FIGURE 12.5 Root loci of single-loop DC-link current control with varying the parameter of the *LC* filter in the z-domain.

This book belongs to Kitab Liaison (ocd1996@gmail.com)
Copyright Elsevier 2023

12.2.3 Experimental validation

Fig. 12.6 presents the experimental waveforms of PCC voltage (phase A voltage V_A), input current (phase A current I_A), and the DC-link current, where the Case I parameters of the *LC* filter is used. It can be seen that the system is unstable. Corresponding to Case II, Fig. 12.7 gives the measured waveforms,

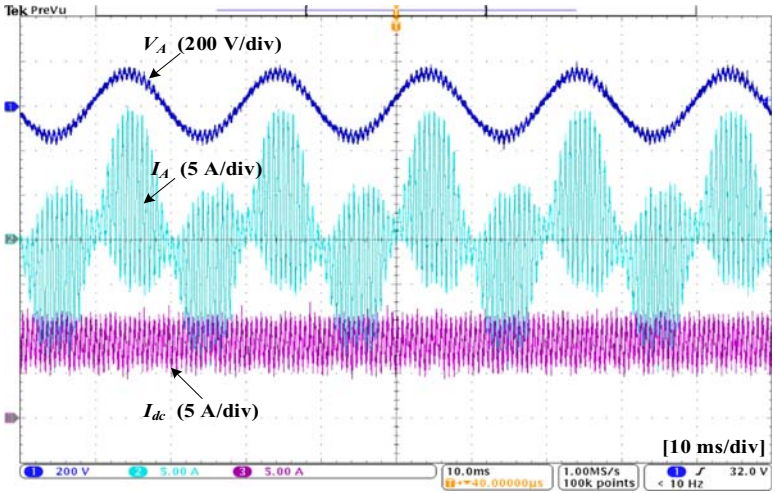

FIGURE 12.6 Measured waveforms of the PCC voltage, input current, and DC-link current corresponding to Case I in Table 12.2.

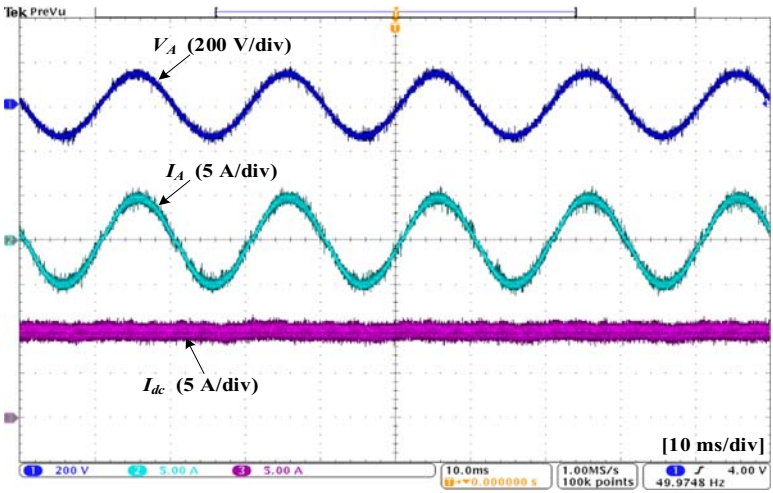

FIGURE 12.7 Measured waveforms of the PCC voltage, input current, and DC-link current corresponding to Case II in Table 12.2.

This book belongs to Kitab Liaison (ocd1996@gmail.com) Copyright Elsevier 2023

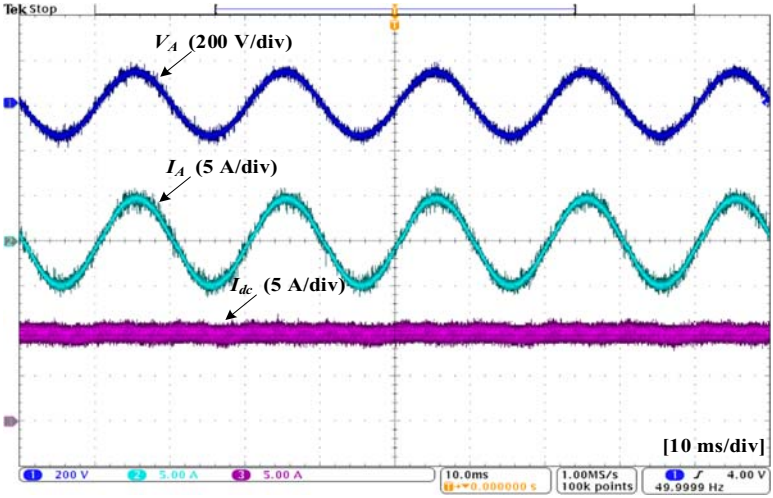

FIGURE 12.8 Measured waveforms of the PCC voltage, input current, and DC-link current corresponding to Case III in Table 12.2.

which indicates that the CSC is stable. By increasing the *LC* filter to meet a larger resonance frequency as Cases III and IV, Figs. 12.8 and 12.9 show the experimental waveforms of PCC voltage (phase A voltage V_A), input current (phase A current I_A), and the DC-link current. Stable operation waveforms can be observed, which matches the analysis of the stable region. Moreover, the

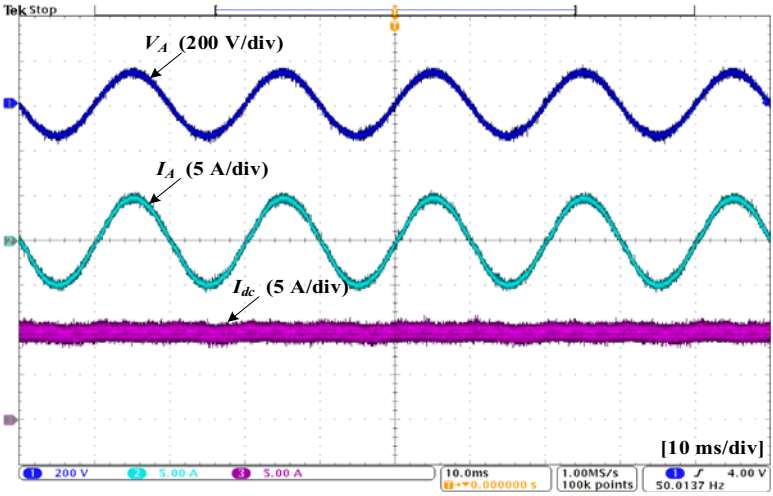

FIGURE 12.9 Measured waveforms of the PCC voltage, input current, and DC-link current corresponding to Case IV in Table 12.2.

This book belongs to Kitab Liaison (ocd1996@gmail.com) Copyright Elsevier 2023

waveforms in Figs. 12.8 and 12.9 also validate that the PI-based single-loop DC-link current control can be used to regulate CSCs, where the current performance becomes higher by increasing the value of the inductor L.

12.3 Active damping methods for high switching frequency CSCs

Based on the stable region analysis, when the LC-filter parameters are located in the high resonance frequency range, which indicates the single-loop DC-link current control is unstable, active damping is a common solution to enhance the power converter's stability.

Redraw the block diagram of the single-loop DC-link current control loop in Fig. 12.10, where the control plant of single-loop DC-link current control is divided into two parts, i.e., from the duty cycle to the input current and from the input current to the DC-link current. To specify the input LC filter, i.e.,

$$\mathbf{Z_C} = \frac{-1}{(s^2+\omega_1^2)C}\begin{bmatrix} s & \omega_1 \\ -\omega_1 & s \end{bmatrix}, \mathbf{Y_L} = \frac{-1}{(s^2+\omega_1^2)L}\begin{bmatrix} s & \omega_1 \\ -\omega_1 & s \end{bmatrix} \tag{12.8}$$

the transfer function matrix from the duty cycle to the input current is further divided into the gain of the converter $\mathbf{G_{Idc}}$ and the LC filter. $\mathbf{G_{Idc}}$ can be thus derived as

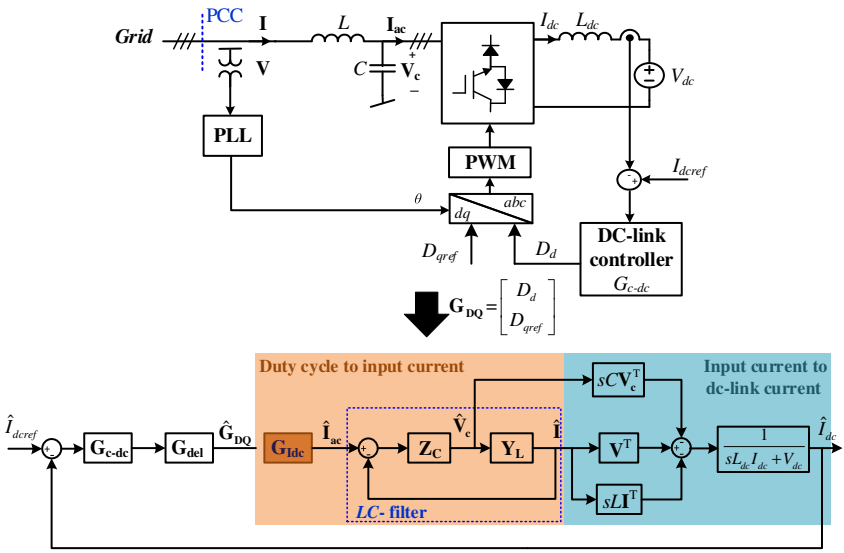

FIGURE 12.10 Block diagram of the single-loop DC-link current control loop to be applied for the active damping control.

This book belongs to Kitab Liaison (ocd1996@gmail.com)
Copyright Elsevier 2023

$$\underbrace{\begin{bmatrix} I_{acd} \\ I_{acq} \end{bmatrix}}_{\mathbf{I_{ac}}} = \begin{bmatrix} D_d \\ D_q \end{bmatrix} I_{dc} \xrightarrow{linearization} \begin{bmatrix} \widehat{I}_{acd} \\ \widehat{I}_{acq} \end{bmatrix} = \begin{bmatrix} \widehat{D}_d \\ \widehat{D}_q \end{bmatrix} \begin{bmatrix} I_{dc} & 0 \\ 0 & I_{dc} \end{bmatrix} + \begin{bmatrix} D_d \\ D_q \end{bmatrix} \widehat{I}_{dc}$$

$$\Rightarrow \begin{bmatrix} \widehat{I}_{acd} \\ \widehat{I}_{acq} \end{bmatrix} = \begin{bmatrix} \widehat{D}_d \\ \widehat{D}_q \end{bmatrix} \begin{bmatrix} I_{dc} & 0 \\ 0 & I_{dc} \end{bmatrix} + \begin{bmatrix} D_d \\ D_q \end{bmatrix} \begin{bmatrix} G_{dc-d} & G_{dc-q} \end{bmatrix} \begin{bmatrix} \widehat{D}_d \\ \widehat{D}_q \end{bmatrix}$$

$$= \underbrace{\begin{bmatrix} I_{dc}+D_d G_{dc-d} D_d G_{dc-q} \\ D_q G_{dc-d} I_{dc} + D_q G_{dc-q} \end{bmatrix}}_{\mathbf{G_{Idc}}} \begin{bmatrix} \widehat{D}_d \\ \widehat{D}_q \end{bmatrix} \tag{12.9}$$

According to the linearization in Eq. (12.9), by including the DC-link current dynamics, $\mathbf{G_{Idc}}$ is no longer equal to the value of the DC-link current I_{dc}, where the frequency responses in respect to $\mathbf{G_{Idc}}$ are given in Fig. 12.11, where the four channels are obtained, which depicts the relations between the two inputs and two outputs. The $d-d$ and $q-q$ channels reflect the active power and reactive power flow, respectively. The $d-q$ and $q-d$ channels show the coupling effects. It can be seen that, in the diagonal elements, compared to the proportional gains of the constant DC-link current, the low frequency range response of $d-d$ channel presents an integral property, while little differences occur in the $q-q$ channel. As for the $d-q$ channel impedance, the magnitude is below 0 dB except the two resonance peaks, which indicates a weak coupling from the q-axis to the d-axis. However, in the $q-d$ channel, the

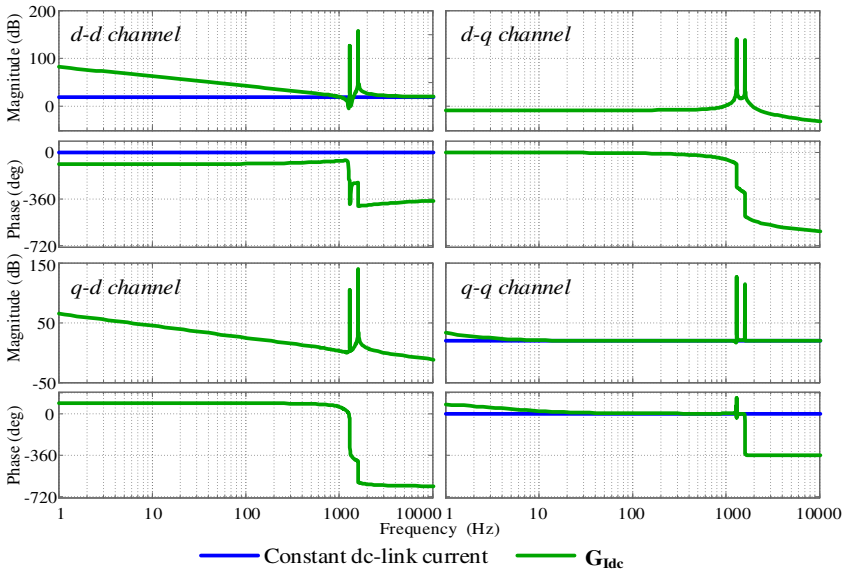

FIGURE 12.11 Frequency responses of $\mathbf{G_{Idc}}$ and constant DC-link current, where the parameters in Table 12.1 are used.

This book belongs to Kitab Liaison (ocd1996@gmail.com)
Copyright Elsevier 2023

magnitude of the impedance is far above 0 dB, which proves that the DC-link current dynamics lead to a nonnegligible impact from the d-axis on the q-axis.

Thus, in the perspective of control, $\mathbf{G_{Idc}}$ can be simplified to

$$\begin{aligned} G_{dc-d} \rightarrow G_{dc-ds} &= \frac{V_{cd}}{sL_{dc}} \\ G_{dc-q} \rightarrow G_{dc-qs} &= 0 \end{aligned} \Rightarrow \mathbf{G_{Idc-s}} = \begin{bmatrix} I_{dc} + \dfrac{D_d V_{cd}}{sL_{dc}} & 0 \\ \dfrac{D_q V_{cd}}{sL_{dc}} & I_{dc} \end{bmatrix} \tag{12.10}$$

12.3.1 Virtual impedance analysis

Based on the above discussions, three possible active damping loops, i.e., capacitor-voltage feedback, capacitor-current feedback, and inductor-current feedback, will be investigated in the following.

The control diagrams of the single-loop DC-link current control with capacitor-voltage feedback, capacitor-current feedback, and inductor-current feedback active damping are shown in Figs. 12.12–12.14, respectively. $\boldsymbol{I_c}$ is the capacitor current. $\mathbf{G_{ad}}$ is the feedback gain of the active damping.

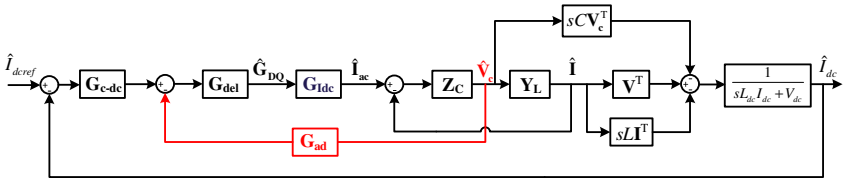

FIGURE 12.12 Block diagram of single-loop DC-link current control with active damping by capacitor-voltage feedback.

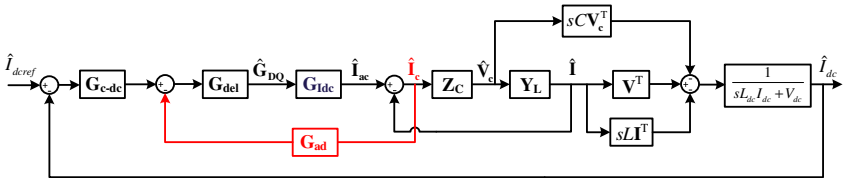

FIGURE 12.13 Block diagram of single-loop DC-link current control with active damping by capacitor-current feedback.

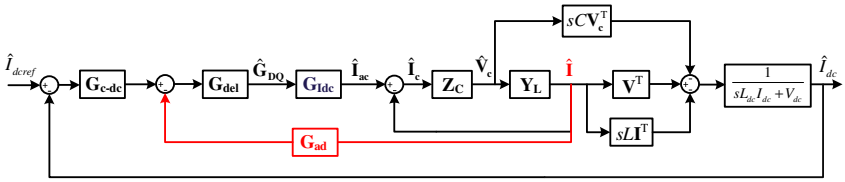

FIGURE 12.14 Block diagram of single-loop DC-link current control with active damping by inductor-current feedback.

This book belongs to Kitab Liaison (ocd1996@gmail.com)
Copyright Elsevier 2023

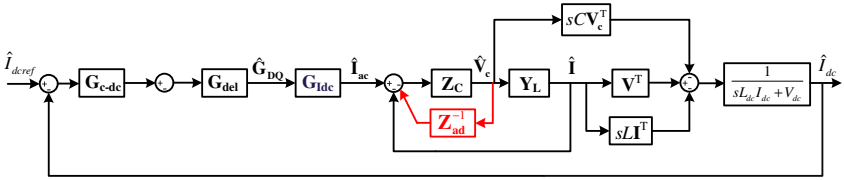

FIGURE 12.15 Equivalent block diagram of Figs 12.12–12.14.

Moreover, all of them can be transformed to Fig. 12.15, where the active damping feedbacks are equivalent to a feedback loop with $\mathbf{Z_C}$, which is equal to a virtual impedance $\mathbf{Z_{ad}}$ in parallel with the filter capacitor C. Since the dynamics of the single-loop DC-link current control are implemented in the d-axis and the active damping is also implemented in the d-axis, $\mathbf{G_{ad}}$ can be expressed as

$$\mathbf{G_{ad}} = \begin{bmatrix} G_{ad} & 0 \\ 0 & 0 \end{bmatrix} \tag{12.11}$$

where G_{ad} is the feedback gain of the active damping in the d-axis control loop.

12.3.1.1 Capacitor-voltage feedback (Fig. 12.12)

Proportional capacitor-voltage feedback has been proved to be effective for active damping in high-power CSCs [14]. However, according to the conventional LC-filter–based analysis, the damping performance is sensitive to the design of the virtual resistance and the employed high-pass filter to avoid overmodulation is not clearly analyzed either.

Based on Figs. 12.12 and 12.15, Fig. 12.16 presents an active damping loop in the d-axis and Fig. 12.17 gives the corresponding diagram with the virtual

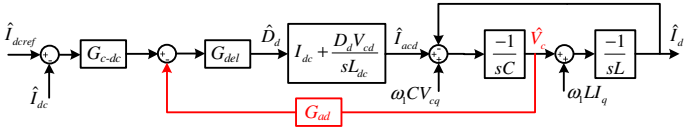

FIGURE 12.16 D-axis capacitor-voltage feedback–based active damping control.

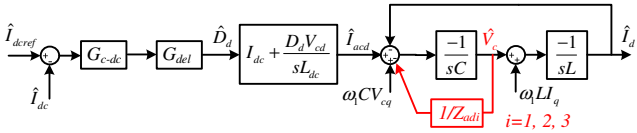

FIGURE 12.17 D-axis block diagram of virtual impedance by active damping control.

This book belongs to Kitab Liaison (ocd1996@gmail.com)
Copyright Elsevier 2023

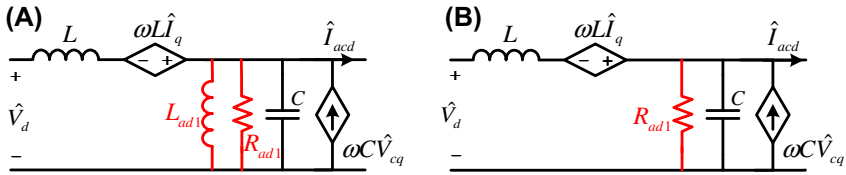

FIGURE 12.18 Equivalent d-axis circuit with capacitor-voltage feedback—based active damping control. (A) Proportional feedback gain, (B) High-pass filter feedback gain.

impedance Z_{ad1}. Considering $G_{del} = 1$, i.e., the CSC system has no time delay, the added virtual impedance Z_{ad1} implemented by the active damping loop is

$$Z_{ad1} = \frac{1}{G_{ad}\left(I_{dc} + \dfrac{D_d V_{cd}}{sL_{dc}}\right)} \tag{12.12}$$

By using a proportional feedback, $G_{ad} = k_{ad1}$, Z_{ad1} is composed of a virtual resistance R_{ad1} and a virtual inductance L_{ad1}, as shown in Fig. 12.18A, which can be derived as

$$\begin{aligned} Z_{ad1} &= \frac{1}{k_{ad1}\left(I_{dc} + \dfrac{D_d V_{cd}}{sL_{dc}}\right)} = R_{ad1}//L_{ad1}s \\ \Rightarrow R_{ad1} &= \frac{1}{k_{ad1} I_{dc}}, L_{ad1} = \frac{L_{dc}}{k_{ad1} D_d V_{cd}} \end{aligned} \tag{12.13}$$

It can be seen that the parallel virtual inductance L_{ad1} depends on the DC-link inductor.

To obtain a virtual resistance R_{ad1} merely, the feedback gain G_{ad} needs a first-order high-pass filter, which is

$$G_{ad} = \frac{\lambda_{ad1} s}{s + \omega_{ad1}} \tag{12.14}$$

where λ_{ad1} and ω_{ad1} are the gain and the cutoff frequency of the high-pass filter, which can be derived as

$$\begin{aligned} Z_{ad1} &= \frac{1}{\dfrac{\lambda_{ad1} s}{s + \omega_{ad}}\left(I_{dc} + \dfrac{D_d V_{cd}}{sL_{dc}}\right)} = R_{ad1} \\ \Rightarrow \lambda_{ad1} &= \frac{1}{R_{ad1} I_{dc}}, \omega_{ad1} = \frac{D_d V_{cd}}{L_{dc} I_{dc}} \end{aligned} \tag{12.15}$$

Therefore, the d-axis equivalent circuit can be obtained as shown in Fig. 12.18B.

This book belongs to Kitab Liaison (ocd1996@gmail.com) Copyright Elsevier 2023

12.3.1.2 Capacitor-current feedback (Fig. 12.13)

Capacitor-current feedback is another possibility to form the active damping in CSCs, which is widely used in *LCL*-filter VSC systems [20]. According to Figs. 12.13 and 12.15, the *d*-axis control diagrams are shown in Fig. 12.19. It can be obtained that, by involving the DC-link current dynamics, the equivalent virtual impedance is

$$Z_{ad2} = \frac{1}{\left(I_{dc} + \frac{D_d V_{cd}}{sL_{dc}}\right) G_{del} G_{ad} sC} \tag{12.16}$$

Firstly, assuming that the CSC system has no delay, i.e., $G_{del} = 1$, with a proportional feedback $G_{ad} = k_{ad2}$, a virtual resistance R_{ad2} and a virtual capacitance C_{ad2} are obtained, which are

$$\begin{aligned} Z_{ad2} &= \frac{1}{\left(I_{dc} + \frac{D_d V_{cd}}{sL_{dc}}\right) k_{ad2} sC} = R_{ad2} // \frac{1}{sC_{ad2}} \\ \Rightarrow R_{ad2} &= \frac{L_{dc}}{k_{ad2} D_d V_{cd} C}, C_{ad2} = k_{ad2} I_{dc} \end{aligned} \tag{12.17}$$

Then, in order to mitigate the virtual capacitance, substituting the feedback proportional gain with a first-order low-pass filter, $G_{ad} = \lambda_{ad2}/(s + \omega_{ad2})$ can be applied. The gain λ_{ad2} and the cutoff frequency ω_{ad2} of the low-pass filter can be derived as

$$\begin{aligned} Z_{ad2} &= \frac{1}{\left(I_{dc} + \frac{D_d V_d}{sL_{dc}}\right) \frac{\lambda_{ad}}{s + \omega_{ad}} sC} = R_{ad2} \\ \Rightarrow \lambda_{ad2} &= \frac{1}{R_{ad2} C I_{dc}}, \omega_{ad2} = \frac{D_d V_{cd}}{L_{dc} I_{dc}} \end{aligned} \tag{12.18}$$

The corresponding *d*-axis equivalent circuits of Eqs. (12.17) and (12.18) are given in Fig. 12.20.

Thus, both the proportional and low-pass filter—based capacitor-current feedback can provide virtual resistance to dampen the CSC system, which has previously been considered impossible for active damping according to the existing literature [16,17]. From Eqs. (12.17) and (12.18), it can be seen that the integral property $V_{cd}/(sL_{dc})$ of the DC-link dynamics contributes to the virtual resistance together with the feedback gain.

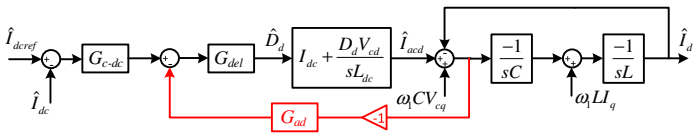

FIGURE 12.19 D-axis capacitor-current feedback—based active damping control.

This book belongs to Kitab Liaison (ocd1996@gmail.com)
Copyright Elsevier 2023

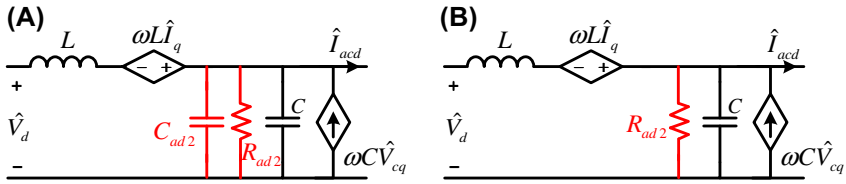

FIGURE 12.20 Equivalent d-axis circuit with capacitor-current feedback—based active damping control. (A) Proportional feedback gain, (B) Low-pass filter feedback gain.

12.3.1.3 Inductor-current feedback (Fig. 12.14)

Besides variables related to the capacitor, inductor-based variables, i.e., the inductor voltage and inductor current, may also be used for active damping by including the DC-link dynamics. Based on Fig. 12.12, the inductor-voltage feedback is equal to the capacitor-voltage feedback by tuning the positive feedback to the negative feedback. Thus, only inductor-current feedback is discussed in the following.

Similarly, according to Figs. 12.14 and 12.15, the equivalent d-axis control diagrams are depicted in Fig. 12.21. The added virtual impedance Z_{ad3} by the inductor-current feedback is

$$Z_{ad3} = \frac{1}{\left(I_{dc} + \frac{D_d V_{cd}}{sL_{dc}}\right) G_{del} G_{ad} \frac{1}{sL}} = \frac{s^2 L L_{dc}}{(sL_{dc} I_{dc} + D_d V_{cd}) G_{del} G_{ad}} \tag{12.19}$$

Considering $G_{del} = 1$ and a proportional feedback, $G_{ad} = k_{ad3}$, the equivalent d-axis circuit is shown in Fig. 12.22 and the corresponding impedance is

$$\begin{aligned} Z_{ad} &= \frac{s^2 L L_{dc}}{(sL_{dc} I_{dc} + D_d V_{cd}) k_{ad}} = sL_1 + sL_2 // R_{ad3} \\ \Rightarrow L_1 &= \frac{L}{k_{ad3} I_{dc}}, L_2 = -L_1, R_{ad3} = -\frac{L D_d V_{cd}}{k_{ad3} L_{dc} I_{dc}^2} \end{aligned} \tag{12.20}$$

As a result, compared to the RL damper by using a capacitor-voltage feedback, a negative virtual inductance, $-L_2$, is added in series. Moreover, by using a first-order phase lead-lag term as the feedback gain, i.e.,

$$G_{ad} = \lambda_{ad3} \frac{s + \omega_{ad3}}{s + \omega_{ad4}}, \omega_{ad3} = -\frac{R_{ad3} \lambda_{ad3} I_{dc}}{L}, \omega_{ad4} = \frac{D_d V_{cd}}{L_{dc} I_{dc}} \tag{12.21}$$

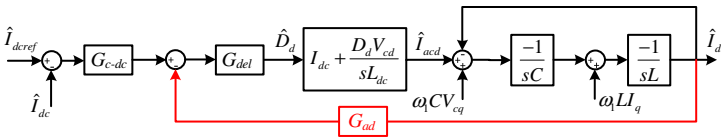

FIGURE 12.21 D-axis inductor-current feedback—based active damping control.

This book belongs to Kitab Liaison (ocd1996@gmail.com)
Copyright Elsevier 2023

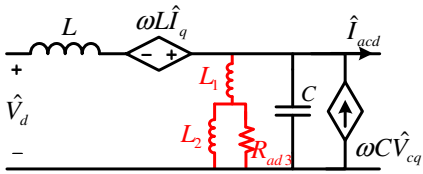

FIGURE 12.22 Equivalent d-axis circuit with inductor-current feedback—based active damping control.

The same combination of the virtual impedance can also be obtained, which is

$$Z_{ad3} = \frac{s^2 L L_{dc}}{(sL_{dc}I_{dc} + D_d V_{cd})G_{ad}} = sL_1 + sL_2//R_{ad3}$$
$$\Rightarrow L_1 = \frac{L}{\lambda_{ad3} I_{dc}}, L_2 = -L_1, R_{ad3} = -\frac{\omega_{ad3} L}{\lambda_{ad3} I_{dc}} \tag{12.22}$$

If only a virtual resistance is desired, a differential sL can be applied as the feedback gain first to make it the same as inductor-voltage feedback. Then, as mentioned before, the design inductor-voltage feedback is equal to the capacitor-voltage feedback by changing the polarity of the feedback gain. However, implementing an ideal differential term sL is not easy in a digital control system.

12.3.1.4 Time delay effect on virtual impedance

Due to the digital control system, a finite time delay, e.g., $G_{del} = e^{-1.5sT_s}$, is introduced, which affects the performance of the active damping through varying the implemented virtual impedance [21,22]. Firstly, considering pure virtual resistances in Eqs. (12.15) and (12.18), by involving the time delay effect, they change to

$$Z_{adi} = R_{adi} e^{1.5sT_s} \Rightarrow Z_{adi}(j\omega) = R_{adi}\cos(1.5\omega T_s) + jR_{adi}\sin(1.5\omega T_s), i = 1, 2 \tag{12.23}$$

It can be obtained that real terms are positive in the frequency range of (0, $1/6\omega_s$), and turn to be negative in the frequency range of ($1/6\omega_s$, $1/2\omega_s$). Regarding to the imaginary terms, they are positive from 0 to $1/3\omega_s$, while they become negative from $1/3\omega_s$ to $1/2\omega_s$. Positive real terms provide the damping effect to the LC resonance. However, negative real terms will lead to open-loop right half plane (RHP) poles to the single-loop DC-link current control, which counteract with the fast dynamic response and even result in instability. Therefore, positive real terms should preferable be guaranteed. In the case of imaginary terms, the positive brings inductance and the negative brings capacitance behaviors virtually, which shift the resonance frequency [22].

This book belongs to Kitab Liaison (ocd1996@gmail.com) Copyright Elsevier 2023

According to the stability analysis in 12.2.2, active damping is essential when the LC resonance frequency is in the high frequency range, which may be in the range of negative real terms. To solve this, a simple method is to invert the polarity of the feedback gain, which thus could provide positive real terms at the resonance frequency.

Next, as with the cases of virtual impedance in Eqs. (12.13), (12.17), and (12.20), it is still required to have a positive $\mathrm{Re}\{Z_{adi}(j\omega)\}$, $i = 1, 2, 3$ in order to avoid a nonminimal-phase property and potential instability. After considering the time delay effect, real parts of the virtual impedance in Eqs. (12.13), (12.17), and (12.20) become Eqs. (12.24), (12.25), and (12.26), respectively.

$$\mathrm{Re}\{Z_{ad1}(j\omega)\} = \frac{\omega L_{dc} I_{dc}}{k_{ad1}\left[(D_d V_{cd})^2 + (\omega L_{dc} I_{dc})^2\right]} \left[\underbrace{\omega L_{dc}\cos(1.5\omega T_s) - D_d V_{cd}\sin(1.5\omega T_s)}_{\tau_1}\right] \tag{12.24}$$

$$\mathrm{Re}\{Z_{ad2}(j\omega)\} = \frac{L_{dc} I_{dc}}{k_{ad2} C\left[(D_d V_{cd})^2 + (\omega L_{dc} I_{dc})^2\right]} \underbrace{\left[D_d V_{cd}\cos(1.5\omega T_s) + \omega\sin(1.5\omega T_s)\right]}_{\tau_2} \tag{12.25}$$

$$\mathrm{Re}\{Z_{ad3}(j\omega)\} = \frac{\omega^2 L L_{dc}^2}{k_{ad3}\left[(D_d V_{cd})^2 + (\omega L_{dc} I_{dc})^2\right]} \underbrace{\left[-D_d V_{cd}\cos(1.5\omega T_s) - \omega L_{dc} I_{dc}\sin(1.5\omega T_s)\right]}_{\tau_3} \tag{12.26}$$

It can be seen that τ_i, $i = 1, 2, 3$, determines the polarity of $\mathrm{Re}\{Z_{adi}(j\omega)\}$, $i = 1, 2, 3$, which are plotted in Fig. 12.23. Compared to $1/6\omega_s$ in the pure resistance cases, the ranges of positive real terms vary in the proportional feedbacks, which are $(0.35\omega_s, 1/2\omega_s)$, $(0, 0.33\omega_s)$, and $(0.26\omega_s, 1/2\omega_s)$ in capacitor-voltage, capacitor-current, and inductor-current feedback, respectively. Moreover, the boundaries depend on the steady-state values and DC-link inductor of the CSC, which increases the complexity of the active damping design.

Thus, based on involving the DC-link dynamics and the simplified model, it is possible to achieve active damping with proportional feedbacks of capacitor-voltage, capacitor-current, and inductor-current in the perspective of controller design, which becomes more flexible in practical applications. Furthermore, by employing a high-pass filter in the capacitor-voltage feedback or a low-pass filter in the capacitor-current feedback, pure virtual resistance

This book belongs to Kitab Liaison (ocd1996@gmail.com) Copyright Elsevier 2023

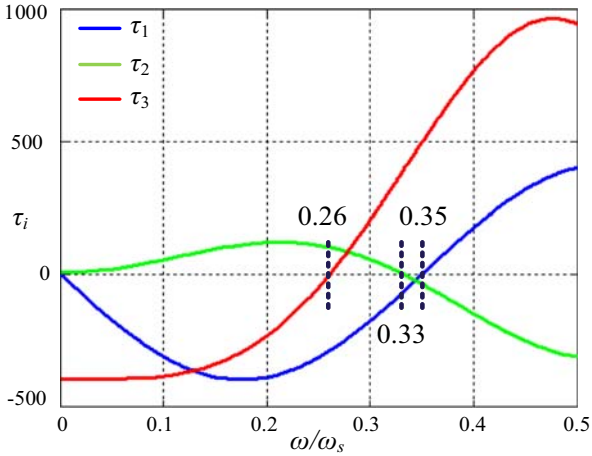

FIGURE 12.23 Critical frequency of $\mathrm{Re}\{Z_{adi}(j\omega)\}$ ($V_g = 173$ V, $L_{dc} = 3$ mH, $I_{dc} = 10$A, $V_{dc} = 100$ V).

can be obtained, which is also simple to be designed including the time delay effect. The solution to maintain a positive real term is to change the polarity of the feedback gain. The design principle of the high-pass filter and the low-pass filter are presented, which depends on the DC-link current dynamics. Lastly, it is noted that by using the inductor-current feedback, which is also an inner-control loop of regulating the inductor-current, performances of the input current can be improved, e.g., implementing harmonic suppression by adding resonant controllers to the feedback loop.

12.3.2 Experimental validation of active damping

The parameters presented in Case I of Table 12.2, i.e., $L = 0.5$ mH, $C = 5$ μF, which need active damping in single-loop DC-link current control, are adopted in the experiments. Fig. 12.24 shows the unstable waveforms when applying the single-loop DC-link current control to the CSC with this *LC* filter, which is the same with Fig. 12.6. Based on the virtual impedance analysis, the used control parameters of the active damping methods are designed as listed in Table 12.3, which will be explained in the following discussions. Subsequently, the step response of the single-loop DC-link current control is tested. The DC-link current is stepped up from 9 to 12 A in each method, which make sure the modeling is effective due to the system is near to the steady-state $I_{dc} = 10$ A. All the experimental results are composed of waveforms of the PCC voltage (phase A voltage V_A), the input current (phase A current I_A), and the DC-link current (I_{dc}).

This book belongs to Kitab Liaison (ocd1996@gmail.com) Copyright Elsevier 2023

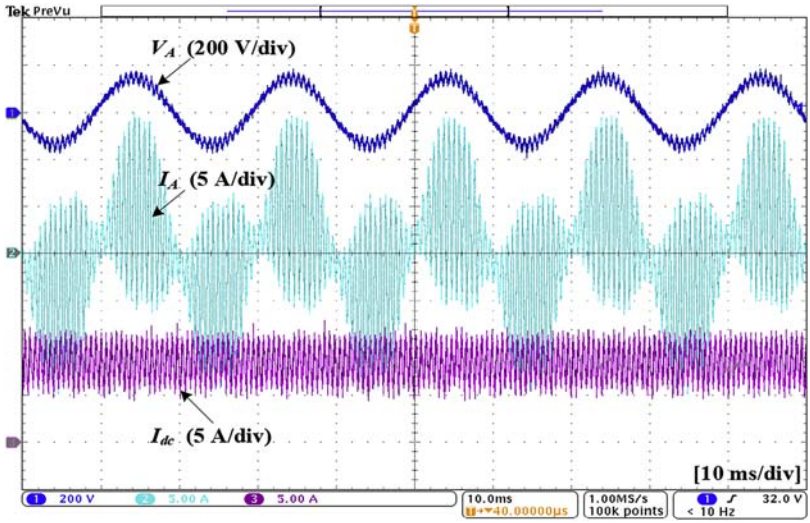

FIGURE 12.24 Measured waveforms of the PCC voltage, input current, and DC-link current corresponding to Case I ($L = 0.5$ mH, $C = 5$ µF).

TABLE 12.3 Parameters of active damping in a three-phase current source converter.

Feedback variable	Parameters of feedback gain	Value
Capacitor voltage (Fig. 12.12)	Proportional feedback gain, k_{ad1}	0.00005
	High-pass filter feedback gain, $G_{ad} = \frac{\lambda_{ad1} s}{s + \omega_{ad1}}$	$\lambda_{ad1} = 0.005$ $\omega_{ad1} = \pm 3333$rad/s
Capacitor current (Fig. 12.13)	Proportional feedback gain, k_{ad2}	± 0.01
	Low-pass filter feedback gain, $G_{ad} = \frac{\lambda_{ad2}}{s + \omega_{ad2}}$	$\lambda_{ad2} = 33$ $\omega_{ad2} = \pm 3333$rad/s
Inductor current (Fig. 12.14)	Proportional feedback gain, k_{ad3}	± 0.0067

12.3.2.1 Capacitor-voltage feedback (see Fig. 12.12)

Firstly, the measured waveforms of proportional feedback gain are presented in Fig. 12.25. According to Eq. (12.13), the virtual resistance is set as $R_{ad1} = 200\ \Omega$, and thus k_{ad1} is designed to be 0.0005. By using the active damping, stable waveforms can be observed in Fig. 12.25, which is no longer distorted like it is shown in Fig. 12.24, which demonstrates the effectiveness of the proportional capacitor-voltage feedback active damping.

This book belongs to Kitab Liaison (ocd1996@gmail.com) Copyright Elsevier 2023

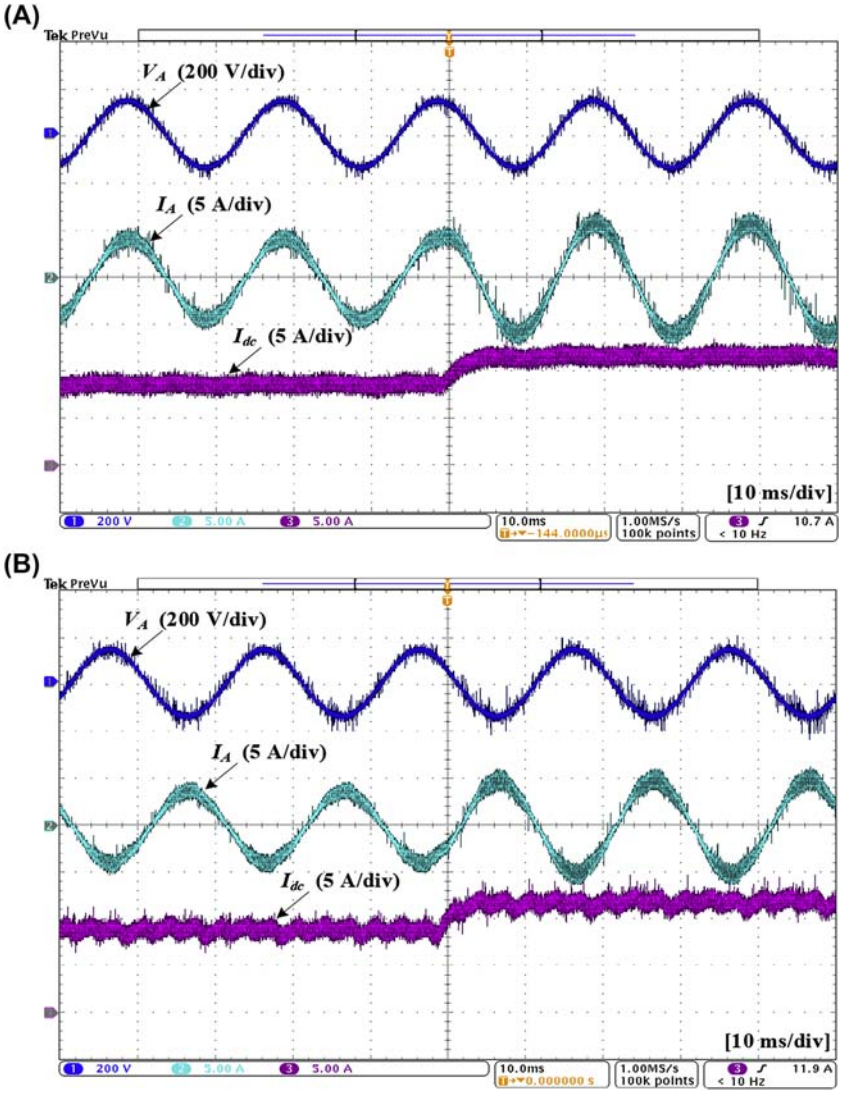

FIGURE 12.25 Measured waveforms of the PCC voltage, input current, and DC-link current with proportional capacitor-voltage feedback (see Figs. 12.12 and 12.18A). (A). Rectifier mode. (B). Inverter mode.

Then, capacitor-voltage feedback with high-pass filter is tested, where the virtual resistance is $R_{ad1} = 20\ \Omega$. The high-pass filter is thus designed based on Eq. (12.15), and its parameters are $\lambda_{ad1} = 0.005$, $\omega_{ad1} = 3333$ rad/s for rectifier mode and $\lambda_{ad1} = 0.005$, $\omega_{ad1} = -3333$ rad/s for the inverter mode.

This book belongs to Kitab Liaison (ocd1996@gmail.com) Copyright Elsevier 2023

Fig. 12.26 shows the waveforms with high-pass filter capacitor-voltage feedback in the rectifier mode and inverter mode. It can be seen that the waveforms are also stable compared to Fig. 12.24, which verifies the high-pass filter capacitor-voltage feedback can dampen the system.

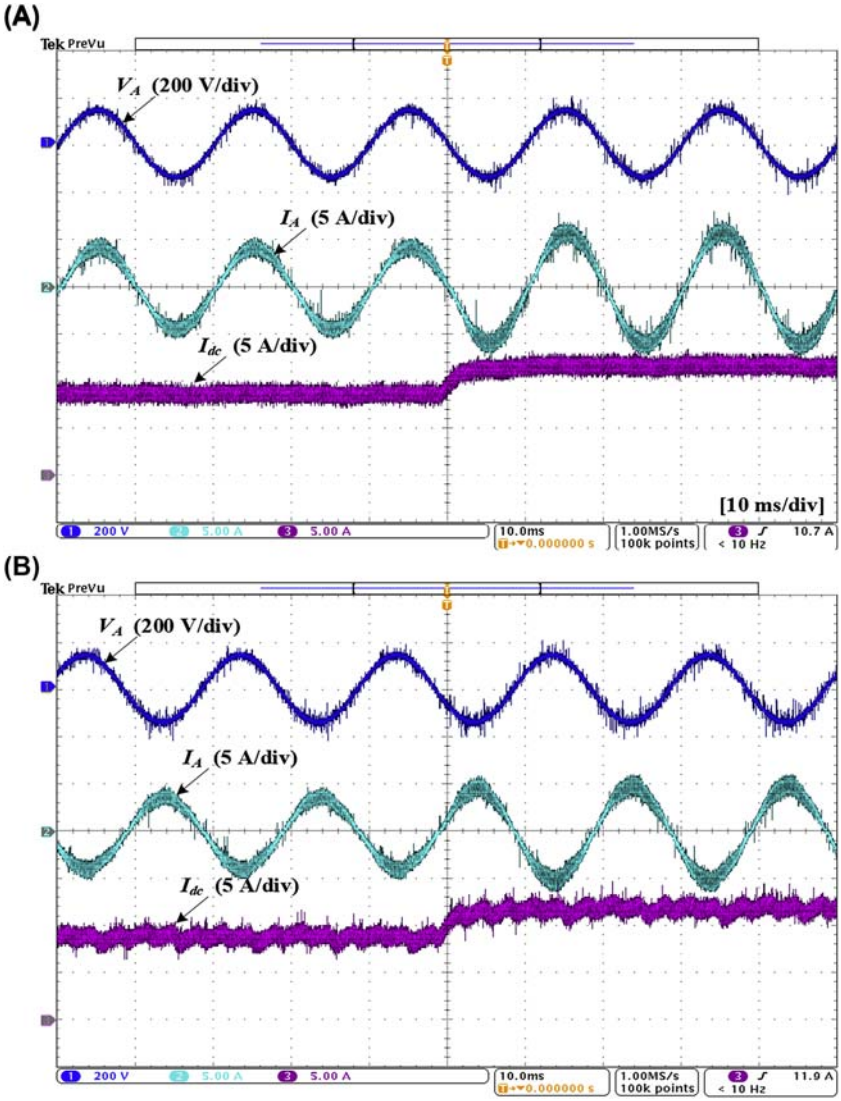

FIGURE 12.26 Measured waveforms of the PCC voltage, input current, and DC-link current with high-pass filter capacitor-voltage feedback (see Figs. 12.12 and 12.18B). (A). Rectifier mode. (B). Inverter mode.

This book belongs to Kitab Liaison (ocd1996@gmail.com)
Copyright Elsevier 2023

12.3.2.2 Capacitor-current feedback (see Fig. 12.13)

Fig. 12.27 presents the measured waveforms when using the proportional capacitor-current feedback in the rectifier mode and inverter mode. The virtual resistance is set to $R_{ad2} = 600\ \Omega$, and based on Eq. (12.17), k_{ad2} is designed to

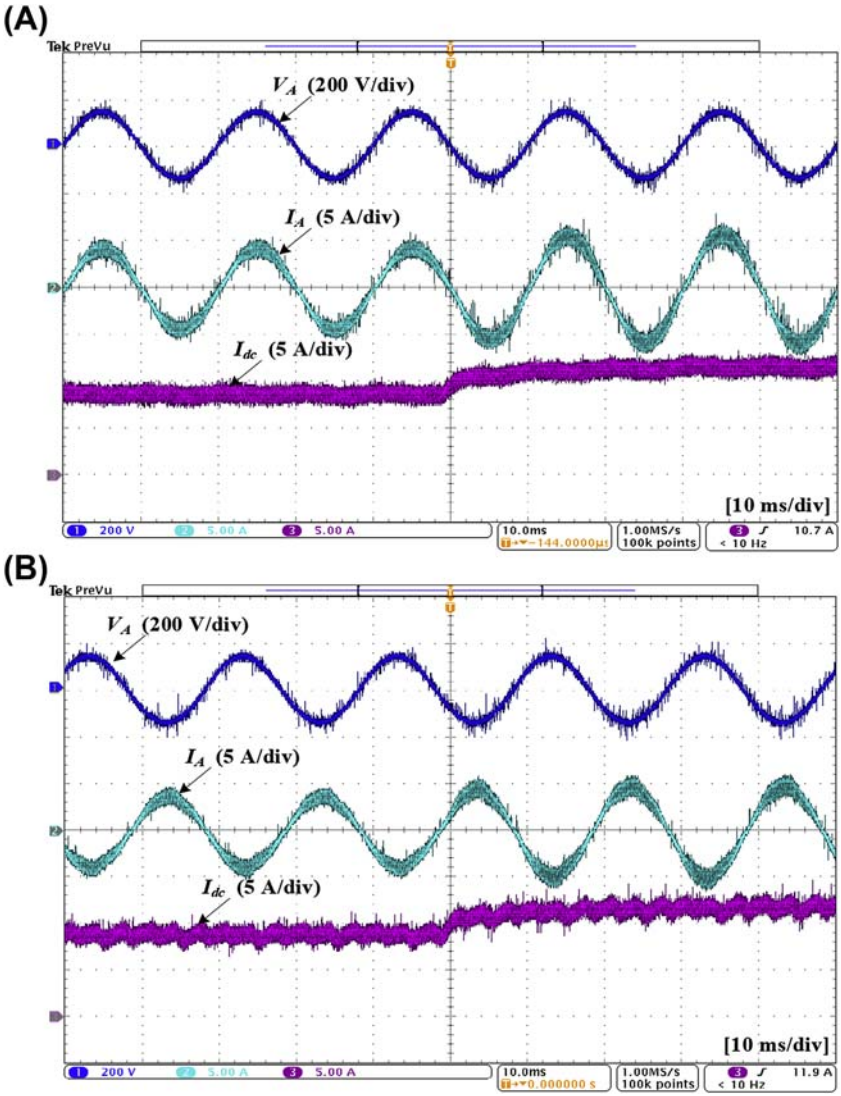

FIGURE 12.27 Measured waveforms of the PCC voltage, input current, and DC-link current with proportional capacitor-current feedback (see Figs. 12.13 and 12.20A). (A). Rectifier mode. (B). Inverter mode.

This book belongs to Kitab Liaison (ocd1996@gmail.com)
Copyright Elsevier 2023

be $k_{ad2} = 0.01$ in the rectifier mode and $k_{ad2} = -0.01$ in the inverter mode. It can be seen that the step responses are stable, which validates the effectiveness of the proposed proportional capacitor-current feedback active damping method. Similarly, due to the same DC-link control parameters, the settling time of step response in the rectifier mode and inverter mode is the same.

Fig. 12.28 presents the measured waveforms when using the low-pass filter capacitor-current feedback in the rectifier mode and inverter mode. By selecting $R_{ad2} = 600\ \Omega$, the low-pass filter is thus designed based on Eq. (12.15), and its parameters are $\lambda_{ad2} = 33$, $\omega_{ad2} = 3333$ rad/s in the rectifier mode and $\lambda_{ad2} = 33$, $\omega_{ad2} = -3333$ in the inverter mode. It can be seen that the waveforms are also stable compared to Fig. 12.24, which verifies the low-pass filter capacitor-current feedback can dampen the system. Moreover, despite realizing the same virtual resistance, the step responses are different, where the settling time of the low-pass filter feedback is larger than the proportional feedback as seen from Figs. 12.27 and 12.28, which indicate the bandwidth of the DC-link current control with using the proportional feedback is larger than when using the low-pass filter feedback. The reason is that the proportional feedback induces a virtual capacitor, which would shift the resonances to lower frequencies and further widen the closed-loop bandwidth of the single-loop DC-link current control.

Different from the capacitor-voltage feedback, it is not possible to use the capacitor-current feedback for realizing a small damping resistance in both proportional and low-pass filter feedback. The reason is that implementing a small virtual resistance needs a large value of k_{ad2} or λ_{ad2}, which will result in overmodulation of the converter.

12.3.2.3 Inductor-current feedback (see Fig. 12.14)

Fig. 12.29 presents the measured waveforms when using the proportional inductor-current feedback in the rectifier mode and inverter mode. Since a *RL* damper is induced, which is not allowed to calculate a proper damping resistance, the feedback gain is given directly and the provided virtual resistance is obtained according to Eq. (12.17). Thus, k_{ad3} is designed to be 0.0067 and the virtual resistance is $R_{ad3} = 25\ \Omega$. It can be seen that the waveforms of the step responses are stable compared to them in Fig. 12.24, which proves the proportional inductor-current feedback can be used to form an active damping loop to the single-loop DC-link current control. The DC-link controller determines the dynamics of the step responses, and thus the responses in the rectifier mode and inverter mode are the same.

Since a pure damping resistance is easier to be designed from the passive damping experience, high-pass filter—based capacitor-voltage feedback and low-pass filter—based capacitor-current feedback are recommended when considering the damping performance. Furthermore, the high-pass filter

This book belongs to Kitab Liaison (ocd1996@gmail.com) Copyright Elsevier 2023

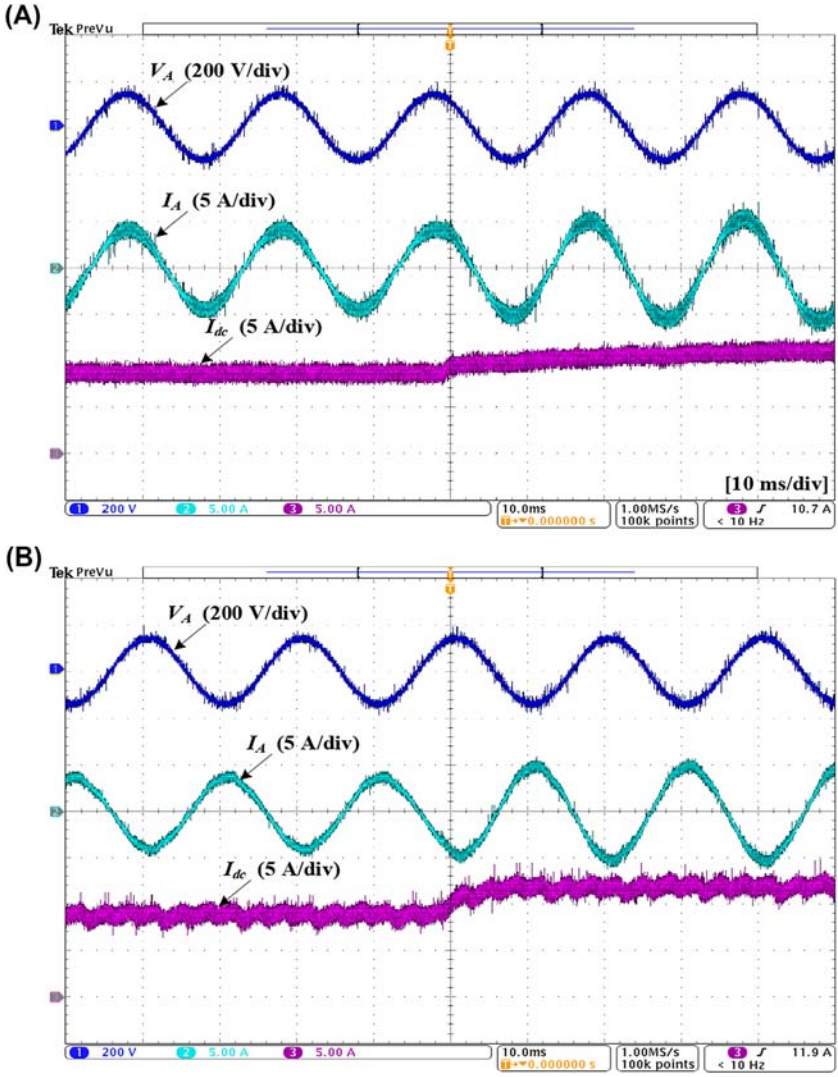

FIGURE 12.28 Measured waveforms of the PCC voltage, input current, and DC-link current with low-pass filter capacitor-current feedback (see Figs. 12.13 and 12.20B). (A). Rectifier mode. (B). Inverter mode.

feedback gain is sensitive to amplify the high frequency noises which may not be captured in the modeling in a practical system. Thus, low-pass filter—based capacitor-current feedback is more flexible to be designed in utilizations of high switching CSCs.

This book belongs to Kitab Liaison (ocd1996@gmail.com)
Copyright Elsevier 2023

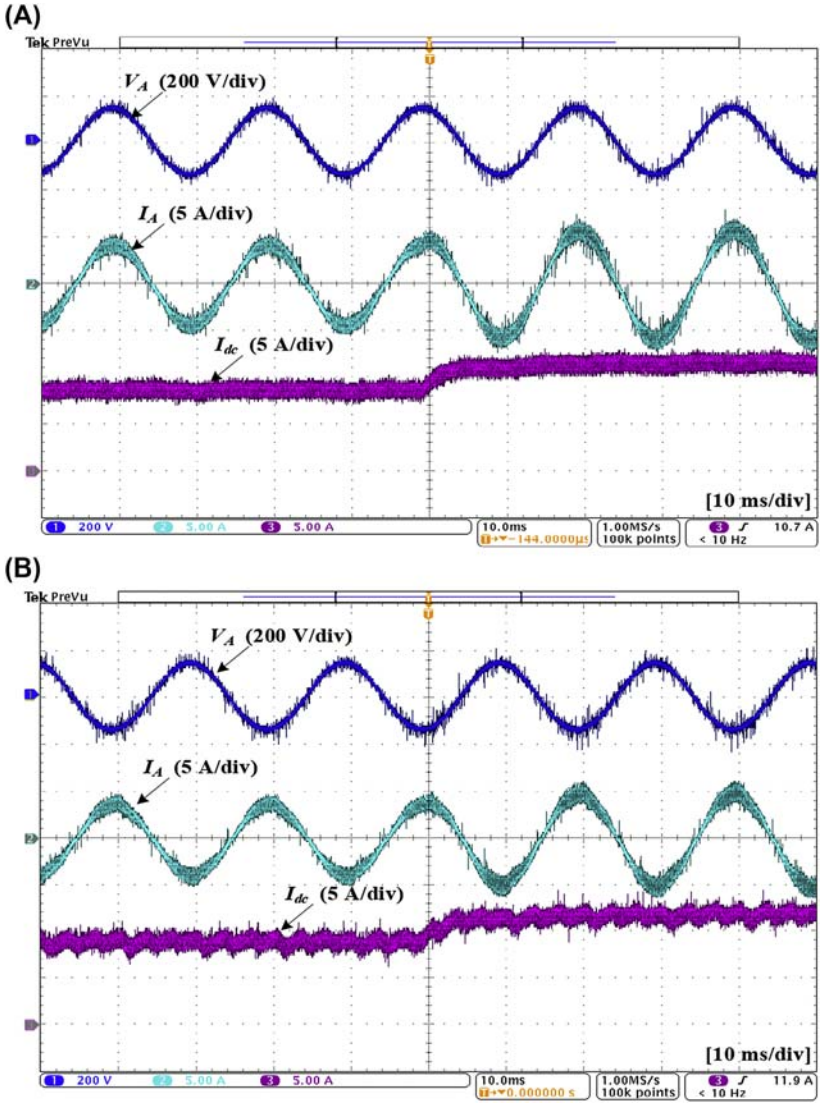

FIGURE 12.29 Measured waveforms of the PCC voltage, input current, and DC-link current with proportional inductor-current feedback (see Fig. 12.14). (A). Rectifier mode. (B). Inverter mode.

12.4 Summary

This chapter has addressed the stability and control of high switching frequency CSCs. The stability of single-loop DC-link current control is discussed, where the stable region is derived, i.e., the CSC can be stabilized when

This book belongs to Kitab Liaison (ocd1996@gmail.com) Copyright Elsevier 2023

the input *LC*-filter resonance frequency is in low frequency range. Furthermore, active damping methods are developed for the unstable cases. The capacitor-voltage feedback, capacitor-current feedback, and inductor-current feedback are analyzed to be designed for active damping, and proved to be effective for stabilizing the system.

References

[1] S. Anand, S.K. Gundlapalli, B.G. Fernandes, Transformer-less grid feeding current source inverter for solar photovoltaic system, IEEE Trans. Ind. Electron. 61 (10) (October, 2014) 5334−5344.

[2] B. Sahan, A.N. Vergara, N. Henze, A. Engler, P. Zacharias, A single-stage PV module integrated converter based on a low-power current-source inverter, IEEE Trans. Ind. Electron. 55 (7) (July, 2008) 2602−2609.

[3] J. Dai, D. Xu, B. Wu, A novel control scheme for current-source-converter-based PMSG wind energy conversion systems, IEEE Trans. Power Electron. 24 (4) (April, 2009) 963−972.

[4] Q. Wei, B. Wu, D. Xu, N.R. Zargari, Further study on a PWM current-source-converter-based wind energy conversion system considering the dc-link voltage, IEEE Trans. Power Electron. 34 (6) (June, 2019) 5378−5387.

[5] F. Xu, B. Guo, Z. Xu, L.M. Tolbert, F. Wang, B.J. Blalock, An all-SiC three-phase buck rectifier for high-efficiency data center power supplies, IEEE Trans. Ind. Appl. 51 (3) (May-June, 2015) 2388−2397.

[6] B. Guo, F. Wang, E. Aeloiza, A novel three-phase current source rectifier with delta-type input connection to reduce the device conduction loss, IEEE Trans. Power Electron. 31 (2) (February, 2016) 1074−1084.

[7] H. Chen, A. Prasai, R. Moghe, K. Chintakrinda, D. Divan, A 50-kVA three-phase solid-state transformer based on the minimal topology: Dyna-C, IEEE Trans. Power Electron. 31 (12) (December, 2016) 8126−8137.

[8] H. Chen, D. Divan, Soft-switching solid-state transformer (S4T), IEEE Trans. Power Electron. 33 (4) (April, 2018) 2933−2947.

[9] P. Parkatti, M. Salo, H. Tuusa, Experimental results for a current source shunt active power filter with series capacitor, Proc. Power Electron. Spec. Con. (PESC) (2008) 3814−3818.

[10] S. Papadopoulos, M. Rashed, C. Klumpner, P. Wheeler, Investigations in the modeling and control of a medium-voltage hybrid inverter system that uses a low-voltage/low-power rated auxiliary current source inverter, IEEE J. Emerg. Sel. Topics Power Electron. 4 (1) (March, 2016) 126−140.

[11] C. Saber, D. Labrousse, B. Revol, A. Gascher, Challenges facing PFC of a single-phase on-board charger for electric vehicles based on a current source active rectifier input stage, IEEE Trans. Power Electron. 31 (9) (September, 2016) 6192−6202.

[12] X. Wang, L. Harnefors, F. Blaabjerg, Unified impedance model of grid-connected voltage-source converters, IEEE Trans. Power Electron. 33 (2) (February, 2018) 1775−1787.

[13] Y. Sato, T. Kataoka, A current-type PWM rectifier with active damping function, IEEE Trans. Ind. Appl. 32 (3) (May-June, 1996) 533−541.

[14] J.C. Wiseman, B. Wu, Active damping control of a high-power PWM current-source rectifier for line-current THD reduction, IEEE Trans. Ind. Electron. 52 (3) (June, 2005) 758−764.

This book belongs to Kitab Liaison (ocd1996@gmail.com) Copyright Elsevier 2023

[15] Y.W. Li, Control and resonance damping of voltage-source and current-source converters with LC filters, IEEE Trans. Ind. Electron. 56 (5) (May, 2009) 1511−1521.

[16] Z. Bai, H. Ma, D. Xu, B. Wu, Y. Fang, Y. Yao, Resonance damping and harmonic suppression for grid-connected current-source converter, IEEE Trans. Ind. Electron. 61 (7) (July, 2014) 3146−3154.

[17] F. Liu, B. Wu, N.R. Zargari, M. Pande, An active damping method using inductor-current feedback control for high-Power PWM current-Source rectifier, IEEE Trans. Power Electron. 26 (9) (September, 2011) 2580−2587.

[18] X. Guo, Y. Yang, X. Zhang, Advanced control of grid-connected current source converter under unbalanced grid voltage conditions, IEEE Trans. Ind. Electron. 65 (12) (December, 2018) 9225−9233.

[19] M. Belkhayat, Stability Criteria for AC Power Systems with Regulated Loads, Ph.D. Dissertation, Purdue University, December, 1997.

[20] S.G. Parker, B.P. McGrath, D.G. Holmes, Regions of active damping control for LCL filters, IEEE Trans. Ind. Appl. 50 (1) (January-February, 2014) 424−432.

[21] D. Pan, X. Ruan, C. Bao, W. Li, X. Wang, Capacitor-current-feedback active damping with reduced computation delay for improving robustness of LCL-type grid-connected inverter, IEEE Trans. Power Electron. 29 (7) (July, 2014) 3414−3427.

[22] X. Wang, F. Blaabjerg, P.C. Loh, Grid-current-feedback active damping for LCL resonance in grid-connected voltage-source converters, IEEE Trans. Power Electron. 31 (1) (January, 2016) 213−223.

This book belongs to Kitab Liaison (ocd1996@gmail.com) Copyright Elsevier 2023

Chapter 13

High-power current source converters

Li Ding, Yunwei Li
Department of Electrical and Computer Engineering, University of Alberta, Edmonton, AB, Canada

13.1 Introduction

Current source converter (CSC) enjoys superior features such as four-quadrant operation, low dv/dt outputs, inherent short circuit protection, as well as voltage boost capacity, which make it widely adopted in industry [1]. There are mainly three types of CSCs, such as current source DC−DC converter, current source rectifier (CSR), and current source inverter (CSI), which have been studied for decades. Compared to the voltage source converter (VSC), which holds a constant voltage on the DC link, the CSC is fed by a constant DC current and the AC-side currents are pulse width modulation (PWM) waveforms. A capacitor filter is required in CSC output side for the commutation of devices and a DC inductor is needed to support the constant DC current. Among which, the load-communicated converter (LCC) and the PWM CSC are commonly used for high-power applications, such as high-voltage direct current (HVDC) systems and medium-voltage (MV) drives. The silicon-controlled rectifier (SCR) thyristors are adopted in LCC whose commutation is assisted by the load with a leading power factor, while integrated gate-commutated thyristor or gate turn-off thyristor is used in PWM CSC, which can be fully controlled. Moreover, PWM CSR and CSI can also be adopted in low-power applications such as photovoltaics (PV) and electrical vehicles (EVs) with the advancement of commercial high switching reverse-blocking devices. On the other hand, the current source DC−DC converters have been widely used for DC voltage boost circuit and multiple-stage voltage conversation, such as data centers.

This chapter focuses on the high-power PWM CSCs for rectifier or inverter applications, particularly in tranformerless MV drives and the essential technical issues. To increase the system power capacity, reliability, and reduce the output harmonics, the parallel connection of modular CSCs with multilevel

Control of Power Electronic Converters and Systems. https://doi.org/10.1016/B978-0-12-819432-4.00003-2
Copyright © 2021 Elsevier Ltd. All rights reserved.

This book belongs to Kitab Liaison (ocd1996@gmail.com)
Copyright Elsevier 2023

current output is becoming a more popular option, which attracted increased attention in recent years. The parallel CSC topologies can be divided into two categories: independent DC link and shared DC link, depends on the DC-link currents need to be shared or not. For parallel CSC-fed high-power MV drives, one of the main considerations is the common-mode voltage (CMV), which can cause motor winding isolation failure if not suppressed. The circulating current (CC) flowing through the parallel modules which cause increased current rating and power loss is another essential issue. Moreover, the DC current balance will be the priority task in shared DC-link structure, since only the total DC current can be regulated. Therefore, the modulation strategies should be designed properly for different parallel CSC structures, and modular modulation method with easy-to-implement ability is always a desirable feature.

13.2 Current source converters and applications

The CSC had been widely adopted in industry for decades and the trends changed with the development of CSC semiconductors. Typical application examples are mainly involved in high-power sites such as HVDC systems and high-power MV drives. Nowadays, more and more PWM CSCs by adopting wide bandgap (WBG) devices for low-power high-switching applications such as PV, EVs, and data center power supplies have been constantly researched.

This section mainly focuses on the CSC-based high-power applications by introducing the typical topologies, modulations, as well as control strategies. More specifically, the transformerless PWM CSC-fed drive will be in focus due to its superior features with reduced size and cost by replacing the normally used isolation transformer. The essential issues that emerged in CSC-fed drives such as CMV and common-mode (CM) resonance are addressed. Various types of CSC modulations such as space vector modulation (SVM), selective harmonic elimination (SHE), carrier-based PWM, and their features will also be investigated.

13.2.1 Thyristor-based technology

Thyristor-based LCC enjoys a long history for the application of HVDC and high-power drives due to its attractive features such as the high-power capacity, lower power losses, and lower cost. HVDC is the preferred connection method for a large offshore grid with long distance to the main grid, which enjoys the advantages such as full power flow control, low cable power losses, and large power transmission capacity [1]. A 12-pulse LCC-based HVDC (LCC-HVDC) is shown in Fig. 13.1, where two identical six pulse converters are series connected along with the use of phase-shifting transformer to reduce the fifth and seventh harmonics. Meanwhile, multiple

This book belongs to Kitab Liaison (ocd1996@gmail.com) Copyright Elsevier 2023

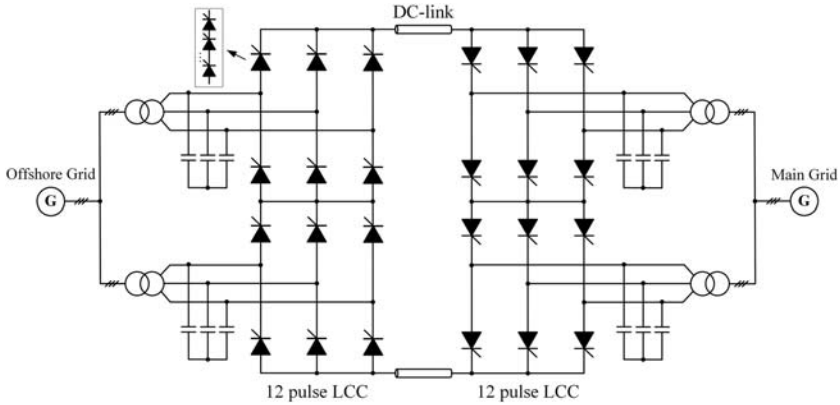

FIGURE 13.1 Load communicated converter (LCC)-based high-voltage direct current configuration.

devices are connected in series to reach higher voltage levels. Although the LCC-HVDC enjoys superior performance with high reliability and low cost, the large footprint due to the needs of the bulky filter and reactive power source makes it a bit challenging for offshore applications [2].

Another typical industry application of CSC is high-power (>1 MW) MV drive applications, such as for pumps, fans, compressors, etc. [3]. Among them, load-communicated inverter (LCI) topology is particularly suitable for very large synchronous motor (SM) drives with a power rating up from 10 to 100 MW due to low manufacturing cost and high-power rating of SCR 2devices. Fig. 13.2 illustrates a typical configuration of LCI-fed SM drive

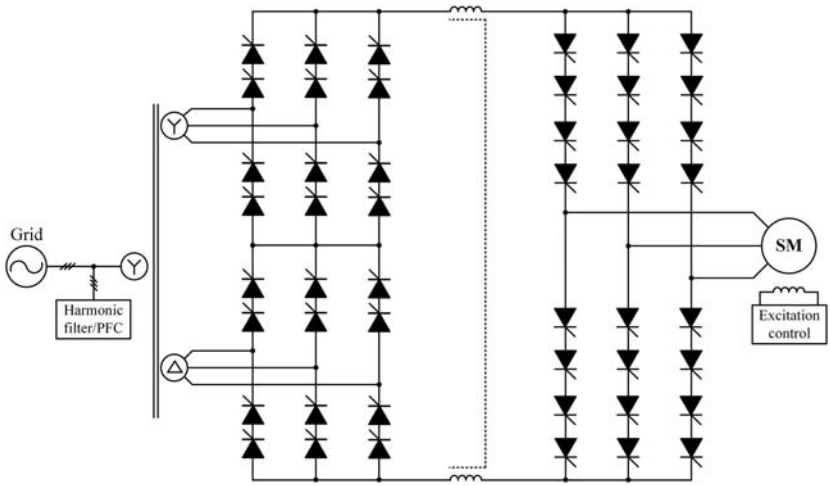

FIGURE 13.2 Load-communicated inverter−fed synchronous motor (SM) drive system.

This book belongs to Kitab Liaison (ocd1996@gmail.com)
Copyright Elsevier 2023

system, which adopts a 12-pulse SCR rectifier with a DC-link choke to provide a controllable DC current. The number of series-connected SCRs depends on the voltage rating and utility supply. The main features of LCI-fed synchronous drive include low cost, high efficiency, and reliability. However, it has some drawbacks such as high torque pulsation, poor dynamic response, and variable input power factor.

13.2.2 PWM CSC-based medium-voltage drives

The PWM CSC by adopting fully controlled semiconductor with turn-off capacity enjoys advantages such as sinusoidal outputs and reactive power control. The grid-side line current quality and power factor can be improved through PWM CSR with power factor compensation and PWM techniques. The low-order harmonics can easily be filtered out. As a result, it is a preferred choice for many MV drives with power rating from 1 to 10 MW [4]. The synchronous gate−commutated thyristor (SGCT) can be connected in series to increase the power capacity. The typical configuration of back-to-back PWM CSC-fed MV drives for 6.6 kV application is shown in Fig. 13.3, which consists of the CSR, DC-link inductor, CSI, and input/output filters.

Typically, an isolation transformer is needed for MV drives to reduce the inverter-side CMV, which is excited by the switching actions of the semiconductor devices. Such CMV can cause motor shaft voltage, bearing current, which would cause premature failure of the motor winding isolations if not mitigated [5]. PWM CSC-based MV drives have been popular due to its capability of eliminating the isolation transformer by using a CM choke or integrated CM and differential mode choke in the DC link [1]. Therefore, the system power losses, cost, and size caused by the bulky transformer can be effectively reduced.

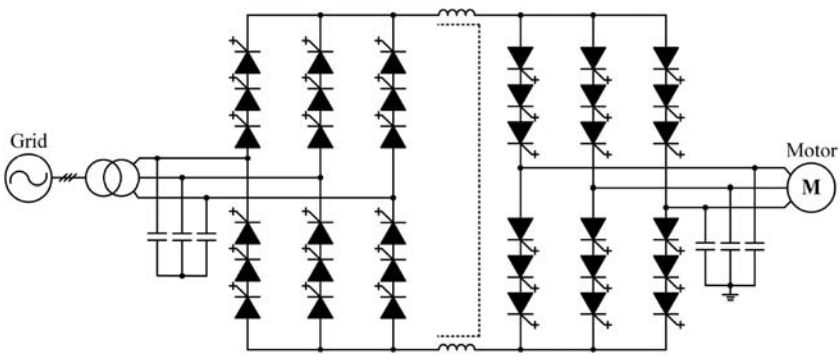

FIGURE 13.3 PWM CSC-fed MV drive with isolation transformer. *CSC*, current source converter; *MV*, medium-voltage; *PWM*, pulse width modulation.

This book belongs to Kitab Liaison (ocd1996@gmail.com) Copyright Elsevier 2023

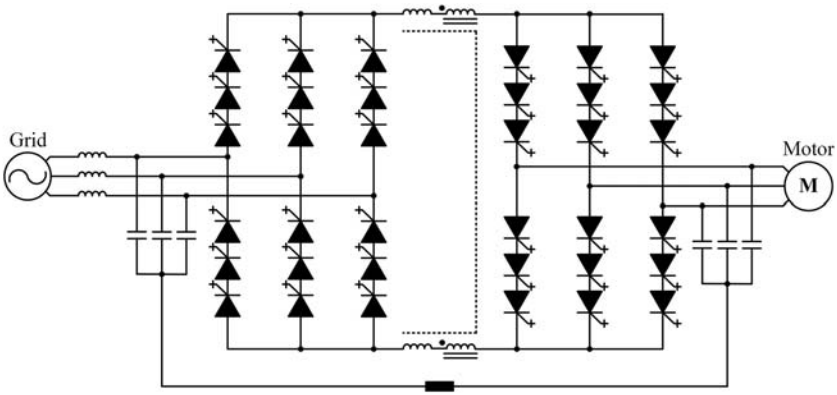

FIGURE 13.4 Transformerless PWM CSC-fed MV drive. *CSC*, current source converter; *MV*, medium-voltage; *PWM*, pulse width modulation.

A transformerless CSC-fed drive configuration is shown in Fig. 13.4, where the isolation or phase-shifting transformer is replaced with a three-phase reactor. However, one of the major concerns in transformerless CSC-fed drive is the CMV, which is determined by the switching actions of the semiconductor devices. To reduce the CMV, an integrated DC choke structure which combines the differential and CM inductances with a single core is equipped on the DC link. The neutral points of input and output filter are connected through a small damping resistor to form a CM loop, where the CM choke can block the majority of CMV. The damping resistor is adopted to suppress the potential CM resonance due to the series connection of CM choke and the capacitor filters. The size and cost of the CM choke strongly depend on the magnitude of CMV and CMC, which are related to the implemented modulation strategies. As a result, it is always desirable to suppress the CMV with improved control and modulation methods.

13.2.3 More potential application

To utilize the superior features of PWM CSC such as reactive power control, operation without commutation voltage, and relatively small footprint with improved harmonic performance over the LCC schemes, a hybrid CSC-based HVDC system was proposed in Ref. [6], which adopted a PWM CSC on the offshore wind farm side to reduce the footprint and connected to onshore grid through DC cable and LCC as shown in Fig. 13.5.

Such topology can combine the advantages of both PWM CSC and LCC techniques in offshore wind applications. To further eliminate the costly and bulky offshore step-up transformer, some literature studied the series-connected PWM CSC system to increase the power rating for high-voltage applications, where each CSC can be regarded as a modular unit. Series-connected PWM

This book belongs to Kitab Liaison (ocd1996@gmail.com) Copyright Elsevier 2023

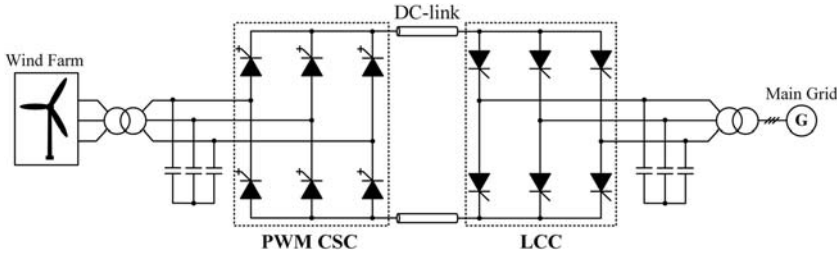

FIGURE 13.5 Hybrid current source high-voltage direct current system for offshore wind power application.

CSC employed on both offshore generator side and onshore grid side was introduced in Ref. [7]. For the offshore generator side, the DC voltage in the range of 100−150 kV can easily be achieved by cascading appropriate numbers of MV wind generators through the PWM CSCs and consequently eliminate the costly and bulky step-up transformer. Moreover, multiple series-connected converters instead of single converter with series-connected devices on the grid side can eliminate the challenge of voltage sharing on each series device. Besides, a mixed series and parallel CSC system as shown in Fig. 13.6 had been researched recently, which can further improve the system performance by combining the advantages of series or parallel modular structure [8].

Besides the high-power applications introduced earlier, CSC can also be adopted in low-power applications with high switching frequency, such as grid-interfacing PV converter, EV application, and data center power supplies.

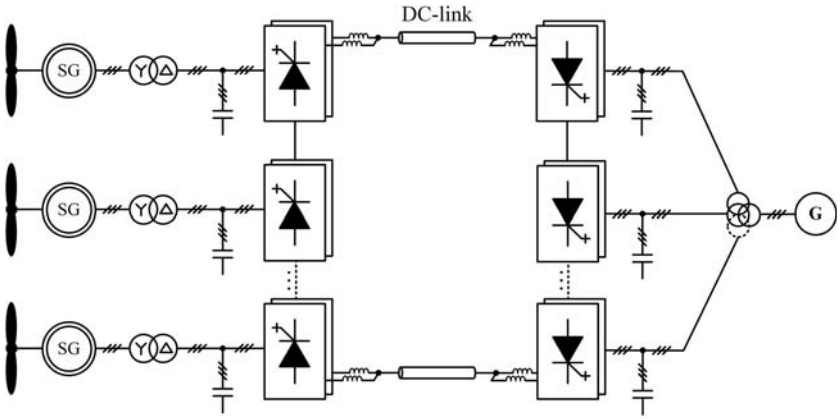

FIGURE 13.6 Series−parallel-connected PWM CSC for HVDC application. *CSC*, current source converter; *HDVC*, high-voltage direct current; *PWM*, pulse width modulation.

This book belongs to Kitab Liaison (ocd1996@gmail.com) Copyright Elsevier 2023

With the help of the boost capacity of CSI, the boost DC/DC converter can be eliminated compared with the two-stage DC/DC plus DC/AC voltage source inverter (VSI)-based system in those applications. Therefore, higher efficiency and a simpler control scheme can be achieved [9,10]. Meanwhile, the CSC-based system enjoys better reliability due to the inherent short circuit protection and elimination of unreliable DC capacitors in the VSI. Moreover, the near sinusoidal output voltage and current can reduce the dv/dt-related electromagnetic noises, as well as the motor losses and bearing current for drive (such as EV) applications.

Other high-frequency CSC applications such as data center power supply by utilizing the buck CSR feature were reported in Ref. [11]. The WBG devices SiC JFET [12] and GaN-HEMT—based reverse-blocking switches adopted for CSC had been studied for efficiency enhancement with much higher switching frequency operation. The newly developed dual-gate monolithic bidirectional GaN e-FET was adopted for CSC-fed motor drives [13], where the power density and efficiency could be significantly increased and competitive with the VSC counterparts. Due to these breakthroughs of CSC semiconductors, the CSCs are likely to be adopted for more and more potential applications in the future.

13.3 Parallel CSC system and modulation strategies

To increase the system power capacity and improve current quality with multilevel output, parallel CSC operation is a practical and easy-to-implement choice. It also provides benefits of modularity, simple structure, improved fault tolerance, and reliability. There are mainly two types of parallel CSC configurations: independent DC link and shared DC link. For independent DC-link structure, the DC-link currents for each CSC module can be controlled independently; thus, most of the modulations or control methods adopted in an independent DC-link structure are mainly developed to improve the PWM sequence, AC output quality, suppress the CM resonance, and reduce CC by reducing the CMV [14].

On the other hand, with shared DC-link parallel structure, the DC current balance is the main concern, which can degrade the AC output quality, make the system unstable, and even damage the devices due to overcurrent [15]. Since only the total DC-link current can be controlled, most of the current balance schemes investigated in literature were choosing or adjusting proper dwell time of small and medium space vectors in the SVM process. In this section, shared DC-link parallel CSC will be selected and its main challenges for MV drive application are introduced. Then, several popular CSC modulation strategies developed for parallel CSC systems will be presented and compared.

This book belongs to Kitab Liaison (ocd1996@gmail.com) Copyright Elsevier 2023

13.3.1 Parallel CSC topology

Series or parallel connected devices to increase the voltage or current rating for higher power applications had been widely adopted in industry, where the series of parallel connected devices can be treated as a single device but with increased power rating. Typically, these devices are driven with synchronous gating signals to achieve the desired power-sharing performance. Therefore, the system output features in terms of PWM sequence, average switching frequency, and harmonic distortion almost stay the same. On the contrary, series or parallel connection based on the converter modules can also easily increase the system power rating. More importantly, the parallel converters can bring other advantages such as improved output quality, reliability, as well as superior control strategy design. As a result, parallel-connected CSCs are becoming popular choices.

There are two types of parallel CSC structures, which are independent DC-link structure and shared DC-link structure. For independent DC-link structure, multiple back-to-back PWM CSC modules are directly connected in parallel with shared input and output filters, where each module has an independent DC link and the current can be controlled through the CSR independently. Since the DC current balance is not a big issue for each module, most of the modulations and control strategies were developed to achieve superior output waveforms and smaller CMV.

On the other hand, a shared DC-link parallel CSC was also investigated in literature where paralleled PWM CSRs or CSIs shared common DC link. A typical shared DC-link structure is shown in Fig. 13.7, where the total DC-link

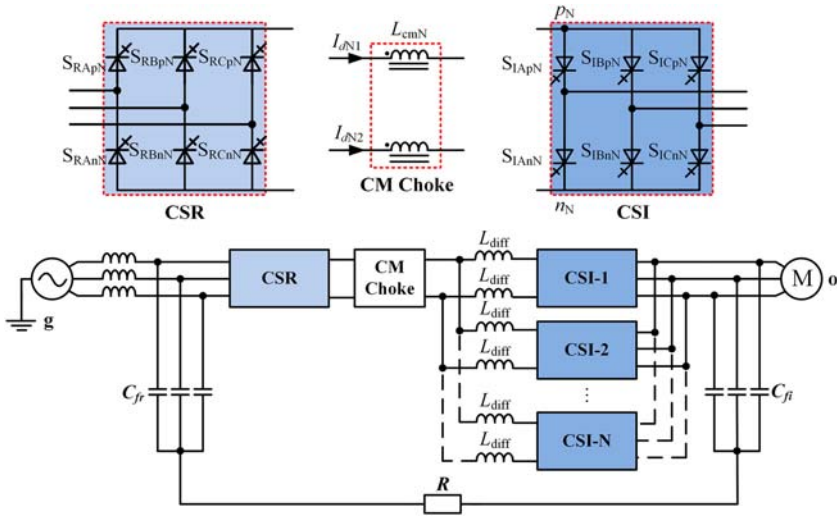

FIGURE 13.7 Transformerless parallel current source converter system with shared DC link.

This book belongs to Kitab Liaison (ocd1996@gmail.com) Copyright Elsevier 2023

current is provided by the shared CSR, and each sub-DC-link current needs to be balanced through proper switching sequence design. Otherwise, the imbalanced currents can result in large CC, deteriorate the output currents, and lead to overcurrent issues which would damage the semiconductor. Therefore, DC current balance strategy development is the priority task for this parallel structure. Meanwhile, other challenges such as CMV and CM resonances should also be considered.

13.3.2 CSC modulation strategies

The performance of CSC is strictly dependent on the modulation strategies. There are three major CSC PWM methods developed as listed in Fig. 13.8. They are SVM, SHE, and carrier-based PWM. The carrier-based PWM can be further divided into trapezoidal PWM (TPWM), bi-trilogical SPWM (BTSPWM) [16], six-step direct PWM (SS-DPWM) [17], and direct duty-ratio PWM (DDPWM) [18]. Both SVM and SHE are difficult to design for N-CSC ($N \geq 3$) parallel system due to a large number of redundant switching state and switching angle optimization. On the other hand, the carrier-based PWM enjoys inherent modularity and can be easily extended into multiple parallel CSC systems by simply shifting the carriers.

The small DC current utilization range and poor harmonic performance of TPWM by adopting trapezoidal references limited its application. The BTSPWM is derived from the developed VSC PWM through logic translation. The line-to-line voltage of VSC is dual to line current of CSC, which causes three-phase line currents that lead to their references by 30 degrees and the linear DC current utilization range is 0−0.866. Meanwhile, the switching frequency of BTSPWM is the same as the carrier frequency. By injecting

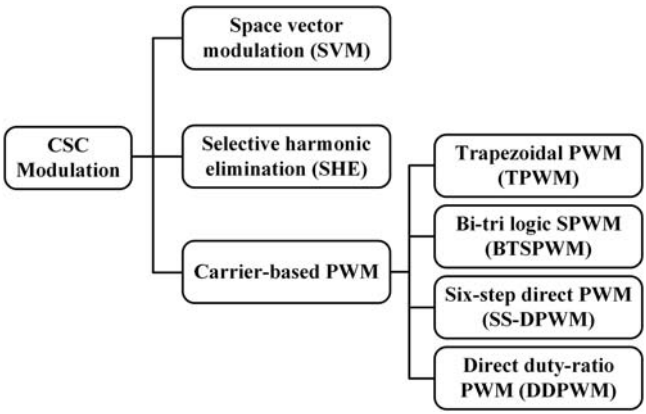

FIGURE 13.8 Modulation strategies of current source converter (CSC).

This book belongs to Kitab Liaison (ocd1996@gmail.com) Copyright Elsevier 2023

third-order harmonics, the DC current utilization range can be increased to 0−1. Among the carrier-based PWMs, DDPWM enjoys the inherent small CMV feature; thus, the DDPWM will be in focus when introducing the carrier-based PWMs.

13.3.2.1 Space vector modulation

Based on the conduction constraint of CSC, only two switches in the converter conduct at any time instant, one in the top half of the CSC bridge and the other in the bottom half. Therefore, the three-phase inverter has a total of nine switching states, which can be classified as six active switching states (I_1−I_6) and three zero switching states (I_7−I_9) as shown in Fig. 13.9. The space vector diagram can be divided into six vectors and the linear modulation range is 0−1. The switching state can be represented by two digital numbers to indicate the turn-on switches. For example, the zero state [1,4] represents that switches S_1 and S_4 in the phase leg A conduct simultaneously.

The current reference can be synthesized by two adjacent active vectors and one zero vector, and the dwell time of each vector is calculated as

$$\begin{cases} T_1 = m_a \sin(\pi/6 - \theta)T_s \\ T_2 = m_a \sin(\pi/6 + \theta)T_s\,; \quad -\dfrac{\pi}{6} < \theta \le \dfrac{\pi}{6} \\ T_0 = T_s - T_1 - T_2 \end{cases} \tag{13.1}$$

where T_1 and T_2 are the total dwell time of the two adjacent active vectors, while T_0 is the dwell time of zero vector. T_s is the carrier period and θ indicates the current reference position in each sector.

13.3.2.2 Selective harmonic elimination

SHE is an offline modulation scheme, which can eliminate a specific number of low-order unwanted harmonics in the output current. Normally, the pause angles are precalculated and imported into the digital controller. Fig. 13.10

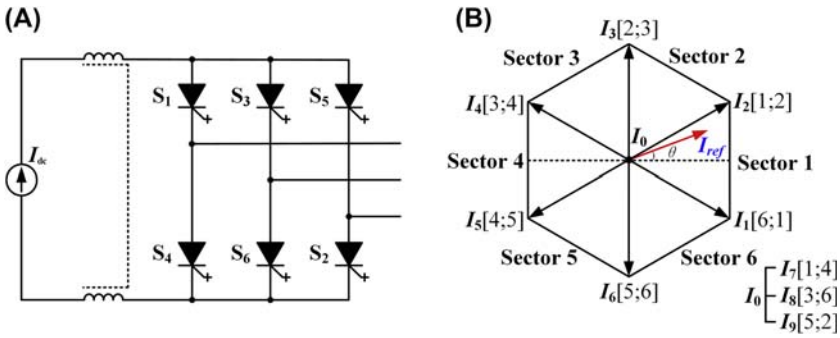

FIGURE 13.9 Space vector modulation of current source converter (CSC). (A) CSC diagram, (B) space vector diagram.

This book belongs to Kitab Liaison (ocd1996@gmail.com) Copyright Elsevier 2023

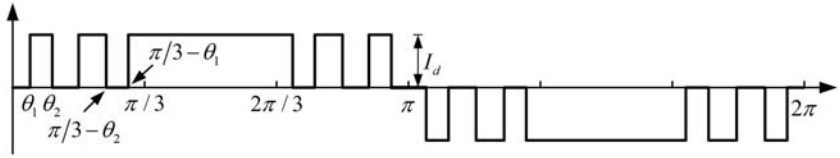

FIGURE 13.10 Example of selective harmonic elimination modulation.

shows a typical SHE waveform; there are five pulses per half-cycle with five switching angles in the first-quarter period, where only two out of the five angles are independent as the PWM is half-wave symmetric and the fifth and seventh harmonics can be eliminated. Multilevel SHE was proposed in Ref. [19] for parallel CSC applications, where the pause angle design will be more flexible, and more orders of unwanted harmonics can be eliminated to achieve better output current. However, the pause angle calculation is much more complex due to a large number of freedoms.

13.3.2.3 Direct duty-ratio pulse width modulation

The DDPWM was first introduced in Ref. [18], which can directly produce the gating signals of CSC without any logic translation. Besides the dual relationship, the isomorphic relationship between VSC and CSC is presented in Ref. [20], which can sufficiently reveal the essential principle of DDPWM. It is verified that the 3-phase CSC and single phase 3-level VSC are isomorphic pairs and they shared the same modulation features.

To achieve DDPWM, the six switches are identified as $S_{p\max}/S_{n\max}$, $S_{p\mathrm{mid}}/S_{n\mathrm{mid}}$, and $S_{p\min}/S_{n\min}$ according to the magnitude of three-phase references (I_A*, I_B*, and I_C*). The output phases are renamed as Max-Mid-Min phase instead of A-B-C phase. The maximum, medium, and minimum values ($I_{\max}$ and $I_{\min}$) among the three-phase references can be obtained as $I_{\max} = \max$ (I_A*, I_B*, I_C*) and $I_{\min} = \min$ (I_A*, I_B*, I_C*) by comparing their magnitudes. In Max-Mid-Min phase, $I_{\max}$, I_{mid}, and $I_{\min}$ are synthesized by $S_{p\max}/S_{n\max}$, $S_{p\mathrm{mid}}/S_{n\mathrm{mid}}$, and $S_{p\min}/S_{n\min}$, respectively. The waveforms of $I_{\max}$ and $I_{\min}$ with balanced three-phase references are shown in Fig. 13.11A. As it can be seen, $I_{\max}$ is always bigger than zero, and $I_{\min}$ is always smaller than zero. Therefore, $I_{\max}$ can be synthesized by using I_{dc} and zero, and $I_{\min}$ can be synthesized by using -I_{dc} and zero. That means the lower leg of Max phase $S_{n\max}$ and upper leg of Min phase $S_{p\min}$ are never turned on ($S_{n\max} = S_{p\min} = 0$). As one and only one switch among the three upper and lower switches should be on, which can be restricted by $S_{p\max} + S_{p\mathrm{mid}} + S_{p\min} = 1$ and $S_{n\max} + S_{n\mathrm{mid}} + S_{n\min} = 1$. The logical switch relations are expressed as

$$S_{p\max} = \begin{cases} 1, & if\ \ I_{\max} >= C_1 \\ 0, & if\ \ I_{\max} < C_1 \end{cases};\ \ S_{n\min} = \begin{cases} 1, & if\ \ I_{\min} < C_2 \\ 0, & if\ \ I_{\min} >= C_2 \end{cases} \tag{13.2}$$

This book belongs to Kitab Liaison (ocd1996@gmail.com) Copyright Elsevier 2023

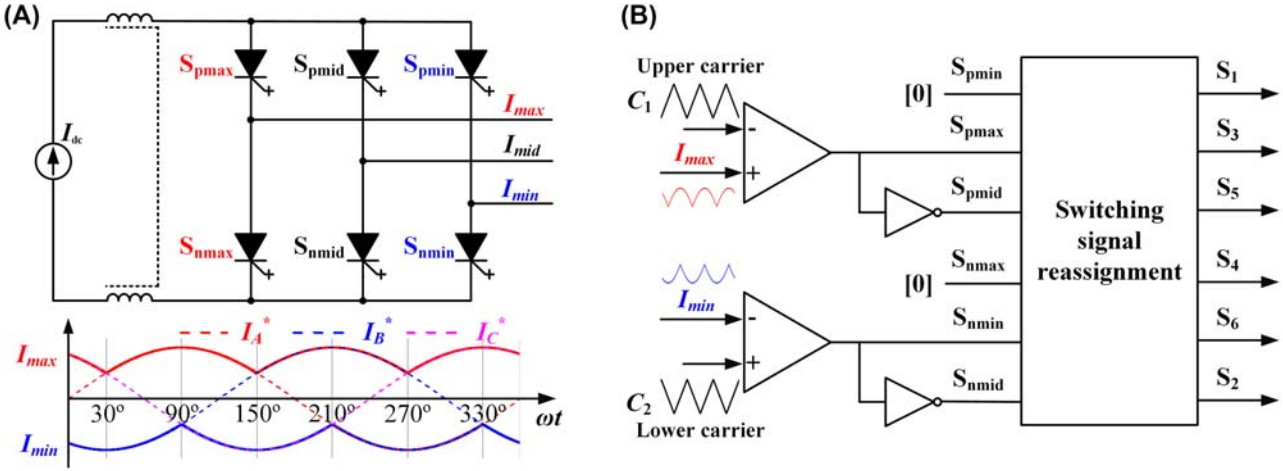

FIGURE 13.11 Direct duty-ratio pulse width modulation principle. (A) Current source converter diagram in Max-Mid-Min phase, (B) digital implement.

This book belongs to Kitab Liaison (ocd1996@gmail.com)

Copyright Elsevier 2023

where C_1 is the upper carrier and C_2 is the lower carrier. Once the gating signals of $S_{p\max}$, $S_{p\mathrm{mid}}$, $S_{p\min}$, $S_{n\max}$, $S_{n\mathrm{mid}}$, and $S_{n\min}$ are obtained based on Eq. (13.2), they can be reassigned to A-B-C phase according to the magnitudes of three-phase current references as shown in Fig. 13.13B. For example, when $I_{\max} = I_C{}^*$, $I_{mid} = I_A{}^*$, and $I_{\min} = I_B{}^*$, the switching signals can be reassigned as $S_{Cp} = S_{p\max}/S_{Cn} = S_{n\max}$; $S_{Ap} = S_{p\mathrm{mid}}/S_{An} = S_{n\mathrm{mid}}$; and $S_{Bp} = S_{p\min}/S_{Bn} = S_{n\min}$.

13.3.2.4 Comparison of different CSC modulations

The PWM output features such as total harmonic distortion (THD), harmonic spectrum, switching frequency, as well as CMV are highly dependent on the sequence design. The PWM sequences of different modulations are compared as shown in Table 13.1, where the numbers 1 to 6 represent the six active vectors and 7 to 9 mean the three zero states.

The PWM sequence of SVM is very flexible and different segment forms can easily be achieved. Normally, the three-segment SVM is adopted for high-power CSC application in order to reduce switching losses. Both SHE and TPWM just utilize the active states, which result in a relatively low switching frequency. Among the three carrier-based SPWMs, the BTSPWM has 6 switching actions in each sampling period and the resulted switching frequency is the same as the carrier frequency. Both SS-DPWM and DDPWM are five-segment PWM and the switching frequency is two-third of the carrier frequency. All three SPWMs adopt two adjacent active vectors and one zero

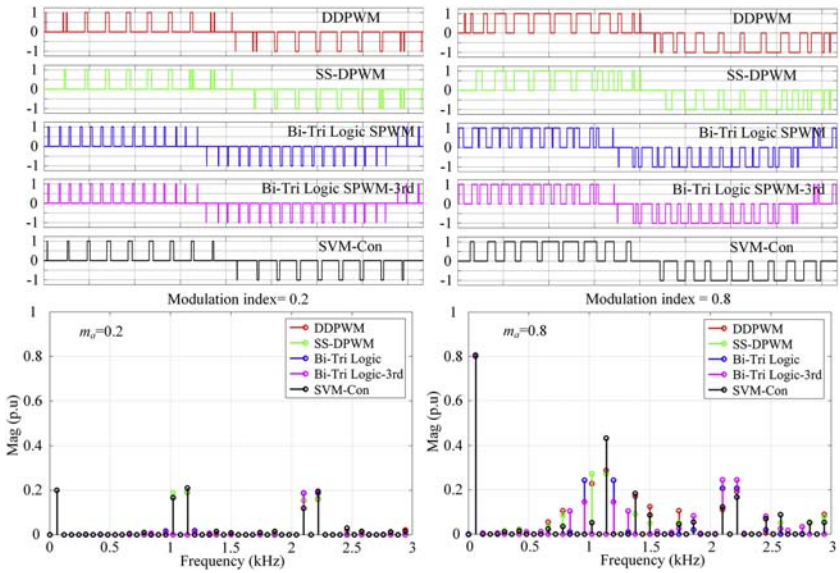

FIGURE 13.12 Pulse width modulation waveforms and harmonic distribution with different modulations.

This book belongs to Kitab Liaison (ocd1996@gmail.com) Copyright Elsevier 2023

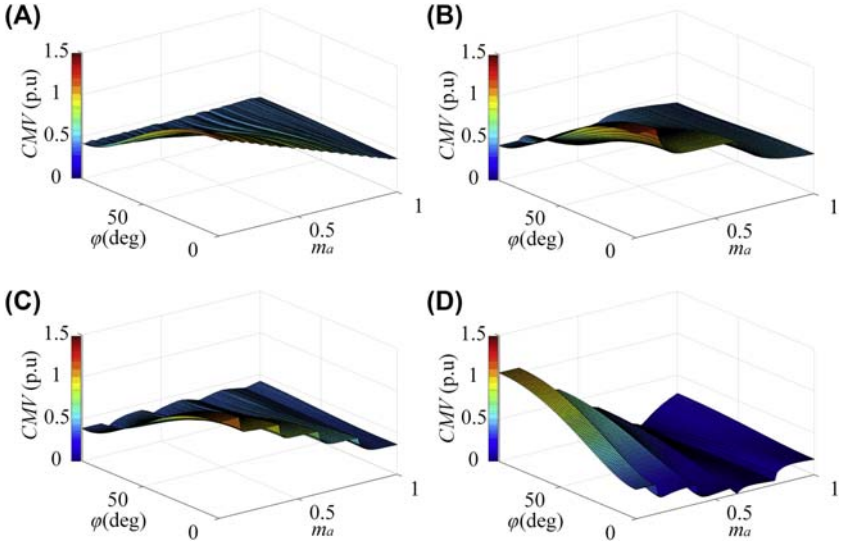

FIGURE 13.13 Third-order CMV of single CSC. (A) Conventional SVM, (B) BTSPWM, (C) SS-DPWM, (D) DDPWM.

TABLE 13.1 Switching sequence with different modulations.

Interval	SVM	SHE/ TPWM	BTSPWM	SS-DPWM	DDPWM
[0–30 degrees]	6-1-8	6–1	8-1-6-8-6-1-8	1-6-8-6-1	6-1-7-1-6
[30–60 degrees]	6-1-8	6–1	7-2-1-7-1-2-7	1-6-8-6-1	1-6-9-6-1
[60–90 degrees]	1-2-7	1–2	7-2-1-7-1-2-7	2-1-7-1-2	1-2-9-2-1
[90–120 degrees]	1-2-7	1–2	9-3-2-9-2-3-9	2-1-7-1-2	2-1-8-1-2
[120–150 degrees]	2-3-9	2–3	9-3-2-9-2-3-9	3-2-9-2-3	2-3-8-3-2
[150–180 degrees]	2-3-9	2–3	8-4-3-8-3-4-8	3-2-9-2-3	3-2-7-2-3

1-6 are active states; 7–9 are zero states.

vector to synthesize the current references. However, the active vector order and zero state selection are different. The DDPWM divides each sector into two subsectors equally due to different active vector orders.

The output PWM waveforms and their harmonic distribution of different modulations are shown in Fig. 13.12. The output frequency (f_0) is 60 Hz, and

This book belongs to Kitab Liaison (ocd1996@gmail.com) Copyright Elsevier 2023

the carrier frequency (f_c) for SPWMs as well as timer frequency (f_t) for SVM are both 1080 Hz. The switching frequency difference is easy to determine as the conventional three-segment SVM enjoys the smallest, while the switching frequency of BTSPWM is the highest. Compared to BTSPWM, other modulations have wider side band harmonics and their overall harmonic performances are similar.

Besides the harmonic performance, the CMV is also an inherent feature and the dominant third-order component is determined by the modulation index (m_a) and the displacement angle (φ) between phase voltage and current as shown in Fig. 13.13. It shows that the DDPWM enjoys the smallest CMV among different carrier-based SPWMs. Moreover, the CMV excited by conventional SVM is high and redundant zero state replacement method was discussed in Ref. [21] to reduce CMV. Since the PWM sequence design of SVM is very flexible and the DDPWM enjoys inherent small CMV as well as modularity, this chapter will continue to focus on these two modulations.

13.4 Parallel CSC and circuit analysis

Generally, the parallel CSC configurations can be classified into an independent DC-link structure and a shared DC-link structure. For independent DC-link structure, the sub-DC-link current can be controlled independently; thus, CMV and CC are the main issues. On the other hand, the DC current balance is the priority task for shared DC-link stricture, since only the total DC-link current can be regulated. This section mainly introduces the CM loop circuit and DC-link circuit analysis for parallel CSC structure with shared DC-link.

13.4.1 CM loop circuit of parallel CSC

The introduction had addressed the possible CMV resonance issue for transformerless CSC-fed MV drives, which also posed a great challenge in parallel CSC systems. To have a detailed analysis, the CM loop circuit for parallel CSC system will be derived from that of a single CSC. The possible CMV resonance point, CC, and CMC features will be investigated through the circuit analysis.

Fig. 13.14A shows the typical CM loop of a back-to-back CSC with an integrated DC choke on the DC link. The neutral points of input (C_{fr}) and output filters (C_{fi}) are connected through a damping resistor and thus creates a CM loop to flow the CMC. With the help of a CM choke, the CMV stress on the motor can be effectively reduced, which can be expressed as

$$V_{og} = i_{cm} \cdot R = V_{cmi} - V_{cmr} - V_L \tag{13.3}$$

where V_{og} is the CMV stress of the motor, R is the damping resistor, and i_{cm} is the total CMC flowing through the CM loop. V_L is the voltage drop on the CM choke. V_{cmi} and V_{cmr} are the CSI- and CSR-side CMVs, which are defined as

This book belongs to Kitab Liaison (ocd1996@gmail.com) Copyright Elsevier 2023

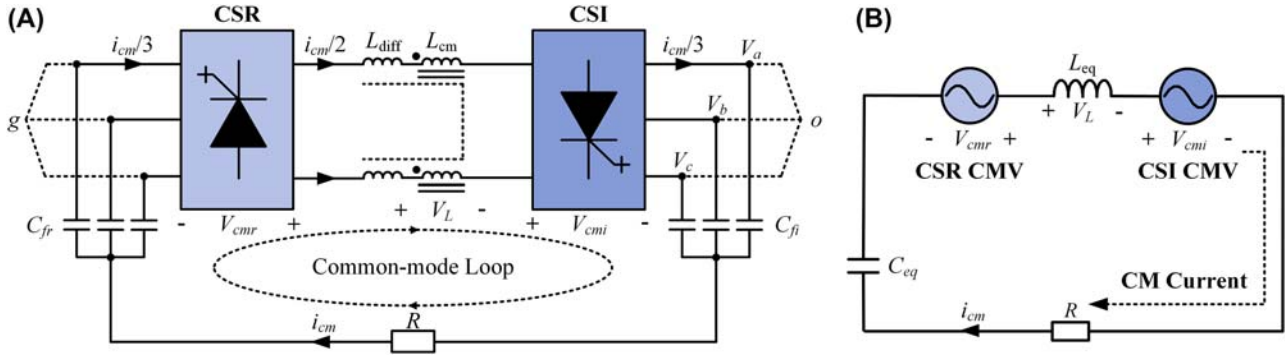

FIGURE 13.14 Common-mode loop circuit of single current source converter system. (A) Common-mode loop, (B) equivalent circuit.

This book belongs to Kitab Liaison (ocd1996@gmail.com)

Copyright Elsevier 2023

the average value of the positive and negative DC-bus voltage and their values are changed with the switching actions of CSI and CSR which are given as

$$V_{cm} = \frac{V_{pN} + V_{nN}}{2} = \frac{1}{2} \cdot [S_1 + S_4 \quad S_3 + S_6 \quad S_5 + S_2] \cdot \begin{bmatrix} V_a \\ V_b \\ V_c \end{bmatrix}; \tag{13.4}$$

$$S_i = \begin{cases} 1, switch\ \ on \\ 0, switch\ off \end{cases} \quad i = 1, 2, \ldots, 6$$

where V_{pN} and V_{nN} are the positive and negative DC-bus voltage with respective to grid- or motor-side neutral points (o or g) which is represented by N. The six switching semiconductors are named as S_1 to S_6, where 1 means the switch is turned on and 0 means it is off. V_a, V_b, and V_c are the three-phase output voltages. Based on Eq. (13.4), the possible CMV values under different switching states can be summarized as in Table 13.2, where the CMVs generated by the three zero states are the same as the phase voltage, while the CMVs are caused by the 6 active states that are half of phase voltages.

To get a deeper look at the CM loop features, the equivalent CM loop circuit of single back-to-back CSC system is shown as in Fig. 13.14B. It consists of the CM choke, equivalent capacitance of input and output filters, and two CMV sources generated by CSR and CSI, respectively. Therefore, the CMC can be expressed as Eq. (13.5),

$$i_{cm} = \frac{V_{cmr} + V_{cmi}}{R - j/\omega/C_{eq} + j\omega \cdot L_{cm}} \tag{13.5}$$

where ω is the CMV dominant angular frequency, L_{cm} represents the CM choke, C_{eq} represents the equivalent capacitance. The resonance frequency in this circuit can be expressed as

$$\begin{cases} F_r = \dfrac{1}{2\pi\sqrt{L_{cm} \cdot C_{eq}}} \\ C_{eq} = 3C_{fr} \cdot C_{fi}/(C_{fr} + C_{fi}) \end{cases} \tag{13.6}$$

TABLE 13.2 Common-mode voltage of single current source converter.

Type	Vector	Switching states	Common-mode voltage
Zero	I_0	[14], [36], [52]	V_a, V_b, V_c
Active	I_1–I_6	[16], [12], [23] [34], [45], [56]	$-0.5V_c$, $-0.5V_b$, $-0.5V_a$ $-0.5V_c$, $-0.5V_b$, $-0.5V_a$

This book belongs to Kitab Liaison (ocd1996@gmail.com) Copyright Elsevier 2023

It indicates that the CM resonance frequency is related to the actual value of system parameters. The excited CMC would be very large on the resonance point, which needs to be addressed. As discussed in Ref. [16], only zero-sequence components are present in the CMV waveform and the dominant component is the third-order component. The rectifier is usually operated under the fixed grid frequency (60 Hz), and the dominant CMV component is 180 Hz. Based on the typical parameters of a CSC-based MV drive system, the *LC* resonance frequency is normally located around 30 Hz. This means that the variable speed drive can excite the CM resonance when the motor operates at around 10 Hz. Thus, the third-order component of the CMV generated by CSI is addressed to suppress the CM resonance.

The equivalent CM loop circuit and *LC* resonance point analysis of a single CSC can be extended into parallel CSC system. The parameters of paralleled CSC modules are assumed to be the same and the detailed equivalent CM loop circuit is shown in Fig. 13.15. The system CMC is influenced by both grid-side and load-side CMVs. Meanwhile, the CC caused by the difference of

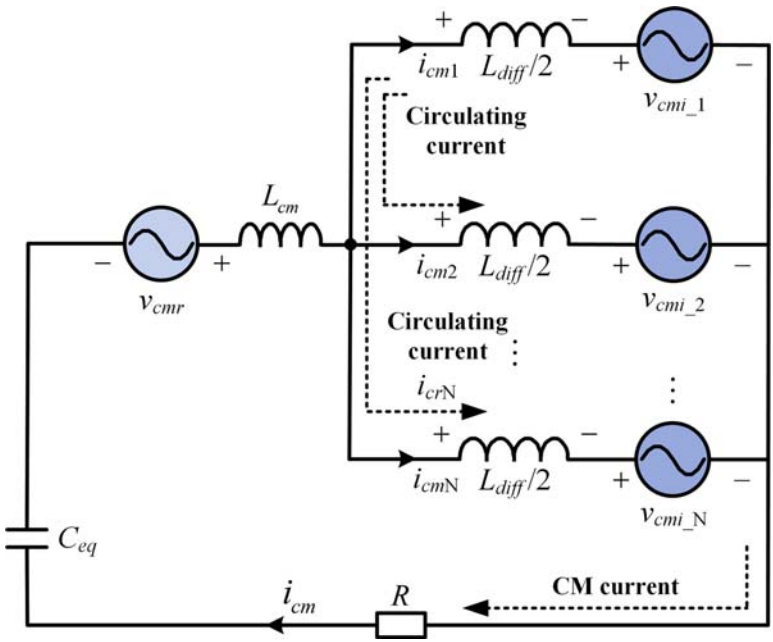

FIGURE 13.15 Equivalent common-mode loop circuit of parallel current source converter system with shared DC link and a damping resistor.

This book belongs to Kitab Liaison (ocd1996@gmail.com) Copyright Elsevier 2023

switching actions between parallel modules also needs to be considered. The expressions of CC and CMC are shown in

$$\begin{cases} i_{crN} = i_{cm1} - i_{cmN} = \dfrac{V_{cmi_N} - V_{cmi_1}}{1/2j\omega L_{diff}} \\ i_{cm} = i_{cm1} + i_{cm2} + \cdots i_{cmN} = \dfrac{V_{cmr} + 1/N \cdot (V_{cmi_1} + V_{cmi_2} + \cdots V_{cmi_N})}{R - j/\omega C_{eq} + j\omega L_{cm}} \end{cases} \tag{13.7}$$

where i_{cmi_1}, i_{cmi_2}, $\cdots$ i_{cmi_N} are the CMC flowing through CSI-1, CSI-2, $\cdots$ CSI-N. i_{crN} is the CC between CSC-1 and CSC-N, which is proportional to the CMV difference between two CSIs. The current i_{cm} flowing to the damping resistor is the total system CMC, which is influenced by the CSR- and CSI-side CMV and can be analyzed separately. The equivalent CMV on the CSI-side is $(V_{cmi_1} + V_{cmi_2} + \cdots + V_{cmi_N})$/N. Similar to the single CSC, the CM resonance also exists in parallel CSC system and the CM resonance frequency for N-CSC parallel system is given as

$$F_{r_N} = \frac{\sqrt{N}}{2\pi\sqrt{L_{cm} \cdot C_{eq}}} \tag{13.8}$$

It shows that the resonance frequency of parallel CSC system increases compared to single CSC. More importantly, the system CMV is normally increased with the operation frequency due to higher phase voltage, and the excited CMC under resonance point will increase correspondingly. Thus, it is also very important to suppress the inverter-side CMV for a paralleled CSC system.

13.4.2 DC-link circuit of parallel CSC

For parallel CSC with shared DC-link structure, since only the total DC-link current can be controlled, the DC current balancing is a priority issue that needs to be addressed. Therefore, the equivalent DC-link circuit should be studied to get a detailed understanding of the causes of current sharing error. Meanwhile, the CM loop circuit is also needed to be simultaneously considered when dealing with the current balance issue.

The sub-DC-link current flowing through the DC choke can be analyzed by considering the voltage stress on the choke, which influences the value of DC-link current continuously. Obviously, the voltage stress on each sub-DC choke is changed with the rectifier-side and inverter-side switching state. Assume that the rectifier-side and inverter-side voltages can be replaced by a changeable voltage source, and the DC-link circuit shared DC-link parallel CSC system can be simplified as shown in Fig. 13.16. V_p and V_n are the rectifier-side positive and negative DC-link voltages. V_{ipN} and V_{inN} ($N = 1, 2, \cdots$) represent the

This book belongs to Kitab Liaison (ocd1996@gmail.com) Copyright Elsevier 2023

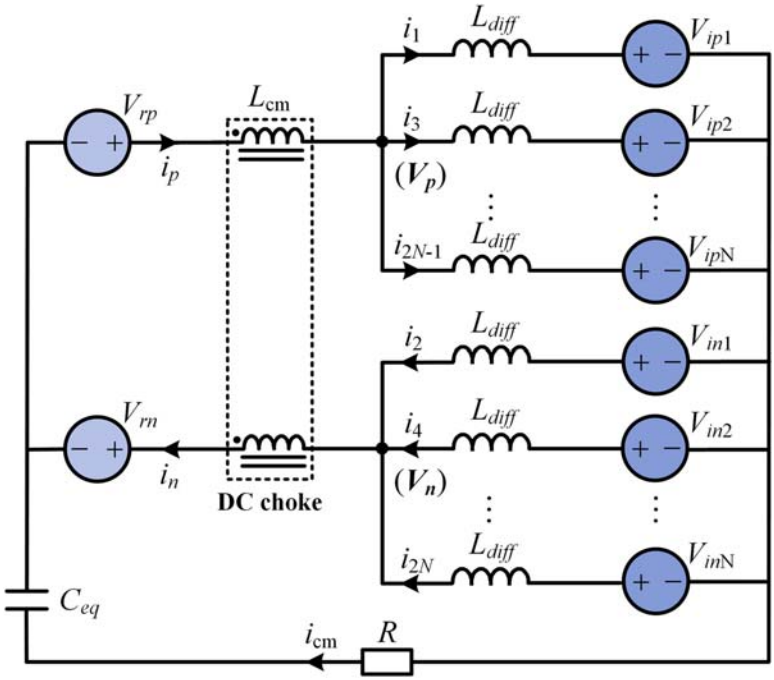

FIGURE 13.16 Equivalent DC-link circuit of parallel current source converter system with shared DC link.

inverter-side positive and negative DC-link voltages, which are related to the inverter-side switching states. i_p and i_n are the total positive and negative DC current, $i_{2N\text{-}1}$ and i_{2N} ($N = 1, 2, \cdots$) represent the positive and negative sub-DC-link currents for CSI-N, which can be expressed as

$$\begin{cases} i_{2N-1} = \dfrac{1}{L_{diff}} \displaystyle\int (V_p - V_{ipN})dt \\ i_{2N} = \dfrac{1}{L_{diff}} \displaystyle\int (V_n - V_{inN})dt \end{cases}, \quad N = 1, 2, \cdots \tag{13.9}$$

The ideal DC current balance condition is that the positive and negative DC current of each CSI module is equal. Thus, the positive and negative DC current sharing errors are introduced to indicate the current balance performance, which can be expressed as

$$\begin{cases} \Delta i_{pN} = i_1 - i_{2N-1} = \dfrac{1}{L_{diff}} \displaystyle\int (V_{ipN} - V_{ip1})dt \\ \Delta i_{nN} = i_2 - i_{2N} = \dfrac{1}{L_{diff}} \displaystyle\int (V_{inN} - V_{in1})dt \end{cases}, \quad N = 2, 3, \cdots \tag{13.10}$$

where Δi_{pN} and Δi_{nN} represent the positive and negative DC current sharing error between CSI-1 and CSI-N. Obviously, the values of current sharing

This book belongs to Kitab Liaison (ocd1996@gmail.com) Copyright Elsevier 2023

errors can be adjusted with $V_{ip\mathrm{N}}$ and $V_{in\mathrm{N}}$ ($\mathrm{N} = 1,\ 2,\ \cdots$). Therefore, the switching sequence of each CSI should be designed comprehensively to regulate both positive and negative DC current sharing errors to converge to zero.

13.5 DC current balance and CMV reduction methods

The CMV puts a great challenge on transformerless parallel CSC-fed drive system and the DC current balance needs to be further considered in a shared DC-link structure. Since the increased number of switching states can be generated through a parallel connection, it is more flexible to design a proper PWM sequence to achieve smaller CMV. To achieve DC current balance, the PWM sequence needs to be properly designed. Due to the flexibility of PWM sequence design, the SVM-based methods to solve the CMV and DC current balance issues will be introduced first. Then, the interleaved DDPWM will be investigated for multiple parallel CSC systems due to inherent modularity.

13.5.1 SVM-based methods

For parallel CSC system, both interleaved SVM and multilevel SVM can be implemented to achieve multilevel output, and the redundant switching states can be utilized to deal with the CMV issue. Specifically, the interleaved SVM can replace the redundant zero states to achieve a minimized CMV, while multilevel SVM can make use of all redundant switching states to balance DC current and reduce CMV, but results in a heavier computational burden.

13.5.1.1 Interleaved SVM

The digital implementation of SVM can be fulfilled by comparing the calculated dwell time and sawtooth timer. The PWM sequence can be flexibly designed to achieve multiple goals such as harmonic optimization and switching time minimization. Different types of SVM-based PWM design such as 3-segment Δ, 4-segment, and 4-segment Δ were proposed in Ref. [21], which result in different harmonic and CMV performance. The 3-segment SVM is shown in Fig. 13.17; two adjacent active states (I_{n}, $I_{\mathrm{n+1}}$) and one zero state are used to synthesize the current reference. The interleaved SVM can easily be implemented by shifting the timer while sharing the same dwell time. For example, the timer can be shifted by $\mathrm{T}_s/2$ for 2-CSC parallel system, where the PWM sequence of each CSC also shifted almost $\mathrm{T}_s/2$ since the dwell time stays constant during adjacent sampling intervals. Therefore, both CSCs enjoy 3-segment PWM sequence and multilevel output can be achieved.

There are three redundant zero states for single CSC, and the conventional SVM selects the proper zero state to minimize the switching frequency. To reduce the CMV, an average value reduction (AVR)-based SVM was proposed in Ref. [14] to minimize the average value of CMV during one sampling

This book belongs to Kitab Liaison (ocd1996@gmail.com) Copyright Elsevier 2023

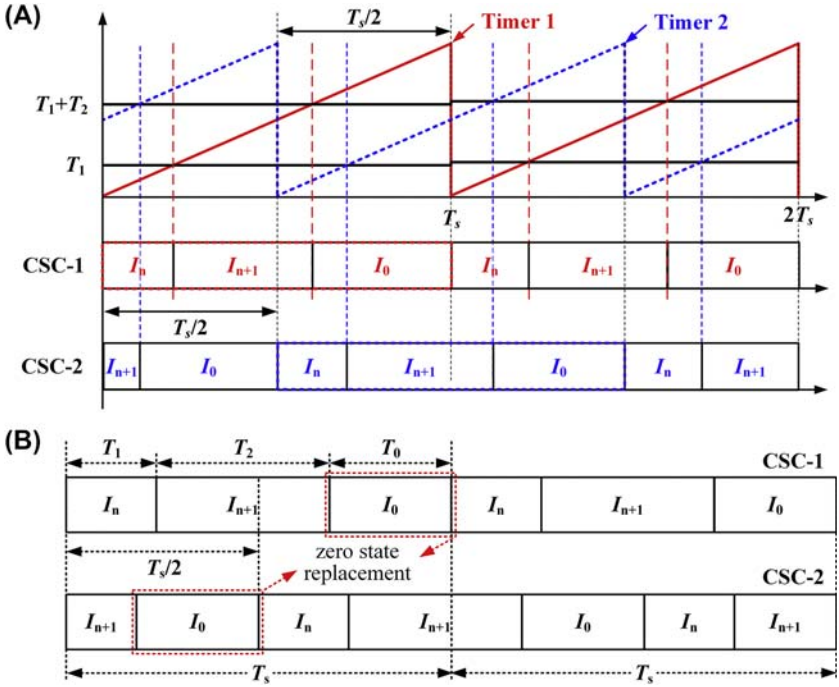

FIGURE 13.17 Interleaved space vector modulation for parallel current source converter (CSC) application with two units. (A) Pulse width modulation sequence, (B) zero state replacement.

period instead of the switching frequency with redundant zero state replacement. The average value of CMV (CMV_{ave}) in each sampling period can be defined as Eq. (13.11),

$$CMV_{ave} = |T_1 \cdot CMV_{act1} + T_2 \cdot CMV_{act2} + T_0 \cdot CMV_{zero}| \tag{13.11}$$

where CMV_{act1}, CMV_{act2}, and CMV_{zero} represent the CMV produced by adjacent active and zero states in one sampling period, respectively. T_1, T_2, and T_0 are the corresponding dwell times.

Fig. 13.18 shows comparative results of interleaved conventional 3-segment SVM and 3-segment AVR SVM for 2-CSC parallel system under certain case ($m_a = 0.8$, $\varphi = 0°$, $f_0 = 60$ Hz, $f_t = 1080$ Hz). 5-level current output can be achieved with interleaved SVM. The equivalent switching frequency is doubled. The output THD of both interleaved conventional 3-segment SVM and 3-segment AVR SVM is 38.30% since the replaced zero state does not influence the output PWM. However, the CMV can be effectively suppressed from 0.48 to 0.07 p.u by adopting an interleaved AVR SVM.

This book belongs to Kitab Liaison (ocd1996@gmail.com) Copyright Elsevier 2023

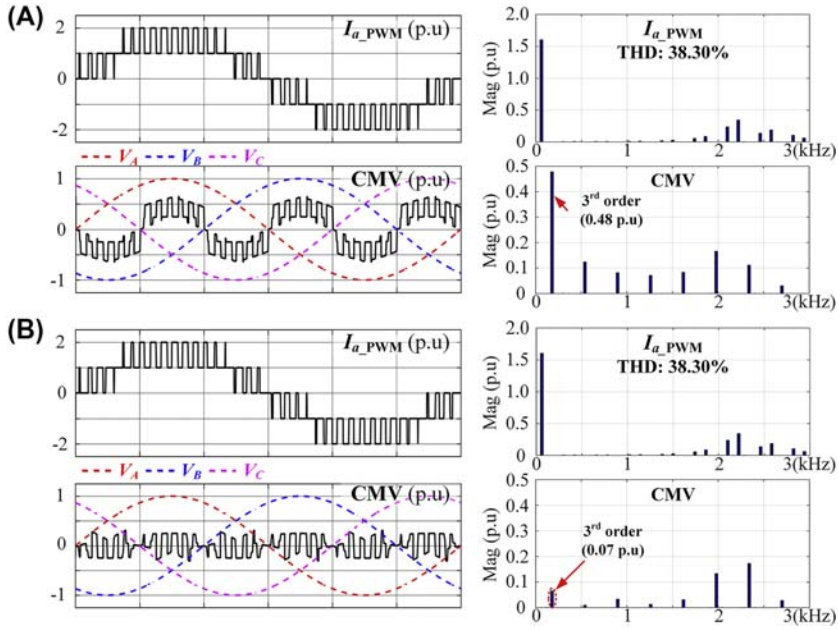

FIGURE 13.18 Output current pulse width modulation (PWM) and common-mode voltage (CMV) waveforms of 2-CSC parallel system ($m_a = 0.8$, $\varphi = 0°$, $f_0 = 60$ Hz, $f_t = 1080$ Hz). (A) Interleaved conventional 3-segment space vector modulation (SVM), (B) interleaved 3-segment average value reduction SVM.

Due to the modularity of interleaved modulation, other AVR SVM-based CMV reduction methods developed for single CSC can easily be extended to parallel CSC system. The third-order CMVs of different interleaved AVR SVMs are shown in Fig. 13.19. Compared to 3-segment AVR SVM and 4-segment AVR SVM, the 4-segment AVR SVM Δ and 3-segment AVR SVM Δ can effectively suppress the CMV in the low modulation index region.

13.5.1.2 Multilevel SVM

Multilevel SVM has been well developed in 2-CSC parallel systems where 19 current vectors and 81 switching states are available as shown in Fig. 13.20A. These vectors can be divided into four types, named as zero, small, medium, and large vectors based on their length. Different from interleaved SVM, the multilevel SVM strategy is implemented by combining the switching states of the paralleled CSC module together. The PWM sequences of parallel module are synchronized with each other. To implement multilevel SVM modulation, three adjacent vectors are selected to synthesize the reference considering the triangle where the reference is located.

This book belongs to Kitab Liaison (ocd1996@gmail.com) Copyright Elsevier 2023

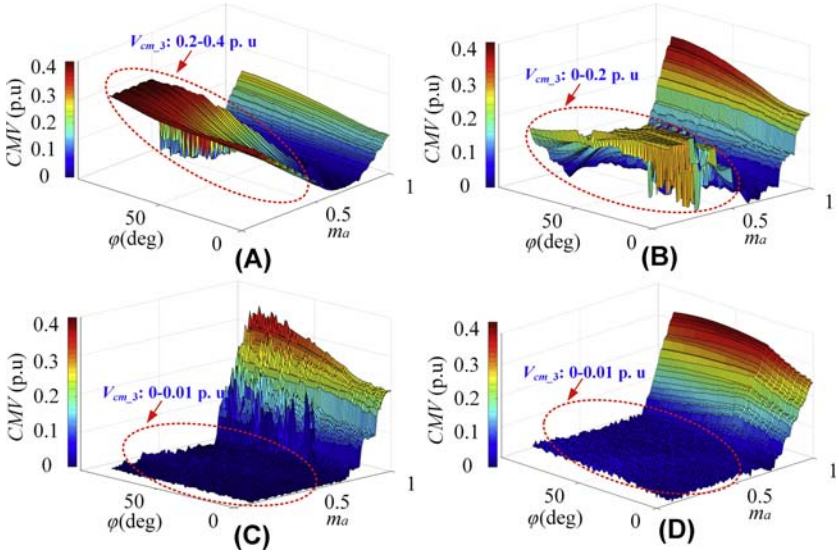

FIGURE 13.19 Third-order common-mode voltage (CMV) with different interleaved AVR SVM. (A) 3-segment AVR SVM, (B) 4-segment AVR SVM, (C) 4-segment AVR SVM Δ, (D) 3-segment AVR SVM Δ.

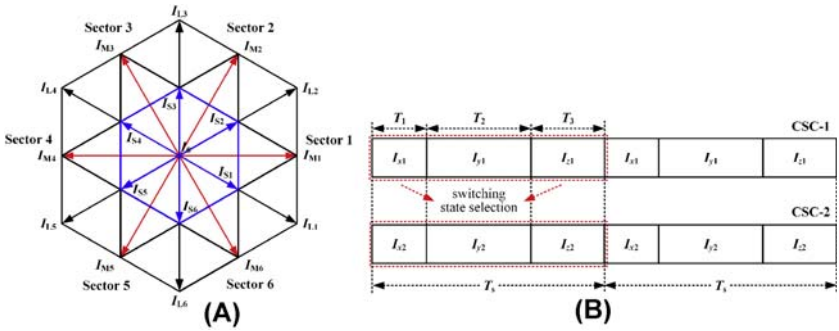

FIGURE 13.20 Multilevel space vector modulation with two parallel units. (A) Space vector diagram, (B) redundant switching state replacement.

Based on the equivalent CM loop circuit analysis, it shows that the system equivalent CMV is the average value of CMV caused by each CSC module. Different switching state combinations can cause different kinds of CMV values, which are summarized in Table 13.3. Each switching state is represented by four digits which show the turned-on devices, the first two digits show the on-state switches in CSC-1, and the last two represent the on-state switches in CSC-2, respectively. For example, one possible switching state [12,16] of medium vector I_{M1} indicates that S_1, S_6 in CSC-1 and S_1, S_2 in CSC-2 are turned on. The types of CMV values are significantly increased

This book belongs to Kitab Liaison (ocd1996@gmail.com) Copyright Elsevier 2023

TABLE 13.3 DC current influence and common-mode voltage with different switching states of 2-CSC parallel system.

Type	Vector	Switching states	Common-mode voltage	DC current influence
Zero	I_0	[14;14], [36;36], [52;52]	V_a, V_b, V_c	Δi_p: x; Δi_n: x
		[14;36], [36;52], [52;14]	$-0.5V_c$, $-0.5V_a$, $-0.5V_b$	If $V_{ab}/V_{bc}/V_{ca}>0$, $\Delta i_p \downarrow$; $\Delta i_n \uparrow$
		[16;34], [32;56], [54;12]	$-0.5V_c$, $-0.5V_a$, $-0.5V_b$	If $V_{ab}/V_{bc}/V_{ca}>0$, $\Delta i_p \downarrow$; $\Delta i_n \downarrow$
Large	I_{L1}	[16;16]	$-0.5V_c$	Δi_p: x; Δi_n: x
Medium	I_{M1}	[16;12]	$0.25V_a$	Δi_p: x; if $V_{bc}>0$, $\Delta i_n \uparrow$
Small	I_{S1}	[16;14]	$0.25(3V_a + V_b)$	Δi_p: x; if $V_{ab}>0$, $\Delta i_n \downarrow$
		[16;36]	$0.25(V_a + 3V_b)$	Δi_n: x; if $V_{ab}>0$, $\Delta i_p \downarrow$
		[16;52]	$0.25V_c$	If $V_{ca}>0$, $\Delta i_p \uparrow$; if $V_{bc}>0$, $\Delta i_n \uparrow$
		[12;56]	$0.25V_c$	If $V_{ca}>0$, $\Delta i_p \uparrow$; if $V_{bc}>0$, $\Delta i_n \downarrow$

compared to single CSC due to the abundance of switching states. Therefore, it is more flexible to choose proper switching states to reduce the CMV with improved modulation schemes.

After determining the three vectors to form the current reference, the specific switching states need to be further determined since some vectors have redundant switching states. The switching state selection for conventional multilevel SVM is to minimize the switching frequency. To reduce the CMV, multilevel AVR SVM can be achieved to deal with the CMV with these redundant switching states. The CMV_{ave} produced in each sampling period with multilevel SVM can be expressed as

$$CMV_{ave} = |T_1 \cdot CMV_1 + T_2 \cdot CMV_2 + T_3 \cdot CMV_3| \tag{13.12}$$

where CMV_1, CMV_2, and CMV_3 are the CMVs produced by the three adjacent vectors I_x, I_y, and I_z, respectively. The possible values are shown in Table 13.3. The CMV_{ave} generated by every possible redundant switching states is compared and the switching states which produce the minimized average CMV_{ave} are selected; therefore, the CMV can be suppressed.

This book belongs to Kitab Liaison (ocd1996@gmail.com) Copyright Elsevier 2023

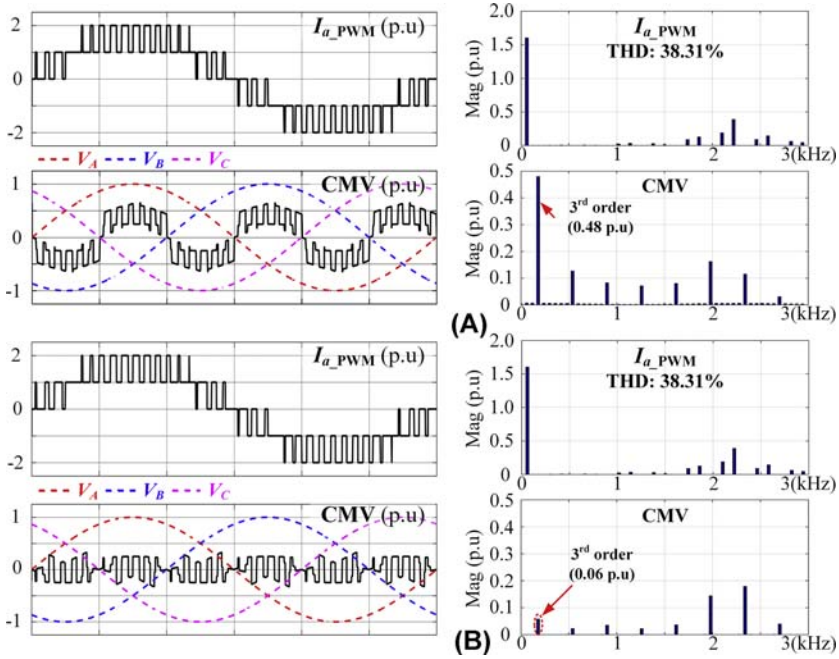

FIGURE 13.21 Output current pulse width modulation (PWM) and common-mode voltage (CMV) waveforms of 2-CSC parallel system ($m_a = 0.8$, $\varphi = 0°$, $f_0 = 60$ Hz, $f_t = 2160$ Hz). (A) Conventional 5-level space vector modulation (SVM), (B) 5-level average value reduction SVM.

To compare the PWM and CMV features of conventional multilevel SVM and multilevel AVR SVM, Fig. 13.21 shows comparative results of conventional 5-level SVM and 5-level AVR SVM for 2-CSC parallel system. Since the switching frequency of conventional 5-level SVM for 2-CSC parallel system is half of 3-level SVM adopted for single CSC, the timer frequency is set as 2160 Hz to guarantee the same switching frequency. As it can be seen, the same 5-level current output can be achieved for both conventional 5-level SVM and 5-level AVR SVM (THD: 38.31%), since replaced redundant switching states of AVR SVM do not influence the output PWM. Different from conventional multilevel SVM, the PWM sequence of multilevel AVR SVM is designed to reduce the CMV_{ave} through Eq. (13.12) instead of switching frequency. As a result, the CMV can be effectively suppressed from 0.48 to 0.06 p.u by adopting 5-level AVR SVM. It is worth to mention that the switching frequency and computational burden proposed method are increased due to numerous redundant switching state replacement, especially the parallel module number increased.

This book belongs to Kitab Liaison (ocd1996@gmail.com) Copyright Elsevier 2023

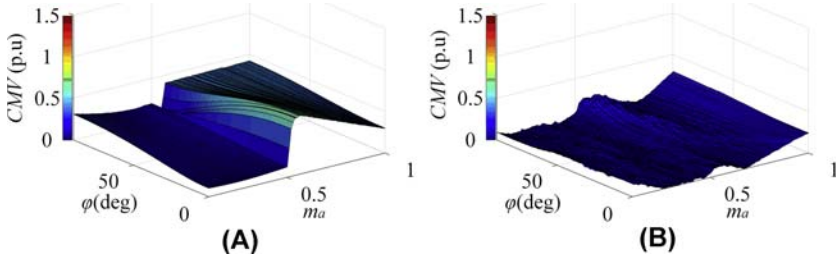

FIGURE 13.22 Third-order common-mode voltage (CMV) of 2-CSC parallel system. (A) Conventional 5-level space vector modulation (SVM), (B) 5-level average value reduction SVM.

Fig. 13.22 shows the third-order CMV caused by conventional 5-level SVM and proposed 5-level AVR SVM adopted for 2-CSC parallel system under different displacement angles and modulation indexes. Compared to conventional 5-level SVM, the proposed 5-level AVR SVM can effectively reduce the third-order CMV in the whole modulation index range. As a result, the CMV resonance can be suppressed.

Besides the CMV reduction methods, the DC current balance for shared DC-link structure also needs to be considered. According to current sharing error in Eq. (13.10), the sub-DC-link currents are influenced by the line-to-line voltage and switching states, which can be summarized as given in Table 13.3, where symbol "x" means no influence, "↓" means DC current decrease, and "↑" means increase.

It shows that the large vectors have no influence on the DC current as the turn-on devices of each CSI are the same, which means the inverter-side DC-link voltage of each CSI is the same. Therefore, the DC currents will stay constant under these switching states. The same conclusion is also applied for some zero vectors with the same switching states for each CSI. The rest switching states can result in different inverter-side DC-link voltages, and the DC currents can be adjusted by them according to the signs of the line-to-line voltages. Based on the above analysis, a general multilevel SVM-based DC current balance strategy is shown in Fig. 13.23, where the desired switching

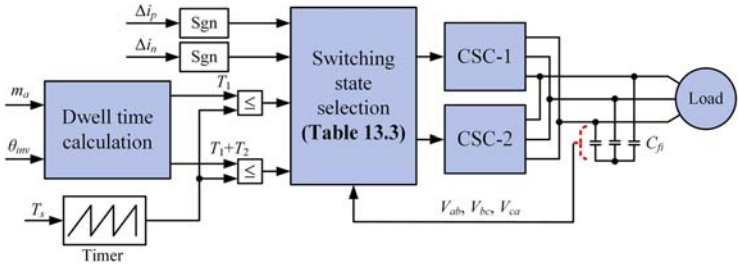

FIGURE 13.23 DC current balance strategy under 2-CSC multilevel converters.

This book belongs to Kitab Liaison (ocd1996@gmail.com) Copyright Elsevier 2023

states can be selected to adjust the DC current by considering the inverter-side line-to-line voltage and the symbols of Δi_p and Δi_n. Once the symbols of Δi_p and Δi_n are detected, the proper switching states can be chosen to make them close to zero based on Table 13.3.

According to Table 13.3, the small vectors can adjust both positive and negative currents, which is key to minimize CMV while considering the DC current balance. When selecting the switching state of small vectors, the CMV_{ave} produced by all possible switching states will be compared, the proper switching state which produces the smallest CMV_{ave} will be selected, and as a result, the DC current balance and CMV reduction can be achieved simultaneously. For example, when the reference located in Sector 1 Area 3, the 3 adjacent vectors I_{L1}, I_{M1}, and I_{S1} are adopted and the PWM sequence is shown as in Fig. 13.24. The medium vector I_{M1} can only adjust Δi_n, while the small vector I_{S1} can adjust both Δi_p and Δi_n; thus, the redundant switching states can be selected to reduce CMV_{ave}.

13.5.2 Carrier-shifted SPWM-based methods

Since the number of redundant switching states has increased significantly due to parallel connection, for example, 729 switching states are available in a 3-CSC parallel system. Multilevel SVM-based redundant switching state selection will be very complex to deal with the CMV and DC current balance issue when the module number is increased. Therefore, most of multilevel SVM-based methods are focusing on 2-CSC parallel system. On the other hand, the carrier-based SPWM enjoys inherent scalability, modularity, and easy-to-implement features for parallel CSC application, which can generate the gating signals by simply comparing the carriers and reference without real-time reference location identification and dwell time calculation. The low computational burden feature makes it very suitable for a modular CSC system, especially for high switching frequency applications where the admitted

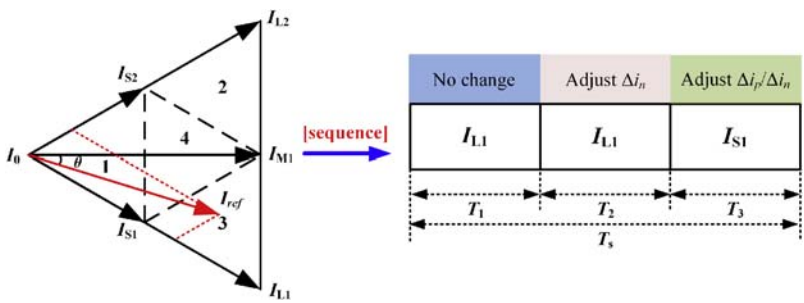

FIGURE 13.24 Space vector sequence and DC current influence of 2-CSC parallel system in Sector 1 Area 3.

This book belongs to Kitab Liaison (ocd1996@gmail.com) Copyright Elsevier 2023

processing time is limited. Among different carrier-based SPWMs, the DDPWM enjoys inherent small CMV feature; thus, this section will focus on an interleaved DDPWM-based CMV reduction and DC current balance methods.

The principle of interleaved SPWM has been introduced in Ref. [22], where the interleaved DDPWM adopted for 2-CSC parallel system with shared DC link is analyzed as an example. Similar to the DDPWM applied in single CSC, the maximum, middle, and minimum values among the three-phase reference currents are first obtained. The six switches in each CSC module are identified as $S_{p\max1(2)}/S_{n\max1(2)}$, $S_{p\mathrm{mid}1(2)}/S_{n\mathrm{mid}1(2)}$, and $S_{p\min1(2)}/S_{n\min1(2)}$ as shown in Fig. 13.25A, and they are used to synthesize the references $I_{\max}$, I_{mid}, and $I_{\min}$, respectively. The phase voltages are marked as V_x, V_d, and V_n. C_{11} and C_{12} are the upper carrier and lower carrier of CSC-1, while C_{21} and C_{22} are the upper carriers and lower carrier of CSC-2, the carrier shifting angle between the two CSCs is 180 degrees. As a result, the PWM sequence of each CSC can be shifted 180 degrees as shown in Fig. 13.25B. A general interleaved DDPWM for N-CSC ($N \geq 3$) parallel system with 360 degrees/N shifting angle was proposed in Ref. [22], where 2N+ 1 level current can be guaranteed with better output quality.

Fig. 13.26 shows the current PWM and CMV waveforms with interleaved DDPWM for 2-CSC parallel system. Similar to the interleaved SVM, the interleaved DDPWM enjoys small CMV while keeping good THD performance (40.64%). The magnitude of third-order CMV is 0.12 p.u which is achieved inherently without redundant switching state replacement. Therefore, the computational burden can be reduced, which makes it very suitable for high switching frequency applications and modular design.

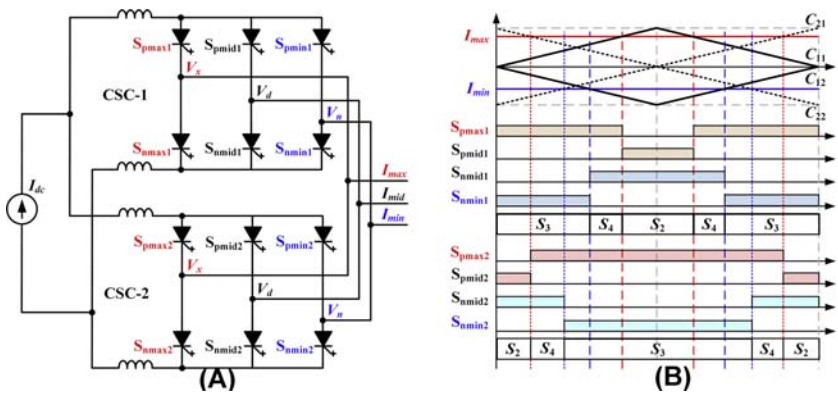

FIGURE 13.25 Pulse width modulation (PWM) sequence of interleaved DDPWM. (A) 2-CSC parallel system with shared DC-link, (B) interleaved DDPWM.

This book belongs to Kitab Liaison (ocd1996@gmail.com) Copyright Elsevier 2023

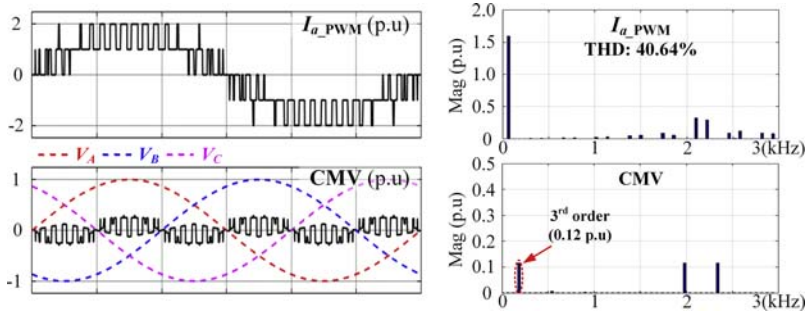

FIGURE 13.26 Output current pulse width modulation (PWM) and common-mode voltage (CMV) waveforms with interleaved DDPWM of 2-CSC parallel system ($m_a = 0.8$, $\varphi = 0°$, $f_O = 60$ Hz, $f_c = 1080$ Hz).

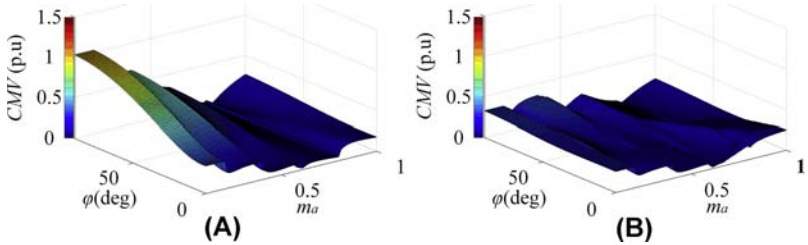

FIGURE 13.27 Third-order common-mode voltage (CMV) of 2-CSC parallel system. (A) Interleaved DDPWM, (B) interleaved AVR DDPWM.

The magnitude of third-order CMV of interleaved DDPWM under different modulation indexes and displacement angles is shown in Fig. 13.27A, which can verify that DDPWM can effectively reduce the CMV under most conditions (high-modulation index or small displacement angle range). To further reduce the CMV, the redundant zero state replacement adopted for interleaved SVM can also be applied for interleaved DDPWM as shown in Fig. 13. 27B. However, the actual CMV value is small due to low base value in the low modulation index range. Therefore, the interleaved DDPWM is competent for most of drive applications.

As introduced in Eq. (13.10), the sub-DC-link currents are influenced by the inverter-side line-to-line voltage and switching states. The DC current influence under different switching states of multilevel SVM is summarized in Table 13.4. Similar analysis can be conducted with interleaved DDPWM. The switching state for DDPWM is defined as [$S_{p\max}$, $S_{p\mathrm{mid}}$, $S_{n\mathrm{mid}}$, $S_{n\min}$], as $S_{p\max}$, $S_{p\mathrm{mid}}$ and $S_{n\mathrm{mid}}$, $S_{n\min}$ are complementary. Therefore, there are four different switching states ([0,1,0,1], [0,1,1,0], [1,0,0,1], and [1,0,1,0]) for one CSC, which are named as S1, S2, S3, and S4, respectively.

This book belongs to Kitab Liaison (ocd1996@gmail.com) Copyright Elsevier 2023

TABLE 13.4 DC current influence with interleaved DDPWM.

	S1	S2	S3	S4
S1	Δi_p: x; Δi_n: x	Δi_p: x; Δi_n: ↑	Δi_p: ↑; Δi_n: x	Δi_p: ↑; Δi_n: ↑
S2	Δi_p: x; Δi_n: ↓	Δi_p: x; Δi_n: x	Δi_p: ↑; Δi_n: ↓	Δi_p: ↑; Δi_n: x
S3	Δi_p: ↓; Δi_n: x	Δi_p: ↓; Δi_n: ↑	Δi_p: x; Δi_n: x	Δi_p: x; Δi_n: ↑
S4	Δi_p: ↓; Δi_n: ↓	Δi_p: ↓; Δi_n: x	Δi_p: x; Δi_n: ↓	Δi_p: x; Δi_n: x

The positive DC-bus voltages under the four switching states are V_d, V_d, V_x, and V_x, while the negative DC-bus voltages are V_n, V_d, V_n, and V_d in Max-Mid-Min phase. Their values are equal to phase voltages V_a, V_b, V_c in A-B-C phase. When considering a 2-CSC parallel system, there are 16 different switching state combinations. The DC current influence with different combinations is shown as in Table 13.4 by assuming $V_x > V_m$ and $V_m > V_n$. Otherwise, the DC current influences are opposite. The positive DC difference Δi_p and negative DC current difference Δi_n are not changed when the switching states of two CSCs are the same.

Based on the PWM sequence of interleaved DDPWM, the PWM sequence of each CSC is 5-segment symmetrical and they are shifted 180 degrees. Based on the DC current influence summarized in Table 13.4, the excited ΔV_p and ΔV_n values are positive and negative line-to-line voltage alternately in each carrier period. That means the resulting Δi_p and Δi_n will keep going up and down around zero in each carrier period. Meanwhile, both ΔV_p and ΔV_n are repetitive in each 120 degrees interval as shown in Fig. 13.28. It indicates that their integral results are exactly the same in each 120 degrees interval; therefore, the DC current error changed value is fixed in each 120 degrees interval. According to the above analysis, the active DC current balance method can be simply fulfilled by taking use of the repetitive features of the voltage differences and shows the results of voltage difference and resulted current sharing error waveforms by reversing the gating signals of the two CSCs. It indicates that the voltage difference waveforms are reversed too, which can keep the current sharing error equal to zero in every two 120 degrees intervals.

13.5.3 Case study results

Experiments are conducted on a 2-CSC parallel CSC system (SGCT module number: 5SHZ 0860F0005) with shared DC link. Two CSIs are paralleled with a shared output filter and the parameters are listed in Table 13.5. The shared DC-link current is supported by a DC source and the carrier frequency is

This book belongs to Kitab Liaison (ocd1996@gmail.com) Copyright Elsevier 2023

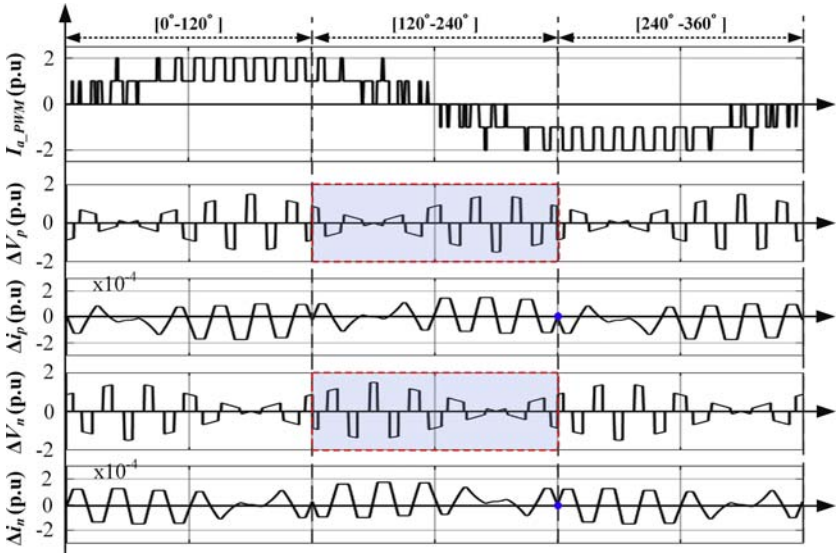

FIGURE 13.28 DC current sharing error of 2-CSC parallel system with interleaved DDPWM.

TABLE 13.5 Experimental parameters for a case study.

Parameters	Experiment value
Power rating	10 kW/208 V
DC-link current	4 A
Carrier frequency	1080 Hz
Differential-mode inductor	10 mH
Output filter capacitance	120 μF
Load resistance	5.76 Ω
Load inductance	5 mH

1080 Hz. Multilevel SVM-based DC current balance and CMV reduction method are verified on a parallel CSC with a shared DC link. Then, different interleaved SPWMs are compared on a 2-CSC parallel system with shared DC link to verify the superior performance of DDPWM.

The experimental results of parallel CSC with shared DC link by adopting multilevel SVM are shown in Fig. 13.29. The output frequency is 10 Hz and the modulation index is 0.8. At the time of 1s, the modulation method is switched from multilevel SVM-based DC current balance modulation to the

This book belongs to Kitab Liaison (ocd1996@gmail.com) Copyright Elsevier 2023

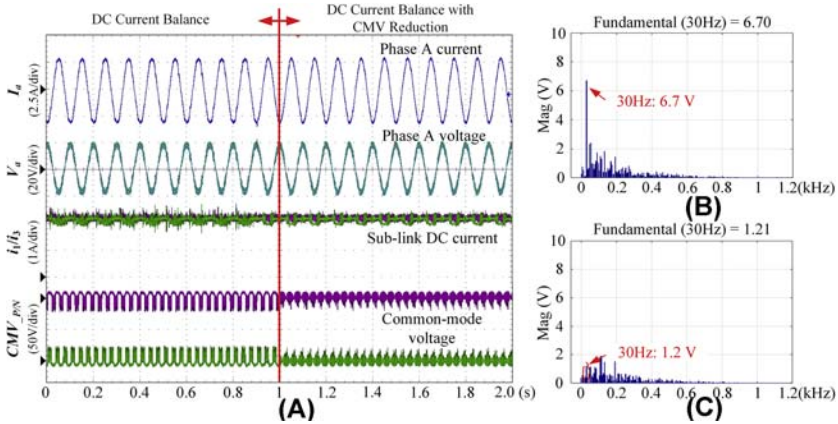

FIGURE 13.29 Experimental results of 2-CSC parallel system with shared DC link. (A) DC-link current and common-mode voltage (CMV) waveforms, CMV FFT results of (B) DC current balance method, (C) DC current balance with CMV reduction method.

DC current balance with CMV reduction method. The positive sub-DC-link currents i_1 and i_3 are constant around 2 A, which shows good DC current sharing performance. More importantly, the CMV reduced effectively when the modulation strategy is switching to simultaneous DC current balance and CMV reduction method. The FFT results show that the dominant component of CMV is the third order, which reduced from 6.7 V to only 1.2 V while keeping the DC current balanced. Thus, the experimental results verify that the proposed method can achieve DC current balance and CMV reduction simultaneously.

To further verify the performance with different carrier-based SPWMs, three interleaved SPWMs (BTSPWM, SS-DPWM, and DDPWM) are implemented on a 2-CSC parallel system with shared DC link as shown in Fig. 13.30. The output frequency is 60Hz and the interleaving angle is 180 degrees for all of the three modulations. The excited CMVs for interleaved discontinuous BTSPWM and SS-DPWM are similar in terms of magnitude as well as FFT spectrum. The third-order component of CMV excited by interleaved discontinuous BTSPWM is 11.20 and 10.81 V when modulation index is 0.6 and 0.8, respectively, where they are 11.12 and 10.86 V for interleaved SS-DPWM. In terms of DC current balance, all of the three SPWMs can achieve good DC current sharing. Moreover, compared to discontinuous BTSPWM and SS-DPWM, the CMV magnitude and third-order component can be effectively reduced with DDPWM. The third-order component is reduced to 0.58 V when the modulation index is 0.6, while it is reduced to 2.14 V when the modulation index is 0.8. It is consistent with theoretical analysis in Section 13.3 and the effectiveness of interleaved DDPWM can be verified.

This book belongs to Kitab Liaison (ocd1996@gmail.com) Copyright Elsevier 2023

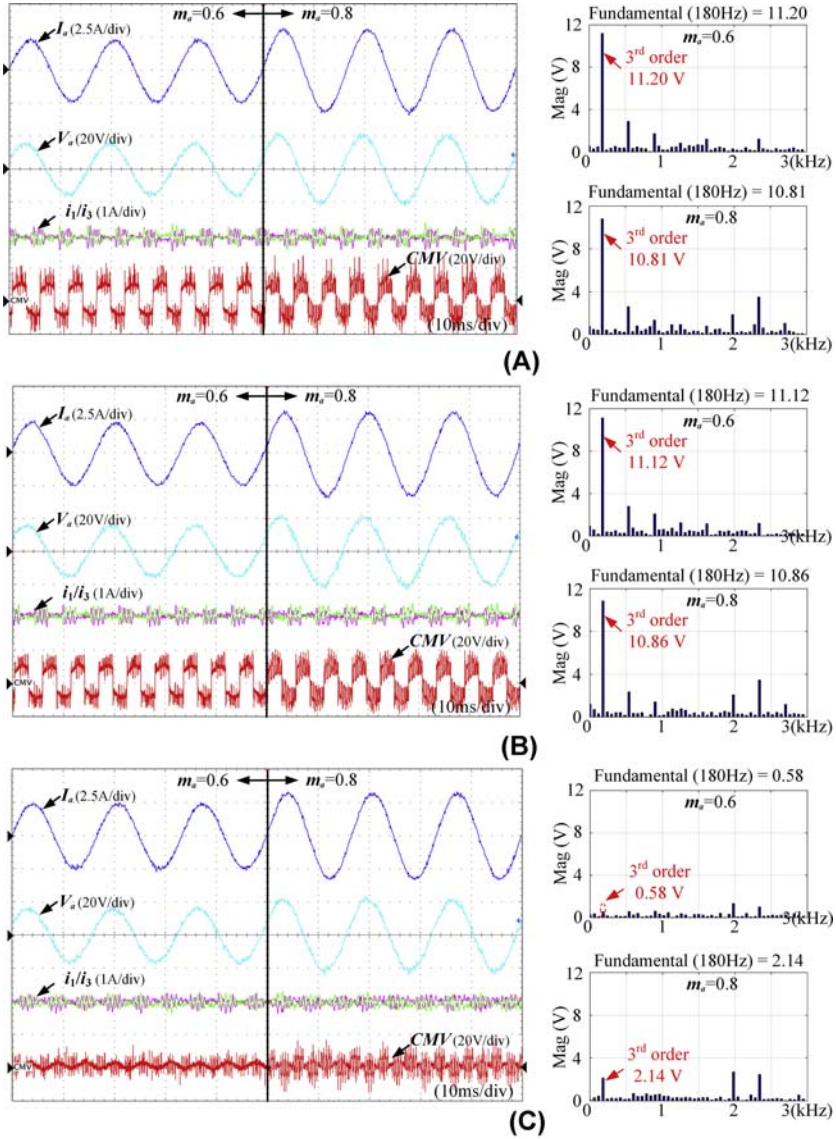

FIGURE 13.30 Experimental results of different carrier-based sinusoidal pulse width modulation for 2-CSC parallel system with shared DC link. (A) BTSPWM, (B) SS-DPWM, (C) DDPWM.

13.6 Conclusions

CSCs have been widely adopted in high-power applications, such as HVDC and industrial drives, for a long history. Parallel CSC configuration can further improve the system power rating, reliability, and also output quality.

This book belongs to Kitab Liaison (ocd1996@gmail.com) Copyright Elsevier 2023

Compared to bulky isolation transformers, transformerless CSC topology by adopting a CM choke can effectively reduce the cost. This chapter mainly studies the transformerless parallel CSC structures and improved modulation and control methods to deal with their potential challenges, such as CMV, CC, and DC current balance. An SVM-based simultaneous DC current balance and CMV reduction method is proposed for parallel CSC system with shared DC link, which can reduce the CMV effectively while keeping a balanced DC current. To achieve a true modular design, an interleaved DDPWM is presented for use with multiple CSC parallel system, which enjoys small CMV as well as having scalability. The analysis and effectiveness of the proposed methods are verified through experiment results. The parallel configurations associated with the proposed methods have the potential benefits of improving the system power rating and power quality, scale down the CM choke and the damping resistor as well as output filter, which are key indicators to improve performance and reduce the cost and size of the CSC-fed drive system.

References

[1] B. Wu, High-Power Converters and AC Drives, Wiley-IEEE Press, 2006, pp. 189–218.

[2] N.M. Kirby, L. Xu, M. Luckett, W. Siepmann, HVDC transmission for large offshore wind farms, Power Eng. J. 16 (3) (June 2002) 135–141.

[3] S. Nishikata, F. Tatsuta, A new interconnecting method for wind turbine/generators in a wind farm and basic performances of the integrated system, IEEE Trans. Ind. Electron. 57 (2) (February 2010) 468–475.

[4] B. Wu, J. Pontt, J. Rodriguez, S. Bernet, S. Kouro, Current-source converter and cycloconverter topologies for industrial medium-voltage drives, IEEE Trans. Ind. Electron. 55 (7) (2008) 2786–2797.

[5] J.M. Erdman, R.J. Kerkman, D.W. Schlegel, G.L. Skibinski, Effect of PWM inverters on AC motor bearing currents and shaft voltages, IEEE Trans. Ind. Appl. 32 (2) (March-April 1996) 250–259.

[6] R.E. Torres-Olguin, A. Garces, M. Molinas, T. Undeland, Integration of offshore wind farm using a hybrid HVDC transmission composed by the PWM current-source converter and line-commutated converter, IEEE Trans. Energy Convers. 28 (1) (2013) 125–134.

[7] M. Popat, B. Wu, F. Liu, N. Zargari, Coordinated control of cascaded current-source converter based offshore wind farm, IEEE Trans. Sustain. Energy 3 (3) (July 2012) 557–565.

[8] L. Ding, Y.W. Li, Mixed Series-Parallel Connected Current Source Converters with Interleaved SPWM, IEEE Energy Conversion Congress and Exposition (ECCE), Baltimore, MD, USA, 2019, pp. 640–645, 2019.

[9] B. Sahan, A.N. Vergara, N. Henze, A. Engler, P. Zacharias, A single stage PV module integrated converter based on a low-power current-source inverter, IEEE Trans. Ind. Electron. 55 (7) (July 2008) 2602–2609.

[10] L. Tang, G. Su, Boost Mode Test of a Current-Source-Inverter-Fed Permanent Magnet Synchronous Motor Drive for Automotive Applications, IEEE 12th Workshop on Control and Modeling for Power Electronics (COMPEL), Boulder, CO, 2010, pp. 1–8, 2010.

This book belongs to Kitab Liaison (ocd1996@gmail.com) Copyright Elsevier 2023

[11] F. Xu, B. Guo, L.M. Tolbert, F. Wang, B.J. Blalock, An all-SiC three-phase buck rectifier for high-efficiency data center power supplies, IEEE Trans. Ind. Appl. 49 (6) (November-December 2013) 2662−2673.

[12] T. Friedli, S.D. Round, D. Hassler, J.W. Kolar, Design and performance of a 200-kHz all-SiC JFET current DC-link back-to-back converter, IEEE Trans. Ind. Appl. 45 (5) (September-october 2009) 1868−1878.

[13] M. Guacci, M. Tatic, D. Bortis, J.W. Kolar, Y. Kinoshita, H. Ishida, Novel Three-Phase Two-Third-Modulated Buck-Boost Current Source Inverter System Employing Dual-Gate Monolithic Bidirectional GaN e-FETs, IEEE 10th International Symposium on Power Electronics for Distributed Generation Systems (PEDG), Xi'an, China, 2019, pp. 674−683, 2019.

[14] L. Ding, Z. Quan, Y.W. Li, Common-mode voltage reduction for parallel CSC-fed motor drives with multilevel modulation, IEEE Trans. Power Electron. 33 (8) (August 2018) 6555−6566.

[15] L. Ding, Y.W. Li, Simultaneous DC current balance and common-mode voltage control with multilevel current source inverters, IEEE Trans. Power Electron. 33 (11) (November 2018) 9188−9197.

[16] X. Wang, B.T. Ooi, Unity PF current-source rectifier based on dynamic trilogic PWM, IEEE Trans. Power Electron. 8 (3) (July 1993) 288−294.

[17] Z. Bai, X. Ruan, Z. Zhang, A generic six-step direct PWM (SS-DPWM) scheme for current source converter, IEEE Trans. Power Electron. 25 (3) (March 2010) 659−666.

[18] N. Choi, K. Lee, B. Han, A Novel Carrier Based PWM for Current Source Converter, IEEE 7th International Power Electronics and Motion Control Conference- ECCE Asia, Harbin, China, 2012. June 2-5, pp. 1945−1950, 2012.

[19] J. Espinoza, G. Jos, J. Guzmn, L. Morn, R. Burgos, Selective harmonic elimination and current/voltage control in current/voltage source topologies: a unified approach, IEEE Trans. Ind. Electron. 48 (1) (2001) 71−81.

[20] Y. Li, L. Ding, Y. Li, Isomorphic relationships between voltage-source and current-source converters, IEEE Trans. Power Electron. 34 (8) (August 2019) 7131−7135.

[21] L. Ding, Y. Lian, Y.W. Li, Multilevel current source converters for high power medium voltage applications, CES Trans. Electric. Machine. Syst. 1 (3) (September 2017) 306−314.

[22] L. Ding, Y. Li, Simultaneous DC current balance and CMV reduction for parallel CSC system with interleaved carrier-based SPWM, IEEE Trans. Ind. Electron. 67 (10) (October 2020) 8495−8505.

This book belongs to Kitab Liaison (ocd1996@gmail.com) Copyright Elsevier 2023

Chapter 14

Parallel operation of power converters and their filters

Ghanshyamsinh Gohil
University of Texas at Dallas, Richardson, TX, United States

14.1 Introduction

Three-phase pulse width modulated (PWM) voltage source converter (VSC) is widely used in many DC/AC and AC/DC power conversion applications, including variable speed motor drives, renewable energy and distributed generation systems, uninterrupted power supply, solid-state transformer, active power filters, fast battery charger for the electric vehicle, etc. The parallel operation of VSC is desired in many of these applications to achieve system cost reduction through modularity. A parallel connection enables the use of the standard VSC module, high availability, and low cost of maintenance and small inventory. Moreover, the flexibility offered by the parallel connection of the VSCs is highly desirable in many applications that require capacity expansion over time. The parallel connection of VSC is also ubiquitous in critical installations, where redundancy is required to ensure minimum downtime. In high-current applications, processing entire power using a single VSC, may not be preferred because of the economic and technical challenges associated with the high-current power semiconductor modules and passive components. Therefore, VSCs are often connected in parallel to divide the total current among parallel VSCs.

The power conversion system (PCS) with parallel VSCs for AC/DC and AC/AC conversion applications is shown in Fig. 14.1. The parallel back-to-back connected VSCs, shown in Fig. 14.1B, have separate DC buses. However, a common DC-bus connection is also possible. In a PCS with parallel VSCs, proper current sharing between the VSCs is highly desirable. However, the filter impedance and semiconductor device parameter mismatch, application of different voltage vectors, and dead-time effect make current sharing very challenging. As a result, circulating current flows between the parallel VCSs due to the existence of the closed path, leading to the underutilization of the system

Control of Power Electronic Converters and Systems. https://doi.org/10.1016/B978-0-12-819432-4.00001-9
Copyright © 2021 Elsevier Ltd. All rights reserved.

This book belongs to Kitab Liaison (ocd1996@gmail.com)
Copyright Elsevier 2023

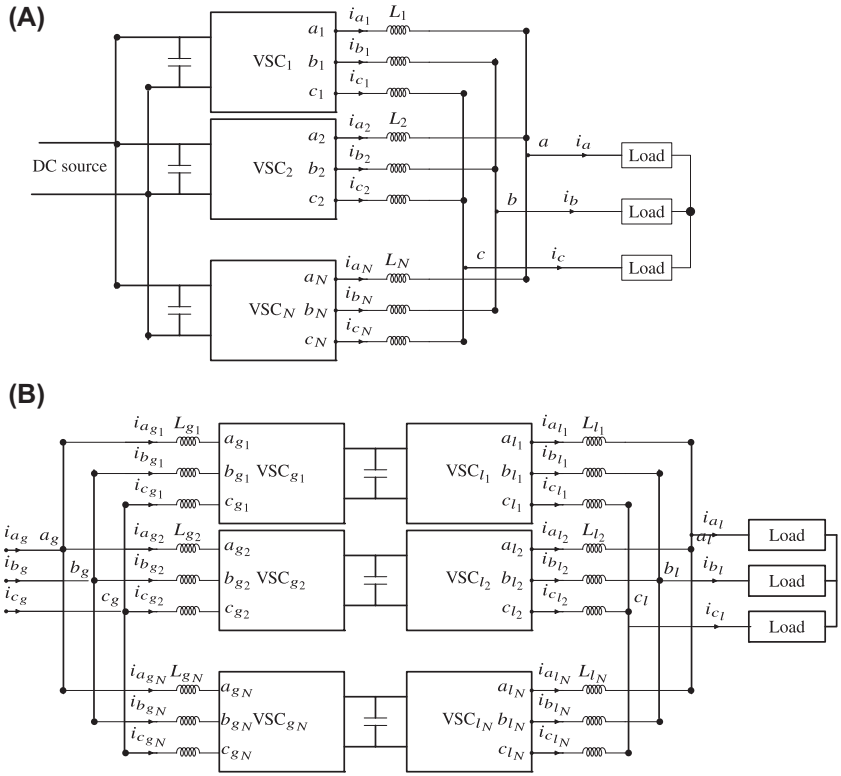

FIGURE 14.1 Power conversion system with parallel voltage source converters. (A) Parallel voltage source converters with a common DC and AC buses in AC/DC conversion applications, (B) AC/AC conversion system using parallel back-to-back connected voltage source converters.

capacity. Moreover, the components (semiconductors and filter) present in the circulating current path experience additional losses due to the flow of the circulating current, which in turn increases stress and may reduce the lifetime of these components. The circulating current may have low-frequency and high-frequency components. The low-frequency circulating current can be reduced by using an appropriate control scheme, whereas modifications in the modulation schemes, carrier signal synchronization, and passive filters are employed for the high-frequency circulating current reduction. The modeling of the circulating current is discussed in Section 2. Various control schemes to achieve desired load sharing and to control the circulating current are discussed in Section 3.

In the conventional PCS with parallel VSCs, control efforts are made to apply the same voltage vector to all the parallel VSCs to ensure minimum

This book belongs to Kitab Liaison (ocd1996@gmail.com) Copyright Elsevier 2023

circulating current. However, the harmonic quality can be improved at the expense of large high-frequency circulating current by applying different vectors to the parallel VSCs. This is typically achieved by interleaving the carrier signals of the parallel VSCs. The concept of harmonic quality improvement of the parallel-connected PWM VSCs by interleaving the carrier signals has been first proposed in Ref. [1]. Various interleaving techniques and their impact on the harmonic performance and circulating current will be presented in Section 4. When VSCs are connected in parallel, the circulating current flows between the VSCs due to the control asymmetry and the impedance mismatch. When the carriers are interleaved, the switched output voltages of the interleaved parallel legs are phase shifted. As a result, the instantaneous voltage difference exists between parallel VSCs, which further increases the high-frequency circulating current. Therefore, the circulating current should be suppressed to realize the full potential of the interleaved carriers in parallel-connected VSCs. The high-frequency circulating current introduced by the carrier interleaving can be eliminated by providing galvanic isolation [2] or can be reduced to a reasonable limit by introducing an impedance in the circulating current path. Various inductive components that are used to offer large impedance to the high-frequency circulating current, including coupled inductor (CI) [1,3], common-mode (CM) inductor [4], and integrated inductor, are discussed in details in Section 5.

The main aim of this chapter is to provide an understanding of the parallel operation of the VSCs. The challenges associated with the load sharing and solutions for the circulating current reduction are described in detail. Harmonic performance improvement using interleaved operation and techniques for the high-frequency circulating current suppression for parallel interleaved operation are illustrated.

14.2 Circulating current modeling

Because of the filter impedance and semiconductor device parameter mismatch, application of different voltage vectors, and dead-time effect, the VSC current may deviate from the desired set point. As a result, the circulating current flows between the VSCs, leading to additional losses in the semiconductor and magnetic components present in the circulating current path. The circulating current for the parallel VSCs with a common DC-bus arrangement (c.f. Fig. 14.1A) and separate DC-bus arrangement (c.f. Fig. 14.1B) is analyzed in this section.

14.2.1 Parallel converters with a common DC bus

For the PCS with parallel VSCs sharing a common DC link shown in Fig. 14.1A, the dynamic behavior of the kth VSC current ($k \in \{1,2,\ldots,N\}$)

This book belongs to Kitab Liaison (ocd1996@gmail.com) Copyright Elsevier 2023

with single-phase inductors having inductance L_k and equivalent series resistance r_k can be expressed as

$$\begin{bmatrix} v_{a_k o} \\ v_{b_k o} \\ v_{c_k o} \end{bmatrix} = \begin{bmatrix} L_k & 0 & 0 \\ 0 & L_k & 0 \\ 0 & 0 & L_k \end{bmatrix} \frac{d}{dt} \begin{bmatrix} i_{a_k} \\ i_{b_k} \\ i_{c_k} \end{bmatrix} + \begin{bmatrix} r_k & 0 & 0 \\ 0 & r_k & 0 \\ 0 & 0 & r_k \end{bmatrix} \begin{bmatrix} i_{a_k} \\ i_{b_k} \\ i_{c_k} \end{bmatrix} + \begin{bmatrix} v_{ao} \\ v_{bo} \\ v_{co} \end{bmatrix} \quad (14.1)$$

where $v_{a_{ko}}$, $v_{b_{ko}}$, and $v_{c_{ko}}$ represents pole voltages (with respect to the arbitary reference point o) of phase a, b, and c, respectively. v_{ao}, v_{bo}, and v_{co} are the load voltages (with the respect to the reference point o) of phase a, b, and c, respectively. The dynamic behavior of the phase x (where $x \in \{a,b,c\}$) currents of all the parallel VSCs can be represented as

$$\frac{1}{N}\boldsymbol{C}\boldsymbol{V_P} = \frac{1}{N}\boldsymbol{C_r}\boldsymbol{I} + \frac{1}{N}\boldsymbol{C_L}\frac{d}{dt}\boldsymbol{I} + \boldsymbol{V} \quad (14.2)$$

where the $\boldsymbol{V_P}$ is the pole voltage vector

$$\boldsymbol{V_P} = [\, v_{x_1 o} \quad v_{x_2 o} \cdots \quad v_{x_N o} \,]^T \quad (14.3)$$

$\boldsymbol{I}$ is a VSC current vector

$$\boldsymbol{I} = [\, i_{x_1} \quad i_{x_2} \cdots i_{x_N} \,]^T \quad (14.4)$$

and

$$\boldsymbol{V} = [\, V_{xo} \quad V_{xo} \cdots \quad V_{xo} \,]^T \quad (14.5)$$

and

$$\boldsymbol{C} = \begin{bmatrix} (N-1) & -1 \cdots & -1 \\ -1 & (N-1) \cdots & -1 \\ \vdots & \vdots & \vdots \\ -1 & -1 \cdots & (N-1) \end{bmatrix} \quad (14.6)$$

$$\boldsymbol{C_r} = \begin{bmatrix} (N-1)r_1 & -r_2 \cdots & -r_N \\ -r_1 & (N-1)r_2 \cdots & -r_N \\ \vdots & \vdots & \vdots \\ -r_1 & -r_2 \cdots & (N-1)r_N \end{bmatrix} \quad (14.7)$$

$$\boldsymbol{C_r} = \begin{bmatrix} (N-1)L_1 & -L_2 \cdots & -L_N \\ -L_1 & (N-1)L_2 \cdots & -L_N \\ \vdots & \vdots & \vdots \\ -L_1 & -L_2 \cdots & (N-1)L_N \end{bmatrix} \quad (14.8)$$

This book belongs to Kitab Liaison (ocd1996@gmail.com) Copyright Elsevier 2023

The load current of a particular phase is the sum of all VSC currents of that phase and it is given as

$$i_x = \sum_{k=1}^{N} i_{x_k};\ \text{where } 1 \le k \le N \tag{14.9}$$

where i_{x_k} is the current through phase x leg of kth VSC. For the parallel-connected VSCs, the VSC current i_{x_k} can be split into two components:

1. The component contributing to the load current $i_{x_k,l}$
2. The circulating current $i_{x_k,c}$

Therefore, the VSC current can be represented as

$$i_{x_k} = i_{x_k,l} + i_{x_k,c} \tag{14.10}$$

where $i_{x_k,l}$ is the load current component of the VSC current i_{x_k} and $i_{x_k,c}$ is the circulating current component of the VSC current. The circulating current components $i_{x_k,c}$ do not contribute to the resultant line current. Therefore, (14.9) can be rewritten as

$$i_x = \sum_{k=1}^{N} i_{x_k,l};\ \text{where } 1 \le k \le N \tag{14.11}$$

and

$$\sum_{k=1}^{N} i_{x_k,c} = 0;\ \text{where } 1 \le k \le N \tag{14.12}$$

14.2.1.1 Impact of the modulator mismatch

In a modular PCS with parallel VSCs, each VSC uses a separate control unit with its own modulator. The mismatch in the reference signals as well as the asynchronous carrier signals leads to the circulating current. A simplified analysis is performed to evaluate the impact of the modular mismatch. A symmetrical filter impedance is assumed to decouple the impact of the impedance mismatch on the circulating current. Under this assumption

$$L_1 = L_2 = L_N = L_f \tag{14.13}$$

and

$$r_1 = r_2 = r_N = r_f \tag{14.14}$$

This book belongs to Kitab Liaison (ocd1996@gmail.com) Copyright Elsevier 2023

Using Eqs. (14.2), (14.13), and (14.14), the dynamics of the circulating current is given as

$$\frac{1}{N}\boldsymbol{CV_P} = \boldsymbol{R_f I_c} + \boldsymbol{L_f}\frac{d}{dt}\boldsymbol{I_c} \tag{14.15}$$

where

$$\boldsymbol{I_c} = \begin{bmatrix} i_{x_1,c} & i_{x_2,c}\cdots & i_{x_N,c} \end{bmatrix} \tag{14.16}$$

$$\boldsymbol{L_f} = \begin{bmatrix} L_f & 0\cdots & 0 \\ 0 & L_f\cdots & 0 \\ \vdots & \vdots & \vdots \\ 0 & 0\cdots & L_f \end{bmatrix} \tag{14.17}$$

and

$$\boldsymbol{R_f} = \begin{bmatrix} r_f & 0\cdots & 0 \\ 0 & r_f\cdots & 0 \\ \vdots & \vdots & \vdots \\ 0 & 0\cdots & r_f \end{bmatrix} \tag{14.18}$$

Since the internal resistance of filter inductor is very small compared to the inductive reactance, resistance of the filter can be neglected. By neglecting the resistance of the VSC current part, the circulating current for the PCS with two parallel VSCs can be expressed as

$$i_{x_1,c}(t) = -i_{x_2,c}(t) = \frac{1}{2L_f}\int (v_{x_1o} - v_{x_2o})dt \tag{14.19}$$

From Eq. (14.21), it clear that any difference in the pole voltages would lead to the flow of the circulating current. Several factors, including mismatch in the reference voltages, asynchronous carriers, and semiconductor devices, contribute to the pole voltage mismatch. The circulating current of all three phases can also be represented in terms of the CM current, and the CM current of kth VSC can be represented as

$$i_{cm_k}(t) = \frac{i_{a_k} + i_{b_k} + i_{c_k}}{3} = \frac{N-1}{NL_f}\int v_{cm_k}dt - \frac{1}{NL_f}\sum_{\substack{j=1 \\ j\neq k}}^{N}\int v_{cm_j}dt \tag{14.20}$$

This book belongs to Kitab Liaison (ocd1996@gmail.com)
Copyright Elsevier 2023

For two parallel VSCs, the CM circulating current can be represented as

$$i_{cm_1}(t) = -i_{cm_2}(t) = \frac{1}{2L_f}\int (v_{cm_1} - v_{cm_2})dt \tag{14.21}$$

14.2.1.2 Impact of the impedance mismatch

The pole voltages of parallel VSCs are assumed to be equal to analyze the impact of the impedance mismatch on the circulating current. Under this assumption, the voltage drop across the filter impedance can be represented as

$$r_k i_{x_k} + L_k \frac{di_{x_k}}{dt} = v_{x_k o} - v_{xo} \tag{14.22}$$

For the two parallel VSCs with equal pole voltages, the voltage drop across the filter impedance is given as

$$r_1 i_{x_1} + L_1 \frac{di_{x_1}}{dt} = r_2 i_{x_2} + L_2 \frac{di_{x_2}}{dt} \tag{14.23}$$

Only considering the fundamental frequency component, the VSC currents can be represented using phasors (represented by bold symbols) as

$$(r_1 + j\omega L_1)\boldsymbol{i_{x_1}} = (r_1 + j\omega L_2)\boldsymbol{i_{x_2}} \tag{14.24}$$

and the phasor representation of the circulating current is

$$\boldsymbol{i_{x_1,c}} = -\boldsymbol{i_{x_2,c}} = \frac{(r_2 - r_1) + j\omega(L_2 - L_1)}{2(r_1 + j\omega L_1)}\boldsymbol{i_{x_2}} \tag{14.25}$$

Therefore, it is evident from Eq. (14.25) that the filter impedance mismatch would lead to the circulating current flow even when the pole voltages are perfectly matched.

14.2.2 Parallel converters with separate DC bus

For the PCS with separate DC bus as shown in Fig. 14.1B, the CM current flows between the parallel-connected back-to-back VSCs. The circulating current behavior of the PCS with two back-to-back connected parallel VSCs with separate DC links is analyzed. The analysis can be simplified by assuming symmetrical impedances ($L_{g_1} = L_{g_2} = L_g$ and $L_{l_1} = L_{l_2} = L_l$). The CM circulating current can be expressed as

$$i_{cm_1}(t) = \frac{1}{2(L_l + L_g)}\int \left(v_{cm_{l_1}} - v_{cm_{g_1}} - v_{cm_{l_2}} + v_{cm_{g_2}}\right)dt \tag{14.26}$$

where i_{cm_1} is the CM circulating current of first back-to-back connected VSCs and $i_{cm_1} = -i_{cm_2}$. $v_{cm_{l_k}}$ and $v_{cm_{g_k}}$ are the CM voltages of the front-end and back-end converter of kth VSC.

This book belongs to Kitab Liaison (ocd1996@gmail.com) Copyright Elsevier 2023

14.3 Circulating current control

The circulating current can be avoided by providing galvanic isolation between the parallel VSCs. The galvanic isolation is often achieved using a bulky line frequency transformer, which adds to the cost and increases the size of the PCS. On the other hand, many grid-connected applications use a transformer between the converter system and a grid for voltage matching. Also, in some applications, the grid codes demand galvanic isolation. In such applications requiring parallel VSCs to meet high current requirements, using a transformer with multiple isolated primary windings [2] is a good solution as it avoids the use of any additional components and control efforts to avoid the circulating current.

The circulating current reduction and proper load sharing between parallel VSCs can be achieved by incorporating a suitable control strategy. One such control strategy is to use communication lines between the parallel VSCs for exchanging information and reference commands to achieve load sharing. Several implementation using communication among the module have been reported, including centralized and distributed control [5–9]. The dependence on the communication channel is a major drawback of these schemes, as the modularity is compromised. Moreover, redundant communication lines are required in critical installations, which increase the cost and complexity of the system. The dependency on communication can be avoided by using droop control techniques [10,11]. The droop control scheme is motivated by the droop control scheme of the synchronous generators in the conventional power grid. The active and reactive power sharing between the parallel VSCs is achieved by adjusting frequency and voltage amplitude set points of each VSC output voltage, defined by their droop equations. The self-regulating action of the droop control makes it communication free. However, a large deviation in the voltage and frequency is inevitable if accurate load sharing is required. Therefore, droop control is often complimented by having additional control information using a slow and noncritical communication channel between the VSCs. As discussed in Section 2, the circulating current flows between the parallel VSCs due to the difference in the pole voltage. Since the circulating current between the parallel VSCs can also be represented as a CM circulating current, it can be reduced by modifying the CM voltage added to the reference signal used for the carrier comparison-based modulator. For the space vector implementation, this can be achieved by adjusting the duty cycle of the zero voltage vector. In this section, control schemes for the circulating current reduction are discussed.

This book belongs to Kitab Liaison (ocd1996@gmail.com) Copyright Elsevier 2023

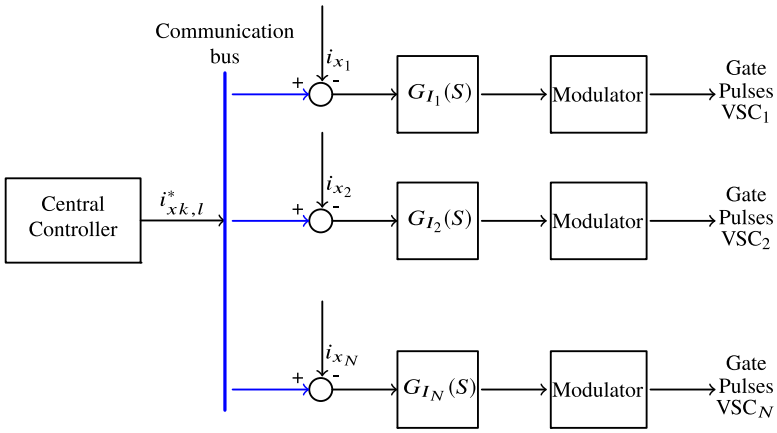

FIGURE 14.2 Parallel voltage source converters with central controller that implements outer voltage/power loop and provides current references for each individual converter inner current loop realization.

14.3.1 Current sharing schemes

In its simplest form, the current sharing scheme can be realized by having a central controller that implements outer voltage or power loop and provides current references for each individual VSC [10], as shown in Fig. 14.2. Each of the VSCs has its own inner current control loop, which processes the current error, obtained by subtracting the measured VSC current from the reference obtained from the central controller [5]. In this scheme, VSC current and load current measurements along with the central controller are required, which compromises the modularity and fault-tolerant operation.

The central controller and total load current measurement can be avoided by employing circular chain control [12], where VSC controllers are connected in the circular chain, as shown in Fig. 14.3. Each VSC has its inner current loop and outer voltage or power loop. The inner current loop tracks the inductor current of the previous module in the circular chain, leading to an equal current sharing.

A master–slave control technique is shown in Fig. 14.4, where the master VSC operates in the voltage-controlled mode and provides current references for the current-controlled slave VSCs [7]. In the master–slave control scheme with the dedicated master VSC, the failure of the dedicated master VSC compromises the availability of the complete PCS. The PCS can be made resilient by incorporating the status line to decide the master VSC [13]. In this scheme, one of the slave VSCs takes over if the master VSC fails. The resiliency can also be improved by adopting auto master–slave control, where the VSC with the highest load current is automatically assigned as a master VSC [14].

This book belongs to Kitab Liaison (ocd1996@gmail.com) Copyright Elsevier 2023

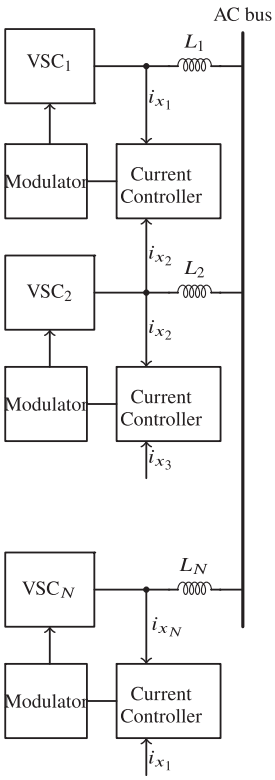

FIGURE 14.3 Circular chain control scheme for parallel voltage source converters.

14.3.2 Droop control scheme

All the current sharing schemes discussed so far require critical communication links between the VSCs and a failure of the communication links compromises the reliability of the PCS. The critical communication link can be avoided by employing a droop control scheme [10]. The droop control of the parallel VSCs is similar to frequency/voltage droop control of the synchronous generator in the conventional power grid. For the VSC connected to the common AC bus using a filter, the active and reactive power of the inverter are

$$P = \left(\frac{EV}{Z}\cos\phi - \frac{V^2}{Z}\right)\cos\theta + \frac{EV}{Z}\sin\phi\sin\theta \tag{14.27}$$

$$Q = \left(\frac{EV}{Z}\cos\phi - \frac{V^2}{Z}\right)\sin\theta + \frac{EV}{Z}\sin\phi\cos\theta \tag{14.28}$$

where E is the amplitude of the fundamental frequency component of the VSC voltage, V is the amplitude of the common AC-bus voltage, Z is the filter

This book belongs to Kitab Liaison (ocd1996@gmail.com) Copyright Elsevier 2023

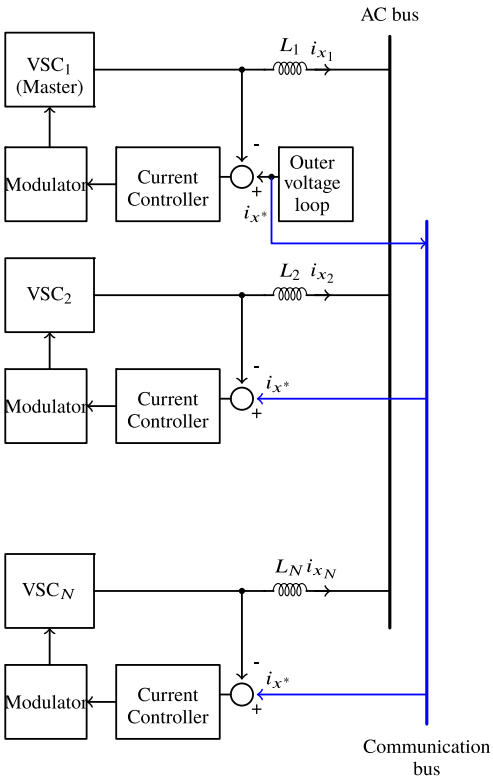

FIGURE 14.4 Master−slave control scheme for parallel voltage source converters.

impedance, θ is the phase angle of the filter impedance, and ϕ is the phase angle. For the VSC with an inductive filter ($X \gg R$), the active and reactive power expressions can be approximated as

$$P = \frac{EV}{X}\sin\phi \approx \frac{EV}{X}\phi \tag{14.29}$$

$$Q = \frac{EV}{X}\cos\phi - \frac{V^2}{X} \approx \frac{V(E-V)}{X} \tag{14.30}$$

where X is the inductive reactance of the filter. From Eqs. (14.29) and (14.30), it is evident that the active power is proportional to the phase angle ϕ and the reactive power is proportional to the voltage amplitude difference $E-V$. Therefore, the active and reactive power of the VSC are regulated by setting appropriate frequency (phase angle) and amplitude of the fundamental frequency component of the VSC output voltage, respectively [11]. Inspired by the synchronous generator control in the conventional power grid, the frequency and amplitude set points of the fundamental frequency component

This book belongs to Kitab Liaison (ocd1996@gmail.com) Copyright Elsevier 2023

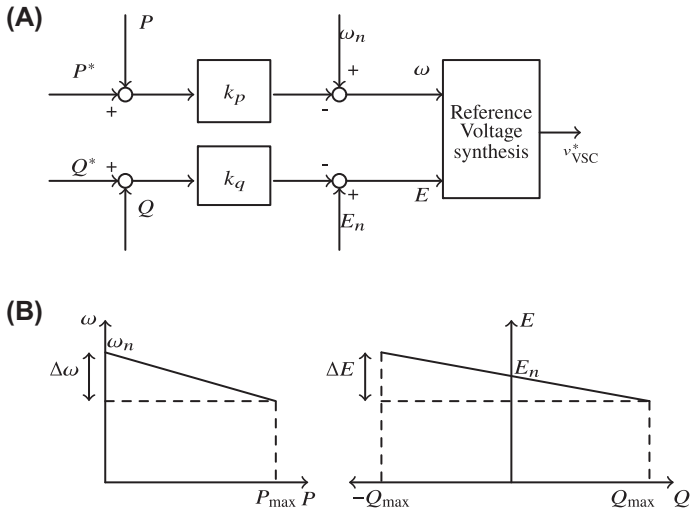

FIGURE 14.5 Droop control scheme for the power sharing among parallel voltage source converters. (A) Control block diagram for reference voltage derivation. (B) Droop control.

of the VSC voltage can be derived using the $P-\omega$ and $Q-V$ droop schemes, as shown in Fig. 14.5, where the control laws can be expressed as

$$\omega = \omega_n - k_p(P - P_n) \tag{14.31}$$

$$E = E_n - k_q(Q - Q_n) \tag{14.32}$$

where k_p and k_q are the frequency and voltage amplitude droop coefficients, respectively. ω_n is the frequency at no load and E_n is the voltage amplitude at no load. As it is evident from Eqs. (14.35) and (14.36) that the droop control law offers negative feedback, and good power sharing between parallel VSCs can be achieved by selecting a sufficiently high value of droop coefficients. However, having a high value of the droop coefficients leads to the larger variation in the frequency and voltages.

The decoupling between the active and reactive power is only valid for the inductively coupled AC sources, and therefore the droop control laws given by Eqs. (14.35) and (14.36) work satisfactorily with good power sharing only in case of the VSC having inductive filters. However, the closed-loop output impedance of the VSC depends on the control strategy. Moreover, the line impedance could be resistive in the low-voltage distribution system, leading to inaccurate power sharing [15]. In such cases, the active and reactive power can be expressed as

$$P = \frac{EV}{R}\cos\phi - \frac{V^2}{R} \approx \frac{V(E-V)}{R} \tag{14.33}$$

This book belongs to Kitab Liaison (ocd1996@gmail.com) Copyright Elsevier 2023

$$Q = \frac{EV}{R}\sin\phi \approx \frac{EV}{R}\phi \tag{14.34}$$

The droop control laws can be adapted as

$$\omega = \omega_n + k_p(Q - Q_n) \tag{14.35}$$

$$E = E_n - k_q(P - P_n) \tag{14.36}$$

The power sharing accuracy can also be improved by adjusting the output impedance of the VSC by employing virtual output impedance control [16]. The desired virtual output impedance Z_o can be inserted by modifying the voltage reference as

$$v_{vsc}^* = E\sin(\omega t) - i_o Z_o(S) \tag{14.37}$$

where i_o is the output current. Moreover, it is also possible to design virtual impedance that exhibits inductive behavior at the fundamental frequency and a resistive behavior at the harmonic frequencies [17]. As a result, good power sharing in the case of linear and nonlinear loads can be obtained.

Proper load sharing can be achieved by combining both the droop control laws and virtual output impedance control [18], as shown in Fig. 14.6. The droop control laws are used to derive voltage references, whereas the virtual output impedance control is used to achieve a symmetrical impedance. The circulating current controller is also incorporated, which modifies the reference current generated using the outer voltage controller. The VSC currents (i_{abc_1} and i_{abc_2}) are transformed into the rotating reference frame, and the circulating current controller is implemented in the rotating reference frame, with the control objective to drive the difference between the VSC currents to zero. Although each of the VSCs has a circulating current controller, it is evident from Eq. (14.21) that controlling the pole voltage of only one VSC can effectively reduce the circulating current.

14.3.3 Zero vector dwell time control

For two parallel VSCs, the circulating CM current behavior can be derived using Eq. (14.2) as

$$v_{cm_1} - v_{cm_2} = (r_1 + r_2)i_{cm} + (L_1 + L_2)\frac{di_{cm}}{dt} \tag{14.38}$$

where i_{cm} is the CM circulating current and it is expressed as

$$i_{cm} = i_{cm_1} = -i_{cm_2} \tag{14.39}$$

This book belongs to Kitab Liaison (ocd1996@gmail.com) Copyright Elsevier 2023

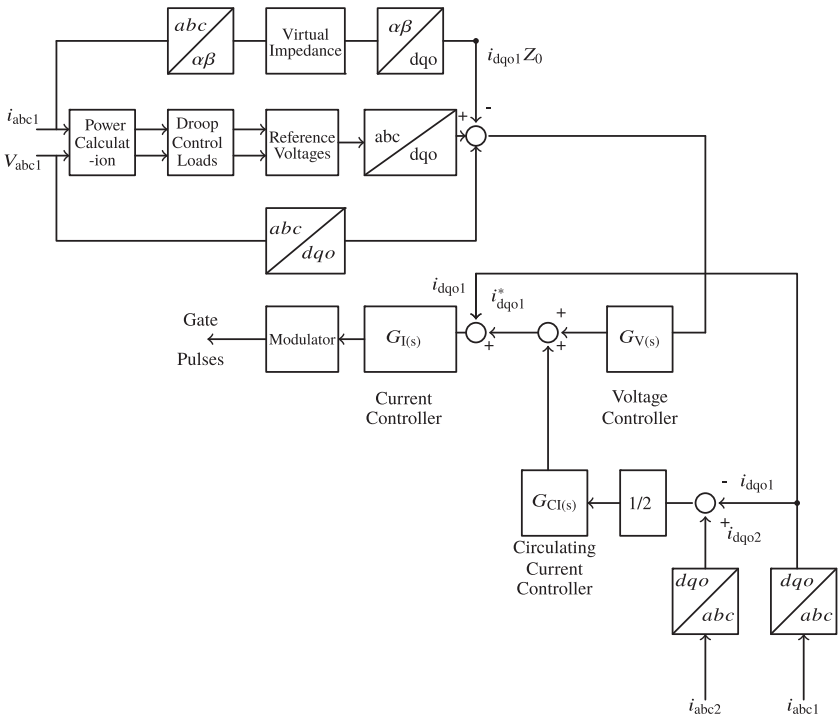

FIGURE 14.6 Load and circulating current control of two parallel converters using a combination of droop control laws and virtual output impedance control.

From Eq. (14.38), it is evident that the low-frequency CM circulating current depends on the difference of the average value of the CM voltages. Therefore, the low-frequency CM circulating current can be reduced through the proper control of the average CM voltage over a switching period.

Using phase-leg averaging technique, the average of the pole voltage over a switching period $\overline{v_{x_k o}}$ can be defined as

$$\overline{v_{x_k o}} = \widehat{d_{x_k}} V_{dc} = \left(d_{x_k} - \frac{1}{2}\right) V_{dc} \tag{14.40}$$

where d_{x_k} is the duty cycle of the x phase leg of kth VSC. Note that the pole voltage is measured with respect to the DC-bus midpoint o. The duty cycle is defined as

$$d_{x_k} = \frac{T_{on}}{T_s} = \frac{v_x^{**}}{V_{dc}} + \frac{1}{2} \tag{14.41}$$

where T_{on} is the on time of the upper switch in the VSC leg, T_s is the switching period, and v_x^{**} is the reference used for the carrier comparison. The reference

This book belongs to Kitab Liaison (ocd1996@gmail.com) Copyright Elsevier 2023

voltage waveform is often derived by adding common voltage v_z in the reference sinusoidal voltage waveform, i.e., the reference waveform of the phase x of kth VSC leg is

$$v_{x_k}^{**} = v_{x_k}^{*} + v_{z_k} \tag{14.42}$$

Using Eqs. (14.40) and (14.42), the average of the CM voltage over a switching period can be obtained as

$$\overline{v_{cm_k}} = v_{z_k} \tag{14.43}$$

Therefore, the CM circulating current can be reduced by controlling v_{z_k}.

The average value of the CM voltage can also be controlled by selecting the appropriate value of the zero vector dwell times. The two-level (2L) VSC has eight voltage vectors defined by the combination of the switch states. These states generate six active vectors ($\overrightarrow{V_1} - \overrightarrow{V_6}$) and two zero vectors ($\overrightarrow{V_0}, \overrightarrow{V_7}$), as shown in Fig. 14.7. The three-phase reference signals can be represented by a complex reference vector $\overrightarrow{V_s^{\star}}$. Based on the magnitude ($|\overrightarrow{V_s^{\star}}|$) and angle ($\psi_s$) of the sampled $\overrightarrow{V_s^{\star}}$, two adjacent active voltage vectors and zero vectors are commonly applied to synthesize the reference vector. The respective dwell time of the active vectors is chosen to maintain the volt−sec balance.

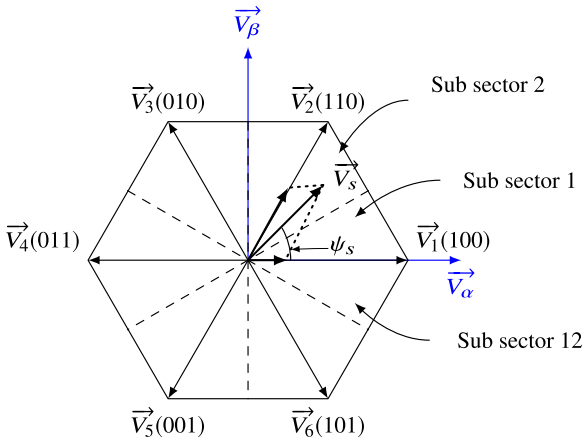

FIGURE 14.7 Basic space vector sectors and states in complex $\alpha\beta$ plane, used for the modulation of the voltage source converter.

This book belongs to Kitab Liaison (ocd1996@gmail.com) Copyright Elsevier 2023

Let T_1, T_2, and T_z be the dwell time of $\overrightarrow{V_1}$, $\overrightarrow{V_2}$, and $\overrightarrow{V_0}/\overrightarrow{V_7}$, respectively, and they are given by

$$T_1 = \frac{2}{\sqrt{3}} \frac{\left|\overrightarrow{V_s^\star}\right|}{V_{dc}} T_s \sin(60^\circ - \psi_s) \tag{14.44}$$

$$T_2 = \frac{2}{\sqrt{3}} \frac{\left|\overrightarrow{V_s^\star}\right|}{V_{dc}} T_s \sin(\psi_s) \tag{14.45}$$

$$T_z = T_s - T_1 - T_2 \tag{14.46}$$

The dwell time of the zero voltage vectors $\overrightarrow{V_0}$ and $\overrightarrow{V_7}$ is given by $K_z T_z$ and $(1 - K_z)T_z$, respectively, where $0 \nleqq K_z \nleqq 1$. Different modulation possibilities exist with variation in the parameter K_z. For example, $K_z = 0.5$ results in the conventional space vector modulation (SVM). By changing the value of K_z between zero and one with a frequency three times higher than the frequency of the reference signal, several discontinuous pulse width modulation (DPWM) schemes can be realized. If the value of K_z is changed from zero to one in the middle of sector 1 (c.f. 7), the reference signals for 60 degrees clamped DPWM (DPWM1) are generated.

Since both the zero voltage vectors do not contribute to any volt−sec toward the reference vector synthesizing, they offer an additional degree of freedom that can be used to control the average CM voltage. The application of $\overrightarrow{V_0}$ and $\overrightarrow{V_7}$ results into the CM voltage of $-\frac{V_{dc}}{2}$ and $\frac{V_{dc}}{2}$, respectively. Therefore, by adjusting the value of the K_z, the desired average CM voltage can be achieved to reduce the CM circulating current [19], as shown in Fig. 14.8. The circulating current controller is implemented for only one of the VSCs in two parallel VSC-based PCS. All three-phase currents are measured, and the CM current is obtained. A proportional integrator (PI) is used to regulate the CM voltage to zero. The PI controller output is K_z, which is then fed to the modulator to determine the dwell time of the voltage vectors $\overrightarrow{V_0}$ and $\overrightarrow{V_7}$.

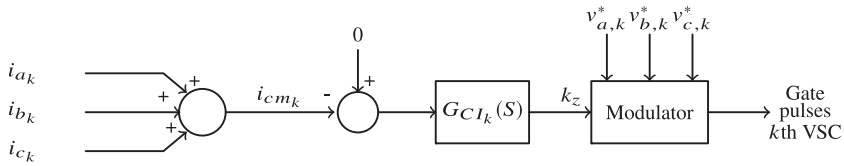

FIGURE 14.8 Circulating current controller implementation for two parallel voltage source converters. Circulating current controller is only implemented for one of the VSCs, as there is only one CM circulating current in two parallel converter system.

This book belongs to Kitab Liaison (ocd1996@gmail.com) Copyright Elsevier 2023

14.4 Harmonic performance improvement through interleaved operation

The harmonic distortion and CM voltage of the PCS with parallel VSCs can be significantly reduced by interleaving operation. Besides, interleaving operation also reduces the DC-link capacitor ripple [20]. As a result, the size of the harmonic filter components and DC-link capacitor can be reduced.

14.4.1 Modulation of parallel interleaved converters

Conventionally the interleaved operation is realized using the phase-shifted carrier signals. Based on the phase-shift angle, the interleaving operation can be classified into two categories:

1. Symmetrical carrier interleaving
2. Asymmetrical carrier interleaving

Symmetrical carrier interleaving is commonly used, where the carrier interleaving angle γ is set to

$$\gamma = \frac{360^\circ}{N} \tag{14.47}$$

where N is the number of parallel VSCs. The impact of the asymmetrical interleaving angle on the harmonic performance has been investigated in Refs. [21,22], where it is demonstrated that the asymmetrical carrier interleaving could lead to improved harmonic performance under some operating conditions.

Two parallel VSCs are shown in Fig. 14.9A. Carrier signals of both the VSCs are phase shifted by 180 degrees, as shown in Fig. 14.9B. As a result, the switched output voltages of the parallel VSC legs (referred to as pole voltages) are also phase shifted, as shown in Fig. 14.10A and Fig. 14.10B. The resultant voltage is the average of the individual switched output voltage of the parallel legs of that phase and demonstrates three-level voltage waveforms, as shown in Fig. 14.10C. The line-to-line voltage across the phase a and phase b is also shown in Fig. 14.10E. It demonstrates a five-level voltage waveform. As a result, compared to the 2L-VSC, superior harmonic performance can be achieved. The harmonic performance of PCS with parallel interleaved VSCs is strongly influenced by the modulation scheme, interleaving angle, and the number of parallel VSCs.

14.4.2 Symmetrically interleaved converters

In addition to the desired fundamental frequency component, the pole voltages have undesirable harmonic frequency components due to the modulation.

This book belongs to Kitab Liaison (ocd1996@gmail.com) Copyright Elsevier 2023

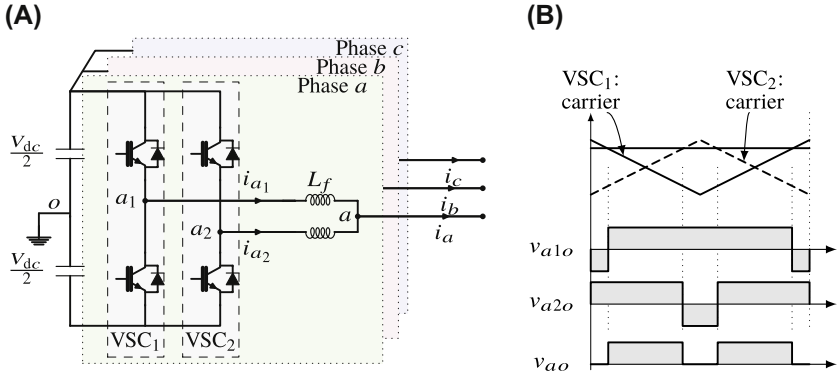

FIGURE 14.9 Parallel interleaved voltage source converters. (A) Power conversion system with two parallel interleaved voltage source converters (VSC_1 and VSC_2), (B) Interleaving implementation using phase-shifted carrier signals. Pole voltages of each voltage source converter and their average voltage for phase a are shown.

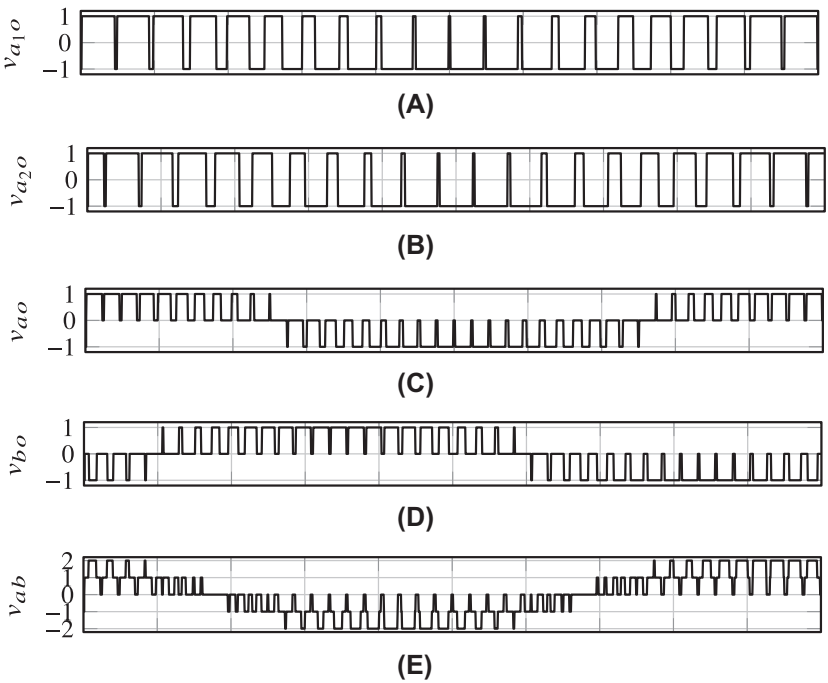

FIGURE 14.10 Simulated voltage waveforms for two parallel interleaved voltage source converters. The carrier signals of the two voltage source converters are phase shifted by 180 degrees. (A) Switched output voltage of leg a_1, (B) Switched output voltage of leg a_2, (C) Resultant voltage of phase a, (D) Resultant voltage of phase b, (E) Line-to-line voltage V_{ab}. The voltage waveforms are normalized with respect to $V_{dc}/2$.

This book belongs to Kitab Liaison (ocd1996@gmail.com) Copyright Elsevier 2023

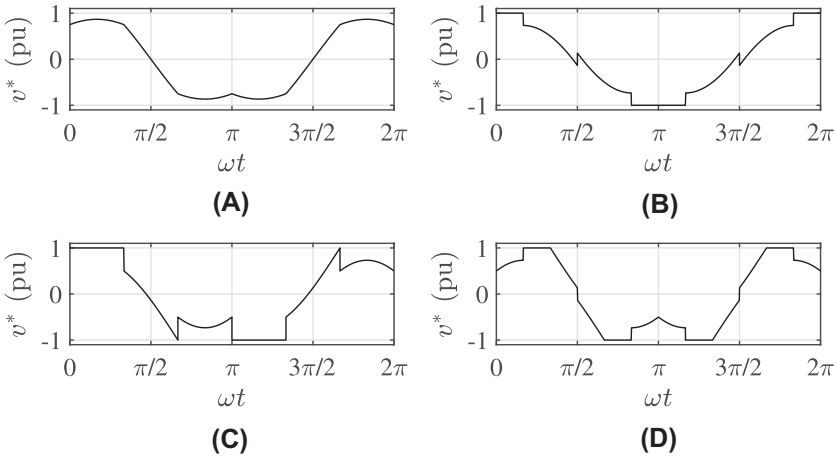

FIGURE 14.11 Representative modulation waveforms for modulation index $M = 1$. (A) Center-aligned space vector modulation (SVM), (B) 60 degrees clamp discontinuous PWM (DPWM1), (C) 30 degrees lagging clamp discontinuous PWM (DPWM2), and (D) 30 degrees clamp discontinuous PWM (DPWM3).

Every PWM scheme has a unique harmonic spectrum, which dictates the load current quality and harmonic filter sizing. The harmonic performance of the following four conventional PWM schemes is evaluated:

- Center-aligned SVM
- 60 degrees clamp discontinuous PWM (DPWM1)
- 30 degrees lagging clamp discontinuous PWM (DPWM2)
- 30 degrees clamp discontinuous PWM (DPWM3)

The representative modulation waveform for each of these PWM schemes is shown in Fig. 14.11. The harmonic performances of these PWM schemes are compared by evaluating the normalized weighted total harmonic distortion (NWTHD), which is defined as

$$\text{NWTHD} = \frac{M\sqrt{\sum_{h=2}^{\infty}(v_h/h)^2}}{v_f} \tag{14.48}$$

where v_f is the fundamental component and v_h is the magnitude of the hth harmonic component.

This book belongs to Kitab Liaison (ocd1996@gmail.com) Copyright Elsevier 2023

The harmonic components can be represented as the summation series of sinusoids, characterized by the carrier index variable m and the baseband index variable n [23] and it is given as

$$\begin{aligned} f(t) = \frac{A_{00}}{2} &+ \sum_{n=1}^{\infty}[A_{0n}\cos(n[\omega_0 t + \theta_0]) + B_{0n}\sin(n[\omega_0 t + \theta_0])] \\ &+ \sum_{m=1}^{\infty}[A_{m0}\cos(m[\omega_c t + \theta_c]) + B_{m0}\sin(m[\omega_c t + \theta_c])] \\ &+ \sum_{m=1}^{\infty}\sum_{n=-\infty\, n\neq 0}^{\infty}[A_{mn}\cos(m[\omega_c t + \theta_c] + n[\omega_0 t + \theta_0]) \\ &+ B_{mn}\sin(m[\omega_c t + \theta_c] + n[\omega_0 t + \theta_0])] \end{aligned} \tag{14.49}$$

The hth harmonic component is defined in terms of m and n, and it is given as

$$h = m\left(\frac{\omega_c}{\omega_0}\right) + n \tag{14.50}$$

where ω_0 is the fundamental frequency and ω_c is the carrier frequency. The harmonic coefficients A_{mn} and B_{mn} in (14.49) are evaluated for each 60 degrees sextant using the double Fourier integral. These coefficients are evaluated for a single VSC (noninterleaved VSC) under SVM scheme for phase a as

$$Amn_{v_{a1o}} = \frac{4V_{dc}}{q\pi^2} \times \left(\begin{aligned} &\frac{\pi}{6}\sin\left[(m+n)\frac{\pi}{2}\right]\left\{J_n\left(q\frac{3\pi}{4}M\right) + 2\cos\left(\frac{n\pi}{6}\right)J_n\left(q\frac{\sqrt{3}\pi}{4}M\right)\right\} \\ &+\frac{1}{n}\sin\left(\frac{m\pi}{2}\right)\cos\left(\frac{n\pi}{2}\right)\sin\left(\frac{n\pi}{6}\right)\left\{J_0\left(q\frac{3\pi}{4}M\right) - J_0\left(q\frac{\sqrt{3}\pi}{4}M\right)\right\}\Bigg|_{n\neq 0} \\ &+ \sum_{\substack{k=1\\k\neq -n}}^{\infty}\frac{1}{n+k}\sin\left([m+k]\frac{\pi}{2}\right)\cos\left([n+k]\frac{\pi}{2}\right)\sin\left([n+k]\frac{\pi}{6}\right) \\ &\times\left\{J_k\left(q\frac{3\pi}{4}M\right) + 2\cos\left([2n+3k]\frac{\pi}{6}\right)\left\{J_k\left(q\frac{\sqrt{3}\pi}{4}M\right)\right\}\right. \\ &+ \sum_{\substack{k=1\\k\neq -n}}^{\infty}\frac{1}{n-k}\sin\left([m+k]\frac{\pi}{2}\right)\cos\left([n-k]\frac{\pi}{2}\right)\sin\left([n-k]\frac{\pi}{6}\right) \\ &\times\left\{J_k\left(q\frac{3\pi}{4}M\right) + 2\cos\left([2n-3k]\frac{\pi}{6}\right)\left\{J_k\left(q\frac{\sqrt{3}\pi}{4}M\right)\right\}\right. \end{aligned} \right) \tag{14.51}$$

This book belongs to Kitab Liaison (ocd1996@gmail.com)
Copyright Elsevier 2023

where V_{dc} is the DC-link voltage, M is the modulation index, and $q = m + n(\omega_0/\omega_c)$. The expressions contain $J_y(z)$, which represents the Bessel functions of the first kind of the order y and argument z. The double summation term in (14.49) is the ensemble of all possible frequencies, formed by taking the sum and the difference between the carrier harmonics, the fundamental waveform, and its associated baseband harmonics. The harmonic coefficients for phase b are also obtained to evaluate the harmonic performance of the line-to-line voltage v_{ab}. The harmonic spectrum of the line-to-line voltage of a single VSC with the SVM scheme is shown in Fig. 14.12 for the modulation index of $M = 1$. The major harmonic components are concentrated around the carrier frequency harmonics, as shown in Fig. 14.12A.

To evaluate the harmonic performance, the harmonic coefficients of the average pole voltage of phase a are calculated for two symmetrically interleaved VSCs under SVM as

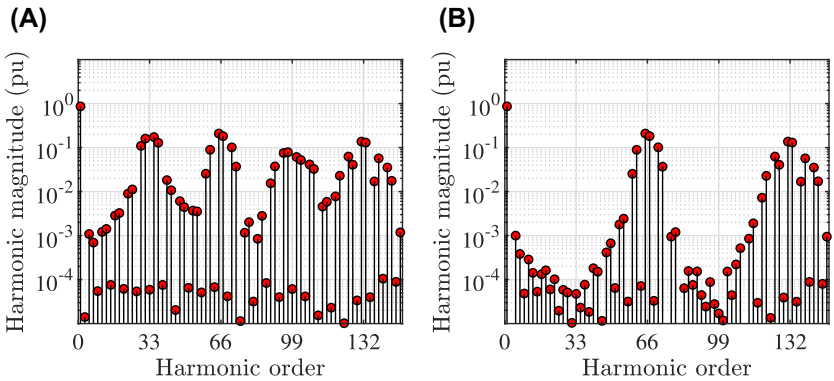

FIGURE 14.12 Harmonic spectrum of the line-to-line voltage under space vector modulation scheme with modulation index $M = 1$ and pulse ratio $\omega_c/\omega_0 = 33$. The pulse ratio is defined as the ratio of the carrier frequency to the fundamental frequency. (A) Line-to-line voltage of the single voltage source converter (noninterleaved), (B) Line-to-line voltage of two symmetrically interleaved voltage source converters.

This book belongs to Kitab Liaison (ocd1996@gmail.com)
Copyright Elsevier 2023

$$Amn_{v_{ao}} = \frac{4V_{\mathrm{dc}}}{q\pi^2} \times \left(\begin{array}{l} \frac{\pi}{6}\cos\left(m\frac{\pi}{2}\right)\sin\left(n\frac{\pi}{2}\right)\left\{J_n\left(q\frac{3\pi}{4}M\right) + 2\cos\left(\frac{n\pi}{6}\right)J_n\left(q\frac{\sqrt{3}\pi}{4}M\right)\right\} \\ + \sum\limits_{\substack{k=1 \\ k\neq -n}}^{\infty} \frac{1}{n+k}\cos\left(m\frac{\pi}{2}\right)\sin\left(k\frac{\pi}{2}\right)\cos\left([n+k]\frac{\pi}{2}\right)\sin\left([n+k]\frac{\pi}{6}\right) \\ \times\left\{J_k\left(q\frac{3\pi}{4}M\right) + 2\cos\left([2n+3k]\frac{\pi}{6}\right)\left\{J_k\left(q\frac{\sqrt{3}\pi}{4}M\right)\right\}\right. \\ + \sum\limits_{\substack{k=1 \\ k\neq -n}}^{\infty} \frac{1}{n-k}\cos\left(m\frac{\pi}{2}\right)\sin\left(k\frac{\pi}{2}\right)\cos\left([n-k]\frac{\pi}{2}\right)\sin\left([n-k]\frac{\pi}{6}\right) \\ \times\left\{J_k\left(q\frac{3\pi}{4}M\right) + 2\cos\left([2n-3k]\frac{\pi}{6}\right)\left\{J_k\left(q\frac{\sqrt{3}\pi}{4}M\right)\right\}\right. \end{array} \right) \tag{14.52}$$

Using Eq. (14.52), the harmonic coefficients of the line-to-line voltages are given as

$$Amn_{v_{ab}} = \frac{4V_{\mathrm{dc}}}{q\pi^2} \times \left(\begin{array}{c} \frac{\pi}{6}\cos\left(m\frac{\pi}{2}\right)\sin\left(n\frac{\pi}{2}\right)\left[1 - \cos\left(2n\frac{\pi}{3}\right)\right. \\ \times\left\{J_n\left(q\frac{3\pi}{4}M\right) + 2\cos\left(\frac{n\pi}{6}\right)J_n\left(q\frac{\sqrt{3}\pi}{4}M\right)\right\} \\ + \sum\limits_{\substack{k=1 \\ k\neq -n}}^{\infty} \frac{1}{n+k}\cos\left(m\frac{\pi}{2}\right)\sin\left(k\frac{\pi}{2}\right)\cos\left(\left[n+k\frac{\pi}{2}\right)\sin\left(\left[n+k\frac{\pi}{6}\right)\right.\right. \\ \times\left\{J_k\left(q\frac{3\pi}{4}M\right)\left[1 - \cos\left([n+3k]\frac{\pi}{3}\right)\right]\right\} \\ +2\left[\cos\left([2n+3k]\frac{\pi}{6}\right) - \cos\left([n-3k]\frac{\pi}{6}\right)\cos\left(n\frac{\pi}{6}\right)\right]\left\{J_k\left(q\frac{\sqrt{3}\pi}{4}M\right)\right\} \\ + \sum\limits_{\substack{k=1 \\ k\neq -n}}^{\infty} \frac{1}{n-k}\cos\left(m\frac{\pi}{2}\right)\sin\left(k\frac{\pi}{2}\right)\cos\left([n-k]\frac{\pi}{2}\right)\sin\left([n-k]\frac{\pi}{6}\right) \\ \times\left\{J_k\left(q\frac{3\pi}{4}M\right)\left[1 - \cos\left([n-3k]\frac{\pi}{3}\right)\right]\right\} \\ +2\left[\cos\left([2n-3k]\frac{\pi}{6}\right) - \cos\left([n+3k]\frac{\pi}{6}\right)\cos\left(n\frac{\pi}{6}\right)\right]\left\{J_k\left(q\frac{\sqrt{3}\pi}{4}M\right)\right\} \end{array} \right) \tag{14.53}$$

This book belongs to Kitab Liaison (ocd1996@gmail.com)
Copyright Elsevier 2023

$$Bmn_{v_{ab}} = \frac{4V_{\mathrm{dc}}}{q\pi^2} \times \left(\begin{array}{c} \frac{\pi}{6}\cos\left(m\frac{\pi}{2}\right)\sin\left(n\frac{\pi}{2}\right)\sin\left(2n\frac{pi}{3}\right) \\ \times\left\{J_n\left(q\frac{3\pi}{4}M\right) + 2\cos\left(\frac{n\pi}{6}\right)J_n\left(q\frac{\sqrt{3}\pi}{4}M\right)\right\} \\ + \sum_{\substack{k=1 \\ k\neq -n}}^{\infty} \frac{1}{n+k}\cos\left(m\frac{\pi}{2}\right)\sin\left(k\frac{\pi}{2}\right)\cos\left([n+k]\frac{\pi}{2}\right)\sin\left([n+k]\frac{\pi}{6}\right) \\ \times\left\{J_k\left(q\frac{3\pi}{4}M\right)\sin\left([n+3k]\frac{\pi}{3}\right)\right. \\ \left.-2\cos\left(n\frac{\pi}{6}\right)\sin\left([n-3k]\frac{\pi}{6}\right)\left\{J_k\left(q\frac{\sqrt{3}\pi}{4}M\right)\right\}\right. \\ + \sum_{\substack{k=1 \\ k\neq -n}}^{\infty} \frac{1}{n-k}\cos\left(m\frac{\pi}{2}\right)\sin\left(k\frac{\pi}{2}\right)\cos\left([n-k]\frac{\pi}{2}\right)\sin\left([n-k]\frac{\pi}{6}\right) \\ \times\left\{J_k\left(q\frac{3\pi}{4}M\right)\sin\left([n-3k]\frac{\pi}{3}\right)\right. \\ \left.-2\cos\left(n\frac{\pi}{6}\right)\sin\left([n+3k]\frac{\pi}{6}\right)\left\{J_k\left(q\frac{\sqrt{3}\pi}{4}M\right)\right\}\right. \end{array} \right) \tag{14.54}$$

Using Eqs. (14.53) and (14.54), the harmonic spectrum of the line-to-line voltage of two symmetrical interleaved VSCs is obtained as shown in Fig. 14.12B. The odd multiple of the carrier frequency harmonics and their sidebands are highly reduced, leading to significant improvements in the harmonic quality.

14.4.3 Harmonic performance evaluation

14.4.3.1 Two symmetrically interleaved VSCs

Using the approach illustrated in the section 14.4.2, the NWTHD is obtained for different modulation schemes and the NWTHD variation with the modulation index for different modulation schemes for two symmetrical interleaved VSCs is shown in Fig. 14.14. The carrier frequency is taken to be the same in all cases; thus, the number of commutations in DPWM schemes is 2/3 times than the number of commutation in the SVM. The DPWM schemes demonstrate superior harmonic performance compared to the SVM in the entire operating modulation range. At low modulation indices range, all the DPWM

This book belongs to Kitab Liaison (ocd1996@gmail.com) Copyright Elsevier 2023

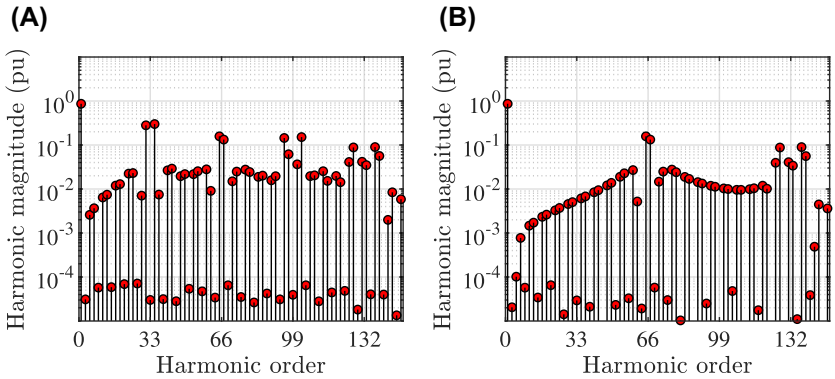

FIGURE 14.13 Harmonic spectrum of the line-to-line voltage under 60 degrees clamp discontinuous (DPWM1) modulation scheme with modulation index $M = 1$ and pulse ratio $\omega_c / \omega_0 = 33$. (A) Line-to-line voltage of the single voltage source converter (noninterleaved), (B) Line-to-line voltage of two symmetrically interleaved voltage source converters.

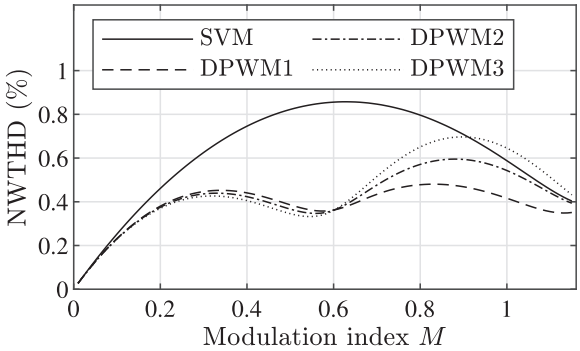

FIGURE 14.14 Harmonic performance of various pulse width modulation schemes for two symmetrically interleaved voltage source converters. The carrier frequency is the same for all the pulse width modulation schemes.

schemes have a similar harmonic distortion, far more superior than the SVM. For modulation indices higher than 0.6, DPWM1 has the lowest harmonic distortion compared to other methods.

This surprising result can be explained using the harmonic energy distribution characteristic of the SVM and DPWM. For the noninterleaved VSC, it is well known that the SVM leads to the lowest harmonic distortion. This is due to the cancelation of the odd harmonics around the first carrier frequency in the line-to-line voltage and distribution of the harmonic energy into the outer sideband harmonics and sidebands of the second carrier frequency harmonic group, as shown in Fig. 14.12A. On the other hand, the odd harmonic cancelation around the first carrier frequency group does not happen in

This book belongs to Kitab Liaison (ocd1996@gmail.com) Copyright Elsevier 2023

DPWM1, and the harmonic energy is mostly distributed with significantly low roll-off in the magnitude of sidebands of the first harmonic carrier group, as shown in Fig. 14.13A. For two symmetrically interleaved VSCs, the sidebands of the first carrier frequency harmonic group are significantly reduced due to the interleaving, whereas the sidebands of the second carrier frequency harmonic group remain unaffected, leading to superior harmonic performance of DPWM1, as shown in Fig. 14.13B. Moreover, the switching losses in the discontinuous modulation schemes are lower compared to the SVM, leading to an improved efficiency. For the applications where the unity power factor operation is required, the use of DPWM1 is advantageous for two symmetrically interleaved VSCs due to low NWTHD and lowest switching losses.

14.4.3.2 Three symmetrically interleaved VSCs

A harmonic performance comparison of different modulation schemes for three symmetrically interleaved VSCs is shown in Fig. 14.15B. The SVM demonstrates superior harmonic performance at low and high modulation indices. However, it is important to note that the carrier frequency is taken to be the same for all the PWM schemes for this comparison. Since the switching losses in the discontinuous modulation schemes are lower than the SVM due to fewer switch transitions, the carrier frequency of the discontinuous modulation schemes can be adjusted to achieve the same number of switch transitions as that of the SVM. The harmonic performance of various modulation schemes with the adjusted carrier frequency is shown in Fig. 14.15B. The SVM offers low harmonic distortion at low modulation indices, whereas discontinuous modulation schemes have a superior harmonic performance at high modulation indices.

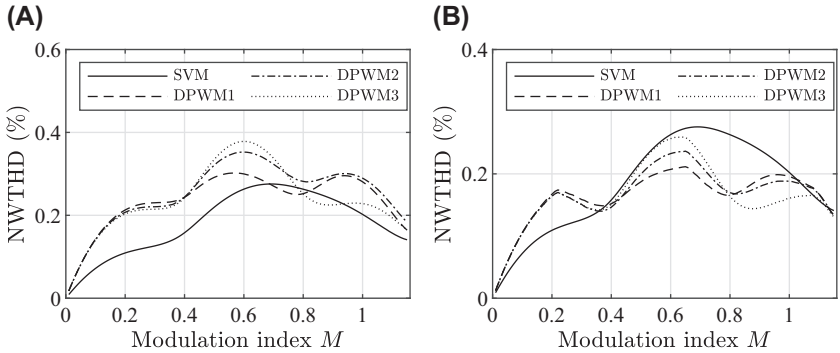

FIGURE 14.15 Harmonic performance of various pulse width modulation schemes for three symmetrically interleaved voltage source converters (interleaving angle is 120 degrees). (A) The carrier frequency is the same for all the pulse width modulation schemes, (B) The carrier frequency of the discontinuous modulation scheme is 3/2 times compared to the SVM.

This book belongs to Kitab Liaison (ocd1996@gmail.com)
Copyright Elsevier 2023

14.4.4 Nearest three vector modulation

Since interleaving of the parallel 2L VSCs leads to the multi-level resultant voltage, parallel VSCs can be treated as a multi-level converter and can be modulated using the multi-level modulation schemes. The switched output voltages of phase a of each of the VSCs (for $\left|\overrightarrow{V_s^{\star}}\right| = 3\sqrt{3}\big/8$ and $\psi_s = 20^{\circ}$) are shown in Fig. 14.16A. The carrier signals of the three VSCs are symmetrically phase shifted by an interleaving angle of 120 degrees. The resultant switched output voltages of all the phases are also shown in Fig. 14.16B, which demonstrate four-level voltage waveforms. The switching sequences

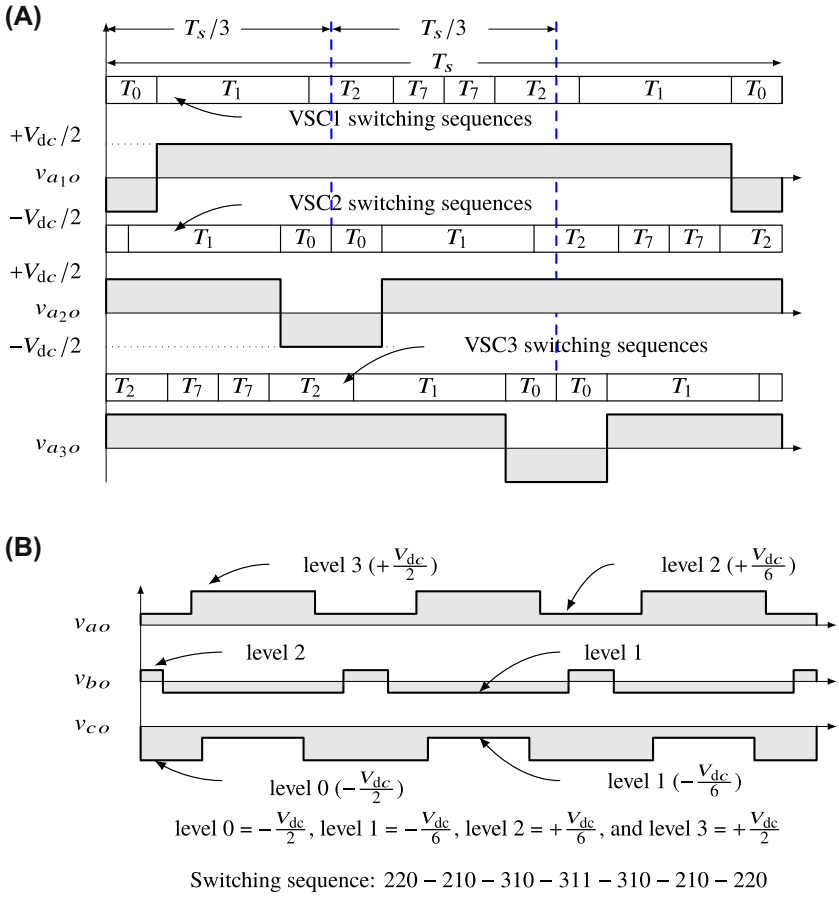

FIGURE 14.16 Switched output voltages of three symmetrically interleaved voltage source converters for $\left|\overrightarrow{V_s^{\star}}\right| = 3\sqrt{3}\big/8$ and space vector angle $\psi_s = 20^{\circ}$. Each of the VSCs is modulated using two-level space vector modulation. (A) Switched output voltage of phase a of all three VSCs, (B) Resultant switched output voltages of all three phases.

This book belongs to Kitab Liaison (ocd1996@gmail.com) Copyright Elsevier 2023

220 – 210 – 310 – 311 – 310 – 210 – 220 are employed, where each of the digits represents the voltage level of the resultant output voltage of the phase a, b, and c, respectively (e.g., 210 represents that voltage levels of phase a, phase b, and phase c are level 2, level 1, and level 0, respectively). As the three parallel VSCs give four-level voltage output, the $\overrightarrow{V_s^\star}$ can be projected on the space vector diagram of the four-level converter, as shown in Fig. 14.17, where the reference space voltage vector is located in the triangle Δ_s. It is well known that the lowest harmonic distortion can be achieved by using the nearest three vectors (NTVs) [24], which are located on the vertices of the triangle Δ_s (210–310–311). However, that is not the case when the symmetrical interleaving is used (an additional voltage vector 220 is also employed), as shown in Fig. 14.16B. Therefore, it is evident that the PS PWM is not an optimal solution for the modulation of the parallel VSCs.

This issue can be mitigated by using asymmetrical interleaving. It is shown in Ref. [21] that the interleaving angle strongly influences harmonic performance. For a given modulation scheme, the lowest harmonic performance can be achieved by varying the interleaving angle with the modulation index. Further improvement can be achieved by selecting an optimal combination of switching sequences and interleaving angle to synthesize the reference space vector $\overrightarrow{V_s^\star}$ [25]. In this scheme, several combinations of the switching sequences and the phase-shift are used in one fundamental cycle of the reference space voltage vector. This would substantially increase the complexity and make it very difficult to implement.

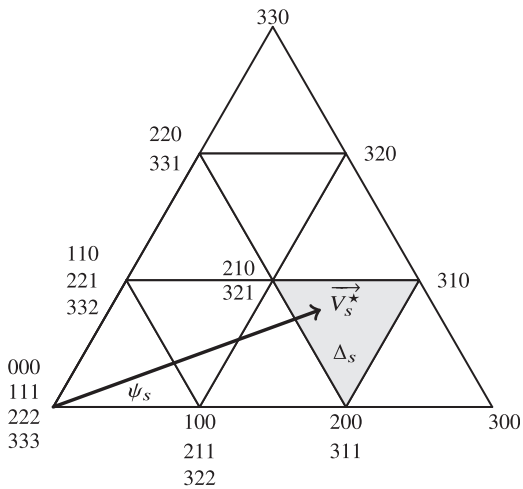

FIGURE 14.17 Projection of the reference space voltage vector $\overrightarrow{V_s^\star} = 3\sqrt{3}/8\angle 20^\circ$ in the first sextant of the space vector diagram of the four-level converter, realized using interleaved operation of three parallel voltage source converters.

This book belongs to Kitab Liaison (ocd1996@gmail.com) Copyright Elsevier 2023

For the parallel-connected 2L-VSCs, multilevel voltage waveforms can be achieved by interleaving the carrier signals. Therefore, the parallel-connected 2L-VSCs can be treated as a multilevel converter. For the multilevel converter, the harmonic profile of the synthesized voltage can be improved by using the NTV [24]. For the carrier comparison implementation, NTV can be achieved using the phase disposition (PD) modulator. The harmonic performance of the parallel VSCs with the symmetrical interleaving and with PD modulator is evaluated and shown in Fig. 14.18. However, the conventional implementation of PD PWM implementation cannot be readily used for the modulation of interleaved VSCs, as it introduces a DC component in the circulating current during band transition [26]. As a result, the magnetic components present in the circulating current path may saturate. This issue can be addressed by introducing additional switchings during the band transition, as also presented in Ref. [26,27]. The load current waveform for the PD-modulated parallel VSCs is shown in Fig. 14.19B. The load current ripple is significantly lower compared to the ripple in the load current with symmetrical interleaving, as shown in Fig. 14.19A.

14.5 Circulating current suppression in parallel interleaved converters

When VSCs are connected in parallel, the circulating current flows between the VSCs due to the control asymmetry and the impedance mismatch. When the carriers are interleaved, the switched output voltages of the interleaved parallel legs are phase shifted. As a result, the instantaneous voltage difference exists between parallel VSCs, which further increases the high-frequency circulating current. Therefore, the circulating current should be suppressed to realize the full potential of the interleaved carriers in parallel-connected VSCs. The high-frequency circulating current introduced by the carrier

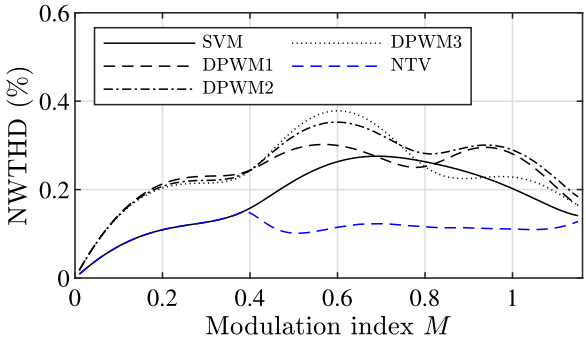

FIGURE 14.18 Harmonic performance of three parallel interleaved converters under nearest three vector modulation. The NWTHD of various modulation schemes with the conventional phase-shifted carrier signals are also shown for the comparison.

This book belongs to Kitab Liaison (ocd1996@gmail.com) Copyright Elsevier 2023

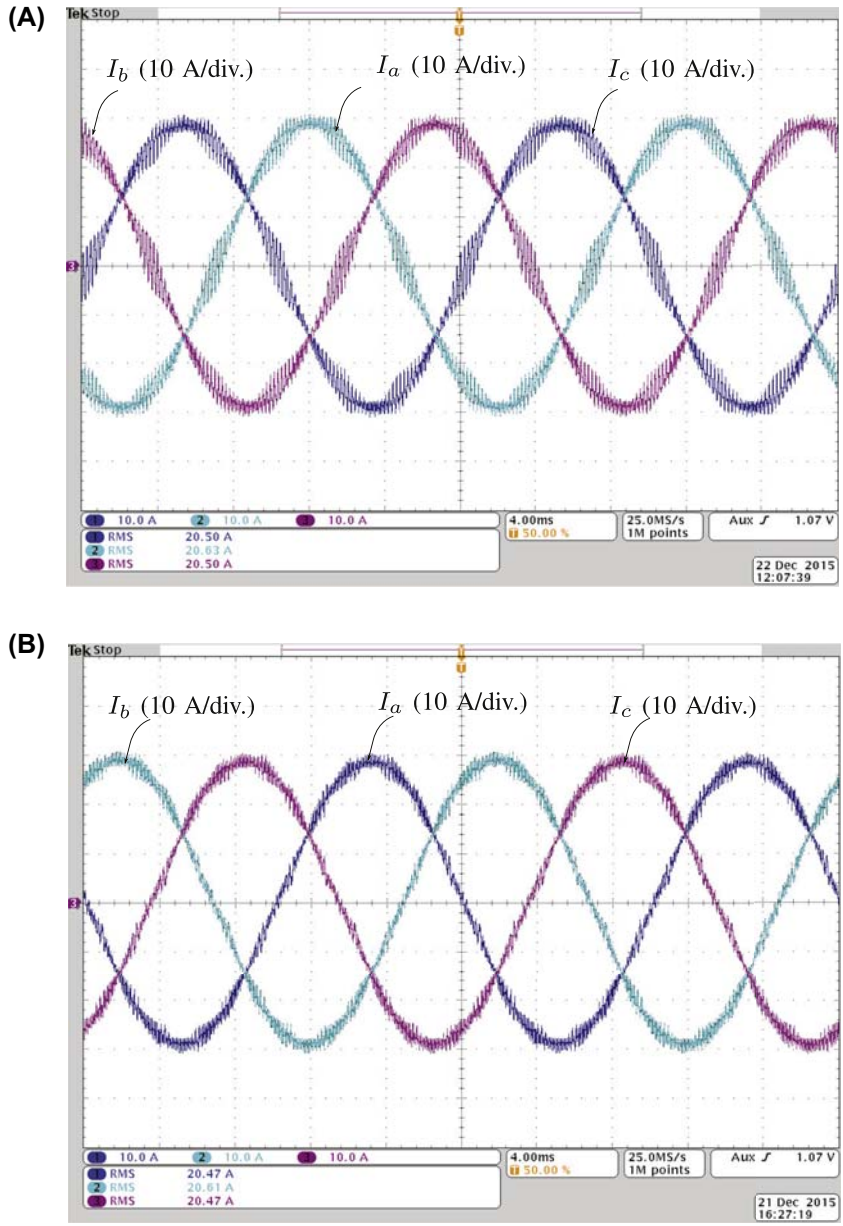

FIGURE 14.19 Load current waveform for three parallel converters. (A) Symmetrically interleaved VSCs with three 120 degrees phase-shifted carrier signals, (B) Phase disposition modulation [26] scheme for parallel interleaved VSCs.

This book belongs to Kitab Liaison (ocd1996@gmail.com)
Copyright Elsevier 2023

interleaving can be eliminated by providing galvanic isolation [2] or can be reduced to a reasonable limit by introducing an impedance in the circulating current path. Various inductive components that are used to offer large impedance to the high-frequency circulating current, including CI [1,3], CM inductor [4], and integrated inductor, are discussed in this section.

14.5.1 Galvanic isolation

The circulating current can be avoided by providing galvanic isolation between the parallel VSCs using the multiple winding line frequency transformer [2], as shown in Fig. 14.20. This solution is preferred in applications requiring a transformer for voltage matching and for providing isolation. The harmonic filter inductor L_f represents a series combination of the leakage inductance of the transformer and external inductor (if leakage inductance is not sufficient). For the three parallel VCSs, the phase-shifted voltages are applied to the isolated primary windings, leading to the cancelation of the major harmonic component that is concentrated around the first and second carrier frequency harmonics in the magnetic flux. As a result, the induced electromotive force (EMF) has major harmonic components that are concentrated around the third carrier frequency component. As a result, the load current has very low harmonic distortion, as it is shown in Fig. 14.21B. On the contrary, the individual VSC current has a major harmonic current concentrated around the first and second carrier harmonic frequency, as shown in Fig. 14.21A. This is due to the fact that these components of the switched output voltage appear across the L_f (since these harmonic components are negligible in the induced EMF). As a result, these harmonic components in the individual VSC currents are only limited by the L_f. Therefore, significant harmonic frequency components are present in the individual VSC currents if a sufficiently large value of L_f is not selected. This current will flow through the primary windings of the transformer and external filter inductors, leading to significant winding losses.

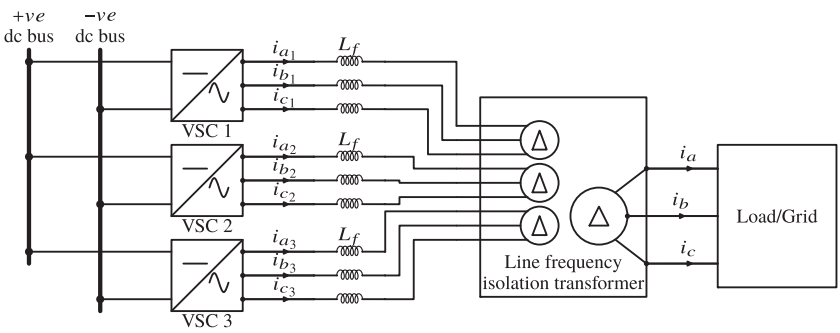

FIGURE 14.20 Three parallel interleaved voltage source converters. A line frequency isolation transformer with multiple windings is used for providing galvanic isolation.

This book belongs to Kitab Liaison (ocd1996@gmail.com) Copyright Elsevier 2023

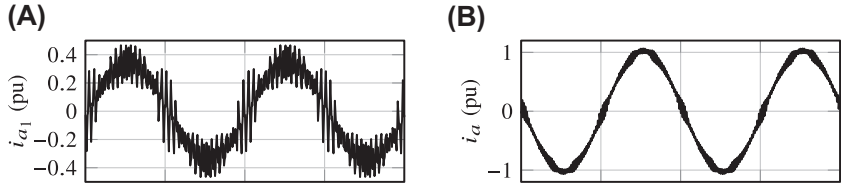

FIGURE 14.21 Simulated current waveform for three parallel interleaved VSCs with isolated transformer windings (see Fig. 14.20). Currents are normalized to the rated current. (A) Individual converter leg current i_{a1}, (B) Load current i_a.

14.5.2 Coupled inductor

The circulating current between the parallel interleaved VSCs can be suppressed by introducing a high impedance in the circulating current path without affecting the impedance in the load current path. This can be achieved by using CI. It suppress the circulating current by providing magnetic coupling between the parallel interleaved legs of the corresponding phases. The magnetic structure of the CI in one of the phases in a three-phase system for N parallel interleaved VSCs is shown in Fig. 14.22A. It consists of N magnetically coupled coils. The start terminal of the coils is connected to the AC terminals of the VSC legs of phase a (a_1, a_2, a_N), whereas the end terminals are connected to form a common connection node a_c.

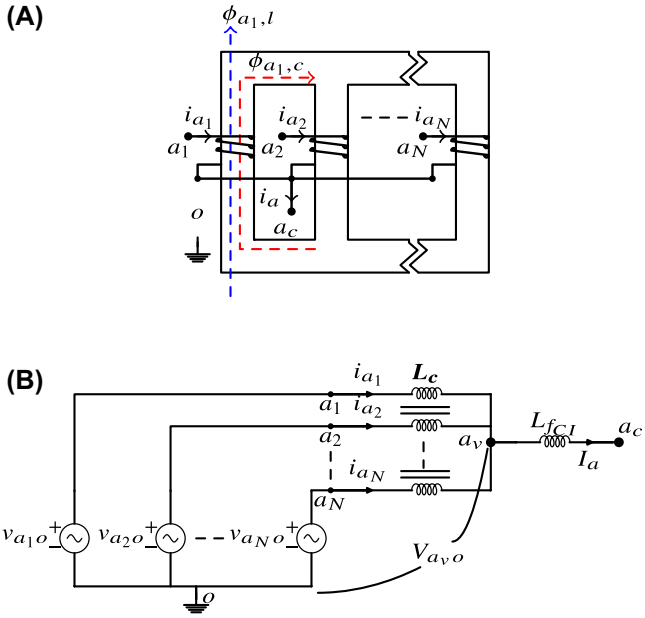

FIGURE 14.22 Circulating current suppression in parallel interleaved voltage source converter using coupled inductor. (A) Magnetic structure of the coupled inductor, (B) Equivalent electric circuit of the phase a of N parallel interleaved voltage source converters with the coupled inductor.

This book belongs to Kitab Liaison (ocd1996@gmail.com) Copyright Elsevier 2023

14.5.2.1 Equivalent electric circuit

The phase-shifted pole voltages are applied between the starting terminals of the coils and fictitious midpoint of the DC bus o, which can be expressed as

$$\boldsymbol{V_P} = \boldsymbol{RI} + \boldsymbol{L}\frac{d}{dt}\boldsymbol{I} + \boldsymbol{V} \tag{14.55}$$

where the $\boldsymbol{V_P}$ is the pole voltage vector

$$\boldsymbol{V_P} = [\, v_{a_1 o} \quad v_{a_2 o} \cdots \quad v_{a_N o} \,]^T \tag{14.56}$$

$\boldsymbol{I}$ is a VSC current vector

$$\boldsymbol{I} = [\, i_{a_1} \quad i_{a_2} \cdots i_{a_N} \,]^T \tag{14.57}$$

and

$$\boldsymbol{V} = [\, V_{a_c o} \quad V_{a_c o} \cdots \quad V_{a_c o} \,]^T \tag{14.58}$$

$\boldsymbol{L}$ and $\boldsymbol{R}$ represent the inductance and resistance matrix, respectively.

$$\boldsymbol{L} = \begin{bmatrix} L_{a_1 a_1} & L_{a_1 a_2} \cdots & L_{a_1 a_N} \\ L_{a_2 a_1} & L_{a_2 a_2} \cdots & L_{a_2 a_N} \\ \vdots & \vdots & \vdots \\ L_{a_N a_1} & L_{a_N a_2} \cdots & L_{a_N a_N} \end{bmatrix} \tag{14.59}$$

$$\boldsymbol{R} = \begin{bmatrix} r_{a_1} & 0 \cdots & 0 \\ 0 & r_{a_2} \cdots & 0 \\ \vdots & \vdots & \vdots \\ 0 & 0 \cdots & r_{a_N} \end{bmatrix} \tag{14.60}$$

Let the average of the switched output voltages of phase x of N parallel VSCs be $V_{x_v o}$ and it is represented as

$$V_{x_v o} = \frac{1}{N}\sum_{k=1}^{n} V_{x_k o}; \text{ where } 1 < k \leq N \tag{14.61}$$

where $V_{x_k o}$ represents the pole voltage of phase x of kth VSC with respect to the common reference point o. Assuming an equal line current sharing between the parallel VSCs, the common component of the leg current is obtained as

$$i_{x_k, l} = \frac{i_x}{N} \tag{14.62}$$

This book belongs to Kitab Liaison (ocd1996@gmail.com) Copyright Elsevier 2023

Using Eq. (14.9) and (14.62), the current through the coils can be represented as

$$i_{x_k} = \frac{i_x}{N} + i_{x_k,c} \tag{14.63}$$

where $\frac{1_x}{N}$ is the load current component of VSC current and $i_{x_k,c}$ is the circulating current component. Since the common current component is in phase for all the coils of the CI, the flux produced by this component (referred to as the common flux component) does not link with other coils and completes its path through the air (c.f. $\phi_{a_1,l}$ in Fig. 14.22A). This leakage flux has a dominant fundamental frequency component and may lead to significant eddy current losses in the laminated magnetic structure (due to the flux component which is orthogonal to the lamination layers) and the metal enclosures [28], especially in high-current applications.

The voltage of the common node ($v_{x_c o}$) is the average of all the pole voltages (see Eq. 14.61). Therefore, the phase-shifted harmonic components present in the pole voltage will be canceled out in $v_{x_c o}$. As a result, the phase-shifted harmonic components only appear across the CI coils. The flux induced by these phase-shifted harmonic frequency components of the pole voltages will link with other coils of the CI due to the availability of a low reluctance path through other limbs of the CI.

Considering a symmetrical magnetic structure, the inductances can be represented as

$$L_{a_j a_j} = L_s \text{ for all } 1 \le j \le N \tag{14.64}$$

and

$$L_{a_j a_k} = -L_m \tag{14.65}$$

$$\text{for all } 1 \le j \le N, 1 \le k \le N, \text{ and } j \ne k$$

Neglecting the resistance in Eq. (14.55) and segregating the load current and circulating current components of the VSC current yields

$$\frac{1}{N}\sum_{k=1}^{n} V_{x_k o} - v_{a_c o} = \left(\frac{L_s - (N-1)L_m}{N}\right)\frac{di_a}{dt} \tag{14.66}$$

Using Eqs. (14.61) and (14.66), the behavior of the load current component can be described as

$$v_{a_v o} - v_{a_c o} = L_{f_{CI}}\frac{di_a}{dt} \tag{14.67}$$

where $L_{f_{CI}}$ is the inductance offered to the load current and it is given as

$$L_{f_{CI}} = \left(\frac{L_s - (N-1)L_m}{N}\right) \tag{14.68}$$

This book belongs to Kitab Liaison (ocd1996@gmail.com) Copyright Elsevier 2023

The behavior of the circulating current components can be described as

$$\boldsymbol{V_P} = \boldsymbol{L_c}\frac{d}{dt}\boldsymbol{I_{a,c}} + V_{a_v o} \tag{14.69}$$

where

$$\boldsymbol{I_{a,c}} = [\, i_{a_1,c} \quad i_{a_2,c} \quad \dots \quad i_{a_n,c} \,]^T \tag{14.70}$$

$$\boldsymbol{L_c} = \begin{bmatrix} L_s & -L_m & \cdots & -L_m \\ -L_m & L_s & \cdots & -L_m \\ \vdots & \vdots & \vdots & \vdots \\ -L_m & -L_m & \cdots & L_s \end{bmatrix} \tag{14.71}$$

Since a high value of the mutual inductance L_m can be achieved using the CI, the circulating current can be effectively suppressed.

14.5.2.2 Impact of the modulation scheme

The PWM scheme has a strong influence on the core losses. Therefore, the design of the CI, especially the thermal design, is strongly impacted by the selection of the PWM scheme. The impact of the PWM scheme on the core losses of the CI for two parallel VSCs has been analyzed. By neglecting the leakage flux, the flux linkage in the CI is given as

$$\lambda_a(t) = \lambda_{a_1}(t) + \lambda_{a_2}(t) = \int (v_{a_1 O} - v_{a_2 O})dt \tag{14.72}$$

The differential voltage that appears across the CI ($v_{a_1 O} - v_{a_2 O}$) determines the flux linkage, which entirely depends on the PWM scheme. The flux density in the CI can be obtained as

$$B_a(t) = \frac{1}{2N_c A_c}\int (v_{a_1 O} - v_{a_2 O})dt \tag{14.73}$$

where N_c is the number of turns in a coil, and A_c is the core cross-sectional area.

The variation in the peak flux linkage with the modulation index for different PWM schemes is plotted in Fig. 14.23 [29]. The maximum value of the peak flux linkage is the same in all PWM schemes. However, the flux linkage pattern is different. As a result, the core losses would be different in each of the schemes, which is an important factor in determining the size and efficiency of the CI. The impact of the modulation schemes on the CI core losses is shown in Fig. 14.24. The core losses are obtained using the improved generalized Steinmetz equation. The core losses are normalized with respect to the core losses in the case of the SVM. When compared to the SVM, all the discontinuous PWM schemes lead to lower core losses at low modulation

This book belongs to Kitab Liaison (ocd1996@gmail.com) Copyright Elsevier 2023

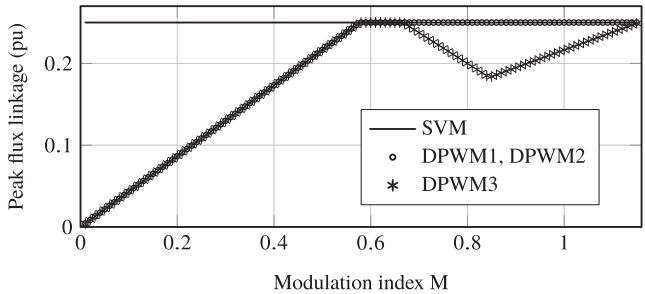

FIGURE 14.23 Variation of the maximum peak flux linkage with the modulation index. The flux linkage is normalized with respect to the $V_{dc}T_s$.

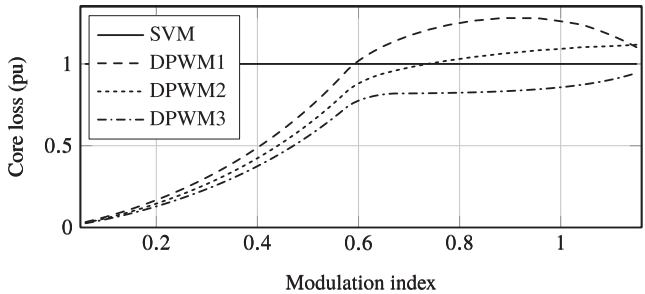

FIGURE 14.24 The core losses in the coupled inductor for different PWM schemes. The core losses are normalized with respect to that of the SVM. The carrier frequency is taken to be the same in all cases.

indices. For high modulation indices, the use of DPWM1 leads to the highest losses, followed by DPWM2. The core losses in the case of DPWM3 are lowest in the entire modulation index range.

14.5.3 Common-mode inductor

Although the CI is very effective in suppressing the circulating current, it has a serious limitation when it comes to modularity. Moreover, unequal current sharing between the parallel VSCs is not possible without overdesigning or saturating the CI. The circulating current (which mainly appears as a CM current) can be suppressed using the CM inductor [4], and it is the preferred solution when unequal load sharing between the parallel VSCs and modularity is desired. The CM inductor is realized using three coils that are wound in the same direction. The coils are connected to the three-phase AC terminals of the VSC, as shown in Fig. 14.25. Each VSC also uses differential mode (DM) inductor for suppressing the harmonics in the load current.

This book belongs to Kitab Liaison (ocd1996@gmail.com) Copyright Elsevier 2023

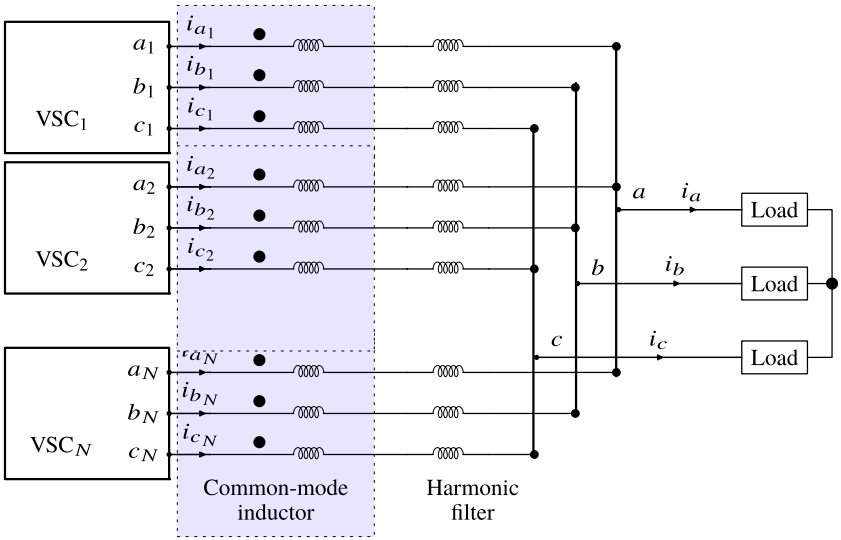

FIGURE 14.25 Schematic illustration of the parallel interleaved voltage source converters. Each converter is connected to the common AC connection using a series combination of differential and common-mode inductors.

For the system shown in Fig. 14.25, the kth VSC currents can be represented as

$$\begin{bmatrix} v_{a_k o} \\ v_{b_k o} \\ v_{c_k o} \end{bmatrix} = \begin{bmatrix} L_{s_c} + L_{s_d} & L_{m_c} - L_{m_d} & L_{m_c} - L_{m_d} \\ L_{m_c} - L_{m_d} & L_{s_c} + L_{s_d} & L_{m_c} - L_{m_d} \\ L_{m_c} - L_{m_d} & L_{m_c} - L_{m_d} & L_{s_c} + L_{s_d} \end{bmatrix} \frac{d}{dt} \begin{bmatrix} i_{a_k} \\ i_{b_k} \\ i_{c_k} \end{bmatrix} + \begin{bmatrix} v_{ao} \\ v_{bo} \\ v_{co} \end{bmatrix} \tag{14.74}$$

where the subscript k represents the kth VSC. L_{s_c} and L_{m_c} are the self- and mutual inductances of the CM inductor, whereas L_{s_d} and L_{m_d} are the self- and mutual inductances of the DM inductor. $v_{x_k o}$ and i_{x_k} represent pole voltage and VSC current of phase x of kth VSC, v_{xo} is the voltage at the load terminal. The VSC current can be represented as

$$i_{x_k} = \frac{i_x}{N} + i_{cm_k} \tag{14.75}$$

where i_x is the load current of phase x and i_{cm_k} is the CM current of kth VSC and represented as

$$i_{cm_k} = \frac{i_{a_k} + i_{b_k} + i_{c_k}}{3} \tag{14.76}$$

This book belongs to Kitab Liaison (ocd1996@gmail.com)
Copyright Elsevier 2023

The dynamic behavior of the CM current of kth VSC can be represented as

$$v_{cm_k} = (L_s - 2L_M)\frac{di_{cm_k}}{dt} + v_{cm} \tag{14.77}$$

where $L_s = L_{s_c} + L_{s_d}$ and $L_m = L_{m_c} - L_{m_d}$, v_{cm_k} is the CM voltage of kth VSC

$$v_{cm_k} = \frac{v_{a_k o} + v_{b_k o} + v_{c_k o}}{3} \tag{14.78}$$

and

$$v_{cm} = \frac{v_{ao} + v_{bo} + v_{co}}{3} \tag{14.79}$$

By assuming a strong coupling between the DM inductor, the flux linkage in the CM inductor can be given as

$$\lambda_{cm_k}(t) = \frac{N-1}{N}\int v_{cm_k}dt - \frac{1}{N}\sum_{\substack{j=1\\ j\neq k}}^{N}\int v_{cm_j}dt \tag{14.80}$$

The volume of the CM inductor is proportional to the maximum value of the CM flux linkage, which strongly depends on the PWM scheme. The maximum value of the peak CM flux linkage as a function of the modulation index for two parallel VSCs is plotted in Fig. 14.26 [30].

For the SVM, the maximum value of the peak flux linkage increases as the modulation index decreases. Therefore, for the applications demanding operation over the full modulation range, the CM inductor has to be designed for the maximum flux linkage, which occurs at low modulation indices. On the other hand, the CM is subjected to maximum flux linkage for a modulation index $M = 2/3$ if DPWM1 is employed. The maximum value of the peak flux linkage in DPWM is almost 33% lower than the SVM, leading to a smaller CM inductor.

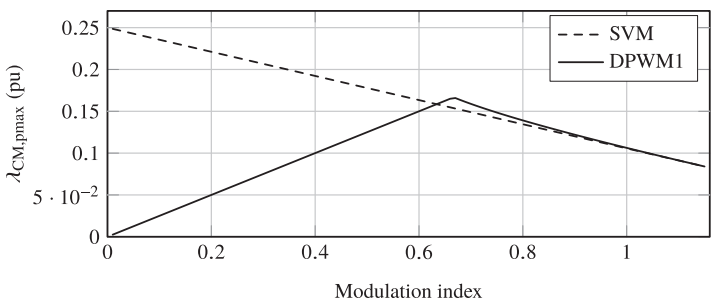

FIGURE 14.26 Comparison of the maximum values of the peak CM flux linkage as a function of the modulation index. The flux linkage is normalized with respect to $V_{dc}T_s$.

This book belongs to Kitab Liaison (ocd1996@gmail.com) Copyright Elsevier 2023

14.5.4 Integrated inductor

The circulating current between the parallel VSCs can be suppressed by introducing impedance in the circulating current path. This can be achieved using the CI. Therefore, for the interleaved operation of parallel VSCs, two distinct magnetic components may be required:

- Inductor for the circulating current suppression.
- Line filter inductor L_f (commonly referred to as a boost inductor) for improving the line current quality.

The volume of the inductive components can be reduced by integrating both of these functionalities into a single magnetic component, as shown in Fig. 14.27 [31].

The simplified arrangement of the magnetic structure is shown in Fig. 14.28. It consists of three CIs for a three-phase system. The CIs of all the three phases are magnetically coupled using the top and bottom bridge yokes. The necessary air gaps are inserted between the cells and the bridge yokes. The top and bottom yokes provide low reluctance for the magnetic coupling between the phases. Considering a symmetrical cell structure, the inductances can be represented as

$$L_{a_jb_j} = L_{b_jc_j} = L_{c_ja_j} = -L_m \text{ for all } 1 \le j \le N \tag{14.81}$$

$$\begin{aligned} &L_{a_jb_k} = L_{b_jc_k} = L_{c_ja_k} \cong 0 \\ &\text{for all } 1 \le j \le N, 1 \le k \le N, \text{and } j \ne k \end{aligned} \tag{14.82}$$

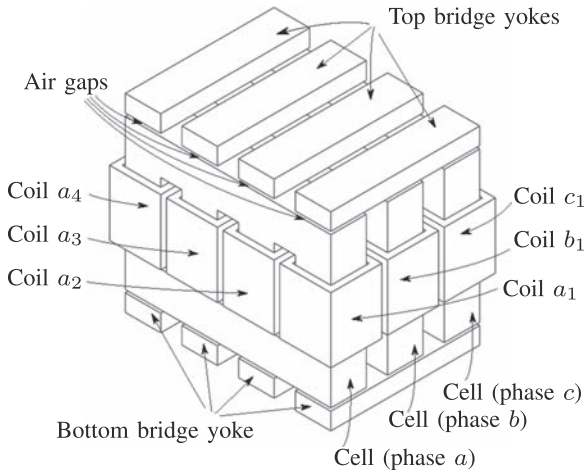

FIGURE 14.27 Magnetic structure of the proposed integrated three-phase inductor for N number of parallel-connected VSCs ($N = 4$ in this illustration).

This book belongs to Kitab Liaison (ocd1996@gmail.com) Copyright Elsevier 2023

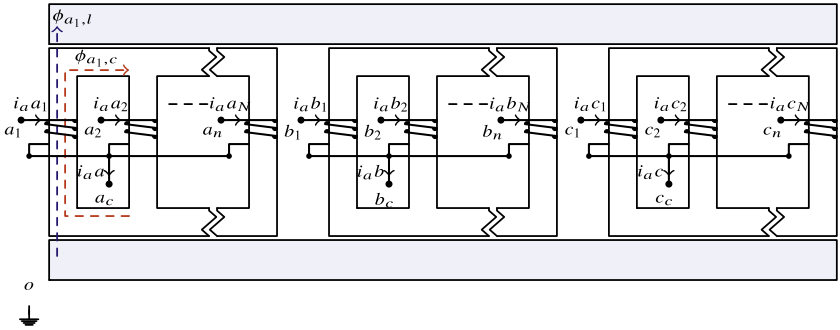

FIGURE 14.28 Simplified magnetic structure of the integrated inductor shown in Fig. 14.27.

$$L_{x_j x_k} = -L_{m_1} \text{ for all } 1 \le j \le N, 1 \le k \le N, \text{and } j \ne k \tag{14.83}$$

The $-ve$ sign is used to represent the L_m and L_{m_1}. Neglecting the leakage flux, the self-inductance of each of the coils is given as

$$\begin{aligned} &L_{a_j a_j} = L_{b_j b_j} = L_{c_j c_j} = (N-1)L_{m_1} + 2L_m \\ &\text{for all } 1 \le j \le N \end{aligned} \tag{14.84}$$

Using these inductance values and averaging the pole voltages of each of the phases gives

$$\begin{bmatrix} v_{a_v o} - v_{a_c o} \\ v_{b_v o} - v_{b_c o} \\ v_{c_v o} - v_{c_c o} \end{bmatrix} = \frac{1}{N} \begin{bmatrix} 2L_m & -L_m & -L_m \\ -L_m & 2L_m & -L_m \\ -L_m & -L_m & 2L_m \end{bmatrix} \frac{d}{dt} \begin{bmatrix} i_a \\ i_b \\ i_c \end{bmatrix} \tag{14.85}$$

For the three-phase three-wire system, $i_a + i_b + i_c = 0$ and the inductance offered to the resultant line current is given as

$$L_f = \frac{v_{x_v o} - v_{x_c o}}{di_x/dt} = \frac{3}{N} L_m \tag{14.86}$$

The behavior of the circulating current can be described by subtracting the average pole voltage from the pole voltages of the corresponding phases and further simplification of those equations gives

$$\boldsymbol{V}_{\boldsymbol{S_x}} = \boldsymbol{L_c} \frac{d}{dt} \boldsymbol{I_{x,c}} + V_{x_v o} \tag{14.87}$$

where

$$\boldsymbol{V}_{\boldsymbol{S_x}} = \begin{bmatrix} v_{x_1 o} & v_{x_2 o} & \dots & v_{x_N o} \end{bmatrix}^T \tag{14.88}$$

This book belongs to Kitab Liaison (ocd1996@gmail.com)
Copyright Elsevier 2023

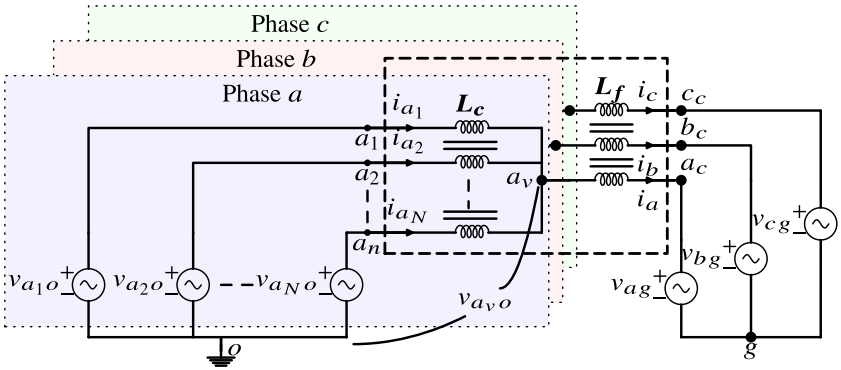

FIGURE 14.29 Equivalent electrical circuit of the parallel interleaved VSCs with the integrated inductor.

$$\boldsymbol{I_{x,c}} = [\, i_{x_1,c} \quad i_{x_2,c} \quad \dots \quad i_{x_N,c} \,]^T \tag{14.89}$$

$$\boldsymbol{L_c} = \begin{bmatrix} (N-1)L_{m_1} & -L_{m_1} & \cdots & -L_{m_1} \\ -L_{m_1} & (N-1)L_{m_1} & \cdots & -L_{m_1} \\ \vdots & \vdots & \vdots & \vdots \\ -L_{m_1} & -L_{m_1} & \cdots & (N-1)L_{m_1} \end{bmatrix} \tag{14.90}$$

Using (14.86) and (14.87), the electrical equivalent circuit is obtained and it is shown in Fig. 14.29. Here, x_v is the virtual common point and the potential of this point with respect to the midpoint of the DC link is the averaged pole voltage v_{x_vo}. The potential difference of $v_{x_vo} - v_{x_co}$ appears across the line filter inductor L_f, as shown in Fig. 14.29. The advantage offered by the integrated inductor in terms of the size reduction is demonstrated in Ref. [31] by comparing the volume of the integrated inductor with the state-of-the-art solution of using three CIs and the three-phase line filter inductor, where 15% reduction in the active material usage was demonstrated for a specific PCS with three interleaved VSCs.

14.6 Summary

The parallel connection of the VSCs is used in multiple applications to realize modular, reliable, and cost-effective PCS. To achieve the full potential of the parallel operation of VSCs, it is very important to reduce the circulating current to a reasonable level. In a PCS with parallel-connected VSCs, the circulating current may flow between the VSCs because of the filter impedance and semiconductor device parameter mismatch, application of different

This book belongs to Kitab Liaison (ocd1996@gmail.com) Copyright Elsevier 2023

voltage vectors, and dead-time effect, etc. The flow of the unwanted circulating current leads to additional losses in the active and passive components present in the circulating current path. The impacts of the application of different applied voltage vectors and impedance mismatch are analyzed. Moreover, the correlation between the circulating current that flows between the VSC legs of a particular phase and the CM circulating current is derived.

Various control schemes for load sharing and circulating current reduction are discussed. The control scheme with the central controller can achieve good load sharing. However, it requires fast communications between the parallel VSCs, which compromises modularity and degrades the redundancy. The droop control scheme can be used to avoid critical communication lines and to achieve good load sharing. The virtual output impedance control can be incorporated to alleviate the impedance mismatch between the parallel VSCs. The droop control, combined with the virtual output impedance control and circulating current controller, can achieve good load sharing and minimize circulating current. The low-frequency component of the CM circulating current can be reduced by controlling the average CM voltage using a closed-loop circulating current controller. The average value of the CM voltage in a switching period can be controlled by appropriately sharing the zero vector dwell time between two zero voltage vectors.

The harmonic performance of the parallel VSCs can be improved by interleaving control. The harmonic performance of various conventional PWM schemes with the symmetrical interleaving is evaluated, where it is shown that the DPWM1 modulation scheme demonstrates superior harmonic performance and low switching losses for the two parallel VSCs, whereas for three parallel VSCs, the continuous SVM has low harmonic distortion. In fact, parallel-connected 2L VSCs can be treated as a multilevel converter. Therefore, superior harmonic performance can be achieved by modulating parallel VSCs as a single multilevel converter using an NTV (PD) modulation scheme. However, the conventional PD modulator cannot be used for parallel VSCs as it may saturate the filter inductors. A detailed discussion on the modified PD modulator, suitable for the parallel VSCs, has been provided.

In the interleaving control, different voltage vectors are applied to the parallel VSCs to improve the harmonic performance. The application of the different voltage vectors gives rise to the high-frequency circulating current. Various filter arrangements for the high-frequency circulating current suppression are discussed. The impact of the PWM scheme on the peak flux linkage and core losses is also analyzed. It is also shown that the size of the passive components can be reduced through the magnetic integration of the circulating current filter and line filter inductor.

This book belongs to Kitab Liaison (ocd1996@gmail.com) Copyright Elsevier 2023

References

[1] K. Matsui, Y. Murai, M. Watanabe, M. Kaneko, F. Ueda, A pulsewidth-modulated inverter with parallel connected transistors using current-sharing reactors, IEEE Trans. Power Electron. 8 (2) (April 1993) 186−191.

[2] H. Akagi, A. Nabae, S. Atoh, Control strategy of active power filters using multiple voltage-source pwm converters, IEEE Trans. Ind. Appl. IA-22 (3) (May 1986) 460−465.

[3] I.G. Park, S.I. Kim, Modeling and analysis of multi-interphase transformers for connecting power converters in parallel, in: Proc. 28th Annual IEEE Power Electronics Specialists Conference, vol. 2, June 1997, pp. 1164−1170.

[4] L. Asiminoaei, E. Aeloiza, P.N. Enjeti, F. Blaabjerg, Shunt activepower- filter topology based on parallel interleaved inverters, IEEE Trans. Ind. Electron. 55 (3) (March 2008) 1175−1189.

[5] A.P. Martins, A.S. Carvalho, A.S. Araujo, Design and implementation of a current controller for the parallel operation of standard upss, Proc. 21st Annual Conf. IEEE Ind. Electron. 1 (November 1995) 584−589.

[6] J. Holtz, K. Werner, Multi-inverter ups system with redundant load sharing control, IEEE Trans. Ind. Electron. 37 (6) (December 1990) 506−513.

[7] J.-F. Chen, C.-L. Chu, Combination voltage-controlled and current-controlled pwm inverters for ups parallel operation, IEEE Trans. Power Electron. 10 (5) (September 1995) 547−558.

[8] X. Sun, Y.-S. Lee, D. Xu, Modeling, analysis, and implementation of parallel multi-inverter systems with instantaneous averagecurrent- sharing scheme, IEEE Trans. Power Electron. 18 (3) (May 2003) 844−856.

[9] Y.J. Cheng, E.K.K. Sng, A novel communication strategy for decentralized control of paralleled multi-inverter systems, IEEE Trans. Power Electron. 21 (1) (January 2006) 148−156.

[10] T. Kawabata, S. Higashino, Parallel operation of voltage source inverters, IEEE Trans. Ind. Appl. 24 (2) (March 1988) 281−287.

[11] M.C. Chandorkar, D.M. Divan, R. Adapa, Control of parallel connected inverters in standalone ac supply systems, IEEE Trans. Ind. Appl. 29 (1) (January 1993) 136−143.

[12] T.-F. Wu, Y.-K. Chen, Y.-H. Huang, 3c strategy for inverters in parallel operation achieving an equal current distribution, IEEE Trans. Ind. Electron. 47 (2) (April 2000) 273−281.

[13] H. Van Der Broeck, U. Boeke, A simple method for parallel operation of inverters, in: Proc. 20th International Telecommunications Energy Conference, October 1998, pp. 143−150.

[14] Y. Pei, G. Jiang, X. Yang, Z. Wang, Auto-masterslave control technique of parallel inverters in distributed ac power systems and ups, in: Proc. IEEE 35th Annual Power Electronics Specialists Conference, vol. 3, June 2004, pp. 2050−2053.

[15] A. Engler, N. Soultanis, Droop control in lv-grids, in: Proc. International Conference on Future Power Systems, November 2005, p. 6.

[16] J.M. Guerrero, L. Garcia de Vicuna, J. Matas, M. Castilla, J. Miret, Output impedance design of parallel-connected ups inverters with wireless load-sharing control, IEEE Trans. Ind. Electron. 52 (4) (August 2005) 1126−1135.

[17] S.J. Chiang, J.M. Chang, Parallel control of the ups inverters with frequency-dependent droop scheme, in: Proc. IEEE 32nd Annual Power Electronics Specialists Conference, vol. 2, June 2001, pp. 957−961, vol. 2.

[18] B. Wei, J.M. Guerrero, J.C. Vásquez, X. Guo, A circulating-current suppression method for parallel-connected voltage-source inverters with common dc and ac buses, IEEE Trans. Ind. Appl. 53 (4) (July 2017) 3758−3769.

This book belongs to Kitab Liaison (ocd1996@gmail.com) Copyright Elsevier 2023

[19] Z. Ye, D. Boroyevich, J.-Y. Choi, F.C. Lee, Control of circulating current in two parallel three-phase boost rectifiers, IEEE Trans. Power Electron. 17 (5) (September 2002) 609−615.

[20] S.K.T. Miller, T. Beechner, J. Sun, A comprehensive study of harmonic cancellation effects in interleaved three-phase vscs, in: Proc. IEEE Power Electronics Specialists Conference, June 2007, pp. 29−35.

[21] D. Zhang, F. Wang, R. Burgos, R. Lai, D. Boroyevich, Impact of interleaving on ac passive components of paralleled three-phase voltagesource converters, IEEE Trans. Ind. Appl. 46 (3) (May 2010) 1042−1054.

[22] J.S. Siva Prasad, G. Narayanan, Minimization of grid current distortion in parallel-connected converters through carrier interleaving, IEEE Trans. Ind. Electron. 61 (1) (January 2014) 76−91.

[23] D.G. Holmes, T.A. Lipo, Pulse Width Modulation for Power Converters: Principles and Practice, Wiley-IEEE Press, Hoboken, NJ, 2003.

[24] N. Celanovic, D. Boroyevich, A fast space-vector modulation algorithm for multilevel three-phase converters, IEEE Trans. Ind. Appl. 37 (2) (March 2001) 637−641.

[25] X. Mao, A.K. Jain, R. Ayyanar, Hybrid interleaved space vector pwm for ripple reduction in modular converters, IEEE Trans. Power Electron. 26 (7) (July 2011) 1954−1967.

[26] G. Gohil, L. Bede, R. Teodorescu, T. Kerekes, F. Blaabjerg, Fluxbalancing scheme for pd-modulated parallel-interleaved inverters, IEEE Trans. Power Electron. 32 (5) (May 2017) 3442−3457.

[27] B. Cougo, G. Gateau, T. Meynard, M. Bobrowska-Rafal, M. Cousineau, Pd modulation scheme for three-phase parallel multilevel inverters, IEEE Trans. Ind. Electron. 59 (2) (February 2012) 690−700.

[28] I. Trintis, G. Gohil, M. Wurzer, M. Franzen, S.L. Pallesgaard, S. Munk- Nielsen, P. Carne Kjaer, Line reactor for parallel-interleaved high power inverters, in: Proc. 19th European Conference on Power Electronics and Applications (EPE'17 ECCE Europe), September 2017, pp. 1−10.

[29] G. Gohil, L. Bede, R. Maheshwari, R. Teodorescu, T. Kerekes, F. Blaabjerg, Parallel interleaved vscs: influence of the pwm scheme on the design of the coupled inductor, in: Proc. 40th Annual Conference of the IEEE Industrial Electronics Society, October 2014, pp. 1693−1699.

[30] G. Gohil, R. Maheshwari, L. Bede, T. Kerekes, R. Teodorescu, M. Liserre, F. Blaabjerg, Modified discontinuous pwm for size reduction of the circulating current filter in parallel interleaved converters, IEEE Trans. Power Electron. 30 (7) (July 2015) 3457−3470.

[31] G. Gohil, L. Bede, R. Teodorescu, T. Kerekes, F. Blaabjerg, An integrated inductor for parallel interleaved three-phase voltage source converters, IEEE Trans. Power Electron. 31 (5) (May 2016) 3400−3414.

This book belongs to Kitab Liaison (ocd1996@gmail.com) Copyright Elsevier 2023

This page intentionally left blank

This book belongs to Kitab Liaison (ocd1996@gmail.com)

Copyright Elsevier 2023

Chapter 15

Advanced power control of photovoltaic systems

Ariya Sangwongwanich, Jinkui He, Yiwei Pan
Aalborg University, Aalborg, Denmark

15.1 Introduction

Conventional control of photovoltaic (PV) system aims at maximizing the PV power production with the maximum power point tracking (MPPT) control. This control method is mandatory for maximizing the energy harvesting of the PV system and thereby minimize the levelized cost of energy of the whole PV plant [1]. However, as the penetration level of the PV systems increases, the variability of the PV power generation, which varies with the weather condition (e.g., solar irradiance and temperature), may impose more and more grid-integration challenges. For instance, overloading of the grid during the peak PV power generation periods (e.g., midday) may occur more frequently in the distribution network with a high PV penetration [2]. Grid voltage fluctuation due to the intermittent PV power generation is another concern, which can occur during a cloudy day [3]. Moreover, the system operator may also face a challenge related to frequency regulation capability, since a majority of PV systems cannot easily be dispatched [4,5].

The above concerns have driven new requirements to the control functionality of PV systems in the grid code. Most of the grid codes, especially for countries with high penetration level of PV systems, have been revised and included new requirements in terms of advanced control functionalities of PV systems [6–10]. Instead of always operating with MPPT control, the PV systems are expected to provide certain flexibility in the power regulation. For instance, active power control functionalities such as absolute power constraint, delta power constraint, and power ramp-rate constraint have been defined in some grid codes, and the PV systems need to fulfill these requirements [8]. In order to achieve these requirements, the PV systems should be able to regulate its output power to a certain limit during the operation (depending on the constraints), which can be enabled through the constant power generation (CPG) control strategies.

Control of Power Electronic Converters and Systems. https://doi.org/10.1016/B978-0-12-819432-4.00012-3
Copyright © 2021 Elsevier Ltd. All rights reserved.

This book belongs to Kitab Liaison (ocd1996@gmail.com)
Copyright Elsevier 2023

15.2 Overview of PV inverter control

In general, two main fundamental tasks should be achieved by the grid-connected PV inverters: (1) the MPPT control to extract the maximum available power from the PV panels, and (2) the injection of grid current with high power quality. For the grid current control, a detailed discussion has been provided in Chapter 8, and thus, only the most popular control structures of PV inverters will be discussed. For the MPPT control, two of the most popular MPPT methods, the perturb and observe (P&O) MPPT and fractional open circuit voltage MPPT, are introduced to exemplify the operating principle of the MPPT control.

15.2.1 Control structure

Although many topologies have been proposed and applied to the PV applications, they can generally be divided into two categories: the single-stage and double-stage configurations [11], as shown in Fig. 15.1, where the control diagrams are also illustrated. For the single-stage configuration, the inverter is responsible for both of the aforementioned tasks, which means that the

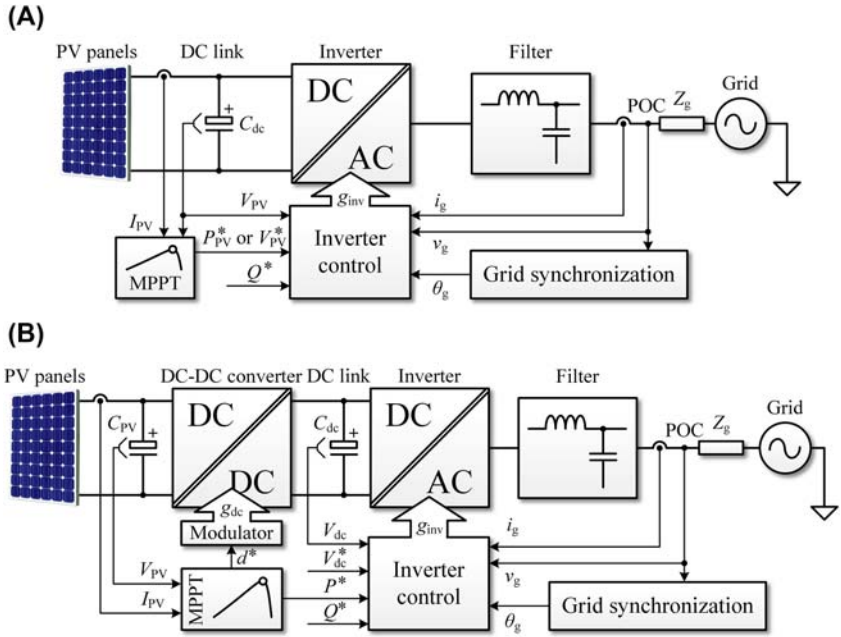

FIGURE 15.1 Configurations of photovoltaic (PV) inverter systems: (A) the single-stage PV system and (B) the double-stage PV system, where g_{inv} and g_{dc} are the gate signals for the inverter and the DC−DC converter, respectively, POC is the point of connection, and C_{dc} denotes for the DC-link capacitance.

This book belongs to Kitab Liaison (ocd1996@gmail.com) Copyright Elsevier 2023

dynamics of the PV power point tracking will affect the dynamics of the power control of the inverter. On the other hand, the interaction between these two control tasks can be decoupled with the double-stage configuration, where the MPPT is performed on the DC−DC stage, and the inverter is in charge of power injection. It can be observed in Fig. 15.1 that the output of the MPPT controller can be different variables depending on the configuration of the system, being the PV voltage reference V_{PV}^*, power reference P_{PV}^*, or the duty cycle d^*. For the inverter control, it can be realized with two cascaded loops: the power/voltage outer loop and the current inner loop [12], as shown in Fig. 15.2. A simple PI regulator can be adopted for the outer loop to regulate the real power or DC voltage according to the reference from the MPPT controller, and generate a current reference i_d^* for the inner loop. The inner loop can be designed under various reference frames, i.e., the natural *abc*-, the stationary $\alpha\beta$-, and the rotating *dq*-reference frames. In the *dq* frames, PI regulators are always employed for the inner loop, and in the *abc* and $\alpha\beta$ frames, PR regulators are recommended to ensure the zero steady-state errors for the inner loop, as shown in Fig. 15.2A and B, respectively. For the three-phase systems, the control is typically in the $\alpha\beta$- and *dq*-reference frames, with the help of Clarke and Park transformations, as it has been discussed in

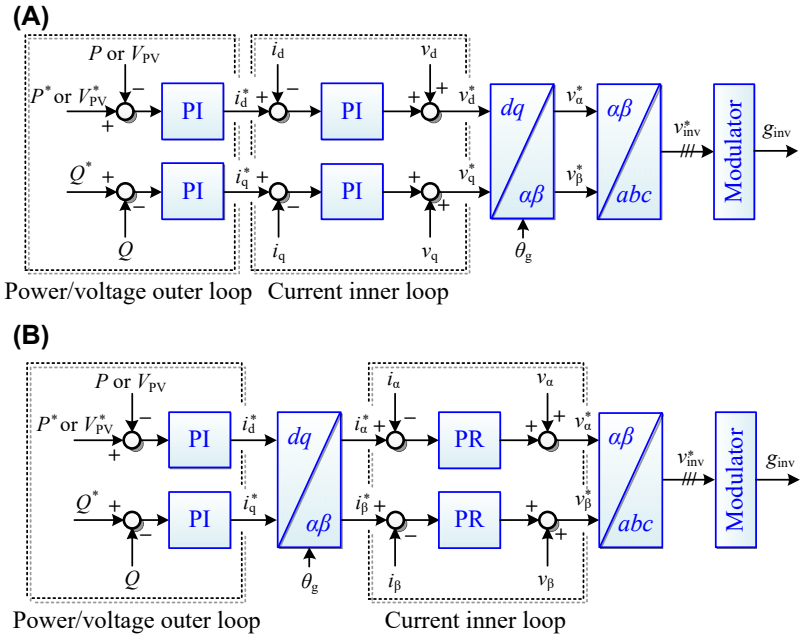

FIGURE 15.2 Control structure of photovoltaic inverter systems: (A) in the rotating *dq* frames using PI controllers, and (B) in the stationary $\alpha\beta$ frames using PI and PR controllers. Here, v_{inv}^* is the modulation index for the inverter.

This book belongs to Kitab Liaison (ocd1996@gmail.com)
Copyright Elsevier 2023

Chapter 8. In single-phase systems, the inner loop control can also be designed under the $\alpha\beta$- and dq-reference frames, with the introduction of an imaginary AC coordinate [13]. Moreover, it can be seen in Fig. 15.1 that the phase angle of the grid voltage is also required for the grid-connected control of the inverter, which can be extracted by a phase-locked loop. The dual-loop control and grid synchronization have been discussed in Chapters 8 and 9.

15.2.2 MPPT algorithm

Since the irradiance and temperature vary throughout a day, the MPPs of PV panels will also change accordingly. Therefore, to extract the maximum power from PV panels regardless of the variation of environmental conditions, the MPPT control should be implemented in the PV inverters. Despite the fact that hundreds of MPPT algorithms have been proposed, they can generally be divided into two categories: the extremum-seeking algorithms and the characteristic-based algorithms [14]. In general, there is always a tradeoff between efficiency (e.g., tracking accuracy) and complexity (e.g., parameterization) for different MPPT algorithms. For the extremum-seeking algorithms, the optimal operating point is online searched, while for the characteristic-based algorithms, the operating point is adjusted mainly according to initial characteristics (e.g., according to the datasheet of PV panels). In the following, two typical MPPT methods are introduced to exemplify these two kinds of algorithms.

15.2.2.1 Perturb and observe MPPT

One of the simplest extremum-seeking MPPT algorithms is the P&O MPPT method, which is also the most popular method in practical applications. The flowchart of the P&O algorithm is shown in Fig. 15.3. As shown in Fig. 15.3, the PV power is online calculated and compared with the power value of the previous MPPT period. If the power increases, the MPPT controller will continue the perturbation following the same direction. If the power decreases, the perturbation direction will be reversed. To better illustrate the operating principle of the P&O algorithm, in Fig. 15.4, the operating points of the PV panels are alphabetically marked starting from the initial reference value to the steady state. It can be clearly observed from the figure that the operating point will oscillate around the MPP in a steady state. This means that a certain amount of power in proportion to the perturbation step-size will be lost because the operating point cannot stay exactly at the MPP all the time [14,15]. Besides, this oscillation may also introduce interharmonics to the grid [16]. Moreover, in fast-changing environmental conditions, the P&O algorithm may loose its MPPT performance [17]. To implement the P&O algorithm, voltage and current sensing circuits are both needed, which will also increase

This book belongs to Kitab Liaison (ocd1996@gmail.com) Copyright Elsevier 2023

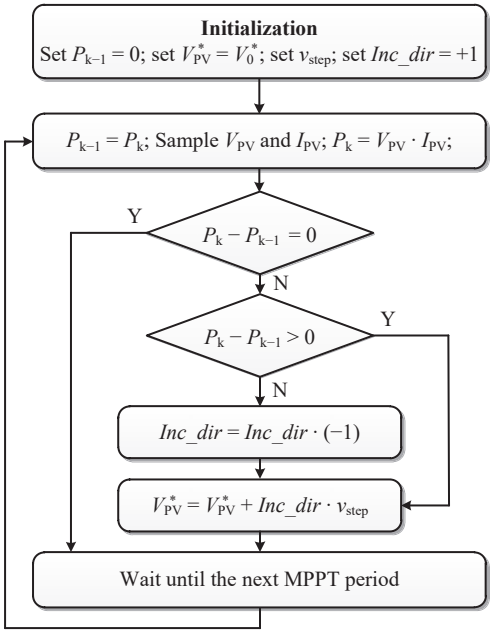

FIGURE 15.3 Flowchart of the P&O MPPT algorithm, where P_k denotes the measured power on the kth MPPT period. V_0^* and v_{step} are the initial voltage reference and perturbation step-size for MPPT, respectively. *Inc_dir* is the increment direction for the MPPT perturbation, with its value being $+1$ or -1.

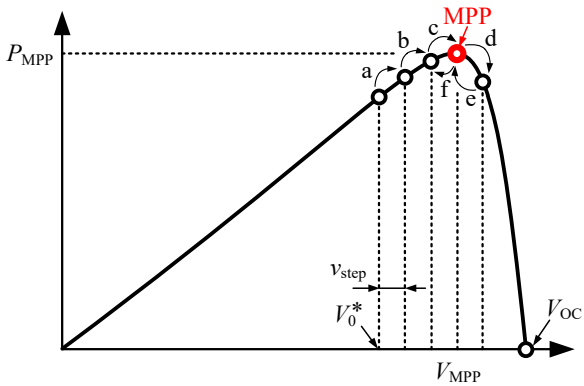

FIGURE 15.4 Illustration of the P&O MPPT algorithm on the P/V curve of PV panels, where V_{MPP} and P_{MPP} refer to the voltage and power on the MPP, respectively, and V_{OC} refers to the open circuit voltage of PV panels.

This book belongs to Kitab Liaison (ocd1996@gmail.com) Copyright Elsevier 2023

the cost and volume of the system. However, despite these limitations, the P&O is still a simple and effective method to maximize the power utilization of the PV panels.

15.2.2.2 Fractional open circuit voltage MPPT

The fractional open circuit voltage MPPT is one of the simplest characteristic-based MPPT algorithms, which adopts a fraction of the open circuit voltage of PV panels as the MPP voltage. This is because the ratio between the MPP voltage and the open circuit voltage is approximately consistent under different environmental conditions. In practice, the ratio is generally within 70%−80%, and the exact fraction value can be determined according to the datasheet of the PV panels. The flowchart of the fractional open circuit voltage MPPT is shown in Fig. 15.5. As shown in Fig. 15.5, this method periodically measures the open circuit voltage of PV panels, and adjusts the voltage reference as a fraction of it. Inevitably, during the time interval of the open circuit voltage sampling, no power will be generated by the PV panels. Therefore, there is a tradeoff between the MPPT accuracy and the power loss caused by the open circuit voltage measurement. In practice, the open circuit voltage MPPT is measured every hundreds of milliseconds, and the PV panels should keep open circuited for tens of microseconds to ensure a reliable sampling result. Moreover, there are still inaccuracies of this method in

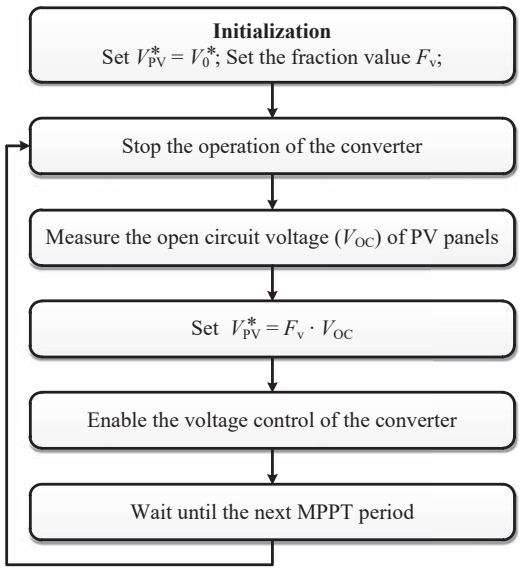

FIGURE 15.5 Flowchart of the fractional open circuit voltage maximum power point tracking (MPPT) algorithm, where F_v is the designed fractional value.

This book belongs to Kitab Liaison (ocd1996@gmail.com) Copyright Elsevier 2023

tracking the MPP, since the fraction of the open circuit voltage cannot coincide exactly with the MPP voltage. Due to this, there will also be energy losses. However, compared with the P&O algorithm, there will be no oscillation in the steady state, which will bring about better interharmonic performances [18]. Once the open circuit voltage is obtained, the voltage reference can be quickly set as a fraction of the open circuit voltage, thus the dynamic performance is better than the P&O method. Besides, since only the voltage sensing circuit is required for this method, the fractional open circuit MPPT method is more cost-effective.

15.3 Requirement of advanced control functionality

Grid-connected PV systems are becoming one of the essential renewable energy sources in today's power grid. With the main purpose of increasing renewable power production, both the number of installation and system capacity of PV plants are expected to be increased even further in the near future [6,11]. In order to cope with this transition, the design, control, and operation of grid-connected PV systems should comply with the currently active grid requirements, defined as the grid codes, which include not only the power quality requirements of grid-connected PV systems but also the advanced control functionalities they should provide [11]. In the following, the main requirements of advanced control functionalities defined in the current grid codes are reviewed, including both general requirements and active power control requirements.

15.3.1 Grid code

15.3.1.1 Requirements under normal grid conditions

In general, the grid-connected PV systems should meet certain fundamental demands, such as the power quality demand within the normal power production range. Also, the DC content of the supplied AC current should not exceed 0.5% of the nominal current, and the total harmonic distortion level should be lower than 5%.

According to the current active grid regulations, the grid-connected PV systems must be able to withstand frequency and voltage deviations in the point of connection while reducing their active power as little as possible. For instance, when the normal operating voltage is within $U_c \pm 10\%$ and the frequency range is 47.00−52.00 Hz, the overall requirements for active power production are as shown in Fig. 15.6 [8]. In the U_c to $U_c + 10\%$ voltage range, the active power is limited to the nominal output. In the U_{min} to U_c voltage range, the active power is limited by the potential nominal current.

This book belongs to Kitab Liaison (ocd1996@gmail.com) Copyright Elsevier 2023

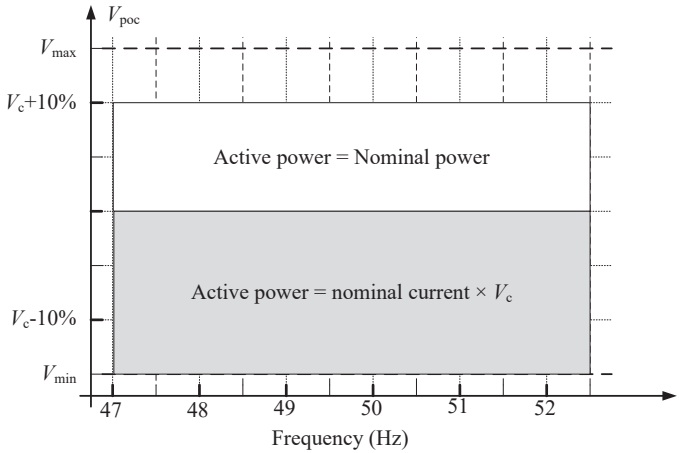

FIGURE 15.6 Requirements of active power production in the event of frequency and voltage deviations [8].

15.3.1.2 Requirements under abnormal grid conditions

A grid is not always ideal, where the grid voltage and frequency may exceed the prescribed limits, which may negatively affect the surrounding equipment (e.g., influencing equipment lifetime) or even challenge the entire system stability (e.g., during grid disturbances and also low SCR). The grid-connected PV systems thus should succeed in riding through grid disturbances and help restore the stability of the power grid.

Due to power line short circuit, starting of large motors, etc., the grid voltage amplitude may drop to a certain level (10%–90% of the nominal voltage or even to zero) for a short time (several milliseconds to several seconds), which is referred to as voltage sags. To maintain the stability of the power grid, firstly, the PV inverters should not be disconnected from the grid in case of a large inrush transient current, which usually occurs at the beginning of a sudden and deep voltage sag [19]. Furthermore, the PV systems should provide their maximum voltage support by injecting a controlled amount of additional reactive current to the grid. This is known as the low-voltage ride-through (LVRT) capability. Fig. 15.7 shows an overview of the LVRT requirements in different countries, where the PV systems should remain connected to the grid when the grid voltage is above the curves in Fig. 15.7. In contrast, the disconnection of these power sources during voltage sags may further lead to the instability of the grid.

15.3.2 Active power control requirement

With the increasing installation of grid-connected PV plants, the grid may face overloading issues during peak power generation periods (e.g., noon hours

This book belongs to Kitab Liaison (ocd1996@gmail.com) Copyright Elsevier 2023

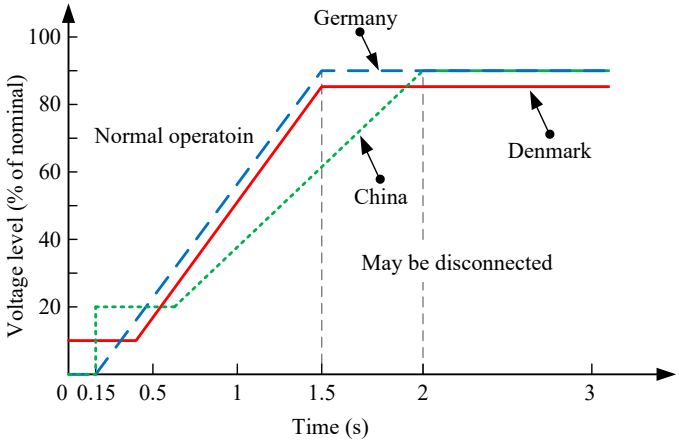

FIGURE 15.7 Low-voltage ride-through requirements for photovoltaic system in different countries [8,20,21].

with high solar radiation) [22]. To maintain the stability of the power network, modern grid codes in many countries dictate that these grid-tied PV systems should be able to control the active power according to the following remote power constraints:

- Absolute power constraint (to protect the power grid against overloading during peak power generation periods)
- Delta power constraint (to establish a regulating power reserve for other ancillary services, e.g., frequency control)
- Ramp-rate constraint (to prevent the changes in active power from negatively impacting the grid stability)

Fig. 15.8 depicts an overview of the active power constraint requirements. It should be noted that the active power control functions may comply with the requirements of frequency response/control, as shown in Fig. 15.8D. It is clear that for enabling grid-friendly systems, the grid-connected PV systems should not solely maximize the energy harvesting but also be active in grid regulation with the various integrated advanced control functions.

15.4 Constant power generation control strategy

In order to achieve the active power control requirements, the PV system needs to be able to regulate its power production to a certain level during the operation. This control strategy is referred to as the CPG control [22,23], which will be implemented with the PV system in Fig. 15.1B and demonstrated in this section. The main objective of the CPG control strategy is to limit the PV output power to a certain power-limit level. This requirement can

This book belongs to Kitab Liaison (ocd1996@gmail.com) Copyright Elsevier 2023

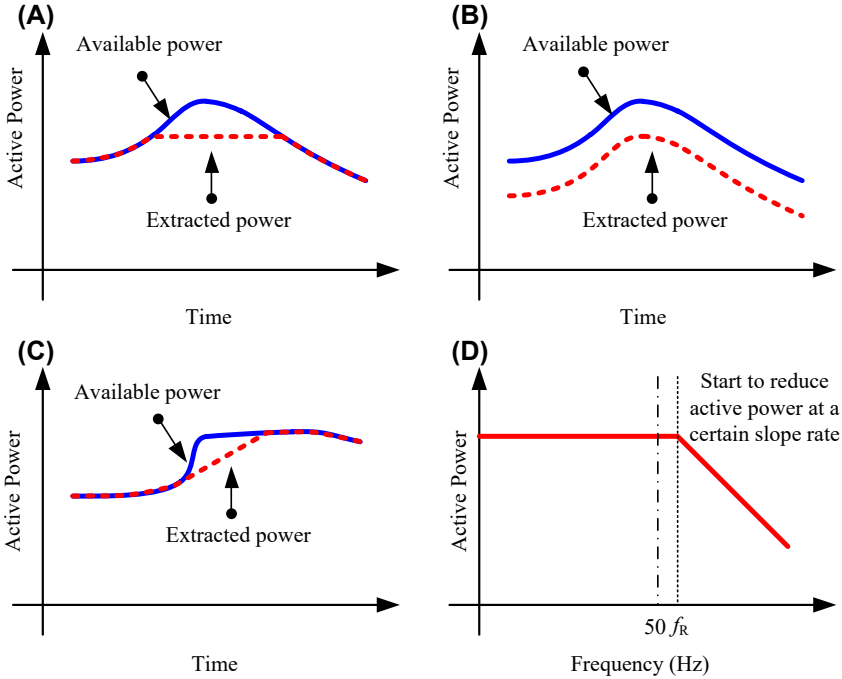

FIGURE 15.8 Active power control functions for grid-connected photovoltaic systems: (A) absolute power constraint, (B) delta power constraint, (C) ramp-rate constraint, and (D) frequency response/control (f_R: grid frequency) [8].

be achieved by regulating the operating point of the PV array below the MPP, as it is illustrated in Fig. 15.9. In principle, there are two possible operating points—CPP-L and CPP-R for a certain power-limit level at a certain solar irradiance and temperature condition. Therefore, the main task of the CPG strategy is to regulate the operating point of the PV arrays at one of these two CPPs. However, the solar irradiance and temperature condition change dynamically during the operation, and thus the P−V characteristic curve. Thus, the CPG strategy also needs to follow the change in the P−V curve and track the CPP under dynamic conditions. In general, the demands of the CPG strategy are as follows:

- During steady state (e.g., constant solar irradiance), the CPG strategy should keep the operating point of the PV array at the CPP with minimum deviation, in order to minimize the power loss.
- During transient (e.g., changing solar irradiance), the CPG strategy should track the CPP and follow the change in the P−V curve. Moreover, it should also ensure a smooth transition, e.g., between MPPT and CPG operation.

This book belongs to Kitab Liaison (ocd1996@gmail.com) Copyright Elsevier 2023

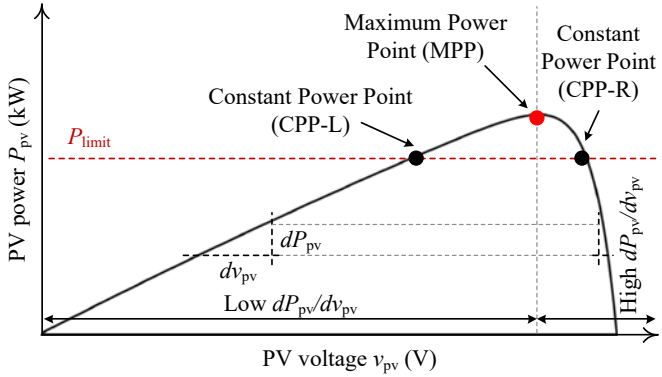

FIGURE 15.9 Possible operating points of the photovoltaic (PV) system in the power–voltage curve of the PV arrays during the CPG operation (i.e., CPP) at a certain power-limit and solar irradiance condition (CPP-L and CPP-R are the operating points at the left and right side of the MPP, respectively).

15.4.1 Direct power control (P-CPG)

One possible way to achieve the CPG operation is by directly regulating the PV output power through the closed-loop power control. In this approach, the reference PV current obtained from the MPPT algorithm is multiplied with the measured PV voltage in order to determine the reference PV power in the MPPT mode. Then, a saturation block is employed to limit the reference PV power to a certain level according to the power-limit set-point. In this way, it can be ensured that the reference PV power will be kept at the power-limit level once the available power is higher than the power-limit, and thereby achieving the CPG operation. Afterward, the modified PV power reference is used in the closed-loop control, where a PI controller is employed to regulate the PV output power following the control structure in Fig. 15.10. The PV power reference with this control method can be summarized as in the following:

$$P^*_{pv} = \begin{cases} P_{MPPT}, & \text{when} \quad P_{MPPT} \le P_{limit} \\ P_{limit}, & \text{when} \quad P_{MPPT} > P_{limit} \end{cases} \tag{15.1}$$

where P_{MPPT} is the maximum available power (according to the MPPT operation), and P_{limit} is the power-limit level during the CPG operation.

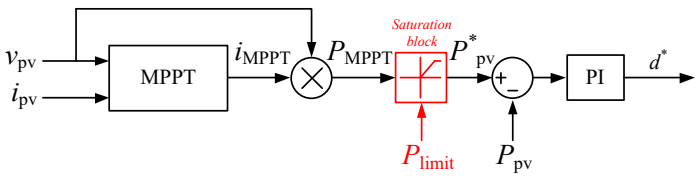

FIGURE 15.10 Control diagram of the CPG strategy based on Direct Power Control method (P-CPG).

This book belongs to Kitab Liaison (ocd1996@gmail.com) Copyright Elsevier 2023

The performance of CPG operation based on the P-CPG method is demonstrated in Fig. 15.11A, where different power-limit levels are considered during the test. It can be seen from the results that the PV output power can be limited accurately according to the set-point with an error of only 0.61% during the operation (e.g., when $P_{limit} = 80\%$). It also achieves a smooth transition between the MPPT and CPG operating modes, as it can be observed from the operating trajectory in the P−V curve of the PV arrays in Fig. 15.11B. In this case, the operating point of the PV arrays is regulated at the right side of the MPP (i.e., CPP-R) during the CPG operation.

15.4.2 Current-limiting control (I-CPG)

The power-limiting operation during the CPG mode can also be achieved through the regulation of the PV output current. According to the I−V characteristic of the PV array, there is an operating region where the PV voltage is

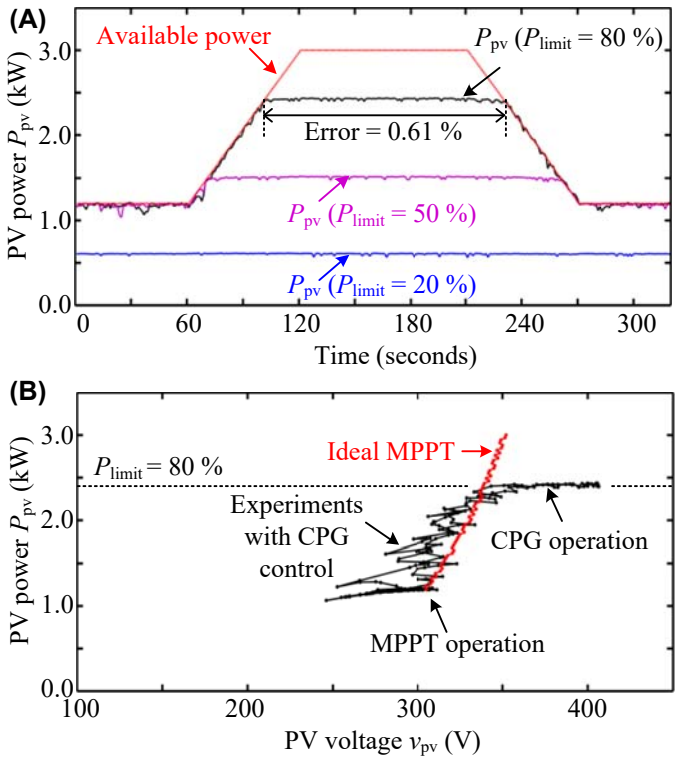

FIGURE 15.11 Experimental results of CPG strategy based on the Direct Power Control method (P-CPG): (A) Photovoltaic (PV) output power and (B) operating trajectory in power-voltage curve of the PV arrays.

This book belongs to Kitab Liaison (ocd1996@gmail.com)
Copyright Elsevier 2023

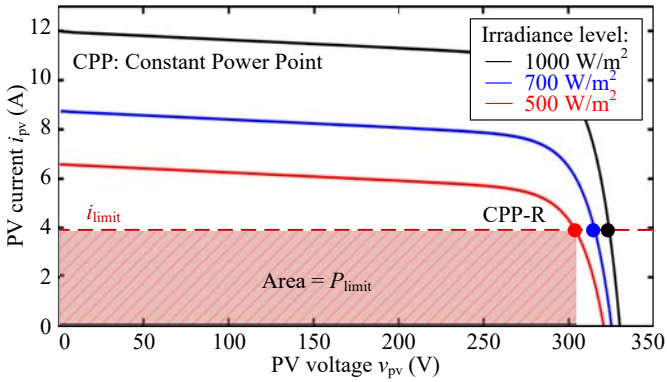

FIGURE 15.12 Operational principle of the CPG strategy based on Current-Limiting Control method (I-CPG).

almost constant, which is located at the right side of the MPP, as it is illustrated in Fig. 15.12. Therefore, the regulation of the PV current in this region can effectively regulate the PV output power, which corresponds to the rectangular area under the CPP-R shown in Fig. 15.12. In this case, the reference PV current needs to be limited according to

$$i_{pv}^{*} = \begin{cases} i_{MPPT}, & \text{when} \quad P_{MPPT} \leq P_{limit} \\ \dfrac{P_{limit}}{v_{pv}}, & \text{when} \quad P_{MPPT} > P_{limit} \end{cases} \tag{15.2}$$

which can be implemented with a saturation block, as illustrated in Fig. 15.13. The reference PV current is then regulated with a PI controller to determine the duty cycle of the DC−DC converter. According to (15.2), the saturation block will not be activated during the MPPT operation (e.g., $P_{MPPT} \leq P_{pv}$). Thus, the modification of the I-CPG method will not affect the performance of the MPPT algorithm during normal operation.

The performance of the I-CPG method is demonstrated in Fig. 15.14A under different power-limit levels. According to the results, the CPG operation

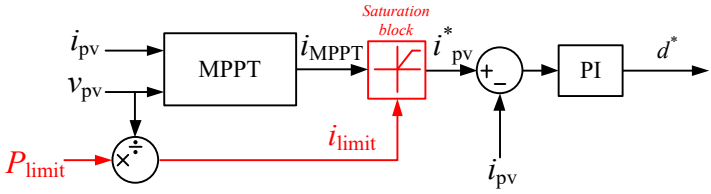

FIGURE 15.13 Control diagram of the CPG strategy based on Current-Limiting Control method (I-CPG).

This book belongs to Kitab Liaison (ocd1996@gmail.com) Copyright Elsevier 2023

can be achieved according to the required power-limit level with the I-CPG method. It can further be seen from the case when $P_{limit} = 80\%$ that the operating mode transition between the MPPT and CPG is achieved smoothly with no overshoot. As it can be seen from Fig. 15.14B, the operating point of the PV arrays is regulated at the right side of the MPP (i.e., CPP-R) during the CPG operation, which is the operating region where the PV voltage is almost constant. In that case, the tracking error during the CPG mode is only 0.36%. However, there is a risk of unstable operation during a decreasing solar irradiance condition, where the operating point of the PV arrays may fall into short circuit condition, as it is shown in Fig. 15.14B. This is mainly due to the steepness of the power−current characteristic of the PV arrays, which may also occur during the MPPT operation [24].

15.4.3 Perturb and observe−based control (P&O-CPG)

A P&O-based control algorithm, which has been employed in the MPPT operation, can also be implemented for the CPG control strategy. However, in

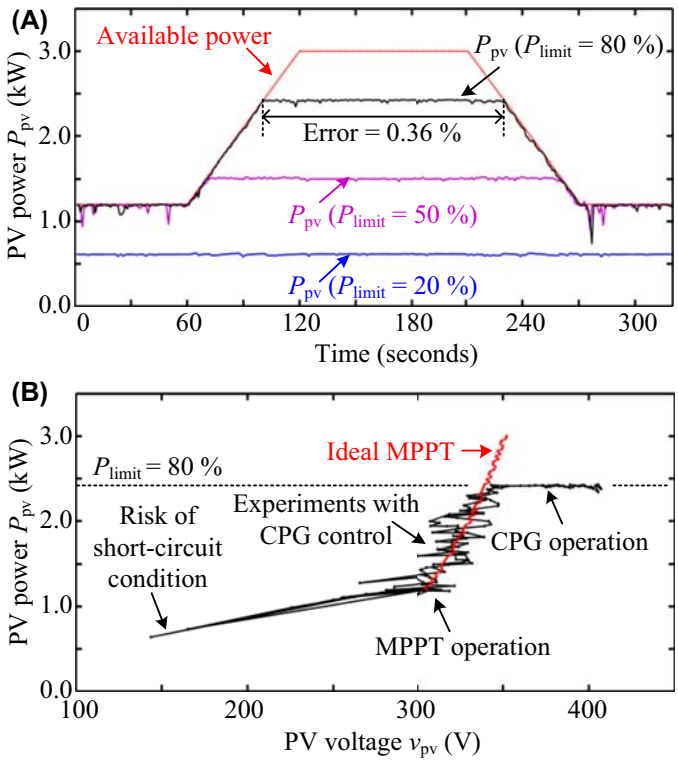

FIGURE 15.14 Experimental results of CPG strategy based on the Current-Limiting Control method (I-CPG): (A) Photovoltaic (PV) output power and (B) operating trajectory in power-voltage curve of the PV arrays.

This book belongs to Kitab Liaison (ocd1996@gmail.com)
Copyright Elsevier 2023

this case, the control algorithm should track the CPP in order to achieve the power-limit constraint, instead of tracking the MPP like in normal MPPT operation. In fact, the operating point of the PV array needs to be continuously perturbed toward one of the CPPs, e.g., $P_{pv} = P_{limit}$, as it is illustrated in Fig. 15.15. After a number of iterations, the operating point of the PV array will reach and oscillate around the corresponding CPP during steady state.

In this CPG strategy, it is possible to regulate the PV output power at either the CPP-L or CPP-R, depending on the perturbation direction. It should also be noted that the operating point at the right side of the MPP, i.e., CPP-R, will result in a larger power oscillation during steady state due to the high slope of the P−V curve (i.e., large dP_{pv}/dt). On the other hand, operating the PV array at the CPP-L may be restricted in a single-stage PV inverter due to the minimum DC-link voltage requirement. The control structure of the P&O-CPG method is shown in Fig. 15.16, where the reference PV voltage v_{pv}^* can be calculated as

$$v_{pv}^* = \begin{cases} v_{MPPT}, & \text{when} \quad P_{MPPT} \le P_{limit} \\ v_{pv} - v_{STEP}, & \text{when} \quad P_{MPPT} > P_{limit} \end{cases} \tag{15.3}$$

if the operating point is regulated at the CPP-L, or

$$v_{pv}^* = \begin{cases} v_{MPPT}, & \text{when} \quad P_{MPPT} \le P_{limit} \\ v_{pv} + v_{STEP}, & \text{when} \quad P_{MPPT} > P_{limit} \end{cases} \tag{15.4}$$

if the operating point is regulated at the CPP-R.

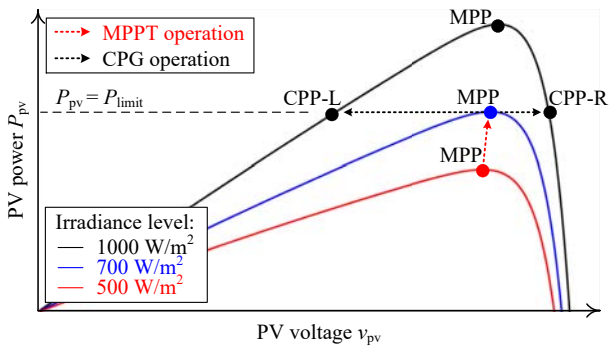

FIGURE 15.15 Operational principle of the CPG strategy based on the P&O control method.

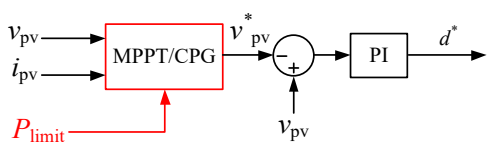

FIGURE 15.16 Operational principle of the CPG strategy based on the P&O control method.

This book belongs to Kitab Liaison (ocd1996@gmail.com) Copyright Elsevier 2023

The performance of the P&O-CPG method when the operating point of the PV arrays is regulated at CPP-R and CPP-L is demonstrated in Figs. 15.17 and 15.18, respectively. According to the results in Fig. 15.17, the operating point at the CPP-R results in a larger power oscillations. Consequently, the tracking error during the CPG operation is 1.22%. On the other hand, regulating the operating point at the CPP-L during the CPG operation results in a lower power oscillation, where the tracking error is only 0.37%, as shown in Fig. 15.18. Nevertheless, there is a small overshoot in the PV power during the operating mode transition (e.g., from MPPT to CPG) when employing P&O-CPG method for both the operating points. This is due to the fact that the P&O-CPG method requires a number of iterations until the operating point of the PV array reaches the corresponding CPP. Notably, the performance of the P&O-CPG algorithm can be improved by employing an adaptive step-size during dynamic and steady-state conditions, as it has been demonstrated in Refs. [25,26].

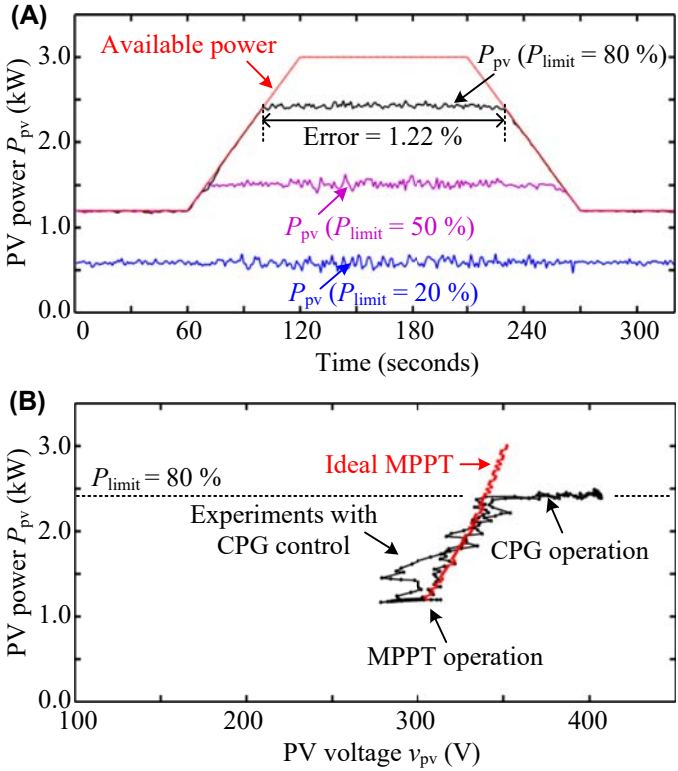

FIGURE 15.17 Experimental results of CPG strategy based on the Perturb and Observe method (P&O-CPG) operating at the right side of the MPP (i.e., CPP-R): (A) Photovoltaic (PV) output power and (B) operating trajectory in power−voltage curve of the PV arrays.

This book belongs to Kitab Liaison (ocd1996@gmail.com)
Copyright Elsevier 2023

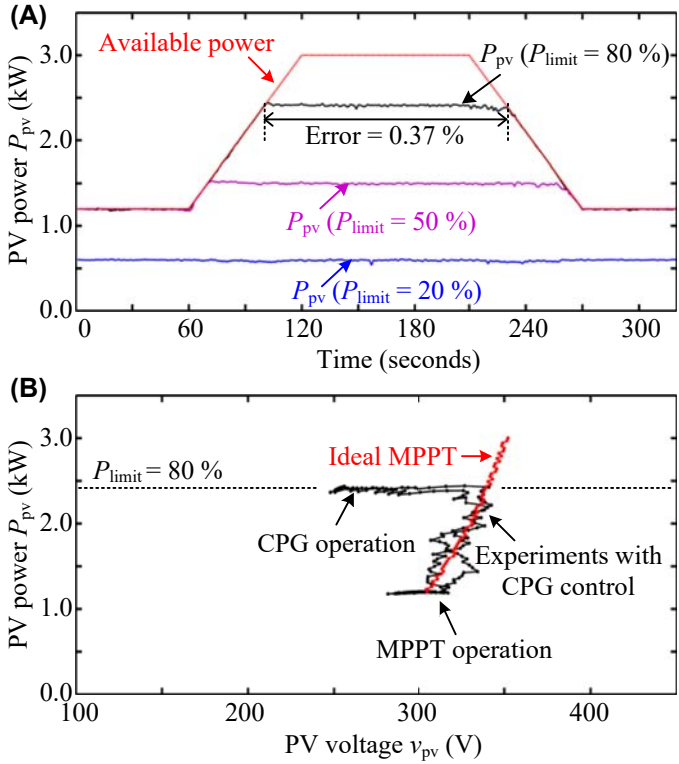

FIGURE 15.18 Experimental results of CPG strategy based on the Perturb and Observe method (P&O-CPG) operating at the left side of the MPP (i.e., CPP-L): (A) Photovoltaic (PV) output power and (B) operating trajectory in power–voltage curve of the PV arrays.

15.5 Benchmarking of constant power generation control strategy

The performance of different CPG strategies is compared through experimental results. Two different operating conditions during cloudy-day and clear-day conditions are considered where a power-limit level of $P_{limit} = 50\%$ is employed, as it is shown in Figs. 15.19 and 15.20, respectively. The performance benchmarking is carried out by considering dynamic responses, steady-state responses, tracking error, stability, and complexity.

15.5.1 Dynamic responses

The dynamic responses of the CPG strategies can be evaluated by considering the operation during a cloudy day, as shown in Fig. 15.19. During this operating condition, the solar irradiance and thus available PV power fluctuate with

This book belongs to Kitab Liaison (ocd1996@gmail.com) Copyright Elsevier 2023

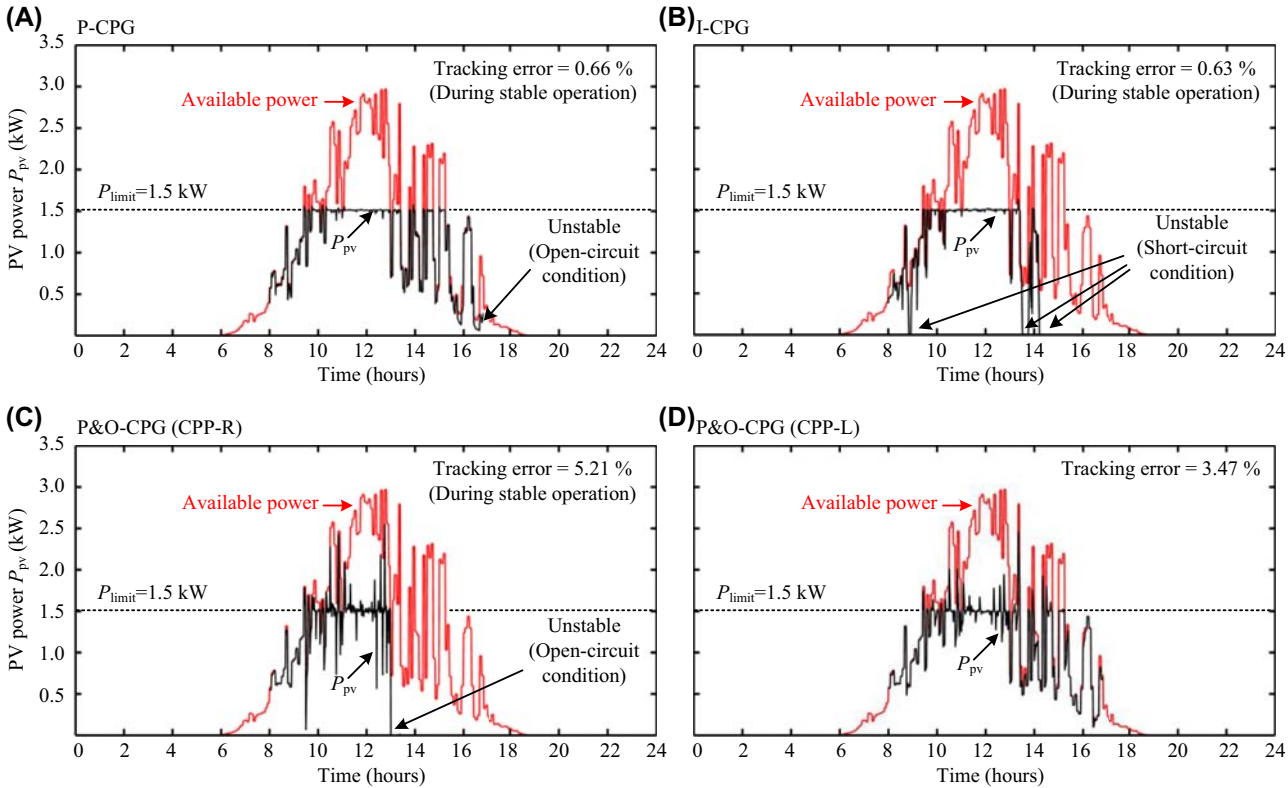

FIGURE 15.19 Experimental results of CPG strategies under a cloudy-day condition with power-limit level of $P_{limit} = 50\%$ based on (A) direct power control, (B) current-limiting, (C) Perturb and Observe at the CPP-R, and (D) perturb and observe at the CPP-L.

This book belongs to Kitab Liaison (ocd1996@gmail.com)

Copyright Elsevier 2023

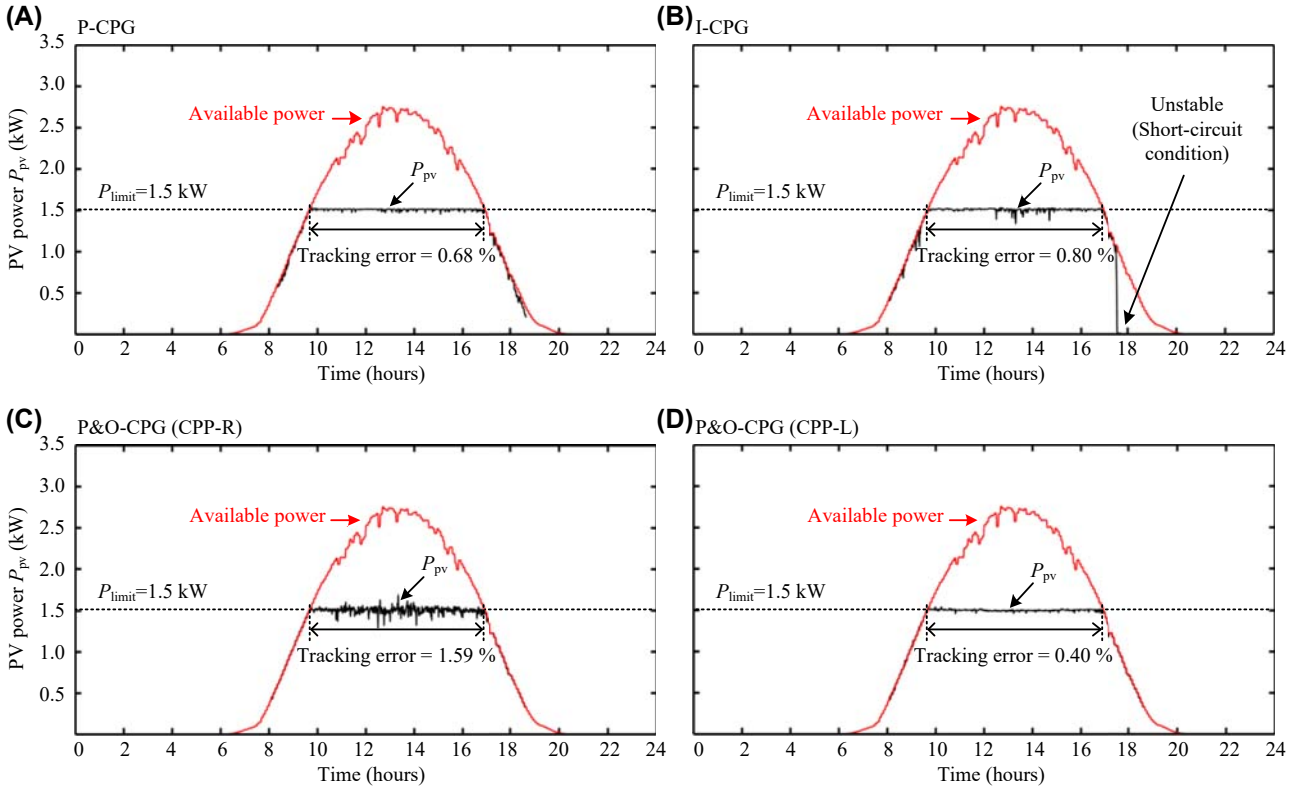

FIGURE 15.20 Experimental results of CPG strategies under a clear-day condition with the power-limit level of $P_{limit} = 50\%$ based on (A) the direct power control, (B) current-limiting, (C) perturb and observe at the CPP-R, and (D) perturb and observe at the CPP-L.

This book belongs to Kitab Liaison (ocd1996@gmail.com)

Copyright Elsevier 2023

a fast-changing rate. This challenges the dynamic performance of the CPG strategy, which needs to keep the PV output power constant at the power-limit regardless of the variation in the available PV power condition.

According to the experimental results in Fig. 15.19, it can be observed that both the CPG strategies based on the direct power control (P-CPG) and current-limiting control (I-CPG) can achieve a fast dynamic performance where there is no overshoot in the PV output power during the fluctuation of the available PV power. Therefore, the PV output power can be limited to 1.5 kW during the entire operation. In contrast, the P&O-based CPG method presents a large power overshoot during the fluctuation of the available power. This slow dynamic response is due to the fact that the control algorithm requires a number of iterations to regulate the operating point at the CPP. This is applied for both the operating point at the CPP-R and CPP-L, as shown in Fig. 15.19C and D, respectively. In that case, the power-limit constraint is violated during the fast-changing of the solar irradiance level.

15.5.2 Steady-state responses

The steady-state performance of the CPG strategies can be evaluated during the clear-day condition, where the available PV power changes smoothly during the daily operation. According to the experimental results in Fig. 15.20, all of the CPG strategies are capable of limiting the PV output power according to the power-limit level during the operation with a very small deviation. Only the P&O-based CPG method presents a power oscillation during the operation when the operating point is regulated at the CPP-R, as it is shown in Fig. 15.20C. This is mainly due to a large dP_{pv}/dv_{pv} at the CPP-R, where even a small perturbation in the PV voltage dv_{pv} can result in a large PV power change dP_{pv}.

15.5.3 Tracking error

The tracking error is a quantitative measure of the accuracy of the CPG strategies. It is calculated from the difference between the actual PV output power and the power-limit level during the operation and then divided by the total energy yield (i.e., $|P_{pv}—P_{limit}|/E_{pv}$). For instance, the dynamic performance of the CPG strategy can be evaluated quantitatively by considering the tracking error during the cloudy-day condition. It can be seen from the results in Fig. 15.19C that a large error occurs when the P&O-based CPG method is employed. On the other hand, the tracking error during the clear-day condition can reflect the steady-state response of the CPG strategies. In all cases, the tracking error during steady state is minimal. The largest error occurs when the P&O-based CPG method regulates the operating point at the CPP-R, which is in an agreement with the power oscillation in the time-domain waveform of the PV output power (see Fig. 15.20C).

This book belongs to Kitab Liaison (ocd1996@gmail.com) Copyright Elsevier 2023

15.5.4 Stability

It is important for the CPG strategy to ensure a stable operation and continuously deliver power to the grid. However, instability may occur for the CPG strategies during the fast decreasing solar irradiance condition. Due to the rapid change in the power-voltage characteristic of the PV arrays, the operating point during the CPG operation may fall into either open circuit or short circuit conditions. For instance, the short circuit condition may occur when the current-limiting CPG strategy is employed, as it has been demonstrated in Fig. 15.19B. On the other hand, the operating point of the PV arrays may also fall into an open circuit condition when the direct power control or the P&O-based CPG strategies operating at CPP-R are employed during a fast decreasing solar irradiance condition, as it is shown in Fig. 15.19A and C. Therefore, only the P&O-based operating at CPP-L is robust against the stability issue during the fast-changing solar irradiance condition.

15.5.5 Complexity

The complexity of the control algorithm plays a major role in the real implementation of the CPG strategy. When comparing all the CPG strategies, the current-limiting CPG strategy offers the simplest control structure where only one saturation block needs to be added to the original MPPT controller. On the other hand, the P&O-based CPG strategy requires a modification at the MPPT algorithm level, while the direct power control CPG strategy needs both the modification of the MPPT algorithm (to be able to provide the reference PV power) and an additional saturation block to limit the PV power reference.

The performance benchmarking of the CPG strategies under different aspects are further summarized in Table 15.1, where + indicates less tracking error, better stability, and less complexity of the CPG strategy.

TABLE 15.1 Benchmarking of the CPG strategies.

CPG strategy	Dynamic responses	Steady-state responses	Tracking error	Stability	Complexity
P-CPG	++	+	+	−	−
I-CPG	++	+	+	−−	++
P&O-CPG at CPP-R	−−	−−	−−	−	−
P&O-CPG at CPP-L	−−	++	−	++	−

Note: the more +, the less tracking error, better stability, and less complexity.

This book belongs to Kitab Liaison (ocd1996@gmail.com) Copyright Elsevier 2023

15.6 Summary

With an increasing installation of PV systems, a more grid-friendly control strategy is required to address the challenging issues related to the overloading of the grid, grid voltage fluctuation, and frequency regulation capability. This chapter has presented an advanced control of PV systems by means of CPG control. Three different approaches to implement the CPG control strategy have been discussed and their performance has been benchmarked in terms of dynamic responses, steady-state responses, tracking error, stability, and complexity. According to the evaluation results, the direct power and the current-limiting control strategies can achieve fast dynamic responses, which results in low tracking errors. However, the P&O-based control strategy has a superior steady-state performance and is more robust, e.g., against unstable operation during the fast decreasing solar irradiance conditions. Therefore, it is a suitable method to be implemented in practical applications.

References

[1] F. Blaabjerg, Z. Chen, S.B. Kjaer, Power electronics as efficient interface in dispersed power generation systems, IEEE Trans. Power Electron. 19 (5) (September 2004) 1184−1194.

[2] T. Stetz, J. von Appen, F. Niedermeyer, G. Scheibner, R. Sikora, M. Braun, "Twilight of the grids: the impact of distributed solar on Germany's energy transition, IEEE Power Energy Mag. 13 (2) (March 2015) 50−61.

[3] A. Woyte, V.V. Thong, R. Belmans, J. Nijs, Voltage fluctuations on distribution level introduced by photovoltaic systems, IEEE Trans. Energy Convers. 21 (1) (March 2006) 202−209.

[4] S. Shivashankar, S. Mekhilef, H. Mokhlis, M. Karimi, Mitigating methods of power fluctuation of photovoltaic (PV) sources - a review, Renew. Sustain. Energy Rev. 59 (2016) 1170−1184.

[5] B. Kroposki, Can solar save the grid? IEEE Spectr. 53 (11) (November 2016) 42−47.

[6] Y. Yang, P. Enjeti, F. Blaabjerg, H. Wang, Wide-scale adoption of photovoltaic energy: grid code modifications are explored in the distribution grid, IEEE Ind. Appl. Mag. 21 (5) (September 2015) 21−31.

[7] Y.K. Wu, J.H. Lin, H.J. Lin, Standards and guidelines for grid-connected photovoltaic generation systems: a review and comparison, IEEE Trans. Ind. Appl. 53 (4) (July-August 2017) 3205−3216.

[8] Energinet.dk, Technical regulation 3.2.2 for PV power plants with a power output above 11 kW, Tech. Rep. Doc. (2016), 14/17997-39.

[9] BDEW, Technische richtlinie erzeugungsanlagen am mittelspannungsnetz − richtlinie fur anschluss und parallelbetrieb von erzeugungsanlagen am mittelspannungsnetz, June 2008.

[10] E. Troester, New German grid codes for connecting PV systems to the medium voltage power grid, in: Proc. of 2nd Int. Workshop Concentrating Photovoltaic Power Plants: Opt. Design, Prod., Grid Connection, 2009.

[11] Y. Yang, K.A. Kim, F. Blaabjerg, A. Sangwongwanich, Advances in Grid-Connected Photovoltaic Power Conversion Systems, Publisher: Woodhead Publishing, 2018.

This book belongs to Kitab Liaison (ocd1996@gmail.com) Copyright Elsevier 2023

[12] F. Blaabjerg, R. Teodorescu, M. Liserre, A.V. Timbus, Overview of control and grid synchronization for distributed power generation systems, IEEE Trans. Ind. Electron. 53 (5) (October 2006) 1398−1409.

[13] M. Saitou, T. Shimizu, Generalized theory of instantaneous active and reactive powers in single-phase circuits based on Hilbert transform, in: Proc. 2002 IEEE 33rd Annu. IEEE Power Electron. Specialists Conf. Proceedings (Cat. No.02CH37289), vol. 3, 2002, pp. 1419−1424.

[14] T. Esram, P.L. Chapman, Comparison of photovoltaic array maximum power point tracking techniques, IEEE Trans. Energy Convers. 22 (2) (June 2007) 439−449.

[15] N. Femia, G. Petrone, G. Spagnuolo, M. Vitelli, Optimization of perturb and observe maximum power point tracking method, IEEE Trans. Power Electron. 20 (4) (July 2005) 963−973.

[16] A. Sangwongwanich, Y. Yang, D. Sera, H. Soltani, F. Blaabjerg, Analysis and modeling of interharmonics from grid-connected photovoltaic systems, IEEE Trans. Power Electron. 33 (10) (October 2018) 8353−8364.

[17] D. Sera, R. Teodorescu, J. Hantschel, M. Knoll, Optimized maximum power point tracker for fast-changing environmental conditions, IEEE Trans. Ind. Electron. 55 (7) (July 2008) 2629−2637.

[18] A. Sangwongwanich, Y. Yang, D. Sera, F. Blaabjerg, Interharmonics from grid-connected PV systems: mechanism and mitigation, in: Proc. 2017 IEEE 3rd Int. Future Energy Electron. Conf. (IFEEC-ECCE Asia), June 2017, pp. 722−727.

[19] Z. Li, R. Zhao, Z. Xin, J.M. Guerrero, M. Savaghebi, P. Li, Inrush transient current analysis and suppression of photovoltaic grid-connected inverters during voltage sag, in: Proc. 2016 IEEE APEC, Long Beach, CA, 2016, pp. 3697−3703.

[20] P. Chao, et al., A unified modeling method of photovoltaic generation systems under balanced and unbalanced voltage dips, IEEE Trans. Sustain. Energy 10 (4) (October 2019) 1764−1774.

[21] Y. Bak, J. Lee, K. Lee, Low-voltage ride-through control strategy for a grid-connected energy storage system, Appl. Sci. 8 (2018) 57.

[22] A. Sangwongwanich, Y. Yang, F. Blaabjerg, H. Wang, Benchmarking of constant power generation strategies for single-phase grid-connected photovoltaic systems, IEEE Trans. Ind. Appl. 54 (1) (Febuary 2018) 447−457.

[23] H.D. Tafti, et al., Extended functionalities of photovoltaic systems with flexible power point tracking: recent advances, IEEE Trans. Power Electron. 35 (9) (September 2020) 9342−9356, https://doi.org/10.1109/TPEL.2020.2970447.

[24] N. Femia, G. Petrone, G. Spagnuolo, M. Vitelli, Power Electronics and Control Techniques for Maximum Energy Harvesting in Photovoltaic Systems, CRC press, 2012.

[25] A. Sangwongwanich, Y. Yang, F. Blaabjerg, High-performance constant power generation in grid-connected PV systems, IEEE Trans. Power Electron. 31 (3) (March 2016) 1822−1825.

[26] H.D. Tafti, A. Sangwongwanich, Y. Yang, J. Pou, G. Konstantinou, F. Blaabjerg, An adaptive control scheme for flexible power point tracking in photovoltaic systems, IEEE Trans. Power Electron. 34 (6) (June 2019) 5451−5463.

This book belongs to Kitab Liaison (ocd1996@gmail.com) Copyright Elsevier 2023

This page intentionally left blank

This book belongs to Kitab Liaison (ocd1996@gmail.com)

Copyright Elsevier 2023

Chapter 16

Low voltage ride-through operation of single-phase PV systems

Zhongting Tang[1], **Yongheng Yang**[2]
[1]*Central South University, Changsha, China;* [2]*Aalborg University, Aalborg, Denmark*

16.1 Introduction

As one of the eco-friendly renewable energy sources, the photovoltaic (PV) energy has experienced a very rapid growth rate of installation, which, however, is highly intermittent [1,2]. This inherent intermittent characteristic (i.e., the power generation is dependent on the environmental conditions) causes many challenging issues when the PV power is injected into the utility grid, such as power quality and network stability [3–6]. In order to overcome the above challenges, the grid-connected PV systems are required to have fully and flexibly supportive functions for the grid, when various disturbances (e.g., voltage and frequency faults) appear [7–9].

Especially, with a high penetration of PV power, the abnormal conditions of the utility grid may trigger wide area unintentional disconnection, threatening the equipment security and the entire grid stability (e.g., a large-scale outage). There are various abnormal conditions in the grid, as exemplified in Fig. 16.1, including the voltage and frequency disturbances [10,11]. Generally, the events can be separated into long-term disturbances (e.g., harmonic distortion [13], unbalanced three-phase voltages, flickering, and frequency variations) and short-term disturbances (e.g., voltage sags, voltage swells, voltage spikes, and power outage). By comparison, the short-term events are more likely to cause interruptions to the grid [10]. Therefore, advanced control strategies for grid-connected PV systems should be developed to provide a stable and grid-friendly operation under such abnormal grid conditions (e.g., voltage sags) [7,12].

A voltage sag is a short and fast transient event in grid-connected systems occurring due to various accidents (e.g., lightning strikes, power line short circuit, etc.). The temporary drop of the grid voltage amplitude may exceed the

Control of Power Electronic Converters and Systems. https://doi.org/10.1016/B978-0-12-819432-4.00006-8
Copyright © 2021 Elsevier Ltd. All rights reserved.

This book belongs to Kitab Liaison (ocd1996@gmail.com)
Copyright Elsevier 2023

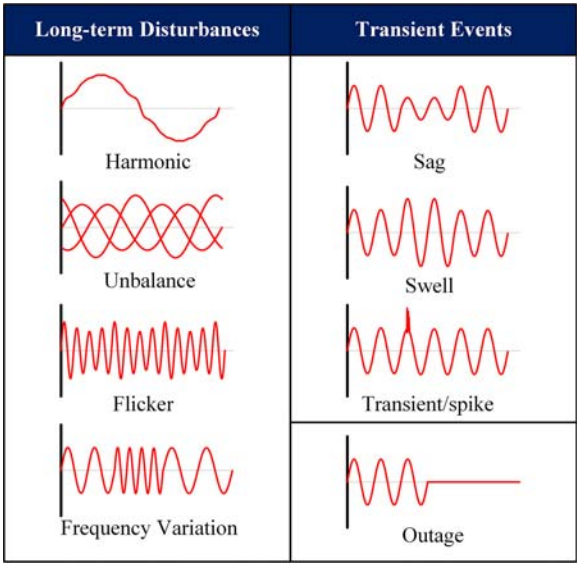

FIGURE 16.1 Abnormal conditions in the utility grid voltage (i.e., including the disturbances/events in amplitude and frequency).

normal voltage threshold, and, subsequently, trigger the islanding protection [14], causing the power supply interruption. When the amount of stoppage of power generation from PV systems reaches a certain level, the stability of the grid may be threatened. This chapter then focuses on the advanced control strategies under a typical transient disturbance (i.e., the voltage sag) in single-phase grid-connected PV systems.

Thus, many grid codes and standards require grid-connected PV systems to have the capability to ride-through the transient voltage sags [15]. Meanwhile, the voltage regulation capability should be provided by the PV generation systems to support the grid voltage recovery during short-term events [16]. This is known as low voltage ride-through (LVRT) operation. The response and voltage ride-through requirements of the distributed energy resources (DERS) in the IEEE Std 1547-2018 (i.e., revision of IEEE Std 1547-2003) are shown in Fig. 16.2 [17,18]. As shown in Fig. 16.2, the operation zone is divided into different regions, containing the continuous operation region (i.e., normal operation mode), mandatory voltage ride-through operation regions (i.e., mandatory connection to the utility grid), momentary cessation regions, trip regions, and undefined regions, where the PV systems may be tripped or may ride-through.

Additionally, the voltage regulation capability demanded in the IEEE Std 1547-2018 includes the voltage-reactive power regulation and voltage-active

This book belongs to Kitab Liaison (ocd1996@gmail.com) Copyright Elsevier 2023

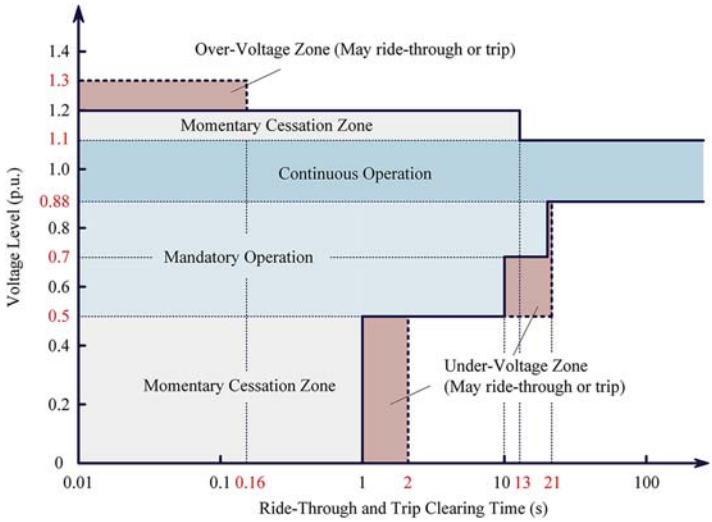

FIGURE 16.2 Response and voltage ride-through requirements for distributed energy resources to grid voltage faults adapted according to the IEEE Std 1547-2018. When outside the shaded areas, the system shall trip.

power regulation [7,18]. More specifically, in the case of LVRT operation, it is mandatory that the grid-connected PV systems should operate the following mutually exclusive regulation modes of reactive power control:

- Constant power factor mode;
- Voltage-reactive power mode;
- Active power-reactive power mode; and
- Constant reactive power mode.

For instance, Fig. 16.3 shows the voltage-reactive power characteristic as an example, where the grid-connected PV systems should actively control the reactive power output according to the piecewise linear characteristics. The minimal reactive power injection (RPI) should arrive at 25% of the nameplate apparent power in normal DERs, while 44% is required in the area where the aggregated DERs penetration is high or the overall DERs power output has frequent large variations (e.g., due to the fluctuation of the PV energy resource). In addition to the requirements for the RPI, the voltage should also be regulated by changing the active power, following the voltage-active power characteristic. This requirement aims to limit the maximum active power during the voltage sag to avoid inverter tripping. Fig. 16.4 exemplifies two characteristics for different DERs (i.e., one can only generate active power, while the other can generate and absorb active power).

This book belongs to Kitab Liaison (ocd1996@gmail.com) Copyright Elsevier 2023

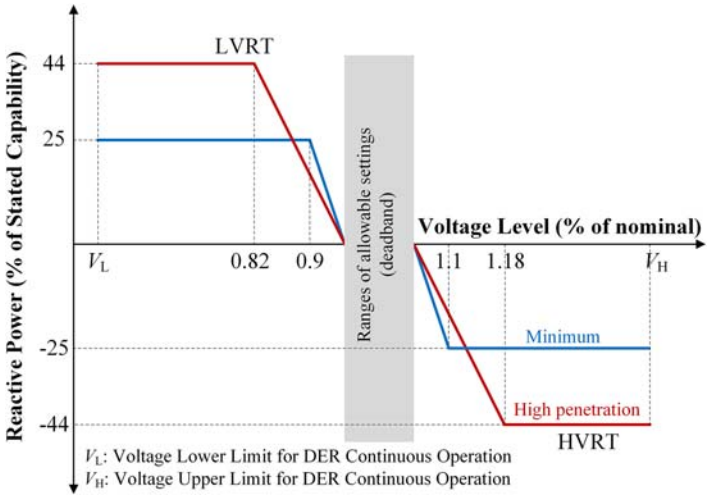

FIGURE 16.3 Requirement of the voltage-reactive power characteristic in the case of fault ride-through operation (i.e., low voltage ride-through (LVRT) operation) according to the IEEE Std 1547.

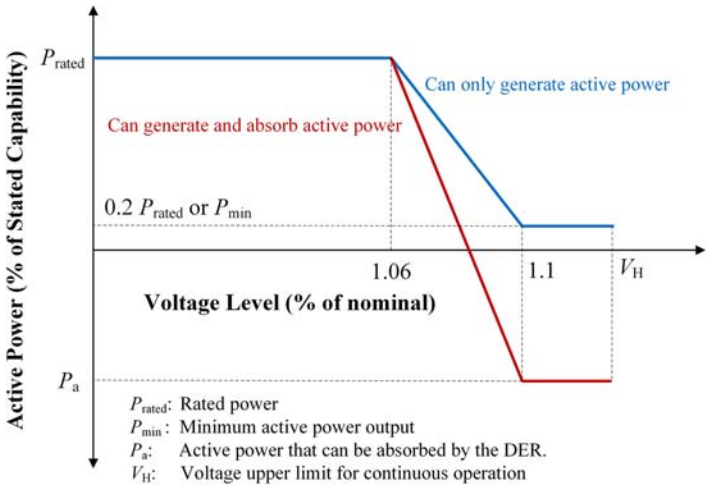

FIGURE 16.4 Requirement of the voltage-active power characteristic according to the IEEE Std 1547-2018.

The above operation modes are allowed to be flexibly adjusted by the utility grid operator, such as the power factor and the parameters in the adjustable range of the voltage-reactive/active power characteristics [18].

Without special requirements from the utility grid operator, the PV systems should operate in the maximum power point tracking (MPPT) mode at the

This book belongs to Kitab Liaison (ocd1996@gmail.com) Copyright Elsevier 2023

unity power factor and remain in the continuous operation region, as shown in Fig. 16.2 [19]. Once a grid voltage fault occurs (i.e., the mandatory ride-through regions in Fig. 16.2), the grid-connected PV systems are demanded to stay connected to the utility grid [12,20]. In practice, the transient grid voltage faults occur more frequently, especially in remote areas with a weak grid. Thus, advanced control strategies should be developed for the grid-connected PV systems to provide a seamless operation transition between the normal operation (i.e., MPPT at the unity power factor) and LVRT operation (i.e., ride-through voltage sags with voltage regulation capability). To provide dynamic grid support, the control method should enhance the RPI capability from the PV grid-connected converters [7,16,18]. Therefore, in addition to the voltage-active regulation capability, shown in Fig. 16.4, the active power should also be reduced to prevent overcurrent caused by the excessive apparent power, as discussed previously.

In this chapter, solutions to LVRT operations for single-phase PV systems are firstly reviewed. To achieve flexible, grid-friendly, and grid-supporting PV systems, the LVRT operations for both the single-stage and double-stage PV systems are introduced. Since the voltage-reactive regulation capability is demanded to provide dynamic supports for the grid voltage, RPI strategies considering the active power regulation for single-phase PV inverters are then presented in this chapter.

16.2 Low voltage ride-through operations

As mentioned previously, the LVRT operation means that the grid-connected PV systems must remain connected and ride-through the grid voltage sags of a certain level (see Fig. 16.2) [21]. Simultaneously, the utility grid operator can require a certain amount of reactive power to be injected at the point of common coupling [14] from the grid-connected PV systems to support the grid voltage recovery, and by that, providing dynamic grid support capability [7,16,18]. The single-phase inverter is suitable to be applied in the low-power or medium-power PV systems, which means it has limited contribution to the utility grid voltage regulation. However, with the increasing penetration of PV systems, the total PV power is becoming much larger to affect the entire system stability [1]. Thus, the advanced and flexible control strategy should be developed for the individual grid-connected PV inverter to avoid the stoppage under the transient voltage sag (due to islanding protection) and to provide voltage regulation for the overcurrent protection and the grid voltage recovery. In general, the basic LVRT operation of the grid-connected PV systems (either single-phase or three-phase) can be summarized in three steps:

(1) ***Monitoring***—Since the grid voltage amplitude is the basic judgment for the switchover of the normal operation and LVRT operation, the grid voltage online monitoring is very critical for fast detection. The prior-art

This book belongs to Kitab Liaison (ocd1996@gmail.com) Copyright Elsevier 2023

research efforts have verified that a phase-locked loop (PLL) system can provide a fast and accurate detection of the grid voltage [22]. Nevertheless, more advanced monitoring techniques, e.g., combined with artificial intelligence, are always of interest.

(2) ***Continuous connection and accurate current reference generation***—It is mandatory to continuously connect to the utility grid in a required period. In addition, the controller should generate accurate current references to satisfy the demands in grid codes (i.e., reactive and active power regulation) and to prevent overcurrent or overvoltage tripping. The continuous connection can easily be implemented when a voltage sag happens. In addition, the major control is switched to the LVRT operation state to generate the current references as required [21]. As mentioned previously, various strategies (e.g., active power and reactive power control) can be implemented when generating the current references.

(3) ***Recovery***—When the grid voltage sag is cleared, the PV system should provide seamless transitions back to the normal operation (i.e., in the MPPT mode at unity power factor) [23]. The recovery further requires a robust and fast synchronization technique to avoid any potential large transient disturbances and to protect the equipment.

Without physical inertia (i.e., the inherent characteristics in large wind power systems and conventional power generation systems with rotating machines) [10], PV systems have fast dynamics coming from the power electronic control. However, as increasing RPI under the LVRT operation is required, the active power should be reduced correspondingly to prevent the overcurrent tripping. When compared to the single-stage PV converter, the double-stage PV converter (i.e., including a DC−DC stage and an inverter stage) accepts a wider voltage range of the PV panels, enhanced by the front-end DC−DC converter [24]. Additionally, the double-stage structure can provide more flexible control due to the separated control for the grid-connected PV systems, where the DC−DC stage mainly aims to achieve the MPPT of the PV panels, and the inverter stage satisfies the requirements from the utility grid. Correspondingly, the solutions to reduce the active power for double-stage inverter are easier than those for the single-stage inverter. Possible methods to active power reduction for the single-phase PV systems can be summarized as follows:

- *Modifying the MPPT control*: The PV systems regulate the power tracking according to the power−voltage (P-V) characteristics of PV panels to reduce the active power (see also Chapter 14).
- *Integrating storage systems*: The PV systems with a storage device can store the excessive active power during the LVRT operation, and then provide the power to the local equipment in the islanding operation [7].

This book belongs to Kitab Liaison (ocd1996@gmail.com) Copyright Elsevier 2023

- *Adopting a DC chopper*: The excessive active power can be dissipated in the chopper resistor (i.e., the same as the braking resistor in wind turbine systems with rotating machines).

Compared to the above methods, modifying the MPPT is the most promising one due to its low system cost (i.e., no extra hardware). However, the conversion efficiency of the PV panel may be reduced. The second method can allow the MPPT control and ensure the conversion efficiency under the LVRT. Although being an advanced and promising technology in smart PV systems, the high price of the storage may lead to a relatively low cost-efficient of the PV systems. Nevertheless, along with the further development of storage technologies, the second solution will become much attractive and flexible. Regarding the conventional solution, i.e., employing a DC chopper, the MPPT control also can be continuous. Yet, the extra active power is only wasted as heat on the chopper resistor. Considering the above, the advanced control methods of the LVRT operation for single-phase PV systems will be implemented through modifying the MPPT control, which will be introduced in the following.

16.2.1 LVRT control using the single-phase PQ theory

The RPI and active power regulation are critical tasks for the grid-connected PV systems during the LVRT operation. It seems that the droop control is a suitable choice to implement the reactive/active power regulation [25]. The relationship of the conventional droop-control method includes the voltage-reactive power and frequency-active power, where the system should be mainly inductive (i.e., a high X/R ratio) [21]. Seen from this aspect, the droop control is not a very feasible method for the LVRT operation of single-phase PV systems, which are generally connected to low-voltage feeders (i.e., being resistive lines with a low X/R ratio).

Consequently, to have a flexible control of the reactive/active power, one way is the control strategy based on the single-phase PQ theory to directly synthesize the power references under the LVRT operation for single-phase PV systems [26,27]. With additional adaptive filters, the LVRT control based on the single-phase PQ theory facilitates to regulate the RPI [21,28,29]. In addition, the control schemes can be implemented in either the stationary or the rotating reference frame [4]. Considering the entire control complexity and harmonic compensation capability, the control strategy implemented in the stationary reference frame (i.e., $\alpha\beta$) is more advantageous.

Fig. 16.5 shows the entire control system for the single-stage single-phase PV system, and the control is based on single-phase PQ theory. Since there is only a full-bridge (DC−AC) inverter to control, the PV input voltage (DC-link voltage) v_{pv} is regulated through the MPPT control (gives the active power reference, P^*), and it must be higher than the peak value of the grid voltage. As

This book belongs to Kitab Liaison (ocd1996@gmail.com) Copyright Elsevier 2023

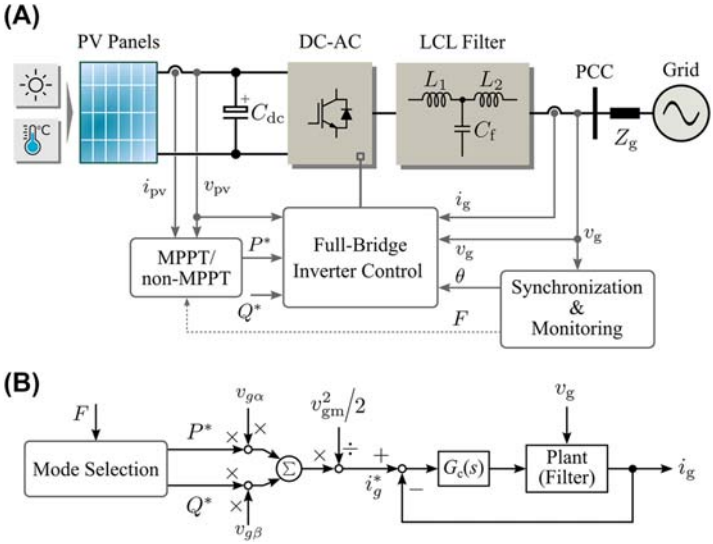

FIGURE 16.5 Control structure of the single-stage single-phase grid-connected photovoltaic (PV) system: (A) hardware schematic and (B) multimode control structure based on the single-phase PQ theory, where F is the fault signal and θ is the grid phase. Here, the control is implemented in the $\alpha\beta$ frame with $v_{g\alpha} = v_g$ being the grid voltage, $v_{g\beta}$ being the orthogonal in-quadrature voltage, and v_{gm} being the grid voltage amplitude, $G_c(s)$ is the current controller, point of common coupling (PCC) is the point of common-coupling, Z_g is the grid impedance, and C_{dc} is the DC-link capacitor.

shown in Fig. 16.5A, a synchronization and monitoring unit is adopted for the synchronization and the voltage information detection (e.g., the instantaneous grid voltage level). When there is a voltage sag fault, the signal F will then change the operation mode to the LVRT mode. Furthermore, for grid-connected system, the current controller should ensure the injection of high-quality currents that are synchronized with the grid voltage phase [4,19]. Considering the control structure in Fig. 16.5B, the fundamental-frequency current controller can be a periodic controller (e.g., a proportional resonant (PR) controller, a repetitive controller, or a deadbeat controller [30–33]) instead of the conventional proportional integral (PI) controller. Additionally, harmonic compensation based on parallel resonant controllers and repetitive controllers can be employed to further improve the current quality.

In normal operation mode, the PV system should operate in the MPPT mode at unity power factor, thus ensuring the maximization of the power production from PV panels. According to Fig. 16.5A, the active power reference is determined by the MPPT control, i.e., $P^* = P_{MPP}$ with P_{MPP} representing the maximum power of the PV panels, while the reactive power reference is 0 var ($Q^* = 0$ var) for the unity power factor. Once the grid voltage level is in the Mandatory Operation zone shown in Fig. 16.2, the power

This book belongs to Kitab Liaison (ocd1996@gmail.com) Copyright Elsevier 2023

reference should be reconstructed as a function of the voltage amplitude following the required linear voltage-reactive/active power capability. For instance, according to the requirements of the IEEE Std 1547-2018 in Fig. 16.3 [18], the reactive power that should be injected during grid faults is given as

$$Q = \begin{cases} 0 & 0.9 \text{ p.u.} \le v_{\text{gm}} < 1.1 \text{ p.u.} \\ k(1 - v_{\text{gm}})P_{\text{N}} & V_{\text{L}} \text{ p.u.} \le v_{\text{gm}} < 0.9 \text{ p.u.} \\ P_{\text{N}} & v_{\text{gm}} < V_{\text{L}} \text{ p.u.} \end{cases} \tag{16.1}$$

where V_{L} is the lower limit of the voltage for continuous operation, v_{gm} is the grid voltage level, P_{N} is the nominal grid power, Q is the required reactive power, and k is an adjustment factor that is given as

$$k = \frac{Q/P_{\text{N}}}{1 - v_{\text{gm}}} \ge 2 \text{ p.u.} \tag{16.2}$$

According to the single-phase PQ theory, the active power P and reactive power Q can be calculated in the $\alpha\beta$-reference frame as

$$\begin{cases} P = \dfrac{1}{2}(v_\alpha i_\alpha + v_\beta i_\beta) \\ Q = \dfrac{1}{2}(v_\beta i_\alpha - v_\alpha i_\beta) \end{cases} \tag{16.3}$$

in which the subscript α and β represents the corresponding α and β component of the grid voltage v_{g} and grid current i_{g}. Then, the currents in the $\alpha\beta$-reference frame can be expressed as

$$\begin{bmatrix} i_\alpha \\ i_\beta \end{bmatrix} = \frac{2}{v_\alpha^2 + v_\beta^2} \begin{bmatrix} v_\alpha & v_\beta \\ v_\beta & -v_\alpha \end{bmatrix} \begin{bmatrix} P \\ Q \end{bmatrix} \tag{16.4}$$

with ${v^2}_\alpha + {v^2}_\beta = {v^2}_{\text{gm}}$. As the active and reactive power should be adjusted in the LVRT mode, it is intuitive to generate the current references according to Eq. (16.4) as

$$i_{\text{g}}^* = i_\alpha^* = \frac{2}{v_\alpha^2 + v_\beta^2} \begin{bmatrix} v_\alpha & v_\beta \end{bmatrix} \begin{bmatrix} G_{\text{PI-P}}(s)(P^* - P) \\ G_{\text{PI-Q}}(s)(Q^* - Q) \end{bmatrix} \tag{16.5}$$

with $G_{\text{PI-P}}(s)$ and $G_{\text{PI-Q}}(s)$ being the PI controller for the active power and reactive power, respectively. Clearly, the current reference is an AC signal, and thus, the current controllers working in the $\alpha\beta$-reference frame should be adopted, as discussed previously. It should be noted that the current reference

This book belongs to Kitab Liaison (ocd1996@gmail.com) Copyright Elsevier 2023

can be obtained directly from the power references (i.e., the power is not directly controlled, and the PI controllers are set as unity gains), according to Eq. (16.5), as

$$i_g^* = \frac{2}{v_\alpha^2 + v_\beta^2}\begin{bmatrix} v_\alpha & v_\beta \end{bmatrix}\begin{bmatrix} P^* \\ Q^* \end{bmatrix} \tag{16.6}$$

which simplifies the control design.

In order to validate the effectiveness of the above-discussed control strategies, simulations have been carried out on a single-stage single-phase PV system and the control in Eq. (16.6) was adopted. The system parameters are listed in Table 16.1 and the MPPT sampling frequency is 200 Hz. In the simulations, the rated power was set as $P_N = 1.03$ kW. The current controller is a PR controller, where the proportional and resonant control gains (k_p and k_r) are set as 22 and 3000. In addition, the proportional and integral gains of $G_{PI\text{-}P}(s)$ and $G_{PI\text{-}Q}(s)$ are 6.2 and 1.5 for active power, respectively, and 1 and 50 for the reactive power. A second-order generalized integrator PLL is adopted for synchronization and fault detection [21], i.e., the grid-monitoring system. A perturb and observe (P&O) MPPT algorithm (see Chapter 14) has been applied in this case study. The voltage lower limited V_L is set to 0.5 p.u. in the simulations. The simulation results are shown in Figs. 16.6 and 16.7.

Fig. 16.6 shows that the grid has a voltage sag of 0.35 p.u. In the beginning, the single-stage single-phase PV system runs in the normal operation (i.e., MPPT control in unity power). Then, at around 0.05 s, the grid voltage drops to 0.65 p.u., and then the system enters the LVRT operation mode. This voltage sag lasts for about 320 ms. It is noted that the entire generating unit should

TABLE 16.1 System and control parameters of a single-phase photovoltaic inverter with an *LCL* filter.

Parameter	Symbol	Value
DC-link voltage (at the maximum power point)	V_{dc}	400 V
Grid voltage amplitude	v_{gm}	325 V
Grid nominal frequency	f_0	50 Hz
LCL filter	L_1	3.6 mH
	C_f	2.35 μF
	L_2	4 mH
Sampling frequency	f_s	10 kHz
Switching frequency	f_{sw}	10 kHz

This book belongs to Kitab Liaison (ocd1996@gmail.com) Copyright Elsevier 2023

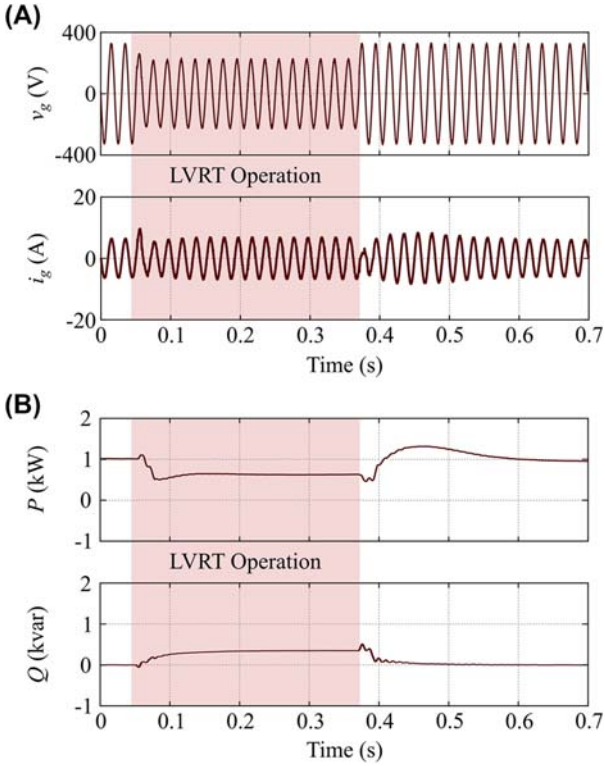

FIGURE 16.6 Simulation results of a single-stage single-phase photovoltaic system under a grid voltage sag with the low voltage ride-through (LVRT) control based on the single-phase PQ theory: (A) grid voltage v_g and grid current i_g, (B) injected active power P and reactive power Q.

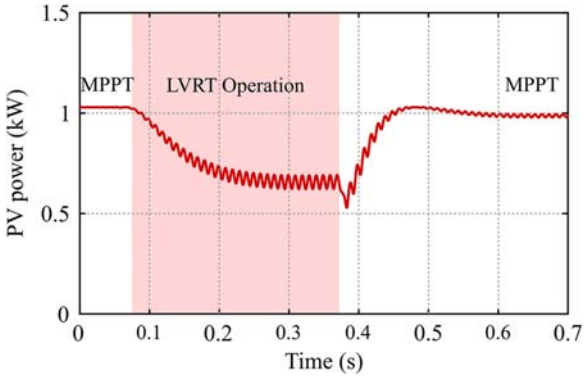

FIGURE 16.7 Output power from the photovoltaic (PV) panels of the single-stage single-phase system under grid faults with the low voltage ride-through (LVRT) control based on the single-phase PQ theory.

This book belongs to Kitab Liaison (ocd1996@gmail.com) Copyright Elsevier 2023

cease energizing if the short-term voltage sag lasts too long (i.e., requiring tripping if the grid voltage sags to 0.65 p.u. for more than 21 s, as shown in Fig. 16.2). Additionally, it will take a few milliseconds for the PLL (i.e., for the grid voltage detection) to respond to sudden changes of the grid voltage. During this period, the PV system stays in the MPPT operation at unity power factor. The grid current thus has a transient rise, as it is shown in Fig. 16.6A. Due to the same reason, the grid current has a temporary drop when the grid voltage recovers, which can also be seen in Fig. 16.6A.

Once the grid voltage is detected, the control scheme switches to the LVRT operation from the MPPT, where the active power is reduced and reactive power increases according to the requirement in Eq. (16.1), as shown in Fig. 16.6B. It should be pointed that, on one hand, the active power regulation capability may be determined by the utility grid operator. On the other hand, the active power reduction should be enabled to prevent overcurrent tripping. This is mainly because the grid code demands the PV system provide RPI for dynamic grid support during the LVRT operation. However, the increasing of the reactive power may trip the overcurrent protection if the active power is the same as operating in MPPT mode. After the grid voltage sag is cleared (i.e., the voltage level back to 0.9 p.u.), the PV system recovers its normal operation to track the maximum output power of the PV panels again and only generating active power to the utility grid, as depicted in Fig. 16.7.

As mentioned previously, the DC-link voltage should be larger than the peak value of the grid voltage due to the simple hardware structure of the single-stage single-phase inverter. Therefore, when switching to the LVRT operation mode from the normal MPPT operation, the system can only operate in the right region of the maximum power point (MPP), i.e., a higher voltage, to reduce the active power output from the PV panels. There is no doubt that the switching losses will be increased due to the increased DC-link voltage. Nevertheless, the above results have illustrated that the advanced control method based on the single-phase PQ theory can achieve the LVRT operation of single-stage single-phase grid-connected PV inverters, including the reactive/active power regulation.

16.2.2 LVRT control based on the power-voltage curve

To have a wider input voltage range for PV panels, a conventional DC−DC converter is normally inserted between the PV panels and the inverter to form a double-stage PV converter, as shown in Fig. 16.8. Additionally, the double-stage structure can provide a flexible control strategy due to the separated control. More specifically, the DC−DC stage mainly aims to achieve the MPPT of the PV panels, and the inverter satisfies the requirements from the utility grid by controlling the DC-link voltage and the grid current. In the

This book belongs to Kitab Liaison (ocd1996@gmail.com) Copyright Elsevier 2023

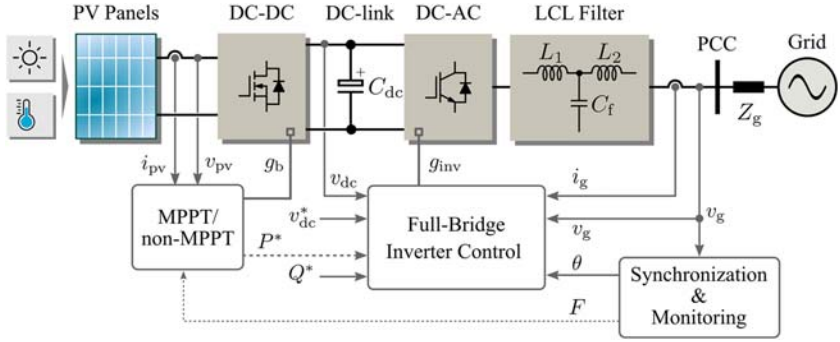

FIGURE 16.8 Control structure of the double-stage single-phase grid-connected photovoltaic (PV) system with the low voltage ride-through capability, where g_{inv} is the gate signals for the DC−AC (full-bridge) inverter, and g_b is the gate signal for the DC−DC converter. Here, the fault is continuously monitored, F is the monitored grid voltage amplitude that is fed to the control unit for the DC−DC converter, point of common coupling is the point of common-coupling, Z_g is the grid impedance, and C_{dc} is the DC-link capacitor.

case of grid voltage faults, an advanced control strategy is developed by directly linking the active power from the PV panels with the voltage grid sag level [34].

According to Fig. 16.8, the advanced control strategy can be developed, as shown in Fig. 16.9, which should be able to provide seamless transitions between the normal operation and LVRT operation. In this control scheme, one loop is the conventional control system separated into the MPPT control of the DC−DC stage and a single-phase PQ control of the inverter, and the other is a proportional LVRT controller plugged into the DC−DC controller. Since the plug-in controller is automatically enabled during the LVRT (the fault signal F is fed back), it becomes a promising method for the seamless transition control for the double-stage single-phase PV system. Moreover, as shown in Fig. 16.9, the inverter employs a dual-loop control structure. In details, the outer loop is a voltage controller based on a PI controller to control the DC-link voltage, while a PR controller with a parallel repetitive controller forms the internal current controller to compensate for harmonics of the injected current.

As mentioned above, the novel control scheme links the active power with the voltage sag. To further explain this control strategy, the linear droop curve (i.e., the relationship between the PV voltage v_{pv} and the PV power P_{pv}) of the PV panels can be used. Fig. 16.10 shows the power−voltage characteristics of the PV panels, including the MPP and the LVRT points A and B (i.e., Point A, below the voltage at the MPP, is in the low voltage region, where dP_{pv}/dv_{pv} is small; while at B, dP_{pv}/dv_{pv} is large). As mentioned, the single-stage inverter can only operate at B, where, however, the increasing PV voltage v_{pv} leads to higher switching losses. For the double-stage inverter, the PV system can be controlled to operate at both points in theory, but the steady-state performance

This book belongs to Kitab Liaison (ocd1996@gmail.com) Copyright Elsevier 2023

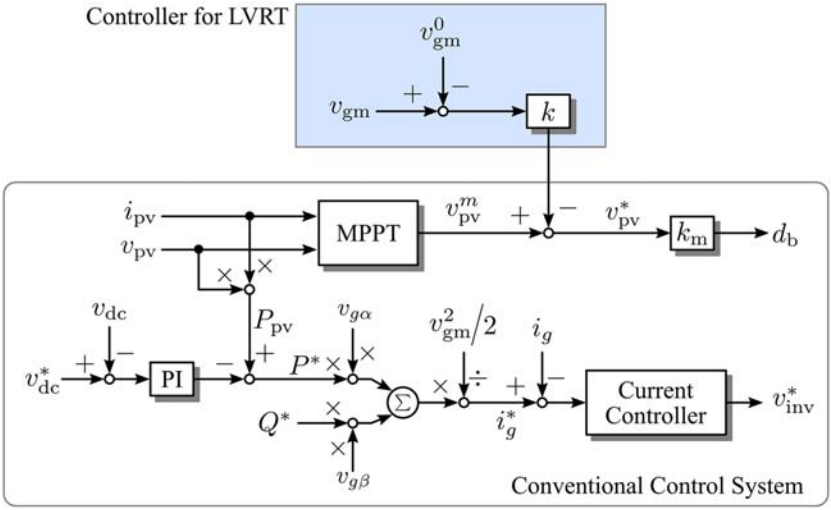

FIGURE 16.9 Detailed control structure of the single-phase grid-connected photovoltaic system, where a simple controller is plugged in the control loop for the DC−DC converter to enable the low voltage ride-through (LVRT) operation and PI is a proportional integral controller. Here, k is the control gain for the plug-in controller, d_b is the duty cycle for the boost converter (to generate the gate signal g_b), v_{inv}^* is the reference voltage (to generate the gate signals g_{inv}) for the inverter, and v^0_{gm} is the initial grid voltage amplitude (prefault value).

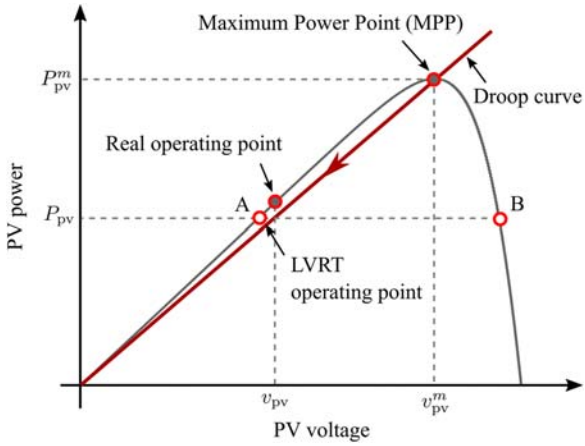

FIGURE 16.10 Power−voltage linear characteristics of photovoltaic (PV) panels for double-stage grid-connected PV systems. The linear droop relationship can be utilized to implement the low voltage ride-through (LVRT), i.e., automatic active power reduction during the LVRT operation. Here, v_{pv} and P_{pv} are the PV voltage and power, respectively, with the superscript "m" denoting the corresponding variable at the maximum power point.

This book belongs to Kitab Liaison (ocd1996@gmail.com) Copyright Elsevier 2023

is different, where the power variations of point A are smaller than point B. Additionally, the PV voltage of point B may be larger than the designed DC-link voltage, where the boost converter becomes inactive, and in turn, the entire system acts as a single-stage inverter. With the above concerns, the double-stage single-phase PV system normally chooses to operate at point A during the LVRT. According to Fig. 16.10, the PV voltage at point A can be approximated as

$$v_{\mathrm{pv}} \approx v_{\mathrm{pv}}^{m} + k_{\mathrm{pv}}\left(P_{\mathrm{pv}} - P_{\mathrm{pv}}^{m}\right) \tag{16.7}$$

where the superscript "m" represents the variable at the MPP, and k_{pv} is the droop coefficient. Obviously, the droop coefficient is affected by the operating conditions. To estimate the information of k_{pv}, only the voltage and power at the MPP are needed in the normal operation (i.e., the DC−DC stage operates at the MPPT under certain conditions, e.g., 25°C ambient temperature and 1-kW/m^2 solar irradiance level, and the inverter performs at unity power factor).

Furthermore, referring to the previous discussions, for single-phase PV systems, the feeders are typically resistive with small X/R ratios. In such a case, the grid voltage frequency is affected by the reactive power, while the grid voltage level can be regulated through the active power control based on a droop relationship as

$$v_{\mathrm{gm}} = v_{\mathrm{gm}}^{0} - k_{\mathrm{d}}\left(P_{\mathrm{g}} - P_{\mathrm{g}}^{0}\right) \tag{16.8}$$

with v_{gm} being the amplitude of the grid voltage, P_{g} being the active power injected into the grid, k_{d} is the active power derating factor (determined by the grid code or the inverter rating), and the superscript "0" indicating the corresponding initial value. Neglecting the power losses of the PV inverter, P_{g} is approximately equal to P_{pv}, which is expressed as

$$P_{\mathrm{pv}} \approx P_{\mathrm{g}} \tag{16.9}$$

Therefore, an approximate linear relationship can be found to enable an automatic active power reduction under the grid voltage sag. Combining Eqs. (16.7)−(16.9) gives the linear relationship between the grid voltage amplitude changes and the PV voltage changes as

$$v_{\mathrm{gm}} - v_{\mathrm{gm}}^{0} \approx -\frac{k_{\mathrm{d}}}{k_{\mathrm{pv}}}\left(v_{\mathrm{pv}} - v_{\mathrm{pv}}^{m}\right) \tag{16.10}$$

which implies that the grid voltage amplitude has no changes during the normal operation of the PV system, i.e., $v_{\mathrm{gm}} = v^{0}{}_{\mathrm{gm}}$. Therefore, the DC−DC stage should operate at the MPP, i.e., the PV voltage is $v^{0}{}_{\mathrm{pv}}$. When the grid voltage sag happens, the PV voltage will be regulated as the grid voltage changes, i.e., v_{gm}−$v^{0}{}_{\mathrm{gm}}$, according to the linear relationship in Eq. (16.10).

This book belongs to Kitab Liaison (ocd1996@gmail.com) Copyright Elsevier 2023

With the above, seamless transitions can be achieved by simply setting the reference voltage for the PV panels as

$$v_{\mathrm{pv}}^{*} = v_{\mathrm{pv}}^{m} - k\left(v_{\mathrm{gm}} - v_{\mathrm{gm}}^{0}\right) \tag{16.11}$$

where $k = k_{\mathrm{pv}}/k_{\mathrm{d}}$ is a linear coefficient. The proportional controller (i.e., the proportional gain is k) with the linear relationship in Eq. (16.11) can be directly plugged into the control of the DC−DC converter of the double-stage single-phase system. Since the PV system is controlled to operate at A, it can be derived that the control gain k is a positive value. According to Fig. 16.9, the grid fault will increase the PV voltage reference v_{pv}^{*}, corresponding to an increase of the duty cycle d_{b}. As a result, the PV voltage v_{pv} will be moved to the left side of the MPP in practice during the LVRT operation.

Compared to the conventional control method for the double-stage single-phase PV system, only one parameter k is added. Since $k = k_{\mathrm{pv}}/k_{\mathrm{d}}$, it is affected by the PV panel characteristics, the operation conditions (i.e., solar irradiance and ambient temperature), and also the grid impedance characteristics. Specifically, the power-voltage droop coefficient k_{pv} of the PV panels can be expressed as

$$k_{\mathrm{pv}} = \frac{v_{\mathrm{pv}}^{m}}{P_{\mathrm{pv}}^{m}} \tag{16.12}$$

in which $v^{\mathrm{m}}{}_{\mathrm{pv}}$ and $P^{\mathrm{m}}{}_{\mathrm{pv}}$ are the PV voltage and PV power when the PV system is operating at the MPPT mode under a uniform solar irradiance profile. It can be seen from Fig. 16.10 that the relationship of the droop curve is approximately linear. Thus, the gain of the droop curve k_{pv} in Eq. (16.12) can be refined by using an accurate PV panel model or based on lookup tables. However, the design of the droop control coefficient k_{d} at the grid side is related to the entire PV system (i.e., requiring a detailed analysis using small-signal modeling). It should be designed from the aspect of stability analysis of the entire system. Nevertheless, substituting Eq. (16.12) into Eq. (16.11) leads to

$$v_{\mathrm{pv}}^{*} = v_{\mathrm{pv}}^{m} - \frac{v_{\mathrm{pv}}^{m}}{P_{\mathrm{pv}}^{m} k_{\mathrm{d}}}\left(v_{\mathrm{gm}} - v_{\mathrm{gm}}^{0}\right) \tag{16.13}$$

which is implemented in Fig. 16.9.

Simulations are carried out on a double-stage single-phase grid-connected PV system (i.e., a DC−DC boost converter with a single-phase full-bridge inverter referring to Fig. 16.8) to validate the automatic control strategy. The parameters of the system are listed in Table 16.2 and the MPPT sampling frequency is 200 Hz. The control strategy shown in Fig. 16.9 has been implemented. There are three PV strings with 15 panels in series for each, and the panel parameters are also shown in Table 16.2. Accordingly, the maximum

This book belongs to Kitab Liaison (ocd1996@gmail.com) Copyright Elsevier 2023

TABLE 16.2 System parameters of a double-stage single-phase photovoltaic (PV) inverter with an *LCL* filter.

Parameter	Symbol	Value
DC-link voltage	v_{dc}	450 V
Boost converter inductor	L	2 mH
DC-link capacitor	C_{dc}	2200 μF
Grid voltage amplitude	v_{gm}	325 V
Grid nominal frequency	f	50 Hz
LCL filter	L_1	4.76 mH
	C_f	4.28 μF
	L_2	4 mH
Sampling frequency	f_s	8 kHz
Full-bridge inverter switching frequency	f_{sw}	8 kHz
Boost converter switching frequency	f_b	16 kHz
PV panels (3 strings and 15 panels per string)		
Rated maximum power	P_{mpp}	65 W
Voltage at the maximum power	v_{mpp}	17.6 V
Current at the maximum power	i_{mpp}	3.69 A
Open-circuit voltage	v_{OC}	21.7 V
Short-circuit current	i_{SC}	3.99 A

power of the PV array under the standard test condition (i.e., 1-kW/m^2 solar irradiance level, 25°C ambient temperature) is 2.9 kW. As mentioned previously, the dual-loop controller employs a PI controller for the DC-link voltage control, a PR controller with a repetitive controller for the grid current control. Similar to the single-stage case, a second-order generalized integrator-based PLL has been utilized to create the orthogonal voltage, and thus enabling the current control in the $\alpha\beta$-reference frame. The P&O MPPT algorithm is employed in the DC−DC converter stage to track the PV power. All the control parameters are shown in Table 16.3.

Fig. 16.11 shows the simulation results of the double-stage single-phase PV system in the same case of the LVRT operation. The performance of the active power regulation is presented in Fig. 16.11A, where the PV power is automatically reduced with the increase of the duty cycle d_b. In this simulation, the active power regulation aims to prevent inverters from exceeding the rated

This book belongs to Kitab Liaison (ocd1996@gmail.com) Copyright Elsevier 2023

TABLE 16.3 Control parameters for simulations referring to Fig. 16.9.

Parameter	Symbol	Value
DC-link PI controller	k_p	60
	k_i	250
Proportional resonant controller	k_{pr}	20
	k_{ir}	4500
Repetitive control gain	k_{rc}	6.5
Maximum power point tracking control gain	k_m	0.00167
Photovoltaic droop coefficient	k_{pv}	0.09
Active power droop gain	k_d	0.0317

power, which is done automatically according to the scheme in Fig. 16.9. The dynamics of the control system are also fast, as observed in Fig. 16.11. In addition, it can be illustrated in Fig. 16.11B that the DC-link voltage can be maintained as a relatively stable value. During the LVRT operation, the reactive power is also injected from the PV system to the grid, as it is illustrated in Fig. 16.11A. As mentioned previously, the single-phase PV system has normally a low X/R ratio. Therefore, the injection of the reactive power has a minor contribution to the grid voltage recovery. Nevertheless, as it is demonstrated in Fig. 16.11, the plug-in control strategy presented in Fig. 16.9 can effectively enable the RPI by directly setting the reactive power reference.

In all, the above simulation results verify the effectiveness of the simple LVRT scheme for double-stage single-phase PV systems in terms of dynamics and control. To better understand the operation principle, Fig. 16.12 shows the trajectories of the PV panels under the grid fault (i.e., including the LVRT and recovery). It can be seen in Fig. 16.12 that with the LVRT scheme, the PV system can seamlessly transit between the MPPT mode and LVRT operation with fast dynamics. Moreover, the LVRT scheme regulates the active power automatically by monitoring the grid voltage amplitude instead of calculating the grid active power. However, when the PV inverter is controlled by a droop controller, the calculation may be inevitable. Notably, the active power droop coefficient employed in this case is not optimal, and it is related to the inverter system characteristics.

16.3 Reactive power injection strategies under LVRT

As the penetration of PV energy is still increasing, many grid codes have updated the requirements on the RPI under grid faults [36]. As the critical

This book belongs to Kitab Liaison (ocd1996@gmail.com) Copyright Elsevier 2023

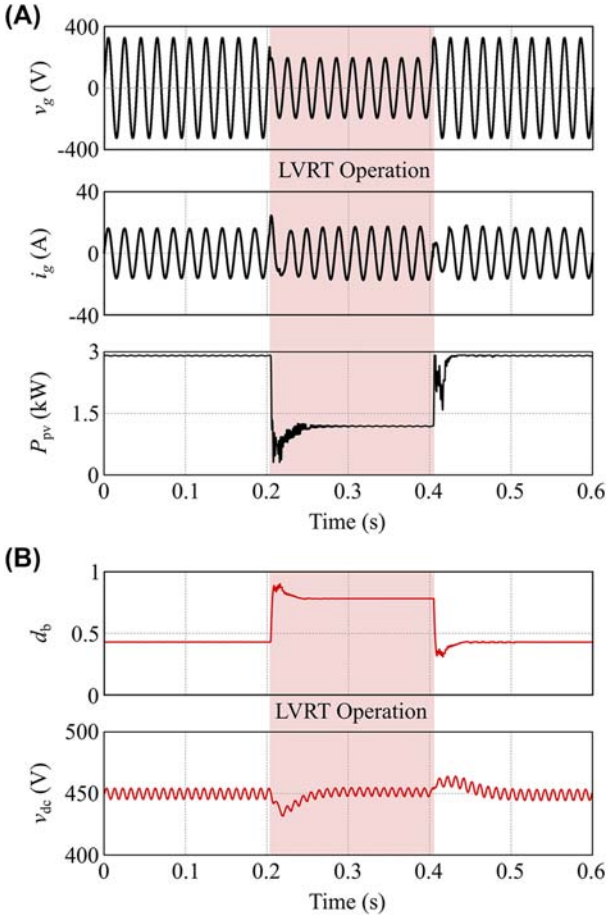

FIGURE 16.11 Simulation results of a 3-kW single-phase double-stage photovoltaic (PV) system under grid faults with the low voltage ride-through (LVRT) control considering the PV panel inherent power-voltage characteristics: (A) grid voltage v_g, grid current i_g, and PV output power P_{pv}; (B) duty cycle d_b and DC-link voltage v_{dc}.

interface of the PV energy and the utility grid, the PV inverter can implement the RPI, which can contribute significantly for smart PV systems to improve system stability and reliability, and thus reduced cost. Considering the dynamic grid support requirement (i.e., the demands from the utility grid operator) and the maximum apparent power of PV inverters (i.e., as exemplified in Fig. 16.13), three RPI strategies [35,36] for single-phase systems are introduced in this section, i.e., the constant average active power control strategy (*Const.-P*), constant active current control strategy (*Const.-I_d*), and constant peak current control (*Const.- I_{max}*).

This book belongs to Kitab Liaison (ocd1996@gmail.com) Copyright Elsevier 2023

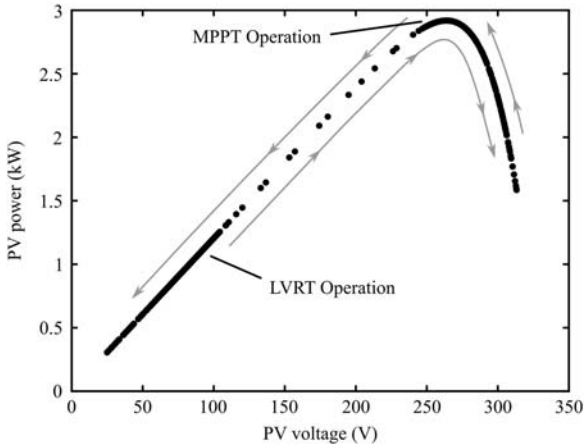

FIGURE 16.12 Operation trajectories of photovoltaic (PV) panels of the 3-kW single-phase system under the low voltage ride-through operation based on the inherent power-voltage characteristics with the dynamic waveforms shown in Fig. 16.11.

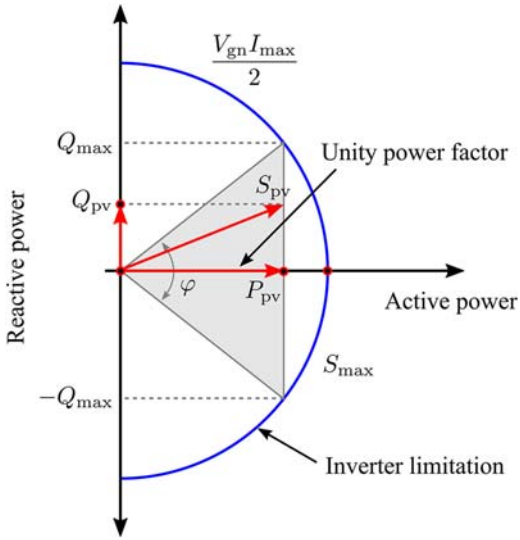

FIGURE 16.13 PQ diagram of a single-phase photovoltaic (PV) inverter, where Q_{max} indicates the maximum reactive power exchange capability of the inverter with the maximum power point tracking control, P_{pv} is the PV inverter active power (can be below the MPP power), and V_{gn} and I_{max} are the grid voltage nominal amplitude and the rated current, respectively.

This book belongs to Kitab Liaison (ocd1996@gmail.com)
Copyright Elsevier 2023

16.3.1 Constant average active power control strategy (*Const.-P*)

The objective of the *Const.-P* strategy is to maximize the power production of the PV panels even during the LVRT operation. In this case, the active power is maintained constant either by the MPPT control or an active power reduction scheme in the short-term low-voltage period. As a consequence, the amplitude of the injected grid current will inevitably increase. Considering the reactive power requirements (i.e., shown in Fig. 16.13) and the single-phase PQ theory, the currents in the *dq*-synchronous rotating reference frame can be expressed as

$$\begin{cases} i_{\mathrm{d}} = \dfrac{k_{\mathrm{d}}}{v_{\mathrm{gm}}} I_{\mathrm{N}} \\ i_{\mathrm{q}} = k(1 - v_{\mathrm{gm}}) I_{\mathrm{N}} \end{cases} \tag{16.14}$$

where $k_{\mathrm{d}} = P_{\mathrm{pv}}/P_{\mathrm{N}}$ is the power derating factor (determined by the inverter rating) with P_{pv} being the injected active power and P_{N} being the nominal power of the system and

$$\left(1 - \frac{1}{k}\right) \text{ p.u. } \leq v_{\mathrm{gm}} \leq 0.9 \text{ p.u. and } I_{\mathrm{gm}} = \sqrt{i_{\mathrm{d}}^2 + i_{\mathrm{q}}^2} \tag{16.15}$$

with I_{gm} being the amplitude of the grid current and k being an adjustable factor ($k \geq 2$ p.u.). When the grid voltage amplitude is lower than $(1-1/k)$ p.u., the system should inject a 100% current as demanded. During this period, the PV active power may still be injected to ensure the output power of the PV panels. However, if a large amount of active and reactive power is injected into the grid at the same time, the operation may trigger the overcurrent protection of the PV inverter, and subsequently, leading to a failure of the fault ride-through operation. In order to tackle this issue (i.e., avoid the failure of the LVRT), the following constraints should be satisfied:

(1) When the voltage sag occurs at the condition as $\left(1 - \frac{1}{k}\right)$ p.u. $\leq v_{\mathrm{gm}} \leq$ 0.9 p.u., the constraint can be expressed as

$$\frac{1}{v_{\mathrm{gm}}} \sqrt{k_{\mathrm{d}}^2 + k^2 \left(v_{\mathrm{gm}} - v_{\mathrm{gm}}^2\right)^2} \leq \frac{I_{\max}}{I_{\mathrm{N}}} \tag{16.16}$$

(2) In addition, if the grid voltage drops to $v_{\mathrm{gm}} \leq \left(1 - \frac{1}{k}\right)$ p.u., a full RPI may be mandatory (depending on the grid codes). Then, the limitation for the active power derating factor can be expressed in an inequality as

$$\frac{1}{v_{\mathrm{gm}}} \sqrt{k_{\mathrm{d}}^2 + v_{\mathrm{gm}}^2} \leq \frac{I_{\max}}{I_{\mathrm{N}}} \tag{16.17}$$

where $I_{\max}$ is the maximum inverter current limitation.

This book belongs to Kitab Liaison (ocd1996@gmail.com) Copyright Elsevier 2023

Eqs. (16.16) and (16.17) illustrate the LVRT capability of the PV systems, which can be one of the design criteria for the component design of grid-connected PV inverters. Obviously, a larger design margin means a better LVRT capability (i.e., withstanding higher currents). On the other hand, this may lead to the selection of high-rating devices (thus, increased cost). Seen from another perspective, the LVRT capability can be enhanced by adjusting the active power derating factor k_d at the predesigned PV inverter. Fig. 16.14 shows the design considerations for a PV inverter with the LVRT capability and $k = 2$ p.u. Clearly, the derating factor k_d can affect the operation range of the PV inverter under LVRT operation. For instance, if the allowable maximum current of a PV inverter is $I_{max} = 1.5\ I_N$ in this case, the PV inverter has to reduce the active power when the voltage is below 0.72 p.u. Otherwise, the inverter will be shut down due to overcurrent.

16.3.2 Constant active current control strategy (*Const.-I_d*)

Another alternative RPI strategy is called *Const.-I_d* strategy, which aims to maintain a constant active current in the LVRT operation. The *Const.-I_d* strategy can automatically reduce active power output in response to voltage sags as

$$i_d = \frac{2P}{v_{gm}} = mI_N = Const. \tag{16.18}$$

where m is a scaling factor and $0 \le m \le 1$. Similarly, in the case of voltage sags, the injection of active currents according to Eq. (16.18) may also lead to

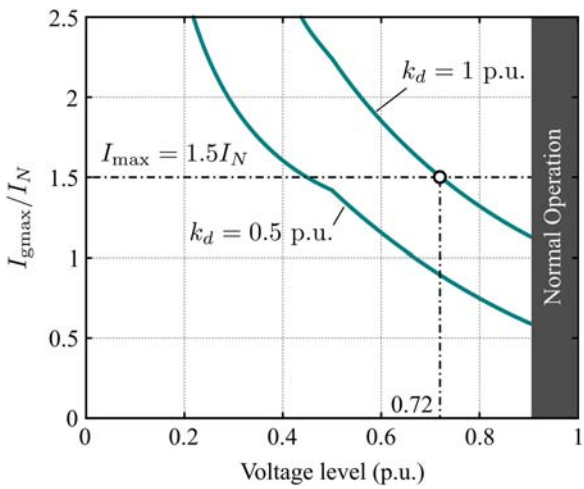

FIGURE 16.14 Photovoltaic inverter fault ride-through capability with the *Const.-P* strategy considering the reactive power injection requirement ($k = 2$ p.u.).

This book belongs to Kitab Liaison (ocd1996@gmail.com) Copyright Elsevier 2023

overcurrent. To avoid so, the following conditions should be kept when the control strategy is employed under the voltage sag.

(1) If the monitored instantaneous grid voltage amplitude (e.g., through a PLL) v_{gm} is within $\left(1-\frac{1}{k}\right)$ p.u. $\leq v_{gm} \leq 0.9$ p.u., the controller should satisfy

$$\sqrt{m^2+k^2(1-v_{gm})^2} \leq \frac{I_{max}}{I_N} \tag{16.19}$$

(2) Otherwise, v_{gm} sags severely to the range $v_{gm} \leq \left(1-\frac{1}{k}\right)$ p.u., and the PV inverter should meet the constraint as

$$\sqrt{m^2+1} \leq \frac{I_{max}}{I_N} \tag{16.20}$$

Thus, the LVRT performance of the PV inverter is dependent on the scaling parameter m and the RPI demand, i.e., the gain k. The design consideration for the *Const.-*I_d strategy is presented in Fig. 16.15. Compared with the *Const.-P* strategy, the PV inverter with the *Const.-*I_d scheme can be designed with a lower I_{max}/I_N. That means when targeting the same LVRT capability, the PV inverter with the *Const.-*I_d strategy can select lower rated power devices, leading to a lower cost. Furthermore, in order to ensure the safety of the inverter in the LVRT operation, a lower m can be considered, i.e., the derating operation.

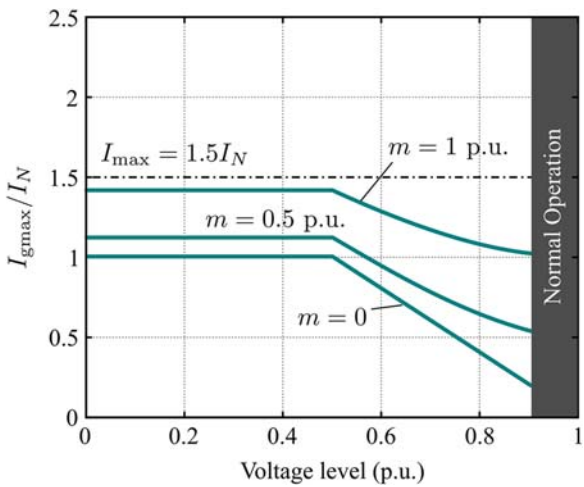

FIGURE 16.15 Photovoltaic inverter fault ride-through capability with the *Const.-*I_d strategy considering the reactive power injection requirement ($k = 2$ p.u.).

This book belongs to Kitab Liaison (ocd1996@gmail.com) Copyright Elsevier 2023

16.3.3 Constant peak current control (*Const.-I_{gmax}*)

It is known from the above discussions that the LVRT capability of the PV inverter with the two RPI strategies may be affected by the design of the control gains (k_d and m) (i.e., the overcurrent protection may be easily enabled due to the improper gains). Therefore, to strictly avoid the inverter overcurrent tripping, the PV inverter can maintain a constant peak value of the injected current during LVRT operation. In this case, the peak of the grid current is given as

$$I_{gmax} = nI_N = Const. \leq I_{max} \tag{16.21}$$

where n is introduced to assist the design. Considering the RPI requirement as exemplified in Eq. (16.1), the grid current in the dq-reference frame can be generated directly. Similarly, when the *Const.-I_{gmax}* strategy is adopted, two conditions should be considered:

(1) When the voltage sag is within $\left(1 - \frac{1}{k}\right)$ p.u. $\leq v_{gm} \leq 0.9$ p.u., the reference grid current can be derived as

$$\begin{cases} i_d = I_N\sqrt{n^2 - k^2(1 - v_{gm})^2} \\ i_q = I_N \cdot k(1 - v_{gm})I_N \end{cases} \tag{16.22}$$

(2) When the grid voltage level is lower and falls in $v_{gm} \leq \left(1 - \frac{1}{k}\right)$ p.u., the grid currents in the dq-reference frame will become

$$\begin{cases} i_d = I_N\sqrt{n^2 - 1} \\ i_q = I_N \end{cases} \tag{16.23}$$

It should be pointed out that n has a maximum value of I_{max}/I_N. With this constraint, the inverter has no risk of overcurrent tripping during the LVRT operation.

However, in the design and operation phases of the PV inverters, the above constraints should be considered. A comparison of the above three RPI strategies for PV inverters is depicted in Fig. 16.16, where the inverter current limitation is $I_{max} = 1.5\ I_N$ and $k = 2$ p.u. Observations in Fig. 16.16 indicate that the parameters (k_d, m, and n) affect the operation ranges of the PV inverters under the LVRT operation. For the *Const.-I_{gmax}* control strategy, the PV inverter will not be tripped off over a wide range of voltage sags. A similar capability for the PV inverters is also enabled when the *Const.-I_d* control strategy is adopted, as indicated in Figs. 16.15 and 16.16. However, the voltage range that the PV inverter can withstand during the LVRT is significantly

This book belongs to Kitab Liaison (ocd1996@gmail.com) Copyright Elsevier 2023

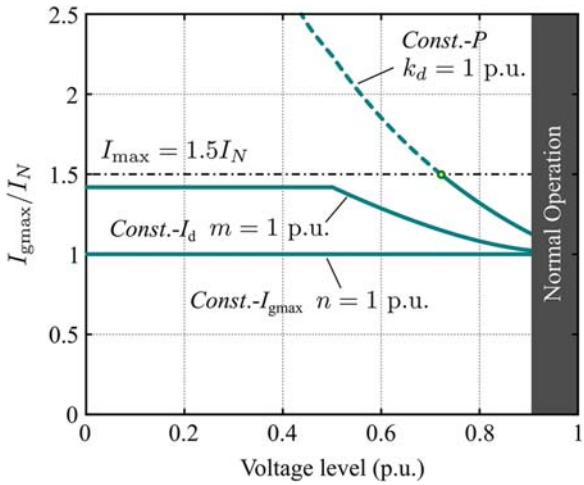

FIGURE 16.16 Comparison of the three reactive power injection strategies for single-phase photovoltaic inverters ($k = 2$ p.u.), where $I_{max} = 1.5I_N$.

limited when the *Const.-P* control strategy is adopted if the derating operation is disabled. Nevertheless, with the above reactive control strategies, both active power and reactive power (following the demands) can be regulated under the LVRT operation.

16.4 Summary

This chapter has reviewed the grid code (i.e., IEEE 1547) requirements under an abnormal grid condition—grid voltage sags that may affect the stability of the entire utility grid when the penetration level of the renewable energy system is high. Then, control strategies for the seamless transition under the voltage sag have been discussed, and the strategies are designed for single-phase grid-connected PV systems. Furthermore, for single-stage single-phase PV systems, an advanced control strategy which directly generates the reference reactive/active power has been implemented based on the single-phase PQ theory. Also, another advanced power control strategy has been developed by regulating reactive/active power automatically in accordance to the grid voltage sag level for double-stage single-phase PV systems. Both advanced control strategies can achieve seamless transitions between the LVRT operation and the normal operation of single-phase PV systems, but they have different dynamic performances. The advanced LVRT strategies have been validated through simulations. Furthermore, this chapter has also introduced various RPI strategies, as a dynamic grid support ability for single-phase grid-connected PV systems, which is required under grid voltage faults. The audience is recommended to validate the reactive power injection strategies as exercises to better understand them.

This book belongs to Kitab Liaison (ocd1996@gmail.com) Copyright Elsevier 2023

References

[1] F. Blaabjerg, Y. Yang, D. Yang, X. Wang, Distributed power-generation systems and protection, Proc. IEEE 105 (7) (July, 2017) 1311−1331.

[2] F. Blaabjerg, D.M. Ionel, Y. Yang, H. Wang, Renewable energy systems- technology overview and perspectives, in: Renewable Energy Devices and Systems with Simulations in MATLAB® and ANSYS®, CRC Press, 2017, pp. 1−16.

[3] V. Knazkins, Stability of Power Systems with Large Amounts of Distributed Generation, KTH, Stockholm, Sweden, 2004. Ph.D. Dissertation.

[4] F. Blaabjerg, R. Teodorescu, M. Liserre, A.V. Timbus, Overview of control and grid synchronization for distributed power generation systems, IEEE Trans. Ind. Electron. 53 (5) (October, 2006) 1398−1409.

[5] H. Wang, M. Liserre, F. Blaabjerg, Toward reliable power electronics: challenges, design tools, and opportunities, IEEE Ind. Electron. Mag. 7 (2) (June, 2013) 17−26.

[6] E. Koutroulis, F. Blaabjerg, Design optimization of transformerless grid-connected PV inverters including reliability, IEEE Trans. Power Electron. 28 (1) (January, 2013) 325−335.

[7] Y. Yang, P. Enjeti, F. Blaabjerg, H. Wang, Wide-scale adoption of photovoltaic energy: grid code modifications are explored in the distribution grid, IEEE Ind. Appl. Mag. 21 (5) (September, 2015) 21−31.

[8] E. Serban, M. Ordonez, C. Pondiche, Voltage and frequency grid support strategies beyond standards, IEEE Trans. Power Electron. 32 (1) (January, 2017) 298−309.

[9] Y. Xue, K.C. Divya, G. Griepentrog, M. Liviu, S. Suresh, M. Manjrekar, Towards next generation photovoltaic inverters, in: Proceedings of 2011 IEEE Energy Conversion Congress and Exposition (ECCE), 17−22 September, 2011, pp. 2467−2474.

[10] K.C. Divya, P.S. Nagendra Rao, Effect of grid voltage and frequency variations on the output of wind generators, Elec. Power Compon. Syst. 36 (6) (2008) 602−614.

[11] M.H.J. Bollen, I.Y.H. Gu, Signal Processing of Power Quality Disturbances, IEEE Press and John Wiley & Sons, Inc., 2006.

[12] A. Luna, et al., Grid voltage synchronization for distributed generation systems under grid fault conditions, IEEE Trans. Ind. Appl. 51 (4) (July-August, 2015) 3414−3425.

[13] Y. Yang, K. Zhou, F. Blaabjerg, Current harmonics from single-phase grid-connected inverters-examination and suppression, IEEE J. Emerg. Sel. Topics Power Electron. 4 (1) (March, 2016) 221−233.

[14] L.A.C. Lopes, S. Huili, Performance assessment of active frequency drifting islanding detection methods, IEEE Trans. Energy Convers. 21 (1) (March, 2006) 171−180.

[15] Q. Zheng, J. Li, X. Ai, J. Wen, J. Fang, Overview of grid codes for photovoltaic integration, in: Proc. Of 2017 IEEE Conference on Energy Internet and Energy System Integration (EI2), Beijing, 2017, pp. 1−6.

[16] R. Walling, A. Ellis, S. Gonzalez, Implementation of Voltage and Frequency Ride-Through Requirements in Distributed Energy Resources − Interconnection Standards, Sandia National Laboratories, April, 2014. Tech. Rep., SAND 2014-3122.

[17] IEEE Standard Committee, IEEE standard for interconnecting distributed resources with electric power systems, IEEE Std. 1547 (2003).

[18] IEEE Standard Committee, IEEE Standard for Interconnection and Interoperability of Distributed Energy Resources with Associated Electric Power Systems Interfaces, April, 2018, pp. 1−138. IEEE Std 1547-2018 (Revision of IEEE Std 1547-2003).

This book belongs to Kitab Liaison (ocd1996@gmail.com) Copyright Elsevier 2023

[19] Y. Yang, F. Blaabjerg, Overview of single-phase grid-connected photovoltaic systems, Elec. Power Compon. Syst. 43 (12) (2015) 1352−1363.

[20] L. Meegahapola, M. Datta, I. Nutkani, J. Conroy, Role of fault ride- through strategies for power grids with 100% power electronic - interfaced distributed renewable energy resources, in: Proc. Of WIREs Energy Environ, March, 2018, pp. 1−24.

[21] Y. Yang, F. Blaabjerg, Z. Zou, Benchmarking of Grid Fault Modes in Single-Phase Grid-Connected Photovoltaic Systems, IEEE Trans. Ind. Appl. 49 (5) (September−October, 2013) 2167−2176.

[22] S. Kumar, A.K. Verma, I. Hussain, B. Singh, C. Jain, Better control for a solar energy system: using improved enhanced phase-locked loop-based control under variable solar intensity, IEEE Ind. Appl. Mag. 23 (2) (March-April, 2017) 24−36.

[23] A. Mojallal, S. Lotfifard, Enhancement of grid connected PV arrays fault ride through and post fault recovery performance, IEEE Trans. Smart Grid 10 (1) (January, 2019) 546−555.

[24] M. Mirhosseini, J. Pou, V.G. Agelidis, Single- and two-stage inverter-based grid-connected photovoltaic power plants with ride-through capability under grid faults, IEEE Trans. Sustain. Energy 6 (3) (July, 2015) 1150−1159.

[25] Q.-C. Zhong, T. Hornik, Robust droop control with improved voltage quality, in: Control of Power Inverters in Renewable Energy and Smart Grid Integration, John Wiley & Sons/ IEEE, 2012, pp. 335−346.

[26] M. Ebrahimi, S.A. Khajehoddin, M. Karimi-Ghartemani, Fast and robust single-phase DQ current controller for smart inverter Applications, IEEE Trans. Power Electron. 31 (5) (May 2016) 3968−3976.

[27] M. Saitou, T. Shimizu, Generalized theory of instantaneous active and reactive powers in single-phase circuits based on Hilbert transform, in: Proc. 2002 IEEE 33rd Annual IEEE Power Electronics Specialists Conference. Proceedings (Cat. No.02CH37289), vol. 3, 2002, pp. 1419−1424.

[28] Y. Yang, F. Blaabjerg, H. Wang, M.G. Simões, Power control flexibilities for grid-connected multi-functional photovoltaic inverters, IET Renew. Power Gener. 10 (4) (4 2016) 504−513.

[29] Y. Yang, F. Blaabjerg, H. Wang, Low-voltage ride-through of single-phase transformerless photovoltaic inverters, IEEE Trans. Ind. Appl. 50 (3) (May-June 2014) 1942−1952.

[30] M. Ciobotaru, R. Teodorescu, F. Blaabjerg, Control of single-stage single-phase PV inverter, in: Proceedings of 2005 European Conference on Power Electronics and Applications (EPE), Dresden, Germany, 2005, pp. 1−10.

[31] Y. Yang, K. Zhou, H. Wang, F. Blaabjerg, D. Wang, B. Zhang, Frequency adaptive selective harmonic control for grid-connected inverters, IEEE Trans. Power Electron. 30 (7) (July, 2015) 3912−3924.

[32] T. Jakub, P. Zdenek, B. Vojtech, Central difference model predictive current control of single-phase H-bridge inverter with LCL filter, in: Proceedings of 2013 European Conference on Power Electronics and Applications (EPE), Lille, France, 2−6 September, 2013, pp. 1−8.

[33] J.-F. Stumper, V. Hagenmeyer, S. Kuehl, R. Kennel, Deadbeat control for electrical drives: a robust and performant design based on differential flatness, IEEE Trans. Power Electron. 30 (8) (August, 2015) 4585−4596.

This book belongs to Kitab Liaison (ocd1996@gmail.com) Copyright Elsevier 2023

[34] Y. Yang, A. Sangwongwanich, H. Liu, F. Blaabjerg, Low voltage ride-through of two-stage grid-connected photovoltaic systems through the inherent linear power-voltage characteristic, in: Proceedings of 2017 IEEE Applied Power Electronics Conference and Exposition (APEC), Tampa, FL, 2017, pp. 3582−3588.

[35] Y. Yang, H. Wang, F. Blaabjerg, Reactive power injection strategies for single-phase photovoltaic systems considering grid requirements, IEEE Trans. Ind. Appl. 50 (6) (Novembr-December, 2014) 4065−4076.

[36] Y. Yang, K.A. Kim, F. Blaabjerg, A. Sangwongwanich, Advances in Grid-Connected Photovoltaic Power Conversion Systems, Woodhead Publishing, 2018, p. 213.

This book belongs to Kitab Liaison (ocd1996@gmail.com) Copyright Elsevier 2023

Chapter 17

Grid-following and grid-forming PV and wind turbines

P. Rodriguez, N.B. Lai
Luxembourg Institute of Science & Technology, Esch-Sur-Alzette, Luxembourg

17.1 Introduction

The share of renewable energy in global power capacity has grown rapidly in the last decade. As a consequence, more stringent grid interconnection requirements have been imposed by grid operators aiming to increase grid flexibility and maintain grid stability. Both photovoltaic (PV) power and wind power (WP) plants are connected to the grid through power converters which, besides transferring the generated DC power to the AC grid, should now be able to provide some services to the grid, such as dynamic control of active and reactive power, frequency and voltage ride-through, reactive current injection during faults, and participation in a grid voltage and frequency control, etc. In this chapter, we introduce the typical structures of PV and WP systems with a particular focus on the power electronic parts, especially grid-connected power converters. These power converters can operate either in the grid-following or grid-forming mode. The former has been widely used in PV and WP plants with maximum power injection as a primary objective, whereas the latter has emerged in the last few years due to growing concerns regarding the displacement of synchronous generation units by converter-interfaced resources and recent advances in energy storage systems. In addition to an overview of the typical control structures, this chapter analyzes different strategies for the control and synchronization of grid-following and grid-forming power converters. In Section 17.2, the latest development of PV and WP systems is reviewed. In Section 17.3, the grid-following converter is discussed. Here, popular synchronization strategies and current controllers are explained. Building upon these control blocks, serval representative implementations of grid forming is considered in Section 17.4. Finally, this chapter summary is discussed in Section 17.5.

Control of Power Electronic Converters and Systems. https://doi.org/10.1016/B978-0-12-819432-4.00022-6
Copyright © 2021 Elsevier Ltd. All rights reserved.

This book belongs to Kitab Liaison (ocd1996@gmail.com)
Copyright Elsevier 2023

17.2 PV and wind turbine systems

The installed capacity of PV and WP has increased exponentially in the last decade with annual additions of just above 30% and 10%, respectively [1], as shown in Fig. 17.1. This amount of additions accounts for approximately 83% of renewable power and 62% of all net power capacity installed in 2018 [2]. It is forecasted that the growth for PV and WP will reach 2264 GW by 2024. The major players are China, the European Union, the United States, and India, which contribute to about 75% of PV and WP capacities. Depending on the power ratings and technologies used, there are different configurations for these systems. The typical structures of PV and WP systems are outlined in the following subsections.

17.2.1 PV structures

There are four most common types of inverter used in PV plants, namely microinverter, string inverter, multistring inverter, and central inverter. The configuration for different types of inverters is as depicted in Fig. 17.1. The choice of PV inverters is often based on the required peak power and net efficiency [3]. For instance,

- Microinverter: typically, in the 50−500 Wp range for only one panel.
- String inverters: typically, in the 0.4−2 kWp range for small rooftop plants with panels connected in one string.
- Multistring inverters: typically, in the 1.5−150 kWp range for medium-large rooftop plants with panels configured in several strings.
- Central inverters: typically, in the 80−4000 kW range with three-phase topology and modular design for large power plants ranging to hundredths of a MWp.

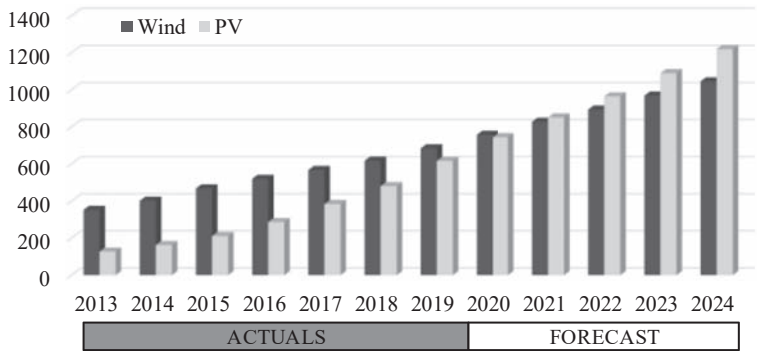

FIGURE 17.1 Global cumulative installations for photovoltaic (PV) and wind power in GW. *Source: IEA.*

This book belongs to Kitab Liaison (ocd1996@gmail.com)
Copyright Elsevier 2023

Microinverter is the most effective way to utilize PV modules as each inverter is attached to a module, as shown in Fig. 17.2A. This also makes this configuration easy to expand. However, for large PV plants, a high number of power converters are required resulting in high installation and maintenance costs. On the contrary, the central inverter structure depicted in Fig. 17.2D uses only one power converter for all PV modules, thus reducing the total capitalization and operation cost of the system. The most popular implementation is based on a string converter Fig. 17.2B. In this setup, each string is connected to a power converter which balances the cost and efficiency of the system. For larger PV plants, a multistring inverter can also be used as in Fig. 17.2C.

17.2.2 Grid converter for wind turbine systems

WP is generated by using wind turbine generators (WTGs), particularly, induction generators, double-fed induction generators, or synchronous generators. Generally speaking, the WTG can be connected to the grid either directly or through a power converter. The arrangement of the WTG and power converter in WP systems makes up four major topologies of wind turbines, as shown in Fig. 17.3, which can be classified as follows:

- Type 1: Induction generator (fixed speed—1%−2% regulation)
- Type 2: Induction generator with variable rotor resistance (limited variable speed—10% regulation)
- Type 3: Double-fed induction generator (variable speed—30% regulation)
- Type 4: Synchronous or asynchronous generators with full converter (variable speed—100% regulation).

Fixed-speed wind turbines are the first generation of wind turbines. Even though they are directly connected to the grid, they require additional components, such as a soft starter to reduce current transients during the start-up

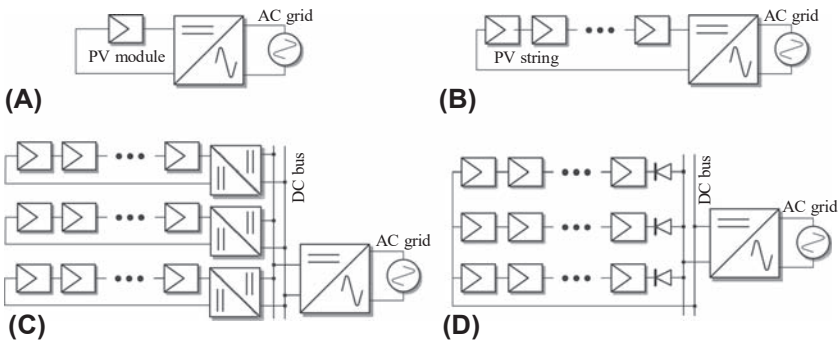

FIGURE 17.2 Configuration of photovoltaic (PV) systems: (A) Microinverter, (B) String inverter, (C) Multistring inverter, (D) Central inverter.

This book belongs to Kitab Liaison (ocd1996@gmail.com) Copyright Elsevier 2023

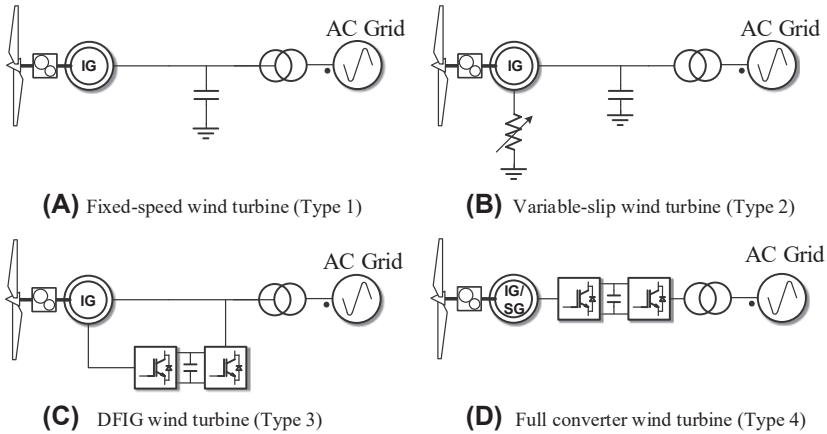

FIGURE 17.3 Configuration of wind turbine generators in wind power systems. (A) Fixed-speed wind turbine (Type 1); (B) Variable-slip wind turbine (Type 2); (C) Double-fed induction generator wind turbine (Type 3); (D) Full converter wind turbine (Type 4).

and a capacitor bank to compensate for reactive power. They need to operate at a rather constant speed (1%−2% regulation range). The speed governing is generally achieved by changing the aerodynamic profile of the WT blades, which has a quite slow response. Thus, the Type 1 wind turbine is rather sensible to wind disturbances. Wind turbines based on induction generators with variable slip were often used to slightly extend the speed regulation range (10% regulation range). This design, often referred to as Type 2 wind turbines, incorporates controllable rotor resistance to control the rotor slip. To eliminate the power loss on rotor resistance and extend the speed regulation range (30% regulation range), double-fed induction generator turbines are employed. Type 4 wind turbines employ a full back-to-back power converter, which extends the WT speed controllability (100% regulation range), increasing energy extraction under high and low wind speeds, and improves the interaction with the electrical grid under abnormal operating conditions, e.g., during grid faults.

17.3 Grid-following power converters

17.3.1 Definition

Grid-following power converters are grid-connected converters operated as controllable current sources to deliver the desired value of active and reactive power to an energized grid [4]. The regulation of active and reactive power delivered to the grid is achieved by characterizing (following) the grid voltage and calculating corresponding references for the current controller. As grid-following power converters work as current sources, they are suitable for parallel operation in grid-connected mode. A simplified representation for a

This book belongs to Kitab Liaison (ocd1996@gmail.com) Copyright Elsevier 2023

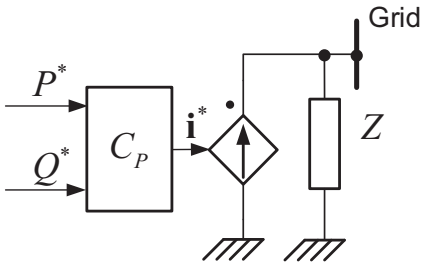

FIGURE 17.4 Simplified diagram of grid-following power converter.

grid-following power converter is shown in Fig. 17.4, where P^* and Q^* are the active and the reactive power references to be delivered to the grid, respectively. In this operation mode, it is important to highlight that the power controller should be perfectly synchronized with the AC voltage at the connection point (amplitude, frequency, and phase angle), in order to regulate accurately the instantaneous active and reactive power exchanged with the electrical grid.

Currently, most of the power converters employed in PV or WP systems operate in grid-following mode [5]. Even though these power converters use to operate at the maximum power point to maximize renewable energy yield, they can also contribute to control of the grid voltage amplitude and frequency by including some additional control loop to adjust the active and reactive power references, P^* and Q^*, respectively [6,7]. In principle, grid-following power converters cannot operate in islanded mode if there is not a local synchronous generator or a grid-forming power converter, to set the grid voltage amplitude and frequency of the islanded part. Fig. 17.5 shows a typical control structure for a grid-following power converter. The control system of grid-following power converters is primarily composed of a grid synchronization unit, a current controller, and a power controller.

17.3.2 Synchronization strategies

The accuracy in the estimation of the AC grid voltage parameters has a strong influence on the overall performance of grid-following power converters. A precise synchronization algorithm is needed to estimate the grid voltage parameters, i.e., voltage amplitude, frequency, and phase angle, as these values are needed for conducting a precise control of the instantaneous active and the reactive power delivered to the grid. Additionally, precise monitoring of the grid conditions is mandatory in order to determine the most suitable operation mode of the converters, as well as for properly supporting connection and disconnection sequences. In this regard, two widely used types of phase-locked loop (PLL) will be introduced in the following.

This book belongs to Kitab Liaison (ocd1996@gmail.com) Copyright Elsevier 2023

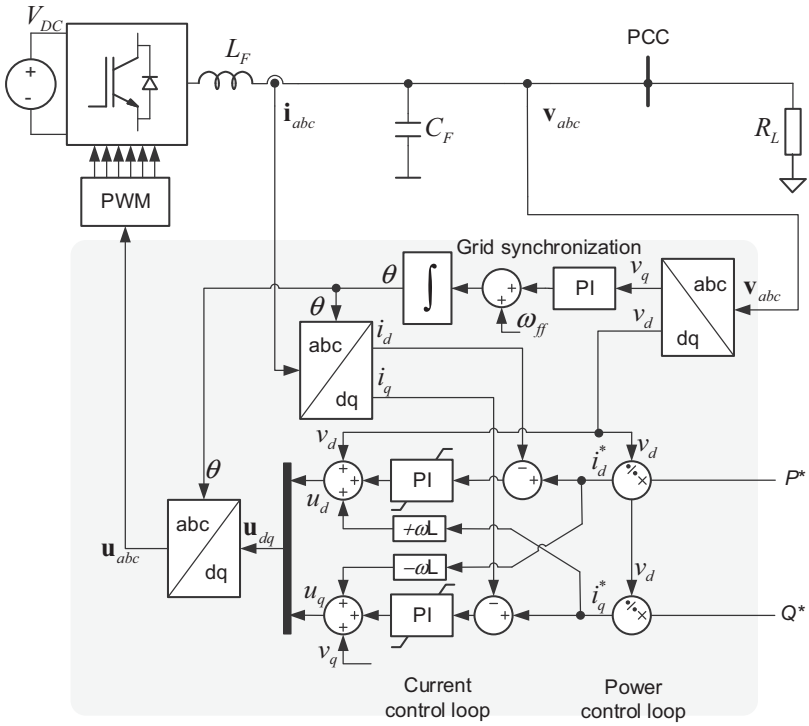

FIGURE 17.5 Basic control structure of grid-following power converter.

17.3.2.1 Synchronous reference frame phase-locked loop

The PLL technology has been extensively used to synchronize grid-connected power converters with the grid. In three-phase systems, the synchronous reference frame phase-locked loop (SRF-PLL) has been broadly used for this purpose. The structure of the SRF-PLL is depicted in Fig. 17.6. The SRF-PLL translates the three-phase instantaneous voltage waveforms from the *abc* reference frame into the *dq* rotating reference frame through the Park transformation. The angular position of this *dq*-reference frame is controlled through a feedback control loop which drives the v_q component to zero [8,9]. As depicted in Fig. 17.6, the estimated grid frequency is ω', being the value for rated frequency normally included as a feedforward term, ω^*, to improve the dynamics of the phase estimation, θ', which is obtained by integrating ω' [10,11].

Despite the good behavior of the SRF-PLL under balanced grid conditions, its performance is deteriorated when the three-phase input signal becomes unbalanced or distorted. To overcome such a drawback, some advanced grid synchronization techniques have been proposed in the literature. This is, for

This book belongs to Kitab Liaison (ocd1996@gmail.com) Copyright Elsevier 2023

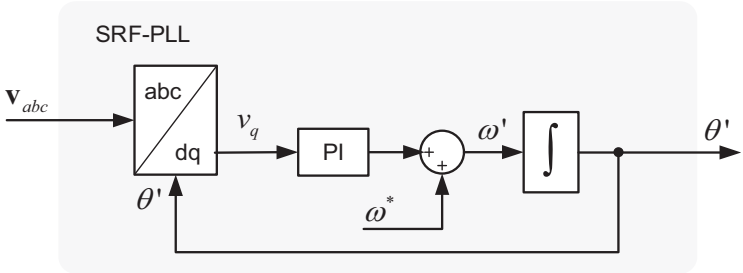

FIGURE 17.6 Block diagram of synchronous reference frame phase-locked loop (SRF-PLL).

instance, the case of the decoupled double-SRF PLL, which is an enhanced PLL that stems from the same operation principle as the SRF-PLL with improved phase angle and magnitude estimation under unbalanced conditions [12,13].

17.3.2.2 Stationary reference frame frequency-locked loop

The grid voltage vector can experience relevant phase angle jumps during grid faults, which can give rise to significant transient synchronization errors that might threaten the stability of grid-following power converters. As a consequence, other implementations based on a frequency-locked loop (FLL) can be used, since frequency presents a more stable evolution during grid faults. Among different proposals, the synchronization structures based on a second-order generalized integrator (SOGI) and an FLL to detect the grid voltage components, $\mathbf{v}'_{\alpha\beta}$ and $q\mathbf{v}'_{\alpha\beta}$, as well as the grid frequency, ω' [14], as it is presented in Fig. 17.7, have proven to be effective and accurate under arbitrary

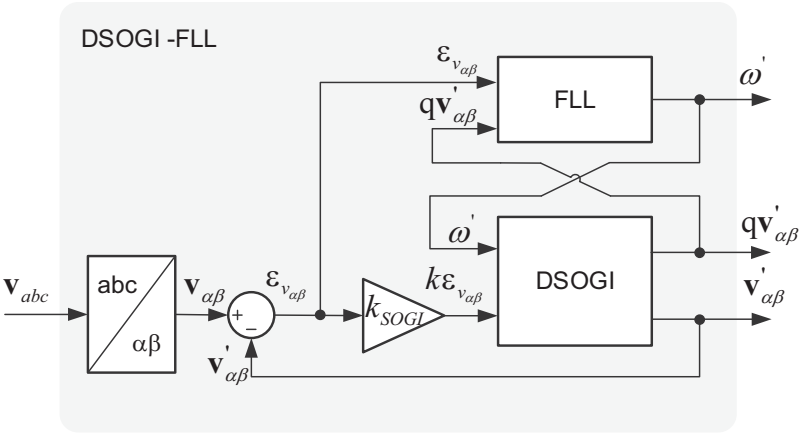

FIGURE 17.7 Block diagram of dual second-order generalized integrator frequency-locked loop (DSOGI-FLL).

This book belongs to Kitab Liaison (ocd1996@gmail.com) Copyright Elsevier 2023

grid conditions. The SOGI is implemented in both α- and β-axes, giving rise to a dual SOGI (DSOGI) structure, which is an adaptive band-pass filter that provides the filtered version of the input voltage vector, $\mathbf{v}'_{\alpha\beta}$, as well as its quadrature component, $q\mathbf{v}'_{\alpha\beta}$. The resonance frequency of the DSOGI is the grid frequency estimated by the FLL.

As previously mentioned, one of the main advantages of using an FLL lays on the fact that this structure is less sensitive than the PLL to phase angle jumps occurred in the grid voltage during transient grid faults, improving, thus, the power converter response under abnormal grid conditions. This interesting feature of the FLL provides a fast dynamic response with small overshoot, allowing thus a fast and smooth transition between the grid-connected and the islanded operating modes.

17.3.3 Current controllers

The inner control loop of grid-following power converters is based on fast current controllers that regulate the current injected into the grid [15]. The references for current controllers are often generated by power controllers which determine the amount of power to be exchanged with the grid [16,17]. Such reference currents are usually calculated as a function of the reference powers, P^* and Q^* [18,19].

The most widely used solutions for implementing linear current controllers in three-phase systems are those based on the well-known PI controller working on a dq-SRF or the ones based on the implementation of a resonant controller working on an $\alpha\beta$-stationary reference frame [15]. In addition to these proposals, those controllers based on nonlinear control structures, such as hysteresis, sliding mode, or predictive controllers, can be also used for tracking sinusoidal reference currents in a fast and robust way [19].

17.3.3.1 PI controller on the SRF

The implementation of current controllers based on the dq-SRF has been extensively used in the control of AC currents in three-phase systems. Through the Park transformation, the sinusoidal currents under control can be represented as DC quantities on an orthogonal dq frame, rotating synchronously at the detected grid fundamental frequency. In this reference frame, two independent control loops are in charge of regulating the direct and quadrature current components. In the case of grid-following converters, the reference currents i_d^* and i_q^* are usually provided by a power controller, which regulates the active and reactive power delivered to the grid. The instantaneous active and reactive power components are calculated by

$$p = v_d i_d + v_q i_q \; ; \; q = v_d i_q - v_q i_d. \tag{17.1}$$

This book belongs to Kitab Liaison (ocd1996@gmail.com) Copyright Elsevier 2023

Fig. 17.5 shows the structure of a dq-based synchronous current control, including the grid voltage feedforward and the decoupling network used to improve the performance of the controller [19]. However, in this standard structure, the PI controllers are unable to suppress the oscillations that appear in the dq signals under unbalanced grid conditions. To overcome this drawback, two dq synchronous controllers may be implemented in order to regulate independently both the positive- and the negative-sequence current components of the injected current. Likewise, multiple reference frames [20], rotating at multiples of the fundamental frequency, should be implemented to properly control the harmonic currents injected into the AC grid.

17.3.3.2 Resonant controller in a stationary reference frame

This kind of controllers work with AC variables expressed on the $\alpha\beta$-stationary reference frame [21]. In this case, the PI controllers are replaced by proportional resonant (PR) controllers, whose resonance frequency is tuned at the fundamental grid frequency estimated by the grid synchronization system [22,23]. The transfer function of a PR controller can be written as follows:

$$G_{\mathrm{PR}}^{\alpha\beta}(s) = k_P + \frac{k_R s}{s^2 + \omega_0^2} + \sum_{h=2}^{n} \frac{k_{ih} s}{s^2 + (h\omega_0)^2}, \tag{17.2}$$

where k_P is the proportional gain, k_R is the resonant gain at the grid fundamental frequency, k_{ih} is the resonant gain at the h-harmonic to be controlled, and ω_0 is the estimated fundamental frequency [15]. Similar to the case of dq synchronous controllers, the reference currents on the $\alpha\beta$-stationary reference frame are calculated by the power controller, which is in charge of regulating the power exchanged with the grid. The instantaneous active and reactive power components in the $\alpha\beta$-stationary reference frame are calculated by

$$p = v_\alpha i_\alpha + v_\beta i_\beta \ , \ q = v_\beta i_\alpha - v_\alpha i_\beta. \tag{17.3}$$

There is a significant advantage in the implementation of PR controllers in a stationary reference frame, instead of using PI controllers working in a dq-SRF, when unbalanced sinusoidal currents control is intended. In such a case, those implementations based on PR controllers do not need to use any decoupling network, neither independent sequence controllers, since resonant controllers are able to regulate both positive and negative-sequence components simultaneously. This feature makes PR controllers a very convenient candidate to be applied to regulate the current injected by grid-following power converters under generic grid conditions, even under grid faults. Moreover, additional harmonic compensators can be implemented straightforwardly, through tuning multiple PR controllers at the desired harmonic frequencies $(h \cdot \omega')$ working in parallel. The control structure of a grid-following converter based on resonant controllers is shown in Fig. 17.8.

This book belongs to Kitab Liaison (ocd1996@gmail.com) Copyright Elsevier 2023

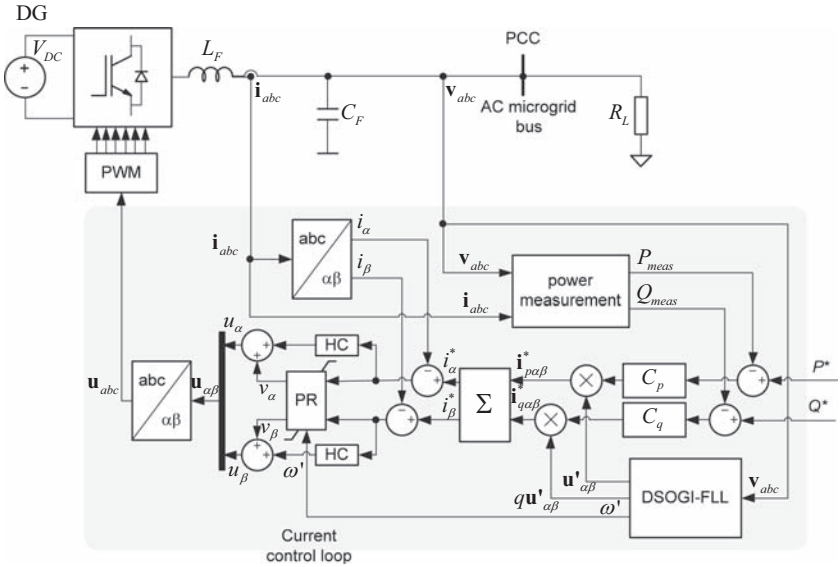

FIGURE 17.8 Basic structure of the grid-following converter implemented in Stationary Reference Frame Control, with proportional resonant controller (PR) and Harmonic Compensator (HC).

17.4 Grid-forming power converters

17.4.1 Definition

According to recent definitions, a grid-forming power converter should be able to support the operation of the AC power system under normal, alerted, emergency, blackout, and restoration states without having to rely on services from synchronous generators [24]. Therefore, a grid-forming power converter could be represented in a simplified manner as controlled AC voltage source with a given amplitude E^* and frequency ω^*, as shown in Fig. 17.9. As a voltage source, such a power converter would present low output impedance, which might complicate its operation in parallel with other grid-forming converters, e.g., when operating in interconnected grids. In such a case, the natural (unregulated) current sharing among paralleled grid-forming converters would depend on the value of their physical output impedances, which are rather low. Therefore, in a realistic implementation of a grid-forming power converter, it will be necessary to include an inner current controller to regulate and limit the maximum current injected by the power converter to the grid. Moreover, in order to naturally regulate the current sharing among multiple grid-forming power converters connected in parallel, it would be interesting to incorporate a dedicated mechanism to emulate the output impedance shown by the power converter to the grid. In addition, some outer

This book belongs to Kitab Liaison (ocd1996@gmail.com) Copyright Elsevier 2023

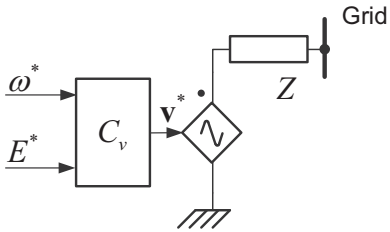

FIGURE 17.9 Basic representation of a grid-forming power converter.

control loops would be enabled to contribute to grid frequency and voltage regulation by modifying the active and reactive power references of the power converter. These loops would play a similar role to the governor and the automatic voltage regulator in the case of synchronous generators.

A simple example of a grid-forming power converter could be a stand-alone UPS. This system remains connected from the main grid when the operating conditions are within certain limits. In the case of a grid failure, the power converter of the UPS forms the grid voltage. In the islanded part of the grid, the AC voltage generated by the grid-forming power converter will be used as a reference for the rest of grid-following power converters connected to it.

17.4.2 Control schemes for grid-forming power converter

Fig. 17.10 shows an example of a controller for a simplified grid-forming power converter, which is implemented by using two cascaded PI controllers working on the *dq*-reference frame. The inputs to the control system are the grid voltage amplitude V^* and the grid frequency ω^* to be formed by the power converter at the point of common coupling (PCC). The outer loop controls the grid voltage to match its reference value, while the inner control loop regulates the current supplied by the converter. Therefore, the controlled current flowing through the inductor L_F charges the capacitor C_F to keep the output voltage close to the reference provided to the voltage control loop. Usually, in industrial applications, these power converters are fed by stable DC voltage sources driven by PV panels, batteries, fuel cells, or other primary sources.

It should be pointed out that, in the simplified implementation shown in Fig. 17.10, the voltage control loop of the grid-forming power converter will be enabled only when it is disconnected from the main network and works in islanded mode. Otherwise, several grid-forming converters would compete each other to set the grid voltage when working in parallel. As previously mentioned, the inner current loop of the cascade configuration in Fig. 17.10 regulates the current supplied by the power converter, tracking the reference

This book belongs to Kitab Liaison (ocd1996@gmail.com) Copyright Elsevier 2023

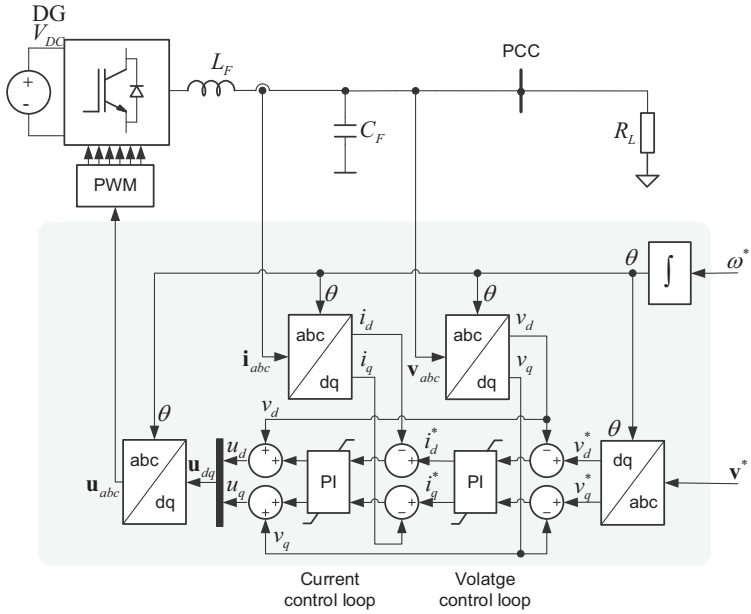

FIGURE 17.10 Cascaded implementation of grid-forming power converter.

current provided by the outer voltage loop. It is worth noting that the grid-forming power converters can be controlled in both the *dq*-synchronous [25] and the $\alpha\beta$-stationary reference frames as in the case of grid-following power converters [26].

Some typical schemes for the control loops previously mentioned to regulated current and power sharing among paralleled grid-forming converters are discussed in following sections.

17.4.3 Droop control in grid-forming power converters

The implementation of the grid-forming power converter shown in Fig. 17.10 does not allow controlling power sharing control among paralleled power converters. To overcome such a shortcoming, several power-sharing strategies have been proposed in the literature, such as centralized controllers, master–slave, average load sharing, or circular chain controls [27]. However, such solutions use to assume that paralleled converters are physically connected close to each other and linked through high-bandwidth communication networks. In real cases, distributed generator systems and loads may be spread over larger geographic areas, so communication-based solutions can become impractical due to technical and economic reasons. To address this issue, droop control algorithms have been traditionally used to control the power sharing among grid-connected power converters without using any

This book belongs to Kitab Liaison (ocd1996@gmail.com) Copyright Elsevier 2023

communication link, thereby eliminating the limits imposed by physical location and improving the grid performance [28]. The droop regulation techniques are implemented in grid-forming power converters to regulate the exchange of active and reactive powers with the grid, thereby contributing to regulate the grid voltage frequency and amplitude, respectively.

17.4.3.1 Grid impedance influence on droop control

Considering the power converter as an ideal controllable voltage source that is connected to an infinite bus through a given line impedance, as shown in Fig. 17.11A, the active and reactive powers that it will deliver to the grid can be written as follows:

$$P_A = \frac{V_A}{R^2 + X^2}[R(V_A - V_B \cos\delta) + XV_B \sin\delta], \tag{17.4}$$

$$Q_A = \frac{V_A}{R^2 + X^2}[-RV_B \sin\delta + X(V_A - V_B \cos\delta)], \tag{17.5}$$

where P_A and Q_A are the active and reactive powers, respectively, flowing from the source A (power converter) to the B (grid), V_A and V_B are the voltage magnitudes of these sources, δ corresponds to the phase angle difference between the two voltage vectors, $Z = R + jL$ is the interconnection line impedance, and θ is the impedance angle. As $R = Z \cdot \cos\theta$ and $X = Z \cdot \sin\theta$, the performance of this simplified electrical system can be depicted by its vector representation as shown in Fig. 17.11B [29].

17.4.3.1.1 Inductive grid

The inductive component of the line impedances in high-voltage (HV) and medium-voltage (MV) transmission networks is typically much higher than the resistive one, as shown in Table 17.1 [30].

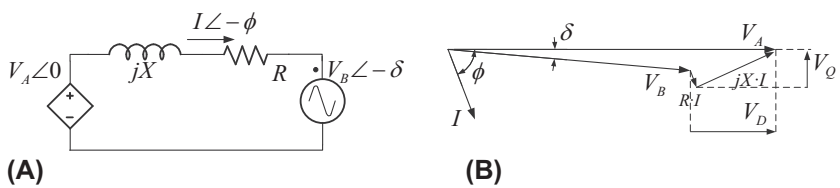

FIGURE 17.11 Simplified modeling of power converter connection to a distribution network. (A) Equivalent circuit, (B) phasor diagram.

This book belongs to Kitab Liaison (ocd1996@gmail.com) Copyright Elsevier 2023

TABLE 17.1 Typical line impedances values.

Type of line	R (Ω/km)	X (Ω/km)	R/X (p.u.)
Low-voltage line	0.642	0.083	7.7
Medium-voltage line	0.161	0.190	0.85
High-voltage line	0.06	0.191	0.31

Therefore, the resistive part can be neglected without losing generality. Additionally, the power angle, δ, in such lines is rather small, so it can be assumed that $\sin\delta \approx \delta$ and $\cos\delta \approx 1$ [31]. Therefore, Eqs. (17.4) and (17.5) can be rewritten as follows:

$$P_A \approx \frac{V_A}{X}(V_B \sin\delta) \quad \Rightarrow \quad \delta \approx \frac{XP_A}{V_A V_B}, \tag{17.6}$$

$$Q_A \approx \frac{V_A}{X}(V_A - V_B \cos\delta) \quad \Rightarrow \quad V_A - V_B \approx \frac{XQ_A}{V_A}. \tag{17.7}$$

Expressions Eqs. (17.6) and (17.7) show a direct relationship between the power angle δ and the active power P, as well as between the voltage difference $V_A - V_B$ and the reactive power Q. From Eqs. (17.6) and (17.7), a small-signal analysis allows determining the relationship between the active power variation and grid frequency variation, as well as between reactive power variation and voltage variation. Such expressions are known as droop control expressions and can be described by Eqs. (17.8) and (17.9) for inductive lines as follows:

$$f - f_0 = -k_p(P - P_0), \tag{17.8}$$

$$V - V_0 = -k_q(Q - Q_0), \tag{17.9}$$

where $f - f_0$ and $V - V_0$ represent the grid frequency and the voltage deviations, respectively, from their rated values, and $P - P_0$ and $Q - Q_0$ are the variations in the active and reactive powers delivered by the power converter to compensate such deviations. These relationships permit regulating the grid frequency and voltage at the point of connection of the power converter, by controlling the value of the active and reactive powers delivered to the grid and can be graphically represented by the droop characteristics shown in Fig. 17.12, where the gain of the control action in each case, i.e., the slope of the frequency and voltage droop characteristic, is set by the k_p and k_q parameters, as indicated in Eqs. (17.8) and (17.9). Therefore, as depicted in Fig. 17.12, each of the grid-forming power converters will adjust its active and reactive power reference according to its P/f and Q/V droop characteristics to participate in the regulation of the grid frequency and voltage, respectively.

This book belongs to Kitab Liaison (ocd1996@gmail.com) Copyright Elsevier 2023

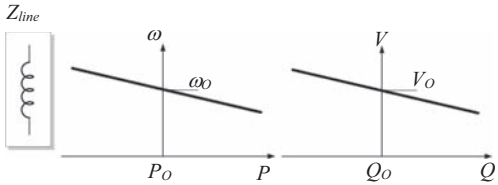

FIGURE 17.12 Frequency and voltage droop characteristics in grids with dominant inductive behavior.

17.4.3.1.2 Resistive grid

On the contrary to the case of HV networks, the grid impedance in low-voltage (LV) networks is mainly resistive, as it is shown in Table 17.1, and thus the inductive part can be neglected. As a consequence, maintaining the assumption that the power angle, δ, is small, the expressions Eqs. (17.4) and (17.5) give rise to the following:

$$P_A \approx \frac{V_A}{R}(V_A - V_B \cos\delta) \quad \Rightarrow \quad V_A - V_B \approx \frac{RP_A}{V_A}, \tag{17.10}$$

$$Q_A = -\frac{V_A \cdot V_B}{R}\sin\delta \quad \Rightarrow \quad \delta \approx -\frac{RQ_A}{V_A V_B}. \tag{17.11}$$

Therefore, the voltage amplitude in LV networks depends mainly on the active power flow, while their frequency is mainly affected by the reactive power injection. From Eqs. (17.10) and (17.11), the following droop control expressions can be written for resistive lines:

$$V - V_0 = -k_p(P - P_0), \tag{17.12}$$

$$f - f_0 = k_q(Q - Q_0), \tag{17.13}$$

being their droop characteristics represented in Fig. 17.13, which depicts the P/V and the Q/f droop control actions to be taken in resistive networks for regulating the grid voltage and frequency.

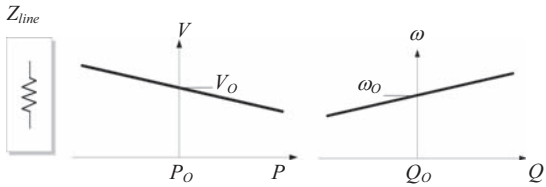

FIGURE 17.13 Voltage and frequency droop characteristics in mainly resistive grids, generally in low-voltage systems.

This book belongs to Kitab Liaison (ocd1996@gmail.com) Copyright Elsevier 2023

17.4.3.1.3 General case

In the general case, the combined effect of the resistive and inductive line impedance components should be taken into account in the droop control equations. To do that, a rotation matrix **T** is used to transform the active and reactive powers, P and Q, into the rotated power components, P' and Q', as detailed in the following:

$$\begin{bmatrix} P' \\ Q' \end{bmatrix} = [\mathbf{T}] \cdot \begin{bmatrix} P \\ Q \end{bmatrix} = \begin{bmatrix} \cos\phi & -\sin\phi \\ \sin\phi & \cos\phi \end{bmatrix} \cdot \begin{bmatrix} P \\ Q \end{bmatrix} = \begin{bmatrix} X/Z & -R/Z \\ R/Z & X/Z \end{bmatrix} \cdot \begin{bmatrix} P \\ Q \end{bmatrix}, \tag{17.14}$$

where $\phi = \pi/2 - \theta = \arctan(R/X)$, ϕ is the rotation angle of the matrix **T** and θ is the angle of the line impedance, $\mathbf{Z} = Z\angle\theta$.

Provided that δ takes a small value, the application of the **T** rotation matrix to Eqs. (17.4) and (17.5) results in the following simplified equations:

$$P'_A \approx \frac{V_A}{Z}(V_B \sin\delta) \quad \Rightarrow \quad \delta \approx \frac{ZP'_A}{V_A V_B}, \tag{17.15}$$

$$Q'_A \approx \frac{V_A}{X}(V_A - V_B \cos\delta) \quad \Rightarrow \quad V_A - V_B \approx \frac{ZQ'_A}{V_A}, \tag{17.16}$$

where P'_A and Q'_A are the rotated components of P_A and Q_A.

From Eqs. (17.15) and (17.16), it can be concluded that the power angle, δ, can be controlled by regulating the rotated active power, P'_A, while the voltage difference $V_A - V_B$ can be changed by regulating the rotated reactive power, Q'_A. Therefore, in a general case, the droop control equations can be written as follows:

$$f - f_0 = -k_p\left(P' - P'_0\right) = -k_p\frac{X}{Z}(P - P_0) + k_q\frac{R}{Z}(Q - Q_0), \tag{17.17}$$

$$V - V_0 = -k_q\left(Q' - Q'_0\right) = -k_p\frac{R}{Z}(P - P_0) - k_q\frac{X}{Z}(Q - Q_0). \tag{17.18}$$

According to Eqs. (17.17) and (17.18), the contribution in the compensation of the frequency and the voltage amplitude variations by each grid-forming power converter can be adjusted by changing the values k_p and k_q.

17.4.3.2 Virtual impedance control

Conventional P/f and Q/V droop controls have been proven to be an effective solution for regulating the voltage magnitude and frequency in transmission networks, where the lines have a predominant inductive behavior. However, as shown previously, the performance of this kind of control is highly dependent on the R/X ratio of the line [32]. Due to this feature, this method cannot be directly applied in all kinds of MV networks, unless some grid impedance

This book belongs to Kitab Liaison (ocd1996@gmail.com) Copyright Elsevier 2023

estimation algorithms are implemented to calculate the rotated powers as indicated in Eq. (17.14). This issue is even more important when the droop control is applied to LV distribution networks, as stated in Refs. [28,33]. In such a case, a small mismatch in the grid impedance estimation results in an inefficient power sharing among the droop-controlled generations.

As an intuitive solution to address these drawbacks, resulting from the strong dependence of the conventional droop controller performance on the line impedance value, large inductors could be used to link the power converter to the AC bus, and thereby the line impedance would be predominantly inductive. However, this is not an efficient solution since, in addition to the increase in the size and the costs, the DC-bus voltage level should be significantly increased to compensate for the high voltage drop across these inductors, reducing thus the overall efficiency. A more effective solution is to virtually introduce the effect of this link impedance into the control system of the grid-forming power converter.

This concept was successfully implemented in Refs. [32,34], where an adjustable virtual output impedance was used for regulating the power sharing among parallelized inverters and for limiting overcurrent under grid disturbances. It is worth to remark that the value of the virtual impedance should be higher than the actual line impedance, otherwise it will not have a predominant effect in the power flow equations.

The virtual impedance modifies the power converter output voltage reference as indicated in Eq. (17.19), where the modified voltage reference, v^{**}, is obtained by subtracting the virtual voltage drop across the virtual impedance, $Z_V \cdot i_{\text{grid}}$, from the reference value originally provided by the droop equations, v^*.

$$v^{**} = v^* - Z_V \cdot i_{\text{grid}}. \tag{17.19}$$

The value of Z_V sets the controller response, hence it must be considered as a control variable and should be selected according to the nominal power of the converter. An example of the implementation of the virtual impedance concept in a grid-forming power converter is shown in Fig. 17.14.

Fig. 17.14. also represents the implementation of the droop equations shown in Eqs. (17.8) and (17.9) to regulate the frequency amplitude of the virtual electromotive force (emf), $e = E \cdot \sin(\omega t)$, assuming the virtual output impedance of the power converter is predominantly inductive. Conceptually, these droop control loops enable the grid-forming power converter to conduct grid synchronization based on power balance, instead on direct grid voltage parameters estimation through a PLL or FLL. For instance, in case the grid frequency was lower than the frequency of the virtual emf of the power converter, the power angle δ would trend to increase. As a consequence, according to Eq. (17.6), the active power delivered by the power converter

This book belongs to Kitab Liaison (ocd1996@gmail.com) Copyright Elsevier 2023

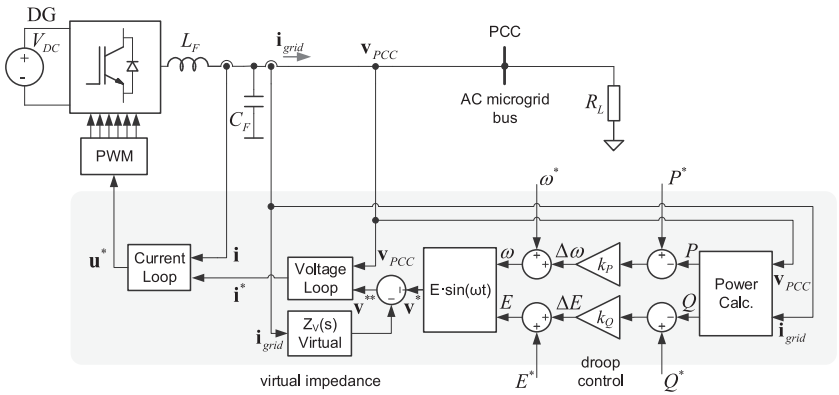

FIGURE 17.14 Block diagram of the virtual output impedance loop working with P and Q droop method in the grid power converter.

would trend to increase as well. Such an increment in the output active power would be detected by the P/ω droop control loop of Fig. 17.14, and according to Eq. (17.8), the internal frequency of the grid-forming converter would be reduced according to the parameter k_P. A similar process, but driven by reactive power given by Eq. (17.9), would be followed in case of deviations in the value of the voltage at the PCC.

17.4.4 The synchronous power controller

Although droop controllers somehow allow implementing grid-forming functionalities in power converters, they do not physically describe the dynamic response of electromechanical synchronous generators. This is particularly interesting when the grid-forming converters are required to provide inertial response in case of transient grid frequency deviations. Actually, the inertia-less behavior of most of conventional grid-following power converters has raised significant concerns about power system stability, particularly when their share in power systems becomes substantial. This has led to a new implementation of grid-forming power converters which is based on the concept of virtual synchronous machine (VSM). In this implementation, the control system of the power converter is altered to mimic the dynamic response of an electromechanical synchronous machine.

There have been various proposals for VSM including the VISMA [34], the synchronverter [35], the synchronous power controller (SPC) [36], to name a few of them. Among these approaches, the SPC has stood out as one of most the simple and effective practical implementations. The block diagram of the SPC is shown in Fig. 17.15, where the power converter is controlled as a current source. This enables the SPC to be implemented in most of the

This book belongs to Kitab Liaison (ocd1996@gmail.com) Copyright Elsevier 2023

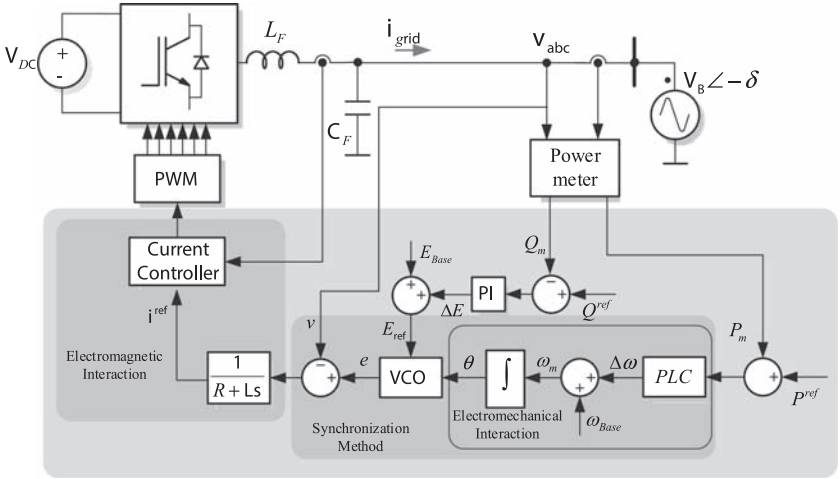

FIGURE 17.15 Block diagram the synchronous power controller.

grid-following power converters currently available in the market, which generally use current controllers similar to the ones described in Section 17.2. Since gird-forming converter should provide support services during grid transients, such as inertia emulation, the main requirements for current controller are often low settling time and robustness. The fact of using a current-controlled voltage source converter to connect to the electrical grid requires to substitute the virtual impedance block shown in Fig. 17.14 by a virtual admittance block. In this manner, the references for the current controller are generated by such a virtual admittance block, whose input is the difference between measured grid voltage, v, and the virtual emf, e. Actually, such a current reference results from solving the i_{grid} current in Eq. (17.19). Therefore, the transfer function of the virtual admittance block can be written as follows:

$$G_a(s) = \frac{1}{R + Ls}, \tag{17.20}$$

where R and L represent the value for the virtual resistance and the virtual inductance, respectively. It is worth noting that Eq. (17.20) has the form of a low-pass filter rather than a derivative term that would result from Eq. (17.19) [37], which results in a more stable implementation of the virtual impedance (admittance) effect. Parameters of the virtual admittance block are usually chosen to meet the reactive power support requirements [38]. Combining multiple virtual admittance blocks to control different voltage sequences and frequencies is also used [39].

This book belongs to Kitab Liaison (ocd1996@gmail.com) Copyright Elsevier 2023

The virtual emf, e, of the SPC is generated by using a voltage-controlled oscillator, which combines the outputs of the power loop controller (PLC) and the PI-based reactive controller. Similar to a synchronous generator, the grid synchronization through input/output power balancing is achieved by such PLC. As shown in Ref. [40], several transfer functions can be used to implement the PLC. For instance, it can be implemented through a simple first-order low-pass filter transfer function as follows:

$$\mathrm{PLC}(s) = k\frac{\omega_c}{s+\omega_c}, \tag{17.21}$$

where k and ω_c are the proportional gain and the cut-off frequency, respectively. This feature allows the SPC to provide synthetic inertia to support the grid. For designing the PLC, a small-signal model of the SPC is often adopted, as the one shown in Fig. 17.16, where $P_{\max} = EV/X$ results from the synchronous power expression shown in Eq. (17.6).

From Fig. 17.16, the closed loop of the closed-loop transfer function of the resulting power-locked loop can be given as follows:

$$\frac{P_s}{P_{in}} = \frac{kP_{\max}\omega_c}{s^2+\omega_c s+kP_{\max}\omega_c} = \frac{\omega_n^2}{s^2+2\xi\omega_n s+\omega_n^2}, \tag{17.22}$$

where ξ and ω_n are the damping factor and natural frequency. From Eq. (17.22), the gain and cut-off frequency can be calculated as follows:

$$\omega_c = 2\xi\omega_n \text{ and } k = \frac{\omega_n}{2\xi P_{\max}}, \tag{17.23}$$

giving rise to the following expression to calculate the virtual moment of inertia emulated by the SPC controller:

$$J = \frac{P_{\max}}{\omega_n^2\omega_s}, \tag{17.24}$$

where ω_s is fundamental grid frequency in rad/s. It is worth to notice that multiple PLCs can be paralleled and tuned with different subsynchronous frequencies to damp multiple modal oscillations in power systems [41].

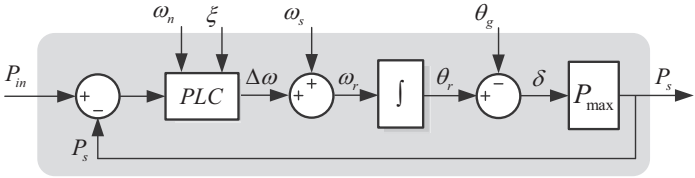

FIGURE 17.16 Small signal of active power control loop of the synchronous power controller.

This book belongs to Kitab Liaison (ocd1996@gmail.com)
Copyright Elsevier 2023

17.5 Conclusions

In this chapter, various control schemes for the grid-connected power converters used in PV and WP systems have been discussed. The most relevant concepts presented in this chapter are the following:

- There are four main configurations for power converter in PV systems, namely microinverter, string inverter, multistring inverter, and central inverter.
- Depending on the combination of the induction machine and the power converter, WP systems are classified into four types: fixed-speed, variable-slip, double-fed induction generator, and full converter wind turbines.
- A grid-connected power converter in PV and WP can be operated either in grid-following or grid-forming mode.
- The most frequently used synchronization mechanisms for grid connected are the SRF-PLL and the FLL in the rotating and the stationary reference frames, respectively.
- Current controllers can be implemented by using PI controllers in SRF or PR controller in the stationary reference frame.
- Grid-forming power converters need some current/power sharing mechanism to operate in parallel or grid-connected mode.
- Grid-forming power converters can be implemented by using both conventional droop strategies or VSMs approaches.
- Droop-based strategies are sensitive to line impedance. Virtual impedance/admittance can be used to address such a limitation.
- The SPC is one of the most effective strategies to implement a grid-forming power converter, which can provide not only steady-state voltage and frequency regulation but also dynamic support to the grid such as inertial response and power oscillation damping.

References

[1] IEA, Renewables 2019, 2019. Paris.
[2] REN21, Renewables 2019 Global Status Report, REN21 Secretariat, Paris, 2019.
[3] Fraunhofer Institute for Solar Energy, Photovoltaics Report, 2020.
[4] J. Rocabert, A. Luna, F. Blaabjerg, P. Rodríguez, Control of power converters in AC microgrids, IEEE Trans. Power Electron. 27 (11) (2012) 4734–4749.
[5] J.T. Bialasiewicz, Renewable energy systems with photovoltaic power generators: operation and modeling, IEEE Trans. Ind. Electron. 55 (7) (July 2008) 2752–2758.
[6] H.H. Zeineldin, A Q–f droop curve for facilitating islanding detection of inverter-based distributed generation, IEEE Trans. Power Electron. 24 (3) (March 2009) 665–673.
[7] H.H. Zeineldin, E.F. El-saadany, M.M.A. Salama, Distributed generation micro-grid operation: control and protection, in: In 2006 Power Systems Conference: Advanced Metering, Protection, Control, Communication, and Distributed Resources, 2006, pp. 105–111.

This book belongs to Kitab Liaison (ocd1996@gmail.com) Copyright Elsevier 2023

[8] P. Rodriguez, A. Lunar, R. Teodorescu, F. Iov, F. Blaabjerg, Fault ride-through capability implementation in wind turbine converters using a decoupled double synchronous reference frame PLL, in: In 2007 European Conference on Power Electronics and Applications, 2007, pp. 1−10.

[9] V. Kaura, V. Blasko, Operation of a phase locked loop system under distorted utility conditions, IEEE Trans. Ind. Appl. 33 (1) (January 1997) 58−63.

[10] S.K. Chung, A phase tracking system for three phase utility interface inverters, IEEE Trans. Power Electron. 15 (3) (May 2000) 431−438.

[11] A. Timbus, R. Teodorescu, F. Blaabjerg, M. Liserre, Synchronization methods for three phase distributed power generation systems. An overview and evaluation, in: In PESC Record - IEEE Annual Power Electronics Specialists Conference, 2005, 2005, pp. 2474−2481.

[12] P. Rodríguez, J. Pou, J. Bergas, J.I. Candela, R.P. Burgos, D. Boroyevich, Decoupled double synchronous reference frame PLL for power converters control, IEEE Trans. Power Electron. 22 (2) (March 2007) 584−592.

[13] S. Cobreces, E.J. Bueno, D. Pizarro, F.J. Rodriguez, F. Huerta, Grid impedance monitoring system for distributed power generation electronic interfaces, IEEE Trans. Instrum. Meas. 58 (9) (2009) 3112−3121.

[14] P. Rodríguez, A. Luna, M. Ciobotaru, R. Teodorescu, F. Blaabjerg, Advanced grid synchronization system for power converters under unbalanced and distorted operating conditions, in: In IECON Proceedings (Industrial Electronics Conference), 2006, pp. 5173−5178.

[15] F. Blaabjerg, R. Teodorescu, M. Liserre, A.V. Timbus, Overview of control and grid synchronization for distributed power generation systems, IEEE Trans. Ind. Electron. 53 (5) (October 2006) 1398−1409.

[16] N. Pogaku, M. Prodanovic, T.C. Green, Modeling, analysis and testing of autonomous operation of an inverter-based microgrid, IEEE Trans. Power Electron. 22 (2) (March 2007) 613−625.

[17] M.C. Chandorkar, D.M. Divan, R. Adapa, Control of parallel connected inverters in standalone AC supply systems, IEEE Trans. Ind. Appl. 29 (1) (January 1993) 136−143.

[18] P. RodrÍguez, A. Timbus, R. Teodorescu, M. Liserre, F. Blaabjerg, Reactive power control for improving wind turbine system behavior under grid faults, IEEE Trans. Power Electron. 24 (7) (July 2009) 1798−1801.

[19] A. Timbus, M. Liserre, R. Teodorescu, P. Rodriguez, F. Blaabjerg, Evaluation of current controllers for distributed power generation systems, IEEE Trans. Power Electron. 24 (3) (March 2009) 654−664.

[20] M. Liserre, R. Teodorescu, F. Blaabjerg, Multiple harmonics control for three-phase grid converter systems with the use of PI-RES current controller in a rotating frame, IEEE Trans. Power Electron. 21 (3) (May 2006) 836−841.

[21] E. Clarke, Circuit Analysis of A-C Power Systems, vol. 1, Wiley, New York, NY, 1943.

[22] R. Cárdenas, C. Juri, R. Peña, P. Wheeler, J. Clare, The application of resonant controllers to four-leg matrix converters feeding unbalanced or nonlinear loads, IEEE Trans. Power Electron. 27 (3) (March 2012) 1120−1129.

[23] A.M. Roslan, K.H. Ahmed, S.J. Finney, B.W. Williams, Improved instantaneous average current-sharing control scheme for parallel-connected inverter considering line impedance impact in microgrid networks, IEEE Trans. Power Electron. 26 (3) (March 2011) 702−716.

This book belongs to Kitab Liaison (ocd1996@gmail.com) Copyright Elsevier 2023

[24] ENTSO-E Technical Group on High Penetration of Power Electronic Interfaced Power Sources, High Penetration of Power Electronic Interfaced Power Sources and the Potential Contribution of Grid Forming Converters, January 2020.
[25] F. Katiraei, R. Iravani, N. Hatziargyriou, A. Dimeas, Microgrids management, IEEE Power Energy Mag. 6 (3) (May 2008) 54−65.
[26] R. Teodorescu, F. Blaabjerg, Flexible control of small wind turbines with grid failure detection operating in stand-alone and grid-connected mode, IEEE Trans. Power Electron. 19 (5) (2004) 1323−1332.
[27] J.M. Guerrero, L. Hang, J. Uceda, Control of distributed uninterruptible power supply systems, IEEE Trans. Ind. Electron. 55 (8) (August 2008) 2845−2859.
[28] J.M. Guerrero, J. Matas, L.G. De Vicuña, N. Berbel, J. Sosa, Wireless-control strategy for parallel operation of distributed generation inverters, in: In IEEE International Symposium on Industrial Electronics, vol. II, 2005, pp. 845−850.
[29] K. De Brabandere, Voltage and Frequency Droop Control in Low Voltage Grids by Distributed Generators with Inverter Front-End, October 2006, p. 227.
[30] A. Engler, Applicability of droops in low voltage grids, Int. J. Distrib. Energy Resour. Smart Grids 1 (1) (2005) 1−5.
[31] H. Laaksonen, P. Saari, R. Komulainen, Voltage and frequency control of inverter based weak LV network microgrid, in: 2005 International Conference on Future Power Systems, 2005, 2005, p. 6.
[32] W. Yao, M. Chen, J. Matas, J.M. Guerrero, Z. Qian, Design and analysis of the droop control method for parallel inverters considering the impact of the complex impedance on the power sharing, IEEE Trans. Ind. Electron. 58 (2) (February 2011) 576−588.
[33] J.M. Guerrero, L. Garcia de Vicuna, J. Matas, M. Castilla, J. Miret, Output impedance design of parallel-connected UPS inverters with wireless load-sharing control, IEEE Trans. Ind. Electron. 52 (4) (August 2005) 1126−1135.
[34] H. Beck, R. Hesse, Virtual synchronous machine, in: In 2007 9th International Conference on Electrical Power Quality and Utilisation, 2007, pp. 1−6.
[35] Q. Zhong, G. Weiss, Synchronverters: inverters that mimic synchronous generators, IEEE Trans. Ind. Electron. 58 (4) (April 2011) 1259−1267.
[36] P. Rodríguez, C. Citro, J.I. Candela, J. Rocabert, A. Luna, Flexible grid connection and islanding of SPC-based PV power converters, IEEE Trans. Ind. Appl. 54 (3) (May 2018) 2690−2702.
[37] S. D'Arco, J.A. Suul, O.B. Fosso, Control system tuning and stability analysis of virtual synchronous machines, in: In 2013 IEEE Energy Conversion Congress and Exposition, 2013, pp. 2664−2671.
[38] W. Zhang, J. Rocabert, J.I. Candela, P. Rodriguez, Synchronous power control of grid-connected power converters under asymmetrical grid fault, Energies 10 (7) (July 2017) 950.
[39] A. Tarrasó, J.I. Candela, J. Rocabert, P. Rodriguez, Grid voltage harmonic damping method for SPC based power converters with multiple virtual admittance control, in: 2017 IEEE Energy Convers. Congr. Expo. ECCE, January 2017, pp. 64−68.
[40] W. Zhang, et al., Comparison of different power loop controllers for synchronous power controlled grid-interactive converters, in: 2015 IEEE Energy Conversion Congress and Exposition, Montreal, QC, 2015, pp. 3780−3787.
[41] P. Rodriguez, J.I. Candela, J. Rocabert, R. Teodorescu, Virtual Controller of Electromechanical Characteristics for Static Power Converters, US20140067138A1, 2012.

This book belongs to Kitab Liaison (ocd1996@gmail.com) Copyright Elsevier 2023

This page intentionally left blank

This book belongs to Kitab Liaison (ocd1996@gmail.com)

Copyright Elsevier 2023

Chapter 18

Virtual inertia operation of renewables

Rasool Heydari[1], Mehdi Savaghebi[1], Frede Blaabjerg[2]
[1]*University of Southern Denmark, Odense, Denmark;* [2]*Department of Energy Technology, Aalborg University, Aalborg, Denmark*

18.1 Introduction

Currently, around 28% of the overall greenhouse gas emissions are produced by fossil fuel—based electricity generations [1]. "Replacing fossil fuels as an energy source with green renewable energy is the most important action we can take to address the impacts of climate change," Rame Hemstreet, Chief Energy Officer [2]. Therefore, the European Union (EU) has set energy targets to reduce greenhouse gas emissions to 90% by 2050 [3]. For instance, Germany has already decided to shut down all the coal-based generation by 2038 [4]. An increasing number of countries, e.g., Ireland and Denmark, some states in the United States, e.g., California and Hawaii, as well as utilities, e.g., American Electric Power and Xcel Energy, set targets of 100% renewables or 100% carbon-free generation [5].

Distributed renewable energy sources (RESs) connected by power converters are becoming prominent components in the modern power system. Based on the international renewable energy agency reports, the proportion of the installed microsource distributed generation units capacity has been increased from 77.5 GW in 2000 to 1225 GW in 2018, as shown in Fig. 18.1 [6]. Furthermore, the global wind energy council has reported that more than 341,000 wind turbines generated electricity in 2017 [7], and the EU has set a binding target of 20% electrical generation from renewable sources by 2020 [6].

However, high penetration of RESs leads to some technical challenges such as instability problems, frequency deviations, and synchronization problems in the power grid due to the low-inertia characteristics of nonsynchronous generators (NSGs).

Power converters, which serve as interfaces between an RES and the common AC bus, have no mechanical kinetic energy. Therefore, high penetration of the converter-based generations and NSGs, with zero inertia,

Control of Power Electronic Converters and Systems. https://doi.org/10.1016/B978-0-12-819432-4.00011-1
Copyright © 2021 Elsevier Ltd. All rights reserved.

This book belongs to Kitab Liaison (ocd1996@gmail.com)
Copyright Elsevier 2023

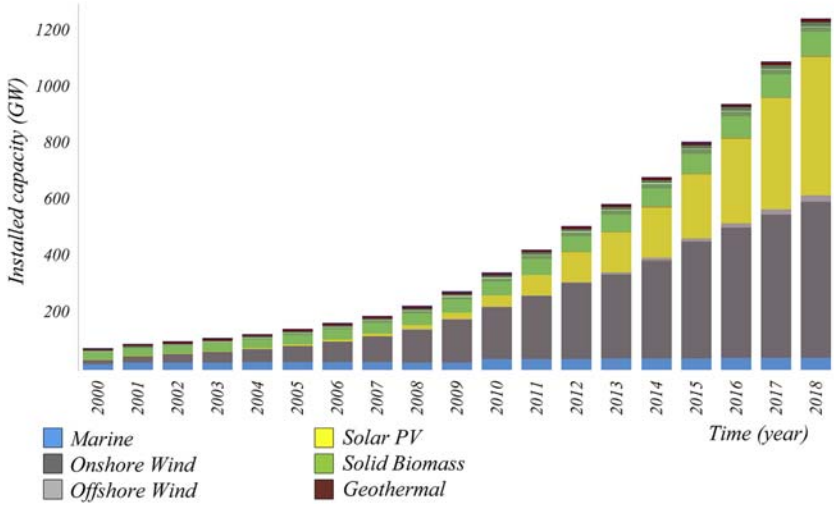

FIGURE 18.1 Global cumulative installed DGU capacity trend from 2000 to 2018 [4].

introduces new challenges in terms of frequency and voltage control as well as stability of the grid. Lower inertia in the grid yields a more considerable impact of disturbances on the system frequency and voltage control. The rotating parts of the synchronous generators and turbines interchange inertial energy with the grid so that the primary controllers have time to react to the grid disturbance or load/generation imbalance. However, the converter-interfaced RES does not provide any inertial response toward the power grid. Consequently, a large generation/load imbalance or a perturbation on the system may lead to the significant frequency and voltage deviations, which in turn may lead to load shedding or system instabilities in the power system and in worst case power outage.

This so-called *low-inertia* challenge is stated as the main bottleneck to integrate a high penetration of NSG in the power network in both literature and industry. For instance, due to the increasing penetration of NSG, frequency violations have increased in the Nordic grid [8]. In Ireland and Northern Ireland, the inadequate grid inertia significantly affected the frequency and voltage regulations [9].

Many aspects should be considered in the design phase of RES integration regarding inertia challenges and providing virtual inertia as a solution. Efficiency, reliability, and stability are the significant concerns of operation and control of NSG-based systems. This chapter first overviews the low-inertia grid challenges and main resultant difficulties in the world power systems. Then, the focus is on virtual inertia concept, theory, and control solutions in a grid with a high penetration of renewables. Design examples and some PowerFactory simulation results are also provided.

This book belongs to Kitab Liaison (ocd1996@gmail.com) Copyright Elsevier 2023

18.2 Evolution of green energy transition

Wind and solar photovoltaics (PV) generation are currently the fastest growing sources of electricity due to the drop in the price of power electronic components and renewable energy technologies [6].

There are two main challenges with high penetration of NSGs from the power system operation point of view. First, PV and wind are variable energy resources, and their outputs are uncertain and change over minutes, hours, or days. This variable characteristic leads to challenges with power system balancing and resource adequacy during peak demand. Secondly, these NSGs, e.g., wind and PV, are connected to the main grid through power converters, which means they are nonsynchronously coupled to the main grid. Changing fault behavior from power converters, lower short circuit capability, and decreasing system inertia are sources of concern as SGs are displaced by NSGs massively. This low-inertia challenge degrades the grid reliability, stability, and performance, if not addressed appropriately. The main focus of this chapter is on the second challenge, i.e., low-inertia grids with high penetration of RESs.

18.2.1 Low-inertia grid challenges

The green transition from conventional rotational synchronous generators toward power converter–based NSG, as in the case of RESs, battery energy storages, or high-voltage DC (HVDC) links, will pose major challenges to the control, operation, and stability of power grid due to [10–13]

- The loss of kinetic energy stored in the rotating mass of the synchronous generator.
- The loss of a robust and stable synchronization mechanism, which is physically inherent in a synchronous machine.
- The loss of a global rotating speed and frequency signal, and consequently, loss of a robust frequency and voltage control.

In the modern power grid, these functionalities have to be addressed by proper control of the power converters.

For instance, Fig. 18.2 shows a frequency response comparison between a *low-inertia* system and a synchronous generator–based high-inertia grid. In the low-inertia grid, in the event of a generation loss, the rate of change of frequency (RoCoF) is higher, and consequently, the frequency nadir is lower due to the lack of system inertia [14,15]. This problem may lead to major instability and cascading failures in the power system. Experiences from Ireland indicate that at the high level of wind power penetration (above approximately 50%), the frequency deviations and dynamic stability deteriorate significantly (see Fig. 18.3 [16]).

This book belongs to Kitab Liaison (ocd1996@gmail.com) Copyright Elsevier 2023

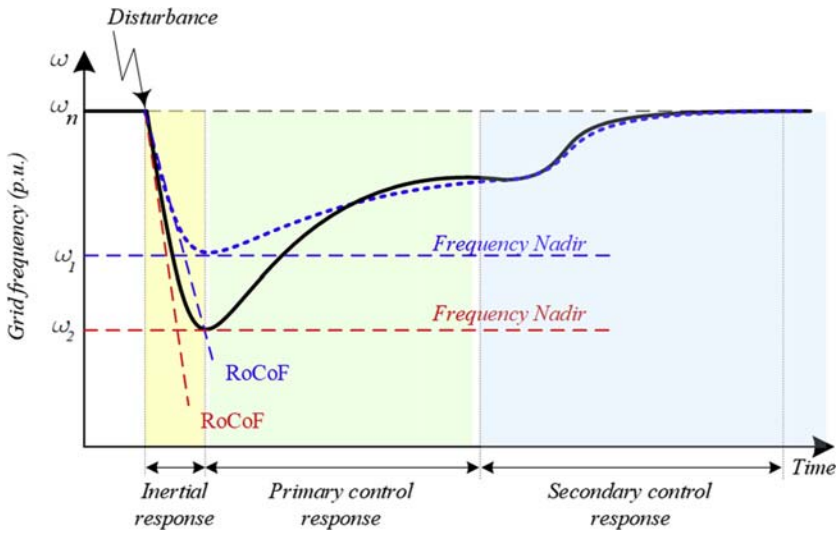

FIGURE 18.2 A comparison between the system frequency response in a low-inertia grid (*solid black line*) and an SG-based high-inertia network (*dashed*).

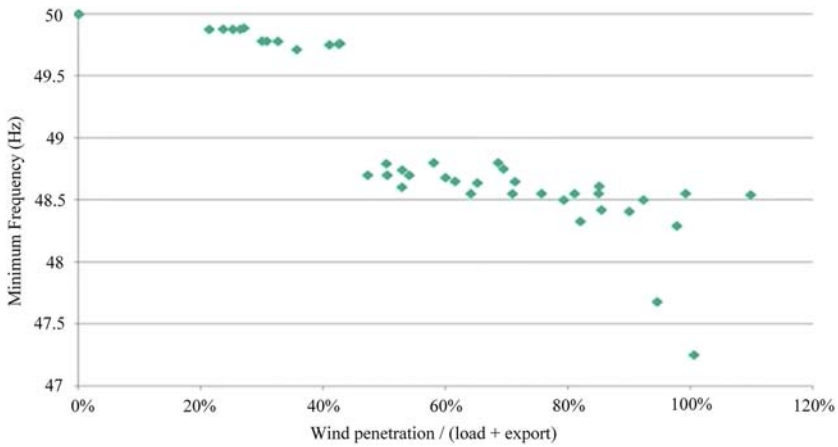

FIGURE 18.3 The frequency deviation versus wind penetration in Ireland [16].

The grid of South Australia state is located at the end of the Eastern Australian interconnection. On September 28, 2016, cascading failure of the electricity transmission network led to a huge blackout in South Australia, where 40% of generation in this region is provided by the wind turbines. When a fault had occurred, 9 out of 15 wind farms did not respond to the system accurately and just shut off, which resulted in almost the entire state losing its electricity supply [17].

This book belongs to Kitab Liaison (ocd1996@gmail.com) Copyright Elsevier 2023

Therefore, Australian Electricity Market Operator studied a large electromagnetic transient and electromechanics model of the South Australian interconnected grid, which includes all synchronous generators, grid-connected RESs, generation protection systems, and the transmission network. The results of the studies have identified the following:

(1) The technical requirement for a minimum of four or five, 150–200 MVA, synchronous generators to keep online in South Australia at all times.
(2) The limited maximum wind output under low-inertia conditions. These constraints resulted in the curtailment of 4% of output wind generation in winter, 2018 [17].

Eastern and Western Denmark are connected to the large interconnected synchronous areas in Scandinavia and Continental Europe, respectively [18]. In 2003, technical errors on the Swedish power plants resulted in substantial power outages in large parts of Sweden and Eastern Denmark. The first contingency has been occurred with the outage of a 1200-MW nuclear unit in Southern Sweden, due to some problems with a steam valve. Consequently, the system experienced voltage collapse leading to the separation of a region of the Southern Swedish and Eastern Denmark systems. Therefore, this low-inertia islanded system collapsed in both frequency and voltage, and thus led to a huge blackout in Copenhagen and Eastern Denmark [19].

The plans for decommissioning nuclear plants, e.g., in Germany and Sweden [20], will adversely affect the interconnected grid inertia so that it would be a major challenge for the integration of NSG in Denmark and Europe in the near future.

Considering the aforementioned problems, Ireland currently limits its instantaneous penetration of RES to 55% [9]. Ireland's grid is islanded with limited DC interconnection to Great Britain. During November and December 2018, the wind power supplied around 43% of the total electrical energy consumed in Ireland (over the year, wind provides approximately 30% of entire demand). In 2008, the transmission system operator of Ireland and Northern Ireland (EirGrid) analyzed the impact of high penetrations of NSG on the grid transient stability. The results indicate that the operator faces several daunting challenges to reaching 75% system nonsynchronous penetration and 1-Hz/s RoCoF [5,16]. Today, EirGrid operates the interconnected grid up to 55% NSG with a 0.5-Hz/s RoCoF limit [9]. With high NSG penetration levels, the grid instability issues significantly arise due to the low kinetic energy and synchronizing torque [21].

18.2.2 Control of power converter–interfaced renewables

In the conventional power system, synchronous generators provide the inertial response and ensure system stability. However, the power converter–interfaced RES does not contribute to such ancillary services [22].

This book belongs to Kitab Liaison (ocd1996@gmail.com) Copyright Elsevier 2023

All the rotating mass of synchronous generators in power systems are electromechanically coupled to each other; hence, during stable operation, they rotate with synchronous speed. It equivalently can be represented as a huge shaft rotating at the nominal synchronous frequency (60 or 50 Hz). Fig. 18.4 shows the strong coupling of synchronous generators in the conventional power system and equivalent rotating shaft. This huge shaft equivalently represents the inertia of the system, which consists of all the rotating mass of synchronous generators in the grid. By operating renewables, they just follow the reference angular speed of the synchronous generators in the system, since the power converter–interfaced renewables have no rotating mass to contribute in power system kinetic energy. Power converter–interfaced renewables should be able to provide inertia for the system in order to allow their high penetration in the modern grids.

In a general structure, the power converter controllers can be divided into two main structures: grid following and grid forming [23,24]. Grid-following controllers represent the most common type of control structure for grid-connected wind or PV converters. At the core of its operation, a grid-following control strategy employs a phase-locked loop in order to determine the instantaneous sinusoidal voltage angle at the converter output. Therefore, the power electronics are operated to inject a controlled current

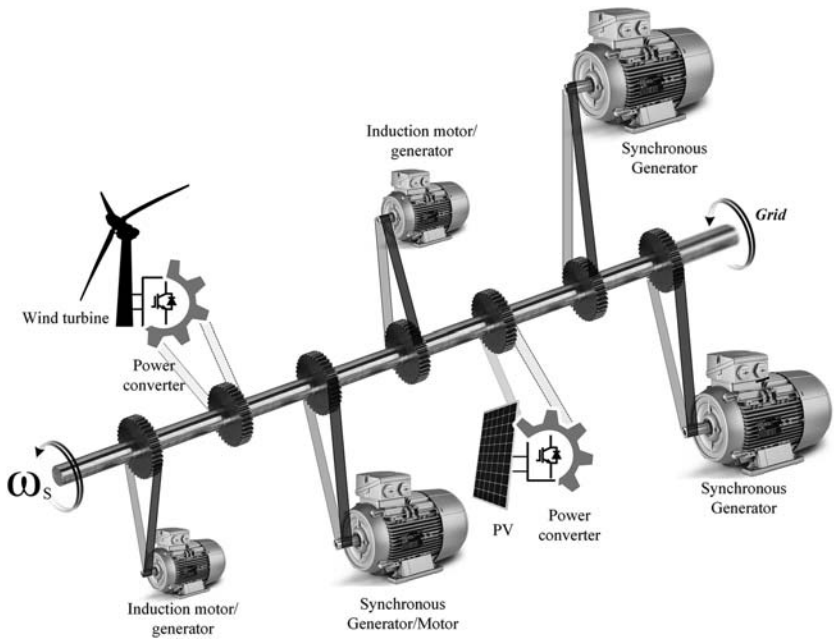

FIGURE 18.4 The strong coupling of synchronous generator in the electric power grid, where also renewables are interconnected.

This book belongs to Kitab Liaison (ocd1996@gmail.com) Copyright Elsevier 2023

into the main power grid that "*follows*" the sinusoidal reference voltage. Thus, it is called a grid-following unit. As the main limitation, grid-following converters work under the presumption that a stiff AC voltage with minimal amplitude and frequency deviations is maintained at its terminals so that it can only follow its local voltage and inject a controlled current.

In practice, this translates to the assumption that the collective behavior of the synchronous machines, the generator and system controllers, as well as voltage regulating equipment on the system, provides a sufficiently stiff frequency and voltage at any point on the grid. Conventionally, this assumption has held up relatively well because the cumulative amount of converter-interfaced RES with grid-following inverters has been relatively small compared to conventional synchronous generators that regulate the system frequency and voltages [24]. Moreover, the grid-following control structure allows all the harvested energy to be exported to the main grid and provides accurate control of the current flow [25,26].

However, with higher penetration of grid-following converter-interfaced RESs, various significant concerns are raised:

- Increasing the RoCoF, and consequently, frequency instability.
- Loss of synchronizing power/torque.
- Voltage instability challenges during postfault, e.g., voltage collapse, or postfault overvoltage.
- Challenges with modeling the electricity power systems dynamic behavior.
- Subsynchronous oscillations and possible interaction with conventional synchronous generator in the system.

To overcome this shortcoming of a conventional grid-following control structure, it is necessary to develop the next-generation grid-forming control strategies that enable the transition to a converter-based generation and which are capable of regulating the system voltages and frequency, directly, through local decentralized control structure.

18.3 Virtual inertia-based control

A solution toward stabilizing the low-inertia grid and increasing the penetration of RESs and NSGs while the system maintained stable is to virtually provide additional inertia. The virtual inertia can be provided by RESs utilizing short-term energy storages together with a power converter and a proper control structure. Inertia can be also emulated directly from RESs, with the cost of operating the wind or PV below the maximum power point [27]. Notice that to employ the controller providing virtual inertia for an NSG converter, a certain amount of energy storage or a high-speed responding energy source is needed to interchange synthetic inertial energy with the grid [28].

This book belongs to Kitab Liaison (ocd1996@gmail.com) Copyright Elsevier 2023

18.3.1 Virtual synchronous machine

The concept of virtual synchronous machine (VSM) or virtual synchronous generator control strategy is presented in the literature with different original variants:

(1) VISMA: VIrtual Synchronous MAchine (VISMA) is proposed in Ref. [29], in which a stand-alone power converter mimics a synchronous machine. Virtual torque and virtual excitation are embedded into the VISMA to regulate the output power. Furthermore, a cascaded structure is implemented where voltage and frequency controllers feed references to the current controller.

(2) Synchronverter: Operating a power converter to mimic a synchronous generator is the so-called Synchronverter and initially presented in Ref. [30]. A synchronverter is equivalent to a synchronous machine with a capacitor bank connected in parallel to the stator terminal.

(3) PSC: Power synchronization control (PSC) is presented in Ref. [31], which emulates the power synchronization mechanism between synchronous machines in the power system. The proposed PSC is a grid-forming control structure for the grid-connected power converters, but may be of most importance for HVDC connected to a weak AC grid system.

The power converter in all various aforementioned approaches will then operate like a synchronous machine, providing inertia and damping properties of a conventional synchronous generator. In this chapter, the notation of "*VSM*" is employed.

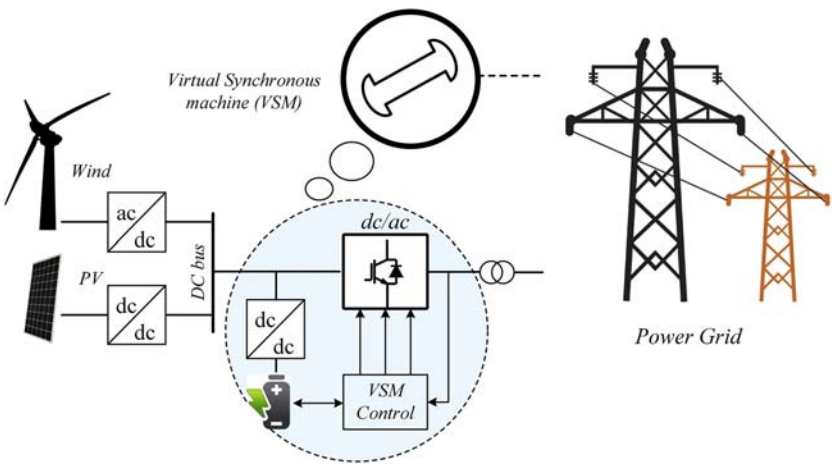

FIGURE 18.5 The general concept of virtual synchronous machine (VSM).

This book belongs to Kitab Liaison (ocd1996@gmail.com) Copyright Elsevier 2023

The aim of VSM control is the emulation of a synchronous machine dynamics by a power converter, so that, from the power system point of view, the converter should be able to have very similar dynamics as a synchronous machine (Fig. 18.5). The major objectives of VSM control of power converters are as follows [32]:

- Providing virtual inertia to contribute to system frequency control.
- Enhancing the stability properties for connection to low-inertia grids and weak grids.
- Enabling stable operation with higher penetration of NSGs.
- Improving the frequency nadir (maximum frequency deviation) and the RoCoF in the system.

Mostly, the various approaches for VSM control are based on emulating the swing equation of a synchronous machine, which is shown in Fig. 18.6.

18.3.2 Concepts and fundamentals

The kinetic energy (E_r) of the rotating mass in a synchronous machine with the moment of inertia $J\left[kg \times m^2\right]$ and angular rotor speed $\omega_r\left[rad/s\right]$ is as follows:

$$E_r = \frac{1}{2} J \omega_r^2 \tag{18.1}$$

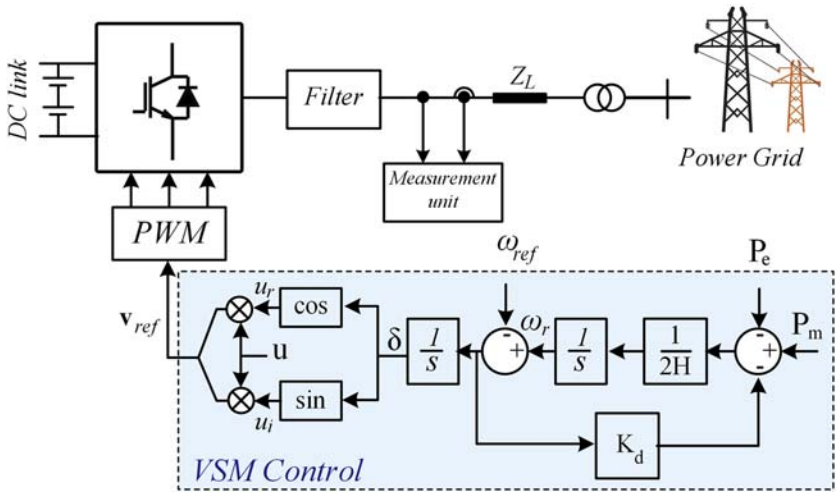

FIGURE 18.6 Virtual synchronous machine (VSM) control structure emulated from the dynamic model of a synchronous machine.

This book belongs to Kitab Liaison (ocd1996@gmail.com)
Copyright Elsevier 2023

The power, which accelerates the rotating mass, can be obtained by differentiating (18.1) as follows:

$$\frac{dE_r}{dt} = J\omega_r \frac{d\omega_r}{dt}. \tag{18.2}$$

If the variables are expressed in the per-unit system, and the angular speed varies slightly around the nominal angular synchronous frequency $\omega_{r_0}[rad/s]$, the first-order swing equation can be expressed as follows:

$$P_m - P_e = 2H\frac{d\omega_r}{dt} + P_D \tag{18.3}$$

$$H = \frac{J\omega_{r_0}^2}{2S_{Base}} \tag{18.4}$$

$$\frac{d\delta}{dt} = \omega_r - \omega_g \tag{18.5}$$

$$P_D = K_d(\omega_r - \omega_g) \tag{18.6}$$

where P_m is the prime mover mechanical power, P_e is the electrical power. The damping term $P_D = K_d(\omega_r - \omega_g)$ is used to emulate the effect of damper windings in the synchronous machine to suppress the grid frequency oscillations. Furthermore, ω_r, ω_g, and δ are the rotor angular speed, grid reference machine rotor angular speed, and the rotor angle, respectively. Finally, H $[s]$ is the inertia constant and S_{Base} $[VA]$ is the base rating of the machine. Note that in a practical case, ω_g (the speed of the reference machine) is not available. Thus, the damping term loop presented here is hard to realize without remote measurements, and a wide area control system [28].

By employing the control law in (18.3), the VSM control should enable the power converter to appear as a VSM, with a similar inertial response, in the grid. Fig. 18.6 shows the control schematic of VSM emulating the proposed swing Eq. (18.3).

18.4 VSM implementation

In order to evaluate the performance of the proposed control structure, a 50Hz, four-machine test system inspired by that of Ref. [33] is implemented in PowerFactory DIgSILENT. This is a 230 kV power grid containing four synchronous generators and two main loads in its original form. All the generators are equipped with the automatic voltage regulator, and G1 and G3 are equipped with hydrofrequency governors. Fig. 18.7 shows the electrical network of the test system.

This book belongs to Kitab Liaison (ocd1996@gmail.com) Copyright Elsevier 2023

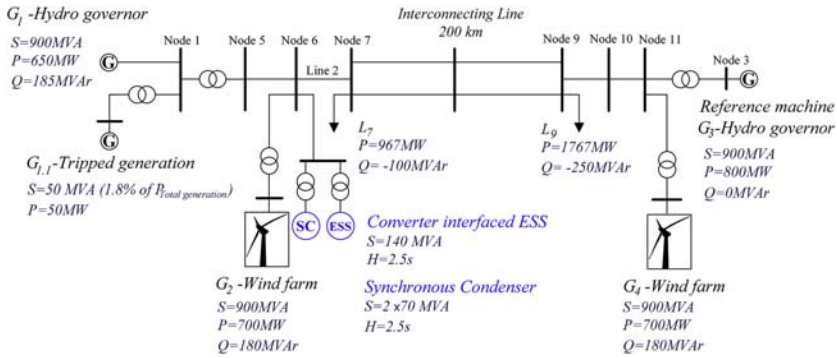

FIGURE 18.7 A four-machine test bench implemented in PowerFactory DIgSILENT, to illustrate inertia influence.

18.4.1 NSG penetration level

In the first study, the penetration level of NSGs is increased in order to analyze the system behavior. Generator 2 (G_2) and generator 4 (G_4) of the original model are replaced with wind turbine generators with the same power rating in three scenarios, without inertia emulation:

- Scenario 1: All the generators in the system are synchronous hydro-generators with hydroturbines.
- Scenario 2: 25% of the generators are replaced with NSG. (G_2 is replaced with a wind turbine generator with the same power rating.)
- Scenario 3: 50% of the generators are replaced with NSG. (G_2 and G_4 are replaced with wind turbine generators with the same power rating.)

As it is expected and shown in Fig. 18.8, when a generation trip ($G_{1.1}$) is applied, by increasing the penetration of NSGs, the RoCoF is increased, and also the maximum frequency deviation is increased.

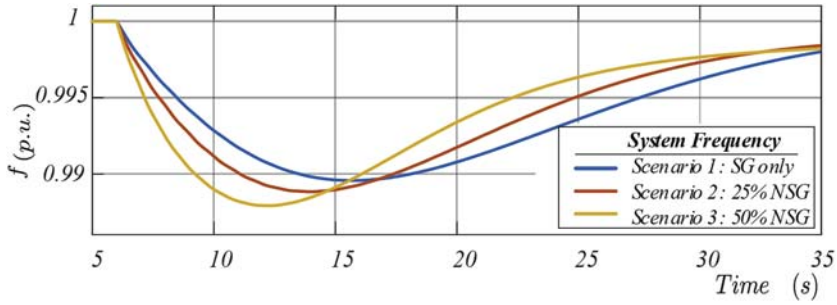

FIGURE 18.8 Effect of increasing the penetration of nonsynchronous generator.

This book belongs to Kitab Liaison (ocd1996@gmail.com)
Copyright Elsevier 2023

18.4.2 VSM performance

As it can be seen from Fig. 18.7, a 140 MVA synchronous condenser (SC) and a converter-interfaced energy storage system (ESS) with the same power rating are included at node 6 to be alternatively connected in different scenarios. SC is a synchronous machine where its rotating shaft spins freely. The SC is connected to the same node as the converter-interfaced ESS to serve as a benchmark for analyzing the behavior of a converter controlled by the VSM. As shown in Table 18.1, the SC and converter-interfaced ESS, controlled by the VSM, have same parameters. The studies are implemented by means of RMS, phasor-based simulation in DIgSILENT PowerFactory. The converter at node 6 is controlled by the proposed VSM approach with the inertia constant $H = 5$ like the SC. Therefore, it should have a similar dynamic behavior as the SC, which is connected to the same node. A generation trip at node 1 is applied for two cases, i.e., the SC is connected or the converter controlled by the VSM is connected. As depicted in Fig. 18.9, the converter controlled by the VSM has a very similar dynamic behavior as a synchronous machine. Therefore, from the power system point of view, the VSM control performance is validated.

18.4.3 Fault right through capability

It is important to note that in a controller based on the swing equation, the current is not controlled in the short time frame directly. However, the converter current needs to be limited, especially during a fault, in order to avoid overcurrent blocking of the converter [28,34]. Therefore, a current limitation controller should be implemented inside the VSM control. Fig. 18.10 shows

TABLE 18.1 Parameters of the virtual synchronous machine (VSM) controller and synchronous condenser benchmark.

Parameters	Synchronous condenser	Converter controlled by the VSM
S_n (MVA)	140	140
Inertia constant H (s)	2.5	2.5
Inductance L_c (p.u.)	0.25	0.25
Damping factor K_d	–	25
Current control loop bandwidth	–	20
Current limit (p.u.)	–	1.0

This book belongs to Kitab Liaison (ocd1996@gmail.com) Copyright Elsevier 2023

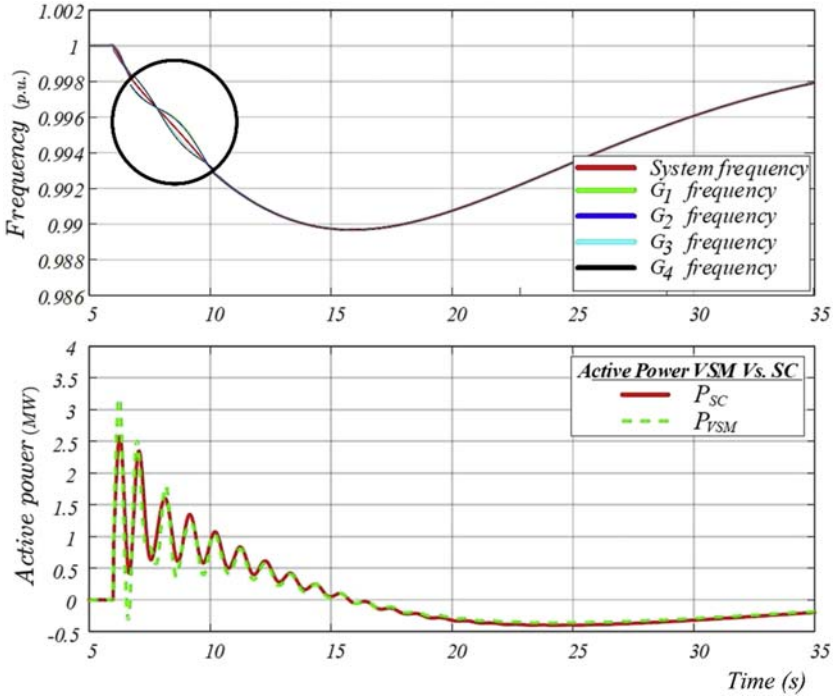

FIGURE 18.9 System frequency and the active output power of a synchronous condenser (P_{SC}) and a power converter (P_{VSM}) as the virtual synchronous machine (VSM).

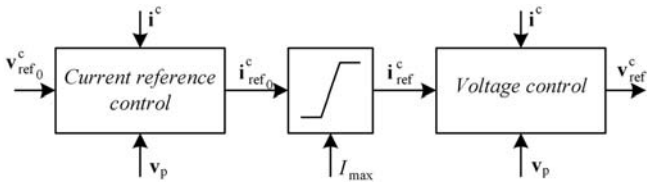

FIGURE 18.10 Current limitation control of voltage source converters proposed in Ref. [28].

the current limitation strategy proposed in Ref. [28]. In case that the converter current is above its limit (I_{max}), the desired voltage control law is defined as follows:

$$\mathbf{v}_{ref}^{c} = \alpha_c L_c \left(i_{ref}^{c} - i^{c}\right) + j\omega_1 L_c \mathbf{i}^{c} + \mathbf{v}_p \tag{18.7}$$

Here, α_c is the desired current control loop bandwidth, and i_{ref}^{c} stands for the converter inner current reference. i^c, L_c, and ω_1 stand for the converter current, the converter inductance, and the network angular frequency, respectively. The term $j\omega_1 L_c \mathbf{i}^c$ represents the feedback decoupling of the

This book belongs to Kitab Liaison (ocd1996@gmail.com) Copyright Elsevier 2023

voltage across the converter inductor and $\mathbf{v}_p$ is a feedforward of the point of common coupling voltage filtered through a low-pass filter. In normal operation, when the converter current is less than the current limit, $i^c_{ref_0} = i^c_{ref}$ and $\mathbf{v}^c_{ref_0} = \mathbf{v}^c_{ref}$. In this case, the reference current can be defined as follows:

$$i^c_{ref_0} = \frac{1}{\alpha_c L_c}\left(\mathbf{v}^c_{ref_0} - j\omega_1 L_c \mathbf{i}^c - \mathbf{v}_p\right) + \mathbf{i}^c \tag{18.8}$$

The current reference i^c_{ref} in (18.8) is an indication of the converter real current flow. During a fault, the current limitation is achieved automatically by limiting the magnitude of i^c_{ref} to the predefined maximum current (I_{max}).

In the next study, a three-phase to ground fault cleared without line disconnection at t = 6 s is applied in the middle of the line 2, between nodes 6 and 7, near the converter controlled by the VSM and SC, as shown in Fig. 18.7.

Fig. 18.11 shows the output voltage and current of the SC during the fault. As can be seen, the output current is larger than 2 p.u. The same fault is applied for the ESS/VSM without the current limitation controller. Fig. 18.12 shows the voltage and current of the ESS/VSM. As it is expected, a similar dynamic behavior as for the SC can be observed. However, for the converter, it is essential to respect the current limitation. Thus, the current limit control is activated for the same fault case, see Fig. 18.13. As it can be seen, during the fault, the current is limited by the VSM controller to 1 p.u.

18.5 Summary and future trend

The synchronous rotating inertia is the key parameter of power system stability. Increasing the penetration of NSGs, e.g., wind turbine, PV, and ESS, in

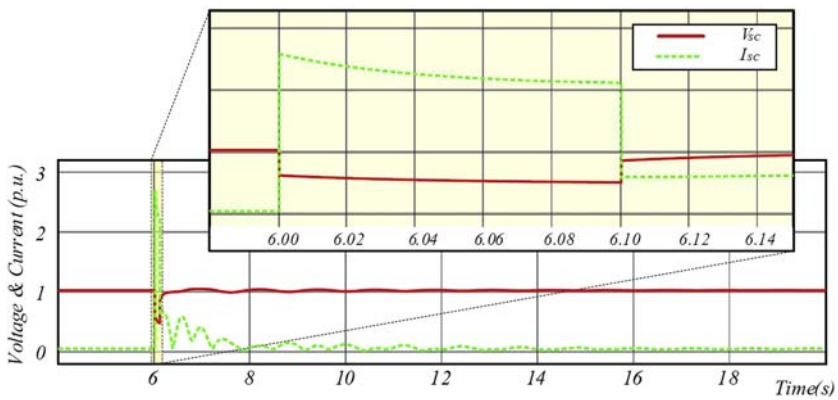

FIGURE 18.11 Voltage and current of the synchronous condenser during a 100-m three-phase to ground fault at line 2 in Fig. 18.7.

This book belongs to Kitab Liaison (ocd1996@gmail.com) Copyright Elsevier 2023

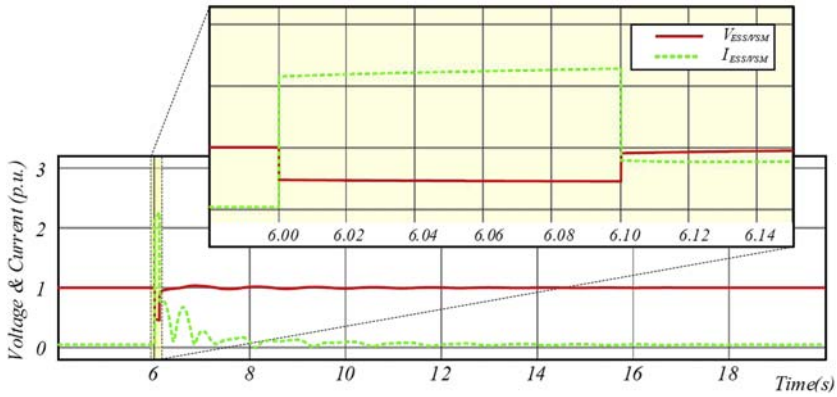

FIGURE 18.12 Voltage and current of converter controlled by virtual synchronous machine without current limitation during a 100-m three-phase to ground fault at the line 2, in Fig. 18.7.

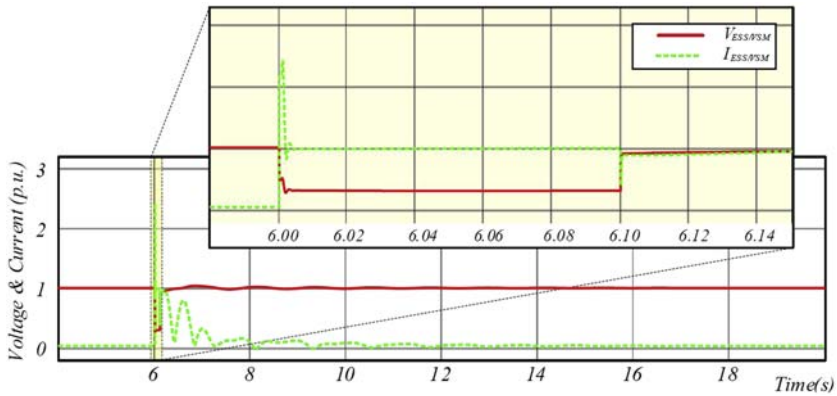

FIGURE 18.13 Voltage and current of converter controlled by virtual synchronous machine with the current limitation controller, during a 100-ms three-phase to ground fault at the line 2, in Fig. 18.7.

the power grids leads to some stability challenges due to the lack of rotating mass and kinetic inertia in the system. In this chapter, the effect of high penetration of renewables on power system stability is shown. Moreover, the recent low-inertia grid challenges in Europe and South Australia are discussed. Technically, in order to achieve 100% renewables, providing virtual inertia is a demand. The VSM is a promising solution to emulate the behavior of a synchronous machine and provide inertia virtually. In this chapter, the theoretical concept of VSM, as well as the control structure, is presented.

Furthermore, the VSM implementation in the power system is investigated, and some RMS simulation results are provided in a fault situation. Since in a

This book belongs to Kitab Liaison (ocd1996@gmail.com) Copyright Elsevier 2023

controller based on the swing equation, the current is not controlled in the short time frame directly, a current limitation controller has also been implemented in VSM and scrutinized in this chapter.

Although several aspects of the virtual operation of renewables are investigated in this chapter, there are still some open issues:

- Inertia estimation: Determining the system inertia is going to be crucial for the power system operators in the modern power grid with the high RES penetrations. Accurate inertia estimation will help the grid operators to set up a framework for planning and procuring the inertial services.
- Improvement of modeling and analysis: Although there are many of the challenges related to the control structure of converter-interfaced RESs, and their inertial responses have been highlighted in the recent publications, a lack of VSM modeling and implementation in power system−level studies is still observed.
- Storage system for virtual inertia: Typically, batteries, capacitors, and supercapacitors have been proposed as ESS for dynamic control of power converter−interfaced RESs. Coordination, price, lifetime, and reliability of the designed ESS should be examined.
- Coordination between VSM and synchronous machines: Standards related to overall power system performance, with higher penetration of RESs controlled by VSM, and their coordination, should comprehensively be analyzed.

References

[1] EPA. United Stated Environmental Protection Agency, Sources of Greenhouse Gas Emissions, Climate Change, 2015 [Online]. Available, http://www.epa.gov/climatechange/ghgemissions/sources/transportation.html. (Accessed 8 April 2020).

[2] Importance of Renewable Energy in the Fight against Climate Change, World Wildlife Magazine (WWF), 2015 [Online]. Available: https://www.worldwildlife.org/magazine/issues/summer-2015/articles/importance-of-renewable-energy-in-the-fight-against-climate-change–3. (Accessed 22 April 2020).

[3] European Commission, Energy Roadmap 2050, 2011.

[4] German commission proposes coal exit by 2038 | Clean Energy Wire. [Online]. Available: https://www.cleanenergywire.org/factsheets/german-commission-proposes-coal-exit-2038. (Accessed 08 April 2020).

[5] D. Lew, et al., Secrets of successful integration: operating experience with high levels of variable, inverter-based generation, IEEE Power Energy Mag. 17 (6) (2019) 24−34.

[6] International renewable energy agency (IRENA), Trends in Renewable Energy. [Online]. Available: https://www.irena.org/Statistics/View-Data-by-Topic/Capacity-and-Generation/Statistics-Time-Series. (Accessed 08 April 2020).

[7] Global Wind Energy Council, Global Wind Report 2019. [Online]. Available: https://gwec.net/global-wind-report-2019/. (Accessed 08 April 2020).

[8] ENTSO-E, High Penetration of Power Electronic Interfaced Power Sources, HPoPEIPS), 2017.

This book belongs to Kitab Liaison (ocd1996@gmail.com) Copyright Elsevier 2023

[9] B. Kroposki, et al., Achieving a 100% renewable grid: operating electric power systems with extremely high levels of variable renewable energy, IEEE Power Energy Mag. 15 (2) (2017) 61−73.

[10] F. Dorfler, S. Bolognani, J.W. Simpson-Porco, S. Grammatico, Distributed control and optimization for autonomous power grids, in: 2019 18th European Control Conference, ECC 2019, 2019, pp. 2436−2453.

[11] T. Ackermann, T. Prevost, V. Vittal, A.J. Roscoe, J. Matevosyan, N. Miller, Paving the way: a future without inertia is closer than you think, IEEE Power Energy Mag. 15 (6) (2017) 61−69.

[12] L. Zhang, H.P. Nee, L. Harnefors, Analysis of stability limitations of a VSC-HVDC link using power-synchronization control, IEEE Trans. Power Syst. 26 (3) (2011) 1326−1337.

[13] C. Li, I. Cvetkovic, R. Burgos, D. Boroyevich, C. Engineering, V. Tech, Assessment of virtual synchronous machine based control in grid-tied power converters, in: 2018 Int. Power Electron. Conf. (IPEC-Niigata 2018 -ECCE Asia), 2018, pp. 790−794.

[14] Y. Khayat, R. Heydari, et al., On the secondary control architectures of AC microgrids: an overview, IEEE Trans. Power Electron. 35 (6) (2020) 6482−6500.

[15] R. Heydari, T. Dragicevic, F. Blaabjerg, High-bandwidth secondary voltage and frequency control of VSC-Based AC microgrid, IEEE Trans. Power Electron. 34 (11) (2019) 11320−11331.

[16] L. M. Robbie Aherne, Operating High Variable, Renewable Generation Power Systems Lessons Learned from Ireland and Northern Ireland. [Online]. Available: https://cleanenergysolutions.org/training/high-variable-renewable-generation-power-systems-ireland. (Accessed 08 April 2020).

[17] AEMO, Update Report − Black System Event in South Australia on an Update to the Preliminary Operating Incident Report for the National Electricity Market, October 2016.

[18] dk Energinet, New Paths to the Energy of the Future Annual Report 2017, no. 28980671, 2017.

[19] G. Andersson, et al., Causes of the 2003 major grid blackouts in North America Europe, and recommended means to improve system dynamic performance, IEEE Trans. Power Syst. 20 (4) (2005) 1922−1928.

[20] Decommissioning of Nuclear Facilities: Germany's Experience, International Atomic Energy Agency, 2016 [Online]. Available: https://www.iaea.org/newscenter/news/decommissioning-of-nuclear-facilities-germanys-experience.

[21] J. Chen, T. O'Donnell, Parameter constraints for virtual synchronous generator considering stability, IEEE Trans. Power Syst. 34 (3) (2019) 2479−2481.

[22] F. Milano, F. Dorfler, G. Hug, D.J. Hill, G. Verbič, Foundations and challenges of low-inertia systems (Invited Paper), in: 20th Power Syst. Comput. Conf. PSCC 2018, 2018, pp. 1−25.

[23] B.J. Matevosyan, H. Urdal, S. Achilles, J. Macdowell, J.O. Sullivan, R. Quint, Grid-forming inverters: are they the key for high renewable penetration? IEEE Power Energy Mag. 17 (3) (2019) 89−98.

[24] J. Rocabert, A. Luna, F. Blaabjerg, Control of power converters in AC microgrids, IEEE Trans. Power Electron. 27 (11) (2012) 4734−4749.

[25] B.K. Poolla, D. Groß, F. Dörfler, Placement and implementation of grid-forming and grid-following virtual inertia and fast frequency response, IEEE Trans. Power Syst. 34 (4) (2019) 3035−3046.

This book belongs to Kitab Liaison (ocd1996@gmail.com) Copyright Elsevier 2023

[26] Z. Wang, F. Zhuo, H. Yi, J. Wu, F. Wang, Z. Zeng, Analysis of dynamic frequency performance among voltage-controlled inverters considering virtual inertia interaction in microgrid, IEEE Trans. Ind. Appl. 55 (4) (2019) 4135−4144.

[27] J. Fang, H. Li, Y. Tang, F. Blaabjerg, On the inertia of future more-electronics power systems, IEEE J. Emerg. Sel. Top. Power Electron. 7 (4) (2019) 2130−2146.

[28] R. Heydari, N. Johansson, L. Harnefors, F. Blaabjerg, A VSM converter controller implemented for RMS simulation studies of electrical power systems, in: 18th Wind Integration Workshop, 2019, pp. 1−6.

[29] H.P. Beck, R. Hesse, Virtual synchronous machine, in: 2007 9th International Conference on Electrical Power Quality and Utilisation, EPQU, 2007.

[30] Q.C. Zhong, G. Weiss, Synchronverters: inverters that mimic synchronous generators, IEEE Trans. Ind. Electron. 58 (4) (2011) 1259−1267.

[31] L. Zhang, L. Harnefors, H. Nee, Power-synchronization control of grid-connected voltage-source converters, IEEE Trans. Power Syst. 25 (2) (2010) 809−820.

[32] R. Heydari, M. Savaghebi, F. Blaabjerg, Fast frequency control of low-inertia hybrid grid utilizing extended virtual synchronous machine, in: Power Electron. Drive Syst. Technol. Conf. (PEDSTC 2020), 2020, pp. 1−5.

[33] P. Kundur, Power System Stability and Control, McGraw Hill, 1998.

[34] P. Control, L. Zhang, L. Harnefors, S. Member, H. Nee, S. Member, Interconnection of two very weak AC systems by VSC-HVDC links using, IEEE Trans. Power Syst. 26 (1) (2011) 344−355.

This book belongs to Kitab Liaison (ocd1996@gmail.com) Copyright Elsevier 2023

Chapter 19

Virtual inertia emulating in power electronic–based power systems

Yousef Khayat[1], Mobin Naderi[1], Hassan Bevrani[1], Frede Blaabjerg[2]
[1]*University of Kurdistan, Sanandaj, Kurdistan, Iran;* [2]*Department of Energy Technology, Aalborg University, Aalborg, Denmark*

19.1 Introduction

The concept of virtual inertia is adopted from the moment of inertia of synchronous generator (SG) rotating masses operating in a power system. The conventional power systems profit from the inertial function of numerous existing SGs to solve or improve the frequency challenges, e.g., low damping and high nadir due to load/generation disturbances. However, the modern power systems are becoming penetrated by a large number of the inertia-less power electronic–interfaced distributed energy resources (DERs) while typically are voltage source converters with a DC link. Hence, the rotational DER portion decreases impressively and the power system frequency experiences more intensive changes due to disturbances than the conventional SG-dominated power systems. In order to solve the low-inertia challenges of the power electronic–based power systems, the concept of virtual inertia is introduced, which is realized by applying a control function on the power electronic–interfaced DERs to mimic the SG inertial dynamics and to provide the inertia, virtually. The main source of the virtual inertia is the short-term stored energy in the DC link of the DER power converters, which should be injected to the AC side according to the virtual inertia control objective. In fact, the DER power converters are controlled to surmount the low-inertia challenges including high-frequency nadir and high rate of change of frequency (RoCoF), low frequency/power oscillation damping, frequency instability, severe changes triggering protection devices mistakenly, and all key functions for power system operation, as mentioned before in Chapter 17.

The idea of emulating inertia dynamics for power electronic–interfaced DERs has been presented in different control structures using many control methods. Firstly, the virtual synchronous machine is introduced to allow a grid

Control of Power Electronic Converters and Systems. https://doi.org/10.1016/B978-0-12-819432-4.00019-6
Copyright © 2021 Elsevier Ltd. All rights reserved.

This book belongs to Kitab Liaison (ocd1996@gmail.com) Copyright Elsevier 2023

compatible integration of DERs to be electromechanical SGs [11]. The idea is presented as a solution for injecting the virtual inertia by the inverter-based DERs in the form of virtual synchronous generator (VSG) [1], and it has developed extensively until now [2,3]. In Ref. [4], an internal synchronization mechanism has been proposed for the grid-connecting voltage source converters, where the synchronous machine dynamics is mimicked. Finally, the grid-connected operation of an inverter with the ideal DC link is realized by emulating the SG dynamics entitled Synchronverter [5], which is developed employing the nonlinear stabilizer [6], mimicking a synchronous condenser [7], and improving the dynamic response [8].

Among the virtual inertia control structures, the VSG is more taken into account and developed. The VSG-based grid-supporting DERs are allowed to be some active components to support the frequency dynamics of the microgrids [9]. By adjusting the VSG inertia and/or damping coefficient, the output power oscillations and the overall VSG behavior can be improved significantly, which is demonstrated by small-signal modeling and sensitivity analysis [10,11]. A virtual capacitor control to enhance the reactive power sharing in VSG-based MGs in Ref. [12] and an adaptive linear quadratic regulator—based VSG in Ref. [13] to improve the inertial response of the system, have also been presented. In order to minimize the frequency deviation and output power oscillation of the VSG, a self-adaptive VSG control method based on RoCoF [14] and a self-tuning—based algorithm [15] have been employed to continuously optimize the virtual inertia among predefined amounts of inertia moment and damping coefficient. Similar methods are addressed in Refs. [16,17], where different values of the parameters have been employed to improve the frequency response. The virtual inertia response is improved by tuning droop gain in Ref. [18,19]. In Ref. [20], a fuzzy control method is used to improve the frequency response of a wind turbine system, which is developed for islanded and grid-connected microgrids in Ref. [3,21], and at the same time emulate virtual inertia.

The rest of this chapter is organized as follows: Section 19.2 basically deals with the inertia concept. Inertia challenges of the power electronic—based power systems are introduced in Section 19.3. In Section 19.4, the virtual inertia is presented as a fundamental solution. Finally, a case study is addressed in Section 19.5 to show the benefits of the virtual inertia using an adaptive control method.

19.2 Inertia concept

Inertia is the property of an object to continue its existing rest state or uniform motion into a straight line, unless its state is changed by an external force/disturbance. In fact, inertia is the object resistance to its velocity changes. It can be simply said that the larger inertia of the object leads to a slower velocity changes. The inertia of an object corresponds to its mass. It is easy to know

This book belongs to Kitab Liaison (ocd1996@gmail.com) Copyright Elsevier 2023

that objects of higher mass resist against changes in motion/velocity more than objects of lower mass. In other words, heavier objects have larger inertia.

The moment of inertia or rotational inertia can be considered as the required torque for a desired angular acceleration similar to the object mass, which determines the force required for a desired linear acceleration. Considering T as the torque applied to a rotatable mass and α as the angular acceleration, the moment of inertia J is obtained as follows:

$$T = J\alpha. \tag{19.1}$$

For a given α, a larger moment of inertia causes a higher torque. The moment of inertia is also known as the dual of mass in the angular motion. It is realized for a differential mass dm rotating at a perpendicular distance r from the rotation axis as follows:

$$J = \int r^2 dm. \tag{19.2}$$

Generally, it is obvious that a larger mass results in a higher inertia.

The SGs as the backbone of the traditional power systems benefit from the concept of inertia. The SG rotor with other coupling masses, especially turbines, provides an inertia to resist the frequency (electrical velocity) changes, i.e., acceleration/deceleration caused by power system disturbances, e.g., faults and load changes. Eq. (19.1) shows such a resistance, where T is the accelerating torque as follows:

$$T = T_m - T_e, \tag{19.3}$$

and α is the angular acceleration as follows:

$$\alpha = \frac{d\omega}{dt}. \tag{19.4}$$

T_m is the mechanical torque rotating the SG rotor to produce electromotive force, T_e is the electrical restraining torque against T_m, and ω is the angular frequency or mechanical rotor speed. Substituting Eqs. (19.3) and (19.4) into Eq. (19.1), the well-known swing equation can be found as follows:

$$J\frac{d\omega}{dt} = T_m - T_e. \tag{19.5}$$

Without any disturbance and in the steady-state condition, T_e equals to T_m. Thus, $d\omega/dt$ equals to zero and the frequency is remained constant. During power disturbances, T_e, which equals to P_e/ω, starts to change immediately. However, T_m related to the mechanical and control instruments cannot be influenced immediately, and it varies with a delay around a few seconds according to the rotating mass amount and controller delays. Therefore, in the first moments of the disturbance, the difference between T_e and T_m causes frequency variations. According to the disturbance size, a damped oscillation,

This book belongs to Kitab Liaison (ocd1996@gmail.com) Copyright Elsevier 2023

constant oscillation, or instability may occur. Obviously, for a given $T_m - T_e$, a larger amount of inertia J leads to a lower RoCoF ($d\omega/dt$). Moreover, considering ω_0 as the predisturbance frequency, and integrating Eq. (19.5), one can find the frequency ω as follows:

$$\omega = \omega_0 + \frac{1}{J}\int_{t_0}^{t}(T_m - T_e)dt, \tag{19.6}$$

where the right term can be considered as the overshoot/undershoot of the transient response. Therefore, a larger amount of inertia results in a lower frequency overshoot/undershoot.

The swing equation is generalized to the power system load-generation balance [22,23]. For a power system including a number of SGs and loads interconnected through a power network, the electrical torque can be considered as follows:

$$T_e = T_{eS} + T_{eD}, \tag{19.7}$$

where T_{eS} is the synchronizing torque and T_{eD} is the damping torque, generally provided by the load damping and SG rotor damping windings. T_{eD} can be considered as a coefficient of the frequency changes given as follows:

$$T_{eD} = K_{TD}\Delta\omega, \tag{19.8}$$

where K_{TD} is the damping torque coefficient. The synchronizing torque can also be considered as a coefficient of the rotor angle changes $\Delta\delta$. Substituting Eq. (19.8) into Eq. (19.5), the swing equation is rewritten as follows:

$$J\frac{d\omega}{dt} = T_m - T_{eS} - K_{TD}\Delta\omega. \tag{19.9}$$

Since the active power is a more common variable in the power system studies, Eq. (19.9) is desired to be rewritten as follows considering $P = T\omega$:

$$J\omega\frac{d\omega}{dt} = P_m - P_{eS} - K_D\Delta\omega, \tag{19.10}$$

where P_m and P_{eS} are the mechanical power and synchronizing electrical power of the power system, and K_D is known as the damping coefficient. Eq. (19.10) is a nonlinear model of the power system swing equation due to the term $\omega(d\omega/dt)$. Nevertheless, in the literature [24], the frequency variation is considered as being low enough as for small disturbances such that the ω multiplied by $d\omega/dt$ is considered constant as ω_0. Hence, a linear perturbed form of the swing equation is achieved as follows:

$$J\omega_0\frac{d\Delta\omega}{dt} = P_m - P_{eS} - K_D\Delta\omega, \tag{19.11}$$

where P_m-P_{eS} can be considered as the network power changes ΔP independent of the frequency changes. Hence, the linear frequency model of

This book belongs to Kitab Liaison (ocd1996@gmail.com) Copyright Elsevier 2023

the power system load-generation balance in the Laplace domain is calculated as follows:

$$\Delta\omega = \frac{1}{J\omega_0 s + K_D}\Delta P. \tag{19.12}$$

In this linear model, the inverse relationship between the frequency changes and the moment of inertia is also obvious. Furthermore, the s coefficient of J means its different influence on the frequency changes and RoCoF proportion to the frequency value of the disturbances. In fact, the moment of inertia J has a larger impact for larger frequencies, i.e., the term $J\omega_0 s$ is larger. Since the high-frequency disturbances occur in transients, the moment of inertia impacts on the transients more than the steady state. RoCoF and overshoot/undershoot (frequency nadir) are the most common indices to recognize the inertia influence on the transients, which were already explained. The following example shows these facts for a simple typical swing equation.

Example 1. Consider a single SG power system with $K_D = 300$ W s/rad affected by the main damping sources such as RL loads.

(a) Compare nonlinear and linear models of the swing equation for $J = 2$ W s^2/rad and $\Delta P = 2000u(t) - 2000e^{-2(t-10)}u(t-10)$ W.

(b) Investigate the impact of inertia amount on the transients of the swing equation for $J_1 = 0$, $J_2 = 0.5$, $J_3 = 1$, $J_4 = 2$, and $J_5 = 4$ W s^2/rad.

Solution. Fig. 19.1A shows the power changes, which is a constant step before $t = 10$ s and is suddenly reduced at $t = 10$ s, then it is exponentially returned back to zero. Fig. 19.1B shows the frequency of both nonlinear and linear models of the swing equation, i.e., Eqs. (19.10) and (19.12). The frequency error of the linear model calculated as $E_\omega = 100 \times (\omega_{NL} - \omega_L)/\ \omega_{NL}$ is shown in Fig. 19.1C, which can be absolutely negligible for both power changes at $t = 0$ s and $t = 10$ s. The frequency error is investigated for larger power changes as 10 kW. The largest frequency error is obtained as 0.1%. Therefore, the linear model is validated comparing the nonlinear model, and it is creditable for small-signal studies.

Fig. 19.2 shows the angular frequency for different moments of inertia when the damping coefficient and the input are permanent in the all situations. $J_1 = 0$ is equivalent to a power system without rotating generation units, e.g., a power electronic−based microgrid. The transients of the power changes completely appear in the frequency dynamics. Such an inertia-less system suffers from the very large RoCoF and frequency overshoot/undershoot, which may trigger protection relays by mistake for small disturbances and noncritical situations, and subsequently cause frequency instability. As shown in Fig. 19.2, the RoCoF is as 13.33, 6.15, 2.88, and 1.78 rad/s^2 for $J_1 = 0$, $J_2 = 0.5$, $J_3 = 1$, $J_4 = 2$, and $J_5 = 4$, respectively. Therefore, in an inertia-less power electronic−based power system, one can decrease the RoCoF by designing the controller of power electronic devices to provide a virtual

This book belongs to Kitab Liaison (ocd1996@gmail.com) Copyright Elsevier 2023

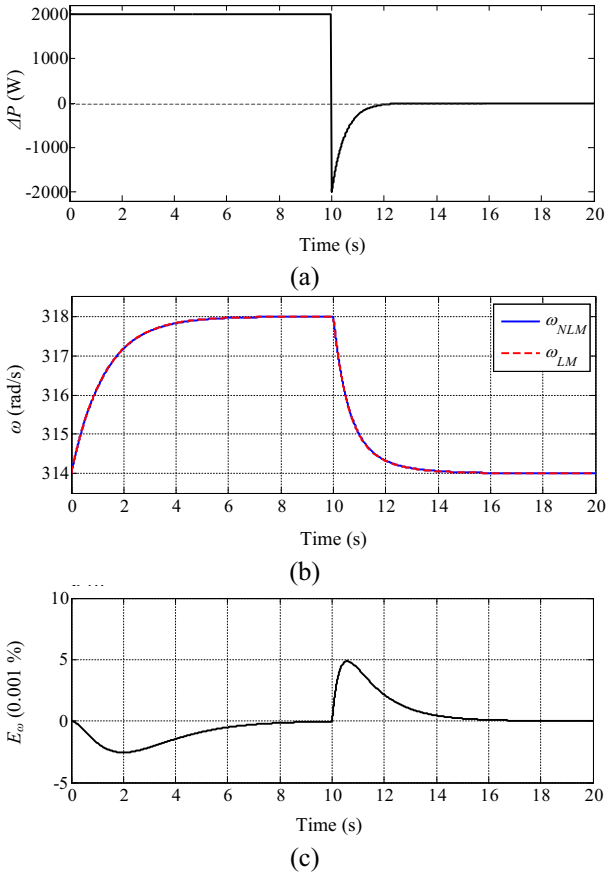

FIGURE 19.1 Comparison between linear and nonlinear models of the swing equation. (A) Active power changes, (B) angular frequency changes, (C) relative frequency error.

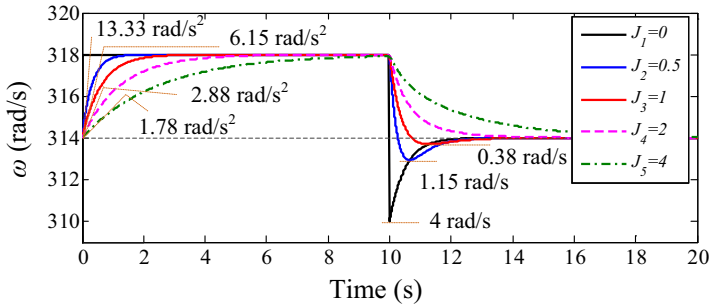

FIGURE 19.2 The impact of inertia amount on the transients of the nonlinear swing equation for $J_1 = 0$, $J_2 = 0.5$, $J_3 = 1$, $J_4 = 2$, and $J_5 = 4$.

This book belongs to Kitab Liaison (ocd1996@gmail.com) Copyright Elsevier 2023

inertia. Obviously, a larger (virtual) moment of inertia leads to a lower RoCoF. The second span of the frequency response from $t = 10$ s is against to the transient power change. For this span, the frequency undershoot/nadir is shown in Fig. 19.2, which decreases when the moment of inertia is reduced. It was already discussed based on Eq. (19.6). Both low RoCoF and low frequency nadir are vital during transients for power systems. However, they cannot be achieved for inertia-less power electronic−based power systems without applying virtual inertia control algorithms and schemes.

19.3 Inertia challenges of power electronic−based power systems

Installing renewable energy sources like wind and solar power units to power systems is becoming bulky, such that the total installed capacity of wind energy was reached 592 GW by 2018, and it is expected to be added more than 300 GW until 2023 [41]. The same growth for solar power through PV technologies are expected, since by the end of 2018 the total installed PV capacity was reached 509 GW [42]. These show a transition and an evolution for the energy paradigms, which needs a comprehensive remodeling and dynamic analysis of the modern power electronic−dominated power systems in a multi-timescale manner.

Transition from rotating mass−based SGs toward power electronic interfaces, which are employed to converse renewable energies in a more controllable way, is becoming more and more important and challengeable. This transition leads to a power electronic−dominant power system with no or few rotating mass−based SGs. As mentioned before, it leads to a low-inertia power electronic−based power system, which presents a stochastic and time-dependent inertial feature as they are weather dependent. The inertial features for these systems are expected to be a function of the expected wind power, solar power, and ESS's state of charge among all. It means that the system's inertia is going to be a stochastic variable and mainly dependent on weather conditions. In addition, sometimes, situations may be emerged in which a required inertial support or an acceptable inertial response cannot be provided properly, as discussed in technical reports [25−27]. Possible solutions to provide a sufficient level to satisfy the inertial requirements are needed not only remodeling through a time-dependent stochastic manner but also considering the prime mover's type and capacity regarding to the employed device, its energy form, and its possible costs/limitations.

Self-synchronization of SGs through the grid, their kinetic energy as safeguard against grid-side disturbance, and their well-known dynamics and control is going to be replaced with no inherent synchronization through the grid and no (a sufficient) energy storage as inertial support of power electronic interfaces. In confront, inertial emulation in power electronic−based power systems has not been matured enough. Some possible forms and techniques to emulate the inertial response are summed up in Table 19.1.

This book belongs to Kitab Liaison (ocd1996@gmail.com) Copyright Elsevier 2023

TABLE 19.1 Inertia emulating methods in power electronic–based power systems.

Emerging technology	Inertial type	Being a function of	Energy form	Main challenges
Energy storages	ESS′ capacity and charge and discharge rate	ESS′ capacity and SoC	Electrical	Costly and need appropriate planning and control studies.
Wind generation	Rotating mass (depending to the type of wind turbine)	The mass, speed, and shape of the turbine's rotor, and the MPP	Kinetic	Based on the wind turbine types the emulation complication changes. For example, for a Type IV wind turbine, inertial emulation needs more complicated control approach regarding a Type I wind turbine and an MPP algorithm.
Solar generation	Adjusting the operating point on the voltage –power curve	MPP	Electrical	Coordinated control for ESS and DC-link capacitor for the inertial provision, balancing the PV output power (by an MPP).

In addition, Table 19.2 sums up technical aspects to be considered for inertial proposes in both the planning and operating steps. These issues can be employed to find a better solution for concerns like which storage solution is better for (inductive/resistive) weak and very weak grids, how much capacity is needed for inertial support? What is the dynamic effect of ESSs on the inertial response during contingencies? How can designers find the best position of ESSs for inertial purposes? Which required control and coordination of ESSs can be done for inertial support?

A number of control solutions for different types of grid-connected systems are given in Table 19.3. Possible ways to emulate the virtual inertia for grid-feeding (in electromagnetic timescale) and grid-supporting and grid-forming (in electromechanical timescale) converters are further summarized.

This book belongs to Kitab Liaison (ocd1996@gmail.com) Copyright Elsevier 2023

TABLE 19.2 Challenges for inertia emulating in power electronic–based power systems.

Planning challenges	Cost evaluation	Capital costs, repair and maintenance costs, power losses [28]
	ESS type	Fly-wheels, supercapacitors, Li-Ion batteries, etc. [29]
	Sizing issues	Arbitrary, simulation based, probabilistic based [30,31]
	Market design	Considering RoCoF and nadir constraints for frequency control in market designs [32,33]
	Placement considerations	Power limit of converters, SoC, and line capacity constraints [34]
Control challenges	Adaptive and robust manners [14–16]	
	Time-delay considerations [35]	
	Saturation drawbacks for power injection in inner loops [36]	

TABLE 19.3 Control solutions for inertia emulation.

Grid-tied type	Operation mode	Inertia realization
Grid feeding	Current source converters	Viable by mapping the PLL such as swing equation [37] and [44]
Grid supporting	Synchronous condensers	Second-order nonlinear swing [38]
Grid forming	*First orders:* Power synchronization control [4], droop control based [39], etc.	Viable by augmenting a low-pass filter
	Second orders: VSG, synchronous power control [40], synchronverters [5], etc.	Second-order linear swing equation

19.4 Adaptive inertia for grid-connected VSGs

The circuit topology of a grid-connected VSG with associated setup equipment is shown in Fig. 19.3. As it can be seen, a three-phase inverter converses the DC-side power to the AC side, like a Type IV wind turbine system. An ideal voltage source in series with the impedance Z_g is considered as the grid's model. An LCL filter is incorporated to reduce the switching ripples of the voltage and currents of the converter. Current control loop, as the first control

This book belongs to Kitab Liaison (ocd1996@gmail.com) Copyright Elsevier 2023

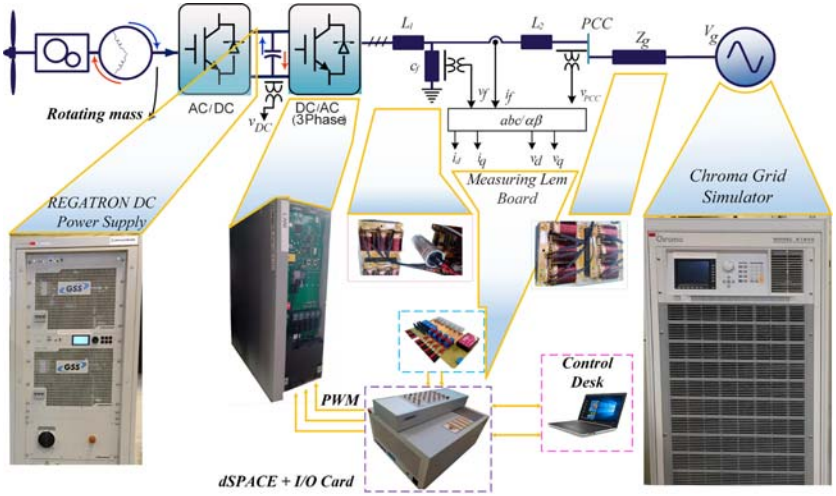

FIGURE 19.3 The overall system of a grid-forming grid-tied virtual synchronous generator connected to an external Thevenin modeled grid (circuit diagram and setup equipment).

loop, tracks the reference currents generated by a virtual impedance loop. Moreover, it provides also fault ride-through capability by limiting the converter current during transients. The virtual impedance loop, which is an emulation of the SG's stator dynamics, is also employed to generate the reference currents, and limit the inrush fault currents as well [43].

19.4.1 VSG principle

Mechanical features of the SG rotor is emulated through the rotor inertia and damping behavior by forming the active power balance and the virtual rotor angle correlation in the active power loop. In the same way, reactive power loop tunes the voltage amplitude of the VSG. A control block diagram for a typical VSG is shown in Fig. 19.4. According to the active and reactive power set-points P_{set} and Q_{set}, the governor and droop controllers adjust the active and reactive power references for the active and reactive power loops, as like as the governor and automatic voltage regulator (AVR) units are doing, respectively. For instance, the active power loop adjusts the frequency, based on the active power changes from the droop controller with a defined moment of inertia and a damping coefficient.

The $Q - V_{pcc}$ AVR and $P - \omega_{vsg}$ governor droops can be expressed as follows:

$$\begin{aligned} P^* &= P_{set} + (\omega_0 - \omega_{vsg})k_{gov}, \\ Q^* &= Q_{set} + (E_0 - V_{pcc})k_{avr}, \end{aligned} \tag{19.13}$$

where ω_0 and E_0 are the nominal frequency and voltage amplitude, respectively. ω_{vsg} is the generated virtual frequency by the active power loop, V_{pcc} is

This book belongs to Kitab Liaison (ocd1996@gmail.com) Copyright Elsevier 2023

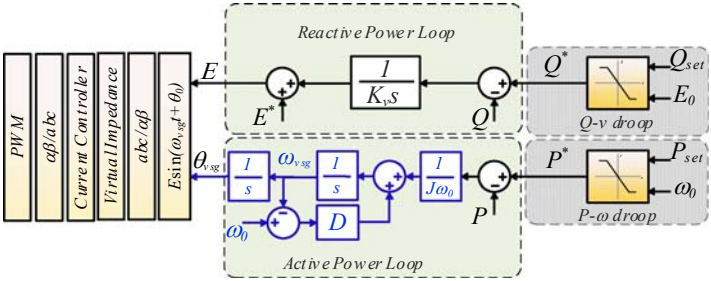

FIGURE 19.4 Control block diagram of the studied virtual synchronous generator implemented in the system in Fig. 19.3.

the root mean square value of the PCC voltage, and k_{gov}, k_{avr} are the constant droop gains for the governor and the AVR loops, respectively. The governor and AVR droop gains are calculated by considering the operational constraints as

$$k_{gov} = \frac{P_{\max}}{\frac{P - droop\%}{100} \times \omega_0}, \quad k_{avr} = \frac{Q_{\max}}{\frac{Q - droop\%}{100} \times E_0}, \tag{19.14}$$

where $P{-}droop\%$ and $Q{-}droop\%$ are constant droop rates. In the active power control loop, the swing equation, which describes the electromechanical dynamics of an SG, can be realized for a grid-connected VSG as

$$J\frac{d^2 q_{vsg}}{dt^2} = (T^* - T_{em}) - D(w_{vsg} - w_0), \tag{19.15}$$

where J stands for the virtual inertia, D denotes the damping constant, $T^* = P^*/\omega_0$ means the governor torque, and $T_{em} = P_e/\omega_0$ is the electromechanical torque. In the same way, the reactive power control loop dynamics is implemented as

$$K_v\frac{dE}{dt} = (Q_s - Q_e) - k_{avr}(V_{pcc} - E_0), \tag{19.16}$$

where K_v is the integrator gain for the voltage control loop. P_e and Q_e stand for the active and reactive powers transferred from the VSG toward the grid side, which can be expressed as

$$\begin{aligned} P_e &= E^2G + EV_gB\sin\delta - EV_gG\cos\delta, \\ Q_e &= E^2B - EV_gB\cos\delta - EV_gG\sin\delta, \end{aligned} \tag{19.17}$$

where $G = r_t/\left(r_t^2 + x_t^2\right)$, and $B = x_t/\left(r_t^2 + x_t^2\right)$. The x_t and r_t are the total inductance and resistance of the connection impedance between the VSG and the grid side, respectively.

19.4.2 Adaptive inertia

The value of the virtual inertia J together with the damping constant D determines the time constant of the VSG unit. How to select the proper values for

This book belongs to Kitab Liaison (ocd1996@gmail.com) Copyright Elsevier 2023

them is a challenging issue without a straightforward routine for the weak grids. Mimicking a synchronous machine, J can be described as

$$J = \frac{2HS_{base}}{\omega_0^2}, \tag{19.18}$$

where H is the machine inertia constant based on second, S_{base} is the machine base power, and ω_0 is the nominal frequency of the system. The parameter H states that for which period of time the machine is able to inject its nominal power toward the grid based merely on the stored energy in the rotating mass. The higher H results in a slower response but smaller frequency deviation after a change or disturbance. However, it depends on the machine size and power, for a typical SG, H varies between 2 and 10 s.

In addition to grid-forming VSGs with a constant value for the moment of inertia, alternating inertia based on a simple bang-bang approach can be proposed. To this end, considering the power angle curve shown in Fig. 19.5, with its initial operating point α_0. After a disturbance in the system, the operating point moves along the curve between α_1 and α_3. The machine mode during each segment of the curve has been summarized in Table 19.4, which shows the acceleration or deceleration mode. From Eq. (19.15), it can be concluded that the rate of acceleration or deceleration $\frac{d\omega}{dt}$ has a reverse relation with J, i.e., $\frac{d\omega}{dt} \propto \frac{1}{J}$. According to this, selecting a large value for J during the acceleration modes, and a small value during deceleration modes, is recommended [16]. However, in this chapter, inspired from the alternative based bang-bang inertia, we have employed a weighting-based alternative inertia as

$$J = J_0 + J_1 \cdot \mathrm{sgn}(\Delta\omega) \cdot \mathrm{sgn}\left(\frac{d\omega}{dt}\right) \cdot k \cdot (\omega - \omega_0)^2, \tag{19.19}$$

where multiplication of $\mathrm{sgn}(\Delta\omega) \cdot \mathrm{sgn}\left(\frac{d\omega}{dt}\right)$ shows the acceleration or deceleration mode, and the weighting factor k shows the effective weighting gain for correcting the moment of the inertia J for smaller deviation.

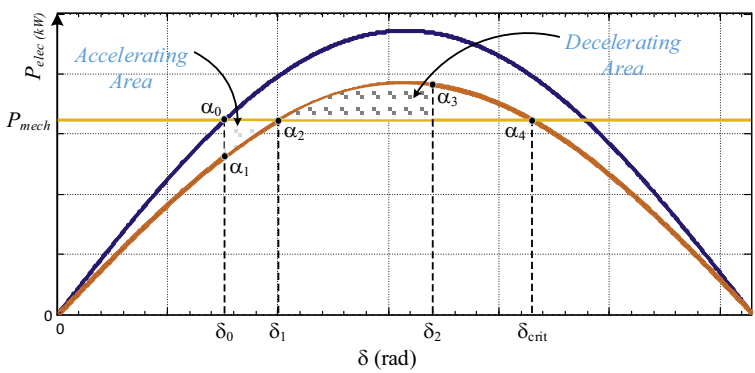

FIGURE 19.5 Power-angle curve of a typical synchronous generator to detect acceleration and deceleration modes: blue (black in print version) curve for before disturbance, and orange (gray in print version) curve for during disturbance.

This book belongs to Kitab Liaison (ocd1996@gmail.com) Copyright Elsevier 2023

TABLE 19.4 Alternative J determining for different machine modes illustrated in Fig. 19.5.

Segment	sgn($\Delta\omega$)	sgn($\frac{d\omega}{dt}$)	Mode	Alternative J
$\alpha_1-\alpha_2$	+	+	Accelerating	Big *J*
$\alpha_2-\alpha_3$	+	−	Decelerating	Small *J*
$\alpha_3-\alpha_2$	−	−	Accelerating	Big *J*
$\alpha_2-\alpha_1$	−	+	Decelerating	Small *J*

19.5 Simulation and experimental results

In this section, both simulation and experimental results are presented to demonstrate the proposed adaptive inertia control method of the VSG. A comparison with the existing methods is also given.

19.5.1 Simulation results

Simulations based on Simulink models in Matlab software are performed to evaluate the proposed strategy for the case study which its single line diagram is shown in Fig. 19.3. A Type IV wind turbine configuration consisting of an SG using a back to back converter interfaced with the grid through an LCL filter has been considered. Parameters used for the simulation and experimental verification of the system are shown in Table 19.5. As the turbine-side converter is tightly regulated with its independent control objectives and has been separated by a DC link, the grid-side converter can be considered as a decoupled system. Therefore, only a grid-side converter with a constant

TABLE 19.5 Test system parameters for the control technique shown in Fig. 19.4.

Parameter	Value	p.u.	Parameter	Value	p.u.
P_{set}	1.3 kW	1.0	Q_{set}	0	0.0
E_0	110 V	1.0	L_1, L_2	3 mH	0.105
V_g	110 V	1.0	C_f	10 μF	35.44
ω_0	314 rad/s	1.0	Zg	$j\omega_g 0.01\ \Omega$	0.37
k_{gov}	$P_{set}/0.06\omega_0$ W.s/rad	0.06	k_{avr}	$Q_{max}/0.04V_g$ Var/v	0.04
J	6 kg m^2		D	10 rad/s.W	

This book belongs to Kitab Liaison (ocd1996@gmail.com) Copyright Elsevier 2023

DC-voltage source is considered for the analysis and some comparisons are performed throughout this section.

The proposed adaptive inertia is compared to the constant inertia, which represents a comprehensive and implementable inertia response for a grid-forming VSG converter during fault conditions. To assess the effect of the inertia control on the stability of the studied systems, a symmetrical three-phase voltage sag which reduces 10% nominal voltage magnitude and the duration of 0.15 s was applied from the grid side, and the performance of the system is analyzed.

The reference power and damping coefficient of the VSG were 1 p.u. and 10 rad/s.W, respectively, and a fixed inertia factor of 6 kg m^2 is applied. Fig. 19.6 shows the PCC voltages, three-phase injected currents, active and reactive powers, the fixed moment of the inertia $J = 6$ kg m^2, and the VSG's frequency. The three-phase currents are limited to 20% more than their rated value 1 p.u. during grid faults where the converter should be saturated in order to be in a safe operation. During the voltage sag, the grid-forming converters show of course their grid supporting feature by injecting the reactive power to

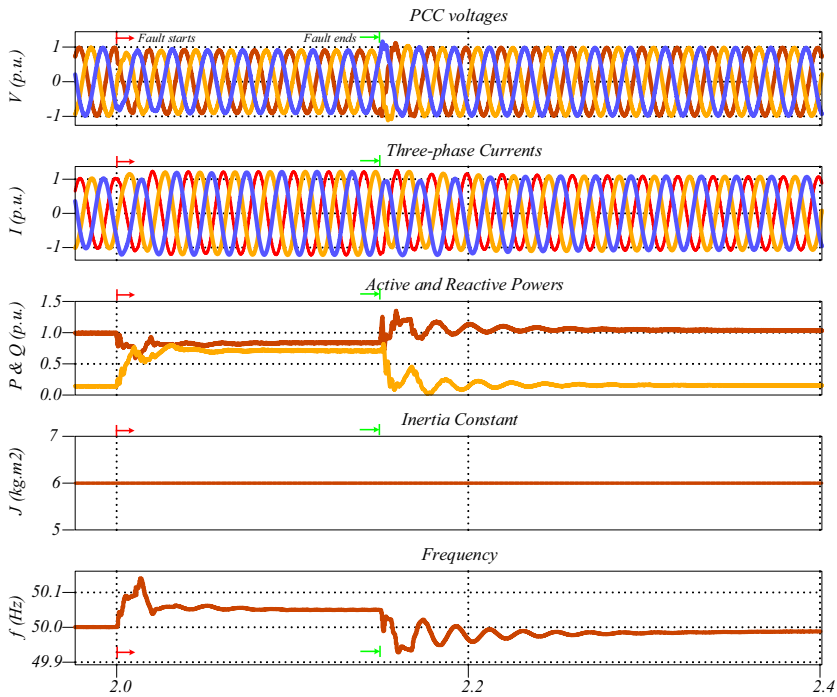

FIGURE 19.6 PCC voltages, three-phase currents, active and reactive powers, constant moment of inertia of VSG with fixed $J = 6$ kg m^2, and frequency waveforms during a grid-side fault to the system shown in Fig. 19.3.

This book belongs to Kitab Liaison (ocd1996@gmail.com) Copyright Elsevier 2023

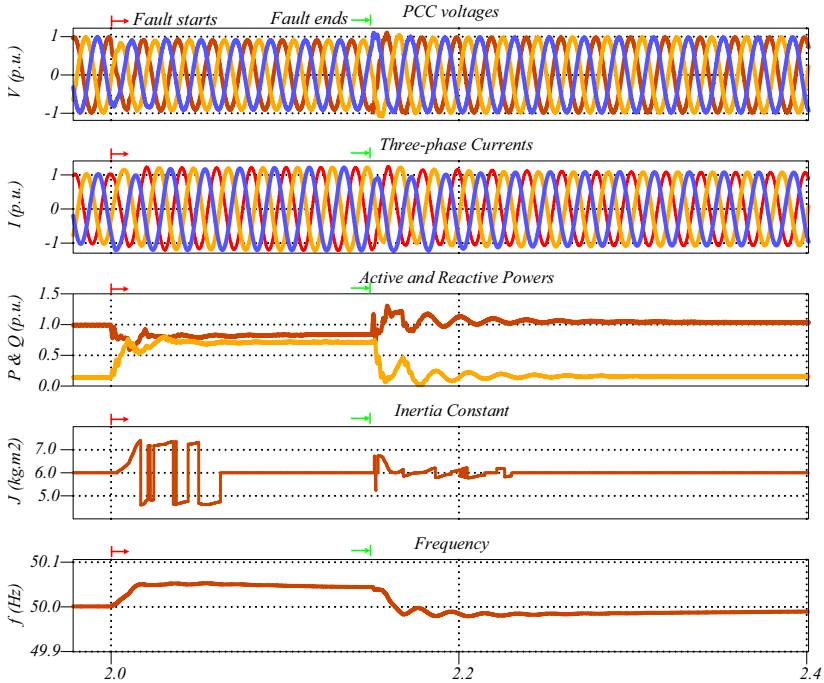

FIGURE 19.7 PCC voltages, three-phase currents, active and reactive powers, where the adaptive moment of inertia of virtual synchronous generator is a weighting function of frequency error, and frequency waveforms during a grid-side fault for the system shown in Fig. 19.3.

support the voltage as it can be observed. Consequently, active power injection will be reduced due to V_g reduction in Eq. (19.19), and the VSG frequency will have a jump, and for preventing the RoCoF relays in the system from malfunctioning an inertial support is needed.

The same test is simulated using the proposed structure Eq. (19.19) as it can be perceived in Fig. 19.7. For the proposed case, a better inertial response is obtained, as can be observed. In the proposed method, the moment of the inertia equipped with a weighting function of the frequency error which regarding to the machine mode leads to a better response. In this regard, a comparison of frequency responses has, realized by different methods, has been shown in Fig. 19.8.

19.5.2 Experimental results

To further verify the proposed adaptive inertia control, simulated cases are tested experimentally in the laboratory setup as shown in Fig. 19.3. A Regatron DC power source is used as the DC power supply with desired DC value of

This book belongs to Kitab Liaison (ocd1996@gmail.com) Copyright Elsevier 2023

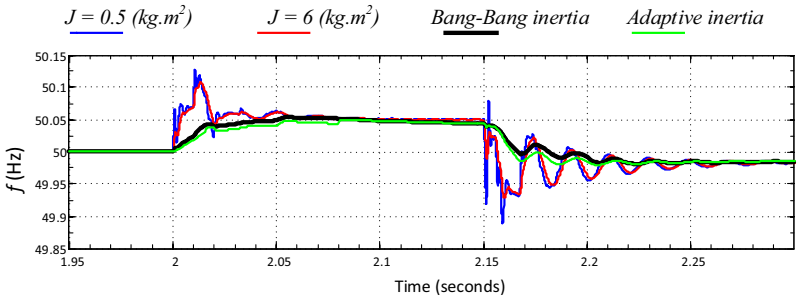

FIGURE 19.8 A comparison of frequency responses for different virtual inertia realizations.

650 V. The converter under test is the grid-tied converter, which is a Danfoss FC-302 2.2 kVA frequency inverter. The PCC voltages, converter currents, active and reactive powers, moment of inertia, and frequency are being measured. Between the LCL filter and Chroma 61845 (grid simulator), a line impedance is inserted. The grid simulator is specifically programmed to emulate the grid fault, i.e., voltage sag, by directly controlling the three-phase voltages at its output. By this, at the fault instant of interest, the amplitudes of the three-phase voltages are reduced to 0.9 pu for 0.16 ms as shown in Fig. 19.9. From the measurements, the actual programming, control, and data acquisition are processed through a dSPACE expansion box consisting of a DS1007 PPC processor board for code compiling, a DS5101 digital waveform output board for PWM pulse signal generation, and a DS2004 high-speed A/D board for measuring of the currents and voltages. The parameter values for the setup and control can be seen in Table 19.5 respectively. The response for constant J and adaptive J are depicted in Figs. 19.10 and 19.11. The experimental results are in good agreement with the simulation results where it is clear that appropriate inertia solutions can provide properly sufficient inertial support.

As it can be seen from Figs. 19.10 and 19.11, a significant role of inertial control in RoCoF and nadir values can be observed, where for a constant $j = 6\,\text{kg.m}^2$ these values are 10 Hz/s and 50.16 Hz, respectively. For the

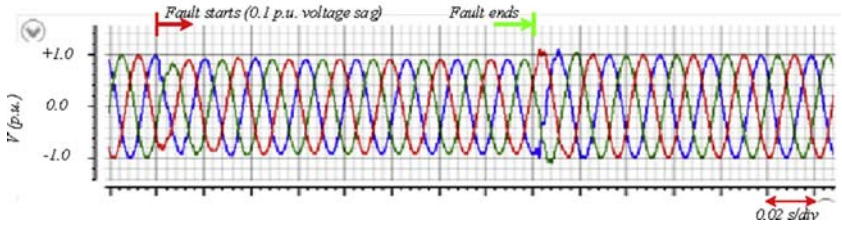

FIGURE 19.9 Experimental Results: the grid-side three-phase PCC voltages during a voltage sag of 10%.

This book belongs to Kitab Liaison (ocd1996@gmail.com) Copyright Elsevier 2023

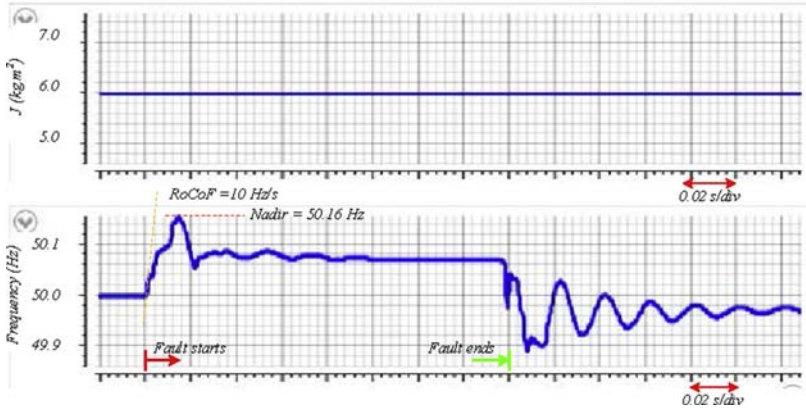

FIGURE 19.10 Fixed value moment of inertia of the virtual synchronous generator and the frequency response during a low voltage ride-through.

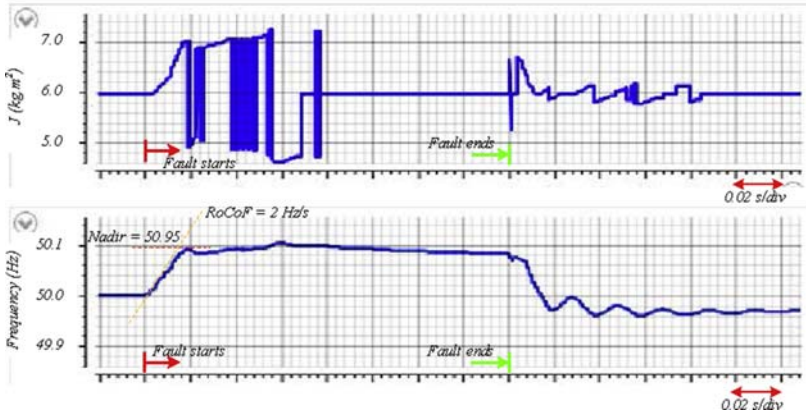

FIGURE 19.11 The proposed adaptive moment of inertia and the frequency response control during a low voltage ride-through.

proposed adaptive control using a weighting function of frequency changes, the results as shown provide a RoCoF equals to 2 Hz/s and a nadir equals to 49.95 Hz.

19.6 Summary

In this chapter, after discussing the inertia concept, the key role of inertial control in future modern power electronic—based power systems have been mentioned. Ways to provide inertial requirements, device and current technologies, grid-tied topologies, design considerations, planning concerns,

This book belongs to Kitab Liaison (ocd1996@gmail.com) Copyright Elsevier 2023

market and operation challenges, and control solutions in power electronic–based power systems have been reviewed and further summarized. A promising role of advanced virtual inertia control approaches, which may present better inertial response, have been investigated, not only by simulations studies but also by experimental test. Experiments show good agreements with the simulation studies to demonstrate how an improved virtual inertia can be obtained.

References

[1] J. Driesen, K. Visscher, Virtual synchronous generators, IEEE Power Energy Soc. General Meeting-Conv. and Del. of Electr. Energy the 21st Century (2008) 1–3.

[2] H. Bevrani, T. Ise, Y. Miura, Virtual synchronous generators: a survey and new perspectives, Int. J. Electr. Power Energy Syst. 54 (2014) 244–254.

[3] A. Karimi, Y. Khayat, M. Naderi, T. Dragicevic, R. Mirzaei, F. Blaabjerg, H. Bevrani, Inertia response improvement in microgrids: a fuzzy-based virtual synchronous generator control, IEEE Trans. Power Electron. (2019), https://doi.org/10.1109/TPEL.2019.2937397.

[4] L. Zhang, L. Harnefors, H.P. Nee, Power-synchronization control of grid-connected voltage-source converters, IEEE Trans. Power Syst. 25 (2) (2009) 809–820.

[5] Q.C. Zhong, G. Weiss, Synchronverters: inverters that mimic synchronous generators, IEEE Trans. Ind. Electron. 58 (4) (2010) 1259–1267.

[6] M. Ashabani, M.Y. Abdel-Rady, A flexible control strategy for grid-connected and islanded microgrids with enhanced stability using nonlinear microgrid stabilizer, IEEE Trans. Smart Grid 3 (3) (2012) 1291–1301.

[7] P.L. Nguyen, Q.C. Zhong, F. Blaabjerg, J.M. Guerrero, "Synchronverter-based operation of STATCOM to mimic synchronous condensers, 7th IEEE Conf. Ind. Electron. and Appl. (ICIEA) (2012) 942–947.

[8] S. Dong, Y.C. Chen, Adjusting synchronverter dynamic response speed via damping correction loop, IEEE Trans. Energy Convers. 32 (2) (2016) 608–619.

[9] S.A. Khajehoddin, M. Karimi-Ghartemani, M. Ebrahimi, Grid supporting inverters with improved dynamics, IEEE Trans. Ind. Electron. 66 (5) (May 2019) 3655–3667.

[10] J. Liu, Y. Miura, H. Bevrani, T. Ise, Enhanced virtual synchronous generator control for parallel inverters in microgrids, IEEE Trans. Smart Grid 8 (5) (September, 2017) 2268–2277.

[11] H. Wu, et al., Small-signal modeling and parameters design for virtual synchronous generators, IEEE Trans. Ind. Electron. 63 (7) (July, 2016) 4292–4303.

[12] H. Xu, X. Zhang, F. Liu, R. Shi, C. Yu, R. Cao, A reactive power sharing strategy of VSG based on virtual capacitor algorithm, IEEE Trans. Ind. Electron. 64 (9) (September, 2017) 7520–7531.

[13] U. Markovic, Z. Chu, P. Aristidou, G. Hug-Glanzmann, LQR-based adaptive virtual synchronous machine for power systems with high inverter penetration, IEEE Trans. Sustain. Energy 10 (3) (July, 2019) 1501–1512.

[14] D. Li, Q. Zhu, S. Lin, X. Bian, A self-adaptive inertia and damping combination control of VSG to support frequency stability, IEEE Trans. Energy Convers. 32 (1) (March, 2017) 397–398.

This book belongs to Kitab Liaison (ocd1996@gmail.com) Copyright Elsevier 2023

[15] M.A. Torres L, L.A. Lopes, L.A. Moran T, J.R. Espinoza C, Self-tuning virtual synchronous machine: a control strategy for energy storage systems to support dynamic frequency control, IEEE Trans. Energy Convers. 29 (4) (December, 2014) 833−840.
[16] J. Alipoor, Y. Miura, T. Ise, Power system stabilization using virtual synchronous generator with alternating moment of inertia, IEEE J. Emerg. Sel. Topics Power Electron. 3 (2) (June, 2015) 451−458.
[17] J. Alipoor, T. Ise, Y. Miura, Stability assessment and optimization methods for microgrid with multiple VSG units, IEEE Trans. Smart Grid 9 (2) (March, 2018) 1462−1471.
[18] N. Soni, S. Doolla, M.C. Chandorkar, Improvement of transient response in microgrids using virtual inertia, IEEE Trans. Power Deliv. 28 (3) (July, 2013) 1830−1838.
[19] D.K. Dheer, N. Soni, S. Doolla, Improvement of small signal stability margin and transient response in inverter-dominated microgrids, Sustain. Energy, Grids Netw. 5 (2016) 135−147.
[20] S. Zhang, Y. Mishra, M. Shahidehpour, Fuzzy-logic based frequency controller for wind farms augmented with energy storage systems, IEEE Trans. Power Syst. 31 (2) (March, 2015) 1595−1603.
[21] A. Karimi, Y. Khayat, M. Naderi, R. Mirzaee, H. Bevrani, Improving transient performance of VSG based microgrids by virtual facts'functions, in: Proc. IEEE Smart Grid Conf., March, 2017, pp. 1−6.
[22] H. Bevrani, Robust Power System Frequency Control, second ed., Springer, New York, NY, USA, 2014.
[23] H. Bevrani, B. François, T. Ise, Microgrid Dynamics and Control, Wiley, Hoboken, NJ, USA, 2017.
[24] J.J. Grainger, W.D. Stevenson, Power System Analysis, McGraw-Hill, 1994.
[25] Global Wind Energy Council, Global Wind Report 2018," GEWC, Tech. Rep, Brussels, Belgium, April, 2019.
[26] Solar Power Europe, Global Market Outlook for Solar Power 2019- 2023, Tech. Rep., Brussels, Belgium, May, 2019.
[27] N. Miller, D. Lew, R. Piwko, Technology capabilities for fast frequency response, GE Energy Consulting, Tech. Rep. (2017).
[28] F. Statnett, Challenges and opportunities for the nordic power system, Tech. Rep. (2016).
[29] ERCOT, Future ancillary services in ERCOT, Tech. Rep. (2013).
[30] H. Thiesen, C. Jauch, A. Gloe, Design of a system substituting today's inherent inertia in the European continental synchronous area, Energies 9 (8) (July, 2016) 582.
[31] G. Delille, B. Francois, G. Malarange, Dynamic frequency control support by energy storage to reduce the impact of wind and solar generation on isolated power system's inertia, IEEE Trans. Sustain. Energy 3 (4) (October, 2012) 931−939.
[32] V. Knap, S.K. Chaudhary, D.-I. Stroe, M. Swierczynski, B.-I. Craciun, R. Teodorescu, Sizing of an energy storage system for grid inertial response and primary frequency reserve, IEEE Trans. Power Syst. 31 (5) (September, 2016) 3447−3456.
[33] S. Wogrin, D.F. Gayme, Optimizing storage siting, sizing, and technology portfolios in transmission-constrained networks, IEEE Trans. Power Syst. 30 (6) (November, 2015) 3304−3313.
[34] E. Ela, V. Gevorgian, A. Tuohy, B. Kirby, M. Milligan, M. O'Malley, Market designs for the primary frequency response ancillary service—part I: motivation and design, IEEE Trans. Power Syst. 29 (1) (January, 2014) 421−431.
[35] E. Ela, V. Gevorgian, A. Tuohy, B. Kirby, M. Milligan, M. O'Malley, Market designs for the primary frequency response ancillary service—part II: case studies, IEEE Trans. Power Syst. 29 (1) (January, 2014) 432−440.

This book belongs to Kitab Liaison (ocd1996@gmail.com) Copyright Elsevier 2023

[36] B.K. Poolla, S. Bolognani, F. Dorfler, Optimal placement of virtual inertia in power grids, IEEE Trans. Automat. Contr. 62 (12) (December, 2017) 6209−6220.

[37] A.F. Hoke, M. Shirazi, S. Chakraborty, E. Muljadi, D. Maksimovic, Rapid active power control of photovoltaic systems for grid frequency support, IEEE J. Emerg. Sel. Topics Power Electron. 5 (3) (September, 2017) 1154−1163.

[38] M.G. Taul, X. Wang, P. Davari, F. Blaabjerg, Current limiting control with enhanced dynamics of grid-forming converters during fault conditions, IEEE Trans. Emerg. Sel. Topics Power Electron. 8 (2) (2019) 1062−1073.

[39] Q. Hu, J. Hu, H. Yuan, H. Tang, Y. Li, Synchronizing stability of dfig-based wind turbines attached to weak ac grid, in: Proc. IEEE ICEMS, October, 2014, pp. 2618−2624.

[40] H. Zhang, J. P. Hasler, N. Johansson, L. Ängquist, and H. P. Nee. Frequency response improvement with synchronous condenser and power electronics converters. In 2017 IEEE 3rd International Future Energy Electronics Conference and ECCE Asia (IFEEC 2017-ECCE Asia) (pp. 1002-1007). IEEE.

[41] Y. Khayat, R. Heydari, et al., On the secondary control architectures of AC microgrids: an overview, IEEE Trans. Power Electron. 35 (6) (2020) 6482−6500.

[42] P. Rodriguez, I. Candela, A. Luna, Control of pv generation systems using the synchronous power controller, in: Proc. IEEE ECCE, September, 2013, pp. 993−998.

[43] X. Lu, J. Wang, J.M. Guerrero, D. Zhao, Virtual-impedance-based fault current limiters for inverter dominated ac microgrids, IEEE Trans. Smart Grid 9 (3) (2016) 1599−1612.

[44] Y. Khayat, S. Golestan, J. Guerrero, J.C. Vasquez, H. Bevrani, DC-link voltage control aided for the inertial support during severe faults in weak grids, IEEE J. Emerg. Sel. Topics Power Electron. (2020), https://doi.org/10.1109/JESTPE.2020.3033657.

Further reading

[1] H. Beck, R. Hesse, Virtual synchronous machine, 9th IEEE Int. Conf. Electr. Power Qual. Utilisat. (2007) 1−6.

This book belongs to Kitab Liaison (ocd1996@gmail.com) Copyright Elsevier 2023

Chapter 20

Abnormal operation of wind turbine systems

Dao Zhou, Mads Graungaard Taul
Department of Energy Technology, Aalborg University, Aalborg, Denmark

20.1 Introduction

This chapter starts with the various grid fault types in the power system and the evolution progress of wind turbine systems. Aligned with modern grid codes on low-voltage ride-through, Type III and Type IV wind turbine configurations are preferred nowadays. In the case of the doubly fed induction generator (DFIG)-based wind turbine system (Type III), due to the direct link between the generator stator and power grid, the power faults introduce the transient stator flux, which may cause the rotor overvoltage. Consequently, the control scheme of the rotor-side converter (RSC) is comprehensively addressed subject to symmetrical and asymmetrical faults. In respect to the permanent magnet synchronous generator—based wind turbine system (Type IV), as the power grid is fully decoupled from the generator, the control scheme of the grid-side converter (GSC) is in focus. Different controller strategies for both symmetrical and asymmetrical faults are thoroughly studied and tested. To that end, a control method that injects asymmetrical converter current in compliance with recent grid code requirements is demonstrated.

20.1.1 Classification of grid faults

Grid faults in power systems are classified into symmetrical faults (three-phase fault 3Φ-g) and asymmetrical faults (single-phase fault Φ-g, phase-to-phase fault 2Φ, and two-phase fault 2Φ-g) [1,2]. Compared to symmetrical grid faults, an asymmetrical grid fault contains a negative-sequence component and possibly a zero-sequence component.

A typical configuration between the power grid and a wind farm is shown in Fig. 20.1. T1 represents the step-up transformer in order to increase the low voltage of wind turbine terminals to a medium voltage (Bus1) used in the wind farm collector grid, which is typically located in the nacelle of the wind turbine. Then, a large collector step-up transformer T2, sized at the nominal

Control of Power Electronic Converters and Systems. https://doi.org/10.1016/B978-0-12-819432-4.00004-4
Copyright © 2021 Elsevier Ltd. All rights reserved.

This book belongs to Kitab Liaison (ocd1996@gmail.com) Copyright Elsevier 2023

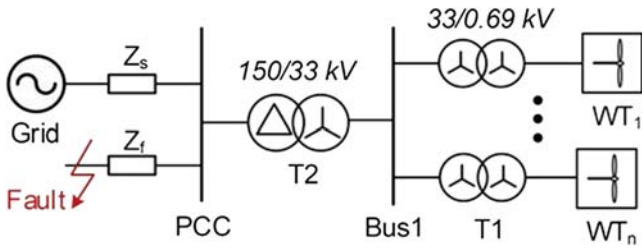

FIGURE 20.1 A typical configuration for a wind farm which is linked to the power transmission grid.

capacity of the wind farm, is used to increase the collection grid voltage to the transmission-level voltage (PCC). Due to the existence of a Y/d transformer in the power transmission system, the zero-sequence component of the voltage circulates within the delta transformer and cannot be propagated, so the type of the asymmetrical grid fault may be changed remarkably.

A short circuit fault happens typically at the terminals of the transmission line. Depending on the source impedance Z_s and the impedance between the point of common coupling (PCC) and fault location Z_f, the dip level p_{dip} can be defined as follows:

$$p_{dip} = \frac{Z_s}{Z_f + Z_s} \tag{20.1}$$

For simplicity, only the parasitic resistance is considered in the transmission line, which avoids the phase angle jump between the grid and PCC voltage. It can be seen that the dip level can be varied from 0 to 1 because of the fault distance to the PCC.

Assuming that various asymmetrical grid faults may occur at the same location, the calculation of the voltage at the turbine terminal will be different [3]. With various dip levels, the positive, negative, and zero components of the voltages at PCC and Bus1 are listed and summarized in Table 20.1. As shown in Fig. 20.2, it can be seen that fault type can be changed through the Y/d transformer. Moreover, it is noted that the positive-sequence component remains the same, while the negative component becomes inverse. It is evident that the 2Φ fault introduces the highest negative component.

20.1.2 Grid code requirements on low-voltage ride-through

Wind turbines and large wind power plants are subject to grid code requirements listing needed functionalities in order to be connected to the grid. Most countries have their own set of requirements, designed for the specific power system needs, and may differ among different countries and transmission system operators [4]. Despite this, most grid codes include requirements on the following: extended operation range of grid frequency and

This book belongs to Kitab Liaison (ocd1996@gmail.com) Copyright Elsevier 2023

TABLE 20.1 Positive (Pos.), negative (Neg.), and zero components of grid faults through Y/d transformer.

Fault types		3Φ-g	Φ-g	2Φ	2Φ-g
PCC	Dip level	p_{dip}	p_{dip}	p_{dip}	p_{dip}
	Classification	A	B	C	E
	Pos., neg., and zero components	$1-p_{dip}$; 0; 0	$1-p_{dip}/3$; $-p_{dip}/3$; $-p_{dip}/3$	$1-p_{dip}/2$; $p_{dip}/2$; 0	$1-2\ p_{dip}/3$; $p_{dip}/3$; $p_{dip}/3$
Bus1	Classification	A	C	D	F
	Pos., neg., and zero components	$1-p_{dip}$; 0; 0	$1-p_{dip}/3$; $p_{dip}/3$; 0	$1-p_{dip}/2$; $-p_{dip}/2$; 0	$1-2\ p_{dip}/3$; $-p_{dip}/3$; 0

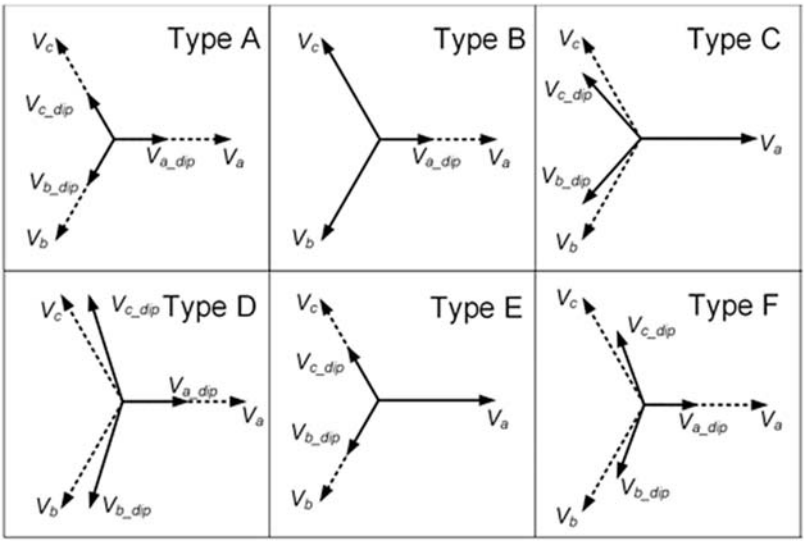

FIGURE 20.2 Classification of various fault types: Phasors of three-phase voltage before (*dotted*) and during fault (*solid*) are displayed.

voltage, frequency stabilization through active power control, voltage stabilization through reactive power control, and low-voltage ride-through (LVRT) requirements [5]. This section will specifically address the LVRT requirements, which are to define the proper control actions of wind turbines during different grid faults in the remainder of this chapter.

This book belongs to Kitab Liaison (ocd1996@gmail.com) Copyright Elsevier 2023

With wind power generators providing a significant part of the total electrical power generation, direct disconnection following a grid fault cannot be tolerated since this will imply an increased risk of a large loss of generation and decreased security of supply. To alleviate such undesired events, wind turbines must be able to ride-through low-voltage conditions and provide dynamic voltage support via injection of reactive current. Discussion and analysis of recurring faults and high-voltage ride-through requirements due to capacitor energization or large load drops is beyond the scope of this chapter.

LVRT capability is defined by a voltage sag tolerance curve and the necessary injection of reactive current during voltage sags. For most grid codes, one single voltage sag tolerance curve is defined to both address symmetrical as well as asymmetrical faults. Other requirements as the ones specified in VDE-AR-N-4110/20 have individual requirements for symmetrical and asymmetrical faults. This is shown in Fig. 20.3A where it can be noticed that more stringent requirements on the voltage sag are present for two-phase faults (2Φ, 2Φ-g) compared to three-phase symmetrical faults (3Φ-g). Also, for high-voltage connections, ride-through at the point of connection should be accomplished during zero-voltage conditions for a specified amount of time. Besides this, the grid-connected converter should provide dynamic voltage support through reactive current injection when the voltage deviates from its nominal value, as shown in Fig. 20.3B. Here, a proportionality constant of 2 is used between the reactive current component and the change in the voltage sequences. Mathematically, the required injection of reactive current is

$$\Delta i_Q^{+,-} = 2 \cdot \Delta v^{+,-} \tag{20.2}$$

where

$$v^+ = \frac{V^+ - V_{pf}}{V_N}, \quad v^- = V^-/V_N. \tag{20.3}$$

V_{pf} is the mean value of the prefault network voltage measured over 50 fundamental cycles, and V_N is the nominal voltage.

In this regard, the required response time of reactive current injection is usually limited to be below 20–30 ms. The defined voltage drop is usually measured at the point of connection of the wind turbine or wind farm and often at the point of generator connection, i.e., directly at the high-voltage transformer terminal of each individual turbine. The reactive current support curve is typically defined from the positive-sequence voltage where during asymmetrical faults, a limit on the voltage swell in the nonfaulty phases is often included. However, to address that most grid faults are asymmetrical and to avert overvoltages in nonfaulty phases, the German VDE-AR-N-4110/20 grid codes require an injection of both positive- and negative-sequence reactive

This book belongs to Kitab Liaison (ocd1996@gmail.com) Copyright Elsevier 2023

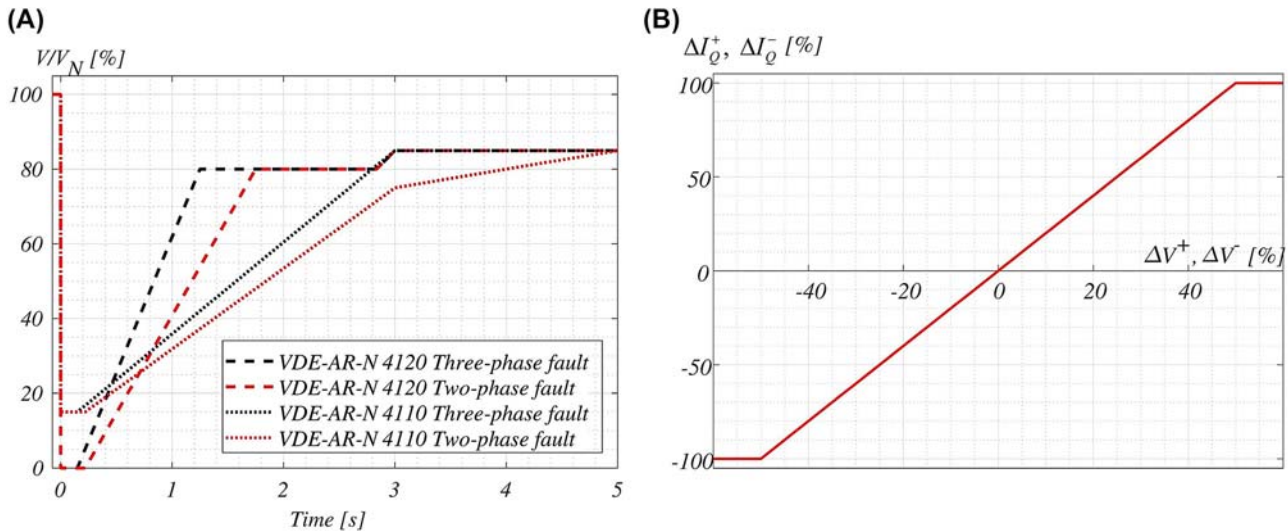

FIGURE 20.3 Low-voltage ride-through requirements of VDE-ARN-4110/20: (A) voltage sag tolerance curve for three-phase and two-phase faults, (B) reactive current provision as a function of change in voltage sequence components.

This book belongs to Kitab Liaison (ocd1996@gmail.com)

Copyright Elsevier 2023

current during asymmetrical faults [6,7]. This is evident from Fig. 20.3B where the injected current in either the positive or negative sequence is proportional to the voltage deviation in the respective sequence frame.

20.1.3 Fundamental wind turbine configurations

Up until now, wind turbine configurations can be generally categorized into four concepts (Type I–IV) [8,9]. The main differences between these concepts lie in the types of generator, the controllability of generator speed, and the usage of power electronics.

A Type I wind turbine configuration is shown in Fig. 20.4, which was very popular in the 1980s. The wind turbine is equipped with a squirrel-cage induction generator, and a smooth grid connection can be achieved using a soft starter that consists of bidirectional thyristors.

As a capacitor bank is required to compensate for the reactive power to excite the asynchronous generator, it becomes the main drawback of this concept. Besides, since the rotational speed is fixed without any controllability, the wind fluctuations are directly transferred into electrical power pulsations, which affect stability issues, especially in the case of a weak grid and need to be dealt with in the design.

As presented in Fig. 20.5, the Type II wind turbine configuration emerged in the mid-1990s. It introduced a variable rotor resistor and thus limited speed

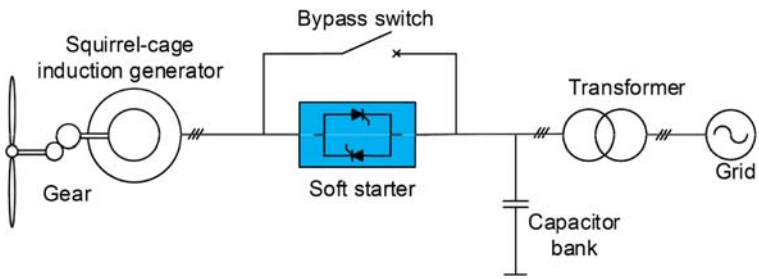

FIGURE 20.4 Type I—fixed speed wind turbine with a direct grid connection.

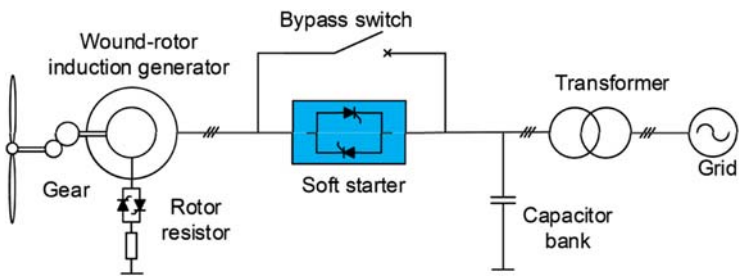

FIGURE 20.5 Type II—partial variable speed wind turbine with a rotor resistor.

This book belongs to Kitab Liaison (ocd1996@gmail.com) Copyright Elsevier 2023

controllability of the generator rotor speed. A wound-rotor induction generator and corresponding capacitor compensator are typically used, and the generator is directly connected to the grid through a soft starter.

The improvement of this concept is that the rotational speed of the generator can be partially adjusted by changing the rotor resistance. This feature contributes to mechanical stress relief. However, the constant power dissipation in the rotor resistor is the main disadvantage.

The Type III topology is shown in Fig. 20.6, which is usually based on a DFIG. It employs a power converter rated at approximately 30% of the nominal generator power in order to handle the slip power from the rotor of the generator. The power converter is connected to the rotor through slip rings and makes the rotor current as well as rotor speed under control, while the stator is directly linked to the grid.

The fraction of slip power through the converter makes this concept attractive from an economic point of view. However, the main drawbacks lie in the use of slip rings, and also an additional crowbar is needed to protect the generator-side converter under grid faults.

As shown in Fig. 20.7, the Type IV configuration equipped with an asynchronous or a synchronous generator is considered as a promising technology for multiMW wind turbine systems. The stator windings of the generator are connected to the grid through a full-scale power converter, which

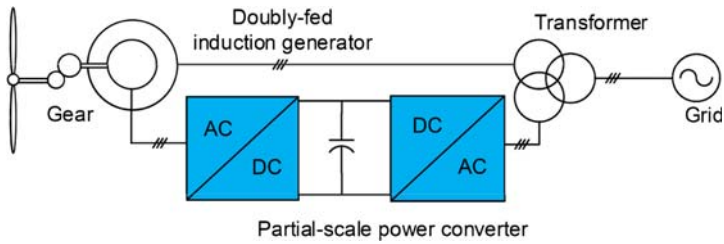

FIGURE 20.6 Type III—variable speed wind turbine with a partial-scale power converter and a doubly fed induction generator.

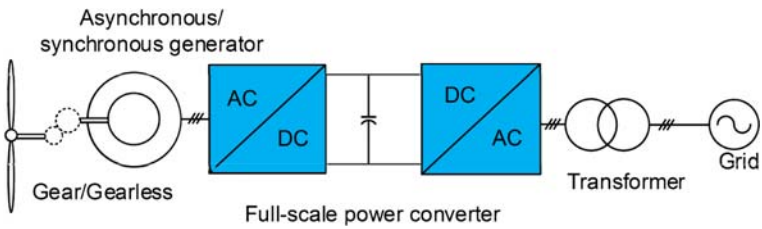

FIGURE 20.7 Type IV—variable speed wind turbine with a full-scale power converter.

This book belongs to Kitab Liaison (ocd1996@gmail.com) Copyright Elsevier 2023

performs the reactive power compensation and also a smooth grid connection for the entire operating speed. Some variable speed wind turbine systems may be gearless by the introduction of a multipole generator.

The elimination of slip rings, more straightforward gearbox, and full power controllability during the grid faults are the main advantages. However, to satisfy the power rating, the widely used approach nowadays is to implement several converter modules or power devices in parallel, which are challenging the complexity and reliability of the whole wind turbine system.

20.2 Control of type III wind turbine during grid faults

20.2.1 Existing challenges during grid faults

This section begins with a description of the DFIG model during grid faults. Since the stator of the DFIG is directly linked to the power grid, any disturbance in the grid can change the stator voltage immediately but not the stator flux due to that the inductor current needs to change continuously. The internal challenge for the fault ride-through lies in the introduction of the natural and negative stator flux, caused by the direct connection between the DFIG stator and the power grid. Moreover, the external challenge comes from the reactive current injection imposed by the grid codes.

20.2.1.1 Internal challenge from DFIG configuration

A typical DFIG configuration is depicted in Fig. 20.8, where the RSC and the GSC are named owing to their positions. It can be seen that the DFIG stator is linked to the power grid directly, which implies that the stator flux cannot be changed abruptly.

With the help of the DFIG model under the stator reference frame [10], the relationship between the stator voltage u_s and the stator flux φ_s can be found as follows:

$$\overline{u_s^s} = R_s \overline{i_s^s} + \frac{d}{dt}\overline{\varphi_s^s} \tag{20.4}$$

where R_s and i_s denote the stator resistance and stator current, and superscript s denotes the stator reference frame.

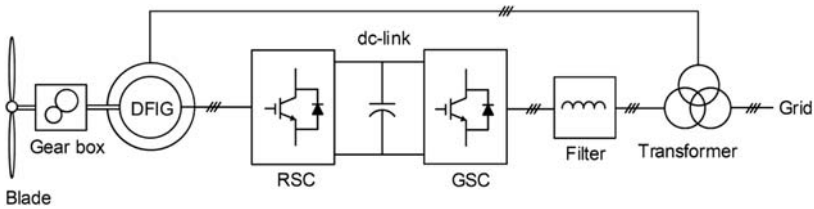

FIGURE 20.8 A typical configuration of the doubly fed induction generator (DFIG) wind turbine system. *GSC*, grid-side converter; *RSC*, rotor-side converter.

This book belongs to Kitab Liaison (ocd1996@gmail.com) Copyright Elsevier 2023

For an MW-level DFIG used in wind turbines, the voltage drop across the stator resistance only contributes to 1% of the stator voltage [10], so this component can be neglected. Consequently, the stator flux becomes the integral of the stator voltage.

In the case of grid faults, according to the positive-sequence and negative-sequence voltage components as listed in Table 20.1, the positive- and negative-sequence stator flux can be calculated. The negative-sequence stator flux rotates in the opposite direction of the positive-sequence stator flux, which leads to a steady-state elliptical trajectory from the original circular trajectory, similarly to what is depicted in Fig. 20.29. In respect to the natural stator flux φ_{sn}, it is inevitably introduced during the symmetrical grid fault. However, in the case of the asymmetrical grid faults, the natural flux may be introduced, whose value depends on the time instant of the fault occurrence [10,11]. For different types of grid faults, the maximum and minimum natural stator flux are summarized in Table 20.2.

Since the stator flux and the rotor flux are coupled with the stator current and the rotor current, the rotor flux φ_r can be expressed by the stator flux φ_s and rotor current i_r as

$$\overline{\varphi_r} = \frac{L_m}{L_s}\overline{\varphi_s} + \sigma L_r \overline{i_r} \tag{20.5}$$

where L_m, L_s, and L_r denote the magnetizing inductance, the stator inductance, and the rotor inductance, respectively, and σ denotes the leakage coefficient.

Meanwhile, according to the voltage equation of the DFIG, the rotor voltage yields

$$\overline{u_r^r} = R_r \overline{i_r^r} + \frac{d}{dt}\overline{\varphi_r^r} \tag{20.6}$$

where R_r denotes the rotor resistance, and superscript r denotes the rotor reference frame.

TABLE 20.2 Maximum and minimum natural flux components at various types of grid faults.

Fault types	3Φ-g	Φ-g	2Φ	2Φ-g
Max. natural flux (pu)	p_{dip}	$p_{dip}/3$	p_{dip}	p_{dip}
Min. natural flux (pu)	p_{dip}	0	0	$p_{dip}/3$

This book belongs to Kitab Liaison (ocd1996@gmail.com)
Copyright Elsevier 2023

Substituting Eq. (20.3) into Eq. (20.4), the rotor voltage can be related to the stator flux as well as the rotor current as follows:

$$\overline{u_r^r} = \frac{L_m}{L_s}\frac{d}{dt}\overline{\varphi_s^r} + \left(R_r + \sigma L_r \frac{d}{dt}\right)\overline{i_r^r} \tag{20.7}$$

where the first term denotes the emf induced by the stator flux in the rotor e_r. The second term denotes the voltage drop across the rotor resistor alongside the transient inductor.

Accordingly, the stator flux under the rotor reference frame can be obtained based on Eq. (20.2) considering the stator voltage to rotate at an arbitrary speed ω, as

$$\overline{\varphi_s^r} = \frac{U_s}{j\omega} e^{j(\omega-\omega_r)t} \tag{20.8}$$

where U_s denotes the phasor of the stator voltage, and ω_r denotes the rotor speed.

As the positive, negative, and natural stator flux can occur during grid faults, the dynamic model of the DFIG consists of a positive machine, a negative machine, and a natural machine, all of which are shown in Fig. 20.9.

Substituting Eq. (20.6) into Eq. (20.5), it can be inferred that in the case of the positive machine, the positive rotor emf e_{r+} is almost the product of the slip s and the positive stator voltage U_{s+}.

$$e_{r+} = \frac{L_m}{L_s} s \cdot U_{s+} \tag{20.9}$$

In the case of the negative machine, the negative rotor voltage e_{r-} is related to the negative-sequence component of the stator voltage U_{s-},

$$e_{r-} = \frac{L_m}{L_s}(2-s)\cdot U_{s-} \tag{20.10}$$

where the rotor emf is (2 − s) times higher than the negative stator voltage. Typically, the slip value varies from −0.2 to 0.2, which results in much higher emf due to the negative-sequence stator voltage.

For the natural stator flux, since it stands still seen from the stator reference frame, it rotates at ω with respect to the rotor reference frame. The natural component of the stator voltage e_{rn} is deduced by

$$e_{rn} = \frac{L_m}{L_s}(1-s)\cdot U_{sn} \tag{20.11}$$

where U_{sn} denotes the virtual natural stator voltage caused by the existence of the natural stator flux.

As aforementioned, since the stator of the induction generator is directly linked to the power grid, a natural stator flux is inevitably introduced in the

This book belongs to Kitab Liaison (ocd1996@gmail.com) Copyright Elsevier 2023

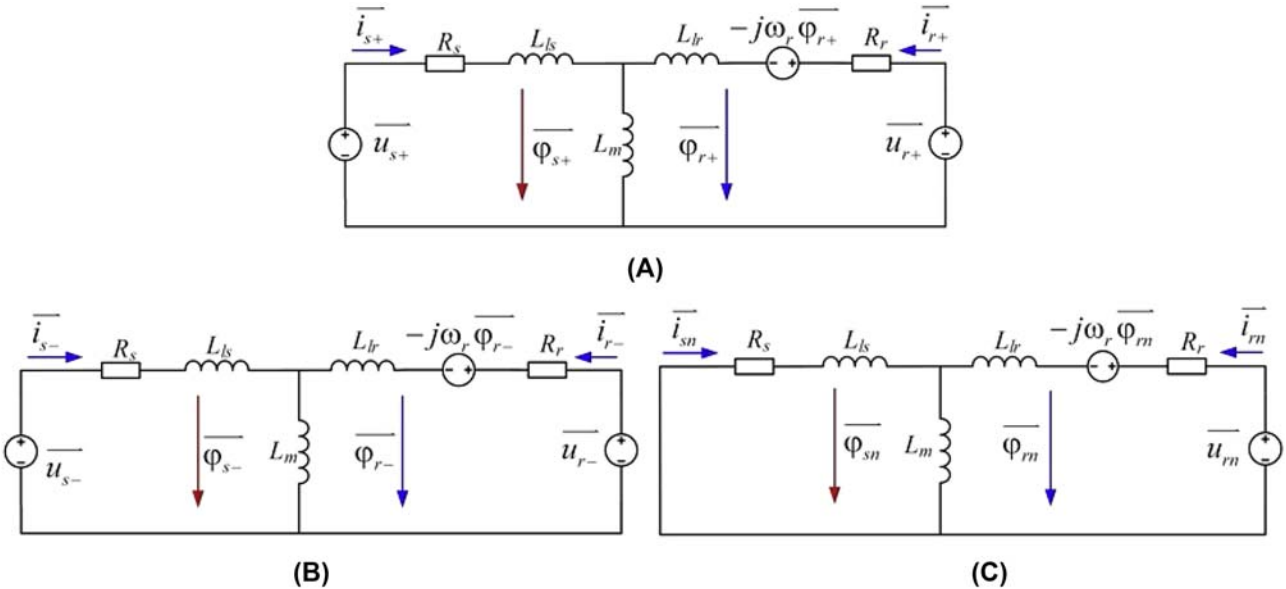

FIGURE 20.9 The dynamic model of the doubly fed induction generator under the stator reference frame during grid faults. (A) Positive machine, (B) Negative machine, (C) Natural machine.

This book belongs to Kitab Liaison (ocd1996@gmail.com)

Copyright Elsevier 2023

case of the stator voltage change, which may induce overvoltage and overcurrent issues of the RSC. The state-of-the-art fault ride-through approaches consist of hardware and software solutions [12–16]. In respect to hardware solutions, as shown in Fig. 20.10, the Dynamic Voltage Restorer can maintain a constant stator voltage, and can avoid the occurrence of the natural stator flux [12]. On the other hand, the rotor-side crowbar or DC-side chopper can be used to accelerate the damping of the natural stator flux and prevent the fragile power devices from overvoltage and overcurrent [13,14]. Under serious voltage dips, the RSC may be saturated. In this case, the DFIG will be out of control, a large rotor current will be produced and flow into the DC bus of the RSC, the converters may be overloaded, and the DC voltage will be too high. Besides, large electromagnetic torque fluctuation will be introduced, and this may reduce the life time of the gearbox. Under grid faults, the crowbar is enabled to protect the RSC after the voltage dips or the over rotor current is detected. The rotor of the DFIG is short circuit and the RSC is disabled. The active crowbar with a diode rectifier and IGBT switch is usually used.

A software solution like the demagnetizing current control is also promising due to its cost-effectiveness [15,16], but the extent of this application is closely related to the power rating of the RSC, and it becomes challenging during the serious voltage dips. During the grid fault, this chapter focuses on the feasibility of the demagnetizing current control.

20.2.1.2 External challenge from grid codes

Although a severe grid fault may cause saturation of the RSC and loss of rotor current control, modern grid codes rarely encourage disconnection of the DFIG from the grid, owing to a high penetration of renewable energy [17,18]. As shown in Fig. 20.3A, a wind turbine system is generally required to remain connected for a certain period of time with various dip levels.

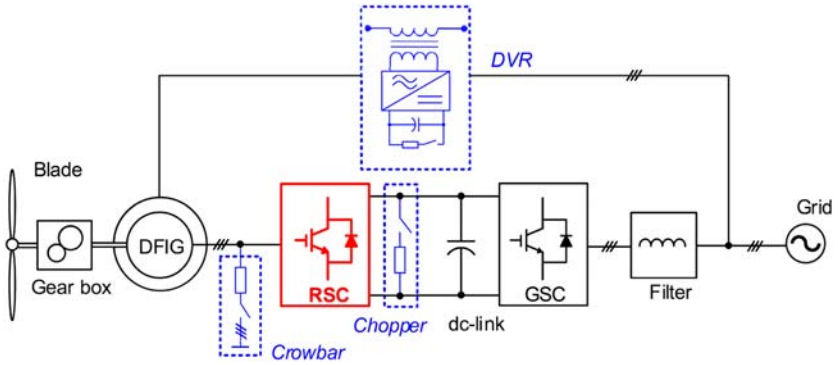

FIGURE 20.10 State-of-the-art hardware solutions for doubly fed induction generator (DFIG) to ride-through grid faults. *DVR*, dynamic voltage restorer; *GSC*, grid-side converter; *RSC*, rotor-side converter.

This book belongs to Kitab Liaison (ocd1996@gmail.com) Copyright Elsevier 2023

Apart from the fault ride-through of the DFIG itself, the reactive current is provided to the power grid within dozens or hundreds of milliseconds after the voltage dip. As shown in Fig. 20.3B, the higher dip level demands a larger reactive current provision, and up to 1.0 pu reactive current is expected if the dip level is higher than 0.5 pu. The requirement of reactive current injection results in an additional increase of the rotor current and it can be considered as an external challenge of the fault ride-through.

As aforementioned, the natural stator flux is inevitably introduced in the case of a symmetrical grid fault, while both the natural and negative stator flux may be produced in the case of an asymmetrical fault. The control strategies under the symmetrical and asymmetrical grid faults will be discussed individually.

20.2.2 Control strategies during symmetrical grid faults

In the case of a symmetrical grid fault, the positive and natural stator flux exists in the DFIG. As expressed in Eqs. (20.9) and (20.11), since the positive component of the rotor emf is linearly related to the slip, while the natural component of the rotor emf is proportional to $(1 - s)$, it can be expected that the natural machine mainly determines the saturation of the RSC. However, traditional vector control only takes care of the positive machine and provides the rotor current at the slip angular frequency, which hardly contributes to cancel out the natural component of the rotor emf.

According to Eq. (20.5), the relationship between the rotor voltage and the rotor current is shown in Fig. 20.11A under the natural machine. As shown in Fig. 20.11B, it is noted that the natural stator flux lags the stator voltage by 90 degrees, and the rotor emf again lags the natural flux by 90 degrees. Also, owing to the inductive characteristic of the DFIG rotor side, the voltage drop across the rotor side u_{rn_RL} lags the rotor current by almost 90 degrees.

Demagnetizing control is used to reduce the rotor voltage during a grid fault [19–21]. It tries to regulate the rotor current in the opposite direction of

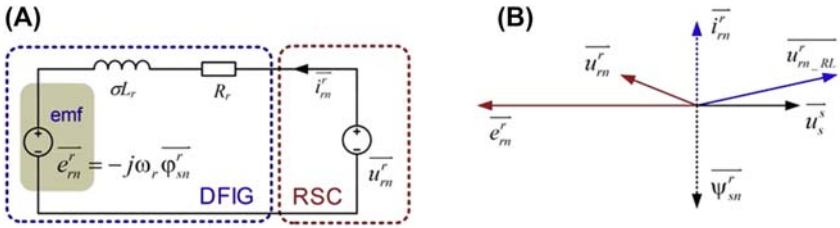

FIGURE 20.11 Relationship between the rotor voltage and the rotor current under the natural machine. (A) Equivalent doubly fed induction generator (DFIG) model seen from the rotor, (B) Vector diagram of the DFIG under the rotor reference frame.

This book belongs to Kitab Liaison (ocd1996@gmail.com) Copyright Elsevier 2023

the natural stator flux, as shown in Fig. 20.11 [22]. Because the preferred current contributes solely to absorbing the reactive power, demagnetizing control is regarded as the most effective way to overcome the transient natural flux.

With the specifications of the induction generator as well as the important parameters of the RSC listed in Tables 20.3 and 20.4, a case study is performed on a 2 MW DFIG system. The Safe Operation Area (SOA) of the RSC is closely related to the capacity of the power semiconductors. Together with the power semiconductor ratings and the rated rotor current, it is evident that the RSC can support up to a 2.0 pu rotor current. Moreover, a 1050 V DC-link voltage at a full modulation index can be transferred into a 2.0 pu rotor voltage. For a 1.7 kV power module, the DC-link voltage should be limited to under 1300 V during the transient period. Then, a 2.5 pu rotor voltage is regarded as the limitation of the voltage stress to ensure safe operation.

TABLE 20.3 Specification and control parameters of doubly fed induction generator.

Rated power	2 MW
Operational range of rotor speed	1050–1800 rpm
Rated amplitude of stator phase voltage	563 V
Rated amplitude of stator phase current	2368 A
Rated frequency	50 Hz
Stator resistance	1.69 mΩ
Rotor resistance	1.52 mΩ
Mutual inductance	2.91 mH
Stator leakage inductance	0.04 mH
Rotor leakage inductance	0.06 mH
Time constant of stator flux	1.75 s
Ratio of stator winding and rotor winding	0.369
Switching frequency	2 kHz
Proportional coefficient of current controller	0.5
Integral coefficient of current controller	7.5
Proportional coefficient of power controller	9.0e − 5
Integral coefficient of power controller	1.35e − 2
Demagnetizing coefficient	1.65

This book belongs to Kitab Liaison (ocd1996@gmail.com)
Copyright Elsevier 2023

TABLE 20.4 Specification of rotor-side converter.

Rated power	400 kW
Rated amplitude of rotor phase current	915 A
Rated amplitude of rotor phase voltage	305 V
DC-link capacitor	20 mF
DC-link voltage V_{dc}	1050 V
Switching frequency f_{sw}	2 kHz
Used power module in each arm	1 kA/1.7 kV; two in parallel

According to Eq. (20.5), the relationship between the rotor current and the rotor voltage can be found using demagnetizing control. As a result, the capability of the DFIG RSC can be calculated with various amounts of demagnetizing current, as shown in Fig. 20.12. Assuming that a maximum 2.0 pu demagnetizing current is applied, the RSC can fully ride-through a symmetrical grid fault at a rotor speed of 1050 rpm. However, if the rotor speed increases to 1500 and 1800 rpm, the DFIG can ride-through a dip level of around 0.8 and 0.7, respectively. Compared to the DFIG capability with 1.0 and 2.0 pu demagnetizing current, a higher amount of demagnetizing current facilitates a higher fault ride-through capability. In short, it can be found that both a higher dip level and higher rotor speed cause a higher rotor emf, which hinders the fault ride-through of the DFIG.

Owing to the existence of the natural stator flux, the control scheme of the RSC during the grid fault occurrence and clearance is shown in Fig. 20.13. At the instant of the fault occurrence, the control priority of the RSC shifts to inject demagnetizing current, in order to maintain the RSC within its SOA and to accelerate the decay of the natural stator flux. Afterward, a certain amount of the reactive current is injected at the stator of the DFIG within dozens or hundreds of milliseconds in accordance with the grid code. As the natural stator flux also occurs during the fault clearance, the demagnetizing control is again applied before the normal vector control becomes effective.

In order to verify the proposed control scheme, a simulation of a 2 MW DFIG system is carried out. The key parameters are consistent with Table 20.3. It is noted that the switching frequency of the two power converters is set at 2 kHz. Further, the DC chopper activates if the DC-link voltage is higher than 1300 V, but deactivates if the DC-link voltage is lower than 1100 V. Assuming that a symmetrical grid fault with a dip level of 0.6 occurs for 500 ms, according to the grid codes, a 1.0 pu reactive current is injected after 150 ms of fault detection, and the original active power is provided after 150 ms of fault clearance. For the traditional vector control, once a grid fault is detected, the

This book belongs to Kitab Liaison (ocd1996@gmail.com) Copyright Elsevier 2023

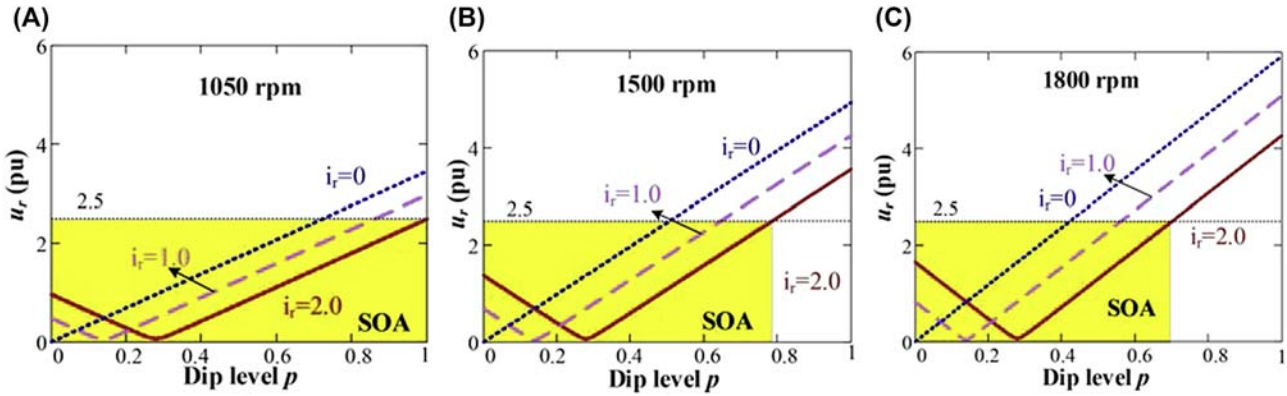

FIGURE 20.12 The safe operation area (SOA) of the doubly fed induction generator to ride-through various dip levels p. (A) 1050 rpm, (B) 1500 rpm, (C) 1800 rpm.

This book belongs to Kitab Liaison (ocd1996@gmail.com)

Copyright Elsevier 2023

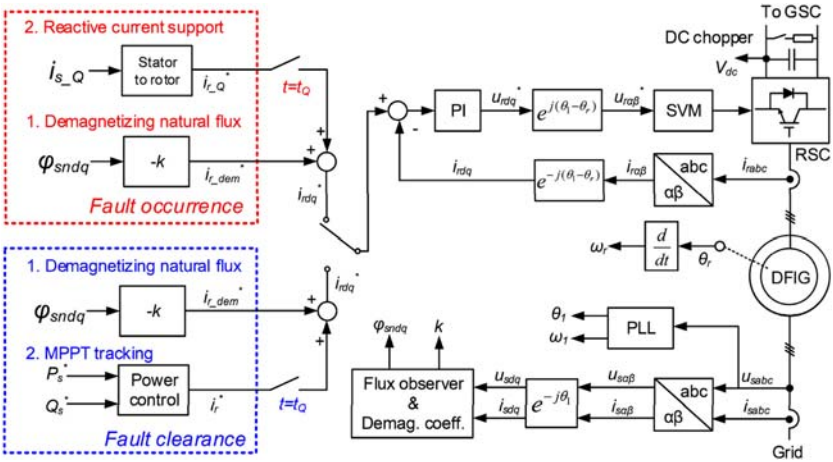

FIGURE 20.13 Control schemes of the rotor-side converter in the cases of the symmetrical grid fault occurrence and clearance.

stator active and reactive power switch to zero before the required reactive current is supplied. During the fault recovery, the stator active and reactive power is again switched to zero before the original active power is provided. In the case of the demagnetizing control, the control objective is changed to the elimination of the natural stator flux during the fault period, and the reactive current is additionally supplied after 150 ms of fault detection. Similarly, the demagnetizing current is applied again during the fault recovery, before the original active power is provided at a fault clearance of 150 ms.

At a rotor speed of 1800 rpm, traditional vector control and the demagnetizing control are compared as shown in Fig. 20.14. For traditional vector control, as shown in Fig. 20.14A, once the grid fault is detected, the rotor current reference is switched to zero in order to minimize the rotor voltage and contribute to the ride-through of the RSC. However, owing to the existence of the natural stator flux, its corresponding rotor voltage exceeds the limit that the DC link can provide, and the rotor current (i_{rd} and i_{rq}) cannot effectively track its reference (i_{rd}^* and i_{rq}^*). As shown in Fig. 20.14B, when the grid fault occurs, a 1.65 pu demagnetizing current is selected. During the fault period, the rotor current is kept almost within the desired value. Moreover, the stator active power and reactive power of the DFIG oscillate at the grid frequency and has an exponential decay. With respect to the DC-link voltage, it is more stable by using demagnetizing control. In addition, as the stator flux decays much faster when the proposed demagnetizing control is used, the stator flux, active power, and reactive power almost reach the steady state at the instant of the fault recovery. This results in a separated evaluation during the grid fault

This book belongs to Kitab Liaison (ocd1996@gmail.com) Copyright Elsevier 2023

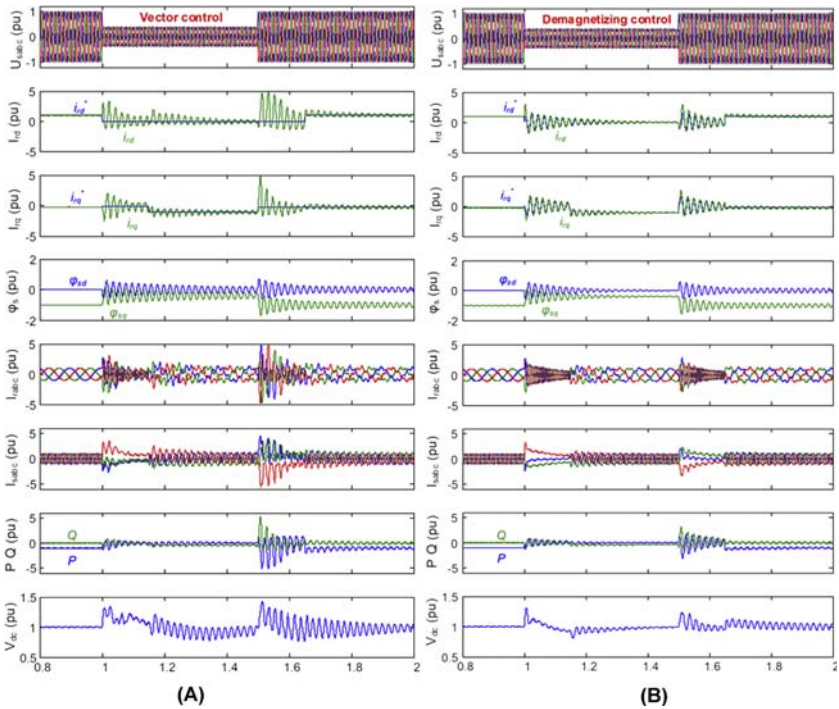

FIGURE 20.14 Simulation results in the case of the doubly fed induction generator at 1800 rpm to ride-through a 0.6 dip balanced grid fault with various control schemes. (A) Traditional vector control, (B) Optimized demagnetizing control.

and recovery. However, vector control does not significantly contribute to the acceleration of the natural stator flux decay, which may be superposed at the instant of the fault recovery.

20.2.3 Control strategies during asymmetrical grid faults

Compared with the symmetrical grid fault, a negative-sequence stator flux exists in the case of the asymmetrical grid fault, which demands a different control strategy. A study of fault ride-through capability, which indicates that the converter is able to operate within the rated current and voltage specified in power module datasheet, is analyzed for the 2 MW DFIG system. The main parameters of the DFIG and its RSC are listed in Tables 20.3 and 20.4. During the normal operation, although the winding ratio between the stator and rotor behaves as a step-up transformer, the yield rotor voltage inferred from Eq. (20.7) is much smaller than the stator voltage because the rated slip value is only −0.2.

This book belongs to Kitab Liaison (ocd1996@gmail.com) Copyright Elsevier 2023

As previously mentioned, various components of the stator flux may have different impacts on the emf e_r. In the case of a single-phase fault, the introduced emf can also be categorized as the positive, negative, and natural components. If the minimum natural stator flux is taken into account, the capability of the DFIG in the case of the Φ-g fault can be estimated in Fig. 20.15A by summing up all the emf components. It is noted that the negative component of the stator flux causes a much higher rotor voltage than usual, which may even exceed the output voltage that DC link can maximum provide (2.5 pu rotor current). Similarly, the capability in the case of a 2Φ fault and a 2Φ-g fault of the DFIG can be seen in Fig. 20.15B and C, respectively. Due to the smallest positive rotor voltage at synchronous operation, the DFIG can endure the highest dip level among various rotor speeds. Besides, as the 2Φ fault has the highest negative component of the stator flux, the ride-through capability of the DFIG becomes worse under this situation (0.29 pu at a rotor speed of 1050 rpm).

Due to the existence of the negative-sequence stator flux, the control objective of the DFIG may be shifted away from maximum power provision in order to comply with the LVRT requirement. Based on the DFIG model seen from the rotor side, the DFIG capability during asymmetrical grid faults will be improved by using a proper rotor current control.

During normal grid conditions, if the supersynchronous operation is used as a case study, the phasor diagram of the DFIG stator and rotor variables is shown in Fig. 20.16A. In order that the stator current is controlled in the opposite direction of the stator voltage, the rotor current is almost in reverse with the stator current. As the rotor transient reactance is dominant compared to the rotor resistance, the voltage across the rotor resistor and transient inductor U_{RL+} is lagging 90 degrees with respect to the rotor current. As a result, the caused rotor voltage is almost the same as the emf, and the control objectives focus on the maximum power generation as well as the excitation supply in order to realize the unity power factor in the DFIG stator side.

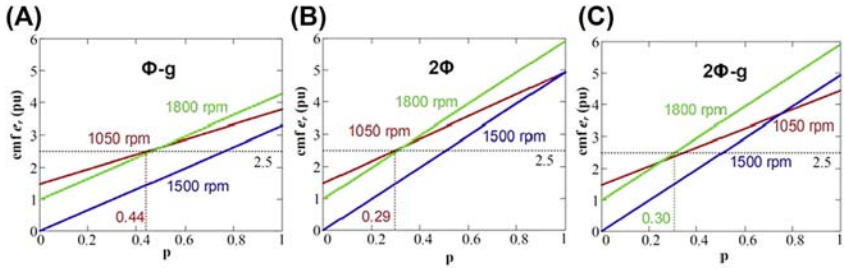

FIGURE 20.15 The capability of the doubly fed induction generator for various asymmetrical grid faults with dip level p. (A) Φ-g fault, (B) 2Φ fault, (C) 2Φ-g fault.

This book belongs to Kitab Liaison (ocd1996@gmail.com) Copyright Elsevier 2023

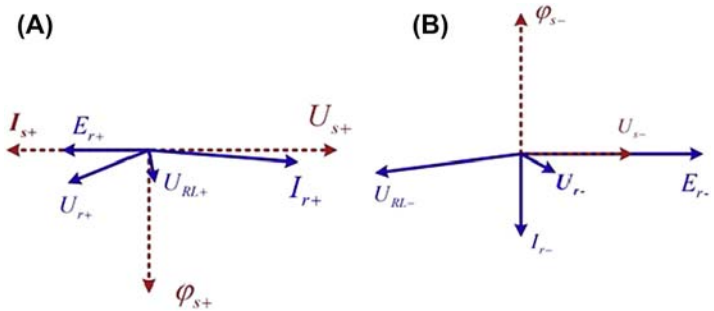

FIGURE 20.16 Phasor diagram of doubly fed induction generator stator and rotor variables. (A) Positive component, (B) Negative component. (Note: supersynchronous operation is used as a case study.)

In the case of asymmetrical faults, as mentioned before, the negative sequence of the stator flux introduces a significant increase in the emf, which may quickly saturate the RSC. In order to enhance the capability of the DFIG, the control target is expected to switch from the active and reactive power control to the minimum rotor voltage, and this can be achieved by controlling the rotor current in the opposite direction of the negative stator flux. As shown in Fig. 20.16B, since the negative stator flux is leading 90 degrees with respect to negative stator voltage, the voltage across the rotor resistor and transient inductor U_{RL-} is almost in the opposite direction in respect to negative stator voltage. As the negative emf is in the same direction with the negative stator voltage, this control can cancel out the effect of the negative emf and causes lower rotor voltage.

According to the voltage equation for the DFIG rotor side, the relationship between the rotor voltage and rotor current can be found. Due to the power rating of the IGBT module as listed in Table 20.3, up to 2.0 pu rotor current can be applied. In order to have similar loading stress of power semiconductor in normal operation, 1.0 pu rotor current is selected. The DFIG capability under Φ-g fault can be summarized and found in Fig. 20.17A, where the DFIG

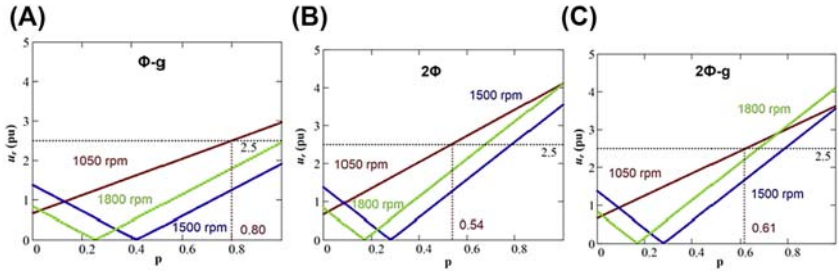

FIGURE 20.17 Improved doubly fed induction generator capability using 1.0 pu negative rotor current with various rotor speed. (A) Φ-g fault, (B) 2Φ fault, (C) 2Φ-g fault. (Note: *p* denotes the dip level.)

This book belongs to Kitab Liaison (ocd1996@gmail.com) Copyright Elsevier 2023

LVRT capability is restricted by the rotor speed of 1050 rpm. Under this circumstance, the RSC can withstand up to 0.80 dip level, which is remarkably improved than 0.44 dip level of the traditional control. Similarly, the DFIG capability in the cases of 2Φ and 2Φ-g faults can be summarized in Fig. 20.17B and C, respectively. It can be seen that the rotor speed at 1050 rpm will limit the DFIG fault ride-through capability. However, the capability ranges become 0.54 and 0.61 dip level, which are much more enhanced compared to the traditional control, as shown in Fig. 20.15B and C.

In order to reduce the rotor voltage in asymmetrical faults, the control scheme of the RSC is comprehensively addressed. Moreover, the improved DFIG capability is validated by simulation in the case of the Φ-g fault. In the condition of the positive dq^+ frame, the negative component during the asymmetrical grid fault will no longer become a DC component but an AC component with the frequency of 100 Hz. It prevents the application of a traditional PI controller, which can only track the DC component without any error. Correspondingly, a negative dq^- frame is introduced, and a notch filter is also applied to extract the positive and negative component after the positive dq^+ or negative dq^- frame.

As mentioned in Ref. [11,23], the negative component of the rotor current reference can be set in order to achieve balanced stator current, balanced rotor current, constant output active power, and constant electromagnetic torque under unbalanced network conditions. However, this is the long-term steady-state condition because of the weak power grid, and the focus will be changed if a sudden asymmetrical fault happens, which highlights the successful ride-through of the DFIG RSC.

Since the negative component of the stator voltage causes very high emf in the DFIG rotor side, the rotor current is controlled in the opposite direction with the negative stator flux, which makes the voltage across the rotor resistance and transient inductor counteract the emf. The amplitude of the rotor current reference is decided by the gain coefficient k. The complete control scheme of the RSC is then shown in Fig. 20.18 [24]. It is noted that in a normal situation, the Maximum Power Point Tracking is implemented through the positive component of the rotor current, while there is no negative component of the rotor current because no negative component exists in the DFIG system. During the fault period, the reference of the positive component of the rotor current is set to supply the reactive power according to the grid codes, while the reference of the negative component of the rotor current becomes to follow the negative stator flux.

The 2 MW DFIG is simulated in order to verify the improved capability under the asymmetrical fault, in which the Φ-g fault is used as a case study. Assuming the DC capacitor is large enough to maintain a constant DC voltage, and the DFIG operates at 1800 rpm, in case of the dip level of 0.5, the

This book belongs to Kitab Liaison (ocd1996@gmail.com) Copyright Elsevier 2023

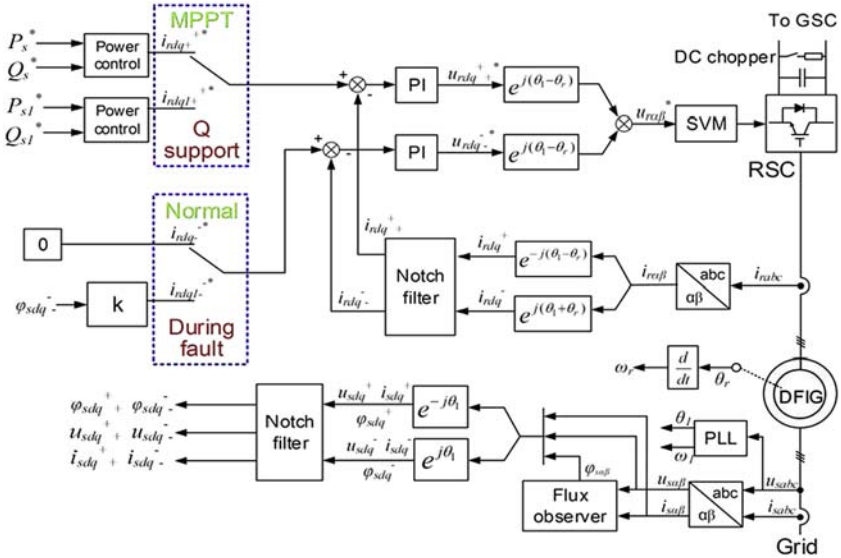

FIGURE 20.18 Control scheme of the doubly fed induction generator (DFIG) to reduce the required rotor voltage during asymmetrical faults having two operational modes.

traditional vector control cannot ride-through as shown in Fig. 20.15A, while the proposed control can withstand this fault successfully, as shown in Fig. 20.17A. As shown in Fig. 20.19A, the reference of the rotor current remains the same in the traditional vector control, where no negative component of the rotor current is injected. It is noted that during the fault period, the current reference cannot be well tracked, which indicates the saturation of the RSC. Meanwhile, the maximum rotor current almost reaches 4.0 pu, which can easily breakdown the power modules used in the RSC. The proposed control scheme is shown in Fig. 20.19B. The positive rotor current reference reduces to zero, while the negative current is 1.0 pu to track the opposite direction of the negative stator flux. It can be seen that the rotor current can be followed after dozens of milliseconds, and the maximum rotor current is almost 1.0 pu, which implies a successful fault ride-through.

20.3 Control of type IV wind turbine during grid faults

In this section, the modeling and control of a grid-connected back-to-back configured converter during grid faults are addressed. This is done to specifically describe the control and operation of a Type IV wind turbine, as shown in Fig. 20.20 during fault conditions. The section includes a brief description of a sufficient modeling principle of the system alongside identifying its main

This book belongs to Kitab Liaison (ocd1996@gmail.com) Copyright Elsevier 2023

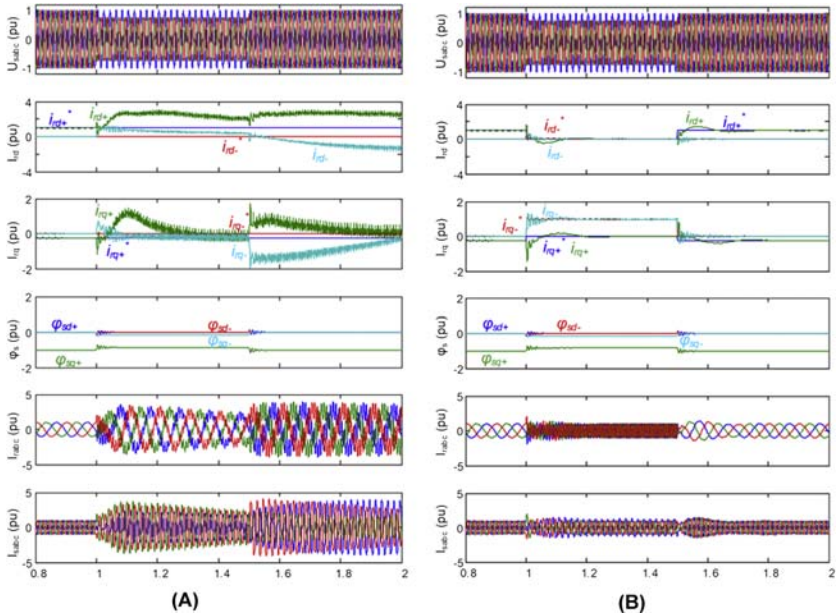

FIGURE 20.19 Simulation results of the doubly fed induction generator in the case of the Φ-g fault at the dip level of 0.5. (A) Traditional vector control, (B) Proposed control.

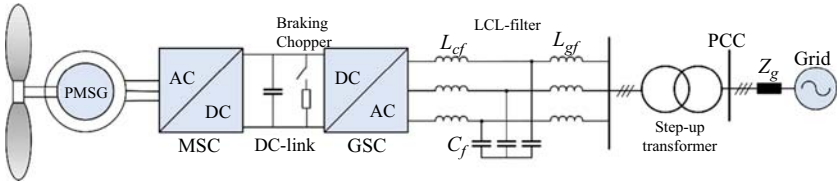

FIGURE 20.20 Type IV wind turbine system with a full-scale power converter connected to the grid through an output LCL filter and a step-up transformer. *GSC*, grid-side converter; *MSC*, machine-side converter; *PMSG*, permanent magnet synchronous generator.

control parts and its design. Subsequently, the control and operation of the Type IV wind turbine system during symmetrical as well as asymmetrical fault conditions are carefully addressed.

20.3.1 Modeling and control of grid-side converter

The GSC, with its basic control functionalities, including voltage synchronization using a phase-locked loop (PLL), a DC-link voltage controller, and an inner current controller with voltage feedforward, is visualized in Fig. 20.21.

This book belongs to Kitab Liaison (ocd1996@gmail.com)
Copyright Elsevier 2023

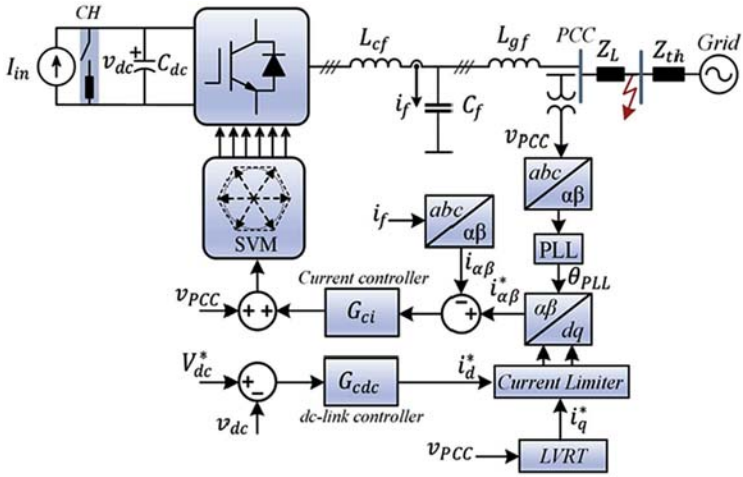

FIGURE 20.21 The control structure of a grid-following grid-side converter where the machine-side converter is represented as a constant current source. The control structure shows a grid-following structure with a phase-locked loop (PLL), a DC-link voltage controller, and an inner current controller with voltage feedforward. *CH*, DC chopper circuit; *SVM*, space vector modulation.

During fault conditions, chopper control is performed to avoid overvoltage on the DC link. For simplicity, any externally set reactive power reference is neglected during this analysis and assumed to be zero. Accordingly, the reactive current injection is only determined by the LVRT requirements stated by the considered grid code. Usually, the GSC is a two-level voltage source converter which may be paralleled or interleaved for an increased power rating of the converter. For the design of the converter control, only the average behavior of the converter operation is considered. In this manner, the switching ripple can be eliminated while the control and system dynamics may still be characterized. With an averaged representation of the system, the converter can be modeled as an ideal voltage gain as $K_C = 0.5v_{dc}$ acting on the computed reference duty cycle. To fully utilize the DC-link voltage, Space Vector Modulation may be used for pulse width modulation generation, which is the case in this section.

20.3.1.1 Converter current control

From the stationary reference frame current references, a proportional resonant (PR) current controller, which has zero tracking error at both the positive and negative fundamental frequency, is used. Additionally, feedforward of the

This book belongs to Kitab Liaison (ocd1996@gmail.com) Copyright Elsevier 2023

voltages at the connection point is included to enhance the transient performance during the fault occurrence and recovery. During weak grid conditions, the voltage feedforward decreases the stability margin of the system and may be included as a compromise between sufficient stability margin and enhanced transient response.

For the converter current control, the relationship between the converter voltage and the converter current is needed and can be described as follows:

$$G_{if}(s) = \left.\frac{i_f(s)}{v_{inv}(s)}\right|_{V_g=0} = \frac{s^2 + \omega_{LC}^2}{L_{cf}s\left(s^2 + \omega_r^2\right)}, \tag{20.12}$$

where

$$\omega_{LC} = \frac{1}{\sqrt{L_{gf}C_f}}, \quad \omega_r = \sqrt{\frac{L_{cf} + L_{gf}}{L_{cf}L_{gf}C_f}}. \tag{20.13}$$

The open-loop transfer function of the current control loop is then

$$G_{ol,c}(s) = G_{PR}(s)e^{-T_d s}G_{if}(s), \tag{20.14}$$

where the stationary reference frame PR controller is

$$G_{PR} = K_p + \frac{K_r s}{s^2 + \omega_0^2}, \tag{20.15}$$

and $T_d = 1.5T_s$ is the time delay of the system originating from the digital implementation (T_s) and the digital modulator ($0.5T_s$) where T_s is the sampling period. From Eq. (20.14), it is evident that the actual converter model is not included. This is because when considering the linear averaged model of the inverter, it merely cancels out in the control block diagram since the voltage reference obtained from the output of the current regulator should be divided by $0.5v_{dc}$ to get the duty cycles. Using Eq. (20.14), the PR controller gains can be tuned based on the desired phase margin and bandwidth alongside with the parameter of the system. Detailed information on how accurately to implement the PR controller in a discrete manner can be found in Ref. [25].

20.3.1.2 Phase-locked loop for grid synchronization

For grid synchronization, a synchronous reference frame phase-locked loop (SRF-PLL) is employed. The main idea is to control the q-axis component of the input voltage to zero by using a PI controller. The nominal grid frequency is fed forward in the SRF-PLL to enhance the design of the small-signal model used for design, and an outer integrator is used to achieve zero steady-state error for the phase angle, which is a ramp function. The block diagram of the SRF-PLL is visualized in Fig. 20.22A. The principle of operation of the SRF-PLL can be understood from Fig. 20.22B. By regulating v_q to zero, the

This book belongs to Kitab Liaison (ocd1996@gmail.com) Copyright Elsevier 2023

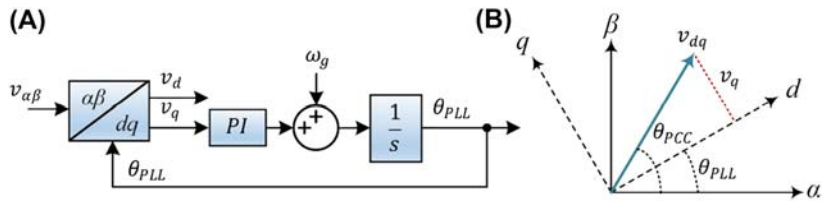

FIGURE 20.22 Synchronous reference frame phase-locked loop. (A) Control block diagram, (B) representation of stationary reference and synchronous reference frame for the phase-locked loop operation.

input voltage vector will be aligned with the rotating frame direct axis. When this is the case, $\theta_{PLL} = \theta_{PCC}$ and the phase angle of the input voltage will be locked and extracted. The closed-loop small-signal transfer function of the SRF-PLL can be written as follows:

$$\frac{\theta_{PCC}(s)}{\theta_{PLL}(s)} = \frac{T(s)}{1+T(s)} = \frac{V_{PCC}K_p s + V_{PCC}K_i}{s^2 + V_{PCC}K_p s + V_{PCC}K_i}, \tag{20.16}$$

where V_{PCC} is the magnitude of the input voltage. During fault conditions where this magnitude changes, one may use a voltage normalization scheme in the SRF-PLL to make the design of the SRF-PLL independent on the input voltage magnitude [26]. Eq. (20.16) is a second-order system on the normalized form. Using this, the PI parameters of the SRF-PLL may be selected to give an approximate damping and natural frequency as follows:

$$K_p = \frac{2\zeta\omega_N}{V_{PCC}}, \quad K_i = \frac{\omega_N^2}{V_{PCC}}. \tag{20.17}$$

20.3.1.3 DC-link voltage controller

During the design of the PR controller, the DC-link voltage is assumed constant. Nevertheless, for wind turbine applications, the machine-side converter is usually controlled to maximize its active power injection to the grid. In this case, the voltage at the DC link is not constant but determined from the power balance between the machine-side converter and the GSC. Considering a varying DC-link voltage, also the duty cycle will be time varying, which makes the modeling and control nonlinear. To cope with this, the DC-link voltage controller and the PR controller can be assumed independently by designing the DC-link controller much slower than the control loop for the converter current.

This book belongs to Kitab Liaison (ocd1996@gmail.com) Copyright Elsevier 2023

For the DC-link voltage controller, the average exchange of power on the DC bus is used to compute an AC-current reference, which results in a constant DC-link voltage. The power stored in the DC-link capacitor can be expressed as

$$P_{dc} = \frac{dW_{dc}}{dt} = \frac{1}{2} C_{dc} \frac{d(v_{dc})^2}{dt}, \tag{20.18}$$

from where it becomes evident that one can regulate the power error by using the square of the DC-link voltage error. Consequently, the control law for the reference AC-side power neglecting converter losses is

$$P^* = \left(K_{p,dc} + \frac{K_{i,dc}}{s}\right) \frac{\left(V_{dc}^*\right)^2 - v_{dc}^2}{2} + H_{dc}(s) P_{WT} \tag{20.19}$$

where $P_{WT} = I_{in} v_{dc}$ and

$$H_{dc}(s) = \frac{\alpha_d}{s + \alpha_d} \tag{20.20}$$

where $\alpha_d < 0.1\alpha_c$ and α_c is the bandwidth of the inner current control loop [27]. Here, the wind turbine generator power (P_{WT}) is low-pass filtered and fed forward to enhance the control. Lastly, the d-axis current reference is calculated from the active power reference and a filtered PCC voltage magnitude as follows:

$$i_d^* = \frac{P^*}{E_f} \quad \text{where} \quad E_f = H_{dc}(s) \| V_{PCC} \|. \tag{20.21}$$

with the wind turbine power being used as a feedforward, the integral gain can be selected as a small value just to remove any steady-state errors. Consequently, by considering the integral gain to be small, the proportional gain can be set as follows:

$$K_{p,dc} = \alpha_d C_{dc} \tag{20.22}$$

where α_d is the desired bandwidth of the DC-link voltage controller. The control block diagram of the DC-link voltage controller can be seen in Fig. 20.23, where the PI controller is set to be negative since the DC-link control plant is inherently incrementally negative.

20.3.2 Symmetrical grid fault control

Even though symmetrical grid faults are responsible for only a small percentage of all grid faults, the resulting voltage sag represents the most severe of all grid faults [28]. This may introduce low-frequency instability as a result

This book belongs to Kitab Liaison (ocd1996@gmail.com) Copyright Elsevier 2023

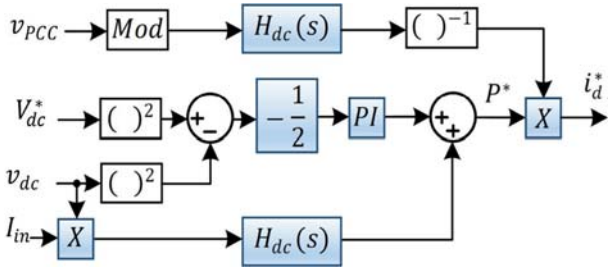

FIGURE 20.23 Block diagram and implementation of the DC-link voltage controller shown in Fig. 20.21.

of the interactions between the converter control and the grid [29]. Also, since the network positive-sequence voltage can reach shallow values, supporting the grid with reactive current is essential. As it is stated by the grid codes, reactive current injection should be prioritized during symmetrical faults in order to support and boost the local grid voltage. Since the current-mode/grid-following controller inherently does not support the grid, the current reference generation needs to be modified during the fault. This implies that instead of active current provision, as provided during normal operating conditions, capacitive reactive current injection is required during low-voltage conditions.

To that end, the control strategy should consider the current rating of the converter semiconductor devices in case of a fault condition and limit the current between rated and two times rated current, dependent on design margins and application [30]. Limiting the converter current can be achieved in numerous ways depending on whether balanced or unbalanced currents are to be injected during the fault [31]. This will be more carefully discussed in the next section. Considering a symmetrical fault where the converter injects balanced currents, the converter current can be limited as follows:

$$I_{\text{lim}} = \sqrt{i_d^{*2} + i_q^{*2}}. \tag{20.23}$$

During low-voltage conditions where the reactive current is prioritized, i_d^* is set to fulfill Eq. (20.23).

The active current reference is obtained from the DC-link voltage controller, whereas the reactive current reference is calculated according to the LVRT requirements. Given the per-unit value of the voltage at the converter connection point, the reactive current reference can be calculated as follows:

This book belongs to Kitab Liaison (ocd1996@gmail.com) Copyright Elsevier 2023

$$i_q^* = \begin{cases} 0 & \text{if} \quad V_{pu} > 0.9 \\ -2I_{nom}(1 - V_{pu}) & \text{if} \quad 0.5 < V_{pu} < 0.9 \\ -I_{nom} & \text{if} \quad V_{pu} < 0.5 \end{cases} \tag{20.24}$$

where I_{nom} is the rated converter current and V_{pu} is calculated as a low-pass filtered response of

$$V_{pu1} = \sqrt{\frac{3}{2}} \cdot \frac{\sqrt{v_\alpha^2 + v_\beta^2}}{V_b} \tag{20.25}$$

where V_b is the rms line-to-line base voltage.

20.3.2.1 Protection of DC-link capacitor through chopper control

If a grid fault happens in the vicinity of the voltage terminals of the wind turbine, very low voltage levels may arise at the point of connection. When this is the case, the power transfer capability between the wind turbine and the grid is altered. If an inductive grid is considered, the active power transfer can be expressed as follows:

$$P = \frac{V_{WT} V_g}{X_g} \sin(\delta), \tag{20.26}$$

where V_{WT}, V_g, X_g, δ are the wind turbine voltage, the grid voltage, the grid reactance, and the relative phase angle between the wind turbine and grid voltages, respectively.

If the grid voltage approaches zero, active power cannot be transferred from the wind turbine to the grid, which causes destructive overvoltages on the DC-link capacitor if not correctly managed. This is true even though a dedicated controller for the DC-link voltage is used since the generator power cannot be injected into the grid. The energy stored in the DC-link is

$$E_{dc} = \frac{1}{2} C_{dc} v_{dc}^2 \quad \rightarrow \quad v_{dc} = \sqrt{2E_{dc}/C_{dc}}. \tag{20.27}$$

Utilizing that the capacitor energy is the integral of the power being accumulated at the DC side, the DC-link voltage may be written as follows:

$$v_{dc} = \sqrt{\frac{2}{C_{dc}}} \int (P_{WT} - P_g)\, dt \tag{20.28}$$

where P_g and P_{WT} are the power delivered to the grid and power from the wind turbine, respectively. Thus, if P_g is reduced, the DC-link voltage will increase. To manage this issue, a chopper circuit is usually implemented on the DC link to dissipate the accumulated energy [32]. This consists of a parallel-connected resistor, as shown in Fig. 20.20. In case the grid voltage drops to zero, the chopper resistance should be selected based on the rated power and DC-link

This book belongs to Kitab Liaison (ocd1996@gmail.com) Copyright Elsevier 2023

voltage of the converter. In the analysis to be presented in this section, a PI controller is used to regulate the chopper circuit during the fault. The control law for the chopper control is

$$d_{chop} = \left(v_{dc} - v_{dc}^{*}\right)\left(K_{p,chop} + \frac{K_{i,chop}}{s}\right)S_F \tag{20.29}$$

where S_F is the fault signal, which is set high when a fault is detected. Thus, practically, the controller only performs calculations when a fault is detected.

20.3.2.2 Verification of symmetrical fault control

The presented control methodology with the specifications listed in Table 20.5 is tested during a symmetrical three-phase fault where the fault magnitude drops to 0.3 pu for 150 ms.

TABLE 20.5 Specification for the test system in Fig. 20.21.

Symbol	Description	Physical value
S_b	Rated power	7.5 kVA
V_N	Nominal grid voltage	400 V
f_n	Nominal frequency	50 Hz
V_{dc}^{*}	DC-link voltage reference	730 V
Q_{ext}^{*}	External reactive power reference	0
C_{dc}	DC-link capacitance	0.5 mF
L_{cf}	Converter-side inductor	0.071 pu
L_{gf}	Grid-side inductor	0.043 pu
C_f	Filter capacitor	0.068 pu
f_{sw}	Switching frequency	10 kHz
f_s	Sampling frequency	10 kHz
Z_L	Line reactance	0.1 pu
Z_g	Grid impedance	0.1 pu
SCR	Short circuit ratio	5
I_{lim}	Maximum temporary converter current	1.2 pu
$K_{p,ic}$	Proportional gain PR controller	12
$K_{r,ic}$	Resonant gain of PR controller	2000

This book belongs to Kitab Liaison (ocd1996@gmail.com)
Copyright Elsevier 2023

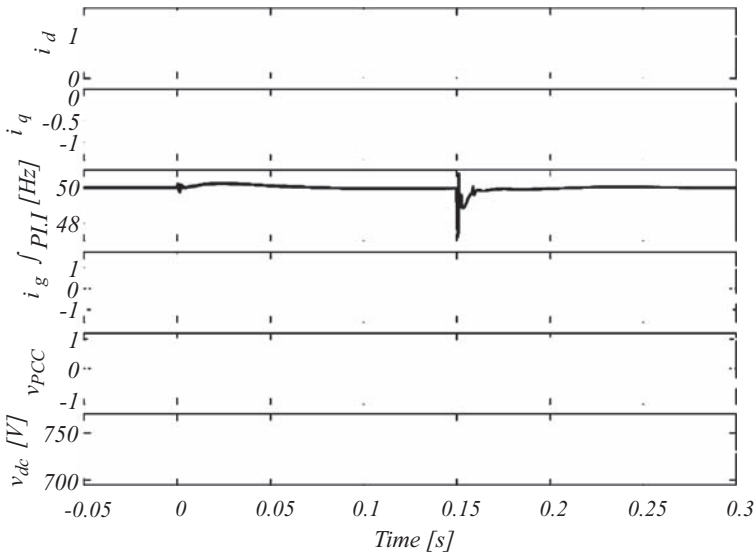

FIGURE 20.24 Simulated fault response of a three-phase symmetrical fault with a voltage magnitude of 0.3 pu. From top to bottom, the visualized variables are the d-axis reference (white) and realized (black) current, q-axis reference (white) and realized (black) current, estimated PLL frequency, three-phase grid currents, three-phase PCC/point of connection voltages, and the DC-link voltage.

The simulated response is shown in Fig. 20.24, where it can be seen that full reactive current is injected, while the active current is reduced such that the current magnitude is limited to 1.2 pu, which is considered as the allowable converter overload in this case.

The chopper circuit is enabled quickly when the fault is detected, effectively dissipating the excess energy to avoid any DC overvoltage during the fault. When the fault is cleared, the chopper circuit is deactivated, which gives a transient in DC-link voltage when the active power is again raised to its prefault state. It is observed that the converter injects nominal reactive current in compliance with the grid code requirements and allocated the remaining current capability for active current injection.

20.3.2.3 Zero-voltage ride-through capability

Today, the vast majority of GSCs for wind turbine systems are controlled as grid-following units. For such a control structure to operate acceptably, a rather stiff network voltage must be established by other units, either synchronous machines or grid-forming converters. This necessity is met in most operating cases, including normal operation and most grid faults. However, events may occur where the grid-following converter becomes separated from the grid-forming units, either as a result of an extremely severe three-phase

This book belongs to Kitab Liaison (ocd1996@gmail.com) Copyright Elsevier 2023

fault where the network voltages at that point essentially drop to zero or during line openings by circuit breakers where redundant parallel lines are not present. In either case, the grid-following converter has no well-established voltage to follow and hence will lose stability if not adequately controlled. During such zero-voltage conditions, the converter should be able to ride-through, i.e., remain connected, and support the local voltages with reactive power, as shown in Fig. 20.3. In some previous work [1,2], it is assumed that the voltages drop to zero at the point where the measurements are taken for the PLL. During this scenario, the control error in the PLL immediately drops to zero, making the PLL operate at its prefault phase and frequency stably. However, in a realistic scenario where some impedance (e.g., a wind turbine transformer) will be present between the voltage measurement and the fault location, some small voltages, generated by the converter itself, will be present at the measurement point. This condition will cause instability since the grid-following properties completely break down. To be able to ride-through in this case, the grid-following converter must be able to detect the abnormal operation (islanded connection) and switch into a stand-alone mode, either by adopting a grid-forming control structure during the fault [3] or intentionally nullifying the PLL control error [4–6]. Due to its simplicity and robust performance, the control which nullifies the PLL control error (also known as the PLL freezing method) is demonstrated in this chapter. The control diagram of the PLL freezing method is shown in Fig. 20.25. Since the magnitude of the input voltages affects the desired dynamics selected during PLL parameter tuning, an adaptive voltage normalization is performed to make the design independent of the input voltage magnitude. As can be seen from Fig. 20.25, the instantaneous per-unit value of the voltage magnitude is compared to a

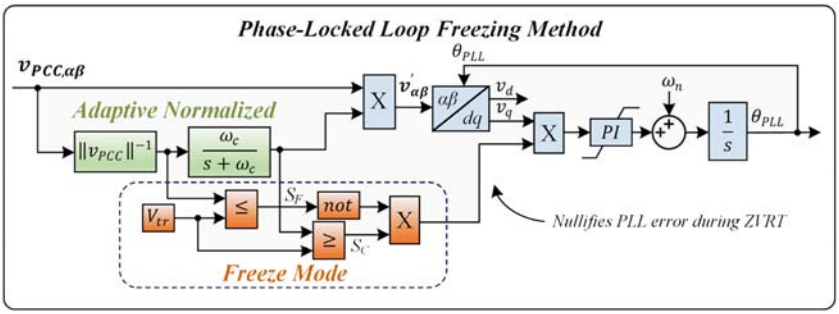

FIGURE 20.25 Structure of the phase-locked loop (PLL) freezing method activated during zero-voltage conditions to possess ZVRT. V_{tr} is the threshold voltage for activating the freezing method. A low-pass filter with cut-off frequency ω_c is used for adaptive normalization of the PLL control design and to reenable normal PLL operation with some delay after voltage recovery. S_F is the fault signal and S_C is the clear signal. Saturation limits on the PI controller frequency are $\pm$ 10 Hz.

This book belongs to Kitab Liaison (ocd1996@gmail.com) Copyright Elsevier 2023

threshold parameter V_{tr}. When the voltage drops below the threshold, $S_F = 1$, which nullifies the PLL control error, keeping its prefault frequency and phase angle during the fault. When the fault is cleared and the voltage recovers, the PLL is switched back to normal operation with a delay defined by the low-pass filter in the adaptive normalization.

The responses of the GSC to a zero-voltage grid fault using the PLL structure in Fig. 20.25 without and with the PLL freezing method are shown in Fig. 20.26. The converter control without PLL freeze is unstable and cannot operate in stand-alone mode, and hence cannot comply with ZVRT capability. To that end, a slow fault-recovery response is observed since the PLL is operating at its lower saturation limit due to the instability. On the other hand, using the PLL freezing method as shown in Fig. 20.26B, the converter can successfully ride-through the zero-voltage fault with a fast fault-recovery response. Using the PLL freezing method, the converter can operate in stand-alone mode during extremely severe faults where the external established voltage is either fully absent or too low for adequate stable synchronization.

20.3.3 Asymmetrical grid fault control

To achieve converter control during asymmetrical faults, three distinct functionalities are needed for successful operation: (i) extraction of the sequence components of the voltage at the converter point of connection, (ii) dual-sequence current tracking capability, and (iii) a current reference generation strategy fulfilling the target of operation without overloading the converter's active devices [33]. Each of these functionalities will be briefly explained in the following sections.

The extraction of the sequence components can be accomplished in several different ways including a Dual Second-Order Generalized PLL (DSOGI-PLL) [34], a Decoupled Double Synchronous Reference Frame PLL (DDSRF-PLL) [35], or a Multiple Complex Coefficient Filter—based PLL (MCCF-PLL) [36], among others [34,37]. All methods serve the task of observing the positive and negative sequences of the unbalanced voltage, and the method being most favorable depends on the control structure employed. In this chapter, the MCCF-PLL is used since it operates in $\alpha\beta$-coordinates, which are used throughout the remainder of the control in this section. To that end, it offers straightforward modularity toward dealing with a distorted environment of multiple positive- and negative-sequence harmonics. If it is desirable to work in the synchronous reference frame or utilize the frequency-locked loop (FLL) synchronization, detailed analysis on the DSOGI-FLL and the DDSRF-PLL can be found in Ref. [38].

This book belongs to Kitab Liaison (ocd1996@gmail.com) Copyright Elsevier 2023

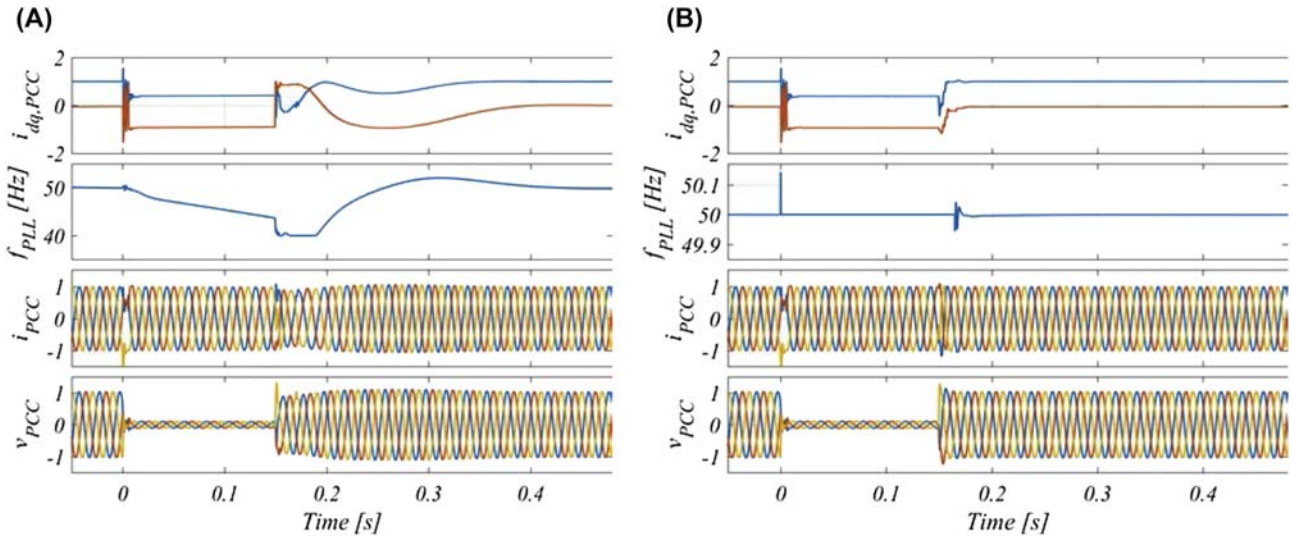

FIGURE 20.26 Simulation results of the grid-side converter from Fig. 20.21 under a zero-voltage fault with impedance $Z = 0.04 + 0.1j$ pu between PCC and fault location. (A) Adaptive normalized phase-locked loop (PLL) without freezing method, (B) Adaptive normalized PLL with the freezing method.

This book belongs to Kitab Liaison (ocd1996@gmail.com)

Copyright Elsevier 2023

20.3.3.1 Grid synchronization during asymmetrical faults

During ideal grid conditions, the often-used SRF-PLL is adequate for grid synchronization. However, under distorted conditions and especially during unbalanced operation, the negative-sequence component causes second-harmonic oscillations in the estimations [39]. As a result of this, more elaborate synchronization methods are needed in this case, including prefiltering and sequence extraction. For attenuating the fundamental negative-sequence component passing through the fundamental positive-sequence frequency, a frequency-shifted low-pass filter shifted by the fundamental frequency (ω_0) can be used to obtain unity gain at the positive sequence while providing attenuation at the fundamental negative sequence. Such a shifted first-order low-pass filter can be expressed as follows:

$$CCF(s) = \frac{\omega_{cf}}{s - j\omega_0 + \omega_{cf}} = \frac{\dfrac{\omega_{cf}}{s - j\omega_0}}{1 + \dfrac{\omega_{cf}}{s - j\omega_0}} \tag{20.30}$$

where ω_{cf} is the cut-off frequency of the filter. Eq. (20.30) can be represented as a feedback loop in the $\alpha\beta$ coordinates, as shown in Fig. 20.27A. The transfer function between the filtered voltage and the input voltage is

$$\frac{v'_{\alpha\beta}(s)}{v_{\alpha\beta}(s)} = \frac{R_{+1}(s)}{1 + R_{+1}(s)} \quad \text{where} \quad R_{+1}(s) = \frac{\omega_{cf}}{s - j\omega_0}. \tag{20.31}$$

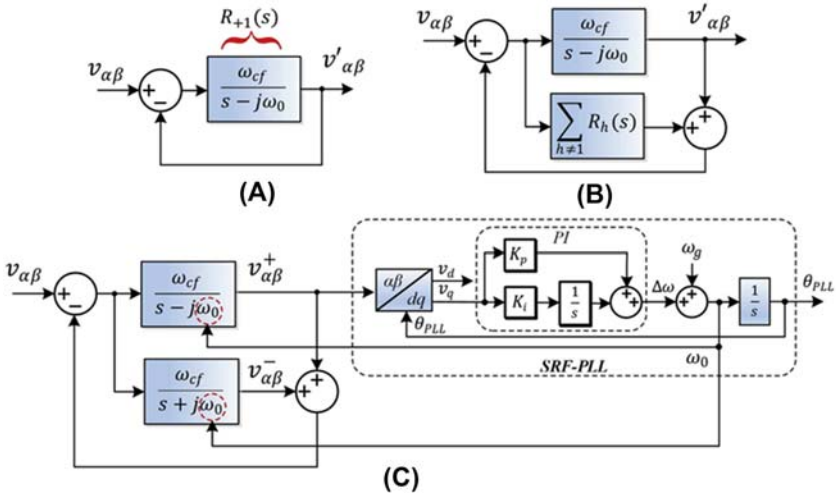

FIGURE 20.27 Block diagram of complex coefficient filter used to attenuate grid harmonics and extract the positive- and negative-sequence components of the input voltage. (A) Complex filter shifted to the positive fundamental frequency, (B) Complex filter, which can remove any arbitrary positive/negative-sequence component at a desired frequency, (C) Example of implementation for extracting the fundamental frequency sequence components only.

This book belongs to Kitab Liaison (ocd1996@gmail.com) Copyright Elsevier 2023

As can be seen, for $s \rightarrow j\omega_0$, the open-loop gain approaches infinity. This makes the closed-loop gain tend to one, which is desired since the filter will not attenuate the positive-sequence fundamental component. Additionally, infinite attenuation at the negative-sequence fundamental frequency should be provided for proper extraction. This is not achieved since by letting $s \rightarrow -j\omega_0$, the open-loop system tends to $\omega_{cf}/j2\omega_0$ and not to zero. To do so, the open-loop transfer function is modified such that it tends to infinity when $s \rightarrow -j\omega_0$. This is done by including the term $R_{-1}(s) = \omega_{cf}/(s+j\omega_0)$ in the denominator of Eq. (20.30) as follows:

$$\frac{v'_{\alpha\beta}(s)}{v_{\alpha\beta}(s)} = \frac{R_{+1}(s)}{1 + R_{+1}(s) + R_{-1}(s)} \rightarrow 0 \quad \text{as} \quad s \rightarrow -j\omega_0. \tag{20.32}$$

This procedure can be extended to any positive- and negative-sequence harmonics for distortion attenuation. Consequently, the filter transfer function can be written as follows:

$$\frac{v'_{\alpha\beta}(s)}{v_{\alpha\beta}(s)} = \frac{R_{+1}(s)}{R_{+1}(s) + \sum_{h \neq 1} R_h(s)} \tag{20.33}$$

which is visualized in its block diagram form in Fig. 20.27B. Furthermore, the implementation of the MCCF with positive- and negative-sequence voltage extraction is visualized in Fig. 20.27C.

Finally, an SRF-PLL is used to estimate the angular frequency of the measured input voltage (ω_0), which is fed back to tune the adaptive complex filters.

20.3.3.2 Current-reference generation methods

With the sequence components of the voltage at the connection point being determined, a proper method for generating the desired current references is needed. A general fault control, including the three required functionalities, is shown in Fig. 20.28, where the reference generator is highlighted since this is to be discussed in the following. Methods for current reference generation are extensive in number, all with different control objectives. These include suppression of active power and DC-link voltage oscillations, suppression of

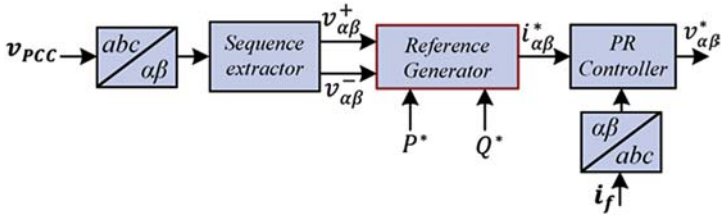

FIGURE 20.28 General fault control of grid-side converter during asymmetrical faults.

This book belongs to Kitab Liaison (ocd1996@gmail.com) Copyright Elsevier 2023

oscillations in the injected reactive power, injection of purely balanced currents, or injection of positive- and negative-sequence currents used to support the positive-sequence voltage while suppressing the negative-sequence one [40]. Since updates of requirements of wind turbine systems demand sophisticated grid voltage support [7], this text focuses primarily on describing the current reference generation for such LVRT compliance. Many of the above-described methods can be realized using a so-called Flexible Positive- and Negative-Sequence Control (FPNSC) [41–43], which will be briefly examined in the consecutive part.

Considering a three-phase three-wire system and utilizing instantaneous power theory [44], the stationary reference frame current references using FPNSC [33,42,43] are

$$i_\alpha^* = P^*\frac{2}{3}\left(\frac{k_1 v_\alpha^+}{(V^+)^2}+\frac{(1-k_1)v_\alpha^-}{(V^-)^2}\right)+Q^*\frac{2}{3}\left(\frac{k_2 v_\beta}{(V^+)^2}+\frac{(1-k_2)v_\beta^-}{(V^-)^2}\right) \tag{20.34}$$

$$i_\beta^* = P^*\frac{2}{3}\left(\frac{k_1 v_\beta^+}{(V^+)^2}+\frac{(1-k_1)v_\beta^-}{(V^-)^2}\right)-Q^*\frac{2}{3}\left(\frac{k_2 v_\alpha}{(V^+)^2}+\frac{(1-k_2)v_\alpha^-}{(V^-)^2}\right) \tag{20.35}$$

where $(V^+)^2 = \left(v_\alpha^+\right)^2 + \left(v_\beta^+\right)^2$, $(V^-)^2 = \left(v_\alpha^-\right)^2 + \left(v_\beta^-\right)^2$ and P^*, Q^* are the references for the active and reactive power, respectively. The first term in each expression represents the current vector contributing to active power, whereas the second term is the current vector contributing to reactive power. Notably, as this current reference strategy both consist of its positive and negative sequences, an expression for the three-phase converter currents is needed in order to avoid destructive overcurrents during the fault. For this to be carried out, the relationship between the active and reactive power references k_1, k_2, and the corresponding converter phase currents must be identified to limit the current references during the fault. Calculation of the peak value of the asymmetrical phase currents is accomplished by expressing the phase current in the stationary reference frame. Then, by use of the inverse Clarke transformation, the amplitude of each phase current can be readily computed [33,45–47]. The procedure of this will be briefly reviewed in the subsequent part.

20.3.3.3 Calculation of phase current magnitude

Given the voltage sequence components extracted using the MCCF-PLL, the $\alpha\beta$-axis components may be written as follows:

$$v_\alpha^+ = V^+\cos(\omega t+\phi^+), \quad v_\beta^+ = V^+\sin(\omega t+\phi^+), \tag{20.36}$$

This book belongs to Kitab Liaison (ocd1996@gmail.com) Copyright Elsevier 2023

$$v_\alpha^- = V^- \cos(-\omega t + \phi^-), \quad v_\beta^- = V^- \cos(-\omega t + \phi^-), \tag{20.37}$$

where

$$\phi^+ = \tan^{-1}\left(\frac{v_\beta^+}{v_\alpha^+}\right), \quad \phi^- = \tan^{-1}\left(\frac{v_\beta^-}{v_\alpha^-}\right). \tag{20.38}$$

Using this while defining

$$I_p^+ = \frac{2k_1P^*}{3V^+},\ I_p^- = \frac{2(1-k_1)P^*}{3V^-},\ I_q^+ = \frac{2k_2Q^*}{3V^+},\ I_q^- = \frac{2(1-k_2)Q^*}{3V^-}, \tag{20.39}$$

the current references from Eqs. (20.34) and (20.35) are equivalent to

$$i_\alpha^* = I^+ \cos(\omega t + \phi^+ - \theta_p) + I^- \cos(\omega t - \phi^- + \theta_n), \tag{20.40}$$

$$i_\beta^* = I^+ \sin(\omega t + \phi^+ - \theta_p) - I^- \sin(\omega t - \phi^- + \theta_n), \tag{20.41}$$

where

$$I^+ = \sqrt{\left(I_p^+\right)^2 + \left(I_q^+\right)^2}, \quad \theta_p = \tan^{-1}\left(\frac{I_q^+}{I_p^+}\right), \tag{20.42}$$

$$I^- = \sqrt{\left(I_p^-\right)^2 + \left(I_q^-\right)^2}, \quad \theta_n = \tan^{-1}\left(\frac{I_q^-}{I_p^-}\right). \tag{20.43}$$

The positive-sequence and negative-sequence currents in Eqs. (20.40)–(20.41) are depicted in Fig. 20.29. Here, the addition of the positive and negative sequences assembles the resulting asymmetrical current, shown as the elliptical loci in the stationary reference frame. From this, the objective is to derive an expression for the maximum value of the elliptical current projected to the *abc*-axes, shown as $(\widehat{I}_a, \widehat{I}_b, \widehat{I}_c)$ in Fig. 20.29. Employing the inverse Clarke transformation, an expression for the maximum three-phase currents can be given as follows:

$$\mathbf{i}_{\mathbf{abc}}^* = \cos(\gamma) i_\alpha^* - \sin(\gamma) i_\beta^*, \tag{20.44}$$

where

$$\gamma = \begin{cases} 0 & \text{for phase a} \\ -2\pi/3 & \text{for phase b} \\ +2\pi/3 & \text{for phase c} \end{cases} \tag{20.45}$$

This book belongs to Kitab Liaison (ocd1996@gmail.com)
Copyright Elsevier 2023

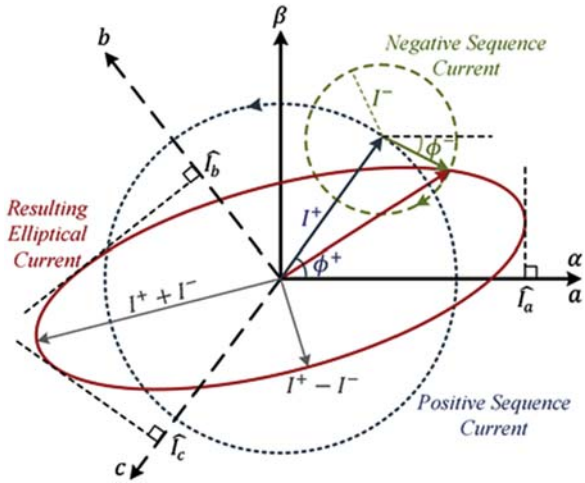

FIGURE 20.29 Positive- and negative-sequence current resulting in the elliptical stationary reference frame current reference. The magnitude of the phase currents is highlighted as the projection of the ellipse to the *abc*-axes.

Through some mathematical manipulations, the magnitude of the phase current can be expressed as follows:

$$\hat{I} = \sqrt{(I^+)^2 + (I^-)^2 + 2I^+I^- \cos(2\gamma + \delta - \theta_n - \theta_p)}, \tag{20.46}$$

with $\delta = \phi^+ - \phi^-$. For details on this derivation, please refer to Ref. [33]. This expression for the peak value of the phase currents will be applied when calculating the power references of the control system.

20.3.3.4 Selection of k_1, k_2, P^*, Q^*

Usually, the control gains k_1 and k_2 may be selected as a constant value based on different controller objectives of the converter including the provision of constant active power or constant reactive power [47,48]. These methods are usually based on requirements seen from the converter point of view where other research [33,49] aims to inject an unbalanced set of currents as required in Refs. [6,7]. In addition to the selection of the FPNSC controller gains, the power references must be picked, such as to avoid violation of the maximum converter current capability.

Defining the reactive power reference to be comprised of its sequence components, i.e., $Q^* = Q^+ + Q^-$ where

$$Q^+ = Q^* k_2, \quad Q^- = Q^*(1 - k_2), \tag{20.47}$$

it is explicitly shown that the reactive power reference can be divided into its sequence components using k_2, which is often assumed constant during the fault. However, considering that some grid codes require dynamic

This book belongs to Kitab Liaison (ocd1996@gmail.com) Copyright Elsevier 2023

dual-sequence current injection, k_2 could be directly set dependent on the voltage unbalance of the grid. After the occurrence of a fault, the maximum reactive power is achieved when the full current capability is used for reactive power injection. Using this, the reactive power reference based on the grid code can be expressed as follows:

$$Q^+ = \begin{cases} 0 & \text{if} \quad V^+ > 0.9 \\ 2Q_{\max}(1 - V^+) & \text{if} \quad 0.5 < V^+ < 0.9 \\ Q_{\max} & \text{otherwise} \end{cases} \tag{20.48}$$

and

$$Q^- = \begin{cases} 0 & \text{if} \quad V^- < 0.1 \\ 2Q_{\max}V^- & \text{if} \quad 0.1 < V^- < 0.5 \\ Q_{\max} & \text{otherwise} \end{cases} \tag{20.49}$$

with this, the reactive power reference can be written as follows:

$$Q^* = Q^+ + Q^- = 2Q_{\max}(1 - V^+ + V^-) \tag{20.50}$$

where k_2 can be calculated as follows:

$$k_2 = \frac{Q^+}{Q^*} = \frac{1 - V^+}{1 - V^+ + V^-}. \tag{20.51}$$

The reactive power is now split between the positive and negative sequences depending on the voltage unbalance factor, rather than a defined fixed value. This means that during symmetrical conditions $k_2 = 1$ since the negative-sequence voltage is zero. Likewise, for an increasing negative-sequence voltage component, k_2 will approach zero, indicating that more efforts are devoted to decreasing the negative-sequence component instead of supporting the positive-sequence component. From Eqs. (20.48) and (20.49), it is clear that $Q_{\max}$ needs to be known in order to set the reactive power reference. By expanding Eq. (20.46), the maximum phase current can be expressed as a function of active and reactive power together with control coefficients as [38]

$$\begin{aligned} \hat{I}^2 = {} & P^{*2}\underbrace{\frac{4}{9}\left(\frac{k_1^2(V^-)^2 + (1-k_1)^2(V^+)^2 + 2k_1(1-k_1)\cos(2\gamma)V^+V^-}{(V^+)^2(V^-)^2}\right)}_{a} \\ & \underbrace{-\frac{4}{9}Q^*\left(\frac{2V^+V^-\sin(2\gamma)(k_1 + k_2 - 2k_1k_2)}{(V^+)^2(V^-)^2}\right)}_{b} P^* \\ & + \underbrace{\frac{4}{9}Q^{*2}\left(\frac{k_2^2(V^-)^2 + (1-k_2)^2(V^+)^2 - 2k_2(1-k_2)\cos(2\gamma)V^+V^-}{(V^+)^2(V^-)^2}\right)}_{c}. \end{aligned} \tag{20.52}$$

This book belongs to Kitab Liaison (ocd1996@gmail.com)
Copyright Elsevier 2023

During a fault, the reactive power is prioritized over active power since the local voltages should be supported. Accordingly, $Q_{\max}$ is computed where the active power reference is set to zero. Doing so, the maximum obtainable reactive power without exceeding $I_{\lim}$ is

$$Q_{\max} = \min\left(\frac{3}{2}\sqrt{\frac{I_{\lim}^2 (V^+)^2 (V^-)^2}{k_2^2 (V^-)^2 + (1-k_2)^2 (V^+)^2 - 2k_2(1-k_2)\cos(2\gamma)V^+V^-}}\right). \tag{20.53}$$

With the expression for $Q_{\max}$, Q^+ and Q^- are evaluated from Eqs. (20.48)–(20.49) and the reactive power reference is $Q^* = Q^+ + Q^-$. Notably, if $Q^* > Q_{\max}$, then $Q^* = Q_{\max}$. After calculating the reactive power reference required by the grid code, any remaining current capability can be allocated to the active power. This remaining capacity is found by solving

$$0 = aP_r^{*2} + bP_r^* + c \quad \rightarrow \quad P_r^* = \frac{-b + \sqrt{-4ac + b^2}}{2a} \tag{20.54}$$

For actual implementation where the outer DC-link voltage controller usually determines the active power reference of the GSC, P_r^* should be compared to the commanded reference obtained from the DC-link voltage controller. If the remaining capacity is higher than the request from the DC-link voltage controller, the active power reference can be achieved without violating the converter current limitation. Alternatively, if the remaining capacity for active power is less than the DC-link request, active power curtailment should be performed by reducing the reference to P_r^* in order to avoid destructive converter overcurrents. In that case, a chopper circuit might be employed to dissipate the accumulation of energy on the DC-link capacitor. For a more thorough walkthrough on these implementation steps, please refer to Ref. [33]. The above-presented strategy is denoted as the FPNSC + GC (FPNSC with Grid Code compliance) in the following verification section.

20.3.3.5 Verification of asymmetrical fault control

Based on the extracted sequence voltages from the MCCF-PLL, k_2 is calculated from Eq. (20.51), whereas $k_1 = 1$ since the active power should only be provided in the positive sequence, and the active and reactive power references are computed from Eqs. (20.50) and (20.54), respectively. All of these values are inserted in Eqs. (20.34)–(20.35) from where the stationary reference frame current references can be directly calculated, which comply with grid codes requirements on dual-sequence current injection and limit the phase current amplitude to a selected maximum. The described method is implemented in simulation and verified on the test system in Fig. 20.30 with the parameters from Table 20.5.

This book belongs to Kitab Liaison (ocd1996@gmail.com) Copyright Elsevier 2023

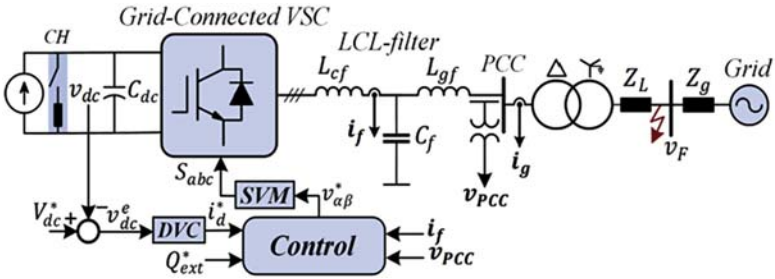

FIGURE 20.30 Grid-connected three-phase converter connected to the grid via a step-up transformer. The asymmetrical fault is highlighted with the *red arrow* (*dark gray arrow* in print version). *CH*, DC chopper circuit; *DVC*, direct voltage control (DC-link voltage controller); *SVM*, space vector modulation.

Two asymmetrical fault types are considered: a single line-to-ground fault and a line-to-line fault both tested for the above methodology (FPNSC + GC) and the highly used BPSC [41]. For BPSC, this is simply achieved using FPNSC and setting $k_1 = 1$ and $k_2 = 1$. These two test cases are shown in Fig. 20.31A and B, where the described methodology using the FPNSC and grid code requirements on dual-sequence current injection is denoted as FPNSC + GC. In both cases, the wind turbine is considered to inject half of its rated power to the grid prior to the fault. It is evident that the injection of both positive-sequence and negative-sequence currents has several advantages compared to only positive-sequence current injection.

At first, using the BPSC, overvoltage occurs on the primary side of the transformer during a single line-to-ground fault. This is despite the fact that the converter in the case of BPSC is not utilizing the full converter current capability since the reactive current is only injected as a requirement of the positive-sequence voltage drop, not the negative-sequence voltage increase.

Similarly, during a line-to-line asymmetrical fault, overvoltages are experienced on the secondary side of the transformer. In contrast, the full converter current capability is utilized since the positive-sequence PCC voltage is lower than the case for the single line-to-ground fault. In both cases, the FPNSC + GC eliminates the phase overvoltage by injection of currents in both the positive- as well as the negative-sequence frame. To that end, the voltage unbalance factor, which is the ratio between the positive-sequence and negative-sequence voltage components, is significantly reduced in both cases using FPNSC + GC. Accordingly, as required by some grid codes, the injection of dual-sequence reactive current support has benefits seen from the grid point of view.

This book belongs to Kitab Liaison (ocd1996@gmail.com) Copyright Elsevier 2023

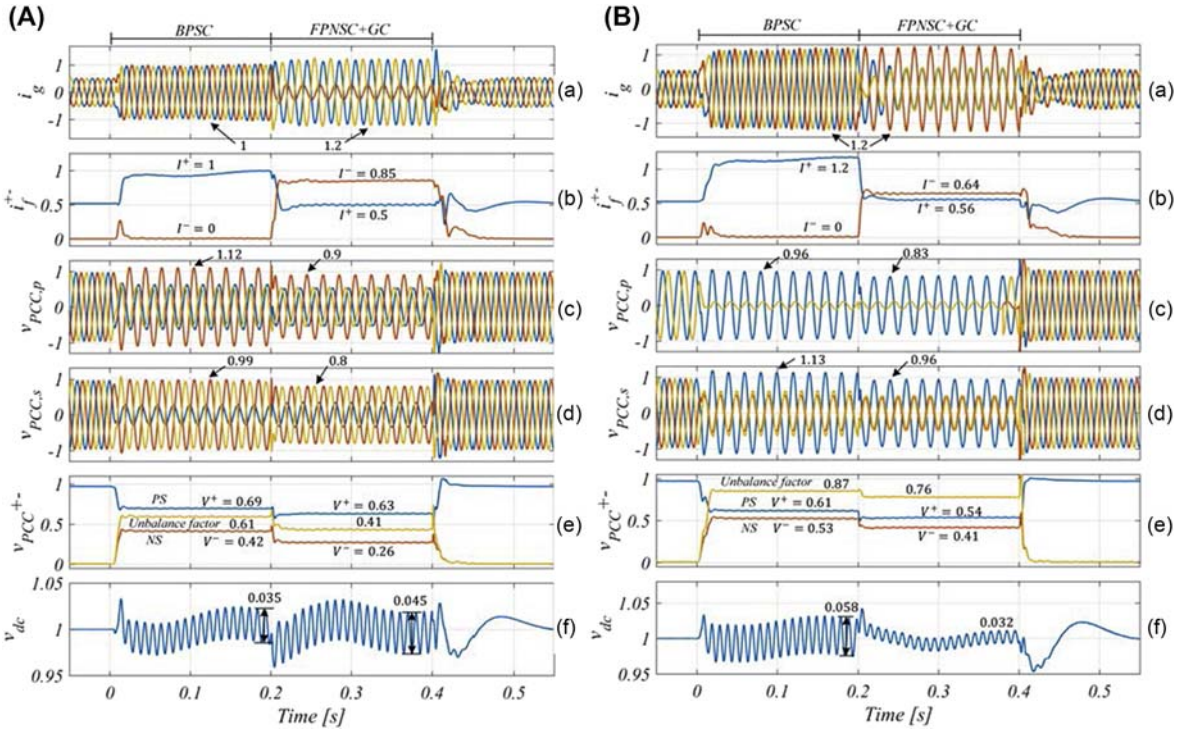

FIGURE 20.31 Simulation results for a single line-to-ground solid fault (A) and line-to-line solid fault (B) for BPSC and FPNSC + GC. Variables of subfigures are as follows: (a) three-phase injected grid currents, (b) positive- and negative-sequence component of controlled converter current, (c) three-phase voltages of transformer primary side, (d) three-phase voltages of transformer secondary side, (e) positive sequence, negative sequence, and voltage unbalance factor of PCC voltage, and (f) DC-link voltage.

This book belongs to Kitab Liaison (ocd1996@gmail.com)

Copyright Elsevier 2023

20.4 Summary

This chapter starts with the investigation of various grid fault types in the power system, where the positive-, negative-, and zero-sequence components of the grid voltage can be classified with a typical step-up Y/d transformer. Aligned with modern grid codes for low-voltage ride-through, Type III and Type IV wind turbine configurations are highly penetrated nowadays. In the case of the DFIG-based wind turbine system, due to the direct link between the generator stator and power grid, the power faults introduce the natural and negative stator flux, which may cause the RSC out of control. Consequently, the control scheme of the RSC is comprehensively addressed subject to the symmetrical and asymmetrical faults. With respect to the permanent magnet synchronous generator—based wind turbine system, as the power grid is fully decoupled from the generator by using full-scale back-to-back power converters, the control scheme of the GSC is in focus. During the symmetrical and asymmetrical faults, two different controller strategies have been presented. For asymmetrical fault control, a novel current reference generation method is studied, which complies with dual-sequence current provision during the fault.

References

[1] M. Mohseni, S. Islam, M.A.S. Masoum, Impacts of symmetrical and asymmetrical voltage sags on DFIG-based wind turbines considering phase-angle jump, voltage recovery, and sag parameters, IEEE Trans. Power Electron. 26 (5) (May 2011) 1587—1598.

[2] G. Saccomando, J. Svensson, A. Sannino, Improving voltage disturbance rejection for variable-speed wind turbines, IEEE Trans. Energy Convers. 17 (3) (September 2002) 422—428.

[3] M.H.J. Bollen, Understanding Power Quality Problems: Voltage Sags and Interruptions, IEEE Press, New York, 1999.

[4] Y. Wu, S. Chang, P. Mandal, Grid-connected wind power plants: a survey on the integration requirements in modern grid codes, IEEE Trans. Ind. Appl. 55 (6) (November-December 2019) 5584—5593.

[5] M. Mohseni, S.M. Islam, Review of international grid codes for wind power integration: diversity, technology and a case for global standard, in: Renewable & Sustainable Energy Reviews, 2012, pp. 3876—3890.

[6] VDE, VDE-AR-N 4120: Technical Requirements for the Connection and Operation of Customer Installations to the High-Voltage Network (TCC High-Voltage), 2015.

[7] VDE, VDE-AR-N 4110: Technical Requirements for the Connection and Operation of Customer Installations to the Medium-Voltage Network (TCC Medium-Voltage), 2017.

[8] F. Blaabjerg, K. Ma, Future on power electronics for wind turbine systems, IEEE Trans. Emerg. Sel. Topics Power Electron. 1 (3) (Sep. 2013) 139—152.

[9] R. Cardenas, R. Pena, S. Alepuz, G. Asher, Overview of control systems for the operation of DFIGs in wind energy applications, IEEE Trans. Ind. Electron. 60 (7) (July 2013) 2776—2798.

This book belongs to Kitab Liaison (ocd1996@gmail.com) Copyright Elsevier 2023

[10] G. Abad, J. Lopez, M. Rodriguez, L. Marroyo, G. Iwanski, Doubly Fed Induction Machine-Modeling and Control for Wind Energy Generation, IEEE Press, Piscataway, NJ, 2011.
[11] H. Geng, C. Liu, G. Yang, LVRT capability of DFIG-based WECS under asymmetrical grid fault condition, IEEE Trans. Ind. Electron. 60 (6) (June 2013) 2495−2509.
[12] C. Wessels, F. Gebhardt, F.W. Fuchs, Fault ride-through of a DFIG wind turbine using a dynamic voltage restorer during symmetrical and asymmetrical grid faults, IEEE Trans. Power Electron. 26 (3) (March 2011) 807−815.
[13] J. Morren, S.W.H. Haan, Ridethrough of wind turbines with doubly-fed induction generator during a voltage dip, IEEE Trans. Energy Convers. 20 (2) (June 2005) 435−441.
[14] G. Pannell, B. Zahawi, D.J. Atkinson, P. Missailidis, Evaluation of the performance of a DC-link brake chopper as a DFIG low-voltage fault-ride-through device, IEEE Trans. Energy Convers. 28 (3) (September 2013) 535−542.
[15] J. Lopez, E. Gubia, E. Olea, J. Ruiz, L. Marroyo, Ride through of wind turbines with doubly fed induction generator under symmetrical voltage dips, IEEE Trans. Ind. Electron. 56 (10) (October 2009) 4246−4254.
[16] W. Chen, D. Xu, N. Zhu, M. Chen, F. Blaabjerg, Control of doubly-fed induction generator to ride-through recurring grid faults, IEEE Trans. Power Electron. 31 (7) (July 2016) 4831−4846.
[17] E. ON-Netz, Requirements for Offshore Grid Connections, April 2008.
[18] M. Tsili, S. Papathanassiou, A review of grid code technical requirements for wind farms, IET Renew. Power Gener. 3 (3) (September 2009) 308−332.
[19] G. Pannell, D.J. Atkinson, B. Zahawi, Minimum-threshold crowbar for a fault-ride-through grid-code-compliant DFIG wind turbine, IEEE Trans. Energy Convers. 25 (3) (September 2010) 750−759.
[20] W. Chen, F. Blaabjerg, N. Zhu, M. Chen, D. Xu, Doubly fed induction generator wind turbine systems subject to recurring symmetrical grid faults, IEEE Trans. Power Electron. 31 (2) (February 2016) 1143−1160.
[21] D. Zhou, F. Blaabjerg, Optimized demagnetizing control of DFIG power converter for reduced thermal stress during symmetrical grid fault, IEEE Trans. Power Electron. 33 (12) (December 2018) 10326−10340.
[22] D. Xiang, L. Ran, P.J. Tavner, S. Yang, Control of a doubly fed induction generator in a wind turbine during grid fault ride-through, IEEE Trans. Energy Convers. 21 (3) (September 2006) 652−662.
[23] L. Xu, Y. Wang, Dynamic modeling and control of DFIG-based wind turbines under unbalanced network conditions, IEEE Trans. Power Syst. 22 (1) (February 2007) 314−323.
[24] D. Zhou, F. Blaabjerg, Improved DFIG capability during asymmetrical grid faults, in: Proc. of IECON, 2015, pp. 1152−1157, 2015.
[25] A.G. Yepes, Digital Resonant Current Controllers for Voltage Source Converters, Doctoral dissertation, 2011.
[26] M.G. Taul, X. Wang, P. Davari, F. Blaabjerg, Robust fault ride-through of converter-based generation during severe faults with phase jumps, IEEE Trans. Ind. Appl. 56 (1) (January-February 2020) 570−583.
[27] L. Harnefors, M. Bongiorno, S. Lundberg, Input-admittance calculation and shaping for controlled voltage-source converters, IEEE Trans. Ind. Electron. 54 (6) (December 2007) 3323−3334.
[28] N. Tleis, Power Systems Modelling and Fault Analysis - Theory and Practice, 1st ed., Elsevier, 2008. ISBN: 978-0-7506-8074-5.

This book belongs to Kitab Liaison (ocd1996@gmail.com) Copyright Elsevier 2023

[29] M.G. Taul, X. Wang, P. Davari, F. Blaabjerg, An overview of assessment methods for synchronization stability of grid-connected converters under severe symmetrical grid faults, IEEE Trans. Power Electron. 34 (10) (October 2019) 9655−9670.

[30] J.M. Bloemink, M.R. Iravani, Control of a multiple source microgrid with built-in islanding detection and current limiting, IEEE Trans. Power Deliv. 27 (4) (October 2012) 2122−2132.

[31] H. Chen, C. Lee, P. Cheng, R. Teodorescu, F. Blaabjerg, A low-voltage ride-through technique for grid-connected converters with reduced power transistors stress, IEEE Trans. Power Electron. 31 (12) (December 2016) 8562−8571.

[32] S.B. Naderi, M. Negnevitsky, K.M. Muttaqi, A modified DC chopper for limiting the fault current and controlling the DC-link voltage to enhance fault ride-through capability of doubly-fed induction-generator-based wind turbine, IEEE Trans. Ind. Appl. 55 (2) (March-April 2019) 2021−2032.

[33] M.G. Taul, X. Wang, P. Davari, F. Blaabjerg, Current reference generation based on next generation grid code requirements of grid-tied converters during asymmetrical faults, in: IEEE Journal Emerg. Sel. Topics Power Electron, 2020.

[34] S. Golestan, J.M. Guerrero, J.C. Vasquez, Three-phase PLLs: a review of recent advances, IEEE Trans. Power Electron. 32 (3) (March 2017) 1894−1907.

[35] P. Rodriguez, J. Pou, J. Bergas, J.I. Candela, R.P. Burgos, D. Boroyevich, Decoupled double synchronous reference frame PLL for power converters control, IEEE Trans. Power Electron. 22 (2) (March 2007) 584−592.

[36] X. Guo, W. Wu, Z. Chen, Multiple-complex coefficient-filter-based phase-locked loop and synchronization technique for three-phase grid-interfaced converters in distributed utility networks, IEEE Trans. Ind. Electron. 58 (4) (April 2011) 1194−1204.

[37] S. Golestan, J.M. Guerrero, J.C. Vasquez, A.M. Abusorrah, Y. Al-Turki, A study on three-phase FLLs, IEEE Trans. Power Electron. 34 (1) (January 2019) 213−224.

[38] R. Teodorescu, M. Liserre, P. Rodriguez, Grid Converters for Photovoltaic and Wind Power Systems, 1st ed., Wiley, 2011.

[39] X. He, H. Geng, G. Yang, A generalized design framework of notch filter based frequency-locked loop for three-phase grid voltage, IEEE Trans. Ind. Electron. 65 (9) (September 2018) 7072−7084.

[40] Ö. Göksu, R. Teodorescu, C.L. Bak, F. Iov, P.C. Kjær, Impact of wind power plant reactive current injection during asymmetrical grid faults, IET Renew. Power Gener. 7 (5) (September 2013) 484−492.

[41] X. Du, Y. Wu, S. Gu, H. Tai, P. Sun, Y. Ji, Power oscillation analysis and control of three-phase grid-connected voltage source converters under unbalanced grid faults, IET Power Electron. 9 (11) (September 7, 2016) 2162−2173.

[42] A. Camacho, M. Castilla, J. Miret, A. Borrell, L.G. de Vicuña, Active and reactive power strategies with peak current limitation for distributed generation inverters during unbalanced grid faults, IEEE Trans. Ind. Electron. 62 (3) (March 2015) 1515−1525.

[43] J. Jia, G. Yang, A.H. Nielsen, A review on grid-connected converter control for short-circuit power provision under grid unbalanced faults, IEEE Trans. Power Deliv. 33 (2) (April 2018) 649−661.

[44] H. Akagi, E.H. Watanabe, M. Aredes, Instantaneous Power Theory and Applications to Power Conditioning, 1st ed., IEEE Press on Power Engineering, 2007.

[45] C. Lee, C. Hsu, P. Cheng, A low-voltage ride-through technique for grid-connected converters of distributed energy resources, IEEE Trans. Ind. Appl. 47 (4) (July-August 2011) 1821−1832.

This book belongs to Kitab Liaison (ocd1996@gmail.com) Copyright Elsevier 2023

[46] K. Schönleber, E. Prieto-Araujo, S. Ratés-Palau, O. Gomis-Bellmunt, Extended current limitation for unbalanced faults in MMC-HVDC-connected wind power plants, IEEE Trans. Power Deliv. 33 (4) (August 2018) 1875−1884.

[47] F. Wang, J.L. Duarte, M.A.M. Hendrix, Pliant active and reactive power control for grid-interactive converters under unbalanced voltage dips, IEEE Trans. Power Electron. 26 (5) (May 2011) 1511−1521.

[48] S. Mortazavian, M.M. Shabestary, Y.A.I. Mohamed, Analysis and dynamic performance improvement of grid-connected voltage−source converters under unbalanced network conditions, IEEE Trans. Power Electron. 32 (10) (October 2017) 8134−8149.

[49] S.K. Chaudhary, Ö. Göksu, R. Teodorescu, P.C. Kjaer, Impact of negative sequence current injection by wind power plants, in: Proc. IEEE PESGM, Vancouver, BC, 2013, pp. 1−5.

This book belongs to Kitab Liaison (ocd1996@gmail.com) Copyright Elsevier 2023

This page intentionally left blank

This book belongs to Kitab Liaison (ocd1996@gmail.com)

Copyright Elsevier 2023

Chapter 21

Wind farm control and optimization

Weihao Hu, Qi Huang, Xiawei Wu, Jian Li, Zhenyuan Zhang
University of Electronic Science and Technology of China, Chengdu, Sichuan, China

21.1 Introduction

With the fast development of renewable energy, wind energy is increasingly recognized by both the public and the market to be an important energy source. According to the report of GWEC (Global Wind Energy Council) 2018 [1], wind energy has maintained rapid growth in recent years and its installed capacity cannot be underestimated, and will further continue to grow in the next few years as shown in Fig. 21.1.

Wind energy has already provided more new power production than any other forms of energies [1]. Wind farms as a power plant source are relatively cost effective and it is a clean fuel source. Wind power has already enabled many countries industry upgrade and provided many increasing job opportunities. Besides, this sustainable energy can be developed both on onshore and offshore, which is more flexible to convert wind resources into clean energy and make benefits to economy. The advantages and disadvantages of onshore and offshore wind farms are compared, and these basic conditions are the basis for wind farm control and optimization in Table 21.1.

The study of wind farms attracts a lot of interests of researchers all over the world. For the sake that it is a relatively new technology, there should be more space left for the researchers to investigate the cost reduction method. For wind farm optimization work, it can be mainly divided into wind farm layout optimization and various levels of wind farm control [3–5]. Generally speaking, the wind farm level control will be considered comprehensively first, and then there will be some more specific decentralized control. Even a small improvement in the wind farm control or wind farm optimization would lead to a large sum of money saving. Hence, much work is aimed at maximizing the energy production of whole wind farms or minimizing the investment cost.

Control of Power Electronic Converters and Systems. https://doi.org/10.1016/B978-0-12-819432-4.00002-0
Copyright © 2021 Elsevier Ltd. All rights reserved.

This book belongs to Kitab Liaison (ocd1996@gmail.com)
Copyright Elsevier 2023

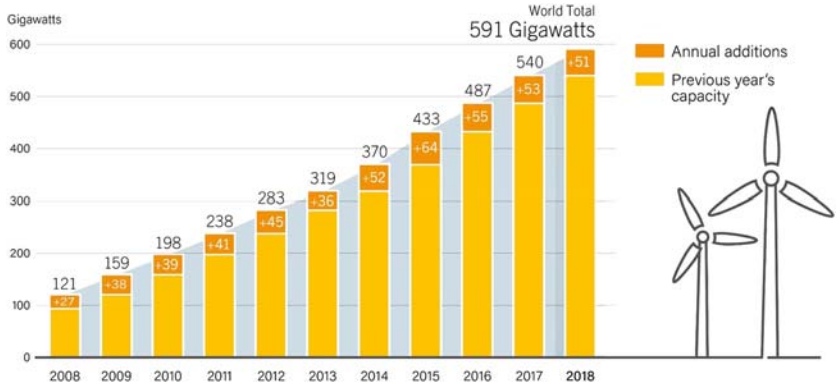

FIGURE 21.1 Global annual installed capacity of wind from 2008 to 2018 [1].

TABLE 21.1 Comparison between onshore and offshore wind farms [2].

Offshore		Onshore	
Advantage	**Disadvantage**	**Advantage**	**Disadvantage**
Wind speed increase in the afternoon corresponds to the increase trend of power demand	Complex structures are needed to support the turbines in the sea	Simpler technologies compared with offshore wind generation	Wind turbines (WTs) operated at lower efficiency
The cities with largest power demand are always located near shorelines, which means that the electricity generated by offshore wind farm do not need to be transmitted over long expensive transmission lines	Additional wear and tear from higher wind speeds or even storms makes the WTs more expensive than onshore ones		Long transmission lines are often required
Higher and smooth wind speed	The maintenance is more complicated and expensive. Skilled technicians with experiences are required	Overall lower investment and it is easy to do maintenance	Marring landscapes
No impacts on residents			Wind speed will often increase in the night

This book belongs to Kitab Liaison (ocd1996@gmail.com)
Copyright Elsevier 2023

This chapter is organized as follows: Section 21.2 introduces wind farm active dispatch methods. And wind farm reactive dispatch is analyzed in Section 21.3. And wind farm layout optimization is presented in Section 21.4. In the end, this chapter is summarized in Section 21.5.

21.2 Wind farm active dispatch

Maximizing the power production of wind farms using proper control strategy has become an important issue for wind farm operators. A proper active dispatch method can help achieve better economic benefits of operating the wind farms. The wake effect is firstly introduced then two regular wind farm control strategies are mentioned. After that, a recent wind farm control strategy for less noise is analyzed and compared with previous two methods.

21.2.1 Wake effect

Whether it is wind farm control problem or wind farm layout optimization, it cannot be introduced without wake effect. When the wind passes through a wind farm, different positions of the wind turbine (WT) will see different wind speeds. Generally speaking, the wind speed will gradually decrease as the number of passing WTs increases. This phenomenon is called wake effect [6,7]. The wind velocity of x-th downstream WT caused by one upstream WT is calculated according to the Jensen model as follows:

$$V_x = V_0 - V_0\left(1 - \sqrt{1 - C_T}\right)\left(\frac{R_0}{R_x}\right)^2\left(\frac{S_{overlap}}{S_0}\right) \tag{21.1}$$

where C_T is a thrust coefficient for the WT, V_0 is the initial velocity at upstream WT, and $S_{overlap}$ is the actual overlap area between wake area and downstream blade sweeping area S_0. Then, R_x is the wake radius generated by linear expansion of WT radius R_0 with distance x between upstream and downstream WT.

$$R_x = R_0 + kx \tag{21.2}$$

where k is the wake decay constant.

There is a phenomenon called wake combination where one downstream WT is affected by several upstream WTs in the wind farm [8]. The wind velocity at the x-th downstream WT caused by N WTs can be derived as follows:

$$V_y = V\left[1 - \sqrt{\sum_{y=1}^{N}\left[1 - \left(\frac{V_x}{V_0}\right)\right]}\right] \tag{21.3}$$

This book belongs to Kitab Liaison (ocd1996@gmail.com)
Copyright Elsevier 2023

Based on the basic Jensen model, some works also propose developed wake model due to specific situations [9−11].

21.2.2 Single MPPT and global MPPT

Jensen wake model is taken to calculate the velocity here [12]. Then, a simplified static model is selected to calculate the mechanical power production for a WT in a wind farm:

$$P_{mec} = \frac{1}{2}\rho\pi R^2 V^3 C_p(\beta, \lambda) \tag{21.4}$$

where ρ is the air density, R is the rotor radius, V is the effective wind velocity on WT, and C_p is the power coefficient. C_p and C_t are two lookup tables, both are determined by blade pitch angle β and tip speed ratio λ. Tip speed ratio can be derived as follows:

$$\lambda = \frac{\omega R}{V} \tag{21.5}$$

ω represents the rotational speed of WT.

The mode of WT operation is presented to serve wind farm control strategies [13,14]. Generally, there are two operation ways for WTs: normal operation and derate operation. As for normal operation, there are five regions according to different wind speeds, which are shown in Fig. 21.2. In Region 1, because the extracted wind energy is less than the losses, WT does not work. In Region 2, WT extracts wind energy at maximum power. In order to achieve this goal, WT must change the rotational speed ω to get the maximum C_p and the pitch angle β is set at 0 degree. In Region 3, the wind energy available is more than the capacity of WT. So, the pitch angle control is activated to make the rotational speed of rotor and active power of WT is equal to the rated value.

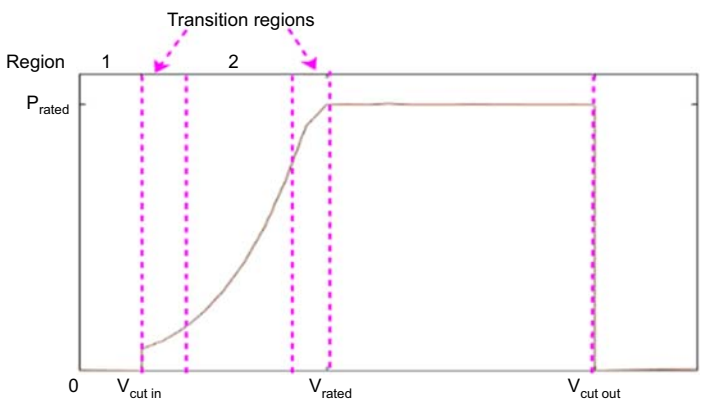

FIGURE 21.2 Normal operation curve of wind turbine.

This book belongs to Kitab Liaison (ocd1996@gmail.com)
Copyright Elsevier 2023

Otherwise, the rotor and turbine may overload, which will cause WT breakdown. In the two transition regions: Region 1 to Region 2 and Region 2 to Region 3, the rotor rotational speed is fixed to the value of lower limit and the value of higher limit, respectively.

The derating operation is a variation of the normal operation. In Region 2, the derating operation aims to make WT yield power at a set value from WF controller instead of maximizing the power production. The power production of each WT is determined by C_p as well as the wind velocity V, which is related to C_t. Both of C_p and C_t are lookup tables that are determined by the blade pitch angle β and tip speed ratio λ. Hence, the value of WT power production can be controlled by adjusting β and λ. Fig. 21.3 shows the contour curve when the power coefficient C_p equals 0.4. From the curve, it is can be seen that there are many options for operation point (β, λ) to get a given power reference. Each operation point represents a control strategy of the WT. Therefore, there is a freedom to choose WT control strategy under the constraints of ω and β. Constant tip speed ratio (Const-λ) control strategy is selected when the operation point of whom is marked as shown in Fig. 21.3. In this strategy, the tip speed ratio λ is set to be equal to the λ that makes C_p to maximize until ω reaches its rated value ω_{rated}. In the initial stage of wind farm control, the maximum power point track (MPPT) strategy is widely used for each WT and can ensure the maximum power captured for each WT [15]. The principle is tracking the maximum power coefficient (C_p) and the maximum power corresponding to the wind flow through rotor [16]. Under this strategy which is called single MPPT, each WT works independently and yields energy freely without any constraints. However, due to the impact of wake effect, the wind at the downstream WTs will be reduced. There is a

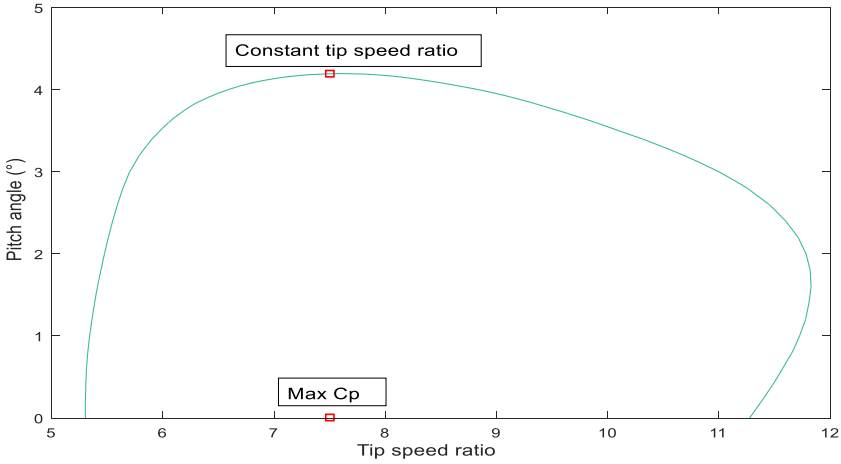

FIGURE 21.3 A contour curve of $C_p = 0.4$ for different pitch angle and tip speed ratio.

This book belongs to Kitab Liaison (ocd1996@gmail.com)
Copyright Elsevier 2023

possibility named global MPPT to reduce the total wake losses by controlling the operation point of each WT so that the total power production of the wind farm may be increased. Using a pitch angle control method to improve the wind farm efficacy has already been studied in Refs. [17,18]. The control target for the whole wind farm and not just for every single WT is a more ideal solution for wind farm controllers.

21.2.3 Noise impact reduction

The power dispatch strategy for wind farms generally focuses on maximizing the captured power or minimizing the levelized production cost (LPC). However, some environmental impacts could be considered if needed. Noise caused by wind farms may cause interference to the surrounding living environment and the power dispatch strategy should combine power production and environmental factors. An optimal power dispatch strategy with limited WTs noise impact is proposed for a better environmental performance as well as maximizing the power generation [19].

WT noise consists of the following parts: the noise caused by the inflow turbulence, the noise caused by the interaction between the turbulent boundary layer and the blade trailing, and the noise caused by the vortex shedding at the trailing edge. Compared with the first two parts, the third part of WT noise is too small. Therefore, it can be ignored because the blade trailing edge of WTs is mostly pointed nowadays.

The modeling of WT noise is developed by Hubbard et al. in the 1980s based on the aerodynamics and helicopter noise model. Hubbard's noise model is complete without simplified factors and considers the influence of wind velocity on the turbine noise. Absolutely, each turbine noise also can be assumed as a fixed value, and then the propagation model is adopted to calculate through distances. However, what that method considers is just a part of the noise concern: wind velocity magnitude is not considered regarding the turbine noise. In fact, the wind velocity is combined with the wake effect, power production, and also turbine noise and these are all interacted. So, the evaluation of the WT noise can be estimated based on Hubbard model as the following two parts [20]:

$$SPL_1(f) = 10\lg\left[\frac{B\sin^2\varphi\rho^2 C_{0.7}R\sigma^2 V_{0.7}^4}{r_0^2 c_0^2}\right] + K_a(f) \tag{21.6}$$

$$f_{peak} = SV_{0.7}/(h - 0.7R) \tag{21.7}$$

$$SPL_2(f) = 10\lg\left\{\frac{V_r^5 BD\delta l}{r_0^2}\left(\frac{S}{S_{\max}}\right)^4\left[\left(\frac{S}{S_{\max}}\right)^{1.5} + \frac{1}{2}\right]^4\right\} + K_b \tag{21.8}$$

This book belongs to Kitab Liaison (ocd1996@gmail.com) Copyright Elsevier 2023

where $V_{0.7}$ is the rotating speed of WT blade at 0.7 radius. And r_0 is the distance from the WT noise source to the noise observation site. More parameters can be seen in Ref. [20].

Just like multiple wakes above, one noise observation site can be affected by not only one WT in a wind farm. In acoustics, multiple noise sources from multiple WTs can be accumulated by a logarithmic method. This method also can be applied in the different parts of the one WT noise. So, the accumulated noise L_2 for two WTs as an example can be obtained as follows:

$$L_2 = 10\lg\left(10\hat{}(L_i / 10) + 10\hat{}(L_j / 10)\right) \tag{21.9}$$

where L_i is one WT noise resource, and L_j is another noise resource. Analogically, no matter how many WTs are in the wind farm, they can be accumulated in this equation to get the total noise from the target wind farm.

Without considering WT noise problem and wake effect, the optimal power curve C_p (β, λ) is adjusted by the β and λ to take the optimal pitch angle β_{opt} and the optimal tip speed ratio λ_{opt} based on the individual MPPT strategy. And WTs can capture their own maximum wind energy. However, the maximum power production of each single WT does not mean that the entire wind farm reaches the maximum power production. The noise problem in onshore wind farms should be controlled for meeting specific noise regulations. For power dispatch method, β and λ can be variables to adjust both the wind velocity arrived at the downstream and the captured power for optimization. Thus, the control optimization strategy is carried out to avoid noise problem caused by WTs as well as increase the power generation. Noise caused WTs is mainly determined by the distance from WTs to the observation site and the WTs rotational speed related to the control strategy. While WTs layout and the observation site are fixed, the noise of the wind farm depends on the control strategy of WTs. And parts of WTs are chosen to operate in the constant-ω control strategy for a limiting noise value, since the superposition of sound is mainly determined by the nearest sources. Then, other WTs will be operated to increase the power generation of wind farms considering power losses and topography by adjusting λ and β.

Although limiting the rotational speed may have a slight risk on entering the stall area, there will be a smoother transition between full load and partial load. For noise problems of wind farms, it is totally worthwhile to slightly increase the risk of stalling for some WTs to achieve the purpose of controlling noise for good environmental performances and to increase power generation of wind farms in the case of nonextreme wind conditions. And the noise caused by all WTs at observation site is controlled no more than a specified value $Noi_{\max}$ according to the ISO standard:

$$L_N = 10\lg\left[\sum_{n=1}^{N} 10^{0.1L_n}\right] \le Noi_{\max} \tag{21.10}$$

This book belongs to Kitab Liaison (ocd1996@gmail.com) Copyright Elsevier 2023

Then, the objective for optimization can be presented as follows:

$$\max(POUT) = \max(POUT(\beta_i, \lambda_i)) \tag{21.11}$$

$$dB_{\text{obse}}(\beta_i, \lambda_i) = 10\lg\left[\sum_{i=1}^{n} 10^{0.1dB_i}\right] \le Noi_{\max} \tag{21.12}$$

$$\beta_{\min} \le \beta_i \le \beta_{\max} \quad \forall i = 1, 2, \ldots, n \tag{21.13}$$

$$\lambda_{\min,i} \le \lambda_i \le \lambda_{\max} \quad \forall i = 1, 2, \ldots, n \tag{21.14}$$

$$\lambda_{ne,\ i} = \frac{\omega_c R}{v} \quad \forall i = 1,\ 2, \ldots,\ n_1 \tag{21.15}$$

$$\lambda_{fa,i,\min} = \lambda_{opt}(\beta_i) \quad \forall i = n_1 + 1, \ldots, n \tag{21.16}$$

$$0 \le P_i(\beta, \lambda) \le P_{av,i} \tag{21.17}$$

where $P_{av,i}$ is the available captured power of each WT. And β and λ are limited to upper and lower limits. $\lambda_{fa,i,\min}$ is the optimal tip speed ratio obtained by MPPT of the whole wind farm, although some WTs cannot be operated like this for noise control needs. To ensure noise problem priority, the nearest WTs are operated by limiting their rotational speed due to the wind direction, and then other more WTs are operated on more attention to increase power generation.

One onshore wind farm with the terrain is adopted to verify the effectivity and practicality of the proposed optimized operating control strategy as shown in Fig. 21.4.

The layout of wind farm is fixed as the reference wind farm with 80 DTU 5 MW WTs used for analysis. As it can be seen in Fig. 21.4, the observation points as shown by the green house are 800 m far away from the side of the reference wind farm and the interval of WTs is fixed as 4D (diameter). 45 dB(A) is chosen as the evaluation value for WT noise. It can be explained that the wind farm noise is not permitted to exceed 45 dB(A) under control strategies of WTs operation.

The onshore wind farm is assumed on the construction area with a three-degree slope as shown in Fig. 21.5. The wind speed for simulation is firstly chosen to be slightly higher than the rated wind speed, taking 11.8 m/s. This will make some WTs to operate above the rated speed of the reference WT, and some of them below the rated speed, respectively, due to the wake effect, which will have a comprehensive impact on the WT noise. And the wind direction comes from the 90 degrees direction as shown in Fig. 21.4.

Some nearest WTs are chosen for noise reduction according to the wind direction. It means that the red (dark gray in print version) WTs in Fig. 21.4. are operated at a constant rotational speed to make sure the noise reduction for the onshore wind farm.

This book belongs to Kitab Liaison (ocd1996@gmail.com) Copyright Elsevier 2023

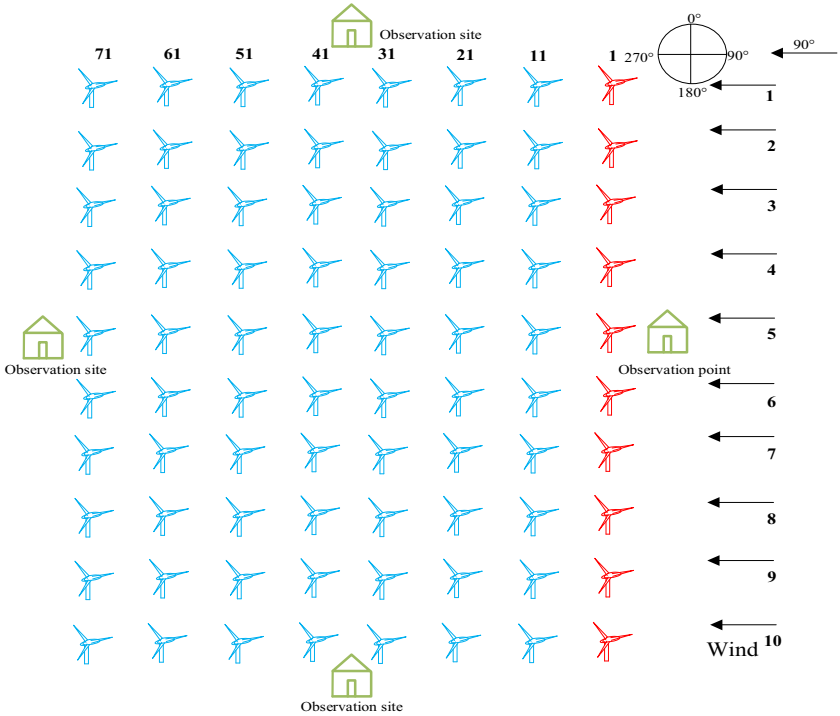

FIGURE 21.4 Reference wind farm.

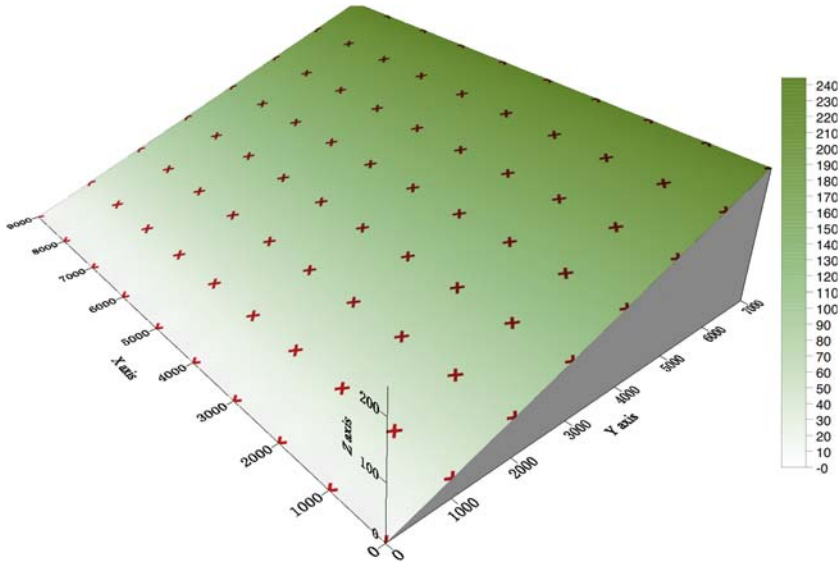

FIGURE 21.5 Onshore wind farm with a slope for studying noise reduction (Units: m).

This book belongs to Kitab Liaison (ocd1996@gmail.com)
Copyright Elsevier 2023

The result of the novel optimized power dispatch strategy (NOPDS) is presented and compared with two conventional strategies as shown in Table 21.2. The first is the MPPT strategy for a single WT, and the second is the MPPT strategy for the entire wind farm. It is noticed that not all WT operating data are shown for similarities, and the representative ones are shown for details.

From Table 21.2, the wind farm noise is reduced compared with the individual MPPT. The noise from the onshore wind farm is effectively contained to a reasonable range. Furthermore, noise can be reduced even more if needed. Besides, the power generation of the whole wind farm is increased by 14.15%. The power generation of MPPT has a relatively large reduction compared with NOPDS because the distance of WTs is smaller to make the wake effect obvious. As for the comparison with global MPPT, although the power generation is slightly higher than NOPDS, the noise of the entire wind farm is even higher than the individual MPPT. In fact, a better environmental performance may be more beneficial than a small increase in the power production.

The red (dark gray in print version) WTs in Fig. 21.4 represent the first row in the wind farm, followed by the second to eighth rows. And the total amount of electricity from each row WTs can be found in Fig. 21.6, and this MPPT indicates an individual MPPT. The row of red (dark gray in print version) WTs is selected to reduce the noise of the entire wind farm by limiting the rotational speed because they are closest to the observation point on the right. Also the power generation is reduced. On the basis of the above, for the latter rows of WTs along the wind direction, the wake losses are reduced by adjusting the pitch angle and the tip speed ratio, thereby increasing the power generation of the entire wind farm.

21.3 Wind farm reactive dispatch

In addition to the active power dispatch, the reactive power dispatch is also important for the control optimization of wind farms. Wind farms are normally required to provide reactive power to the system. When the power system operator gives a reactive power reference to a wind farm, wind farm controller gives reactive power references to each WT according to the reactive power dispatch strategies. This section introduces a regular method for the wind farm reactive dispatch and presents two novel strategies for better performances.

21.3.1 Regular method

As the increase of wind farm scales, wind energy accounts for more and more capacities in power system. According to the wind power technology standard, wind farms need to provide reactive power to support the Point of Common Coupling (PCC) voltage in power systems.

This book belongs to Kitab Liaison (ocd1996@gmail.com) Copyright Elsevier 2023

TABLE 21.2 Optimized results comparison of two regular strategies and proposed one in the wind farm shown in Fig. 21.4.

	Individual MPPT				Global MPPT				NOPDS			
WT numbers	λ	B	Ω	V	λ	β	ω	v	λ	B	ω	v
1	6.89	3.39	12.10	11.59	6.89	7.41	12.10	11.59	6.43	6.40	11.29	11.59
2	6.89	3.39	12.10	11.59	6.89	3.91	12.10	11.59	6.43	5.58	11.29	11.59
3	6.89	3.39	12.10	11.59	6.89	3.70	12.10	11.59	6.43	3.73	11.29	11.59
4	6.89	3.39	12.10	11.59	6.89	3.28	12.10	11.59	6.43	4.25	11.29	11.59
5	6.89	3.39	12.10	11.59	6.89	4.31	12.10	11.59	6.43	5.93	11.29	11.59
6	6.89	3.39	12.10	11.59	6.89	4.18	12.10	11.59	6.43	4.65	11.29	11.59
7	6.89	3.39	12.10	11.59	6.89	2.60	12.10	11.59	6.43	4.35	11.29	11.59
8	6.89	3.39	12.10	11.59	6.89	6.30	12.10	11.59	6.43	4.78	11.29	11.59
9	6.89	3.39	12.10	11.59	6.89	4.50	12.10	11.59	6.43	4.61	11.29	11.59
10	6.89	3.39	12.10	11.59	6.89	4.68	12.10	11.59	6.43	4.26	11.29	11.59
11	7.5	0	11.73	10.32	7.23	3.63	12.10	11.03	7.35	3.26	12.10	10.86
21	7.5	0	10.89	9.58	7.50	3.30	12.10	10.64	7.5	5.66	11.96	10.52
31	7.5	0	10.88	9.57	7.49	4.36	12.10	10.66	7.19	4.80	12.10	11.10

Continued

This book belongs to Kitab Liaison (ocd1996@gmail.com)

Copyright Elsevier 2023

TABLE 21.2 Optimized results comparison of two regular strategies and proposed one in the wind farm shown in Fig. 21.4.—cont'd

	Individual MPPT				Global MPPT				NOPDS			
WT numbers	λ	B	Ω	V	λ	β	ω	v	λ	B	ω	v
41	7.5	0	11.02	9.69	7.23	4.40	12.10	11.04	7.09	3.35	12.10	11.26
51	7.5	0	11.17	9.83	7.06	3.81	12.10	11.30	7.14	2.25	12.10	11.17
61	7.5	0	11.33	9.97	7.00	2.71	12.10	11.40	7.24	4.46	12.10	11.03
71	7.5	0	11.49	10.11	7.05	0	12.10	11.32	6.92	3.23	12.10	11.54
Wake loss	33.18%				19.44%				19.95%			
Cable loss	0.43 MW				0.26 MW				0.26 MW			
P (E_{total})	267.27 MW				322.24 MW				320.22 MW			
WT noise	45.54 dB(A)				46.16 dB(A)				44.99 dB(A)			

This book belongs to Kitab Liaison (ocd1996@gmail.com)

Copyright Elsevier 2023

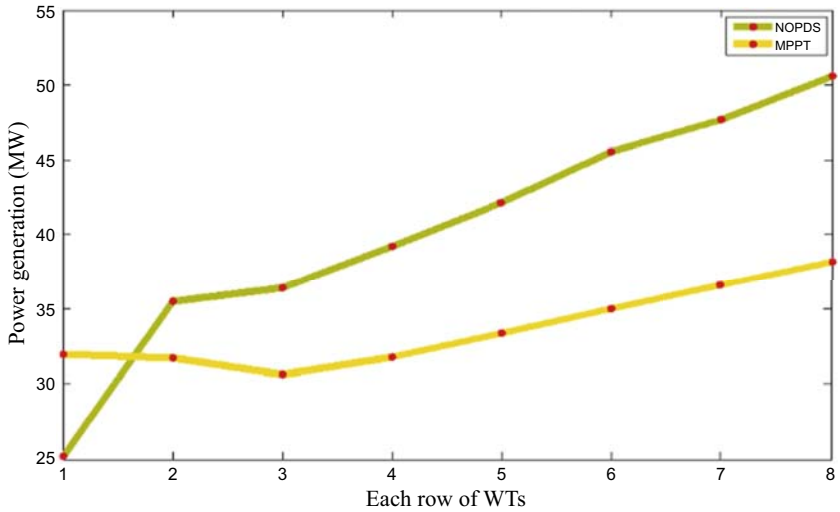

FIGURE 21.6 Total power generation of each row of wind turbines (WTs) for the scenario: 11.8 m/s wind speed.

To meet the requirements for reactive power, it is a tradition to add reactive power sources from capacitor banks, Static Synchronous Compensators, Static Var Compensators, etc., for the PCC. These strategies are adopted for small wind farms without power electronic devices installed. However, as the wind farm scale increases, more and more doubly fed induction generators and permanent magnet synchronous generators (PMSGs) are used in wind farms. Also, this makes more options for wind farms such as being a reactive power source because these power electronic devices can be beneficial. In addition, the investment for original reactive power sources can be reduced in these novel reactive power dispatch methods.

Once the power system requires a reference for the reactive power from wind farms, the wind farm owners need to dispatch the reactive power reference to each WT due to their reactive dispatch method. The regular method is to dispatch proportionally and dispatching the reactive power references is based on their available range [21]. In the proportional strategy, the reference reactive power is dispatched among all the WTs as follows:

$$Q_{WT,\,k}^{ref} = \frac{Q_{WT,\,k}^{avail}}{\sum_{k=1}^{n} Q_{WT,\,k}^{avail}} Q_{WF}^{ref} \tag{21.18}$$

where $Q_{WT,k}^{ref}$ and Q_{WF}^{ref} are the reference reactive powers of WT k and the whole wind farm, respectively, $Q_{WT,k}^{avail}$ is the available reactive power of WT k, n is the number of WTs. Obviously, this approach is simple and feasible, and it

This book belongs to Kitab Liaison (ocd1996@gmail.com) Copyright Elsevier 2023

can be guaranteed not to exceed the limit. From the view of optimization works that differ from the basic method, different algorithms and objectives are optional to be chosen to deal with the reactive dispatch problem for different operating requirements. Among them, losses minimization, investment reduction, voltage stability, etc., are all common objective functions.

As for the algorithm aspect, Particle Swarm Optimization (PSO) algorithm, Feasible Solution Search algorithm, Seeker Optimization Algorithm, and other algorithms can be chosen to improve the reactive dispatch optimization process. Recently, some optimization works are updated to specifically solve this problem from various objectives.

21.3.2 Loss minimization

The power losses of wind farms basically come from the losses from WT components and the losses from the transmission collector system. Fig. 21.7 shows the main components of a wind farm structure: PMSG, converter, filter, transformer, and the cables. Since the system losses in the generator are independent of the reactive power of the wind farm, the loss model of PMSG is not considered here.

For larger scale of wind farms with PMSG, it is more economical to provide PCC with reactive power from the power electronic devices of each WT. When the power system operator gives a reactive power reference to a WF at PCC, the WF controller gives reactive power references to each WT according to some reactive power dispatch strategy. The traditional strategy is proportional dispatch. Literature [10–13] uses this strategy to distribute the reactive power reference of each WT according to their available reactive power capacities. It is easy to calculate, and it can be ensured that the reactive power of each

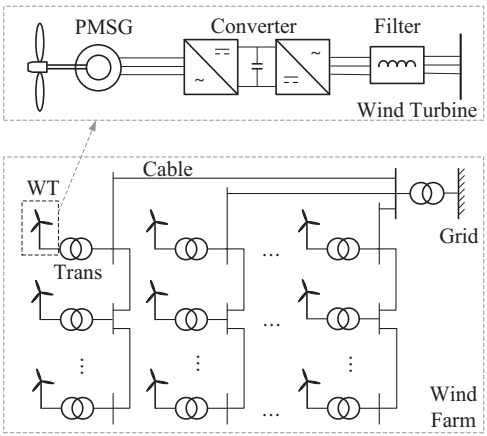

FIGURE 21.7 Components of a wind farm structure.

This book belongs to Kitab Liaison (ocd1996@gmail.com)
Copyright Elsevier 2023

WT does not exceed the limit. Recently, a novel optimized reactive power dispatch of PMSG wind farm is proposed to minimize the power losses including the losses inside WTs and the losses of transmission system [21]. This strategy for the loss minimum chooses an optimization algorithm to get the reference reactive power of each WT. The objective considers not only the transmission system loss but also the WT interior loss:

$$\min\left\{\sum_{k=1}^{n}\left(P_{con,\,k}+P_{filter,\,k}+P_{trans,\,k}\right)+\sum_{l=1}^{m}P_{calbe,\,l}\right\} \tag{21.19}$$

The related constraints are as follows:

$$P_j=|V_j|\sum_{i=1}^{N_B}|V_i||V_{ji}|\cos(\theta_{ji}-\delta_j+\delta_i) \tag{21.20}$$

$$Q_j=-|V_j|\sum_{i=1}^{N_B}|V_i||V_{ji}|\sin(\theta_{ji}-\delta_j+\delta_i) \tag{21.21}$$

$$Q_{PCC}=Q_{WF}^{ref} \tag{21.22}$$

$$V_j^{\min}\le V_j\le V_j^{\max} \tag{21.23}$$

$$I_{GSC,\,k}^{rms}\le I_{GSC}^{rated} \tag{21.24}$$

where P_j and Q_j are the active and reactive powers at bus j, and formulas (21.19) and (21.20) are the power flow balance limits. Q_{PCC} is the reactive power at the PCC, and (21.21) is the WF reference reactive power constraint. V_j is the voltage at bus j, and formula (21.22) is the bus voltage constraint. $I_{GSC,\,k}^{rms}$ is the RMS value of grid-side converter (GSC) current, and formula (21.23) is the GSC current constraint. This section mainly focuses on the dispatch of reactive power, so the traditional MPPT control strategy for each WT is chosen as the active power dispatch.

As shown in Fig. 21.8, a wind farm with 25 PMSG WTs is adopted for the scenario and ranged in 5 rows and 5 columns. The 5 MW NREL WT is chosen as the WT in the simulation wind farm and its parameters can refer to Ref. [22]. The distance between each WT is 882 m. Considering the different load of each cable, the cables between row 1 and row 3 use the 95 mm^2 XLPE-Cu, the cables between row 3 and row 5 use the 150 mm^2 XLPE-Cu, and the cables between row 5 and PCC use the 240 mm^2 XLPE-Cu [23]. The velocity and direction of wind are set to 10 m/s and 270 degrees.

Three strategies are presented: Strategy A is the proportional dispatch strategy [24–26], Strategy B is the optimal dispatch strategy with wind farm transmission loss minimization [27,28], and Strategy C is the proposed optimal dispatch strategy with wind farm total loss minimization. Fig. 21.9 shows the

This book belongs to Kitab Liaison (ocd1996@gmail.com) Copyright Elsevier 2023

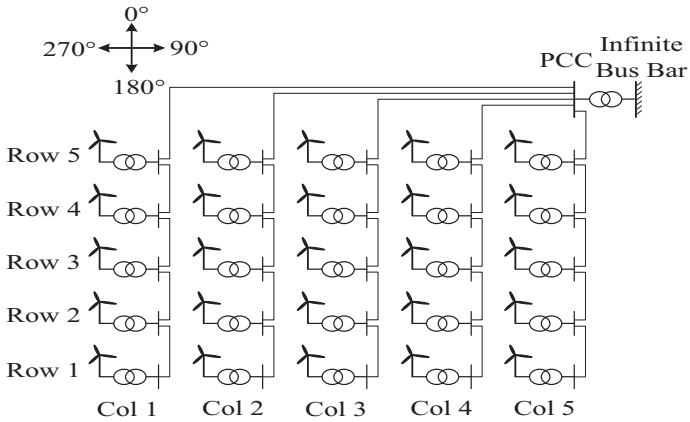

FIGURE 21.8 The layout of the studied wind farm for optimized reactive power control.

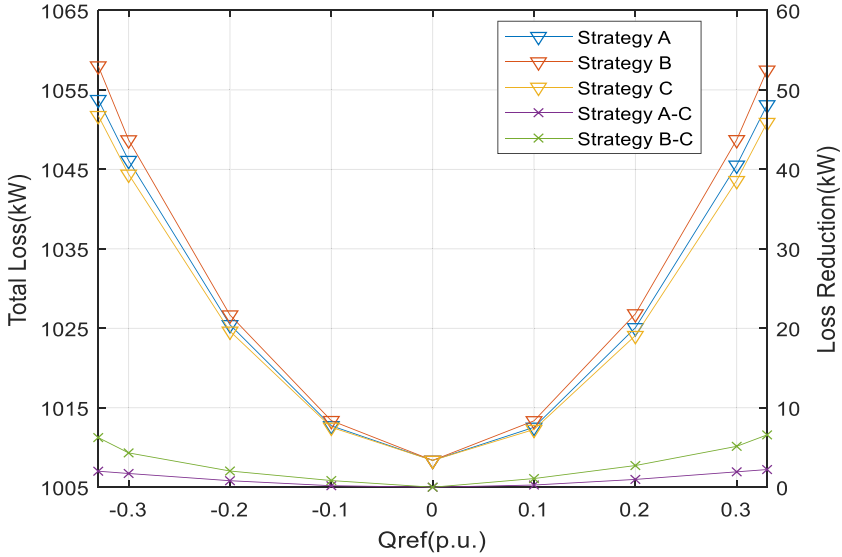

FIGURE 21.9 The total power loss of WF using each strategy at different Q_{WF}^{ref}.

total power loss of WF using each strategy at different Q_{WF}^{ref}. It is obvious that Strategy C always gets the lowest total loss, while Strategy B gets the highest. The reason is that the target of Strategy B is minimizing the loss of cables and transformers, which may cause the rising of the loss inside WTs, so the total loss of WF will be bigger. As Fig. 21.9 shows, the bigger the absolute value of Q_{WF}^{ref}, the higher the difference between each Strategy. Because when $Q_{WF}^{ref} = 0$, the $Q_{WT,\,k}^{ref}(k = 1, \ldots, 25)$ tends to be 0, while the absolute value of Q_{WF}^{ref} is

This book belongs to Kitab Liaison (ocd1996@gmail.com) Copyright Elsevier 2023

rising, the difference of $Q_{WT,\,k}^{ref}$ becomes obvious, so the difference in the total power losses of WF also becomes significant.

Then, set $Q_{WF}^{ref} = 0.2$. The strategies are compared at different wind velocities and different wind directions. Fig. 21.10A shows the total loss of WF at $Q_{WF}^{ref} = 0.2$ using Strategy A, B, and C, and the reduction of Strategy A and C is shown in Fig. 21.10B, the reduction of Strategy B and C is shown in Fig. 21.10C. In Fig. 21.10A, the total loss of WF rises with wind velocity and then stays the same when the wind velocity exceeds about 14 m/s. But this phenomenon will be earlier when the wind direction is not 0 degree, 90 degrees, 180 degrees, or 270 degrees, and the total loss of WF stays the same when the wind velocity exceeds about 12 m/s. Because in these directions the wake effect is not that strong, there are four gaps in the surface. And the four ridges in Fig. 21.10B and C can be explained, too. As the reductions are all positive, it can be ensured that Strategy C will always be the best in any condition with three sets of data (wind velocity, wind direction, Q_{WF}^{ref}).

21.3.3 Levelized production cost minimization

In order to minimize the LPC, it is crucial to maximize the lifetime of WTs besides minimizing the power loss of wind farms as the previous section. And the reactive power references for WTs are used as the optimization variables. Then, the power loss of wind farms can be rewritten as follows:

$$P_{WF}^{loss} = \sum_{k=1}^{n}\left(P_{PMSG,k}^{loss} + P_{con,k}^{loss} + P_{filter,k}^{loss} + P_{trans,k}^{loss}\right) + \sum_{l=1}^{m} P_{calbe,l}^{loss} \tag{21.25}$$

where $P_{PMSG,k}^{loss}$ is the loss inside the generator of WT k, $P_{con,k}^{loss}$ is the loss of converter in WT k, $P_{filter,k}^{loss}$ is the loss in the filter, $P_{trans,k}^{loss}$ is the loss of transformer of WT k, $P_{calbe,l}^{loss}$ is the loss of *cable l*, m is the total number of cables, n is the total number of WTs.

Regarding the WT lifetime, the maintenance and repair costs for WTs cannot be ignored in currently active wind farms and it is significant to consider the lifetime of WTs. As mentioned above, a WT contains a turbine, a gearbox, a generator, and a converter, etc. Among them, the failure rate of the electrical part has the highest volume. Thus, the lifetime of the power converter is the shortest one to determine the lifetime of the WT. Besides, the reactive power dispatch method will only affect the lifetime of the converter but not the WT; thus, only the lifetime of the converter is evaluated [29].

Fig. 21.11 shows the framework to estimate the converter lifetime in a WT. The input is the active power P and the reactive power Q, and the output is the converter lifetime (AD). In the process, the first step is the power converter loading translation, which means that the voltage V_g, current I_g, and phase angle φ_g of the GSC can be calculated through the PMSG model and the converter model. The second step is loss evaluation in the power converter.

This book belongs to Kitab Liaison (ocd1996@gmail.com) Copyright Elsevier 2023

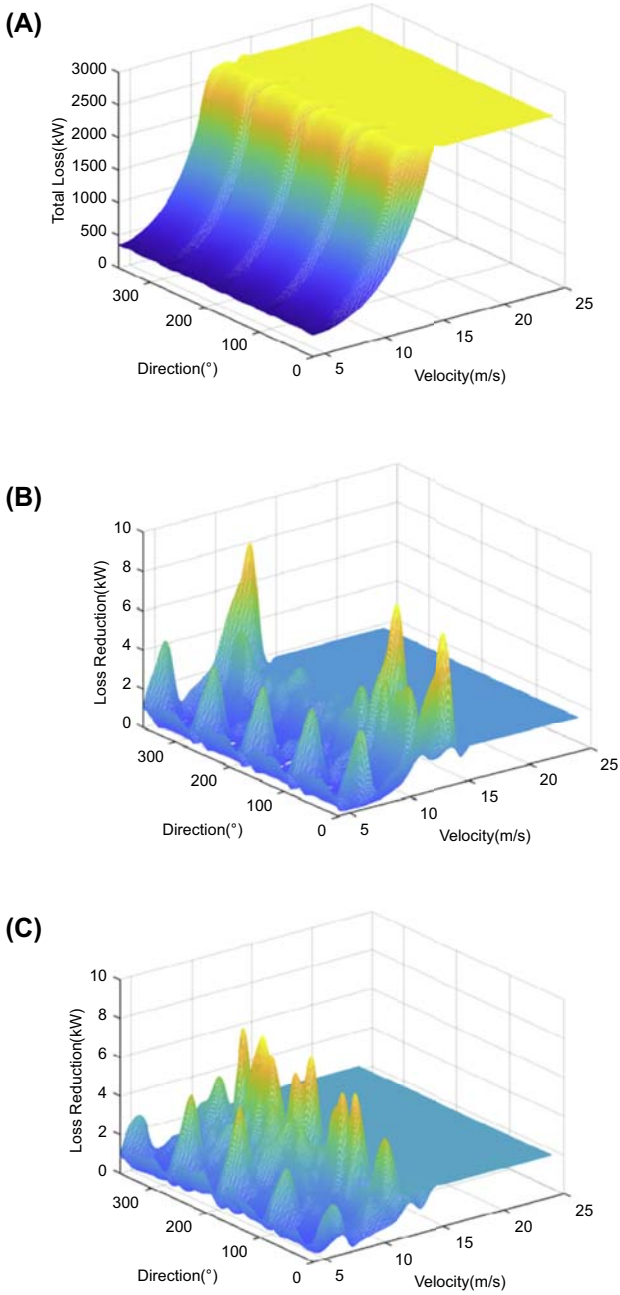

FIGURE 21.10 The total power loss of WF and loss reduction using different strategies at different wind velocities and directions. (A) The total power loss of WF using different strategies at $Q_{WF}^{ref} = 0.2$, (B) the loss reduction of Strategy A−C, and (C) the loss reduction of Strategy B−C.

This book belongs to Kitab Liaison (ocd1996@gmail.com) Copyright Elsevier 2023

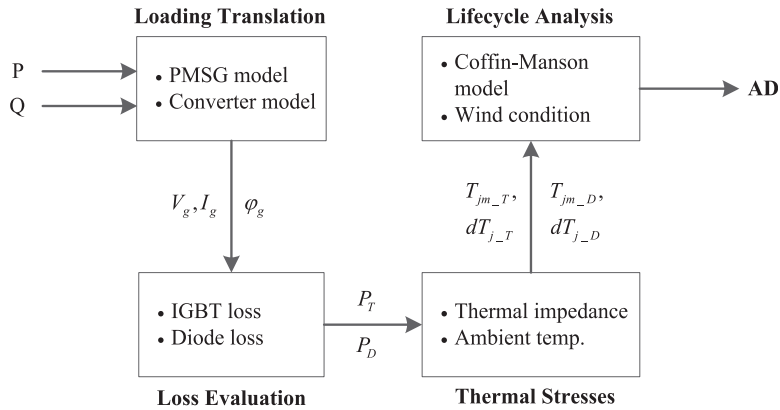

FIGURE 21.11 The framework for estimating converter lifetime to be used in wind farm optimization.

The loss in the internal components is calculated by the converter loss model, including IGBT conduction loss, IGBT switching loss, diode conduction loss, and diode switching loss. The third step is thermal stress evaluation. In this step, the thermal model of the power module is used to evaluate the thermal stress according to the average junction temperature and the junction temperature fluctuation under specific loading conditions, which is closely related to the thermal resistance of the power module and the ambient temperature. Finally, according to the manufacturer's B10 lifetime data under fixed thermal stress, the total endurance power cycle can be further calculated by using the Coffin−Manson equation at specific average junction temperatures and junction temperature fluctuations. According to the wind conditions in a year, the annual damage can be derived, which is the reciprocal volume of the lifetime.

By using this lifetime calculating model, the lifetime of the GSC and the machine-side converter can both be predicted. With respect to the full-scale power converter, the synchronous generator is fully decoupled from the power grid, which results in that the GSC is responsible for the reactive power provision combined with the active power. As a result, the lifetime of IGBT in the GSC will be in focus in this chapter [11]. The objective function LPC is chosen to evaluate both the wind power loss and the wind farm lifetime:

$$\min_{Q^{ref}_{WT,\,k}} \left\{ LPC = \frac{C_0 r(1+r)^{N_y}}{(1+r)^{N_y} - 1} \frac{1}{E_{tol}} \right\} \tag{21.26}$$

$$N_y = \frac{1}{\sum_t^T \left(\frac{1}{N_y^{WF}(t)} * \frac{1}{T} \right)} \tag{21.27}$$

This book belongs to Kitab Liaison (ocd1996@gmail.com) Copyright Elsevier 2023

$$E_{tol} = \sum_{t=1}^{T} \left[\left(\sum_{k=1}^{n} P_{WT,\,k}(t) - P_{WF}^{loss}(t) \right) * \frac{8760}{T} \right] \tag{21.28}$$

where T is the number of sampling points in 1 year, $P_{WT,\,k}(t)$ is the captured active power of WT k at time t, $P_{WF}^{loss}(t)$ is the power loss of WF at time t, $N_y^{WF}(t)$ is the lifetime of WF that can be achieved when the situation at time t is always running, which is limited by the shortest lifetime among WTs. And the lifetime of WF can be calculated as follows:

$$N_y^{WF}(t) = \min\left\{ N_y^{WT,k}(t) \right\} (k = 1, 2, \ldots, n) \tag{21.29}$$

where $N_y^{WT,\,k}(t)$ is the lifetime of WT k at time t, $N_y^{WF}(t)$ is the lifetime of WF at time t.

The proposed strategy and the traditional proportional dispatch strategy are compared in a wind farm in the following scenario: Wind velocity = 6 m/s, wind direction = 270 degrees, and $Q_{WF}^{ref} = 0.33$. The wind farm chosen for simulation consists of 25 5 MW NREL PMSG WTs [22] and they are arranged in five rows and five columns, which is shown in Fig. 21.12. The distance between each two WTs is 882 m. The parameters of the cables can be found in Ref. [23].

A comparison of the traditional control strategy and the proposed strategy are shown in Fig. 21.13, in which the active power, reactive power, and lifetime of all the WTs can be seen. Table 21.3 shows the simulation result.

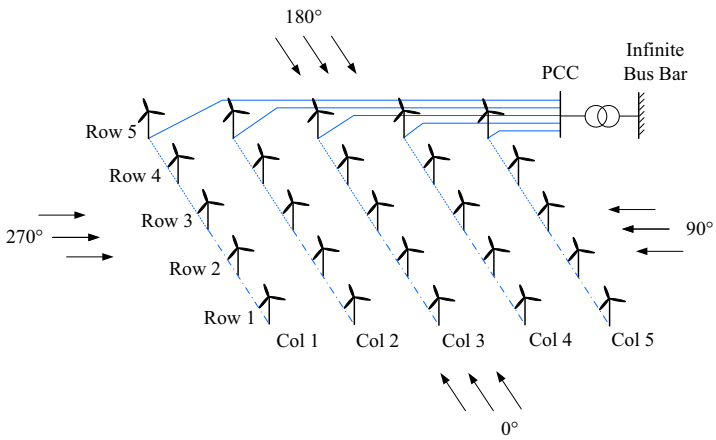

FIGURE 21.12 The layout of the wind farm for lifetime optimization.

This book belongs to Kitab Liaison (ocd1996@gmail.com)
Copyright Elsevier 2023

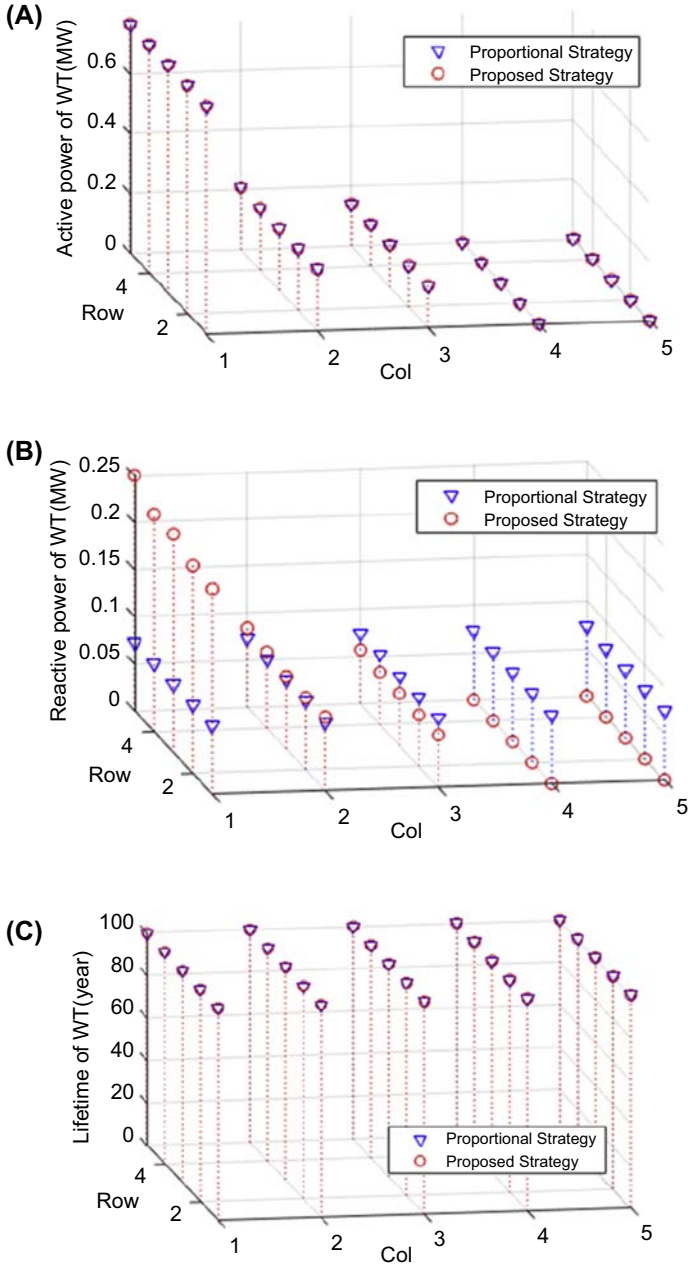

FIGURE 21.13 The active power, reactive power, and lifetime of wind turbines (WTs) using two different optimization methods. (A) The active power of WTs, (B) the reactive power of WTs, and (C) *the lifetime of WTs*.

This book belongs to Kitab Liaison (ocd1996@gmail.com)
Copyright Elsevier 2023

TABLE 21.3 Simulation results using different control strategies for Scenario 1: wind velocity = 6 m/s, wind direction = 270 degrees, $Q_{WF} = 0.33$.

Strategy	Total captured power of WF (MW)	Total power loss of WF (MW)	Lifetime of WF (year)	LPC (DKK/kWh)
Proportional strategy	5.57	0.41	100.00	110,167.12
Proposed strategy	5.57	0.40	100.00	110,042.95
Reduction	0	0.01	0	124.17

Comparisons of the proportional strategy and the proposed strategy are shown in Fig. 21.14, in which the active power, reactive power, and lifetime of all the WTs can be seen. Table 21.4 shows the case results at Scenario 2: wind velocity = 12 m/s, wind direction = 270 degrees, $Q_{WF} = 0.33$.

In Table 21.4, the LPC of WF using the proposed strategy is 171.37 DKK/kWh lower than that of the proportional strategy. In Scenario 2, the lifetime of WF can be greatly improved by using the proposed strategy. As shown in Fig. 21.14, the lifetime of WTs at Col.1 is 48.55 years by using the proportional strategy. While using the proposed strategy, the WTs at Col.1 are assigned to give lower reactive power since they generate higher active power. Thus, their lifetime increases to 53.68 years. As the active power of WTs at Col.2−5 is low, they have a larger threshold to generate reactive power while maintaining the lifetime of 100 years. So, the reactive power of WTs at Col.2−5 can be higher to offset the lower reactive power of WTs at Col.1. As a cost of obtained longer lifetime, the total loss of WF increases. The total loss of WF by using the proposed strategy is 0.02 MW higher than that of the proportional strategy. However, its growth has less impact on the LPC minimization than the lifetime's increasing, so the optimization of LPC is still very obvious. In summary, when the wind velocity is at a suitable value in the middle area, the proposed method mainly optimizes the lifetime of WF.

Then, a comparison of the proportional strategy and the proposed strategy is shown in Fig. 21.15, in which the active power, reactive power, and lifetime of all the WTs can be seen. Table 21.5 shows the simulation result at Scenario 3.

In Table 21.5, the LPC of WF using the proposed strategy is 0.35 DKK/kWh lower than that of the proportional strategy, which is a small number. In this scenario, the wind velocity is large enough so that the output of each WT reaches a maximum of 5 MW. All WTs do not have a large margin to regulate reactive power. So, the LPC reduction is small.

This book belongs to Kitab Liaison (ocd1996@gmail.com) Copyright Elsevier 2023

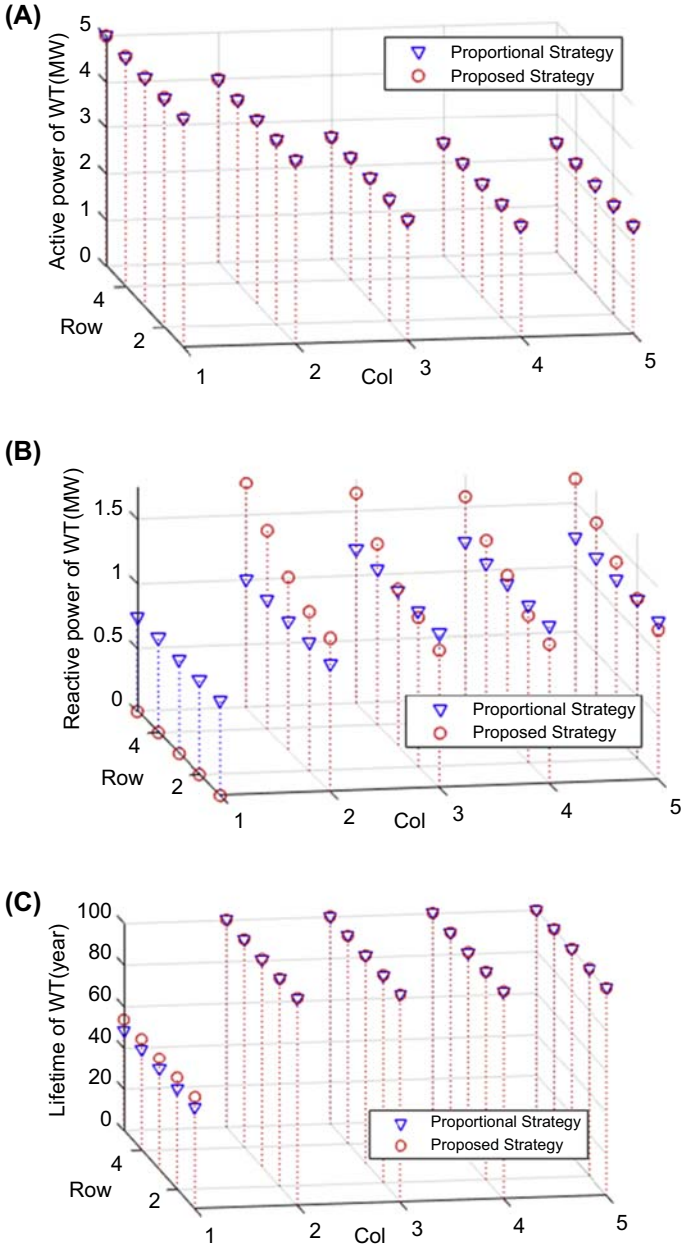

FIGURE 21.14 The active power, reactive power, and lifetime of wind turbines (WTs) at Scenario 2. (A) The active power of WTs, (B) the reactive power of WTs, and (C) the lifetime of WTs.

This book belongs to Kitab Liaison (ocd1996@gmail.com) Copyright Elsevier 2023

TABLE 21.4 Simulation results using different control strategies for Scenario 2: wind velocity = 12 m/s, wind direction = 270 degrees, $Q_{WF} = 0.33$.

Strategy	Total captured power of WF (MW)	Total power loss of WF (MW)	Lifetime of WF (year)	LPC (DKK/kWh)
Proportional strategy	82.11	1.81	48.55	7752.34
Proposed strategy	82.11	1.83	53.68	7580.97
Reduction	0	−0.02	−5.13	171.37

In addition, all wind speeds from 4 to 25 m/s were sampled at 1 m/s intervals to do the simulation. The active power captured by WF and the LPC of WF under different wind velocities are shown in Figs. 21.16 and 21.17, respectively.

As shown in Figs. 21.16 and 21.17, the downward trend of the LPC is similar to the upward trend of the active power of WF because the LPC is inversely proportional to the active power of WF. The LPC reduction shown in Fig. 21.17 can be separated into three areas. In Area 1, when the wind velocity is below 10 m/s, the main contribution of the proposed strategy is minimizing the total loss of WF like Scenario 1 shows. This contribution will be amplified as the total captured power decreases. This explains that the downward trend of LPC reduction is similar to the upward trend of the active power of WF in Area 1. In Area 2, when the wind velocity is between 10 and 14 m/s, the proposed method mainly optimizes the lifetime of WF like Scenario 2 shows. In this area, some but not all WTs have reached their maximum output. This situation creates favorable conditions for optimizing the lifetime. In order to assign a lower reactive power to the WTs that reach the maximum active power output, the remaining WTs are designed to take over more reactive power. Thus, the lifetime of WF can be significantly improved and the LPC reduction is more obvious in Area 2. In Area 3, when the wind velocity is higher than 14 m/s, the LPC reduction is almost zero just like Scenario 3 shows. Because the wind velocity is large enough, the output of each WT reaches a maximum of 5 MW. All WTs do not have a large margin to regulate the reactive power. So, the LPC reduction is small in Area 3.

In order to evaluate the effectiveness of the proposed strategy more comprehensively, it is necessary to simulate over a course of a year. Fig. 21.18 shows a wind rose that reflects the wind velocity and wind direction in a year. The wind data are obtained from the NREL National Wind Technology Center [30], sampled every 3 h, totally 2920 data. Assume that the WF reactive power reference from the grid is normally distributed, and the values and their times

This book belongs to Kitab Liaison (ocd1996@gmail.com) Copyright Elsevier 2023

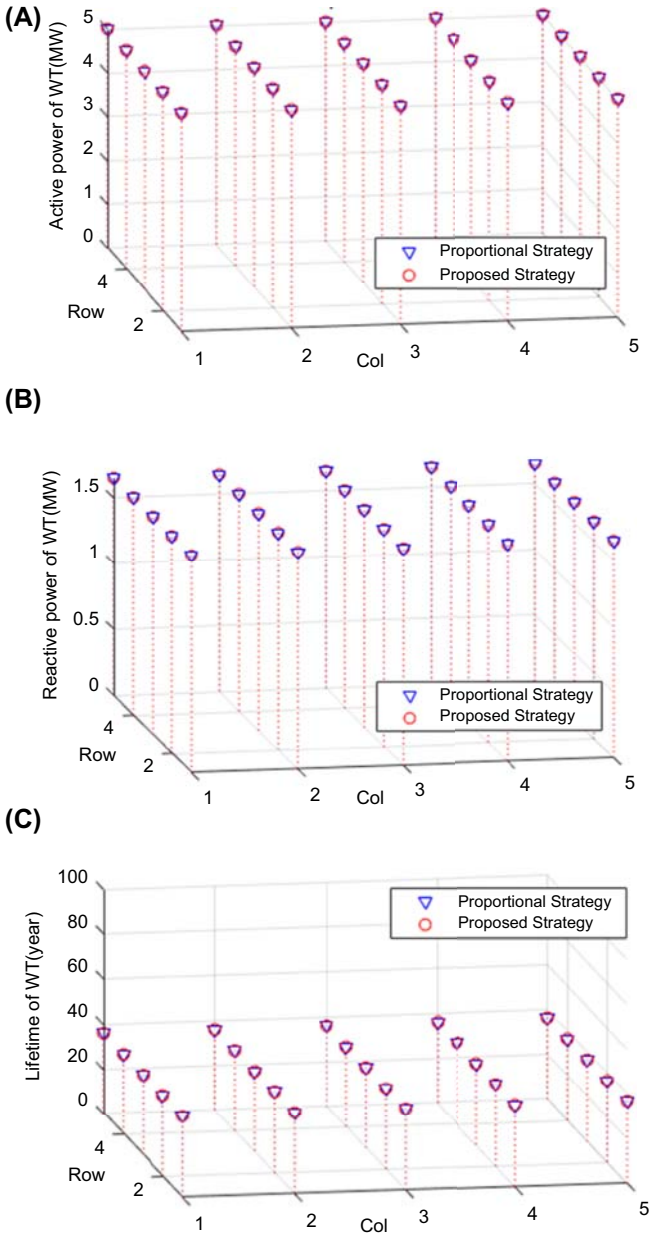

FIGURE 21.15 Active power, reactive power, and lifetime of wind turbines (WTs) at Scenario 3: wind velocity = 18 m/s, wind direction = 270 degrees, $Q_{WF} = 0.33$. (A) The active power of WTs, (B) the reactive power of WTs, and (C) the lifetime of WTs.

This book belongs to Kitab Liaison (ocd1996@gmail.com) Copyright Elsevier 2023

TABLE 21.5 Simulation results at Scenario 3 using different strategies.

Strategy	Total captured power of WF (MW)	Total power loss of WF (MW)	Lifetime of WF (year)	LPC (DKK/kWh)
Proportional strategy	125.00	2.81	36.24	5568.05
Proposed strategy	125.00	2.81	36.25	5567.69
Reduction	0	0.00	−0.01	0.35

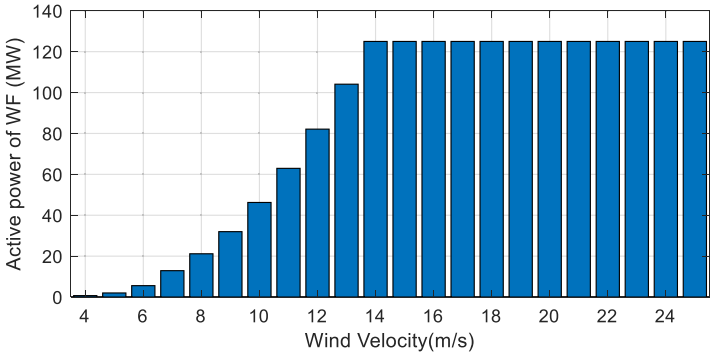

FIGURE 21.16 Active power captured by the wind farm for different wind speeds.

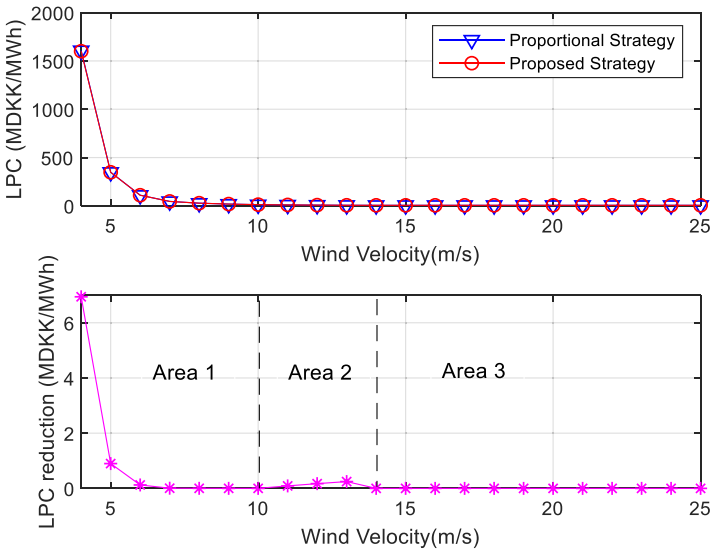

FIGURE 21.17 The levelized production cost (LPC) of the wind farm and LPC reduction for different wind speeds.

This book belongs to Kitab Liaison (ocd1996@gmail.com) Copyright Elsevier 2023

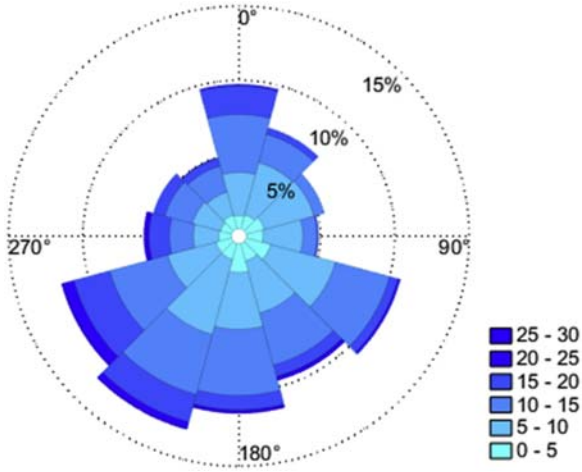

FIGURE 21.18 Wind rose of a year for case study (m/s).

of appearance are shown in Fig. 21.19. The sum of appearance times at each value is 2920, which aims to match the data of wind velocity and wind direction.

The LPC of WF using the proportional strategy and the proposed strategy is compared for 1-year condition. The total captured power of WF, the total loss of WF, the lifetime of WF, and the LPC are listed in Table 21.6.

As the active power dispatch of WF is the same in these two strategies, the total captured power of WF in a year of these two strategies is 606.44 GWh. The total power loss of WF in a year of the proposed strategy is 0.01 GWh higher than that of the proportional strategy, which is the price of lifetime optimization. Table 21.6 shows that the WF can operate 70.84 years using the

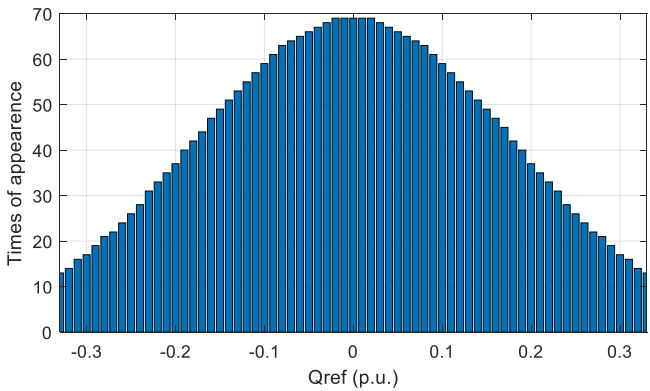

FIGURE 21.19 A year's Q_{WF}^{ref} in *pu*.

This book belongs to Kitab Liaison (ocd1996@gmail.com)
Copyright Elsevier 2023

TABLE 21.6 Simulation result of a year.

Strategy	Total captured power of WF (GWh)	Total power loss of WF (GWh)	Lifetime of WF (year)	LPC (DKK/kWh)
Proportional strategy	606.44	13.19	70.57	8607.32
Proposed strategy	606.44	13.19	70.84	8603.73
Reduction	0	−0.01	−0.27	3.59

proposed strategy, which is 0.27 years longer than that of the proportional strategy. As a result, the LPC of WF using the proposed strategy is 3.59 DKK/kWh smaller than that of the traditional strategy.

In fact, the lifetime of a WT is usually 20−25 years, which is much shorter than the 70.84 years mentioned above. However, the lifetime calculated in this chapter can reflect the fatigue of the converter. Extending the lifetime of the converter can effectively reduce the number and cost of maintenance of the converter.

21.4 Wind farm layout optimization

The optimization of a wind farm contains both an operation and a planning problem. The operation problems of a wind farm including its active and reactive dispatch are as analyzed above. This section aims to investigate the planning problems of a wind farm, namely, wind farm layout optimization. In planning stage, wind farm layout optimization is important to efficiently reduce investment costs or increase power production. Notably, wind farms are usually not designed on flat grounds. This section analyzes the impact of topography and wind direction and the layout optimization problem.

21.4.1 Topography and wind direction impact for layout

With the increasing size of onshore wind farms, the impact of the wake effect on energy production becomes more and more evident. WT siting in onshore wind farms usually takes topographical conditions into consideration, generally including the topographic height and slope. However, optimized WT layout for wind farms with different topographic heights considering the wake effect is realistic. An approach for an optimized layout of WTs in onshore wind farms considering the topography as well as the wake effect is proposed [31]. Based on LPC, the placement of WTs is optimized considering topography and the effect of this on the WTs interactions.

This book belongs to Kitab Liaison (ocd1996@gmail.com) Copyright Elsevier 2023

While the WTs are on flat ground, the center of the wake area generated by the wake effect of the upstream WT will be on the same level as the center of the downstream blade swept area of the downstream WT. The wake area generated by the upstream WT in the downstream WT is shown as a circle consisting of purple (light gray in print version) and red (gray in print version) in Fig. 21.20. However, when there is a difference in topography, the center of the blade swept area will be shifted upward by the same distance as the height difference between the upstream and downstream WTs, like shown by blue (dark gray in print version) and red (gray in print version) circles in Fig. 21.20. The shift makes the distance between the centers of the swept areas more separate, and then the area of the overlap of the downstream rotor's swept area with the upstream rotor's wake is decreased. If the wind farm is constructed in a zone with different topographic amplitudes and slopes, the wind velocity at the downstream WT is affected by the following:

(1) Wind shear effect (The wind speed will increase slightly with the elevation of the air.)
(2) Wake effect from upstream WTs (The wind speed will be reduced in downstream WTs.)

The wind direction is facing the WT in the case of Fig. 21.20, and if the wind direction changes, the description and corresponding model will be as presented below. The downstream WT in the different topographic heights is affected partially by the wake generated by the upstream WT. If both the upstream and the downstream WTs are at the same topographic height which means the circle centers are also at the same height, the wake effect area is unchanged. If the WTs are not at the same topographic height, then there are two cases, where the affected wake area will be reduced because of the different heights of the topography L_h as illustrated in Fig. 21.21A and B.

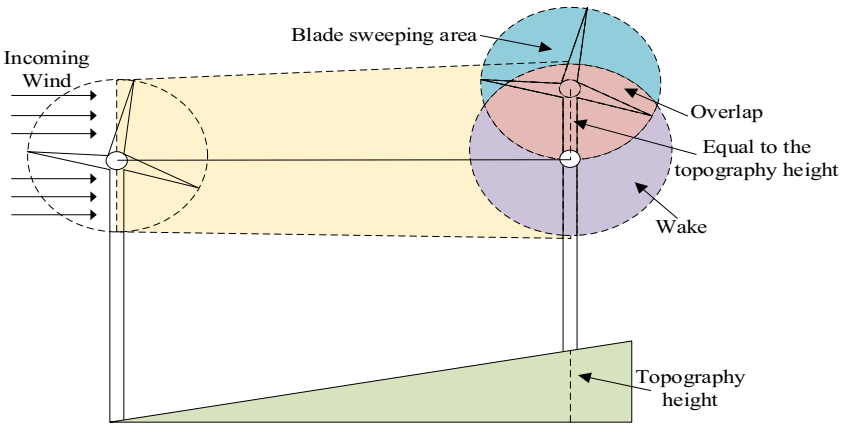

FIGURE 21.20 Wake effect between two wind turbines on a slope in the landscape.

This book belongs to Kitab Liaison (ocd1996@gmail.com)
Copyright Elsevier 2023

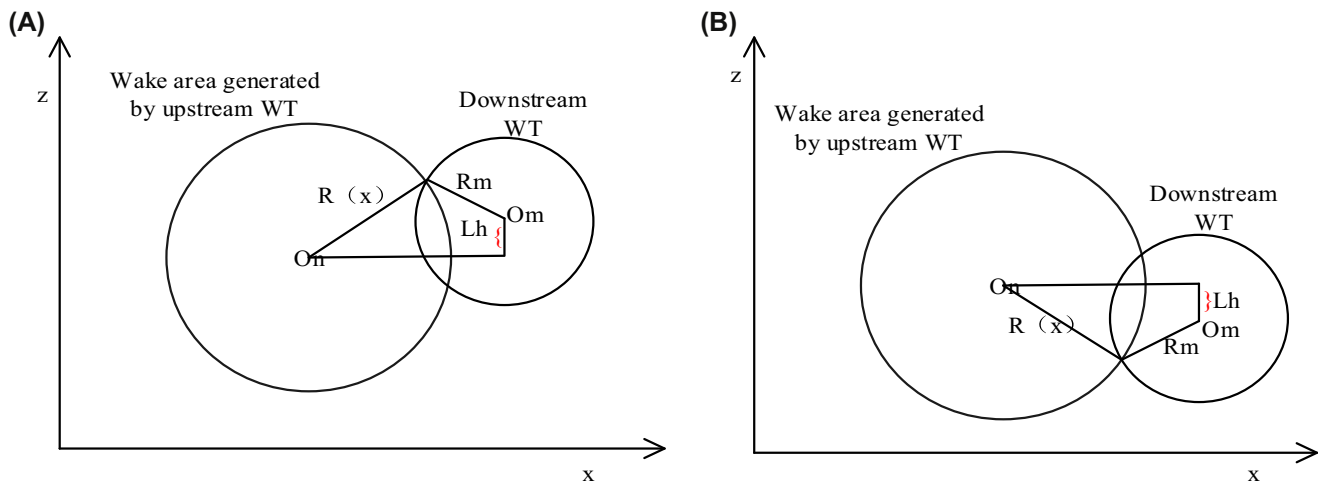

FIGURE 21.21 Wake model considering topographical difference. (A) Downstream wind turbine (WT) is at a higher elevation than the upstream one and (B) downstream WT is at a lower elevation than the upstream one.

This book belongs to Kitab Liaison (ocd1996@gmail.com)

Copyright Elsevier 2023

In this model, two cases corresponding to Fig. 21.21 need to be analyzed in detail like shown in Fig. 21.22. All extra circles are for expressing the state of moving up and down, left and right in Fig. 21.22. The solid circle represents the wake area of the upstream WT in the downstream moving left and right, and the dotted circle represents the changes in height of the wake area moving up and down based on a solid circle. If the WTs are at the same topographical

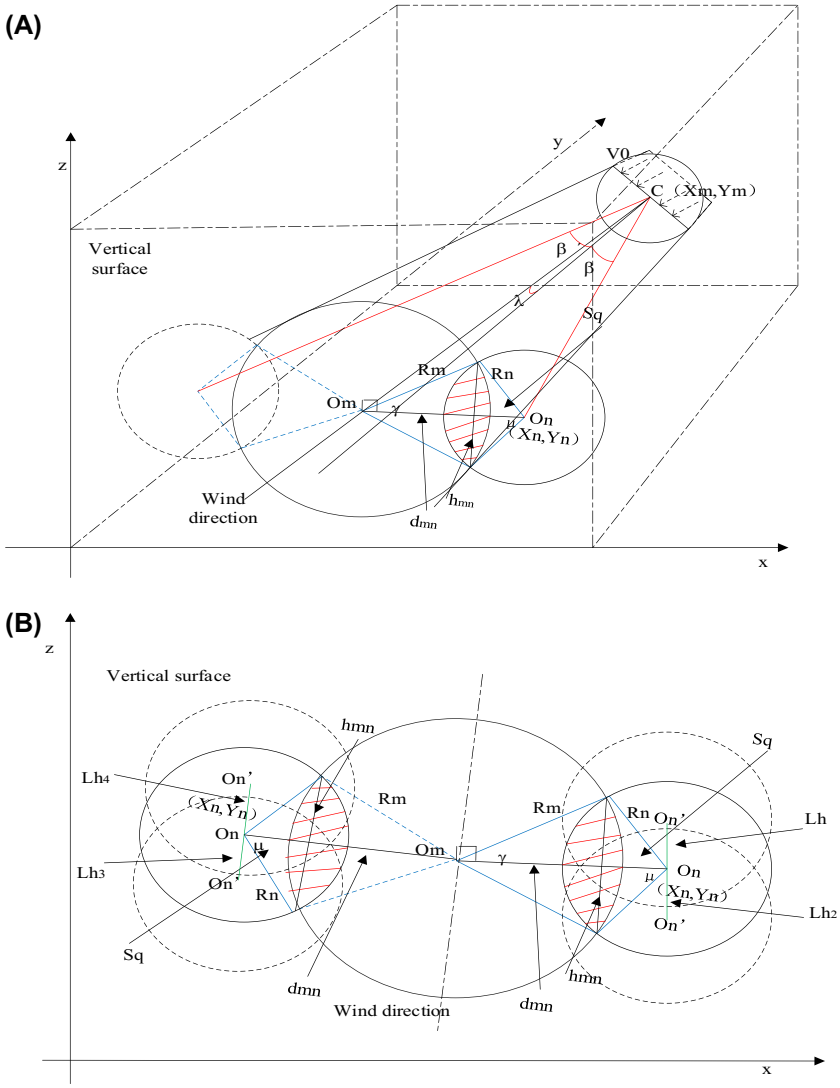

FIGURE 21.22 Three-dimensional wake overlaps for different topographic conditions. (A) Wind turbines (WTs) in the same topographic height presented in three-dimensional coordinate system z−x−y. (B) WTs in different topographic heights presented in vertical coordinate z−x.

This book belongs to Kitab Liaison (ocd1996@gmail.com)
Copyright Elsevier 2023

height, a 2D wake model will be adopted to calculate the energy yields of onshore wind farms as shown in Fig. 21.22A. The vertical z–x plane portion of Fig. 21.22B is the same as that of Fig. 21.22B. Only the z–x plane is selected for illustration and analysis to make it more intuitive, where the z-axis represents translation in the z-direction due to changes in terrain height. Here, the blue (light gray in print version) line L_{mn} is the distance between the center of the upstream WT and the downstream one. The overlapping areas are indicated as the shaded area as Overlap. The blue (light gray in print version) quadrangle area is denoted as S_q. While the new version of 3D wake model by taking the topographic height difference's impact on the wake area into consideration, the related analyses are shown in Fig. 21.22B.

The 2D wake model is shown in Fig. 21.22A, while (B) dotted circles refer to the proposed model. When the downstream WT is on the left of the wind direction, a series of mathematical equations for the 3D wake model can be derived given as (21.30)–(21.40).

$$L_{mn} = \sqrt{(x_n - x_m)^2 + (y_n - y_m)^2} \tag{21.30}$$

$$L_h = O_n O'_n = d_y \cdot \sin\alpha \tag{21.31}$$

$$d_{mn} = \sqrt{(L_{mn}|\sin(\beta + \lambda)|)^2 + (L_h)^2} \tag{21.32}$$

$$R_n = R_m + kL_{mn}|\cos(\beta + \lambda)| \tag{21.33}$$

$$\mu = 2\cos^{-1}\frac{R_n^2 + d_{mn}^2 - R_m^2}{2R_n d_{mn}} \tag{21.34}$$

$$\gamma = 2\cos^{-1}\frac{R_m^2 + d_{mn}^2 - R_n^2}{2R_m d_{mn}} \tag{21.35}$$

$$h_{mn} = 2R_m|\sin(\mu/2)| \tag{21.36}$$

$$S_m = \gamma\frac{R_m^2}{2} \tag{21.37}$$

$$S_n = \mu\frac{R_n^2}{2} \tag{21.38}$$

$$S_q = \frac{h_{mn}d_{mn}}{2} \tag{21.39}$$

$$S_{overlap} = S_m + S_n - S_q \tag{21.40}$$

here L_{mn} is the distance of the upstream WT and the downstream WT, and d_y is the distance of every WT. The overlapping area $S_{overlap}$ is calculated by the area of the sector circle with a radius of R_m and a chord angle of μ plus the area

This book belongs to Kitab Liaison (ocd1996@gmail.com) Copyright Elsevier 2023

of the sector circle with a radius of R_n and a chord angle of λ, then minus the rectangular area of the blue (light gray in print version) side in Fig. 21.22. All other variables are defined like drawn in Fig. 21.22A and B to illustrate the overlap area change due to height differences. More variables defined can refer to Ref. [31].

So, the $S_{overlap}$ should be adjusted:

$$V_x = V_0\left[1-\left(1-\sqrt{1-C_{T,\,mn}}\right)\left(\frac{R_0}{R_x}\right)^2\left(\frac{S'_{overlap}}{S_0}\right)\right] \tag{21.41}$$

When the downstream WT is located on the other side of the wind direction, the corresponding formula can be obtained by changing all $(\beta+\lambda)$ to $(\beta-\lambda)$ without changing other parts. It is worth noting that the wake analyses above are steady-state cases and the wake center moves up and down and left and right during operation but averages around a certain position. However, the overlap will change with the wind direction.

21.4.2 Layout optimization for minimum levelized production cost

The distances of the WTs L_x, L_y are related to the length and the types of each cable, which determine the cable investment C_0. Due to wake effect, the annual energy production E_{tol} depends on the wind velocity, which is affected by L_x and L_y. Changing L_x and L_y will change both C_0 and E_{tol}. So, the L_x and L_y are chosen to be the changing variables in the optimization problem. The objective function can be written as follows:

$$\min\{LPC(L_x,\ L_y)\} \tag{21.42}$$

$$\min\left\{\left[\frac{C_0(L_x,\ L_y)r(1+r)^{N_y}}{(1+r)^{N_y}-1}+OAM_t\right]\frac{1}{E_{tol}(L_x,\ L_y)}\right\} \tag{21.43}$$

$$L_x=\left[L_{x,1},L_{x,2},\ldots,L_{x,i}\right],\quad i\in[1,N_row-1] \tag{21.44}$$

$$L_y=\left[L_{y,1},L_{y,2},\ldots,L_{y,j}\right],\quad j\in[1,N_col-1] \tag{21.45}$$

$$\text{Constraint: } 8R\le L_x\le 40R,\ \ 8R\le L_y\le 40R \tag{21.46}$$

The wind farm is assumed to be sited on a steadily rising slope of 2 degrees in the case study. The input time series wind speed and the distribution of direction for the calculation are obtained from the Norwegian Meteorological Institute [30]. Information about cables such as conducting sectional areas, voltage levels, and so on is obtained from Ref. [23]. The 500 and 630 mm^2 XLPE-Cu HVAV cables with 66 kV rated voltage are chosen for the collection system and the commonly used 1000 mm^2 Cu HVDC cable with 300 kV rated

This book belongs to Kitab Liaison (ocd1996@gmail.com) Copyright Elsevier 2023

voltage [32] is chosen for the transmission system as reference standards, respectively. According to the flowchart using PSO algorithm, the resulting wind energy production, the costs of cables, and the optimization results are presented in Table 21.4. And the optimized results are compared with the optimized results on the flat ground, while the other conditions are exactly the same, so that the difference of the optimized variables, results, and the influence of topographical heights can be obtained and compared if the topographical factors are not considered.

According to Table 21.7, no matter what kind of case is chosen, the losses caused by the wake effect reach a nonnegligible proportion about 8.67% and 7.01% of the total energy production. In terms of power production considering the wake effect, the optimization result on the slope is increased by 11.17% compared with the optimized result on the flat ground. There are two main reasons for increasing this increase: one is that the overall height is increased due to the wind shear effect, and the other is that the wake area between the different WTs is relatively reduced due to the height difference. Besides, the LPC is reduced by 10.29%.

TABLE 21.7 Comparison between optimized result of flat ground and slope.

Name	Optimized placement on flat ground	Optimized terrain-induced placement
L_x (m)	1029.22 895.85 1131.78 883.22 898.93 814.68 800.33 838.50 714.39	1743.15 834.51 908.81 739.31 971.44 789.48 679.43 756.43 576.63
L_y (m)	700.21	700.02
Annual energy production (GWh)	4164.30	4629.65
Annual energy production without considering wake effect (GWh)	4559.28	4978.95
Percentage of wake losses (%)	8.67%	7.01%
Cable cost (MDKK)	843.31	841.11
LPC (DKK/MWh)	202.51	181.68

This book belongs to Kitab Liaison (ocd1996@gmail.com) Copyright Elsevier 2023

21.5 Conclusion

This chapter has introduced wind farm control and optimization problems from three aspects: wind farm active dispatch, wind farm reactive dispatch, and wind farm layout optimization. Every aspect introduces its regular methods and some recent research works. Notably, their case performances are shown and compared. Generally, wind farm control and optimization are vital for the initial wind farm design and worth that more researchers are looking into these.

References

[1] Global Wind Report 2018 | Global Wind Energy Council. [Online]. Available: https://gwec.net/global-wind-report-2018/. (Accessed 16 June 2020).

[2] P. Hevia-Koch, H.K. Jacobsen, Comparing offshore and onshore wind development considering acceptance costs, Energy Pol. 125 (2019) 9–19.

[3] X. Wu, W. Hu, Q. Huang, C. Chen, M.Z. Jacobson, Z. Chen, Optimizing the layout of onshore wind farms to minimize noise, Appl. Energy 267 (2020) 114896.

[4] B. Zhang, P. Hou, W. Hu, M. Soltani, C. Chen, Z. Chen, A reactive power dispatch strategy with loss minimization for a DFIG-based wind farm, IEEE Trans. Sustain. Energy 7 (3) (2016) 914–923.

[5] P. Hou, W. Hu, M. Soltani, C. Chen, B. Zhang, Z. Chen, Offshore wind farm layout design considering optimized power dispatch strategy, IEEE Trans. Sustain. Energy 8 (2) (2017) 638–647.

[6] F. González-Longatt, P. Wall, V. Terzija, Wake effect in wind farm performance: steady-state and dynamic behavior, Renew. Energy 39 (1) (2012) 329–338.

[7] S. Mathew, Wind Energy: Fundamentals, Resource Analysis and Economics, Springer, Berlin, 2006.

[8] Wake modeling and simulation - DTU Research Database. [Online]. Available: https://orbit.dtu.dk/files/3453997/ris-r-1653.pdf. (Accessed 16 Jun 2020).

[9] P. Hou, W. Hu, M. Soltani, Z. Chen, A novel energy yields calculation method for irregular wind farm layout, in: IECON 2015 - 41st Annual Conference of the IEEE Industrial Electronics Society, 2015.

[10] X. Wu, W. Hu, Q. Huang, Z. Chen, A novel approach for onshore wind farm energy production calculation with different topographic heights, in: 2018 IEEE Innovative Smart Grid Technologies - Asia (ISGT Asia), 2018.

[11] P. Hou, W. Hu, M. Soltani, Z. Chen, Optimized placement of wind turbines in large-scale offshore wind farm using particle swarm optimization algorithm, IEEE Trans. Sustain. Energy 6 (4) (2015) 1272–1282.

[12] B. Zhang, W. Hu, P. Hou, M. Soltani, Z. Chen, Coordinated power dispatch of a PMSG based wind farm for output power maximizing considering the wake effect and losses, in: 2016 IEEE Power and Energy Society General Meeting (PESGM), 2016.

[13] H. Liao, W. Hu, X. Wu, N. Wang, Z. Liu, Q. Huang, C. Chen, Z. Chen, Active power dispatch optimization for offshore wind farms considering fatigue distribution, Renew. Energy 151 (2020) 1173–1185.

[14] J.S. González, M.B. Payán, J.R. Santos, Á.G.G. Rodríguez, Maximizing the overall production of wind farms by setting the individual operating point of wind turbines, Renew. Energy 80 (2015) 219–229.

This book belongs to Kitab Liaison (ocd1996@gmail.com) Copyright Elsevier 2023

[15] Y. Errami, M. Benchagra, M. Hilal, M. Maaroufi, M. Ouassaid, Control strategy for PMSG wind farm based on MPPT and direct power control, in: 2012 International Conference on Multimedia Computing and Systems, 2012.

[16] Y. Errami, M. Maaroufi, M. Cherkaoui, M. Ouassaid, Maximum power point tracking strategy and direct torque control of permanent magnet synchronous generator wind farm, in: 2012 IEEE International Conference on Complex Systems (ICCS), 2012.

[17] J. Lee, E. Son, B. Hwang, S. Lee, Blade pitch angle control for aerodynamic performance optimization of a wind farm, Renew. Energy 54 (2013) 124−130.

[18] P. Hou, B. Zhang, M. Soltani, Z. Chen, C. Chen, W. Hu, Optimised power dispatch strategy for offshore wind farms, IET Renew. Power Gener. 10 (3) (2016) 399−409.

[19] X. Wu, W. Hu, Q. Huang, C. Chen, Z. Liu, Z. Chen, Optimal power dispatch strategy of onshore wind farms considering environmental impact, Int. J. Electr. Power Energy Syst. 116 (2020) 105548.

[20] H.H. Hubbard, K.P. Shepherd, Aeroacoustics of large wind turbines, J. Acoust. Soc. Am. 89 (6) (1991) 2495−2508.

[21] N. Wang, J. Li, W. Hu, B. Zhang, Q. Huang, Z. Chen, Optimal reactive power dispatch of a full-scale converter based wind farm considering loss minimization, Renew. Energy 139 (2019) 292−301.

[22] J. Jonkman, S. Butterfield, W. Musial, G. Scott, Definition of a 5-MW Reference Wind Turbine for Offshore System Development, 2009.

[23] XLPE Submarine Cable Systems Attachment to XLPE Land Cable … [Online]. Available: https://new.abb.com/docs/default-source/ewea-doc/xlpe-submarine-cable-systems-2gm5007.pdf. (Accessed 16 June 2020).

[24] G. Tapia, A. Tapia, J.X. Ostolaza, Proportional−integral regulator-based approach to wind farm reactive power management for secondary voltage control, IEEE Trans. Energy Convers. 22 (2) (2007) 488−498.

[25] J. Saenz, A. Tapia, G. Tapia, F. Jurado, X. Ostolaza, I. Zubia, Reactive power control of a wind farm through different control algorithms, 4th IEEE International Conference on Power Electronics and Drive Systems. IEEE PEDS 2001 - Indonesia. Proceedings (Cat. No.01TH8594).

[26] F. Merahi, E.M. Berkouk, S. Mekhilef, New management structure of active and reactive power of a large wind farm based on multilevel converter, Renew. Energy 68 (2014) 814−828.

[27] M. Martinez-Rojas, A. Sumper, O. Gomis-Bellmunt, A. Sudrià-Andreu, Reactive power dispatch in wind farms using particle swarm optimization technique and feasible solutions search, Appl. Energy 88 (12) (2011) 4678−4686.

[28] B. Kanna, S.N. Singh, Towards reactive power dispatch within a wind farm using hybrid PSO, Int. J. Electr. Power Energy Syst. 69 (2015) 232−240.

[29] J. Li, N. Wang, D. Zhou, W. Hu, Q. Huang, Z. Chen, F. Blaabjerg, Optimal reactive power dispatch of permanent magnet synchronous generator-based wind farm considering levelised production cost minimisation, Renew. Energy 145 (2020) 1−12.

[30] X. Wu, W. Hu, Q. Huang, C. Chen, Z. Chen, F. Blaabjerg, Optimized placement of onshore wind farms considering topography, Energies 12 (15) (2019) 2944.

[31] Norwegian Meteorological Institute. [Online]. Available: https://www.met.no/en. (Accessed 16 June 2020).

[32] HVDC Light® Cables - ABB Group. [Online]. Available: https://library.e.abb.com/public/564b3711c060164dc1257b0c00552e50/HVDC%20Light%20power%20cables.pdf. (Accessed 16 June 2020).

This book belongs to Kitab Liaison (ocd1996@gmail.com) Copyright Elsevier 2023

Chapter 22

Power converters and control of LEDs

Xiaohui Qu[1], **Huai Wang**[2]
[1]*Southeast University, Nanjing, Jiangsu, China;* [2]*Aalborg University, Aalborg, North Jutland, Denmark*

22.1 Introduction

In the past decade, lighting accounts for 22% of the total electrical energy consumption in the United States as reported by the Department of Energy of the United States, and as depicted in Fig. 22.1, and the demands for energy are increasing. To promote more energy saving, there is a popular and prospective trend to employ more energy-efficient lighting alternatives and to gradually reduce energy-inefficient incandescent bulbs. Some governments have introduced measures to phase out incandescent lamps. Brazil and Venezuela started to phase them out in 2005, and other nations are scheduling phase outs of incandescent lamps: Australia, Ireland, and Switzerland in 2009, Argentina, Italy, Russia, and the United Kingdom by 2011, Canada in 2012, and the United States between 2012 and 2014.

The government across the globe are constantly working to phase out inefficient lamps such as incandescent and halogen lamps, promoting the use of environmental lighting lamps. Recently, the European Union announced new regulations to phase out the tungsten halogen and compact fluorescent lamps by 2020. The new regulations under the new Ecodesign Law state the maximum standby power of 0.5 W and a minimum energy requirement of 85 lm for lamps. The government authorities are also offering tax rebates and subsidies to promote the use of more efficient lighting technologies across the globe. Smart Lighting Market size estimated at over USD 7.5 billion in 2018 and is anticipated to grow at a CAGR of more than 15% from 2019 to 2025, as shown in Fig. 22.2. Wired technology captures the major share in the smart lighting market, accounting for more than 70% in 2018. The wireless technology will grow at a CAGR of more than 21% during the forecast period. Indoor lighting accounts for over 78% share in the smart lighting market. Outdoor lighting will grow at a CAGR of approximately 20% during the

Control of Power Electronic Converters and Systems. https://doi.org/10.1016/B978-0-12-819432-4.00021-4
Copyright © 2021 Elsevier Ltd. All rights reserved.

This book belongs to Kitab Liaison (ocd1996@gmail.com)
Copyright Elsevier 2023

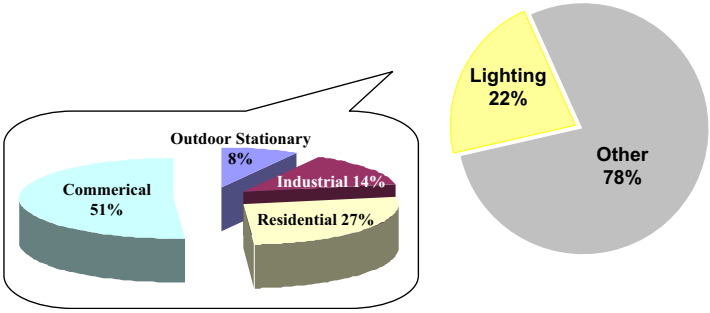

FIGURE 22.1 Distribution of electricity energy utilization in the United States.

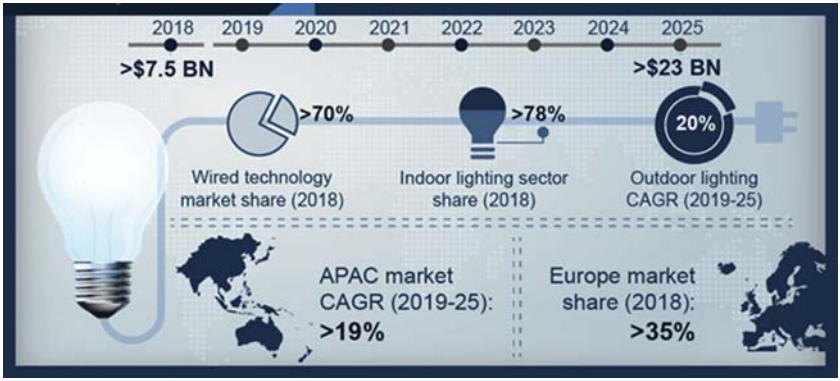

FIGURE 22.2 Industry analysis and forecast of the global smart lighting market. *Source: https://www.gminsights.com/.*

projection timeline. It is estimated that cities account for more than 60% of the world's energy, and lighting alone consumes 19% of the world's electricity. This is encouraging the development of smart city initiatives across the globe, which will aggregate the demand for the smart lighting industry.

With the rigid growth of technology in semiconductors, it is believed that light-emitting diodes (LEDs) will become a major lighting device in the coming years. Figs. 22.3 and 22.4 exhibit a variety of LED lamps and fixtures from different dominant manufacturers, such as Cree, Lumileds, Nichia, Osram, Lamina, Soeul semi, etc. Table 22.1 gives typical LED lamps' characteristics from these manufactures recently, where the lumen per watt is catching up with fluorescent lamps. Improvement in the light output of high-flux LEDs is rapidly giving rise to many new applications and products, particularly in the general illumination area. Besides, LED luminaires offer several desirable advantages over the traditional lamps including compactness, lacking of UV and IR radiation, longevity, mechanical ruggedness, fast response, reliability, mercury-free, wide color range, ease of control, and

This book belongs to Kitab Liaison (ocd1996@gmail.com) Copyright Elsevier 2023

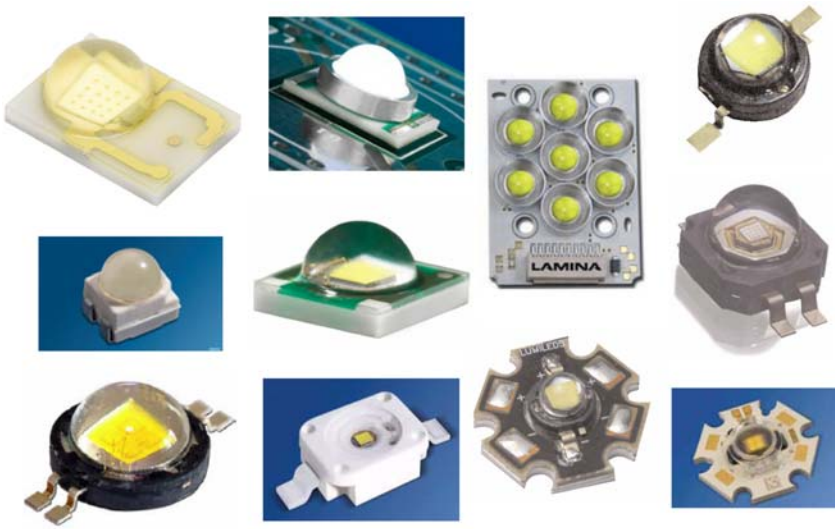

FIGURE 22.3 Various LED lamps from different manufacturers.

FIGURE 22.4 Examples of commercial luminaires.

instant color changing capacity. Consequently, LEDs have great potential in numerous applications from traffic signal, signaling, liquid-crystal display (LCD) back lighting, detector system, biomedical apparatus, general decorative illumination, etc. Therefore, more and more investigations have focused on the new opportunities in lighting design, control of the intensity and the color itself, and spatial distribution of light, along with the practical implementation of LED luminaires.

This book belongs to Kitab Liaison (ocd1996@gmail.com) Copyright Elsevier 2023

TABLE 22.1 Typical LED lamp characteristics from some manufacturers.

White LED		Viewing angle degrees	Typical lumens (lm)								Typical current mA	Typical voltage V_f(V)	Typical power W	Therm. Resist.°C/W	Max. Junct.°C	CRI
			350	500	700	1	1.4	1.5	2.8	5						
			mA	mA	mA	A	A	A	A	A						
Osram	LW W5SM cool	120	52–97	104.3							350	3.2	1.1	6.5	125	80
Lumileds	LXLW-PWC1-0100 cool	120	100								350	3	1.1	10	150	70
	LXML-PWC1-0100 cool	140	100		180						350	3.15	1.1	10	150	70
	LXK2-PWC4-0220 cool	120	105		185	220		300			1000	3.65	3.7	5.5	150	70
	LXK2-PWW4-0180 Warm	120	85		150	180		250			1000	3.65	3.7	5.5	150	75
Cree	XR E series cool	90	107								350	3.3	1.2	8	150	75
	XR E series warm	90	80.6								350	3.3	1.2	8	150	80
	MC E series cool	110	107.5								350	3.2	1.1	3	150	75
	MC E series warm	110	80								350	3.2	1.1	3	150	80
	XP E series cool	115	114								350	3.2	1.1	9	150	75
	XP E series warm	115	87.4								350	3.2	1.1	9	150	80

This book belongs to Kitab Liaison (ocd1996@gmail.com)

Copyright Elsevier 2023

Nichia	NS9W153MT cool	120	350								350	10.5	3.7	10	150	
	NS3W183T cool	120	120								350	3.5	1.2	15	135	
	NS3L183T-H3 warm	120	95								350	3.5	1.2	15	135	85
	NS6W083BT cool	120	100								300	3.3	1.0	10	120	
Seoul semi	W42180 cool	127	100								350	3.25	1.1	7.2	145	75

This book belongs to Kitab Liaison (ocd1996@gmail.com)

Copyright Elsevier 2023

Despite considerable advantages, LEDs have inherent nonlinear characteristics varying with time, current, temperature, and from device to device. As a consequence, there are still some remaining issues involving optical, thermal, electrical, and temporal behaviors to be solved in LED applications, before they can be a dominant force in the general illumination applications.

22.2. Characteristics of LEDs and drivers

In this part, the characteristics of the LED device are introduced. A detailed discussion focusing on thermal, optical, and electrical characteristics of LEDs is given.

22.2.1 Physical principle of LEDs

LEDs are electroluminescence light sources in contrast to pyroluminescence incandescent lamps and photoluminescence fluorescent lamps. The essence of electroluminescence is the charge carrier injection across a p−n junction into a zone where the injected carriers can convert their excess energy to light. The process is the principle of light emission in diodes and detailed in the following.

The so-called p−n junction is a junction formed by combining P-type and N-type semiconductors together in very close contact, as shown in Fig. 22.5. In

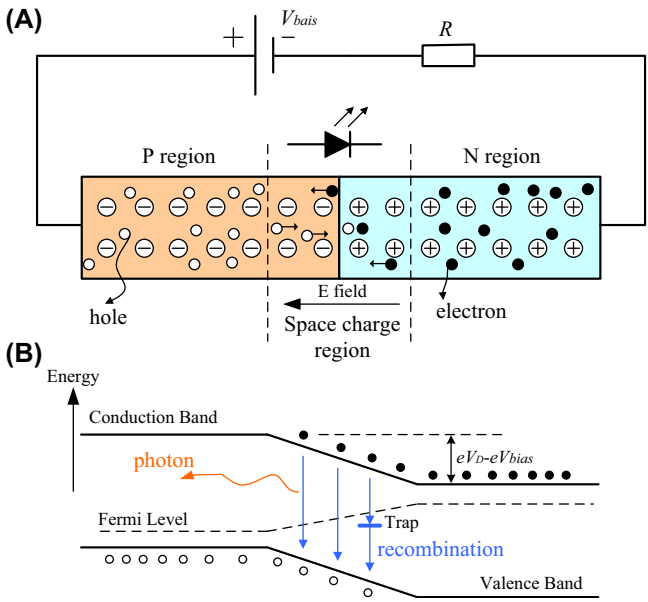

FIGURE 22.5 Effects of bias at the p−n junction of LED. (A) PN junction structure, (B) bandgap energy.

This book belongs to Kitab Liaison (ocd1996@gmail.com) Copyright Elsevier 2023

a p−n junction, without an externally applied voltage, an equilibrium condition is reached in which a potential difference called diffusion voltage V_D is formed across the junction. Electrons near the p−n junction interface tend to diffuse into the P region. As electrons diffuse, they leave positively charged ions (donors) in the N region. The regions nearby the p−n interfaces lose their neutrality and become charged, forming a space charge region or depletion region, whereas the left P region and N region are kept neutral.

If an external bias is applied in forward direction (P region positive, N region negative) as shown in Fig. 22.5A, the barrier height in the energy axis will reduce. If the forward bias is comparable with E_g/e, where E_g is the minimum bandgap energy of the semiconductor material, the barrier height becomes small enough that a large amount of electrons are injected into the P region and holes into the N region. When a diffusing electron meets a hole in the space charge region, it falls from high occupied conduction band into a lower energy level, valence band, and releases energy in the form of photons. This action is known as a *radiative combination*. During *nonradiative recombination*, the electron energy is converted to heat, not lights. Typical nonradiative transitions may take place via such deep levels (traps), as shown in Fig. 22.5B, or localized shallow state due to an impurity atom. Some technologies in the fabrication of LEDs aim to maximize the radiative process and minimize the nonradiative process.

22.2.2 Optoelectrical properties of LEDs

22.2.2.1 Current−voltage characteristic

The current−voltage (I−V) characteristic of LEDs is like a common p−n junction. Its functional equation can be described as follows:

$$I = I_s\left(\exp\frac{eV}{nkT_j} - 1\right), \tag{22.1}$$

where I_S is the diode's reverse saturation current, k is Boltzmann's constant, n is the ideality factor, and T_j is junction temperature in Kelvin scale.

Under reverse-bias conditions, V is negative and diode current saturates. I_S is dependent on many factors such as the active region area, charge carriers concentrations, and their lifetimes. Under typical forward-bias conditions, Eq. (22.1) illustrates that the current strongly increases as the diode voltage becomes large. It is noted that there is a voltage at which the current begins to increase rapidly, named as threshold voltage, V_{th}. This voltage can be given by $V_{th} \approx V_D \approx E_g/e$, determined by the semiconductor materials. Fig. 22.6 shows three I−V characteristics of RGB LEDs made from different materials. Along with different values of bandgap energy, the red, green, and blue LEDs have different threshold voltages.

The junction temperature is a critical parameter to the LED characteristics. High junction temperature leads to low forward voltage when a constant

This book belongs to Kitab Liaison (ocd1996@gmail.com) Copyright Elsevier 2023

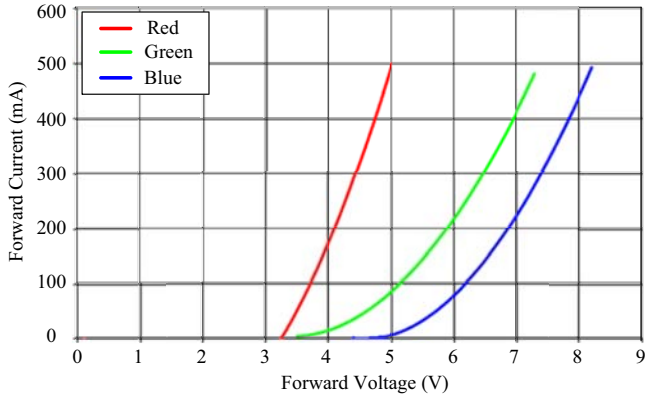

FIGURE 22.6 Forward current versus forward voltage for different color LEDs.

forward current flows across the semiconductor. Fig. 22.7 demonstrates the characteristic variation on a sample red LED semiconductor due to the junction temperature change via adjusting the heat sink temperature.

22.2.2.2 Luminous flux emission

The active region of an ideal LED emits one photon for every electron injected. Higher injection current denotes more recombination of electron–hole pairs and more simultaneous emission of photons. In an ideal LED, all photons emitted by the active region are also emitted into free space. Such an LED has unity extraction efficiency. However, in a real LED, light emitted by the active region may be reabsorbed in the substrate of the LED or reflected back to the substrate, referred to as total internal reflection. The optical flux, also called the radical flux, is the light power of a source emitted into the free space with the unit of watt (W). It is a radiometric quantity.

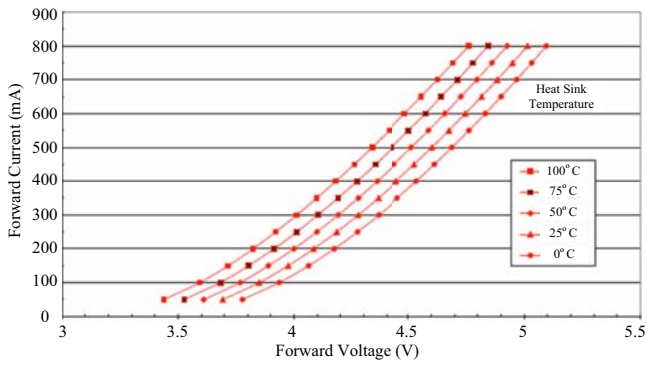

FIGURE 22.7 Forward current versus forward voltage of red Lamp at different heat sink temperatures.

This book belongs to Kitab Liaison (ocd1996@gmail.com) Copyright Elsevier 2023

The recipient of the light is the human eye. It is observed that the sensitivity of the human eye varies with the light wavelength. The luminous efficiency function or eye sensitivity function, $V(\lambda)$, provides the conversion between radiometry and photometry.

Luminous flux is a photometric quantity, representing the light power of a source perceived by the human eye. The unit of luminous flux is the lumen (lm). Accordingly, luminous flux, Φ, is obtained from the radiometric light power using the equation

$$\Phi = 683\frac{\text{lm}}{\text{W}}\int_{\lambda} V(\lambda)P(\lambda)d\lambda, \tag{22.2}$$

where $P(\lambda)$ is the spectral power density, i.e., the light power emitted per unit wavelength. Meanwhile, the optical power emitted by a light source is given by

$$P = \int_{\lambda} P(\lambda)d\lambda. \tag{22.3}$$

Luminous efficacy is defined as giving with the unit of lm/W.

$$\text{luminous efficacy} = \frac{\Phi}{P} = 683\frac{\text{lm}}{\text{W}}\frac{\int_{\lambda} V(\lambda)P(\lambda)d\lambda}{\int_{\lambda} P(\lambda)d\lambda}, \tag{22.4}$$

Larger injection current increases the amount of photons released, therefore luminous flux. But the luminous flux is not linear with the injected current. This is caused by the reduced internal quantum efficiency, where the increased injection electrons increase the chance of nonradiative recombination.

22.2.3 Characteristics of drivers for LEDs

LEDs are operated at a voltage higher than their cut-in voltages, above which their currents increase rapidly. Their powers are, therefore, better controlled with current modulation. Connecting LEDs to the AC power grid, a voltage step-down power converter is needed. This LED power converter must comply with industry standards. The standards consist of current quality, power factor (PF) limitation, current harmonic restriction, lifetime matching, conversion efficiency, etc.

European Union has claimed that the input current harmonics of lighting equipment must meet the requirements specified by EN 61000-3-2 Class C standard [1]. Much research has been directed toward power factor correction (PFC) topologies [2–6] and control schemes [7,8] in LED applications over the past decades. Ye et al. [9] studied and compared several single-stage offline PFC preregulators for driving LEDs, including boost converter, SEPIC converter [10], forward converter, flyback converter [2], and half-bridge converter [5,6]. These topologies are suitable for different power capacities and different

This book belongs to Kitab Liaison (ocd1996@gmail.com) Copyright Elsevier 2023

customer requirements. In general, these papers were devoted to improving PF and efficiency in the preregulator stage. Little attention was directed to the LED current and light control. Besides, these papers did not consider the lifetime of the converters while using high-voltage (up to 450 V) low-lifetime electrolytic capacitors [11], which limited the lifetime of the converter.

LED strings are connected in series so that the output voltage can be as high as 40−50 V. This will facilitate the post-PFC DC/DC converter design with higher efficiency and broader topology selection. Nevertheless, LED characteristics can vary from device to device. Thus, one driver per LED chip would be preferable in terms of high color accuracy for sophisticated lighting applications, like LCD and general illumination. Driving such LEDs from an offline power system to low-voltage loads will introduce many challenges in the converter design. For instance, a high-voltage conversion ratio would be implemented by isolation transformer with a high turns ratio, thus bringing relatively large leakage inductance, which needs passive snubber circuits in reducing either voltage or current stress [12]. In addition, snubber circuits will decrease efficiency and increase the cost of LED drivers. Current control can easily be realized by using a current feedback control loop in the power converter. Traditional control schemes, including average current mode (ACM) control, peak current mode control, hysteresis current mode control, and so on, are available in LED applications.

As a result, a durable LED driver system with high efficiency and independent color or brightness control is still needed for modern and sophisticated applications.

22.3 Color control with a power converter

LEDs are direct bandgap semiconductor p−n junction diodes. The bandgap of the semiconductor, which was controlled by mixing different proportions of the III−V elements from the periodic table, defines the light-color frequency of the diode. The bandgap of the LED may, therefore, change from time to time during operation, where the junction temperature changes with power dissipation and the ambient temperature. LED junction temperature estimation has been done using a linear current driver. However, in practice, LEDs are often driven by switching power converters for better efficiency, causing difficulty in measuring signals that were buried in a noisy switching environment. This setup also poses engineering challenges in correcting color drift due to device and temperature variations.

The data points on the CIE 1976 chromaticity diagram shown in Fig. 22.8 give the color coordinates (u', v') of typical red, green, and blue LEDs having wavelengths from 380 to 700 nm for a step size of 5 nm. The diagram was made in a way to give an even color perceptible difference for the distance of two-color points independent of the absolute positions of the color points. A color distance of $\Delta u'v' = \sqrt{(\Delta u')^2 + (\Delta v')^2} < 0.0035$ is indistinguishable to

This book belongs to Kitab Liaison (ocd1996@gmail.com) Copyright Elsevier 2023

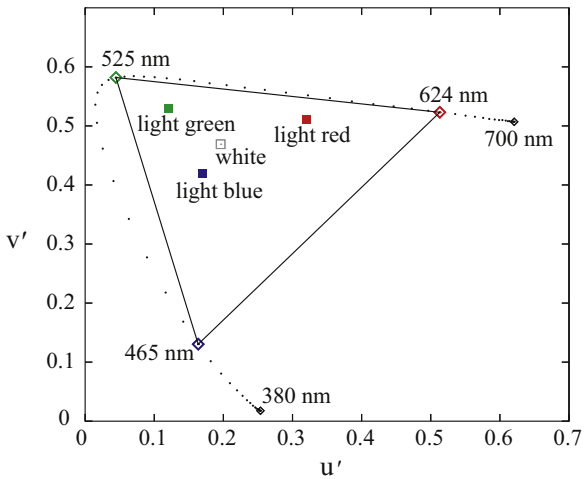

FIGURE 22.8 Color coordinates of typical LED of center wavelengths ranging from 700 to 380 nm.

human eyes. Errors within this small distance are considered very acceptable for most applications. Mixing the light intensity of the three LEDs having wavelengths of 624, 525, and 465 nm can produce all colors within the triangle whose corners are at the color coordinates of the RGB LEDs. The color accuracy of light mixed by the RGB LEDs is, therefore, dependent on (1) the stability of the color points of the RGB LEDs and (2) the accuracy of LED light dimming method.

We assume that the light stability of color points of LEDs is mainly dependent on the junction temperatures TR, TG, and TB of the red, green, and blue diodes. Like in previous studies [5,13−18], the effects of component aging are ignored here. Such effects can be compensated using a similar technique here and taking into consideration the thermal history concerning device aging. Alternatively, the aging speed can be effectively controlled by limiting the LED temperatures below a maximum threshold. The aging process thus is very slow and does not affect the result of different proposed temperature compensation techniques. If desired, it can also be compensated by regular calibrations using additional LED light measurement fixtures for specific applications.

An intended light output is usually expressed in terms of the so-called tristimulus, denoted by $X = (X\ Y\ Z)^t$, and also the dimming factor, denoted by $d = (d_r\ d_g\ d_b)^t$ and given by

$$d = f_T(X), \tag{22.5}$$

where f_T is a column vector function whose parameters change with T, which is a column vector of the LED junction temperatures, i.e., $T = (\mathrm{T_R}\ \mathrm{T_G}\ \mathrm{T_B})^{\mathrm{t}}$. Note that T depends on both d and the ambient temperature.

This book belongs to Kitab Liaison (ocd1996@gmail.com) Copyright Elsevier 2023

Without precise information of the temperature change inside the LED diode junction, the control of the light output from Eq. (22.5) can only be achieved by a feedback loop that senses the light outputs from the RGB LEDs and adjusts the control parameter d to compensate for the light output drifts as defined from f_T [16]. Indirect temperature compensation techniques like sensing the temperature of the heat sink on which the LEDs are mounted [17,19] may suffer from poor response to the change in temperature [18]. Although the method measures the LED forward voltage directly, it does not use pulse width modulation (PWM) control for simplicity. The method of two-diode driving voltages [20] may cause excessive errors in estimating the diode junction temperature and increase system complexity. Thus, light sensing is still important for ensuring high performance.

Eq. (22.5) can be highly nonlinear if inappropriate control methods and/or working color ranges are used. It is widely known that dimming using PWM is preferred over the use of amplitude modulation because of the linear relationship between the duty cycle d and the LED color light output. This is confirmed by experimental measurement, as shown in Fig. 22.9A–C. The

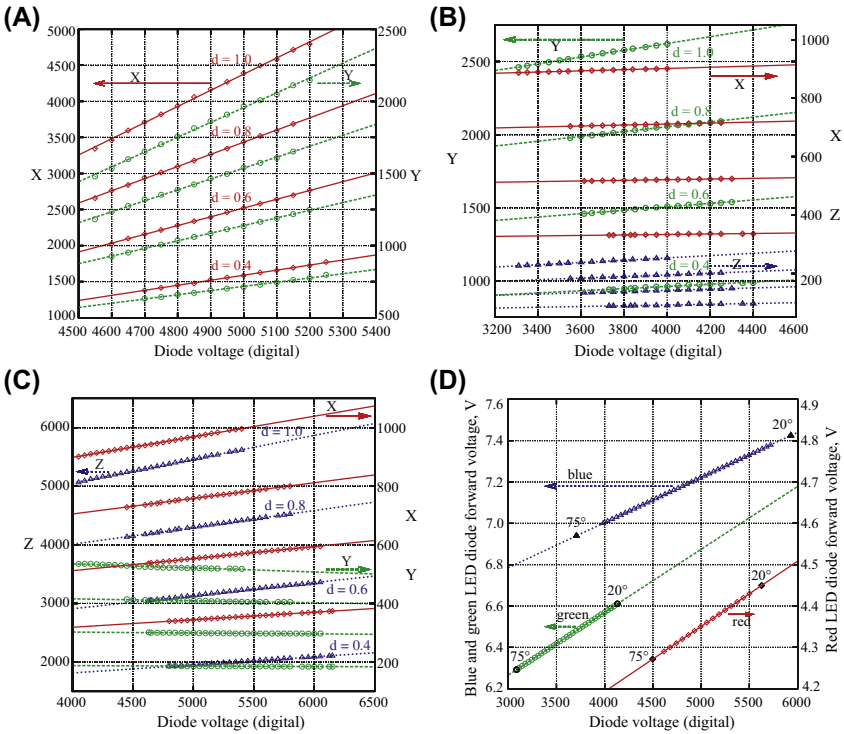

FIGURE 22.9 Experimental light tristimulus X versus diode voltage (digital) of (A) red LED light, (B) green LED light, and (C) blue LED light at different duty cycles. (D) Relationships between actual (two diodes in series connection) diode forward voltage and digital temperature V_{di} for $i = r, g, b$.

This book belongs to Kitab Liaison (ocd1996@gmail.com)
Copyright Elsevier 2023

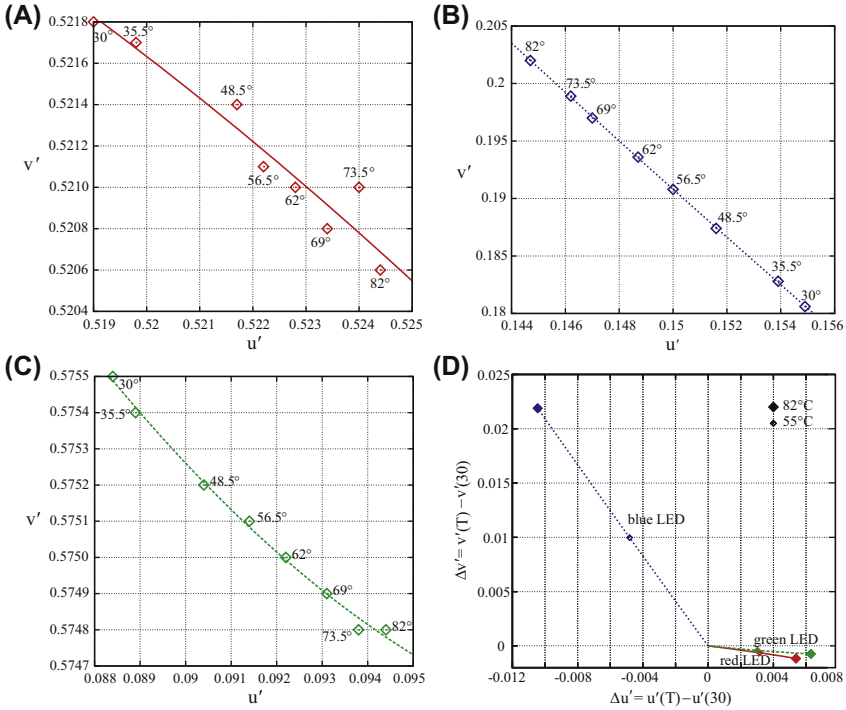

FIGURE 22.10 Evaluation of color points of the LEDs with center wavelengths of 624 nm (red), 525 nm (green), and 465 nm (blue), marked with small diamonds, changing with different heat sink temperatures for a constant current-driven (A) red, (B) blue, and (C) green LEDs. Lines are the least square fits of data points using second-degree polynomials. Shown in (D) are corresponding drifts of color points relative to the color point at a heat sink temperature of 30°C.

tristimulus $X = (X\ Y\ Z)^t$ changes linearly with the junction temperature and hence also with the A/D converted values of RGB diode voltages when drivers operate at a stable duty cycle as in Fig. 22.9D. Also, the tristimulus X changes linearly with the duty cycle at a stable junction temperature. It is possible to measure the above linear correspondence at several duty cycle values, such as in Fig. 22.9A–C and derive the corresponding tristimulus at the other duty cycle values accordingly. The linearity of the dependence of RGB lights on the RGB diode voltages makes programming very simple. Moreover, the color points of the LEDs with center wavelengths of 624 nm (red), 525 nm (green), and 465 nm (blue) in Fig. 22.8 drifts with the increase in junction temperature caused by heat sink temperature are very significant, as illustrated in Fig. 22.10 where the color variation $\Delta u'v'$ can be as high as 0.026 for a change of heat sink temperature from 30 to 82°C for the blue LED.

A Lamina BL-4000 RGB LED light engine to illustrate how essential parameters are contained in f_T of Eq. (22.5) can be found. Each color channel

This book belongs to Kitab Liaison (ocd1996@gmail.com) Copyright Elsevier 2023

of the RGB LED consists of a series connection of two corresponding color LEDs. The LEDs behave essentially as diodes with a higher cut-in voltage. At a typical driving current of 350 mA to each color channel, the LED produces forward diode voltages of 4.5, 6.7, and 7.6 V for red, green, and blue channel LEDs, respectively. At this driving current, they consume a total electrical power of 6.7 W and provide a total luminous flux of 120 lm. At any forward diode voltage below 3 V, the LEDs consume virtually no electrical power. In the experimental setup, a constant current of 330 mA during the turn-on duration of the PWM cycle is applied to all the red, green, and blue LEDs at ambient temperature. The data measured are indicated in Fig. 22.9A–C to obtain X_{or}, X_{og}, and X_{ob} versus diode forward voltages of the LEDs, i.e., V_{dr}, V_{dg}, and V_{db}, at $(d_r, d_g, d_b) = (1, 1, 1)$, (0.8, 0.8, 0.8), (0.6, 0.6, 0.6), and (0.4, 0.4, 0.4). The LED heat sink temperature is used as the variation parameter. Sufficient time is allowed for the forward diode voltages to settle down before taking measurements. Thus, diode forward voltages (junction temperatures) are measured with a one-to-one correspondence to the heat sink temperatures.

As explained in the previous content, the mixed color is therefore given as

$$\begin{pmatrix} X_o \\ Y_o \\ Z_o \end{pmatrix} = d_r \begin{pmatrix} X_{or} \\ Y_{or} \\ Z_{or} \end{pmatrix} + d_g \begin{pmatrix} X_{og} \\ Y_{og} \\ Z_{og} \end{pmatrix} + d_b \begin{pmatrix} X_{ob} \\ Y_{ob} \\ Z_{ob} \end{pmatrix} \tag{22.6}$$

where

$$\begin{pmatrix} X_{oi} \\ Y_{oi} \\ Z_{oi} \end{pmatrix} = \begin{pmatrix} \alpha_{i1} V_{di} + \alpha_{i2} \\ \alpha_{i3} V_{di} + \alpha_{i4} \\ \alpha_{i5} V_{di} + \alpha_{i6} \end{pmatrix} \tag{22.7}$$

with $i = r, g, b$ and α_{ij} being coefficients of least square fits from Fig. 22.9A,B, and C.

Since X_{or}, X_{og}, and X_{ob} are linearly independent, it is always possible to determine a unique d such that (22.6) is satisfied. If X_{or}, X_{og}, and X_{ob} are temperature invariant and d is well controlled, the light-color output will be very stable as given in (22.6). However, the three-color bases X_{or}, X_{og}, and X_{ob} are temperature dependent, as given in (22.7). Using (22.6) and (22.7), the desired color can be achieved.

22.4 Efficiency and lifetime improvement

To promote energy saving, many governments in the world, such as the United States, European Union, and Australia, have implemented measures to phase out energy-inefficient incandescent light bulbs [19]. LED lamps are prospective successors of incandescent lamps with much higher efficacy of about 90

This book belongs to Kitab Liaison (ocd1996@gmail.com) Copyright Elsevier 2023

and 75 lm/W for cool and warm white LEDs, respectively. For cost consideration, the interim lighting fixtures are expected to have the ability to accommodate both incandescent bulbs and LED lamps. Therefore, LED lamps mounted in the existing fixtures, such as PAR30 and PAR16 style housings, can be direct replacements of the incandescent light bulbs with the expectation of more than 80% energy saving and much longer lifetime.

To realize these advantages of LED luminaire, LED ballasts must be durable and efficient. In addition, earlier energy saving lamps for home applications, such as fluorescent lamps and HID lamps, do not work properly with the existing incandescent dimmers, such as the trailing-edge controller shown in Fig. 22.11, where the averaged light output is dimmed by controlling the duty ratio of state-on phase of the input voltage. Therefore, to gain public acceptance, LED replacement lamps should be designed to work with dimmer switches.

To produce 1000 lm (typical luminance flux from a 60-W incandescent lamp), approximately 12 LEDs of 1 W each are needed to be integrated into a PAR30 style housing. Here, high-flux cool white LEDs are used, Cree XREWHT-L1-0000-00C02, as an example. The LED lamp has a luminous efficacy of 100 lm/W driven at a typical current of 350 mA and junction temperature T_j of 25°C. The 12 LEDs are configured in parallel with two branches of six LEDs each in series. Therefore, the LED ballast should provide an output current of 700 mA at a typical loading voltage of approximately (3.3 V × 6 V) 19.8 V at T_j of 25°C from a universal line voltage of 100−240 V_{rms}. For such a high-voltage step-down ratio, a transformer is usually used [20−22]. However, such a transformer has large leakage inductance whose energy needs to be recycled or dissipated properly. Otherwise the energy will appear as voltage or current stress to the devices connected, complicating the ballast design or reducing the converter efficiency. Consequently, transformerless design can be more attractive, especially in the low-power and cost-effective applications.

There are two approaches for dimming an LED. One is to modulate the amplitude of the DC biasing current for LED driving. This amplitude modulation method can easily be implemented by current feedback control in a

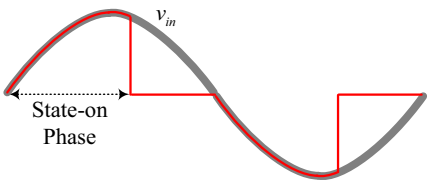

FIGURE 22.11 Trailing-edge control principle. The output power is controlled by state-on phase of input voltage.

This book belongs to Kitab Liaison (ocd1996@gmail.com) Copyright Elsevier 2023

power converter. However, amplitude modulation is not suitable for applications where accurate control of color and intensity is needed, because the output lumen of the LED lamp is not linearly proportional to the driving current. Another dimming method is to use pulse width modulation (PWM). During the turn-on duration, the driving current is constant and it assures a constant color point in the CIE gamut. Adjusting the turn-on duty cycle can permit the desired light intensity to be achieved easily. Hence, one current driver per LED lamp may be needed for precise color and brightness control.

The traditional PWM single-switch buck converter is among the most efficient transformerless step-down converters, as shown in Fig. 22.12A. However, to provide PFC, the buck converter operating in continuous conduction mode (CCM) normally requires an averaged current controller with considerable cost. Such averaged current programmed power converters, due to the need to sense the slow varying input voltage magnitude, are not compatible with existing dimmer switches, reducing the popularity of LED replacement lamps. Considering the large-voltage step-down ratio, the conduction loss of the high-voltage freewheel diode D_1 would be significant because of the long freewheeling time and large-diode forward voltage. The CCM buck converter may also suffer from loss caused by the high reverse-recovery current of D_1.

On the contrary, the buck converter operating in discontinuous current mode (DCM) is almost input resistive due to the relatively low output voltage, providing automatic PFC. The duty cycle control allows instant current tracking with the line input voltage variation, and thus it is compatible with the trailing-edge dimmer. As shown in the freewheeling diode turns off naturally, there is no loss due to zero-diode recovery current. However, the output switching ripple current in the DCM-operated buck converter that flows into the charge-storage capacitor is several times higher than that of the CCM case. This will reduce the lifetime of the capacitor, as well as the lifetime of the replacement lamp. In addition, the freewheeling time of D_1 is still long due to the relatively low output voltage and therefore incurs a considerably large loss, although the loss is still lower than that in CCM.

From the aforementioned analysis, for the ballast input stage, the buck converter operating in DCM can satisfy the requirements of controller simplicity and dimmer compatibility. For the output section, the CCM buck converter can provide continuous LED current that reduces the current stress

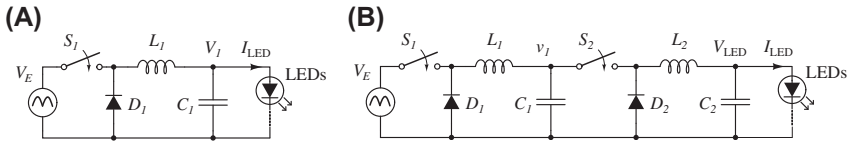

FIGURE 22.12 (A) Buck converter driving several LEDs. (B) Two cascading buck converters driving several LEDs.

This book belongs to Kitab Liaison (ocd1996@gmail.com) Copyright Elsevier 2023

on the charge-storage capacitor and thereby extends its lifetime. Therefore, the use of two buck converters connected in cascade as shown in Fig. 22.12B can readily dim the LED lamps and reduce switching current ripple to the charge-storage capacitor simultaneously. Here, the first buck converter operates in DCM and the last one operates in CCM. However, a two-stage design is less efficient due to the use of intermediate storage.

Driving multiple LED lamps independently from an offline power source poses challenges in many aspects of power converter design. High PF and low input current harmonics are becoming the mandatory design criteria for switching power supplies. In lighting equipment, the input current of ballasted lamps must meet the harmonic limits specified by IEC 61000-3-2-Class C. Ballasts with input power exceeding 25 W are required to comply with stricter requirements as stated in IEC 61000-3-2-Class C. Much research has been directed toward PFC topologies and control schemes. A typical 100-W design using the "classical" two-stage PFC circuit and postcurrent regulators is shown in Fig. 22.13. The specific challenges in using this circuit are described as follows. LED lamps have a lifetime of about 25 years, while conventional PFC power converters employing high-voltage electrolytic capacitors have much shorter lifetimes. These high-voltage electrolytic capacitors are utilized in most single-stage PFC circuits. To generate light with the desired color and brightness, the red, green, or blue LED lamps may be driven by three independent switching mode power converters, respectively, with PWM output current programming in the final stage. However, due to LED device variations, a small number of LED lamps should be driven independently for brightness correction. Thus, three stages are effectively needed, which limit the overall efficiency. A high turns-ratio transformer is required to provide a low-voltage level at the secondary suitable for an LED controller. This, however, is accompanied by a significant leakage inductance on the primary side of the transformer, causing a dramatic increase in power loss due to

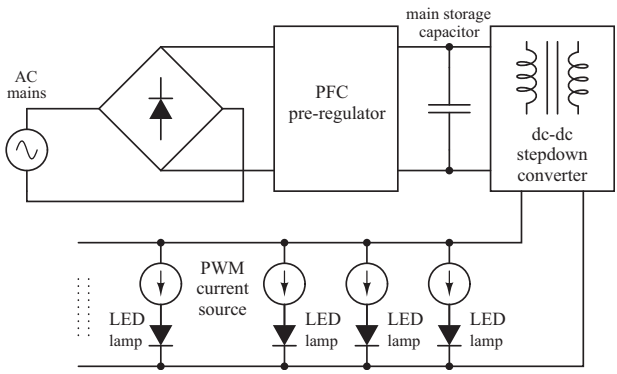

FIGURE 22.13 Classical design of LED power supply consisting of a two-stage PFC voltage regulator driving point-of-load current-regulated LED lamps.

This book belongs to Kitab Liaison (ocd1996@gmail.com) Copyright Elsevier 2023

passive snubbering, thermal stress, and device stress, and making the lifetime of converter much shorter than that of LED lamps. An isolated boost converter that eliminates passive snubbering has been proposed. However, the design utilizes a primary-side high-voltage storage capacitor.

LED lamps with many overwhelming advantages emerge as a potential light solution and find a great deal of applications in the current markets. To generate light with the desired color and brightness in a mono-or multicolor LED luminaire, LEDs should be fed with a constant current controlled by PWM for independent linear dimming. Therefore, one or a bin of LED(s) driven by one driver can minimize the effect of device variation and realize the linear brightness programming. Now, many IC controllers perform the function of accurate, current regulation with high power density and efficiency from a relatively low-voltage bus, 10−20 V. Accordingly, a front-end PFC preregulator is needed to convert the voltage from the universal AC grid (100−240 V/50−60 Hz) to the low DC voltage bus, where the input current should satisfy the current harmonic limits as stated in IEC 61000-3-2 Class C standard for lighting equipment.

A typical LED driver using the "classical" two-stage PFC circuit is shown in Fig. 22.13. Conventional designs of PFC power converters normally use the main storage capacitor on the primary high-voltage side, which is usually a high-density aluminum electrolytic capacitor having a lifetime of 2000−5000 h, which is far shorter than the lifetime of 50,000−100 000 h of LED lamps. A large turns-ratio transformer is needed in the DC/DC step-down converter. The associated large transformer primary side parasitic leakage inductance will make switching components to suffer from higher switching loss, as well as higher thermal, voltage, and current stresses, making their lifetime of operation much shorter than that of LED lamps. In addition, all power is processed thrice and the efficiency cannot be high.

To extend the lifetime of LED ballasts, many researchers have observed that the capacitor will degrade the lifetime of the lamp system and therefore have proposed some techniques to avoid the use of aluminum capacitors at the expense of degraded performances. The main concept is to replace the expensive high-voltage short-lifetime capacitors in the primary of the isolation transformer by less expensive low-voltage long-lifetime capacitors in the secondaries with the same charge-storage capacity. Thus, the high-density low-cost aluminum electrolytic capacitors can be used in this design for achieving a longer lifetime for LED driver applications. A soft-switching half-bridge resonant circuit follows a boost stage to provide a direct energy path from the primary to the secondaries with little storage and loss. The significant primary leakage inductor favors a resonance tank to eliminate the voltage or current spikes of the switches, which is typical in current-fed isolated converters. To improve the efficiency further, a noncascading structure with two output transformer windings is used in the downstreams. One winding output is connected to a current regulator to regulate the LED current and the other is

This book belongs to Kitab Liaison (ocd1996@gmail.com) Copyright Elsevier 2023

directly contributed to power LEDs without power processing loss. Therefore, the high efficiency will be guaranteed without additional cost.

In this part, the circuit is operated in continuous conduction mode (CCM), as shown in Fig. 22.14, to permit the high PF to be achieved easily with the conventional ACM control method.

Two secondary output windings of the transformer are used in the non-cascading output configuration. One of the outputs is connected directly (without being processed) in series with the other output which is then current regulated by a PWM buck converter to drive an LED lamp. Additional buck converters and identical secondary connections can be included to drive more LEDs independently. Since the energy from one output winding can directly be used to drive the LED without going through the other power stage, a higher efficiency can be guaranteed.

η_1 and η_2 are the efficiency of the isolated PFC converter and the buck converter, respectively, and define k as the percentage of the output power from the preregulator that goes directly to the LED load. For the noncascading structure, the overall efficiency η is given as

$$\eta = k\eta_1 + (1-k)\eta_1\eta_2, \tag{22.8}$$

where $k < 1$, $\eta_1 < 1$, and $\eta_2 < 1$.

Rearranging Eq. (22.8) gives

$$\eta = \eta_1(\eta_2 + k(1-k)) = \eta_1\eta_2'. \tag{22.9}$$

Obviously, η_2' is the equivalent efficiency of the "improved" buck converter. The LED is connected in series with two voltage sources consisting of V_{out} and $v_{C_{B2}}$. The power provided by the output of the buck converter and $v_{C_{B2}}$ can be calculated as $I_{\text{LED}}V_{\text{out}}$ and $I_{\text{LED}}v_{C_{B2}}$, respectively, where I_{LED} is the LED driving current. The corresponding input power of the buck converter is therefore given as $I_{\text{LED}}V_{\text{out}}/\eta_2 = I_{\text{LED}}(V_{\text{LED}} - v_{C_{B2}})/\eta_2$, where V_{LED} is the voltage across an LED. Hence, further simplification gives

$$\eta_1' = \frac{V_{\text{LED}}}{v_{C_{B2}} + (V_{\text{LED}} - v_{C_{B2}})/\eta_2}, \tag{22.10}$$

$$k = \frac{v_{C_{B2}}}{v_{C_{B2}} + (V_{\text{LED}} - v_{C_{B2}})/\eta_2}, \tag{22.11}$$

Typical forward diode voltages of red, green, blue, and white LEDs are 2.4, 3.55, 3.75, and 3.75 V, respectively. Different packages of LED lamps may integrate identical LEDs in series or parallel producing forward voltages and currents in multiple of that from a single LED.

From the voltage transfer property of the buck converter, $0 < d_{\text{buck}} = \dfrac{V_{\text{LED}} - v_{C_{B2}}}{v_{C_{B1}}} < 1$, the following inequality can be obtained

$$0 \le v_{C_{B2}} < V_{\text{LED}} < v_{C_{B1}} + v_{C_{B2}} = V_o, \tag{22.12}$$

This book belongs to Kitab Liaison (ocd1996@gmail.com) Copyright Elsevier 2023

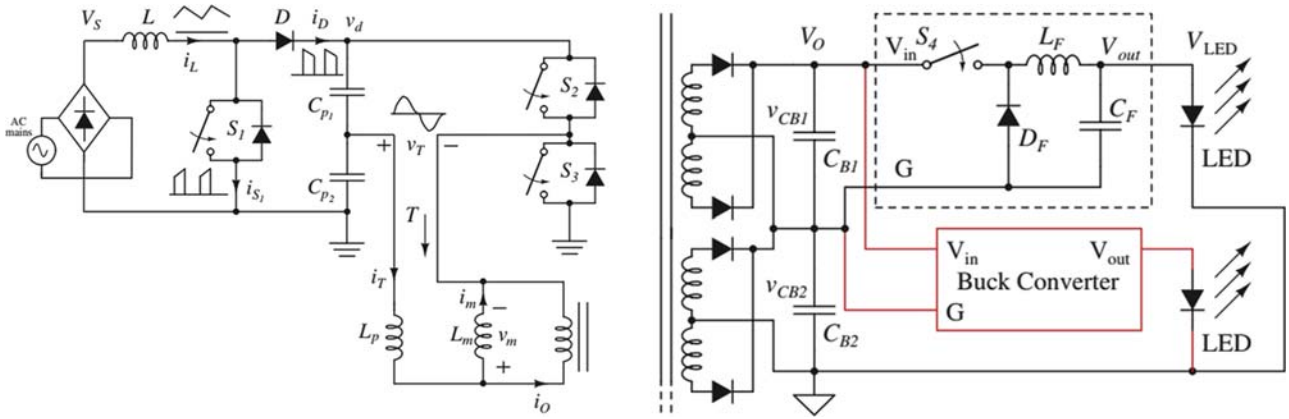

FIGURE 22.14 Circuit schematic of the proposed LED ballast.

This book belongs to Kitab Liaison (ocd1996@gmail.com)

Copyright Elsevier 2023

Specifically, if $v_{C_{B2}}$ is equal to 0, the circuit reduces to the conventional cascading structure. For practical applications, V_{LED} is fixed and η_2 in Eq. (22.11) can be estimated by calculating the power dissipation of the buck converter. Hence, it is available to determine $v_{C_{B2}}$ and V_o for the maximum of η_2'.

As an example is illustrated here, the technique of optimizing efficiency for the noncascading configuration. Suppose that the LED lamps are series-connected, composing of four blue LEDs with $V_{\text{LED}} = 14.45$ V. Three such series-connected LEDs are connected in parallel to draw a driving current of 1020 mA. A current source based on a buck topology using LT1510 operating at a switching frequency of 200 kHz is used for illustration. Fig. 22.15 gives the schematic of the buck switching converter behaving essentially as a current source whose magnitude is controlled by a PWM signal. PWM gate pulses, V_{PWM}, which are applied at a frequency of 200 Hz to the MOS transistors Q_1 and Q_2 respectively, can change the intensity of the lamp instantaneously at a fixed color point. For lighting applications where 100% dimming is normally not necessary, Q_2 in Fig. 22.15 can be removed. Here, without loss of generality, V_{PWM} is kept low and Q_2 is replaced by a short circuit. The power dissipation in the IC circuit is calculated, including loss dissipated in the bias and driver, switch resistance, switch transition, current sensing resistor, conduction loss of the buck inductor, and the freewheeling diode, where the buck inductor parasitic resistance of 0.45 Ω and the Schottky freewheeling diode voltage drop during on-stage of 0.5 V are used in the calculation. Fig. 22.16 plots the efficiency η_2 of the buck converter versus $v_{C_{B1}}$ for different values of $V_o(= v_{C_{B1}} + v_{C_{B2}})$. From Fig. 22.16, when V_o is constant, η_2 increases with $v_{C_{B1}}$ because of larger duty cycle and smaller conduction current flowing into D_F.

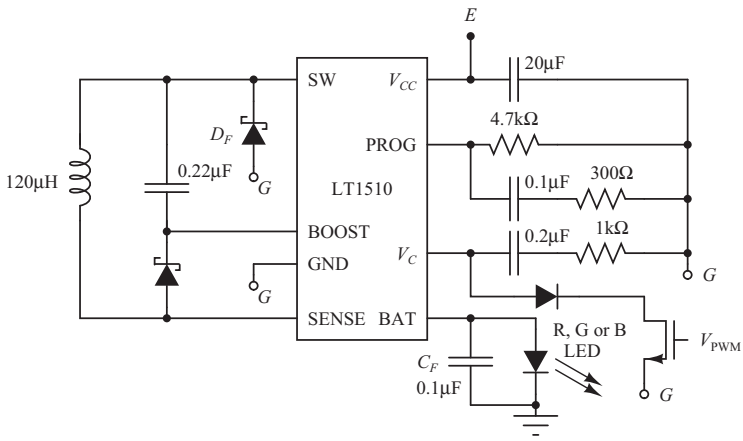

FIGURE 22.15 Switching converter with PWM control.

This book belongs to Kitab Liaison (ocd1996@gmail.com)
Copyright Elsevier 2023

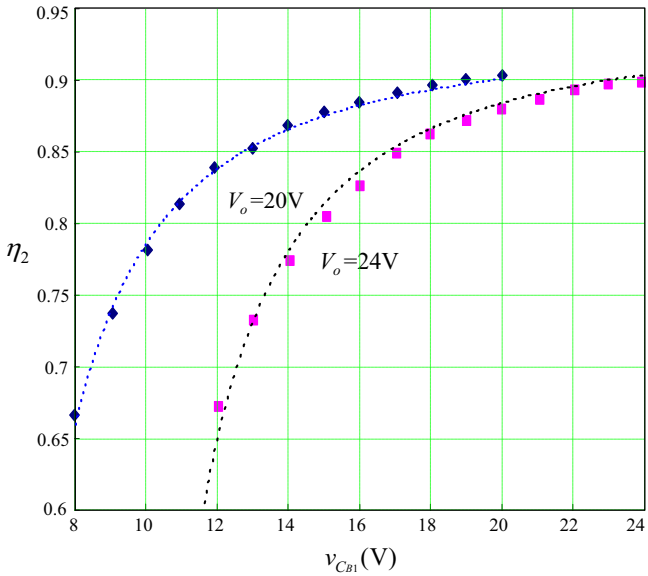

FIGURE 22.16 Efficiency η_2 of the buck converter.

From Eq. (22.10) and Fig. 22.16, we can plot the efficiency η_2' versus $v_{C_{B2}}$ and V_o to form a surface, as shown in Fig. 22.17, where the surface with a projection inside the red (gray in printed version) triangle on the $v_{C_{B2}}-V_o$ plane is nonoperational for the IC as it needs a supply voltage $v_{C_{B1}}$ higher than 7.8 V. To help visualize how η_2' changes with $v_{C_{B2}}$ and V_o, a family of curves are given in Fig. 22.18. These curves illustrate that η_2' is much higher at $v_{C_{B2}} = 12$ V for the whole range of V_o. Therefore, the maximum η_2' must be on the line of interception between the efficiency plane and the vertical plane at $v_{C_{B2}} = 12$ V. The line is redrawn in Fig. 22.19, where the maximum of η_2' occurs at $(v_{C_{B2}}, V_o) = (12\text{ V}, 19.8\text{ V})$, as shown in Fig. 22.14.

The capacitor voltages at $2f_l$ can be expressed

$$v_{C_{B1}}(t) = v_{C_{B1_0}} - v_{C_{B1_1}} \sin(4\pi f_l t), \tag{22.13}$$

$$v_{C_{B2}}(t) = v_{C_{B2_0}} - v_{C_{B2_1}} \sin(4\pi f_l t), \tag{22.14}$$

$$v_o(t) = v_{C_{B1}}(t) + v_{C_{B2}}(t). \tag{22.15}$$

where $v_{C_{B1_1}}$ and $v_{C_{B2_1}}$ depend on the values of the filtering capacitors C_{B1} and C_{B2} and the transformer coupling coefficient. Write by considering their respective reactive powers:

$$C_{B1} = \frac{(1-k)P_o}{4\pi f_l v_{C_{B1_0}} v_{C_{B1_1}}}, \tag{22.16}$$

This book belongs to Kitab Liaison (ocd1996@gmail.com) Copyright Elsevier 2023

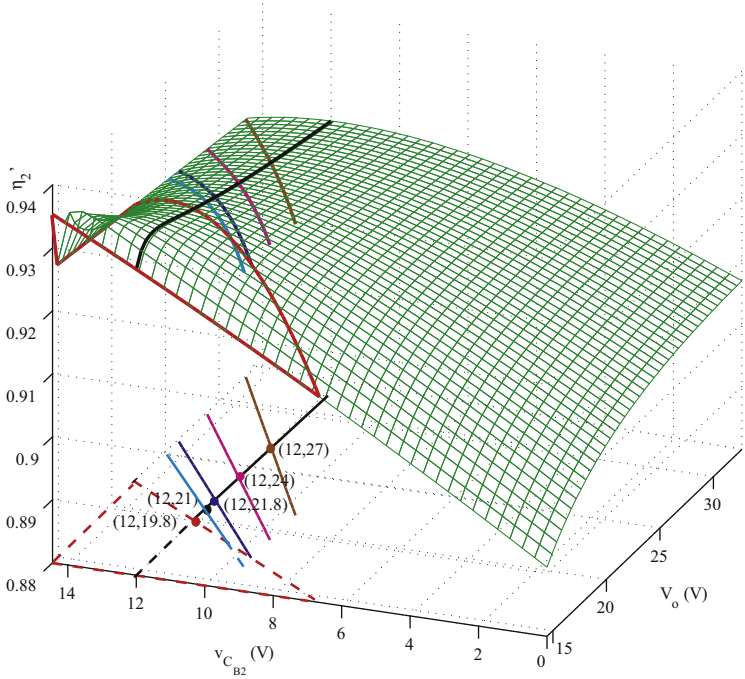

FIGURE 22.17 Efficiency surface η_2'.

$$C_{B2} = \frac{kP_o}{4\pi f_l v_{C_{B2_0}} v_{C_{B2_1}}}. \tag{22.17}$$

It should be noted that $\frac{v_{CB1_0}}{v_{CB2_0}} \equiv \frac{v_{CB1_1}}{v_{CB2_1}} = \frac{m_1}{m_2}$ for unity coupling of the transformer of turns ratio of n: m_1: m_2.

Eqs. (22.13)–(22.17) indicate that the noncascading converter is not operating at a single efficiency point of η_2', but rather operating along the line segments centered at the chosen point of $(v_{C_{B2_0}}, V_{o0})$, as shown in Fig. 22.14. The line segments centered at $v_{C_{B2}} = 12$ V and $V_o = 19.8$, 21, 21.8, 24, and 27 V are illustrated in Fig. 22.14. To minimize the cost of filtering capacitors, the maximum allowable $v_{C_{B2_1}}$ is calculated from (22.12), i.e.,

$$\max(v_{C_{B2_1}}) = V_{\text{LED}} - v_{C_{B2_0}} = 2.45 \text{ V}. \tag{22.18}$$

Shown in Fig. 22.14 are line segments in the v_{CB2} projection limited to $2\max(v_{CB_{2_1}}) = 4.9$ V, where the operating points at (12, 19.8 V) and (12, 21 V) would not lead to the use of minimum filtering capacitors.

Clearly, the efficiency η_2' varies periodically in half-line period along one of the efficiency curves, as illustrated in Fig. 22.14. The average efficiency η_2' for the noncascading converter is seen the following expression:

This book belongs to Kitab Liaison (ocd1996@gmail.com) Copyright Elsevier 2023

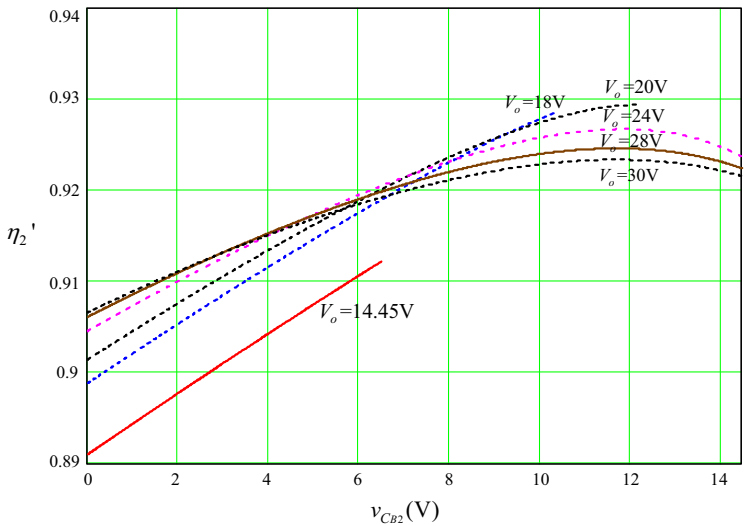

FIGURE 22.18 Efficiency η_2' versus $v_{C_{B2}}$ at different values.

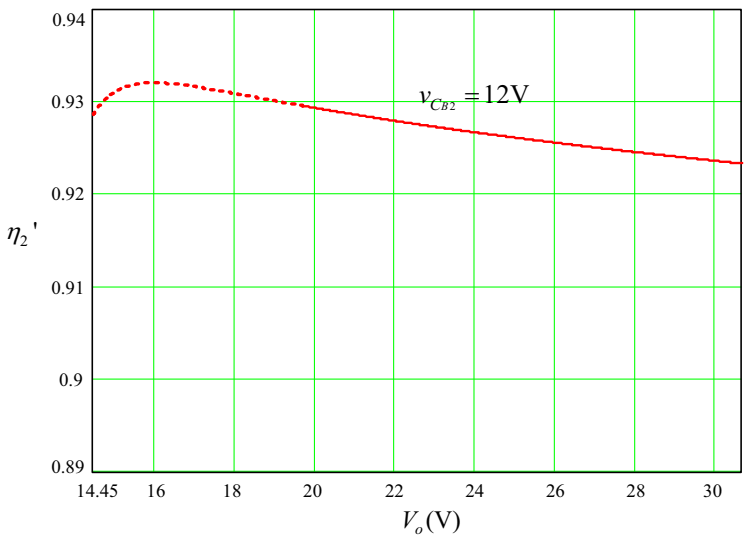

FIGURE 22.19 Efficiency η_2' versus v_o at $v_{C_{B2}} = 12$ V from Fig. 22.17.

$$\bar{\eta_2'}\left(v_{C_{B2_0}}, V_{o0}, v_{C_{B2_1}}\right) = \frac{2}{T_i}\int_0^{T_i/2} \eta_2'(v_{C_{B2}}(t), V_o(t))dt. \tag{22.19}$$

This book belongs to Kitab Liaison (ocd1996@gmail.com)
Copyright Elsevier 2023

22.5 Current sharing schemes

22.5.1 Passive current sharing schemes

The brightness uniformity is the basic requirement for applications involving multiple LEDs. This requirement is directly related to the driving current of the LEDs. The simplest approach is to connect the LEDs in series to form a string. However, the drawback of this connection is that the failure probability of the LED string increases by a factor equaling the number of LEDs connected. Moreover, the terminal voltage of aggregated LEDs can exceed the safety limit if tens of LEDs are connected in series. Therefore, several LED strings connected in parallel with acceptable terminal voltage are a better tradeoff for most applications. It is commonly known that the LED driving voltage will be slightly different due to device and temperature variations. Each LED follows an exponential V−I relationship, where a small voltage disturbance causes a large current variation. Thus, this inherent property of LEDs brings about current imbalance if the LED strings are connected in parallel to the same supply output terminal.

To avoid current imbalance, a direct solution is to connect each LED string from the ground to a different terminal, whose voltage is adaptively varied with the string current [23−25]. This method is effective but requires the use of more components since each LED string needs an individual electrical circuit and control logic. In the mains-operated three-stage configuration, the efficiency is usually hard to optimize. To improve the efficiency, a non-cascading structure [26] has been proposed to allow direct power delivery to the LEDs, minimizing power processing from the source to the load. To further simplify the current control circuit, a mag amp has been used to replace the switching component [27]. However, each LED string in these methods still requires individual active current control to realize current balance. To simplify the current control in each LED string, automatic current sharing methods have been adopted. In Ref. [28], the AC current is separated into its positive and negative half periods. The rectified average currents in the two half periods are naturally equalized to drive two LED strings. Because of the doubled period, the filters become larger. The use of a coupled inductor or transformer is a passive approach to realizing automatic current balance [29−32]. However, it is relatively hard to precisely control the current of each LED string due to the presence of parasitics, component variations, and the absence of feedback control. When the number of paralleled LED strings increases, the complexity of the circuit may increase exponentially.

To maintain simplicity and minimal power conversion, it is more desirable to connect all LED strings to a common voltage terminal. Additional components are needed to absorb the voltage difference between the terminal voltage and the accumulative LED voltage drops of an LED string. To maximize the efficiency, the component should be lossless. Therefore,

This book belongs to Kitab Liaison (ocd1996@gmail.com) Copyright Elsevier 2023

methods involving the use of dissipated components such as resistors and linear current regulators can only be applied to low-power applications [33]. To reduce losses, self-adaptive voltage driving methods [8,34] have been proposed to minimize the voltage drop across the linear current regulator. However, the self-adaptive control utilizing a MOSFET in the low drop-out portion of the linear operation region can be difficult to achieve. Also, the losses of the switch components in linear mode are different for different dimming conditions for a linear regulator. The losses under all dimming conditions are not smaller than in the same linear regulator with the MOSFET operating in saturation mode.

Passive lossless capacitors can also be used to absorb the voltage difference among the LED strings [35–41]. If the reactance of the capacitor is much larger than the total equivalent resistance of LEDs, then the difference in the resistances among LED strings would have a little effect on the string currents and the current balance is automatically realized. However, the presence of the current balancing capacitor increases the bus voltage stress. Other lossless components are the active power switches, such as MOSFETs. The on-resistance is approximately zero. PWM is used to maintain an identical averaged current in each LED string. However, the on-time current level in each string affects the LED luminous efficacy, which is important and often neglected in the derivation of the switch-mode (PWM) LED current balancing methods.

The concept of the current balancing scheme using PWM is to maintain a constant averaged LED current via the tuning of the duty cycle of each LED string as shown in Fig. 22.20, where N LED strings are connected to a common output terminal with DC-bus voltage V_O, which is used to control the duty cycle of each switching regulator to provide the required power of each LED string. Denote the instantaneous current of each LED string as in which is

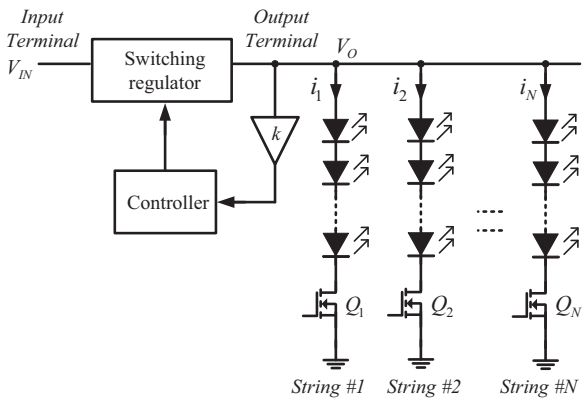

FIGURE 22.20 LED driver with switch-mode current balancing modulation.

This book belongs to Kitab Liaison (ocd1996@gmail.com)
Copyright Elsevier 2023

modulated by the current balancing switch with on-time current I_n, where $n = 1, 2, \ldots, N$. The current waveforms are illustrated in Fig. 22.21 with a common averaged current of I_{LED}.

To achieve current balancing, the turn-on current amplitude I_n and turn-on duty cycle D_n of string n should satisfy

$$I_{\text{LED}} = I_n D_n. \tag{22.20}$$

In the subsequent analysis, X_n will be used to describe the property X of LED-string n, where $n = 1, 2, \ldots, N$. From (22.20), I_n is determined by V_O and the characteristic of the LED string. The PWM current balancing scheme controls a constant I_{LED} by adjusting D_n. Intuitively, V_O must adjust to be no smaller than the accumulative voltage drop of any LED string to guarantee sufficient on-time current. LEDs are nonlinear components with the typical exponential V–I curves shown in Fig. 22.22. A slight voltage difference in V_O

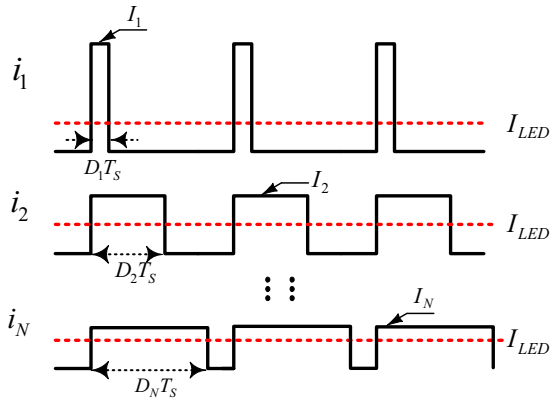

FIGURE 22.21 Current waveform in each LED string with PWM.

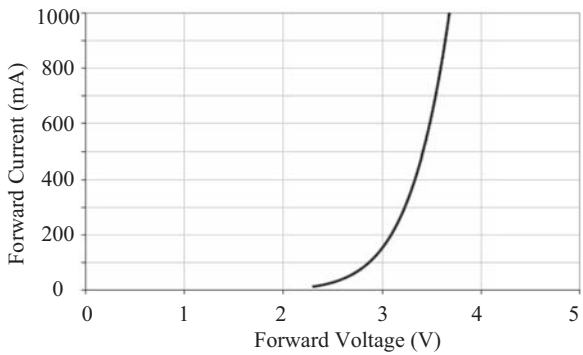

FIGURE 22.22 Typical forward voltage versus forward current of Cree Xlamps XR-E LEDs at $T_j = 25°\text{C}$.

This book belongs to Kitab Liaison (ocd1996@gmail.com)
Copyright Elsevier 2023

will result in a large on-time current variation in I_n. Fig. 22.23 illustrates a typical relationship of the luminous flux versus the driving current I_n. The emitted luminous flux is not linear with the driving current and slowly decreases when the driving current is increasing due to higher junction temperature as a result of more heat dissipation. Normally, the normalized forward voltage varies insignificantly compared with the normalized forward current, and thus it can be assumed constant. Therefore, the slope at a particular point of the curve in Fig. 22.23 can reflect the trend of luminous efficacy (=(luminous flux)/($V_{LED}I_{LED}$)) at that specific position. The general photo-electro-thermal theory also verifies that the luminous efficacy will decrease when the forward current exceeds a certain point. This threshold point depends on the thermal design. Manufacturers often provide a typical working current in the datasheet. The Cree XR-E series LED operates at 350 mA. The forward currents in LED strings are expected to be around 350 mA with good luminous performance. If there is current imbalance of the LED strings with different on-time currents I_n, individual adjustment of duty cycles D_n can be used to achieve the required average current of 350 mA. Therefore, the maximum of D_n is unity and the string with unity D_n has the best luminous efficacy among other LED strings having duty cycle smaller than unity. Hence, V_O should better be just above the maximum of all the LED-string voltage drops to produce a set of I_{LED} with maximized D_n ($n = 1, 2, \ldots, N$) and minimized I_n ($n = 1, 2, \ldots, N$). Then, high luminous efficacy of LED sources is achieved.

In general, the forward voltage of LEDs is sensitive to temperature and varies with individual devices. It is hard to determine a fixed V_O for the varying LED operating points and guarantee an optimized system. Thus, the control using a fixed V_O for all operating points is not desirable for LED current balancing. Therefore, the key idea is to optimize the terminal voltage V_O until

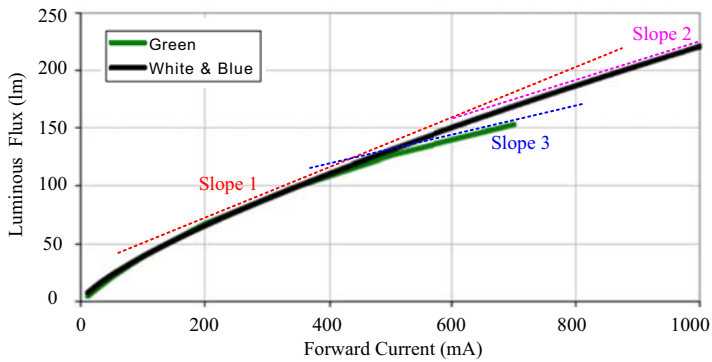

FIGURE 22.23 Typical luminous flux versus forward current of Cree Xlamps XR-E LEDs at $T_j = 25°C$.

This book belongs to Kitab Liaison (ocd1996@gmail.com)
Copyright Elsevier 2023

one of the duty cycle of D_n ($n = 1, 2, \ldots, N$) reaches unity, and the minimum on-time current would equal the balancing current I_{LED} as in

$$\min\{I_n, n \in \{1, 2, \ldots, N\}\} = I_{\mathrm{MIN}} = I_{\mathrm{LED}}. \tag{22.21}$$

22.5.2 Active current sharing schemes

The current imbalance of LED strings within an LED load is caused by unequal V–I curves of the LED strings. To balance currents in multiple LED strings simultaneously, additional balancing circuitry must be inserted within the LED load to regulate the current and absorb the voltage difference in each LED string, as shown in Fig. 22.24. The balancing circuitry can be passive or active. Active balancing circuitry includes switched current regulator, linear regulator, current mirror [33], and so on. Obviously, linear regulators and current mirrors are simple and economical to implement, but the losses on the linear transistors are relatively high. The switched current regulator uses high-frequency on-off switches to control the current of each LED string with high efficiency. However, the switched-mode circuit and control logic is complex and less reliable. Recently, some attempts have been made to improve the efficiency of linear schemes with the penalty of complex control [8,35,42]. In the passive balancing circuit, lossy resistors are not considered in high-power LED applications. The inductor and capacitor without real power dissipation are good candidates. The AC currents from a pair of coupled inductors with 1:1 turns ratio [30] or from two complementary rectified current paths of an AC capacitor can automatically balance the currents of two LED strings according to the principles of electromagnetic induction and capacitive charge balance, as shown in Fig. 22.25 It should be noted that each LED string in capacitive charge balance shares the AC current alternatively for half a period

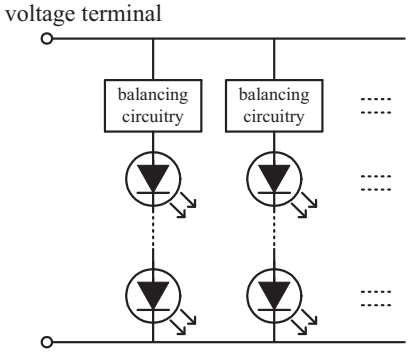

FIGURE 22.24 LED load with balancing circuitry for each string.

This book belongs to Kitab Liaison (ocd1996@gmail.com) Copyright Elsevier 2023

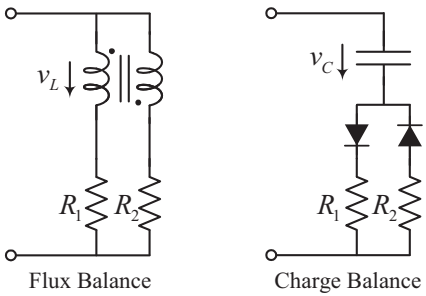

FIGURE 22.25 Inductive flux balance and capacitive charge balance with two LED strings.

by using two additional semicontrolled diodes. The coupled inductors and the capacitor within the charge balancing circuitry also act as voltage snubbers to absorb the voltage difference between two LED strings. To balance currents for more LED strings, the number of coupled inductor will increase exponentially and the number of LED strings having balanced current must be an even number [43,44]. It has been previously proposed to reduce the number of coupled inductors with diploid relation to the number of LED strings and hence eliminate the strict requirement of an even number of balancing strings. Capacitive charge balance also has a similar limitation of only balancing an even number of LED strings. However, implementation of capacitive charge balance is complicated if the number of LED strings is more than two because every two LED strings need a capacitor and some fully controlled switches to facilitate the complementary conduction paths [41]. Generally, the inductive flux balance scheme suffers from low power density and high production cost compared to the capacitive scheme. The capacitive charge balance scheme is hard to implement for multiple LED strings. As a tradeoff, a hybrid structure with coupled inductor and blocking capacitor has been used.

Unlike the balancing circuitries in Fig. 22.25, near-identical current can be achieved by using a reactance in series with the resistive LED string, provided that the reactance is sufficiently larger than the equivalent resistance of each LED string. The differences among the LED equivalent resistances can be neglected and a small current variation among LED strings can be guaranteed. However, direct driving this large reactance brings large reactive power, which will increase the VA rating and decrease the overall efficiency of the LED driver. Alternatively, the reactive loads can be driven indirectly with an opposite reactance to form a resonant tank. At the operating frequency, the impedance of the LED load can be compensated to be resistive for direct driving with minimal power stress. To supply the required current for the LED load, frequency control and/or PWM control can be used. It is well known that LED has nonlinear characteristics and the equivalent resistance varies with driving current and junction temperature. Even when driven at a constant

This book belongs to Kitab Liaison (ocd1996@gmail.com) Copyright Elsevier 2023

current, LED forward voltage still drifts nonlinearly with temperature. In some LED back lighting panels, the number of LEDs in one string is not fixed. The wide load range will widen the frequency variation and/or duty cycle variation, increase the reactive power, and make it difficult for converter optimization. Control using a hybrid of frequency and PWM has been used to prevent the wide variations of these two control variables with improved performance. However, the control is complex.

To simplify the control, the LED driver should operate as a constant current source independent of load variation. With the abundant supply of voltage source, a pure sinusoidal AC voltage-driven parallel resonant tank as shown in Fig. 22.26 can facilitate the transformation of the AC voltage source v_{IN} to an AC current source i_{Oi} to drive the load Z_i, where $i = 1$ or 2.

The frequency-domain analysis of the circuit is used for simplicity. When v_{IN} operates at f_r, it can be readily shown that the output current is a constant given by

$$i_{o1} = -v_{IN} \cdot j\omega_r C \text{ and } i_{o2} = -\frac{v_{IN}}{j\omega_r L}, \tag{22.22}$$

where $\omega_r = 2\pi f_r$. As indicated in Fig. 22.26C, i_{O1} and i_{O2} have the same magnitude and are out of phase that they are load independent. The parallel resonant circuits are inherently output short circuit proof. However, output open circuit is prohibited and an output open circuit protection circuit should be implemented.

In a practical implementation, v_{IN} is generated from a full-bridge or half-bridge switching circuit. The reactive power and circuit VA rating of the switching circuit should be minimized. Effectively, the input impedance of the reactive elements should be resistive. Now, the input impedances of these two circuits are investigated as

$$Z_{IN1} = \frac{v_{IN}}{i_{IN1}} = j\omega_r L + \frac{1}{j\omega_r C} || Z_1 = j\frac{\frac{L}{C}}{\frac{1}{j\omega_r C} + Z_1} \text{ and} \tag{22.23}$$

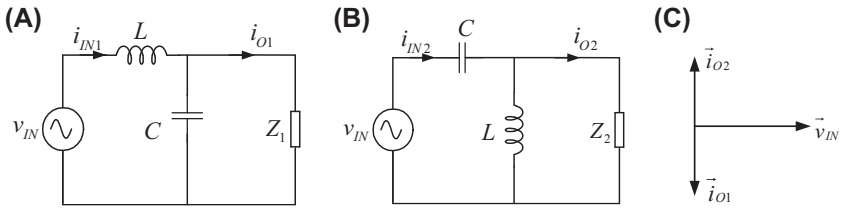

FIGURE 22.26 Two parallel resonant circuits of (A) and (B) with the corresponding vectors of input voltage and output currents in (C).

This book belongs to Kitab Liaison (ocd1996@gmail.com) Copyright Elsevier 2023

$$Z_{IN2} = \frac{v_{IN}}{i_{IN2}} = j\omega_r L + \frac{1}{j\omega_r C} || Z_2 = j\frac{\frac{L}{C}}{j\omega_r C + Z_2} \tag{22.24}$$

So, additional inductive or capacitive component is added in these two parallel resonant circuits to realize the input zero-phase-angle (ZPA), as shown in Fig. 22.27. As a result, the input impedances in (22.23) and (22.24) become

$$Z_{IN} = \frac{v_{IN}}{i_{IN1}} = \frac{v_{IN}}{i_{IN2}} = \frac{L}{RC}. \tag{22.25}$$

Here it is shown that the LCL-T and CLC-T circuits operating at f_r can output a constant AC current and can be driven with zero reactive power. Each LED string driven by one of these two circuits with the same parameters can have near-identical current. Multiple LCL-T circuits are used and connected to a common AC line to realize the current balancing for multiple LED strings. One LED string requires an LCL-T circuit, which is easy for a modular design. However, the component tolerances of the LCL-T circuit affect the accuracy of the output current for each LED string and the power density with each LED string having an LCL-T module is relatively low.

To improve the current balancing performance and power density, the existing large reactance balancing schemes can be integrated within the LCL-T and CLC-T circuits for current balancing. The basic concept is to duplicate the output inductor or capacitor with LED strings in the resonant tank, but keeping the overall reactance the same, as shown in Fig. 22.28. With a much larger reactance of L' or C' than the equivalent LED string loading resistance R_m, $m \in 1, 2, \ldots, N$, each LED string connected with the same L' or C' can equally share the constant output current i_{O1} or i_{O2}. To ensure ZPA (Zero-Phase Angle), the overall reactance should be equal to that as in Fig. 22.27, i.e.,

$$L' = NL \text{ and } C' = \frac{C}{N} \tag{22.26}$$

$$i_{L'1} = i_{L'2} = \cdots = i_{L'N} = \frac{i_{o1}}{N} \tag{22.27}$$

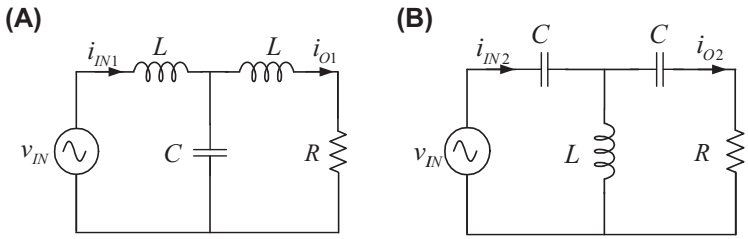

FIGURE 22.27 Circuits with constant output current and input ZPA: (A) LCL-T type and (B) CLC-T type.

This book belongs to Kitab Liaison (ocd1996@gmail.com) Copyright Elsevier 2023

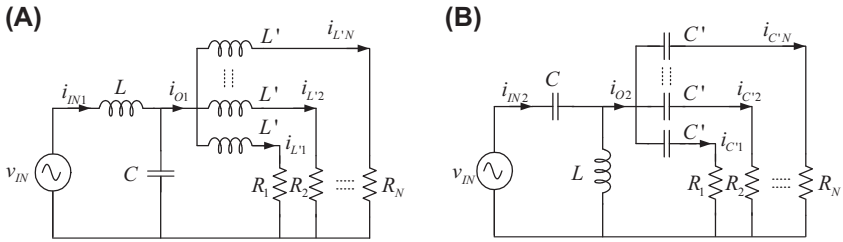

FIGURE 22.28 Improved circuits with constant output current, input ZPA, and reactive current balancing scheme. (A) LCL-T type; (B) CLC-T type.

$$i_{o2} = i_{C'1} + i_{C'2} + \cdots + i_{C'N}. \tag{22.28}$$

Here, N can be odd or even. Compared with the current balancing scheme, the improved current balancing scheme based on an LCL-T or CLC-T circuit only needs one pair of LC or CL and N balancing inductors or capacitors to realize N balanced and constant LED current, which saves $N-1$ pairs of LC or CL. The accuracy of current balance is affected only by the tolerances of N balancing inductors or capacitors.

The tolerance distribution of inductors is determined by the production process. Obviously, an LCL-T circuit with N larger inductors will decrease the power density and increase the production cost. The use of coupled inductors L' will face the original problem of inductive flux balance. Therefore, the CLC-T circuit will be adopted for the subsequent development. The tolerance of film capacitors is normally ±5%. As the total output current i_{O2} is determined by the leading CL impedances, the tolerances of balancing capacitors and load resistors will not affect the accuracy of i_{O2}. Assuming the tolerance of C'_p is α_p, where the subscript $p \in \{1, 2, \ldots, N\}$ denotes the index of LED strings, the following is obtained

$$C'_p = C'\left(1 + \alpha_p\right) \tag{22.29}$$

$$i_{C'1} \cdot \frac{1}{j\omega C'_1} = i_{C'2} \cdot \frac{1}{j\omega C'_2} = \cdots = i_{C'N} \cdot \frac{1}{j\omega C'_N} \tag{22.30}$$

$$i_{O2} = i_{C'1} + i_{C'2} + \cdots + i_{C'N}. \tag{22.31}$$

The current deviation d_p can be calculated by

$$d_p = \frac{\left| i_{C'p} - \dfrac{i_{o2}}{N} \right|}{\dfrac{i_{o2}}{N}} = \frac{\left| N\alpha_p - \sum\limits_{i=1}^{N} \alpha_i \right|}{N + \sum\limits_{i=1}^{N} \alpha_i}. \tag{22.32}$$

This book belongs to Kitab Liaison (ocd1996@gmail.com) Copyright Elsevier 2023

22.6 Reliability assessment

Power LEDs are increasingly applied for indoor and outdoor lighting applications due to their higher efficiency and longer lifetime compared to the traditional lighting sources. The lifetime of LED lamps involving LED drivers and source packages is routinely quoted as 25,000−50,000 h in the market [45−47]. These claimed lifetimes are usually released by the LED manufacturers or standard organizations. However, the customer experiences may be different and some of the LED lamps can fail in a considerable time ahead of the claimed life. The failure could be induced either by the LED drivers or by the LED source packages. The discrepancies between the claimed [48,49] lifetime and the field operation experiences are mainly due to the following reasons [50,51]:

(1) The definition of the specified lifetime of LED lamps is vague. A necessary lifetime definition should include at least four aspects: (a) operation conditions; (b) end-of-life criteria; (c) required minimum reliability at the end of the specified lifetime; (d) confidence level of the specified lifetime.

(2) The claimed lifetime is usually tested or predicted under specific temperature and current level. The environmental and operational conditions in field operation may vary within the operation specifications of the LED lamps, or even exceed the specifications for severe users.

(3) The lifetime mismatch between the LED drivers and the LED packages may occur. Sometimes, the lifetime of LED packages is misused as the claimed lifetime of the whole LED lamps.

The LED lamps could fail due to the following reasons: (1) failure of LED drivers; (2) catastrophic failure of LED package; and (3) wear out failure due to long-term lumen depreciation and color shift [52]. The level of lumen depreciation is usually used as end-of-life criteria. For color quality critical applications, the color shift level is also used as an additional criterion. Fig. 22.29A illustrates the definition of the time-to-failure L_p of an LED individual. For example, L_{70} is the time when the lumen is maintained at 70% of its initial value. With a more stringent requirement on lumen maintenance, the lifetime is shortened (e.g., L_{90} is less than L_{70} for a specific LED). Nowadays, the L_{70} or L_{85} criteria are usually used for commercial and residential outdoor applications and L_{90} is for residential indoor applications [53]. In some applications without the stringent lumen requirement, L_{50} is also used as design criteria.

It is known that the L_p lifetime varies among LED samples even with the same part number from the same manufacturer due to the variances in materials, process control, etc [54]. Therefore, the percentile lifetime B_X for a population of LEDs is of more interest with X% of failures as a result of a gradual loss of luminous flux. Fig. 22.29B shows the definition of B_X lifetime

This book belongs to Kitab Liaison (ocd1996@gmail.com) Copyright Elsevier 2023

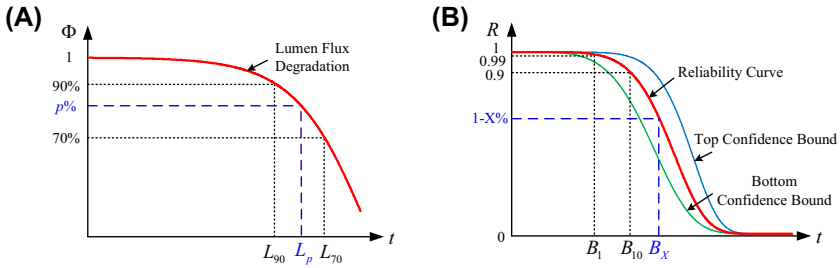

FIGURE 22.29 Two LED lifetime criteria. (A) L_p is defined as the time when $p\%$ of the initial output lumen of an LED is maintained. (B) B_X is defined as the time when $X\%$ of the LEDs have the lumen output below $p\%$ of their initial values.

based on the required minimum reliability level R $(= 1 - X\%)$ at the end of the specified lifetime. For example, B_{10} lifetime means the time when 10% of the LEDs fail (i.e., with a reliability $R = 0.9$), and B_1 lifetime means the time when 1% of the LEDs fail. Accordingly, L_pB_X lifetime refers to the time when $X\%$ of the LEDs have the lumen output below $p\%$ with respect to their initial values. The choices of p and X are application dependent. L_pB_X lifetime is more legitimate to declare the lifespan of the LED package. It is also applicable for LED drivers to evaluate the reliability level. The reliability curve can be plotted using these L_p data arranged by a specific rank method to define the cumulative percentage of the population. Among different data rank methods, the median rank is corresponding to a confidence level of 50%. It is also possible to obtain the reliability range with certain confidence bounds (CBs) as shown in Fig. 22.29B with other data rank methods. For example, the two-sided 90% CBs have the top CB and the bottom CB curve to provide 5% and 95% confidence, respectively. These statistical properties are necessary to define the lifetime of LED lamps.

Since LEDs are basically p−n junctions, the emitted lumen flux and intensity are proportional to the concentration of carriers. The concentration of carriers depends on the current density and junction temperature, which results in LED output lumen, color chromaticity, and the forward voltage characteristics also varying with these two stresses. Hence, a generally accepted Black model in Eq. (22.33) is used to describe the time to failure under different stresses

$$\text{Time to failure} = A_0 J^{-n} \frac{E_a}{e^{k_B T}}. \tag{22.33}$$

where A_0 is a constant, J is the current density, n is a scaling factor, E_a is the activation energy in unit of eV, k_B is the Boltzmann constant, and T is the absolute temperature in Kelvin.

The model in Eq. (22.33) describes the impact of current and temperature on the lifetime of LEDs. Therefore, L_p lifetime, defined as time to failure for

This book belongs to Kitab Liaison (ocd1996@gmail.com) Copyright Elsevier 2023

an LED individual, follows this model. Moreover, B_X lifetime based on a population of L_p lifetime data also follows this equation to specify the reliability of an LED population. The parameters of A_0, n, and E_a are usually obtained according to the accelerated testing data. n and E_a are material dependent, which can be assumed constant for a given type of LEDs with a given failure mechanism. Hence, Eq. (22.33) can be rearranged as

$$L_p(I_F, T_J) = A_p I_F^{-n} e^{\frac{E_a}{k_B T_J}}, \text{ and} \tag{22.34}$$

$$B_X(I_F, T_J) = A_X I_F^{-n} e^{\frac{E_a}{k_B T_J}}. \tag{22.35}$$

where I_F is the LED driving current proportional to the current density, and T_J is the junction temperature of LEDs. Although A_p and A_X are dependent on the different L_p and B_X criteria, Eqs. (22.34) and (22.35) have the same acceleration factors (AFs).

$$AF(n, E_a) = \left(\frac{I_F}{I_{F0}}\right)^{-n} e^{\frac{E_a}{k_B}\left(\frac{1}{T_J} - \frac{1}{T_{J0}}\right)}. \tag{22.36}$$

Here, (I_{F0}, T_{J0}) is the initial stress level, while (I_F, T_J) is the accelerated stress level. To solve factors of n and E_a in Eq. (22.36), the time-to-failure data from at least three different stress levels are required.

With this information, a case study based on an LM-80 test for Lumileds Luxeon Rebel LEDs will show how to establish the models of Eqs. (22.34) and (22.35), where the data in the LM-80 report are experimentally measured by the manufacturers. Weibull distribution is the most widely used to process the lifetime data in reliability engineering, which is adopted here to analyze the reliability information of LEDs. The report provides multiple accelerated life testing conditions with stress levels of IF from 0.35, 0.5, 0.7, to 1 A and air temperature T_a from 55, 85, 105, to 120°C. There are 25 samples in each test to ensure the accurateness of the results, lasting for at least 9000 h. To solve n and E_a in Eq. (22.36), at least three different stress levels of I_F and T_J are randomly chosen. Here, the degradation data and fitted curves at three stress levels of I_F and T_J with (0.35 A, 129°C), (0.7 A, 74°C), and (1 A, 112°C) are plotted by software tool ReliaSoft and shown in Fig. 22.30. The data points are provided by LM-80 report, which are measured every 1000 h for 25 samples in the accelerated testing. Then, the fitting curves are projected by an exponential extrapolation according to TM-21 procedure. With two end-of-life criteria L_{70} and L_{90}, two groups of end-of-life L_p data can be read directly in Fig. 22.30.

Each group of L_p data is then arranged in sequence and ranked by the algebraic approximation of the Median rank in Eq. (22.37)

$$\text{Median rank } r_j = \frac{j - 0.3}{N + 0.4}. \tag{22.37}$$

This book belongs to Kitab Liaison (ocd1996@gmail.com) Copyright Elsevier 2023

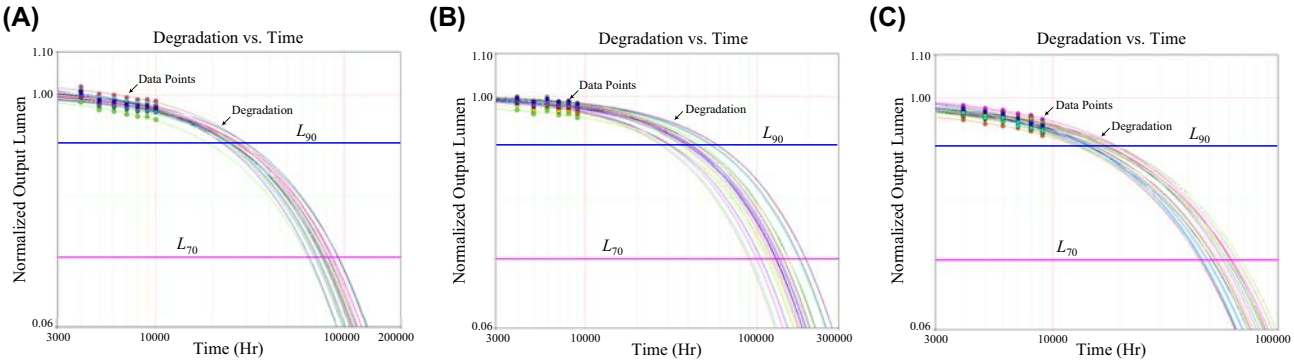

FIGURE 22.30 Lumen degradation curves with L_{70} and L_{90} lifetime criteria under different conditions. (A) $I_F = 0.35$ A, $T_a = 120°C$, $T_J = 129°C$; (B) $I_F = 0.7$ A, $T_a = 55°C$, $T_J = 74°C$; (C) $I_F = 1$ A, $T_a = 85°C$, $T_J = 112°C$.

This book belongs to Kitab Liaison (ocd1996@gmail.com)

Copyright Elsevier 2023

where j is the order number of the sequenced L_p data, $j \in [1, N]$, and N is the total number of failure (i.e., the size of L_p data). The rank r_j is actually the probability of failure for the jth LED. With these ranks and the corresponding L_p group at one stress level, the probability to failure line for this stress level can be generated via *ReliaSoft ALTA* (Accelerated Life Testing Analysis) degradation. Fig. 22.31A and B illustrates the unreliability function $F(t)$ (i.e., probability to failure function) at each operating stress level with 50% confidence level. The unreliability curves with the different confidence levels could also be plotted upon the application requirements. In Fig. 22.31A and B, most data points of the three stress groups are fitted to the Weibull distribution reasonable well. Few data points outside of the probability lines due to the measurement error or LED sample variation can be dismissed here. With the three probability lines, B_X satisfying $F(B_X) = X\%$ can be obtained. The probability lines follow the two-parameter Weibull distribution and the cumulative failure $F(t)$ is described as

$$F(t) = 1 - R(t) = 1 - e^{-\left(\frac{t}{\eta}\right)^{\beta}}. \tag{22.38}$$

where t is time, β is the shape parameter, and η is the scale parameter of characteristic life $B_{63.2}$ (i.e., the life at which 63.2% of the tested samples fail) at each stress condition. For the wear-out failure, $\beta > 1$. With the same failure mechanism, β is assumed constant under different stress levels within the physical limits. In Fig. 22.31A and B, six well-fitted curves show good consistence on β, n, and E_a, where the discrepancies are caused by the distribution variation. Besides, the probability lines under the different stress levels can be readily plotted in Fig. 22.31 with the same β, n, E_a, and different η, such as two lines at the stress level of I_F and T_J with (0.7 A, 25°C, i.e., 298 K) in Fig. 22.31A and B separately.

It is reported that many LED lamps fail in a considerable time ahead of the claimed lifetime and the failure can be induced by both sources and drivers. For example, the catastrophic failure causes the light suddenly going OFF, which mostly occurs in the LED drivers because any internal component failure inside the driver may terminate the driving current output. Meanwhile, the wear-out failure occurs on LED source packages mainly considering the lumen depreciation after a long-term operation. With different failure modes of LED source and driver, the failure of either of them will result in failure of the whole system. Thus, the reliability prediction of an LED lighting system can use the series system reliability model. Then, the reliability R and unreliability F of the system can be expressed as

$$F_{\text{sys}} = 1 - R_{\text{sys}} = 1 - R_{\text{LED}} \cdot R_{\text{dri}} = 1 - (1 - F_{\text{LED}})(1 - F_{\text{dri}}). \tag{22.39}$$

where the subscript LED, dri, and sys denote the R or F of the LED source, driver, and system, respectively. Here, R_{dri} should be the product of reliability

This book belongs to Kitab Liaison (ocd1996@gmail.com) Copyright Elsevier 2023

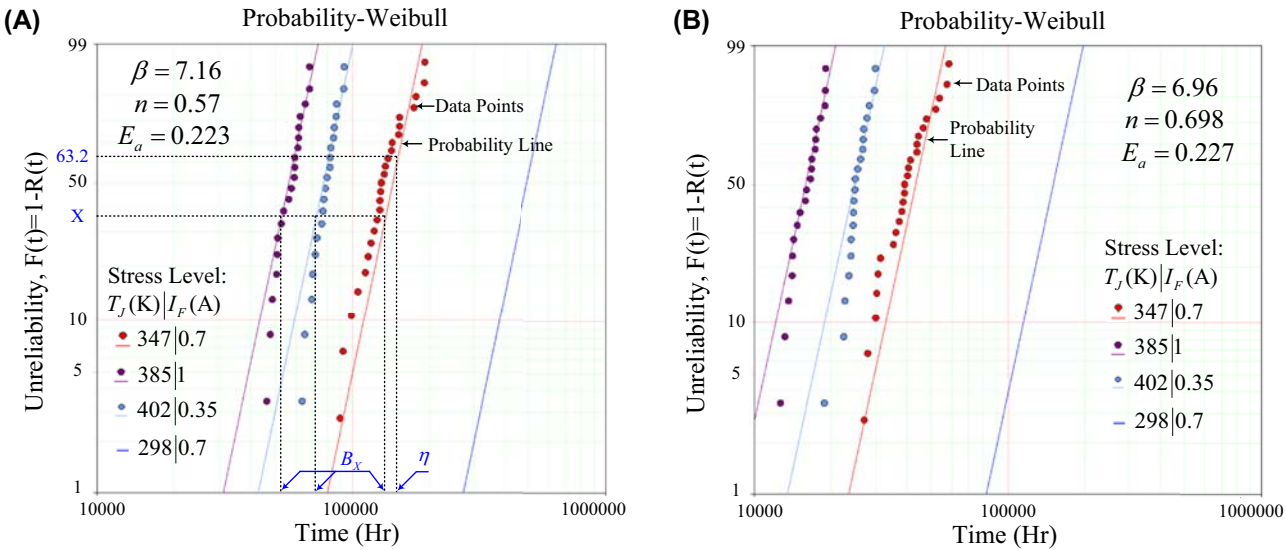

FIGURE 22.31 Unreliability curves under different stress levels. (A) With L_{70} criteria, (B) With L_{90} criteria.

This book belongs to Kitab Liaison (ocd1996@gmail.com)

Copyright Elsevier 2023

of all internal components in the driver. According to Eq. (22.39), the reliability of the whole LED system can be assessed and improved by its LED source and driver individually. Many efforts have been made to the lifetime prediction and thermal design optimization from these two parts. With the research results, lifetime discrepancies between the claimed lifetimes and the field operation experiences are mainly due to the following reasons.

(1) *Diverse End-of-Life Criteria and Vague Lifetime Definition:* For a population of LED sources or drivers, the percentile lifetime B_X is of interest with X% of failures, i.e., the time when X% of the LEDs or drivers fail. For the components with wear-out failure, e.g., LED or capacitors, the time-to-failure L_p for an individual LED or capacitor is the time when its lumen output or capacitance degrades to the end-of-life criteria, p% with respect to its initial value. A group of L_p ranked by one statistical distribution constructs the failure probability density function (pdf) and failure function $F(t)$ is the integral function of pdf over a time, as it is shown in Fig. 22.32. Because p and X are application dependent, the vague definition will cause lifetime discrepancy.

(2) *Various Field Operational Environment:* Accelerated degradation testing is well known to obtain the time-to-failure L_p of each individual sample with the wear-out failure mode. However, the degradation testing for LEDs, presented in the IES LM-80 report, is usually performed under several specific conditions, e.g., constant driving currents and several constant ambient temperatures. The testing for capacitors is also carried out in several constant environment temperatures. The environmental and operational conditions in the field operation may vary within the operation specifications of the LED lamps, or even exceed the specifications for severe users.

(3) *Lifetime Incompatibility Between LED Sources and Drivers:* In a survey of more than 5400 outdoor LED lamps, 59% of failures are related to the LED drivers. The LED driver seems to be the weakest part in the whole lighting system. Sometimes, the lifetime of LED source package is misused as the lifetime of the whole LED lamp.

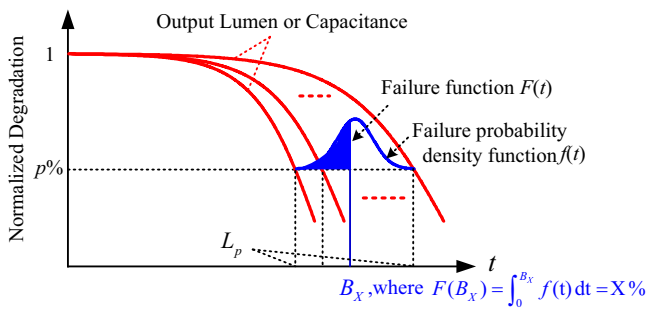

FIGURE 22.32 Definition of L_p and B_X lifetimes.

This book belongs to Kitab Liaison (ocd1996@gmail.com)
Copyright Elsevier 2023

Considering the above-mentioned issues, a lifetime model of LEDs was presented in with well-defined end-of life criteria, operating condition, required minimum reliability, and the confidence level of the specified lifetime. The LED driving current I_F and junction temperature T_J determine the lifetime and reliability of LED source packages. The junction temperature depends on the dissipated heat from LEDs, thermal design of LEDs, and the mission profile of ambient temperature. In residential indoor applications, the ambient temperature is at room temperature. In outdoor applications, the mission profile of ambient temperature is related with the weather records of the location, where the LED sources are placed. The real mission profile-based lifetime prediction of LED sources facilitates the proper design of LED heat sinks with the fulfilled lifetime target while avoiding lack of robustness or overengineering. As the lifetime prediction of LED drivers, research analyzed the lifetimes of electrolytic capacitors and power semiconductors devices, both of which are the vulnerable components having the ease to cause failure among all components in the driver. Having considered the impact of mission profile on component lifetimes, the global and local ambient temperatures are clearly defined outside and inside the LED driver. The global ambient temperature, i.e., environmental ambient temperature, follows the mission profile, while the local ambient temperatures around components are not easy to acquire due to the unknown heat distribution. Thus, an improved thermal modeling assisted by the finite-element method simulation was built in to obtain the local ambient temperatures around each component. Then, the lifetime prediction of an LED driver is more accurate.

References

[1] EN 61000-3-2, Electromagnetic Compatibility (EMC) - Part 3-2: Limits-Limits for Harmonic Current Emissions (Equipment Input Current $\leq$ 16 A Per Phase), 2006.

[2] M. Rico-Secades, A.J. Calleja, J. Ribas, E.L. Corominas, J.M. Alonso, J. Garcia, Driver for high efficiency LED based on flyback stage with current mode control for emergency lighting system, in: Proceedings of IEEE Industry Application Society Conference (IAS), October 2004, pp. 1655–1659.

[3] G. Spiazzi, S. Buso, G. Meneghesso, Analysis of a high-power-factor electronic ballast for high brightness light emitting diodes, in: Record of IEEE Power Electronics Specialists Conference (PESC), June 2005, pp. 1494–1499.

[4] M. Rico-Secades, A.J. Calleja, J. Ribas, E.L. Corominas, J.M. Alonso, J. Cardesin, J. Carcia-Garcia, Evaluation of a low-cost permanent emergency lighting system based on high-efficiency LEDs, IEEE Trans. Ind. Appl. 41 (5) (September/October 2005) 1386–1390.

[5] H.-J. Chiu, S.-J. Cheng, LED backlight driving system for large-scale LCD panels, IEEE Trans. Power Electron. 54 (5) (October 2007) 2751–2760.

[6] G. Carraro, Solving high-voltage off-line HB-LED constant current control-circuit issues, in: Proceedings of IEEE Applied Power Electronics Conference and Exposition (APEC), February 2007, pp. 1316–1318.

This book belongs to Kitab Liaison (ocd1996@gmail.com) Copyright Elsevier 2023

[7] J. Sebastíán, D.G. Lamar, M. Arias, M. Rodriguez, M.M. Hernando, A very simple control strategy for power factor correctors driving highbrightness light-emitting diodes, in: Proceedings of IEEE Applied Power Electronics Conference and Exposition (APEC), February 2008, pp. 537−543.

[8] Y. Hu, M.M. Jovanovíc, LED driver with self-adaptive drive voltage, IEEE Trans. Power Electron. 23 (6) (November 2008) 3116−3125.

[9] Z. Ye, F. Greenfield, Z. Liang, A topology study of single-phase offline AC/DC converters for high brightness white LED lighting with power factor pre-regulation and brightness dimmable, in: In Proceedings of IEEE Conference on Industrial Electronics, Control and Instrumentations (IECON), November 2008, pp. 1961−1967.

[10] Z. Ye, F. Greenfield, Z. Liang, Offline SEPIC converter to drive the high brightness white LED for lighting applications, in: Proceedings of IEEE Conference on Industrial Electronics, Control and Instrumentations (IECON), November 2008, pp. 1994−2000.

[11] S.K. Maddula, J.C. Balda, Lifetime of electrolytic capacitors in regenerative induction motor drives, in: Record of IEEE Power Electronics Specialists Conference (PESC), June 2005, pp. 153−159.

[12] H. Chung, S.Y.R. Hui, W.H. Wang, An isolated ZVS/ZCS flyback converter using the leakage inductance of the coupled inductor, IEEE Trans. Ind. Electron. 45 (4) (August 1998) 679−682.

[13] F. Richard, Light-emitting Diodes: A Guide to the Technology and its Applications, BSRIA, Bracknell, UK, 2005.

[14] C.C. Chen, C.Y. Wu, Y.M. Chen, T.F. Wu, Sequential color LED backlight driving system for LCD panels, IEEE Trans. Power Electron. 22 (3) (May 2007) 919−925.

[15] D.A. Steigerwald, J.C. Bhat, D. Collins, R.M. Fletcher, M.O. Holcomb, M.J. Ludowise, Illumination with solid state lighting technology, IEEE J. Sel. Top. Quant. Electron. 8 (2) (March/April 2002) 310−320.

[16] S. Muthu, F.J. Schuurmans, M.D. Pashley, Red, green, and blue LED based white light generation: issues and control, in: Proceedings of IEEE Industry Application Society Conference (IAS), October 2002, pp. 327−333.

[17] S. Muthu, J. Gaines, Red, green, and blue LED based white light generation: implementation challenges and control design, in: Proceedings of IEEE Industry Application Society Conference (IAS), October 2003, pp. 515−522.

[18] K. Gillessen, W. Schairer, Light Emitting Diodes: An Introduction, Prentice Hall, New Jersey, NJ, 1987.

[19] C. DiLouie, Advanced Lighting Controls: Energy Savings, Productivity, Technology and Applications, The Fairmont Press, Lilburn, GA, 2005.

[20] H. Wei, I. Batarseh, G. Zhu, P. Kornetzky, A single-switch AC-DC converter with power factor correction, IEEE Trans. Power Electron. 15 (3) (May 2000) 421−430.

[21] K. Zhou, J.G. Zhang, G. Meneghesso, Quasi-active power factor correction circuit for HB LED driver, IEEE Trans. Power Electron. 23 (3) (May 2008) 1410−1415.

[22] D. Fu, F.C. Lee, M. Xu, A novel driving scheme for synchronous rectifiers in LLC resonant converters, IEEE Trans. Power Electron. 24 (5) (May 2009) 1321−1329.

[23] Q. Hu, R. Zane, Minimizing required energy storage in off-line LED drivers based on series-input converter modules, IEEE Trans. Power Electron. 26 (10) (October 2011) 2887−2895.

[24] K.I. Hwu, Y.T. Yau, Applying one-comparator counter-based sampling to current sharing control of multichannel LED strings, IEEE Trans. Ind. Appl. 47 (6) (November/December 2011) 2413−2421.

This book belongs to Kitab Liaison (ocd1996@gmail.com) Copyright Elsevier 2023

[25] D. Liu, A. Hu, G. Wang, W. Hu, Current sharing schemes for multiphase interleaved DC/DC converter with FPGA implementation, in: Proc. IEEE Int. Conf. Electr. Control Eng., 2010, pp. 3512−3515.
[26] X. Qu, S.C. Wong, C.K. Tse, Non-cascading structure for electronic ballast design for multiple LED lamps with independent brightness control, IEEE Trans. Power Electron. 25 (2) (February 2010) 331−340.
[27] W. Chen, S.Y.R. Hui, A dimmable light-emitting diode driver with mag-amp postregulators for multistring applications, IEEE Trans. Power Electron. 26 (6) (June 2011) 1714−1722.
[28] J. Zhang, L. Xu, X. Wu, Z. Qian, A precise passive current balancing method for multi-output LED drivers, IEEE Trans. Power Electron. 26 (8) (August 2011) 2149−2159.
[29] K.I. Hwu, S.C. Chou, A simple current-balancing converter for LED lighting, in: Proc. IEEE Appl. Power Electron. Conf., 2009, pp. 587−590.
[30] X. Wu, Z. Wang, J. Zhang, Design considerations for dual-output quasi-resonant flyback LED driver with current-sharing transformer, IEEE Trans. Power Electron. 28 (10) (October 2013) 4820−4830.
[31] K.H. Jung, J.W. Yoo, C.Y. Park, A design of current balancing circuit for parallel connected LED strings using balancing transformers, in: Proc. IEEE Int. Conf. Power Electron.- ECCE Asia, 2011, pp. 528−535.
[32] R. Zhang, H.S.H. Chung, Daisy-chain transformer structure for current-balancing multiple LED strings, in: Proc. IEEE Energy Convers. Congr. Expo., 2013, pp. 3118−3125.
[33] S.N. Li, W.X. Zhong, W. Chen, S.Y.R. Hui, Novel self-configurable current-mirror techniques for reducing current imbalance in parallel lightemitting diode(LED) strings, IEEE Trans. Power Electron. 27 (4) (April 2012) 2153−2162.
[34] H.J. Chiu, Y.K. Lo, J.T. Chen, S.J. Cheng, C.Y. Lin, S.C. Mou, A high-efficiency dimmable LED driver for low-power lighting applications, IEEE Trans. Ind. Electron. 57 (2) (February 2010) 735−743.
[35] S.M. Baddela, D.S. Zinger, Parallel connected LEDs operated at high frequency to improve current sharing, in: Proc. IEEE Ind. Appl. Conf., 2004, pp. 1677−1681.
[36] S. Choi, T. Kim, Symmetric current-balancing circuit for LED backlight with dimming, IEEE Trans. Ind. Electron. 59 (4) (April 2012) 1698−1706.
[37] J. Zhang, J. Wang, X. Wu, A capacitor-isolated LED driver with inherent current balance capability, IEEE Trans. Ind. Electron. 59 (4) (April 2012) 1708−1716.
[38] H. Wu, S. Ji, F.C. Lee, X. Wu, Multi-channel constant current (MC3) LLC resonant LED driver, in: Proc. IEEE Energy Convers. Congr. Expo., 2011, pp. 2568−2575.
[39] K.H. Loo, Y.M. Lai, C.K. Tse, Design and analysis of LCC resonant network for quasi-lossless current balancing in multistring AC-LED array, IEEE Trans. Power Electron. 28 (2) (February 2013) 1047−1059.
[40] X. Wu, J. Zhang, Z. Qian, A simple two-channel LED driver with automatic precise current sharing, IEEE Trans. Ind. Electron. 58 (10) (October 2011) 4783−4788.
[41] S. Zhang, Q. Chen, J. Sun, M. Xu, Y. Qiu, High accuracy passive current balancing schemes for large-scale LED backlight system, in: Proc. IEEE Appl. Power Electron. Conf. Expo., 2011, pp. 723−727.
[42] X. Qu, S.C. Wong, C.K. Tse, A current balancing scheme with high luminous efficacy for high-power LED lighting, IEEE Trans. Power Electron. 29 (6) (June 2014) 2649−2654.
[43] Y. Hu, M.M. Jovanovic, A new current-balancing method for paralleled LED strings, in: Proc. IEEE Appl. Power Electron. Conf. Expo., 2011, pp. 705−712.
[44] R. Zhang, H.S.H. Chung, Use of daisy-chained transformers for current-balancing multiple LED strings, IEEE Trans. Power Electron. 29 (3) (March 2014) 1418−1433.

This book belongs to Kitab Liaison (ocd1996@gmail.com) Copyright Elsevier 2023

[45] Cree LED Lamps, 2016 [Online]. Available: http://creebulb.com/ products.
[46] GE LED Lamps, 2016 [Online]. Available: http://catalog.gelighting.com/ lamp/ led-lamps/.
[47] Philips Lighting, 2016 [Online]. Available: http://www.lighting.philips.com/main/prof.
[48] Daily Mail Reporter, The Great LED Lightbulb Rip-Off: One in Four Expensive 'Long-Life' Bulbs Doesn't Last Anything Like as Long as the Makers Claim, 2014 [Online]. Available: http://www.dailymail.co.uk/news/article-2546363/.
[49] W.D. van Driel, X.J. Fan, Solid State Lighting Reliability: Components to Systems, Springer, New York, NY, USA, 2013.
[50] H. Wang, et al., Transitioning to physics-of-failure as a reliability driver in power electronics, IEEE J. Emerg. Sel. Top Power Electron. 2 (1) (March 2014) 97−114.
[51] H.S.H. Chung, H. Wang, F. Blaabjerg, M. Pecht, Reliability of power electronic converter systems, Institution of Engineering and Technology, 2015, ISBN 978-1-84919-901-8.
[52] N. Narendran, Y. Gu, Life of LED-based white light sources, IEEE/OSA J. Disp. Technol. 1 (1) (September 2005) 167−171.
[53] U.S. Department of Energy, Lifetime of White LEDs, 2015 [Online]. Available: http://apps1.eere.energy.gov/buildings/publications/pdfs /ssl/ lifetime_white_leds.pdf.
[54] M.S. Shur, A. Zukauskas, Solid-state lighting: toward superior illumination, Proc. IEEE 93 (10) (October 2005) 1691−1703.

This book belongs to Kitab Liaison (ocd1996@gmail.com) Copyright Elsevier 2023

Index

Note: 'Page numbers followed by "*f*" indicate figures and "*t*" indicate tables.'

A

Active current sharing schemes, 673–677
Active damping (AD), 221–222, 316–318, 341
  under converter current feedback, 248–251
  experimental validation of, 357–363
  using filter capacitor current feedback, 244–246
  under grid current feedback, 246–248
  for high switching frequency CSCs, 348–363
    capacitor-current feedback, 353
    capacitor-voltage feedback, 351–352
    inductor-current feedback, 354–355
    time delay effect, 355–357
    virtual impedance analysis, 350–357
Active front end power converter (AFE power converter), 116
Active power, 544–545
  control requirement, 454–455
  tracking error, 17
Active power filters (APFs), 149
Adaptive boundary-layer sliding mode control, 85
Adaptive control in power electronic systems, 4, 24, 125
  experimental results, 142–144
  indirect adaptive predictive control, 135–136
  model reference direct adaptive control of UPS, 136–144
  system dynamics on UPS system, 127–128
  system identification, 128–134
    parameters identification, 129
    state identification, 130–134
Adaptive inertia for grid-connected VSGs, 549–552
  experimental results, 555–557
  simulation results, 553–555
  VSG principle, 550–551
Adaptive observer, 126–127, 136
Adaptive sliding mode control, 85–86
Adaptive super-twisting, 91
Advanced control methods of power electronic systems, 1, 4, 5f
  linear controller implementation and analysis, 5–10
  nonlinear controller implementation and analysis, 10–26
Ambient temperature, 685
Artificial intelligence (AI), 4, 26
Artificial neural network (ANN), 150
  for asymmetric selective harmonic current mitigation-PWM, 152–157
Asymmetric selective harmonic current mitigation-PWM (ASHCM-PWM), 150–151
  ANN for, 152–157
Asymmetrical carrier interleaving, 419
Asymmetrical grid fault control, 593–602. *See also* Symmetrical grid fault control
  control gains, 599–601
  current-reference generation methods, 596–597
  grid synchronization during asymmetrical faults, 595–596
  phase current magnitude calculation, 597–599
  verification of, 601–602
Asymmetrical grid faults, control strategies during, 578–582
Australian Electricity Market Operator, 527
Automatic voltage regulator (AVR), 550
Average current mode (ACM), 654
Average value reduction-based SVM (AVR-based SVM), 387–388

B

Backstepping (BS), 3, 15–19
Balanced positive-sequence control (BPSC), 255

This book belongs to Kitab Liaison (ocd1996@gmail.com)
Copyright Elsevier 2023

Balanced three-phase systems, modeling methods in, 222–226
Band-pass filter (BPF), 279
Bi-trilogical SPWM (BTSPWM), 375
Black box method, 172–174
Boost inductor. *See* Line filter inductor
Boundary-layer sliding mode control, 85
Brayton–Moser's Mixed Potential method, 170–171, 182

C

Capacitor-current feedback, 353, 361–362
Capacitor-voltage feedback, 351–352, 358–360
Carbon-neutral electrical power systems, 199
Carrier interleaving, 404–405
Carrier-shifted SPWM-based methods, 394–397
Cascaded H-bridge active power filter configuration, 151
Cascaded H-bridge converter (CHB converter), 150
Central inverters, 500
Circulating current (CC), 367–368
  control, 410–418
    current sharing schemes, 411
    droop control scheme, 412–415
    zero vector dwell time control, 415–418
  modeling, 405–409
    parallel converters, 405–409
  suppression, 430–442
    common-mode inductor, 437–439
    coupled inductor, 433–437
    galvanic isolation, 432
    integrated inductor, 440–442
Clark transformation, 37, 273
Classic SMC, 79, 82–85
Closed-loop stability of observer, 134
Color control with power converter, 654–658
Common-mode inductor (CM inductor), 404–405, 437–439
Common-mode voltage (CMV), 367–368
  reduction methods, 387–399
    SVM-based methods, 387–394
Communication links, 205
Complex coefficient filter–based PLLs (CCF-PLLs), 280–282
Component connection method (CCM), 170
Constant power generation (CPG), 447
  control strategy, 455–462
  current-limiting control, 458–460
  direct power control, 457–458
  perturb and observe–based control, 460–462
Continuous control set MPC (CCS-MPC), 102
Continuous current mode (CCM), 660
Continuous-time averaged model of VSC converter, 224–225
Control
  gains, 599–601
  input calculation, 82
  objectives, 1–2, 80
  of power converter–interfaced renewables, 527–529
  strategies
    during asymmetrical grid faults, 578–582
    during symmetrical grid faults, 573–578
  systems, 125
  of type III wind turbine during grid faults, 568–582
  of type IV wind turbine during grid faults, 582–602
  under unbalanced grid voltages, 251–256
Controller, 71f, 205, 323
Conventional repetitive controller (CRC), 7
Conventional synchronous reference frame PLL, 271–275
Converter control, 583–584
Converter current control, 584–585
Converter current feedback (CCF), 240–241
Converter-side current control
  passivity-based stability analysis for, 309–310, 312–313
  small-signal modeling, 307–308
Coordinated attacks, 209, 214
Coupled inductor (CI), 404–405, 433–437
Current control. *See also* Outer-loop control
  passivity-based stability analysis, 309–313
  robustness enhancement, 313–318
  small-signal modeling, 305–308
  stability and robustness improvement of, 304–318
Current controllers, 506–507
Current sharing schemes
  LED, 669–677
    active current sharing schemes, 673–677
    passive current sharing schemes, 669–673
Current source converters (CSCs), 339, 367. *See also* Voltage source converters (VSCs)

This book belongs to Kitab Liaison (ocd1996@gmail.com) Copyright Elsevier 2023

2-CSC parallel CSC system experiment, 397–399
active damping, 348–363
applications, 368–373
challenges of high switching frequency, 339–341
CMV reduction methods, 387–399
DC current balance, 387–399
parallel CSC system, 373–381
and circuit analysis, 381–387
and modulation strategies, 373–381
single-loop DC-link current control, 342–348
Current source inverter (CSI), 367
Current source rectifier (CSR), 367
Current-limiting control, 458–460
Current-reference generation methods, 596–597
Current–voltage characteristic of LEDs (I–V characteristic of LEDs), 651–652
Cyber attack, 199–200
detection mechanisms in power electronic systems, 205–212
mitigation mechanisms in power electronic systems, 205–212
test cases, 212–217
Cyber physical architecture of power electronic converters, 200–203
cyber stage, 202–203
physical stage, 201–202
Cyber security, 203–204
Cyber threats, 203–204

D

Damping control, 250
DC current balance, 387–399
DC link, 339–340
DC microgrid model, 54–57
robust small-signal stability, 59–60
DC-link circuit of parallel CSC, 385–387
DC-link voltage control (DVC), 303–304
design, 334–336
dynamic impact of, 330–332
DC-link voltage controller, 586–587
DC/DC buck converter model, 54
Decentralized control, 203
Decoupled CCF-PLL (DCCF-PLL), 280–281
Decoupled Double Synchronous Reference Frame PLL (DDSRF-PLL), 284, 593
Delayed signal cancellation–based PLLs (DSC-PLLs), 282–283
Denial of service attack (DoS attack), 199–200, 203–204, 208–209
Differential mode (DM), 437
Diffusion voltage, 650–651
Direct adaptive control (DAC), 125–126
Direct duty-ratio PWM (DDPWM), 375, 377–379
Direct model predictive current control (DMPCC), 108–109, 118–119
Direct power control (DPC), 11–12, 36, 457–458
Discontinuous current mode (DCM), 660
Discontinuous pulse width modulation (DPWM), 418
Distributed energy resources (DERs), 472, 541
Disturbance estimation based on an adaptive observer, 132–134
Double-fed induction generator (DFIG), 115–116, 561
Double-frequency and amplitude compensation–based P-PLLs, 290–291
Droop control
in grid-forming power converters, 510–516
scheme, 412–415
Dual of mass in angular motion. *See* Moment of inertia
Dual second-order generalized integrator –phase-locked loop (DSOGI-PLL), 253–254, 279, 593
Dual SOGI (DSOGI), 505–506
Duty cycle, 416–417
Dynamic performance, 96

E

Eigenvalue method, 170, 174–177, 184–186
component modeling and system integration, 174–176
Eigenvalue stability analysis, 176–177
system modeling, 184–186
verification, 177
Electric vehicles (EVs), 199, 367
Electrical drives, 101–102
Electrical torque, 544
Electromotive force (EMF), 432
Energy storage systems (ESSs), 39, 199, 534
Equivalent electric circuit, 434–436
Equivalent series resistor (ESR), 323
Euler-forward method, 107

This book belongs to Kitab Liaison (ocd1996@gmail.com)
Copyright Elsevier 2023

Explicit model predictive control (EMPC), 102
Exponentially modulated periodic signal (EMP signal), 232

F

False data injection attacks (FDIAs), 203–204
Fault ride-through, 568
Fault right through capability, 534–536
Feedback linearization (FBL), 3, 23
Finite control set MPC (FCS-MPC), 102, 105f
  for PMSM drives, 108–109
  for three-level PMSG systems, 119–121
Flexible positive-and negative-sequence control (FPNSC), 596–597
Fourier coefficients of switching functions, 229–230
Fractional open circuit voltage MPPT, 452–453
Frequency-fixed SOGI-PLLs (FFSOGI-PLLs), 294
Frequency-locked loop (FLLs), 270, 505–506
  stationary reference frame, 505–506
Fuzzy control method, 542

G

Galvanic isolation, 432
Generalized averaged model (GAM), 221, 227–231
Generalized integrator–based PLLs (GI-PLLs), 293–294
Generalized predictive control (GPC), 102
Generalized SSA model method, 172–173
Genetic algorithm–based Lyapunov function searching method, 170–171
Global Wind Energy Council (GWEC), 609
Green energy transition
  control of power converter–interfaced renewables, 527–529
  evolution of, 525–529
  low-inertia grid challenges, 525–527
Grid codes, 472, 488–489
  requirements on low-voltage ride-through, 562–566
Grid converter for wind turbine systems, 501–502
Grid current feedback (GCF), 240–241
Grid faults, 561–562
Grid forming controllers, 528–529
Grid synchronization during asymmetrical faults, 595–596
Grid-connected converter, 564
Grid-connected PV systems, 453–454
Grid-connected voltage source inverter, 38–40
Grid-following controllers, 528–529
Grid-following power converters, 502–507
  current controllers, 506–507
  synchronization strategies, 503–506
Grid-following unit, 528–529
Grid-forming power converters, 508–518
  control schemes for, 509–510
  droop control in, 510–516
  synchronous power controller, 516–518
Grid-forming VSCs, 204–205, 206f
Grid-side converter (GSC), 116, 561
  current, 623
  modeling and control of, 583–587
Grid-side current control, small-signal modeling, 308

H

H_∞ control, 25
Harmonic balance principle, 232–233
Harmonic state space modeling method (HSS modeling method), 172–173, 221, 232–236
High-power CSC, 367
High-switching frequency modulation techniques, 149–150
High-voltage DC (HVDC), 199, 525
  systems, 367
  transmission, 169
Hysteresis control, 3, 11

I

Immersion and invariance theory (I&I theory), 125–126
Impedance mismatch, 409
Impedance-based method, 170, 177–179, 187–188
  impedance modeling, 177–178, 187–188
  network partitioning, 178
  stability analysis, 178–179
  verification of analysis, 179
Impedance-based stability analysis
  system control of *LCL*-filtered VSCs in $\alpha\beta$ frame and dq frame, 258–262
  under weak grid conditions, 256–265

This book belongs to Kitab Liaison (ocd1996@gmail.com) Copyright Elsevier 2023

Indirect adaptive control (IAC), 125–126
Indirect adaptive predictive control, 135–136
  experimental results, 136
Inductive grid, 511–512
Inductor-current feedback, 354–355, 362–363
Inertia, 542–547
  challenges of power electronic–based power systems, 547–548
  emulating methods in, 548t
Infinite impulse response (IIR), 288
Inherent damping (ID), 242
Inner current control loop, 142
Input–output linearization method (IOL method), 35–36
Instantaneous power theory, 11–12
Integral sliding mode control, 87
Integrated inductor, 440–442
Interleaved SVM, 387–389
Inverse park transformation–based PLL (IPT-PLL), 292
Islanded AC MG, MPC for robust and fast operation of, 112–113

J

Jensen model, 611
Junction temperature, 651–652

K

Kalman filter, 131–132
KERAS software, 157
Kinetic energy, 531
Kirchhoff's laws, 78–79

L

Large-signal analysis, 170–171
Large-signal stability analysis methods, 180–183
  case studies with practical examples, 192–193
  Lyapunov-based analytical methods, 180–183
  time-domain simulations, 180
LCL filters
  alternative current control of VSCs with, 238–256
  system control of *LCL*-filtered VSCs in $\alpha\beta$ frame and dq frame, 258–262
  voltage source converters with, 222–238
Levelized production cost (LPC), 614
  layout optimization for minimum, 641–642
  minimization, 625–636
Lifetime of LED, 678–685
Light-emitting diode (LED), 646–647
  characteristics and drivers, 650–654
  characteristics of drivers for, 653–654
  classical design of, 661f
  color control with power converter, 654–658
  current sharing schemes, 669–677
  efficiency and lifetime improvement, 658–668
  lamp characteristics, 648t–649t
  lamps, 647f
  optoelectrical properties of, 651–653
  reliability assessment, 678–685
Line filter inductor, 440
Linear control methods, 35
Linear controllers, 2
  application and design, 2–3
  implementation and analysis, 5–10
Linear matrix inequality (LMI), 181
Linear quadratic estimation technique. *See* Kalman filter
Linear quadratic Gaussian (LQG), 35
Linear quadratic regulator (LQR), 2, 9–10, 35
Linear time-invariant system (LTI system), 42, 221
Linear time-periodic system (LTP system), 221
Linearization techniques, 150
Liquid-crystal display (LCD), 646–647
Load-communicated converter (LCC), 367
Lookup table–based direct power control (LUT-DPC), 11–14
Loop controller, 270
Loop filter (LF), 270
Loop-shaping controller, 25
Loss minimization, 622–625
Low pass filter (LPF), 280
  low pass filter–based P-PLLs, 288
Low-inertia grid challenges, 524–527
Low-voltage ride-through (LVRT), 454, 472, 475–488, 562–563
  capability, 564
  on power-voltage curve, 482–488
  requirements, 565f
  RPI strategies, 488–495
  single-phase PQ theory, 477–482
Luenberger observer, 130–131

This book belongs to Kitab Liaison (ocd1996@gmail.com) Copyright Elsevier 2023

Luminous efficacy, 653
Luminous flux emission, 652–653
Lur'e type model, 51–57
  DC microgrid model, 54–57
  DC/DC buck converter model, 54
Lyapunov function, 3, 18, 21, 46, 85–86, 134
Lyapunov stability theory, 140
Lyapunov-based analytical methods, 170–171, 180–183
  Brayton–Moser's mixed potential, 182
  optimal Lyapunov function generation, 183
  Takagi–Sugeno multimodel method, 181–182

M

Machine learning, 150
  ANN for asymmetric selective harmonic current mitigation-PWM, 152–157
  cascaded H-bridge active power filter configuration, 151
  simulation and experimental results, 157–163
Man-in-the-middle attack (MITM attack), 203–204
Mathematical approaches, 150
MATLAB/Simulink, 47
Maximum power point tracking (MPPT), 447, 474–475, 613–614
  algorithm, 450–453
  fractional open circuit voltage, 452–453
  P&O MPPT method, 450–452
  single and global MPPT, 612–614
Maximum torque per Ampere law (MTPA law), 108–109
Medium-voltage drives (MV drives), 367
Microgrids (MGs), 199
  dynamic stabilization of DC MG using MPC, 113
  dynamics and predictive model of VSC-based MG, 111–112
  MPC for, 110–115
  passivity-based control design in, 63–65
  performance evaluation with experimental results, 113–115
  for robust and fast operation of islanded AC MG, 112–113
Microinverter, 500–501
Model predictive control (MPC), 3, 14–15, 101, 126–127
  classification of, 104t
  for microgrids, 110–115
  performance evaluations of MPC with simulations, 109
  for permanent-magnet synchronous motor drives, 102–110
  for renewable energy applications, 115–121
Model reference adaptive control (MRAC), 125–126
Model reference adaptive system (MRAS), 24
Modified mixer PD-Based P-PLL (MMPD-P-PLL), 291
Modulator mismatch, 407–409
Module-based approach, 170
Moment of inertia, 543
Moving average filter (MAF), 277
  moving average filter–based P-PLLs, 288–289
  moving average filter–based PLLs, 277
Multilevel SVM, 389–394
Multiple Complex Coefficient Filter–based PLL (MCCF-PLL), 593
Multiple SRF filter–based PLLs (MSRF-PLLs), 283–284
Multiple-input and multiple-output model (MIMO model), 304
  MIMO-based stability analysis, 326–332
Multistring inverters, 500

N

Nearest three vectors (NTVs), 428–429
  modulation, 428–430
Network partitioning, 178
Neural network (NN), 26
Noise impact reduction, 614–618
Noncoordinated attack, 214
Nonlinear controller implementation and analysis, 10–26
  adaptive control, 24
  artificial intelligence, 26
  backstepping control, 15–19
  feedback linearization, 23
  H_∞ control, 25
  hysteresis control, 11
  lookup table–based direct power control, 11–14
  model predictive control, 14–15
  passivity control, 23–24
  sliding mode control, 19–23
Nonradiative recombination, 651
Nonsynchronous generators (NSGs), 523
  penetration level, 533

This book belongs to Kitab Liaison (ocd1996@gmail.com) Copyright Elsevier 2023

Normalized weighted total harmonic distortion (NWTHD), 421
Notch filter (NF), 246, 278
  notch filter—based P-PLLs, 289—290
  notch filter—based PLLs, 278
Novel optimized power dispatch strategy (NOPDS), 618

O

Observability condition, 130—131
Optical flux, 652
Optimal Lyapunov function generation, 183
Optimal switching sequence MPC (OSS-MPC), 102
Optimal switching vector MPC (OSV-MPC), 102
Optoelectrical properties of LEDs, 651—653
Outer voltage control loop, 137—141
Outer-loop control, 319—336. *See also* Current control
  MIMO-based stability analysis, 326—332
  robustness enhancement, 332—336
  small-signal modeling, 319—326

P

Parallel converters
  with common DC bus, 405—409
  with separate DC bus, 409
Parallel CSC system
  and circuit analysis, 381—387
  and modulation strategies, 373—381
Parallel interleaved converters, 419
Parallel operation of VSCs, 405
  circulating current control, 410—418
  circulating current modeling, 405—409
    parallel converters, 405—409
  circulating current suppression, 430—442
  harmonic performance, 419—430
    NTVs modulation, 428—430
    parallel interleaved converters, 419
    symmetrically interleaved converters, 419—425
    symmetrically interleaved VSCs, 425—427
Parameters identification, 129
Park transformation, 37, 225—226, 273
Participation factor analysis, 176, 186
Particle Swarm Optimization algorithm (PSO algorithm), 622
Passive current sharing schemes, 669—673
Passive damping (PD), 221—222, 243—244. *See also* Active damping (AD)
Passivity control, 23—24
Passivity-based control (PBC), 36. *See also* Model predictive control (MPC)
  design, 61—70
  in microgrid, 63—65
  port-controlled Hamiltonian system, 62—63
  in STATCOM, 67—70
Passivity-based stability analysis, 309—313
  for converter-side current control, 309—310, 312—313
Perfect-matching of reference model and closed-loop system, 140
Permanent-magnet synchronous generator (PMSG), 115, 621
  modeling of PMSG wind turbine system with back-to-back power converter, 116—118
Permanent-magnet synchronous motor (PMSM), 102
  FCS-MPC for, 108—109
  model, 106—108
  performance evaluations of MPC with simulations, 109
Perturb and observe MPPT (P&O MPPT), 448, 450—452
Perturb and observe—based control, 460—462
Phase current magnitude calculation, 597—599
Phase detection (PD), 270
Phase disposition (PD), 430
Phase shift—pulse width modulation (PS-PWM), 149—150
Phase-leg averaging technique, 416—417
Phase-locked loops (PLLs), 269, 303—304, 503, 583—584
  control and design, 270—271
  design, 334
  dynamic impact of, 326—330
  freezing method, 591—593
  for grid synchronization, 585—586
  linearization of, 320
  single-phase, 287—298
  small-signal model of VSC with, 321—322
  SRF-PLL, 504—505
  three-phase, 271—287
Phasor measurement units (PMUs), 203
"Phasor" concept, 37
Photovoltaics (PV), 169, 199, 367, 525

This book belongs to Kitab Liaison (ocd1996@gmail.com) Copyright Elsevier 2023

Photovoltaics (PV) (*Continued*)
active power control requirement, 454–455
advanced control functionality, 453–455
constant power generation control strategy, 455–467
grid code, 453–454
inverter control, 448–453
control structure, 448–450
MPPT algorithm, 450–453
power, 499
structures, 500–501
system, 447
PLECS, 47
p–n junction, 650–651, 650f
Point of common coupling (PCC), 78–79, 127–128, 149, 201–202, 256–258, 509, 562, 618
Pole placement control, 2, 9
Port-controlled Hamiltonian system (PCH system), 61–63
Power conversion system (PCS), 403–404
Power converters, 1–2, 523–525
color control with, 654–658
current control, 304–318
modeling, 172–174
black box method, 173–174
generalized SSA model method, 172–173
HSS modeling method, 173
SSA approach, 172
outer-loop control, 319–336
power converter–interfaced renewable, control of, 527–529
Power electronic converters, 77, 169
Power electronic systems, 35
Power electronic–based power systems, inertia challenges of, 547–548
Power factor (PF), 653
Power factor correction (PFC), 653–654
Power synchronization control (PSC), 530
Power system stability, 169–170, 536–537
Power-based PLLs (P-PLLs), 287
Proportional and integral (PI), 35, 477–478
controller, 2
implementation, 5–6
Proportional and resonant controller (PR controller), 2
implementation, 6–7
Proportional integral derivative controller (PID controller), 277
Proportional integrator (PI), 418
Proportional resonant (PR), 477–478
controllers, 507
current controller, 584–585
Pulse width modulation (PWM), 307, 367, 403, 656, 659–660
CSC-based medium-voltage drives, 370–371

Q

Quadrature signal generation–based PLLs (QSG-PLLs), 287
Quarter-wave symmetric modulation techniques, 150–151

R

Radiative combination, 651
Radical flux. *See* Optical flux
Rate of change of frequency (RoCoF), 525, 541
Reachability condition in sliding mode control, 81–82
Reaching law, 81–82
Reaching phase, 84
Reactive current support curve, 564–566
Reactive power injection (RPI), 473–474
constant active current control strategy, 492–493
constant average active power control strategy, 491–492
constant peak current control, 494–495
strategies under LVRT, 488–495
Receding horizon control. *See* Model predictive control (MPC)
Rectangular window filter, 288
Recursive least-square estimator (RLS estimator), 125–126, 129
Regular method, 618–622
Reliability assessment, 678–685
Renewable energy sources (RESs), 35, 199, 523
Renewables, 524
Repetitive controller (RC), 2
implementation, 7–9
Repetitive regulator/controller inside SRF-PLL control loop (RR-PLL), 284
Resistive grid, 513
Resonance damping technique, 242–251
Resonant controller, 2
Robust controller design, 42–49
simulation results, 47–49
tracking controller, 44–45

This book belongs to Kitab Liaison (ocd1996@gmail.com) Copyright Elsevier 2023

voltage-modulated direct power control, 43–44
Robust small-signal stabilization control design, 49–60
Lur'e type model, 51–57
robust small-signal stability analysis problem, 57–58
robust stability analysis method, 58
robust stabilization control design, 58–60
Robustness, 35
current control, 313–318
active damping, 316–318
design of passive filters, 315
time delay reduction, 314
outer-loop control, 332–336
Rotational inertia, 543
Rotor-side converter (RSC), 561

S

Safe Operation Area (SOA), 574
Second-order generalized integrator (SOGI), 253–254, 505–506
Second-order generalized integrator–based PLL (SOGI-PLL), 279–280
Second-Order Lead Compensators (SOLC), 285
Second-order sliding mode control (SOSMC), 77–78, 89–91
adaptive super-twisting, 91
super-twisting, 90–91
twisting SMC, 89–90
Selective harmonic current mitigation-PWM (SHCM-PWM), 149–150
Selective harmonic elimination (SHE), 368, 376–377
Selective harmonic elimination-PWM (SHE-PWM), 149–150
Selective harmonic mitigation-PWM (SHM-PWM), 149–150
Sensitivity analysis, 176–177
Sensors, 205
Short circuit ratio (SCR), 303
Silicon-controlled rectifier (SCR), 367
Single-input and single-output (SISO), 303–304
Single-loop DC-link current control, 342–348
experimental validation, 346–348
small-signal modeling, 342–343
stable region of, 343–345
Single-phase PLLs, 287–298
double-frequency and amplitude compensation–based P-PLLs, 290–291
generalized integrator–based PLLs, 293–294
inverse park transformation–based PLL, 292
low pass filter–based P-PLLs, 288
modified mixer PD-Based P-PLL, 291
moving average filter–based P-PLLs, 288–289
notch filter–based P-PLLs, 289–290
performance comparison and recommendation, 296–298
standard P-PLLs, 287–288
synthesis circuit PLLs, 295
transfer delayed–based PLLs, 291–292
Single-phase PV systems, 475
LVRT operation, 475–488
RPI strategies, 488–495
Sinusoidal signal integrator PLL (SSI-PLL), 278–279
Six-step direct PWM (SS-DPWM), 375
Sliding mode control (SMC), 3, 19–23, 36, 77, 78f, 79–82
adaptive sliding mode control, 85–86
boundary-layer sliding mode control, 85
classical sliding mode control, 82–84
comparison of different SMCs, 91
control input calculation, 82
experimental results, 93–96
integral sliding mode control, 87
reachability condition in, 81–82
second-order sliding mode control, 89–91
system dynamics of voltage source inverter, 78–79
terminal sliding mode control, 87–89
Sliding phase, 84
Sliding variable, 90
Small-signal modeling, 305–308, 319–326
linearization of converter power stage, 305–307
linearization of DC-link voltage control, 322–324
linearization of PLL, 320
single-loop DC-link current control, 342–343
of VSC, 307–308
of VSC with DC-link voltage control loop, 325–326
of VSC with PLL, 321–322

This book belongs to Kitab Liaison (ocd1996@gmail.com) Copyright Elsevier 2023

Small-signal stability analysis methods, 170–180
  case studies with practical examples, 183–191
  comparison of methods, 179–180
  Eigenvalue method, 174–177
  impedance-based method, 177–179
  power converter modeling, 172–174
Space Vector Fourier Transforms (SVFT), 284
Space vector modulation (SVM), 149–150, 368, 376, 387–394, 418
  interleaved, 387–389
  multilevel, 389–394
Stability analysis methods for power electronic–based power systems, 35, 171
  case studies with practical examples, 183–193
  large-signal stability analysis methods, 180–183
  small-signal stability analysis methods, 171–180
Standard P-PLLs, 287–288
STATCOM, 40–42
  passivity-based control design in, 67–70
State identification, 130–134
State space averaging approach (SSA approach), 172
State space model of power electronic systems, 36–42
  grid-connected voltage source inverter, 38–40
  STATCOM, 40–42
Stationary reference frame (SRF), 504
  frequency-locked loop, 505–506
  PI controller on, 506–507
  resonant controller in, 507
  SRF-PLL, 504–505
Steady-state performance, 48–49, 94
String inverters, 500
Super-twisting, 90–91
Supervisory control and data acquisition (SCADA), 199–200
Swing equation, 544
Symmetrical carrier interleaving, 419
Symmetrical grid fault control, 573–578, 587–593
  protection of DC-link capacitor through chopper control, 589–590
  verification of, 590–591
Symmetrically interleaved converters, 419–425
Synchronization, 269–270
Synchronous condenser (SC), 534
Synchronous gate–commutated thyristor (SGCT), 370
Synchronous generators (SG), 527, 541
Synchronous power controller (SPC), 516–518
Synchronous reference frame, control in, 239–242
Synchronous reference frame phase-locked loop (SRF-PLL), 271, 585–586
  characteristics, 274–275
  linearized models, 273
  open-loop and closed-loop transfer functions, 273–274
Synchronverter, 530
Synthesis circuit PLLs, 295
System identification, 128–134
  parameters identification, 129
  state identification, 130–134

T

Takagi–Sugeno multimodeling approach (TS multimodeling approach), 170–171, 181–182
Terminal sliding mode control (TSMC), 77–78, 87–89
Three level back-to-back power converter PMSG WTS (3L back-to-back power converter PMSG WTS), 119
Three-phase PLLs, 271–287. *See also* Single-phase PLLs
  complex coefficient filter–based PLLs, 280–282
  conventional synchronous reference frame PLL, 271–275
  delayed signal cancellation–based PLLs, 282–283
  moving average filter–based PLLs, 277
  multiple SRF filter–based PLLs, 283–284
  notch filter–based PLLs, 278
  performance comparison and recommendation, 285–287
  second-order generalized integrator–based PLL, 279–280
  sinusoidal signal integrator PLL, 278–279
Three-phase two-level VSC, 5–6
Three-phase UPS, 127–128
Threshold voltage, 651

This book belongs to Kitab Liaison (ocd1996@gmail.com) Copyright Elsevier 2023

Thyristor-based technology, 368–370
Time delay
effect, 355–357
reduction, 314
Time-domain simulations, 180
Total demand distortion (TDD), 155
Total harmonics distortion (THD), 42, 379
Total internal reflection, 652
Tracking controller, 44–45
Tracking error, 80, 466
dynamics, 140
Trailing-edge control principle, 659, 659f
Transfer delayed–based PLLs, 291–292
Transient stator flux, 561
Trapezoidal PWM (TPWM), 375
Tristimulus, 655
Twisting SMC, 89–90
Two-level power converter (2L power converter), 102
Two-step MPC, 135
Type III wind turbine control during grid faults, 568–582
control strategies during asymmetrical grid faults, 578–582
control strategies during symmetrical grid faults, 573–578
existing challenges during grid faults, 568–573
external challenge from grid codes, 572–573
internal challenge from DFIG configuration, 568–572
Type IV wind turbine control during grid faults, 582–602
asymmetrical grid fault control, 593–602
modeling and control of grid-side converter, 583–587
symmetrical grid fault control, 587–593

U

Unbalanced grid voltages, control under, 251–256
Unbalanced three-phase systems
generalized averaged model, 227–231
harmonic state space model, 232–236
modeling methods in, 226–236
simulation examples, 236–238
Uninterruptible power supply system (UPS system), 77, 126–127
model reference direct adaptive control of, 136–144
system dynamics on, 127–128

V

Variable structure control (VSC), 77
Verification, 177, 189–191
of asymmetrical fault control, 601–602
of symmetrical fault control, 590–591
Virtual impedance
analysis, 350–357
control, 514–516
loop, 549–550
Virtual inertia, 524, 541
concepts and fundamentals, 531–532
evolution of green energy transition, 525–529
virtual inertia-based control, 529–532
Virtual synchronous generator (VSG), 541–542
adaptive inertia for grid-connected VSGs, 549–552
VSG-based grid-supporting DERs, 542
VIrtual Synchronous MAchine (VISMA), 530
Virtual synchronous machine (VSM), 516, 530–531, 530f
implementation, 532–536
performance, 534
Voltage sags, 454, 471–472
Voltage source converters (VSCs), 4, 110–111, 199, 221, 303, 367, 403. *See also* Current source converters (CSCs)
alternative current control of VSCs with LCL filters, 238–256
current control, 304–318
passivity-based stability analysis, 309–313
robustness enhancement, 313–318
small-signal modeling, 305–308
dynamics and predictive model of VSC-based MG, 111–112
impedance-based stability analysis under weak grid conditions, 256–265
with LCL filters, 222–238
modeling methods in balanced three-phase systems, 222–226
modeling methods in unbalanced three-phase systems, 226–236
outer-loop control, 319–336
vulnerability analysis of cyber attacks on control of, 203–205
Voltage source inverters (VSIs), 77, 126–127
system dynamics of, 78–79
VSI-based system, 372–373

This book belongs to Kitab Liaison (ocd1996@gmail.com) Copyright Elsevier 2023

Voltage tracking error, 140
Voltage-controlled oscillator (VCO), 270
Voltage-modulated direct power control (VM-DPC), 42–44
Vulnerability analysis of cyber attacks on control of VSCs, 203–205
  assessment, 204–205
  cyber security, 203–204

W

Wake combination, 611
Wake effect, 611–612
Weak grids, 304, 548
Wide bandgap (WBG), 368
Wind farm
  active dispatch, 611–618
    noise impact reduction, 614–618
    single MPPT and global MPPT, 612–614
    wake effect, 611–612
  control
    comparison of strategies in, 619t–620t
    onshore *vs*. offshore, 610t
    wind farm active dispatch, 611–618
    wind farm layout optimization, 636–642
    wind farm reactive dispatch, 618–636
  layout optimization, 636–642
  reactive dispatch, 618–636
    levelized production cost minimization, 625–636
    loss minimization, 622–625
    regular method, 618–622
Wind power plants (WP plants), 499
Wind turbine (WT), 611–613
Wind turbine generators (WTGs), 501
Wind turbine systems (WTSs), 35, 115, 500–502, 561
  fundamental wind turbine configurations, 566–568
  grid code requirements on low-voltage ride-through, 562–566
  grid converter for, 501–502
  grid faults, 561–562
  type III wind turbine control during grid faults, 568–582
  type IV wind turbine control during grid faults, 582–602

Z

Zero vector dwell time control, 415–418
Zero-crossing detection-based PLL (ZCD-PLL), 284
Zero-phase-angle (ZPA), 676
Zero-voltage ride-through capability, 591–593
ZOH discretization–based predictive model, 111

This book belongs to Kitab Liaison (ocd1996@gmail.com)
Copyright Elsevier 2023

CONTROL OF POWER ELECTRONIC CONVERTERS AND SYSTEMS

VOLUME 3

EDITED BY FREDE BLAABJERG

Control of Power Electronic Converters and Systems, Volume 3, explores emerging topics in the control of power electronics and converters in applications, including the theory behind control, and the practical operation as well as modeling and control of basic power electronic system. This book introduces the most important controller design methods, including both analog and digital systems. This reference explains the dynamic characterization of terminal behavior for power converters, as well as preserving the stability and power quality of modern power systems. This is useful for engineers in emerging applications of power electronic converters and those combining control design methods into different applications in power electronics technology.

The book is addressing controller interactions—in light of increasing renewable energy integration and discussing related challenges with stability and power quality—which is becoming more frequent in power converters and passive components.

Technological advancements in power electronics enable new applications to emerge and also help in performance improvement in existing applications. These advancements largely rely on the control effectiveness; therefore, it is essential to apply the appropriate control scheme to the converter and to the system to obtain the desired performance as well as robustness to parameter variations.

In this context, this book focuses on applying innovative control techniques for power converters and drives so that the desired behavior can be achieved.

- Discusses different applications and their control in integrated renewable energy systems (wind, solar)
- Introduces the most important controller design methods, both in analog and digital
- Describes different important applications to be used in future industrial products
- Explains the dynamic characterization of terminal behavior for converters

Frede Blaabjerg was with ABB Scandia, Randers, Denmark, from 1987 to 1988. From 1988 to 1992, he was a PhD student with Aalborg University, Aalborg, Denmark. He became an Assistant Professor in 1992, Associate Professor in 1996, and Full Professor of power electronics and drives in 1998. His current research interests include power electronics and its applications such as in wind turbines, PV systems, reliability, harmonics, and adjustable speed drives. He has received 32 IEEE Prize Paper Awards, the IEEE PELS Distinguished Service Award in 2009, the IEEE William E. Newell Power Electronics Award 2014, the Villum Kann Rasmussen Research Award 2014, Global Energy Prize in 2019, and the 2020 IEEE Edison Medal. He has in the last 7 years according to Thomson Reuters been among the most 250 cited researchers in Engineering in the world.

ENGINEERING / ELECTRICAL POWER ENGINEERING

ISBN 978-0-12-819432-4

9 780128 194324

ELSEVIER

ACADEMIC PRESS
An imprint of Elsevier
elsevier.com/books-and-journals

This book belongs to Kitab Liaison (ocd1996@gmail.com)

Copyright Elsevier 2023